INTEGRITY-RELIABILITY-FAILURE

IN ENGINEERING, MATERIALS, MANUFACTURING AND BIOMECHANICS

Proceedings IRF2025
8th International Conference on on Integrity-Reliability-Failure
Porto 15-18 July 2025

Editors

J.F. Silva Gomes
Shaker A. Meguid

FEUP-2025

INTEGRITY-RELIABILITY-FAILURE

IN ENGINEERING, MATERIALS, MANUFACTURING AND BIOMECHANICS

Proceedings IRF2025: 8th International Conference on Integrity-Reliability-Failure, Porto 15-18 July 2025

INTEGRITY-RELIABILITY-FAILURE

IN ENGINEERING, MATERIALS, MANUFACTURING AND BIOMECHANICS

Proceedings IRF2025: 8th International Conference on Integrity-Reliability-Failure, Porto 15-18 July 2025

Editors

J.F. Silva Gomes
Shaker A. Meguid

FEUP

(2025)

Conference Co-Chairs

J.F. Silva Gomes (*U. Porto)*
Shaker A. Meguid (*U. Toronto*)

Organizing Committee

Carlos C. António, Catarina F. Castro, José M. Cirne
J. Reis Campos, Paulo G. Piloto, Teresa Morgado

International Scientific Committee

Alexopoulos, Niko (Greece)
António, Carlos C. (Portugal)
Bandeira, Cirlene (Brazil)
Camanho, Pedro (Portugal)
Castro, Catarina (Portugal)
Chen, Terry Y-F (Taiwan)
Chvojan, Jan (Czech Rep.)
Croccolo, Dario (Italy)
Egner, Halina (Poland)
Hongbing Lu (USA)
Hori, Muneo (Japan)
Huber, Johannes (Sweden)
Johansen, Nicolai (Denmark)
Kepka, Miloslav (Czech Rep)
Kim, Chang-wan (South Korea)
Kowalewski, Zbigniew (Poland)
Kuhn, Erik (Germany)
Meguid, Shaker A. (Canada)
Mileiko, Sergei T. (Russia)
Mond, Michael (Israel)
Mongrain, Rosaire (Canada)
Olmi, Giorgio (Italy)
Outeiro, José C.M. (USA)
Pieczyska, Elzbieta (Poland)
Pinto, Sónia (Portugal)
Schneider, Martin (Austria)
Senner, Veit (Germany)
Seruga, Domen (Slovenia)
Silva Gomes, J.F. (Portugal)
Silva, Arlindo (Singapore)
Sinha, Jyoyi (UK)
Skarka, Wojciech (Poland)
Sousa, Luisa C. (Portugal)
Sturm, Ralf (Germany)
Umehara, Noritsugu (Japan)
Van Hemelrijc, Danny (Belgium)
Varum, Humberto (Portugal)
Vaz, Mário A.P. (Portugal)
Ville, Fabrice (France)
Wang, Wei-Chung (Taiwan)
Yuan, Huang (China)
Zhang, Xiong (China)

Institutional Sponsors

FEUP (University of Porto, Portugal)
MADL (University of Toronto, Canada)
APAET (Society of Experimental Mechanics, Portugal)

Other Sponsors

EuraSEM - European Society for Experimental Mechanics
SPM - Sociedade Portuguesa de Materiais
SEM - American Society for Experimental Mechanics
JSME - Japanese Society of Mechanical Engineering
IMEKO - International Measurement Confederation
DYMAT - European Association for Dynamics of Materials
INEGI - Instituto de Ciência e Inovação em Engenharia Mecânica e Engenharia Industrial
ABREU - PCO Professional Congress Organizer
Materials - An Open Access Journal from MDPI
Applied Sciences - An Open Access Journal MDPI
Actuators - An Open Access Journal from MDPI
Aerospace - An Open Access Journal from MDPI
Drones - An Open Access Journal from MDPI
Sensors - An Open Access Journal from MDPI

Publisher

FEUP-Faculty of Engineering, University of Porto
Rua Dr Roberto Frias, 4200-465 Porto - Portugal
Tel: +351 225 081 400; Email: feup@fe.up.pt
URL: https://www.up.pt/feup/pt/

July, 2025

ISBN: 978-972-752-323-8 | DOI: https://doi.org/10.24840/978-972-752-323-8

All rights reserved. No part of this publication may be reproduced, stored in a retrieval system, or transmitted in any form or by any means, electronic, mechanical, optical, recording, or otherwise, without the prior written permission of the Editors.

Conference Secretariat

Maria João Coelho, Lurdes Catalino
With the support of
ABREU-PCO, Professional Congress Organizer (http://abreuevents.com/)
Mercatura Conference System (http://www.mercatura.pt)

Proceedings IRF2025: 8th International Conference on Integrity-Reliability-Failure
In Engineering, Materials, Manufacturing and Biomechanics. Porto 15-18 July 2025
DOI: https://doi.org/10.24840/978-972-752-323-8

PREFACE

IRF2025 is the eighth international gathering of a prestigious series of Integrity-Reliability-Failure conferences coordinated by the International Scientific Committee on Mechanics and Materials in Design. This series of conferences started in 1999 and they are wholly devoted to advances in assessing the integrity, reliability and failure of engineering systems, materials, manufacturing and biomechanics. IRF2025 is jointly sponsored by the University of Porto, the University of Toronto and the Portuguese Society of Experimental Mechanics. The conference attracted over 160 contributions, with 148 accepted submissions involving 454 authors from 27 different countries.

The conference themes, which address novel and advanced topics on Integrity, Reliability and Failure, focused on Theory, Experiments and Applications in Engineering, including Composite and Advanced Materials, Fatigue and Fracture Mechanics, Structural Dynamics, Mechanical Design and Prototyping, Civil Engineering Applications, Biomechanical Applications, Energy and Thermo-Fluid Systems, and Industrial Engineering, among other topics.

We believe that the meeting and these proceedings offered our delegates an excellent opportunity for the discussion and dissemination of their recent work in assessing the integrity, reliability and failure of engineering structures, components and systems. They fostered research that integrates mechanics and materials in the design process, and promoted exchange of ideas and international co-operation among scientists and engineers in this important field of engineering.

We are particularly indebted to the authors and special guests for their contributions. Each of the 138 approved papers offers an opportunity for thorough discussions with the authors and the scientific community. Particularly, we acknowledge the excellent contributions of the participants, their innovative ideas and research directions, the novel modelling and simulation techniques, and the invaluable critical comments. We also take this opportunity to thank the members of the International Scientific Committee and the reviewers for their time and helpful suggestions, the symposia organizers for their efforts and valuable contributions to the success of conference and this publication, and the local organizing committee for an absolutely superb organization of this "*virtual*" meeting. To all of them, we offer our deepest gratitude.

Porto/Portugal, July 2025

J.F. Silva Gomes and Shaker A. Meguid
(Conference Co-Chairs and Editors)

Proceedings IRF2025: 8th International Conference on Integrity-Reliability-Failure
In Engineering, Materials, Manufacturing and Biomechanics. Porto 15-18 July 2025
DOI: https://doi.org/10.24840/978-972-752-323-8

CONTENTS

INVITED KEYNOTE PAPERS 1

22140 THERMAL BARRIER COATINGS FOR GAS TURBINE ENGINES: STATUS AND PROSPECTS. Shaker A. Meguid. 3

22141 SEISMIC BEHAVIOUR OF CONCRETE BUILDINGS: FIELDS LESSONS, STANDARDS AND RESEARCH NEEDS. Humberto S.A. Varum. 5

CONFERENCE MAIN TOPICS (TRACKS) 7

TRACK-A: COMPOSITE AND ADVANCED MATERIALS 9

22181 PERFORMANCE ENHANCEMENT STRATEGY AND MICROSTRUCTURE-PROPERTIES OF A ROCK-BREAKING CUTTER RING STEEL USED IN TUNNEL BORING MACHINE. Jingbo Guo, Mengze Han. 11

22316 ANELASTIC DEFORMATIONS IN SiO2, NANOCOMPOSITES OF MULTIWALLED CARBON NANOTUBES AND POLYMERS. A.P. Onanko, L.V. Kuzmych, Y.A. Onanko, O.P. Dmytrenko, M.P. Kulish, T.M. Pinchuk-Rugal, A.G. Rugal, V.V. Kuryliuk, A.M. Kuryliuk, O.L. Pavlenko, T.O. Busko, A.M. Gaponov, S.A. Kuzmych, P.P. Il'in. 13

22378 CARBON TEXTILE REINFORCED MORTAR (CTRM) TO MASONRYBOND UNDER FATIGUE LOADING. Kuanysh Makashev, Savvas Triantafyllou, Georgia Thermou. 15

22387 THE INFLUENCE OF SELECTED PARAMETERS OF EXPLOSION WELDING ON THE PROPERTIES AND STRUCTURE OF ZIRCONIUM - CARBON STEEL BIMETALLIC SYSTEMS. Mariusz Prażmowski, Aleksander Karolczuk, Henryk Paul. 21

22395 EVALUATION OF THE EFFECT OF TI, SR AND MO ON THE SOLIDIFICATION CHARACTERISTICS OF ADC12 ALLOY BY COOLING CURVE THERMAL ANALYSIS. Xiangjie Wang. 23

22404 CONTROL OF THE COMPOSITION OF BIOCERAMICS - COMPOSITE STRUCTURAL ABUTMENTS - USED IN DENTISTRY. Cirlene F. Bandeira, Carla C.G. Nogueira, Renata M. Parreira, Sérgio R. Montoro, Izabel O. Mota. 25

22405 MECHANICAL EVALUATION OF LDPE BERTHOLLETIA EXCELSA BARK COMPOSITES. Izabel O. Mota, Jairo O. Silva, Alexandre A. Palmeira, Ana C.C. Pereira, Sérgio R. Montoro, Cirlene F. Bandeira. 27

22425 COAXIAL STRUCTURAL BATTERIES: A NEW APPROACH FOR THE NEXT GENERATION OF ENERGY STORAGE. Beatriz A. Maia, Maria H. Braga. 29

22433 STUDY ON THE MECHANICAL PROPERTIES AND DAMAGE MECHANISM OF C/C-SIC COMPOSITES FOR HIGH-SPEED TRAIN BRAKE DISCS. Xiangli Zeng, Wenjing Wang, Junsheng Qu, Ruiguo Yan, Yiming Shangguan. 31

22438 A PERSPECTIVE ON CATHODE MATERIALS FOR ELECTRICAL VEHICLE INDUSTRY. José M. Pinheiro, Beatriz Gomes, Maria H. Braga. 33

22450 ENHANCING SOLID-STATE STRUCTURAL BATTERY PERFORMANCE WITH NANOSTRUCTURED COPPER CURRENT COLLECTORS. Tomás Prior, Ângela Freitas, Beatriz Gomes, Beatriz Maia, Manuela Baptista, Hugo Lebre, Nuno Guerreiro, Joana Figueira, Joana V. Pinto, David Carvalho, Rodrigo Martins, M. Helena Braga. 35

22451 3D INCONEL 625 SODIUM ELECTROLYTE ENERGY STORAGE DEVICE. Antonio B. Vale, Manuela C. Baptista, Jose M. Costa, M. Helena Braga, Manuel F. Vieira. 37

22453 THERMAL CHARACTERIZATION OF PLA, ABS, PETG, AND NYLON FILAMENTS FOR 3D PRINTING APPLICATIONS. Alexandre M. Oliveira, Lindomar M. Gonçalves, Amir Z. Mesquita. 39

22461 LOCAL DEFORMATION AND FAILURE OF COMPOSITES DURING SELF-PIERCING RIVETING: A CT BASED MICROSTRUCTURE INVESTIGATION. Alrik Dargel, Johannes Gerritzen, Benjamin Gröger, Daniel Köhler, Malte Schlichter, Gerson Meschut, Maik Gude, Robert Kupfer. 41

22464 CURE PERCENTAGE DETERMINATION IN EPOXY RESIN/CARBON FIBER STRUCTURAL COMPOSITES. Cirlene F. Bandeira, André M. Santos, Onofre R. Lima Jr., Julia C. Landim, Michelle L. Costa, Edson C. Botelho, Sérgio R Montoro, Izabel O. Mota. 53

22568 GEOMECHANICAL BEHAVIOR OF OIL SHALES FROM ARARIPE BASIN, BRAZIL. José A. Soares, Anne B. Guedes Sobrinho, Juliana T. Batista. 55

22602 MULTI-MATERIALS COMPONENTS DEVELOPMENT FOR POWER APPLICATIONS BY DIRECTED ENERGY DEPOSITION. Ying Li, Jan Dzugan, Daniel Melzer, Michal Brazda, Anna Reis, Martina Koukolikova. 61

22616 PREDICTION OF INTERNAL DAMAGE IN GFRP LAMINATES CAUSED BY REPEATED LOW VELOCITY IMPACTS USING ARTIFICIAL INTELLIGENCE METHODS. Djalel Eddine Tria, Houssem Habbouche, Abdel Wahhab Lourari, Sid Ali Boukhaoua. 63

22632 FLAW DETECTION IN THERMOPLASTIC MATRIX CARBON FIBER REINFORCED COMPOSITE BY ULTRASOUND. João P. Learth, Camila A. Farias, Cesar G. Camerini, Celio A.C. Neto. 67

22641 THE POSSIBILITY OF INCREASING THE IMPACT RESISTANCE OF AN EPOXY RESIN-BASED MATRIX BY USING POWDER ADDITIVES. Pawel Przybylek, Joanna Masiewicz, Tomasz Zahorski, Robert Szczepaniak. 69

22643 THE INFLUENCE OF THE MOLD SIZE ON PROPERTIES OF GFRP MADE BY INFUSION METHOD. Jacek Janiszewski, Andrzej Komorek, Daniel Śliwiński. 71

22646 TENSILE STRENGTH OF A COMPOSITE WITH A POWDER AEROGEL EXPOSED TO A THERMAL FLOW. Robert Szczepaniak, Andrzej Komorek, Paweł Przebyłek, Mateusz Bak. 73

22838 A STRENGTH ASSESSMENT OF STRUCTURAL COMPOSITES WITH MODIFIED EPOXY MATRIX UNDER LOW-ENERGY STATIC AND DYNAMIC LOADS. Joanna Masiewicz, Pawel Przybylek, Robert Szczepaniak. 75

23459 MANUFACTURING MONITORING IN FULL-SCALE CFRP WING BY EMBEDDED FIBRE OPTIC DISTRIBUTED SENSORS. Lorenzo Pellone, Monica Ciminello, Gianvito Apuleo, David Bardenstein, Umberto Mercurio, Antonio Concilio. 77

23491 A MEMETIC ALGORITHM FOR THE MULTI-OBJECTIVE OPTIMIZATION OF GEOMETRICALLY NONLINEAR COMPOSITE STRUCTURES. Carlos C. António, Ricardo Oliveira de Faria. 81

TRACK-B: FATIGUE AND FRACTURE MECHANICS 83

22228 A STAGGERED GRID SHELL PARTICLE METHOD FOR SHELL STRUCTURAL DAMAGE SUBJECTED TO UNDERWATER EXPLOSION. Jiasheng Li, Xiong Zhang. 85

22243 FATIGUE LIFE UNDER CYCLIC BENDING CONDITIONS OF WELDED JOINTS MADE OF 6060 ALUMINUM ALLOY WITH VARIOUS WELDING TECHNOLOGIES. Sebastian Skrobacz, Joanna Małecka, Mariusz Prażmowski, Karolina Głowacka, Tadeusz Łagoda. 87

22252 FATIGUE BEHAVIOUR IN PRESENCE OF ELASTIC ANISOTROPY AND STRESS CONCENTRATION. Riccardo Nobile. 89

22255 FATIGUE RELIABILITY ANALYSIS OF GH4169 ALLOY UNDER THE COUPLING EFFECT OF TEMPERATURE AND STRESS. Lei Wang, Yang Liu, Hanzhong Deng, Xiu Song. 91

22261 DAMAGE MECHANISMS IN SHOT-PEENED 7010-T7451 ALUMINIUM ALLOYS UNDER CYCLIC LOADING. Maxime Tissot, Catherine Mabru, Michel Chaussumier, Martin Surand. 93

22274 CRACK PLANES AFTER IMPACT TREATMENT OF 6XXX ALUMINUM ALLOYS. Joanna Małecka, Marta Kurek, Aleksander Hebda, Sławomir Małys, Tadeusz Łagoda. 95

22317 ELASTIC, ANELASTIC DEFORMATIONS IN HYDRO TECHNICAL STRUCTURES CONCRETES, NANOCOMPOSITES OF MULTIWALLED CARBON NANOTUBES AND POLYMERS. A.P. Onanko, L.V. Kuzmych, Y.A. Onanko, O.P. Dmytrenko, M.P. Kulish, T.M. Pinchuk-Rugal, A.G. Rugal, V.V. Kuryliuk, A.M. Kuryliuk, L.I. Kurochka, S.A. Popov, S.V. Yehorov, S.A. Kuzmych, P.P. Il'in. 97

22374 EXPERIMENTAL INVESTIGATION ON THE MOTORCYCLE SWINGARM DEFORMABILITY AND STABILITY. Beatriz Almeida, António Leite, Sérgio Dias, Miguel Oliveira, Isidro Arce, Fábio Pereira. 99

22376 A MEAN LIFE BASED FATIGUE CRITERION AND PROBABILISTIC FATIGUE LIFE PREDICTION APPROACH. Liyang Xie. 101

22382 SURVIVAL ANALYSIS TECHNIQUES FOR PROBABILISTIC FATIGUE LIFE EVALUATION IN BRIDGES CONSIDERING LOADING SEQUENCE EFFECTS. Farhad Farajiani, Habib Tabatabai. 111

22403 FATIGUE CHARACTERIZATION OF L-PBF AlSi10Mg RELATED TO SAMPLE TOPOLOGY, LOAD TYPE AND PROCESS SETUP. Giorgio De Pasquale, Luca Margaria, Antonio Coluccia. 113

22406 MICROSTRUCTURAL EFFECTS ON STATIC AND CYCLIC CRACK GROWTH BEHAVIOR OF NODULAR CAST IRON EN-GJS-600-3. Sebastian Henschel, Sarah Hübner, Lutz Krüger. 115

22419 INDUCING COMPRESSIVE RESIDUAL STRESSES USING WATER JET PEENING FOR FATIGUE LIFE EXTENSION IN A STAINLESS STEEL. E.D. McMullan, A.H. Mahmoudi. 123

22426 OPTIMIZING THE FRACTURE TOUGHNESS OF POLYMER CONCRETE WITH VARIABLE MIXTURES BY TAGUCHI METHOD. Mohammad R.M. Aliha, Hossein Parsania, Tomasz Sadowski, Daniel Pietras, Rasoul Ghayomian, Somayeh Moshatghi, Camellia Rafiei. 125

22428 A COMPARATIVE CRACK GROWTH EVALUATION FOR REACTOR COMPONENTS. Heejun Yang, Hwan-Jae Joo, Yoon-Suk Chang. 127

22436 COMPARATIVE ANALYSIS OF EXPERIMENTAL AND NUMERICAL DURABILITY IN BUS STRUCTURES USING FREQUENCY Domain Methods. Gabriel R.P. Reis, Rogério J. Marczak. 129

22439 APPLICATION OF MACHINE LEARNING FOR PREDICTING AND OPTIMIZING FRACTURE ENERGY IN ASPHALTIC MIXTURES AT INTERMEDIATE TEMPERATURES. Mohammad R.M Aliha, Hossein Parsania, Daniel Pietras, Tomasz Sadowski, A. Rajabi-Kafshgar, A. Mousavi, S. Momenian, Javad Hosseinzadeh. 131

22445 PLASMA INDUCED HYDROPHILIC MODIFICATION ON ELECTROPLATED SILVER SURFACE IMPROVING SILVER SINTER QUALITY FOR POWER SEMICONDUCTOR DIE ATTACH. Min-Su Kim, Minju Yu. 133

22593 AN ANALYTICAL CORRELATION TO OPTIMIZE THE RESULTS OF FLATTENED BRAZILIAN TEST. R. Gutiérrez-Moizant, D.J. Guerrero-Miguel, M. Ramírez-Berasategui. 135

22597 POST-FATIGUE TENSILE BEHAVIOR OF SINGLE LAP JOINTS WITH GRAPHENE NANO PARTICLE REINFORCED ADHESIVE. Güntaç Bali, Tolga Topkaya. 141

22645 A COMBINED FATIGUE INDICATOR PARAMETER (FIP) FOR PREDICTING MICROCRACK PROPAGATION PATH IN POLYCRYSTALLINE NICKEL. Arash Valiollahi, Haiying Huang. 143

22657 DEVELOPMENT OF 16MnCr5 CD STEEL NEW FATIGUE LIMIT PREDICT MODEL. Teresa Morgado, Tiago Bancaleiro, José Simões, Mário Pereira, Alexandre Velhinho, Suzana Lampreia. 145

22658 DURABILITY STUDY OF ST-52 AND R304 SUBJECT TO CORROSION ENVIRONMENT AND FATIGUE LOADS. Teresa Morgado, Pedro Amaral, José Simões, Mário Pereira, Suzana Lampreia. 147

22714 STUDY ON THE INFLUENCE OF RANDOM VIBRATION LOADING UNSTEADY STATE ON DAMAGE ESTIMATION. Roger Serra, Yuzhu Wang. 149

23480 UNCERTAINTIES IN LOW-CYCLE FATIGUE OF COILED-TUBING. Silvia Corbani, Emmanuel A.A.M. Costa, Lucas S.K. Camp, Daniel A. Castello, Thiago G. Ritto. 151

TRACK-C: STRUCTURAL DYNAMICS 153

22233 INVESTIGATION OF A METALLIC SANDWICH DESIGN WITH THERMOPLASTIC CORE FOR IMPROVED PEDESTRIAN PROTECTION. Ralf Sturm. 155

22294 STUDY ON TEMPORAL CHANGES IN WHEEL LOAD AND ROLLING RESISTANCE OF AIRLESS TIRE DURING ROLLING MOTION. Katsuhide Fujita, Takuma Suzuki, Toshihiko Okano, Kensuke Sasaki. 157

22303 THE EFFECT OF CUMULATIVE POST-SEISMIC DEFORMATIONS ON THE CAPACITY OF BOLTED T-STUB CONNECTIONS UNDER MONOTONIC LOADING. Florea Dinu, Calin Neagu, Denis Ivascu, Paul Zdrenghea, Andreea Constantinescu, Mihai Senila. 159

22306 HELICOPTER VIBRATION MONITORING USING REGULAR NEURAL NETWORKS. Diego M.G. Pereira, Helio A. Pegado. 169

22397 NUMERICAL SIMULATION AND OPTIMIZATION OF BALLISTIC PROTECTION STRUCTURES. Giovanni Garofalo, Patrice Longère, Kamel Moussaoui. 179

22412 REPEATED DYNAMIC TESTS AND NUMERICAL ANALYSES OF MULTI-SPAN OLD REINFORCED CONCRETE BRIDGE. Michal Venglar, Milan Sokol, Katarina Lamperova, Martin Marton. 181

22435 TRANSPORTATION OF SMALL PARTS ON A PLATFORM EXCITED IN TWO PERPENDICULAR HORIZONTAL DIRECTIONS BY SINUSOIDAL VAWES WITH A PHASE SHIFT. Kristina Liutkauskiene, Ramunas Cesnavicius, Sigitas Kilikevicius. 187

22459 DESIGN, SIMULATION AND EXPERIMENTAL VERIFICATION OF A DYNAMIC INERTIAL TABLE. Jocinaldo A.P. Silva, Antônio A. Silva, Márcio D. Silva. 191

22467 COST-EFFICIENT SEISMIC RETROFIT OF HIGH-VOLTAGE CURRENT TRANSFORMERS USING SEISMIC DAMPERS. Mohammad Ali Jafari, Arash Y. Fallah, Alireza Rahnavard, Amir H. Khalvati. 193

22480 NUMERICAL AND EXPERIMENTAL MODAL ANALYSIS OF A SMALL-SCALE WIND TURBINE BLADE. Vanessa N.P. Moura, Antônio A Silva, Andersson G. Oliveira, Rômulo P.B. Reis. 195

TRACK-D: MECHANICAL DESIGN AND PROTOTYPING 199

22254 PREDICTION OF CENTRAL BURSTING IN AXISYMMETRIC EXTRUSION PROCESS THROUGH DIES OF ARBITRARY SHAPE. Amir Parghazeh, Yaser Khaledi, Soroush Khaledi. 201

22358 APPLICATION GENERATIVE DESIGN TO A MOUNTAIN BIKE FRAME WITH CONSIDERATION OF THE STRUCTURAL WEIGHT REDUCTION. L.J Juiña, D. Rubio, A. Villalba, V.H. Cabrera-Moreta. 205

22375 TEMPERATURE-DEPENDENT EXPERIMENTAL CHARACTERIZATION OF A STRETCHABLE STRAIN SENSOR. Beatriz Almeida, José R. Fernandes, Miguel Oliveira, Raul Morais, Fábio Pereira. 213

22408 MATHEMATICAL MODEL FOR KINEMATICS OF A KNUCKLE JOINT PRESS. Luísa R. Madureira, Francisco Q. Melo. 215

22418 DESIGN OPTIMIZATION USING MULTI-PHYSICS MODELLING FOR UNMANNED AERIAL VEHICLES. Arun W. Amaladoss, Wojciech Skarka, Jacek Rduch. 221

22421 TOWARDS HUMAN TRUST IN ARTIFICIAL INTELLIGENCE: AN EXPERIMENT THROUGH AUTONOMOUS VEHICLE. Peer M. Sathikh, Zong R.D. Fang. 231

22423 MECHANICAL DESIGN OF A PROTOTYPE OF ROBOT FOR NON-DESTRUCTIVE INSPECTION OF CORROSION IN NUCLEAR SPENT FUEL SEALED CONTAINERS. David A. Rio, Pablo Garcia-Gil, Irea Lopez Garcia, Marcos Lopez Lago, Miguel Miguez Coto, Enrique Casarejos. 233

22458 THE ROLE OF PLASTIC STRAIN DISTRIBUTION ON MICROSTRUCTURAL EVOLUTION IN BAINITIC STEEL DURING THERMOMECHANICAL CONTROL PROCESSING. M. Karam-Abian, P. Parandavar, M. Tong, S.B. Leen. 235

22490 RESEARCH ON THE TRIBOLOGICAL FAILURE OF MECHANICAL COMPONENTS INDUCED BY ENVIRONMENTAL NANOPARTICLES UNDER HUMID CONDITIONS. Jim C. Yeh, Shin Y. Chern, Sheng J. Liao, Wei L. Liu, Jeng-Haur Horng. 237

22635 SIMULATION-BASED STRUCTURAL DESIGN AND RELIABILITY EVALUATION OF AN INDICATOR SPRING. Domen Seruga, Lovro Novak, Marko Nagode, Jernej Klemenc. 239

22797 ReDesignFX NOVEL METHODOLOGY: APPLICATION IN PRODUCT (RE)DESIGN-FOR-REMANUFACTURING. António J. Baptista, João N. Ruivo, Gabriele Marchello, Farshad N. Heravi. 243

TRACK-E: CIVIL ENGINEERING APPLICATIONS 257

22234 CUTTING-EDGE GROUND PENETRATING RADAR FOR HIGH- PRCEISION IDENTIFICATION OF BARS IN CONCRETE SLABS. Wael Zatar, Hien Nghiem. 259

22235 POST-TENSIONED RODS OF AGING WATER NAVIGATION STRUCTURES: A NOVEL EVALUATION STRATEGY FOR ENHANCED SAFETY AND INTEGRITY. Wael Zatar, Hien Nghiem. 267

22258 STRUCTURAL DAMAGE ALERT THROUGH ARTIFICIAL NEURAL NETWORKS. Danilo S. Nunes, José Luis V. Brito, Graciela N. Doz. 275

22290 DAMAGE DETECTION IN BRIDGES USING COMBINED MODAL STRAIN ENERGY AND SPECTRAL FINITE ELEMENT METHODS. Mohammad Vahidi, Gholamreza Ghodrati Amiri. 277

22377 DAMAGE STATE PREDICTION OF RC BRIDGES SUBJECTED TO PIER SCOURING AND EARTHQUAKES. Aref Jozi, Ali R.M. Hosseini, Mehran S. Razzaghi. 279

22388 PUR SANDWICH PANELS SUBJECTED TO BLASTS AT SHORT STANDOFF DISTANCES. Florea Dinu, Calin Neagu, Andreea Oneea, Paul Zdrenghea, Mihai Senila, Robert Laszlo, Emilian Ghicioi. 281

22394 PRELIMINARY SCENARIO OF EXPECTED EARTHQUAKE DAMAGE IN THE BUILDING STOCK OF SÃO MIGUEL, AZORES. Maria João Barros, Margarida Machado Pires. 283

22402 EFFECT OF SUSTAINABLE GRAPHENE DERIVATIVE ON 3D PRINTING OF CEMENTITIOUS MATERIALS. Mohd M. Ali, Rashid K. Abu Al-Rub, Fawzi Banat, Tae-Yeon Kim. 293

22414 THERMAL AND MECHANICAL RESISTANCE OF WOOD CONNECTIONS IN SINGLE SHEAR, WITH AND WITHOUT PROTECTION. João C. Aguiar, Elza M.M. Fonseca. 295

22415 PROGRESSIVE COLLAPSE OF THE SURFSIDE CONDOMINIUM POOL DECK. Mehrdad Sasani. 303

22416 EVALUATION OF CONTACT AREAS FOR EACH CONSTITUENT MATERIAL USING X-RAY CT IMAGE ANALYSIS. Kosei Shibahara, Kotaro Sasai, Kiyoyuki Kaito. 305

22420 FWI IMAGING OF FAULTS AND FRACTURES IN ROCKS. Paula R.L. Andrade, José S. Agnelo, Carlos A. Mendonça, Carlos M. Chaves, Andre L.F. Silva. 307

22422 ESTABLISHMENT OF A LOAD CARRYING CAPACITY FORMULA FOR REINFORCING FOUNDATIONS OF POWER TRANSMISSION TOWERS. Nanaka Sakamura, Tomonori Murakami, Manabu Matsushima, Hidenori Yoshida. 317

22427 IMPORTANCE OF FAILURE MODES IN THE ROBUSTNESS OF 4 BOLT-PER-ROW END-PLATE STEEL CONNECTIONS. Daniel L. Nunes, Adrian L. Ciutina. 331

22429 WONDERING ABOUT FIRE RESISTANCE OF TRADITIONAL PORTUGUESE CONSTRUCTION. João Rodrigues, Daniela Miranda, Naim Sedira, Cristina Reis, Sandra Cunha, Jorge Pinto. 333

22434 DETERMINATION OF THE AERODYNAMIC FORCE DISTURBANCE INDEX FOR ANALYSIS OF NEIGHBORHOOD EFFECTS IN TALL BUILDINGS SUBJECTED TO WIND. Gabriela Villoslada, Thiarly F.A. Lavôr, José L.V. Brito, João C. Pantoja. 335

22441 NUMERICAL SIMULATION OF THE FIRE PROTECTION EFFECT AND LOAD LEVEL ON GLT TIMBER COLUMNS. Paulo A.G. Piloto, Manuel D. Lorenzo, Ana B. Ramos Gavilán, Javier Sánchez-Haro. 337

22443 COHESIVE ZONE MODEL STRATEGY IN FINITE ELEMENTS SIMULATION OF MECHANICAL BEHAVIOR OF REINFORCED CONCRETE CORBEL STRENGTHENED BY CFRP. Veselin Stankov, Dimitar Dontchev, Ivelina Ivanova, Jules Assih. 339

22446 SENSITIVITY ANALYSIS OF A RAILWAY TEMPERATURE PREDICTION MODEL. Ary V.N. Frigeri, Rubia M. Bosse, Paulo A.G Piloto, Manuel Minhoto. 351

22449 STRUCTURAL REHABILITATION: SOLAR DA BARONESA, SÃO JOÃO DEL REI - MG. Luciana B. Coimbra, Paloma S. Silva. 353

22465 NUMERICAL AND EXPERIMENTAL INVESTIGATION OF REINFORCED CONCRETE BEAM STRENGTHENED WITH NATURAL FABRICS. Veselin Stankov, Dimitar Dontchev, Ivelina Ivanova, Jules Assih. 355

22572 CONTRIBUTION TO THE STUDY OF THE INFLUENCE OF DATE PALM FIBERS ON THE CREEP AND RUTTING OF BITUMINOUS MIXTURES. Ferkous S. Abdelhakim, Ramdane Kahlouche. 359

22577 NUMERICAL ANALYSIS OF THE SHORT-TERM BEHAVIOR OF A SEMI-INTEGRAL ABUTMENT UNDER CYCLIC LATERAL LOADING. Pedro H.S. Silva, Yuri D.J. Costa, Carina M.L. Costa, Jorge G. Zornberg. 373

22603 NUMERICAL ASSESSMENT OF PROGRESSIVE COLLAPSE IN REINFORCED CONCRETE FRAMES WITH MASONRY INFILL. Jessenia G. Peñaloza Morán, Ingrid Xavier de Oliveira, Fábio Fleming Leitão, Nathan Shauer, Hugo L. Oliveira, Gustavo H. Siqueira. 375

TRACK-F: BIOMECHANICAL APPLICATIONS 385

22237 FAILURE OF AN AUTO-BELAY DEVICE. David Eager. 387

22417 THERMOMECHANICAL SIMULATION MODELS FOR EVALUATING THERMAL RISKS IN BONE DRILLING FOR DENTAL IMPLANTS. Irea López García, David Agudo del Río, Jose A. López Campos, Jose R. Fernández García, Jacobo González Baldonedo, Miguel Miguez Coto, Sofía Suárez García, Mercedes Gallas-Torreira. 389

22447 PVA-BG58S-CL-BASED BARRIER MEMBRANES FOR GUIDED TISSUE/BONE REGENERATION THERAPY. Isabela S. Gonçalves, Vitor G.P. Lima, Tiago B.M. Campos, Marcos Jacobovitz, Paulo H.S. Carvalho, Luana R.M. Vasconcellos, Ivone R. Oliveira. 391

22448 SILK FIBROIN-PVP-NPG-BASED BARRIER MEMBRANES FOR TISSUE REGENERATION THERAPY. Ivone R. Oliveira, Isabela S. Gonçalves, Tiago M.B. Campos, Leandro J. Raniero, Luana M.R. Vasconcellos, Fernando. S. Ortega, João H. Lopes. 393

22454 MECHANICAL ANALYSIS OF THE KNEE OF A BIPED ROBOT. Gerardo G. Liñán, Sergio S. Segura, Juan C.B. Morales, Pedro J.C. Zugasti, Ludy M.V. Martínez, Juan G.S. Granja, Juana E.R. Hernández. 395

22457 INVESTIGATING THE DISTAL CONNECTION STRENGTH OF A FUSED FILAMENT FABRICATED PROSTHETIC SOCKET. Clara Phillips, Aaryan Nagpal, Mark Kortschot, Fae Azhari. 401

TRACK-G: ENERGY AND THEMO-FLUID SYSTEMS 403

22558 THE FLUID-STRUCTURE ANALYSIS OF VACUUM PUMPS IN SEMICONDUCTOR FABRICATION FACILITY FOR IDENTIFYING THE STRUCTURAL DAMAGE AND CRACK. Chan Lee. 405

22600 TECHNICAL-ECONOMIC ASSESSMENT OF ETHANOL CONVERSION TO JET FUEL PRODUCTION CONSIDERING CADO TECHNOLOGY. York C. Santiago, Rafael M. de Almeida, Leandro Novaes, Jeiveison G.S. Maia, Stefano F. Interlenghi. 407

22642 A DELAYED ACCEPTANCE APPROACH WITH MARKOV CHAIN MONTE CARLO METHOD TO CONTACT FAILURES IDENTIFICATION IN MULTILAYERED COMPOSITES MEDIUM. Luiz A.S. Abreu, Helcio R.B. Orlande. 417

23498 AN EXPERIMENTAL METHOD TO MEASURE BICYCLE TIRES ROLLING RESISTANCE AT THE SANGALHOS VELODROME. Pedro F.V. Carvalheira, Octávio N.C.F. Cardoso. 419

23499 AN EXPERIMENTAL METHOD TO MEASURE BICYCLE TIRES ROLLING RESISTANCE AT A ROAD ROUNDABOUT. Pedro F.V. Carvalheira, Octávio N.C.F. Cardoso. 421

23512 HIERARCHICAL CARBON NANOTUBE ARCHITECTURES FOR EFFICIENT INTER-FACIAL SOLAR-DRIVEN WATER EVAPORATION. Yongyi Zhang. 423

TRACK-H: INDUSTRIAL ENGINEERING 425

22173 NEW DESIGN FOR SEMI-INDUSTRIAL 6-APA PRODUCTION: TECHNICAL AND ECONOMIC REVIEW. Akbar Esmaeili. 427

22188 SOME OF THE GOVERNING PARAMETERS OF THE MACHINE SETTINGS DURING THE MANUFACTURING PROCESSES OF MASS PRODUCTION IN METALWORKING INDUSTRIES. Jayanta Banerjee, Julián Rivera-Rodríguez, Luis Cruz-Zapata. 429

22398 STRUCTURE FORMATION IN LUBRICATING GREASES AS A RESULT OF APPLIED FRICTIONAL STRESS. Erik Kuhn. 431

22409 SmartMTQM - SIMPLIFICATION OF THE MTQM METHOD FOR APPLICABILITY IN SMEs. Christian Kern, Robert Refflinghaus, Jochen Deuse, David Lenze. 433

22432 COMPUTATIONAL MATHEMATICAL MODELING OF AIRFLOW IN A CABIN-TYPE SOLAR DRYER USED FOR DRYING SUGAR CANE BAGASSE. Lindomar M. Gonlçalves, Alexandre M. Oliveira, Amir Z. Mesquita, Daniel J.O. Ferreira, Hugo C.C. Michel. 435

22440 ENHANCING MULTI-MATERIAL RECYCLING IN THE AUTOMOTIVE INDUSTRY: A STUDY ON CRYOGENIC TREATMENT FOR IMPROVED MATERIAL SEGREGATION. Romeu Matos, Ivan Pereira, F. Bruna Oliveira, Flávia Barbosa, Vitor Paulo, Maria Fernandes. 445

22466 DEVELOPMENT OF WOK SEVERITY INDEX FOR BAKERY OPERATIONS. Olasunkanmi S. Ismaila, Desmond A. Oladeji. 451

22571 RELIABILITY ESTIMATION IN INDUSTRIAL SYSTEMS: A PROBABILITY-BASED APPROACH TO FAILURE PREDICTION. Daniel Sanin-Villa, Juan C. Tejada, Adrian F. Martinez. 455

SPECIAL SESSIONS (SYMPOSIA) 457

SYMP-1: EXPERIMENTAL MECHANICS AND INSTRUMENTATION 459

22146 OPTICAL TECHNIQUES IN EXPERIMENTAL MECHANICS: A STATE-OF-THE-ART OVERVIEW. J.F. Silva Gomes. 461

22178 DETERMINE WATER VELOCITY IN CHECK VALVES WITH DIFFERENT GEOMETRY IN MICROCHANNELS MANUFACTURED BY 3D PRINTING (SLA). Richard Chamorro, Victor H. Cabrera-Moreta. 463

22384 ULTRA-SENSITIVE MICROCRACK-BASED STRAIN SENSORS FOR REAL-TIME STRUCTURAL INTEGRITY MONITORING. Jae-Hwan Lee, Seung-Kyun Kang. 477

22389 LABORATORY INVESTIGATION OF MECHANICAL PROPERTIES ON HALF-SCALLED GLASS FIBRE REINFORCED PLASTIC BOGIE FOR THE FREIGHT WAGONS. Jan Chvojan, Roman Jozefy. 479

22413 IN-LINE ALTERNATIVE FOR NON-DESTRUCTIVE TESTING IN WIRE ARC ADDITIVE MANUFACTURING BASED ON ELECTROMAGNETIC EMISSIONS. Douglas S.M. Serrati, João P.S. Oliveira, Telmo G. Santos. 481

22424 COMPARISON OF X-RAY AND TERAHERTZ METHODS IN NON-DESTRUCTIVE TESTING OF PYROTECHNIC OBJECTS. Waldemar Swiderski, Tomasz Krzeminski. 483

22437 RELIABLE CONTINUOUS FORCE MEASUREMENT AT AMBIENT AND ELEVATED TEMPERATURES WITH STRAIN GAUGES USING THE EXAMPLE OF BOLTED JOINTS. Tobias Held, Jens Peth, Christoph Friedrich. 485

22634 EFFECT OF CARBON /ARAMID FIBER REINFORCEMENT ON THE IMPACT TOLERANCE OF LAMINATES. Przybylek Pawel, Andrzej Komorek, Robert Szczepaniak, Tomasz Zahorski. 499

22644 CORRELATING FLEXURAL ULTRASOUND ATTENUATION PARAMETER TO SENSITIZATION BASED ON FABRY-PEROT RESONATOR PRINCIPLE. Songwei Wang, Haiying Huang. 501

SYMP-3: DIGITAL MANUFACTURING 503

22462 EXPERIMENTAL EVALUATION AND NUMERICAL SIMULATION OF HIGH-SPEED MILLING OF INCONEL 718 USING CERAMIC TOOLS. Marcos V. Ribeiro, Necati Uçak, Ahmed Razin, Jose Outeiro. 505

22463 DEVELOPMENT OF A DIGITAL TWIN OF AN INTELLIGENT ROBOT-ASSISTED FINISHING SYSTEM FOR POLISHING METAL ADDITIVE MANUFACTURED COMPONENTS. Jose Outeiro, Tero Kaarlela, Necati Ucak, Noel Greis, Harish Cherukuri. 507

22578 MEMETIC-BASED BIOGEOGRAPHY HYBRID ALGORITHM FOR OPTIMIZATION OF MECHANICAL SYSTEMS. Arcílio C.F. Peixoto, Carlos C. António. 509

22723 DYNAMIC TRACKING WITH INTELLIGENT COLLISION AVOIDANCE BASED ON OCTREE STRUCTURE FROM POINT CLOUD FOR AUTOMATIC COLLABORATION. Wen-Yang Chang. 515

22783 INTEGRATED TWIN-TRANSITION MATURITY MODEL: APPLICATION TO A MECHATRONIC SME. João N. Ruivo, AntónioJ. Baptista, Américo L. Azevedo. 521

SYMP-5: COMPUTER METHODS, ARTIFICIAL INTELLIGENCE AND EXPERIMENTS IN BIOMEDICINE 533

22471 NUMERICAL MODELING OF RED BLOOD CELLS INTERACTIONS WITH VISCOELASTIC MEMBRANES. Rosaire Mongrain, Hristo Valtchanov, Renzo Cecere. 535

22580 COMPUTED FFR USING WINDKESSEL AND VISCOELASTIC MODELS - VALIDATION WITH LEFT CORONARY PATIENT CASES. Maria Fernandes, Luísa C. Sousa, Marco P.L. Parente, Samuel Silva, Sónia I.S. Pinto. 537

22581 ANALYSIS OF HYPEREMIC STATE GENERATED IN PATIENT-SPECIFIC RIGHT CORONARY ARTERIES USING CURRENT OR AUTOMATIC IN-HOUSE SOFTWARE. Francisco P. Oliveira, Gonçalo Rodrigues, Luísa C. Sousa, João Festas, Sónia I.S. Pinto. 545

22583 SEMI-AUTOMATIC CONSTRUCTION OF 3D CORONARY GEOMETRIES IN HYPEREMIA CONDITIONS FOR FFR ACHIEVEMENT - DEVELOPMENT OF A PYTHON SOFTWARE. C. Rodrigues, M. Fernandes, L.C. Sousa, J. Festas, Sónia.I.S. Pinto. 555

22584 EQUIPMENT AND ADVANCES FOR MEASURING FATIGUE IN OFFICE SETTINGS: A SYSTEMATIC REVIEW ABSTRACT. Seyed I. Pezeshki, Joana Guedes, Joao S. Baptista. 559

22640 PRINCIPAL COMPONENT ANALYSIS AND HIDDEN MARKOV MODELS OF ELECTRICAL SUBMERSIBLE PUMPS DATA TO FAILURE DETECTION. Paulo Y. Kuga, Alberto L. Serpa. 563

22648 ALIGNING CORONARY AND VENTRICULAR SEGMENTATIONS FOR AN INTEGRATED ASSESSEMENT OF CARDIAC FUNCTION. J. Festas, A.F.A. Senra, Luisa C. Sousa, Sónia I.S. Pinto. 565

SYMP-6: INNOVATIVE ENGINEERING EDUCATION: FROM LESSONS TO EMERGING PRACTICES 573

22472 IMPLEMENTATION OF DESIGN ACTIVITIES FOR CAPSTONE ENGINEERING TEAMS FOR COMMUNICATION SKILLS. Rosaire Mongrain, Mark Driscoll. 575

22592 SUCCESS LEVEL OF MECHANICAL ENGINEERING STUDENTS OF THE ENGINEERING FACULTY OF UNIVERSITY OF PORTO IN MATHEMATICAL ANALYSIS III COURSE UNIT FROM 2017 TO 2023. Sónia I.S. Pinto, Luísa Madureira, Susan M. Zvacek. 577

22620 ENHANCING MECHANICAL ENGINEERING EDUCATION: HANDS-ON MACHINING PROJECTS FOR SKILL DEVELOPMENT. Abílio M.P. Jesus, Rúben D.F.S. Costa, Vítor F.C. Sousa, Tiago E.F. Silva. 581

22637 DISCUSSING INTERNATIONAL STUDENT MOBILITY IN AND OUT OF PORTUGAL. Catarina F. Castro. 591

23600 ENHANCING ENGAGEMENT IN COMPUTATIONAL FLUID MECHANICS: A REVIEW ON THE USE OF INTERACTIVE VIDEOS AND IN-CLASS QUIZZES IN HIGHER EDUCATION. S.I.S. Pinto. 593

SYMP-7: CONDITION-BASED MAINTENENCE: RELIABILITY, PROACTIVITY AND PRACTICE 595

22460 FAILURE MODES, EFFECTS, MECHANISM AND CRITICALITY ANALYSIS (FMMECA) OF THE INTERVAL CONTROL VALVE (ICV). Iara Tammela, Rodolfo Cardoso, Igor S. Pinto, Luiz A.O. Chaves, Mateus C. Amaral, Nelson V.C. Silva. 597

22468 MAIS METHOD FOR GULLY'S RISK ANALYSIS. Ana L.A. Oliveira, Nathaly N. Sarasty, João C. Pantoja. 599

22519 DATA-DRIVEN POST-EARTHQUAKE REPAIRABILITY ASSESSMENT OF CORRODED RC BRIDGE PIERS. Melina Sadeghi, Pooria P. Anzabi, Mahmoudreza Shiravand. 609

22598 DETERMINATION OF ACOUSTOELASTIC COEFFICIENTS FOR STRESS ESTIMATION OF A CONCRETE ELEMENT SUBJECTED TO FLEXURAL LOADING. Aayush Joshi, Kranti Jain, Ajay Chourasia. 611

22633 ADOPTION OF INDUSTRY 4.0 TECHNOLOGIES FOR PRODUCTIVITY IMPROVEMENT IN MANUFACTURING SYSTEMS - A REVIEW. Mohammed I. Quraishi, Prashant M. Ambad. 613

AUTHOR INDEX 615

LIST OF TOPICS AND SYMPOSIA

LIST OF MAIN TOPICS

TOPIC – A: COMPOSITE AND NEW MATERIALS ……..... 9

TOPIC – B: FATIGUE AND FRACTURA MECHANICS ……..... 83

TOPIC – C: STRUCTURAL DYNAMICS ……..... 153

TOPIC – D: MECHANICAL DESIGN AND PTOTOTYPING ……..... 199

TOPIC – E: CIVIL ENGINEERING APPLICATIONS ……. 257

TOPIC – F: BIOMECHANICAL APLICATIONS …… 385

TOPIC – G: ENERGY AND THERMO-FLUID SYSTEMS ……. 403

TOPIC – H: INDUSTRIAL ENGINEERING ……. 425

LIST OF SYMPOSIA

SYMP – 1: EXPERIMENTAL MECHANICS AND INSTRUMENTATION. Promoted by J.F. Silva Gomes (FEUP, U.Porto, Portugal). 459

SYMP – 3: DIGITAL MANUFACTURING. Promoted by J.C. Outeiro and H.P. Cherukuri (DMEES, University of North Carolina at Charlotte, U.S.A.). 503

SYMP – 5: COMPUTER METHODS, ARTIFICIAL INTELLIGENCE AND EXPE-RIMENTS IN BIOMEDICINE. Promoted by S.I.S. Pinto and L.C. Sousa (FEUP/INEGI, Portugal). 533

SYMP – 6: INNOVATIVE ENGINEERING EDUCATION: FROM LESSONS TO EMERGING PRACTICES. Promoted by S.I.S. Pinto (FEUP/INEGI, Portugal) and Rosaire Mongrain (McGill University,Canada). 573

SYMP – 7: CONDITION-BASED MAINTENENCE: RELIABILITY, PROACTI-VITY AND PRACTICE. Promoted by Suzana Lampreia (Portuguese Naval Academy, Portugal), T.L. Morgado (Polytechnic University of Lisbon, Portugal) and A.M. Pereira (Polytechnic University of Leiria, Portugal). 595

KEYNOTE PAPERS

Proceedings IRF2025: 8th International Conference on Integrity-Reliability-Failure
In Engineering, Materials, Manufacturing and Biomechanics. Porto 15-18 July 2025
DOI: https://doi.org/10.24840/978-972-752-323-8

PAPER REF: 22140

THERMAL BARRIER COATINGS FOR GAS TURBINE ENGINES: STATUS AND PROSPECTS

Shaker A. Meguid(*)
Mechanics and Aerospace Design Laboratory (MADL),
University of Toronto, Toronton, Canada
(*)*Email:* meguid@mie.utoronto.ca

ABSTRACT

Thermal barrier coatings (TBCs) were adopted in gas turbine engines (GTEs) since the 1950s for high temperature components, such as combustors, high pressure turbine and nozzle (Figure 1). The use of TBC, along with the advancement in GTEs air-cooling techniques, had enabled higher operating temperature and improved engine thermodynamics efficiency. Alumina and zirconia-calcia are some examples of the early ceramic materials used in GTEs. These early coating materials have been replaced by highly advanced material systems that consist of four layers: substrate, bond coat, thermally grown oxide and a ceramic top coat, as depicted in Figure 2. They are designed to protect high temperature components in GTEs against corrosion, erosion and creep, thus leading to improved engine efficiency and durability. In this keynote lecture, Meguid will review the structure, material properties, inelastic thermo-mechanical behavior of coating, and the resulting failure mechanisms as well as outline future directions of TBCs and summarize current TBC research activities in his laboratory.

Keywords: Thermal Barrier Coatings, Gas Turbine Engines, Modeling & Characterization.

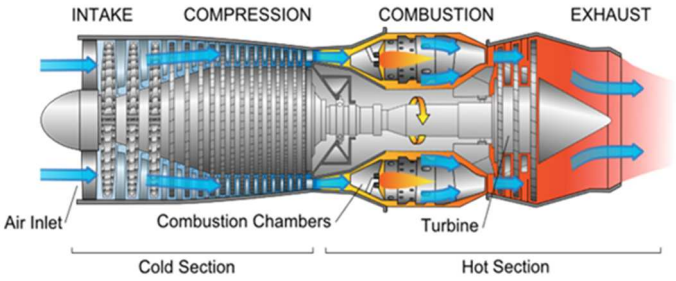

Fig. 1 - A schematic of aviation GTE showing the hot sections that require thermal barrier coatings (Credit: Rolls Royce Inc.).

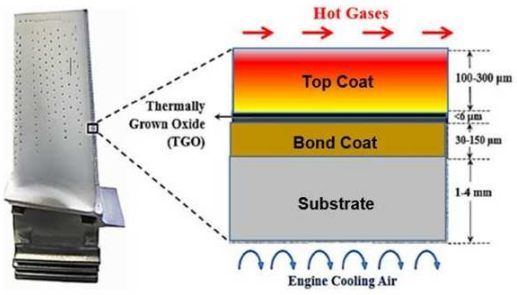

Fig. 2 - Constituents of thermal barrier coatings.

AUTHOR'S SHORT BIOGRAPHIC NOTE

Professor Shaker Meguid is an internationally renowned scholar with significant contributions in computational and experimental mechanics at varied length scales. Undoubtedly, his research activities have contributed significantly to the areas of multiscale modelling, advanced and smart nanocomposites, crashworthiness, fracture mechanics and failure prevention. He has published 354 papers in leading tier-1 scientific journals, 260 presentations in international conferences of significance with a large number being invited as keynote and plenary speaker. He authored 4 books on fracture mechanics, nanomechanics and micromechanics, edited18 international conference proceedings and contributed 19 book chapters.

He is the Founding Editor-in-Chief of Int. Journal of Mechanics and Materials in Design, former Technical Associate Editor of ASME J. of Engineering Materials and Technology (for two consecutive terms), former Associate Editor of IMechE Journal of Mechanical Process Engineering, Guest Editor to a number of Journals including Mechanics of Materials and a member of the editorial board of numerous journals. He is also the Founding Head of the Aerospace Engineering Division of Nanyang Technological University, Singapore. He taught different branches of mechanics in 4 continents: Europe (Manchester, Oxford (England) and Milano Polytecnico (Italy)), North America (Toronto, Canada), and Asia (NTU, Singapore), Hunan, Peking, and BIT (China), and Africa (Cairo University, Egypt).

He is an Engineering Consultant to the United Nations, a lifetime senior member of AIAA, member of the American Academy of Mechanics, Professional Engineer in the Province of Ontario (PEng), Chartered Engineer in Great Britain (CEng), Fellow of ASME, Fellow of IMechE and Fellow of the Engineering Institute of Canada. He works closely with the aerospace and automotive industries and is regularly approached by members of the media for clarification of engineering issues and accidents.

Professor Meguid and his research team won numerous awards, with the most recent honor being the nomination by his department for the gold medal by the Governor General of Canada, holder of the Robert Hooke Award bestowed by the European Society for Experimental Mechanics, Engineering Award-Research and Development by the Professional Engineers of Ontario for his significant contribution to research and development in Canada.

Proceedings IRF2025: 8th International Conference on Integrity-Reliability-Failure
In Engineering, Materials, Manufacturing and Biomechanics. Porto 15-18 July 2025
DOI: https://doi.org/10.24840/978-972-752-323-8

PAPER REF: 22141

SEISMIC BEHAVIOUR OF CONCRETE BUILDINGS: FIELDS LESSONS, STANDARDS AND RESEARCH NEEDS

Humberto S.A. Varum(*)
FEUP/CONSTRUCT, University of Porto, Porto, Portugal
(*)*Email:* hvarum@fe.up.pt

ABSTRACT

Recent earthquakes demonstrate that many of the existing reinforced concrete buildings structures may not perform adequately in future seismic events, due to several factors, including the design strategy adopted in the project, the irregular characteristics of the structural system, inadequate detailing and the potential influence of non-structural elements in the structural response. In some design situations, designers report difficulties in applying certain rules and requirements included in the codes. On the other hand, the materials, technical solutions and construction systems used in structures and non-structural elements continue to evolve, introducing new levels of complexity and uncertainty in the project. This justifies the research and continued development of seismic design rules and requirements to be included in codes with the aim of achieving rigorous design guidelines, but with an acceptable level of complexity.

Keywords: Civil Engineering, Buildings Structures, Earthquakes, Seismic Design.

AUTHOR'S SHORT BIOGRAPHIC NOTE

Professor Humberto Varum is a full professor at the Civil Engineering Department of the Faculty of Engineering of the University of Porto, Portugal. He is integrated member of CONSTRUCT research unit: Institute of R&D in Structures and Construction.

He has been Seconded National Expert to the ELSA laboratory, Joint Research Centre, European Commission, Italy, in the period July 2009 to August 2010. Since 2015, he is member of the directorate body of the Construction Institute from the University of Porto, and President since 2019. He was member of the Project Team 2 for the development of the 2nd generation of EN Eurocodes (SC8.T2 - material dependent sections of EN 1998-1).

Professor Varum is member of the National Committee of the International Council on Monuments and Sites (ICOMOS), since 2009, and Expert Member of the ICOMOS's International Scientific Committee of Earthen Architectural Heritage (ISCEAH).

He has participated to post-earthquake field reconnaissance missions, in particular in L'Aquila (Italy, 2009), Lorca (Spain, 2011), Emilia-Romagna (Italy, 2012), Gorkha (Nepal, 2015) and Puebla (Mexico, 2017).

His main research interests include: assessment, strengthening and repair of structures, earthquake engineering, historic constructions conservation and strengthening.

MAIN TOPICS / TRACKS

TRACK - A: Composite and Advanced Materials

Multiscale Modelling and Characterisation
Multifunctional Composites
Nanomaterials and Nanotechnologies
Interfacial Properties at Varied Length Scales
Smart Structures and Materials,
Processing/Fabrication/Recycling
Durability/Damage/Fracture
Health Monitoring and Repairability
Adhesive Bonding
Case Studies

Proceedings IRF2025: 8th International Conference on Integrity-Reliability-Failure
In Engineering, Materials, Manufacturing and Biomechanics. Porto 15-18 July 2025
DOI: https://doi.org/10.24840/978-972-752-323-8

PAPER REF: 22181

PERFORMANCE ENHANCEMENT STRATEGY AND MICROSTRUCTURE-PROPERTIES OF A ROCK-BREAKING CUTTER RING STEEL USED IN TUNNEL BORING MACHINE

Guo Jingbo(*), Han Mengze

School of Mechanical Engineering, Shijiazhuang Tiedao University, Shijiazhuang 050043, China
(*)*Email:* guojingbo66@163.com

ABSTRACT

To enhance the service life of the tunnel boring machine (TBM) cutter ring in extremely hard rock, the HR1 steel was developed by refining chemical composition and optimizing heat treatment, achieving high hardness and toughness. Compared to conventional cutter ring material DC53 steel, the HR1 steel quenched at 1050 ℃ and tempered at 540 ℃ increases hardness by 2.1 HRC and impact toughness by 225.7%. In low-stress wear, the abundant primary carbides in the microstructure of DC53 steel result in lower wear mass loss compared to the HR1 steel. However, the wear resistance of HR1 steel outperforms under high-stress wear due to its favorable matching of hardness and toughness.

Keywords: TBM, disc cutter ring, heat treatment, mechanical property, wear resistance.

INTRODUCTION

When excavating extremely hard rock strata, the high abrasion and strong impact load of rock can seriously shorten the working life of cutter rings (Ling et al., 2021). In engineering practice, it has been demonstrated that the time spent on inspecting, replacing, and maintaining the cutter ring due to failures constitutes approximately 30% to 40% of the total tunneling construction time, with the associated costs making up about one-third of the total tunneling construction cost (Ren et al., 2018). To solve the issue that many TBM cutter rings made of DC53 steel were prone to wear and fracture under extremely hard rock geology in an underground project in China. In this study, the internal relationships among processing, microstructure, mechanical properties and wear behavior of the HR1 steel cutter ring after performance enhancement were mainly investigated, and compared to the structure and properties of the DC53 steel cutter ring.

RESULTS AND CONCLUSIONS

The experimental materials include HR1 and DC53 steel. The DC53 steel sample was obtained from a fractured cutter ring on site. After sampling the HR1 finished steel, the samples were quenched at 990, 1050 °C, 1110 °C and tempered at 540 °C. The microstructure and mechanical properties of the two test materials were analyzed by a metallographic microscope, Rockwell hardness tester, and pendulum impact tester. To compare the wear resistance of DC53 and HR1 steel. Low-stress and high-stress cyclic wear tests were performed on the HCCW-1 wear tester. The low-stress test used a rubber wheel with quartz sand, while the high-stress test was carried out at the condition of steel wheel quartz sand.

The microstructure of DC53 steel primarily consists of tempered sorbite and chain-like distributed primary carbides, Figure 1(a). The microstructural defect leads to stress concentration and crack propagation, thereby reducing impact toughness. Figures 1(b)-(d) show

the microstructure of HR1 steel at dissimilar quenching temperatures. With the increase of quenching temperature, the primary carbides in the HR1 steel structure are continuously dissolved, and the matrix structure is gradually grown from fine acicular martensite to acicular martensite, Figures 1(b)-(d).

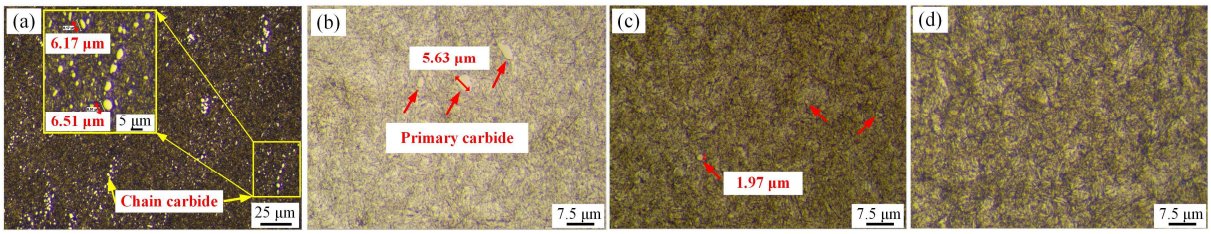

Fig. 1 - Microstructure of the DC53 steel (a) and the HR1 steel (b)-(d).

When the heat treatment process is quenching at 1050 ℃ and tempering at 540 ℃, which results in HR1 steel having satisfying hardness and toughness.Compared with the DC53 steel, the HR1 steel increases in hardness by 2.1 HRC, reaching 60.2 HRC, with the impact absorption energy increasing by about 225.7% to 49.6 J, as shown in Figure 2. Figure 3 exhibits the wear mass loss of HR1 steel with the best comprehensive mechanical properties and DC53 steel under two wear conditions. Under low-stress cyclic wear, HR1 steel exhibits lower wear resistance than DC53, with a mass loss of 323.3 mg, 25.12% more than DC53. However, under high-stress cyclic wear, wear mass loss of both steels significantly rises, reaching 937.1 mg for HR1 and 984.6 mg for DC53. In this high-stress condition, HR1 outperforms DC53 with 4.82% less wear, indicating better wear resistance.

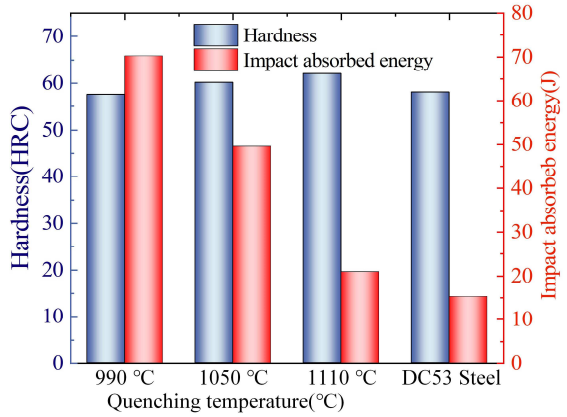

Fig. 2 - Mechanical properties of the DC53 steel and the HR1 steel

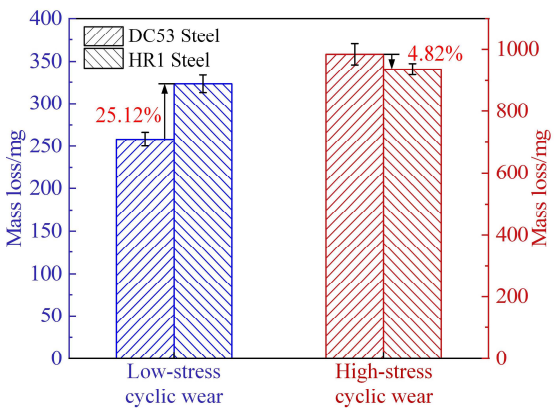

Fig. 3 - Comparison of wear resistance of DC53 steel and HR1 steel.

Through improving the content of C, Cr, V, and other alloying elements and optimizing the heat treatment process. The impact toughness and hardness of HR1 steel are synergistically improved compared to DC53 steel. The results of the abrasive wear test show that good hard-tough matching can make the cutter ring material have better impact wear resistance.

REFERENCES

[1] Ling JX, Cheng L, Tong X, Wu ZH. Research on rock breaking mechanism and load characteristics of TBM cutter based on discrete element method, Advances in Mechanical Engineering, 2021, 13, pp. 1-15.

[2] Ren DJ, Shen SL, Arulrajah A, Cheng WC. Prediction model of TBM disc cutter wear during tunnelling in heterogeneous ground, Rock Mechanics and Rock Engineering, 2018, 51, pp. 3599-3611.

Proceedings IRF2025: 8th International Conference on Integrity-Reliability-Failure
In Engineering, Materials, Manufacturing and Biomechanics. Porto 15-18 July 2025
DOI: https://doi.org/10.24840/978-972-752-323-8

PAPER REF: 22316

ANELASTIC DEFORMATIONS IN SiO_2, NANOCOMPOSITES OF MULTIWALLED CARBON NANOTUBES AND POLYMERS

A.P. Onanko(*), L.V. Kuzmych, Y.A. Onanko, O.P. Dmytrenko, M.P. Kulish, T.M. Pinchuk-Rugal, A.G. Rugal, V.V. Kuryliuk, A.M. Kuryliuk, O.L. Pavlenko, T.O. Busko, A.M. Gaponov, S.A. Kuzmych, P.P. Il'in

Taras Shevchenko National University of Kyiv, Kyiv, Ukraine
(*)*Email:* onanko@i.ua

ABSTRACT

Anelastic deformations in SiO_2, radiation and structural functionalized nanocomposites of multiwalled carbon nanotubes (MCNT) and polyamide, polyvinylchloride, polyethylene were investigateded.

Keywords: Anelastic deformations, elastic stress, electron irradiation, nanocomposites, carbon nanotubes.

INTRODUCTION

Poisson's ratio μ and elastic modulus E fully characterize the elastic properties of a polymer nanocomposite (Onanko et al., 2022; Trus et al., 2019). The increase of Debye temperature θ_D indicates the strengthening of interatomic interaction (Bereka et al., 2021; Onanko et al., 2019; Onanko et al., 2023).

RESULTS

Elastic, anelastic deformations in SiO_2, radiation functionalized nanocomposites of multiwalled carbon nanotubes (MCNT) and polyamide-6 $(NH(CH_2)_5CO)_n$ (Figure 1), polyvinylchloride $(C_2H_3Cl)_n$, polyethylene $(C_2H_4)_n$ were measured.

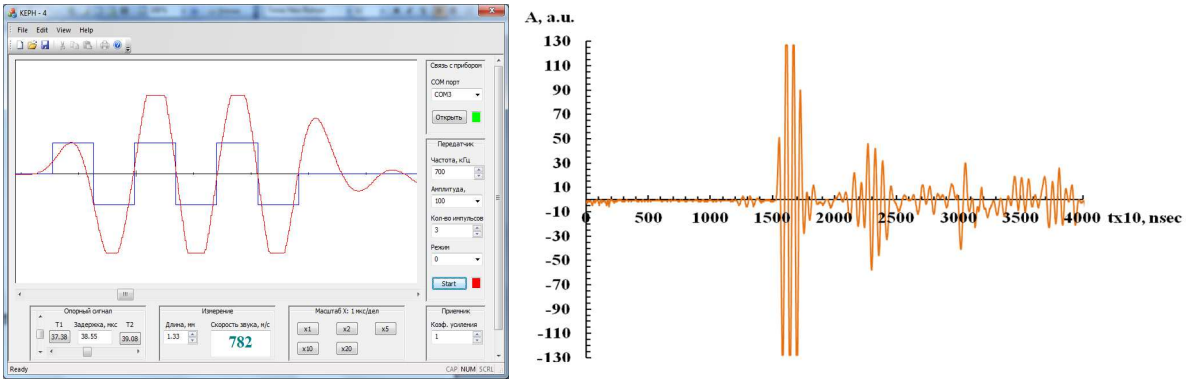

Fig. 1 - Illustration of the window for processing data of quasitransversal elastic waves velocity measuring $V\perp$ = 782 m/sec in nanocomposite polyamide-6 $(NH(CH_2)_5CO)_n$ + 0.1% MCNT by impulse phase ultrasonic (US) method at frequency $f\perp \approx 0.7$ MHz after electron irradiation with dose $D_{e^-} \approx 20$ Mrad with energy $E_{e^-} \approx 2.0$ Mev. Logarithmic decrement of attenuation $\delta = ln\left(\frac{A_{n+1}}{A_n}\right) = ln\left(\frac{127}{90}\right) \approx (3.44 \pm 0.1) \times 10^{-1}$.

Complex elastic modulus E^* nanocomposite is equal to the sum of dynamic elastic modulus $E' = \rho V_{\parallel}^2$ and loss modulus $E'' = E'\delta$ (Onanko et al., 2022; Radovenchyk et al., 2021):

$$E^* = E'(1+\delta) = \rho V_{\parallel}^2(1+\delta) = \rho V_{\parallel}^2(1+\pi Q^{-1}), \quad (1)$$

where δ - logarithmic decrement of US attenuation, ρ - nanocomposite density, $V_{\parallel}$ - longitudinal US elastic waves velocity, Q^{-1} - internal friction.

CONCLUSIONS

1. After electron irradiation with dose $D_{e^-} \approx 20$ Mrad with energy $E_{e^-} \approx 2.0$ Mev the presence of the strong interaction for nanocomposites between multiwalled carbon nanotubes and polymers was confirmed by mechanical studies.

2. The phenomenon of change of Poisson coefficient μ, Debye temperature θ_D, dynamic elastic modulus $E' = \rho V_{\parallel}^2$, dynamic shear modulus $G = \rho V_{\perp}^2$ under the influence of radiative electronic e^- radiation is caused by the appearance of primary radiation defects (RD). As the result of interdefect interactions primary RD form secondary RD.

ACKNOWLEDGMENTS

This work has been supported by the Ministry of Education and Science of Ukraine: Grant of the Ministry of Education and Science of Ukraine for the prospective development of the scientific direction "Mathematical sciences and natural sciences" at Taras Shevchenko National University of Kyiv.

REFERENCES

[1] Bereka V., Boshko I., Kondratenko I. et al. Efficiency of plasma treatment of water contaminated with persistent organic molecules. Journal of Environmental Engineering and Science, 2021, 16(1), pp.40-47.

[2] Onanko A.P., Charny D.V., Onanko Y.A. et al. Inelastic, elastic characteristics of SiO2, porous polystyrene and automated system. 18th International Conference on Geoinformatics - Theoretical and Applied Aspects, 2019, 2019, pp.1-5.

[3] Onanko A.P., Dmytrenko O.P., Pinchuk-Rugal T.M. et al. Characteristics of Monitoring and Mitigation of Water Resources Clay Particles Pollution by ζ-Potential Research. 16th International Conference Monitoring of Geological Processes and Ecological Condition of the Environment, 2022, 2022, pp.1-5.

[4] Onanko A., Kuzmych L., Onanko Y., Kuzmych A. Indicatory surface of anelastic-elastic properties of Ti alloys. Materials Research Express, 2023, 10(10), 106511.

[5] Onanko Yu., Charnyi D., Onanko A. et al. Oil and Gas Reservoir Rock Sandstone SiO2 Porosity Research by Internal Friction Method. International Conference of Young Professionals «GeoTerrace-2022», 2022, 2022, pp.1-5.

[6] Radovenchyk I., Trus I., Halysh V. et al. Evaluation of Optimal Conditions for the Application of Capillary Materials for the Purpose of Water Deironing. Ecological Engineering & Environmental Technology, 2021, 22(2), pp.1-7.

[7] Trus I., Gomelya N., Trokhymenko G. et al. Determining the influence of the medium reaction and the technique of magnetite modification on the effectiveness of heavy metals sorption. Eastern-European Journal of Enterprise Technologies, 2019, 6(10 (102), pp. 49-54.

Proceedings IRF2025: 8th International Conference on Integrity-Reliability-Failure
In Engineering, Materials, Manufacturing and Biomechanics. Porto 15-18 July 2025
DOI: https://doi.org/10.24840/978-972-752-323-8

PAPER REF: 22378

CARBON TEXTILE REINFORCED MORTAR (CTRM) TO MASONRY BOND UNDER FATIGUE LOADING

Kuanysh Makashev[1,*], Savvas Triantafyllou[2], Georgia Thermou[3]

[1]Faculty of Architecture and Civil Engineering Toraighyrov University, Pavlodar, Kazakhstan
[2]School of Civil Engineering, National Technical University of Athens, Athens, Greece.
[3]Faculty of Engineering, University of Nottingham, Nottingham, United Kingdom
[(*)]*Email:* makashev.kt@teachers.tou.edu.kz

ABSTRACT

The Textile-Reinforced Mortar (TRM) is a well-established solution for reinforcing unreinforced masonry (UM) structures. A key factor in the effectiveness of this technique is the bond between the TRM and the masonry substrate. Although considerable work has shed light in the mechanics of this bond under static loading, few studies have focused on examining the effect of cyclic loading. In this study, we present preliminary research on the bond behaviour at the interface of Carbon Textile Reinforced Mortar and masonry under fatigue loading conditions and attempt a comparison with the quasi-static case. Even at established bond length, our results show a consistent shift in the failure mode, i.e., from textile slippage at the static case to matrix detachment at the cyclic case.

Keywords: TRM, carbon, fatigue, masonry, bond.

INTRODUCTION

Efficient strengthening of unreinforced masonry (UM) structures is a timely and pressing challenge of engineering practice. The Textile Reinforced Mortar (TRM) is an effective solution for strengthening UM structures, offering enhanced flexural and shear resistance. As with every strengthening technique, the key weak link is found in the bond between the UM and TRM. To this end, the quasi-static scenario gained primary attention in the research community. Conversely, research on the TRM response under fatigue loading is scarce. Cyclic loading scenarios are of prevalent in transport infrastructure, e.g., masonry arch bridges operating under repeated cycles of loading that result in damage initiation at stresses that are lower than the maximum stress level corresponding to the static case (Harrewijn and Vergoossen, 2022; D'Antino, et al., 2015; Carozzi, et al., 2009). As a result, failure occurs unpredictably, often before the structure exhibits sufficient visible damage.

Until now, there is no standard for the fatigue bond tests. Most studies used the RILEM TC 250-CSM standardized single-lap test protocol for testing the bond between TRM and masonry under static loading (de Felice et al., 2018). The load envelope in most studies is in a range of 60%, 70%, and 80% of the critical load and 15% as a lower load, indicating that tests are performed under low-cycle fatigue conditions (see, e.g., Carloniet al., 2012). More recent studies on TRM to masonry strengthening under cyclic loading have investigated the effectiveness of TRM for strengthening rammed earth walls under in-plane cyclic loads**.** The strengthened specimens displayed a 104% recovery of shear strength**,** with a 600% increased drift capacity compared to the unstrengthened case (Romanazzi et al. 2023).

EXPERIMENTAL PROGRAM

Test Specimens and Experimental Setup

This experimental campaign involved two test series, i.e., under quasi-static and fatigue loading conditions using the single lap experimental setup shown in Figure 1. The specimens were masonry wallets comprising five clay bricks with individual dimensions of 215 x 102.5 x 65 mm. The total height of the wallet was 365 mm. The thickness of the joint mortar was 10mm in all cases. The bonded area was positioned at a 25 mm distance from the prism edges to eliminate potential edge effects. The width and length of the bonded area in this research were 120 and 250 mm, respectively. The TRM layer had an approximate thickness of 6 mm.

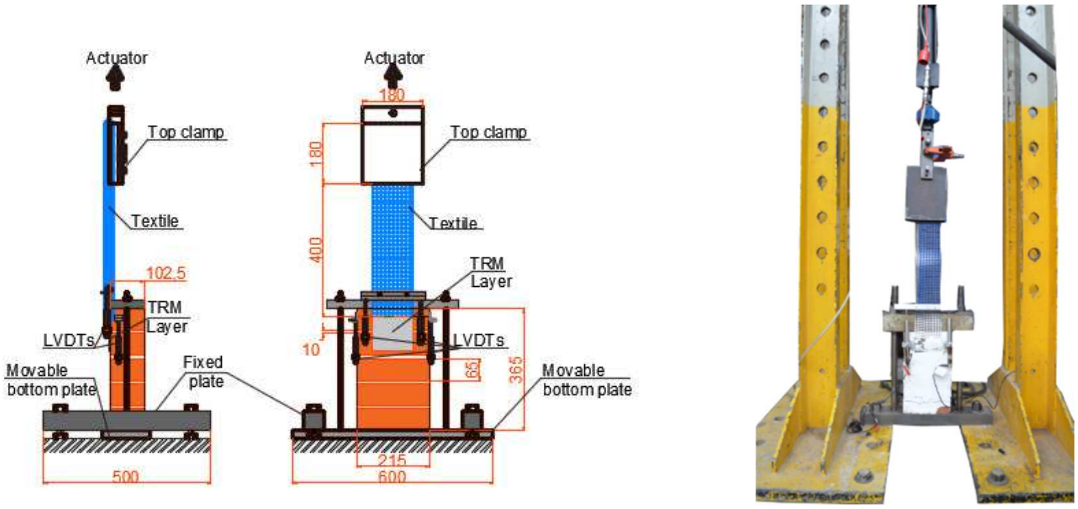

(a) (b)

Fig. 1 - Test setup (a) test setup details (all dimensions in mm), (b) actual test setup.

The displacement measurement was organised as follows: two Linear Variable Differential Transducers (LVDTs) were directly attached to the wall. Two similar LVDTs were used to measure the relative displacement of the textile to the wall. The maximum stroke of the LVDTs was 15mm. The load-displacement was recorded with a fully computerized data accusation system with a constant rate of 4 Hz.

Materials

A commercially available carbon textile was used, with a mesh size of 10mm on both sides and weight of 348 g/m^2 (Figure 2). The corresponding equivalent thickness was evaluated to be 0.097 mm. The textile fibre material properties are summarized in Table 1 as per the manufacturer's datasheets.

The joint mortar was a 1:4 cement to sand mix. A cement-based mortar was utilized for the application of the TRM strengthening composite system. This was an inorganic dry binder comprising cement and polymers at a ratio 8:1 by weight. A 0.23 water-to-mortar ratio was used in all cases; this was established after trial mixes to achieve the desired workability. The properties of the joint and strengthening mortars were identified according to EN 1015-11 test standard. The flexural strength was determined by conducting 3 three-point bending tests on 40 x 40 x 160 mm prisms. Then the failed parts with a dimension of 40 x 40 mm were tested in compression (6 specimens). The resulting average values of the compressive and flexural strength are shown in Table .

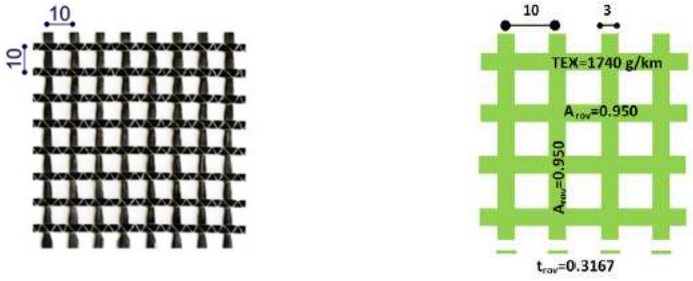

a b

Fig. 1 - Geometry of textile.

Table 1 - Property of the textile.

Material	Weight [g/m^2]	Nominal thicknesses [mm]	Tensile Strength [MPa]	Young's Modulus [GPa]	Density [g/cm^3]
Carbon	348	0.097	3800	225	1.8

Table 2 - Properties of the mortar.

Mortar	Compressive strength [MPa]	Flexural strength [MPa]
Join mortar	7.82 (0.36*/0.04**)	1.85 (0.5*/0.26**)
M1: ready mix mortar (W/C:0.23)	28.9 (0.17*/0.02**)	4.95 (0.17*/0.03**)
*Standard deviation/**Coefficient of Variation		

RESULTS AND DISCUSSION

Quasi Static Bond Tests

The quasi-static test results are summarized in Table 3. As expected, in all cases the stress increases linearly until failure. In every instance, the failure mode was textile slippage (Figure 3a). The average stress global slip plot is shown in Figure 3b. Four identical specimens with a bond length of 250mm were tested under the static case to determine the average value of the maximum load (6.9 kN).

Table 3 - Test result for monotonic quasi-static tests.

Specimen bond length	Test result by specimen [kN]				Mean value [kN]	Standard deviation	Coefficient of variation
	a	b	c	d			
C_250_s	6.6	6.53	7.22	7.4	6.9	0.37	0.05

Fatigue Bond Tests

The quasi-static tests aimed to establish a baseline for the maximum load and the corresponding failure mode. The attained maximum load was then used to establish the upper and lower bounds of the cyclic envelope during fatigue testing. The present work considered the case of a typical low-cycle fatigue envelope (Carloni et al. 2012), where the upper and lower boundaries of the load were defined as P_{max}^{f} and P_{min}^{f} respectively, where the actual recorded P_{max}^{f} and P_{min}^{f} is shown in Table 4.

The average stress versus slip plots and the corresponding failure modes for the cyclic cases are shown in Figure 3cd. Conversely to the quasi-static, in the case of cyclic loading failure occurred via matrix detachment, albeit at a significantly lower level of load. Failure occurred after 8632 (average value) loading cycles. The last stable cycle is shown in the plot.

Table 4 - Fatigue test results.

Specimen	Sample	P_{max}^{f} [kN]	|Rd| [%]	P_{min}^{f} [kN]	|Rd| [%]	Ns
Ch_250_f	a	4.49	-7.49	1.28	23.00	9325
	b	4.63	-4.53	1.22	17.00	8534
	c	4.64	-4.26	1.14	9.72	8036
Mean		4.59	0.67	1.21	17.00	8632
St.d		0.08	0.49	0.03	7.03	260
CoV.		0.01	0.73	0.02	0.41	0.03

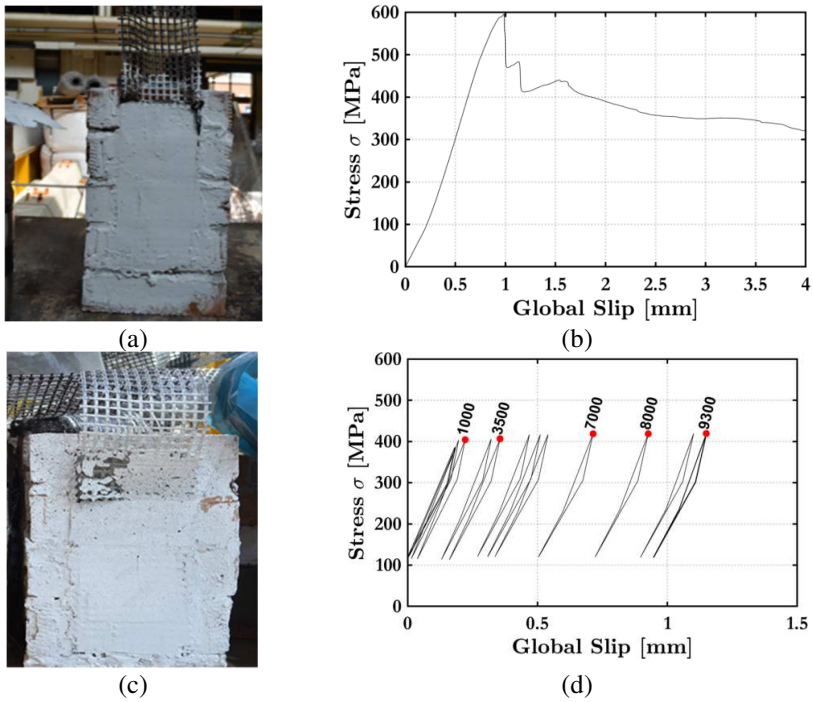

Fig. 2 - Failure mode and applied load versus slip paths for the static (a), (b) and cyclic cases (c), (d), respectively.

The cyclic response is manifested in three distinct stages, i.e.:

Initial Crack Formation: This stage usually starts at the first 100-500 cycles. Initial cracks appear in the vicinity of the here as the load repeatedly stretches and compresses the composite material, concentrating stress at the top border where the bond connection is weaker. During this stage, the loading cycles evolve practically over the same slip range.

Crack Propagation: Once the cracks form, they propagate as cyclic loading continues. The duration of this stage is approximately 5000 cycles. Even though the cyclic load causes micro-cracks to merge and extend, the structure still retains enough integrity to delay immediate failure, however severe ratcheting is observed.

Matrix Detachment: In this part, the cracks spread through the bonded area extensively. Then detachment initiates at the mortar to masonry interface. This in contrast to the quasi-static case where the mortar remains intact and the interface properties are governed by the chemistry of the bond between the textile and the matrix.

Conversely, in the quasi-static tests, the failure mechanism initiates with cracks in the mortar matrix followed by matrix detachment. It may occur due to the mortar matrix experiencing localized fatigue and weakening under cyclic loading, leading to its inability to hold the textile in a matrix.

CONCLUSIONS

In this study, preliminary results were presented on an ongoing experimental campaign investigating the TRM to masonry bond under one-sided cyclic loading conditions. The key observations derived from experimental analysis are:

- Under the single lap bond test considered in this study, a shift in the failure mode is observed. Under quasi-static loading, textile slippage occurred, whereas cyclic loading resulted in textile detachment.
- The adhesion between the textile and the mortar matrix is subjected to progressive degradation under cyclic loading. The repeated stress disrupts the integrity of the adhesive property at the interface, eventually causing detachment rather than slippage.
- Previous research by the authors on cyclic loading, where the basalt textile was used also manifested by shift of failure mode. This highlights the influence of textile property and mesh size on the bond performance factors. Also, it shows the need for careful material selection to enhance durability under repeated loading conditions.

ACKNOWLEDGMENTS

The first author would like to acknowledge: This research has been funded by the Science Committee of the Ministry of Education and Science of the Republic of Kazakhstan (Grant No. AP25793581)

REFERENCES

[1] Harrewijn, R. Vergoossen, Assessment of masonry arch bridges, in: Proceedings of the IABSE Symposium Prague, 2022: Challenges for Existing and Oncoming Structures - Report, 2022, pp. 562 - 568.

[2] T.D'Antino, C. Carloni, L. Sneed, C. Pellegrino, Fatigue and post-fatigue behavior of pbo FRCM- concrete joints, International Journal of Fatigue 81 (2015) 91-104.

[3] Carozzi, F.G. et al. Experimental investigation of tensile and bond properties of Carbon-FRCM composites for strengthening masonry elements. Composites Part B: Engineering 128, 100-119 (2017).

[4] de Felice, G. et al. Recommendation of RILEM Technical Committee 250-CSM: Test method for Textile Reinforced Mortar to substrate bond characterization. Materials and Structures/Materiaux et Constructions 51 (4), 1-9 (2018).

[5] C. Carloni, K.V. Subramaniam, M. Savoia, C. Mazzotti, Experimental determination of FRP–concrete cohesive interface properties under fatigue loading, Composite Structures 94 (2012) 1288-1296.

[6] Romanazzi, A.; Silva, R.A.M.; Barontini, A.; Mendes, N.; Oliveira, D.V. (2024). In-plane strenghtening of a rammed earth wall with a compatible TRM-strengthening solution.

Proceedings IRF2025: 8th International Conference on Integrity-Reliability-Failure
In Engineering, Materials, Manufacturing and Biomechanics. Porto 15-18 July 2025
DOI: https://doi.org/10.24840/978-972-752-323-8

PAPER REF: 22387

THE INFLUENCE OF SELECTED PARAMETERS OF EXPLOSION WELDING ON THE PROPERTIES AND STRUCTURE OF ZIRCONIUM/ CARBON STEEL BIMETALLIC SYSTEMS

Mariusz Prażmowski[1(*)], Aleksander Karolczuk[1], Henryk Paul[2]

[1]Faculty of Mechanical Engineering, Opole University of Technology, Opole, Poland
[2]Institute of Metallurgy and Materials Science, Polish Academy of Sciences, Krakow, Poland
[(*)]*Email:* m.prazmowski@po.edu.pl

ABSTRACT

This paper discusses the problems of the transformations taking place in the joint area of the system of plates carbon steel P355NL2 and zirconium Zr700. The clads were produced in explosive welding technologies with diversified proces parametrers (detonation velocities and stand-off distance). Then the interrelation between proces parameters and strength properties of the clad were analysed. The microstructure changes were analyzed with the use of scanning electron microscopy (SEM) and they were correlated with the results of the mechanical tests.

Keywords: Layered structure Zr/(carbon steel), explosion welding, interface, intermetallic phases.

INTRODUCTION

Leyered products are often used in industry for structure application. Their production is justified not only by the economical factors but also by the necessity to fulfil particular funcional requirements. It is usually sufficient to apply a thin layer of a material, of high anti-corrosive properties at elevated temperatures applied on a relatively inexpensive base (construction) material to meet the operation requirements, i.e. to obtain element characterized both by high corrosion resistance and strength.

Materials, such as zirconium, titanium, tantalum, niobium, tungsten, etc., and their alloys, perfectly fulfill the above expectations. They show high corrosive resistance in numerous environments and therefore, they are widely used in the construction of processing apparatus used both in the chemical and the power generation industry. Taking into account the high cost of such materials, it is advisable to use them in the form of plated coatings, most often on carbon as two layered composites. However, joining these metals (e.g. in the form of metal sheets) still is a big technological problem. That is why, one increasing interest in the technology of explosive treatment of materials, including the technology of explosive cladding, is observed.

Achieving such a connection requires particularly careful selection of the parameters of the explosive welding process, namely the energy of the explosion, the detonation velocity, and the distance between the sheets being joined [1] (Figure 1). An inappropriate selection of these parameters, for example, below the threshold values, may lead to the formation of discontinuities or a complete lack of connection. On the other hand, exceeding the critical values results in the melting of the surfaces of the joined sheets, ultimately leading to the formation of unfavorable areas of fusion that are characterized by high hardness and brittleness from the perspective of connection quality.

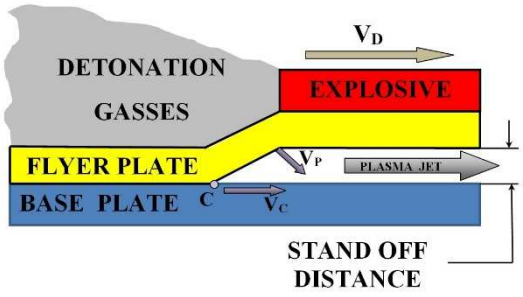

Fig. 1 - Scheme of the parallel system and the shape of the ejector die in the welding process. The basic parameters are: V_D – detonation velocity, V_P – velocity of plate collision, V_C – velocity at the collision point, β – collision angle, h – distance between the plates, C – collision point.

RESULTS AND CONCLUSIONS

The results received allowed to conclude that for the assumed parameters it is possible to obtain Zr /(carbon steel) bi-metallic strips with properties meeting the standard's requirements. Performed metallographic analysis shows that the detonation velocities affect the quality of the welded sheets as well as the quantity of the transition zones near the interface. Smaller velocities promotes the formation of waves with lower parameters (of length and height), whereas greater velocities allow forming the bond of a more pronounced, repetitive wavy character, however, increasing the quantity of the transition zones at the same time (Figure 2). Also, the initial distance between the materials to be joined makes for the strengthening in the areas adjacent to the interface. SEM observations proved that the location of the intermetallic phase and the shape of the transition zone are strictly dependent on technological parameters of the process. The analysis of the chemical composition allowed to recognize three main intermetallic phases in the intermediate layer, i.e. FeZr, $FeZr_2$ and Fe_2Zr_3 (Figure 3).

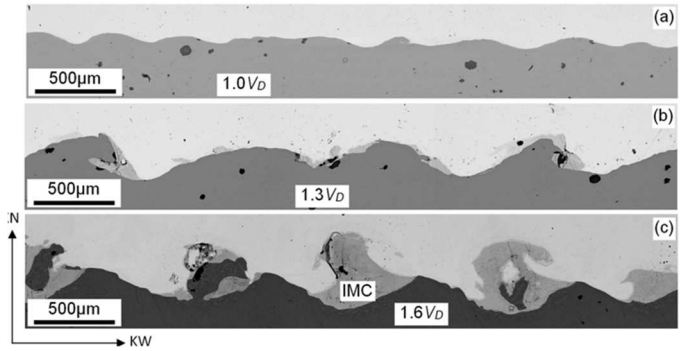

Fig. 2 - Morphological changes observed near the bonding zone of (carbon steel)/Zr composites manufactured at different detonation velocities: (a) 2200m/s, (b) 2800m/s and (c) 3500m/s.

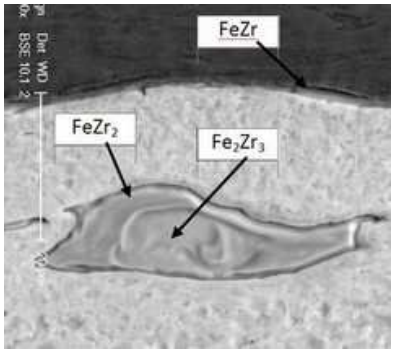

Fig. 3 - The changes in concentration of Zr and Fe elements inside the melted zone.

REFERENCES

[1] Blazynski T.Z. (ed.) Explosive welding, forming and compaction, Applied Science Publishers, London and New York.

Proceedings IRF2025: 8th International Conference on Integrity-Reliability-Failure
In Engineering, Materials, Manufacturing and Biomechanics. Porto 15-18 July 2025
DOI: https://doi.org/10.24840/978-972-752-323-8

PAPER REF: 22395

EVALUATION OF THE EFFECT OF TITANIUM, STRONTIUM AND MOLYBDENUM ON THE SOLIDIFICATION CHARACTERISTICS OF ADC12 ALLOY BY COOLING CURVE THERMAL ANALYSIS

Xiangjie Wang[1,2(*)]

[1]Key Laboratory of Electromagnetic Processing of Materials, Ministry of Education, Northeastern University, Shenyang, Liaoning, 110819, PR China
[2]School of Materials Science and Engineering, Northeastern University, Shenyang, Liaoning, 110819, PR China
[(*)]*Email:* wangxj011@163.com

ABSTRACT

The influence of Al-5Ti-B, Al-10Sr and Al-5Mo on the temperature-based parameters of ADC12 alloy were investigated using cooling curve thermal analysis. Results show that the alloy with 2 wt.% Al-5Ti-1B addition, under-cooling and nucleation rate of primary a-Al significantly increase. The nucleation and growth temperature of eutectic Si in ADC12 aluminum alloy with 0.04 wt.%Sr addition significantly decreases. The nucleation and growth temperature of eutectic Al_2Cu in ADC12 alloy with 0.1 wt.% Mo addition are the lowest. Evaluating the solidification structure of ADC12 aluminum alloy through characteristic temperature parameters optimizes the effect of trace elements on the microstructure and properties of ADC12 alloy.

Keywords: ADC12 alloy, trace element, solidification characteristics, thermal analysis.

INTRODUCTION

Cooling curve thermal analysis (CCTA) is a non-equilibrium thermal analysis method that can evaluate the quality of the smelting process and optimize the addition of elements. Because it is a non-destructive quantitative technique that can be used before casting (Emadi D, 2005). In the process of melt solidification, the nucleation and growth of the structure in the alloy will release or absorb heat, thus showing a specific temperature value (Mackay R I, 2000). CCTA technology is to record the change of temperature with time during solidification. Therefore, the phase transition process in metal melt can be predicted and judged by CCTA method, and the information of alloy composition, solidification latent heat, solid fraction evolution, solidification phase type and dendrite phase can be obtained. In addition, thermal analysis can also be used to analyze the degree of modification and refinement, determine the liquidus and solidus temperatures, and obtain the characteristic temperatures related to the formation of eutectic zones and metal compound phases (Farahany S, 2012).

RESULTS AND CONCLUSIONS

Figure 1(a) illustrates a cooling curve recorded during the solidification of ADC12 casting alloy, along with its corresponding first derivative curve (dT/dt) and second derivative curves (d^2T/dt^2). The cooling curve shows three main reactions associated with phase formation, marked by arrows on the curves. Specifically, the solidification process of ADC12 alloy involves the formation of primary Al dendrites, the Al-Si eutectic reaction and Al-Cu eutectic reaction. To identify characteristic temperatures for primary Al, eutectic Si and eutectic Al-Cu,

namely nucleation temperature (T_N), minimum temperature (T_M), and growth temperature (T_G). Specifically, T_N is identified as the intersection point between the zero line and the second derivative curve when d^2T/dt^2 shifts upward. T_M corresponds to the peak on the d^2T/dt^2 curve, which aligns with the zero point on the dT/dt curve, indicating the onset of latent heat release. T_G is determined when the d^2T/dt^2 curve descends and then rises to intersect the abscissa, corresponding to another zero point on the dT/dt curve. (Saeed Farahany S, 2014).

Figure1(b) is the cooling curve of ADC12 alloy with different trace elements. It can be seen that after adding Al-5Ti-1B, the T_N and T_G of α-Al increase, while adding Sr or Mo, T_N and T_G decrease. For the eutectic Si reaction, the T_N and T_G of the alloy with Al-5Ti-1B and Mo have little change, while Sr has a great influence on the nucleation temperature of the eutectic Si reaction, which affects the nucleation and growth of the eutectic Si. For the eutectic Al-Cu reaction, the T_N and T_G of the alloy with Al-5Ti-1B are slightly increased, while the T_N and T_G of the eutectic Al-Cu reaction are decreased to varying degrees by Sr and Mo. It shows that differences have little effect on the growth temperature of primary α-Al, but produce a greater effect on the eutectic growth temperature.

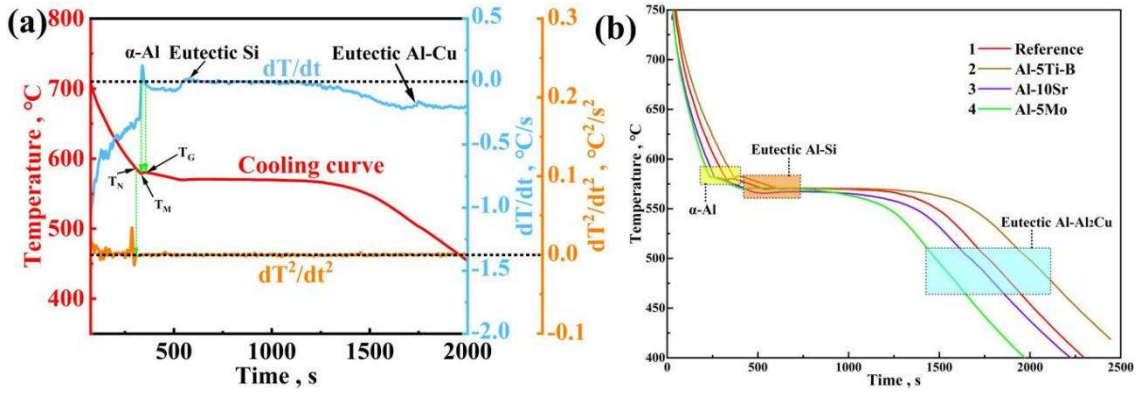

Fig. 1 - (a) Cooling curve, first derivative and second derivative curves of ADC12 alloy indicating the three main phase reactions, (b) Cooling curves of ADC12 with different trace elements.

In summary, thermal analysis is mainly applied to the solidification process of the alloy. The addition of A1-5Ti-1B, Sr and Mo has a certain influence on the solidification characteristic parameters of primary α-Al, eutectic silicon and eutectic copper in ADC12 alloy. In the study, the relationship between alloy elements and solidification characteristic parameters can be established to provide reference for optimizing the influence of alloy elements on the microstructure and properties of the alloy.

REFERENCES

[1] Emadi D, Whiting L V, Nafisi S. Application of thermal analysis in quality control of solidification process. Journal of Thermal Analysis and Calorimetry, 2005, 81, pp.235-42.

[2] Mackay R I, Djurdjevic M B. Effect of cooling rate on fraction solid of metallurgical reactions in 319 alloy. Transactions of the American Foundry Society, 2000, 108, pp.521-530.

[3] Farahany S, Ourdjini A, Idris M H. The usage of computer-aided cooling curve thermal analysis to optimise eutectic refiner and modifier in Al-Si alloys. Journal of thermal analysis and calorimetry, 2012, 109, pp.105-111.

[4] Farahany S, Ourdjini A, Abu Bakar T A. A new approach to assess the effects of Sr and Bi interaction in ADC12 Al-Si die casting alloy. Thermochimica Acta, 2014, 575, pp.179-187.

Proceedings IRF2025: 8th International Conference on Integrity-Reliability-Failure
In Engineering, Materials, Manufacturing and Biomechanics. Porto 15-18 July 2025
DOI: https://doi.org/10.24840/978-972-752-323-8

PAPER REF: 22404

CONTROL OF THE COMPOSITION OF BIOCERAMICS - COMPOSITE STRUCTURAL ABUTMENTS - USED IN DENTISTRY

Cirlene Fourquet Bandeira(*), Carla Cristina Guimarães Nogueira, Renata Martins Parreira, Sérgio Roberto Montoro, Izabel de Oliveira da Mota

UNIFOA/MeMat, Volta Redonda University Center, Volta Redonda, Brazil
(*)*Email:* cirlenefourquet@yahoo.com.br

ABSTRACT

To ensure the reproducibility of the results, strict quality control is required in sample preparation. However, these analysis methods are generally expensive and complex. In order to reduce the time, the amount of sample required for analysis, the cost and ensure efficiency in the methodology, an approach was taken using thermogravimetric analysis (TGA) to control the composition and degradation temperature of ceramic pieces (Zirconia with stearic acid - 40%) bound with high and low densities polyethylene (HDPE and LDPE) and paraffin (60%). This makes it possible to control the percentage of zirconia through the residue obtained after heating and to determine, quickly and at a low cost, the initial degradation temperature (Ti) of the binders, which in this study are 196°C (Stearic acid and paraffin), 282°C (HDPE and paraffin) and 232°C (1st Event) and 447°C (2nd Event) (paraffin, HDPE and LDPE).

Keywords: Zirconia, HDPE and LDPE, paraffin, TGA, prosthetic rehabilitation.

INTRODUCTION

Zirconia is a bioceramic used in dental processes, especially in prosthetic applications. For the production of these parts, injection molding of ceramic powders is the most commonly technique used because it allows the fabrication of complex structures at a low cost. However, due to the weak cohesiveness and low plasticity of the ceramic material, it is necessary to use binders or adhesive to favor molecular interactions and promote processability in all stages of production until the final sintered parts. Therefore, the composition of the mixture is of paramount importance (Belo et al., 2013; He et al., 2017; Nogueira, 2024). For this purpose, the compositions of the materials with and without the addition of binders were analyzed to evaluate the zirconia content and the temperature at the beginning of degradation through the TGA technique.

RESULTS AND CONCLUSIONS

The results of all triplicates were consistent with each other. In the case of residue, the coefficient of variation (CV) is less than 5%. Furthermore, the value of the calculated Student's t-test distribution is lower (9.925) than the tabulated t-value (9.2901), which indicates that the theoretical value is within the permitted variation range with a 99% confidence level; therefore, there is no statistically significant difference between the mass used and the established one (Bandeira, 2015).

Another important point (Table 1) is that stearic acid and paraffin present an initial degradation temperature (Ti), in a single stage, of 196.0°C, while the paraffin and HDPE mixture, also degraded in a single stage, has a Ti of 282.4°C. In this case, paraffin and HDPE degrade

concomitantly, with the highest percentage of loss occurring at approximately 490°C. In the case of the paraffin, HDPE and LDPE mixture, the formation of two decay stages is due to the degradation of HDPE and LDPE, which, despite having similar degradation ranges, have different crystallinities, and therefore different Ti, and an initial degradation temperature of 232°C (Ti- 1st Event) and 447°C (Ti- 2st Event) (Euzébio Jr., 2017).

In this way, it is possible to determine the percentage of zirconia through the proposed methodology, as well as the initial degradation temperatures of the mixtures, quickly and at a low cost, since at 700°C, the binders are eliminated.

Table 1 - Results obtained using the thermogravimetric analysis (Authors).

Composition	Stage	Ti (ºC) Event 1	Ti (ºC) Event 2	Mass loss (%) Event 1	Mass loss (%) Evento 2	Residue (%)
Zirconia – 40% Stearic acid – 4% Paraffin – 56%	1	196.0±6.6	---	44.56±0.58	---	52.39±2.31
HDPE – 44% Paraffin – 56%	1	282.4±9.6	---	99.99±0.01	---	0.01±0.01
HDPE – 33% LDPE – 11% Paraffin – 56%	2	232.4±3.1	446.6±2.6	54.22±0.84	45.78±0.84	0.01±0.01

REFERENCES

[1] Belo Y D, et al. Yttria-stabilized tetragonal zirconia: mechanical behavior, adhesion and clinical longevity. Ceramics, 2013, 59, p. 352 (in Portuguese).

[2] He J., et al. Investigation of inhomogeneity in powder injection molding of nano zirconia. Powder Technology, 2017, 17, pp. 31035-5.

[3] Nogueira CCG. Characterization and selection of binders for production of aesthetic temporary zirconia abutments for implant-based prosthesis using the injection molding technique. 2024, Dissertation (Professional Master's Degree in Materials) – UniFOA – Volta Redonda - Brazil, 2024, 67p. (in Portuguese).

[4] Bandeira CF. Obtaining and characterizing benzoxazine/carbon fiber composites. 2015, Thesis (PhD in Mechanical Engineering) – UNESP–FEG – Guaratinguetá - Brazil, 2015, 206p. (in Portuguese).

[5] Euzébio Jr. SH. Influence of organic waxes on the properties of LDPE tubular films. Dissertation (Master in Engineering) – UFRGS – Porto Alegre - Brazil, 2017, 91p. (in Portuguese).

Proceedings IRF2025: 8th International Conference on Integrity-Reliability-Failure
In Engineering, Materials, Manufacturing and Biomechanics. Porto 15-18 July 2025
DOI: https://doi.org/10.24840/978-972-752-323-8

PAPER REF: 22405

MECHANICAL EVALUATION OF LDPE BERTHOLLETIA EXCELSA BARK COMPOSITES

Izabel de Oliveira da Mota, Jairo de Oliveira Silva, Alexandre Alvarenga Palmeira, Ana Carolina Callegário Pereira, Sérgio Roberto Montoro, Cirlene Fourquet Bandeira(*)

UNIFOA/MeMat, Volta Redonda University Center, Volta Redonda, Brazil
(*)*Email:* cirlene.bandeira@foa.org.br

ABSTRACT

Aiming to reduce environmental impacts, several "green" composites have been developed. Among them, thermoplastic materials with reinforcement from agribusiness have stood out. However, these materials need to be mechanically analyzed to determine their potential and applicability. In order to evaluate this property, mixtures of LDPE (low-density polyethylene) and Bertholletia excelsa bark were made in proportions of 10%, 20% and 30% to be compared with the pure material. This made it possible to obtain a composite that presented an increase in the elastic modulus and yield stress with the addition of reinforcement compared to the pure polymer. However, with the increase in the percentage of biomass, there was a decrease in the maximum stress, thus presenting a non-linear mechanical behavior. The composites obtained can be used in the automotive sector or in boxes and will contribute to reducing the use of oil and the disposal of waste from the agro-industry.

Keywords: Brazil nuts, green composites, agribusiness, reuse, biomass.

INTRODUCTION

Bertholletia excelsa or Brazil nut is a plant native to the Amazon region with great economic importance. Its fruits, called ouriços, weigh about 2 kg and only the nuts are edible, with about 90% of the total being discarded. In an attempt to reinsert this material into the production cycle, green composites using thermoplastic matrix (LDPE) that has low cost and easy processability were manufactured and injected to obtain the test specimens (Carvalho, 2019; Silva, 2024). However, to determine its applicability and behavior, mechanical tensile tests were performed. For this purpose, three families of composites (10, 20 and 30%) were tested and the result compared with the pure material worked under the same conditions.

RESULTS AND CONCLUSIONS

The shells were cleaned, dried, crushed and then sieved, obtaining a biomass with particle size lower than 50 meshes. The samples were then weighed in the appropriate proportions for the composition of the three families and mixed in a thermokinetic mixer (Dryzer). These mixtures were then injected (EMIC, with a 5 kN load cell at 1.4 mm.min-1), forming the six specimens for each tensile test (ASTM D 638, 2014). The tests (Table 1) show that LDPE has a yield stress of 2.90 ± 0.32 MPa, being the least resistant material to yielding. The incorporation of fibers into the composite progressively increases the yield stress, which is related to the presence of this material that acts as a reinforcing agent in the composite, improving the material's resistance to initial plastic deformation due to its superior rigidity and the effect of transferring stresses from the matrix to the fiber. The continuous increase with the addition of fiber,

indicates good adhesion between the polymer matrix and the fibers, which is crucial for the efficiency of the composite (Callister Jr.; Rethwisch, 2021). At maximum stress, the materials exhibit varied behaviors in relation to pure LDPE. This behavior may be due to several factors. Therefore, the increase with 10% fiber can be attributed to moderate reinforcement of the matrix. However, with an increase in the fiber fraction (20% and 30%), there is a reduction in maximum stress, possibly due to fiber agglomerates and their poor dispersion, resulting in stress concentration points, composite fragility due to a high percentage of fibers that lead to a reduction in the ductility of the matrix, making the material more susceptible to fracture, or structural discontinuity due to imperfect adhesion between matrix and fiber that can create weak interfaces that compromise the overall strength (Callister Jr.; Rethwisch, 2021; Silva, 2024).

However, composites show a significant increase in elastic modulus with the addition of fiber, which reflects an increase in the stiffness of the materials. This increase is expected, since fibers have a higher modulus of elasticity compared to the polymer matrix. This results in a composite that is more resistant to elastic deformation. However, the proportional increase in fiber content also highlights the importance of uniform dispersion and fiber-matrix adhesion, which ensure good stress transfer. This behavior makes composites more suitable for applications that require greater rigidity (Callister Jr.; Rethwisch, 2021; Silva, 2024).

Therefore, it is possible to conclude that the addition of fibers improves the yield stress and elastic modulus of composites, making them stronger and stiffer, that the maximum stress shows a non-linear behavior, with a slight improvement at low fiber contents and a reduction at high contents, probably due to dispersion or adhesion problems, and that composites with intermediate fiber contents (~10%-20%) can present the best balance between strength and ductility, while composites with 30% fiber are stiffer but less resistant to maximum load.

Table 1 - Results of tensile tests of composites (Authors).

Material	Yield Stress (MPa)	Maximum Stress (MPa)	Elastic Modulus (MPa)
LDPE	2.90 ±0.32	10.18 ±0.27	35.19 ±1.14
LDPE 10% fiber	3.58 ±0.24	10.51 ±0.45	48.27 ±0.91
LDPE 20% fiber	3.99 ±0.16	9.86 ±0.17	57.30 ±2.34
LDPE 30% fiber	4.23 ±0.15	9.22 ±0.22	64.55 ±3.65

REFERENCES

[1] Carvalho JAL. Benzoxazine resin composites / biomass extracted from açaí washing residue: Obtaining and characterization. Dissertation (Professional Master's Degree in Materials) – UniFOA – Volta Redonda - Brazil, 2019, 103p. (in Portuguese).

[2] Silva JAL. Obtaining and characterization of low-density polyethylene composites reinforced with biomass from the bark of Bertholletia excelsa. Dissertation (Professional Master's Degree in Materials) – UniFOA – Volta Redonda - Brazil, 2024, 103p. (in Portuguese).

[3] American Society for Testing and Material. ASTM D 638: standard test method for tensile properties of plastics. U.S., 2014.

[4] Callister Jr. WD; Rethwisch DG. Materials science and engineering: an introduction. 10th ed. - Rio de Janeiro: LTC, 2021 (in Portuguese).

Proceedings IRF2025: 8th International Conference on Integrity-Reliability-Failure
In Engineering, Materials, Manufacturing and Biomechanics. Porto 15-18 July 2025
DOI: https://doi.org/10.24840/978-972-752-323-8

PAPER REF: 22425

COAXIAL STRUCTURAL BATTERIES: A NEW APPROACH FOR THE NEXT GENERATION OF ENERGY STORAGE

Beatriz Arouca Maia[1,2,3,4], M. Helena Braga[2, 3,4(*)]

[1]INEGI, Institute of Science and Innovation in Mechanical and Industrial Engineering, 4200-465 Porto, Portugal
[2]FEUP, Engineering Faculty, University of Porto, 4200-465 Porto, Portugal
[3]MatER - Materials for Energy Research Laboratory, Engineering Faculty, University of Porto, Portugal
[4]LAETA -Associated Laboratory of Energy, Transports and Aeronautics, Portugal
[(*)]*Email:* mbraga@fe.up.pt

ABSTRACT

The global push for a green and sustainable energy economy has intensified the focus on developing and optimizing advanced battery systems. This study advances Na^+ all-solid-state structural batteries, combining the high ionic conductivity of $Na_{2.99}Ba_{0.005}OCl$ with the mechanical strength of CFRP. The resulting coaxial cells are cost-effective, sustainable, and durable, offering a promising solution for energy storage in modern transportation systems.

Keywords: Structural batteries, all-solid-state electrolyte, energy storage systems.

INTRODUCTION

Recognized as a cornerstone technology by the European Union and numerous governments and organizations worldwide, batteries play a pivotal role in addressing human-driven climate change and achieving net-zero CO_2 emissions targets (Titirici et al., 2024). Looking ahead, advanced, optimized, and eco-friendlier energy storage solutions have become the driving force behind modern transportation systems. In this context, materials scientists have been inspired to enhance battery functionality by integrating multiple primary roles, leading to the development of multifunctional devices that combine a perspective on energy storage capabilities with mechanical performance - known as structural batteries. The NGS – New Generation Storage project aligns with the EU's energy transition strategy for 2050 by enhancing Na^+ all-solid-state structural batteries through systematic studies of component interactions and scalability. A key innovation lies in the coaxial battery geometry first developed by Braga's group, which combine the high electrochemical performance from the Braga's glassy electrolyte $Na_{2.99}Ba_{0.005}OCl$ (Danzi et al., 2022; Gomes et al., 2024) with the high mechanical performance of carbon-fiber reinforced polymer (CFRP) composites (Valente et al., 2023). This electrolyte exhibits exceptional properties, including an ionic conductivity of 25 $mS.cm^{-1}$ and a dielectric constant (ε_r) of 10^8 at room temperature, enabling the fabrication of electrodeless batteries where only current collectors (e.g., copper, carbon, aluminum, or zinc) are employed as electrodes. This work explores the effect of aluminum rod diameters (4 mm, 6 mm, and 8 mm) on the electrochemical behavior of coaxial cells, maintaining other parameters constant (cell diameter ~10 mm, effective length ~10 cm).

RESULTS AND CONCLUSIONS

Coaxial cells are constituted by an aluminium rod current collector, and a copper foil current collector which are separated by the glassy electrolyte $Na_{2.99}Ba_{0.005}OCl$. To provide mechanical robustness, a CFRP laminate is wrapping the structure, as suggested in Figure 1.

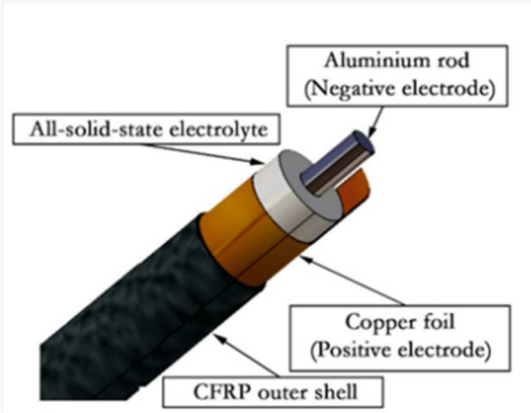

Fig. 1 - Schematic representation of a structural coaxial cell.

The Nyquist plots revealed that a 6 mm aluminum rod minimized internal resistance. When connected to a 10 kΩ resistor for 24 hours, the cell delivered an output voltage of 1.1 V after a 3-minute charge at 1.5 V (< 2.8 mA), demonstrating a discharge plateau voltage between 0.85–1.1 V over 32 days and sustaining this plateau for over 40 days. These cells are safe, cost-effective (< 10 €/kWh), sustainable, and mechanically robust, offering a viable alternative for energy storage in multifunctional applications, particularly in transportation.

REFERENCES

[1] Danzi, F.; Valente, M.; Terlicka, S.; Braga, M.H. (2022). Sodium and potassium ion rich ferroelectric solid electrolytes for traditional and electrode-less structural batteries. APL Materials, 10(3), 031111. https://doi.org/10.1063/5.0080054.

[2] Gomes, B.M.; Ribeiro Moutinho, J.F.; Braga, M. H. (2024). A perspective on the building blocks of a solid-state battery: from solid electrolytes to quantum power harvesting and storage. J. Mater. Chem. A, 12(2), 690–722. https://doi.org/10.1039/D3TA04228F.

[3] Titirici, M.: Johansson, P.; Crespo Ribadeneyra, M.; Au, H.; Innocenti, A.; Passerini, S.; Petavratzi, E.; Lusty, P.; Tidblad, A.A.; Naylor, A.J.; Younesi, R.; Chart, Y.A.; Aspinall, J.; Pasta, M.; Orive, J.; Babulal, L.M.; Reynaud, M.; Latham, K.G.; Hosaka, T.; Antuñano, N. (2024). 2024 roadmap for sustainable batteries. Journal of Physics: Energy, 6(4), 041502. https://doi.org/10.1088/2515-7655/ad6bc0.

[4] Valente, M.; Silva, S.; Braga, M. (2023). Cork: Enabler of sustainable and efficient coaxial structural batteries. Heliyon, 9, e15063. https://doi.org/10.1016/j.heliyon.2023.e15063.

Proceedings IRF2025: 8th International Conference on Integrity-Reliability-Failure
In Engineering, Materials, Manufacturing and Biomechanics. Porto 15-18 July 2025
DOI: https://doi.org/10.24840/978-972-752-323-8

PAPER REF: 22433

STUDY ON THE MECHANICAL PROPERTIES AND DAMAGE MECHANISM OF C/C-SIC COMPOSITES FOR HIGH-SPEED TRAIN BRAKE DISCS

Xiangli Zeng, Wenjing Wang(*), Junsheng Qu, Ruiguo Yan, Yiming Shangguan

School of Mechanical and Electronic Control Engineering, Beijing Jiaotong University, Beijing 100044, China
(*)*Email: wjwang@bjtu.edu.cn*

ABSTRACT

Due to their exceptional low density, superior wear resistance and favorable thermodynamic characteristics, C/C-SiC composites have emerged as the prime choice for lightweight high-speed train brake discs. In this study, the mechanical properties of 2.5D needled C/C-SiC composites under tensile, compression, and shear loading at both room and elevated temperatures were explored. Furthermore, the changes in material properties subsequent to a 1:1 dynamic fatigue test were analyzed. The results indicate that the in-plane tensile properties of the material initially increase and subsequently decrease with temperature. Cracks are present within the C/C-SiC after the test. The interlayer properties of the material decreased with increasing temperature, whereas the in-plane properties either increased or remain constant. Material fracture is predominantly caused by matrix cracks and the propagation of composite cracks. The initiation of fiber debonding predominantly occurs along the fiber cracks and the fiber-matrix interface.

Keywords: C/C‑SiC, damage mechanism, high-speed trains, composite brake discs.

INTRODUCTION

Due to their excellent properties, carbon-ceramic composites have considerable potential in the braking systems of high-speed trains (Li Z, 2016). When 2.5D C/C-SiC is subjected to uniaxial loading, the microscopic damage involves crack propagation and debonding of the carbon fibers and SiC shell (Dalmaz A, 1999). The brake disc endured 618 braking cycles under various working conditions. The test essentially simulated 618 thermal cycles with a maximum temperature of 889 ° C. The material properties of the disc change significantly when the surface temperature is high during braking. The C/C-SiC properties before and after the fatigue test were analyzed. Combined with the results of the CT scan and SEM analysis, the damage mechanisms such as internal crack propagation, fiber debonding, and matrix cracking of C/C-SiC were explored.

RESULTS AND CONCLUSIONS

Tests were performed in accordance with ASTM, GJB and GB/T standards, and data acquisition was performed on an Instron 5982 universal materials testing machine with a DIC test system. High-temperature in-plane tensile tests were performed on ZWICK/Z100 machines at temperatures of 200 ° C, 400 ° C, 600 ° C and 800 ° C. Figure 1 shows the test setup used and some of the results.

The results of the mechanical property at room temperature are shown in Table 1. A comparison of the material properties before and after the test revealed that the properties of the materials

deteriorated among the layers after use. However, the performance in the plane has improved or remained unchanged. As shown in Figure 1(e), the in-plane tensile strength of the C/C-SiC composites first increased but then decreased with increasing temperature, reaching a maximum value of 148.12 MPa at 200 ° C and only 15% of the normal temperature at 800 ° C.

A high-resolution CT scan was conducted on the material after the fatigue test, as depicted in Figure 2(a). After actual use, the carbon ceramic material exhibited matrix cracks and fiber cracks, with composite cracks that penetrated both the fibers and the matrix simultaneously. Figure 2(b) reveals cracking, slipping, debonding of the fiber bundles, and cracking of the matrix. Material fracture was caused by matrix cracks and composite crack propagation. The fiber bundle debonding primarily along the position of fiber cracks and the interfaces between the fiber and the matrix.

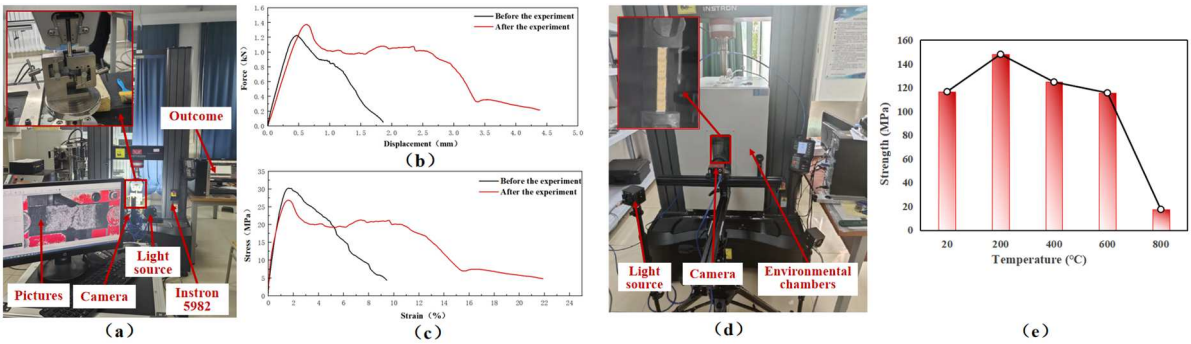

Fig. 1 - Materials testing: (a) DIC testing system (interlayer shear); (b) load-displacement results; (c) stress-strain results; (d) high-temperature tensile equipments; (e) results of tensile strength at different temperatures.

Table 1 - Mechanical property test results.

Strength test	New (MPa)	Used (MPa)	Strength test	New (MPa)	Used (MPa)
In-plane tensile	116.60	116.73	Interlayer tensile	13.16	9.14
In-plane shear	55.23	59.12	Interlayer shear	33.77	30.48
In-plane compressive	195.35	216.42	Interlayer compressive	315.29	258.26

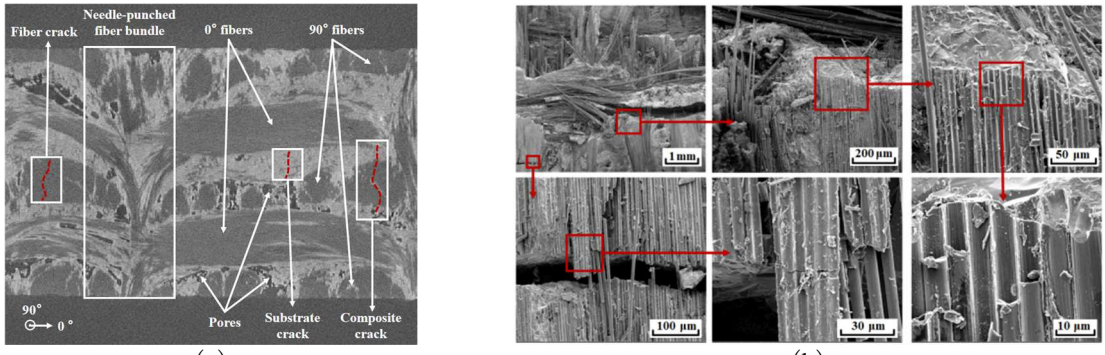

Fig. 2 - Microstructure: (a) CT scan image and (b) SEM results of in-plane tensile fractures.

REFERENCES

[1] Li Z, Xiao P, Zhang B G, et al. Preparation and Dynamometer Tests of 3D Needle-Punched C/C-SiC Composites for High-Speed and Heavy-Duty Brake Systems. International Journal of Applied Ceramic Technology, 2016, 13, pp. 423-433.

[2] Dalmaz A, Reynaud P, Rouby D, et al. Cyclic fatigue behaviour at room temperature and at high temperature under inert atmosphere of a C SiC multilayer composite. High Temperature Ceramic Matrix Composites III, 1999, 164-1, pp. 325-328.

Proceedings IRF2025: 8th International Conference on Integrity-Reliability-Failure
In Engineering, Materials, Manufacturing and Biomechanics. Porto 15-18 July 2025
DOI: https://doi.org/10.24840/978-972-752-323-8

PAPER REF: 22438

A PERSPECTIVE ON CATHODE MATERIALS FOR ELECTRICAL VEHICLE INDUSTRY

José Maria Pinheiro[1,2], Beatriz Gomes[1,2], M. Helena Braga[1,2(*)]

[1]LAETA, University of Porto, Engineering Faculty, 4200-465 Porto, Portugal
[2]MatER - Materials for Energy Research Laboratory, Engineering Faculty, University of Porto, Portugal
[(*)]*Email :* mbraga@fe.up.pt

ABSTRACT

The electric vehicle (EV) market has experienced exponential growth, becoming a centrepiece in the global effort to reduce carbon dioxide emissions and fight climate change. The success of this market depends on advancements in battery technology to deliver higher energy density, greater capacity, longer lifespans, and affordability. A critical component of all battery systems—whether conventional lithium-ion batteries (LIBs) or next-generation solid-state batteries— is the cathode. Comprising the active material, binder, and conductive agent, the cathode plays a pivotal role in defining the specific capacity and energy density of a battery, while also representing a significant fraction of the overall cost [1]. This underscores the need for continuous innovation to achieve a balance between performance and cost-effectiveness. As of 2022, the EV industry has been dominated by three primary active materials: NMC (Nickel-Manganese-Cobalt), LFP (Lithium Iron Phosphate), and NCA (Nickel-Cobalt-Aluminum) [2–4]. In this poster, the authors present a comprehensive perspective on the development and selection of cathode materials for solid-state batteries, examining their alignment with evolving industry demands and addressing key challenges. Furthermore, it is emphasized the importance of adopting a life cycle perspective to ensure batteries serve as a truly sustainable energy storage solution and follow the environmental guidelines of the European Union, from the extraction of raw materials to end-of-life management.

Keywords: Cathode, Electric Vehicles, Solid-State, Batteries, Sustainability.

INTRODUCTION

The electric vehicle (EV) market has seen rapid growth, attracting substantial investment and becoming a central element in efforts to reduce carbon emissions and combat climate change. The market's success depends on the development of batteries with high energy density, long lifespan, capacity, and affordability. The performance of these batteries largely depends on three key components: the cathode, anode, and electrolyte. A major milestone in battery technology was the birth of solid-state batteries (SSBs). Unlike traditional lithium-ion batteries (LIBs), which use liquid electrolytes, SSBs utilize solid-state electrolytes that are non-flammable (especially the inorganic) and more resistant to dendrite formation, greatly reducing the risk of explosions. These solid electrolytes also offer a broader electrochemical window, making them better suited for high-energy-density cathodes and anodes [5,6] .For high-energy-density batteries, the development of stable cathodes with increased specific capacity is crucial. Cathodes are composed of three main parts: active material, binder, and conductive agent. The active material is particularly important as it determines the cathode's capacity. By 2022, three types of active materials dominated the EV industry: NMC, LFP, and NCA [2–4]. Among them, NMC stands out due to its excellent balance of energy density, cycle life, and thermal stability. NMC's structure can incorporate various combinations of transition metals—nickel (Ni), cobalt

(Co), and manganese (Mn)—each contributing different performance benefits. Optimizing these metals' proportions is essential to meet the EV industry's ambitious targets and reduce its environmental footprint [7]. However, a major challenge is balancing performance, stability, cost, and sustainability. NMC cathodes currently rely on cobalt (Co). Besides its toxicity, cobalt is primarily sourced from the Democratic Republic of Congo, where its extraction is linked to exploitative labor practices and unsustainable economic conditions [8,9]. As a result, there is growing pressure to reduce cobalt content in cathodes [10]. Additionally, the use of PVDF, a common binder in cathode production, is being phased out in the European Union due to environmental concerns [11]. In large-scale cathode synthesis, it is also critical to select eco-friendly solvents to mitigate environmental impact. To truly position batteries as sustainable energy storage solutions, their entire lifecycle must be considered—from mineral extraction to disposal. The end-of-life management of batteries is particularly important, as they contain materials that are difficult to dispose of safely. Improper storage and disposal of batteries can lead to environmental hazards, including contamination of water systems due to their toxicity and flammability. In recent years, however, strategies for recycling or reusing batteries and their components have gained traction, fueling the development of a circular economy in the industry [12].

REFERENCES

[1] A. Tron; R. Hamid; N. Zhang; A. Beutl Rational Optimization of Cathode Composites for Sulfide-Based All-Solid-State Batteries. Nanomaterials 2023, 13, 327.

[2] Celadon, A.; Sun, H.; Sun, S.; Zhang, G. Batteries for Electric Vehicles: Technical Advancements, Environmental Challenges, and Market Perspectives. SusMat 2024, doi:10.1002/sus2.234.

[3] Mohammadi, F.; Saif, M. A Comprehensive Overview of Electric Vehicle Batteries Market. e-Prime - Advances in Electrical Engineering, Electronics and Energy 2023, 3.

[4] Salgado, R.M.; Danzi, F.; Oliveira, J.E.; El-Azab, A.; Camanho, P.P.; Braga, M.H. The Latest Trends in Electric Vehicles Batteries. Molecules 2021, 26.

[5] Huo, S. et al.. Challenges of Polymer Electrolyte with Wide Electrochemical Window for High Energy Solid-State Lithium Batteries. InfoMat 2023, 5.

[6] Gomes, B.M.; Ribeiro Moutinho, J.F.; Braga, M.H. A Perspective on the Building Blocks of a Solid-State Battery: From Solid Electrolytes to Quantum Power Harvesting and Storage. J Mater Chem A Mater 2023, 12, 690–722.

[7] Manthiram, A. A Reflection on Lithium-Ion Battery Cathode Chemistry. Nat Commun 2020, 11.

[8] Faber, A.; Krause, B.; Sánchez de la Sierra, B. UC Berkeley CEGA White Papers Title Artisanal Mining, Livelihoods, and Child Labor in the Cobalt Supply Chain of the Democratic Republic of Congo Permalink Https://Escholarship.Org/Uc/Item/17m9g4wm Publication Date;

[9] Schleich, K. Unveiling the Dark Side of Innovation: Sustainability, Cobalt Mining, and Modern-Day Slavery. SMU Science and Technology Law Review 2024, 27, 135, doi:10.25172/smustlr.27.1.8.

[10] Kim, Y.;et al., A. Cobalt-Free, High-Nickel Layered Oxide Cathodes for Lithium-Ion Batteries: Progress, Challenges, and Perspectives. Energy Storage Mater 2021, 34, 250–259.

[11] PFAS Restriction Proposal RECHARGE Statement for 2 Nd Call for Evidence-October 2021.

[12] Tembo, P.M.; Dyer, C.; Subramanian, V. Lithium-Ion Battery Recycling—a Review of the Material Supply and Policy Infrastructure. NPG Asia Mater 2024, 16.

Proceedings IRF2025: 8th International Conference on Integrity-Reliability-Failure
In Engineering, Materials, Manufacturing and Biomechanics. Porto 15-18 July 2025
DOI: https://doi.org/10.24840/978-972-752-323-8

PAPER REF: 22450

ENHANCING SOLID-STATE STRUCTURAL BATTERY PERFORMANCE WITH NANOSTRUCTURED COPPER CURRENT COLLECTORS

Tomás Prior[1,2], Ângela Freitas[1,2,3], Beatriz Gomes[1,2,3], Beatriz Maia[1,2,3,4], Manuela Baptista[1,2,3], Hugo Lebre[1,2], Nuno Guerreiro[1,2,3], Joana Figueira[5], Joana Vaz Pinto[5], David Carvalho[5], Rodrigo Martins[5], M. Helena Braga[1, 2, 3(*)]

[1]Engineering Faculty, University of Porto, 4200-465 Porto, Portugal
[2]MatER – Materials for Energy Research Laboratory, Engineering Faculty, University of Porto, Portugal
[3]LAETA –Associated Laboratory of Energy, Transports and Aeronautics, Portugal
[4]INEGI, Institute of Science and Innovation in Mechanical and Industrial Engineering, 4200-465 Porto, Portugal
[5]i3N/CENIMAT, and CEMOP/UNINOVA, NOVA School of Science and Technology, Caparica, Portugal
[(*)]*Email:* mbraga@fe.up.pt

ABSTRACT

Batteries are pivotal in the transition to renewable energy, with current collectors playing a crucial role in optimizing battery efficiency. This study, part of the New Generation Storage (NGS) PRR project, explores the enhancement of solid-state structural battery performance through the incorporation of nanostructured copper current collectors (CCs). The initial stages, conducted by a collaborating group, involved coating PEN substrates with parylene-C and structuring them using Langmuir-Blodgett deposition of polystyrene spheres followed by O2 plasma etching. These micro-structured substrates were subsequently coated with copper through thermal evaporation. Our research focuses on the topological characterization of these copper CCs and the electrochemical characterization of sodium solid-state batteries that incorporate them.

Keywords: NGS, current-collectors, nanostructured, solid-state, structural batteries.

INTRODUCTION

Batteries are essential in the transition to renewable energy sources, serving critical roles across various applications, from grid storage solutions to electric vehicles. As the demand for more efficient and integrated energy storage solutions increases, the development of structural batteries, which combine load-bearing capabilities with energy storage, emerges as a particularly innovative area. These batteries serve a dual purpose: they provide structural support while also functioning as power sources, Figure 1. This dual functionality reduces the number of components and overall weight, making them ideal for applications where weight is a critical factor in the [1], [2]. In structural batteries, the function and efficiency of current collectors are of paramount importance. Current collectors influence battery performance significantly by affecting the interface connections between electrodes and electrolytes. The introduction of nanostructured current collectors can enhance these connections, particularly with solid-state electrolytes, potentially improving efficiency and battery life.

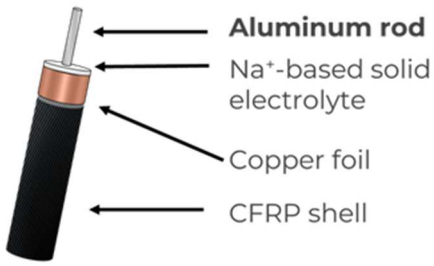

Fig. 1 - Representation of a coaxial structural battery with major components highlighted.

RESULTS AND CONCLUSION

The herein presented study was conducted under the New Generation Storage (NGS) PRR project and explores the enhancement of solid-state structural battery performance through the incorporation of nanostructured copper current collectors (CCs). These nanostructures aim to improve interface connections between the sodium ferroelectric solid-state electrolyte and the copper CCs, which lead to enhanced battery performance. The initial stages of this project involved collaborative efforts where PEN substrates were coated with parylene-C and structured using Langmuir-Blodgett deposition of polystyrene spheres, followed by O2 plasma etching to create micro-structures. These substrates were then coated with copper through thermal evaporation to produce the current collector samples. This work focuses on the detailed characterization and performance evaluation of copper current collectors (CCs) in solid-state batteries. Atomic Force Microscopy (AFM) is used to analyze surface topology, total surface area, and surface potential, Figure 2.

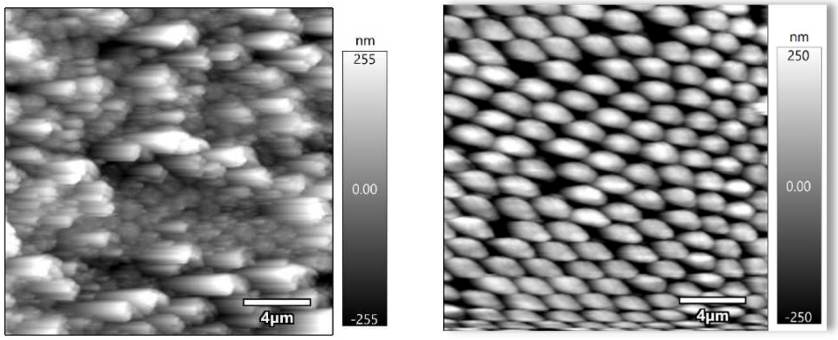

Fig. 2 - Topological height images of nanostructured CC's with different etching times obtained with AFM.

Following the characterization, the copper current collectors are integrated into a real battery system. Each battery is constructed with two distinct current collectors: one made of aluminum and the other of nanostructured copper. These collectors are positioned opposite each other within the battery, separated by a sodium-based ferroelectric solid-state electrolyte[3],[4]. The setup is specifically designed to isolate and underscore the effects of different current collector materials, allowing for a clear comparison of traditional versus nano-engineered designs. Battery testing procedures include Cyclic Voltammetry, Potentiostatic Electrochemical Impedance Spectroscopy, and long-term charge and discharge cycles to evaluate the performance and stability of the batteries. Finally, post-mortem analyses such as EDM/XPS are conducted to study the interface formation and degradation processes, providing insights into the electrochemical interfaces and their impact on battery efficiency and lifespan.

This comprehensive approach highlights the potential of nano-engineered surfaces and structural battery configurations in enhancing the performance and durability of batteries, which are crucial for advancing renewable energy technologies.

REFERENCES

[1] F. Danzi, P.P. Camanho, M.H. Braga, "An All-Solid-State Coaxial Structural Battery Using Sodium-Based Electrolyte," Molecules, vol. 26, no. 17, p. 5226, Aug. 2021, doi: 10.3390/molecules26175226.

[2] M. Valente, S.M. Silva, M.H. Braga, "Cork: Enabler of sustainable and efficient coaxial structural batteries," Heliyon, vol. 9, no. 4, p. e15063, Apr. 2023, doi: 10.1016/j.heliyon. 2023.e15063.

Proceedings IRF2025: 8th International Conference on Integrity-Reliability-Failure
In Engineering, Materials, Manufacturing and Biomechanics. Porto 15-18 July 2025
DOI: https://doi.org/10.24840/978-972-752-323-8

PAPER REF: 22451

3D INCONEL 625 SODIUM ELECTROLYTE ENERGY STORAGE DEVICE

M. Helena Braga[1,2,3(*)], Manuela C. Baptista[1,2,3], Antonio B. Vale[1,2], Jose M. Costa[2,3], Manuel F. Vieira[2,3]

[1]Materials for Energy Research Laboratory, Faculty of Engineering, University of Porto, Porto, Portugal
[2]Faculty of Engineering, University of Porto, Porto, Portugal
[3]LAETA, Institute of Science and Innovation in Mechanical and Industrial Engineering, Porto, Portugal
[(*)]*Email:* mbraga@fe.up.pt

ABSTRACT

Inconel 625 has been widely used in several applications due to its resistance to corrosion, oxidation protection in reducing environments, and mechanical strength. Performs well in environments containing chlorides, strong acids, and seawater. It shows good weldability and the production of functional components by Additive Manufacturing (AM) [1]. In energy storage applications, it has applications in flow batteries (e.g., vanadium redox flow batteries), which use aggressive electrolytes. Inconel 625's resistance to strong acids and chlorides makes it an excellent choice for (1) electrolyte containers and tanks; (2) piping and flow systems; (3) bipolar plates or current collectors exposed to corrosive environments. In battery manufacturing, particularly in lithium-ion or sodium-ion batteries, Inconel 625 may be used in machinery or systems exposed to corrosive chemicals, such as: (1) chemical reactors used for synthesizing cathode/anode materials and (2) acid-resistant processing tanks or pipelines for recycling spent batteries. Herein, we categorized electrochemically and electrostatically an Al/$Na_{2.99}Ba_{0.005}ClO$/Inconel625 3D cell containing a chloride-based alkali ferroelectric-electrolyte, $Na_{2.99}Ba_{0.005}ClO$ [2]. A caveat of the latter electrolyte is its hygroscopicity, which we tried to overcome by closing the cell in an epoxy resin enclosure. Results show a discharge voltage of 1.1 V, self-cycling with a 2.4 h period and 24 h, and self-charge of 30 mV when the cell is set to discharge with a 47 kΩ. The 3D cell was able to retain the voltage for more than 62.5 days, while the Inconel 625 performed as a current collector/cathode.

Keywords: Inconel 625, all-solid-state batteries, ferroelectric-electrolyte, Na^+-based electrode-less batteries, cathodes.

INTRODUCTION

Inconel 625 contains (in weight percent): 20-23% Cr, 8-10% Mo, 3.15–4.15% Nb + Ta, <5% Fe, <1% Co, <0.5% Mn, <0.5% Si, <0.4% Al, <0.4% Ti, <0.1% C, <0.015% P, <0.015% S, balanced with Ni. Due to its chemical composition, Inconel 625 is resistant to chlorides and seawater [3]. Therefore, here we studied Inconel, not as a container, but as a AM current collector/electrode. Our hypothesis is that the material fixes the electrode's chemical potential without reacting with the alkaline solid electrolyte. To determine if Inconel performs as a cathode or anode, we performed μm-Scanning Kelvin Probe (SKP) analysis. Then, in the face of the latter results, the second electrode was chosen. Subsequently, an Al/$Na_{2.99}Ba_{0.005}ClO$/Inconel625 3D cell was fabricated, tested, and compared to previous analyses [2].

RESULTS AND CONCLUSIONS

The results demonstrate that Inconel 625 may perform as a cathode (Figure 1). Figure 2 shows the fabrication of an Al/$Na_{2.99}Ba_{0.005}ClO$/Inconel 625 3D cell in an Ar filled glove box.

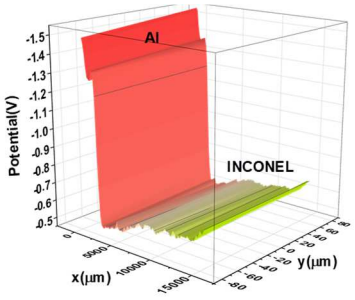

Fig. 1 - SKP analysis for Al//Inconel showing a potential difference of ~1 V and Al and Inconel 625 surface chemical potential in the Standard Hydrogen Electrode (SHE) scale.

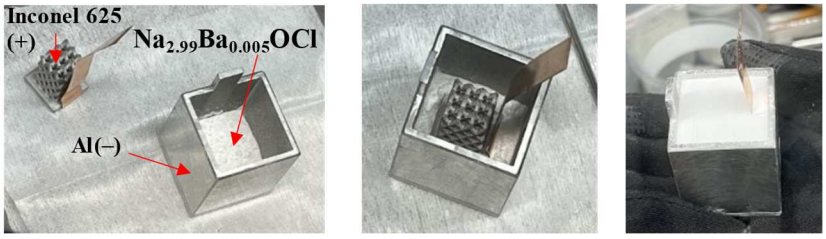

Fig. 2 - Al/$Na_{2.99}Ba_{0.005}ClO$/Inconel625 3D cell fabricated in an Ar filled glovebox.

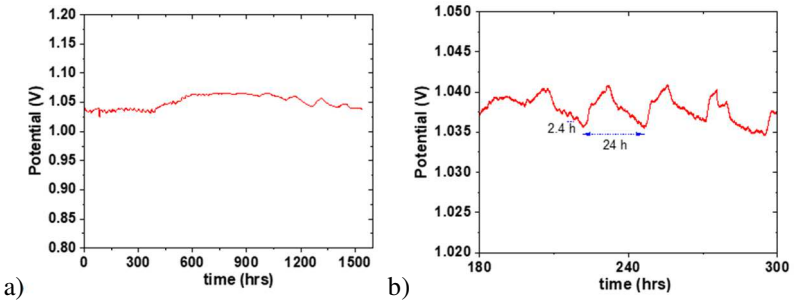

Fig. 3 - Al/$Na_{2.99}Ba_{0.005}ClO$/Inconel625 3D cell set to discharge with a 47 kΩ resistor for > 1500 hrs, showing self-cycling with two periods 2.4 and 24 h and a small self-charging effect corresponding to 30 mV observed after 350 hrs; a) full graph; b) inset.

The electrochemical analysis (Figure 3) reinforces that Inconel 625 performs as a cathode showing a potential difference (1.05 V), as expected. When set to discharge with a 47 kΩ resistor, the cell may hold the potential between 1.035 to 1.065 V for more than 62.5 days. This data shows that the Inconel 625 may fix the potential without reacting with the ferroelectric Na^+ electrolyte, which is an advantage in increasing the cells' cycle life. The electrolyte holds the capacity of the cell as it contains all mobile species [4].

REFERENCES

[1] Costa, J., et al. Additive Manufacturing: Material Extrusion of Metallic Parts. U.Porto Journal Engineering 2021, 7, 53-69, doi: https://doi.org/10.24840/2183-6493_007.003_0005.

[2] Manuela C. Baptista, et al. Adv. Funct. Mater. 2023, 2212344 (pp. 1-13).

[3] https://www.specialmetals.com/documents/technical-bulletins/inconel/inconel-alloy-625.pdf, retrieved in January 2025.

[4] M. Helena Braga, Chem. Commun. 60 (2024) 5395-5398.

Proceedings IRF2025: 8th International Conference on Integrity-Reliability-Failure
In Engineering, Materials, Manufacturing and Biomechanics. Porto 15-18 July 2025
DOI: https://doi.org/10.24840/978-972-752-323-8

PAPER REF: 22453

THERMAL CHARACTERIZATION OF PLA, ABS, PETG, AND NYLON FILAMENTS FOR 3D PRINTING APPLICATIONS

Alexandre Melo de Oliveira[1], Lindomar Matias Gonçalves[2], Amir Zacarias Mesquita[3]

[1]IFSP, Federal Institute of São Paulo, Votuporanga campus, Brazil.
[2]UNIFEI, Institute of Pure and Applied Sciences, Federal University of Itajubá, Itabira campus, Brazil
[3]CDTN, Nuclear Technology Development Center, Belo Horizonte, Brazil.
(*)*Email:* alexandre.melo@ifsp.edu.br

ABSTRACT

This study investigates the thermal characterization of PLA, ABS, PETG, and Nylon filaments, widely used in 3D printing, to understand their behavior during additive manufacturing processes. Thermogravimetry (TGA) and differential scanning calorimetry (DSC) were employed to assess key thermal properties, including thermal stability, glass transition temperatures, and melting points. The research also examined how printing temperature affects the mechanical and dimensional stability of fabricated parts. Experiments involved 23 polymer samples, including virgin and recycled PLA, to evaluate sustainability and material performance. A 3D printer equipped with precise thermal control and calibrated analytical instruments ensured accurate evaluations. Results highlighted correlations between thermal properties and the quality of printed components, providing data to optimize print settings and minimize defects. The findings contribute to advancing sustainable 3D printing practices by identifying efficient material usage and reducing waste. This project addresses industrial needs for high-quality additive manufacturing, emphasizing eco-friendly material development and the importance of standardizing thermophysical data for improved processes and products.

***Keywords**:* PLA, ABS, PETG, Nylon, thermal characterization, additive manufacturing.

INTRODUCTION

Additive manufacturing (AM), commonly known as 3D printing, has revolutionized how objects are fabricated, offering unparalleled design flexibility and material efficiency (Ambrosi; Pumera, 2016) (Atakok et al., 2022; Pakkanen et al., 2017). Among AM techniques, Fused Deposition Modeling (FDM) is widely used due to its simplicity, cost-effectiveness, and versatility (Wojtyła et al., 2017). However, optimizing material performance requires understanding the thermal properties of the polymers involved, particularly during processing (Song et al., 2016). This study focuses on four commonly used thermoplastics—PLA, ABS, PETG, and Nylon - analyzing their thermal stability and transitions using TGA and DSC. These analyses aim to provide insights into material suitability for various industrial applications, with additional emphasis on sustainability through recycled PLA studies.

RESULTS AND DISCUSSION

Experiments were conducted using 23 polymer samples, comprising 14 PLA, 7 ABS, 1 PETG, and 1 Nylon. Sample preparation included standard extrusion into filaments followed by thermal characterization. Preliminary results demonstrated that PLA exhibits excellent printability but is sensitive to thermal fluctuations, whereas ABS offers higher impact resistance

but requires precise temperature control due to its higher thermal expansion. PETG and Nylon showed intermediate characteristics, with PETG excelling in chemical resistance and Nylon offering superior flexibility.

Recycled PLA presented comparable performance to virgin PLA, though with slight reductions in mechanical properties, emphasizing its potential for sustainable applications. Numerical analyses confirmed that optimal temperature ranges for each material improved dimensional stability and minimized warping.

CONCLUSION

This study highlights the importance of thermal characterization in optimizing 3D printing processes. By correlating material properties with print performance, this research provides valuable data for selecting and processing polymers in additive manufacturing. The insights gained support the development of eco-friendly and cost-effective fabrication methods, contributing to the advancement of sustainable manufacturing practices.

Future work will focus on expanding the dataset to include additional materials and exploring the effects of hybrid material blends on performance metrics.

REFERENCES

[1] Ambrosi, A.; Pumera, M. 3D-printing technologies for electrochemical applications. Chemical Society reviews, v. 45, n. 10, pp. 2740-2755, 2016.

[2] Atakok, G.; Kam, M.; Koc, H. B. Tensile, three-point bending and impact strength of 3D printed parts using PLA and recycled PLA filaments: A statistical investigation. Journal of materials research and technology, v. 18, pp. 1542-1554, 2022.

[3] Pakkanen, J. et al. About the use of recycled or biodegradable filaments for sustainability of 3D printing. Em: Sustainable Design and Manufacturing 2017. Cham: Springer International Publishing, 2017. pp. 776-785.

[4] Wojtyla, S.; Klama, P.; Baran, T. Is 3D printing safe? Analysis of the thermal treatment of thermoplastics: ABS, PLA, PET, and nylon. Journal of occupational and environmental hygiene, v. 14, n. 6, pp. D80-D85, 2017.

[5] Song, C. et al. My smartphone knows what you print: Exploring smartphone-based side-channel attacks against 3D printers. Proceedings of the 2016 ACM SIGSAC Conference on Computer and Communications Security. New York, NY, USA: ACM, 2016.

Proceedings IRF2025: 8th International Conference on Integrity-Reliability-Failure
In Engineering, Materials, Manufacturing and Biomechanics. Porto 15-18 July 2025
DOI: https://doi.org/10.24840/978-972-752-323-8

PAPER REF: 22461

LOCAL DEFORMATION AND FAILURE OF COMPOSITES DURING SELF-PIERCING RIVETING: A CT BASED MICROSTRUCTURE INVESTIGATION

Alrik Dargel[1(*)], Johannes Gerritzen[1], Benjamin Gröger[1], Daniel Köhler[1], Malte Schlichter[2], Gerson Meschut[2], Maik Gude1[1], Robert Kupfer[1]

[1]Dresden Univ. of Tech., Institute of Lightweight Engineering and Polymer Technology, Dresden, Germany
[2]Paderborn University, Laboratory for Material and Joining Technology (LWF), Paderborn, Germany
[(*)]*Email:* alrik.dargel@tu-dresden.de

ABSTRACT

The use of continuous fiber-reinforced thermoplastics (FRTP) in automotive industry increases due to their excellent material properties and possibility of rapid processing. The scale spanning heterogeneity of their material structure and its influence on the material behavior, however, presents significant challenges for most joining technologies, such as self-piercing riveting (SPR). During mechanical joining, the material structure is significantly altered within and around the joining zone, heavily influencing the material behavior. A comprehensive understanding of the underlying phenomena of material alteration during the SPR process is essential as basis for validating numerical simulations. This study examines the material structure at ten stages of a step-setting test of SPR with two FRTP sheets with glass-fiber reinforcement. Utilizing X-ray computed tomography (CT), the damage phenomena within different areas of the setting test are analyzed three-dimensionally and key parameters are quantified. Dominating phenomena during the penetration of the rivet into the laminate are fiber failure (FF), interfiber failure (IFF) and fiber bending, while delamination, fiber kinking and roving splitting are also observed. At the final stages, the bottom layers of the second sheet collapse and form a bulge into the cavity of the die.

Keywords: Self-piercing riveting; computed tomography; thermoplastic composites; process-structure-interaction.

INTRODUCTION

The increasing use of FRTP in automotive and lightweight applications is driven by their high specific strength, stiffness, and superior processability compared to thermoset composites [17]. However, their integration into structural assemblies presents significant challenges, like high degrees of deformation in the context of mechanical joining [16].

Mechanical Joining Technologies for continuous fiber reinforced thermoplastic composites

Several mechanical joining techniques have been explored to enable the assembly of thermoplastic composite structures. [3] introduced a method using braided thermoplastic rivets that are directly formed within pre-punched composite laminates. Similarly, [14] and [21] investigated thermoplastic composite fasteners, including 3D-printed and interference-fit solutions. While these approaches demonstrate effective joining strategies, they primarily address composite-to-composite joints and do not necessarily apply to hybrid joints involving metals. Furthermore, the necessity of a pilot hole requires an additional process step.

Hybrid metal-composite structures offer distinct advantages in lightweight design by combining the mechanical benefits of both material classes. However, joining FRTP with metals is particularly challenging due to differences in material properties, limited composite ductility, and stress concentrations at the joint interface [15]. A broad overview of multi-material mechanical joining techniques is provided by [5] and [13]. [19] developed a thermoforming process, by combining flow drilling in metals and warm forming of boreholes in thermoplastic composites. Additionally, inductive contact joining [1] and thermally assisted clinching processes, such as thermoclinching, hotclinching and insert clinching [7] were investigated. Notably, techniques such as joint stamp riveting [10] and macro-scale mechanical interlocking [18] have been developed to improve the integrity of metal-composite joints by reducing fiber damage and enhancing interlocking efficiency.

While many of these methods rely on forming processes adapted from metal joining technologies, these are now limited to metal-composite joints. SPR on the other hand has emerged as a viable mechanical joining approach for joining metal-composites as well as metal-metal-joints, which reduces the variety of joining technologies. Additionally, SPR has gained attention as a robust technique for composite-metal joining due to its adaptability to different material combinations [13].

Self-Piercing Riveting for Hybrid Joints

SPR is a mechanical joining technique used to assemble two joining partners without the need for pre-drilled holes. As illustrated in Figure 1, the process involves pressing a semi-tubular rivet into stacked sheets using a punch, while a die supports the assembly from below. The rivet penetrates the upper layers and expands in the lower sheet due to the die's cavity, forming a mechanical interlock.

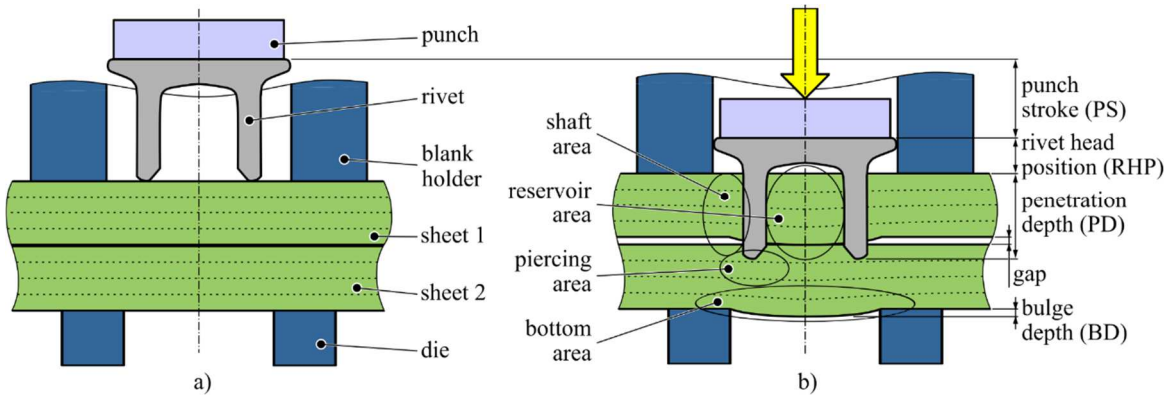

Fig. 1 - Schematic view of SPR-process with a) component labelling; b) areas of interest and key parameters.

Current research on SPR is focused on improving the versatility of the process, particularly in joining dissimilar materials. [9] contributed to this effort by optimizing rivet-die combinations to enhance the robustness of SPR for dissimilar metal joining. The application of SPR in composite-metal joints was first explored by [4], who investigated the joining of glass-fiber-reinforced epoxy panels with aluminum. He observed limited plastic deformation of the rivet due to residual composite material inside the rivet cavity. Subsequent studies, such as [12] and [22], identified damage mechanisms including fiber fracture and delamination in carbon-fiber-reinforced plastics (CFRP) and polyamide-based FRTPs. [12] also defined three different phases of the joining process: Piercing, Flaring and Compression in the force-displacement diagram. [8] further extended the understanding of SPR in fiber-reinforced laminates by

developing numerical models to predict failure behavior. **Error! Reference source not found.** emphasized the need for improved process understanding to validate predictive simulations of SPR joints. Addressing this challenge requires a detailed characterization of local deformation and failure mechanisms within the composite structure, as these significantly influence joint performance.

Advanced Characterization Techniques

Traditional methods for analyzing joints, such as micrograph-based cross-sectional imaging, provide valuable insights but come with significant limitations. [20] used micrographs to analyze the material structure of hybrid joints. However, obtaining meaningful data requires an extensive number of micrographs, making the method highly labor-intensive. Additionally, damage phenomena, which may extend through the laminate in several directions, might not be traced across individual micrographs, since they only represent one single cross-section. Furthermore, inherent discontinuity of phenomena across different specimens significantly restricts the ability to provide a comprehensive and precise description of the spatial progression of such phenomena.

In contrast, CT imaging enables a three-dimensional evaluation of damage phenomena, ensuring greater reliability in the identification and characterization of composite-related failure phenomena. CT has emerged as a powerful non-destructive tool for characterizing internal joint structures and fiber orientations [2]. In situ CT allows for the time efficient analysis of the joint structure, without elastic resetting effects [10]. However, in situ CT is not easily applicable, since the whole process needs to take place inside the CT. [6] used ex situ CT combined with step-setting tests – where the joining process is terminated at defined intervals – to enable detailed analysis of transient deformation states for thermally assisted clinching processes.

Objective of this Study

Building on these advancements, this study employs CT-based analysis to investigate the local deformation and failure mechanisms in SPR step-setting tests with FRTP-FRTP joining partners. By examining the material structure at different process stages, this study aims to characterize the evolution of damage phenomena in three dimensions. The findings deepen the understanding of the process-structure interaction in SPR, giving the possibility for validation of numerical simulations and process optimization in future research.

MATERIALS AND METHODS

Material and Laminate Structure

FRTP sheets with a thickness of 2 mm consisting of eight unidirectional layers of glass fiber-reinforced polypropylene (PP) with a $[0°/90°/0°/90°]_s$ layup and 45 vol% fiber content are used. The fibers have a weight per unit area of 307 g/m^2 and a fineness of 600 tex. The material contains a stitching yarn in each layer.

Figure 2 a) shows a CT scan of the initial material structure. The eight UD layers in 0° and 90° are clearly visible. The dark grey areas between the yarns represent matrix rich zones. The stitch yarn is only visible close to the top and bottom sheet (cf. Figure 2 c)). A slight undulation due to the textile architecture is visible in the 0° layers of the section view. No pre-damage is detected in the scan of the initial material structure (cf. Figure 2 b)).

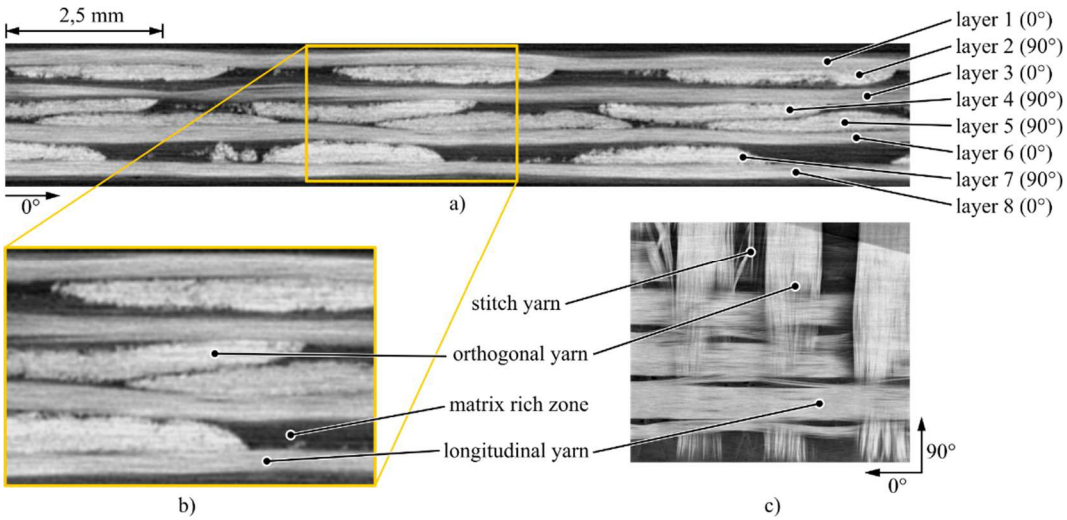

Fig. 2 - CT-Scan of the initial material structure: a) cross section; b) maginfication and c) top view.

Step Setting Tests

For the step setting tests, sheets with a size of 23x23 mm were water jet cut out of the base sheet. For joining, the sheets were aligned in such a way that the outer fiber orientation was parallel to each other. A servo-hydraulic C-frame unit by TUCKER GmbH was used for this study. The punch speed was set to 20 mm/s and the spring loaded blank holder was loaded with 2 kN. A FM 095 2117 was used as a die for all joints. The position of the punch is stroke-controlled and can be set to a defined rivet head position during the joining process (cf. Figure 1). For this purpose, the punch was calibrated to an end position of 0 mm, which corresponds to the contact of the punch on the sheet. For the stepwise setting tests, the targeted punch strokes were set to ten different positions. Figure 3 shows the advancement of the performed SPR setting test for selected stages.

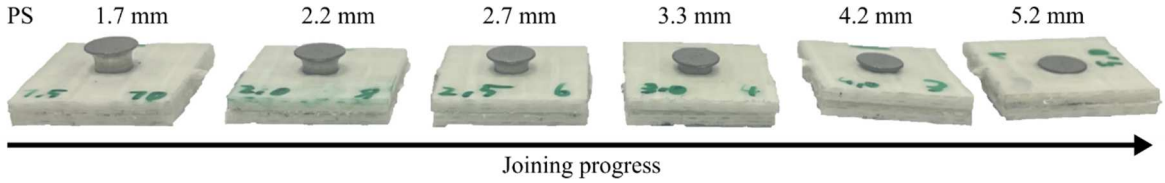

Fig. 3 - Advancement of setting test.

Table 1 shows the used punch strokes. It must be noted, that the punch stroke has an offset of approximately 0.2 mm compared to the targeted positions due to positioning tolerances. For punch strokes ranging from 0.3 to 0.7 mm, a shorter C5.3x4.5 H4 rivet was used. This was due to requirements for the C-frame unit, where the final rivet head position must not exceed 4.5 mm. A C5.3x5.5 H4 rivet was used for all subsequent strokes in order to ensure a progressive joining process. Apart from the different length, the rivets, made of 38B2, are identical. The rivets and the die were produced by Böllhoff GmbH.

Table 1 - Scope of experiments with allocation of the rivets used per punch stroke (PS).

Stage	I	II	III	IV	V	VI	VII	VIII	IX	X
Target PS in mm	0.1	0.3	0.5	1.0	1.5	2.0	2.5	3.0	4.0	5.0
Actual PS in mm	0.3	0.4	0.7	1.2	1.7	2.2	2.7	3.3	4.2	5.2
Rivets	C5.3x4.5 H4			C5.3x5.5 H4						

Analysis Methods

CT scans were performed at each step of the joining process to analyze the evolving process phenomena. For the early stages from 0.3 to 0.7 mm punch stroke, the rivet did not naturally adhere to the laminate due to the low penetration depth. Therefore, the rivet was attached to the top of the laminate with a drop of cyanoacrylate glue before the scan. For all investigated stages, the both sheets were glued together at the edges before the scan to ensure positional stability during scanning, since the rivet alone did not provide sufficient holding force.

The specimens are investigated with a CT-system V|TOME|X L450CT (300 kV micro-focus X-ray tube) with the parameters in Table 2. To enhance signal quality, each radiograph was averaged from three images, whereby one image was skipped at the beginning. To minimize CT time, a helical scan was used in which four samples were scanned simultaneously. The samples were arranged in two planes, with the samples on the same plane offset from each other. During the scan the samples were in a 90°-angle to the central beam to reduce the radiation length. The acquired CT data were reconstructed into three-dimensional models using the FDK algorithm implemented in Phoenix datos|x 2. The reconstruction process was optimized for low noise and included region of interest selection as well as beam-hardening correction for multi material on level 8. Subsequent volume data analysis was performed using VG Studio 2.2. To mitigate metal artifacts caused by the high X-ray absorption of the rivet, the rivet representation in the images was adapted to a darker rendering, improving contrast and visibility of surrounding material structures.

Table 2 - Applied parameters for the CT measurement and image analysis.

Parameter	Unit	Value
Acceleration voltage	kV	150
Tube current	µA	150
Cu-Filter	mm	1
X-ray projections		1440
Exposure time	ms	500
Voxel size	µm	16
Magnification		12.5

EXPERIMENTAL RESULTS

Analysis of the Force-Displacement Curves in the Step-Setting Tests

The force-displacement curves of the step-setting tests are depicted in Figure 4. The diagram includes the curves of all ten investigated stages. For a better representation, the curves were standardised by defining the punch stroke as zero at the point where the preload force was reached. The overall conformity of the individual curves is adequate, indicating good repeatability of the test procedure. Distinct phases of the setting process appear in the force-displacement curves.

In the first phase until 3.3 mm punch stroke, the rivet penetrates the first sheet. The second piercing phase begins afterwards, when the second sheet is penetrated. A force increase during the second piercing phase indicates the beginning of the compression phase, where the rivet shoulder begins to penetrate the laminate. Notably, this compression phase is superimposed on the ongoing piercing phase of the second sheet. The sharp decline in joining force marks the conclusion of the second piercing phase. The compression phase ends when the final rivet head position is reached.

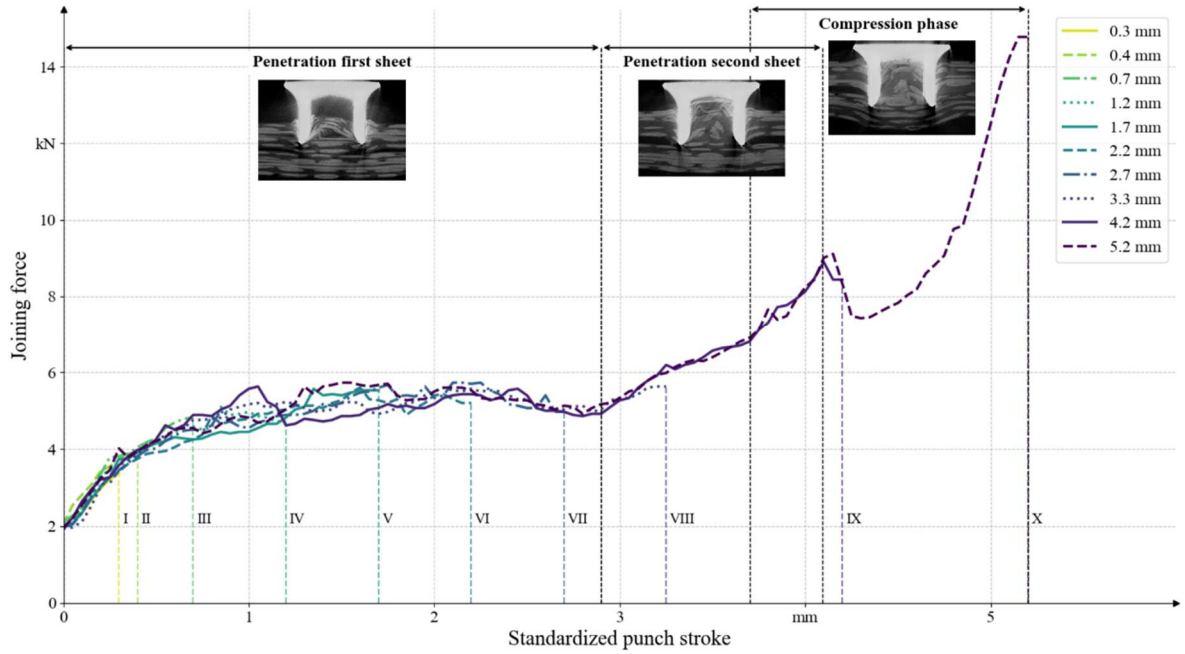

Fig. 4 - Force-displacement curve during SPR.

Global Phenomena

The material structure was assessed with CT scans at ten different stages of the setting process, with cross-sections along the 0° and 90° directions shown in Figure 5. The observed deformation and damage phenomena in the laminate include FF, IFF, fiber bending, fiber kinking, roving splitting, delamination and the collapse of the remaining bottom layers near the end of the process. The phenomena are assigned to four areas of interest: the piercing area, the reservoir area, the shaft area and the bottom area (cf. Figure 5). The phenomena in these areas are described in detail in the following subchapters.

Notably, an initial gap between the sheets is observed (cf. Figure 5). During the punching process, the rivet displaces material from sheet 1 into the gap between both sheets. Along with the deflection, this accumulation of material leads to a widening of the gap. This gap is most likely enlarged due to the elastic springback effect after unloading. As the sheets are fixed with glue for scanning, the gap is fixed in its current position.

Occasionally, IFF on the top and bottom layers of both sheets was detected, which is most likely not induced by the joining process itself. Instead, this damage was probably introduced prior to the process, likely during specimen cutting.

In addition to qualitative observations, specific key parameters (cf. Figure 1) were measured and summarized in Table 3. Along with the punch stroke, the rivet head position, the penetration depth as well as the gap provide information on the actual rivet movement relative to the laminate. The bulge depth allows to quantify the laminate deformation. The identified damage phenomena were categorized into two groups: phenomena occurring on the rivet side (RS), caused by the rivet piercing through the laminate, and phenomena on the die side (DS), resulting from the laminate being compressed against the die. For both categories, the extent of the influence zone (IZ), i.e. the area in which damage occurs, was characterized by two primary parameters. Firstly, the radial width of the influence zone was measured, defined as the distance from the rivet shaft to the final identifiable damage feature.

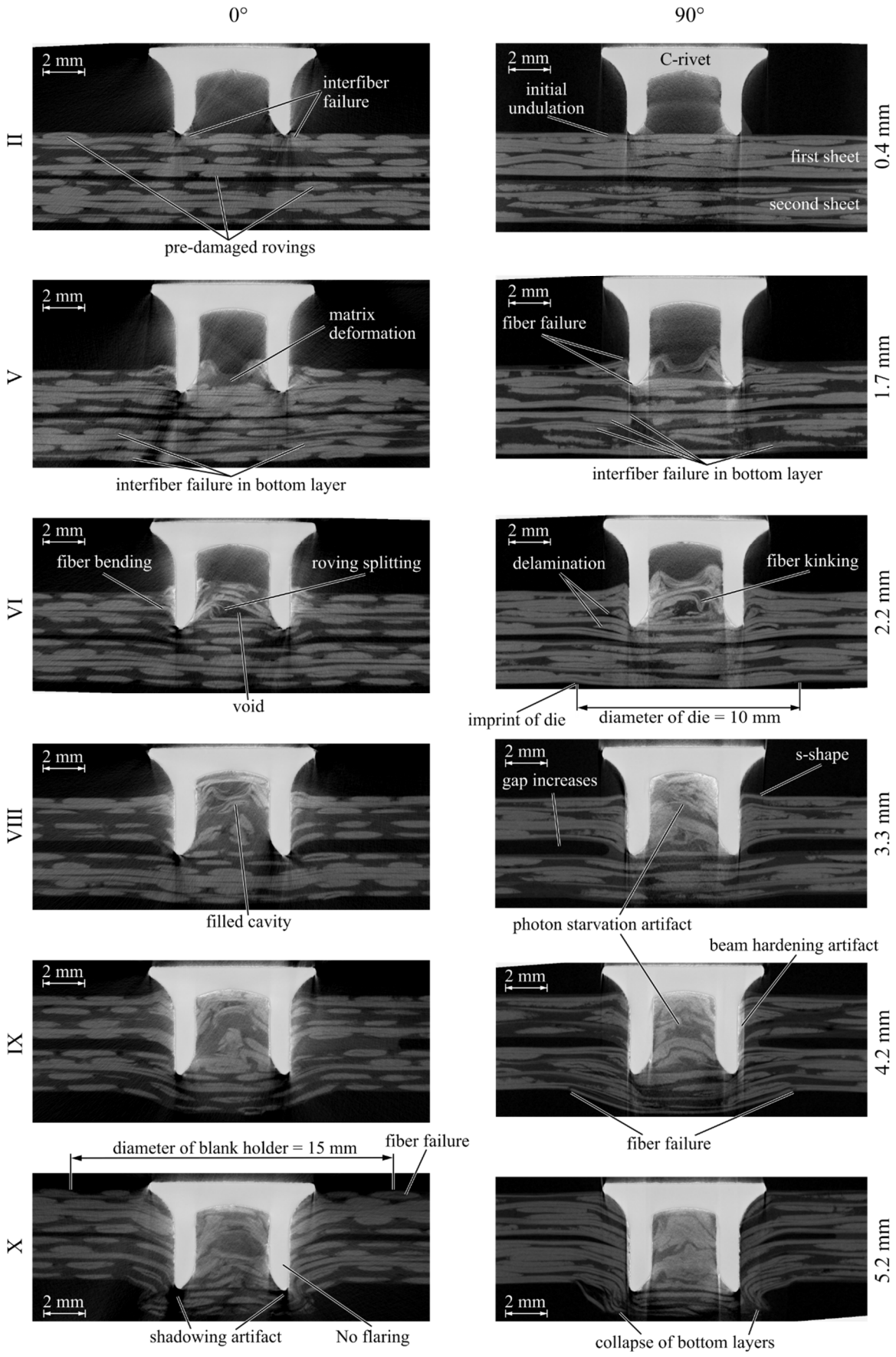

Fig. 5 - CT scans of setting test stages.

Secondly, the depth of the influence zone was quantified by the number of damaged layers. Damage was further classified into FF and IFF. These parameters were systematically documented for each stage, along with measurements of the gap and the bulge depth (cf. Figure 1).

The initial penetration phase is characterized by local IFF. As punch stroke progresses to 0.7 mm, the influence zone expands, with material being displaced downward over the entire rivet contour. At a punch stroke of 1.2 mm, compaction effects extend throughout the thickness of the first sheet and become apparent in the second sheet as well. Upon reaching a punch stroke of 1.7 mm, the influence zone of the rivet expands into the second sheet, where it overlaps with the influence zone of the die. Subsequent to this stage, both influence zones undergo continuous expansion, resulting in the manifestation of damage across all layers in the final stage.

Although the imprint of the die is clearly visible from 1.2 mm onwards, no detectable imprint of the blank holder (diameter 15 mm) is observed at any stage. However, at the final stage, IFF of the outermost 0° layer at the edge of the blank holder becomes apparent.

No deformation of the rivet (flaring) is observed at any stage of the process (cf. Figure 5).

Table 3 - Key parameters of damage phenomena during setting test.

Stage	PS in mm	Force in kN	RHP in mm	PD in mm	No. of layers with IFF/ FF RS	No. of layers with IFF/ FF DS	Width of IZ on RS/DS in mm	BD in mm	Gap in mm
I	0.3	3.43	4.04	0.03	-	-	-	-	0.06
II	0.4	4.00	4.01	0.02	1/0	0/0	1/-	0.07	0.19
III	0.7	4.69	3.90	0.12	3/1	3/0	2.0/2.5	0.06	0.25
IV	1.2	4.79	4.37	0.65	8/2	7/0	2.4/1.9	0.16	0.28
V	1.7	5.42	3.87	1.18	9/3	8/0	2.7/1.4	0.12	0.23
VI	2.2	5.16	3.43	1.60	9/5	8/0	2.8/2.5	0.24	0.25
VII	2.7	5.02	2.72	2.28	15/7	8/0	4.0/2.0	0.34	0.42
VIII	3.3	5.58	2.33	2.74	15/8	8/0	3.2/2.5	0.42	0.58
IX	4.2	8.65	1.35	3.66	16/11	8/1	2.9/2.2	1.01	0.51
X	5.2	14.78	0.31	4.71	16/16	8/1	3.5/1.6	1.60	0.28

Piercing Area

At the initial stage of 0.3 mm punch stroke, no detectable material damage occurs. The first significant interaction is observed at 0.4 mm, where the rivet begins to penetrate the first sheet, causing radial displacement and IFF within the 0° yarns. FF is not yet detectable at this stage. With further penetration, the influence zone of the rivet expands causing IFF in a progressing number of layers (cf. Table 3). The Material is pressed downward over the entire rivet contour. Initial FF is detected at 0.7 mm, as the rivet pierces through the first 0° layer, which is already bend downwards. At 1.2 mm punch stroke, IFF, caused by compression of the laminate against the die, occurs in all layers of the first sheet. The radial expansion of IFF is limited to 2 to 4 mm, while FF only occurs at the tip of the rivet, when a deformed layer is finally pierced. Because the laminate of the first sheet is pressed downwards, it requires at punch stroke of 3.3 mm until the first sheet with a thickness of 2 mm is nearly completely penetrated. At 4.2 mm,

FF occurs in the bottom layer at the edge of the die as the second sheet is pressed into the die cavity. In the final position, the last four layers of the second sheet remain unpenetrated as they are pressed downward, forming a bulge. However, visibility in this region is significantly obstructed by severe shadow artifacts in the CT scans, limiting further analysis.

Reservoir Area

From a punch stroke of 1.2 mm onwards, the already pierced layers begin to bend upwards into the reservoir. At 1.7 mm, the reservoir of the rivet is starting to fill with laminate residues of pierced layers, accompanied by additional FF, fiber kinking, roving splitting and matrix deformation inside the reservoir as the laminate is bend inwards. As a result, a void forms between the layers in the reservoir and the remaining layers outside. The residues in the reservoir protrude beyond the original sheet surface by approximately 1 to 1.4 mm. At 3.3 mm punch displacement, the reservoir is fully filled with debris and the internal material structure within the reservoir becomes increasingly indistinct. In the final position, the first four layers of the second sheet are fully compacted inside the reservoir, further compressing the laminate residues already present within it.

Shaft Area

Similar to the reservoir area, the first pierced layer begins to bend upwards, accompanied by FF and IFF due to the large deformation. At 2.2 mm, while the first layer remains bent upwards, all subsequent layers of the first sheet are bend downward, following the movement of the rivet. This deformation causes IFF in all layers of the first sheet outside the shaft region as well as delamination. As the second sheet is further penetrated, the upper layers of the second sheet are also forced downward, accompanied by the same damage phenomena. In the final position, the first layer of the first sheet, which had initially been bent upwards, is ultimately forced downwards by the rivet head.

Bottom Area

At 0.7 mm, the first bottom layers of the second sheet exhibit initial IFF due to compression of the laminate against the die. From 1.2 mm onward, the imprint of the inner outline of the die becomes increasingly visible, as fibers are bend inside the cavity. The measured dimensions of this imprint correspond to the die diameter of 10 mm (cf. Figure 5). During the whole process the die does not directly induce IFF in the first sheet, since the sheets are not in contact at this area due to the gap between both sheets. At 4.2 mm, FF occurs at the edge of the die in the bottom layer, converting the bend down fibers into a bulge. As a result, the material protrudes 1.2 mm into the die cavity, while the overall material structure remains clearly distinguishable. In the final position, progressive IFF and FF in the remaining layers lead to a fully developed bulge, as the material is pressed downward through the die opening. However, at the edges of the bulge, the material structure becomes unrecognizable due to severe FF and IFF. Additionally, kinking of the bottom layer occurs at the edge of the bulge, further contributing to structural degradation.

Artifacts

As clearly visible in Figure 5, certain artifacts obstruct the analysis of the material structure, primarily due to the presence of the steel rivet, which exhibits significantly higher X-ray attenuation than the surrounding glass fiber-reinforced thermoplastic laminate. The resulting artifacts are predominantly beam hardening, shadowing, and photon starvation effects, which influence the accuracy of material characterization.

A shadowing artifact is particularly pronounced at the rivet peak, limiting direct visibility of the contact zone between the rivet and the laminate. This artifact extends radially into surrounding regions, reducing contrast and obscuring fine structural details. Beam hardening effects cause overexposure artifacts along the surfaces of the rivet, leading to an artificial brightening of adjacent regions, most notably along the shaft extension and in the reservoir area. In the later stages of the joining process, the reservoir area is subject to a superposition of these overexposure effects, reducing contrast between fiber and matrix. Additionally, photon starvation in highly attenuated regions increases image noise, particularly near the rivet-laminate interface.

Despite these artifacts, the fiber structure and associated damage mechanisms remain largely discernible.

DISCUSSION

The penetration phases as well as the compression phase are cleary visible in the force-displacement-diagram in Figure 4. The material structure in the CT scans provides additional reliability regarding the beginnings and endings of the phases. Compared to the force-displacement diagrams of SPR with CFRP-aluminum sheets, the curves show a good compliance except for the apex at 4.2 mm. This can be explained with higher loads due to a second piercing phase instead of a flaring phase at CFRP-aluminum. The sharp decline after the apex of the joining force can be explained with the collapse of the remaining bottom layers between 4.2 and 5.2 mm punch stroke, which is documented in Figure 5.

It is noticable, that in Table 3 the penetration depth as well as the rivet head position do not develop according to the punch stroke for the first two stages. At the same time, the gap increases by roughly the same amount. This indicates, that the punch stroke mainly bends down the first sheet instead of piercing through. At the 0.7 mm, the penetration depth and rivet head position develop accordingly, while the gap remains constant until material accumulation widens the gap. The initial offset of 0.5 mm remains throughout the process and can also be noticed at the final stage of 5.2 mm punch travel, where the rivet has only penetrated to 4.7 mm, while the rivet head is 0.3 mm above the sheet of the surface.

It should be noted that the use of two FRTP sheets in combination with a C-rivet does not result in the formation of a typical SPR joint. This is because the rivet primarily cuts through the second FRTP sheet. Consequently, the required flaring of the rivet does not occur, preventing the establishment of an undercut.

The analysis of damage phenomena during the SPR process demonstrated that the layered structure of FRTP sheets allows for a layer wise detection of damage phenomena. This enabled the designation of specific phenomena and the quantification of influence zones at each stage of the process.

The main driving force behind the observed damage is the rivet piercing through the laminate, accompanied by significant compressive loading. In the piercing area, IFF occurs extensively around the rivet and die due to compressive forces, while FF is primarily confined to the immediate vicinity of the piercing rivet shaft. In the shaft area, fiber bending, FF, IFF and delamination dominate. The reservoir area exhibits the most severe deformation, where all damage mechanisms occur simultaneously, leading to a highly compacted and unstructured material state. In contrast, the bottom layers maintain their integrity for a prolonged phase of the process, until they eventually collapse due to FF at the edge of the die, forming a bulge with an indistinct material structure at the edges.

The use of CT analysis proved highly effective in examining the joining zone in three dimensions, offering significant advantages over conventional micrographic analysis. The ability to analyze multiple cross-sections of the same specimen enables a continuous description of damage progression, which is particularly valuable given the heterogeneous nature of composites.

CONCLUSION

This paper presents a CT-based analysis of the stepwise setting process of SPR in FRTP sheet materials. The occurring damage phenomena were systematically described and quantified at ten distinct stages, ranging from initial contact to the final rivet position. These phenomena were further categorized based on their spatial distribution and correlated with the different phases observed in the force-displacement curve of the process. The study contributes to a deeper understanding of the SPR process in FRTP laminates and provides valuable quantitative data to support and validate future numerical simulations of SPR joints.

It would be interesting to further analyse the mechanics behind the rivet flaring. A parametric simulation study varying the material parameters of the sheets could provide deeper insights into their influence on the SPR process and joint formation.

Additionally, optimizing CT parameters is essential to reduce artifacts and improve the visibility of damage phenomena. While key mechanisms were identified despite imaging limitations, refining scanning and reconstruction settings would enhance data quality and support more accurate validation of numerical simulations.

ACKNOWLEDGMENTS

The author(s) disclosed receipt of the following financial support for the research, authorship, and/or publication of this article: This research was funded by the Deutsche Forschungsgemeinschaft (DFG, German Research Foundation) – TRR 285/2 – 418701707 subprojects C04, A01 and A03.

DATA AVAILABILITY

Data is available upon request from https://trr285.uni-paderborn.de/en/publications.

REFERENCES

[1] Al-Obaidi A, Rochala P, Kroll M, et al. Thermal and Mechanical Joining of Basalt Fiber Reinforced Thermoplastic Laminates. IOP Conf. Ser.: Mater. Sci. Eng. 2020, 947(1), p. 12011.

[2] Dierig T, Becker B, Reinhart C, et al. Fiber composite material analysis in aerospace using CT data. 2012.

[3] Fortier V, Brunel J-E, Lebel L. Fastening composite structures using braided thermoplastic composite rivets. J Compos Mater, 2019, 54(6), pp. 801-812.

[4] Fratini L, Ruisi VF. Self-piercing riveting for aluminium alloys-composites hybrid joints. Int J Adv Manuf Technol, 2009, 43(1-2), pp. 61-66.

[5] Galińska A, Galiński C. Mechanical joining of fibre reinforced polymer composites to metals—a review. Part II: riveting, clinching, non-adhesive form-locked joints, pin and loop joining. Polymers, 2020, 12(8), p. 1681.

[6] Gröger B, Köhler D, Vorderbrüggen J, et al. Computed tomography investigation of the material structure in clinch joints in aluminium fibre-reinforced thermoplastic sheets. Prod Eng Res Devel, 2022, 16(2-3), pp. 203-212.

[7] Gröger B, Troschitz J, Vorderbrüggen J, et al. Clinching of Thermoplastic Composites and Metals - A Comparison of Three Novel Joining Technologies. Materials, 2021, 14(9).

[8] Hirsch F, Müller S, Machens M, et al. Simulation of self-piercing rivetting processes in fibre reinforced polymers: Material modelling and parameter identification. J Mater Process Technol, 2017, 241, pp. 164-177.

[9] Kappe F, Schadow L, Bobbert M, et al. Increasing flexibility of self-piercing riveting by reducing tool–geometry combinations using cluster analysis in the application of multi-material design. J Mater Des Appl, 2022, 236(6), pp. 1310-1320.

[10] Köhler D, Popp J, Kupfer R, et al. In-Situ Computed Tomography — Analysis of a Single-Lap Shear Test with Composite-Metal Pin Joints. J Phys Conf Ser, 2023, 2526(1), p. 12067.

[11] Krassmann D, Moritzer E. Development of a new joining technology for hybrid joints of sheet metal and continuous fiber-reinforced thermoplastics. Weld World, 2022, 66, pp. 45-60.

[12] Kroll L, Mueller S, Mauermann R, et al. Strength of self-piercing riveted joints for CFRP/aluminium sheets. 18th Int Conf Compos Mater (ICCM18), 2011.

[13] Lambiase F, Scipioni SI, Lee C-J, et al. A State-of-the-Art Review on Advanced Joining Processes for Metal-Composite and Metal-Polymer Hybrid Structures. Materials, 2021, 14(8).

[14] Li W, Guo S, Giannopoulos IK, et al. 3D-printed thermoplastic composite fasteners for single lap joint reinforcement. Compos Struct, 2022, 282, p. 115085.

[15] Merklein M, Jäckisch M, Kuball C-M, et al. Mechanical joining of high-strength multi-material systems – trends and innovations. Mech Ind, 2023, 24, p. 16.

[16] Meschut G, Merklein M, Brosius A, et al. Review on mechanical joining by plastic deformation. J Adv Joining Processes, 2022, 5, p. 100113.

[17] Offringa, A. Thermoplastic composites - rapid processing applications. In: Composites Part A: Applied Science and Manufacturing, 1996, 27 (4), S. 329-336.

[18] Phadatare A, Jo E, Pokkalla DK, et al. Fastenerless Joining of Carbon Fiber Reinforced Thermoplastic Composite to Aluminum. ASME Int Mech Eng Congr Expo, 2023, 3.

[19] Seidlitz H, Ulke-Winter L, Kroll L. New Joining Technology for Optimized Metal/Composite Assemblies. J Eng, 2014.

[20] Vorderbrüggen J, Gröger B, Kupfer R, et al. Phenomena of forming and failure in joining hybrid structures – Experimental and numerical studies of clinching thermoplastic composites and metal. ESAFORM Conf Mater Forming, 2019.

[21] Yao C , Qi Z, Chen W. Lightweight and high-strength interference-fit composite joint reinforced by thermoplastic composite fastener. Thin-Walled Structures, 2022, 179, p. 109471.

[22] Zhang J, Yang S. Self-piercing riveting of aluminum alloy and thermoplastic composites. J Compos Mater, 2015, 49(12), pp. 1493-1502.

Proceedings IRF2025: 8th International Conference on Integrity-Reliability-Failure
In Engineering, Materials, Manufacturing and Biomechanics. Porto 15-18 July 2025
DOI: https://doi.org/10.24840/978-972-752-323-8

PAPER REF: 22464

CURE PERCENTAGE DETERMINATION IN EPOXY RESIN/CARBON FIBER STRUCTURAL COMPOSITES

Cirlene Fourquet Bandeira [1(*)], André Marques dos Santos[2], Onofre Rodrigues de Lima Júnior[1], Julia Cardoso Landim[1], Michelle Leali Costa[3], Edson Cocchieri Botelho[3], Sérgio Roberto Montoro[1], Izabel de Oliveira da Mota[1]

[1]UNIFOA/MeMat, Volta Redonda University Center, Volta Redonda, Brazil
[2]UFRRJ/Department of Biochemistry, Federal Rural University of Rio de Janeiro, Seropédica, Brazil
[3]UNESP-FEG/Materials Department, Federal University of São Paulo, Guaratinguetá, Brazil
[(*)]*Email:* cirlenefourquet@yahoo.com.br

ABSTRACT

Due to their high performance, low molecular weight and flexible *design*, structural composites have been applied in several sectors, especially aerospace and energy. However, these advanced engineering materials require a curing process suitable for their transport and use. To do so, it is necessary to determine its degree of curing (after autoclaving the piece). In order to ensure efficiency in the methodology, an approach using differential scanning calorimetry (DSC) was taken to control this parameter in structural composites of epoxy resin and carbon fiber (63%). With this, an average degree of cure of 97% was obtained, which is in agreement with data found in the literature (<5%).

Keywords: Epoxy resin, carbon fiber, DSC, autoclaving, engineering materials.

INTRODUCTION

The degree of curing obtained in a polymer composite is defined as the ratio between the number of interconnected unsaturations and the number of initial unsaturations. Thus, the curing reaction is directly related to obtaining quality parts at a low cost, with the temperature during the process, the speed and the curing time being fundamental parameters (Bandeira, 2015; Costa, 2018). However, to ensure the quality of the materials obtained, it is necessary to evaluate the post-cured part. The literature determines that the crosslinking content, after curing, should be greater than 95%. However, it is often necessary that part of the material is not cured, in order to allow greater movement of the chains, improving the impact resistance of the final product and increasing the lifespan of the artifacts (Bandeira, 2015; Resende; Costa; Botelho, 2011). For this purpose, epoxy resin composites (bisphenol-A diglycidyl ether or DGEBA) and carbon fibers (HexPly® F584TM) were analyzed using the DSC technique.

RESULTS AND CONCLUSIONS

The results, performed in triplicate, were consistent with each other with a coefficient of variation (CV%) of 1.24 (Table 1).

In the present work, the degree of residual cure and the cure of the material were obtained from the relationship between the total cure enthalpy of the epoxy resin ($\Delta HT = -287\ J.g^{-1}$) and the enthalpy value obtained from the cured composite or residual cure ($\Delta HR = -9.61\ J.g^{-1}$) (Equation 1 and 2).

$$\text{Degree of residual healing } (\%) = \left(\frac{\Delta H_R}{\Delta H_T}\right) * 100 \quad (1)$$

$$\text{Degree of cure } (\%) = 100 - \left(\left(\frac{\Delta H_R}{\Delta H_T}\right) * 100\right) \quad (2)$$

Therefore, it is possible to determine the degree of curing of the material after it is exposed to the autoclaving process. Furthermore, it is possible to state that the curing degree of the composite is in accordance with the recommendations found in the literature, which is less than 5% (Bandeira, 2015; Costa, 2018; Resende; Costa; Botelho, 2011), and that the material can be applied in several sectors.

Tab. 1 - Enthalpy values and degree of cure of the epoxy/carbon fiber composite (Authors)

Samples	Residual curing enthalpy (mJ/mg)	Mean	Standard Deviation	CV (%)	Total curing enthalpy (mJ/mg)	Degree of cure (%)	Degree of residual cure (%)
1	-9.48						
2	-9.71	-9.61	0.119	1.24	-287	96.6	3.4
3	-9.65						

REFERENCES

[1] Bandeira CF. Obtaining and characterizing benzoxazine/carbon fiber composites. 2015, Thesis (PhD in Mechanical Engineering) – UNESP–FEG – Guaratinguetá - Brazil, 2015, 206p. (in Portuguese).

[2] Carvalho JAL. Benzoxazine resin composites / biomass extracted from açaí washing residue: Obtaining and characterization. Dissertation (Professional Master's Degree in Materials) – UniFOA – Volta Redonda - Brazil, 2019, 103p. (in Portuguese).

[3] Costa ACA. Obtaining and characterization of benzoxazine resin composites reinforced with macadamia nut shell biomass. Dissertation (Professional Master's Degree in Materials) – UniFOA – Volta Redonda - Brazil, 2018, 83p. (in Portuguese).

[4] Rezende MC.; Costa ML.; Botelho EC. Structural composites: technology and practice. 1st ed. -São Paulo: Artlibre Editora, 2011(in Portuguese).

Proceedings IRF2025: 8th International Conference on Integrity-Reliability-Failure
In Engineering, Materials, Manufacturing and Biomechanics. Porto 15-18 July 2025
DOI: https://doi.org/10.24840/978-972-752-323-8

PAPER REF: 22568

GEOMECHANICAL BEHAVIOR OF OIL SHALES FROM ARARIPE BASIN, BRAZIL

José Agnelo Soares[1(*)], Anne Beatrice Guedes Sobrinho[1], Juliana Targino Batista[1]

[1]LabPetro, Department of Mining and Geology, Federal University of Campina Grande, Brazil
[(*)]*Email:* jose.agnelo@professor.ufcg.edu.br

ABSTRACT

This study aims to characterize the geomechanical properties of oil shales occurring in the Araripe Basin, located in northeastern Brazil. This knowledge is essential for exploration and exploitation activities involving this type of natural energy resource. To achieve this, characterization techniques such as optical petrography, XRD, XRF, X-ray microCT, gas pycnometry, and uniaxial and triaxial geomechanical tests were applied to shale samples extracted from three gypsum mine fronts where oil shale is also found. The results indicate that these shales are composed of clay minerals, carbonates, quartz, and muscovite, and are relatively homogeneous. Macropores occur as microfractures, while micropores are mainly found in clay minerals. The geomechanical behavior of these shales can be classified as moderately to highly friable.

Keywords: Non-conventional reservoirs, hydraulic fracturing, schist.

INTRODUCTION AND METHOD

The economic exploitation of hydrocarbons contained in unconventional oil shale reservoirs requires techniques such as hydraulic fracturing and horizontal drilling, whose proper application heavily depends on prior knowledge of the mechanical properties of these rocks. The shales in this study were extracted from gypsum mines located in the Araripe Basin. They are part of the Post-Rift I sequence, dating to the Aptian/Albian age, within the Ipubi Formation of the Santana Group (Assine, 2007). Laboratory tests were conducted to measure porosity, permeability, and grain density of shale samples, using a gas porosimeter and permeameter. To characterize the mineral composition of the samples, optical microscopy, X-ray diffraction and fluorescence, besides microCT analyses were performed. Geomechanical properties were investigated through uniaxial and triaxial tests.

RESULTS

Thin sections were prepared from oil shale samples extracted from the three mines. Figure 1 shows examples of these thin sections. In all of them, a typical lamellar pattern of shales can be observed, with dark phases composed of clay minerals and organic matter, and light phases composed mainly of carbonate minerals (oolites, fossil shell fragments, and micrite), quartz, and muscovite. XRD and XRF analyses (Figure 2) indicate presence of the following minerals, in decreasing order of abundance: illite, smectite, calcite, quartz, anhydrite, montmorillonite, muscovite, gypsum and dolomite.

Cylindrical core samples of shale from the MPB mine were subjected to gas pycnometry tests to determine porosity, permeability, and grain density, as well as X-ray microtomography

imaging for three-dimensional visualization of the internal depositional architecture of the core samples. According to laboratory experiments, porosity ranges from 14% to 31%, permeability from 1 mD to 4 mD, and grain density from 2.2 g/cm³ to 2.6 g/cm³. The linear trend seen in Figure 3A is a consequence of this relative rock samples homogeneity. Since the permeability of these rocks is given by microfissures, there is no a clear trend with porosity.

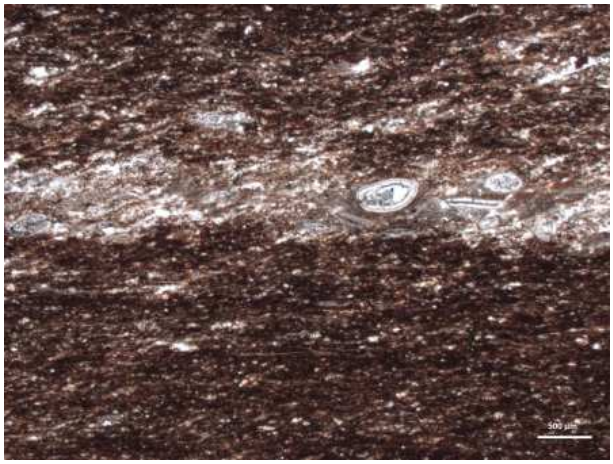

(A)

(B)

(C)

Fig. 1 - Petrographic thin sections of shales samples. A) MPB; B) Campevi; C) Royal.

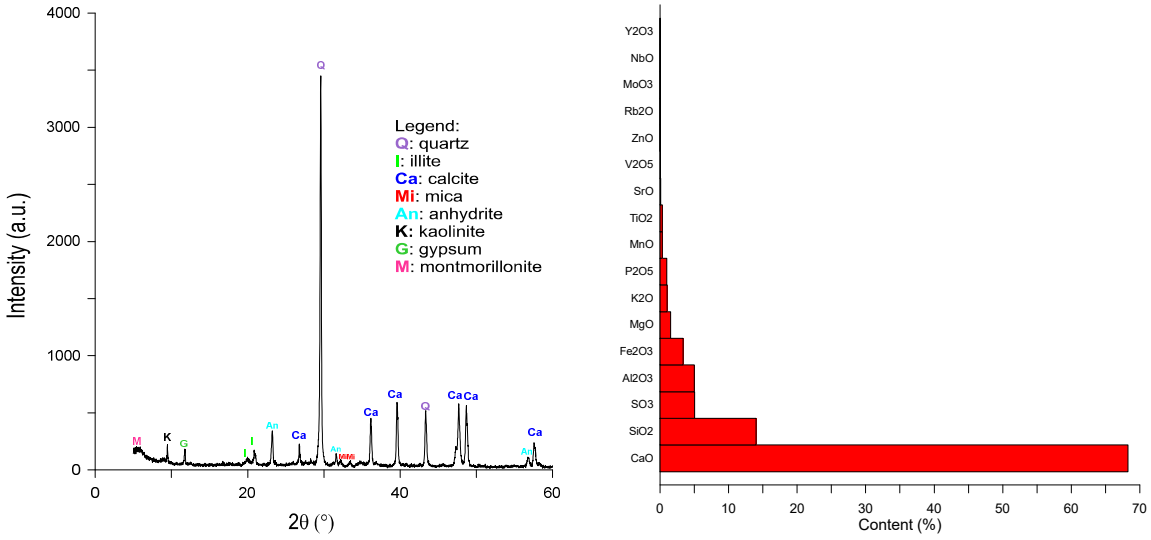

(A) (B)

Fig. 2 - DRX (A) and FRX (B) analyses of a MPB shale sample.

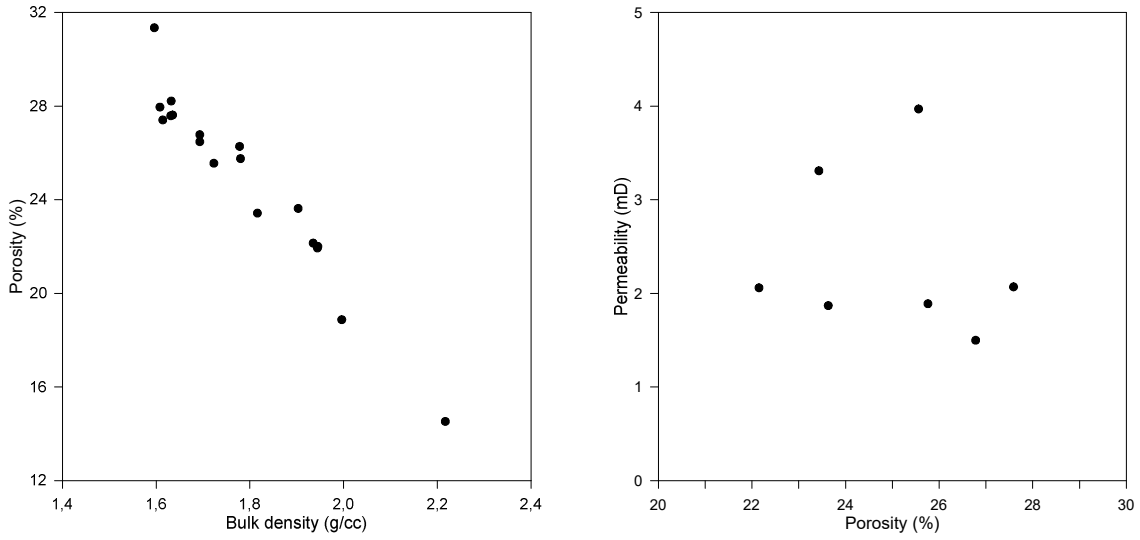

(A) (B)

Fig. 3 - For MPB rock samples, relationship between A) porosity and bulk density; and B) permeability and porosity.

X-ray microtomography imaging allowed for the investigation of the internal spatial arrangement of the various phases that make up the shale samples. Figure 4 presents an example of a digital rock model representative of an oil shale sample from the Araripe Basin, highlighting the internal spatial distribution of its different phases. The macroporosity of the shales is primarily due to microfractures, which develop predominantly along the fissility planes, as well as the dissolution of microfossil shells. On the other hand, microporosity is essentially found in the clay and micritic phases. Silica and carbonate grains are present in a disseminated form.

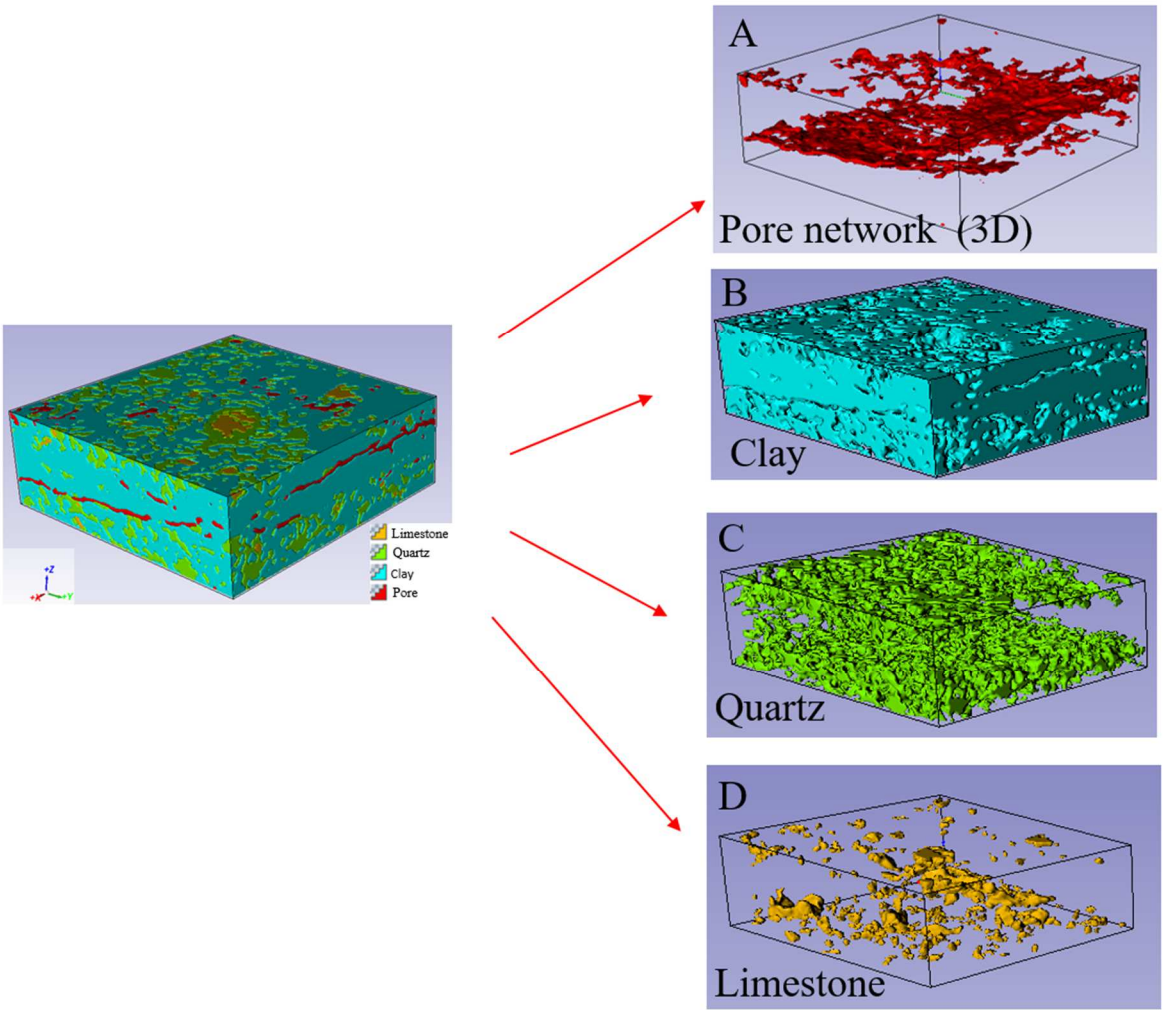

Fig. 4 - Representative digital rock model of the oil shales from the Araripe Basin.

Rock mechanics tests indicate uniaxial strength ranges from 5.2 MPa to 8.1 MPa (Figure 5A), while triaxial strength varies from 28.2 MPa, at a confining pressure (Pc) of 5 MPa, to 36.9 MPa, at Pc = 10 MPa (Figure 1B). A nonlinear failure envelope was fitted (Figure 6) considers the concept of dynamic cohesion and internal friction angle (Soares & Dillon, 2000). It was observed that cohesion and friction angle vary from 1.4 MPa and 50°, under a normal stress of 5 MPa, to 13.8 MPa and 0.6°, at a normal stress of 40 MPa. A failure envelope was defined to predict the maximum shear stress supported by this rock type under a given normal stress condition.

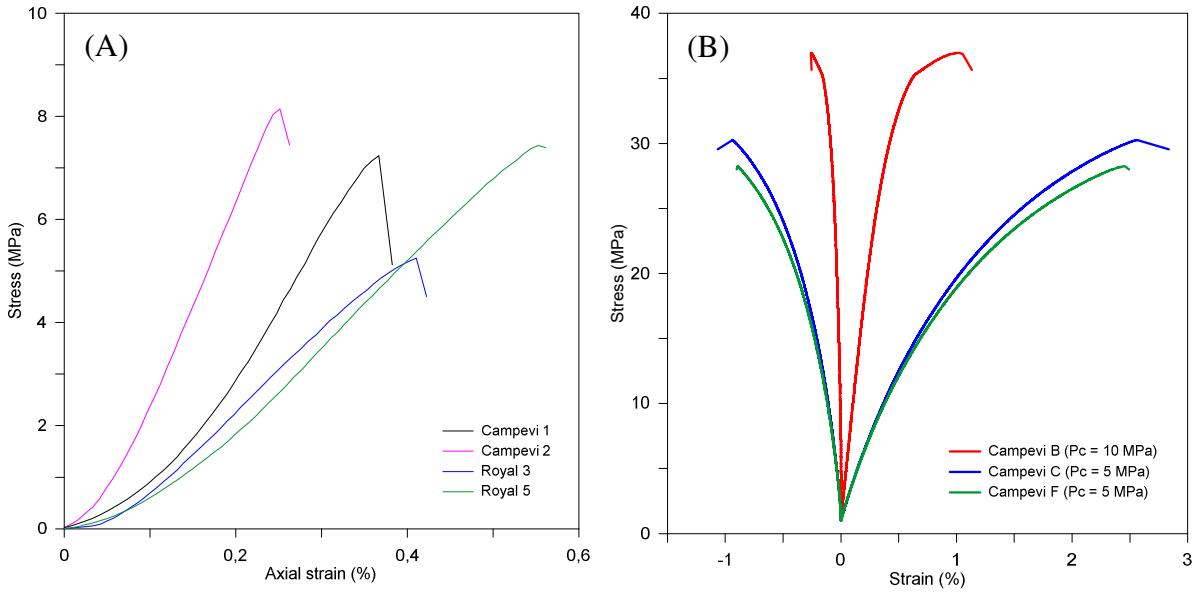

Fig. 5 - (A) Uniaxial and (B) Triaxial tests.

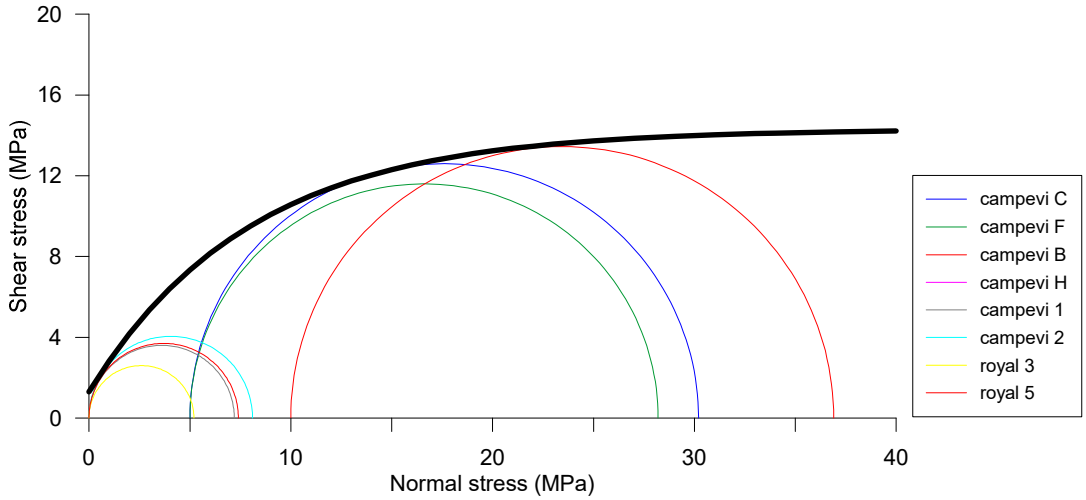

Fig. 6 - Mohr-Coulomb failure envelope.

Table 1 presents the values of static elastic moduli measured in triaxial and uniaxial tests (in the latter case, only E-modulus values). Compared to typical values for shales (Anderson et al., 1986), the oil shales from the Araripe Basin can be classified as moderately to highly friable.

Table 1 - Static elastic moduli of Araripe black shales.

Test type	**Rock sample**	**E (G,Pa)**	**K (GPa)**	**G (GPa)**	**Poisson´s ratio**
Triaxial	Campevi B	8,8	4,0	3,9	0,13
	Campevi C	2,8	2,2	1,1	0,29
	Campevi F	2,8	2,3	1,1	0,30
Uniaxial	Campevi 1	3,0	Not applicable		
	Campevi 2	4,0			
	Royal 3	1,7			
	Royal 5	1,7			

CONCLUSIONS

This study presents the compositional, petrophysical, and geomechanical characterization of oil shales extracted from three mines located in the Araripe Basin, Brazil. The samples exhibit a typical lamellar pattern of shales and are primarily composed of clay minerals, carbonate minerals (oolites, fossil shell fragments, and micrite), quartz, and muscovite. The homogeneity of the samples is reflected in the narrow range of grain density values. Macropores are mainly observed in the form of microfractures contained within the shale's fissility planes and in moldic porosity. Micropores are found in the clay minerals, carbonate mud, and organic matter. Regarding geomechanical behavior, the oil shales from the Araripe Basin can be classified as moderately to highly friable. The failure envelope defines the geomechanical behavior of the black shales from the Araripe Basin and can be applied to predict the mechanical strength of this rock under a wide range of normal stresses. This result is applicable to support analyses of hydraulically induced fracture propagation, aiming to produce hydrocarbons in unconventional reservoirs in similar rocks.

REFERENCES

[1] Anderson R, Coates G, Denoo S, Edwards D, Risnes R. Formation collapse in a producing well. In: The Technical Review, 1986.

[2] Assine M L Bacia do Araripe. Boletim de Geociências da Petrobras, 2007, 15, p.371-389.

[3] Soares J A, Dillon, L D. Deriving cohesion and angle of friction from well logs. In: 31st International Geological Congress, Rio de Janeiro, 2000.

Proceedings IRF2025: 8th International Conference on Integrity-Reliability-Failure
In Engineering, Materials, Manufacturing and Biomechanics. Porto 15-18 July 2025
DOI: https://doi.org/10.24840/978-972-752-323-8

PAPER REF: 22602

MULTI-MATERIALS COMPONENTS DEVELOPMENT FOR POWER APPLICATIONS BY DIRECTED ENERGY DEPOSITION

Ying Li[1(*)], Jan Dzugan[1], Daniel Melzer[1], Michal Brazda[1], Anna Reis[2], Martina Koukolikova1, Libor Kraus[1]

[1]COMTES FHT, Prumyslova 995, Dobrany, Czech Republic
[2]INEGI, Campus da FEUP, Rua Dr. Roberto Frias, 400 4200 - 465 Porto, Portugal
[(*)]*Email : ying.li@comtesfht.cz*

ABSTRACT

In many applications, single-material components struggle to meet all the service requirements for specific parts. Additionally, the need to join dissimilar materials often arises, which is more effectively accomplished under controlled conditions in a production facility rather than during final equipment assembly on-site. In such cases, using an interconnecting part made of different materials on each side can facilitate similar-material welds at the installation site, ensuring a simpler and safer assembly process. This paper highlights key factors that significantly influence the joint quality of multi-material components, focusing on Inconel alloys 718 and 625 joined with 316 austenitic stainless steel and 42C martensitic stainless steel. All materials under investigation were deposited using powder-blown laser-directed energy deposition processes. The study examines the impact of material deposition order for both material combinations—Inconel 718–SS316 and Inconel 625–SS42C—while also exploring the effects of interface orientation and surface quality on the first combination, Inconel 718–SS316.

Keywords: Composite structures, directed energy deposition, joint quality, deposition order.

INTRODUCTION

Additive manufacturing (AM), especially directed energy deposition (DED), is revolutionizing the production of functionally graded materials (FGMs) for applications like engine blocks, medical devices, and turbine blades (Ansari et al., 2021). AM enables complex shapes, customization, and controlled material property variations. While early research focused on single-material AM properties, current studies emphasize FGMs produced via powder bed fusion (PBF) or DED. Powder-blown laser DED, with its separate powder feeders and adjustable parameters, excels in multi-material deposition and component repair. FGMs often combine Fe-based stainless steels (e.g., SS316L, SS304) with Ni-based Inconel alloys (e.g., Inconel 625, 718), leveraging their compatibility and synergistic properties (Chen et al., 2020; Feenstra et al., 2020; Zhang et al., 2021). However, structural integrity and mechanical properties depend on process parameters, deposition sequence, interface orientation, and surface quality, as explored in recent studies. This work investigates these key factors affecting FGMs.

RESULTS AND CONCLUSIONS

The components investigated here were deposited by powder blown laser directed energy deposition (L-DED) systems. The materials combination of Inconel 718 and stainless steel 316 were deposited by INSSTEK MX 600 equipped with 2 kW Yttrium fibre laser. While the

combinations of Inconel 625 and martensitic stainless steel 42C were deposited by machine consisting of a modular coaxial processing head and equipped with a fibre-coupled laser diode, model Laserline LDF 3000–100, with a nominal beam power of 6000 W. The powder nozzle is mounted on a KUKA KR 90 R3100 industrial robot, with six axes connected to the robot control unit.

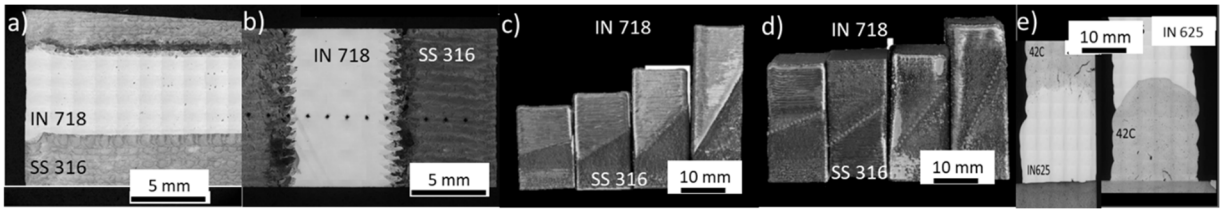

Fig. 1 - Deposited multi-material combinations: a) Vertical interface IN 718-SS316 [1, 2], b) horizontal interface IN 718-SS316 [3], c) Inclined machined interface IN 718-SS316 [4], c) Inclined as-deposited interface IN 718-SS316 [4], e) Horizontal interface IN 625-42C.

The specimens obtained in this study are illustrated in Figure 1. For the IN 718 and 316 stainless steel combination, material interfaces were deposited at various angles, ranging from horizontal to vertical orientations (Figure 1a-d). Inclined interfaces were prepared in two variants: one with the substrate surface machined before depositing the second material (Figure 1c) and the other with an as-deposited interface (Figure 1d). For the IN625-42C steel combination, horizontal deposition was used, with the order of material deposition varied. Both metallographic and mechanical property analyses were conducted.

The results highlight the significant influence of material deposition order on the microstructure of the transition zone and the resulting mechanical properties. In both material combinations, stronger joints were achieved when Inconel was deposited onto the steel substrate.

The study also revealed that the orientation of the inclined surface significantly affected joint quality, particularly for the as-deposited interfaces. The best results were observed for horizontal interfaces, with a slight decline in properties for angles up to 45° for machined surfaces and up to 30° for as-deposited interfaces.

REFERENCES

[1] Ansari M, Jabari E, Toyserkani E. Opportunities and challenges in additive manufacturing of functionally graded metallic materials via powder-fed laser directed energy deposition: A review. Journal of Materials Processing Technology, 2022, 294.

[2] Chen N, Khan H A, Wan Z, et al. Microstructural characteristics and crack formation in additively manufactured bimetal material of 316L stainless steel and Inconel 625. Additive Manufacturing, 2020, 32.

[3] Feenstra D R, Molotnikov A, Birbilis N. Effect of energy density on the interface evolution of stainless steel 316L deposited upon INC 625 via directed energy deposition. Journal of Materials Science, 2020, 27, pp.13314-13328.

[4] Zhang W, Lei Y, Meng W, et al. Effect of Deposition Sequence on Microstructure and Properties of 316L and Inconel 625 Bimetallic Structure by Wire Arc Additive Manufacturing. Journal of Materials Engineering and Performance, 2021, 12, pp.8972-8983.

Proceedings IRF2025: 8th International Conference on Integrity-Reliability-Failure
In Engineering, Materials, Manufacturing and Biomechanics. Porto 15-18 July 2025
DOI: https://doi.org/10.24840/978-972-752-323-8

PAPER REF: 22616

PREDICTION OF INTERNAL DAMAGE IN GFRP LAMINATES CAUSED BY REPEATED LOW VELOCITY IMPACTS USING ARTIFICIAL INTELLIGENCE METHODS

Djalel Eddine Tria(*), Houssem Habbouche, Abdel Wahhab Lourari, Sid Ali Boukhaoua
Ecole Militaire Polyechnique, BP17, Bordj el Bahri,16111, Algiers, Algeria.
(*)*Email:* djaleleddine.tria@gmail.com

ABSTRACT

Repeated low-velocity impacts pose a critical threat to the structural integrity of composite materials in aerospace and offshore applications. This study investigates the progressive damage accumulation and failure mechanisms in glass fiber-reinforced epoxy composite laminates subjected to cyclic low-velocity impacts. By integrating comprehensive experimental testing with advanced AI-driven tools, we develop a robust framework for automated damage assessment that quantifies both microscale (e.g., matrix cracking) and macroscale (e.g., delamination and fiber fractures) impairments. Our approach leverages deep learning techniques inspired by recent methodologies to analyze impact-generated propagating waves and surface image data, achieving high accuracy in damage classification and prognostics. The experimental results demonstrate the cumulative effects of repeated impacts, underscoring the challenges in maintenance and safety assurance, and highlight the potential of tailored AI models to enhance inspection processes. This integrated methodology offers a cost-effective solution for monitoring composite health, thereby improving durability and ensuring the safety of critical aerospace structures.

Keywords: Composite structures, low velocity impact, internal damage, artificial intelligence, structure integrity.

INTRODUCTION

Composite structures used in aerospace and offshore applications frequently experience repeated low-velocity impacts in localized regions during service [1]. These impacts gradually lead to matrix cracking, delamination, and fiber fractures, which compromise structural integrity and increase the risk of unexpected failure [2]. Artificial intelligence (AI)-based methods have shown significant potential for automating damage assessment, including damage classification, quantification, and predicting the remaining useful life of structures. For instance, Zargar and Yuan [3] demonstrated the use of a physics-inspired deep learning (DL) model to characterize impact damage by analyzing the evolution of impact-generated propagating waves. Similarly, Fotouhi et al. [4] utilized DL techniques for quantitatively assessing microscale damage (e.g., matrix cracking) and macroscale damage (e.g., impact and erosion). By analyzing images of impacted and non-impacted surfaces, their model achieved validation accuracies of 96% and 87%, respectively, underscoring the potential of DL to automate visual inspections. However, their findings also emphasized the need for improved datasets and customized classifiers to enhance DL model performance. While a single low-velocity impact may not visibly damage composite structures, repeated impacts often lead to cumulative effects, making maintenance and safety assurance more challenging. Fiber-reinforced composites, widely valued for their lightweight, high strength, and stiffness, are particularly susceptible to low-velocity impacts due to their limited transverse load-bearing

capacity. Although much research has addressed single-impact scenarios [1-5], repeated impacts better reflect real-world conditions, where cumulative damage can surpass that caused by a single high-energy impact.

This study focuses on understanding the damage accumulation and failure mechanisms in glass fiber-reinforced epoxy composite laminates subjected to repeated low-velocity impacts. By combining experimental data with AI-driven tools, this research provides a robust framework for assessing damage, offering cost-effective inspection solutions, improving durability, and enhancing the safety of aerospace structures.

RESULTS AND CONCLUSIONS

Experiments were conducted using an instrumented drop-weight tower, applying localized impacts at energy levels of 6J and 25J with hemispherical, conical, and truncated-conical impactors. Mechanical responses were characterized through force-time, displacement-time, and energy-time curves, and visual inspection images of damage zones. For each impact, key metrics, including delamination area, energy absorption, peak impact force, bending stiffness, maximal displacement, and impact duration, were analyzed.

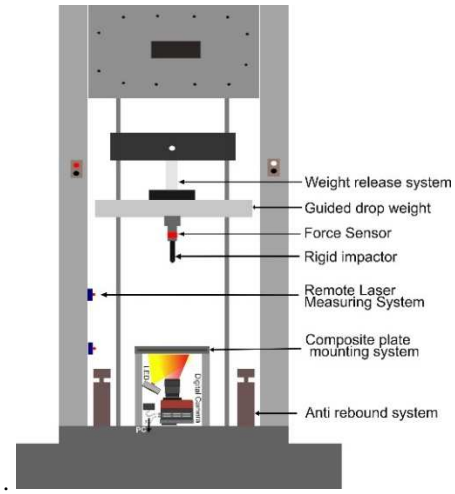

Fig.1 - Drop weight tour system.

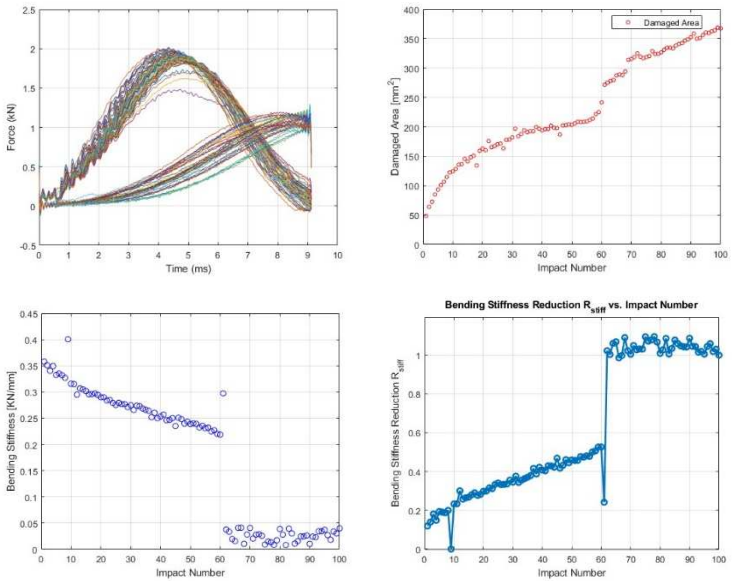

Fig. 2 - Low velocity impact data.

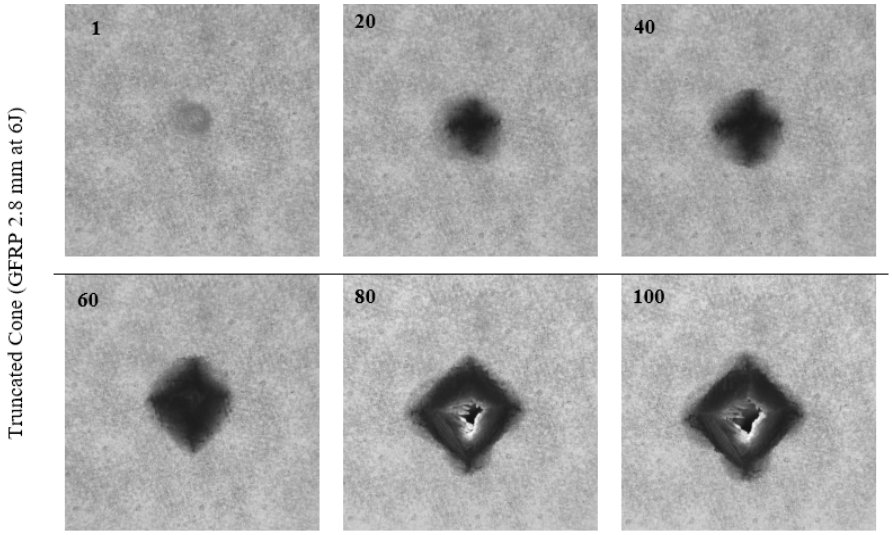

Fig. 3 - Visual inspection images showing damage area evolution.

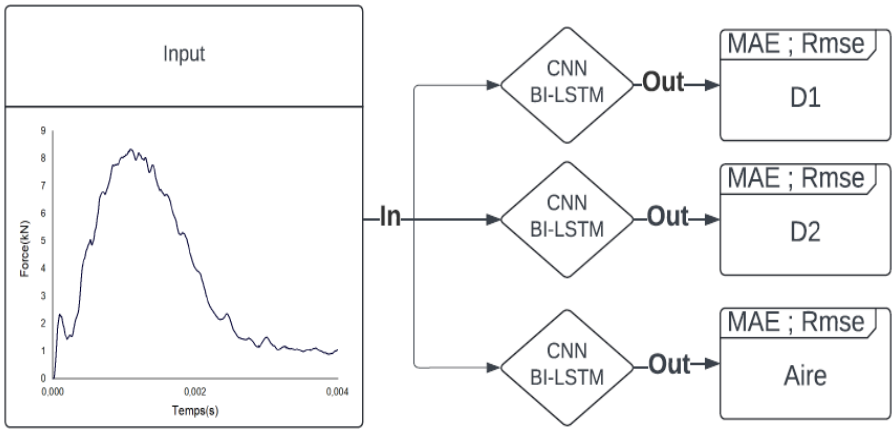

Fig. 4 - Combined CNN and Bi-LSTM models for predicting damaged area size.

Based on this experimental data, an artificial intelligence (AI) methodology was developed to predict damage dimensions and their influence on mechanical properties. A database was constructed from the experimental results, capturing diverse damage profiles induced by repeated low-velocity impacts. This database served as input for training deep learning and machine learning models, which were tested in both parallel and sequential architectures.

The results revealed that delamination growth ceased after a certain number of impacts, while bending stiffness continued to decrease due to progressive fiber rupture. The evolution of delamination areas varied with impactor geometry and laminate thickness, underscoring the need for advanced methods to predict damage progression and assess structural integrity. The AI models demonstrated high reliability and efficiency in predicting internal damage characteristics and assessing the residual performance of composite structures.

REFERENCES

[1] Zhou J, Liao B, Shi Y, Zuo Y, Tuo H, Jia L. Low-velocity impact behavior and residual tensile strength of CFRP laminates. Compos J. Part B-Eng 2019; 161:300-13.

[2] Cao Y, Cao Z, Zhao Y, Zuo D, Tay TE. Damage progression and failure of single-lap thin-ply laminated composite bolted joints under quasi-static loading. Int J Mech Sci 2020; 170:105360.

[3] Zargar SA, Yuan FG. Impact diagnosis in stiffened structural panels using a deep learning approach. Struct Health Monit 2021;20:681‑91.

[4] Fotouhi S, Pashmforoush F, Bodaghi M, Fotouhi M. Autonomous damage recognition in visual inspection of laminated composite structures using deep learning. Compos Struct 2021;268:113960.

[5] Paolino DS, Cavatorta MP, Belingardi G. Effect of thickness on the damage tolerance of lass/epoxy laminates subject to repeated impacts. P I Mech Eng C-J Mec 2017; 232:1363-73.

Proceedings IRF2025: 8th International Conference on Integrity-Reliability-Failure
In Engineering, Materials, Manufacturing and Biomechanics. Porto 15-18 July 2025
DOI: https://doi.org/10.24840/978-972-752-323-8

PAPER REF: 22632

FLAW DETECTION IN THERMOPLASTIC MATRIX CARBON FIBER REINFORCED COMPOSITE BY ULTRASOUND

João Pedro Learth Lourenço[1(*)], Camila Alves Farias[1], Cesar Giron Camerini[2], Celio Albano da Costa Neto[1]

[1]LPCM/COPPE, Federal University of Rio de Janeiro, Rio de Janeiro, Brazil
[2]LNDC/COPPE, Federal University of Rio de Janeiro, Rio de Janeiro, Brazil
[(*)]*Email:* jplearth@metalmat.ufrj.br

ABSTRACT

This work aims to validate ultra-sound defect detection in PVDF/CF composites. For this, two plates were manufactured using two different fiber ply angles (unidirectional and [60º/-60º] stacking). Defect-generating seeds were introduced during the pressing stage. The plates were characterized through density measurements to ensure compatibility with the values sent by the supplier. Then, the plates were inspected with ultrasound, using a phased array transducer. Lastly, the plates were scanned using micro computational tomography in order to validate the results obtained by the ultra-sound analysis, allowing a comparison of the effectiveness of each method. The results obtained indicate the validity of ultrasound as a defect detection tool for carbon fiber reinforced thermoplastic composites, regardless of ply angle.

Keywords: Thermoplastic composite, ultrasound, PVDF, carbon fiber, nondestructive testing.

INTRODUCTION

Thermoplastic matrix composites have been on the rise as the oil and gas industry is adopting thermoplastic composite pipes (TCPs) as potential replacements to the traditional flexible risers. However, not much is known about their behavior in operational conditions, so detecting internal damage in early stages is critical to maintain the integrity of the pipes. Ultrasound has been widely used as a nondestructive testing method due to its ease of use and wide range of applications, yet its application in TCPs is not well documented. The goal of this work is to validate ultrasound as a reliable defect detection tool for PVDF/CF composites.

RESULTS AND CONCLUSIONS

The material studied in this work is a composite made of a PVDF matrix reinforced with carbon fibers. The material was made available in prepreg tapes, with a 50/50 blend by weight. In order to manufacture plates out of the prepreg tapes, the compression molding technique was chosen.

PVDF is an engineering polymer widely used in oil and gas applications that require good mechanical properties, low chemical reactivity and, especially, high thermal stability (Saxena, 2021). Carbon fiber is a common reinforcement for polymer matrix composites due to its low weight, high mechanical strength and overall chemical stability (Zweben, 2005).

In order to determine the capability of defect detection in PVDF/CF composites, two plates of 8 mm thickness were pressed with circular defect-generating seeds interspersed between laminae. One plate was made with a unidirectional ply angle, with the second being made using a [60º/-60º] ply angle. The seeds were made using paper and Kapton tape, organized into four

rows of four disks with diameters of 2 mm, 4 mm, 8 mm and 16 mm, spread among four tapes at 1 mm intervals. This resulted in four lines of same size defects at the four different depths of 4 mm, 5 mm, 6 mm and 7 mm, measuring from the surface in contact with the transducer. Each of the lines was scanned using a time gain compensation curve made specifically for each size.

The phased array scan proved capable of identifying the seeded defects above the 2 mm diameter, while seemingly reaching its limit around this size threshold. The naturally occurring defects around this size within the pressed plate interfered with the detection of the seeds, partially or totally obscuring them in some cases. The identified defect zones also seem to preferentially follow the ply angle of the plate, which indicates that the zones could be delaminations caused by air bubbles being trapped along the fibers, Figure 1.

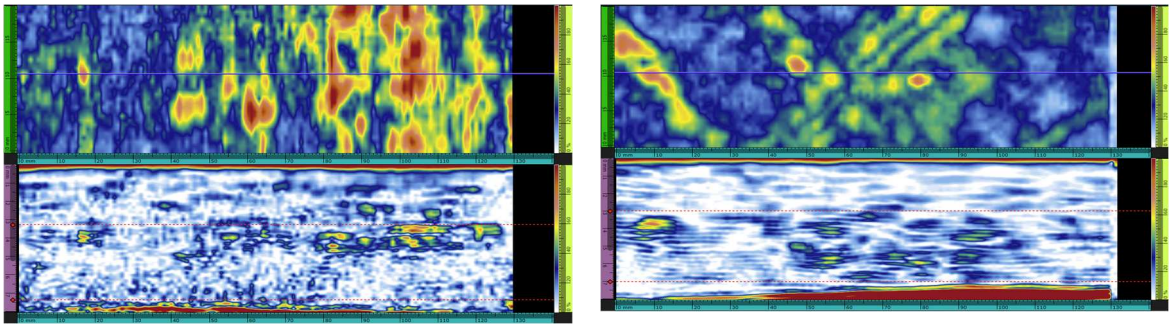

Fig. 1 - C-Scan and B-Scan results obtained with 2 mm TGC curve for unidirectional and [60º/-60º] ply plates.

The results were validated by micro computational tomography (microCT), where all the seeded defects were able to be identified, although the defects showed poor contrast against the plate, Figure 2. Their positions and sizes were matched to the results obtained by ultrasound, confirming their compatibility.

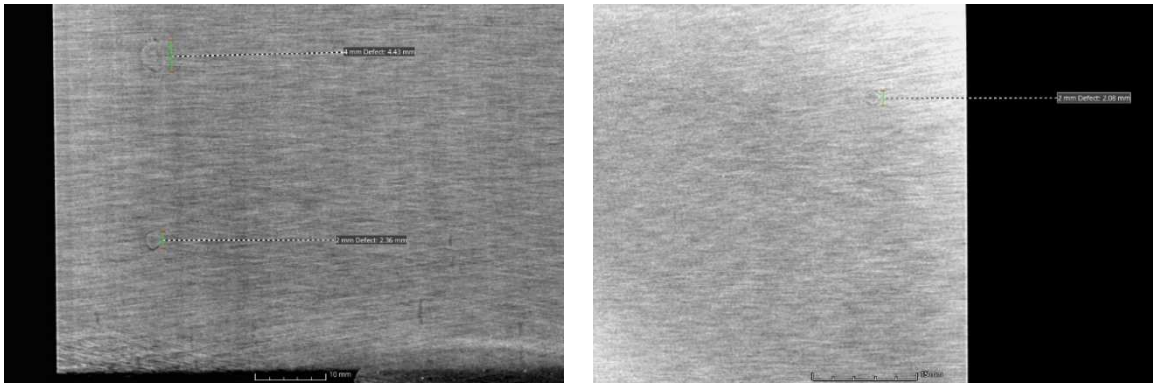

Fig. 2 - Tomography results for unidirectional and [60º/-60º] ply plates, showing 2 mm diameter defects.

This concludes that the ultrasound technique is a viable tool to investigate the internal state of thermoplastic matrix fiber reinforced composites and their eventual changes, such as defects, cavities, delaminations, etc., providing a quick and reliable nondestructive defect detection alternative for thermoplastic composites, while also not being restricted to lab conditions.

REFERENCES

[1] Saxena P, Shukla P. A comprehensive review on fundamental properties and applications of poly(vinylidene fluoride) (PVDF). Adv Compos Hybrid Mater 4, 2021, pp. 8-26.

[2] Zweben C. Mechanical Engineers' Handbook, Volume 1, 4th ed., John Wiley & Sons, Inc., New York, 2015, pp. 401-438.

Proceedings IRF2025: 8th International Conference on Integrity-Reliability-Failure
In Engineering, Materials, Manufacturing and Biomechanics. Porto 15-18 July 2025
DOI: https://doi.org/10.24840/978-972-752-323-8

PAPER REF: 22641

THE POSSIBILITY OF INCREASING THE IMPACT RESISTANCE OF AN EPOXY RESIN-BASED MATRIX BY USING POWDER ADDITIVES

Paweł Przybylek(*), Joanna Masiewicz, Tomasz Zahorski, Robert Szcepaniak
Tme Polish Air Force University, Faculty of Aviation, Dyvwizonu 303 str. No.35, 08-530 Dęblin
(*)*Email: p.przybylek@law.mil.pl*

ABSTRACT

The physical modification of the epoxy matrix is an effective form of influence to improve the strength properties of composites. The aim of this study was to analyse the effect of the addition of powder fillers to the matrix of a composite with carbon fibre fabric reinforcement on the impact resistance. For this purpose, four composites from L 285 resin matrix cured H 285 hardener with powder fillers were fabricated. Three kind of powder fillers were used: halloysite nanoclay, TiO_2 and CeO_2 in certain proportions amounting to 2,5%, 5% and 10%of weight share. In order to evaluate the effect of the additive, the tested materials were subjected to transverse impact loads of 0,5 [J] and 1 [J]. Based on the results obtained, it was observed that each of the three powder additives with a 2.5 percent share increases the values of the above-mentioned parameters compared to samples without filler. However, as the amount of powder increases, these values decrease, and at 10% they are even lower than samples made from resin alone. The exception is the addition of titanium oxide TiO_2, which with a 5% share and an impact energy of 0.5 [J] achieves the highest values of all batches.

Keywords: Composites, powder fillers, impact resistances.

INTRODUCTION

Epoxy resin and carbon fiber composite materials are widely used in the aerospace industry due to their strength, high modulus of elasticity and low weight. [Dutton, at a.l 2004]. The use of epoxy resins as a matrix is very popular due to their good structural properties, which include high stiffness and strength, creep resistance, chemical resistance and good adhesion to many substrates. [Karnati, at al. 2020]. A commonly used method of modifying composite materials is the use of powder fillers.. Typically, traditional composites require a substantial amount of filler (more than 10 wt%) to fulfill the necessary functions and applications. Higher filler loading increases the composite's density and creates processing difficulties. This degrades the overall mechanical performance of composites [Shelly,at al. 2024]. Powder additives are used as functional fillers in many polymer-based composites where the dominant factors are particle uniformity, shape, diameter and surface chemistry, which influence the physical and material properties of the final product. These properties include, for example, mechanical strength, fracture resistance, thermal behavior and electrical conductivity. [Lapčík, at al. 2019].

RESULTS AND CONCLUSIONS

To produce composite samples, L285 epoxy resin with H285 hardener was used, which was modified by adding the following powder materials: halloysite nanoclay, dwutlenek tytanu TiO_2 and CeO_2 in specific proportions of 2,5%, 5% and 10% weight share. 10 groups of 4 samples of each composite were made. The Instron 9440 drop hammer (drop tower) was used

to measure the impact resistance of the finished composite samples.. To analyze the results, the time courses of force and energy changes, as well as the force and energy changes in relation to deformation, were used. In addition, the obtained properties were analyzed: the impact resistance [force on thickness N/m], the impact resistance [energy on thickness J/m], peak force, peak energy, displacement corresponding to the maximum force.

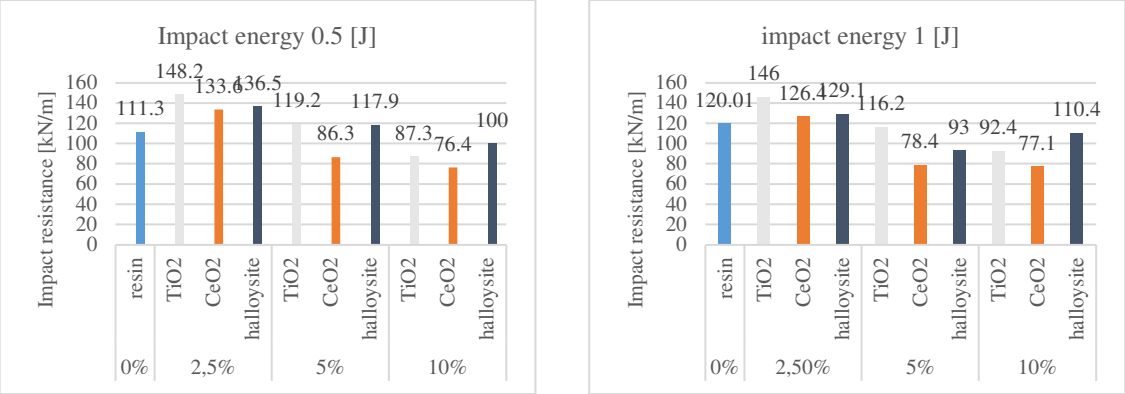

Fig. 1 - Impacy resistance [N/m] depending on the type and percentage of filler for 0,5[J] and 1[J].

- t was observed that each of the three powder additives at a share of 2.5 percent increased the values of the above-mentioned parameters compared to the samples without filler.
- With the increase in the amount of powder, the parameter values decrease, and at 10% they are even lower than samples made of resin alone.
- The exception is the addition of titanium oxide TiO_2, which with a 5 percent share at an impact energy of 0.5J achieves the highest values of all batches, except for the deformation parameter.
- In the case of an impact with twice the energy, the largest increase in value was also recorded for TiO_2, but for a share of 2.5%.
- In terms of deformation at maximum force, the results were consistent, with almost all samples with powder fillers achieving higher values than the nominal values of pure resin.

REFERENCES

[1] Dutton, S.; Baker, A.A. Aircraft Applications and Design Issues. In Composite Materials for Aircraft Structures, 2nd ed.; Baker, A.A., Dutton, S., Kelly, D., Eds.; AIAA, American Institute of Aeronautics and Astronautics, Inc.: Reston, VA, USA, 2004; pp. 435-476.

[2] Karnati SR, Agbo P, Zhang L. Applications of silica nanoparticles in glass/carbon fiber-reinforced epoxy nanocomposite, composites. Communications. 2020; 17: pp. 32-41. doi:10.1016/j.coco.2019.11.003.

[3] Lapčík L., Vašina M., Lapčíková B. et al. Materials characterization of advanced fillers for composites engineering applications. Nanotechnology Reviews, 2019, nr 8.

[4] Shelly, D.; Singhal, V.; Nanda, T.; Mehta, R.; Aepuru, R.; Lee, S.-Y.; Park, S.-J. A review of the emerging approaches for developing multi-scale filler-reinforced epoxy nanocomposites with enhanced impact performance. Polym. Compos. 2024, 45, pp. 9647-9676.

Proceedings IRF2025: 8th International Conference on Integrity-Reliability-Failure
In Engineering, Materials, Manufacturing and Biomechanics. Porto 15-18 July 2025
DOI: https://doi.org/10.24840/978-972-752-323-8

PAPER REF: 22643

THE INFLUENCE OF THE MOLD SIZE ON PROPERTIES OF GFRP MADE BY INFUSION METHOD

Jacek Janiszewski(*), Andrzej Komorek, Daniel Śliwiński
Faculty of Aviation, Polish Air Force University, Dęblin, Poland
(*)*Email:* j.janiszewski@law.mil.pl

ABSTRACT

The aim of the work is to investigate the influence of the mold size on the properties of a layered composite produced by the infusion method, i.e. how the form affects the propagation of the resin composition and the strength characteristics of the laminate. The scope of the work includes the following activities: production of one composite by the infusion method (which was divided into twelve research sectors), examination of individual samples from each sector under a microscope (in terms of the content of air voids in the material structure), examination of the internal and external structure of the laminates under a microscope, tests of the mechanical properties of samples prepared from the produced composite (bending strength test, impact strength test and tensile strength test).

Keywords: Layered composites, composite manufacturing processes, infusion method, GFRP (glass fiber reinforced polymer).

INTRODUCTION

Modern industry, especially aviation, is constantly striving to develop innovative materials that can create structures with maximum strength while maintaining minimum weight. One of the most important achievements in this field are composite materials. Composites consist of at least two separate phases: reinforcement and matrix. They have unique properties compared to traditional materials such as metals and alloys. Reinforcement, often in the form of fibers (e.g. glass fiber, carbon fiber), is responsible for transferring loads and providing high strength. Meanwhile, the matrix bonds the elements and protects them from environmental influences. Composite materials are becoming increasingly important in the aviation industry, because they reduce the weight of aircraft, which leads to lower fuel consumption and lower operating costs. Composite technology allows the development of materials for specific applications due to their anisotropic properties, which makes them extremely versatile. Manufacturing methods such as infusion allow the creation of elements with complex shapes and large dimensions while ensuring high quality and structural coherence. Thanks to the continuous development and improvement of production methods, composite materials have become the basis of modern industrial structures and have set new standards of strength and efficiency. Thanks to this technology, it was possible to produce inexpensive composites that meet the requirements of the aviation industry.

For the purpose of this work, the nine layers composite was made with reinforcement of glass fiber roving fabric with a weight of 390 g/m^2 and a saturation of 370 g/m^2 and a "twill" weave. MGS L285 epoxy resin and H287 hardener were used for production. The resin and hardener were mixed in a 100:40 ratio (according to the manufacturer's recommendations). In order to facilitate the removal of the composite from the mold, a delamination fabric was used. In addition, a special mesh was used to facilitate the propagation of the resin mixture and its even

flow through the mold. The final dimensions of the composite were 100 x 100 cm. The composite was divided into 12 zones and tested.

RESULTS AND CONCLUSIONS

The tested samples were cut using water, thanks to which they had very accurate dimensions. This enabled the generation of reliable results. However, after measuring the thickness of individual samples, a tendency was noticed to reduce it with each tested zone. In the first zone, the average thickness of the tested elements was 3.01 mm, and in the tenth it was already 2.86 mm. This tendency also resulted from the calculations of the percentage share of reinforcement in the laminate. In the first samples it was 62% and in the last 64%. Visual examination using a microscope showed many differences in the surface and internal structure of the samples. The tested elements from the first zone of the composite had many air voids. Numerous air voids of small diameter were visible in the surface structure. On the other hand, in the internal cross-section, there were fewer cavities, but they were larger. The tendency of air voids to appear inside the composite decreased until the sixth zone, where the least were observed. Under the microscope, an increase in the number of air voids in the structure of samples from further zones could be seen. There were not as many of them as in the first zone, but their diameter was larger. The strength tests began with the Charpy impact test. The samples were tested for edge and surface impact strength. Regardless of the tested zones from which the test elements were taken, they were damaged in a similar way. The results that were obtained did not indicate significant differences between the impact strength properties. The only thing that can be noted is that the results of the average edge impact strength were higher than the surface impact strength. The bending strength test of individual samples showed a certain trend as in the visual test. The strength modulus increased up to the fifth zone and then decreased. This may be related to the number of air voids in the laminate, which significantly change its properties. The course of the bending strength graph is diametrically different from the modulus graph. It also increases up to the fifth zone, but then drops rapidly. Large air voids located in the last zones and a smaller thickness of the laminate may affect its strength results. During the determination of tensile strength, all samples showed a similar value of Young's modulus. The difference between the highest average value and the lowest was 3.5%. Tensile strength depends to a large extent on the reinforcement used, which is the same throughout the composite. This may be the reason for such small differences in the obtained results. Based on the conducted tests and the obtained results, it can be concluded that the size of the mold in which the composite is created plays one of the key roles in the infusion process. It affects the propagation of the resin composition and the strength properties of the composite. The highest bending strength was demonstrated by samples from sector five. In the tensile test, the best result was achieved by zone seven. The ambiguous results show the high influence of the mold (especially its size) on the propagation of the resin mixture in the infusion process.

REFERENCES

[1] Lunn, P. Cost-effective resin infusion. Reinf. Plast. 2009.

[2] Janiszewski J., Komorek A., Bakuła M., Bieńczak. R., Pękala B. The influence of pressure in the infusion method upon mechanical properties of polymer composites. Adv. Sci. Technol. Res. J. 2023, 17(6), pp. 217-227.

[3] Mehdikhani, M., Gorbatikh, L., Verpoest, I., Lomov, S.V. Voids in fiber-reinforced polymer composites: A review on their formation, characteristics, and effects on mechanical performance. J. Compos. Mater. 2019.

Proceedings IRF2025: 8th International Conference on Integrity-Reliability-Failure
In Engineering, Materials, Manufacturing and Biomechanics. Porto 15-18 July 2025
DOI: https://doi.org/10.24840/978-972-752-323-8

PAPER REF: 22646

TENSILE STRENGTH OF A COMPOSITE WITH A POWDER AEROGEL EXPOSED TO A THERMAL FLOW

Robert Szczepniak, Andrzej Komorek(*), Paweł Przybyłek, Mateusz Bąk
Polish Air Force University, Dęblin, Poland
(*)*Email:* a.komorek@law.mil.pl

ABSTRACT

Composite materials have been used in aviation for many years. Their use is becoming increasingly popular due to the unique properties of these materials. Due to the increasing need to protect various aircraft devices from the effects of high-temperature heat flux, it was proposed to produce a polymer composite with reinforcement in the form of aerogel powder. The research presented in the article presents the results of tensile strength tests of this type of ablation composite subjected to the action of high-temperature heat flux. Composites with different contents of powder aerogel were produced and cross-linked at different temperatures, and after taking the necessary measurements, they were subjected to the action of a hot gas stream, after which mechanical properties were tested and microscopic observations of fractures were performed. The results obtained during the tests and the analysis carried out allow us to state that both the amount of additive and the temperature at which the composite will cross-link have a significant effect on its strength properties.

Keywords: Polymer composite, aerogel, tensile strength, heat flux.

INTRODUCTION

Dynamically developing technology and constantly growing demand of the industry have led to a significant advantage of composites over other materials combining features such as excellent mechanical and strength parameters, low specific gravity and low production costs (Karsandik, et al., 2023). Aerogel, in turn, is a material that is characterized by excellent thermal insulation properties, strength and an incredibly low specific gravity. Thanks to its unusual structure, it has properties that have found application in the construction, space, chemical and electronics industries. It is the lightest solid material with the lowest value of the thermal conductivity coefficient λ (Sachithanadam, et al., 2016). Combining epoxy resin with a material with ultra-low thermal conductivity can enable the production of a material with acceptable mechanical strength and very good thermal protection.

RESULTS AND CONCLUSIONS

The test samples were made by casting in silicone molds. The polymer material was a composition of L286 resin and H287 hardener. The aerogel particles used in the tests had a diameter of 1.2–4.0 mm. During the preparation of the resin and aerogel composition, a technique was used to limit sedimentation of the mixture. The samples were characterized by the content of aerogel in the mass fraction from 0 to 4%. After casting into the molds, the samples were left to cross-link for 24 hours. After removal from the molds, the samples were divided into 3 series, which were then annealed at different temperatures. Then the geometry

of the samples was verified, the allowances were ground and their geometric dimensions and mass were determined.

For the ablation tests, the samples were placed in special holders resistant to high temperatures and exposed to a high-temperature gas stream. After cooling, the samples were successively placed in the holders of a universal testing machine and subjected to a tensile test. An analysis of the change in the thickness of the tested samples was also carried out based on measurement data before and after the heat flux impact on individual samples. On this basis, the mass loss of individual samples was determined and the effect of the annealing temperature and the share of the aerogel additive on this parameter was analyzed. The samples were additionally subjected to a Shore hardness test, which noted, among other things, that in samples annealed at 55°C, the hardness increases with the increase in the aerogel content.

Analyzing the results of the tensile strength tests, it can be seen that the highest strength values among the samples with aerogel are characterized by samples exposed to the high-temperature flux for the longest time (30 seconds). In turn, observing the nature of the changes in the Young's modulus value of samples heated after cross-linking at 80°C, it can be seen that extending the time of exposure to the high-temperature flux (the tests used a time of 10 or 30 seconds) causes an increase in the Young's modulus value regardless of the percentage of aerogel content. The results obtained during the tests and the analysis performed allow us to conclude that both the amount of additive and the temperature at which the cross-linking of the tested composite was carried out have a significant influence on its strength properties.

REFERENCES

[1] Karsandik, Y., Sabuncuoglu, B., Yildirim, B., Silberschmidt, V.V. Impact behavior of sandwich composites for aviation applications: a review. Composite Structures, 314, 116941, 2023.

[2] Sachithanadam M., Joshi S. C.: Silica aerogel composites, Engineering materials, Springer Singapore, 2016.

Proceedings IRF2025: 8th International Conference on Integrity-Reliability-Failure
In Engineering, Materials, Manufacturing and Biomechanics. Porto 15-18 July 2025
DOI: https://doi.org/10.24840/978-972-752-323-8

PAPER REF: 22838

A STRENGTH ASSESSMENT OF STRUCTURAL COMPOSITES WITH MODIFIED EPOXY MATRIX UNDER LOW-ENERGY STATIC AND DYNAMIC LOADS

Joanna Masiewicz(*), Paweł Przybylek, Robert Szczepaniak

Faculty of Aviation, Polish Air Force University, Dęblin, Poland
(*)*Email:* j.masiewicz@law.mil.pl

ABSTRACT

Structural composites with a foam core and modified epoxy matrix represent an interesting solution in the field of energy-absorbing materials for low-energy impact resistance. Chemical modification of the structural composite matrix by the addition of liquid polyurethane was used, an innovative element in the manufacture of sandwich composites used as energy-absorbing structures. A lightweight and flexible XPS foam core bonded with composite reinforcing layers was also used. A maximum composite thickness of up to 10 ± 1 mm was retained and the core was spread over 3 graded layers. Impact bending tests of the short beam, three-point bending, damage tolerance, puncture resistance and dynamic mechanical analysis of the matrix layer were carried out.

Keywords: Composite structures, mechanical properties, low-energy impact, BVID

INTRODUCTION

Energy-absorbing materials are subjected to specific exposure to impact loads, bending or compression, in 'emergency' situations where there is an accidental or intentional static or dynamic impact. In practice, this means preserving a material that has an effective energy absorption capacity (Haq, 2021). The right choice of materials and design, fabrication technique, as well as repair and maintenance strategies can guarantee the production of highly efficient composite structures for low-energy impact shielding (Isaac, 2021). The effect of low-energy impacts is often subsurface delamination, which is difficult to identify visually or manifests itself as a very slight deformation of the composite surface, is referred to as Barely Visible Impact Damage (BVID) (Polimeno et al., 2009). This paper presents the effect of chemical modification of the matrix on the mechanical properties of the composite with plain glass fabric and XPS foam. The introduction of the modifier is attributed not only to an improvement in the strength properties of the matrix layer, but also to an improvement in the adhesion properties between the composite phases, the inhibition of crack propagation throughout the cladding layer.

RESULTS AND CONCLUSIONS

Based on previous experimental studies using PU in the range of 0 - 20% and an analysis of the literature (Kostrzewa et al., 2015), used a modification of the matrix in the amount of wt. 0-10%. The liquid polymer modification used in this study led to the formation of interpenetrating polymer networks between the reactive groups - OCN in the structural chain of the polyurethane and the resin. It was noteworthy that polyurethane could also form chemical bonds with hydroxyl groups present on the glass surface.

The DMA test made it possible to characterise the composite layer and confirm the mechanism of reinforcement depending on the modifier content in the negative and positive temperature range and under constant, repeated loading. The addition of 5 wt% modifier in the epoxy matrix with GF250 reinforcement in the positive temperature range resulted in an increase in the loss modulus E' (169.80 MPa), Figure 1 and Table 1. The ratio of material stiffness to viscoelastic properties (tgδ) was lowest for the EP0250GF composite (0.18) and highest for the 10PU250GF composite (0.37). The conservative modulus of the composites, which determines the stiffness of the material, showed that the modified composites exhibited a sharp decrease in stiffness at temperatures around 60 - 70°C.

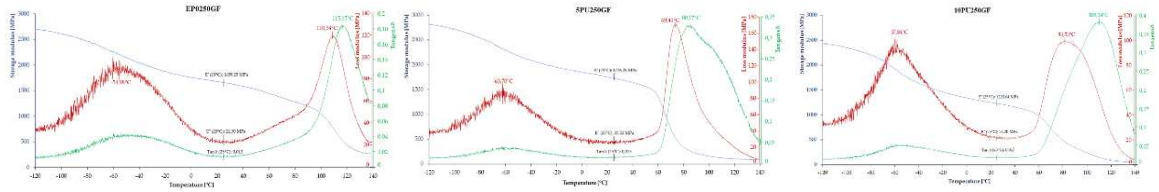

Fig. 1 - Comparison of dynamic mechanical analysis of EP/PU/250GF composites.

Tab. 1. – Comparison of selected mechanical properties

	Charpy impact strength [kJ/m^2]		Energy absorbed [J]	Flexural modulus [MPa]	Compresion modulus [MPa]
	Perpendicular	Parallel			
EP0250GF	10,84	14,08	7,89	41,95	130
5PU250GF	11,28	17,67	7,92	35,57	175
10PU250GF	11,82	18,58	7,76	40,75	175

Visual identification of surface damage showed the impactor point impact trace and linear cracks radiating in two directions. The unmodified composites cracked in the matrix layer, also damaging the fibres in the reinforcement layer. Modified composites maintained structural continuity in the composite layer due to the elasticising effect of the modifier.

REFERENCES

[1] Haq A.U. A brief review on various high energy absorbing materials. Materials Today: Proceedings 38, 2021, pp. 3198-3204.

[2] Isaac C.W., A review of the crashworthiness performance of energy absorbing composite structure within the context of materials, manufacturing and maintenance for sustainability. Composite Structures 257, 2021, 113081.

[3] Polimeno U., Meo M. Detecting barely visible impact damage detection on aircraft composites structures. Composite Structures, Volume 91, December 2009, pp.398-402.

[4] Kostrzewa M., Effect of polyurethane type on mechanical properties of composites based on epoxy resin with IPN structure, Przetwórstwo Tworzyw 2, 2015, pp. 131-134.

Proceedings IRF2025: 8th International Conference on Integrity-Reliability-Failure
In Engineering, Materials, Manufacturing and Biomechanics. Porto 15-18 July 2025
DOI: https://doi.org/10.24840/978-972-752-323-8

PAPER REF: 23459

MANUFACTURING MONITORING IN FULL-SCALE CFRP WING BY EMBEDDED FIBRE OPTIC DISTRIBUTED SENSORS

Lorenzo Pellone[1(*)], Monica Ciminello[1], Gianvito Apuleo[2], David Bardenstein[2], Umberto Mercurio[1], Antonio Concilio[1],

[1]CIRA, Italian Aerospace Research Centre, Capua, Italy
[2]Piaggio Aerospace, Research and Technology Development, Villanova d'Albenga, Italy
[3]Israel Aerospace Industries, Ben Gurion International Airport, Tel Aviv 70100, Israel
[(*)]*Email:* l.pellone@cira.it

ABSTRACT

The adoption of integrated sensing has significantly improved the maintenance and failure inspection of CFRP aircraft structures. Fiber optic (FO) sensor networks, known for their compactness and multiplexing capabilities, enable real-time structural health monitoring (SHM) by detecting damage in bonded joints and manufacturing defects such as porosity, delamination, and inadequate adhesive curing. However, Non-Destructive Inspection (NDI) techniques remain limited due to the lack of standardized defect generation methods, affecting inspection accuracy. This study presents an SHM system developed by CIRA under the OPTICOMS project (CLEAN SKY2 program) for monitoring the structural integrity of a full-scale P180 aircraft wing during a static test campaign at Piaggio Aerospace (PA) Laboratory. The system, featuring fiber optic sensors embedded within adhesive layers, successfully detected manufactured defects, with size and location confirmed by ultrasonic NDI inspections performed by Israelian Aerospace Industries (IAI). The results demonstrate the high reliability of fiber optic-based SHM as a viable solution for bonded joint integrity assessment, supporting compliance with aviation safety regulations.

Keywords: Composite structures, full-scale wing, fibre optics, adhesive bonding, damage characterization, structural health monitoring, adhesive joint

AIM OF THE WORK - OPTICOMS PROJECT

The aim of this work is the development and validation of an SHM system designed by the Italian Aerospace Research Centre (CIRA) within the OPTICOMS project, funded by the CLEAN SKY2 program. The system was deployed for real-time monitoring of the structural integrity of a full-scale P180 aircraft wing (Figure 1-a), manufactured using CFRP materials, during an experimental static test campaign at the Piaggio Aerospace (PA) Laboratory. The objective was to evaluate the SHM system's capability to detect, locate, and quantify defects within the structure, comparing its performance with conventional NDI techniques.

DATA PROCESSING METHODOLOGY

The proposed SHM system utilized an embedded fiber optic sensing network within the adhesive paste layers of a composite wing box to enable real-time strain monitoring and damage detection. The full-scale wing demonstrator was tested under static loading conditions without artificial damage to allow a direct comparison between the L.H.E.O. algorithm and NDI inspections. Eight embedded fiber optics were installed between caps of the spars and the lower

skin during the manufacturing process by IAI to maximize damage detection sensitivity (Figure 1-b). To enable real-time data acquisition, an optical fiber interrogator (LUNA OdisiB) was used alongside a laptop-based monitoring system.

1.Length: 6846 mm
2.Max section height: 198 mm
3.Root chord: 708.55 mm
4.Tip chord: 282.9 mm

(a)

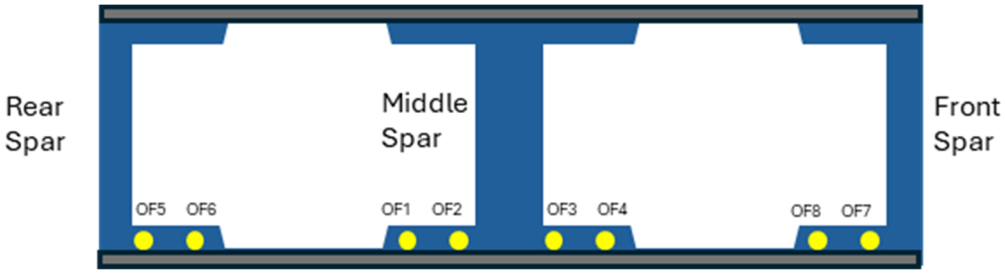

(b)

Fig. 1 - Piaggio P180 Full-Scale Wing and OF location at cross section schematic view.

The L.H.E.O. algorithm, developed by CIRA in Matlab™, employs edge detection techniques and cross-correlation filtering to identify localized strain variations linked to structural damage. It defines Damage Indices (DI) and Threshold Levels (TL) to detect anomalies, ensuring precise fault localization (Figure 2**Error! Reference source not found.**). The experimental tests were conducted at Piaggio Aerospace's Structural Lab using a whiffletree test rig, replicating a Limit Load (L.L.) at Maximum Takeoff Weight (MTOW) positive gust maneuver. A comprehensive sensor network, including strain gauges, LVDTs, and high-resolution cameras, was integrated to monitor structural behavior and capture failure mechanisms.

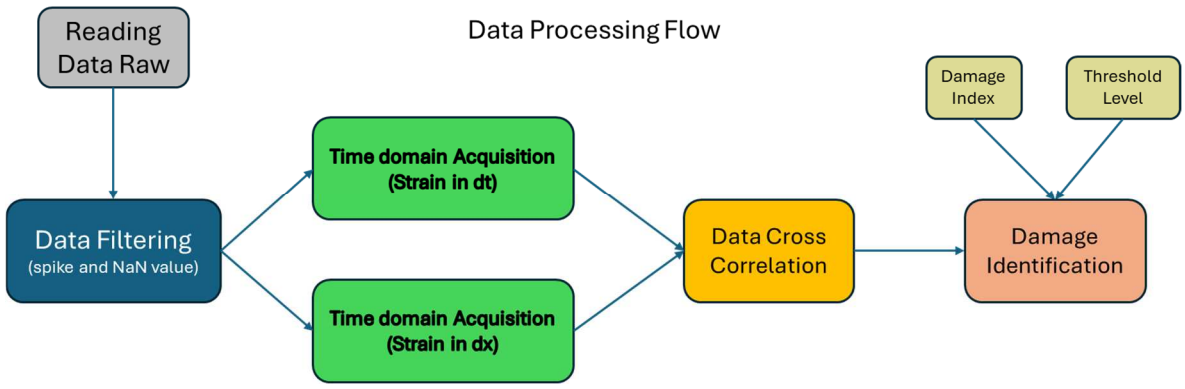

(a)

Fig. 2 - LHEO Algorithm workflow scheme.

RESULTS AND DISCUSSION

Figure 3-a) shows the case of a full-scale composite wing box demonstrator designed and manufactured by IAI to replicate the wing structure of the Piaggio P180 Avanti EVO aircraft. The assembly includes a lower section made of co-cured spars, along with an upper skin panel and a lower panel, the latter of which is bonded in a subsequent curing process. Tests were conducted at Piaggio Aerospace's Structural Lab with using a dedicated whiffletree test rig to apply a representative load configuration defined in the test matrix, and on that base, a distributed load schematic was designed able to replicate at a good extent the actual stress-strain filed related to that load configuration (Figure 3-a).

The experimental campaign was conducted in phases, starting with load applications from 20% up to 70% of the Limit Load (L.L.). At 70% L.L., an unexpected nonlinear strain response was detected, prompting an immediate test stoppage. Strain analysis revealed localized strain spikes in OF6, installed between the lower skin and the cap of the rear spar, suggesting potential disbonding or delamination. The L.H.E.O. algorithm was applied to process the data, identifying a 40 mm damage length along the rear spar, aligning with residual strain anomalies (Figure 3-b).

(a)

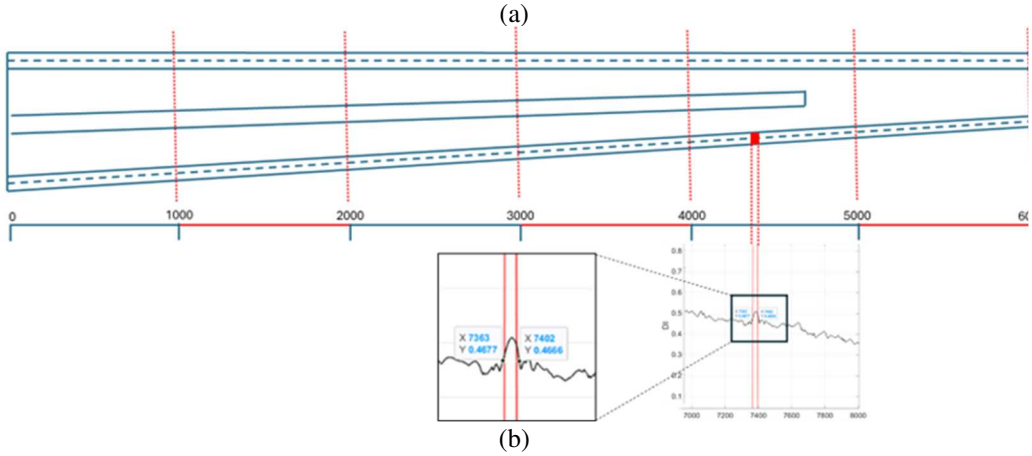

(b)

Fig. 3 - Piaggio Lab. Wing Test Rig (a) and (b) SHM final readout on RS edge cap along rear spar.

The results were validated using Ultrasonic NDI inspections, performed by IAI, which confirmed the presence of delamination at the same location and size. This strong correlation demonstrates the effectiveness of the L.H.E.O. algorithm in detecting and characterizing structural damage. The findings highlight the potential of fiber optic-based SHM systems as a reliable, real-time alternative to traditional NDI methods, contributing to improved structural health monitoring.

CONCLUSION

The SHM system demonstrated high reliability in detecting both the position and size of manufactured defects within the bonded joints of the composite wing. The system effectively identified structural anomalies that were later confirmed through ultrasonic NDI inspections, validating the accuracy and robustness of the fiber optic-based monitoring approach.

The results highlight the potential of fiber optic-based SHM as a viable, non-intrusive, and highly accurate solution for ensuring bonded joint integrity. By addressing the limitations of conventional NDI techniques, this approach aligns with aviation regulatory requirements, supporting the development of safer and more reliable aircraft structures.

Proceedings IRF2025: 8th International Conference on Integrity-Reliability-Failure
In Engineering, Materials, Manufacturing and Biomechanics. Porto 15-18 July 2025
DOI: https://doi.org/10.24840/978-972-752-323-8

PAPER REF: 23491

A MEMETIC ALGORITHM FOR THE MULTI-OBJECTIVE OPTIMIZATION OF GEOMETRICALLY NONLINEAR COMPOSITE STRUCTURES

Carlos Conceição António(*), Ricardo Oliveira de Faria
INEGI/LAETA, Faculty of Engineering, University of Porto, Porto, Portugal
(*)*Email:* cantonio@fe.up.pt

ABSTRACT

A multi-objective optimization framework for the sizing and anisotropic topology of geometrically nonlinear beam-stiffened shell structures made of fiber-reinforced plastics is proposed. The objective functions for the proposed robust design approach are the minimization of mass and the strain energy's mean value, standard deviation and coefficient of variation. Their trade-offs are optimized while adhering to stress, displacement and buckling constraints. The design variables are the ply angles of the shell laminates, the ply widths of the beam laminates and the thicknesses and materials of all layers in the structure. The proposed Multi Objective Memetic Algorithm (MOMA) exploits the synergy between multiple Lamarckian and Baldwinian learning procedures, whose relative performance determines their selection for future offspring generation. Design space decomposition is achieved through the use of multiple sequentially-evolving subpopulations, while a virtual population with age-dominance dual nature updates the Pareto front and accelerates the global search. The concept of species serves as an abstraction of the search space discontinuities due to the presence of integer type design variables. The MOMA is validated through its application to two bi-objective and two tri-objective optimization problems.

Keywords: Memetic, multi-objective, hybrid composites, geometric nonlinearity.

INTRODUCTION

In an effort to reduce the costs associated with the manufacturing of FRP composite structures, considerable research has been devoted to the hybridization between expensive and higher stiffness materials and less expensive and lower stiffness materials. Memetic Algorithms have been shown to be an effective and efficient approach to this complex design problem (António, 2024).

RESULTS AND CONCLUSIONS

The MOMA was applied to the multi-objective optimization of a spherical composite structure composed of three shell laminates and three beam laminates, hinged along its perimeter and with a point load acting on its central node (Figure 1).

The MOMA was extended to be able to handle optimization problems with any number of objectives. Subsequently, the tri-objective optimization problem addressing the minimization of mass and the strain energy's mean value and standard deviation was studied. The results that were obtained illustrate its effectiveness in finding optimal solutions.

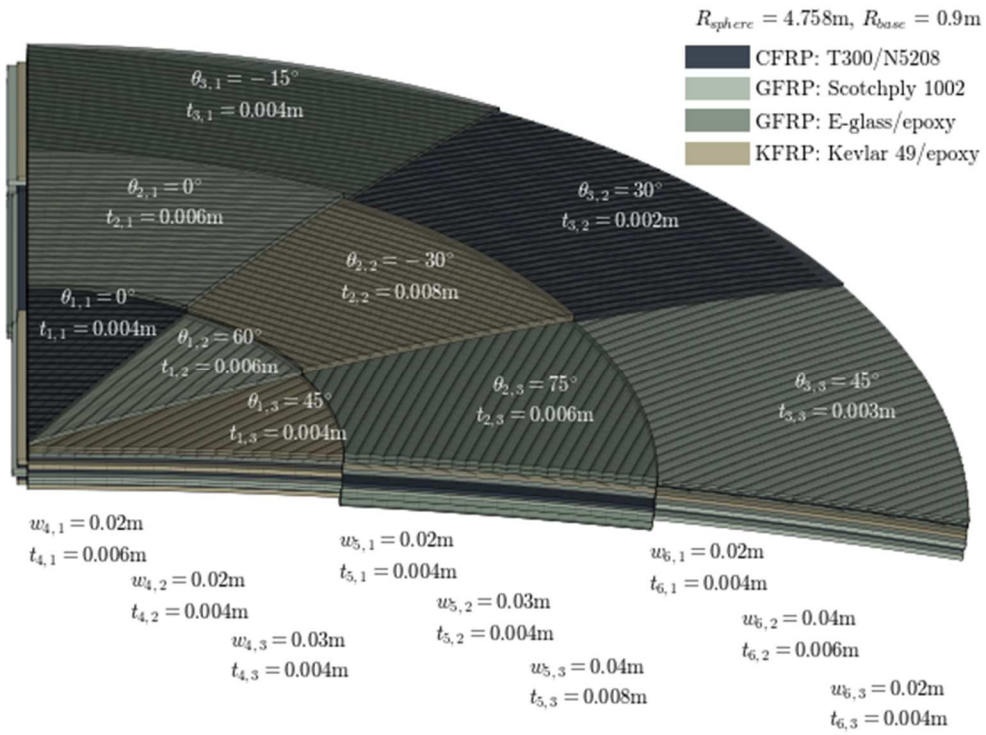

Fig. 1 - Beam-reinforced shallow shell structure for a given set of design variables.

The MOMA was extended to be able to handle optimization problems with any number of objectives. Subsequently, the tri-objective optimization problem addressing the minimization of mass and the strain energy's mean value and standard deviation was studied. The results that were obtained illustrate its effectiveness in finding optimal solutions.

The study of species distribution on the Pareto front revealed a niching effect that validated the adopted domain decomposition that was based on the assumption that different material combinations offer specific trade-offs. Furthermore, this effect suggests that hybrid composites may unlock otherwise unattainable design solutions.

REFERENCES

[1] António, C.C. Memeplex-based memetic algorithm for the multi-objective optimal design of composite structures. Composite Structures, pp. 2024, 329, 117789.

TRACK - B: Fatigue and Fracture Mechanics

Fracture Behaviour at Varied Length Scales
Mechanisms for Crack Propagation`
Tribological Effects and Surface Damage
Thermomechanical Fatigue
Corrosion-Fatigue Interaction
Crack Closure in Crack Healing
Fatigue Fracture of Intelligent Materials
Effect of Surface Treatments
Crack Monitoring Techniques
Case Studies

Proceedings IRF2025: 8th International Conference on Integrity-Reliability-Failure
In Engineering, Materials, Manufacturing and Biomechanics. Porto 15-18 July 2025
DOI: https://doi.org/10.24840/978-972-752-323-8

PAPER REF: 22228

A STAGGERED GRID SHELL PARTICLE METHOD FOR SHELL STRUCTURAL DAMAGE SUBJECTED TO UNDERWATER EXPLOSION

Jiasheng Li, Xiong Zhang(*)

School of Aerospace Engineering, Tsinghua University, Beijing, P R China
(*)*Email:* xzhang@tsinghua.edu.cn

ABSTRACT

A novel staggered grid shell particle method (SGSPM) is proposed in this work to model the shell structural damage subjected to underwater explosion. The material point method (MPM) is used to model the fluid in underwater explosion, and the solid shell material point method (SSMPM) is adopted to model the shell structures. A staggered grid scheme is employed to eliminate the cell crossing noise, mitigate the volumetric locking and improve the accuracy of fluid simulation, and a conversion algorithm is proposed to handle the dynamic fracture of shell structures. In addition, a local multi-mesh contact method is introduced into the staggered grid scheme for modelling the fluid-structure interaction.

Keywords: Material point method, solid shell, staggered grid, structural damage, underwater explosion.

INTRODUCTION

Underwater explosion is a class of extreme deformation problems and always causes severe damage to ship shell structures in engineering practice. To guide the design of engineering structures, the structural damage subjected to underwater explosion has attracted great attention. Experimental research and numerical research are important methods for evaluating the damage of ship structures. However, the cost of damage experiments on large engineering structures is extremely high. Therefore, the development of efficient and powerful numerical methods to simulate structural damage subjected to underwater explosion remains an active field of research. In the present work, a novel staggered grid shell particle method (SGSPM) is developed by introducing the staggered grid scheme and conversion algorithm into the SSMPM (Li et al., 2024) and employing a local multi-mesh contact method.

RESULTS AND CONCLUSIONS

The large deformation of a plate subjected to underwater explosion is simulated. Ramajeyathilagam and Vendhan (Ramajeyathilagam and Vendhan, 2004) carried out the experiment. Due to symmetry, the first octant of the model is simulated, as shown in Figure 1.

The final deformed configurations of the plate are shown in Figure 2. The plate has undergone large deformation, which can be seen from the deflection contours of simulations. The deformed configurations in the simulations are in good agreement with the experimental result.

The final center deflections of experiment and simulation are 57.8 and 58.5 respectively, which are consistent. The results verify the accuracy of SGSPM in simulating shell structures subjected to underwater explosion.

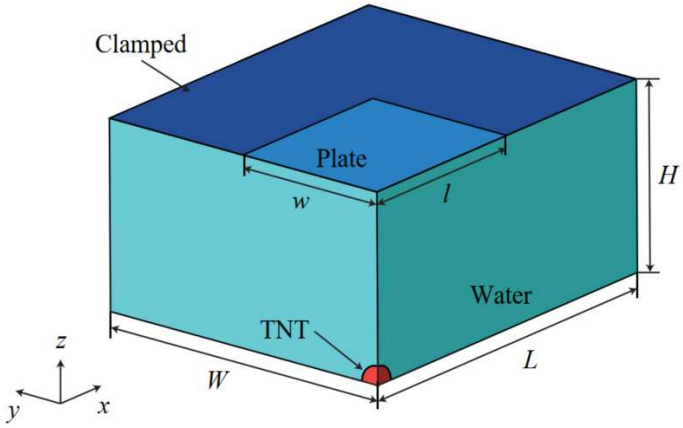

Fig. 1 - Diagram of plate subjected to underwater explosion.

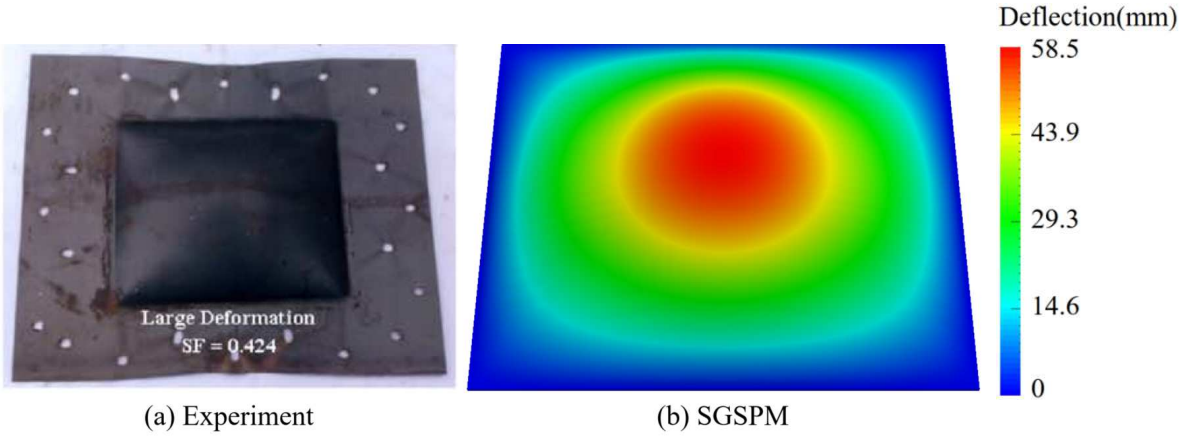

Fig. 2 - Final deformed configurations of the plate.

REFERENCES

[1] J. Li, R. Ni, Z. Zeng, X. Zhang, An efficient solid shell material point method for large deformation of thin structures, International Journal for Numerical Methods in Engineering 125 (1) (2024) e7359.

[2] K. Ramajeyathilagam, C. Vendhan, Deformation and rupture of thin rectangular plates subjected to underwater shock, International Journal of Impact Engineering 30 (6) (2004), pp. 699-719.

Proceedings IRF2025: 8th International Conference on Integrity-Reliability-Failure
In Engineering, Materials, Manufacturing and Biomechanics. Porto 15-18 July 2025
DOI: https://doi.org/10.24840/978-972-752-323-8

PAPER REF: 22243

FATIGUE LIFE UNDER CYCLIC BENDING CONDITIONS OF WELDED JOINTS MADE OF 6060 ALUMINUM ALLOY WITH VARIOUS WELDING TECHNOLOGIES

Sebastian Skrobacz, Joanna Małecka, Mariusz Prażmowski, Karolina Głowacka, Tadeusz Łagoda(*)
Faculty of Mechanical Engineering, Opole University of Technology, Opole, Poland
(*)*Email:* t.lagoda@po.edu.pl

ABSTRACT

The study uses various manufacturing technologies to compare the fatigue life of welded samples of 6060 aluminum alloy in T6 and 64 states. It has been shown that the manufacturing technology has virtually no effect on fatigue characteristics. However, the scatters for manually-made samples are much larger than those automat makes. The fatigue factor of the notch is approximately 2 regardless of thermal treatment. Additionally, the hardness in the joint vicinity was analyzed, and the surface topography of fatigue cracks in the welded joint was analyzed.

Keywords: Cyclic bending, aluminium alloy, welding joints.

INTRODUCTION

Light materials, including aluminium alloys, are increasingly used for mechanical structures. Alloys from the 6xxx family are commonly used for engineering structures, including the production of windows and doors installed in trains. Among others, a comparison of fatigue tests can be found in (Łagoda et al., 2024). However, such a structure must be welded after forming by bending. This raises the question of the impact of welding on the fatigue life of such joints. Some solutions can be found in the literature (Hobbacher, 2008). However, these solutions are better known for steel than for aluminium alloys.

RESULTS AND CONCLUSIONS

Samples made of aluminium alloy 6060-T6 and 6060-T64 were subjected to fatigue tests. The tests were performed under cyclic bending for "diabolo" samples as shown in Fig. 1a and welded samples, the diagram of which is shown in Fig. 1b. Based on the experimental tests performed, the fatigue characteristics of Basquin were determined according to the formula

$$\sigma_a = \sigma'_f N_f^b \tag{1}$$

Table 1 lists the parameters of the Basquin (1) characteristics for cyclic bending of samples without notches and samples welded using two technologies. On this basis, the fatigue action factor of the notch can be determined. From the data analysis in the table, it can be seen that the fatigue characteristics are almost parallel, and the fatigue notch action factor is approximately $K_f = 2$.

Figure 1 shows the fatigue characteristics for cyclic bending for samples made of 6060-T6 and T64 aluminum alloy for samples without notches and welded joints in the nominal system. From the analysis of both the drawing and the table, it can be seen that the fatigue characteristics

of joints made manually and by automatic machines practically coincide. However, in the case of hand-made joints, there are much larger scatters, which is related to the level of confidence.

Table 1 - Basquin (1) characterization parameters for cyclic bending of un-notched and dual-welded specimens.

	T6				T64			
	σ'_f, MPa	m	R^2	$K_f(10^6)$	σ'_f, MPa	m	R^2	$K_f(10^6)$
Un-notched	941.27	-0.141	0.958	-	503.81	-0.108	0.924	-
Manual	763.73	-0.178	0.602	2.05	230.68	-0.100	0.690	1.96
Automat	774.93	-0.177	0.883	2.00	349.29	-0.133	0.870	2.04

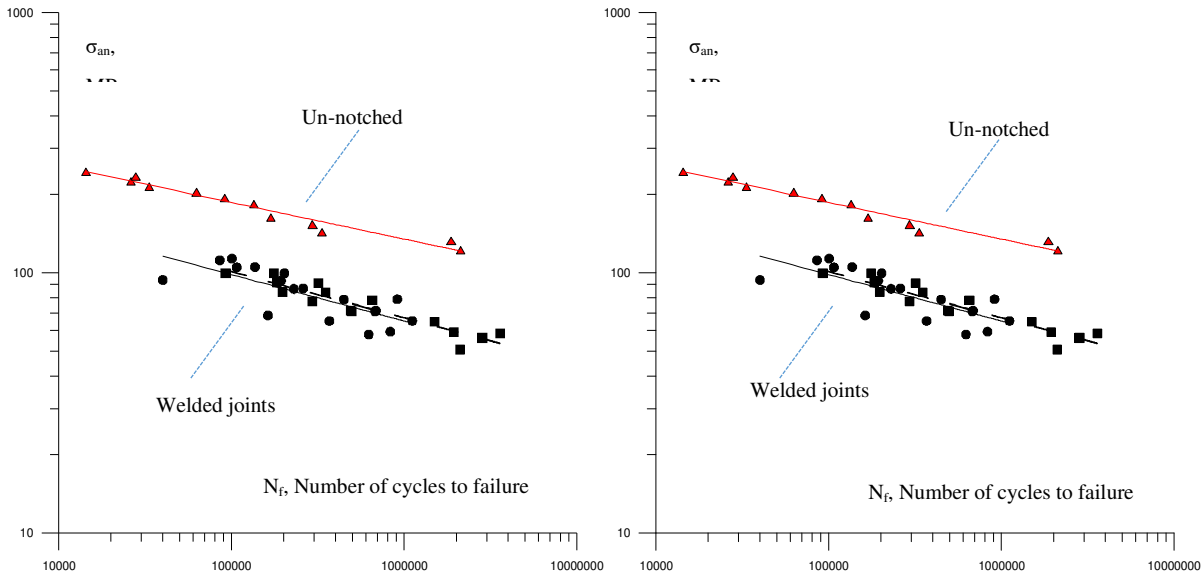

Fig. 1 - Fatigue characteristics for cyclic bending for samples made of aluminium alloy 6060-a) T6 and b) T64 (wheels - manual, squares - automat).

ACKNOWLEDGMENT

This work was financially supported by the Opole University of Technology as part of the DELTA project no. 260/24.

REFERENCES

[1] Hobbacher A., Recommendations for Fatigue Design of Welded Joints and Components. International Institute of Welding, doc. XIII-2151r4-07/XV-1254r4-07.Paris, France, October 2008.

[2] Łagoda T, Małecka J, Małys S, Derda S, Kuś J, Krysiński P, Fatigue fracture cross-sections after cyclic tests with a combination of cyclic bending and torsion of samples made of aluminum alloy 6060, Eksploatacja i Niezawodność – Maintenance and Reliability 2024: 26(1).

Proceedings IRF2025: 8th International Conference on Integrity-Reliability-Failure
In Engineering, Materials, Manufacturing and Biomechanics. Porto 15-18 July 2025
DOI: https://doi.org/10.24840/978-972-752-323-8

PAPER REF: 22252

FATIGUE BEHAVIOUR IN PRESENCE OF ELASTIC ANISOTROPY AND STRESS CONCENTRATION

Riccardo Nobile(*)

Department of Engineering for Innovation, University of Salento, Lecce, Italy
(*)*Email:* riccardo.nobile@unisalento.it

ABSTRACT

The rolling process used to produce metal laminates gives the material a moderate anisotropy in the elastic range. The different behaviour of the material can be neglected in many cases, even if it certainly plays a role in the propagation phase of fatigue cracks. In this work, the changes that the anisotropy of the material introduces in the stress field originated by a hole in a plate were evaluated. Fatigue tests carried out on perforated specimens with different orientations showed the effective influence of the direction of application of the load, which can be justified by the different severity of the notch effect.

Keywords: Elastic anisotropy, stress concentration, fatigue.

INTRODUCTION

Metallic plates are manufactured by lamination that introduce a moderate anisotropy of the material in the elastic range. This effect is originated by the deformation and alignment of grain in the rolling direction and is generally negligible. However, in certain cases, as for example the crack behaviour of thin aluminium plate, this effect plays an important role in determining a different crack propagation speed and crack toughness along L and T directions (Wei et al., 2014; Xia et al., 2018; Kalina et al., 2023). Starting from an experimental evaluation of constitutive properties of Al1050 commercial plates, which has been carried out comparing dynamic measurements and static load tests (Messina et al., 2024), the effect of the elastic anisotropy on the stress concentration factor has been determined by FEM numerical models in case of perforated rectangular specimen. Finally, these specimens having an orientation of 0°, 90°, and 45° (respectively L, T, S) with respect to the rolling direction have been loaded in fatigue to determine the Wöhler curves for a load ratio R = 0.1 and a runout of 10^7 cycles.

RESULTS AND CONCLUSIONS

Stress concentration factor associated to a hole in a finite plate can be easily evaluated using the classical diagrams of Peterson. According to the ratio of hole diameter and plate width, the stress concentration factor k_t is given by:

$$\frac{d}{H} = \frac{2.67}{20} \quad \rightarrow \quad k_t = 2.654 \tag{1}$$

However, this value is referred to an isotropic behaviour. Introducing a different material behaviour, the stress field around hole is depending by the direction of the applied load with respect to the ortotropy direction. Using a FEM model, constituted by quadrangular element with a parabolic formulation and assuming the ortotropy parameters determined in a previous work (Messina et al., 2023), the stress concentration factor has been determined varying the

ortotropy direction between ± 90° with a step of 15° (Figure 1). As a result, k_t value in T direction is reduced of 2.53% with respect to the case of the isotropic behaviour, corresponding to a maximum difference of elastic moduli in direction 1 and 2 of 4.9%.

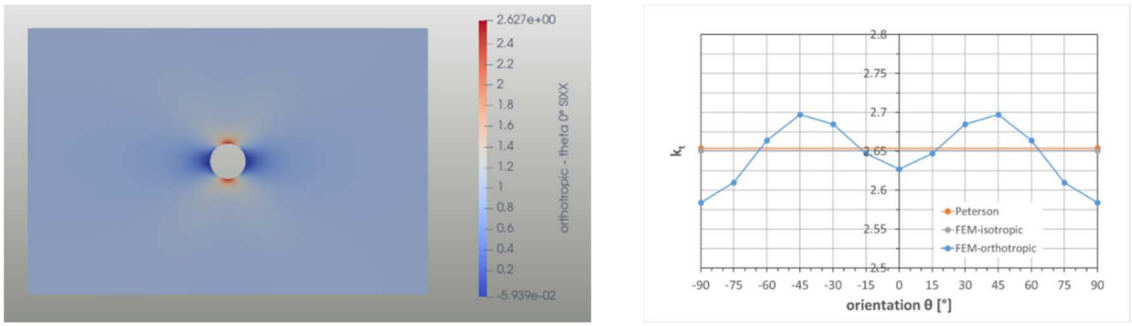

Fig. 1 - Numerical evaluation of stress field and stress concentration factor k_t for different orientation.

The fatigue behaviour (Figure 2) shows an effect of the different orientation of specimens that is clearly associated to the different value of stress concentration k_t. The high fatigue limit is in fact obtained for T direction, for which an increase of 13% of fatigue limit is reached as effect of the reduction of 2.53% of stress concentration.

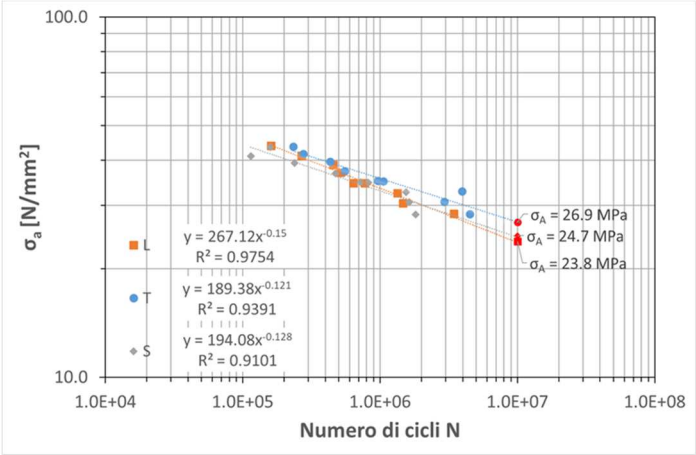

Fig. 2 . Wöhler curves of notched specimen for different orientation.

REFERENCES

[1] Wei L, Pan Q, Huang H, Feng L, Wang Y. Influence of grain structure and crystallographic orientation on fatigue crack propagation behavior of 7050 alloy thick plate. Int J Fatigue, 2014, 66, pp.55-64.

[2] Xia P, Liu Z, Wu W, Zhao Q, Ying P, Bai S. Texture effect on fatigue crack propagation behavior in annealed sheets of an Al-Cu-Mg alloy. J Mater Eng Perform, 2018, 27(9), pp.4693-4702.

[3] M. Kalina, V. Schöne, B. Spak, F. Paysan, E. Breitbarth, M. Kästner. Fatigue crack growth in anisotropic aluminium sheets - phase-field modelling and experimental validation. Int J Fatigue, 2023, 176, 107874.

[4] A. Messina, R. Nobile, N. I. Giannoccaro, A. V. De Nunzio. Anisotropic plates identification through analyses of dynamic behaviour. Mechanics of Advanced Materials and Structures, 2024, 31(21), pp.5125-5141.

Proceedings IRF2025: 8th International Conference on Integrity-Reliability-Failure
In Engineering, Materials, Manufacturing and Biomechanics. Porto 15-18 July 2025
DOI: https://doi.org/10.24840/978-972-752-323-8

PAPER REF: 22255

FATIGUE RELIABILITY ANALYSIS OF GH4169 ALLOY UNDER THE COUPLING EFFECT OF TEMPERATURE AND STRESS

Lei Wang[1(*)], Yang Liu[1], Hanzhong Deng[2], Xiu Song[1]

[1]School of Materials Science and Engineering, Northeastern University, Shenyang, China
[2]College of Materials Science and Engineering, Liaoning Technical University, Fuxin, China
[(*)]*Email:* wanglei@mail.neu.edu.cn

ABSTRACT

Based on the analysis of the fatigue crack propagation behaviour of GH4169 superalloy under 300 MPa stress aging at different temperatures, the fatigue reliability of the alloy under temperature/stress coupling was evaluated. The results show that the fatigue crack growth rate of the alloy treated with temperature/stress coupling aging is higher than that of the alloy treated with single temperature aging, the fatigue threshold is lower, and the overall fatigue reliability is decreased. It is found that the orientation difference of the restricted dislocation plane slip and the activated slip system between adjacent grains will be reduced with the coarsening of γ" phase, at the same time, the localizing plastic deformation and reducing crack deflection. The accelerated coarsening γ" phase caused by coupled stress/temperature aging is the key factor for the decline of fatigue reliability of the alloy.

Keywords: Fatigue crack propagation, microstructure evolution, temperature/stress coupled effect, reliability, GH4169 superalloy.

INTRODUCTION

The reliability of aero-engine turbine disk is directly related to the service safety of aircraft. In particular, especially for the modern large aviation aircraft, which the engines have to be servicing for a long time under high load at high temperature. Therefore, it is of great significance to investigate the fatigue reliability of a superalloy used for aeroengine under the coupling effect of temperature and stress. Based on such back ground, a systematic study has been made on the microstructure evolution behavior of GH4169 alloy under the coupling effect of temperature and stress, and the fatigue reliability of the alloy under the coupling effect of temperature and stress has also been carried out using the experimental study of the fatigue crack growth rate of the alloy with different microstructure, in order to provide a foundation for the safe servicing of the alloy.

RESULTS AND CONCLUSIONS

Fatigue crack propagation behaviour of GH4169 superalloy aged at 650 ℃, 700 ℃ and 730 ℃ with or without a stress of 300 MPa were investigated, respectively. Fatigue crack propagation rate (FCGR) tests were carried out with compact tensile specimens, typical results were shown in Figure 1. Both microstructural characteristics and fracture surface morphology were examined with an optical microscopy (OM), scanning electron microscope (SEM) and confocal laser scanning microscope (CLSM). The typical microstructure and statistical results of alloy microstructure evolution under different aging states are shown in Figure 2.

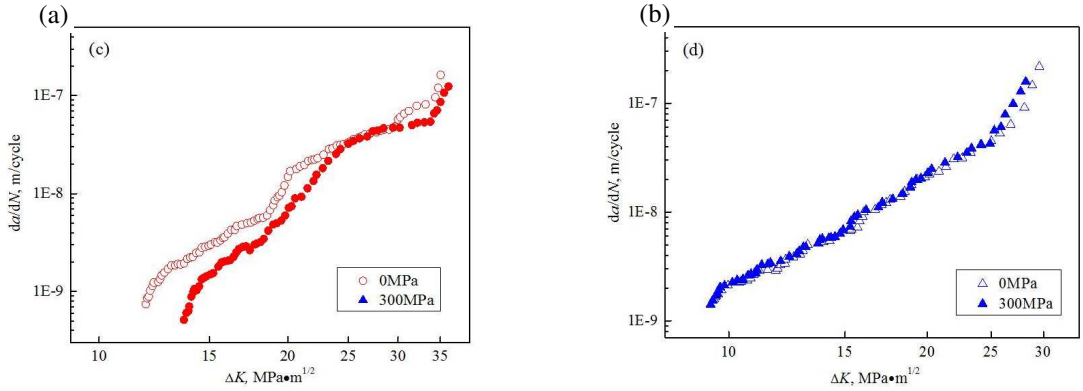

Fig. 1 - da/dN curves of the alloy aged at (a) 650 ℃ and (b) 700 ℃ for 1000 h without or with stress.

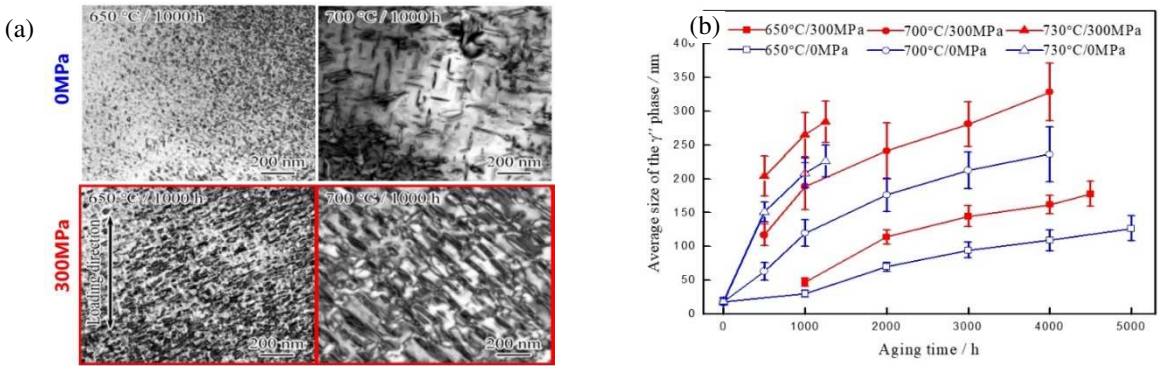

Fig. 2.- Morphologies (a) and size (b) of γ″ phases of the alloy aged with different conditions.

The results show that in the range of threshold value region the fatigue reliability of alloy aged at 650 ℃ for 1000 h with 300 MPa stress are the highest, while the FCGR is the slowest. It is mainly caused by the transition of dislocation approaching the γ" phase from the cutting to the by-pass where there is a critical size of γ" phase during ageing. However, the FCGR of alloys aged at 700 ℃for 1000 h with 300 MPa stress is lower than that of alloy aged at the same temperature and time without stress, which is considered due to the high bearing capacity of δ phase exceeding the critical length to diameter ratio during the ageing. The detail fatigue reliability mechanism also deeply discussed with quantitative analysis from the view point of both microstructure and fracture surface.

REFERENCES

[1] Sujata M, Madan M, Bhaumik SK. Investigation of failure in main fuel pump of an aeroengine. Eng Fail Anal, 2014, 42, pp. 377-389.

[2] Wang K, Li MQ, Luo J, Li C. Effect of the δ phase on the deformation behavior in isothermal compression of superalloy GH4169. Mater Sci Eng A, 2011, 528, pp. 4723-4731.

[3] An JL, Wang L, Liu Y, Cai WL, Song X. The role of δ phase for fatigue crack propagation behavior in a Ni base superalloy at room temperature. Mater Sci Eng A, 2017, 684, pp. 312-317.

[4] Pataky GJ, Sehitoglu H, Maier HJ. High temperature fatigue crack growth of Haynes 230. Mater Charact, 2013, 75, pp. 69-78.

Proceedings IRF2025: 8th International Conference on Integrity-Reliability-Failure
In Engineering, Materials, Manufacturing and Biomechanics. Porto 15-18 July 2025
DOI: https://doi.org/10.24840/978-972-752-323-8

PAPER REF: 22261

DAMAGE MECHANISMS IN SHOT-PEENED 7010-T7451 ALUMINIUM ALLOYS UNDER CYCLIC LOADING

Tissot Maxime[1,2(*)], Mabru Catherine[2], Chaussumier Michel[2], Surand Martin[1]

[1]Safran Landing Systems, Vélizy-Villacoublay, France
[2]Institut Clément Ader (ICA) ; Université de Toulouse ; CNRS, UPS, INSA, ISAE-SUPAERO, IMT Mines Albi; Toulouse, France
[(*)]*Email:* maxime.tissot@safrangroup.com

ABSTRACT

This study investigates the impact of shot-peening on the fatigue performance of 7010-T7451 aluminum alloy under cyclic loading conditions through fatigue testing and fractographic analysis. Surface parameters such as surface roughness, microstructure and residual stress profiles were carefully evaluated and correlated to fractographic features, in order to understand their roles in delaying crack initiation and propagation. Results demonstrate a significant improvement in fatigue life for shot-peened specimens compared to untreated ones, validating the effectiveness of shot-peening.

Keywords: Shot-peening, aluminum alloy, fractographic analysis, fatigue testing.

INTRODUCTION

High-strength aluminum alloys are often used in the aerospace industry due to their favorable strength-to-weight ratio. However, these alloys are prone to fatigue damage under cyclic loading, which limits their service life in structural applications. To reduce the detrimental effect of surface integrity, shot-peening is often applied as a surface treatment [J. Barralis et al, 1999]. This process induces beneficial surface compressive residual stresses and hardening, which can improve resistance to surface fatigue initiation and slow early crack growth. According to applied process parameters, the effectiveness of shot-peening varies with loading conditions and the complex interactions between surface modifications and intrinsic material properties [D. W. Hammond et al, 1990]. Under cyclic loading, the fatigue damage involves various mechanisms, such as surface-induced initiation and subsurface propagation, which must be thoroughly understood to predict and to assess the effect of surface integrity on fatigue performance [K. Takahashi et al, 2018]; [L. Trško et al, 2014]. The aim of the present paper is therefore to precisely characterize and assess the damage mechanisms in the case of shot-peened 7010-T7451 aluminum alloy.

RESULTS AND CONCLUSIONS

Axial tension fatigue tests have been performed on machined and shot-peened cylindrical specimens with two different surface roughness at a load ratio of 0.1 and a frequency of 20 Hz. Fatigue tests results show: i) a detrimental effect of the surface roughness for as-machined specimens, ii) a beneficial effect of shot-peening, whatever the initial roughness, iii) an identical fatigue resistance of the shot-peened specimens, whatever the initial roughness. The results indicate a marked increase in fatigue life for shot-peened specimens compared to untreated ones. According to the applied load level and shot-peening conditions, fatigue life performance

has been improved from a factor of 1.75 for higher stress levels, up to 30 times for lower stress levels, highlighting the effectiveness of the tested shot-peening process on fatigue specimens. In addition, the baseline roughness of the specimens no longer influences fatigue performance once shot-peening is applied. The compressive residual stresses introduced by the treatment thus completely counteract the detrimental effect of surface roughness. Residual stress measurements confirmed the presence of compressive stresses at the surface of the shot-peened specimens, which play a critical role in delaying crack initiation and propagation even after their relaxation due to mechanical cycling. Observation of the fracture surfaces revealed that crack initiations of untreated specimens predominantly occurred at surface singularities. In contrast, the shot-peened specimens present fatigue crack initiations located further from the surface for lower stress levels. Figure 1 illustrates examples of crack initiation sites for both untreated and shot-peened specimens. The fractography also showed the presence of secondary cracks in shot-peened specimens, indicating that the presence of compressive residual stresses alters crack paths, contributing to a more complex fracture mechanism.

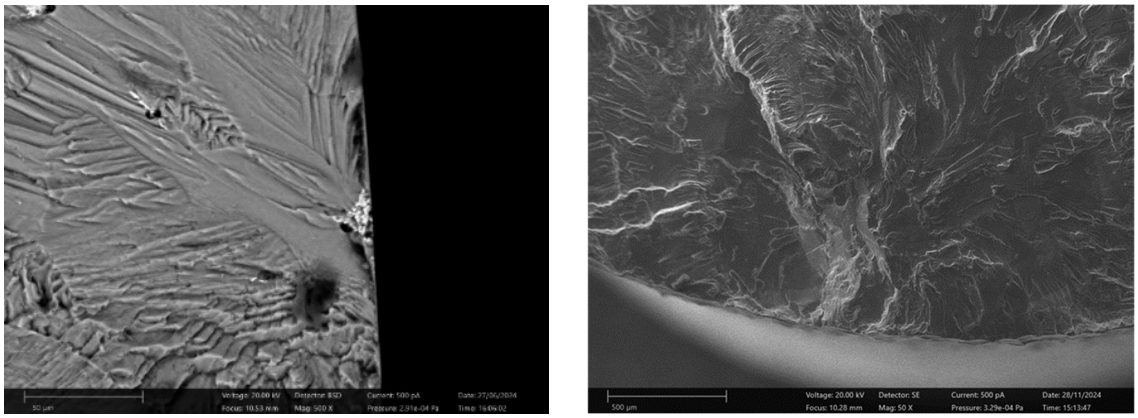

Fig. 1 - SEM images of crack initiation as-machined (left) and shot-peened (right) 7010-T7451 aluminum alloys.

The experimental results of this study highlight the significant beneficial effect of shot-peening on the fatigue behavior of 7010-T7451 aluminum alloys mainly due to the introduction of compressive residual stresses. The insights gained from the experimental and fractographic analyses lay the groundwork for the development of a fatigue life model in order to increase the accuracy of number of cycles calculations.

REFERENCES

[1] J. Barralis, L. Castex, G. Maeder. Précontraintes et traitements superficiels. Techniques de l'Ingénieur, 1999.

[2] D. W. Hammond, S. A. Meguid. Crack propagation in the presence of shot-peening residual stresses. Engineering Fracture Mechanics, vol. 37, no 2, pp. 373-387, 1990.

[3] K. Takahashi, H. Osedo, T. Suzuki, S. Fukuda. Fatigue strength improvement of an aluminum alloy with a crack-like surface defect using shot peening and cavitation peening. Engineering Fracture Mechanics, vol. 193, 2018.

[4] L. Trško, M. Guagliano, O. Bokuvka, F. Novy. Fatigue life of AW 7075 Aluminium Alloy after Severe Shot Peening Treatment with Different Intensities. Procedia Engineering, vol. 74, pp. 246-252, 2014.

Proceedings IRF2025: 8th International Conference on Integrity-Reliability-Failure
In Engineering, Materials, Manufacturing and Biomechanics. Porto 15-18 July 2025
DOI: https://doi.org/10.24840/978-972-752-323-8

PAPER REF: 22274

CRACK PLANES AFTER IMPACT TREATMENT OF 6XXX ALUMINUM ALLOYS

Joanna Małecka(*), Marta Kurek, Aleksander Hebda, Sławomir Małys, Tadeusz Łagoda
Faculty of Mechanical Engineering, Opole University of Technology, Opole, Poland
(*)*Email:* j.malecka@po.edu.pl

ABSTRACT

This paper presents the results of impact bending tests, primarily focusing on the surface topography of the resulting fractures. Three aluminum alloys were used for the study: aluminum alloy 6060 in two heat treatment conditions, T6 and T64, and aluminum alloy 6063 in the T6 heat treatment condition. The studies related to fracture surface topography were conducted using a scanning electron microscope. The results show that both the sample size and the material condition significantly affect the obtained surface parameters, which can be important in the design of impact-treated parts.

Keywords: Aluminum alloy 6XXX, impact bending, topography of fracture plane.

INTRODUCTION

The type of material influences its strength and impact strength. In the case of aluminum alloy, heat treatment is also important. Aluminum alloys from the 6XXX group are often used in structures, including rail transport (Łagoda et al., 2023). The standard EN ISO performed impact tests. The tests and analysis used large and small samples of 3 and 5 mm thickness.

RESULTS AND CONCLUSIONS

Images of cracks obtained at low magnification are shown in Figure 1, for larger samples (a) and smaller ones (b). In the case of the 6060-T6 aluminum alloy, deep and wide cracks can be observed, indicating the material's relatively high ability to absorb energy before the final crack. Large voids in the material reflect places where fragments of the material detached under the influence of impact bending. The irregularity of the surface in the form of numerous peaks and depressions indicates the material's relatively low plasticity and high brittleness. Photos of cracks in samples made of 6060-T64 aluminum alloy show a greater plastic nature of the crack than in the case of T6. We observe a much more uniform structure with finer cracks that are well dispersed. The fracture surface is relatively smooth and contains fewer voids, suggesting better plastic properties and a greater ability of the tested material to dissipate energy during loading.

It should be noted that there are distinct slip lines, which suggest the ability of the material to undergo plastic transformations under load, which reflects a higher impact strength value than for T6. The third aluminum alloy tested is 6063-T6, whose fracture surface is characterized by large and irregular cracks. Additionally, there are numerous voids of various sizes on the surface, which indicate significant detachment of the material during bending. The obtained surface structure highlights the low ability of the 6063 aluminum alloy to absorb energy and its tendency to brittle fracture under the influence of impact bending loads. Impact strength, for the tested aluminum samples are presented in Table 1.

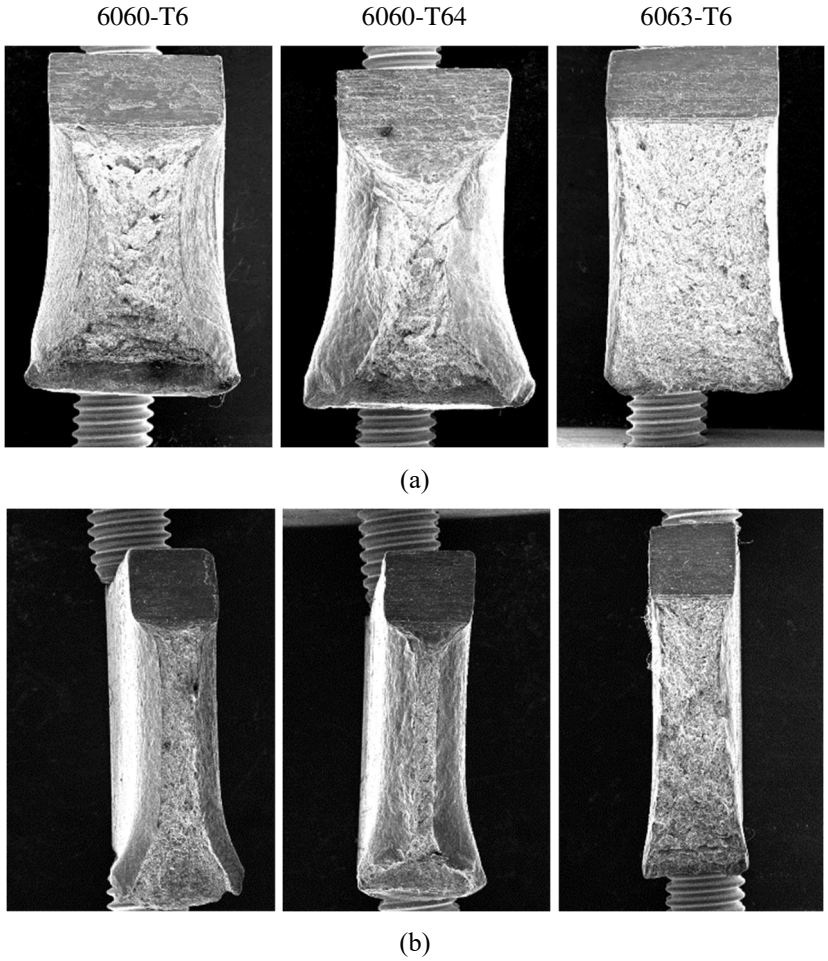

Fig. 1 - SEM photos of the overall samples used in the study: (a) large specimens; (b) small specimens.

Table 1 - Impact strength, kJ/m^2 for the tested aluminum samples.

Alumi□ium alloy	larger □ample□	□maller □ample□
6060-T6 (AlMgSi0.5)	455.42	332.69
6060-T64 (AlMgSi0.5)	577.44	430.71
6063-T6 (AlMgSi0.7)	154.03	172.22

ACKNOWLEDGMENT

This work was financially supported by the Opole University of Technology as part of the DELTA project no. 259/24.

REFERENCES

[1] Łagoda T, Małecka J, Małys S, Derda S, Kuś J, Krysiński P. Fatigue fracture cross-sections after cyclic tests with a combination of cyclic bending and torsion of samples made of aluminum alloy 6060. Eksploat i Niezawodn - Maint Reliab 2023.

Proceedings IRF2025: 8th International Conference on Integrity-Reliability-Failure
In Engineering, Materials, Manufacturing and Biomechanics. Porto 15-18 July 2025
DOI: https://doi.org/10.24840/978-972-752-323-8

PAPER REF: 22317

ELASTIC, ANELASTIC DEFORMATIONS IN HYDRO TECHNICAL STRUCTURES CONCRETES, NANOCOMPOSITES OF MULTIWALLED CARBON NANOTUBES AND POLYMERS

A.P. Onanko(*), L.V. Kuzmych, Y.A. Onanko, O.P. Dmytrenko, M.P. Kulish, T.M. Pinchuk-Rugal, A.G. Rugal, V.V. Kuryliuk, A.M. Kuryliuk, L.I. Kurochka, S.A. Popov, S.V. Yehorova, S.A. Kuzmych, P.P. Il'in

Taras Shevchenko National University of Kyiv, Kyiv, Ukraine
(*)*Email:* onanko@i.ua

ABSTRACT

Elastic, anelastic deformations in concretes, radiation and structural functionalized nanocomposites of multiwalled carbon nanotubes (MCNT) and polyamide, polyvinylchloride, polyethylene was researched.

Keywords: Nanocomposites, carbon nanotubes, mechanical treatments, stress, deformations.

INTRODUCTION

Concretes, polymers strength increasing is achieved by changing their structure, the decreasing of overstrain coefficient γ, as the cracks healing at annealing, reducing the velocity of their germination (Bereka et al., 2021; Kuzmych et al., 2022; Onanko et al., 2022; Radovenchyk et al., 2021).

RESULTS

Anelastic deformations in hydro technical structures concrete (Fig. 1), structural functionalized nanocomposites of multiwalled carbon nanotubes (MCNT) and polyamide-6 $(NH(CH_2)_5CO)_n$, polyvinylchloride $(C_2H_3Cl)_n$, polyethylene $(C_2H_4)_n$ were represented.

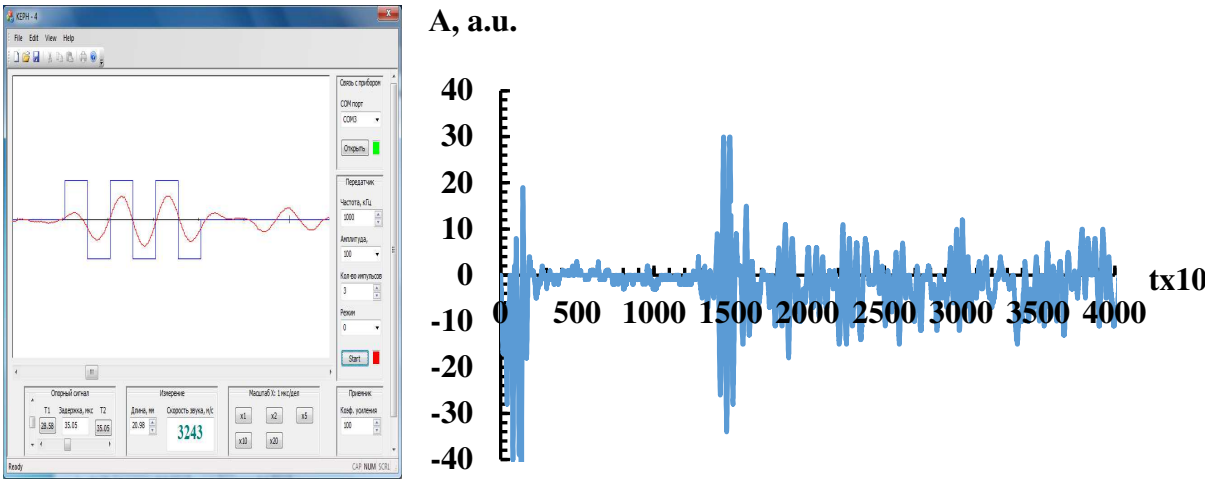

Fig. 1 - Illustration of the window for processing data of quasilongitudinal elastic waves velocity measuring $V_{\parallel}$ = 3243 m/sec in concrete ZSh-35 by pulse-phase US method at frequency $f_{\parallel} \approx 1$ MHz. Logarithmic decrement of attenuation $\delta = ln\left(\frac{A_{n+1}}{A_n}\right) = ln\left(\frac{30}{9}\right) \approx 1.2 \pm 0.1$.

For any point of a quasihomogeneous medium Hooke's law is valid (Onanko et al., 2022; Onanko et al., 2023; Trus et al., 2019):

$$\sigma_{\mathrm{ij}}(\vec{x}) = C_{\mathrm{ijkl}}(\vec{x})\varepsilon_{\mathrm{kl}}(\vec{x}), \quad (1)$$

where $\sigma_{ij}(\vec{x})$, $\varepsilon_{kl}(\vec{x})$ - tensors of strains and deformations at point $\vec{x}$; $C_{ijkl}(\vec{x})$ - tensor of elastic constants at this point.

CONCLUSION

The value of internal friction background Q_0^{-1} after mechanical treatments, temperature describes the changes of the elastic stress σ_i fields in concrete, nanocomposite.

ACKNOWLEDGMENTS

This work has been supported by the Ministry of Education and Science of Ukraine: Grant of the Ministry of Education and Science of Ukraine for the prospective development of the scientific direction "Mathematical sciences and natural sciences" at Taras Shevchenko National University of Kyiv.

REFERENCES

[1] Bereka V., Boshko I., Kondratenko I. et al. Efficiency of plasma treatment of water contaminated with persistent organic molecules. Journal of Environmental Engineering and Science, 2021, 16(1), pp.40-47.

[2] Kuzmych L., Volk L., Kuzmych A. et al. Simulation of the Influence of Non - Gaussian Noise During Measurement. 2022 IEEE 41st International Conference on Electronics and Nanotechnology (ELNANO), 2022, 2022, pp. 595-599.

[3] Onanko A.P., Dmytrenko O.P., Pinchuk-Rugal T.M. et al. Characteristics of Monitoring and Mitigation of Water Resources Clay Particles Pollution by ζ-Potential Research. 16th International Conference Monitoring of Geological Processes and Ecological Condition of the Environment, 2022, 2022, pp.1-5.

[4] Onanko A., Kuzmych L., Onanko Y., Kuzmych A. Indicatory surface of anelastic-elastic properties of Ti alloys. Materials Research Express, 2023, 10(10), 106511.

[5] Onanko Yu., Charnyi D., Onanko A. et al. Oil and Gas Reservoir Rock Sandstone SiO2 Porosity Research by Internal Friction Method. International Conference of Young Professionals «GeoTerrace-2022», 2022, 2022, pp.1-5.

[6] Radovenchyk I., Trus I., Halysh V. et al. Evaluation of Optimal Conditions for the Application of Capillary Materials for the Purpose of Water Deironing. Ecological Engineering & Environmental Technology, 2021, 22(2), pp.1-7.

[7] Trus I., Gomelya N., Trokhymenko G. et al. Determining the influence of the medium reaction and the technique of magnetite modification on the effectiveness of heavy metals sorption. Eastern-European Journal of Enterprise Technologies, 2019, 6(10 (102), pp. 49-54.

Proceedings IRF2025: 8th International Conference on Integrity-Reliability-Failure
In Engineering, Materials, Manufacturing and Biomechanics. Porto 15-18 July 2025
DOI: https://doi.org/10.24840/978-972-752-323-8

PAPER REF: 22374

EXPERIMENTAL INVESTIGATION ON THE MOTORCYCLE SWINGARM DEFORMABILITY AND STABILITY

Beatriz Almeida[1(*)], António Leite[1], Sérgio Dias[1], Miguel Oliveira[2], Isidro Arce[1,3], Fábio Pereira[4]

[1]University of Trás-os-Montes and Alto Douro, Engineering Department, Vila Real, Portugal
[2]A.J.P. Motos S.A., Lousada, Portugal
[3]INEGI, Institute of Mechanical Engineering, Porto, Portugal
[4]University of Trás-os-Montes and Alto Douro, Engineering Department, Center for the Research and Technology Agro-Environmental and Biological Sciences, CITAB, Vila Real, Portugal
[(*)]*Email :* beatriz@utad.pt

ABSTRACT

The growing interest on sustainable transportation has pushed innovations in motorcycle design. This study combines numerical and experimental methodologies to mechanically characterize the swingarm of an electrical motorcycle, a critical structural component. Topology optimization is also applied to reduce production costs and enhance efficiency while maintaining structural integrity. The identification of deformation and stiffness characteristics are analysed and discussed.

Keywords: Electric motorcycle swingarm, finite element simulations, topology optimization, experimental methods, sustainable transportation.

INTRODUCTION

Motorcycles are among the most commonly used vehicles worldwide, the pursuit of sustainable transportation has driven to innovations such as lightweight designs to reduce fuel consumption and emissions (Ahmed and Gupta, 2022). A key component in this context is the swingarm, which connects the rear wheel to the chassis and accommodates the rear suspension system, directly influencing vehicle stability (Risitano et al., 2012). Numerical and experimental methods have significantly advanced the understanding of the mechanical properties of structural components, allowing accurate predictions of their behavior under different load conditions (Taraborrelli et al., n.d.). Additionally, topology optimization enhances designs by removing unnecessary material while preserving essential mechanical performance (Frizziero et al., 2022). This study aims to characterize the mechanical properties of an electric motorcycle swingarm through finite element simulations and topology optimization. The results aim to contribute to the development of safer, more efficient, and sustainable electric motorcycles.

RESULTS AND CONCLUSIONS

The swingarm was specifically designed for an electric motorcycle with a symmetric, bulky and compact design, weighing 4.1kg. The experimental testing procedure was conducted on a custom-designed test bench for static tests (Figure 1) to evaluate the bending stiffness and deformation of the swingarm using an Instron 8801 machine. The swingarm structure was fixed at both ends, and the load was applied at the suspension connection point through a pin connection attached to the load cell. A 5000 kg load cell, aligned with the actuator axis, was used to measure the force applied by the actuator.

To validate the results of numerical simulation with finite element method, the experimental results were used. These simulations predicted stress and strain distribution in the swingarm under various load conditions. Additionally, topology optimization was applied to refine swingarm design.

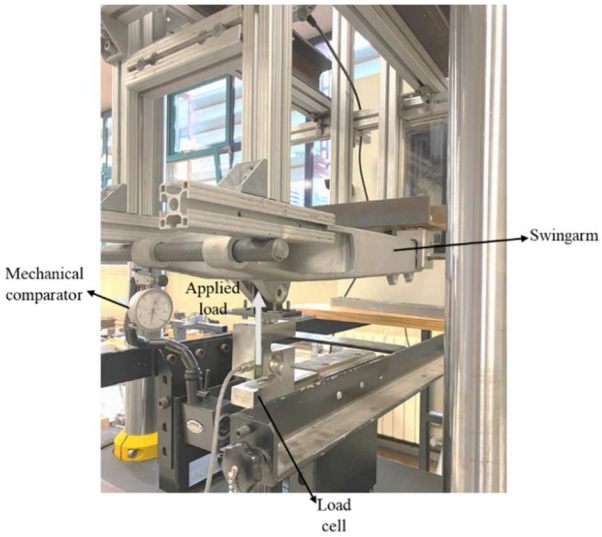

Fig. 1 - Test bench.

The results of topology optimization are presented in Figure out what 2, showing a 13% reduction in weight. Numerical and experimental tests were performed on the original design to evaluate its structural performance, focusing on the stress field. These results provide as a baseline for validating the optimized design, highlighting its potential for enhanced performance in mechanical applications.

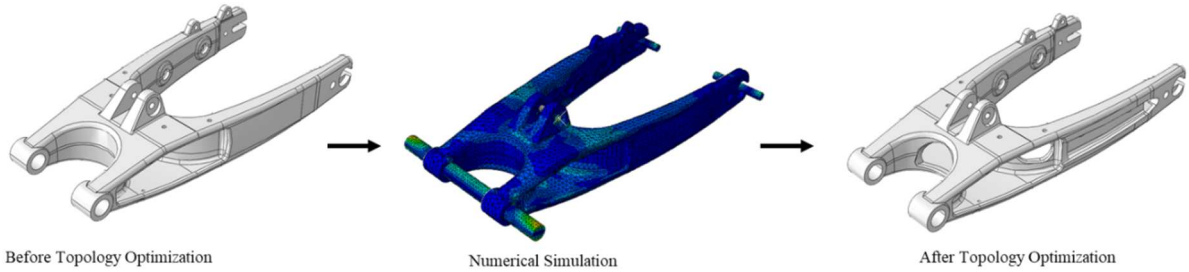

Fig. 2 - Comparison of two swingarm designs: original (left) and optimized (right) for weight reduction.

REFERENCES

[1] S. Ahmed and M. K. Gupta, "Investigations on motorbike frame material and comparative analysis using generative design and topology optimization," Materials Today: Proceedings, vol. 56, pp. 1440-1446, Jan. 2022, doi: 10.1016/j.matpr.2021.12.040.

[2] G. Risitano, L. Scappaticci, C. Grimaldi, and F. Mariani, "Analysis of the Structural Behavior of Racing Motorcycle Swingarms," Apr. 2012. doi: 10.4271/2012-01-0207.

[3] L. Taraborrelli, V. Favaron, and A. Doria, "The effect of swingarm stiffness on motorcycle stability: experimental measurements and numerical simulations".

[4] L. Frizziero et al., "IDeS Method Applied to an Innovative Motorbike—Applying Topology Optimization and Augmented Reality," Inventions, vol. 7, no. 4, Art. no. 4, Dec. 2022, doi: 10.3390/inventions7040091.

Proceedings IRF2025: 8th International Conference on Integrity-Reliability-Failure
In Engineering, Materials, Manufacturing and Biomechanics. Porto 15-18 July 2025
DOI: https://doi.org/10.24840/978-972-752-323-8

PAPER REF: 22376

A MEAN LIFE BASED FATIGUE CRITERION AND PROBABILISTIC FATIGUE LIFE PREDICTION APPROACH

Liyang Xie
Northeastern University, Shenyang 110819, China
Email: lyxie@me.neu.edu.cn

ABSTRACT

A probabilistic fatigue criterion is constituted by means of deterministic damage and random critical damage. The critical damage, a material capability to endure fatigue load, is defined as random fatigue life divided by its median. Fatigue damage caused by a stress cycle is defined based on median life under the cyclic stress, it is therefore a deterministic variable easy to deal with. The equivalence between fatigue damages accumulated at different stress histories is defined based on failure probability, based on that probabilistic fatigue life under variable amplitude load histories can be predicted.

Keywords: Probabilistic fatigue life, failure probability, damage accumulation rule, load uncertainty, reliability.

INTRODUCTION

Fatigue life of a structure is a random variable even under a deterministic load history, because of the dispersion of material property and structure quality. Traditional fatigue life predictions are mostly concern the mean only. Nowadays, probabilistic fatigue life estimation methods have received more attention (Kamala et al., 2018; Noel, 2019) since high reliability is usually required in engineering practice.

P-S-N (stress - probabilistic fatigue life) equation based method has been widely applied to predict probabilistic fatigue life of structures (Lan et al., 2018), given a deterministic load history. Such a method provides only an approximate way to predict the fatigue life associated with a particular survival probability. Especially, in situations of variable amplitude load history, the conventional damage accumulation rule may not be suitable for probabilistic fatigue life prediction.

To reflect random stress effect, stress-strength interference model is applied (Lambert et al., 2010; Roux et al., 2014; Yue et al., 2020). Obviously, stress-strength interference analysis is applicable only to the situation of constant amplitude cyclic stress or endurance assessment (infinite life). Investigations and methods/models on the probability characteristic of fatigue under variable amplitude load history are mostly object specific (Petryna et al., 2002; Zhang et al., 2011; Song et al., 2018). On probabilistic fatigue criterion, almost all are based on random damage and deterministic critical value (Ahmad et al., 2019; Songa et al., 2019; Kliman, 1985; Liao et al., 2020; Fu et al., 2020), and for the majority of probabilistic fatigue criteria the critical damage is a constant, except for the Kliman model (Kliman, 1985) where critical damage is a deterministic function of cyclic stress level. Alternatively, it is noted that a probabilistic threshold value rather than a deterministic threshold value is more appropriate (Zhu et al., 2014).

Taking fatigue damage as a random variable makes probabilistic fatigue damage accumulation difficult and fatigue probability computation cumbersome. To avoid these problems, a fatigue criterion with deterministic damage and random critical damage was introduced (Ren et al., 2020). Besides, random critical damage or reference damage is introduced and a lognormal critical damage with median of 1.0 and deviation of 0.3 is simply assigned (Wirsching et al., 1985; Losberg et al., 2016; Karadeniz et al., 2001; D'Angelo et al., 2015; Mansour et al., 1995).

The present paper presents a deterministic cumulative fatigue damage - random critical damage based fatigue criterion, develops a probabilistic fatigue life prediction method. Where, an "equivalent damage" is defined according to equal failure probability, thus the "equivalent damage means identical failure probability" restriction is intrinsically satisfied.

P-S-N EQUATION BASED FATIGUE DAMAGE ACCUMULATION AND DAMAGE EQUIVALENCE

To predict the fatigue life of a structure under variable amplitude load histories, damage accumulation rule is indispensable. As assumed by the Miner's rule, same cycle ratio n_i/N_i means same fatigue damage (where, n_i stands for the action number of cyclic stress s_i, N_i stands for the fatigue life under cyclic stress s_i), no matter of the cyclic stress level. In other words, fatigue damage produced by n cycles of a certain level of cyclic stress under which the fatigue life is N can be quantified as n/N. According to the Miner's rule (developed under deterministic framework, fatigue life is taken as a deterministic function of cyclic stress amplitude), the cumulative fatigue damage produced by a variable amplitude load history containing n stress cycles equals to the sum of the damages produced by the every stress cycles, and fatigue occurs when the cumulative fatigue damage reaches to unity (the critical damage). In such a situation, the Miner's rule can be expressed as

$$\sum_{i=1}^{n} 1/N_i = 1 \tag{1}$$

However, fatigue life is a random variable. To predict the fatigue life related to an intended survival probability under a variable amplitude load history, P-S-N equation is usually used to calculate fatigue damage. However, such obtained equivalent damage does not really mean the same failure probability, making the fatigue life prediction result plausible. It can be demonstrated by the following example.

Associated with a survival probability R, the fatigue life under cyclic stress s_i is denoted by $N_{R,i}$. If the fatigue life under the cyclic stress s_i follows the Weibull distribution W(η_i, β_i) (η_i and β_i are the scale parameter and shape parameter, respectively), the relationship between the survival probability R and the associated fatigue life $N_{R,i}$ is

$$R = e^{-(N_{R,i}/\eta_i)^{\beta_i}}$$

or

$$N_{R,i} = \eta_i(-\ln \mathrm{R})^{1/\beta_i}$$

According to the conventional damage equivalence concept and the P-S-N equation, n_i cycles of s_i being equivalent to n_j cycles of s_j means

$$n_i / N_{R,i} = n_j / N_{R,j}$$

i.e.

$$n_j = n_i\,(\eta_j / \eta_i)(-\ln(R))^{1/\beta_j - 1/\beta_i}$$

Since

$$P(N_i < n_i) = 1 - \mathrm{e}^{-(\frac{n_i}{\eta_i})^{\beta_i}}$$

$$P(N_j < n_i\,(\eta_j / \eta_i)(-\ln(R))^{1/\beta_j - 1/\beta_i}) = 1 - \mathrm{e}^{-(\frac{n_i}{\eta_i})^{\beta_j}(-\ln(R))^{1-\beta_j/\beta_i}}$$

Therefore

$$P(N_i < n_i) = P(N_j < n_i\,(\eta_j / \eta_i)(-\ln(R))^{1/\beta_j - 1/\beta_i})$$

if and only if $\beta_i = \beta_j$.

where, N_i and N_j are the life random variables under the cyclic stress s_i and s_j, respectively.

It indicates that the P-S-N equation based conventional "damage equivalence" does not coincide with failure probability equivalence. That is, the failure probability caused by n_i cycles of s_i does not equal to that caused by $n_i\,(\eta_j / \eta_i)(-\ln(R))^{1/\beta_j - 1/\beta_i}$ (i.e. the equivalent cycle number n_j converted according to the conventional damage equivalence concept) cycles of s_j, unless the shape parameter of the Weibull-distributed fatigue life random variable is independent on stress level.

PROBABILISTIC FATIGUE CRITERIA

Probabilistic Miner's Rule

Fatigue life of a structure is a random variable even under a deterministic load history, of which the scatter depends on material property, manufacturing quality and stress level. With regard to an intended survival probability R, fatigue criterion can be expressed as the number of stress cycles n being greater than the fatigue life related to the intended survival probability R, i.e.

$$n \geq N_R \tag{2}$$

where, n stands for cycle number of cyclic stress, N_R stands for fatigue life under the cyclic stress associated with the intended survival probability R.

Alternatively, such a probabilistic fatigue criterion can be expressed as:

$$P(n \leq N) < R \tag{3}$$

i.e. fatigue is defined to occur when the probability that the number of stress cycles n is less than the fatigue life random variable N (the probability is denoted by P(n<N)) is less than the intended survival probability R.

It is equivalent to

$$P(n/N \leq 1) < R \tag{4}$$

i.e. fatigue is defined to occur when the probability that fatigue damage (n/N, a random variable) is less than unity (the critical fatigue damage, a deterministic constant) is less than R.

In situations of variable amplitude load history, a probabilistic fatigue damage accumulation rule can be established by taking the fatigue life N_i in the Miner's rule (Eq.1) as a random variable:

$$P(\sum_{i=1}^{n} 1/N_i \leq 1) < R \tag{5}$$

Such a fatigue criterion is difficult to apply since it is difficult to obtain the probability density function (pdf) of the fatigue damage $1/N_i$.

Median life based fatigue damage and probabilistic fatigue criterion

An easy-to-use probabilistic fatigue criterion can be established based on the median life $\bar{N}$, by defining $n/\bar{N}$ as the (median) fatigue damage (a deterministic variable) and defining $N/\bar{N}$ as the critical damage (a random variable). Obviously, a deterministic fatigue damage is simple to deal with and the relevant fatigue damage accumulation is mathematically tractable.

Since

$$P(n < N) = P(\frac{n}{\bar{N}} < \frac{N}{\bar{N}})$$

the probabilistic fatigue criterion can be expressed as

$$P(D < \Delta) < R \tag{6}$$

where, $D = n/\bar{N}$ stands for the fatigue damage produced by n cycles of cyclic stress s, $\Delta = N/\bar{N}$ the critical damage (random variable) under the cyclic stress s.

Eq.6 indicates that the fatigue damage produced by a certain number of stress cycles, i.e. $n/\bar{N}$ is a deterministic value, while the material capability against fatigue damage, i.e. the critical damage, defined as $N/\bar{N}$, is a random variable. In such a probabilistic fatigue criterion, the randomness of material property is characterized by the critical damage random variable.

PROBABILITY DENSITY FUNCTION OF CRITICAL DAMAGE

Fatigue life can be well described by the Weibull distribution. The probability density function (pdf) and the cumulative distribution function (cdf) of the Weibull-distributed fatigue life are as the following, respectively:

$$f(n) = \frac{\beta n^{\beta-1}}{\eta^{\beta}} \mathrm{e}^{-(\frac{n}{\eta})^{\beta}} \tag{7}$$

$$F(n) = 1 - \mathrm{e}^{-(\frac{n}{\eta})^{\beta}} \tag{8}$$

where, n stands for fatigue life; β and η stand for the shape parameter and the scale parameter of the Weibull distribution, respectively.

With respect to a cyclic stress s_i, the critical damage random variable is

$$\Delta_i = N_i / \bar{N}_i \tag{9}$$

where, N_i stands for the fatigue life random variable under cyclic stress s_i, $\bar{N}_i$ stands for the median of the life random variable N_i.

Obviously, the pdf $f(\delta)$ and the cdf $F(\delta)$ of the critical damage random variable Δ can be derived from Eq.7, Eq.8 and Eq.9:

$$f(\delta) = \frac{\beta \bar{N}^{\beta} \delta^{\beta-1}}{\eta^{\beta}} \mathrm{e}^{-(\frac{\bar{N}\delta}{\eta})^{\beta}} \tag{10}$$

$$F(\delta) = 1 - \mathrm{e}^{-(\frac{\bar{N}\delta}{\eta})^{\beta}} \tag{11}$$

As $\bar{N} = \eta \ln(2)^{1/\beta}$, Eq.10 and Eq.11 can be rewritten, respectively as:

$$f(\delta) = \beta \ln(2) \delta^{\beta-1} \mathrm{e}^{-\ln(2)\delta^{\beta}} \tag{12}$$

$$F(\delta) = 1 - \mathrm{e}^{-\ln(2)\delta^{\beta}} \tag{13}$$

It illustrates that, when fatigue life follows the Weibull distribution, the critical damage is also the Weibull-distributed random variable, and the shape parameter β is the same as that of the life distribution, the scale parameter is $\ln(2)^{-1/\beta}$. Therefore, the median equals to unity.

MEAN LIFE BASED PROBABILISTIC FATIGUE DAMAGE ACCUMULATION RULE

Damage equivalence and fatigue probability equivalence

A fatigue damage accumulation rule is necessary for fatigue life prediction under variable amplitude load histories. It declares how fatigue damage is characterized and accumulated, and when fatigue occurs. Necessarily, probabilistic fatigue life prediction requires a probabilistic damage accumulation rule.

For probabilistic fatigue damage accumulation, damage equivalence implies failure probability equivalence, i.e. the same damage means identical failure probability, regardless of the cyclic stress level or stress history by that the damage is produced.

For a Weibull-distributed fatigue life random variable denoted by N_i~W(η_i, β_i) (where η_i is the scale parameter, β_i is the shape parameter, and the subscript i indicates that the associated cyclic stress is s_i), the critical fatigue damage Δ_i is also a Weibull-distributed random variable: $\Delta_i \sim W(\ln(2)^{-1/\beta_i}, \beta_i)$. The damage δ_i produced by n_i cycles of cyclic stress s_i equals to $n_i / \bar{N}_i$, and the failure probability caused by n_i cycles of cyclic stress s_i is $P(n_i > N_i) = 1 - \mathrm{e}^{-(n_i/\eta_i)^{\beta_i}}$, that is the probability of the stress cycle number n_i exceeding the fatigue life random variable N_i,

On the other hand, the failure probability equals to the probability that the fatigue damage $n_i / \bar{N}_i$ is greater than the critical damage random variable Δi, i.e. $P(\delta_i > \Delta_i) = 1 - \mathrm{e}^{-\ln(2)(n_i/\bar{N}_i)^{\beta_i}}$.

Obviously, the failure probability characterized by critical fatigue damage distribution (denoted by P_D) and that characterized by fatigue life distribution (denoted by P_N) is equal, i.e.

$$\begin{aligned} P_D &= 1-e^{-\ln(2)(n_i/\bar{N}_i)^{\beta_i}} \\ &= 1-e^{-\ln(2)(n_i/(\eta_i \ln(2)^{1/\beta_i}))^{\beta_i}} \\ &= 1-e^{-(n_i/\eta_i)^{\beta_i}} \\ &= P_N \end{aligned}$$

It demonstrated that the critical damage random variable based failure probability is consistent with the conventional fatigue life random variable based failure probability.

Probabilistic fatigue damage accumulation rule

To accumulate damage is an essential work for fatigue life prediction under variable amplitude stress histories. According to the principle that "the equivalent damage means the same failure probability", the converted cycle number $n_{i\to j}$ under stress level s_j, equivalent to n_i cycles of stress s_i (i.e. $n_{i\to j}$ cycles of s_j is equivalent to n_i cycles of stress s_i in sense of fatigue damage and fatigue probability), should be figured out as below.

If n_j cycles of stress s_j is equivalent to n_i cycles of stress s_i, then the respective failure probabilities are equal, i.e.

$$1-e^{-(n_j/\eta_j)^{\beta_j}} = 1-e^{-(n_i/\eta_i)^{\beta_i}}$$

or

$$1-e^{-\ln(2)(n_j/\bar{N}_j)^{\beta_j}} = 1-e^{-\ln(2)(n_i/\bar{N}_i)^{\beta_i}}$$

Therefore, with respect to the cyclic stress s_j, the cycle number equivalent to n_i cycles of stress s_i equals to

$$n_{i\to j} = \bar{N}_j \left(\frac{n_i}{\bar{N}_i}\right)^{\beta_i/\beta_j} \tag{14}$$

and the corresponding fatigue damage is

$$D_{i\to j} = \frac{n_{i\to j}}{\bar{N}_j} = \left(\frac{n_i}{\bar{N}_i}\right)^{\beta_i/\beta_j} \tag{15}$$

For a two-level cyclic stress block containing n_1 cycles of s_1 and n_2 cycles of s_2, the cumulative fatigue damage with respect to the cyclic stress level of s_2 equals to

$$D_{1:2} = \frac{n_{1\to 2}+n_2}{\bar{N}_2} = \left(\frac{n_1}{\bar{N}_1}\right)^{\beta_1/\beta_2} + \frac{n_2}{\bar{N}_2} \tag{16}$$

It means that the fatigue damage $n_1/\bar{N}_1$ related to the critical damage Δ_1 is equivalent to the fatigue damage $(n_2/\bar{N}_2)^{\beta_1/\beta_2}$ related to the critical damage Δ_2.

Therefore, the probabilistic fatigue damage accumulation rule can be expressed as

$$P((\frac{n_1}{\bar{N}_1})^{\beta_1/\beta_2}+\frac{n_2}{\bar{N}_2}<\Delta_2)<R \tag{17}$$

For a multi-level stress history (n_1, s_1) - (n_2, s_2) - (n_3, s_3) -…, an iterative procedure should be applied to calculate the respective equivalent stress cycle numbers, equivalent cumulative fatigue damages and failure probability increments. Taking a three-level stress block (n_1, s_1) - (n_2, s_2) - (n_3, s_3) as an example, n_1 cycles of s_1 and n_2 cycles of s_2 are equivalent to $n_{1,2\to3}$ cycles of s_3, $n_{1,2\to3}$ can be determined by failure probability equivalence principle as

$$n_{1,2\to3}=\bar{N}_3(\frac{n_{1\to2}+n_2}{\bar{N}_2})^{\beta_2/\beta_3}=\bar{N}_3((\frac{n_1}{\bar{N}_1})^{\beta_1/\beta_2}+\frac{n_2}{\bar{N}_2})^{\beta_2/\beta_3}$$

Similarly,

$$n_{1,2,3\to4}=\bar{N}_4(((\frac{n_1}{\bar{N}_1})^{\beta_1/\beta_2}+\frac{n_2}{\bar{N}_2})^{\beta_2/\beta_3}+\frac{n_3}{\bar{N}_3})^{\beta_3/\beta_4}$$

$$n_{1,2,\ldots,(n-1)\to n}=$$

$$\bar{N}_n(\ldots((\frac{n_1}{\bar{N}_1})^{\beta_1/\beta_2}+\frac{n_2}{\bar{N}_2})^{\beta_2/\beta_3}+\ldots+\frac{n_{n-1}}{\bar{N}_{n-1}})^{\beta_{n-1}/\beta_n}$$

For a n-level stress history containing n_i cycles of s_i (i=1,2,…,n), the probabilistic fatigue damage accumulation rule can be expressed as (ref. Eq.17)

$$\begin{aligned}&P((\ldots((\frac{n_1}{\bar{N}_1})^{\beta_1/\beta_2}+\frac{n_2}{\bar{N}_2})^{\beta_2/\beta_3}+\ldots\\&+\frac{n_{n-1}}{\bar{N}_{n-1}})^{\beta_{n-1}/\beta_n}+\frac{n_n}{\bar{N}_n}<\Delta_n)<R\end{aligned} \tag{18}$$

since the cumulative fatigue damage caused by all the Σn_i (i=1,2,...,n) stress cycles is

$$D_{1:n}=(\ldots((\frac{n_1}{\bar{N}_1})^{\beta_1/\beta_2}+\frac{n_2}{\bar{N}_2})^{\beta_2/\beta_3}+\ldots+\frac{n_{n-1}}{\bar{N}_{n-1}})^{\beta_{n-1}/\beta_n}+\frac{n_n}{\bar{N}_n} \tag{19}$$

PROBABILISTIC FATIGUE LIFE PREDICTION APPROACH

According to the probabilistic fatigue damage accumulation rule (ref. Eq.18), the fatigue life N_R (the total cycle number to fatigue under a load history composed of n_i cycles of s_i (i=1,2,…,n) associated with survival probability R can be obtained by the following equations:

$$e^{-\ln(2)(\frac{n_{1,2,\ldots,(n-1)\to n}+n_n}{\bar{N}_n})^{\beta_n}} = R \tag{20}$$

or

$$(\frac{n_{1,2,\ldots,(n-1)\to n}+n_n}{\bar{N}_n})^{\beta_n} = -\frac{\ln(R)}{\ln(2)} \tag{21}$$

$$N_R = \sum_{i=1}^{n} n_i \tag{22}$$

For the typical situation of n_i=1 (i=1,2,..., n),

$$N_R = n \tag{23}$$

In one word, the probabilistic fatigue life, i.e. the number of the total stress cycles to the survival probability R is determined by Eq.20 (or Eq.21), summarized by Eq.22 or Eq.23 in a special case, i.e. all the n_i's equal to 1, and $e^{-\ln(2)(\frac{n_{1,2,\ldots,(n-1)\to n}+1}{\bar{N}_n})^{\beta_n}} = R$.

The fatigue probability or probabilistic fatigue life of a structure can be predicted through accumulating fatigue damage cycle by cycle as the following: calculate fatigue damage produced by the first stress cycle → calculate failure probability caused by the first stress cycle → calculate the damage-equivalent cycle number of the second stress level → calculate cumulative fatigue damage produced by the preceding two stress cycles → calculate the failure probability caused by the preceding two stress cycles → calculate the damage-equivalent cycle number of the third stress level → ... ..., until the intended failure probability is reached. The number of the total stress cycles involved in the process is the fatigue life related to the failure probability or survival probability.

RESULTS AND CONCLUSIONS

Based on the median damage and the related critical fatigue damage random variable, a probabilistic fatigue criterion is established. With respect to variable amplitude stress histories, the equivalent stress cycle number under different stress levels is defined based on failure probability equivalence, and cumulative fatigue damage is calculated iteratively.

The fatigue probability and the probabilistic fatigue life of a structure can be predicted by means of the proposed probabilistic fatigue damage criterion: fatigue occurs when the probability that the cumulative fatigue damage is greater than the critical damage random variable equals to the intended failure probability.

REFERENCES

[1] Kamala M, Rahman M M. Advances in fatigue life modelling: A review. Renewable and Sustainable Energy Reviews, 2018, 82, pp.940-949.

[2] Noel M. Probabilistic fatigue life modeling of FRP composites for construction. Construction and Building Materials, 2019, 206, pp.279-286.

[3] Lan C, Bai N, Yang H T et al. Weibull modeling of the fatigue life for steel rebar considering corrosion effects. Int. J. Fatigue, 2018, 111, pp.134-143.

[4] C.M. Lan, Y. Xu, C.P. Liu et al. Fatigue life prediction for parallel-wire stay cables considering corrosion effects. Int. J. Fatigue 114 (2018), pp. 81-91.

[5] S. Lambert, E. Pagnacco, L. Khalij, A probabilistic model for the fatigue reliability of structures under random loadings with phase shift effects. Int. J. Fatigue, 2010, 32: pp. 463-474.

[6] C. Roux, X. Lorang, and H. Maitournam et al, Fatigue design of railway wheels: a probabilistic approach. Fatigue and Fracture of Engineering Materials and Structures, 37 (2014), pp. 1136-1145.

[7] Yue P., Ma J., Zhou C., et al. A fatigue damage accumulation model for reliability analysis of engine structures under combined cycle loadings. Fatigue & Fracture of Engineering Materials & Structures 43 (2020), pp. 1880-1892.

[8] Petryna Y.S., Pfanner D., Stangenberg F. et al. Reliability of reinforced concrete structures under fatigue. Reliability Engineering and System Safety 77 (2002), pp. 253-261.

[9] Zhang D., Hong J., Ma Y., et al. A probability method for prediction on high cycle fatigue of blades caused by aerodynamic loads. Advances in Engineering Software 42 (2011), pp. 1059-1073.

[10] L.K. Song, G.C. Bai, C.W. Fei. Reliability-based fatigue life prediction for complex structure with time-varying surrogate modeling. Advances in Materials Sci. and Eng. 2018, ID 3469465, doi.org/10.1155/2018/3469465.

[11] H.W. Ahmad, J.H. Hwang, K. Javed et al. Probabilistic fatigue life prediction of dissimilar material weld using accelerated life method and neural network approach. Computation 7 2019, 10 DOI 10.3390/computation7010010.

[12] L.K. Songa, G.C. Baia, C.W. Fei. Probabilistic LCF life assessment for turbine discs with DC strategy-based wavelet neural network regression. Int. J. Fatigue 119 (2019), pp. 204-219.

[13] Kliman V. Fatigue life estimation under random loading using the energy criterion. Int. J. Fatigue, 1985, 7(1): pp. 39-44.

[14] D. Liao, S. P. Zhu, B. Keshtegar et al. Probabilistic framework for fatigue life assessment of notched structures under size effects. Int. J. Mechanical Sciences 181 (2020) 105685

[15] B. Fu, J. Zhao, B. Li, Fatigue reliability analysis of wind turbine tower under random wind load, Structural Safety 87 (2020) 101982.

[16] S.P. Zhu, H.Z. Huang, Y.F. Li et al, Probabilistic modeling of damage accumulation for time-dependent fatigue reliability analysis of railway axle steels, Proc IMechE Part F: J Rail and Rapid Transit 2014, 0(0), pp. 1-11.

[17] J.G. Ren, B.F. Zhao, L.Y. Xie. Fatigue Reliability Analysis of a Compressor Disk Based on Probability Cumulative Damage Criterion. Materials 2020, 13, 2182; doi:10.3390/ma13092182.

[18] Wirsching BPH, Asce M. Fatigue reliability for offshore structures. J Struct Eng, 110 (1985) 2340-56.

[19] I. Losberg, G. Sigrudsson, A. Fjeldstad et al, Probabilistic methods for planning of inspection for fatigue cracks in offshore structures, Marine Structures 46 (2016), pp. 167-192.

[20] H. Karadeniz, Uncertainty modeling in the fatigue reliability calculation of offshore structures, Reliability Engineering and System Safety 74 (2001), pp. 323-335.

[21] L. D'Angelo, A. Nussbaumer, Reliability based fatigue assessment of existing motorway bridge, Structural Safety 57 (2015), pp. 35-42.

[22] A. E. Mansour, P. H. Wirsching, Sensitivity factors and their application to marine structures, Marine Structures 8 (1995), pp. 229-255.

Proceedings IRF2025: 8th International Conference on Integrity-Reliability-Failure
In Engineering, Materials, Manufacturing and Biomechanics. Porto 15-18 July 2025
DOI: https://doi.org/10.24840/978-972-752-323-8

PAPER REF: 22382

SURVIVAL ANALYSIS TECHNIQUES FOR PROBABILISTIC FATIGUE LIFE EVALUATION IN BRIDGES CONSIDERING LOADING SEQUENCE EFFECTS

Farhad Farajiani, Habib Tabatabai(*)

Department of Civil & Environmental Engineering, University of Wisconsin-Milwaukee, Milwaukee, USA
(*)*Email:* ht@uwm.edu

ABSTRACT

Fatigue is one of the primary causes of structural deterioration in steel bridges. In the United States, fatigue life estimation for steel bridges is generally based on non-probabilistic S-N curves prescribed by the AASHTO bridge design specifications. The conventional remaining fatigue life analyses are based on Miner's rule and the AASHTO S-N curves, which overlook the effects of loading sequence and conditional probability on remaining fatigue life. Survival analysis, commonly used in medical research, is an emerging method in engineering fatigue analyses that can address fatigue life estimation in a probabilistic manner while considering loading sequence. This work presents the development of probabilistic S-N curves for steel bridges using survival analysis techniques and proposes a methodology for probabilistic remaining life assessments considering loading sequence and conditional survival estimates.

Keywords: Fatigue, survival analysis, steel bridges, Miner's rule.

INTRODUCTION

Survival analysis, mainly used in medical research, has been adapted to study "time-to-event" phenomena in various fields, including engineering. The approach focuses on the time that it takes until a specific event, such as structural failure, occurs. By treating the number of cycles as a fictitious "time parameter, the existing survival analysis techniques can be applied to engineering fatigue. The following functions are the key functions for the survival analysis in engineering fatigue:

$$S(n_c) = P(N_c > n_c) = 1 - F(n_c) \tag{1}$$

$$f(n_c) = \lim_{\Delta n_c \to 0} P\,(n_c < N_c < n_c + \Delta n_c)/\Delta n_c \tag{2}$$

$$h(n_c) = \lim_{\Delta n_c \to 0} P\,(n_c < N_c < n_c + \Delta n_c | N_c > n_c)/\Delta n_c \tag{3}$$

where $S(n_c)$ is the survival function, $f(n_c)$ is the probability density function, and $h(n_c)$ is the hazard rate function. Additionally, N_c is the number of cycles to failure, n_c is the number of applied stress cycles, and $F(n_c)$ is the cumulative probability of failure (Nabizadeh & Tabatabai, 2020).

Nabizadeh and Tabatabai (2020) proposed survival functions for various steel bridge detail categories and different stress ranges using the original data that was the basis for the current AASHTO provisions. These survival functions were then used to develop probabilistic S-N curves in which the user can select their choice of probability of failure associated with the S-N curve for each detail category.

Traditional fatigue analyses do not consider the sequence of loading (as in Miner's rule) and make predictions for the remaining fatigue life based on the S-N curve of a new structure. This wrongly assumes that the fatigue life already spent without failure does not change the remaining life in the original S-N curve. However, as structures age without fatigue failure, the original survival curves require adjustments based on the conditional probability theory. Conditional survival analysis dynamically updates survival probabilities at different stages in fatigue life. Conditional survival is the likelihood of surviving a future number of cycles, assuming that survival has been previously achieved up to a particular number of cycles n_{cs} (Nabizadeh et al., 2020). The conditional survival function (CS), expressed as Equation 4.

$$CS(n_c, n_{cs}) = \begin{cases} 1 & 0 \le n_c \le n_{cs} \\ \dfrac{S(n_c)}{S(n_{cs})} & n_c > n_{cs} \end{cases} \tag{4}$$

It should be noted that bridges are subjected to variable amplitude loading conditions in the field. The corresponding effective stress range for the variable amplitude loads is typically estimated using Equation 5, which is based on Miner's linear damage accumulation equation. This approach assumes that the damage fraction associated with any stress range is a linear function of the ratio of the number of cycles of applied load cycles to the total number of cycles required for failure at that stress range (AASHTO, 2020; Ghahremani & Walbridge, 2011).

$$\Delta S_r = \left(\frac{\sum_{i=1}^{n} N_i \, \Delta S_i^3}{N_{total}}\right)^{1/3} \tag{5}$$

This linear theory would introduce inaccuracies in remaining fatigue life predictions, despite its ease of application. Its major flaws include assuming that damage develops at a particular stress level at the same rate without taking previous stress history into account and ignoring the impact of the order in which different stress levels are applied (Oh, 1991). Survival analysis, however, provides a rational approach for addressing the probabilistic effects of loading sequence through a process of alternating between survival curves associated with different stress ranges while considering the conditional survival effect presented in Equation 4.

REFERENCES

[1] Aashto, B.D.S. (2020). American Association of State Highway and Transportation Officials. Washington, DC, 4.

[2] Ghahremani, K., Walbridge, S. (2011). Fatigue testing and analysis of peened highway bridge welds under in-service variable amplitude loading conditions. International Journal of Fatigue, 33(3), pp. 300-312. https://doi.org/10.1016/j.ijfatigue.2010.09.004.

[3] Nabizadeh, A., Tabatabai, H. (2020). Development of nonlinear probabilistic S-N curves using survival analysis techniques with application to steel bridges. International Journal of Fatigue, 141, 105892. https://doi.org/10.1016/j.ijfatigue.2020.105892.

[4] Nabizadeh, A., Tabatabai, H., Tabatabai, M. A. (2020). Conditional survival analysis for concrete bridge decks. Life Cycle Reliability and Safety Engineering, 9(1), pp. 63-75. https://doi.org/10.1007/s41872-019-00100-4.

[5] Oh, B. H. (1991). Cumulative damage theory of concrete under variable-amplitude fatigue loadings. Materials Journal, 88(1), pp. 41–48.

Proceedings IRF2025: 8th International Conference on Integrity-Reliability-Failure
In Engineering, Materials, Manufacturing and Biomechanics. Porto 15-18 July 2025
DOI: https://doi.org/10.24840/978-972-752-323-8

PAPER REF: 22403

FATIGUE CHARACTERIZATION OF L-PBF AlSi10Mg RELATED TO SAMPLE TOPOLOGY, LOAD TYPE AND PROCESS SETUP

Giorgio De Pasquale(*), Luca Margaria, Antonio Coluccia
Smart Structures and Systems Lab, Politecnico di Torino, Torino, Italy
(*)*Email:* giorgio.depasquale@polito.it

ABSTRACT

The development of interlocking joints between metals and composites seeks to replace traditional fasteners and adhesives, offering distinct advantages in terms of structural integrity and manufacturing efficiency. The metal surface includes three-dimensional anchors specifically tailored to engage the carbon fibers of the composite counterpart. These features are fabricated using laser powder bed fusion (L-PBF) additive manufacturing (AM). In addition to the anchor geometry and interfacial adhesion design, the fatigue performance of the metal alloy plays a critical role. The metal adherend exhibits a combination of bulk and thin geometries, with notch effects that induce local stress concentrations and varying growth orientations. Furthermore, the standard heat treatments for additively manufactured metals are modified during the thermal curing of the composite adherend in an autoclave. This study presents an experimental characterization of the fatigue behavior of standard specimens made of AlSi10Mg alloy. The investigation evaluates the effects of geometric parameters (sample aspect ratio, notching), loading conditions (mean stress effects), and process-related factors (growth direction, surface finish, and heat treatment).

Keywords: Multi-material joints, AlSi10Mg, L-PBF, fatigue, heat treatments.

INTRODUCTION

In the field of multi-material joints, particularly those involving metals and composites, an innovative engineering approach employs interlocking mechanisms by fabricating three-dimensional anchoring features directly on the metal surface [1]. These features interact with the carbon fibers of the composite material during the autoclave co-curing process, creating a permanent bond. This approach eliminates the need for mechanical fasteners and adhesives, improving manufacturing efficiency, enhancing structural integrity by avoiding holes, and reducing overall weight.

In this study, the L-PBF process is utilized to produce the metal side of the joint in AlSi10Mg alloy. The fatigue characterization of this alloy fabricated through AM has been previously investigated [2, 3]. In this work, process parameters optimized for interlocking joints (1344 mm/s infill laser speed, 352 W laser power, 672 mm/s contour laser speed, 304 W contour laser power, 0.03 mm layer thickness, and 0.124 mm hatch distance) are employed to fabricate fatigue test specimens according to ASTM E466. The standard sample is then modified to assess the influence of joint-specific factors on fatigue behavior. These factors include: a) Sample shape: variations in aspect ratio to evaluate the fatigue behavior of miniaturized anchors and bulk regions, notches effect with stress concentration factors Kt of 1.5 and 2.5. b) Load type: symmetric alternating load and additional mean load. c) Fabrication process-related parameters: growth directions of 45° and 90°, surface conditions (as-built roughness and machined surfaces with Ra < 0.2 μm), and modified heat treatments simulating joint curing in

autoclave. Two heat treatments are considered. a) HT7: solution annealing at 530°C for 30 minutes, water quenching, aging at 165°C for 360 minutes (air cooling), followed by autoclave curing at 175°C for 175 minutes (air cooling). The HT7 treatment corresponds to the precipitation hardening process referred to as T6 for AlSi10Mg in the ASTM-F3318 standard. b) HT22: no solution annealing, aging at 140°C for 360 minutes (air cooling), followed by autoclave curing at 175°C for 175 minutes (air cooling).

RESULTS AND CONCLUSIONS

The fatigue experimental results are presented in the form of Wöhler (S-N) curves and Haigh diagrams. The results indicate low sensitivity to the growth direction of the samples, attributed to the precise calibration of the L-PBF process. Conversely, the modified heat treatment, which includes additional exposure to the autoclave, leads to a reduction in the fatigue limit (from 80 MPa to 60 MPa). The effect of mean load is measured on the fatigue limit variation using the staircase method. The findings reveal a dependency on the mean load, as illustrated in Figure 1. Finally, low influence is observed due to stress concentration factors Kt of 1.5 and 2.5.

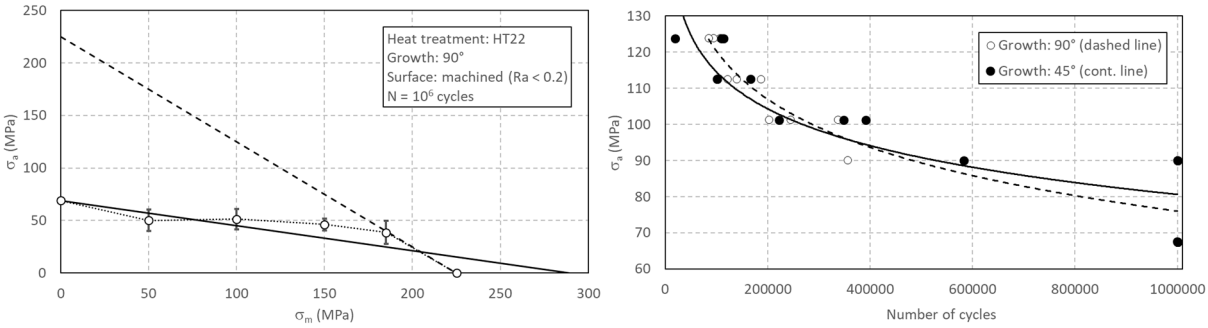

Fig. 1 - ASTM E66 samples. Left: Haigh diagram at 106 number of cycles, HT22 heat treatment, machined surface, 90° growth direction (dashed line: yield limit, continuous line: Goodman limit). Right: Wöhler diagram, HT22 heat treatment, as-built surface, 90° and 45° growth directions (dashed and continuous lines respectively).

ACKNOWLEDGMENT

This work has been funded by the H.E. grant "HORIZON-CL4-2022-RESILIENCE-01", Project MIMOSA (Project 101091826).

REFERENCES

[1] Von HPF Silva MT et al. 3D-reinforcement techniques for co-bonded CFRP/CFRP and CFRP/metal joints: a brief review. Ciência & Tecnologia dos Mat., 2017, 29(1), pp. e102-e107.

[2] Matušů M et al. Fatigue analysis and heat treatment comparison of additively manufactured specimens from AlSi10Mg alloy. International Journal of Fatigue, 2024, 185, 108357.

[3] Santos Macias J et al. Fatigue crack nucleation and growth in laser powder bed fusion AlSi10Mg under as built and post-treated conditions. Materiasl & Design, 2021, 210, 110084.

[4] De Pasquale G, Coluccia A. Modeling and Experimental Validation of CFRP-Metal Joints Utilizing 3D Additively Manufactured Anchors. ASME Journal of Manufacturing Science and Engineering, 2023, 145 (11), 111004.

[5] De Pasquale G, Altunok FE. Multiphase modeling of matrix/fiber-related damaging mechanism in multimaterial additively manufactured joints with 3D interlocking. Engineering Failure Analysis, 2025, 170, 109272.

Proceedings IRF2025: 8th International Conference on Integrity-Reliability-Failure
In Engineering, Materials, Manufacturing and Biomechanics. Porto 15-18 July 2025
DOI: https://doi.org/10.24840/978-972-752-323-8

PAPER REF: 22406

MICROSTRUCTURAL EFFECTS ON STATIC AND CYCLIC CRACK GROWTH BEHAVIOR OF NODULAR CAST IRON EN-GJS-600-3

Sebastian Henschel(*), Sarah Hübner, Lutz Krüger
Institute of Materials Engineering, TU Bergakademie Freiberg, Freiberg, Germany
(*)*Email:* sebastian.henschel@iwt.tu-freiberg.de

ABSTRACT

The effect of cooling conditions on the microstructure in a thick-walled rotor shaft made of nodular cast iron EN-GJS-600-3 was investigated. Furthermore, the impact of the microstructure on the fracture toughness behavior under quasi-static and cyclic loading was studied. Samples from different positions within the rotor shaft were taken. Consequently, microstructural characteristics, strength and deformation behavior, quasi-static fracture toughness, and cyclic crack propagation at different stress ratios were measured. It was observed that an increase in cooling time leads to an increase in graphite nodule size and nodule distance and less Bull's-eye ferrite. This finding correlates to a decrease in quasi-static fracture toughness at both 20 °C and −40 °C. There was no significant effect of the size and mean distance of the graphite nodules on the threshold value for fatigue crack growth ΔK_{th}. However, this threshold value increased with decreasing stress ratio.

Keywords: Nodular cast iron, microstructure, static fracture toughness, cyclic crack growth.

INTRODUCTION

The increasing performance of wind turbines goes hand in hand with higher forces and moments endured by the rotor shaft and other components of the wind turbine. Among optimizations of geometry, the application of affordable high-strength materials is necessary. One approach is to use nodular cast iron EN-GJS-600-3 that has higher strength due to the pearlitic matrix compared to conventionally used EN-GJS-400-18LT with a ferritic matrix.

An economic production route is casting of the hollow rotor shaft, i.e. using a chill mold in combination with a sand core. Since there is a large gradient in cooling rates in such a thick-walled component, microstructural gradients are observed. In regions with high solidification times, i.e. a high wall thickness, a heterogenous microstructure is typical. Such a microstructure may consist of degenerated graphite nodules which are few in number but large in size (Borsato et al. 2017). The solidification time also affects the formation of the pearlitic matrix. It was shown that so-called Bull's-eye ferrite will form (Hübner et al. 2023). Such ferrite can reduce stress concentration around the graphite nodules by plastic deformation. Furthermore, the ferrite phase may build up compressive residual stresses (Cavallini et al. 2008).

The main material requirement in the hollow rotor shaft is damage tolerance that can be expressed by quasi-static and cyclic fracture toughness. The pearlitic microstructure in the matrix leads to higher crack growth rates in comparison to a ferritic matrix. However, the strength of a pearlitic matrix is higher (Öberg, Wallin 1986).

In the present study, the microstructure under different cooling conditions, quasi-static fracture toughness and damage behavior were investigated. Furthermore, the cyclic crack propagation behavior was investigated with respect to the fatigue threshold and stable (subcritical) crack

propagation. The crack propagation behavior was modelled by the NASGRO approach. The mechanical properties were correlated with the cooling conditions and the microstructure at different positions in a hollow rotor shaft made of EN-GJS-600-3.

MATERIALS AND METHODS

Nodular cast iron EN-GJS-600-3 (5.3201) from a real component, i.e. a hollow rotor shaft cast in a chill mold with a sand core, was investigated, see Figure 1. From the mechanical and thermal analysis, characteristic sections of the rotor shaft were identified, i.e. main section (inner and outer radius, referred to as MI and MO), shaft head (SH) and a reference section within the flange (RA). The solidification times in the whole component range from about 500 to over 7000 s. The reference section can be used for sampling during actual production of the shaft. Near the main section, the main bearing is located. This section experiences cyclic loading with different stress ratios R. Since there is a thermal gradient, samples near the inner and outer radius are of interest. At the outer radius, the chill mold results in high solidification times. Near the sand core at the inner radius, solidification times are much higher. Samples from the shaft head were also investigated. Near the sand core, the solidification times are highest. Since not all relevant specimens could be machined from position MI, also some specimens were taken from the shaft head, but closer to the chill mold. At this position, referred to as SH*, the solidification time was nearly the same as at position MI.

The microstructure was analyzed with respect to graphite morphology and distribution (graphite diameter d_G, mean distance λ, shape factor f), and pearlite/ferrite distribution in the matrix (relative area of the Bull's-eye ferrite A_F). The measures of the graphite nodules were quantified at metallographic sections in the polished state. The sections were then etched with 2 % alcoholic nitric acid (Nital) to reveal the ferritic/pearlitic microstructure of the matrix. Figure 2 shows a schematic definition of these microstructural parameters.

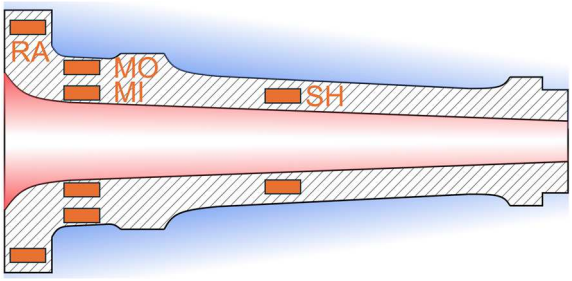

Fig. 1 - Schematic hollow rotor shaft with regions of higher/lower (red/blue) temperatures during casting.

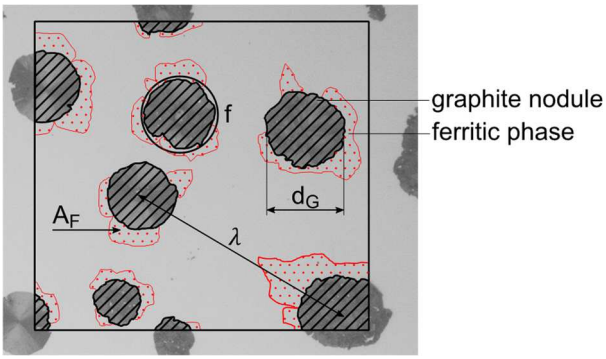

Fig. 2 - Microstructural parameters of the graphite nodules (d_G, λ, f) and the matrix (A_F).

The strength and deformation behavior was studied by tensile tests according to ISO 6892 (ISO 6892-1) at ambient temperature and at –40 °C. To this end, cylindrical tensile specimens (gage length 30 mm, diameter of 6 mm) and a clip-on gage were applied. The low-temperature tensile tests were performed in a chamber with forced-air cooling.

The fracture toughness at quasi-static loading was measured according to ISO 12135 (ISO 12135) at both temperatures at position MO. Furthermore, the position SH* was used that has a similar solidification regime like MI. Compact tension (CT) specimens with dimensions $B = 25$ mm and $W = 50$ mm were used. For position RA, single-edge notched bending (SEB) specimens with dimension $B = 10$ mm and $W = 20$ mm were applied in 3-point bending

mode. In each case, the crack opening displacement (COD) was measured by a clip-on gage at the load line. To achieve low temperatures, cool gaseous N_2 was directed to the specimen under closed-loop control. Since there was a transition in fracture mechanism between 20 and −40 °C, fracture toughness characteristics K_{Ic} or K_{Jc} were derived. Fractography was performed by means of scanning electron microscopy.

The crack growth behavior at cyclic loading was determined according to ASTM E 647 (ASTM E 647-15) at all positions at ambient temperature. SEB specimens in 8-point bending mode were used. Analogously to the quasi-static experiments, the elastic compliance of the specimen was used to calculate the crack length. The fatigue threshold ΔK_{th} was identified. Furthermore, the fatigue crack growth behavior at different stress ratios was comprehensively modeled by the NASGRO equation (Forman, Mettu 1992):

$$\frac{\mathrm{d}a}{\mathrm{d}N} = C_{\mathrm{FM}} \cdot \left(\left(\frac{1-f}{1-R} \right) \cdot \Delta K \right)^{m_{\mathrm{FM}}} \cdot \frac{\left(1 - \frac{\Delta K_{\mathrm{th}}}{\Delta K}\right)^{p}}{\left(1 - \frac{K_{\mathrm{max}}}{K_{\mathrm{c}}}\right)^{q}} \tag{1}$$

RESULTS AND DISCUSSION

Microstructure. The effect of sampling position, and thus the solidification time t_{Solid}, on the microstructure is shown in Figure 3. The thermal conditions at different positions in the hollow rotor shaft not only affect t_{Solid} but also the further cooling, and hence the diffusion processes.

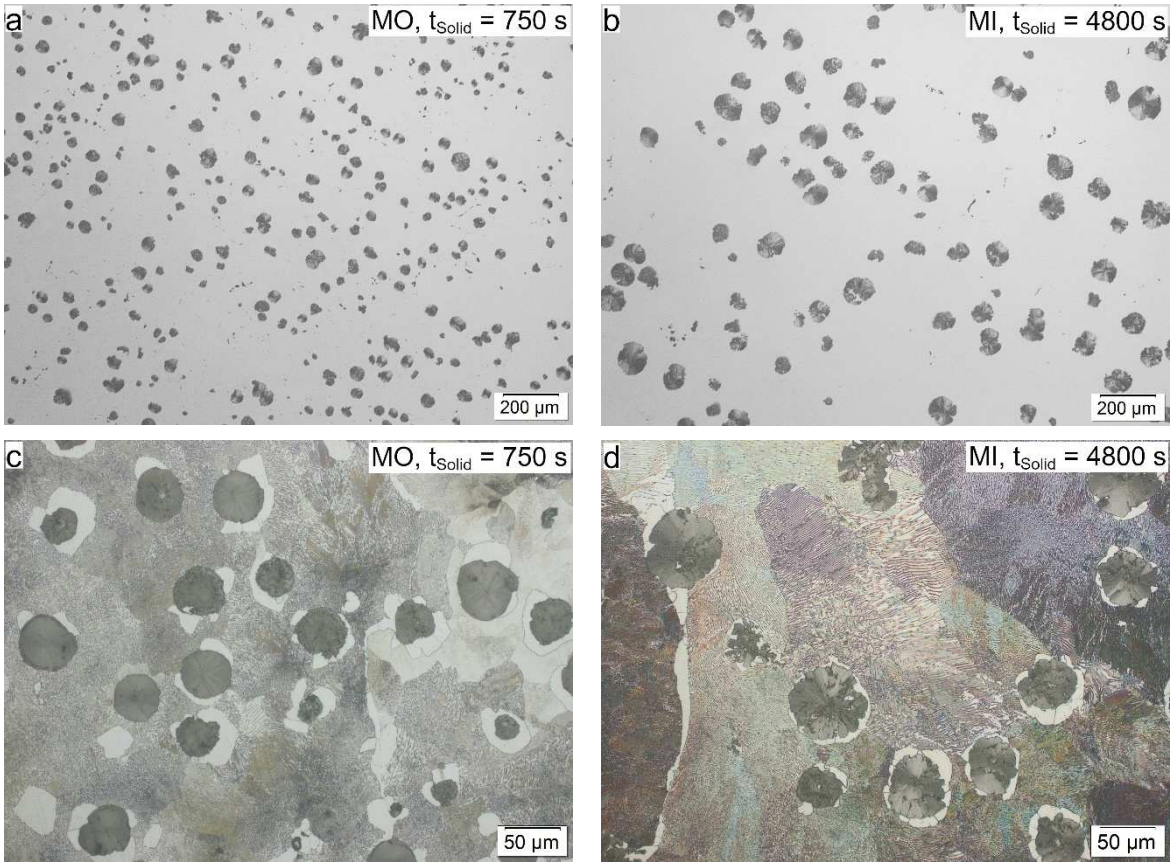

Fig. 3 - Effect of sampling position on microstructure. The shape and distribution of the graphite nodules is best visible in the unetched state (a+b). The distribution of ferrite and perlite can be detected from the etched state (c+d).

It was observed that a slower cooling rate results in much coarser graphite nodules which are fewer in number. Consequently, their distance is higher. Furthermore, the shape of the graphite nodules becomes less circular ($f = 1$ for an ideal circle). At the micrographs of the etched states, a decrease of the ferrite content around the graphite nodules (Bull's-eye ferrite) was found with increasing solidification time.

The microstructural parameters were quantified at multiple micrographs, see Figure 4. At least 1,000 graphite nodules were evaluated for each position. In addition to the interdependencies already mentioned, the analysis revealed, for example, an upper limit of d_G and λ at high solidification times. Similarly, f and A_F have a lower limit. Furthermore, the spatial distribution of the graphite nodules become more heterogenous, as can be seen from the large scatter bars at higher t_{Solid}. Consequently, a linear extrapolation from measurements at low solidification times is not acceptable.

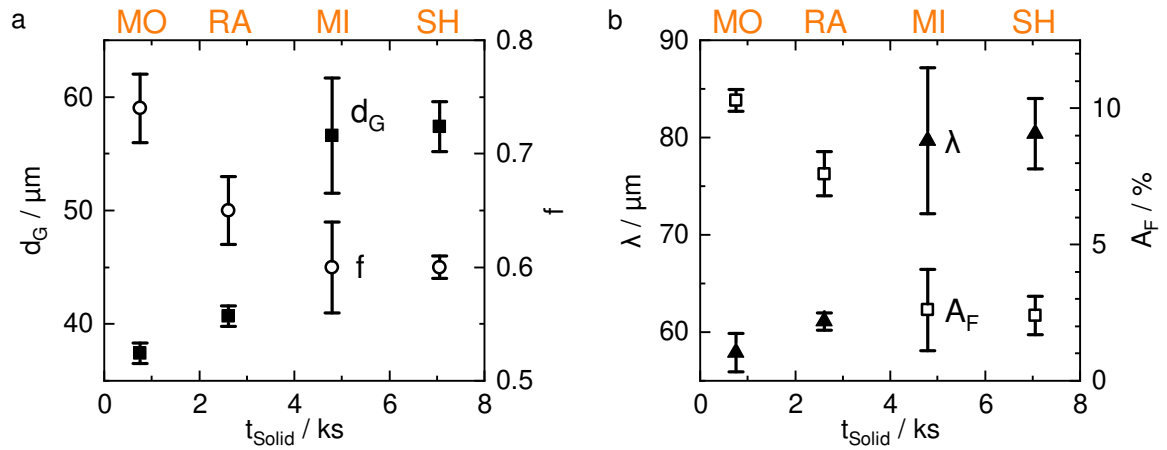

Fig. 4 - Effect of solidification time t_{Solid} on microstructural parameters. (a) Graphite diameter d_G and shape factor f, (b) Mean distance λ and area of ferrite A_F.

Strength and deformation behavior: The effect of the solidification time and thus of the microstructure on the strength and deformation behavior is shown in Figure 5.

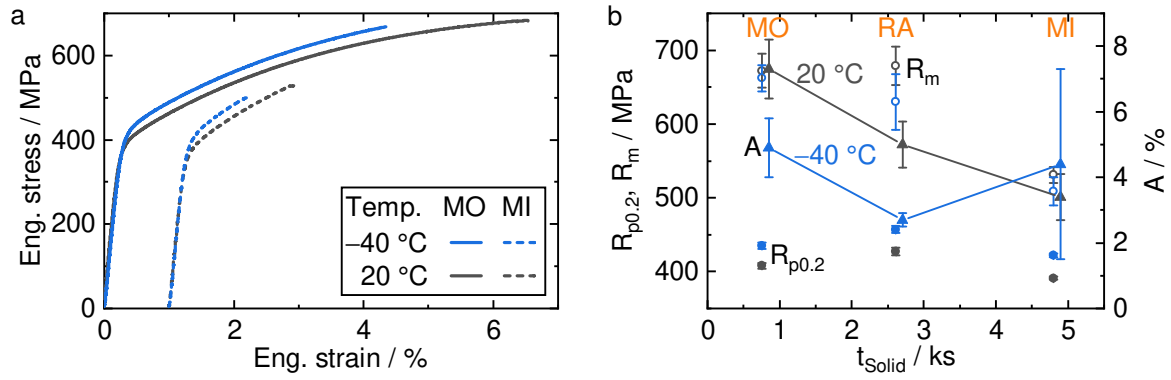

Fig. 5 - (a) Stress/strain curves for selected positions and temperatures. Curves for position MI were shifted. (b) Effect of t_{Solid} on characteristics of the tensile tests. Data points for A (with lines) are slightly shifted to the right.

Figure 5a reveals stress/strain behaviors which are typical for nodular cast irons. The 0.2% offset *yield* strength ($R_{p0.2}$) has increased with decreasing temperature. However, due to embrittlement of the matrix, the ultimate tensile strength (R_m) and fracture elongation (A) were reduced with decreasing temperature.

The effect of t_{Solid} is shown in Figure 5b. While $R_{p0.2}$ is less affected by t_{Solid}, R_m and A are significantly reduced with increasing t_{Solid}. This behavior was explained by the coarsened graphite nodules which are more degenerated (lower f) and are more heterogeneously distributed. The heterogenous distribution is demonstrated by the large scatter bars of A at position MI.

Quasi-static fracture toughness: Depending on the material behavior, see Figure 6a, the plane-strain fracture toughness K_{Ic} or the fracture toughness K_{J_c}, which is equivalent to the critical J integral at unstable fracture (J_c), were calculated, see Figure 6b. At 20 °C, the first significant pop-in was observed after some amount of crack growth and plastic deformation. After such a pop-in, some further stable crack growth was detected (more pop-ins were also possible). However, the first significant pop-in must be defined as the critical point according to ISO 12135. At –40 °C, there was an insignificant amount of crack growth until the first pop-in.

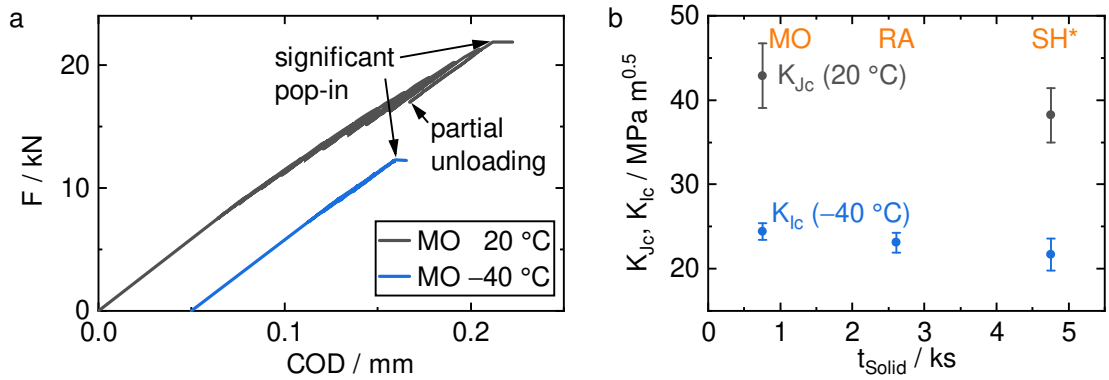

Fig. 6 - (a) Selected force/displacement curves for position MO. Curve at –40 °C was shifted; (b) Effect of t_{Solid} and testing temperature on the fracture toughness characteristics. Position SH* has nearly the same t_{Solid} as position MI.

At a low testing temperature of –40 °C, plane-strain fracture toughness K_{Ic} was measurable at all positions. The embrittlement of the matrix is the main reason for this, see Figure 7b. At ambient temperature, Figure 7a, some regions of ductile fracture were observed.

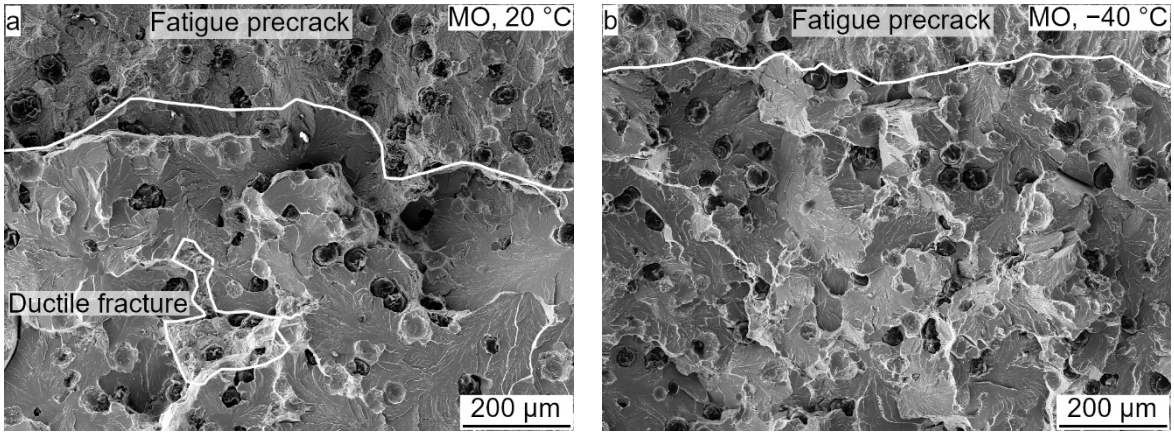

Fig.7 - Fracture surfaces showing mostly unstable crack extension by cleavage fracture, position MO. (a) At 20 °C, some ductile fracture zones are visible. (b) At –40 °C, ductile fracture is negligible.

High solidification rates at position MO result in the highest fracture toughness. The decrease of the fracture toughness with increasing t_{Solid} was explained by the increased notch effect of less globular graphite nodules and the more heterogenous spatial distribution.

Cyclic crack growth behavior: Figure 8a shows $\mathrm{d}a/\mathrm{d}N$-ΔK curves used for measuring the fatigue crack threshold ΔK_{th} at position MO and different stress ratios R. Figure 8b shows the effects of t_{Solid} and R on ΔK_{th}.

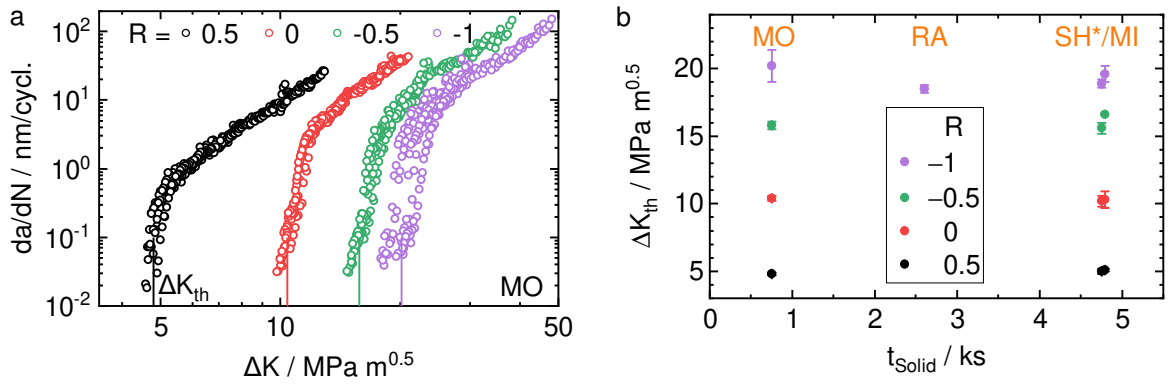

Fig. 8 - (a) $\mathrm{d}a/\mathrm{d}N$-ΔK curves for different stress ratios R at position MO at ambient temperature. At least 4 samples per R. (b) Fatigue threshold ΔK_{th} for different microstructures and stress ratios. Position SH* has a slightly lower t_{Solid} than position MI.

At all sampling positions, higher mean stresses, i.e. higher R, result in lower values of ΔK_{th}. This behavior is typical, not only for the present nodular cast iron, and is explained by crack closure effects at negative R(*Elber* 1970). In contrast, ΔK_{th} is relatively insensitive to higher solidification times. Consequently, the properties of the pearlitic matrix determine the threshold behavior. An interaction with the graphite nodules is less relevant. At negative R, the scatter is increased. However, this scatter can be tolerated. The present EN-GJS-600-3 shows similar or higher fatigue thresholds then typical characteristics given in the literature (Hübner et al. 2023).

At the position RA and at stress ratio $R = -1$, which is most relevant for practical application of the hollow rotor shaft, the slightly lower values of ΔK_{th} were measured. Hence, samples from this reference position can be used to conservatively estimate ΔK_{th} for the whole component.

With the NASGRO equation (Equation 1), the $\mathrm{d}a/\mathrm{d}N$-ΔK curves for all stress ratios R were modelled. The suitability of this approach was demonstrated in Figure 9 for positions MO and MI. Similarly to ΔK_{th}, it can be observed that the effect of different solidifications times is relatively weak.

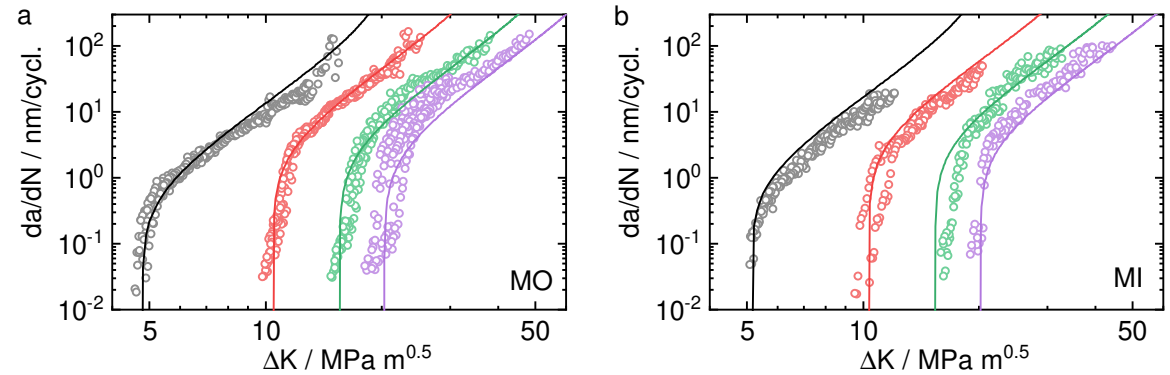

Fig. 9 - $\mathrm{d}a/\mathrm{d}N$-ΔK curves at positions (a) MO and (b) MI at ambient temperature. Lines represent the NASGRO description. Colors represent different stress ratios R, see Figure 8.

The coefficients needed in Equation 1 are given in Table indicate the small effect of t_{Solid}. Depending on the stress ratio R, the respective value for ΔK_{th} must be used, Figure 8b. K_{c} used

in Equation 1 was essentially set to K_{Jc} (see Figure 6b). However, in order to achieve a good description of the experimental data, the values were slightly adjusted.

Tab. 1 - Coefficients of Eq. 1 for positions MO and MI.

Position	C_{FM} / 10^{-2} nm/ MPa$\sqrt{\mathrm{m}}$	m_{FM}	f	p	q	K_{c} / MPa$\sqrt{\mathrm{m}}$
MO	1.1	3.12	0.26	0.70	0.70	43.0
MI	1.4	3.11	0.26	0.67	0.67	42.8

SUMMARY AND CONCLUSION

The nodular cast iron EN-GJS-600-3 from a real thick-walled casting was studied with respect to microstructure, quasi-static fracture toughness and fatigue crack growth behavior. The key findings are summarized below:

- A slower solidification at positions with heat accumulation results in coarse and less round graphite nodules. Furthermore, the so-called Bull's-eye ferrite is less pronounced after slow solidification. The main matrix phase is pearlite.
- The ultimate tensile strength and deformability is reduced by a coarser microstructure. In contrast, the yield strength is relatively unaffected by different cooling conditions.
- The quasi-static fracture toughness is reduced at positions with slow solidification. Due to matrix embrittlement, the cooling to −40 °C further decreases the fracture toughness.
- The pearlitic matrix determines the fatigue behavior. Consequently, the threshold for fatigue crack growth and the shape of the $\mathrm{d}a/\mathrm{d}N$-ΔK curves is insensitive to different cooling conditions. An increase of the stress ratio reduces the fatigue crack growth.
- Mechanical properties measured at samples taken from the reference area (RA) in the flange can be used for quality assessment. Those mechanical properties are representative of the highly loaded main area or slightly conservative in case of ΔK_{th}.

ACKNOWLEDGMENTS

The authors are grateful to the Federal Ministry of Economic Affairs and Energy for funding the joint project (0324329B) at the Institute of Materials Engineering (IWT) at the Technische Universität Bergakademie Freiberg. The authors thank Dr.-Ing. Peter Trubitz and Dr.-Ing. Sebastian Henkel for fruitful discussions.

REFERENCES

[1] Borsato, Thomas; Ferro, Paolo; Berto, Filippo; Carollo, Carlo (2017): Mechanical and fatigue properties of pearlitic ductile iron castings characterized by long solidification times. In Eng. Fail. Anal. 79, pp. 902-912. DOI: 10.1016/j.engfailanal.2017.06.007.

[2] Hübner, Sarah; Trubitz, Peter; Henschel, Sebastian; Krüger, Lutz (2023): Influence of Microstructure on Static and Cyclic Fracture Toughness of EN-GJS-600-3 Nodular Cast Iron. In Int. J. Metalcast. 17 (2), pp. 1217-1228. DOI: 10.1007/s40962-022-00849-y.

[3] Cavallini, Mauro; Di Bartolomeo, Ornella; Iacoviello, Francesco (2008): Fatigue crack propagation damaging micromechanisms in ductile cast irons. In Eng. Fract. Mech. 75 (3-4), pp. 694-704. DOI: 10.1016/j.engfracmech.2007.02.002.

[4] Öberg, Tero; Wallin, Kim (1986): Fracture properties of ferritic, ferritic-pearlitic, pearlitic and bainitic nodular cast irons. Espoo: VTT (Tutkimuksia / Valtion Teknillinen Tutkimuskeskus, 430).

[5] ISO 6892-1, 2019: Metallic materials – Tensile testing – Part 1: Method of test at room temperature.

[6] ISO 12135, 2016: Metallic materials – Unified method of test for the determination of quasistatic fracture toughness.

[7] ASTM E 647-15, 2015: Standard test method of measurement of fatigue crack growth rates.

[8] Forman, Royce G.; Mettu, Sambi R. (1992): Behavior of surface and corner cracks subjected to tensile and bending loads in a Ti-6Al-4V alloy. In Hugo Ernst, Ashok Saxena, David L. McDowell (Eds.): Fracture mechanics: twenty-second symposium, vol. 1. Philadelphia: American Society for Testing and Materials (ASTM STP, 1131), pp. 519-546.

[9] Elber, Wolf (1970): Fatigue crack closure under cyclic tension. In Eng. Fract. Mech. 2 (1), pp. 37-45. DOI: 10.1016/0013-7944(70)90028-7.

Proceedings IRF2025: 8th International Conference on Integrity-Reliability-Failure
In Engineering, Materials, Manufacturing and Biomechanics. Porto 15-18 July 2025
DOI: https://doi.org/10.24840/978-972-752-323-8

PAPER REF: 22419

INDUCING COMPRESSIVE RESIDUAL STRESSES USING WATER JET PEENING FOR FATIGUE LIFE EXTENSION IN A STAINLESS STEEL

E.D. McMullan, A.H. Mahmoudi(*)
School of Engineering, University of West England, Frenchay Campus, BS16 1QY, Bristol, UK,
(*)*Email:* Amir.Mahmoudi@uwe.ac.uk

ABSTRACT

The Water Jet Peening (WJP) technology first introduced in the 1980s is a surface modification process that can induce compressive residual stresses within metals, therefore improving fatigue life of components. In this paper a finite element model simulating the WJP was established using ANSYS and MATLAB. The study focuses on analysing the compressive residual stress, surface roughness and fatigue cycle numbers after waterjet peening. The numerical findings are validated using the experiments.

Keywords: Water Jet Peening (WJP), Finite Element Modelling, residual stresses, Roughness, Fatigue Life.

INTRODUCTION

Water Jet Peening is a cold working process that can induce compressive residual stresses within metals. In recent years the process has undergone research and experimentation with different materials and methods of modelling (Kunaporn. S et al, 2005). Here, 316L stainless steel was used as a corrosion resistant material. This stainless steel has accommodated a wider use in industry fields where higher product properties are required. In this paper the parabolic distribution p(r) provided by Leach and Walker (Leach and Walker, 1966) is used to model the radial impact pressure (Ramulu. M, 1999) on the material surface. The effects of different peening parameters on the residual stresses have been predicted using the finite element simulations.

RESULTS AND CONCLUSIONS

Equation (1) models the impact pressure distribution of the WJP by substituting Leach and Walkers P(r) parabolic with the Kunaporn pressure distribution model.

$$P(r) = 3C_0 \frac{P_s}{u} \left(\frac{d_n}{d_n + 2(SOD)\tan\frac{\alpha}{2}} \right)^3 \left[2\left(\frac{r}{a}\right)^3 - 3\left(\frac{r}{a}\right)^2 + 1 \right] \quad (1$$

In Equation (1) P(r) is impact pressure across the radial impact zone, c_0 is the wave velocity, d_n is the nozzle diameter, r is the variable radius impact zone, P_s is the supply pressure, SOD is the stand-off distance, u is the nozzle feed rate, α is the jet angle and a is the contact area radius. The assembly presented in Figure 1 better illustrates the variables of equation (1)

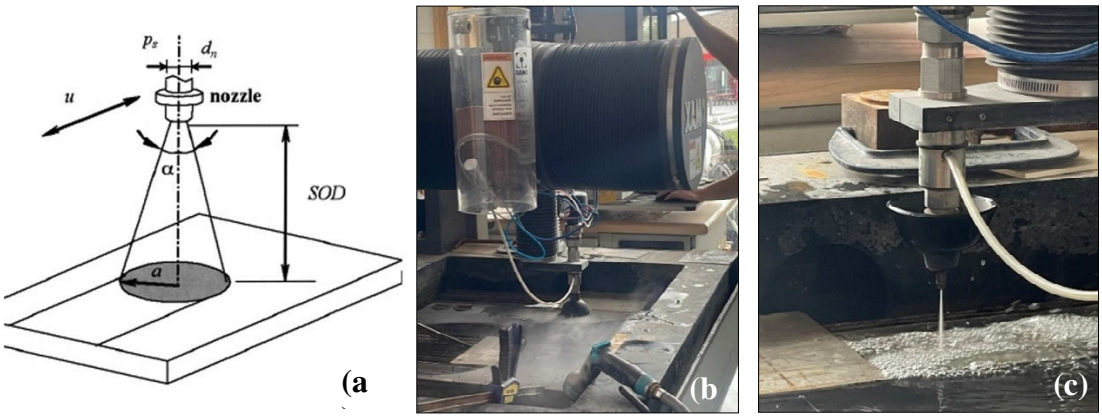

Fig. 1 - (a) Water Jet Peening Schematic (Mahmoudi A.H et al, 2020). (b) & (c) WJP Assembly.

The Supply pressure, Stand-Off Distance and nozzle feed rate were changed in respect to the residual stress induced. The impact distribution produced from Equation (1) was incorporated into a FE model to generate the residual stresses post unloading.

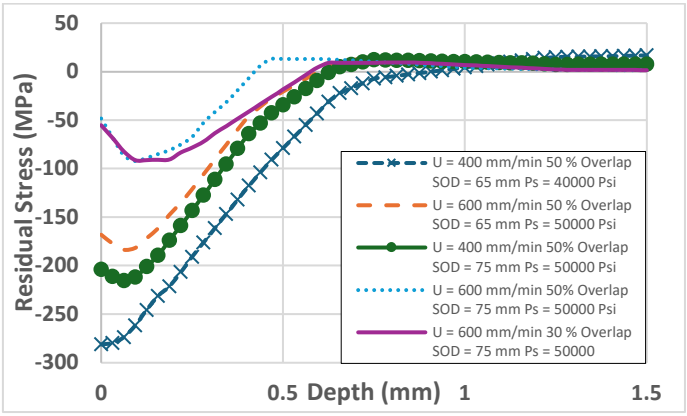

Fig. 2 - FE Residual stresses induced across depth.

The specimens inducing the optimal residual stress relative to surface roughness were subjected to fatigue testing to investigate the effects of WJP on fatigue life. For comparison, the same method was applied to unpeened specimens.

REFERENCES

[1] Kunaporn, S., Ramulu, M. and Hashish, M. (2005) Mathematical Modeling of Ultra-High-Pressure Waterjet Peening. Journal of Engineering Materials and Technology 127 (2), pp. 186-191.

[2] Leach, S.J. and Walker, C.L. (1966) A discussion on deformation of solids by the impact of liquids Philosophical Transactions of the Royal Society of London. Series A, Mathematical and Physical Sciences. 260 (1110), pp. 295-310.

[4] Mahmoudi, A.H., Jamali, A.M., Salahi, F. and Khajeian, A. (2020) Effects of water jet peening on residual stresses, roughness, and fatigue. Surface Engineering. 37 (8), pp. 972-981.

[8] Ramulu, M., Kunaporn, S., Arola, D., Hashish, M. and Hopkins, J. (1999) Waterjet Machining and Peening of Metals. Journal of Pressure Vessel Technology. 122 (1), pp. 90-95.

Proceedings IRF2025: 8th International Conference on Integrity-Reliability-Failure
In Engineering, Materials, Manufacturing and Biomechanics. Porto 15-18 July 2025
DOI: https://doi.org/10.24840/978-972-752-323-8

PAPER REF: 22426

OPTIMIZING THE FRACTURE TOUGHNESS OF POLYMER CONCRETE WITH VARIABLE MIXTURES BY TAGUCHI METHOD

MRM. Aliha[1(*)], Daniel Pietras[2], Hossein Parsania[1], Rasoul Ghayomian[1], Somayeh Moshatghi[1], Camellia Rafiei[1], Rafiee[1], T. Sadowski[2]

[1]Welding and Joining Research Centre, Iran University of Science and Technology (IUST)Tehran, Iran.
[2]Department of Solid Mechanics, Lublin University of Technology, Lublin, Poland
[(*)]*Email:* mrm_aliha@iust.ac.ir

ABSTRACT

Fracture toughness is a key and important design parameter for assessing the integrity and service life of structures and materials containing crack or defects. Polymer Concrete (PC) is a multi-ingredients composite that can be manufactured with different ingredients and contents. Accordingly, the mix design can affect the structural integrity and resistance of PC materials against cracking. In this research, Taguchi method was employed to find the optimum percentages of a silicious aggregate + polyester resin + chopped glass fiber PC mixture to achieve the highest K_{Ic}. The initial window of input variables were: 0% <glass fiber <1.5%, 39% <coarse aggregate <55%, 20%<fine aggregate<37% and 11%< epoxy resin <30%. The fracture toughness tests were done using a novel sub-sized short bend beam (SBB) sample. The SBB tests were performed according to a L32 Taguchi DoE technique and the optimum percentages of PC ingredients and the importance of each ingredient on K_{Ic} value were obtained.

Keywords: Polyester-silicious polymer concrete, mode I failure, Taguchi method.

INTRODUCTION

Polymer concrete (PC) is a type of concrete that can be made by mixing different components namely (i) a polymeric resin, (ii) fine and coarse aggregate and filler materials and (iii) reinforcing fiber materials in suitable percentages. This material has several specific applications in different civil structures such as composite structures, roads and pavement systems, overlay of bridges, repairing and reinforcing of the damaged structures and offshore structures. Mechanical and strength properties in such multi-ingredient composite materials is affected by the type and dosage of the components. The usage of design of experiment (DoE) methods (such as Taguchi) can help the PC designers in determining the optimum mix design parameters to obtain the best achievable strength and mechanical properties with lesser number of laboratory experiments. Since PC mixtures may exhibit dominantly brittle or quasi-brittle behaviour in real field applications, catastrophic failure and fracture due to sodden crack growth is one of the major failure modes for reducing the reliability of structures made of PC materials.

Some experimental testing methods have been utilized and employed by several researchers to determine the fracture toughness of PC materials. Rectangular beam [1,2], semi-circular [2,3] disc [2] and circular [2,4] shape cracked specimens subjected to bending or compressive forces are some of the samples for K_{Ic} testing of PC materials. In this research a novel sub-sized short beam bend (SBB) sample that requires less amount of material for K_{Ic} testing compared to other conventional test samples is utilized for conducting the fracture tests on different mix designs of PC composition to obtain the highest cracking resistance value. The experiments are done according to the suggestions of Taguchi optimization method. The importance of input parameters and optimum range of each ingredient to achieve the highest fracture toughness is then obtained via the analyses of the Taguchi method.

RESULTS AND CONCLUSIONS

The PC mixture of this research was composed of polyester resin, silicious coarse grain aggregates, fine grain filler and chopped glass fibers in the following weight percentage ranges: 0% <glass fiber <1.5%, 39% <coarse aggregate <55%, 20%<fine filler <37% and 11%< polyester resin <30%. A L32 Taguchi DoE technique (with four input variables and four levels for each input factor) was utilized to prepare different PC mixtures and to investigate the effect of each ingredient on the cracking resistance of the PC. Accordingly, a number of fracture toughness tests were done using the short bend beam (SBB) made of different PC mixtures as shown in Figure 1. The fracture toughness for each test was determined by means of Eq. (1).

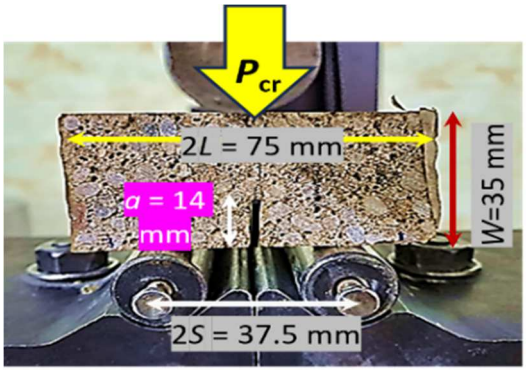

Fig. 1 - SBB test sample for conducting fracture toughness tests on different PC mixtures.

$$K_{\mathrm{Ic}} = \frac{3P_{\mathrm{cr}}S}{2tW^2}\sqrt{\pi a}\,Y_{\mathrm{I}}\left(\frac{a}{W},\frac{S}{L}\right) \quad (1)$$

where P_{cr} is the critical applied load to the SBB sample, t is the thickness of sample and Y_{I} is the geometry factor that depends on the crack length ratio and loading span ratio. For the tested SBB samples of this research Y_{I} was determined equal to 1.94 by finite element modelling. The corresponding average values of mode I fracture toughness (K_{Ic}) for different PC mix designs were obtained in the range of 1.45 to 3.75 MPa.m$^{0.5}$. This reveals the significant influence of mixture type on cracking resistance of PC materials. Based on the main effect parameters obtained from the Taguchi analyses, the best composition of PC mixture is achieved for the following contents of the ingredients: 26% polyester resin, 29% filler, 44% silicious aggregates and 1% glass fiber. Also, based on the signal to noise analyses, the resin content and coarse aggregate percentage showed the highest impact on the change of PC fracture toughness.

REFERENCES

[1] Reis JM, Ferreira AJ. Assessment of fracture properties of epoxy polymer concrete reinforced with short carbon and glass fibers. Construction and Building Materials. 2004, 18, pp. 523-528.

[2] Aliha MR, Kouchaki HG, Mohammadi MH, Haghighatpour PJ, Choupani N, Asadi P, Akbari M, Darvish MG, Sadowski T. Fracture toughness determination for epoxy-based polymer concrete mixtures: Applicability of different rectangular beam and circular disc specimens. Composites Part C: Open Access. 2024, 14, p. 100446.

[3] Aliha MR, reza Karimi H, Abedi M. The role of mix design and short glass fiber content on mode-I cracking characteristics of polymer concrete. Construction and Building Materials. 2022, 317, p. 126139.

[4] Asdollah-Tabar M, Heidari-Rarani M, Aliha MR. The effect of recycled PET bottles on the fracture toughness of polymer concrete.

Proceedings IRF2025: 8th International Conference on Integrity-Reliability-Failure
In Engineering, Materials, Manufacturing and Biomechanics. Porto 15-18 July 2025
DOI: https://doi.org/10.24840/978-972-752-323-8

PAPER REF: 22428

A COMPARATIVE CRACK GROWTH EVALUATION FOR REACTOR COMPONENTS

Heejun Yang[1], Hwan-Jae Joo[1], Yoon-Suk Chang[2(*)]

[1]Department of Nuclear Engineering, Kyung Hee University, Republic of Korea
[2]Department of Nuclear Engineering, Faculty of Engineering, Kyung Hee University, Republic of Korea
[(*)]*Email:* yschang@khu.ac.kr

ABSTRACT

The reliable assessment of structural integrity is essential for ensuring safe design and operation of nuclear power plants. This study introduces a specific crack growth evaluation to demonstrate the applicability of extended finite element method. A case study highlights the suitability of this versatile numerical method for reactor components and provides deeper insights into plausible failure phenomena. Its validity is confirmed through comparisons with an engineering evaluation method and actual images. Key findings are outlined, with discussions on expanded applications and potential limitations.

Keywords: Crack growth simulation, extended finite element method, reactor components.

INTRODUCTION

Integrity of nuclear components must be rigorously ensured. In particular, reactor vessel internals (RVIs) which are exposed to high-temperature and neutron irradiation environments require reliable material performance. However, cracking in complex RVIs has been reported globally within their design life, necessitating a comprehensive risk management strategy for such failures. To address the cracking issue, various methods have been employed to predict initiation and propagation behaviors. Among these, experimental tests are constrained by the challenges of preparing hot-cell facilities, engineering evaluation methods are inherently simplistic and conservative, and conventional numerical methods incur high costs due to the need for crack modeling and re-meshing. The extended finite element method (XFEM) (Moës and Belytschko, 2002), known for its advantages of relatively simple modeling and reasonable accuracy, has been successfully applied to fracture mechanics assessments of compact tension specimens and nuclear piping (Sim and Chang, 2019), in conjunction with degradation mechanisms such as primary water stress corrosion cracking and thermal aging embrittlement. This paper utilizes XFEM for reactor components, aiming to provide an enhanced structural integrity assessment and deeper insights into irradiation-related failure mechanisms.

RESULTS AND CONCLUSIONS

Unlike previous XFEM applications, two separate numerical analyses were conducted. The first involves conventional finite element (FE) analyses using a global-local approach. Stress, strain and displacement profiles of the RVIs were calculated taking into account irradiation embrittlement, irradiation-enhanced creep, void swelling and irradiation-assisted stress corrosion cracking (IASCC) (Jyung et al., 2024). For the subsequent XFEM analyses, the displacement vector function is approximated as described in Equation (1) and Figure 1.

$$u = \sum_I^N N_I(x)[u_I + H(x)a_I + \sum_{\alpha=1}^4 F_\alpha(x)b_I^\alpha] \quad (1)$$

Here, $N_I(x)$ is the nodal shape function, u_I is the nodal DOF, Heaviside function $H(x)$ along with discontinuity-related nodal DOF a_I capture the crack path. Additionally, crack tip enrichment function $F_\alpha(x)$ and nodal enriched DOF $b_I{}^\alpha$ represent the crack tip behavior.

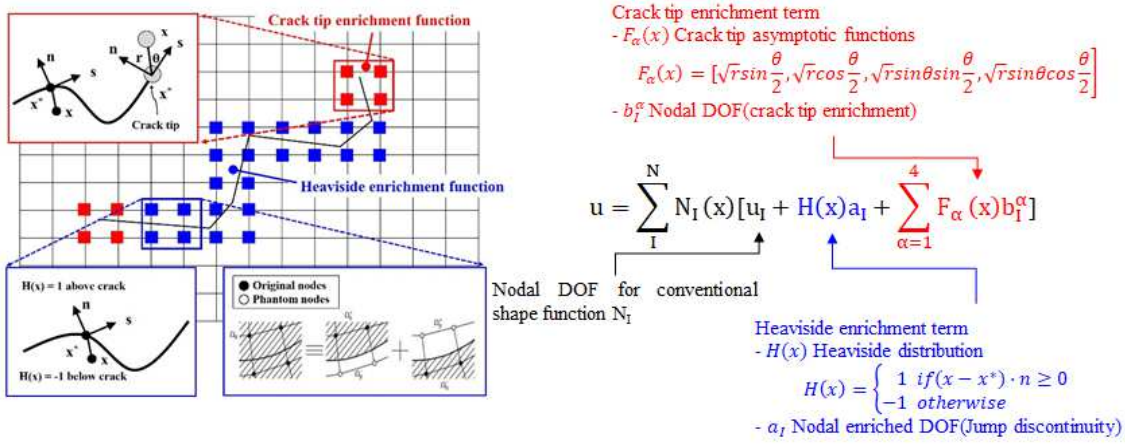

Fig. 1 - Schematic of XFEM and adopted functions.

Out of available options, the quadratic stress criterion and virtual crack closure technique were adopted. The crack evolution energy was calculated from the relationship between forces and displacements, while the threshold value was determined by considering irradiation-adjusted properties of the RVI material, namely stainless steel.

On the other hand, as a typical engineering evaluation method, the procedure specified in the well-known ASME Boiler & Pressure Vessel Code was employed. Stress profiles obtained from the conventional FE analyses were substituted into the stress intensity factor calculation equations provided in the code. The IASCC crack growth rate was defined as follows:

$$\frac{da}{dt} = 4.73 \times 10^{-17}\, \sigma_{0.2}^{2.547} K^{2.504} \quad (2)$$

The validity of crack propagation results was assessed by comparing them with results from the engineering evaluation method and actual 3D data obtained through an advanced imaging technique, which depicted the grown crack shapes and sizes of the defective component.

ACKNOWLEDGMENTS

This work was supported by the Innovative Small Modular Reactor Development Agency grant funded by the Korea Government (MOTIE) (No. RS-2024-00405419).

REFERENCES

[1] Moës, N and Belytschko, T. Extended finite element method for cohesive crack growth. Engineering Fracture Mechanics, 2002, 69, pp .813-833.

[2] Sim, JM and Chang, YS. Crack growth evaluation by XFEM for nuclear pipes considering thermal aging embrittlement effect. Fatigue and Fracture of Engineering Materials and Structures, 2019, 42, pp.775-791.

[3] Jyung, JM, Joo, HJ and Chang, YS. Irradiation-induced age-related degradation mechanisms effect on integrity of baffle former bolts. International Journal of Pressure Vessels and Piping, 2024, 208, 104429.

Proceedings IRF2025: 8th International Conference on Integrity-Reliability-Failure
In Engineering, Materials, Manufacturing and Biomechanics. Porto 15-18 July 2025
DOI: https://doi.org/10.24840/978-972-752-323-8

PAPER REF: 22436

COMPARATIVE ANALYSIS OF EXPERIMENTAL AND NUMERICAL DURABILITY IN BUS STRUCTURES USING FREQUENCY DOMAIN METHODS

Gabriel Ramires Peixoto Reis(*), Rogério José Marczak
PROMEC/UFRGS, Faculty of Engineering, Federal University of Rio Grande do Sul, Porto Alegre, Brazil
(*)*Email:* reisgabrielramires@gmail.com

ABSTRACT

This study compares experimental durability and virtual durability calculation through numerical models, aiming to reduce costs and speed up the development of vehicle structures, specifically bus bodies. The results show a good correlation between the durability measured in the physical prototype and the one calculated in the virtual model, demonstrating the robustness and reliability of the applied methods.

Keywords: Experimental durability, virtual durability, Dirlik methodology, finite element method (FEM).

INTRODUCTION

Many automotive companies use well-established experimental methodologies to evaluate the durability of their structures, conducting advanced tests on special tracks and correlating the damage caused per kilometre on these tracks with the damage on public roads (Lee et al., 2005; Park JS et al., 2018). In bus structures, sensor instrumentation is costly due to the number needed to cover the entire length and structural joints. With the advances in numerical methods and the processing capacity of new computers, this study describes a methodology for calculating the virtual durability of a bus structure and correlating these values with the durability obtained from a physical prototype.

RESULTS AND CONCLUSIONS

To calculate numerical and experimental durability, a track signal obtained from a physical prototype was used. In the vehicle, 4 triaxial accelerometers were used to map the input loads and several uniaxial strain gauges to verify the deformation/stress response along the track and subsequently calculate the durability of the vehicle's structural joints (Benasciutti D, 2004; Pascualinotto, 2021).

Durability through conventional methods was calculated using the Rainflow method for cycle counting and the Palmgren-Miner rule for accumulated linear damage calculation. For virtual durability calculation, the Dirlik methodology was used for cycle counting and accumulated damage, using acceleration values obtained by the accelerometers as input loads (Lee et al., 2005; Park JS et al., 2018). The accelerations were converted from the time domain to the frequency domain, resulting in 12 PSDs (Power Spectrum Density) and 44 Cross-PSDs (CPSD), each containing amplitude and phase angle between the correlated PSDs (Broussinos et al., 1990). The highest damage observed through conventional methodologies was 0.0077,

and the damage value obtained through numerical calculation was 0.008. Other damage values through both methodologies are presented in the Table 1 below, and Figure 1 shows an image of the finite element model (FEM) used for numerical damage calculation.

Table 1 – Comparison of damage values.

	Local of the test	Damage Experimental Method	Damage Virtual Method
LD01	SPECIAL TRACKS (TATUI)	0,00773	0,008
LD02	SPECIAL TRACKS (TATUI)	0,00048	0,00079
LD04	SPECIAL TRACKS (TATUI)	0,00043	0,003

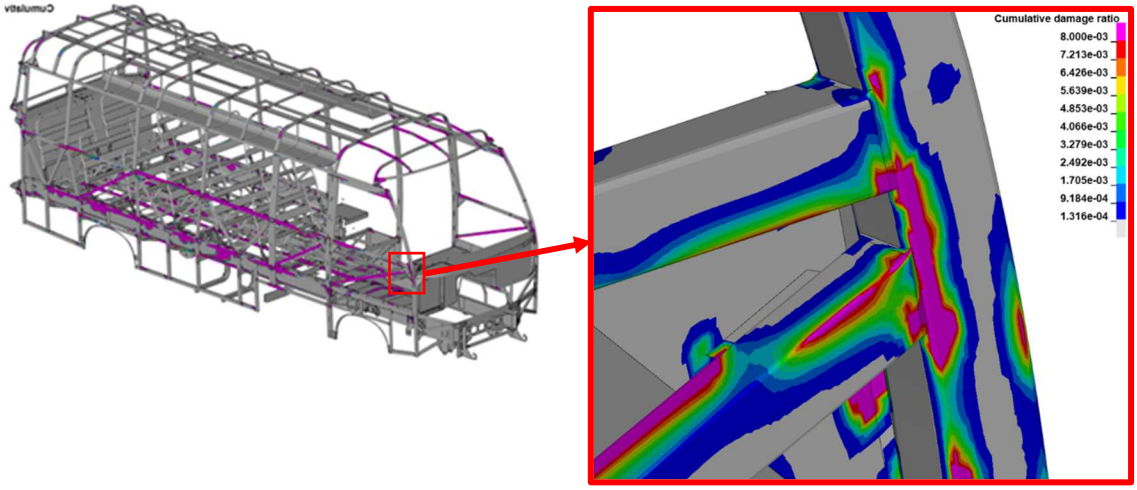

Fig. 1 - FEM model and region of highest cumulative damage.

The results indicate a good correlation between virtual durability via numerical model and the durability obtained with a physical prototype. This provides greater agility and lower cost in the development of new vehicle structures, reducing the number of prototypes and sensors needed and allowing structural changes to be evaluated without compromising the validated structure's durability.

REFERENCES

[1] Benasciutti D. Fatigue Analysis of Random Loadings (PhD Thesis). University of Ferrara. 2004.

[2] Broussinos P, Kabe A. Multi-mode random response analysis procedure. The Aerospace Corp., TR SSD-TR-90-53, Los Angeles. 1990 Jan 1.

[3] Lee YL, Pan J. Fatigue Testing and Analysis: Theory and Practice. Elsevier; 2005. pp. 1-350.

[4] Park JS, Dospati R, Pan YC, Nair A. Random Vibration Fatigue Life Simulation of Bolt-on Metal Brackets using LS-DYNA®. 15th International LS-DYNA Users Conference 2018. pp. 123-130.

[5] Pascualinotto Junior V. Fatigue life estimation of a notched component using frequency domain technique and probabilistic linear cumulative damage model (Doctoral dissertation, Universidade de São Paulo, 2021). pp. 1-200.

Proceedings IRF2025: 8th International Conference on Integrity-Reliability-Failure
In Engineering, Materials, Manufacturing and Biomechanics. Porto 15-18 July 2025
DOI: https://doi.org/10.24840/978-972-752-323-8

PAPER REF: 22439

APPLICATION OF MACHINE LEARNING FOR PREDICTING AND OPTIMIZING FRACTURE ENERGY IN ASPHALTIC MIXTURES AT INTERMEDIATE TEMPERATURES

MRM Aliha[1(*)], H. Parsania[1], D. Pietras[2], A. Rajabi-Kafshgar[1], M. Daghighi[1], A. Mousavi[1], S. Momenian[1], T. Sadowski[)]

[1]Welding and Joining Research Center, Iran University of Science and Technology (IUST)Tehran, Iran.
[2] Department of Solid Mechanics, Lublin University of Technology, Lublin, Poland
[(*)]*Email:* mrm_aliha@iust.ac.ir

ABSTRACT

This study explores the use of machine learning (ML) to optimize asphalt mixture design for improved durability and performance. By analyzing fracture energy from pre-cracked semi-circular bend (SCB) tests under varying conditions, a neural network with regression techniques and genetic algorithms identified the optimal asphalt mixture. The Multi-Layer Perceptron (MLP) model, known for capturing complex nonlinear relationships, used to map input variables such as aggregate composition, air voids, temperature, and loading rate to fracture energy. Bayesian regression applied to train the model, improving predictive accuracy and generalization for optimizing durable asphalt designs.

Keywords: Asphalt Mix Design, Machine Learning, Fracture Energy, , Pavement reliability.

INTRODUCTION

Optimizing asphalt mix design is vital for enhancing pavement performance, durability, and cost-efficiency. Traditional empirical methods, while effective, are resource-intensive and lack adaptability to varying conditions, leading to growing interest in machine learning (ML) models. ML techniques like Gene Expression Programming (GEP), Artificial Neural Networks (ANN), and Support Vector Machines (SVM) have shown success in predicting key asphalt composite properties (such as fracture energy, stiffness modulus, and Marshall stability). Studies by Majidifard et al. [1], Ghanizadeh et al. [2], and Jalota and Suthar [3] demonstrated that ML models can analyze large datasets, identifying complex relationships between variables like aggregate type, air void content, temperature, and loading rate. However, gaps remain in predicting the fracture energy as the critical measure of structural integrity in pavement systems. This study addresses these gaps by combining ML with fracture tests, focusing on pre-cracked asphalt mixtures to optimize designs under intermediate temperature conditions. This data-driven framework promises to improve asphalt durability and reliability of pavement structures while reducing testing time and costs.

RESULTS AND CONCLUSIONS

At intermediate service temperatures (5 to 25°C), hot mix asphalt (HMA) in pavement overlay layers experiences varying loading rates due to vehicle speeds, affecting its mechanical properties and fracture resistance. HMA mixtures were compacted using different gyratory rotations to obtain air void contents of 3%, 5%, and 7%. Manufactured cylindrical HMA specimens (with diameter and height of 150 mm and 140 mm, respectively) were cut into semi-circular bend (SCB) samples with a 25 mm vertical edge crack (shown in Figure 1). The SCB

fracture tests were conducted under mode I loading at intermediate temperatures (5°C, 15°C, and 25°C) and loading rates (1, 5, 10 mm/min). A total of 88 SCB specimens were tested, highlighting trends in fracture resistance and mechanical properties of asphalt mixtures under controlled conditions. Results showed that loading rate, air void content and aggregate type significantly can impact the fracture energy and cracking behavior.

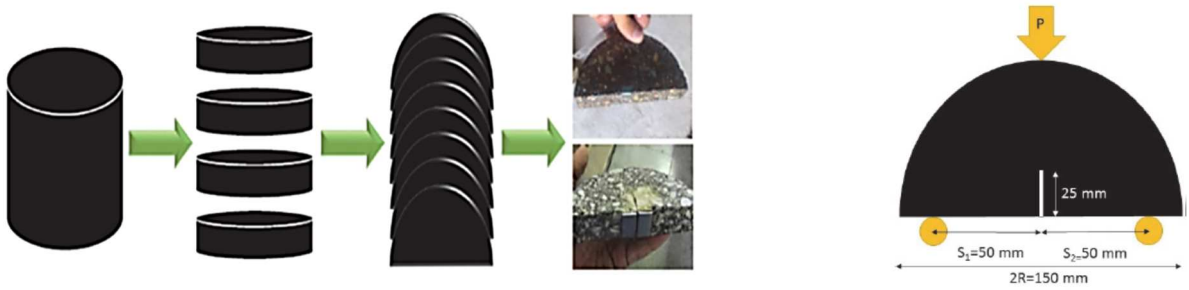

Fig. 1 - SCB sample preparation form the HMA gyratory compacted cylinders.

This study utilized a three-layer neural network topology to predict target variables with simplicity and efficiency. The Multilayer Perceptron (MLP) model was designed with an optimal number of neurons to prevent over fitting, adhering to best practices for small datasets. For an MLP with n input variables and m neurons in the hidden layer, the predicted output $\hat{y}$ can be expressed as:

$$\hat{y} = f\left(\sum_{j=1}^{m} w_j g\left(\sum_{i=1}^{n} w_{ji} x_i + b_j\right) + b_0\right)$$

Data was split into 80% for training and 20% for testing to balance learning and generalization. The network employed hyperbolic tangent sigmoid functions in the hidden layer and a linear activation function in the output layer, enabling accurate gradient flow and reliable predictions. Bayesian regression back propagation was used to train the network, combining back propagation with Bayesian inference to optimize weights while quantifying uncertainty. By updating a probability distribution over weights, the model accounted for data variability, enhancing robustness and predictive accuracy. This integration of Bayesian inference improved generalization and allowed the model to effectively capture complex, nonlinear relationships, as demonstrated in Figure 2.

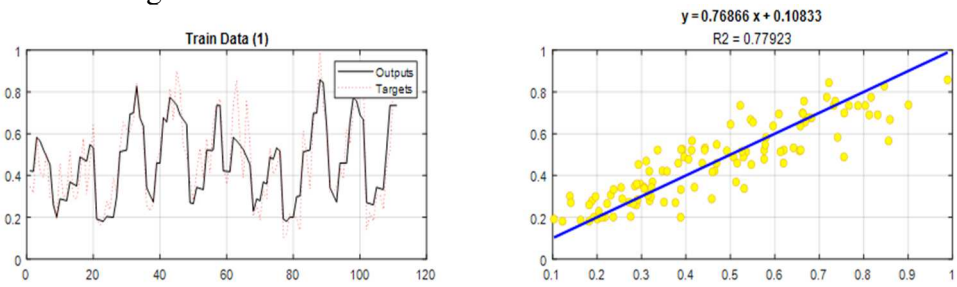

Fig. 2 - Neural network train.

REFERENCES

[1] Majidifard, H., et al. Deep machine learning approach to develop a new asphalt pavement condition index. Construction and building materials, 2020, 247, p.118513.

[2] Ghanizadeh, A.R., et al. A formulation for asphalt concrete air void during service life by adopting a hybrid evolutionary polynomial regression and multi-gene genetic programming. Scientific Reports, 2024, 14, p.13254.

[3] Jalota, Samrity, and Manju Suthar. "Modelling of Marshall stability of polypropylene fibre reinforced asphalt concrete using support vector machine and artificial neural network." International Journal of Transportation Science and Technology 2024, 14, p.28.

Proceedings IRF2025: 8th International Conference on Integrity-Reliability-Failure
In Engineering, Materials, Manufacturing and Biomechanics. Porto 15-18 July 2025
DOI: https://doi.org/10.24840/978-972-752-323-8

PAPER REF: 22445

PLASMA INDUCED HYDROPHILIC MODIFICATION ON ELECTROPLATED SILVER SURFACE IMPROVING SILVER SINTER QUALITY FOR POWER SEMICONDUCTOR DIE ATTACH

Min-Su Kim[1(*)], Minju Yu[1,2]

[1]Advanced Packaging Integration Center, Korea Institute of Industrial Technology, Incheon, Republic of Korea
[2]Department of Materials Science and Engineering, Inha University, Incheon, Republic of Korea
[(*)]*Email:* mskim927@kitech.re.kr

ABSTRACT

The effect of pre-cleaning methods (ethanol ultrasonic cleaning and Ar/O_2 plasma treatment) on Ag sintered joints was investigated. It emphasizes the significance of pre-cleaning in the bonding process and offers new approaches to creating more uniform and durable Ag sintered joints, comparing the effects with conventional ultrasonic cleaning. This method proves effective for applications requiring higher bonding quality. The Ar/O_2 plasma-treated samples exhibited the highest bonding strength, interfacial connection ratio, necking thickness, and failure energy, while showing the lowest values in porosity. These improvements are attributed to the uniformity, enhanced thermal conductivity, and the presence of hydroxyl groups formed on the surface.

Keywords: Ag sinter, die attach, wide bandgap, plasma treatment, hydrophilic treatment.

INTRODUCTION

Wide bandgap (WBG) power semiconductors, such as SiC and GaN, are attracting attention as next-generation power semiconductors as interest in electric vehicles and autonomous vehicles, and renewable energy increases. Power semiconductor packaging processes, including die attach, wire bonding, molding, are crucial process for ensuring the performance and reliability of power module [1]. Among these, we focused on the Ag sinter die attach process to maximize the performance of power module. Here, we used Ar/O_2 plasma pre-cleaning as a method to uniformly remove contaminants without affecting the coating layer (Figure 1). It was confirmed that the shear strength of Ag sintered joint increased by the plasma pre-cleaning by the comparison with the non-cleaned sample. The surface characterization tests, including wettability, photoelectron spectroscopy, and atomic force microscopy, were investigated to reveal the role of pre-cleaning of Ag plated surface on the Ag sintering behavior.

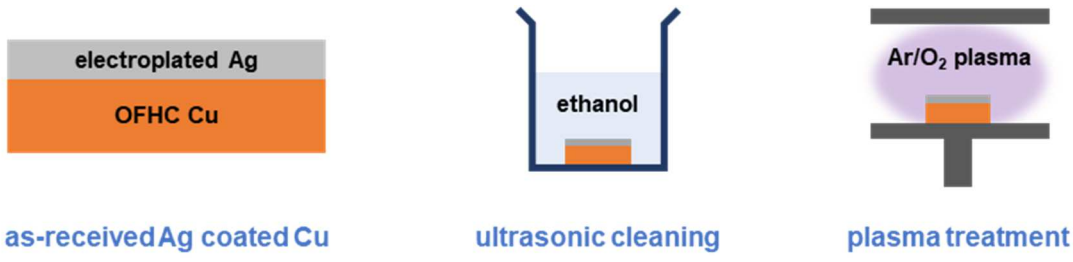

Fig. 1 - Surface cleaning methods for Ag sintering: non-cleaned, ultrasonic cleaning, and plasma treatment.

RESULTS AND CONCLUSIONS

The bonding strength of the non-cleaned sample was 35.9 MPa. After ethanol ultrasonic cleaning, the bonding strength increased to 42.57 MPa (18.58% improvement), and with both ethanol and Ar/O_2 plasma cleaning, it reached 49.38 MPa, a further 16% improvement. X-ray analysis showed no significant difference in porosity across the pre-cleaning methods. The non-cleaned sample exhibited minimal necking, while ethanol and Ar/O_2 plasma cleaning increased the neck thickness and bonding area, as shown in Figure 2.

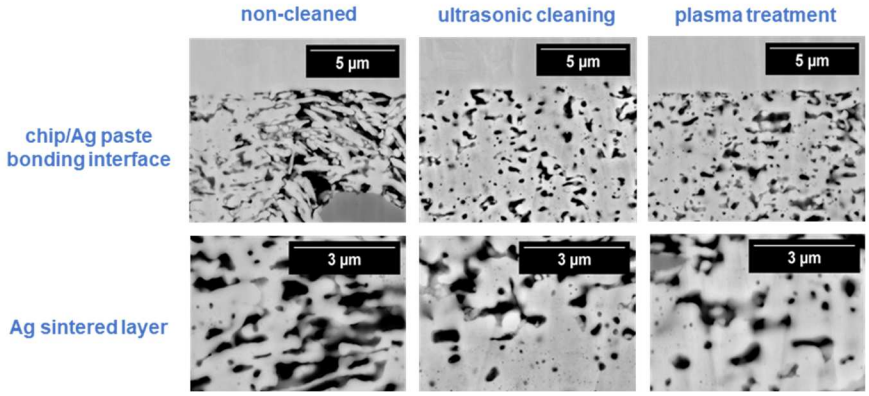

Fig. 2 - SEM micrograph of Ag sinter bonding interface and Ag sinter layer for non-cleaned, ultrasonic cleaned and plasma treated samples.

Figure 3 shows core-level XPS analysis results for the surface of substrate according to the pre-cleaning methods. This result revealed that both ultrasonic and plasma cleaning are effective in removing organic contaminants. After Ar/O_2 plasma cleaning, a large amount of hydroxyl groups (-OH) were formed. These hydroxyl functional groups increase the surface energy, polarizing the surface and strengthening the interaction with the solvent. As a result, the hydrophilicity increases, allowing the solvent to spread better over the surface.

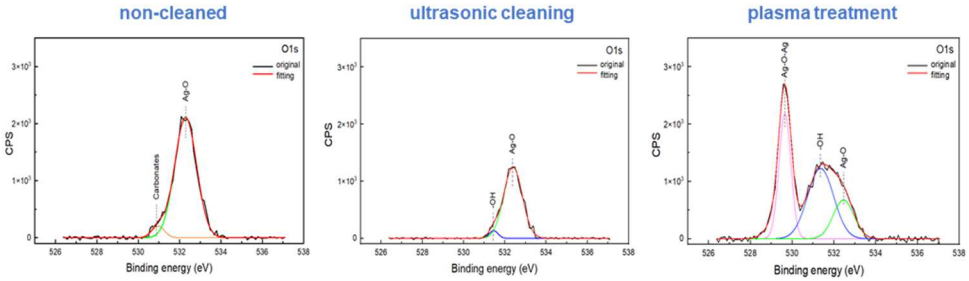

Fig. 3 - SEM micrograph of Ag sinter bonding interface and Ag sinter layer for non-cleaned, ultrasonic cleaned and plasma treated samples.

In conclusion, the combination of ethanol ultrasonic cleaning and Ar/O_2 plasma treatment improve surface wettability of electroplated Ag surface significantly, resulting in improving shear strength of Ag sintered joint

REFERENCES

[1] Zhang H, Wang W, Bai H, Zou G, Liu L, Peng P, Guo W, Microstructural and mechanical evolution of silver sintering die attach for SiC power devices during high temperature applications, Journal of Alloys and Compounds, 2019, 774, pp. 487-494.

[2] Aydemir C, Altay B, Akyol M. Surface analysis of polymer films for wettability and ink adhesion, Color Research & Application, 2021, 46, pp. 489-499.

Proceedings IRF2025: 8th International Conference on Integrity-Reliability-Failure
In Engineering, Materials, Manufacturing and Biomechanics. Porto 15-18 July 2025
DOI: https://doi.org/10.24840/978-972-752-323-8

PAPER REF: 22593

AN ANALYTICAL CORRELATION TO OPTIMIZE THE RESULTS OF FLATTENED BRAZILIAN TEST

R. Gutiérrez-Moizant[1], D.J. Guerrero-Miguel[2], M. Ramírez-Berasategui[1(*)]

[1]Mechanical Engineering Department, Universidad Carlos III de Madrid, Leganés, Madrid 28911, Spain
[2]Construction and Manufacturing Engineering Department, Universidad de Oviedo, Gijón, Spain
[(*)]*Email:* mrami@ing.uc3m.es

ABSTRACT

The Brazilian test is broadly used to determine the indirect tensile strength of most brittle materials, such as rocks or concrete. The effectiveness of this method remains under debate as numerous investigations have concluded that specimen's failure may occur in the vicinity of the contact with the compressing platens. To reduce the stress concentration, a flattened Brazilian splitting test was proposed, by machining two parallel flat ends on the disc, which are subsequently loaded using flat plates. However, several researchers have observed that the stress concentration problem still persists and that the final contact angle between the flattened disc and the horizontal plates is a key point for the success of the test. Under these circumstances, the objective of this work is to analyse the factors of influence, notably the potential lack of parallelism of the flattened faces due to machining imperfections. To achieve this, a set of finite element method (FEM) simulations will be conducted to derive significant results regarding the improvement of predicted Griffith's theoretical equivalent stress by means of an analytical expression.

Keywords: Flattened Brazilian disc, indirect tensile strength, contact stress distribution.

INTRODUCTION

In the fields of civil and mining engineering projects, the accuracy and reliability of the experimental test providing the mechanical properties of the rocks present in the project site is one of the key issues. Among the several testing methods, the Brazilian testing methods remains one of the most popular ones, due to its relatively easy preparation (Yan et al. 2021). However, the conventional Brazilian test has been criticized due to an unwanted high stress concentration in the contact area between the disc and the compression plates (García et al. 2017). One of the proposed alternatives is the flattened Brazilian splitting test shown in Figure 1. (Wang et al. 2004; Huang et al. 2015). According to previous researchers, the factors that can influence the success of this indirect test include the contact angle 2α and the parallelism between the flattened surfaces (Wang et al. 2004; Huang et al. 2015; Lin et al. 2016; Pourya and Mehrnoosh 2016; García et al. 2017). Hence, a detailed analysis of these variables has been conducted in the present study.

Several authors (Wang et al. 2004; Lin et al. 2016; Huang et al. 2015) have already stated that the stress condition for the initiation of the crack in a flattened disc is:

$$3\sigma_\theta + \sigma_r < 0 \tag{1}$$

Being σ_θ and σ_r the tangential and radial stresses, respectively. Due to the symmetry of the test, the vertical diameter is a principal direction; hence, no shear stresses are induced along it.

Therefore, there exists a direct relationship between cartesian and polar coordinates along the vertical diameter, where $\sigma_x = \sigma_\theta$ and $\sigma_y = \sigma_r$. Consequently, the equivalent Griffith stress can be calculated using the following equation:

$$\sigma_G = -\frac{(\sigma_x - \sigma_y)^2}{8(\sigma_x + \sigma_y)} \tag{2}$$

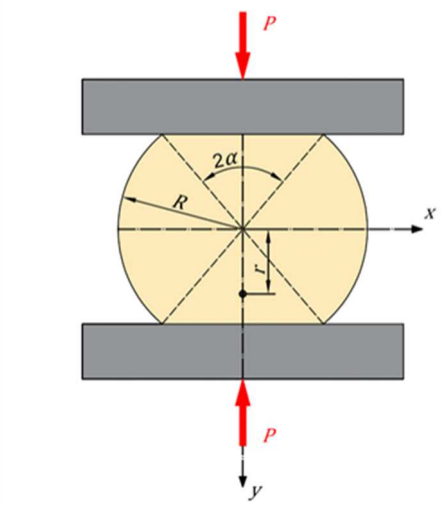

Fig. 1 - Flattened Brazilian splitting test.

The solution for the flattened Brazilian disc subjected to uniformly distributed stress along the contact was developed by Huang et al. (2015). According to this author, the maximum tensile stress region is located along the vertical diameter and, thereby identifying it as the likely initiation region for failure. Due to the symmetry of the test, shear stresses are absent at the vertical radius. Consequently, the maximum and minimum principal stresses are directly correlated with σ_x andσ_y , respectively. Hence, the stress field along the vertical radius of the specimen due to uniformly distributed stress along the contact is expressed as:

$$\sigma_x = \frac{P\cos\alpha}{\pi R t} + \frac{P}{\pi R t \sin\alpha}\left(\frac{B_1}{A_1} + C_1 + \frac{B_3}{A_3} + C_3\right) \tag{3}$$

$$\sigma_y = \frac{P\cos\alpha}{\pi R t} - \frac{P}{\pi R t \sin\alpha}\left(\frac{B_1}{A_1} - C_1 + \frac{B_3}{A_3} - C_3\right) \tag{4}$$

Where P is the applied load, α is the semi-loading angle, R is the radius of the flattened disc, t is the thickness of the disc and r is the distance between any point of the vertical radius and the centre of the disc.:

$$\begin{aligned} A_1 &= (R\cos\alpha + r)^2 + (R\sin\alpha)^2 \\ A_3 &= (R\cos\alpha - r)^2 + (R\sin\alpha)^2 \\ B_1 &= (R\cos\alpha + r)R\sin\alpha \\ B_3 &= (R\cos\alpha - r)R\sin\alpha \\ C_1 &= -\arctan\left(R\sin\alpha\,/(R\cos\alpha + r)\right) \\ C_3 &= -\arctan\left(R\sin\alpha\,/(R\cos\alpha - r)\right) \end{aligned} \tag{5}$$

INFLUENCE OF THE TOLERANCE OF PARALLELISM BETWEEN THE FLATTENED FACES

One of the first issues of the present work is to confirm that the optimal contact angle is $2\alpha = 30°$. To do so, a series of simulations were conducted using the material properties listed in Table 1, with contact angles of 20º, 25º and 30º. In this case, a three-dimensional model was developed with Abaqus Software to precisely replicate the experimental test. The mesh size was set to 1 mm for the disc and 3 mm for the platens, both of which were meshed using 8-node linear brick elements. Notably, these mesh sizes have been previously and successfully employed by various authors (Lin et al., 2015, 2016; Komurlu et al., 2016) to model Brazilian tests. In all three-dimensional models, a representative friction factor of μ=0.5 was applied at the interface between the platens and the flattened disc (Gorst et al et al., 2003). A uniform pressure was applied to the top platen, while the bottom platen was constrained to replicate the actual test conditions.

Table 1 - Geometrical and mechanical properties for the 2D numerical models.

Elastic Body	Diameter D (mm)	Thickness t (mm)	Young's Modulus E (GPa)	Poisson's coefficient $\nu(\mu\epsilon/\mu\epsilon)$
Specimen	53.60	27	30	0.31
Platen	30.00	30.00	210	0.33

Figure 2 shows the map of the equivalent Griffith stress for ideal three-dimensional models that is, with perfect parallelism. The stresses have been obtained directly from the FEM software, by means of a new field output including equation (2). The maximum equivalent stress in red, is located at the centre of the disc. However, it is possible to visualize areas of stress concentration respectively and yellow at the edge of the flattened faces that decrease as the contact angle increases. These results coincide with those observed by (Pourya and Mehrnoosh 2016), who recommend the loading arc configuration of 30° to reduce the risk of unwanted cracks at the flattened ends of the disc.

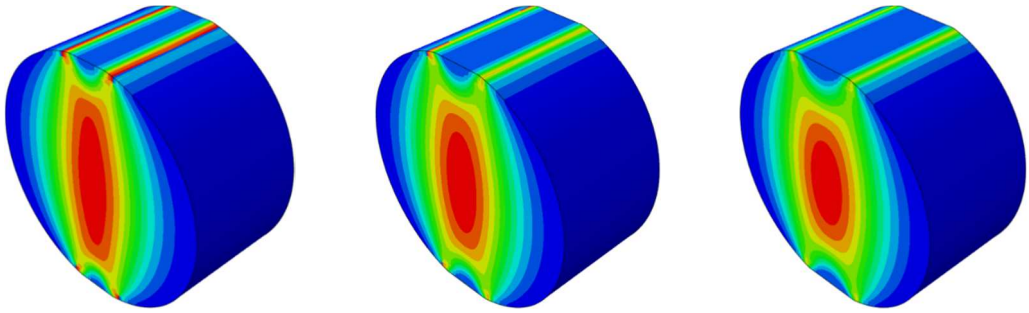

2α = 20° 2α = 25° 2α = 30°

Fig. 2 - Distribution map of the Griffith´s equivalent stress for the contact angles analysed.

Based on these results, it can be confirmed that the contact angle of 30° is the optimal configuration in terms of the central crack initiation, provided that the flattened faces have no parallelism deviation.

The machining process of the flattened Brazilian disc is difficult in terms of the parallelism of the flat surfaces. It is thus necessary to quantify its influence in the achievement of the central crack initiation. Thus, this section aims to quantify how the lack of parallelism can affect the failure of the disc. The analysis has been performed starting with the FEM 3D model of 2α = 30°, but assuming that the bottom flat face is parallel to the horizontal plane, while the top face

is slightly inclined. The lack of parallelism is expressed in terms of the difference in high between the edges of the top surface.

Figure 3 presents the front view of the four 3D models with tolerances ranging from 0.03 mm to 0.10 mm. The equivalent stress according to Equation 2 is represented, indicating in grey the possible zone of failure. The colour scale then goes from red to blue to indicate the stress in decreasing order.

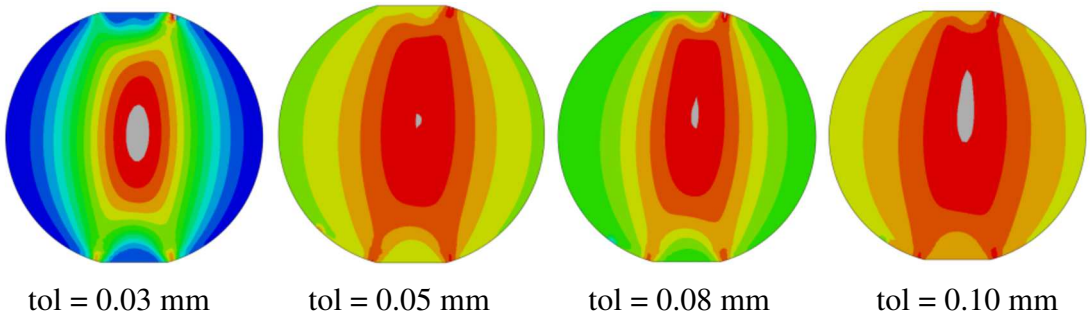

Fig. 3 - Distribution of the Griffith equivalent stress for the flattened disc of 30° with different tolerance of parallelism of the flattened faces.

The proposed tolerances collected in Figure 3 are close in value and may be hard to achieve during the preparation process, but they prove how small differences in parallelism deviate the initiation of failure from the centre, increasing the possibility of premature failure in the vicinity of the contact. Particularly, Figure 3 illustrates that as the tolerance of parallelism increases, the probability of unexpected cracks at the flattened ends of the disc also increases. According to the simulation results, the central and unique crack is guaranteed when the tolerance of parallelism is lower than 0.05 millimetres. For higher tolerances, the crack zone enlarges and tends to be oriented towards the edge with higher stress concentration. In a less strict sense, the test could be considered valid up to a tolerance of 0.10 mm, as the differences between the central equivalent stress and the maximum stress is less than 1.1%.

RESULTS AND CONCLUSIONS

The four simulations performed also allow to determine the real contact angle at the instant of the crack initiation. Table 5 shows that the increase in the lack of parallelism generates a logical decrease in the final contact angle. If the two magnitudes (tolerance of parallelism and final contact angle) are represented for the four simulations in Figure 4, there is evidence of a strong linear relation between them.

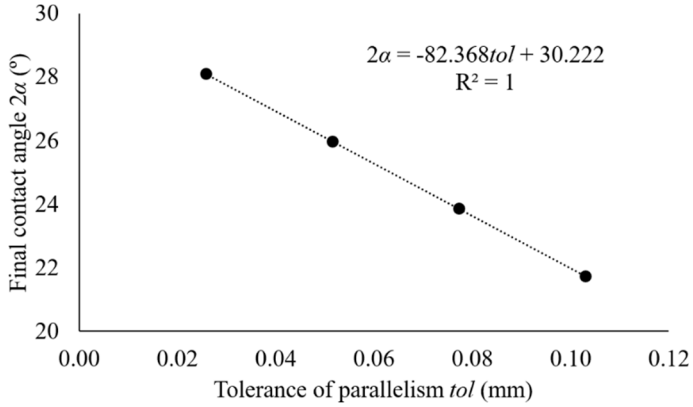

Fig. 4 - Evolution of the final contact angle with respect to the tolerance of parallelism.

The linear regression of Figure 4 could be taken into account when a more accurate result wants to be found as the lack of parallelism of the flat surfaces will be always present in real specimen. Thus, before performing the test, the tolerance of parallelism can be quantified and by using an equation like equation 6 (the one defined by specimen dimensions), a more realistic contact angle can be considered in the calculus of the equivalent Griffith stress, as the expected contact angle would be altered during the test, leading to the maximum α value corrected by equation 6:

$$2\alpha = -82.368tol + 30.222 \quad (6)$$

In the case of the disc and the tolerances chosen in these simulations, we have calculated the relative error of the equivalent Griffith stress considering the theoretical angle of 30º and the final contact angle found in each simulation. Table 5 shows the differences between the FEM results and the theoretical ones for these two cases.

As it can be inferred from Table 5, the lack of parallelism between the flattened faces results in an increased discrepancy between Griffith's theoretical results (2α = 30°) and the numerical ones. If the contact angle resulting from Equation (6) is considered, the analytical predictions are improved, since the larger percentage of error between the equivalent stress corresponding to the new analytical expressions and the maximum equivalent stress of the numerical models do not exceed 3%.

Table 5 - Comparison between the FEM models for 2α=30° and considering parallelism deviations with the theoretical model proposed for both cases, with and without tolerance correction.

Tolerance of parallelism (mm)	Final load P (N)	2α from FEM simulation (°)	$\%Error = \frac{\lvert\sigma_G - \sigma_{G_FEM}\rvert}{\sigma_{G\ FEM}} 100$	
			For $2\alpha = 30°$	For corrected 2α with Eq.(6)
0.03	12410	28.10	4.3	2.2
0.05	12052	25.97	7.0	2.9
0.08	11884	23.88	8.3	2.1
0.10	11815	21.73	8.9	1.1

According to these findings, it can be said that lacks of parallelism higher than 0,05 mm compromise the success of the flattened Brazilian test as there is a high probability of failure in the center but also in the contact with the plates. The preparation of the testing specimens is therefore crucial for the reliability of the results.

In this work, it is proven that the analysis and quantification of the discrepancies between the ideal and real specimens under test can be carried out in numerical models so that the results are then considered to improve the accuracy of the theoretical model. This methodology has been applied with success in the case of the Brazilian test with flattened faces, where the unavoidable lack of parallelism of the faces can be well studied in numerical models to improve the result of the analytical equivalent Griffith stress.

ACKNOWLEDGMENTS

This research was funded by the Ministry of Science and Innovation of Spain through Grant MCINN-23-PID2022-142015OB-I00 funded by MCIN/AEI/10.13039/501100011033 and by "ERDF A way of making Europe".

REFERENCES

[1] García VJ, Márquez CO, Zúñiga-Suárez AR, et al (2017) Brazilian Test of Concrete Specimens Subjected to Different Loading Geometries: Review and New Insights. Int J Concr Struct Mater 11: pp. 343-363. https://doi.org/10.1007/s40069-017-0194-7.

[2] Gorst N., Williamson S., Pallett P., Clark L.Friction in temporary works. Birmingham,UK: Health & Safety Executive; 2003.

[3] Huang YG, Wang LG, Lu YL, et al (2015) Semi-analytical and Numerical Studies on the Flattened Brazilian Splitting Test Used for Measuring the Indirect Tensile Strength of Rocks. Rock Mech Rock Eng 48:1849–1866. https://doi.org/10.1007/s00603-014-0676-8.

[4] Komurlu E, Kesimal A, Demir S (2016) Experimental and numerical study on determination of indirect (splitting) tensile strength of rocks under various load apparatus. Canadian Geotechnical Journal 53: pp. 360-372. https://doi.org/10.1139/cgj-2014-0356.

[5] Lin H, Xiong W, Yan Q (2016) Modified formula for the tensile strength as obtained by the flattened Brazilian disk test. Rock Mech Rock Eng 49: pp. 1579-1586. https://doi.org/10.1007/s00603-015-0785-z.

[6] Lin H, Xiong W, Xiong Z, Gong F (2015) Three-dimensional effects in a flattened Brazilian disk test. International Journal of Rock Mechanics and Mining Sciences 74: pp. 10-14. https://doi.org/10.1016/j.ijrmms.2014.11.006.

[7] Pourya K, Mehrnoosh H (2016) Numerical and experimental studies on the effect of loading angle on the validity of flattened Brazilian disc test. Journal of Geology and Mining Research 8: pp. 1-12. https://doi.org/10.5897/jgmr15.0243.

[8] Wang QZ, Jia XM, Kou SQ, et al (2004) The flattened Brazilian disc specimen used for testing elastic modulus, tensile strength and fracture toughness of brittle rocks: Analytical and numerical results. International Journal of Rock Mechanics and Mining Sciences 41: pp. 245-253.

[9] Yan, Z., Dai, F., Liu, Y., Wei, M., You, W. (2021). New insights into the fracture mechanism of flattened Brazilian disc specimen using digital image correlation. Engineering Fracture Mechanics, 252, 107810.

Proceedings IRF2025: 8th International Conference on Integrity-Reliability-Failure
In Engineering, Materials, Manufacturing and Biomechanics. Porto 15-18 July 2025
DOI: https://doi.org/10.24840/978-972-752-323-8

PAPER REF: 22597

POST-FATIGUE TENSILE BEHAVIOR OF SINGLE LAP JOINTS WITH GRAPHENE NANO PARTICLE REINFORCED ADHESIVE

Güntaç Bali, Tolga Topkaya(*)

Department of Mechanical Engineering, Faculty of Engineering, Batman University, Batman Turkiye
(*)*Email:* tolga.topkaya@batman.edu.tr

ABSTRACT

Adhesive joints are preferred for joining the materials in low weight and high strength applications. Adhesive joints are exposed not only to static loads but also to dynamic loads such as fatigue and impact due to the effects of the structures they are used in. We investigate the fatigue and post-fatigue behaviours of single-lap joints experimentally. For improving the strength of adhesive, graphene nanoparticle was used as a modifier. Test samples were prepared with neat adhesive, 0.25 wt.% graphene used, 0.5 wt.% graphene used, and 1 wt.% graphene used adhesives. Tensile and fatigue strength of samples increased with adding graphene nanoparticle to the adhesive. Increasing the number of cycles applied before tensile tests, decreased the post-fatigue tensile strength of samples for all graphene contents.

Keywords: Adhesive joint, fatigue testing, graphene, post-fatigue.

INTRODUCTION

Carbon-based materials such as graphene, fullerene and carbon nano tube can be used for reinforcing the adhesive materials (Saraç et al., 2019), (Bali and Topkaya, 2023). Nanoparticle reinforcements can improve mechanical properties of adhesive joints with the aid of better adhesion to the adherends (Demir et al., 2022). Daggumati et al. reported that stiffness of the test samples increased by 7-8% with the application of fatigue loading (Daggumati et al., 2013). In this study, we investigate the post-fatigue tensile behavior of single lap joints with graphene nanoparticle- reinforced adhesive. Post-fatigue tensile tests were conducted following the tensile and fatigue tests of the samples. For reinforcing the adhesive material 3 different amount of GNP was used in addition to neat samples.

RESULTS AND CONCLUSIONS

Tensile test results showed that reinforcing adhesive with GNP increased the sample strength and increasing the GNP content increased the sample strength. Failure load for neat adhesive used samples was observed as 15.516 kN. While failure load was 16.461 kN for samples with 0.25 wt% GNP containing adhesive, it was determined as 16.539 kN and 16.786 kN for samples with 0.5 wt% GNP and 1 wt% GNP containing adhesives, respectively.

After determining the tensile strengths of samples, tensile- tensile fatigue tests were carried out for samples. Number of fatigue cycles to failure is given in Figure 1 as a function of load ratio (Fmax/Fult). Using GNP as a reinforcing material improved fatigue strength of samples. Maximum tensile fatigue strength observed on 0.5 wt.% GNP modified samples. Increasing the GNP content after 0.5 wt.% decreased the fatigue strength of samples. But using 1 wt.% GNP still has higher fatigue strength than neat adhesive samples for all load levels.

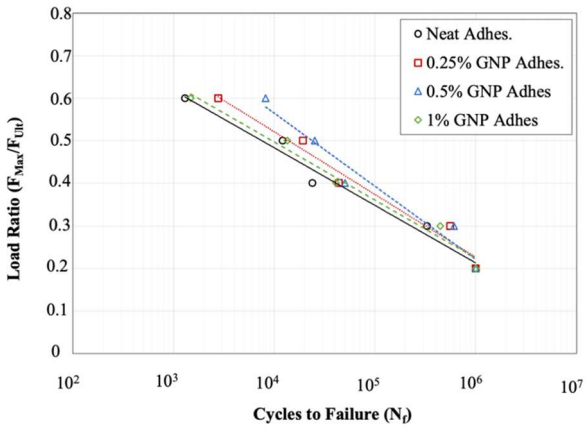

Fig. 1 - Fatigue test results for different GNP content.

For neat adhesive-used samples, the tensile failure load is 15.516 kN without fatigue loading. Applying fatigue load to the samples decreased the sample strength. Tensile failure load determined as 14.740 kN, 11.792 kN, and 10.254 kN after Nf=50,000 cycles, Nf=100,000 cycles, and Nf=200,000 cycles, respectively. Applying 50,000 cycles of fatigue loading decreased the tensile failure load from 16.461 kN to 15.333 kN for 0.25 wt.% GNP samples. Tensile failure load continued to decrease with increasing fatigue cycles and tensile failure loads were determined as 12.784 kN and 8714.1 kN for Nf=100,000 cycles, and Nf=200,000 cycles, respectively. A minimum decrease in tensile failure load was observed for 0.5 wt.% GNP samples for Nf=50,000 cycles compared to without fatigue-loaded samples. After Nf=50,000 cycles fatigue loading tensile failure load determined as 16.527 kN, while tensile failure load was 16.539 kN for without fatigue- loaded sample. A minimum tensile failure load was determined as 8.581 kN for Nf=200,000 cycles sample. tensile failure load was 12.694 kN for Nf=100,000 cycles sample. Tensile failure load determined as 16.786 kN, 16.609 kN, 12.758 kN, and 8548.4 kN after without fatigue- loaded, Nf=50,000 cycles, Nf=100,000 cycles, and Nf=200,000 cycles samples, respectively.

Following conclusions can be made according to limited study results:

- Maximum fatigue strength observed in 0.5 wt.% GNP samples for all load levels.
- Applying fatigue cycles to the samples decreased the tensile strength of the samples.
- Post-fatigue tensile strength decreased with increasing the fatigue cycles.

REFERENCES

[1] Saraç İ, Adin H, and Temiz Ş Investigation of the effect of use of Nano-Al2O3, Nano-TiO2 and Nano-SiO2 powders on strength of single lap joints bonded with epoxy adhesive, Composites Part B Engineering, 2019, 166, pp.472-482.

[2] Güntaç G and Topkaya T, Effect of graphene nano-particle reinforcement on the fatigue behavior of adhesively bonded single lap joints, International Journal of Adhesion and Adhesives, 2023, 120, p.103279.

[3] Demir K, Gavgali E, Yetim A F, Akpinar S, The effects of nanostructure additive on fracture strength in adhesively bonded joints subjected to fully reversed four-point bending fatigue load," International Journal of Adhesion and Adhesives, 2022, 110, p.102943.

[4] Daggumati S, Baere I D, Paepegem W V, Degrieck J, Xu J, Lomov S V, Verpoest I, Fatigue and post-fatigue stress–strain analysis of a 5-harness satin weave carbon fibre reinforced composite, Composites Science and Technology, 2013, 74, pp.20-27.

Proceedings IRF2025: 8th International Conference on Integrity-Reliability-Failure
In Engineering, Materials, Manufacturing and Biomechanics. Porto 15-18 July 2025
DOI: https://doi.org/10.24840/978-972-752-323-8

PAPER REF: 22645

A COMBINED FATIGUE INDICATOR PARAMETER (FIP) FOR PREDICTING MICROCRACK PROPAGATION PATH IN POLYCRYSTALLINE NICKEL

Arash Valiollahi, Haiying Huang(*)

Department of Mechanical and Aerospace Engineering, University of Texas at Arlington, Arlington, TX, USA
(*)*Email:* huang@uta.edu

ABSTRACT

Predicting the propagation path of microcracks in polycrystalline metal alloys is extremely challenging because the crack path is sensitive to local microstructure textures. Many fatigue indicator parameters (FIPs) have been proposed for crack nucleation and propagation prediction, but experimental validation is lacking. This study evaluates an FIP that combines effective strain and surface roughness to predict the future propagation path of micro-cracks in polycrystalline nickel. Validating such an FIP could provide a powerful tool for understanding the driving mechanism of fatigue crack nucleation and propagation in polycrystalline metal alloys.

Keywords: Fatigue, microstructure sensitive crack, fatigue indicator parameter, effective strain, surface roughness, crack propagation.

INTRODUCTION

Despite recent progresses in characterization techniques, simulation tools, and data-driven learning, predicting the propagation of microcracks in polycrystalline metals remains an unsolved engineering problem. This is because numerous microstructure features, including microtextures, grain/twin boundaries, pores, inclusions, etc., contribute to crack nucleation and propagation. Many different fatigue indicator parameters (FIPs) have been proposed and studied for predicting crack nucleation and propagation. However, many of these studies were carried out using simulated data and no FIP has been experimentally validated to be capable of predicting the crack nucleation site or microcrack propagation. This work presents an FIP that combines effective plastic strain and surface roughness changes and assesses its performance for microcrack propagation prediction in terms of accuracy, confidence, and consistency.

RESULTS AND CONCLUSIONS

A middle tension (MT) sample with a center notch was fatigue tested using a mechanical tester integrated with a Whitelight Scanning Interferometer (SWLI) surface profiler. The sample was made of pure nickel and its surface was finely polished to an average surface roughness of 12 nm. The vicinity of the notch tips was slightly etched to reveal the grain boundaries, increasing the average surface roughness to 110 nm. For digital image correlation (DIC) analysis, a speckle pattern with an average speckle size of around 1.1 μm was coated on the surface. At selected fatigue intervals, the sample was unloaded, and an area of $1 \times 1\ mm^2$ (0.1 mm behind and 0.9 mm in front of the notch tip) was imaged using the SWLI surface profiler.

The high resolution SWLI surface topography images were processed using an in-house DIC program to measure both the in-plane and out-of-plane surface deformations at sub-grain scale.

The in-plane strains ε_{xx}, ε_{yy}, and γ_{xy} were calculated from the in-plane deformations u_x and u_y. The out of plane normal strain, ε_{zz}, was determined assuming plane stress condition and plastic incompressibility, i.e., $\varepsilon_{zz} = -(\varepsilon_{xx} + \varepsilon_{yy})$, while the out of plane shear strains, ε_{xz} and ε_{yz} were assumed to be zero. The effective plastic strain, which has been considered as an FIP in ductile materials, is calculated from these strain components as

$$\varepsilon_{eff} = \sqrt{\frac{2}{3}(\varepsilon_{m,n} \times \varepsilon_{m,n})} \quad m,n = 1,2,3 \tag{1}$$

The surface roughness change of the sample surface was calculated from the out-of-plane surface topography of fatigued samples before and after fatigue.

To calculate the FIPs, the imaged area was divided into 23 columns and 21 rows with a total of 483 subsets, each contains 50 pixels. Three FIPs, i.e., the effective plastic strain FIP_{ε}, surface roughness FIP_{Ra}, and combined FIP_c, were calculated for each subset to construct the FIP maps. FIP_c was calculated by multiplying FIP_{Ra} and FIP_c normalized with their respective maximum value.

To predict the future crack path in front of a crack tip, the most critical subsets in each column were determined using the "confidence threshold" criterion. First, the histogram of the subset intensity in each column is fit to the lognormal fit. The subsets whose damage index above a confidence threshold are then identified. These subsets provide an envelope within which the crack is predicted to pass through, as shown in Figure 1. At 80 percentile confidence threshold, all three FIPs predicted the future crack path reasonably well. Increasing the confidence threshold to 95 percentile leads to disconnected crack paths for FIP_{ε} and FIP_{Ra}. In contrast, FIP_c consistently predicted the crack path well, including the turns along the tortuous crack path. As such, this work demonstrated that an FIP combining the effective strain and the surface roughness is more accurate and reliable in predicting the propagation path of microstructure sensitive cracks.

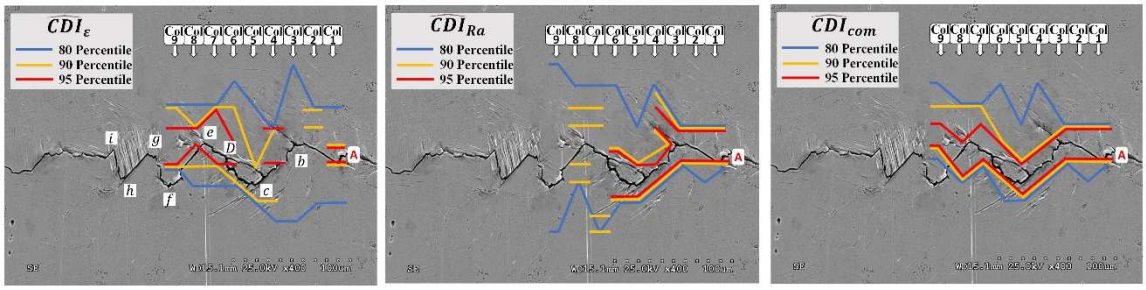

Fig. 1 - the predicted crack path based on (a) FIP_{ε} (b) FIP_{Ra} and (c) FIP_c with 80, 90 and 95-percentile confidence thresholds when the crack was arrested at 'A'.

REFERENCES

[1] Fathi Sola, J., Kelton, R., Meletis, E.I., Huang, H. A surface roughness based damage index for predicting future propagation path of microstructure-sensitive crack in pure nickel. International Journal of Fatigue, 2019, 122, pp. 164-172.

[2] Fathi Sola, J., Kelton, R., Meletis, E.I., Huang, H. Predicting crack initiation site in polycrystalline nickel through surface topography changes. Jnl. of Fatigue, 2019, 124, 70-81.

[3] Valiollahi, A. and Huang, H. Combining in-plane effective strain and out-of-plane surface roughness change for identifying damage accumulation sites in a tensile sample. Experimental Mechanics, 2023, 63, pp. 759-772.

Proceedings IRF2025: 8th International Conference on Integrity-Reliability-Failure
In Engineering, Materials, Manufacturing and Biomechanics. Porto 15-18 July 2025
DOI: https://doi.org/10.24840/978-972-752-323-8

PAPER REF: 22657

DEVELOPMENT OF 16MnCr5 CD STEEL NEW FATIGUE LIMIT PREDICT MODEL

Teresa Morgado[1, 2, 3(*)], Tiago Bancaleiro[3], José Simões[4], Mário Pereira[5], Alexandre Velhinho[6], Suzana Lampreia[2]

[1]UniRE/ISEL, Polytechnic University of Lisbon, Lisboa, Portugal
[2]CINAV/Portuguese Navy School, Portuguese Navy, Alfeite - Almada, Portugal
[3]UNIDEMI/DEMI/FCTNOVA, NOVA University of Lisbon, Caparica, Portugal
[4]ESTS/IPS, Polytechnic University of Setúbal, Setúbal, Portugal
[5]CDRsp/ESTG/IPLeiria, Polytechnic University of Leiria, Leiria, Portugal
[6]CENIMAT-3iN/DEM/FCTNOVA, NOVA University of Lisbon, Caparica, Portugal
[(*)]*Email:* teresa.morgado@isel.pt

ABSTRACT

To prevent fatigue failure of mechanical components is crucial to develop empirical models to predict the fatigue limit of the metallic alloy considering the manufacturing processes, namely intrinsic defects. In this research work, an approach based on Vicker hardness, intrinsic manufacturing defects of casting followed by cold rolling, and experimental fatigue tests were applied to develop a new fatigue limit prediction model for the 16MnCr5 CD steel alloy. This model is crucial for the mechanical design of manganese steel components, such as gears.

Keywords: Fatigue limit, Defects, 16MnCr5 HR, Structural Integrity.

INTRODUCTION

Transmission systems, such as gears, are sensitive to service conditions, such as service loads, lubrication, mounting and manufacturing procedures [1]. The International Organization of Standardization [2] identified fatigue as one of the most frequent failure modes of gears. Fatigue is the most critical failure mode in all industries since it is claimed that about 90% of all failures are related to it [3].

In the last decades, authors such as Murakami et al. [4], Ueno et al. [5], Taijiri et al. [6], Morgado et al. [7, 8], and Alves et al. [9] have studied the structural integrity of mechanical components and developed empirical approaches to predict the fatigue limit (σ_{LF}) of the metallic alloys based on the area of the defects observed or introduced in the material and the Vickers Hardness (HV). The authors [4-9] verified that the results obtained through the different approaches were in agreement with the experimental results, and the slight differences in values can be associated with different metallurgical factors that affect life to the fatigue of the materials.

This work aimed to describe the behaviour of the material DIN 16MnCr5 when subject to a dynamic load and develop a new fatigue limit prediction model. For that purpose, specimens and samples of the material DIN 16MnCr5 HR were used for fatigue tests and to evaluate the Vickers hardness and the intrinsic manufacturing defects. The samples for the hardness tests and manufacturing defects study were prepared following the ASTM E3-95. The Vickers Hardness test was conducted according to ASTM E384-16, and the fatigue specimen dimensions were defined according to ASTM E8/E8M-13a. A sinusoidal wave was used to carry out the fatigue tests, with a stress ratio R= 0.05 and 10 Hz of frequency. The defect analysis was conducted using the reverse optical microscope Leica DMI 5000M that allowed

the swiping extent of the sample using the multistep technology, and the images were post processed using the ImageJ software that allowed the counting and the measurement of the area of the defects observed, this by applying a contrast filter.

RESULTS AND CONCLUSIONS

According to the analysis of the intrinsic manufacturing defects of the DIN 16MnCr5 CD material, namely casting followed by cold rolling, it can be concluded that the large percentage of defect area (49.55%) is in the range of]0.001 to 0.003] mm^2. It was also possible to conclude that the material is homogeneous.

With the microhardness tests, it was concluded that the Vickers hardness of the DIN 16MnCr5 was of $232.2^{+12.9}_{-11.3}$HV 0.5.

The analysis of the lifetime of the material to fatigue, in the number of cycles, N, revealed that the behaviour of the material depends on maximum applied stress, σ_{max} and is described by equation (1).

$$N = e^{\left(\frac{937.45-\sigma_{max}}{35.2}\right)} \quad (1)$$

A new fatigue limit prediction model was developed (equation (2)) for the DIN 16MnCr5 HR based on the Vickers hardness (Hv) and the area of the intrinsic manufacturing defects (area) of casting followed by cold rolling processes.

$$\sigma_{LF} = 1.18\frac{HV+27}{(\sqrt{area})^{1/6}} \quad (2)$$

REFERENCES

[1] Chaari F., Fakhfakh T., Haddar M. Analytical modelling of spur gear tooth crack and influence on gear mesh stiffness. European Journal of Mechanics A/Solids, 2009, vol 28, pp. 461-468.

[2] ISO 10825. Gears. Wear and damage to gear teeth. Terminology. p. 61, 1995.

[3] Olsson E., Olander A., Öberg M. Fatigue of gears in the finite life regime – Experiments and probabilistic modelling. Engineering Failure Analysis, 2016, vol. 62, pp. 276-286.

[4] Murakami Y. Material defects as the basis of fatigue design. International Journal of Fatigue, 2012, vol. 41, pp. 2-10.

[5] Ueno, A., Nishida, M., Miyakawa, S., Yamada, K., Kikuchi, S. ΔK_{th} estimation of aluminum die-casting alloy by means of √ area method. Recent Advances in Structural Integrity Analysis: Proceedings of the International Congress, 2014, (3), pp. 99-103.

[6] Tajiri, A., Nozaki, T., Uematsu, Y., Kakiuchi, T. Fatigue limit prediction of large scale cast aluminum alloy A356. Procedia Materials Science, 2014, 3, pp. 924-929.

[7] Morgado M., Sousa e Brito A., Branco C. M. Influence of casting defects on the fatigue limit of a steel cast railway component. IRF´2009 Integrity Reliability Failure (Challenges and Opportunities), edições INEGI, 2009, 557-558. ISBN: 978-972-8826-22-2.

[8] Morgado T., Paulo D., Velhinho A., Pereira M., Mourão A. Fatigue Life Prediction of 6060 Aluminium Extruded Alloy. Procedia Structural Integrity, 2022, 42, pp. 1545-1551. Elsevier.

[9] Alves J., Morgado T., Galvão I., Pereira A., Pereira M. Development of a Life Prediction Model of Ti-6Al-4V alloy obtained by Additive Manufacturing. Structural Integrity Procedia, 2024, Volume 53, pp. 236-245, Elsevier.

Proceedings IRF2025: 8th International Conference on Integrity-Reliability-Failure
In Engineering, Materials, Manufacturing and Biomechanics. Porto 15-18 July 2025
DOI: https://doi.org/10.24840/978-972-752-323-8

PAPER REF: 22658

DURABILITY STUDY OF ST-52 AND R304 SUBJECT TO CORROSION ENVIRONMENT AND FATIGUE LOADS

Teresa Morgado[1, 2, 3(*)], Pedro Amaral[3], José Simões[4], Mário Pereira[5], Suzana Lampreia[2]

[1]UniRE/ISEL, Polytechnic University of Lisbon, Lisboa, Portugal
[2]CINAV/Portuguese Navy School, Portuguese Navy, Alfeite - Almada, Portugal
[3] UNIDEMI/DEMI/FCTNOVA, NOVA University of Lisbon, Caparica, Portugal
[4]ESTS/IPS, Polytechnic University of Setúbal, Setúbal, Portugal
[5]CDRsp/ESTG/IPLeiria, Polytechnic University of Leiria, Leiria, Portugal
[(*)]*Email:* teresa.morgado@isel.pt

ABSTRACT

The main objective of this work was to obtain the S-N curves for the alloys ST-52 (AISI 1024) and R304 (AISI 304), with and without corrosion and study a fatigue life prediction model to obtain durability under these conditions. The experimental results showed that the corrosion present in the organic waste environment significantly affects both materials, reducing their resistance to fatigue and, consequently, their durability. The predicted model tested showed that durability is lower than the experimental. In conclusion, the fatigue limit stress prediction model showed results that were too conservative, leading to a durability that was quite different from the experimental one. As a result, the prediction model produces premature withdrawals from service and incorrect inspection times.

Keywords: Fatigue limit, Structural durability, S-N curves, Corrosion.

INTRODUCTION

This study allowed to obtain the durability through the experimental procedure and prediction fatigue limit (σ_{LF}) model of Murakami [1]. The Murakami model (equation 1) have as main variable the effect of the defect area (area), the Vickers hardness (HV) and the stress ratio (R) to obtain the value of the fatigue limit stress, with C=1.56 for internal defects and C=1.43 for surface defects and α=0.226+HV×10$^{(-4)}$ in both cases.

$$\sigma_{LF} = C\frac{(HV+120)}{(\sqrt{area})^{1/6}} \times \left(\frac{1-R}{2}\right)^{\alpha} \quad (1)$$

In this work the defect area (area) was obtained by intrinsic manufacturing defects analysis using optical microscopy and the samples analysed followed the ASTM E3-95 in its preparation. Vickers hardness (HV) study followed the ASTM E384-16. For the experimental fatigue limit values were obtained the S-N curves of AISI 1024 and AISI 304 alloys, through fatigue testing, according to the standard ASTM E739. The stress ratio was of R= 0.05. The test specimens were designed according to ASTM-E8/E8M:13a and manufactured through CNC milling and grinding cutting processes. During the testing methodology several specimens of each material were placed in an organic waste solution in order to simulate the predominant corrosion in the solid waste treatment industry and consequently observe its impact on fatigue results.

RESULTS AND CONCLUSIONS

The steel fatigue tests concluded that both undergo a significant reduction in fatigue strength when subjected to an organic waste corrosion environment (Figures 1 and 2). By applying this fatigue strength value in each S-N curve, a correspondent value of durability was obtained to confirm the durability of these alloys applied in organic waste treatment industry studied by Paulo and Morgado [2, 3].

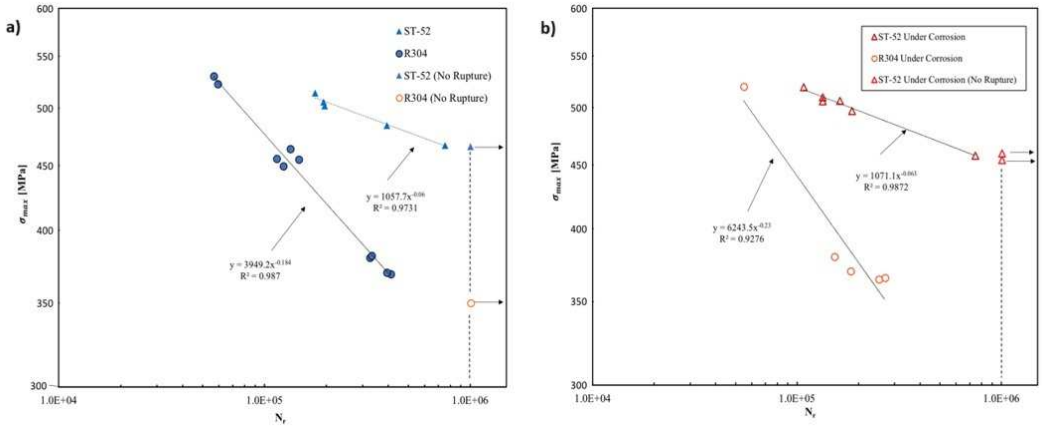

Fig. 1 - ST-52 and R304 S-N curves, submitted to: a) noncorrosive fatigue testing; b) to corrosive fatigue testing.

With the application of the fatigue prediction model (equation 1) it was possible to predict the fatigue limit for each material and compare with the experimental values (Table 1). The R304 alloy presented a highest durability (number of rupture cycles - Nr) than ST-52. These results were confirmed in the presence and absence of organic waste corrosion and verified for both superficial and internal discontinuities. The predicted fatigue limit presents higher values than experimental, for both material and corrosion (Corr.) and non-corrosion (Non corr.) environment.

Table 1 - Fatigue limit stress and respective durability of ST-52 and R304 steel according to the prediction model and experimental results.

Material	**Predict model $Nr_{non\ corr}$ [cycles]**		**Predict model Nr_{corr} [cycles]**		**Predict model σ_{LF}[MPa]**		**Experimental σ_{LF}[MPa]**		**Experimental Nr [cycles]**	
	C=1.43	C=1.56	C=1.43	C=1.56	C=1.43	C=1.56	Non corr.	Corr.	Non Corr.	Corr.
ST-52	26557	10461	19966	8221	574	607	448	461	10^6	
R304	104462	77160	75863	59536	471	498	266	311		

REFERENCES

[1] Murakami Y. Material defects as the basis of fatigue design. International J. Fatigue, vol. 41, pp. 2-10, 2012.

[2] Morgado T., Paulo R., Amaral P., Pereira M., Simoes J., Velhinho J. Durability Study of the AISI 1024HR and AISI 304HR Alloys Applied in the Organic Waste Industry, Revista Mecânica Experimental, APAET, 2020, Vol 32, pp. 1-7. ISSN 1646-7078.

[3] Paulo R., Morgado T. Wear behaviour of AISI 1024, AISI P20 and AISI hot-rolled steels in organic waste treatment industry. Revista Mecânica Experimental, APAET, 2018, Vol 30, pp. 55-60. ISSN: 1646-7078.

Proceedings IRF2025: 8th International Conference on Integrity-Reliability-Failure
In Engineering, Materials, Manufacturing and Biomechanics. Porto 15-18 July 2025
DOI: https://doi.org/10.24840/978-972-752-323-8

PAPER REF: 22714

STUDY ON THE INFLUENCE OF RANDOM VIBRATION LOADING UNSTEADY STATE ON DAMAGE ESTIMATION

Roger Serra[1(*)], Yuzhu Wang[2]

[1]INSA Centre Val de Loire, Laboratoire de Mécanique Gabriel Lamé, Blois, France
[2]China Academy of Railway Sciences, Locomotive Car Research Institute, Beijing, China
[(*)]*Email:* roger.serra@insa-cvl.fr

ABSTRACT

Gaussian vibration and non-Gaussian vibration are usually classified according to the Statistical characteristics of the signal. But another index, unsteady state, will also affect the damage of vibration fatigue. Through a non-stationary index, the damage of non-Gaussian random signals with the same kurtosis is compared, and the relationship between the non-stationary factor and the damage is obtained, Figure 1. The whole research includes generating signals with different kurtosis and different unsteady indexes, and studying their damage.

Keywords: Random vibration fatigue, Non-stationary, Non-Gaussian, Damage, Miner rule, Lifetime.

RESULTS AND CONCLUSION

The research process is realized by virtual test based on the finite element simulations using a series of random signals with the same PSD, but with different kurtosis.

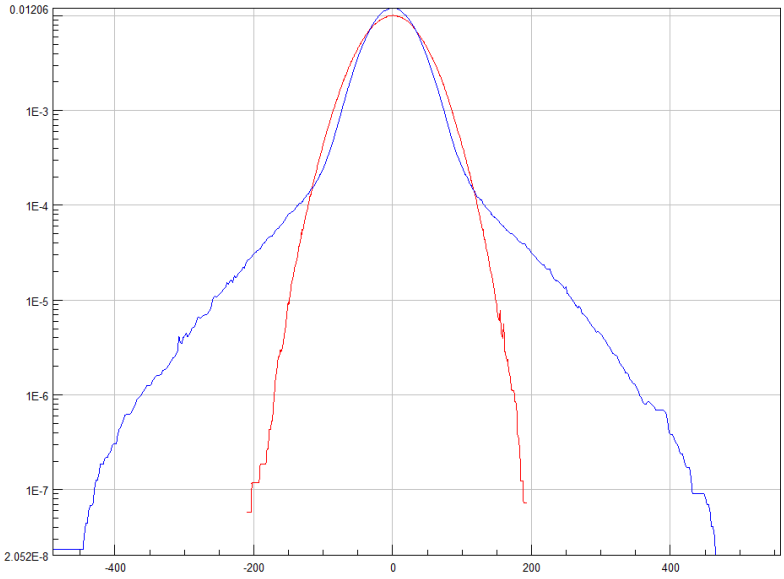

Fig. 1 - Probability Density Function (Log) Red) Gaussian Blue) Non-Gaussian.

The results show that the degree of non-stationary affects the damage, and the farther away from stationary state, the damage will increase accordingly, Figures 2 and 3.

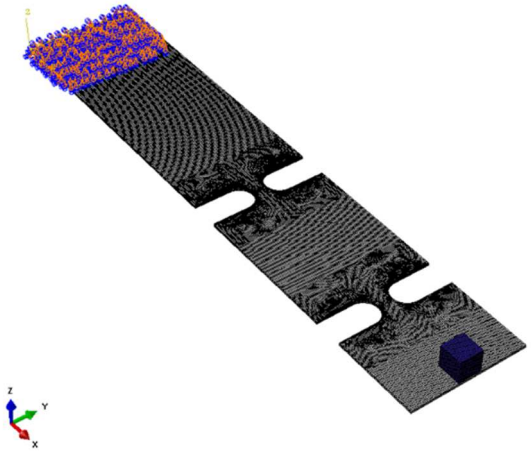

Fig. 2 - FE model of double-notch specimen.

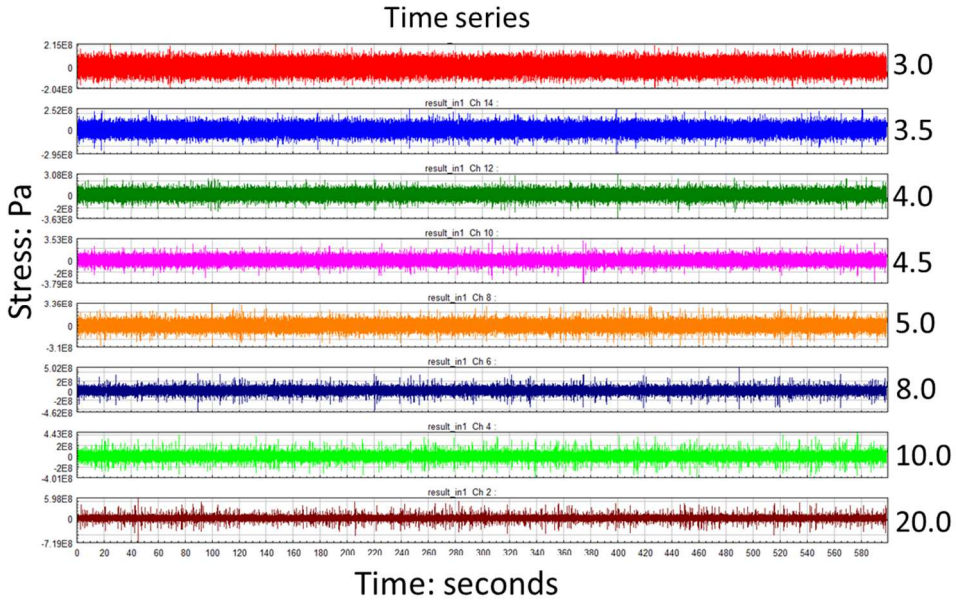

Fig. 3 - FE model of double-notch specimen.

An indicator is introduced to characterize the degree of data discretization within the segmented signal, further reflecting the degree of non-stationarity of the signal. This index better reflects the damage at the same kurtosis compared to the non-stationary index that already exist.

REFERENCES

[1] Yuzhu Wang; Roger Serra. Vibration Fatigue Damage Estimation by New Stress Correction Based on Kurtosis Control of Random Excitation Loadings. Sensors, 2021, 21 (13), pp.4518. ⟨10.3390/s21134518⟩.

[2] Adapted Locati method used for accelerated fatigue test under random vibrations. Yuzhu Wang, Roger Serra,Pierre Argoul. Procedia Structural Integrity, 2019, 19 (19), pp. 674-681. ⟨10.1016/j.prostr.2019.12.073⟩.

Proceedings IRF2025: 8th International Conference on Integrity-Reliability-Failure
In Engineering, Materials, Manufacturing and Biomechanics. Porto 15-18 July 2025
DOI: https://doi.org/10.24840/978-972-752-323-8

PAPER REF: 23480

UNCERTAINTIES IN LOW-CYCLE FATIGUE OF COILED-TUBING

Silvia Corbani[1(*)], Emmanuel A.A.M. Costa[1], Lucas S.K. Camp[2], Daniel A. Castello[2], Thiago G. Ritto[2]

[1]Poli/UFRJ, Dept. of Structures, Federal University of Rio de Janeiro, Rio de Janeiro, Brazil
[2]COPPE/UFRJ, Dept. of Mechanical Engineering, Federal University of Rio de Janeiro, Rio de Janeiro, Brazil
[(*)]*Email:* corbani@poli.ufrj.br

ABSTRACT

The growing need for safer oil drilling processes offshore, with reduced costs, ease of transportation and equipment assembly, requires the implementation of more sophisticated solutions, such as processes applying coiled tubing (CT) wound on reels. The design project requires assessments of fatigue life considering low cycle approaches inasmuch as the deformations attain plastic states. This work assesses the impact of the uncertainties in the material parameters on the service life estimates of a coiled tubing. The deformation cycles are computed using a three-dimensional finite element model, and the low-cycle fatigue analysis considers Ramberg-Osgood and Coffin-Manson models whose computations are performed in a Python-developed code. A reliability analysis is conducted to determine the number of cycles after which periodic monitoring of the structure is required.

Keywords: Coiled tubing, low-cycle fatigue, finite-element, reliability, steel.

INTRODUCTION

The literature provides little information on the material properties of low-cycle fatigue in CTs. Therefore, to understand the importance of each material parameter involved, it becomes important to analyze their uncertainties, focusing on estimating the number of operating cycles that can occur without resulting in failure. Thus, this paper investigates the impact of uncertainties of the CT-110[1] material properties on the low-cycle fatigue life of this structural component.

RESULTS AND CONCLUSIONS

The estimation of low-cycle fatigue life involves modeling the geometry of the coiled tubing (CT) with three-dimensional finite element analysis in the spool and gooseneck sections (see Fig. 1(a)), considering contact, plasticity, and large displacements to obtain the deformation history. In this work, the three-dimensional model is created in Abaqus software for each region of interest (see Figures 1 (b) and (c)). The strains obtained are illustrated in Figures 1 (d) and (e). Based on these strains, the Ramberg-Osgood model (cyclic stress-strain curve) and Coffin-Manson model (strain-life curve), it is possible to calculate fatigue life, N_c. The parameters that are analyzed include the hardening factor, K', Young's modulus, E, fatigue limit of stress and strain, σ_f and ε_f, respectively, and the exponents b and c. The strain hardening exponent, n', is equal to 0.1. The three parameters, K', n' and E, are used in the Ramberg-Osgood model and the four parameters, σ_f, ε_f, b and c, are required in the Coffin-Manson model.

N_c is calculated from a 10^5 randomly samples of material parameters modeled using uniform densities, considering each parameter within ±5%, ±10%, and ±20% around the reference values. Figure 2 (a) presents four realizations of cyclic stress-strain curves. For the failure equation,

$$P_f = N_c - N_f \quad (1)$$

The failure probability is calculated by adopting the desired number of CT usage cycles, N_f, ranging from 1 to 10 operating cycles. The results are shown in Figure 2 (b).

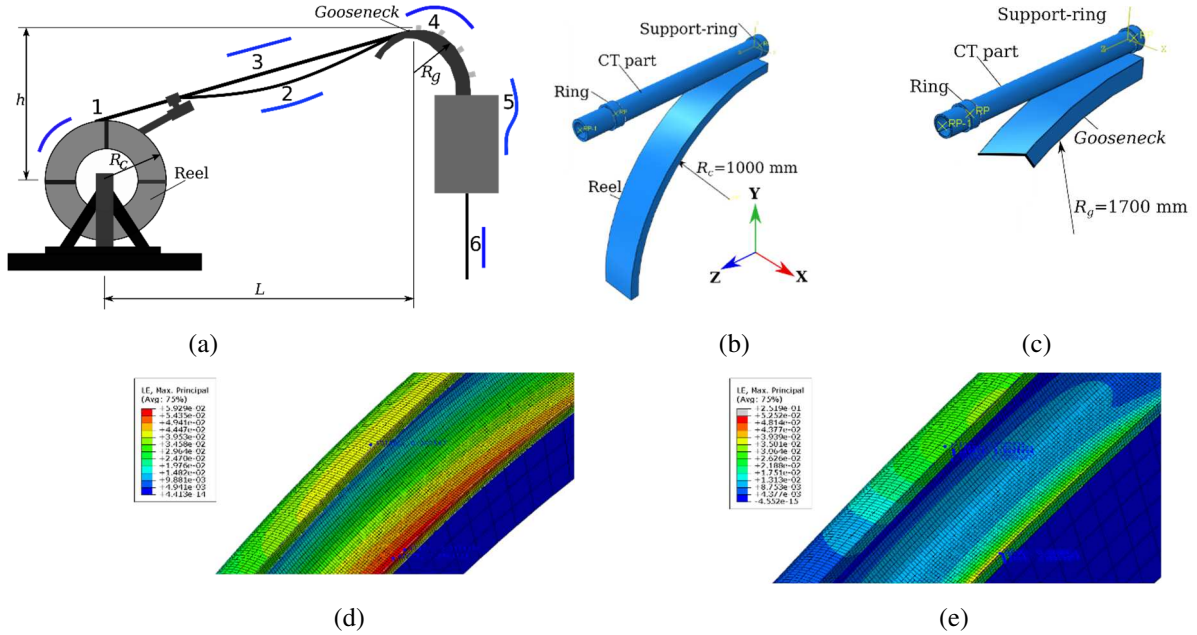

Fig. 1 - (a) Sectors 1-6 describing specific strain patterns of coiled tubing; Model in FE software: (b) Reel and (c) Gooseneck; Longitudinal section of FE with maximum strains: (d) Reel and (e) Gooseneck.

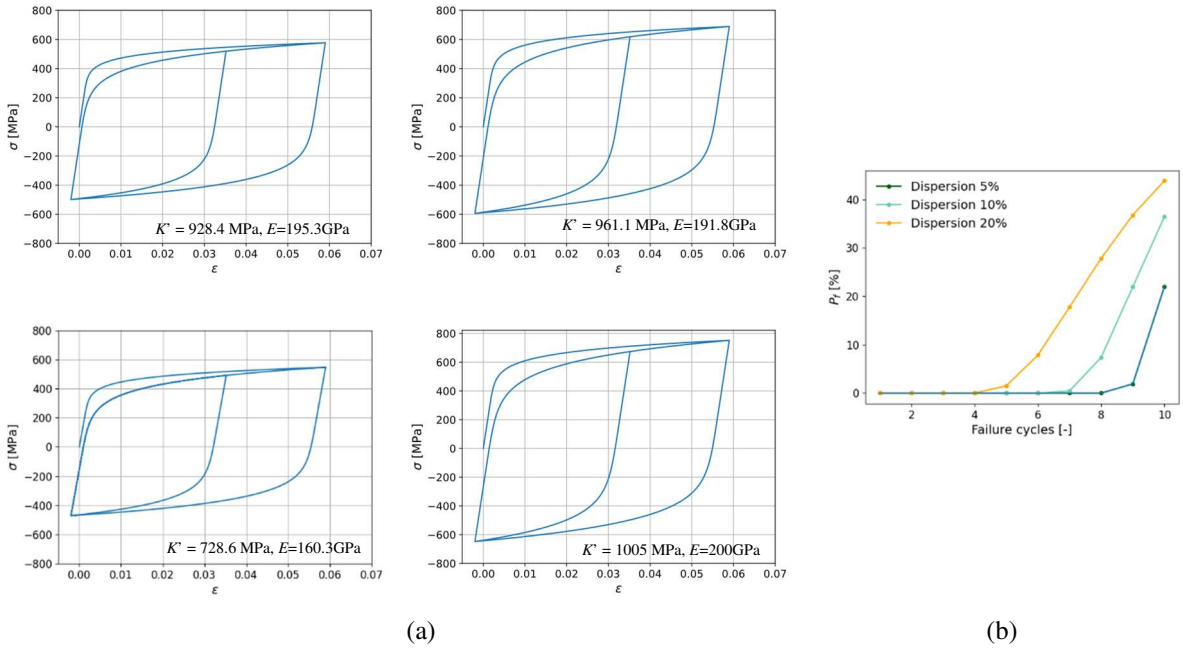

Fig. 2 - (a) Cyclic stress-strain curves. (b) Failure cycles vs failure probability, P_f.

REFERENCES

[1] Shaohu, L., Hao, Z., Hong, Z., Yang, L., Zhen, W. Experimental and numerical simulation study on fatigue life of coiled tubing with typical defects. Journal of Petroleum Science and Engineering, 2021, 198, pp. 63-66.

TRACK - C: Structural Dynamics

Testing Techniques
Measurement in Dynamics
Vibration Analysis
Control Systems
Earthquake Engineering
Crashworthiness
Ballistic Studies
Energetic Materials
Impact Behaviour of Materials
Case Studies

Proceedings IRF2025: 8th International Conference on Integrity-Reliability-Failure
In Engineering, Materials, Manufacturing and Biomechanics. Porto 15-18 July 2025
DOI: https://doi.org/10.24840/978-972-752-323-8

PAPER REF: 22233

INVESTIGATION OF A METALLIC SANDWICH DESIGN WITH THERMOPLASTIC CORE FOR IMPROVED PEDESTRIAN PROTECTION

Ralf. Sturm(*)

Insitute of vehicle concepts, DLR e.V. (German Aerospace Center), Stuttgart, Germany
(*)*Email:* Ralf.Sturm@dlr.de

ABSTRACT

Sandwich structures with PA6 foam as core material were investigated for car applications. For certification, cars have to satisfy certain safety standards required for pedestrian impact scenarios. New solutions are sought for, which offer improved pedestrian protection whilst keeping or reducing the mass of the vehicle. In this study sandwich materials consisting of PA6 foams and aluminium coversheets were analysed. Since the automotive sector is very sensitive to costs, an in-situ joining technique was analysed by directly using the melted thermoplastic material as adhesive. In an experimental study, the performance of the adhesive bonding was characterised. Virtual material descriptions were derived from the sandwich materials by performing quasi-static and dynamic material tests. Finally, impact studies were conducted on the material, testing the performance of the sandwich and validating the numerical models.

Keywords: Sandwich, crash, hybrid, material cards.

INTRODUCTION

For decades, customer demands in terms of comfort and safety have led to ever-increasing vehicle weights in automotive engineering. This constant weight increase has to be reversed due to the need to reduce the CO2 emissions of vehicles. Sandwich designs could offer the possibility to reduce vehicle weight due to the improved structural performance of the sandwich design. According to R. Bhagat at al. [1] hybrid materials as sandwich design could replace the conventional metallic design of bonnets due to the improved stiffness and safety performance. In the field of safety, the pedestrian impacting the bonnet plays a significant role. Qi Liu at al. investigated the performance of a sandwich hood design, identifying that of 12 impact positions covering the main hood area, about half of the impact points meet the HIC<800 and the others achieve HIC from 800 to 1000 [2]. In the presented study, an attempt was made, to investigate a cost-efficient manufacturing technique for sandwich structures by using the contact surface of the thermoplastic core material for the adhesive bonding of the hybrid material.

RESULTS AND CONCLUSIONS

Since the automotive is very cost sensitive, a straight forward manufacturing technique for the generation of a sandwich structure was analysed. Thermoplastic foams melt if a certain temperature level is obtained and this process can be utilised for adhesion whilst the melted material cools down. A simple manufacturing technique was investigated by pressing a heated Aluminium sheet on a thermoplastic sandwich core. Due to the heat on the contact surface the foam melts and bonds as soon as the metallic sheets cool down below 223°C. In this study

surface pretreatment of the metallic surfaces was not considered. Tension and shear specimens were built up for three different densities of the Zotek® N PA6 foam using the described manufacturing technique. In Figure 1 the tension specimen and the obtained test results are shown.

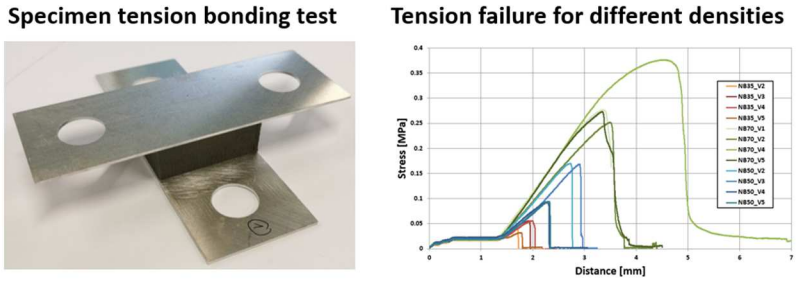

Fig. 1 - Test specimen and tension test results for the bonding of different core densities on metallic face sheets.

The coupon tests were used to identify the obtained bonding properties and the obtained characteristics were integrated into a material description for an explicit solver. Impact simulations on the hybrid material were conducted analysing its impact performance. For validation impact tests were performed using a pendulum with a round impactor. The force displacement characteristics were taken and compared with explicit simulations. The test setup, the impacted specimen and the numerical results are shown in Figure 2.

Fig. 2 - Dynamic validation test and FE-simulation of the hybrid material sandwich structure.

The results show that on the one hand, this manufacturing technique could have the potential for the generation of cost-efficient sandwich structures. However, during the manufacturing it was not possible to have the same heat distribution over the core, leading to a different bonding quality over the plate. Weakly bonded points led to initiated local delamination of the face sheets. Whilst the simulation proved that this technique has the potential for a light sandwich design, more research is required to improve the quality of the bonding. Future research should focus on improving the heat and pressure distribution or implementing additional surface treatment on the metallic face sheets.

REFERENCES

[1] R. Bhagat, A. More, A Review: Analysis and Optimization of Car Bonnet, International Journal of innovative Research & Development, Vol3 Issue 1, 2014, SSN 2278 - 0211.

[2] Qi Liu at al., Design Analysis of a Sandwich Hood Structure for Pedestrian Protection, https://www-nrd.nhtsa.dot.gov/pdf/ESV/Proceedings/21/09-0356.pdf.

Proceedings IRF2025: 8th International Conference on Integrity-Reliability-Failure
In Engineering, Materials, Manufacturing and Biomechanics. Porto 15-18 July 2025
DOI: https://doi.org/10.24840/978-972-752-323-8

PAPER REF: 22294

STUDY ON TEMPORAL CHANGES IN WHEEL LOAD AND ROLLING RESISTANCE OF AIRLESS TIRE DURING ROLLING MOTION

Katsuhide Fujita[1(*)], Takuma Suzuki[2], Toshihiko Okano[2], Kensuke Sasaki[2]

[1]National Institute of Technology, Ube College, Department of Mechanical Engineering, Yamaguchi, Japan
[2]Nissan Motor Corporation, Research Division, EV System Laboratory, Kanagawa, Japan
[(*)]*Email:* katuhide@ube-k.ac.jp

ABSTRACT

In recent years, the automotive industry has been developing autonomous driving systems. There are six levels of autonomous driving, ranging from 0 to 5, with levels 4 and above enabling unmanned driving. However, to ensure the stable operation of unmanned driving, it is considered more important to reduce the frequency of maintenance due to accidental breakdowns. For this reason, airless tires are expected to play a key role as the next-generation tire suitable for future unmanned vehicles, thanks to their puncture-free advantage. Using a scale model airless tire simulating a full-size tire, wheel load and rolling resistance were measured in a rolling experiment. It was confirmed that both wheel load and rolling resistance change over time due to tire deformation caused by preload. In this study, we investigated and analyzed the effects of preload and tire rotation speed on these changes over time.

Keywords: Non-pneumatic tire, Airless tire, Wheel load, Rolling resistance.

INTRODUCTION

In recent years, research on airless tires (non-pneumatic tires, NPT) for passenger cars has received extensive attention (Deng et al., 2023; Nakajima, 2020). This interest is driven by the development of autonomous driving technology. Autonomous driving at Level 4 and above involves unmanned driving, making it increasingly important to reduce the frequency of maintenance due to accidental failures. Puncture-free airless tires are therefore being considered as a suitable for autonomous vehicles. Measurements of the tire forces generated in a rolling experiment using a scale model airless tire confirmed that both wheel load and rolling resistance change over time due to tire deformation caused by preload (Fujita et al., 2023). Consequently, we investigated the temporal changes in wheel load and rolling resistance and analyzed the effects of preload and tire rotation speed on these changes over time.

EXPERIMENTAL EQUIPMENT AND PROCEDURE

In the experiment, a scale model simulating the structure of a full-size airless tire is used. Figure 1 shows the scale model airless tire, which consists of a wheel, spokes, and a tread ring. It has an outer diameter of 200 mm and a width of 50 mm. Figure 2 shows the experimental setup for the rolling test to measure wheel load and rolling resistance. The airless tire is fixed to a cantilevered axle and pressed against a drum with a preload. In this configuration, the tire rotates passively as the drum is rotated by the drive motor. Wheel load and rolling resistance are measured using a 6-component force transducer equipped with the axle. Rolling tests were conducted by varying the preload (100, 200, and 300 N) and the tire rotation speed (180, 360, and 540 rpm). To examine changes over time, measurements were taken immediately after rolling (0 minutes) and then at 1, 2, 5, and 10 minutes thereafter.

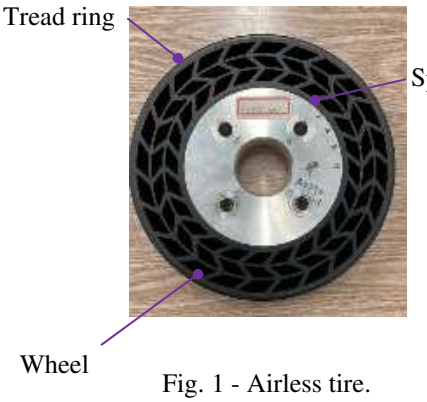

Fig. 1 - Airless tire.

Fig. 2 - Experimental setup.

EXPERIMANTAL RESULTS AND CONCLUSIONS

We investigated the effect of preload and tire rotation speed on the steady-state average values and the amplitude changes over time for wheel load and rolling resistance, respectively. Figure 3 shows the temporal changes in wheel load and rolling resistance for preloads of 100, 200, and 300 N at tire rotation speed of 360 rpm. The average wheel load and rolling resistance values for each elapsed time are plotted, with the amplitude represented by error bars.

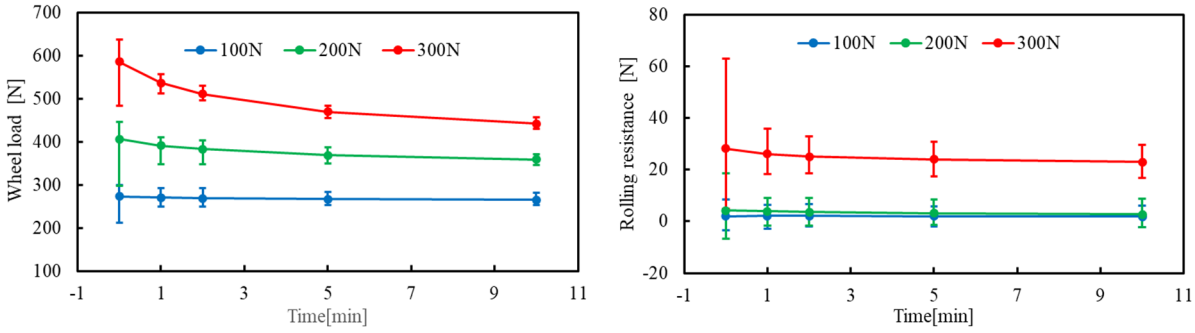

Fig. 3 - Temporal changes in wheel load and rolling resistance.

It was confirmed that the average of the wheel load decreases exponentially over time, with the rate of decrease increasing as the preload increases. This tendency becomes more pronounced as the rotational speed increases. The amplitude of the wheel load nearly converged after 2 minutes, and no effects of preload or tire rotation speed were observed.

The average of the rolling resistance increases with preload, but the decrease over time is much smaller compared to that of the wheel load. The amplitude of the rolling resistance converged after 2 minutes, similar to the wheel load, and it was confirmed that the amplitude tended to increase as tire rotation speed increased.

REFERENCES

[1] Deng Y, Wang Z, Shen H, Gong J, Xiao, Z. A comprehensive review on non-pneumatic tyre research. Materials & Design, 2023, 227.

[2] Nakajima Y. The picture of future tire, Journal of the Society of Rubber Science and Technology, 2020, Vol.93, No.9 (in Japanese).

[3] Fujita K, Suzuki T, Okano T, Washimi Y, Sasaki K, Tanimoto T. Study on clarification of the mechanism for tire force generated in airless tire during rolling motion. Transaction of the JSME, 2023, Vol.89, No.928 (in Japanese).

Proceedings IRF2025: 8th International Conference on Integrity-Reliability-Failure
In Engineering, Materials, Manufacturing and Biomechanics. Porto 15-18 July 2025
DOI: https://doi.org/10.24840/978-972-752-323-8

PAPER REF: 22303

THE EFFECT OF CUMULATIVE POST-SEISMIC DEFORMATIONS ON THE CAPACITY OF BOLTED T-STUB CONNECTIONS UNDER MONOTONIC LOADING

Florea Dinu[1, 2], Calin Neagu[1,2(*)], Paul Zdrenghea[1], Denis Ivascu[1], Andreea Constantinescu[1], Mihai Senila[3]

[1]Politehnica University Timisoara, Timisoara, 300006, Romania
[2]Romanian Academy, Timisoara Branch, Timisoara, 300223, Romania
[3]Technical University of Cluj-Napoca, Cluj-Napoca, Romania
[(*)]*Email:* calin.neagu@upt.ro

ABSTRACT

Bolted end plate joints are widely used for steel frame buildings located in seismic zones. When partial strength joints are employed, the joint ductility is strongly influenced by the properties of the T-stub components. Moreover, in case of multi-hazard scenarios involving local failures after strong earthquakes, the residual capacity may be insufficient to provide alternate load paths, thus resulting in the propagation of failure. The study presents the results of an experimental study on a set of T-stub elements subjected to monotonic loading, cyclic loading, and sequence of loadings, i.e., monotonic after cyclic at different amplitudes. The results showed a significant reduction of stiffness and ductility when T-stubs are tested in sequence of loading.

Keywords: Bolted joint, multi-hazard, robustness, cumulative seismic damage, column loss.

INTRODUCTION

Bolted end plate joints are widely used for steel frame buildings, both in seismic and non-seismic regions. When properly designed and detailed, they exhibit ductile behavior and appropriate seismic performance (Mahin, 1998), (Tremblay et al., 2011). However, their capacity to resist strong seismic aftershocks or localized failures can be seriously diminished. Similar observations have been made about other types of construction materials. One example is the Christchurch (New Zealand) earthquake series of 2010-2011, where not the mainshock of 7.1 Mw, 2010 caused the most losses but the smaller 2011 aftershock (6.2 Mw), which was responsible for 185 fatalities and over 40 billion US$ damage (multi-hazard issues). The seismic list is much longer and include April 2012, Indonesia; Great Tohoku earthquake in Japan, 2011; Chile, February 27, 2010; Wenchuan earthquakes, 2008; New Madrid Earthquakes of 1811-1812) (Li et al., 2014).

A dramatic example is the 32-story building collapse in Bangkok, Thailand, on March 28, 2025, at over 1000 kilometers away from the epicenter of the 7.7 Mw Myanmar earthquake. The progressive collapse took just a few seconds and resulted in the complete destruction of the building, following a so-called pancake collapse. After the earthquake, the safety of other tall buildings in Bangkok started being questioned.

Despite the problems noted above, the existing provisions do not encompass sufficient design rules and requirements, e.g., the description of seismic hazard does not include the probability of aftershocks. As a result, the level of pre-existing damage strongly influences the results of a structural assessment and the capacity to resist further accidental events (Li et al., 2014). And

there are no direct considerations on multi-hazard issues, e.g., column loss (due to fire or explosion) after earthquake, a situation that can be easily described if we mention the Kobe earthquake of January 17, 1995, when major fires sparked throughout the city and caused severe losses (Cole et al., 2013). There are also deliberate attacks and accidental actions (technological, industrial) that may affect building structures, producing damages and endangering the lives of occupants (Guglielmi, 2020).

A step forward is the consideration of resilience, which represents the ability to withstand and recover from deliberate attacks, accidents, or natural hazards (Therese P. McAllister et al., 2022). Two components of resilience are important when considering structural systems, namely the ability to withstand a threat, i.e., robustness (i) and the ability to recover from a threat (ii). The impact of these two components, namely their total or partial lack, has been demonstrated by previous natural or human-made disasters. More important, the post-event reconstruction process has brought to surface the urban resilience as a main goal (Bruneau et al., 2003).

Most research worldwide targeted independently the threats to lateral (seismic) or gravity load resisting systems. The studies on members and connections focused on the response under either cyclic (seismic) or monotonic (column loss, robustness), with or without possible dynamic effects (ElSabbagh et al., 2019), (Adey et al., 1998), (Both et al., 2017), (Landolfo, 2022), (Dinu et al., 2016), (Anwar et al., 2019), (Both et al., 2021), (Demonceau et al., 2019; Demonceau and Jaspart, 2010). As a result, there are no modeling parameters and acceptance criteria for beam to column steel joints under multi-hazard scenarios involving local failures (i.e., columns) following earthquakes. To do this, relevant experimental tests are needed, which are not yet available.

The same problems have been reported for other types of constructions. Thus, in the study performed by (Nojavan et al., 2014), a set of full-scale reinforced concrete columns was tested. The specimens were subjected to large monotonic and cyclic displacement reversals of up to 10% story drift ratio to investigate the behavior at or near collapse conditions. The effect of loading history was investigated by comparing the load-displacement curves and cyclic envelopes of the test specimens. It was observed that columns exhibited faster strength degradation and stiffness deterioration under larger axial load, but, probably more important, under larger number of preceding displacement cycles.

A framework for evaluating the seismic performance of damaged buildings has been proposed in (Polese et al., 2012a), which adopted the residual capacity as a measure of seismic capacity reduced due to damage; the reduction of residual capacity after an earthquake is representative of performance loss. Even the mentioned study refers to existing under-designed reinforced concrete buildings that are typically found in European Mediterranean regions, the methodology may be extended to other structural typologies and sequence of loading (Demonceau et al., 2021).

Also, of special interest are the partial strength / semirigid joints, and their capacity (strength, ductility) to arrest the progressive collapse in the event of a column loss, single or following an earthquake. Thus, the test results reported in (Dinu, 2017) showed that partial strength end plate bolted joints fail before a significant catenary action would develop.

The study presented in the paper investigates the response of end plate bolted joints under large deformation demands. On this aim, bolted T-stub components were tested under different quasi-static loading protocols, i.e., monotonic, cyclic, and combined cyclic and monotonic loading. Some preliminary results have been also presented in (Dinu et al., 2024).

EXPERIMENTAL PROGRAM

The experimental program on T-stubs comprised tests at room temperature, considering quasi-static loading protocols. Geometry of the T-stubs, including the bolt distance (w), end plate thickness (t_f), end plate length (L), and edge distances (e_1) and n, is presented in Figure 1(a). For all T-stubs, bolts are M16 of grade 10.9 HV. To reduce the number of specimens, T-stubs were connected to a more rigid T-stub, with identical geometry but thicker end plate, i.e., 20 mm. The "rigid" T-stub is reused after each test. Figure 1(b) shows one specimen ready for testing in the universal tensile machine. Four LVDT transducers were used to measure the deflection of the T-stub, one at the web-flange transition, two at the end plate edges and one on the rigid T-stub. The load was measured using the 250 kN universal testing machine load cell. The nominal steel grade in end plates is S275. More data about material characteristics may be found in (Dinu et al., 2024).

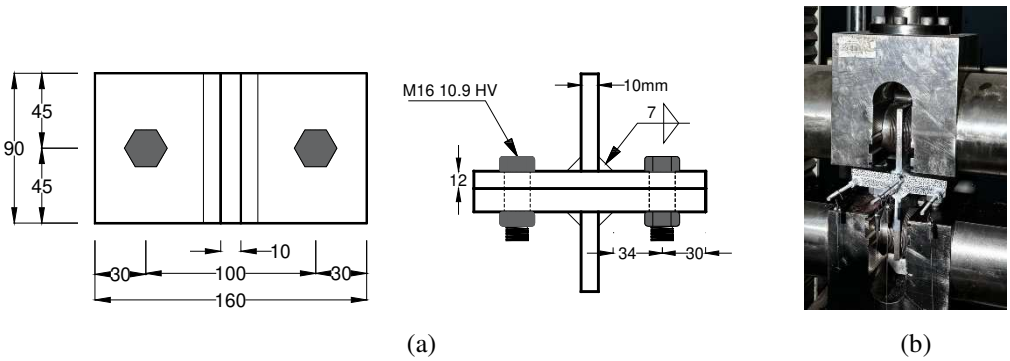

(a) (b)

Fig. 1 - Geometry of the T-stubs (a), and a specimen in the universal machine before testing (b).

Bolted T-stub components were tested under different loading protocols, i.e., monotonic (noted with M), cyclic with increasing amplitudes (noted with C), and combined cyclic and monotonic loading (noted with C_i + M), where the subscript i holds for the maximum level of plastic deformation during the cyclic loading, see Table 1.

For the monotonic tests (M), the quasi-static loading was applied using displacement control and was incremented up to the failure of the specimen, which is given by the fracture of either the bolts or the end plate, or both.

For the cyclic loading (C), the protocol was adapted from the ECCS recommendations (ECCS, 1986), which is governed by the value of the elastic displacement δ_y, corresponding to the point of intersection between two tangent lines, one to the initial stiffness and one to the final stage of the monotonic load (Dinu et al., 2024). The loading protocol starts with four cycles of loading at amplitudes incremented with $\delta_y/4$, until the elastic displacement δ_y is reached. After that, there are three cycles for each displacement incremented with $(2 + 2n)\times \delta_y$, where n = 0, 1, 2, …, see Figure 2(a). T-stubs are subjected to repeated cyclic loading, first in tension and then in compression.

For the combined cyclic and monotonic loading (C_i + M), to consider the pre-existent damage due to an earthquake, the T-stubs were first tested to a certain level of plastic rotation using the cyclic loading protocol. The pre-existent damage level, denoted by the subscript, was set to low, moderate, large and hazardous, i.e., $4d_y$, $6d_y$, $8d_y$, and $10d_y$. Subsequently, the load was applied quasi-statically using displacement control and incremented up to the failure of the specimen, see Figure 2(b).

Table 1 - Summary of experimental program.

T-stub	Loading	
	Cyclic	Monotonic
M		+
C	+	
C_{4dy}+M	$4\times d_y$	+
C_{6dy}+M	$6\times d_y$	+
C_{8dy}+M	$8\times d_y$	+
C_{10dy}+M	$10\times d_y$	+

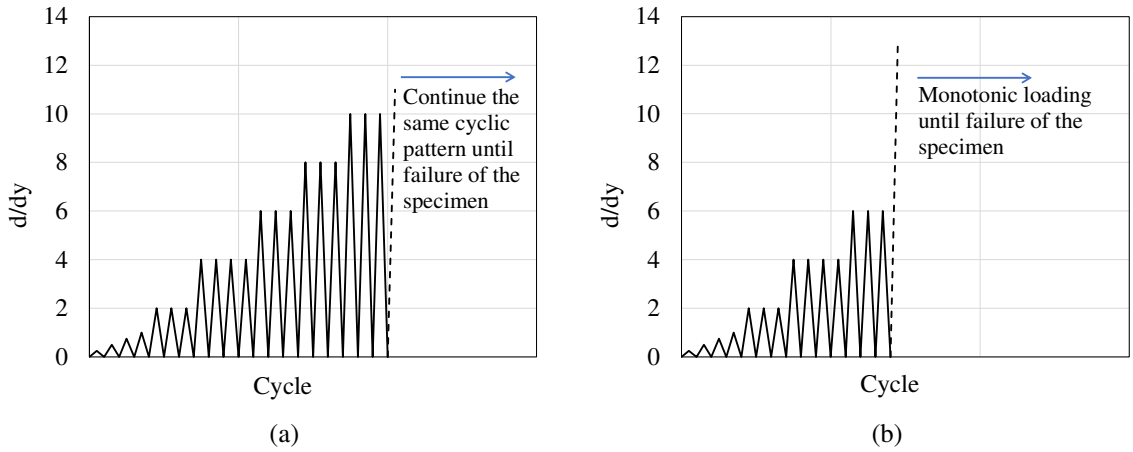

Fig. 2 - ECCS loading protocol adapted to T-stub testing under cyclic loading (a) and combined cyclic + monotonic loading (b).

EXPERIMENTAL RESULTS

A total of twelve T-stubs were tested, 2 for each loading protocol. Table 2 presents the yield and ultimate response parameters, and also the failure mode. Note that for (Ci + M) specimens, the yield point refers to the monotonic loading step that follows the cyclic loading.

Figure 3 shows photos of the failure mode for each loading condition. The failure mode for each loading protocol involved either fracture of the end plate in the heat affected zone HAZ or bolt fracture. However, for tests C6dy + M, one specimen failed due to bolt fracture and one due to end plate fracture. In cases involving bolt fracture, cracks of various extensions were observed in the HAZ. The mixed failure modes is partly given by the value of the yield force in relation to the characteristic resistances in mode 1 and mode 2 calculated in accordance to (EN 1993-1-8, 2011), see Figure 4.

Figure 5 shows the cyclic response and the comparison between force - displacement curve for monotonic test M/1 and 1st cycle envelope for tests C/1, C/2, and the averaged, respectively. While the initial stiffness and yield points are rather identical, the deformation at peak force in the cyclic tests reduces by 25 % for one specimen and by 50% for the second specimen, which is somehow expected. The average of the maximum deformation capacities under cyclic loading supported the decision to limit the cyclic amplitude in the combined protocol (cyclic plus monotonic) to $10d_y$, which is approximately 14 mm.

Table 2 - Experimental results from monotonic (M), cyclic (C) and monotonic after cyclic loading (C_i + M).

T-stub	$F_y^{average}$ [kN]	$d_y^{average}$ [mm]	$F_{max}^{average}$ [kN]	$d_u^{average*}$ [mm]	Failure mode
M	150.00	1.40	228.01	22.37	End plate
C	150.00	1.40	209.07	13.91	End plate
C_{4dy}+M	167.22	3.14	231.80	21.80	Bolt
C_{6dy}+M	201.87	5.62	239.23	24.80	Bolt, end plate**
C_{8dy}+M	193.25	8.80	236.15	30.10	End plate
C_{10dy}+M	-	-	-	-	End plate

Notes:
* Deformation corresponding to peak capacity
** One specimen with bolt fracture, one with end plate fracture

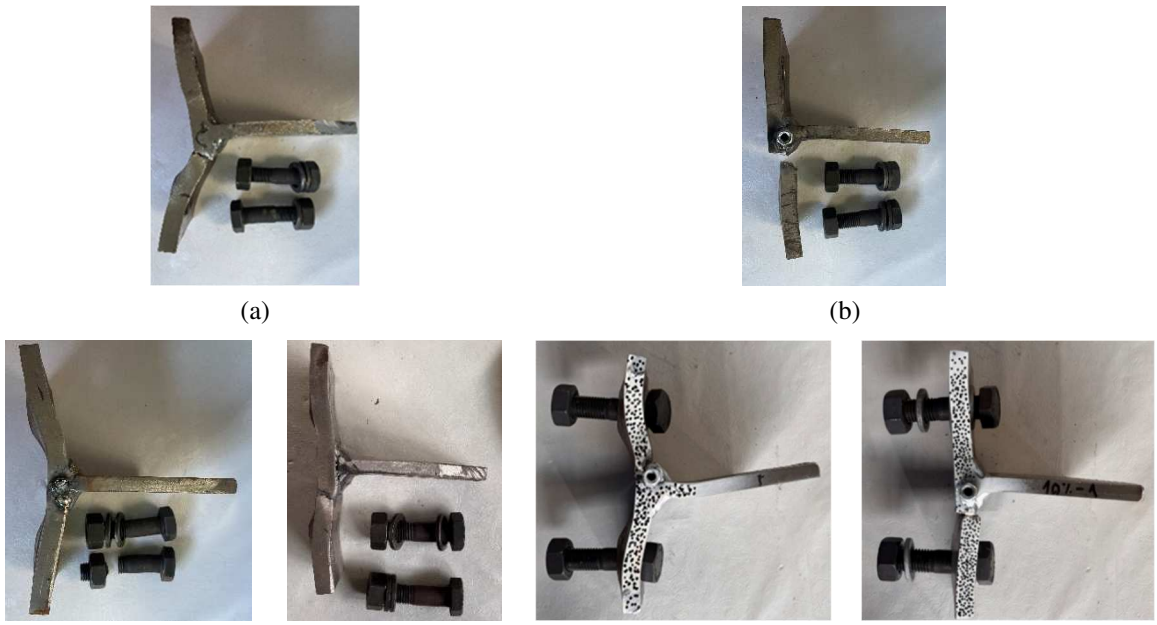

Fig. 3 - Failure modes: a) monotonic; b) cyclic; c) C4dy+M; d) C6dy+M; e) C8dy+M; f) C10dy+M.

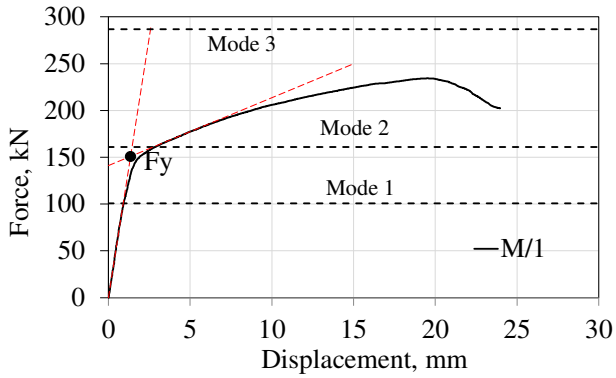

Fig. 4 - Monotonic force displacement-curve vs analytical results (EN 1993-1-8, 2011).

Figure 6 shows the force - displacement curves for T-stubs tested for monotonic loading after cyclic loading at four different amplitudes. For the first two T-stub series, that were tested for low to moderate cyclic plastic deformations, i.e., C_{4dy} + M and C_{6dy} + M, there is a good agreement between the behavior of the specimens of each series, with very close peak force and ultimate deformation. However, for the specimens tested for larger cyclic amplitudes, i.e., C_{8dy} + M and C_{10dy} + M, the cyclic degradation has significant impact on the capacity to resist the last monotonic loading phase. This is, the specimens damaged at this level by an earthquake may fail even with a small increase of the load, e.g., due to a column loss.

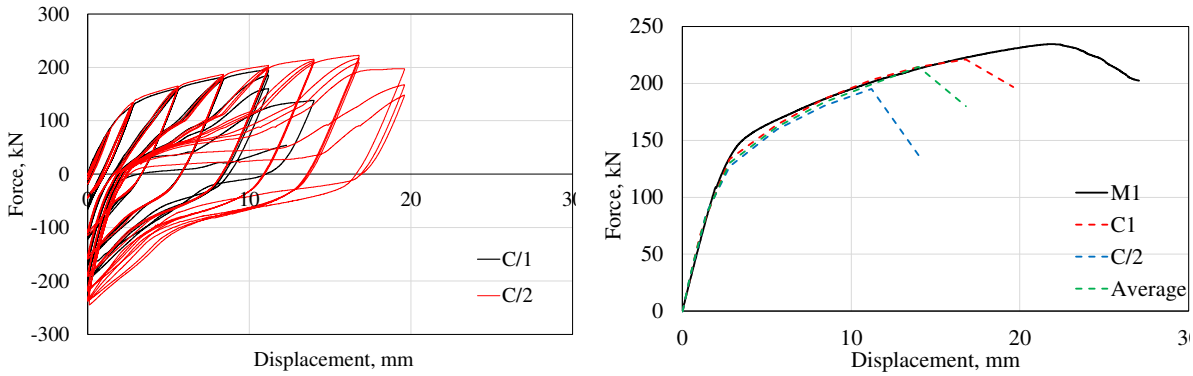

Fig. 5 - Experimental force-displacement curves: (a) cyclic response; (b) monotonic vs backbone curve, 1st cycle.

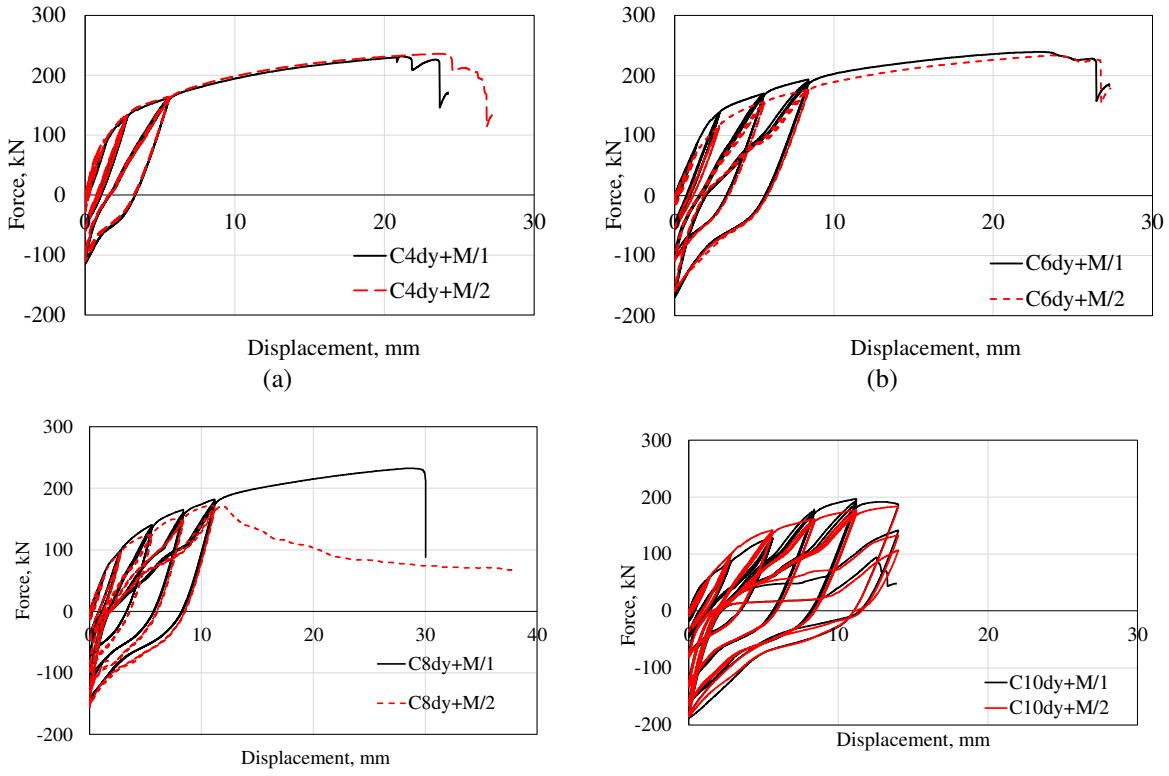

Fig. 6 - Experimental force-displacement curves: a) C_{4dy}+M; b) C_{6dy}+M; c) C_{8dy}+M; d) C_{10dy}+M.

Figures 7(a),(b) show the load-deformation relationship for steel structural components, with a general definition and modelling parameters for intact components (prEN 1998-1-2:2019.3, 2019) and damaged components adapted from (Polese et al., 2012a), (Demonceau et al., 2021). Also, comparative force-displacement curves for monotonic, and monotonic after cyclic tests at different amplitudes are shown in Figure 7(c). Note that the two cyclic curves are based on the average of the envelope curves obtained in each series of tests. Also, for (Ci + M) specimens, the curves refer to the monotonic loading step that follows the cyclic loading. Due to the failure in the cyclic loading phase, no monotonic curve is represented for specimens C10dy + M.

The results are summarized in Table 3. As may be seen, when the cyclic damage in T-stubs is low to moderate (C4dy, C6dy), the initial stiffness and the normalized plastic deformation capacity (or ductility) in a subsequent monotonic loading decrease by different amounts, but the ultimate deformation remains at levels close to that resulting from monotonic tests. However, when the T-stubs are severely damaged by an earthquake (C8dy, C10dy), the residual capacity to sustain any additional load in a subsequent monotonic loading is severely compromised, with 3 out of the four specimens failing at the very end of the cyclic load.

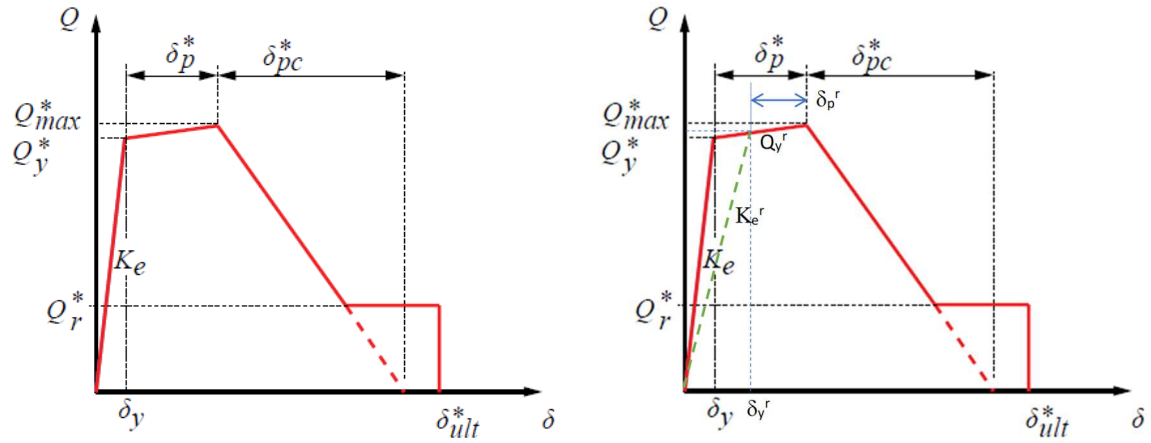

(a) (b)

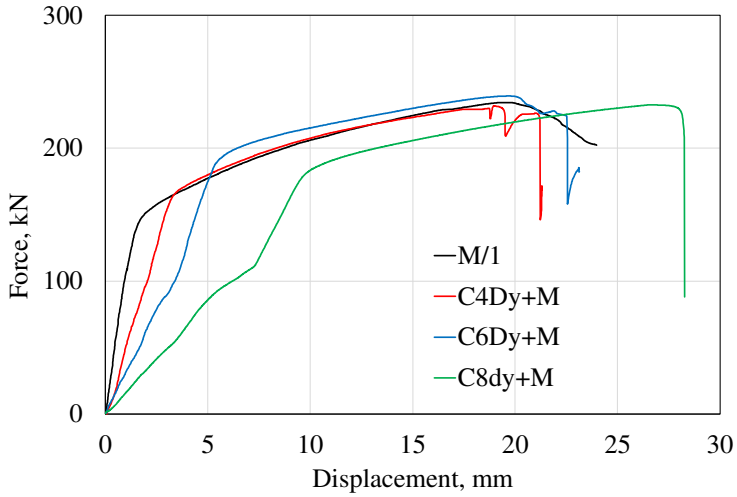

(c)

Fig. 7 - Load-deformation relationship for steel components under monotonic loading: (a) general definition and modelling parameters for "no damage" components (prEN 1998-1-2:2019.3, 2019); (b) modelling parameters for damaged components (Polese et al., 2012b); (c) monotonic after cyclic tests at different amplitudes.

Table 3 - Response parameters for the intact and damaged T-stubs under monotonic loading.

T-stub	Initial stiffness [kN/m]	Ratio damaged/initial	Normalized plastic deformation capacity
Initial (intact), M	110 000		16.0
Damaged C_{4dy}+M	53 000	0.48	6.9
Damaged C_{6dy}+M	29 450	0.27	4.4
Damaged C_{8dy}+M	21 931*	0.19*	3.4*
Damaged C_{10dy}+M	-	-	-
*data are for specimen C_{8dy}+M/1			

CONCLUSIONS

The study presented in the paper investigated experimentally the response of a set of bolted T-stub elements under monotonic loading, cyclic loading, and sequence of loadings, i.e., monotonic after cyclic at different amplitudes. In the following, the concluding remarks and some further developments of the study are presented:

- T stubs are the main contributors to the joint ductility for partial strength joints. Their detailed investigation allowed us to identify the main response parameters (initial stiffness, peak force, ductility).

- When monotonic response is envisaged (e.g., beam to column joints adjacent to a lost column), the T-stubs may provide large ductility, with large deformation capacity of the end plate before bolt fracture.

- Cyclic tests showed ductility is almost halved compared with monotonic. End plate fractures in the heat affected zone (HAZ) before bolt fracture.

- When multi-hazard scenarios are of interest (monotonic after cyclic), moderately damaged T-stubs (C_{4dy}, C_{6dy}) show significantly lower initial stiffness and ductility, but ultimate deformations at levels close to that resulting from monotonic tests. However, when the T-stubs are severely damaged by an earthquake (C_{8dy}, C_{10dy}), the residual capacity to sustain any additional load in a subsequent monotonic load is severely compromised. For such a scenario, a column loss following an earthquake may reveal insufficient capacity to develop alternate load paths and arrest the propagation of collapse.

Further studies will consider other T-stubs configurations (end plate thickness, bolt diameter and distances) under single and multi-hazard scenarios but also dynamic effects due to column loss.

REFERENCES

[1] Adey, B.T., Grondin, G.Y., Cheng, J.J.R., 1998. Extended end plate moment connections under cyclic loading. Journal of Constructional Steel Research 46, pp. 435-436. https://doi.org/10.1016/S0143-974X(98)80073-4.

[2] Anwar, G.A., Dinu, F., Ahmed, M., 2019. Numerical Study on Ultimate Deformation and Resistance Capacity of Bolted T-Stub Connection. Int. J. Steel Struct. 19, pp. 970-977. https://doi.org/10.1007/s13296-018-0186-8.

[3] Both, I., Duma, D., Dinu, F., Dubina, D., Zaharia, R., 2021. The influence of loading rate on the ultimate capacity of bolted T-stubs at ambient and high temperature. Fire Safety Journal 125. https://doi.org/10.1016/j.firesaf.2021.103438.

[4] Both, I., Marginean, I., Neagu, C., Dinu, F., Dubina, D., Zaharia, R., 2017. Experimental Research on T-Stubs Under Elevated Temperatures, in: Wald, F., Burgess, I., Jelcic, R.M., Bjegovic, D., Horova, K. (Eds.), Applications of Structural Fire Engineering. Czech Technical Univ Prague, Prague 6.

[5] Bruneau, M., Chang, S.E., Eguchi, R.T., Lee, G.C., O'Rourke, T.D., Reinhorn, A.M., Shinozuka, M., Tierney, K., Wallace, W.A., von Winterfeldt, D., 2003. A Framework to Quantitatively Assess and Enhance the Seismic Resilience of Communities. Earthquake Spectra 19, pp. 733-752. https://doi.org/10.1193/1.1623497.

[6] Cole, M.A., Elliott, R.J.R., Okubo, T., Strobl, E., 2013. Natural Disasters and Plant Survival: The impact of the Kobe earthquake. Discussion papers.

[7] Demonceau, J.-F., Cerfontaine, F., Jaspart, J.-P., 2019. Resistance of steel and composite connections under combined axial force and bending including group effects: Analytical procedures and comparison with laboratory tests. Journal of Constructional Steel Research 160, pp. 320-331. https://doi.org/10.1016/j.jcsr.2019.05.030.

[8] Demonceau, J.-F., Golea, T., Jaspart, J., Elghazouli, A.Y., Khalil, Z., Santiago, A., Santos, A.F., Silva, L., Kuhlmann, U., Skarmoutsos, G., Baldassino, N., Zandonini, R., Bernardi, M., Zordan, M., Dinu, F., Marginean, I., Jakab, D., Dubina, D., Wertz, F., ANWAAR, O., 2021. Design Recommendations against Progressive Collapse in Steel and Steel-Concrete Buildings [FAILNOMORE].

[9] Demonceau, J.-F., Jaspart, J.-P., 2010. Experimental test simulating a column loss in a composite frame. Advanced steel construction 6, pp. 891-913.

[10] Dinu, F., Marginean, I., Dubina, D., Petran, I., 2016. Experimental testing and numerical analysis of 3D steel frame system under column loss. Eng. Struct. 113, pp. 59-70. https://doi.org/10.1016/j.engstruct.2016.01.022.

[11] Dinu, F., Marginean, Ioan, Dubina, Dan, 2017. Experimental testing and numerical modelling of steel moment-frame connections under column loss. Engineering structures. 151, pp. 861-878.

[12] Dinu, F., Neagu, C., Marginean, I., Dubina, D., Thanopoulos, P., Vayas, I., 2024. Bolted T-stub macro-components under combined cyclic and monotonic loading. Presented at the Behavior of Steel Structures in Seismic Areas, STESSA, Salerno, Italy.

[13] Eccs, E., 1986. Technical Committee 1–Structural Safety and Loadings–Technical Working Group 1.3–Seismic Design Recommended Testing Procedure for Assessing the Behaviour of Structural Steel Elements under Cyclic Loads.

[14] ElSabbagh, A., Sharaf, T., Nagy, S., ElGhandour, M., 2019. Behavior of extended end-plate bolted connections subjected to monotonic and cyclic loads. Engineering Structures 190, pp. 142-159. https://doi.org/10.1016/j.engstruct.2019.04.016.

[15] EN 1993-1-8, 2011. Eurocode 3: Design of steel structures - Part 1-8: Design of joints. European Committee for Standardisation, Brussels.

[16] Guglielmi, G., 2020. Why Beirut's ammonium nitrate blast was so devastating. Nature d41586-020-02361–x. https://doi.org/10.1038/d41586-020-02361-x.

[17] Landolfo, R., 2022. European seismic prequalification of steel beam-to-column joints: EQUALJOINTS and EQUALJOINTS-Plus projects. Journal of Constructional Steel Research 192. https://doi.org/10.1016/j.jcsr.2022.107238.

[18] Li, Y., Song, R., Van De Lindt, J.W., 2014. Collapse Fragility of Steel Structures Subjected to Earthquake Mainshock-Aftershock Sequences. J. Struct. Eng. 140, 04014095. https://doi.org/10.1061/(ASCE)ST.1943-541X.0001019.

[19] Mahin, S.A., 1998. Lessons from damage to steel buildings during the Northridge earthquake. Engineering Structures 20, pp. 261-270. https://doi.org/10.1016/S0141-0296(97)00032-1.

[20] Nojavan, A., Schultz, A., Chao, S.-H., Haselton, C., Simasathien, S., Palacios, G., Liu, X., 2014. Preliminary Results for NEESR Full-Scale RC Column Tests Under Collapse-Consistent Loading Protocols, NCEE 2014 - 10th U.S. National Conference on Earthquake Engineering: Frontiers of Earthquake Engineering. https://doi.org/10.4231/D3C824F6F.

[21] Polese, M., Di Ludovico, M., Prota, A., Manfredi, G., 2012a. Residual capacity of earthquake damaged buildings.

[22] Polese, M., Di Ludovico, M., Prota, A., Manfredi, G., 2012b. Residual capacity of earthquake damaged buildings. prEN 1998-1-2:2019.3, 2019. Eurocode 8 - Design of structures for earthquake resistance - Part 1-2: Rules for new buildings. European Committee for Standardization, Brussels, Belgium.

[23] Therese P. McAllister, Richard Walker, Amy Baker, 2022. Assessment of Resilience in Codes, Standards, Regulations, and Best Practices for Buildings and Infrastructure Systems. https://doi.org/10.6028/NIST.TN.2209.

[24] Tremblay, R., Filiatrault, A., Timler, P., Bruneau, M., 2011. Performance of steel structures during the 1994 Northridge earthquake. Canadian Journal of Civil Engineering. https://doi.org/10.1139/l95-046.

Proceedings IRF2025: 8th International Conference on Integrity-Reliability-Failure
In Engineering, Materials, Manufacturing and Biomechanics. Porto 15-18 July 2025
DOI: https://doi.org/10.24840/978-972-752-323-8

PAPER REF: 22306

HELICOPTER VIBRATION MONITORING USING REGULAR NEURAL NETWORKS

Diego Martins Gomes Pereira, Hélio de Assis Pegado(*)
DEMEC, Universidade Federal de Minas Gerais, Belo Horizonte, Brasil
(*)*Email:* helio@demec.ufmg.br

ABSTRACT

Helicopter vibration monitoring is crucial for ensuring flight safety, reducing maintenance costs, and optimizing operational efficiency. Traditional health monitoring systems, such as Health and Usage Monitoring Systems (HUMS) and Prognostics and Health Management (PHM), rely on extensive sensor networks and pre-defined diagnostic models but often require aircraft grounding to operate. This study explores the application of neural networks for helicopter vibration analysis, using raw acceleration data and its Fast Fourier Transform (FFT) representations as inputs. A simple neural network architecture was trained with various hyperparameter configurations to assess its performance. Initially, raw vibration data were fed into the model to evaluate its capacity to learn without feature extraction. Subsequently, FFT-modified data were used to capture frequency-domain characteristics. The results demonstrate how input choice (raw vs. FFT) and hyperparameter tuning influence the model's ability to detect and classify vibration anomalies. This approach suggests a real-time health monitoring solution that complements existing HUMS and PHM systems, enhancing early fault detection and predictive maintenance in rotorcraft operations.

Keywords: Neural networks, vibration monitoring, helicopter vibration.

INTRODUCTION

Helicopters are a type of rotary-wing aircraft that utilize rotating blades to generate lift, propulsion, and enable flight control (Venkatesan, 2015). The rotor hub is the fundamental component of helicopters, it is attached to the blades and the fuselage, and through this component the aerodynamics forces and vibrations are transmitted to the aircraft. Due to the rotational motion and aerodynamics, natural frequencies arise and vary across different flight phases, inducing vibrations throughout the entire aircraft (Bramwell et al., 2000). Prolonged exposure to these vibrations has the potential to harm critical hub components which can alter vibration patterns, providing valuable data that can be harnessed for proactive measures to prevent incidents and accidents. As technology continues to evolve, new computational resources are being introduced and can be used in vibration-based damage detection techniques, such as Neural Networks (NN). In this study, two vibration detection methods are integrated with computational tools to effectively identify structural damage in helicopters. Publicly available vibration datasets are employed to train NN models using different combinations of techniques and software architectures.

HELICOPTER VIBRATIONAL PATTERNS

According to Bramwell et al. (2000), aerodynamic loads are periodic during steady flight, which can be used to model the force equation in lateral/longitudinal axes and the vertical axis. By defining b as the number of blades on a helicopter and Ψ as the angle of one blade taken as

reference, vertical loads observed from the fuselage can be modeled using Fourier series into the following equation

$$Z = -b \begin{bmatrix} U_0 & +U_b \cos(b\Psi) + U_{2b} \cos(2b\Psi) + U_{3b} \cos(3b\Psi) + \cdots \\ & +V_b \sin(b\Psi) + V_{2b} \sin(2b\Psi) + V_{3b} \sin(3b\Psi) + \cdots \end{bmatrix} \quad (1)$$

in which U and V are constants obtained from the Fourier series. As it can be seen, vertical loads are periodic and dependant only on frequencies that are integer multiples of the number of blades b. Using the same methodology for lateral and longitudinal loads, equations

$$\begin{aligned} X = \quad & -\tfrac{1}{2}b \sum_{m=1}^{\infty} [P_{mb-1} + T_{mb-1} + P_{mb+1} - T_{mb+1}] \cos mb\Psi \\ & -\tfrac{1}{2}b \sum_{m=1}^{\infty} [Q_{mb-1} - S_{mb-1} + Q_{mb+1} + S_{mb+1}] \sin mb\Psi \end{aligned} \quad (2)$$

and

$$\begin{aligned} Y = \quad & +\tfrac{1}{2}b \sum_{m=1}^{\infty} [S_{mb-1} - Q_{mb-1} + S_{mb+1} + Q_{mb+1}] \cos mb\Psi \\ & +\tfrac{1}{2}b \sum_{m=1}^{\infty} [P_{mb-1} + T_{mb-1} - P_{mb+1} + T_{mb+1}] \sin mb\Psi \end{aligned} \quad (3)$$

can be achieved. Both longitudinal (X) and lateral (Y) are dependant on the Fourier constants P, T, Q and S, but this time the trigonometric functions contains the m integer that when combined to the Fourier constants depending on $mb-1$ or $mb+1$ leads to forces only appearing at frequencies multiples of $(mb-1)$ or $(mb+1)$. This mathematical model can be summarised at Table 1, also presented at Prouty (1993), in which Ω is the rotor rotational speed and the primary frequency acting on the rotor hub.

Table 1 - Ideal frequencies transmitted to the fuselage according to frequencies on the hub and blades.

	Frequency of Load Acting on the Hub	Frequencies Transmitted to the Fuselage			
		b=2	b=3	b=4	b=5
Vertical Loads	1Ω	-	-	-	-
	2Ω	2Ω	-	-	-
	3Ω	-	3Ω	-	-
	4Ω	4Ω	-	4Ω	-
	5Ω	-	-	-	5Ω
Longitudinal and Lateral Loads	1Ω	2Ω	-	-	-
	2Ω	-	3Ω	-	-
	3Ω	2Ω e 4Ω	-	4Ω	-
	4Ω	-	3Ω	-	5Ω
	5Ω	4Ω e 6Ω	6Ω	4Ω	-

FAULT DETECTION METHODOLOGY

Helicopter vibration analysis can be performed using different methods, which commonly involve treating data in the time domain or the frequency domain. To make use of existing knowledge in the helicopter vibration field, two approaches will be taken: one developing the raw vibrational acceleration data and the other will use the frequency domain, transforming time series data acquired in real aircraft from accelerometers positioned in the fuselage and hub in different axis to the frequency domain using the Fast Fourier Transform (FFT).

Time Series Classification (TSC) has been one extensive subject of study in the Machine Learning community with researchers investigating the performance of different NN models, architectures and methodologies combinations over multiple datasets such as Bagnall et al. (2017). A study compared different NN models, including the Multi Layer Perceptrons (MLPs)

- denominated “Regular NN” in this study—, Convolutional Neural Networks (CNNs), Encoders and other classifiers, showing that MLPs, although not exceptional, can exceed other models and stand in the average performance range for TSC (Fawaz et al., 2019). The present study explores the potential of MLPs over the TSC problem and in the frequency domain, displaying the capabilities of fault detection with neural networks.

To interpret and generalize the analysis, a NN was developed returning the aircraft health condition using data from the Airbus Challenge Large Scale Machine Learning to the detection of anomalies in accelerometer data (ETH Zürich, 2020). This data is composed of one-minute acceleration samples captured at 1024 Hz, being 1677 healthy samples in the original train dataset and 594 samples in the validation dataset, evenly split between healthy and faulty conditions. Four samples extracted from the validation dataset are represented in Figure 1, in the time and frequency domain.

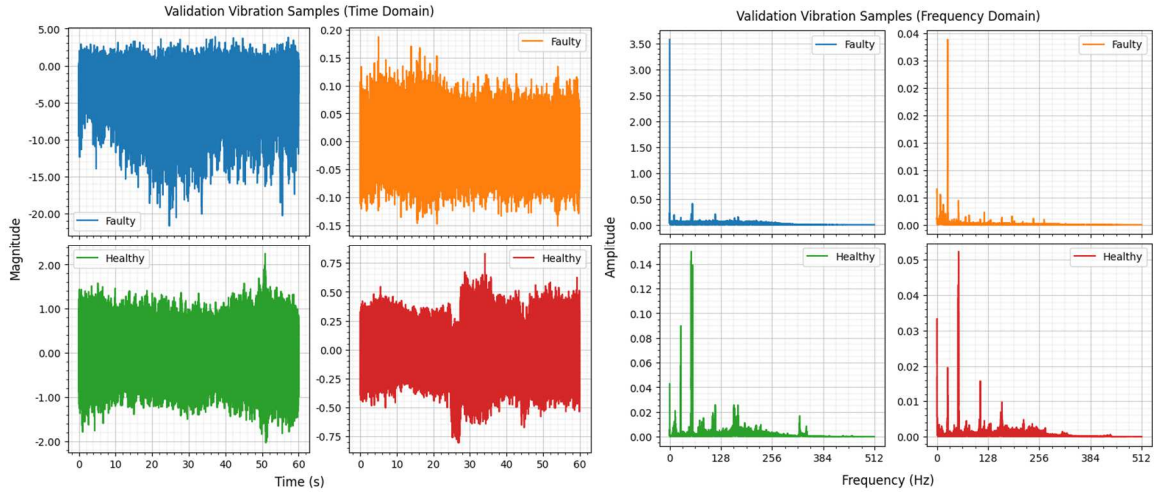

Fig. 1 - Samples extracted from the validation dataset represented in the time and frequency domain.

Creating a regular NN required using the original validation dataset as the training dataset, since the original training dataset contained only healthy samples, which is considered unbalanced and would lead to poor results. Two training routines were created: one using the entire validation dataset; other using a method called stratified k-fold cross-validation, consisting of partitioning the original validation dataset into ‘k’ balanced pieces of samples, training with (k-1) samples and validating with the last piece for every combination possible. After that, samples were divided using the knowledge from Table 1 to verify if separating data would lead to better performances.

A NN with three layers — an input layer, one hidden layer, and an output layer — was designed with configurations of 128, 256, 512, and 1024 neurons. To prevent data memorization, a dropout rate of 25% was applied in the first and second layers. The Rectified Linear Unit activation function was used in these layers to introduce non-linear behaviors, while the Softmax activation function was employed in the output layer to classify data into healthy or anomalous states. The network was optimized using the Categorical Cross Entropy loss function and the Adaptive Momentum (ADAM) optimizer, with predefined learning rates and corresponding decays for each configuration. Additionally, L2 regularization was incorporated with fixed values to penalize high weights, reducing the risk of overfitting caused by memorization. The whole coding was created in Python based on Kinsley & Kukieła (2020). The complete set of hyperparameters used is summarized in Table 2, and a visual representation of the NN architecture is shown in Figure 2.

Table 2 - Hyperparameter combination for different neurons, learning rates (LR), decay and L2 penalization.

Neurons	Learning Rate	Decay	L2 Penalization	Description
128	5e-5	1e-3	5e-4	Small network with lower LR
	1e-4	1e-3	5e-4	Small network with moderate LR
	5e-4	1e-3	5e-4	Small network with higher LR
256	5e-5	1e-3	5e-4	Medium network with lower LR
	1e-4	1e-3	5e-4	Medium network with moderate LR
	5e-4	1e-3	5e-4	Medium network with higher LR
512	5e-5	1e-3	5e-4	Big network with lower LR
	1e-4	1e-3	5e-4	Big network with moderate LR
	5e-4	1e-3	5e-4	Big network with higher LR
1028	5e-5	1e-3	5e-4	Large network with lower LR
	1e-4	1e-3	5e-4	Large network with moderate LR
	5e-4	1e-3	5e-4	Large network with higher LR

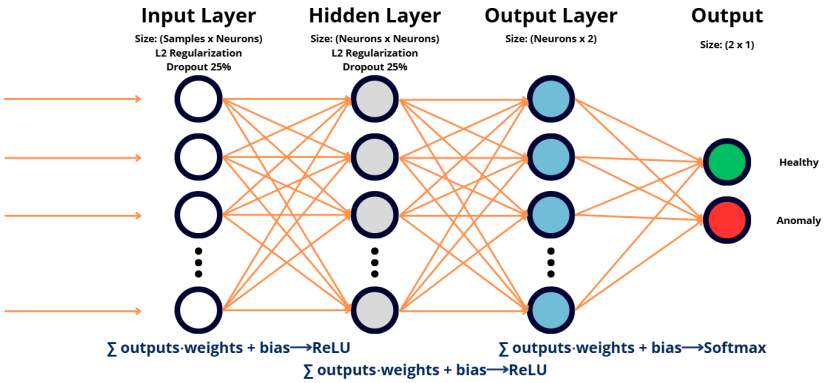

Fig. 2 - Neural Network model used in visual representation.

DATA PREPARATION

The validation dataset contained 25 duplicated faulty samples, which were removed to ensure correct results. This removal created the necessity of balancing the dataset once again, with 25 additional healthy samples being transferred from the original dataset to the training dataset, going from 1677 and 594 samples in the original training and validation dataset to 1702 and 544 samples respectively.

The same dataset was also separated in the vertical and lateral/longitudinal axis to check if it would lead to better performance. The separation methodology applied was according to the region of peaks in the frequency domain. Due to aerodynamics phenomena, lateral and longitudinal vibrations also have noticeable peaks of smaller amplitude in high frequency regions (Bramwell et al., 2000; Prouty, 1993). This behaviour was used to separate samples into vertical, in case the sample has high peaks in low frequency regions (<90 Hz/5400 RPM), or lateral, in case the sample possess high frequency prominent peaks (>=90 Hz/5400 RPM) or frequency peaks are similar in magnitude (<=10%). This separation was only necessary due to the fact that the dataset provider did not specify the direction of each sample, which would not be necessary in a real implementation, with accelerometers capturing data in known directions. After balancing, the new original dataset size, both mixed and separate is exhibited in Table 3.

A common process in NN model training is feature normalization, where columns from each sample are normalized to the interval of [-1,1] or [0,1] in order to avoid large numbers in neuron weights and biases.

Table 3 - Processed datasets sizes.

Mixed Samples		Separated Samples			
Vertical + Lateral Axis		Vertical		Lateral	
Training	Validation	Training	Validation	Training	Validation
1702	544 (179 Healthy, 179 Anomalous)	1000	358 (93 Healthy, 93 Anomalous)	702	186 (74 Healthy, 74 Anomalous)

This feature normalization is not meaningful to acceleration data that is presented in time series, since the data captured in the 30th second mark, for example, does not correlate with other samples captured in the same 30th second mark. However, this feature normalization is useful for the FFT transform of samples, since peaks might appear in the same region of frequency for every sample. The same normalization values applied in the training dataset must be used in the validation dataset, avoiding BIAS. To avoid adding complexity to the analysis, all samples were normalized by the maximum absolute value in the actual training dataset.

PERFORMANCE METRICS

For binary classifiers NN models, the confusion matrix is easily assembled with numbers from the NN guesses. The confusion matrix for helicopter fault detection NN models is represented in Table 4. Loss and accuracy are the main metrics used in this study, the lower the loss, the better overall performance the model will have. Accuracy accounts for the right predictions from the network, given by Equation 4. After evaluating the best models, the True Positive Rate (TPR), False Positive Rate (FPR) are calculated, along with the Area Under the Curve (AUC) and F1 Score (Google, 2024a; 2024b). Great NN models present loss and FPR close to zero and accuracy, TPR, AUC and F1 Score close to 100% during validation.

Table 4 - Confusion matrix for helicopter fault detection neural network models.

	Actual negative	Actual positive
Predicted negative	**True negative (TN):** The network predicts a healthy status when the helicopter is healthy	**False negative (FN):** The network predicts a healthy status when the helicopter has one or more anomalies
Predicted positive	**False positive (FP):** The network predicts an anomaly status when the helicopter is healthy	**True positive (TP):** The network predicts an anomaly status when the helicopter has one or more anomalies

$$Accuracy = \frac{TP+TN}{TP+TN+FN+FP} \tag{4}$$

$$TPR = \frac{TP}{TP+FN} \tag{5}$$

$$FPR = \frac{FP}{FP+TN} \tag{6}$$

$$F1\ Score = \frac{2 \cdot TP}{2 \cdot TP+FN+FP} \tag{7}$$

RESULTS AND CONCLUSIONS

Training with raw data did not lead to impressive results, achieving up to 85.19% accuracy when validating with only healthy samples, as shown in Table 5, and when using both healthy and faulty data the accuracy increased to 89.34±1.9%, shown in Table 6, but still not reaching the desired performance above 95% for safety indications. Using the same input but in the frequency domain, after passing through an FFT algorithm, the accuracy reached up to 98.41% when validating with only healthy samples (Table 7) and 97.24±0.83% when validating with both healthy and anomalous data, exhibited in Table 8. As seen by the low loss, coupled with low standard deviations in both the accuracy and loss of the latter, this is a promising model to be used in a real scenario.

Table 5 - Results for raw data as input in the mixed data analysis. Trained with all validation data and validated with only healthy samples.

Mixed Raw Data Analysis **Training with Validation Samples and Validating with Healthy Samples**							
Learning Rates		**5e-5**		**1e-4**		**5e-4**	
Neurons	**Phase**	**Accuracy**	**Loss**	**Accuracy**	**Loss**	**Accuracy**	**Loss**
128	Training	0.9540	0.3954	0.9577	0.2112	0.9779	0.1236
	Validation	0.8143	0.6582	0.8514	0.4940	0.6398	1.4643
256	Training	0.9577	0.3105	0.9596	0.1527	0.9871	0.1104
	Validation	0.8519	0.5190	0.8261	0.4448	0.6627	1.0618
512	Training	0.9577	0.3269	0.9743	0.1562	0.8125	1.5800
	Validation	0.8114	0.5314	0.7068	0.8965	0.4483	4.1297
1024	Training	0.9632	0.5370	0.9816	0.2086	0.9798	0.2547
	Validation	0.8237	0.4670	0.6651	1.2395	0.6357	1.9275

Table 6 - Results for raw data as input in the mixed data analysis. Results for the 5-fold cross validation.

Mixed Raw Data Analysis **Performance for the 5-fold Cross Validation**				
Neurons	**LR**	**Phase**	**Accuracy**	**Loss**
128	**5e-5**	Training	0.9701±0.0052	0.3867±0.0131
		Validation	0.8712±0.0435	0.3275±0.0793
	1e-4	Training	0.9858±0.0023	0.2672±0.0121
		Validation	0.8271±0.0452	0.4525±0.2547
	5e-4	Training	0.9890±0.0130	0.2040±0.0384
		Validation	0.7554±0.0250	0.9045±0.3564
256	**5e-5**	Training	0.9867±0.0034	0.6325±0.0304
		Validation	0.8934±0.0190	0.3405±0.1230
	1e-4	Training	0.9917±0.0034	0.4873±0.0407
		Validation	0.8106±0.0323	0.5351±0.2843
	5e-4	Training	0.9894±0.0037	0.4382±0.0259
		Validation	0.7297±0.0466	1.210±0.5583
512	**5e-5**	Training	0.9894±0.0011	1.2248±0.0392
		Validation	0.8805±0.0279	0.4258±0.2514
	1e-4	Training	0.9968±0.0031	1.0158±0.0846
		Validation	0.8124±0.0281	0.6575±0.2806
	5e-4	Training	0.9508±0.0692	1.1874±0.6858
		Validation	0.7021±0.0452	2.4603±0.9509
1024	**5e-5**	Training	0.9963±0.0018	2.4953±0.1375
		Validation	0.8822±0.0320	0.4057±0.2627
	1e-4	Training	0.9981±0.0009	1.8880±0.3314
		Validation	0.8088±0.0379	0.6674±0.3301
	5e-4	Training	0.9972±0.0023	2.0934±0.3448
		Validation	0.7408±0.0485	2.7375±0.9370

Since it was observed that the FFT analysis outperformed the raw data analysis, the Separate Samples Analysis were trained and validated similarly to the Mixed Samples Analysis: first validating with the original training dataset; then performing the k-fold cross validation. After training, the best combination of networks achieved 97.80% accuracy in vertical vibrational patterns and 98.58% in lateral when validated with only healthy samples, shown in Table 9. In Table 10, the results are shown after validating with healthy and anomalous data, reaching up to 92.72±4.91% precision in the vertical analysis and 100±0% in the lateral one. Although it may seem impressive to obtain 100% accuracy, it can be attributed to the small validation pool sample, consisting of only 37 or 38 samples for lateral models during the cross validation.

Table 7 - Results for FFT data as input in the mixed data analysis. Trained with all validation data and validated with only healthy samples.

Mixed FFT Data Analysis **Training with Validation Samples and Validating with Healthy Samples**							
Learning Rates		**5e-5**		**1e-4**		**5e-4**	
Neurons	**Phase**	**Accuracy**	**Loss**	**Accuracy**	**Loss**	**Accuracy**	**Loss**
128	Training	0.8033	0.6701	0.8290	0.5588	0.9081	0.3312
	Validation	0.5229	0.6977	0.6298	0.6982	0.9677	0.2663
256	Training	0.8199	0.6094	0.9080	0.4723	0.9191	0.3088
	Validation	0.5329	0.7121	0.8355	0.5990	0.9841	0.2236
512	Training	0.8915	0.5462	0.8952	0.3936	0.9228	0.2887
	Validation	0.8038	0.6171	0.9336	0.3718	0.9818	0.1903
1024	Training	0.8897	0.5173	0.9044	0.3640	0.9301	0.2623
	Validation	0.9177	0.4258	0.9530	0.3103	0.9771	0.1414

Table 8 - Results for FFT data as input in the mixed data analysis. Results for the 5-fold cross validation.

Mixed FFT Data Analysis **Performance for the 5-fold Cross Validation**				
Neurons	**LR**	**Phase**	**Accuracy**	**Loss**
128	**5e-5**	Training	0.9159±0.0058	0.4719±0.0060
		Validation	0.9173±0.0367	0.4367±0.0243
	1e-4	Training	0.9342±0.0070	0.2858±0.0143
		Validation	0.9228±0.0243	0.2556±0.0280
	5e-4	Training	0.9370±0.0068	0.1583±0.0125
		Validation	0.9301±0.0221	0.1401±0.0361
256	**5e-5**	Training	0.9357±0.0062	0.3751±0.0132
		Validation	0.9265±0.0278	0.3096±0.0253
	1e-4	Training	0.9375±0.0067	0.2031±0.0098
		Validation	0.9302±0.0256	0.1747±0.0295
	5e-4	Training	0.9389±0.0053	0.1264±0.0088
		Validation	0.9320±0.0221	0.1143±0.0264
512	**5e-5**	Training	0.9361±0.0053	0.3110±0.0082
		Validation	0.9246±0.0242	0.1931±0.0281
	1e-4	Training	0.9375±0.0067	0.1843±0.0086
		Validation	0.9320±0.0221	0.1540±0.0320
	5e-4	Training	0.9858±0.0057	0.1063±0.0077
		Validation	0.9651±0.0134	0.0986±0.0296
1024	**5e-5**	Training	0.9375±0.0067	0.3727±0.0090
		Validation	0.9320±0.0221	0.1596±0.0317
	1e-4	Training	0.9375±0.0067	0.1744±0.0068
		Validation	0.9320±0.0221	0.1346±0.0280
	5e-4	Training	0.9885±0.0175	0.1124±0.0403
		Validation	0.9724±0.0083	0.1108±0.0454

Table 9 – Results for FFT data as input in the separated data analysis. Trained with all validation data and validated with only healthy samples.

Separated FFT Data Analysis **Training with Validation Samples and Validating with Healthy Samples**								
Learning Rates			**5e-5**		**1e-4**		**5e-4**	
Neurons	**Category**	**Phase**	**Accuracy**	**Loss**	**Accuracy**	**Loss**	**Accuracy**	**Loss**
128	Vertical	Training	0.8743	0.7100	0.8575	0.6299	0.8855	0.3633
		Validation	0.8870	0.6897	0.6510	0.6876	0.9730	0.3159
	Lateral	Training	0.8602	0.7549	0.8065	0.6745	0.9731	0.2279
		Validation	0.7322	0.6926	0.5570	0.6975	0.9473	0.2581
256	Vertical	Training	0.8743	0.7081	0.8799	0.5325	0.8855	0.3533
		Validation	0.6470	0.6903	0.6880	0.6768	0.9780	0.2859
	Lateral	Training	0.7312	0.8012	0.8978	0.6030	0.9892	0.1502
		Validation	0.3461	0.7016	0.7236	0.6841	0.9530	0.1766
512	Vertical	Training	0.8631	0.6765	0.8855	0.4507	0.8883	0.3380
		Validation	0.6360	0.6909	0.8990	0.5108	0.9720	0.2901
	Lateral	Training	0.7742	0.8759	0.9731	0.5295	0.9946	0.1224
		Validation	0.4330	0.7161	0.8718	0.5687	0.9801	0.1081
1024	Vertical	Training	0.8799	0.6992	0.8827	0.4227	0.8855	0.3333
		Validation	0.8210	0.5934	0.9680	0.3531	0.9750	0.2739
	Lateral	Training	0.9516	1.0566	0.9731	0.4505	1.0000	0.0988
		Validation	0.8077	0.6494	0.9430	0.2869	0.9858	0.0930

Table 10 - Results for FFT data as input in the separated data analysis. Results for the 5-fold cross validation.

Separated FFT Data Analysis **Performance for the 5-fold Cross Validation**						
			Vertical		**Lateral**	
Neurons	**LR**	**Phase**	**Accuracy**	**Loss**	**Accuracy**	**Loss**
128	**5e-5**	Training	0.8037±0.0400	0.5590±0.0094	0.5027±0.0045	0.6630±0.0064
		Validation	0.7708±0.0782	0.5165±0.0197	0.5000±0.0121	0.5781±0.0177
	1e-4	Training	0.9043±0.0073	0.3990±0.0048	0.9032±0.0371	0.4783±0.0128
		Validation	0.8993±0.0328	0.3804±0.0361	0.8711±0.0307	0.4280±0.0226
	5e-4	Training	0.9050±0.0085	0.2145±0.0074	1.0000±0.0000	0.0716±0.0046
		Validation	0.8937±0.0344	0.2078±0.0512	0.9946±0.0108	0.0513±0.0055
256	**5e-5**	Training	0.9050±0.0085	0.5128±0.0070	0.7607±0.0729	0.6470±0.0063
		Validation	0.9021±0.0312	0.4299±0.0296	0.7798±0.0724	0.4845±0.0250
	1e-4	Training	0.9036±0.0083	0.2945±0.0102	0.9973±0.0033	0.3449±0.0144
		Validation	0.8797±0.0389	0.2670±0.0352	0.9841±0.0211	0.2608±0.0318
	5e-4	Training	0.9078±0.0069	0.1769±0.0041	1.0000±0.0000	0.0429±0.0012
		Validation	0.8965±0.0331	0.1813±0.0513	1.0000±0.0000	0.0240±0.0047
512	**5e-5**	Training	0.9015±0.0065	0.4788±0.0135	0.9865±0.0085	0.6515±0.0144
		Validation	0.8853±0.0331	0.3111±0.0308	0.9733±0.0166	0.3343±0.0344
	1e-4	Training	0.9050±0.0085	0.2630±0.0087	1.0000±0.0000	0.2551±0.0092
		Validation	0.8881±0.0313	0.2223±0.0407	1.0000±0.0000	0.1143±0.0208
	5e-4	Training	0.9329±0.0173	0.1602±0.0151	1.0000±0.0000	0.0347±0.0012
		Validation	0.9272±0.0491	0.1512±0.0255	1.0000±0.0000	0.0166±0.0052
1024	**5e-5**	Training	0.9043±0.0091	0.5674±0.0101	1.0000±0.0000	0.7861±0.0101
		Validation	0.8853±0.0292	0.2334±0.0372	0.9946±0.0108	0.1562±0.0254
	1e-4	Training	0.9050±0.0085	0.2765±0.0071	1.0000±0.0000	0.2991±0.0049
		Validation	0.8909±0.0262	0.2088±0.0373	1.0000±0.0000	0.0505±0.0052
	5e-4	Training	0.9623±0.0465	0.1824±0.0697	1.0000±0.0000	0.0278±0.0009
		Validation	0.9217±0.0440	0.1755±0.0382	1.0000±0.0000	0.0121±0.0054

After picking the best two models from each analysis, Table 11 was created to show additional metrics. Since some validations occurred with only healthy samples, it is not possible to calculate the TPR, AUC and F1 Score, since these metrics all depend on the number of actual positive (faulty) samples in the dataset.

Table 11 – Additional metrics for the best two models of every analysis. Healthy Only abbreviated as H. O.

Analysis	Validation	Neurons	LR	TPR (%)	FPR (%)	AUC (%)	F1 (%)
Mixed Raw	H. O.	256	5e-5	-	14.81	-	-
Mixed Raw	H. O.	128	1e-4	-	14.86	-	-
Mixed Raw	K-Fold	256	5e-5	92.26±3.79	13.62±6.26	96.92±0.60	89.67±1.78
Mixed Raw	K-Fold	1024	5e-5	94.47±2.35	18.07±7.61	97.58±0.75	89.01±2.82
Mixed FFT	H. O.	256	5e-4	-	1.59	-	-
Mixed FFT	H. O.	512	5e-4	-	1.82	-	-
Mixed FFT	K-Fold	1024	5e-4	94.84±2.18	0.37±0.74	99.26±1.09	97.16±1.01
Mixed FFT	K-Fold	512	5e-4	93.02±2.71	0.00±0.00	99.59±0.59	96.36±1.63
Sep. Vert. FFT	H. O.	256	5e-4	-	2.20	-	-
Sep. Vert. FFT	H. O.	1024	5e-4	-	2.50	-	-
Sep. Lat. FFT	H. O.	1024	5e-4	-	1.42	-	-
Sep. Lat. FFT	H. O.	512	5e-4	-	1.99	-	-
Sep. Vert. FFT	K-Fold	512	5e-4	85.47±9.68	0.00±0.00	99.49±0.45	91.87±6.43
Sep. Vert. FFT	K-Fold	1024	5e-4	84.38±8.68	0.00±0.00	98.87±0.88	91.29±5.73
Sep. Lat. FFT	K-Fold	1024	5e-4	100.00±0.00	0.00±0.00	100.00±0.00	100.00±0.00
Sep. Lat. FFT	K-Fold	512	5e-4	100.00±0.00	0.00±0.00	100.00±0.00	100.00±0.00

It is quickly evident that high learning rates promote better models, which is a great lead for future studies. FFT analysis outperformed the raw data analysis, with higher F1 Scores, AUCs, and smaller FPRs. The separation methodology applied improved models in the lateral axis analysis, but worsened in the vertical axis, which can indicate the creation of a BIAS during the separation.

RESULT COMPARISON WITH BIBLIOGRAPHY

Garcia et al. (2021) performed a similar study over the same dataset, creating a CNN instead of a MLP, which turns slices of the time series signal into visual information through methodologies like Gray-scale encoding, compresses the numeric information of the image to lower dimensions and reconstructs it in the same network. This allows the network to train solely on healthy data, since any faulty data would lead to poor reconstruction of the slice of data. In the study, the latter authors achieved a remarkable model of 85±02% TPR, 01±00% FPR, 91±01 F1 Score and 92±01% AUC, which is close to what the developed regular NN models achieved. The idea of using regular Neural Networks was to simplify the analysis and take advantage of already known faulty modes of a helicopter, which can be simulated in a controlled environment with safety.

CONCLUSIONS

Neural networks and Artificial Intelligence are modern technologies that have plenty of applications in the engineering industry. By using a helicopter vibration database with healthy and faulty samples from an Airbus, models were trained in two methodologies, one in the time domain and other in the frequency domain. An attempt to separate the samples in the vertical axis and lateral/longitudinal axis of vibration was made, leading to better results in the lateral axis but worse results in the vertical axis. This study proposes the application of neural network

models in fault detection and prevention, demonstrating its effectiveness if correctly trained, following different architectures and methodologies.

The best NN models trained can be used to create a real-time analysis in helicopters where pilots get constant feedback on helicopter health based on vibrational patterns. Evidently, more techniques must be applied to further improve the diagnostic provided by the NN, making it more reliable and of easy access, always prioritizing safety. More safety layers also can be used to avoid false alarms, for example, a computer can store a pre-defined number of previous diagnostics and alert the pilot if the number of anomalous diagnostics reach a certain threshold.

ACKNOWLEDGMENTS

The authors would like to thank the PRPq - Pró-Reitoria de Pesquisa - from the Universidade Federal de Minas Gerais for supporting this research paper.

REFERENCES

[1] Bagnall, A., Lines, J., Bostrom, A., Large, J. and Keogh, E. (2016). The great time series classification bake off: a review and experimental evaluation of recent algorithmic advances. Data Mining and Knowledge Discovery, 31(3), pp.606–660. doi:https://doi.org/10.1007/s10618-016-0483-9.

[2] Bramwell, A.; Done, G.; Balmford, D. (Ed.). Bramwell's Helicopter Dynamics (Second Edition).AIAA, Second edition, 2000. pp. 314-318.

[3] ETH Zürich. Airbus Helicopter Accelerometer Dataset. 2020. Available from Internet: <https://doi.org/10.3929/ethz-b-000415151>.

[4] Garcia, G.R., Michau, G., Ducoffe, M., Gupta, J.S. and Fink, O. (2021). Temporal signals to images: Monitoring the condition of industrial assets with deep learning image processing algorithms. Proceedings of the Institution of Mechanical Engineers, Part O: Journal of Risk and Reliability, 236(4), pp.1-11. doi: https://doi.org/10.1177/1748006x21994446.

[5] Google (2024a). Classification: Accuracy, recall, precision, and related metrics. [online] Google for Developers. Available at: https://developers.google.com/machine-learning/crash-course/classification/accuracy-precision-recall.

[6] Google (2024b). Classification: ROC Curve and AUC [online] Google for Developers. Available at: https://developers.google.com/machine-learning/crash-course/classification/roc-and-auc.

[7] Ismail Fawaz, H., Forestier, G., Weber, J., Idoumghar, L. and Muller, P.-A. (2019). Deep learning for time series classification: a review. Data Mining and Knowledge Discovery, 33. doi:https://doi.org/10.1007/s10618-019-00619-1.

[8] Kinsley, H.; Kukieła, D. Neural Networks from Scratch in Python. Available from Internet: <https://nnfs.io>: Sentdex, 2020.

[9] Prouty, R.W. Even More Helicopter Aerodynamics. Phillips Business Information, 1993.

[10] Venkatesan, C. Fundamentals of Helicopter Dynamics. CRC Press, 1 Ed., 2015. p.22.

Proceedings IRF2025: 8th International Conference on Integrity-Reliability-Failure
In Engineering, Materials, Manufacturing and Biomechanics. Porto 15-18 July 2025
DOI: https://doi.org/10.24840/978-972-752-323-8

PAPER REF: 22397

NUMERICAL SIMULATION AND OPTIMIZATION OF BALLISTIC PROTECTION STRUCTURES

Giovanni Garofalo(*), Patrice Longère(*), Kamel Moussaoui(*)
Institut Clément Ader, CNRS, INSA, ISAE-SUPAERO, IMT Mines Albi, Université de Toulouse
(*)*Email:* giovanni.garofalo@isae-supaero.fr

ABSTRACT

The complexity of protection systems has gradually evolved into sophisticated, multi-layered and multi-material solutions to deal with changing levels of threat. Their design requires a numerical optimization. In this context, the present preliminary work focuses on the comparison of different numerical algorithms for the optimization of the mechanical properties of an armor plate perforated by small munitions.

Keywords: Ballistics, simulation, optimisation, ISIGHT, ABAQUS.

INTRODUCTION

Ballistic problems are related to high-speed impacts on structures that can cause irreversible damage and further failures. They include, but are not limited to, impacts of ammunition on armored vehicles, hail on aircraft, and debris/micro-meteorite on satellites. The complexity of ballistic protection systems has progressively evolved from a monolithic configuration into sophisticated, multi-layered and multi-material solutions, aiming to cope with ever-changing threat levels. Their design requires a numerical optimization. In this context, this preliminary work is concerned with the comparison of different numerical algorithms for the optimization of the mechanical properties of an armor plate perforated by small munitions, see Figure 1 and related literature (Cosquer et al., 2023).

RESULTS AND CONCLUSIONS

Numerical simulations are carried out using the commercial finite element computation code Abaqus and optimizations using the numerical environment Isight. The initial-boundary value problem is the impact of a small munition onto a metallic plate. The behaviour of the plate material is described using Johnson-Cook models for plasticity and fracture, see (Johnson and Cook, 1983) and (Johnson and Cook, 1985). We here consider Johnson-Cook models material coefficients A and D1 that respectively represent the initial yield stress and fracture strain at given temperature, strain rate and stress triaxiality ratio (for the latter). For high-enough initial velocity V_{init}, the munition perforates the plate and has a residual velocity V_{res}, see Figure 1.

The optimization problem consists in finding the parameters A and D1 giving a residual velocity V_{res} with the constraint $C=A \cdot D1$. Three numerical optimization algorithms available in Isight are compared: (i) Downhill Simplex, (ii) NLPQLP, and (iii) Hooke-Jeeves. Starting with the same initial values for A and D1, they are expected to converge toward the reference values A and D1 used to carry out the numerical simulation giving the residual velocity V_{res}, see Figure 2.

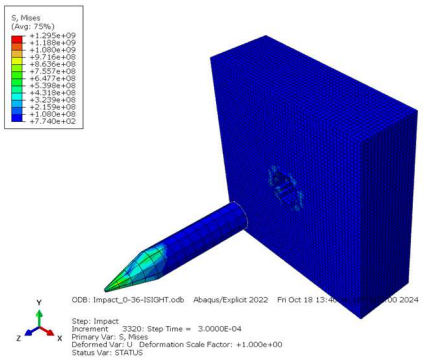

Fig. 1 - Perforation simulation of an aluminium plate.

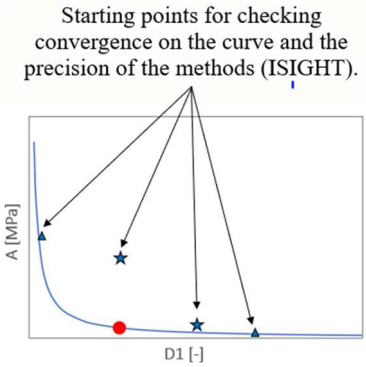

Fig. 2 - Parameters to calibrate.

The results of the optimisation are summarized in Figure 3. All employed algorithms demonstrate convergence toward the residual velocity V_{res}. Values of the parameters A and D1 depend on the specified precision range. The non-gradient-based optimization method Downhill Simplex is the most precise, even though the iteration number is high. The gradient-based method NLPQLP provides less precise results, but it needs fewer iterations. At last, the Hooke-Jeeves method requires a higher number of iterations, while not being the most precise.

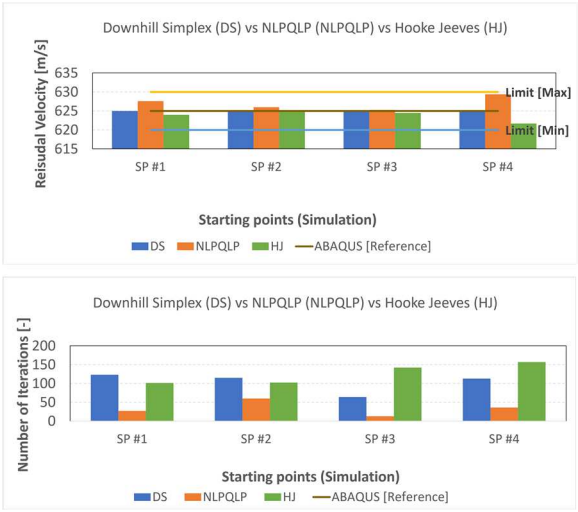

Fig. 3 - Optimization results. SP #i stands for starting point #i.

Further work is needed to refine the process and improve consistency in matching the desired parameters. The computation time itself has not yet been factored into the analysis and should be considered in future studies to provide a more comprehensive evaluation.

REFERENCES

[1] Johnson G.R., Cook W.H. (1983), A constitutive model and data for metals subjected to large strains, high strain rates and high temperatures, Proceedings of the 7th International Symposium on Ballistics.

[2] Johnson G.R., Cook W.H. (1985), Fracture characteristics of three metals subjected to various strains, strain rates, temperatures and pressures, Engineering Fracture Mechanics, 21, pp. 31-48, 1985.

[3] Cosquer Y., Longère P., Pantalé O., Gailhac C. (2023), Experiment/simulation correlation-based methodology for metallic ballistic protection solutions, Defence Technology, 29, pp. 24-38.

Proceedings IRF2025: 8th International Conference on Integrity-Reliability-Failure
In Engineering, Materials, Manufacturing and Biomechanics. Porto 15-18 July 2025
DOI: https://doi.org/10.24840/978-972-752-323-8

PAPER REF: 22412

REPEATED DYNAMIC TESTS AND NUMERICAL ANALYSES OF MULTI-SPAN OLD REINFORCED CONCRETE BRIDGE

Michal Venglar(*), Milan Sokol, Katarina Lamperova, Martin Marton

Slovak University of Technology in Bratislava, Faculty of Civil Engineering, Department of Structural Mechanics Radlinskeho 11, SK-810 05, Bratislava, Slovakia
(*)*Email:* michal.venglar@stuba.sk

ABSTRACT

Bridges are essential for road and railway networks, and their closure can cause significant economic losses. Regular maintenance, including non-destructive testing, is crucial for effective bridge management. However, due to budget constraints, the condition of bridges in Slovakia is deteriorating. This study focuses on a multi-span reinforced concrete bridge built in the 1980s, where traffic had to be controlled due to its deteriorating condition. Repeated dynamic testing was performed to assess the dynamic characteristics and structural integrity of the bridge. The results highlight the importance of repeated measurements and advanced numerical modelling for evaluating the health of aging infrastructure while minimizing traffic disruption.

Keywords: Operational modal analysis, FE model updating system identification, repeated measurements.

INTRODUCTION

Bridges are especially important part of the road or railway network. Due to this fact, any closure can lead to a lot of economic losses (Carvalho et al., 2017). Periodic and careful maintenance covering not only visual inspections, but also non-destructive testing or monitoring can have a positive effect on bridge management and can save money in the future (Rodrigues and Duvnjak, 2021). Nowadays, there is a lot of possibilities how to test the structure and an investigation of dynamic response can be included among non-destructive testing (Horvath et al., 2023). Besides the approaches using new technologies in testing and monitoring, researchers are designing in-depth numerical reliability-oriented assessment methods for bridge systems (Apostolidi et al., 2022) as a hopeful practice. Testing or monitoring has no sense itself and because of that various damage detection methods are currently developed or tested (Jarosinska and Berczynski, 2021; Akahoshi et al., 2023)

On the contrary, due to the insufficient budget for maintenance or the lack of specialists, the "health" of bridges in Slovakia is deteriorating. The similar situation occurred on a multi-span reinforced concrete bridge which was built in the 80s of the 20th century. According to the assessment, the traffic on the bridge had to be decreased and controlled by the traffic lights. This state is provisional, and the repeated measurements were done to have a comprehensive information about the change in the state.

This study presents the findings of repeated dynamic testing of the multi-span reinforced concrete bridge, with the objective of identifying its dynamic characteristics and structural integrity. The bridge, which has been in service for several decades, was subjected to six separate rounds of dynamic testing using high-precision accelerometers to capture its dynamic

responses under real traffic conditions. Due to the necessity of maintaining operational traffic throughout the testing, an operational modal analysis (OMA) was conducted to assess the bridge's dynamic properties without requiring traffic interruption.

(a) (b)

Fig. 1 - The multi-span reinforced concrete bridge: a) side view with Vajnorska street on the right; b) the restricted traffic operation.

The tests were designed to monitor the natural frequencies, mode shapes and damping ratios of the bridge, providing a comprehensive understanding of its dynamic behaviour. A highly detailed numerical model of the bridge was developed using the Finite Element Method (FEM). This model was used to simulate the bridge response to dynamic loads, comparing the numerical results with the measured data to validate the accuracy of the numerical model.

NUMERICAL MODEL

The foundations of the bridge were modelled using shell elements with a height of 1,5 m, which corresponds to the height of the cup foundations. The columns are modelled using beam elements. Height and width of the cross-section is 0,7 m. Due to the gradient of the bridge deck (Figure 1 a)); the columns have a variable height. The axial distance of the columns (violet) in the transverse direction is 2,8 m (Figure 2).

The superstructure of the bridge is modelled in detail (Figure 2). All of its elements, such as the cross girders (blue), beams (red), carriageway (orange), sidewalks (pink), and grouts (green), are created with volumetric elements. In the cross-section of the superstructure, we can see 11 precast beams (type KA-67) placed on the crossbar. The joint between the beams is filled with volumetric element, which is a cast-in-place concrete. At the edges of the bridge, the sidewalks are also formed with the same type of element. The carriageway is modelled in the joint and fixed to the girders at all common points. The cross girder is rigidly connected to the columns at four points. The abutments are modelled by volumetric elements and are flexibly supported by springs in all directions, as well as the foundations under all columns.

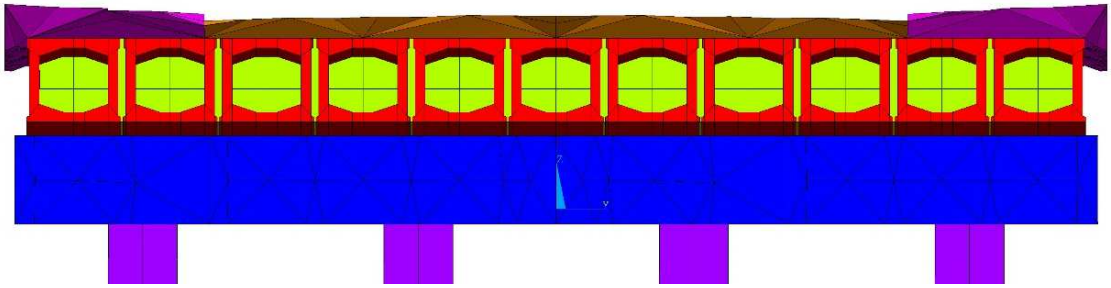

Fig. 2 - The cross-section of the bridge deck.

MEASUREMENTS

Between 2020 and 2024, several measurements were carried out in order to monitor the deteriorating "structural health" of the bridge. The measurements included measurements of the strains at the bottom edge of the eleven beams (type of KA-67) in the chosen span (span. no. 3 in Figure 3) during common operation (as mentioned before traffic is restricted). Vertical deflections over time were also recorded using interferometric radar in the same span. However, the main focus was devoted to the measurement of the ambient vibration and the identification of the first natural frequencies. Figure 3 shows the positions of the accelerometers on the bridge deck according to the initial modal analysis performed on the FE model described in the previous chapter. The sensors oriented perpendicularly to the longitudinal axis of the bridge in the horizontal direction (Y direction) are marked in red in order to identify mode shapes in that direction. The vertical sensors marked in green in order to identify vertical bending and torsional mode shapes. Two sensors were also located in the direction along the bridge (X direction) are marked in blue. In total, 26 sensors were deployed.

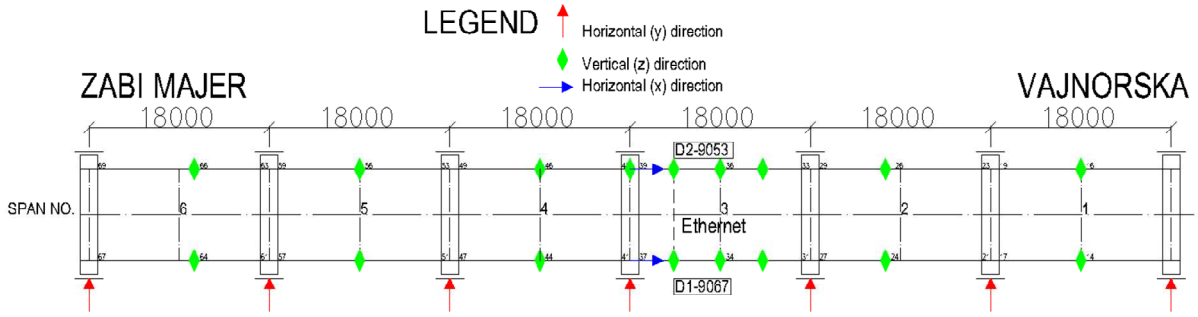

Fig. 3 - Placement of the accelerometers and devices of measuring system (dimensions in millimetres).

Due to the excessive damage of the 7th girder, the third span was measured in more detail (Fig. 3) and therefore there was a greater concentration of vertical sensors. All high sensitivity accelerometers PCB 393B31 were connected to two acquisition devices (D1 and D2 marked on Fig. 3). Connection and synchronisation between them were ensured by ethernet cable and the device D1 was used also for the storage of recorded data.

Thermocouples located in span no. 4 and no. 3 close to the accelerometers in vertical direction were connected to the device D1. As a result, the correlation between temperature and modal parameters could be investigated.

Ambient vibrations were recorded in data sets of 300 s or 600 s to fulfil minimum length of time series according to (Brincker and Ventura, 2015). The necessity of minimum length is caused by the fact that only output (response of structures) is measured. On the contrary, the main advantage of OMA is no need to traffic restriction or stop the traffic. Thanks to that, OMA could be done successfully, and the entire process is described in the following section.

OPERATIONAL MODAL ANALYSIS (OMA)

OMA was performed in ModalVIEW software using previously pre-processed data by own-developed script (Sokol et al., 2020). Due to the hardware restrictions, 2048 samples per seconds were used during measurements. 15 Hz were chosen as the upper limit for filtering in order to identify enough natural frequencies and appropriate mode shapes. According to the upper limit, data could be downsampled in order to analyse data quicker and to store lower amounts of data.

Example is depicted on Figure 4 where bridge deck is moving in the horizontal direction (Y direction) as the first mode shape with the natural frequency of 2,44 Hz. It can be seen that interpolation between measured points and intermediate points was not able to correctly set by the ModalVIEW software. As a result, the amplitudes from the intermediate points were lower as in the reality and the values obtained by numerical model. To compare numerical results and identified from the measurements using MAC (Beutelhauser, Venglar and Honti, 2023), only amplitudes from 26 measured points were used (interpolated values were excluded).

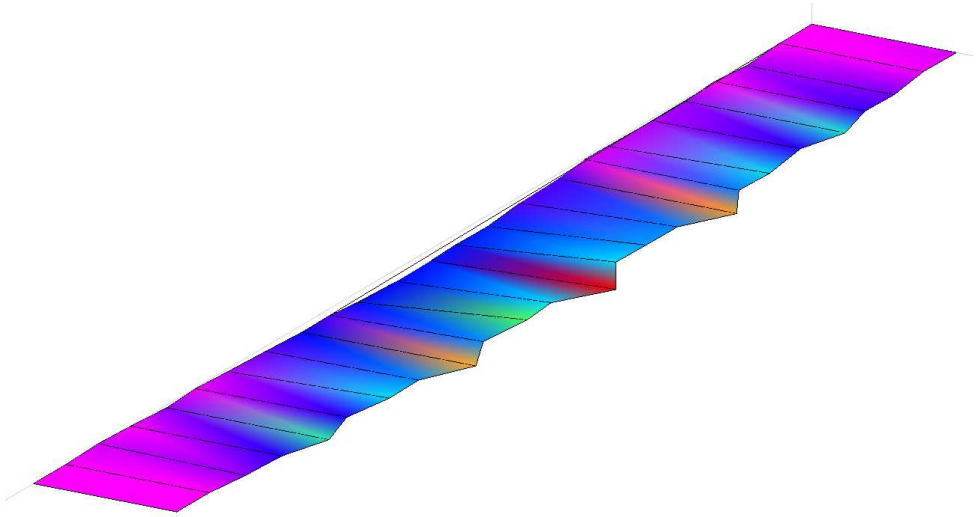

Fig. 4 - The first mode shape identified using OMA (appropriate natural frequency 2,39 Hz) – data from 04/2021.

RESULTS

Similarly to the data from 2021, data from years 2020, 2022 and 2023 were analysed. The first natural frequency from various campaigns is summarised in Table 1. There is also information about the air temperature. It can be seen that the first natural frequency corresponding to the mode shape in horizontal direction is increasing with the increasing temperature and vice versa. This environmental impact can disguise the real damage or in this case, decreasing temperature can signalise the damage that is not present or real, as mentioned in (Wenzel, 2009).

Table 1 - Natural frequencies (in Hz) for the first mode-shape identified during repeated measurements.

MODE NO.	Measurements (month/ year) and air temperature						
	12/2020	04/2021	08/2021	11/2021	06/2022	07/2023	12/2023
	3°C	20°C	29°C	6°C	25°C	19°C	4°C
1	2,34	2,39	2,44	2,36	2,45	2,37	2,35

It is necessary to eliminate the environmental impact (temperature effect on modal parameters) before applying model updating methods in order to prepare a verified and validated numerical model. At the moment, there is not possible to statistically evaluate the impact and due to that there is a plan to monitor the bridge in real time to obtain larger statistical sample. At this stage of the research, the difference between the measured value and the results from the FE model for the first natural frequency is 0,1 Hz (2,39 Hz for the measurement and 2,29 Hz for the initial FE model) with the MAC value of 0,97 (that is showing quite good agreement even before the updating process).

CONCLUSIONS

The lack of maintenance has necessitated restricted operation and more detailed monitoring or testing. The results indicate that the "health" of the bridge during restricted operation over the past three years has remained unchanged. This suggests that the repeated measurement campaigns have been successful.

The findings of this study provide valuable insight into the dynamic performance of an ageing reinforced concrete bridge, emphasising the importance of repeated measurements and evaluation.

The highly detailed FE model can be considered a valuable step in the overall assessment process. In this case, the FE model was used solely as a base for the measurements. After accounting for temperature effects, it will be used to update selected parameters through particle swarm optimisation as a part of the ongoing research project.

ACKNOWLEDGMENTS

Authors thank the Slovak Research and Development Agency (SRDA) for providing grant from research program APVV Nr. 0431-22 as well as this paper has been supported by the Grant Agency of the Ministry of Education, Science, Research and Sports of the Slovak Republic VEGA No. 1/0230/22.

REFERENCES

[1] Carvalho H, Hallal Fakury R, Leite Vilela PM. Structural integrity assessment and rehabilitating of Hercilio Luz bridge. Frattura ed Integrità Strutturale, 2017, 11, pp.93-104.

[2] Rodrigues H, Duvnjak I. Editorial on the Special Issue: Advanced Structural Health Monitoring: From Theory to Applications. Applied Sciences, 2021, 11, pp.1-3.

[3] Horvath P, Hajdu F, Szalai P, Papp, C, Apagyi A et al. Investigation of Traffic Induced Dynamic Response of a Bridge. Strojnícky časopis - Journal of Mechanical Engineering, 2023, 73, 1, pp.85-102. ISSN 2450-5471.

[4] Apostolidi E, Somodikova M, Strauss A, Novak D, Pukl R et al. Modelling of Nonlinear and Uncertain Behavior of Concrete Bridges. Proceedings of the 1st Conference of the European Association on Quality Control of Bridges and Structures. Lecture Notes in Civil Engineering. Cham: Springer International Publishing, 2022, pp. 244-251. ISBN 978-3-030-91876-7.

[5] Jarosinska M, Berczynski S. Changes in Frequency and Mode Shapes Due to Damage in Steel-Concrete Composite Beam. Materials, 2021, 14, 21. ISSN 1996-1944.

[6] Akahoshi K, Hayashi G, Chen Y, Yamaguchi T. Damage identification of corroded arch bridge using vibration characteristics and rotational angle. Life-Cycle of Structures and Infrastructure Systems. London: CRC Press, 2023, pp.562-569. ISBN 9781003323020.

[7] Brincker R, Ventura C. Introduction to operational modal analysis. Chichester, England: Wiley, 2015. ISBN 978-1-118-53516-5.

[8] Sokol M, Venglar M, Lamperova K, Marfoldi M. Performance Assessment of a Renovated Precast Concrete Bridge Using Static and Dynamic Tests. Applied Sciences, 2020, 10, 17. ISSN 2076-3417.

[9] Beutelhauser D, Venglar M, Honti R. Case study - System identification of an old reinforced concrete bridge. AIP Conference Proceedings, 2023, 2887, 020035.

[10]Wenzel H. Health monitoring of bridges. Chichester: Wiley, 2009. ISBN 978-0-470-03173-5.

Proceedings IRF2025: 8th International Conference on Integrity-Reliability-Failure
In Engineering, Materials, Manufacturing and Biomechanics. Porto 15-18 July 2025
DOI: https://doi.org/10.24840/978-972-752-323-8

PAPER REF: 22435

TRANSPORTATION OF SMALL PARTS ON A PLATFORM EXCITED IN TWO PERPENDICULAR HORIZONTAL DIRECTIONS BY SINUSOIDAL VAWES WITH A PHASE SHIFT

Kristina Liutkauskienė[1(*)], Ramūnas Česnavičius[1], Sigitas Kilikevičius[2]

[1]Department of Mechanical Engineering, Kaunas University of Technology, Kaunas, Lithuania
[2]Department of Transport Engineering, Kaunas University of Technology, Kaunas, Lithuania
[(*)]*Email:* kristina.liutkauskiene@ktu.lt

ABSTRACT

This paper proposes a vibrational transportation method of small parts on a platform excited in two perpendicular horizontal directions by harmonic sinusoidal excitation with a phase shift. To investigate the characteristics of the transportation process, dynamic and mathematical models were developed. The mathematical model was implemented by developing simulation codes using MATLAB, and simulations of the process were carried out. The simulation results showed that parts can be transported due to the asymmetry caused by the phase shift between the perpendicular sinusoidal waves. Moreover, the transportation characteristics can be controlled by modifying the excitation parameters. The influence of the input parameters on the transportation characteristics was determined. The method can be applied across various industries, especially those related to high technologies that implement tasks related to feeding, position or automatic assembly of delicate objects.

Keywords: Transportation, control, vibrations, asymmetry.

INTRODUCTION

The transportation of small parts is relevant for various industries, especially those related to high technologies that implement tasks related to feeding, position or automatic assembly of delicate objects. In practice, parts are transported, positioned and manipulated through various active and passive methods. Active approaches rely on sensory approaches [1], feedback systems [2], and computer vision systems [2]. However, these methods are expensive, complex, and require more energy. Therefore, passive methods in certain situations might be more efficient and cost effective. These methods are achievable through an asymmetry of a mechanical transportation system [3]. In practice, this is achieved using transportation surfaces exposed to vibrations with a sawtooth waveform [4] or asymmetric vibrational trajectories [5]. This paper proposes a vibrational transportation method transportation of small parts on a platform excited in two perpendicular horizontal directions by harmonic sinusoidal excitation with a phase shift. In this case, the effect of transportation is achieved through the asymmetry caused by the phase shift between the perpendicular sinusoidal waves.

DYNAMIC AND MATHEMATICAL MODELS OF MOVEMENT OF A PART ON A HORIZONTALLY OSCILLATING PLATFORM

Dynamic and mathematical models were developed to study the transportation of small parts placed on a horizontal platform subjected to sinusoidal vibrations in two perpendicular in-plane directions. To easily and quickly move parts from one place to another, it is necessary to

determine the movement trajectories of the part on the horizontal platform excited in two perpendicular horizontal directions by harmonic sinusoidal excitation with a phase shift. When the harmonic excitation amplitude and frequency are the same in both directions, then any point on the platform follows the same trajectory. Figure 1 shows the dynamic motion model of the part on the platform as it moves in a circular path. The system consists of a fixed base (1) (Figure 1) on which a horizontal moving platform (2) is placed. At the intersection of two horizontal stationary axes χ and ψ is origin of immovable base coordinate system Σ. The coordinate system of the moving platform is named Σ_{pl} and it moves with the platform.

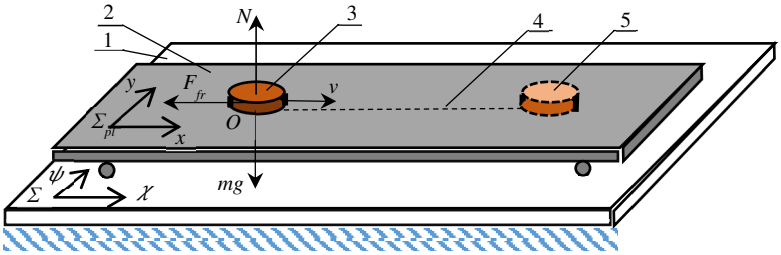

Fig. 1 - Dynamic model of transportation on a platform subjected to circular trajectory of planar oscillations: (1) stationary base; (2) mobile platform; (3) part in initial position; (4) part in final position; (5) distance traveled Δd.

As the platform is excited with the same amplitude in both directions, but with phase shift between the harmonic waves, the equations of motion of the platform are written as follows:

$$\begin{cases} \chi = \chi_0 + A\sin(\omega t) \\ \psi = \psi_0 + A\sin(\omega t - \tau) \end{cases} \tag{1}$$

where t is excitation time, A is the excitation amplitude in x and y directions, ω is the frequency of excitation, and τ is the phase shift between the harmonic waves along the x and y axes (in this case it is equal $\tau = \pi/2$ for circular motion), χ_0 and ψ_0 - platform initial coordinates.

When formulating the equations of motion of a part placed on a platform (Figure 1, (3)), for simplicity, it is assumed that the part is flat, and the mass of the part is concentrated at the center of mass. Also, an assumption is made that the coefficient of dry friction between the part and the platform is constant.

Then equation of motion of the small part, placed on a horizontally vibrating platform:

$$\begin{cases} \ddot{x} = A\omega^2 \, sin(\, \omega t) - \frac{\mu g \dot{x}}{\sqrt{\dot{x}^2 + \dot{y}^2}}, \\ \ddot{y} = A\omega^2 \, sin(\, \omega t + \tau) - \frac{\mu g \dot{y}}{\sqrt{\dot{x}^2 + \dot{y}^2}}. \end{cases} \tag{2}$$

The trajectory of the movement of the part on the platform varies depending on the excitation frequency, friction conditions, and excitation amplitude. By changing these parameters, it is possible to control the velocity of the transfer of the part onto the platform. The average sliding velocity of the part is calculated by dividing the transport path by the transport time:

$$v = \Delta d / \Delta t \tag{3}$$

where Δd is the distance and Δt is the travel time. The equations of motion express the position and velocity vectors of the part with respect to the coordinate system Σ_{pl}.

RESULTS OF SIMULATION

In order to study the influence of the input parameters μ, ω, and A on the movement characteristics of the part, simulations were carried out using software developed for this purpose. The software was written using the MATLAB (Mathsoft, Cambridge, MA, USA) programming language. The equations of motion were solved using the ode45 solver based on the Runge-Kutta (4, 5) formula. All simulated cases are assigned a value of $g = 9.81$ m/s^2.

When a horizontal platform is excited in a circular path, the part initially moves a certain distance in a wavy path (Figure 2, (b)). Later, the wavy trajectory turns into a spiral one. However, the part eventually starts to move around one point, i.e. does not move further forward and the part is no longer transported. The location of the steady movement of the part is perfectly visible in the Figure 2, (a), then the part no longer moves in the x and y directions but only oscillates around the equilibrium point (the vertical red line and the letter E mark the place where the part is no longer transported). The characteristics of the movement and the nature of the trajectory depend on the parameters of the system such as the excitation amplitude, frequency and dry friction coefficient.

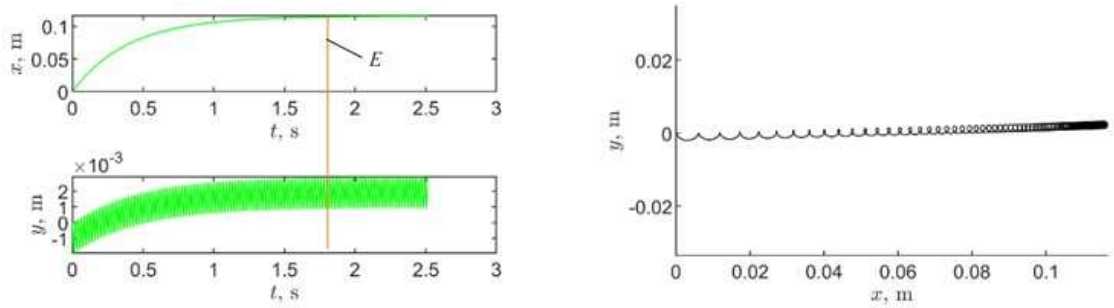

(a) (b

Fig. 2 - Trajectory of movement of the part on the platform, when $\mu = 0.15$, $A = 0.001$ m, $\omega = 300$ rad/s, $\tau = \pi/2$: (a) displacement of the part with respect to time in the x and y directions; (b) trajectory of the part to be transported.

The velocity of transportation is a very important parameter from the practical point of view. Therefore, in order to determine the average velocity of the part on the platform, it is necessary to determine the time during which the part reaches the equilibrium position. An additional program code was developed that calculated the centers of arcs and circles for each oscillation cycle and compared the coordinates of the differences between two adjacent points. When the difference between the center points of the adjacent circles was $\Delta k < 2 \cdot 10^{-4}$ m, the code was terminated and the platform excitation time was recalculated.

During the study, it was found that by increasing the excitation amplitude and frequency, the average transport velocity increases linearly (Figure 3 (a and b)). However, when the excitation frequency is high, the friction coefficient does not have a significant effect on the part's sliding velocity (Figure 3 (c)). Thus, when a horizontal platform is excited in two perpendicular directions by sinusoidal waves of the same amplitude with a phase shift, the excitation frequency and amplitude have the greatest influence on the average transportation velocity of the part.

CONCLUSIONS

A method of transporting small parts on a platform that is excited in two perpendicular horizontal directions by harmonic excitation has been proposed, where the transportation effect is achieved through the asymmetry caused by the phase shift between the perpendicular sinusoidal waves.

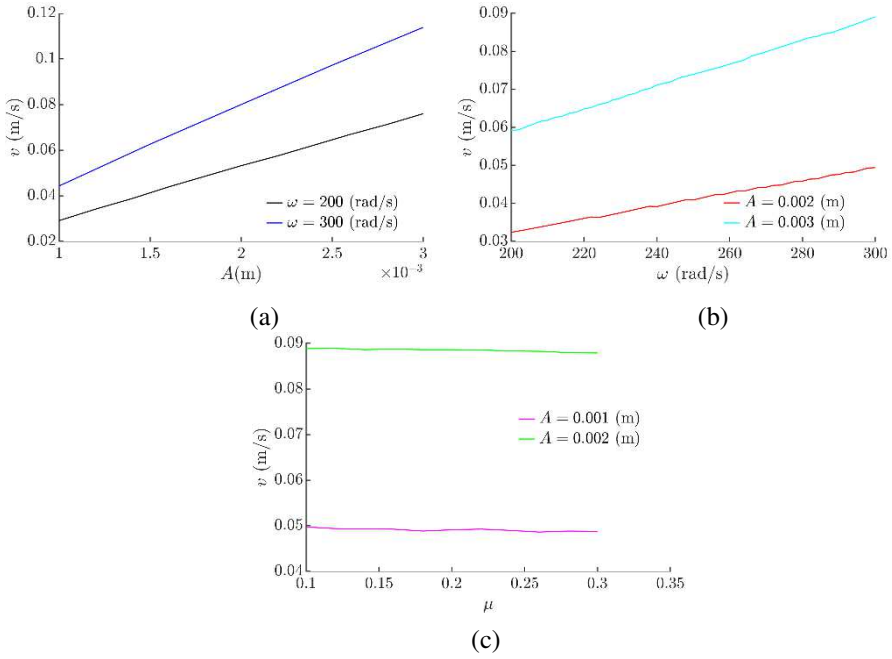

Fig. 3 - Average transportation velocity depending on: (a) excitation amplitude, where $\mu = 0.15$; (b) excitation frequency ω, where $\mu = 0.15$; (c) friction coefficient μ, where $\omega = 300$ rad/s.

Dynamic and mathematical models of small part transportation were developed. Modelling codes were developed using MATLAB, and simulations of the transportation process were performed. It has been found that the excitation frequency and amplitude have the greatest influence on the average transportation velocity of the part. When the excitation amplitude or frequency increases, the average transportation velocity increases linearly. When the excitation frequency is high, the friction coefficient does not have a significant effect on the sliding velocity of the part.

REFERENCES

[1] Tanabe K, Shiota M, Kusui E, Iida Y, Kusama H, Kinoshita R, Tsukui Y, Minegishi R, Sunohara Y, Fuchiwaki O. Precise Position Control of Holonomic Inchworm Robot Using Four Optical Encoders 2023;14:375. https://doi.org/10.3390/mi14020375.

[2] Klemiato M, Czubak P. Control of the transport direction and velocity of the two-way reversible vibratory conveyor 2019;89:1359-73. https://doi.org/10.1007/s00419-018-01507-8.

[3] Zhu M, Zhang G, Zhang L, Han W, Shi Z, Lv X. Object Segmentation by Spraying Robot Based on Multi-Layer Perceptron 2022;16:232. https://doi.org/10.3390/en16010232.

[4] Kilikevičius S, Liutkauskienė K, Česnavičius R, Keršys A, Makaras R. Investigation of the motion characteristics of parts on a platform subjected to planar oscillations 2023;13:9576. https://doi.org/10.3390/app13179576.

[5] Hartig J, Howard HC, Stelmach TJ, Weimer AW. DEM modeling of fine powder convection in a continuous vibrating bed reactor 2021;386:209-20. https://doi.org/10.1016/j.powtec.2021.03.038.

Proceedings IRF2025: 8th International Conference on Integrity-Reliability-Failure
In Engineering, Materials, Manufacturing and Biomechanics. Porto 15-18 July 2025
DOI: https://doi.org/10.24840/978-972-752-323-8

PAPER REF: 22459

DESIGN, SIMULATION AND EXPERIMENTAL VERIFICATION OF A DYNAMIC INERTIAL TABLE.

Jocinaldo Alves Pereira da Silva(*), Antônio Almeida da Silva, Márcio Diniz da Silva
Federal University of Campina Grande, Campina Grande, Brazil
(*)*Email:*jocinaldo.alves@estudante.ufcg.edu.br

ABSTRACT

Vibration isolation is crucial for experiments and measurements of dynamic systems. Among the options, a robust inertial table, supported by helical springs, may be a feasible and affordable solution. However, to guarantee stability and accuracy of tests an appropriate vibrational dimensioning is required. The objective of this work is to describe the necessary steps to design a 3.3-ton inertial table, suspended by helical springs, with rigid body modes under 2Hz. The process includes the choosing and characterizing of springs and the finite element models built to analyse the linear and nonlinear behaviours imposed by the vertical load. Modal analyses were performed to position the six rigid body modes (3 translational and 3 rotational axes) below target. Based on the simulation results the table was physically built and natural frequencies confirmed by experimental frequency response functions (FRF). The comparison between measured and simulated FRFs showed that the dynamic behaviours of the inertial table could be reliably predicted thanks to the use of FEM in the table design.

Keywords: Inertial table, vibration analysis, vibration isolation, modal analysis, linear static analysis, nonlinear static analysis, FEM.

INTRODUCTION

Structural engineering is essential for designing and constructing structures that can withstand loads, including extreme events such as earthquakes and strong winds, ensuring safety, durability, and efficiency. In civil engineering and structural dynamics, passive vibration control in structures subjected to transient loads is crucial for their integrity and performance. With advancements in computational modeling, it is possible to analyze dynamic behavior, validate results through experimental modal analysis, and implement strategies for vibration isolation.

RESULTS AND CONCLUSIONS

For the characterization of the springs, the first step is to perform an analytical analysis to calculate the stiffness modulus in Equation (1) of the springs, using theoretical formulas based on geometric parameters and materials provided by the manufacturer.

$$k = \frac{d^4 \cdot G}{8 \cdot n \cdot D^3} = \frac{16{,}4^4 \cdot 80 \cdot 10^3}{8 \cdot 7 \cdot 119^3} = 61{,}3\frac{N}{mm} \qquad (1)$$

Since the springs are identical, the theoretical stiffness modulus is the same for all of them, resulting in an equivalent stiffness constant, Equation (2).

$$k_{eq} = 4 \cdot k = 4 \cdot 61{,}3 = 245{,}2 \frac{N}{mm} \quad (2)$$

Based on the equivalent stiffness modulus and the inertia table mass of 3300 kg, the table's volume is estimated using the concrete density along with the mass of the steel components of the table. From this, the natural frequency of the table is estimated in Equation (3) and Equation (4).

$$\omega_n = \sqrt{\frac{k_{eq}}{M}} = 8{,}62 \frac{rad}{s} \quad (3)$$

$$f = \frac{\omega_n}{2\pi} = 1{,}37Hz \quad (4)$$

In a simplified analytical model, the table's natural frequency is calculated to be below 2 Hz. After characterizing the springs, a computational simulation of the inertia table is performed using the HyperMesh software. Initially, the springs were simulated separately to verify if they would withstand the applied loads. Subsequently, a simulation was conducted with the complete table model (Figure 1).

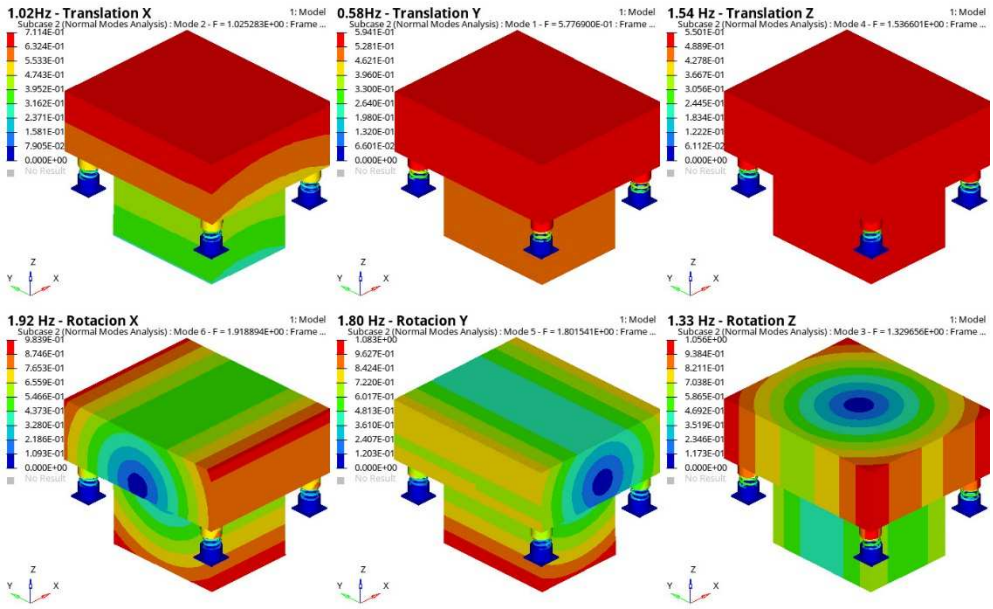

Fig. 1 - Simulation conducted with the complete table model.

In the image above, the results of the frequencies in all six axes are presented, and all of them are below 2 Hz.

REFERENCES

[1] Inman, Daniel J.; SINGH, Ramesh Chandra. Engineering vibration. Englewood Cliffs, NJ: Prentice Hall, 1994.

[2] Altair Engineering. Nonlinear quasi-static analysis. 2021. Disponível em: https://2021.help.altair.com/2021/hwsolvers/os/topics/solvers/os/analysis_nonlinear_quasi_static_c.htm. Acesso em: 24 jan. 2025.

Proceedings IRF2025: 8th International Conference on Integrity-Reliability-Failure
In Engineering, Materials, Manufacturing and Biomechanics. Porto 15-18 July 2025
DOI: https://doi.org/10.24840/978-972-752-323-8

PAPER REF: 22467

COST-EFFICIENT SEISMIC RETROFIT OF HIGH-VOLTAGE CURRENT TRANSFORMERS USING SEISMIC DAMPERS

Mohammad Ali Jafari[1(*)], Arash Yeganeh Fallah[1], Alireza Rahnavard[1], Amir Hossein Khalvati[2]

[1]Niroo Research Institute (NRI), Power Industry Structures Research Department, Tehran, I.R. of Iran
[2]Iran Islamic Azad University, Faculty member of West Tehran Branch, Tehran, I.R. of Iran
[(*)]*Email :* mjafari@nri.ac.ir

ABSTRACT

This paper analytically examines the seismic retrofitting of high-voltage current transformers in power transmission substations using various energy-absorbing dampers. The dampers studied include viscous, friction spring, rotational friction, yielding dampers, and wire-rope isolators. These dampers are considered in two scenarios: between the equipment and support structure, or at the base of the support structure. The best retrofitting option is selected based on efficiency and cost, presented as a prioritization index (PI). The results show that rotational friction dampers perform best when placed between the equipment and structure support.

Keywords: Power transmission substation, Current transformer, seismic damage, seismic retrofit, damper, wire-rope isolator.

INTRODUCTION

Power transmission substations are critical components of the power network. Their behavior and the damages they sustained during past earthquakes reveal their vulnerability. Most damage in high-voltage substations during earthquakes is due to porcelain insulator failure. Current transformers, particularly top-core types, are vital and have shown seismic vulnerability in past earthquakes (Bastami, 2008). Standards like IEEE-693 and IEEE-1527 provide guidelines for designing and improving substation equipment behavior against earthquakes. Extensive research has been conducted to evaluate this behavior. Recently, there is a trend to use seismic protection devices like isolators and dampers to improve equipment behavior (e.g., Alessandri et.al. 2015 and Cochran et.al. 2022). This paper presents an approach for retrofitting current transformers using dampers and suggests the best type through technical and economic analysis.

RESULTS AND CONCLUSIONS

This paper models a 400 kV current transformer weighing 1780 kgf and its support structure in SAP2000 software. It is dynamically evaluated using nonlinear time history analysis subjected to IEEE-matched earthquake ground motions (Takhirov et. al. 2017) for high seismic level (PGA=1g). The transformer is a top-core type with porcelain insulators, supported by a truss structure with steel angle sections. The model, prepared using the manufacturer's drawings, is validated based on the first mode frequency. Various dampers—viscous (FVD), friction spring (FSD), wire-rope isolator (WRI), V-type rotational friction (V-RFD), and yielding metallic (TADAS)—are used in two scenarios: on top of the support structure and at the. The dampers move vertically, causing a rocking isolation effect. Each damper is applied using the NLLink element with parameters provided by the manufacturers, which optimized.

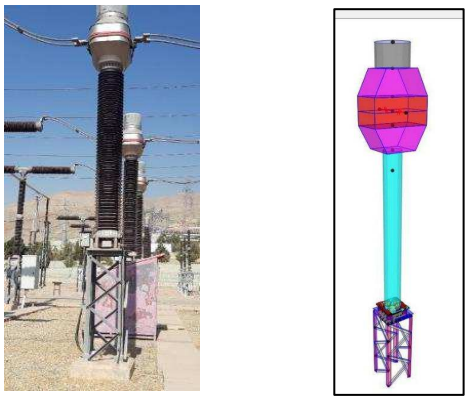

Fig. 1 - Picture of the current transformer and support structure (Left) and analytical model in SAP2000 (right).

In order to determine the best type of damper for retrofitting the equipment, the prioritization index (PI) for each option was calculated using equation (1):

$$PI = \sqrt{(\max(\frac{\Delta_{top}}{\Delta_{All}}, \frac{M_{ins}}{M_{All}}))^{w_1} \times (CR)^{w_2}} \quad (1)$$

Where, CR is the cost ratio, Δ_{top} and Δ_{all} represent the maximum displacement at the top of the equipment and its allowable value, respectively. M_{ins} and M_{all} are the maximum bending moment at the base of the insulator and its allowable value (according to IEEE-693), respectively. w_1 and w_2 are the relative weights, respectively. The cost ratio (CR) is the total cost of retrofitting, normalized to the price of the equipment and support structure. The PI values for the examined options are presented in Table 1.

Table. 1 - Prioritization Index (PI) values for various retrofitting options of the current transformer

Damper Type	FVD (top)	FVD (base)	FSD (top)	FSD (base)	WRI (top)	WRI (base)	RFD (top)	RFD (base)	TADAS (top)	TADAS (base)
PI	0.72	0.76	0.46	0.57	0.55	0.59	0.3	0.43	0.47	0.61

Based on the PI values in Table 1, the preferred retrofitting option is the V-type rotational friction damper, installed between the equipment and its support structure.

REFERENCES

[1] Bastami, M., Seismic Assessment of medium and high voltage power substation equipments, in the 14th World Conference on Earthquake Engineering. October 12-17, 2008: Beijing, China.

[2] Alessandri, S., Giannini, R., Paolacci, F., Malena, M. (2015). Seismic retrofitting of an HV circuit breaker using base isolation with wire ropes. Part 1: Preliminary tests and analyses. Engineering Structures, 98, pp. 251-262.

[3] Alessandri, S., Giannini, R., Paolacci, F., Amoretti, M., Freddo, A. (2015). Seismic retrofitting of an HV circuit breaker using base isolation with wire ropes. Part 2: Shaking-table test validation. Engineering Structures, 98, pp. 263-274.

[4] Cochran, R., Parker, E., Gille, S., Kempner Jr, L. (2022). Damping Devices for Seismic Protection of Substation Equipment. In Electrical Transmission and Substation Structures 2022 (pp. 508-523). Reston, VA: American Society of Civil Engineers.

[5] Takhirov, S., Fujisaki, E., Kempner, L., Riley, M., Low, B. (2017). Development of Time Histories for IEEE693 Testing and Analysis (Including Seismically Isolated Equipment). PEER Report No. 2017/10, Pacific Earthquake Engineering Research Center.

Proceedings IRF2025: 8th International Conference on Integrity-Reliability-Failure
In Engineering, Materials, Manufacturing and Biomechanics. Porto 15-18 July 2025
DOI: https://doi.org/10.24840/978-972-752-323-8

PAPER REF: 22480

NUMERICAL AND EXPERIMENTAL MODAL ANALYSIS OF A SMALL-SCALE WIND TURBINE BLADE

Vanessa da Nóbrega Porto de Moura[1(*)], Antônio Almeida Silva[1], Andersson Guimarães Oliveira[1], Rômulo Pierre Batista dos Reis[2]

[1]UFCG, Federal University of Campina Grande, Campina Grande, Brazil
[2]UFERSA, Federal Rural University of the Semi-Arid Region, Mossoró, Brazil
Email: vanessa.npmoura@gmail.com

ABSTRACT

Technological advancements and climate change have driven the transition to renewable energy sources, with wind energy emerging as one of the leading clean and sustainable alternatives. Increasing the size of wind turbine components, such as blades, has proven to be an effective strategy for increasing the energy power for each machine. However, this structural growth introduces challenges, including higher vibration levels that negatively affect performance, reduce turbine lifespan, and increase maintenance costs. This study presents an experimental and numerical modal analysis of a small-scale wind turbine blade. The objective was to perform a methodology to characterize the dynamic parameters of the wind blade structure and validate by numerical model. For the experimental analysis, triaxial electronic accelerometers, an impact hammer, and a National Instruments data acquisition system were used under free-free boundary conditions. The collected data were processed to generate frequency spectra (FFTs) and determine the structure's natural frequencies. Subsequently, a numerical simulation was performed, and the results were compared with the experimental data. The results showed good agreement between the methods, with relative errors below 5% for most analyzed modes. The accuracy of the numerical analyzes was significantly influenced by the proper control of geometric configurations and boundary conditions. The method demonstrates the continuous improvement of the geometric model and appropriate selection of materials can increase the accuracy of results, contributing to a deeper understanding of the dynamic behavior of wind turbine structures and the optimization of their performance and reliability.

Keywords: Experimental modal analysis, finite element method, wind turbine blades, failure modes.

INTRODUCTION

Wind energy, a rapidly expanding renewable energy source, plays a crucial role in the transition to sustainable energy matrices and in reducing dependence on fossil fuels. With the increase in energy demand and the challenges of climate change, the wind sector has promoted technological advances, such as increasing the length of towers and blades in order to improve the energy efficiency of turbines (Moraes, 2019). However, these innovations bring new structural challenges, such as high levels of vibration, which can compromise the efficiency and integrity of turbines (Awada *et al*., 2021).

Structural deflections, such as edgewise (in the plane parallel to the axis of rotation) and flapwise (in the perpendicular plane), are essential in the analysis of the vibrational behavior of blades, as they directly influence the operational efficiency and durability of the structure. Vibration monitoring, combined with modal analysis, allows the identification of problems

such as misalignments and failures, and is an essential strategy in predictive maintenance. The Finite Element Method (FEM) is widely used in modal analysis to evaluate vibrational properties and ensure structural integrity (Xu *et al*., 2021).

RESULTS AND CONCLUSIONS

In this study, an experimental modal analysis and a numerical simulation were performed using FEM on a VERNE 555 wind turbine blade from ENERSUD. The experimental analysis was performed with the blade in free-vibration condition, using ADXL 335 triaxial electronic accelerometers and a PCB 086C03 impact hammer. The data were acquired by a National Instruments acquisition system and NI DAQ Express software The geometric model initially proposed by Araújo *et al*. (2016), was updated and the geometry was imported into ANSYS® for discretization, using quadratic-order tetrahedral meshes, adjusted to balance computational accuracy and customization. The results identified the natural frequencies and the first modal shapes of the blade, evidencing greater deformations at the tip and smaller ones at the root. The vibrational modes demonstrate a combination of flapwise and edgewise deflections, with deflection in the edgewise direction predominating in modes 3 and 4. Figure 1 shows the vibrational modes of the blade.

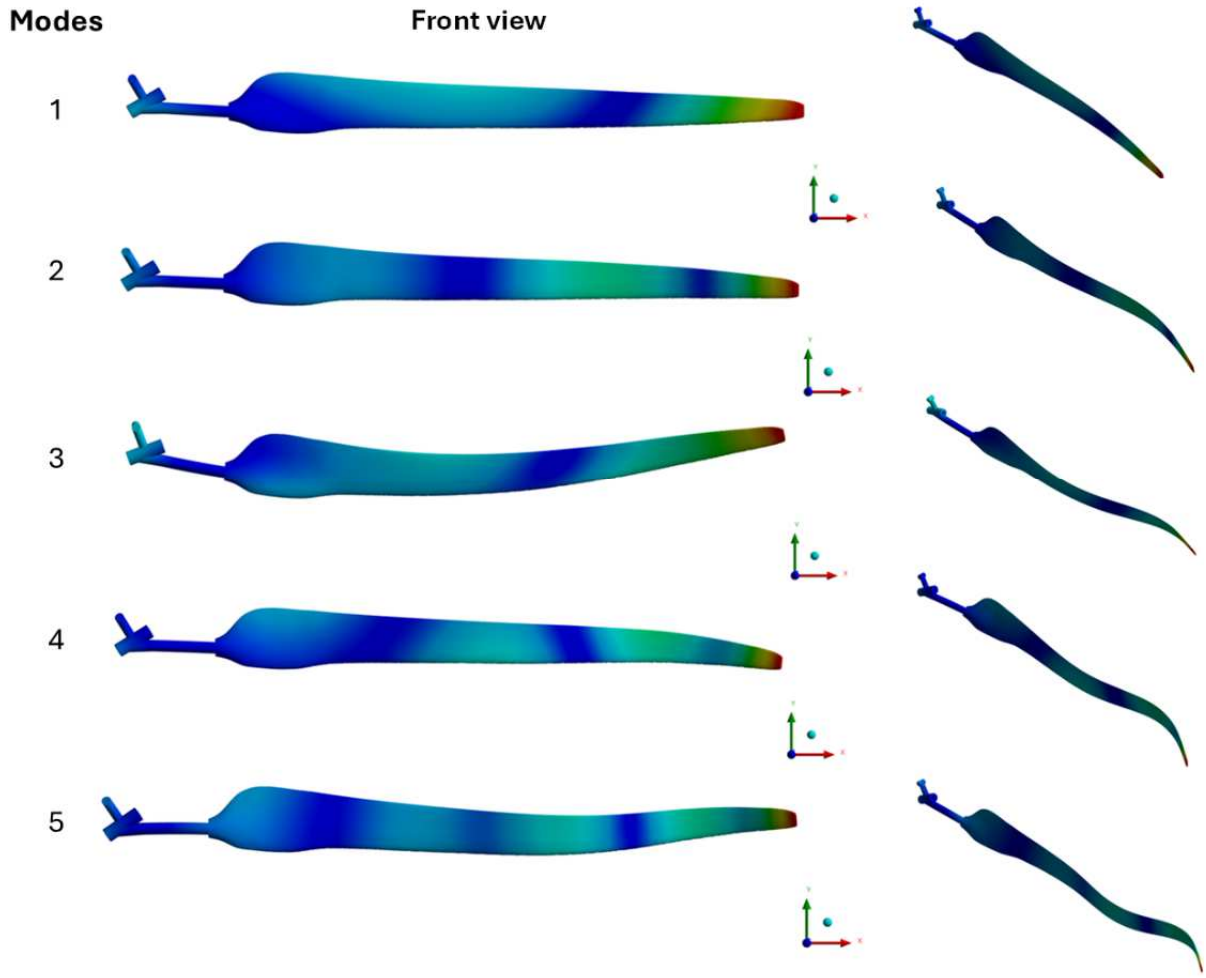

Fig. 1 - Representations of the first 5 vibration modes.

Table 1 shows a summary of the natural frequencies and vibration modes found in the numerical modal analyses and the respective relative errors between the numerical and experimental values.

Table 1 - Results of natural frequencies and vibration modes – free-free condition.

Modes	**Numerical Frequencies (Hz)**	**Experimental Frequencies (Hz)**	**Relative error (%)**
1	12.22	12.12	0.82
2	50.68	53.48	5.23
3	63.72	61.15	4.2
4	99.43	96.12	3.44
5	148.19	150.68	1.65

Considering all the parameters used in the simulation, it can be observed that the updates to the geometric model proposed by Araújo *et al*. (2016), as well as the appropriate choice of materials that make up the blade, directly influenced the accuracy of the results. The analysis of the natural frequencies revealed that, for most of the modes evaluated, the relative errors remained below 5%, which reinforces the effectiveness and suitability of the numerical model based on the Finite Element Method (FEM) to capture the global vibrational behavior of the blade. The more accurately the geometric model is able to represent the reality of the object of study, the greater the convergence between the experimental and numerical results will be, ensuring a more reliable and consistent modal analysis.

REFERENCES

[1] Araújo, D. C. *et al.* Modal identification of a wind turbine. Procedia Engineering. Elsevier Ltd, 2016.

[2] Awada, A.; Younes, R.; Ilinca, A. Review of vibration control methods for wind turbines. Energies, v. 14, n. 11, pp. 1-25, jun. 2021.

[3] He, J.; Fu, Z.-F. Modal analysis. 2. ed. Oxford: Butterworth-Heinemann, 2001.

[4] Moraes, L. F. B. Modeling and analysis of a horizontal axis wind turbine subject to the action of turbulent winds. Dissertation (Master in Mechanical Engineering) – State University of Campinas, Campinas, 2019.

[5] Xu, Ziyang *et al***.** A state-of-the-art review of the vibration and noise of wind turbine drivetrains. Sustainable Energy Technologies and Assessments, v. 48, 2021.

TRACK - D: Mechanical Design and Prototyping

Mechanical Design
Product Development
3-D Printing and Additive Manufacturing
Fastening and Joining Technologies
Prototyping
Design of Sensors and Actuators
Design for Manufacturing
Eco-Design
Conversion Technologies
Case Studies

Proceedings IRF2025: 8th International Conference on Integrity-Reliability-Failure
In Engineering, Materials, Manufacturing and Biomechanics. Porto 15-18 July 2025
DOI: https://doi.org/10.24840/978-972-752-323-8

PAPER REF: 22254

PREDICTION OF CENTRAL BURSTING IN AXISYMMETRIC EXTRUSION PROCESS THROUGH DIES OF ARBITRARY SHAPE

Amir Parghazeh (Amir Armani)[1(*)], Yaser Khaledi[2], Soroush khaledi[3]

[1]Mechanical Engineering, Faculty of Engineering, Razi University, Kermanshah, Iran
[2]Civil Engineering, Azad university of Mahabad, Iran
[3]Biomedical Engineering, Tabriz university, Iran
[(*)]*Email:* Parghazeh@gmail.com

ABSTRACT

This paper presents an upper bound analysis for the axisymmetric extrusion of a perfectly plastic material. It is built a velocity field valid for all die forms possible. This field allows the potential development of a central explosion while extruding. Assuming the boundary at entrance into deformation zone is an arbitrary curved surface and at exit to be a spherical surface. Extrusion pressure is minimized at the entrance to obtain the shape of the boundary. The best effective die profiles that reduce the precious extrusion pressure, along with the specification curves for braided rupture in the midsection and the secure areas for a large set of process variables, are presented. We show that the optimal die profiles also fulfil the central burst prevention conditions. Predictions obtained using the proposed criterion compare well with the FEM simulation data and are consistent with published results.

Keywords: Rod extrusion, Upper bound method, Central bursting defects, Curved die.

INTRODUCTION

In this process a round bar is subjected to plastic deformation under a compressive load; is made to flow through the die opening which has a smaller cross-sectional area than that of the original rod, and may take a conical or curved shape. During this process due to some die geometries, the products may form a crack on their centre line leading to a fracture called as central burst. These defects are insidious due to their hidden nature on the product's surface and require more sophisticated and costly equipment for diagnosis. Thus, computation simulations should be conducted to predict and avoid the central rupturing successfully. The die profile, friction and reduction ratio is particularly influential in solving this problem. Another important aspect of the die design is the specification of a profile which simultaneously reduces the external power along with providing a defect free product. The optimal profile is a profile leading to the lowest extrusion pressure.

Several papers have discussed the subject of central defects in axisymmetric extrusion. Using the upper bound approach on an axisymmetric region with an infinitesimally small radius cylindrical hole, Avitzur studied the central burst phenomenon in extrusion and wire drawing through conical dies of rigid perfectly plastic materials. Two concentric spherical surfaces have been assumed as the boundaries at the entrance and exit regions of the deformation zone which are shear surfaces or velocity discontinuity surfaces respectively. He postulated that it was less force required for that extrusion or drawing process with central bursting started compare to no-central bursting state (Avitzur, 1968). For proof of the concept, an analytical model was introduced by Zimmerman and Avitzur (1970) using the upper bound method, considering

spherical surfaces at inlet and outlet shear boundaries for linear strain hardening materials. Moritoki, 1991 applied a slip line method to predict the central bursting defects during extrusion through conical dies and validated his model predictions with Avitzur results. In the rod extrusion process through rectangular dies for rigid perfectly plastic materials, Wu and Li predicted central bursting defects employing the upper bound analysis (Wu and Li, 1992). Venkata Reddy et al. used the pressure-velocity finite element formulation and predicted the minimizing die profiles in the redundant forming energy in extrusion with the different process conditions. They also demonstrated that the optimal dies by this proposed hydrostatic stress criterion satisfy the condition for central bursting prevention (Reddy et al., 1996). KO and KIM introduced a method to predict central bursting defects while simatraneously inspecting deformation during extrusion and wire drawing. They utilized using the damage model, according to rigid-plastic finite element method (Ko and Kim, 2000).

Plancak et al. propose an idea of forming limit curve to study the forming ability of carbon steel and the central bursting defects (Plancak et al., 2014). Sebek et al. employed a numerical simulation with the use of the package of Abaqus/Explicit to study the effects of die angle, friction and reduction ratio. They used the uncoupled ductile failure models and compared the numerical results with the experimental results (sebek et al., 2015) The analytical model for the prediction of central bursting defects during rod extrusion process through conical dies is proposed by the current authors based on the upper bound method (Parghazeh and Haghighat, 2016).

RESULTS AND CONCLUSIONS

A velocity field kinematically admissible to the predicted axisymmetric extrusion of rigid-perfectly plastic materials is defined in this paper which leads to the central bursting defects through dies of any shape simultaneously with the necessary and sufficient conditions. The inlet shear boundary is approximated as a spherical surface, and the outlet shear boundary is approximated as an arbitrary curved surface in the analysis. The optimized inlet shear boundary and extrusion force are derived by minimizing total power obtained from the analysis velocity field, and the criterion for central bursting defects is achieved. In addition, the effect of process parameters like die length and frictional factor on die wall on the central bursting defects is also established. The upper limit extrusion pressure is compared with the results calculated by the finite element method.

REFERENCES

[1] Avitzur B. Analysis of central bursting defects in extrusion and wire drawing. ASME Journal of Engineering for Industry 1968;90: pp. 79-91.

[2] Balaji, PA, Sundararajan T, Lai, G K. Viscoplastic deformation analysis and extrusion die design by FEM, ASME Journal of Applied Mechanics 1991;58: pp. 644-650.

[3] Gordon WA, Van Tyne CJ, Moon YH. Axisymmetric extrusion through adaptable dies-Part 1: Flexible velocity fields and power terms. International Journal of Mechanical Sciences 2007;49: pp. 86-95.

[4] Gordon WA, Van Tyne CJ, Moon YH. Axisymmetric extrusion through adaptable dies-Part 2. Comparison of velocity fields, International Journal of Mechanical Sciences 2007;49: pp. 96-103.

[5] Gordon WA, Van Tyne CJ, Moon YH. Axisymmetric extrusion through adaptable dies-Part 3: Minimum pressure streamlined die shapes, International Journal of Mechanical Sciences 2007;49: pp. 104-115.

[6] Gordon WA, Van Tyne CJ, Sriram S. Extrusion through spherical dies-an upper bound analysis. ASME Journal of Manufacturing Science and Engineering 2002;124: pp. 92-97.

[7] Gunasekera JS, Gegel HL, Malas JC, Doraivelu SM, Barker D. CAD/CAM of streamlined extrusion dies. Journal of Applied Metalworking 1985;4: pp. 43-49.

[8] Ko DC, Kim BM. The prediction of central burst defects in extrusion and wire drawing. Journal of Materials Processing Technology 2000;102: pp. 19-24.

[9] Moritoki H. The criterion for central bursting and its occurrence in drawing and extrusion under plane strain. International Journal of Plasticity 1991;7: pp. 713-731.

[10] Parghazeh A, Haghighat H, Prediction of central bursting defects in rod extrusion process with the method of upper bound analysis. Transaction of Nonferrous Metals Society of China 2016;23:3392-3399.

[11] Plancak M, Vilotic D, Kacmarcik I. Stress state in forward cold extrusion. Journal for Technology of Plasticity 2014;39: pp. 21-27.

[12] Reddy NV, Dixit PM, Lai GK. Central bursting and optimal die profile for axisymmetric extrusion, ASME Journal of Manufacturing Science and Engineering 1996;118: pp. 579-584.

[13] Sebek F, Kubik P, Petruska J. Prediction of central bursting in the process forward extrusion using the uncoupled ductile failure models. Advances in Materials and Processing Technologies 2015;1: pp. 43-48.

[14] Wu S, Li M. Analysis of the central cavity of axisymmetric forward extrusion by the upper bound approach. Journal of Materials Engineering and Performance 1992;1: pp. 409-414.

[15] Yang DY, Han CH, Lee BC. The use of generalized deformation boundaries for the analysis of axisymmetric extrusion through curved dies. International Journal of Mechanical Sciences 1985;27: pp. 653-63.

[16] Yang DY, Han CH. A new formulation of generalized velocity field for axisymmetric forward extrusion through arbitrarily curved dies. Transactions of the ASME-Journal of Engineering for Industry 1987;109: pp. 161-168.

[17] Yang DY, Lee, CM, Cho JR. Analysis of axisymmetric extrusion of rods by the method of weighted residuals using body-fitted coordinate transformation, International Journal of Mechanical Sciences 1990;32: pp. 101-114.

[18] Zimmerman Z, Avitzur B. Analysis of the effect of strain hardening on central bursting defects in drawing and extrusion. ASME Journal of Engineering for Industry 1970; 90: pp. 135-145.

Proceedings IRF2025: 8th International Conference on Integrity-Reliability-Failure
In Engineering, Materials, Manufacturing and Biomechanics. Porto 15-18 July 2025
DOI: https://doi.org/10.24840/978-972-752-323-8

PAPER REF: 22358

APPLICATION GENERATIVE DESIGN TO A MOUNTAIN BIKE FRAME WITH CONSIDERATION OF THE STRUCTURAL WEIGHT REDUCTION

L.J. Juiña, D. Rubio, A. Villalba, V.H. Cabrera-Moreta(*)
Mechanical Engineering Department, Universidad Politécnica Salesiana (UPS), Quito, Ecuador
(*)*Email:* vcabrera@ups.edu.ec

ABSTRACT

This proposal exposes the application of the generative design to a mountain bike swingarm considering the reduction of the structural weight and model improvement. The process was carried out to obtain the optimized model of the swingarm. Different alternatives generated was observed, to compare between them and obtain the best alternative that complies with the standards. Three different methods were used to obtain the alternatives: own generation, generate by artificial intelligence and optimization a topographic study. A total of seven alternatives were proposed to perform the analysis and determine the quality level. Through the simulation of the different alternatives the best working conditions were verified based on the resistance and compliance with the safety factor of each alternative. The greatest structural reduction was obtained in the alternatives obtained through AI generation with 25.64 %, however, the safety factor of the alternative was not proper. The most encouraging results were obtained in one of the alternatives obtained by self-generated generation when complying with the safety factor of 1.32 and 13.82 % of structural reduction, which translates into 36.12 grams.

Keywords: Generative design, factor of safety, reverse engineering.

INTRODUCTION

Currently the world of cycling has become famous due to the versatility of the sport, which has evolved over time, becoming one of the most practiced sports in the country thanks to its great performance, to thoroughly understand this area is necessary to understand what is available, and the operation of each component that, despite seeming simple, must be well executed to achieve harmony in the movement. Especially if we are talking about mountain biking where the riding conditions are much more aggressive compared to the city [1]. This harmony translates into an excellent convergence between the rider and the bicycle, among the most important parameters is the need for the bicycle to be light, so this research focuses on the application of generative design to the swingarm of a mountain bike with the aim of reducing its structural weight. Generative design uses a different approach to computer aided design where algorithms and artificial intelligence techniques are used to generate design models based on predefined parameters. The results obtained were favorable due to the structural weight reduction obtained, 39.189 g of reduction for the final part obtained, about 15 % of the original weight, which complied with what was proposed when using the generative design.

A. Double suspension mountain

The improvements that were integrated to the model were appearing according to the needs that were appearing in the process, a fork type suspension was implemented, since, with this solution [2] allowed a better driving experience which allowed a pivot with the impact and thus reduce

fatigue to the rider, the first forks used as elastic system to the air and for damping a system of open oil. With this it was possible to counteract the problem of rigidity and soon it did not take long to appear the double suspension bicycles that were much more useful for the mountain descent, an important role was also played by the diameter of the wheel, nowadays there are from 24 in. to 29 in.

It provides an additional level of comfort and is particularly suitable for areas with technical trails and descents, where greater stability, fun and comfort are sought. In addition, the presence of damping systems also facilitates climbs and improves traction, avoiding rear wheel slippage, since both wheels remain in constant contact with the ground for longer. According to the research of Perez [3] double suspension frames are ideal for mountain biking because an evolution can be obtained within mountain biking by optimizing aspects to ensure the adaptability of the bicycle to the rider, which requires knowledge on how the rider's body behaves with respect to the bicycle, thus achieving a correct posture that meets the biomechanical requirements that prevent injuries. In addition to the size that each bicycle should have with respect to the user is different and must be correct to be able to regulate the saddle as shown in Figure 1.

Fig. 1 - Trek Slash 8 Bike.

B. Generative Design

A computer-aided design and engineering approach [4]that uses advanced algorithms and software to automatically generate optimal or efficient designs for a specific product. Itis based on simulation and optimization to find design solutions that meet certain objectives, such as weight reduction, structural strength, or aerodynamic efficiency. It is thus an artificial intelligence used in mechanical engineering to solve design problems [5]. Instead of facing constraints and parameters during the process, designers tell the program the desired objectives and limits of the project. Cloud computing allows the program to generate multiple possible solutions based on these requirements. Generative design introduces changes to the conventional design process, where the engineer sets the overall parameters so that the software can work accordingly [6].

C. Reverse Engineering

It is a discipline in constant evolution due to the fact that its application has been useful in engineering fields. That reverse engineering represents a revolution in the aspect of the product development process [7]. The high potential it has lies in the continuous improvement of machines, tools, technological accessories of the industry. Where the demand for quality increase and price preservation makes it necessary to optimize time and costs in complete research processes, i.e., to start from scratch. With reverse engineering you already have a base part, and a base of necessary data with which hat part works, if you want to make some kind of improvement to this part, by means of 3D information obtained; the process can be greatly expedited. The process involved in reverse engineering, and the difference that exists with

normal engineering, Figure 2 shows the beginning of a normal engineering process starting from base data to obtain a final prototype, as opposed to reverse engineering [8], which is to take the prototype already built, apply design improvements and obtain data and a new database.

D. 3D Scanner

A 3D scanner is a device that is used to capture different geometries in third dimension in a precise digitizing software, thus obtaining a digital model that represents the characteristics of the scanned object [9]. The process used to obtain it is based on an emission camera and a reception camera, through the emission of light beams that interact with the reflection markers are captured by the receiving camera to record three-dimensional information, the diameter of the markers differ in the reflective part of the normal part in Figure 3 shows the size and color that have these markers.

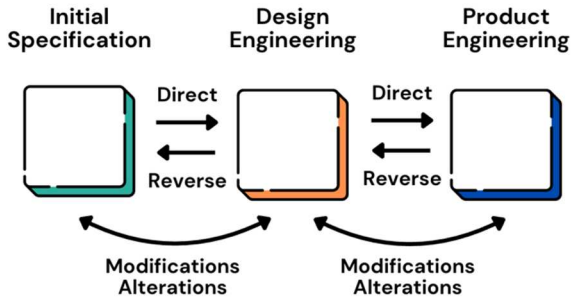

Fig. 2 - Reverse Engineering [9].

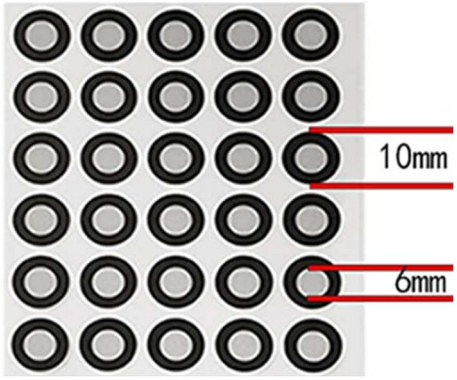

Fig. 3 - Reflective markers.

RESULTS

The swingarm of a Trek bicycle, model Slash 8, was selected as the object of study to apply generative design with the aim of reducing structural weight. To obtain the scanned part, several steps were followed, including the calibration of the scanner using a box with reflection markers. During the scanning process, markers were placed on the rocker and support surface to ensure accuracy and proper reference, as shown in Figure 4.

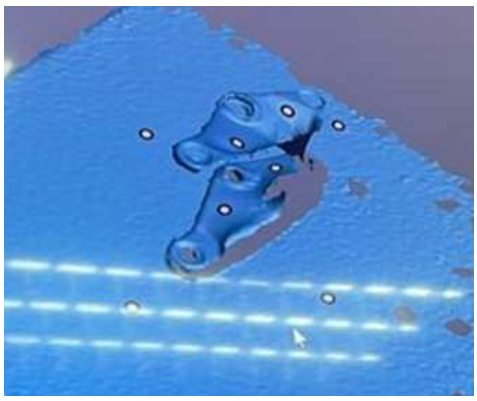

Fig. 4 - Link obtained with 3D scanner.

The scanning progress was monitored through the software, and the total time spent was approximately 35 minutes. However, the model initially obtained did not meet expectations, so additional operations were performed to refine it in SolidWorks software. Details such as bearing holes were adjusted and imperfections were eliminated to prepare the model for optimization by generative design in the Figure 5.

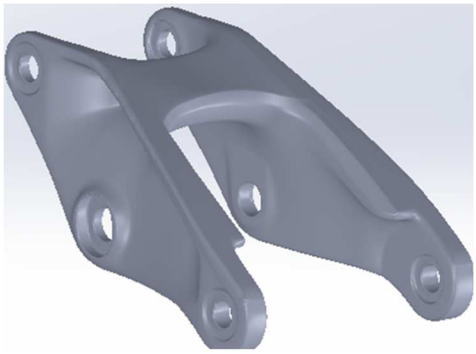

Fig. 5 - refined model.

A. Static Analysis

Static analysis is a crucial step in the design and evaluation of structures, focusing on the equilibrium of bodies and systems under static loads to determine internal forces, deformations and reactions. In the case study of the bicycle, a static analysis was performed at the support points of the wheels to calculate the reactions and forces acting on them as shown in Figure 6.

Fig. 6 - Reaction management at strategic points.

The calculated values for the forces and reactions are shown in Table 1. These results were used as inputs for the simulation of the part and compared with the results obtained during the analysis. This process provides a detailed evaluation of the structural behavior and its suitability for implementation in the bicycle design.

Table 1 - Calculated analysis results.

Forces / Reactions	**Magnitudes (N)**
Weight (W)	1177.2
Ry1	385.87
Ry2	405.45
F1x	559.35
F1y	385.87
F1	679.53
F3y	-318.58
F4y	-704.45

B. Base model simulation

The simulation of the base model of the swingarm was carried out using SolidWorks to observe stresses, displacements and deformations, these being fundamental data for the analysis. Before starting, the initial mass of 261.26 grams in 6061 aluminium alloy was considered. Force F1, with a magnitude of 679.53 N and an inclination of 34.6°, was applied at point A, while points B and C were used as fixtures, one fixed and the other as a bearing support, respectively as shown in Figure 7.

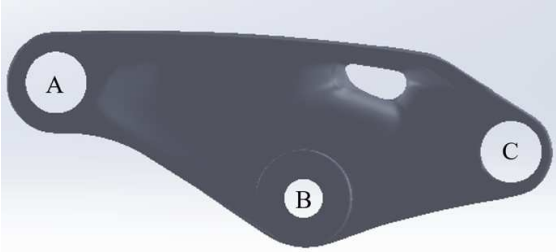

Fig. 7 - Denomination of each hole.

Results included maximum stresses of 37.24 N/mm² and maximum displacements of 0.149 mm. Unit deformations were mainly concentrated in hole B, one of the two direct connections to the bicycle frame, being one of the most stressed parts. The safety factor was calculated at 1.48 as shown in Figure 8, indicating that the original part is suitable for its current use and serves as a reference for the analysis in the optimized model. These results are fundamental to achieve a correct optimization, as they will help determine the percentage of structural weight reduction in the generative design model using artificial intelligence tools.

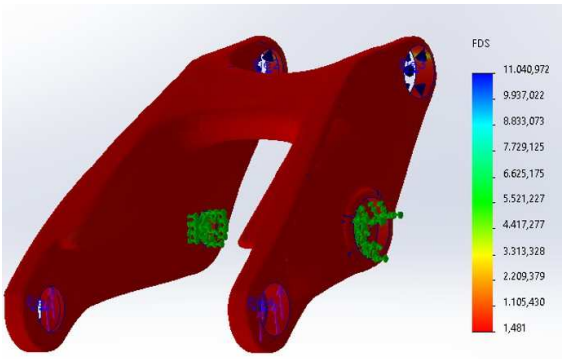

Fig. 8 - Original part safety factor.

C. Design alternative

In house generation

Weight reduction is prioritized, currently at 261.26 grams with a safety factor of 1.48. It is decided to work with a safety factor of 1.2 to observe the eliminated mass. The least affected areas in the original part are in the central part, so it is decided to reduce the weight in these areas.

These results show the importance of finding a balance between weight reduction and part strength in the generative design process as shown in Table 2.

Table 2 - Results of the Analysis Of 3 Alternatives.

Variables	Alternative 1	Alternative 2	Alternative 3
Weight	193.49 gr	214.31 gr	225.14 gr
Maximum tension	208 MPa	256 MPa	43.56 MPa
Maximum displacement	0.22 mm	0.208 mm	0.162 mm
Deformation	0.00157	0.00145	0.00048
Safety factor	0.265	0.354	1.266

Generation using AI

The generative design models in Autodesk's Fusion 360 [10] are based on the selection of geometries to be retained and obstacles, along with constraints and loads [11]. The software uses this data to iteratively calculate a part that fits the initial parameters. Depending on the

complexity, various design options are obtained. In the process, the constraint and obstacle geometries are identified with green and red colors, respectively, as shown in Figure 9 [12]. The generated alternatives may vary in small details, but these can significantly influence the analysis as shown in Table 3.

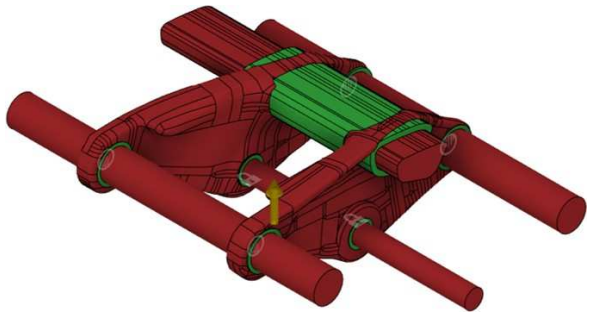

Fig. 9 - Visualization of generative design process on Fusion 360.

None of the AI-generated alternatives were found to be feasible for use. It was determined that the manual design approach, based on the results obtained on the original part, produces better results. Alternative 3 as shown in Figure 10, obtained from this approach, has an excellent ratio of weight reduction to initial strength.

Table 3 - Results of the analysis of 3 alternatives with AI.

Variables	Alternative 1	Alternative 2	Alternative 3
Weight	196 gr	197.58 gr	195.54 gr
Maximum tension	260 MPa	516 MPa	398 Mpa
Maximum displacement	2.57 mm	0.227 mm	0.506 mm
Deformation	0.0374	0.005	0.00493
Safety factor	0.0.0169	0.0107	0.138

Fig. 10 -Alternative of generative with AI.

Generation by topographic survey

The process of generation by topographic survey in SolidWorks involves setting parameters such as mass reduction and the desired factor of safety, together with the selection of surfaces to be retained and free areas for optimization [13].

Parameter settings: The mass reduction (in this case, 15%) and the desired safety factor (1.5) are set to start the study. Surface selection:Areas to be retained are marked in green, while areas free for optimization are highlighted in gray.

Once the parameters have been set, the topographic survey is executed, and an initial parametric model is obtained. However, the initial results do not meet the safety requirements, suggesting that the optimization has not converged properly.

A second study is performed with more conservative parameters (15% mass reduction and safety factor of 1.5). The resulting model requires refinement to correct the surfaces generated by the software. Once refined, a more viable model is obtained for implementation as seen in Figure 11.

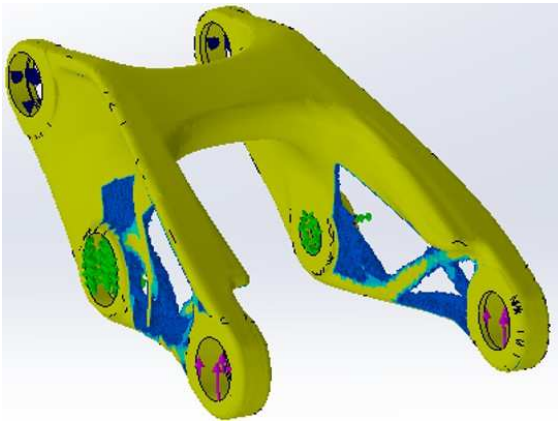

Fig. 11 - Figure with 15% weight reduction.

Analysis of the optimized alternative by topographic survey yields a weight of 226.66 g, a maximum stress of 86.5 MPa, a maximum displacement of 0.178 mm, a maximum unit strain of 0.000934, and a factor of safety of 0.637. Although the refined model shows improvements, the factor of safety is still insufficient, indicating that this alternative is not feasible for the materialization of the project.

Figure 12 details the best option with its own optimization. Figure 13 details the best option with AI optimization.

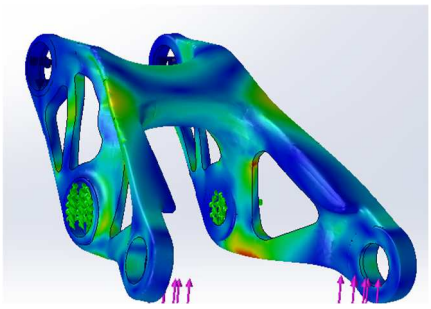

Fig. 12 - The best option con own optimization.

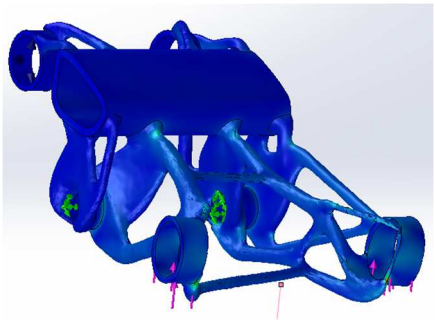

Fig. 13 - The best option con AI optimization.

Figure 14 details the best option with topological optimization.

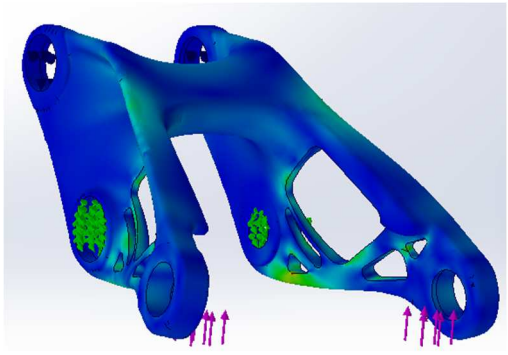

Fig. 14 - The best option con topological optimization.

CONCLUSIONS

Considering the simulations, there is variability in the results obtained in several aspects. Among the five alternatives proposed in the framework of this project, only the third option was able to achieve established objectives. First, the percentage of weight reduction was 10.87

%, equivalent to a decrease of 28.42 g with respect to the initial weight. In addition, there was an increase of 12 MPa in the maximum strength of the part.

The alternative generated by artificial intelligence had the potential to be one of the most viable options due to the type of software used. The weight has a weight reduction of 65.26 gr. Additionally, it shows the lowest safety factor as a result its construction is not feasible.

The results derived from the topological analysis failed to meet all the parameters established at the beginning of the simulation. Although an effectiveness was evidenced in the weight reduction section, reaching 15 % corresponding to a decrease of 39.189 g, the part under consideration does not satisfy the safety factor requirement. This drawback indicates the lack of feasibility of the proposal using the topographic study method, showing the need to reconsider alternative approaches for the optimization of the part in question.

The most accure results were obtained in one of the alternatives obtained by self-generated generation when complying with the safety factor of 1.32 and 13.82 % of structural reduction, which translates into 36.12 grams less.

REFERENCES

[1] A. Laqua, J. Schnee, J. Pletinckx, M. Meywerk, “Identification of factors influencing the riding experience on e-mountain bikes: an analysis of the rider-bicycle interaction,” Transp Res Part F Traffic Psychol Behav, vol. 98, pp. 61-72, 2023.

[2] W. Bauer and Bauer, Hydropneumatic suspension systems. Springer, 2011.

[3] A. Pérez Medina, “Diseño de una suspensión delantera para bicicleta de montaña.” Universitat Politècnica de València, 2016.

[4] Z. Bi, X. Wang, Computer aided design and manufacturing. John Wiley & Sons, 2020.

[5] G. Menéndez, M.D. Somonte, M. Escudero, “Diseño generativo: el estado del arte,” Técnica Industrial, pp. 44-49, 2019.

[6] C.E.N. Alcantar, L.A.P. Gallardo, M. A. M. Bocanegra, M. B. Sánchez, “Diseño generativo aplicado en el diseño de un pedal de frenado para automóvil,” Revista de Ciencias Tecnológicas, vol. 6, no. 4, pp. 1-20, 2023.

[7] D. Palka, “Use of reverse engineering and additive printing in the reconstruction of gears,” Multidisciplinary Aspects of Production Engineering, vol. 3, no. 1, pp. 274-284, 2020.

[8] M. Akerdad, A. Aboutajeddine, M. Elmajdoubi, “Development of a redesign process based on reverse engineering and patent circumvention,” International Journal on Interactive Design and Manufacturing (IJIDeM), vol. 17, no. 1, pp. 261-277, 2023.

[9] R.H. Helle, H.G. Lemu, “A case study on use of 3D scanning for reverse engineering and quality control,” Mater Today Proc, vol. 45, pp. 5255-5262, 2021.

[10] P.R. Shrestha, D. Timalsina, S. Bista, B.P. Shrestha, T.M. Shakya, “Generative design approach for product development,” in AIP Conference Proceedings, AIP Publishing, 2021.

[11] F. Buonamici, M. Carfagni, R. Furferi, Y. Volpe, L. Governi, “Generative design: an explorative study,” Comput Aided Des Appl, vol. 18, no. 1, pp. 144-155, 2020.

[12] R. Savage, “Fusion 360 Introduction to Generative Design,” Retrieved, vol. 1, no. 28, p. 2021, 2020.

[13] Z.-X. Chen, G. Chen, Y. Liu, “Effects of topographic irregularity on seismic site amplification considering input signal frequency: A case study,” Eng Struct, vol. 304, p. 117667, 2024.

Proceedings IRF2025: 8th International Conference on Integrity-Reliability-Failure
In Engineering, Materials, Manufacturing and Biomechanics. Porto 15-18 July 2025
DOI: https://doi.org/10.24840/978-972-752-323-8

PAPER REF: 22375

TEMPERATURE-DEPENDENT EXPERIMENTAL CHARACTERIZATION OF A STRETCHABLE STRAIN SENSOR

Beatriz Almeida[1(*)], José Ramiro Fernandes[2], Miguel Oliveira[3], Raul Morais[4], Fábio Pereira[4]

[1]University of Trás-os-Montes and Alto Douro, Engineering Department, Vila Real, Portugal
[2]University of Trás-os-Montes and Alto Douro, Physics Department, Chemistry Centre, Vila Real, Portugal
[3]A.J.P. Motos S.A., Lousada, Portugal
[4]University of Trás-os-Montes and Alto Douro, Engineering Department, Center for the Research and Technology Agro-Environmental and Biological Sciences, CITAB, Vila Real, Portugal
(*) *Email :* beatriz@utad.pt

ABSTRACT

The increasing demand for advanced wearable technologies has driven innovations in stretchable strain sensors. In this contribution, we investigated the mechanical behaviour of Ecoflex™ Shore 00-30 under varying temperature conditions. The results of the effects of temperature on stiffness, energy dissipation, and failure mechanics were analysed and discussed. Mechanical testing across a range of temperatures revealed no significant changes in these properties, highlighting the material's thermal stability.

Keywords: Stretchable strain sensor; Ecoflex silicone rubber; Temperature dependence; Mechanical characterization.

INTRODUCTION

Stretchable strain sensors, used in various applications such as health monitoring, electronic skin, and motion detection, depend on materials such as silicone polymers for their exceptional physical properties, including biocompatibility, non-toxicity, and thermal stability (del Bosque et al., 2023; Liao et al., 2020). Ecoflex™ Shore 00-30, a rubber-like silicone with excellent stretchability and durability, is particularly promising due to its mechanical resilience and environmental resistance (Lee et al., 2022). While its mechanical behavior has been extensively studied, the influence of temperature on its tensile properties remains underexplored ("Strain rate, temperature and deformation state effect on Ecoflex 00-50 silicone mechanical behaviour - ScienceDirect," n.d.). This study aims to investigate how temperature variations affect the stiffness, energy dissipation, and failure mechanisms of Ecoflex, providing critical insights to optimize the performance of stretchable strain sensors for diverse applications.

RESULTS AND CONCLUSIONS

In this study, Ecoflex™ Shore 00-30 was supplied in two liquid components: which were combined in a 1:1 weight ratio and mixed for 3min. The resulting mixture was poured into a sensor mold and placed in a vacuum oven at 52ºC and 6 bar for 1 hour to remove entrapped air and minimize bubble formation. Four samples were prepared for each experiment, subjected to different temperature treatments: nonheated, heated at 70°C for 2 hours, and heated at 70°C for 4 hours.

Tensile tests were conducted using an Instron Micro-Tester 5848, where each specimen was subjected to a controlled, increasing force while its deformation was measured (Figure 1). The face of each specimen was marked with black points and recorded using a smartphone camera

to capture the material's response during the experiment. The recorded videos were converted into images and then processed using an algorithm developed in MATLAB, to measure displacement and determine the strain values over time (Figure 2).

Fig. 1 - Tensile test.

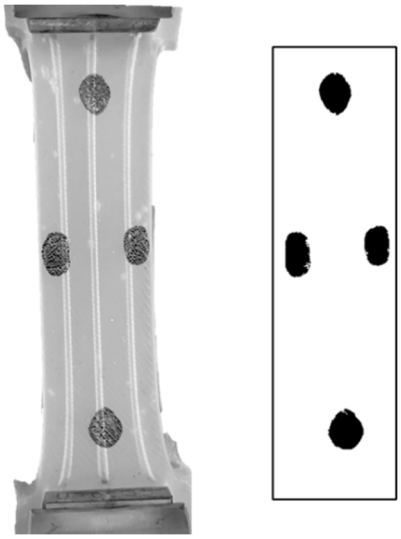

Fig. 2 - Greyscale image (left) and binary image (right).

REFERENCES

[1] A. del Bosque, X. F. Sánchez-Romate, A. Gómez, M. Sánchez, A. Ureña, "Highly stretchable strain sensors based on graphene nanoplatelet-doped ecoflex for biomedical purposes," Sensors and Actuators A: Physical, vol. 353, p. 114249, Apr. 2023, doi: 10.1016/j.sna.2023.114249.

[2] H. J. Lee, R. Joyce, J. Lee, "Liquid Polymer/Metallic Salt-Based Stretchable Strain Sensor to Evaluate Fruit Growth," ACS Appl. Mater. Interfaces, vol. 14, no. 4, pp. 5983-5994, Feb. 2022, doi: 10.1021/acsami.1c21376.

[3] Z. Liao, M. Hossain, X. Yao, "Ecoflex polymer of different Shore hardnesses: Experimental investigations and constitutive modelling," Mechanics of Materials, vol. 144, p. 103366, May 2020, doi: 10.1016/j.mechmat.2020.103366.

[4] "Strain rate, temperature and deformation state effect on Ecoflex 00-50 silicone mechanical behaviour - ScienceDirect." Accessed: Sep. 25, 2024. [Online]. Available: https://www.sciencedirect.com/science/article/pii/S0167663623000066#b16.

Proceedings IRF2025: 8th International Conference on Integrity-Reliability-Failure
In Engineering, Materials, Manufacturing and Biomechanics. Porto 15-18 July 2025
DOI: https://doi.org/10.24840/978-972-752-323-8

PAPER REF: 22408

MATHEMATICAL MODEL FOR KINEMATICS OF A KNUCKLE JOINT PRESS

Maria Luísa Madureira(*), Francisco Queirós de Melo[2]

[1]INEGI/LAETA, Faculty of Engineering, University of Porto, Porto, Portugal
[2]INEGI, Porto, Portugal
(*)*Email:* luisa.madureira@fe.up.pt

ABSTRACT

The exact solution of the trigonometric system of equations for direct kinematic analysis of the driving system of a knuckle mechanical press is difficult to achieve. The authors propose an algebraic system of equations to obtain the solution by an iterative procedure. The method consists of defining the mechanism configuration at a defined time step t. Then the same equations are rewritten for a next time step $t+\Delta t$ and the increments for the stroke, velocity and acceleration of the press slide are evaluated. This way, the updated configuration of the system allows the evaluation of any of the system parameters, which lead to the progressive update of the system variables until a defined time step. A code was generated to allow different geometrical inputs and to achieve solutions iteratively at any time step, usually one cycle.

Keywords: Mechanical press, knuckle joint press, mathematical equations.

INTRODUCTION

The kinematic analysis of these machines and detailed analytical, yet with a lesser mathematical development of the press driving concept, has been focus of some research in book chapters (Dubbel,1979; Schuler, 1998). This mechanism has good potential for short displacement under high forces in metal forming processes (Mäkelt, 1968). When a motion law of the slide machine is identified, it is possible to know the necessary power to plastically process a defined component geometry. Authors Xinyu Dong and Yu Sun (Xinyu et al., 2022) proposed a study of the knuckle mechanism kinematics focusing only on the crankshaft angle, when the slide is close to BDC, a critical point for the machine integrity for reasons of force singularity. In their simulation, the single point multiple connection knuckle mechanism was not considered; instead, they used the modified knuckle mechanism (with two final connection holes). Heinz Tschaetsch (Tschaetsch, 2006) also presented a detailed graphical stroke vs crankshaft kinematics study of knuckle mechanisms. Tschaetsch proved that the knuckle mechanism has a faster tool approach/return slide motion than the classical crank mechanism; moreover, getting close to the workpiece, the speed is much controllable.

The knuckle press driving system, is depicted in Figures 1, 2. A system of equations is obtained by the geometry of the device. Conventional press slide driving mechanisms are 2D kinematics systems. The definition of the system kinematics consists in the characterization of the slide motion, velocity and acceleration as time dependent functions. From previous concepts, the geometry of the press driving system is defined by two equations (now algebraic) for each time step: Equations (1, 2). Then these will be transformed into algebraic equations to be solved iteratively. This system involves a classical crankshaft/connection rod group; respectively parts 1-2 and 2-3. Component 1-2 is the crankshaft and revolves at a prescribed angular velocity about axis 1; then it transmits a motion to main connecting rod 2-3 which imposes an alternative displacement at node 3 either on X and Y axes.

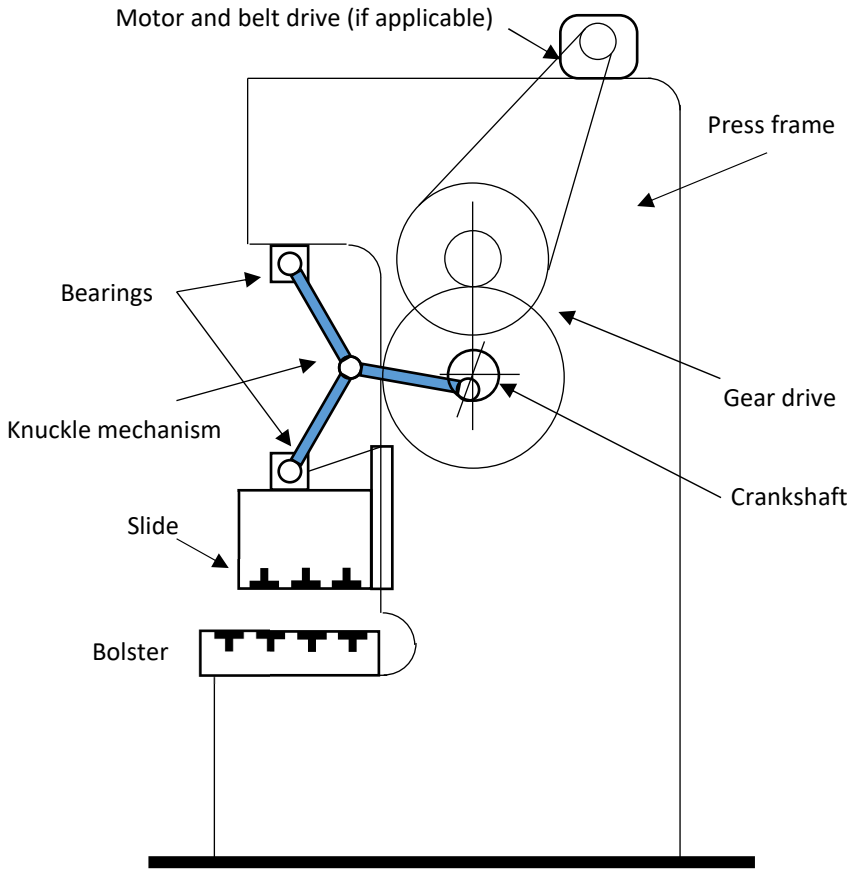

Fig. 1 - Knuckle press (sketch of basic mechanism and kinematics).

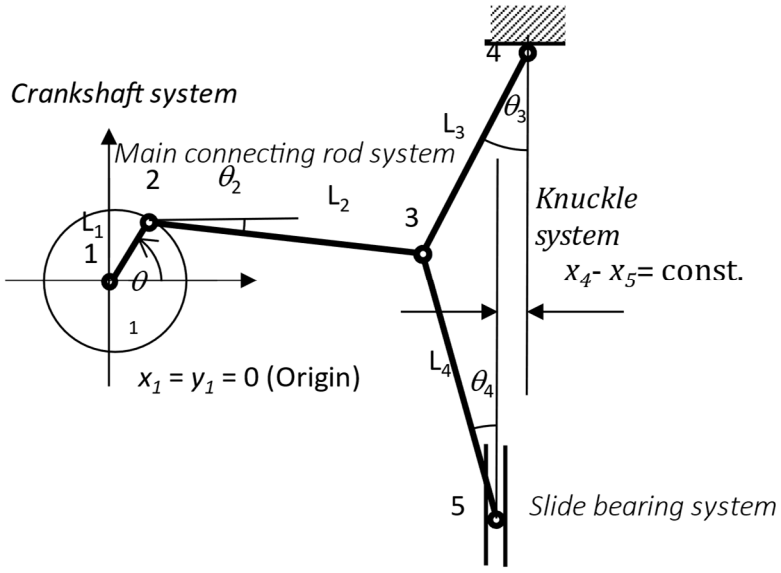

Fig. 2 - Schematic representation of the knuckle system in a mechanical press.

Point 4 is a fixed bearing mounted in the press crown (or press head). It cannot be displaced; however, it allows rotation about X-axis (normal to X-Y plane). For sake of accessibility to tool mounting, there is the option of assuming an offset between vertical axis of the slide 5 and the one passing on bearing 4.

METHODOLOGY

The equations obtained for the geometrical system are Equations 1, 2, below, and the variables of the problem are θ_2, θ_3, θ_4 and y_5

$$(On\ x-axis): \begin{cases} L_1 \cos\theta_1 + L_2 \cos\theta_2 + L_3 \sin\theta_3 = x_4 \\ L_3 \sin\theta_3 - L_4 \sin\theta_4 = x_4 - x_5 \end{cases} \quad (1)$$

$$(On\ y-axis): \begin{cases} L_1 \sin\theta_1 - L_2 \sin\theta_2 + L_3 \cos\theta_3 = y_4 \\ y_4 - L_3 \cos\theta_3 - L_4 \cos\theta_4 = y_5 \end{cases} \quad (2)$$

A numerical method based on step-by-step time increment of the motion mechanism is used for the solution of this system of equations.

The equations are of great importance for the machine design, given that the leading forces and their time dependency when performing a stroke, will heavily condition the machine dynamic behavior and its fatigue endurance. The accurate definition of the system kinematics leads to the characterization *vs* time for the slide displacement, velocity and acceleration. This last parameter is superimposed by the generation of inertial forces, with the material plastic forming forces, so informing about the strength of press structure and additional components of the mechanical driving system.

Resulting from these concepts, the geometry of a press driving system can therefore be defined by a system of two equations:

$$\begin{cases} X_{Slide}(\theta_1, \theta_2, \theta_3, \theta_4, ..) = f_x(\theta_1, \theta_2, \theta_3, \theta_4, ..) \\ Y_{Slide}(\theta_1, \theta_2, \theta_3, \theta_4, ..) = f_y(\theta_1, \theta_2, \theta_3, \theta_4, ..) \end{cases}$$

Here $(\theta_1, \theta_2, \theta_3, \theta_4, ..)$ are angular positions of integrating components of the driving system at a defined time instant (such angles are themselves functions of time).

As mentioned above, this pair of equations refers to the system configuration at a defined time instant *t*. It can be checked what happens if an increment in time, as *t*+ *Δ t*; all angular arguments defining the system geometry also evolve to an "updated" configuration. To solve that problem, it´s necessary to obtain the geometric increment of the machine kinematics during a single time increment *Δt*:

$$\begin{cases} \Delta X_{Slide}(\theta_1, \theta_2, \theta_3, \theta_4, ..) = \left(\frac{\partial X_{Slide}}{\partial \theta_1}\right)_t \times \Delta\theta_1 + \left(\frac{\partial X_{Slide}}{\partial \theta_2}\right)_t \times \Delta\theta_2 + \left(\frac{\partial X_{Slide}}{\partial \theta_3}\right)_t \times \Delta\theta_3 + \dots \\ \Delta Y_{Slide}(\theta_1, \theta_2, \theta_3, \theta_4, ..) = \left(\frac{\partial Y_{Slide}}{\partial \theta_1}\right)_t \times \Delta\theta_1 + \left(\frac{\partial Y_{Slide}}{\partial \theta_2}\right)_t \times \Delta\theta_2 + \left(\frac{\partial Y_{Slide}}{\partial \theta_3}\right)_t \times \Delta\theta_3 + \dots \end{cases} \quad (3)$$

The terms enclosed by brackets refer to the *actual* system or *current* configuration; they are determined from a previous time step and assumed constant during time increment *Δt*. This methodology allows the evaluation of increments $\Delta\theta_i$ during time step *t* for a time increment *Δt*.

This is an algebraic and linear system of equations, but it is frequently indeterminate. However, geometric constraints and some angular arguments may have a prescribed time dependent law, this rendering the system determinate and possible to be solved.

Boundary conditions and prescribed variables:

- θ_1 has a prescribed time dependent law, so it is not an unknown
- Bearing 4 has prescribed coordinates; respectively x_3 and x_4 are given values and do not change with time
- Bearing slide 5 has a prescribed value on *x*-axis (it is guided laterally); so x_5 is known.

Unknown y_5 can be obtained after knowing θ_2, θ_3 and θ_4

Next using incremental procedure in Equations (1, 2) new Equations (3, 4) are obtained:

$(\boldsymbol{On\ x-axis})$

$$\begin{cases} L_1\, cos(\,\theta_1+\Delta\theta_1)+L_2\, cos(\,\theta_2+\Delta\theta_2)+L_3\, sin(\,\theta_3+\Delta\theta_3)=x_4+\underbrace{\Delta x_4}_{(zero)} \\ L_3\, sin(\,\theta_3+\Delta\theta_3)-L_4\, sin(\,\theta_4+\Delta\theta_4)=x_4-x_5+\underbrace{\Delta x_4}_{(zero)}-\underbrace{\Delta x_5}_{(Zero)} \end{cases} \tag{4}$$

$(\boldsymbol{On\ y-axis})$

$$\begin{cases} L_1\, sin(\,\theta_1+\Delta\theta_1)-L_2\, sin(\,\theta_2+\Delta\theta_2)+L_3\, cos(\,\theta_3+\Delta\theta_3)=y_4+\underbrace{\Delta y_4}_{(zero)} \\ y_4+\underbrace{\Delta y_4}_{(Zero)}-L_3\, cos(\,\theta_3+\Delta\theta_3)-L_4\, cos(\,\theta_4+\Delta\theta_4)=y_5+\Delta y_5 \end{cases} \tag{5}$$

It is recalled that values of x_4, y_4 and x_5 are given constants, then no increment is allowed.

As all integrating mechanical components are rigid, their dimensions cannot change with time; only trigonometric functions change, as shown in previous equations. Assuming that the angular increments are small, the following expressions hold:

$$sin(\,\theta+\Delta\theta)=sin\,\theta\,cos\,\Delta\,\theta+cos\,\theta\,sin\,\Delta\,\theta\simeq sin\,\theta+cos\,\theta\,\Delta\theta$$
$$sin(\,\theta+\Delta\theta)=cos\,\theta\,cos\,\Delta\,\theta-sin\,\theta\,sin\,\Delta\,\theta\simeq cos\,\theta-sin\,\theta\,\Delta\theta$$

The results lea to a first order Taylor expansion of incremented trigonometric functions as follows:

$$sin(\,\theta+\Delta\theta)\simeq sin\,\theta+cos\,\theta\,\Delta\theta$$
$$cos(\,\theta+\Delta\theta)\simeq cos\,\theta-sin\,\theta\,\Delta\theta$$

If time is included as independent variable, equivalent expressions can be obtained:

$$sin(\,\theta_{t+\Delta t})\simeq\ \ sin\theta_t+cos\theta_t\times\dot{\theta}_t\Delta t$$
$$cos(\,\theta_{t+\Delta t})\simeq cos\theta_t-sin\theta_t\times\dot{\theta}_t\Delta t$$

It can be understood that a *next* time step, $t+\Delta t$, can result in updating the *current* system state (at time t) by previous recurrence equations.

This results in a new system of equations that can express only the increments of the kinematics state of the driving system, and is written as a matrix equation:

$$\begin{bmatrix} -L_2\, sin\,\theta_2 & L_3\, cos\,\theta_3 & 0 & 0 \\ 0 & L_3\, cos\,\theta_3 & -L_4\, cos\,\theta_4 & 0 \\ -L_2\, cos\,\theta_2 & -L_3\, sin\,\theta_3 & 0 & 0 \\ 0 & L_3\, sin\,\theta_3 & L_4\, sin\,\theta_4 & -1 \end{bmatrix} \begin{Bmatrix} \Delta\theta_2 \\ \Delta\theta_3 \\ \Delta\theta_4 \\ \Delta y_5 \end{Bmatrix} = \begin{Bmatrix} -L_1\, sin\,\theta_1\,\Delta\theta_1 \\ 0 \\ L_1\, cos\,\theta_1\,\Delta\theta_1 \\ 0 \end{Bmatrix} \tag{6}$$

Having obtained the angular increments, the respective angles are updated, leading to *renaming* as *current* values, playing the role of *actual* known parameters in the algebraic system above, so leading to the calculation of new angular increments in an operating recurrence cycle.

RESULTS

An example was studied considering the machine with the following dimensions and operating velocity:

Dimensions

$$L_1 = 0.1m$$
$$L_2 = 0.5m$$
$$L_3 = 0.5m$$
$$L_4 = 0.5m$$

Initial values, increment considered is $\pi/10$

θ_1= -3.1415927 θ_2= 0.08728

θ_3= 0.17456 θ_4= π 0.15

$\Delta\theta_1$= 0.3141592700 Δy_5= 0

Table 1 - Slide displacement values in m.

θ	Δy_5
$\pi/10$	0
$2\pi/10$	0.012
$3\pi/10$	0.024
$4\pi/10$	0.025
$5\pi/10$	0.006
$6\pi/10$	-0.015
$7\pi/10$	-0.025
$8\pi/10$	-0.024
$9\pi/10$	-0.015
π	-0.005

The code used allows to calculate with different increments. Figure 3 shows the displacements obtained with increment defined as $\pi/20$.

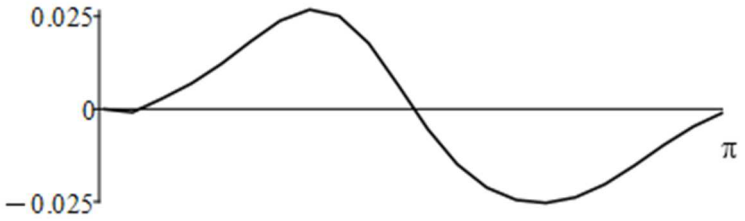

Fig. 3 - Slide displacement y_5 obtained (in *m*).

Fig. 4 - Respective slide velocities obtained.

CONCLUSIONS

The simulation tool presented showed how it was possible to model with accuracy the kinematics of dedicate machine tools as the one here presented, the knuckle press. Despite the low velocity and relatively small amplitude displacements, the involved forces may be very large and this means a high level of plastic work involved during materials forming. A precise information about the displacement and velocity field during the press strokes is valuable to compute the energy spent by the machine and temperature estimation of the processed material in order to predict additional hardening behavior affecting the quality of the processed items.

REFERENCES

[1] Dubbel, H. Handbook of Mech Engineering, Ed W. Beitz k-H Kuttner, Germany, 1979.

[2] Mäkelt H. Mechanical Presses, Ed Edward Arnold, 1968.

[3] Schuler. Metal forming handbook. Springer Science & business media, 1998.

[4] Tschaetsch, H. Metal Forming Practise - Processes - Machines – Tools, Springer, Dresden, Germany, 2006.

[5] Xinyu Dong, Yu Sun. Dynamic modeling and performance analysis of toggle-linkage presses considering mixed clearances and flexibility. International Journal of Nonlinear Mechanics, vol 147, 2022.

Proceedings IRF2025: 8th International Conference on Integrity-Reliability-Failure
In Engineering, Materials, Manufacturing and Biomechanics. Porto 15-18 July 2025
DOI: https://doi.org/10.24840/978-972-752-323-8

PAPER REF: 22418

DESIGN OPTIMIZATION USING MULTI-PHYSICS MODELLING FOR UNMANNED AERIAL VEHICLES

Arun Winglin Amaladoss, Wojciech Skarka(*), Jacek Rduch

RMT6, Department of Fundamentals of Machinery Design, Faculty of Mechanical Engineering,
Silesian University of Technology, Gliwice, Poland
(*)*Email:* wojciech.skarka@polsl.pl

ABSTRACT

Unmanned Aerial Vehicles (UAVs) generally operate in complex and effective environments that impose multiple physical stresses, including thermal, aerodynamic, and structural loads. Conventional analysis methods usually look at these things separately, which can cause problems and lead to less-than-ideal design results. This study aims to implement a Multiphysics modeling framework for comprehensive structural design optimization for UAVs. We designed a Multiphysics framework to analyze and integrate aerodynamic forces and their structural responses using coupled simulations, enabling accurate predictions of unmanned aerial vehicle structural behaviour under real-world conditions. We will apply optimization algorithms to refine UAV designs for enhanced performance, which include improved structural durability, reduced weight, and increased energy efficiency. This paper highlights the practical applications of Multiphysics modeling, such as extended UAV lifetimes, reduced maintenance costs, and improved safety margins. The research concludes by discussing the iterative design approach of the UAV structural design using multi-physics modelling.

Keywords: Unmanned aerial vehicle, UAV, Multiphysics modelling, design optimization.

INTRODUCTION

The highly increased use of Unmanned Aerial Vehicles in the field of defense, logistics, surveillance, and environmental monitoring (N. V. Nguyen et al., 2014; Skarka, 2018) has created an impact on finding modernized UAV design development methods for improving the effectiveness of the UAV design process, development, and reliability of the design (Skarka, 2018; Skarka et al., 2023). In general, the conventional design process follows a step-by-step approach, which helps only to find the solution one step at a time, such as aerodynamic and structural analysis (Ives et al., 2018; Matsson et al., 2016; Khadse et al., 2015) separately. The interdependence of the UAV design process becomes more complex. They involve one another as they evolve, so there is a dire need for new design frameworks that can holistically capture these design complexities.

In the context of design optimization using multi-physics (Cheng H.D et al., 2015) modelling for UAVs, multi-physics modelling will be a more powerful tool that helps simulate (Cheng H.D et al., 2015) various physical phenomena and their interaction in a single computational environment. Using the Multiphysics iterative approach, engineers can run a realistic simulation, and they can decide to find the best structural design (Peruru et al., 2017) configuration based on the simulation results, which are closer to real-world conditions. This iterative approach not only integrates the various fields of physics but also reduces the design cycle by preventing wasted efforts on UAV structural design that won't work.

In this paper, we demonstrated the use of multi-physics-based design optimization for UAV design using coupled simulation in aerodynamics, structural mechanics, and natural frequency response of the UAV structures to create a more robust and high-performing design. This iterative approach will help us to push the boundaries for maximum performance, weight minimization, energy efficiency, and flight efficiency across a wide range of mission profiles.

METHODOLOGY

Multiphysics is the study of the simultaneous simulation of various physical fields within a single framework. This method is crucial in situations where multiple physics interact and influence each other, necessitating their collaboration to achieve accurate and comprehensive outcomes in the UAV design process. The research uses advanced computer tools like computational fluid dynamics (CFD) (Cheng H.D et al., 2015); Matsson et al., 2016) and finite element analysis (FEA) (Cheng H.D et al., 2015; Peruru et al., 2017) to show how the airflow over the UAV structure and the changes in the structure affect one another (Cheng H.D et al., 2015; Son et al., 2016). The methodology employed one-way fluid-structure interaction (FSI) coupling (Cheng H.D et al., 2015; Son et al., 2016) in conjunction with computational fluid dynamics analysis to analyze the structural response of the UAV, which is essential for calculating aerodynamic forces at the specific mission profile velocity. Additionally, this method describes the key role of a repeated process in the design by linking the aerodynamic forces with how the structure responds, including structural analysis and modal analysis, while considering the pre-stress condition.

After making a successful connection, tools like Computational Fluid Dynamics (which studies aerodynamic forces) were added to the information for structural analysis (which examines stress and changes in shape) using one-way FSI. The findings from both the structural analysis and CFD (Cheng H.D et al., 2015; Ives et al., 2018; Peruru et al., 2017; Khadse et al., 2015) were then used to perform modal analysis under pre-stress conditions to find out how the structure naturally vibrates. Along with developing a 3D model based on the trade study, mission profile, and initial sizing, created a loop for the iterative approach.

We will optimize the UAV design through an iterative approach. Once we reach the desired geometry based on the mission profile and aerodynamic results, we will use software for 3D modelling to create a 3D model that incorporates fewer design constraints from our initial concepts. We will then import this model into the previously mentioned coupled simulation to perform Multiphysics simulations (Ives et al., 2018; Matsson et al., 2016) with our designed frameworks. Based on the simulation results, if we obtain the desired result, the optimized design will move on to the detailed one; if not, we will modify it to improve the structural integrity with additional structural components, like skin thickness, spars, ribs (Peruru et al., 2017), and stringers of the UAV, with related structural constraints.

Multiphysics modelling requires the assistance of sophisticated design and simulation software for its execution. This methodology will utilize the technical advancements of the sophisticated software that is available on the market (Ives et al., 2018) for aerodynamic calculations, 3D UAV designs, and Multiphysics simulations. To get the most out of the Multiphysics application in this study, we will be designing a sustainable energy propulsion (Peciak et al., 2022; Skarka, 2018; Peciak et al., 2023) UAV with a fixed wing that strictly follows the UAV design regulations (Raymer, 2018; Skarka et al., 2023). The algorithm of design optimization is as follows, Figure 1:

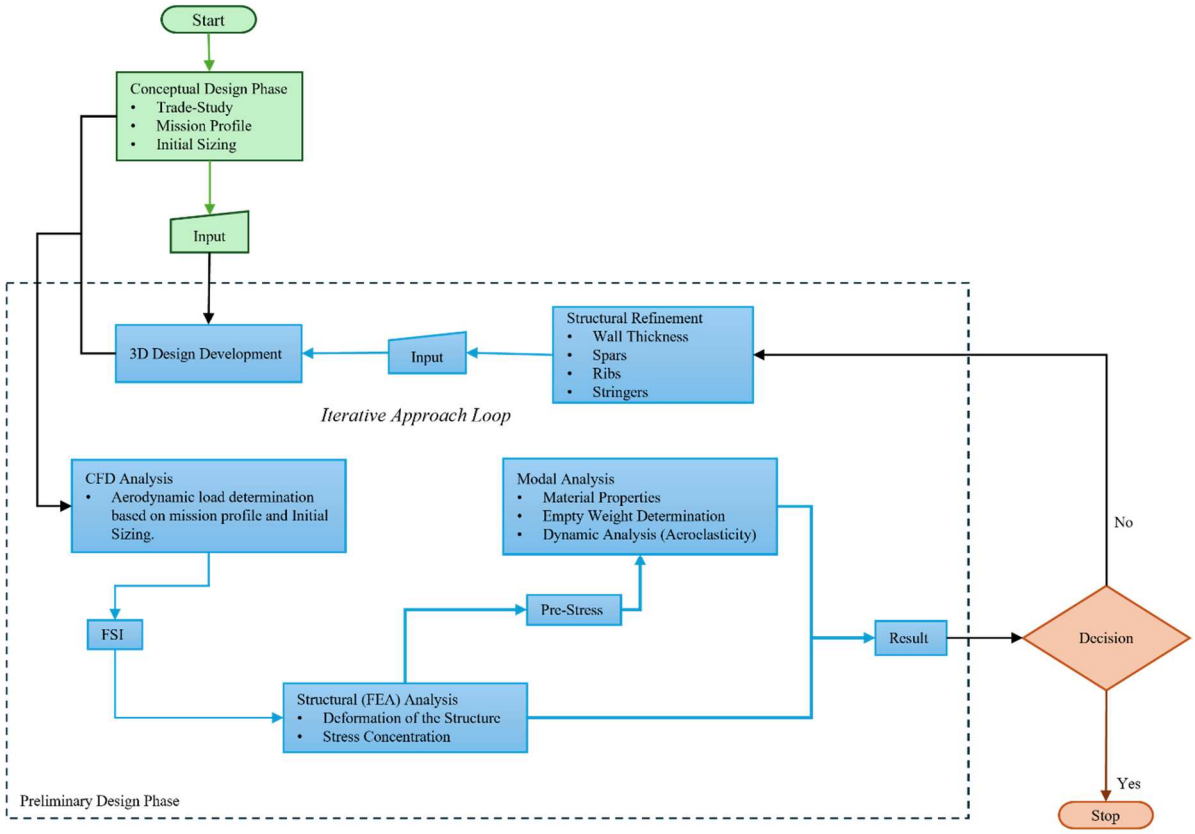

Fig. 1 - Algorithm of multiphysics modeling for UAV design optimization.

RESULTS

This research aims to provide a new approach to optimizing conventional UAV design using Multiphysics modeling, especially for UAV structural design, as mentioned in the algorithm in the methodology section, Figure 1. The research begins with a selection of types of UAVs. We have considered designing the Long-range UAV for its efficiency, range, and sustainable energy propulsion comfort to demonstrate this new approach. A trade study has been conducted to create the perfect mission profile (Raymer, 2018) for the selected type of UAV. The trade study was conducted among six Long-range UAVs that operate in real-time, and the names and parameters considered are mentioned in the Table 1 below:

Table 1 - Collected data of existing long-range UAVs – Trade study.

Parameters	*Airbus Kzo**	*Hesa Ababil-3**	*Yarara**	*Rheinmeta 11 Luna**	*UAVOS Sitaria**
Gross Weight, kg	161	123	40.5	110	45
Wingspan, m	3.42	5	3.98	5.3	5.16
Maximum Speed, km/h	220	200	166.68	153	140
Maximum Speed, m/s	61.11	55.56	46.30	42.50	38.89
Maximum Speed, Mach	0.18	0.16	0.13	0.12	0.11
Range, km	140	100	50	100	120

* The data for the trade study was collected from various sources.

Based on the data collected from multiple long-range UAVs, we have used a graphical method optimization technique to design our mission profile requirements (Raymer, 2018) based on two main criteria, such as range and gross weight, as shown in Figure 2 below.

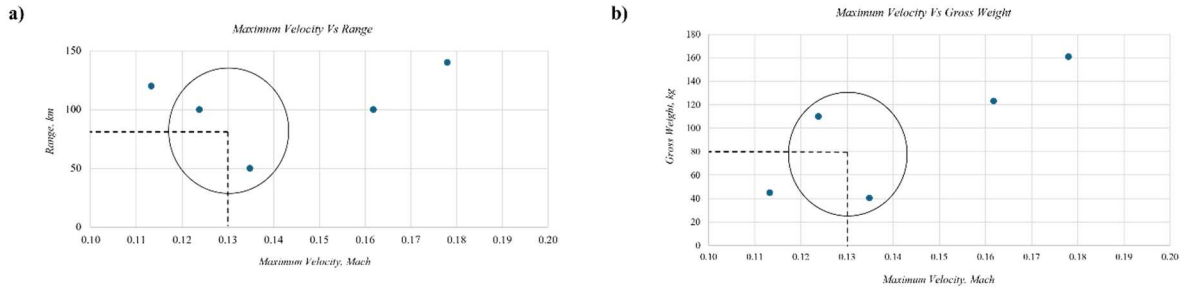

Fig. 2 - Graphical optimization method to define the mission profile: a) Range, b) Gross weight

Based on the results obtained from the trade study, our desired mission profile parameters are mentioned in the Table 2.

Table 2 - Desired mission profile of the UAV.

	Mission Profile Consideration		
1	Flight Maximum Velocity	45	m/s
2	Flight Maximum velocity	216	km/h
3	Flight Maximum velocity	0.13	Mach
4	Gross Weight	80	kg
5	Range	80	km

After deciding on the mission profile parameters, we moved on to find the dimensional and non-dimensional parameters of the long-range UAV wing by utilizing the conceptual design (Raymer, 2018) phase of the conventional UAV design methodology. The wing design parameters that were obtained are shown in the Table.3 below.

Table 3 - Obtained wing design parameters.

1	Type	Monoplane	
2	Location	Mid Wing	
3	Airfoil	NACA2412	
4	Wingspan (b)	3.16	*m*
5	Tip Chord (CT)	0.79	*m*
6	Root Chord (CR)	0.79	*m*
7	Mean Aerodynamic Chord M.A.C (Ĉ)	0.79	*m*
8	Area of the Wing (S)	2.50	*m2*
9	Aspect Ratio (AR)	4.00	
10	Taper Ratio (λ)	1	
11	Wing Loading (W/S)	171.68	*N/m2*
12	Volume of the Wing (Volwing)	0.16	*m3*

All the obtained dimensional non-dimensional parameters and the selected airfoil profile for the long-range rectangular wing configured UAV, the airfoil NACA 2412 (Matsson et al., 2016), have been chosen based on its proven efficiency of lift, drag, and pitching moment characteristics (Ives et al., 2018). It's specially designed for rectangular-wing UAVs. To ensure the flying capabilities of the designed UAV wing, we have compared the aerodynamic performance coefficients (Ives et al., 2018; Matsson et al., 2016) that we obtained from both analytical and numerical methods in the Table 4 below.

Table 4 – Comparison of the designed wing results.

S. No	***Analytical Result***	***Numerical Result***
Lift Co-efficient (C_L)	0.101179	0.1604
Drag Co-efficient (C_D)	0.018824	0.0195

After getting sufficient results, the next step of the methodology algorithm guides us to enter the iterative design approach of the UAV with the help of the Multiphysics Modelling framework. To demonstrate the iterative design approach for the UAV structural design, developing the proper CAD model is important (Peruru et al., 2017). In general, the design of the UAV has a symmetrical structure. So, we are taking one-half of the structure to perform the iterative design approach. The half segment of the developed CAD model of the wing with the calculated dimensional and non-dimensional parameters, along with the profile of the NACA2412 airfoil (Ives et al., 2018; Matsson et al., 2016), has been shown in Figure 3.

Fig. 3 - CAD model of the desired wing geometry.

The next step of the algorithm allows us to perform the Multiphysics simulation that has already been explained in the methodology section. For this simulation, we have employed high-fidelity software such as Ansys Workbench. In general, the forces that act on the aircraft structures are aerodynamic forces (Ives et al., 2018; Matsson et al., 2016). So, we begin our iterative approach with the CFD analysis of the UAV wing structure for the mission profile velocity of 45 m/s. Since our mission profile parameters are fixed, this iterative approach is going to explain how the structural components of the UAV are going to be decided using the Multiphysics simulation model. So, we recommend performing the analysis with the flexible relative aerodynamic forces to make a strong structural design. For that, we have considered 60 m/s velocity as our margin of safety, so the desired UAV structure will be able to carry some more aerodynamic forces other than the mission profile velocity. After setting all the boundary conditions of the wing structure, we performed the CFD analysis in Ansys fluent (Ives et al., 2018; Matsson et al., 2016), and the simulated pressure load is shown in Figure 4.

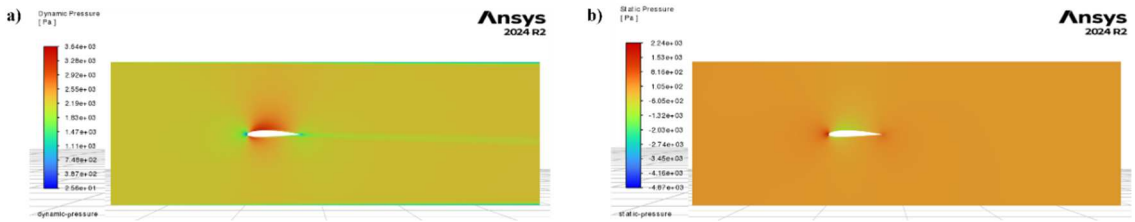

Fig. 4 - Obtained CFD results: a) Dynamic pressure, b) Static pressure.

The algorithm allowed us to move to the coupled simulation of CFD and FEA analysis (Matsson et al., 2016; Peruru et al., 2017), so the Fluid-Structure Interaction (FSI) (Son et al., 2016) has been taken into consideration. In this study, we have considered only One-way FSI , which is often called weak coupling, which means the impact of the fluid over the structure is only considered, and the effect in the fluid will be (Son et al., 2016) ignored. The reason behind choosing the one-way FSI over the two-way FSI is that the one-way will give a realistic pressure distribution, which is very important for the FEA analysis (Peruru et al., 2017), as shown in Figure 5.

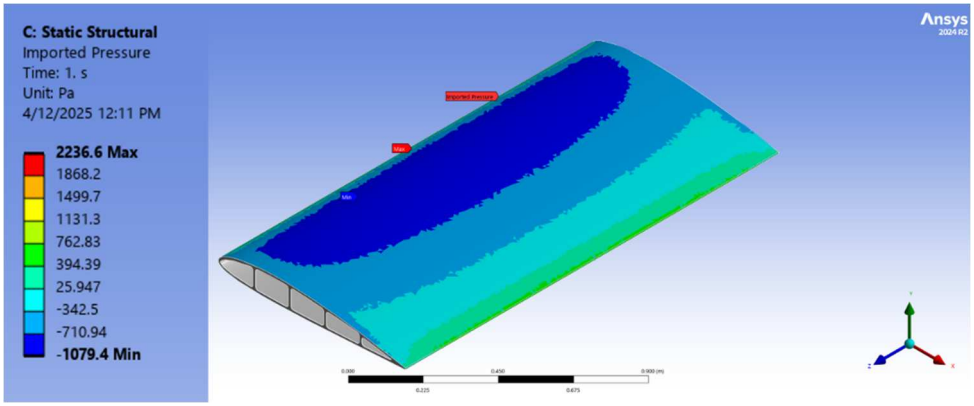

Fig. 5 - Pressure distribution over the wing surface.

The pressure loads of the relative velocity obtained from the CFD analysis (Ives et al., 2018; Matsson et al., 2016) have been taken as the analysis setup for the FEA analysis (Peruru et al., 2017). Further, the algorithm has been structured with the modal analysis (Khadse et al., 2015) to find out the maximum bending and torsion of the wing structure for its natural frequency. Since the pressure load has been applied to the structure, the modal analysis will be performed under the pre-stress condition. For the FEA and Modal analysis (Peruru et al., 2017; Khadse et al., 2015), the material selection is very important. We have taken aluminum alloy 7079 (Yuvraj et al., 2015) for this demonstration, and the material properties (Yuvraj et al., 2015) have been added as the simulation setting of the FEA and Modal (Peruru et al., 2017; Khadse et al., 2015) coupled simulation. The iterative approach loop gave us instructions on how to follow the steps in the process of designing the UAV. In the very first step, the thickness of the skin is set to 2 mm, with ribs at the edges. The design of the wing and the results of the first iterative approach are shown in Figure 6 below.

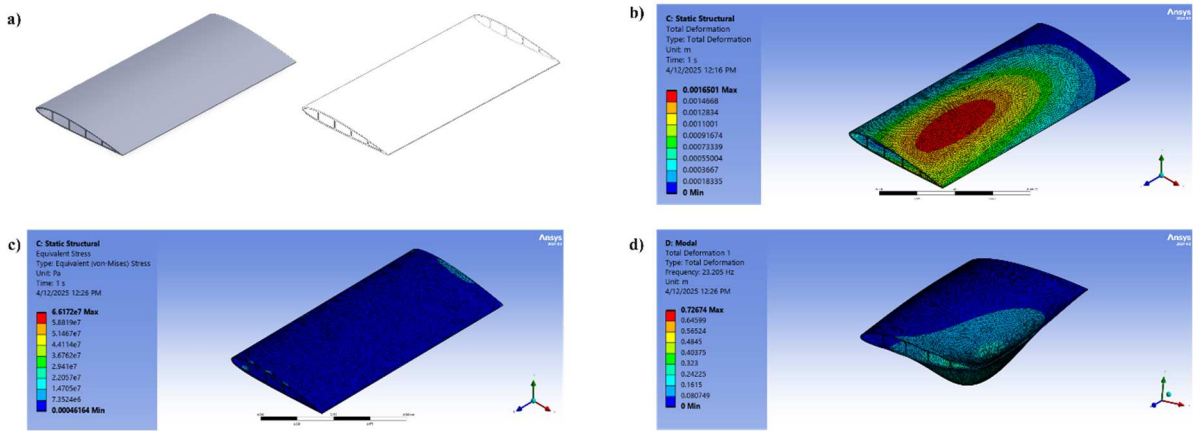

Fig. 6 - Iteration 1: a) CAD model, b) Total deformation, c) Equivalent stress, d) Bending deformation.

Based on the results of Figure 6 (b), we decided to refine our wing with the same skin thickness of four ribs (Peruru et al., 2017), mainly from the left end. Adding more ribs from the free end will give more strength to the place where the maximum deformation happened in the first iteration process; longitudinal spars are placed between ribs to cover the length (Peruru et al., 2017) between the ribs, and the results of the second iterative approach are shown in Figure 6. also, in iteration 2 we have successfully minimized the bending deformation significantly by refining the wing structure.

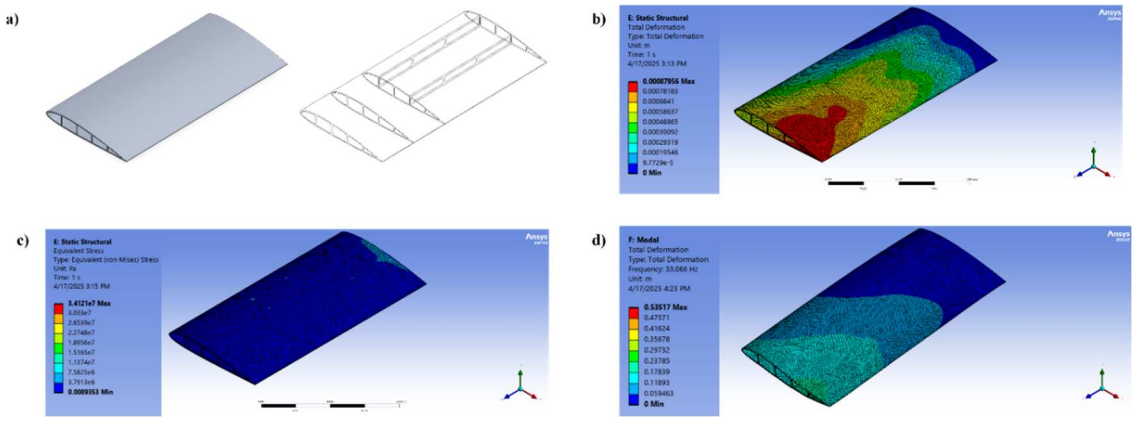

Fig. 7 - Iteration 2: a) Refined CAD model, b) Total deformation, c) Equivalent stress, d) Bending deformation.

Even with significant results in iteration 2, we decided to run iteration one more time to get a finer result and reduce the bending (Khadse et al., 2015) deflection. In iteration 3, the wing geometry was modified further with five ribs and two full-length longitudinal hollow spars (Peruru et al., 2017) across the wingspan to maintain a similar weight and reduce the bending deflection. The result is in Figure 7, and the results of an iterative approach are shown in Table 5.

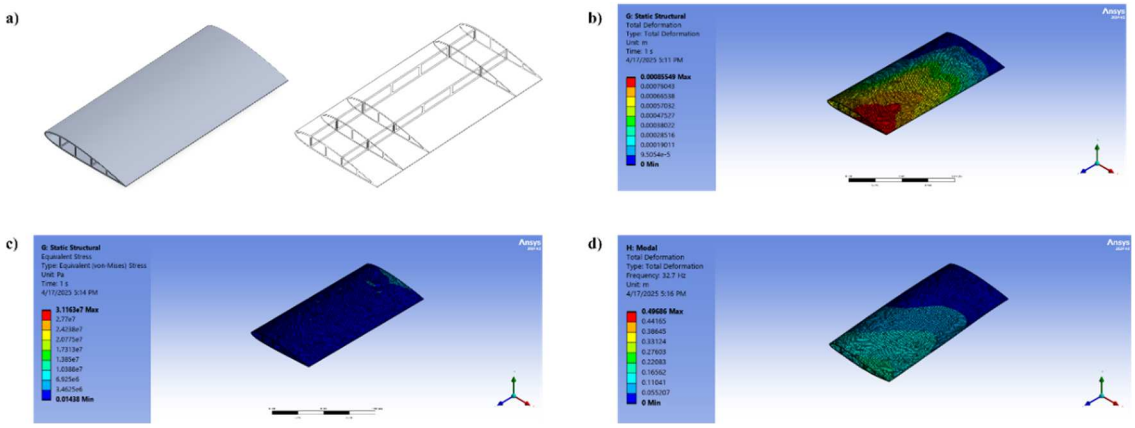

Fig. 8 - Iteration 3: a) Refined CAD model, b) Total deformation, c) Equivalent stress, d) Bending deformation.

Table 5 - Comparison of results from the iterative approach.

S.No	*Velocity, m/s*	*Material*	*Thickness, mm*	*Wing Components*	*Mass, Kg*
Iteration 1	60	Aluminium Alloy	2	Shell, two ribs	14.793
Iteration 2				4 ribs, two spars	15.271
Iteration 3				5 ribs, two long spars	15.349

DISCUSSION

This study proposes a novel design optimization for unmanned aerial vehicles by introducing a new iterative design approach that uses the advantages of Multiphysics during the preliminary design phase. By coupling the following tools, such as Computational Fluid Dynamics (CFD) (Ives et al., 2018; Matsson et al., 2016), Finite Element Analysis (FEA) (Peruru et al., 2017), and Modal Analysis (Khadse et al., 2015), the engineers can understand the effect of aerodynamic forces on the structure and dynamic stability well before entering the detailed design phase. This shows the major shift from the conventional UAV design workflow, where structural design decisions such as the layout of spars, ribs, and skin thickness (Peruru et al., 2017) are usually addressed only in later phases.

One major benefit of this iterative design approach is the use of starting the iterative approach with a shell-based structure to perform the simulation. These shell models are computationally lightweight (Yuvraj et al., 2015) and versatile, allowing rapid analysis of the multi-physics output. Structural refinement can be progressively altered based on the structural stress, deformation, and frequency responses (Ives et al., 2018; Peruru et al., 2017; Khadse et al., 2015) gained from real aerodynamic conditions.

The application of one-way FSI (Son et al., 2016) effectively captures the aerodynamic forces as pressure loads. It has an impact on structural deformation, making it highly recommended for early design optimization, as we explained in the methodology. One-way FSI is more accurate in capturing aerodynamic loads, which is closer to real-world conditions; on the other hand, two-way FSI (Son et al., 2016) offers a higher level of accuracy by allowing mutual fluid-structure feedback, and it remains computationally intensive and more helpful for the final validation.

However, this methodology has limitations. Firstly, high-fidelity software is required to maintain accuracy in both the design of the 3D model and the analysis of the multi-physics framework. During the iterative approach, engineers need to switch between both software systems simultaneously and perform the analysis for each component because putting them all together will require more computational power, which might delay the process. Secondly, this iterative approach is more suitable for lightweight, (Yuvraj et al., 2015) low-altitude, and relatively low-speed platforms like UAVs, where we can manage to analyze the aeroelasticity within the simplified multi-physics framework, due to the requirement of high computational resources and advanced computational strategies applying the same methodology to large commercial or high-speed aircraft requires extreme validation. Hence, the multi-physics system needs to be really sophisticated.

In spite of these limitations, the integration of CFD-derived pressure (Ives et al., 2018; Matsson et al., 2016; Khadse et al., 2015) loads into modal analysis under pre-stress conditions gives a strategic advantage. It also allows us to detect potential issues and dynamic (Khadse et al., 2015) instability. This is specifically important for UAVs, where the mass is low and modal frequencies match the aerodynamic excitation frequencies.

In the end, the methodology provides a flexible and expandable basis for designing UAVs, allowing the integration of structural and aerodynamic performance (Peruru et al., 2017; Khadse et al., 2015) into a single optimization framework.

CONCLUSION

This paper presents a multi-physics modeling framework developed for the structural design Optimization of Unmanned Aerial Vehicles. By combining CFD, FEA, FSI, and modal analysis (Ives et al., 2018; Matsson et al., 2016; Peruru et al., 2017; Khadse et al., 2015) in a

single simulation environment, the methodology allows critical structural decisions to be made much earlier in the preliminary design stage than is possible in conventional workflows. Shell models, enhanced by CFD-derived pressure fields, provide vital insights into stress distribution, modal behavior, and aeroelastic responses at initial design stages. One-way FSI is computationally efficient for the transfer of aerodynamic loads to the structural domain and has adequate accuracy during early development.

It is highly recommended for the development of UAVs, where weight, cost, and fast iteration cycles are of greatest concern. However, it is not necessarily suited to all fluid–structure interactions due to issues in accurate prediction at extreme flexibility (Yuvraj et al., 2015; Matsson et al., 2016) or flown speed. The method also builds the foundation for future developments, such as automated optimization and integration with machine learning-based design tools. Therefore, this methodology represents a valid, practical, and future-oriented approach to UAV design optimization. Thus, it leads to better decision-making at an early stage in the design process, accelerates the design cycle, and helps design UAV structures that are both more efficient and more reliable, both aerodynamically and structurally.

ACKNOWLEDGMENTS

The publication is funded by the European Funds for Silesia 2021-2027 under the program FSD-10.25: Development of Higher Education for the Green Economy. The project, titled "The Modern Methods of Monitoring the Level and Isotopic Composition of Atmospheric CO2 (MONCO2)", is identified as project No. *FESL.10.25-IZ.01-06C9/23-004.*

The publication is supported by the Rector's pro-quality grant. Silesian University of Technology, grant number 10/060/RGJ24/2050

REFERENCES

[1] Cheng H.D., Cen Y.P, Multiphysics Modeling: Numerical Methods and Engineering Applications. Elsevier and Tsinghua University Press, 2015.

[2] Ives, Rob, Edet BASSEY, Faik A. HAMAD. "Investigation of the flow around an aircraft wing of section NACA 2412 utilising ANSYS fluent." INCAS Bulletin, 2018.

[3] Khadse, Nikhil A., S.R. Zaweri. "Modal analysis of aircraft wing using Ansys workbench software package." International Journal of Engineering Research & Technology 4.7 2015: 225-230.

[4] Matsson, John E., et al. "Aerodynamic performance of the NACA 2412 airfoil at Low Reynolds Number." 2016 ASEE Annual Conference & Exposition. 2016.

[5] N.V. Nguyen, J.W. Lee, Y. D. Lee, H.U. Park, "A multidisciplinary robust optimisation framework for UAV conceptual design," The Aeronautical Journal, vol. 118, no. 1200, pp. 123–142, 2014.

[6] Peruru, Sivarama Prasad, Suman Babu Abbisetti. "Design and finite element analysis of aircraft wing using ribs and spars." Int. Res. J. Eng. Technol. (IRJET) 4.06 2017: 2133-2139.

[7] Peciak M, Skarka W. Assessment of the Potential of Electric Propulsion for General Aviation Using Model-Based System Engineering (MBSE) Methodology. Aerospace 2022, 9, 74.

[8] Peciak M, Skarka W, Mateja K, Gude M. Impact Analysis of Solar Cells on Vertical Take-Off and Landing (VTOL) Fixed-Wing UAV. Aerospace, 2023, 10, 247.

[9] Raymer D.P, Aircraft Design: A Conceptual Approach, 6th ed. Reston, VA: AIAA, 2018.

[10] Skarka W. Model-Based Design and Optimization of Electric Vehicles. 25th ISPE Inc International Conference on Transdisciplinary Engineering 2018, 7, pp.566-575.

[11] Skarka W, Nalepa R, Musik R. Integrated Aircraft Design System Based on Generative Modelling. Aerospace 2023, 10, 677.

[12] Son, Seok-Ho, et al. "Wing design optimization for a long-endurance UAV using FSI analysis and the Kriging method." International Journal of Aeronautical and Space Sciences 17.3 (2016).

[13] T.W. Simpson, J.R.R.A. Martins, "Multidisciplinary design optimization for complex engineered systems: report from a National Science Foundation workshop," Journal of Mechanical Design, vol. 133, no. 10, article 101002, 2011.

[14] Yuvraj, S.R., P. Subramanyam. "Design and analysis of Wing of an ultra-light Aircraft." International journal of innovative research in science, engineering and technology 4.8 (2015): 7456-7468.

Proceedings IRF2025: 8th International Conference on Integrity-Reliability-Failure
In Engineering, Materials, Manufacturing and Biomechanics. Porto 15-18 July 2025
DOI: https://doi.org/10.24840/978-972-752-323-8

PAPER REF: 22421

TOWARDS HUMAN TRUST IN ARTIFICIAL INTELLIGENCE: AN EXPERIMENT THROUGH AUTONOMOUS VEHICLE

Peer M Sathikh(*), Dexter Fang Zong Rui
School of Art, Design and Media, Nanyang Technological University, Singapore
(*)*Email:* peersathikh@ntu.edu.sg

ABSTRACT

Artificial Intelligence (AI) as a modern endeavour has a long history in the making. Many early authors have been writing on this topic such as McCorduck [1] who writes, "For nearly as long as we have records, human beings have imagined bestowing their essence upon artifacts – idols, automata, robots, simulacra, unpredictable deities, obedient slaves- animated, artificial intelligences, every one of them". For a very long time the scientific and the engineering world was interested in making inanimate objects intelligent. According to Mijwel [2], "Ancient Greeks had myths about robotics, and Chinese and Egyptian engineers made automatons. We can see the traces of the beginning of modern artificial intelligence as an attempt to define the classical philosophers' system of human thought as a symbolic system". In other words, AI and robots somehow had gotten intertwined into a perceived systems where AI delivers its 'intelligence' through physical objects that could be stationary or mobile or both. While it has become a common sight to see service robots at various places like the airports and restaurants, with more or less 'programmed' intelligence, researchers around the world have been working on 'intelligent' robots with human-like face and body. Hanson Robotics' Sophia is one example of such advanced human-like robot. According to Hanson Robotics, "Sophia is simultaneously a human-crafted science fiction character depicting the future of AI and robotics, and a platform for advanced robotics and AI research". (https://www.hansonrobotics.com/sophia/ retrieved on 15 December 2024). Will AIs always have physical form? Is this the future progress for AI? In this paper the authors research into the possibility of 'pervasive / omnipresent intelligence' which does not require physical form.

Keywords: Artificial intelligence, human-to-AI interaction, reliability and trust.

INTRODUCTION

Opportunity to find answers to the question of interacting with 'formless' AI came in the form of research grants for the development of autonomous vehicle under Singapore's National Research Foundation (NRF) awarded to a research alliance between Nanyang Technological University (NTU) and Technical University of Munich (TUM) called TUMCREATE. Further grant to pursue this has come from the Ministry of Education of Singapore through a Tier 1 Grant from 2022 to 2025.

The research framework for this wider project was to study how human-to-human interactions take place within the findings of Speech Act theory by Searle Speech Act Theory [3] from a human-to-human communication point of view, which requires in a spoken sentence to fulfill the following:

1) Essential Condition, 2) Preparatory Context, 3) Propositional Content and 4) Sincerity

where its intent is carried through 3 different forces, which are Locutionary, Illocutionary and Perlocutionary Forces by itself, and more discerning acts need to be understood for its intentions to be clear. To have clarity and to bring sincerity and authenticity to the way humans communicate with each other, Habermas' [4] Communicative-Action Theory builds on this with the introduction of validity claims which work towards mutual agreement for both speaker and hearer. With an understanding of these two theories, the authors set out to propose the qualities for interacting with pervasive / omnipresent AIs. This takes one to the question on how should/could humans interact with omnipresent AIs if and when the AIs evolve into omnipresent entities.

SIMULATING DESIRED COMMUNICATION THROUGH EXPERIMENTS.

The authors are at present testing their proposal for a 'natural communication' with omnipresent AI through simulation of an autonomous vehicle, testing both the emerging capabilities of Open AIs such as ChatGPT and Claude, as well as how human participants communicate with an autonomous driver. The experiments set up prepares participants through a pre-recorded trip in a virtual mockup of an autonomous vehicle, where they role play as passengers. The conversations are analysed and recorded to assess the effectiveness of these designed experiment with the first level results ready by June 2025.

RESULTS AND CONCLUSIONS

With rapid development in Open AI which can interact directly with human users and with the anticipation of omnipresent AIs with interconnectivity and access to large amounts of data, there is a need for building in communication ability for them to interact with human users which could be more 'normal and social'. In this research the authors and the research team exploring on a more natural mode of communication between humans and future omnipresent AIs. This research has taken into considerations' "...concepts of human communicative theories, nonverbal communication, the use of personality to create presence" [5]. To validate the research direction, experiments are in progress to strengthen the validity and hence the trust in future communication between humans and AIs.

REFERENCES

[1] McCorduck, P. Artificial Intelligence: An Apreçu. Artificial Intelligence, Winter 1988, Vol. 117, No. 1, pp. 65-83.

2] Mijwel, M.M. History of Artificial Intelligence. Computer Science, College of Science, University of Baghdad, Baghdad, Iraq, maadalnaimiy@yahoo.com, April 2015.

[3] Searle, J. R., Kiefer, F., Bierwsich, M (Ed). Speech Act Theory and Pragmatics. Dordrecht, Holland. D. Reidel, 1980.

[4] Habermas, J. The Theory of Communicative Action. Translated by Thomas McCarthy. Boston: Beacon Press, 1981.

[5] Sathikh, P., Fang, Z.R., Tan, G.Y. Achieving Trust in Future Human Interactions with Omnipresent AI: Some Postulates. Proceedings of the Intelligent Systems Conference (IntelliSys) 2021, Intelligent Systems and Applications, 2021, Vol.294, pp.700-718.

Proceedings IRF2025: 8th International Conference on Integrity-Reliability-Failure
In Engineering, Materials, Manufacturing and Biomechanics. Porto 15-18 July 2025
DOI: https://doi.org/10.24840/978-972-752-323-8

PAPER REF: 22423

MECHANICAL DESIGN OF A PROTOTYPE OF ROBOT FOR NON-DESTRUCTIVE INSPECTION OF CORROSION IN NUCLEAR SPENT FUEL SEALED CONTAINERS

David Agudo del Rio[1(*)], Pablo Garcia-Gil[1], Irea Lopez Garcia[2], Marcos Lopez Lago[1], Miguel Miguez Coto[2], Enrique Casarejos[1]

[1]CINTECX, Universidade de Vigo, Dpt. Mech. Engineering, E-36310 Vigo, Spain
[2]Dpt. Mech. Engineering, Universidade de Vigo , E-36310 Vigo, Spain
[(*)]*Email:* david.agudo@uvigo.gal

ABSTRACT

This work presents the mechanical design of a fully functional robot dedicated to the inspection of the steel cells containing dry spent nuclear fuel, and potentially suffering from stress corrosion cracking. The sealed cells made of steel can be placed inside an overpack and hold in open spaces. The challenge is making the inspection without removing the cell out of the overpack, due to radiation issues, and using just the venting wall openings. Both, the radiation condition, and the tough access limitation, would be solved by using a dedicated remote inspection device. The developed design focuses in the widely common HI-STORM overpacks, probing the inspection concept. Autonomous inspection cells can deploy sensors to perform the non-destructive inspection. A real scale prototype and mock-up were used to demonstrate the feasibility of the design concept.

Keywords: Mechanical design, nuclear spent fuel, stress corrosion cracking (SSC).

INTRODUCTION

The dry storage of nuclear spent fuel storage is a suitable option for fuel that has cooled substantially [1]. Dry interim storage of spent nuclear fuels requires the use of specific containers for the entire handling operation and temporary storage (Figure 1, left). Typical solutions used worldwide include containers with some form of sealed pressure capsule (called Multi-Purpose Container MPC) installed inside of an overpack for mechanical and environmental protection (Figure 1-right). MPCs can be designed for 40 years; however, local lifecycle management may include inspections at shorter periods (e.g., 20 years in Spain) to ensure the right safety status.

Fig. 1 - Left: Interim storage at Ascó (Spain). Right: MPC container in an overpack [2].

These devices use passive cooling methods to dissipate the thermal energy of the nuclear waste, avoiding excessive heating of the MPC. These passive systems consist of openings to the outside at different heights and a system of vertical channels (metallic profiles which also serve as centring devices for the correct insertion of the MPC) that create a ventilation stream inside the overpack that cools down the surface of the MPC.

The MPCs are made according to the highest standards for pressurized vessels (ASME B31.3-2016). However, dedicated research programs pointed out that it remains a potential risk in the long-term due to appearance of stress corrosion cracking (SCC) around the welds. SSC can cause cracks by a combination of stress (accumulated in the affected zone from the heat of welding that occurred in the construction of the MPC), and corrosion (caused by the deposition of chlorides on the surface). SSC is difficult to predict, and shows crack opening displacements of 15-30 μm, at the limit of visual inspections [3].

Removing the MPC for inspection is a complex operation (as it is the initial insertion). Indeed, it becomes a dangerous option if an existing crack was under the forces happening in handling or transport of the MPCs, inducing a radiation leak or allowing for oxygen intake that would dangerously alter the state of the stored fuel.

RESULTS AND CONCLUSIONS

All of the above opens up the opportunity to consider a robotic remote inspection. Considering the HI-STORM overpacks (Holtec International, PA, USA), the access from the outside is through the ventilation inlets (650mm x104mm). Then, the inspection of the MPC surface should be done along the vertical channels (4m long, 200mm x 58mm).

We created a mechanical design that allows the simplified insertion of the main body of the robot inside the container. Once on top of the MPC, a mobile arm can rotate and provide access to all the inspection channels. An independent system allows for driving inspection cells through the channels. These cells, equipped with sensors (visual testing, eddy current testing, radiation testing, etc.), can reach all possible and necessary inspection areas for doing a point-wise scanning. A full operational prototype was built using off-the-shelf and rapid prototyping elements. A real size mock-up was used to probe the capability of the prototype and the feasibility to make an appropriate inspection.

REFERENCES

[1] IRSN Report No 2019-00181, Storage of nuclear spent fuel: concepts and safety issues, IRSN, June 2018 (French issue), http://www.irsn.fr/spent-nuclear-fuel-storage.

[2] S.R. Greene, J.S. Medford, S.A. Macy. ATI-TR-13047. Storage and Transport Cask Data for Used Commercial Nuclear Fuel 2013 U.S. Edition 2013, p.65.

[3] A Wale, J., Ekstrom, P. (1995). Crack Characterization for In-service Inspection Planning, SKI, Technical Report, 14.4-940389.

Proceedings IRF2025: 8th International Conference on Integrity-Reliability-Failure
In Engineering, Materials, Manufacturing and Biomechanics. Porto 15-18 July 2025
DOI: https://doi.org/10.24840/978-972-752-323-8

PAPER REF: 22458

THE ROLE OF PLASTIC STRAIN DISTRIBUTION ON MICROSTRUCTURAL EVOLUTION IN BAINITIC STEEL DURING THERMOMECHANICAL CONTROL PROCESSING

M. Karam-Abian[1(*)], P. Parandavar[1], M. Tong[1,2], S.B Leen[1,2,3]

[1]Mechanical Engineering, College of Science and Engineering, University of Galway, Ireland.
[2]I-Form Advanced Manufacturing Research Centre, Ireland.
[3]Ryan Institute for Environmental, Marine and Energy Research, University of Galway.
[(*)]*Email:* m.karamabian1@universityofgalway.ie

ABSTRACT

The effect of plastic strain on the hot deformation behaviour and grain size evolution in bainitic steel was investigated using Gleeble thermo-mechanical physical simulation and finite element simulation. The model was validated by comparing the predictions with the experimentally measured true stress-strain curves. The model allowed quantification of the heterogeneity of plastic strain within the thermomechanical control processing under the investigated conditions. The results reveal that increasing plastic strain enhances dislocation density, promoting the nucleation of recrystallized grains. The recrystallized grain size decreases with higher strain due to enhanced grain boundary migration and subdivision of grains, reaching a saturation grain size at large plastic strain. The inhomogeneous distributions of plastic strain resulted in an inhomogeneous final microstructure, i.e., inhomogeneous distribution of recrystallization, constituent fraction, and average grain size.

Keywords: Thermomechanical control processing, plastic strain, finite element simulation.

INTRODUCTION

The thermomechanical control processing (TMCP) of Bainitic steels plays a critical role in tailoring their microstructural structure to reach optimal mechanical properties [1]. During TMCP, the distribution of plastic strain significantly impacts the evolution of microstructure, particularly in these steels. Understanding the relationship between plastic strain distribution and microstructural evolution is vital for designing advanced TMCP strategies to enhance the properties of bainitic steels [2]. This study explores the mechanisms through which plastic strain affects microstructural changes, aiming to provide insights into optimizing TMCP parameters for improved steel performance.

RESULTS AND CONCLUSIONS

The study showed that plastic strain significantly influences the hot deformation behaviour and microstructural evolution in low alloy steel. The validated finite element model accurately captured the heterogeneity of plastic strain during uniaxial hot compression test (UHCT). The results exhibited that increasing plastic strain enhances dislocation density that facilitates the nucleation of recrystallized grains. Furthermore, the average grain size was decreased with increasing plastic strain due to intensified grain boundary migration and grain subdivision, eventually stabilizing at a saturation grain size. However, the plastic strain was unevenly

distributed throughout the material, leading to an inhomogeneous microstructure characterized by variations in recrystallization fraction, constituent phases, and grain size (Figure1).

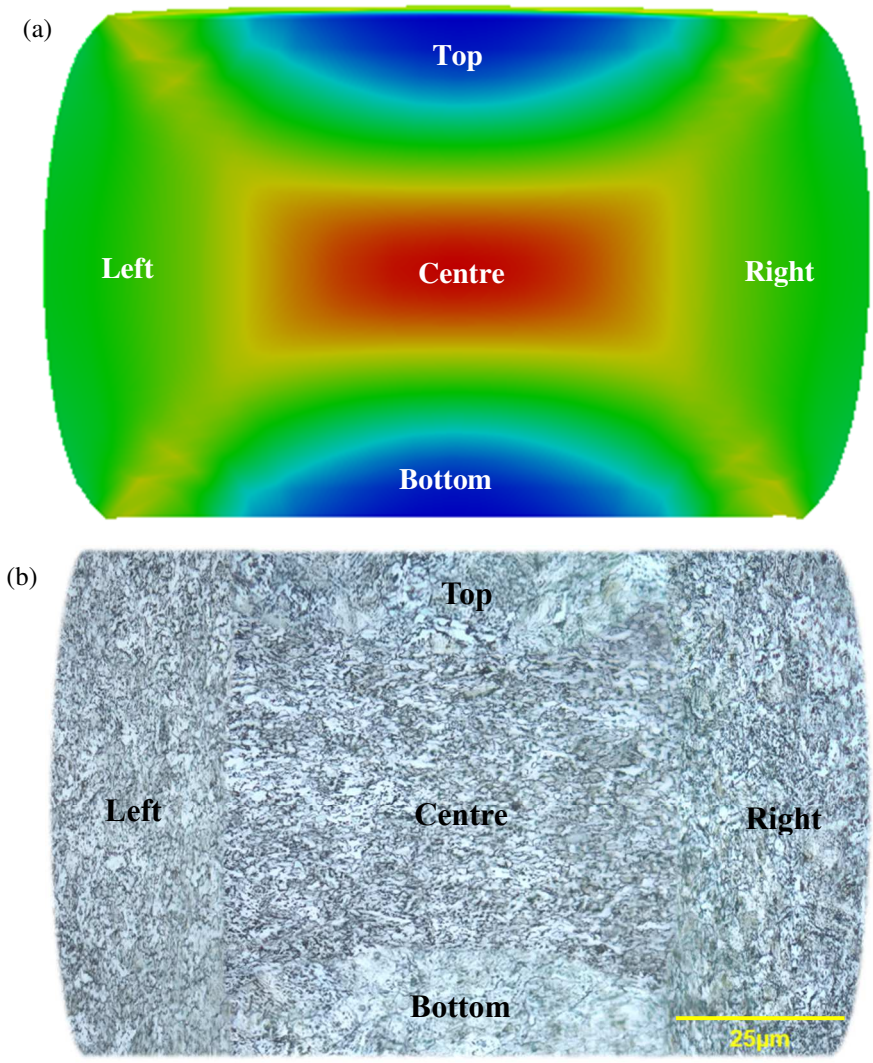

Fig. 1 - (a) FEM plastic strain distribution; (b) OM microstructure of different areas in the UHCT sample.

REFERENCES

[1] M Karam-Abian, A Zarei-Hanzaki, HR Abedi. Micro and macro-mechanical behavior of a transformation-induced plasticity steel developed by thermomechanical processing followed by quenching and partitioning. Materials Science and Engineering: A, 2016, 651, pp.233-240.

[2] Jie Cao, Jun Yan, Jing Zhang. Effects of thermomechanical processing on microstructure and properties of bainitic work hardening steel. Materials Science and Engineering: A, 2015, 639, pp.192-197.

Proceedings IRF2025: 8th International Conference on Integrity-Reliability-Failure
In Engineering, Materials, Manufacturing and Biomechanics. Porto 15-18 July 2025
DOI: https://doi.org/10.24840/978-972-752-323-8

PAPER REF: 22490

RESEARCH ON THE TRIBOLOGICAL FAILURE OF MECHANICAL COMPONENTS INDUCED BY ENVIRONMENTAL NANOPARTICLES UNDER HUMID CONDITIONS

Jim Chwen Yeh[1], Shin Yuh Chern[1], Sheng Jie Liao[1], Wei Lun Liu[1], Jeng Horng Horng[1,2(*)]

[1]Department of Power Mechanical Engineering, Yunlin, National Formosa University
[2]International Master's Program in Interdisciplinary Sustainability Studies, Tainan, National Cheng Kung University
[(*)]*Email:* jhhorng@gmail.com

ABSTRACT

This paper investigates the effects of different sizes and concentrations of environmental nanoparticles on the wear and scuffing performance of lubricants. Experimental results show that the size and concentration of the particles are the main factors affecting tribological performance. In fresh lubricants, larger particles and higher concentrations are associated with increased wear and scuffing. However, deviations from this optimal water content range, regardless of particle size, result in inferior tribological performance compared to fresh lubricant. Therefore, there may be a balance point where the deterioration of the lubricant caused by water and its absorption of frictional heat, and the increase in real contact area caused by nanoparticles, results in better tribological performance than new lubricants.

Keywords: Environmental nanoparticle, tribology failure, scuffing, excessive wear.

INTRODUCTION

The atmospheric environment is filled with numerous tiny water droplets and environmental particles. During the operation of mechanical components, these water and particles interact with the lubricant, causing gradual degradation over time, which reduces the performance of the components and may even shorten their service life. Among them, excessive wear and scuffing are the main reasons for the replacement of transmission components. Excessive wear will cause excessive contact temperatures and surface roughness. (Wu et al., 2015). Scuffing, in particular, lacks an accurate prediction method to this day (Horng and Lin, 1995; Chern et al., 2021). The most widely used method for estimating the service life of bearing grease internationally (ISO281, 2007), where the solid particle contamination factor e_c is only listed in six levels of 0, 0.1-0.3, 0.3-0.5, 0.5-0.6, 0.6-0.8, and 1.0, according to the severity of the contamination described in the text. e_c = 1 represents clean grease, and e_c = 0.5 represents moderately contaminated grease. However, there is no quantitative measure for what is considered moderately contaminated, and the description can only be blindly selected based on experience, indicating a lack of effective quantitative specifications. This paper mainly explores the influence of solid particles on excessive wear and scuffing.

RESULTS AND CONCLUSIONS

In this study, experiments were conducted using the ASTM D4127 four-ball accelerated wear tester, as shown in Figure 1. The balls used in the experiments are SUJ2 bearing steel with a diameter of 12.7 *mm*, a hardness of 64-66 HRC. Lithium-based grease was used as the test lubricant. Figure 2 shows that as the concentration of SiO_2 particles in the grease increases, the

water content also increases, while the total acid number (TAN) decreases. The greatest reduction in TAN occurs at a concentration of 1.480 wt% SiO_2 particles. It is hypothesized that the addition of SiO_2 particles, along with their associated surfactants, contributes to the decrease in TAN. A wear comparison was performed between the condition without particles and the condition with a particle concentration of 0.2 *wt %*. As shown in Figure 3, the wear diameter of SiO_2 in the dust was larger than that of clean grease. Assuming a wear tolerance life L_w = 340 *μm* as a baseline, it can be found that the life with a particle concentration of 0.2 *wt %* (7.2 minutes) is only 9.0% of the life without SiO_2 (80 minutes).

The scuffing test conditions followed the DIN-51350-4 standard, with a rotational speed of 1450 rpm, an oil temperature of 35°C, and an initial load of 10 *kgf*. The scuffing test results are presented in Figures 4(a) and 4(b). These figures illustrate that the grease containing 0.2 *wt %* SiO_2 exhibited higher friction coefficient and contact temperature compared to the clean grease. The scuffing load was observed to be 70 *kgf* for both the test without particles and the test with 0.2 *wt %* SiO_2 particles. However, the grease with 0.2 *wt %* SiO_2 reached the end of its service life approximately 50 seconds earlier. These results indicate that environmental particles tend to reduce the reliability and service life of mechanical components.

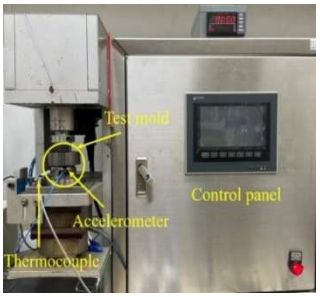

Fig. 1 - Four-balls tribometer.

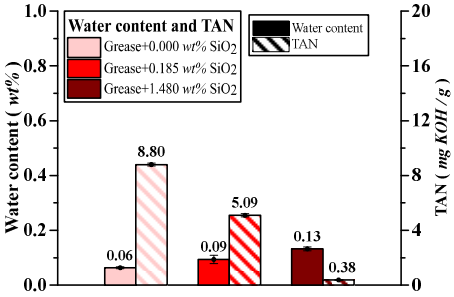

Fig. 2 - Water content and total acid value at the different SiO_2 concentrations of grease.

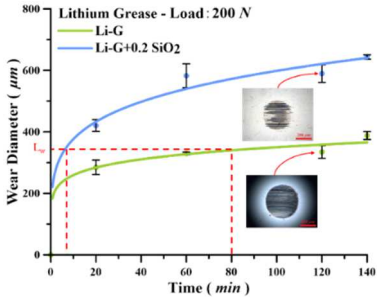

Fig. 3 - Wear life curves of grease with and without SiO_2 particle.

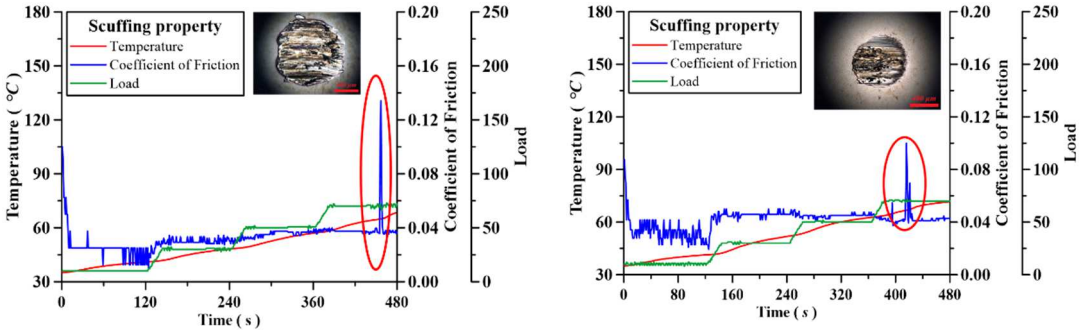

Fig. 4 - Friction and oil temperature of the grease with different particle concentrations (a)0.0 *wt%* (b)0.185 *wt%*.

REFERENCES

[1] Wu H.W. Chen Y.Y. Horng J.H. Contact temperature under three-body dry friction conditions, Wear, 2015, 330, pp. 85-92.

[2] Horng J.H. Lin, J. F. Effect of surface roughness on steel roller ccuffing, Wear, 1995, 184, pp. 203-212.

[3] Chern S.Y, Ta T.N. Horng J.H. Wu Y.S. Wear and vibration behavior of ZDDP-containing oil considering scuffing failure, Wear, 2021, pp. 478-479, 203923.

[4] ISO 281:2007(en) Rolling bearings - Dynamic load ratings and rating life.

Proceedings IRF2025: 8th International Conference on Integrity-Reliability-Failure
In Engineering, Materials, Manufacturing and Biomechanics. Porto 15-18 July 2025
DOI: https://doi.org/10.24840/978-972-752-323-8

PAPER REF: 22635

SIMULATION-BASED STRUCTURAL DESIGN AND RELIABILITY EVALUATION OF AN INDICATOR SPRING

Domen Šeruga[1(*)], Lovro Novak[2], Marko Nagode[1], Jernej Klemenc[1]

[1]University of Ljubljana, Faculty of Mechanical Engineering, Aškerčeva 6, 1000 Ljubljana, Slovenia
[2]Eti Elektroelement d.o.o., Obrezija 5, 1411 Izlake, Slovenia
[(*)]*Email:* domen.seruga@fs.uni-lj.si

ABSTRACT

The introduction of a reliability-based evaluation of fuse elements is an important developmental improvement towards ensuring operational safety. A case study presented here focuses on the essential level of details to be considered in early development stages of a product when it is already necessary to decide on the suitability of the design to ensure the required reliability level during operation. A finite element analysis of an indicator spring on a fuse element is carried out for a given geometry, material properties and operating conditions. The displacement-dependent force signal generated by the indicator spring is then worked out from the simulation results. The comparison of the generated spring force signal with the distribution of the micro-switch activation load yields the reliability assessment of the indication that a fuse has operated and needs replacement.

Keywords: Fuse element, indicator spring, reliability, finite element analysis.

INTRODUCTION

Fuses are used in all electric circuits (Coman et al., 2024; Bayliss and Hardy, 2012; Todorov and Kamberov, 2020; Hajimohammadi et al., 2020; Osmani et al., 2023). They are deliberately made weak so they can break the electric circuit when overloads and short-circuit currents appear which then protects the users and electrostatic components in such events (Bayliss and Hardy, 2012; Torres et al., 2010). The operation of a fuse is usually provided by a built-in fuse element which melts when overloaded (Coman et al., 2024; IEC 60269-1, 2006; Todorov et al., 2020). Typical elements used in an electric fuse are shown in Figure 1(a).

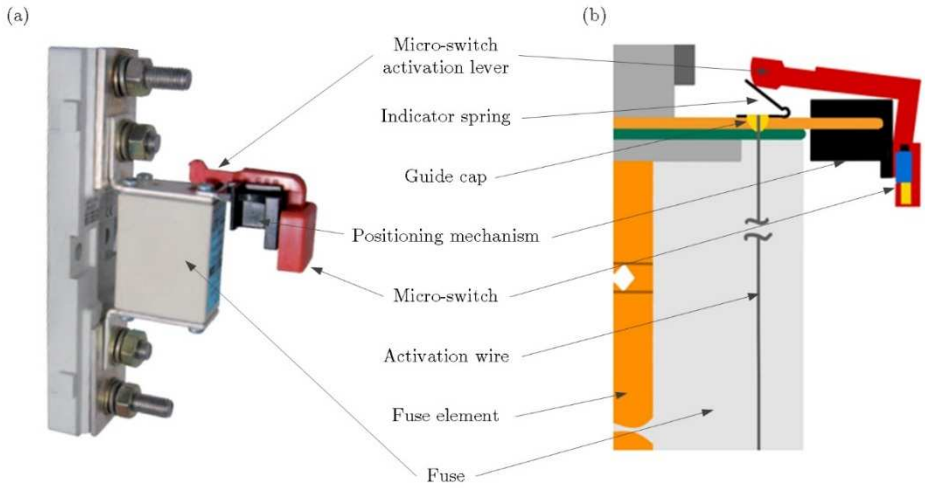

Fig. 1 - Electric fuse: (a) physical component and (b) geometric model with typical elements.

The operation of the fuse can also be shown by an indicator element as the fuse requires replacement after the fault clearance and before the electric circuit is put back into operation. The operation of the fuse can also activate an indicator spring which then turns on a micro-switch, Figure 1(b), and allows for an easier and also remote identification of fuses that need replacement when electric systems consist of a number of fuses (Coman et al., 2024; Plunkett et al., 2021).

METHOD

The force F which can be generated by an indicator spring depends on several factors,

$$F = F\left(u, \mu_1, \mu_2, t, r, h\right) \tag{1}$$

where u, μ_1, μ_2, t, r and h stand for the displacement of the spring at fuse operation, friction coefficient between the indicator spring and the guide cap, friction coefficient between the indicator spring and the micro-switch activation lever, thickness of the activation spring, positioning of the activation wire onto the indicator spring and the initial position of the indicator spring, respectively. The force generation of an indicator spring in this study has been simulated using finite element (FE) analysis in Abaqus 6.13-5. The FE model consisted of 3 parts using 5800 shell and solid structural elements, Figure 2(a).

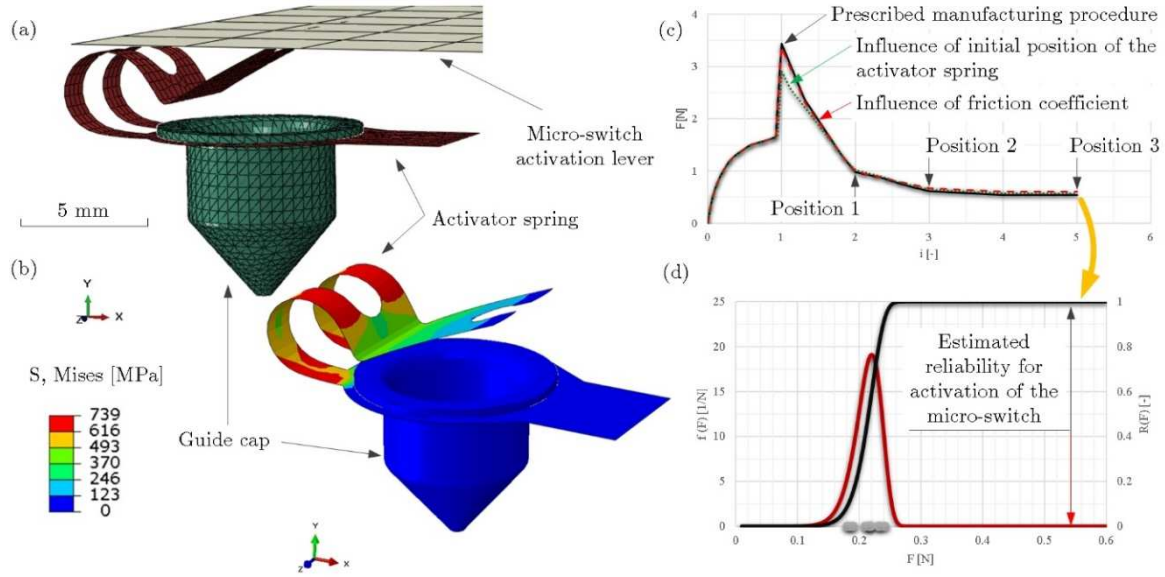

Fig. 2 - (a) Finite element model, (b) equivalent von Mises stress at position 1, (c) force signal of the indicator spring for various boundary conditions and (d) the measured distribution of the micro-switch activation load and estimated reliability at position 3.

The contacts between the parts allowed for the transfer of normal and tangential loads with prescribed coefficients of friction in prescribed range between $\mu_1, \mu_2 = 0.1$ and $\mu_1, \mu_2 = 0.4$. Elastoplastic material properties of a $t = 0.11$ mm X12 CrNi 17-7 steel sheet metal were measured prior to the simulation and were then applied as a bilinear material model with elastic modulus $E = 210000$ MPa, yield stress $\sigma_y = 1114$ MPa and tangential modulus $E_t = 1292$ MPa. Boundary conditions included positioning of the indicator spring with the guide cap, pre-loading of the indicator spring with the activation wire, operation of the fuse (melting of both the fuse element and the activation wire) and generation of force by the

indicator spring against the micro-switch activation lever at three pre-defined positions (positions 1, 2 and 3). Positions 1, 2 and 3 corresponded to pre-defined displacements of $u = 0.76$ mm, $u = 3.0$ mm and $u = 3.5$ mm, respectively. Boundary conditions were applied in steps 1-5 where step 1 represented the pre-loading of the indicator spring and step 2 stood for the initial contact between the indicator spring and the micro-switch activation lever (position 1). Step 3 exhibited the displacement of the lever just before the activation of the micro-switch (position 2) and finally steps 4-5 stood for the activation of the micro-switch and hence the blockage of the indicator spring movement (position 3).

RESULTS AND CONCLUSIONS

During the pre-loading of the indicator spring, stresses beyond the yield stress of the spring material can occur which cause plastic strains in the rounded part of the indicator spring, Figure 2(b). Consequently, the indicator spring does not return to its initial position (before the pre-loading) after the operation of the fuse. Pre-loading hence has the highest impact to the force generation ability of the indicator spring which can be clearly seen by the force peak at step 1, Figure 2(c). If the pre-loading of the indicator spring and hence its initial position is only reduced for 0.15 mm, the force generated is reduced from 3.5 N to 2.9 N, Figure 2(c). Interestingly, the force in positions 2 and 3 in this case is higher due to lower plastic strains and consequently a higher spring-back effect. A similar effect although to a much lower degree is achieved by reducing the friction from $\mu_1, \mu_2 = 0.4$ to $\mu_1, \mu_2 = 0.1$, Figure 2(c).

The micro-switch is activated at position 3 so it is crucial that the force caused by the indicator spring at that position is higher than the force needed to activate the micro-switch. Typical values of the micro-switch activation forces depend on the length of the lever, but in its shortest setting, where highest forces appear, a typical scatter is shown in Figure 2(d) (Novak, 2024; Novak et al. 2024). Comparing a typical force generated by the indicator spring at position 3 to the scatter of the forces needed to activate the micro-switch it can be seen that a high reliability of the fuse operation indication can be expected. Specifically, if the reliability of the micro-switch activation R_s is calculated with respect to the observed indicator spring force at position 3, F_3, as

$$R_s = \int_0^{F_3} f\left(F\right) \mathrm{d}F \tag{2}$$

where the probability density function of the micro-switch activation force $f\left(F\right)$ is described by a two-parametric Weibull distribution function $f\left(F\right) = f_{\mathrm{w}}\left(F, \theta, \beta\right)$ with parameters $\theta = 0.22$ N and $\beta = 11.5$, then a value $R_s \approx 1$ is observed.

CONCLUSIONS

Electric fuses are an important safety element in every electric circuit. It is also important that a reliable indicator is integrated into the fuse to warn the user when and where in the electric circuit a failure has occurred. Here we used a finite element analysis to simulate the behaviour of the indicator spring after the operation of a fuse, i.e. after melting of both the fuse element and the activation wire. It has been shown that an accurate elastoplastic material behaviour, all the crucial assembly parts and contacts between them have to be included in the simulation if the results are to be used in the reliability analysis of the failure indicator.

REFERENCES

[1] Coman P.T, Petrushenko D, Darcy E.C, White R.E. Electrical-thermal modeling and electrical design optimization of fuses in a nickel bus-plate for a Li-ion battery pack, Journal of Energy Storage, 2024, 86, 111226.

[2] Bayliss C, Hardy B. Chapter 11 - fuses and miniature circuit breakers in Transmission and Distribution Electrical Engineering (Fourth Edition), Newnes, Oxford, 2012, pp. 361-395.

[3] Todorov G, Kamberov K. EV fuse design cost reduction based on thermal-electric conduction analyses, Case Studies in Thermal Engineering, 2020, 21, 100692.

[4] Hajimohammadi F, Fani B, Sadeghkhani I. Fuse saving scheme in highly photovoltaic integrated distribution networks, International Transactions on Electrical Energy Systems, 2020, 30, e12148.

[5] Osmani K, Haddad A, Lemenand T, Castanier B, Alkhedher M, Ramadan M. A critical review of PV systems' faults with the relevant detection methods, Energy Nexus, 2023, 12, 100257.

[6] E. Torres, A. Mazón, Fernández E, Zamora I, Pérez J. Thermal performance of back-up current-limiting fuses, Electric Power Systems Research, 2010, 80, pp. 1469-1476.

[7] International Electrotechnical Commission IEC 60269-1, Low-voltage fuses – part 1: General requirements, 2006.

[8] Plunkett S. T, Chen C, Rojaee R, Doherty P, Sik Oh Y, Galazutdinova Y, Krishnamurthy M, Al-Hallaj S. Enhancing thermal safety in lithium-ion battery packs through parallel cell current dumping' mitigation, Applied Energy, 2021, 286, 116495.

[9] Novak L, Optimisation and simplification of fuse link indicator springs (in Slovene), Bachelor's Thesis, University of Ljubljana, Faculty of Mechanical Engineering, 2024.

[10] Novak L, Herman B, Klemenc J, Nagode M, Šeruga D. Determination of operating conditions of indicator springs (in Slovene), Svet strojništva, 2024, 13 – 1/6, pp. 82-83.

Proceedings IRF2025: 8th International Conference on Integrity-Reliability-Failure
In Engineering, Materials, Manufacturing and Biomechanics. Porto 15-18 July 2025
DOI: https://doi.org/10.24840/978-972-752-323-8

PAPER REF: 22797

ReDesignFX NOVEL METHODOLOGY: APPLICATION IN PRODUCT (RE)DESIGN-FOR-REMANUFACTURING

A.J. Baptista[1(*)], J.N. Ruivo[1], F.N. Heravi[2], G. Marchello[2]

[1]INESC TEC - Institute for Systems and Computer Engineering, Technology and Science, Porto, Portugal
[2]IIT - Istituto Italiano di Tecnologia, Genoa, Italy
[(*)]*Email:* antonio.baptista@inesctec.pt

ABSTRACT

Circular Economy challenges demand effective actions in the context of systemic change, production innovation and new product design approaches. Most company products must be redesign applying circular design principles articulated with sustainable design guidelines. Regarding product type, different approaches must be considered, namely in the scenario of novel product versions with updates or new design, and in the scenario of product instance redesign. This work presents a model for product redesign encompassing multidimensional assessment, ReDesignFX, considering design-for-X guidelines, either for new product development or product instance redesign in circular economy strategies application for product life extension. The model is applied as a proof-of-concept of the methodology in a system redesign in the context of a real-based remanufacturing operation of an industrial robot machine, where design-for-disassembly and design-for-repair were assessed for performance in the old machine (reverse engineered) and the new redesigned version.

Keywords: Circular Economy; Product Redesign; Design-for-X; R-Strategies; Design-for Disassembly; Design-for-Repair; Remanufacturing.

1. INTRODUCTION

As we continue to face a massive influx of new products designed following a Linear Economy approach - with minimal consideration for their use phase duration and lifecycle extension beyond legal requirements and warranty cost minimization - the transition to a more Circular Economy requires that products are fundamentally redesigned, in order to meet CE standards, following circular design principles and integrating sustainable design guidelines. To better understand if the correct approach is being taken, the 9R circularity index, as proposed by (Muñoz et al., 2024), can be considered. From the perspective of the producer, depending on the complexity and economic value of its parts and modules, Remanufacturing can be specially appealing, as it could lead to higher profits, by reducing production costs and being environmentally positive (Fegade et al., 2015). Design-for-Remanufacturing encompasses various domains, such as Design-for-Disassembly, Design-for-Repair, Design-for-Retrofit or Design-for-IoT which adds a lot of variables to consider in the design process. All of these have to be taken into account, as the ultimate suitability of a product towards remanufacturing is highly dependent on decisions made in the earlier phases of the design process (Fegade et al., 2015). Unsuitable decisions during the design process prevent products from being remanufacturable, leading to enormous costs in correcting design flaws – correcting a design flaw increases its cost by ten in each development stage (Paul et al., 2024). As an example, if Design-for-Disassembly is one of the X domains selected for the design process, there are several design parameters that will influence the successful application of this domain – part

accessibility, as (Soh et al., 2016) concluded, is essential to determine the optimal disassembly path; (Bogue, 2007) argues that DfD can be enhanced by incorporating modularity, reducing components and standardizing manufacturing processes, as well as designing fasteners, joints and connections for ease of disassembly, preferring mechanical fasteners and being matched to standard tools. Independently of the X domains selected, there are several design parameters which must be taken into consideration during the design process, to ensure that the product will be more likely remanufacturable in the future. These parameters are summarized in Table 1 below.

Table 1 - Design parameters for Remanufacturing.

Parameter	**Description**	**Reference**
Disassemblability and Reassemblability	Easily separate a product into components, enabling repair, refurbish, remanufacture and upgrade	(Mesa, González-Quiroga, 2023) (Mesa, 2023)
Durability/Longevity	Ensure a product lasts, allowing it to be reused and having multiple lifetimes	(Mesa, González-Quiroga, 2023) (Paul et al., 2024) (Mesa, 2023)
Modularity	Allow components to be added, removed or exchanged to modify a product's functionality	(Mesa, González-Quiroga, 2023) (Paul et al., 2024) (Mesa, 2023)
Identifiability	Allow individual parts (components, fasteners) and function and condition (wear, contamination) to be determined	(Paul et al., 2024)
Accessibility	Facilitate the separation of components from the rest of the product by having fasteners and components accessible, to loosen connections during disassembly – position, depth, arrangement and orientation are critical factors	(Paul et al., 2024)
Manageability	Ensure the required disassembly/reassembly tasks are based on human body capacity	(Paul et al., 2024)
Standardization	Use standard parts and low diversity (few materials and low model diversity) as well as standardizing fasteners, tools and components	(Paul et al., 2024) (Mesa, 2023)
Separability	Make it easy to components from each other (eg: detach fasteners from components)	(Paul et al., 2024)
Cleanability	Have products suited for cleaning, resistant to chemicals and high temperatures	(Paul et al., 2024)

Within the context of complex product design and concurrent engineering, where multiple design disciplines and product life cycle dimensions of knowledge must be coherently and efficiently integrated, Lean Design-for-eXcellence (LeanDfX) as proposed by (Atilano et al., 2019), aiming to integrate Lean Thinking and Design-for-X methodologies to enhance product development through various domains and aims to assess the effectiveness and efficiency of a given product design. The present work proposes a new framework, so-called ReDesignFX, which aims to combine the necessity to design products, namely focused on Remanufacturing capability and related R-Strategies, while considering Design-for-X base principles.

2. METHODOLOGY DEVELOPMENT

2.1 Development method

The proposed framework followed a Design Thinking approach (Serrat, 2017), composed of 3 phases in order to achieve the full methodology development (Figure1). Initially, there was a systematic literature review on the relevant topics, which led to the formulation of the respective research question.

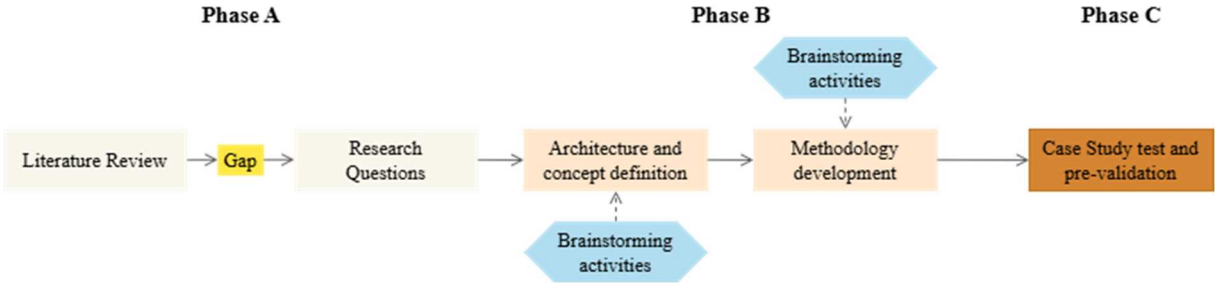

Fig. 1 - Design process for the development of the ReDesignFX methodology.

In the second phase the architecture of the proposed methodology was defined, mainly through brainstorming sessions. Finally, with the methodology fully developed, it was tested for initial validation in a concrete case study.

2.2 Architecture Design and Methodology Description and Guidelines

The research question for this study consist in developing a methodology capable of assessing the performance of product redesign and integrating multiple design dimensions. In Figure 2 is presented the overall architecture developed of ReDesignFX.

The proposed methodology foresees two distinct scenarios of application. The case of a new product design, i.e., a new version (or evolution) of an existing product (scenario A); and the case of redesigning an existing product or updating it, so, instance-based (scenario B) which will be delved deeper further ahead. For both scenarios, despite the urgency to design with these guidelines in mind, it is important not to do it without considering the impact it can have on costs. For this reason, incorporating Lean Design principles is key. In fact, (Dombrowski et al., 2014) defined a group of qualitative guidelines to aid design engineers in the process of converting non-value-added variables. This can be used as the basis for the evaluation of possible design solutions and subsequent new product designs, although it is only qualitatively. Due to this, LeanDfX, as proposed by (Atilano et al., 2019), presents as a powerful solution to combine these concepts, while also providing a quantitative analysis and being a powerful tool for decision making.

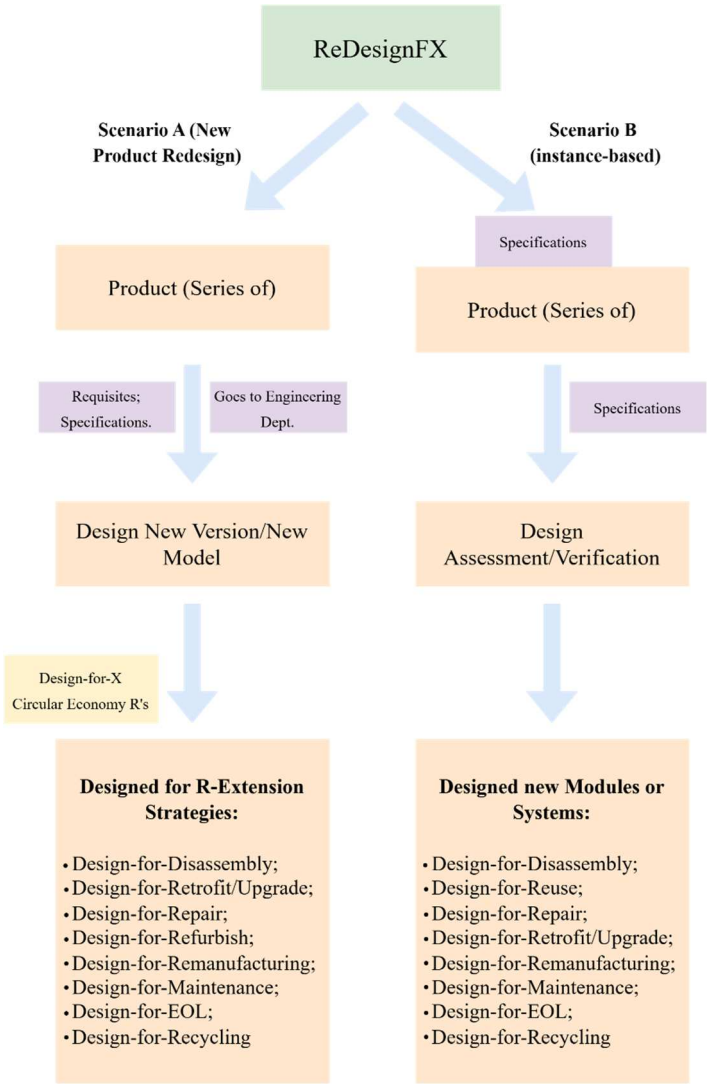

Fig. 2 - ReDesignFX architecture and the two predicted scenarios for application.

2.2.1 Scenario Redesign Product Version

For the considered scenario A, which considers the development of a new version of a given product, redesigned to be suited for remanufacturing, which is regarded as a crucial strategy for achieving circularity. In this scenario, since a new product version is being developed, it is relevant to meet the criteria enlisted above. Nevertheless, it is mandatory to look for areas of improvement and to understand what has not been achieved in the product's previous version. This can be done either through an analysis of historical information of the product's use phase, direct feedback (from end-user, for example) or through quality reports. In fact, (Zhang et al., 2019) suggests that customer reviews have become a crucial data source for product design. This contributes to a better definition of the new version's requirements, better meeting the user's needs, since good requirements are essential for the success of a project (Montgomery et al., 2022). After this information is gathered, it will then be used by the Engineering Design Department (or equivalent) when designing a new version or a new model, where a coherent DfX approach, including Circular Design guidelines, will be taken. In fact, the design of

products that strictly follow Circular Design guidelines is still very limited, with focus being solely given to improving product design, manufacturing, use and final disposal stages (Mesa, 2023). Moreover, (Sassanelli et al., 2020) found that new methods for incorporating DfX in product design are needed, so that they can firmly support design decision-making.

2.2.2 Scenario Redesign an Existing Product Instance

As for scenario B, it presupposes the existence of a product manufactured instance, meaning that a given asset that was designed in the past, where probably it didn't include Design-for-X integration guidelines, circular design or eco-design principles. One thing that plays a vital role during this process is the existence of available documentation in various engineering domains (Mechanical, Electrical, Automation and Electronic, Software, etc) that will support the necessary reverse engineering needed to decompose the product in manageable modules/components and work their way from there. Reverse engineering has become essential in product development, particularly within the context of circular economy and sustainable manufacturing. It typically involves data acquisition through advanced digitization techniques, such as 3D scanning, and subsequent processing steps like point-cloud and surface reconstruction to generate accurate computer-aided design (CAD) models (Várady et al., 1997). Of course, in the case CAD models are available, this first step can be skipped. Feature recognition is crucial, serving as a foundation for functional understanding and design modifications aimed at product optimization (Buonamici et al., 2018). The analytical phase, including finite element and tolerance analyses, ensures structural and functional integrity, supporting original performance standards (Otto & Wood, 1998). Redesign integrates design-for-X (DfX) principles - especially manufacturability, assembly, and remanufacturing-enhancing sustainability and product lifecycle management (Fegade et al., 2015; Atilano et al., 2019; Muñoz et al., 2024). Reverse engineering can significantly differ when applied to new product designs versus existing products. For new products, reverse engineering typically leverages historical product use data, direct consumer feedback, or sensor data to refine design requirements and specifications proactively (Stark et al., 2017). In contrast, reverse engineering of existing products frequently requires deconstructing products to their fundamental components, analyzing existing documentation, and conducting detailed assessments to identify improvement opportunities based on past performance and lifecycle experiences (Raja & Fernandes, 2008). When the principles behind this instance are understood, there should be a new revised definition of both requisites and specifications that the product must match, allowing for its design calculus verification and assessment, and thus providing that the new modules or components can be redesigned to include Circular Design and R-Strategies.

3. USE CASE TESTING AND RESULTS DISCUSSION

3.1 Use Case Description – Machine System Redesign

An exemplary case of industrial application is represented by the Cartesian robot, as show in Fig. 1, manufactured by Campetella, an Italian industry specializing in robotic automation systems. As presented in Figure 3, Campetella's Cartesian robot comprises three orthogonal linear axes complemented by a sophisticated robotic wrist, offering precise and versatile manipulation capabilities suitable for various industrial applications. The vertical axis typically includes components such as a balance bar, servo-motor, and belt-driven mechanism, designed for operational efficiency and accuracy. This modular design supports varying payload capacities and movement dynamics, aligning with industrial flexibility requirements. The integration of precision control systems, underscores performance, reliability, exemplifying

modular design that can facilitate sustainable manufacturing practices based on circular business models.

Fig. 3 - The Campetella's Cartesian robot.

Figure 4 presents the principal robot machine systems considered in this study for redesign in a remanufacturing real-based context. This example maps the ReDesignFX "Scenario B" methodology application, where an existing machine is under a remanufacturing operation. The Vertical Axis System was considered for redesign (Figure 5) and is divided into three main modules: Balance bar (M1); Servo-motor (M2); and Belt-Driven System (M3).

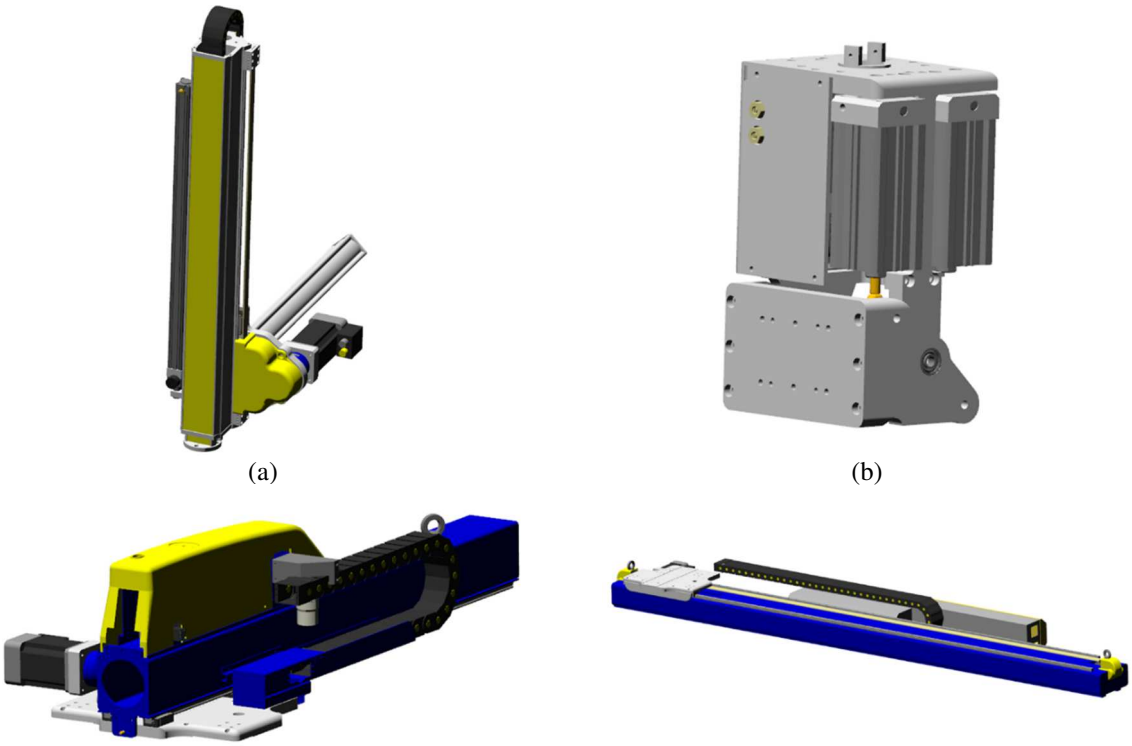

(a) (b)

(c) (d)

Fig. 4 - Systems of Cartesian robot considered: (a) vertical axis; (b) wrist; (c) extraction axis; (d) and transversal axis.

The results presented are based on real remanufacturing operation that deals on machine instances at the end of the use-phase, and for old product versions some modules might need to be redesigned to the updated in the remanufactured machine. Due to confidentiality reasons the example values were distorted, but the results interpretation and methodology validation are not affected.

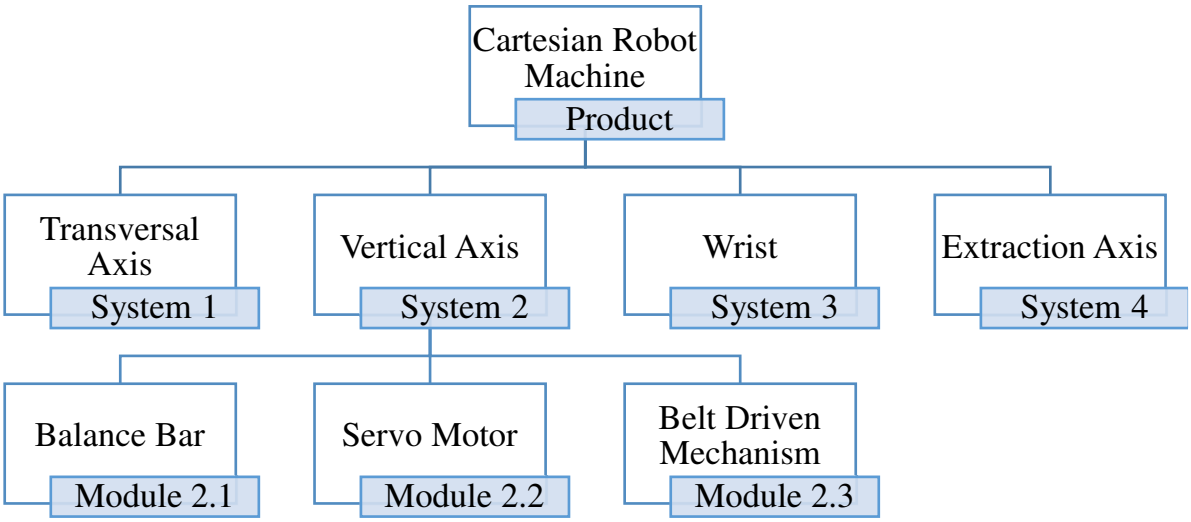

Fig. 5 - Top Levels product breakdown hierarchy of the Cartesian robot machine.

3.2 Parameterization for the selected X-Domains and Design Variables

3.2.1 Selection of X-Domains for the ReDesignFX proof-of-concept

For initial proof-of-concept of ReDesignFX methodology, Scenario B's guidelines were followed, i.e., it considering an instance of the product – in this case, the vertical axis of Campetella's cartesian robot – that is under a Remanufacturing Operation. In order to study the selected system according to the proposed methodology, by applying the LeanDfX integration tool to assess the product design performance, two X-domains were defined as essential in a redesign scenario and to make the product more suitable for remanufacturing: Design-for-Disassembly (DfD) and Design-for-Repair. Each X was then composed of three Design Variables (DV), which would assess the feasibility of the design proposal, both before and after the application of the methodology and its suggestions based on the obtained results (old vs new redesigned modules). The X-domains and respective Design Variables were organized as follows, alongside the proposed levels of assessment for each.

X1 - Design-for-Disassembly

DV1 - Joint/Union type – the reversibility or irreversibility of a joint between two components is known to be one of the main factors influencing ease of disassembly (De Fazio et al., 2021). For example, avoiding non-detachable fastenings (rivets, welding, etc) facilitates non-destructive disassembly (Paul et al., 2024). A 3-level scale was considered:

(i) Using only irreversible joints;
(ii) Using a mix of reversible and irreversible;
(iii) Using only reversible joints;

DV2 - Components accessibility – allow an easy separation of components during disassembly processes, by considering the position and depth of the components in the product, as well as their orientation (Paul et al., 2024). In this work, a 5-level scale is proposed:

(i) Non-serviceable – lack of modularity or access limited due to obstructions or destruction of components needed (because of irreversible joints or similar);
(ii) High complexity – dependence on specialized tools or general high effort needed for component retrieval;
(iii) Moderate – use of commonly available tools but multiple steps required for access;
(iv) Low complexity – use of basic tools and minimal steps required for access;
(v) Fully serviceable – all components accessible from multiple ways and directly available.

DV3 - Standard tools use – using standard tools, by using standard fasteners and components and reducing their diversity (Paul et al., 2024). A 3-level scale was considered:

(i) Heavily dependent on specialized equipment and tools;
(ii) Mix of standard and specialized equipment and tools;
(iii) Mostly dependent on standard equipment and tools.

X2 - Design-for-Repair

DV1 - Ease of Disassembly – This maps lower disassembly times and logical disassembly sequences that make it easier for damaged/non-functional components or modules to be retrieved and repaired, while also minimizing components needing substitution (Roskladka et al., 2023) (Dangal et al., 2025). Since Design for disassembly was already characterized above as X1 dimension, the effectiveness and efficiency will be directed mapped in the analysis results.

DV2 - Availability of spare parts - (Roskladka et al., 2023) (Dangal et al., 2025). For repair operations, the access to substitute parts is a key element. It was considered 5 level qualitative scale:

(i) Spare parts very low availability – very low access to spare parts, that are no more produced or very hard to reach.
(ii) Spare parts low availability – low access to spare parts, that are no more produced or hard to reach.
(iii) Moderate spare parts availability – moderate access to spare parts, that are still on production and available to order or produced.
(iv) Spare parts good availability – good access to spare parts, that are produced or easy to reach.
(v) Spare parts very good availability – very good access to spare parts, that are produced or very easy to reach and order.

DV3 - Material components robustness – using parts made from robust materials that allow for their replacement, without breaking (Roskladka et al., 2023). It was considered a 3 level qualitative scale.

(i) Low material parts robustness – Low material strength or durability in the context of repairability.

(ii) Medium material parts robustness – Medium material strength or durability in the context of repairability.

(iii) High material parts robustness – High material strength or durability in the context of repairability.

DV4 - Repair information – Defines the level of information available for a given product, module or component. It includes also the information type and availability. It was considered a 5 level qualitative scale.

(i) Very low information availability – very low access to product information and its parts, either in digital or non-digital format.

(ii) Low information availability – low access to product information and its parts, either in digital or non-digital format.

(iii) Moderate information availability – sufficient access to product information and its parts, either in digital or non-digital format.

(iv) Good information availability – good access to product information and its parts, either in digital or non-digital format.

(v) Very good information availability – very good access to product information and its parts, either in digital and non-digital format.

3.3 Results discussion and key findings

The analysis of the redesign of the three modules of the Vertical Axis system are presented below in the ReDesignFX scorecards that adopt a LeanDfX approach but in these cases for Design-for-Disassembly and Design-for-Repair context of Remanufacturing operation of a given machine. A particular difference to previous LeanDfX case studies rely on the qualitative design variables assessment and the interconnection of Design-for-Disassembly overall result (effectiveness and efficiency of the design) to the Design-for-Repair, as a dependent DV (DfD).

3.3.1 Assessment to the machine Remanufacturing Instance modules to redesign.

In Figure 6 are presented the results for the Design-for-Disassembly of the 3 modules considered. The “design fail” of some design variables (DV1 Joint / Union type or DV2 Components Accessibility), represent that in this present condition design assessment the design criteria is more demanding that it was when these modules were firstly developed in the past (and the robot machined produced). The design for disassembly was not bad, but should be improved now as more Circular Business Models and R-Strategies are essential to put in place by companies, as Campetella is doing by expanding the Refurbishment and Remanufacturing business area. In the Efficiency assessment it must be clarified that the inefficiency of design is measured face the maximum level of each DV qualitative scale. Thus, since all DV are qualitative, it can’t be straightly interpreted as “overdesign engineering” as many times occurs in continuous design variables.

In Figure 7 it is presented the Design-for-Repair performance assessment of current, reversed engineered, robot machine design. The DV related to Design-for-Disassembly was linked to the overall result of scorecard presented in Figure 6. This interlink is coherent to the instrumental role of DfD in Design-for-Repair, the best DfD the better the reparability performance and vice-versa. The DV2 related to parts availability is observed to be failing as design assessment for Module 2.2 (Servomotor) and M2.3 (Belt Driven Mechanism). The Material Robustness is below threshold 3 in M2.1 (Balance Bar). The repair information is also

insufficient in M2.1 and M2.2. The overall design performance for reparability of the current existing machine modules are thus compromised, to the lens of today needs, and need to be improved in the redesigned version of this study, namely by resolving the downsides of DfD, consider more availability for spare parts, improve the material robustness of M2.1 balance bar and create detailed information for reparation of M2.1 and M2.2.

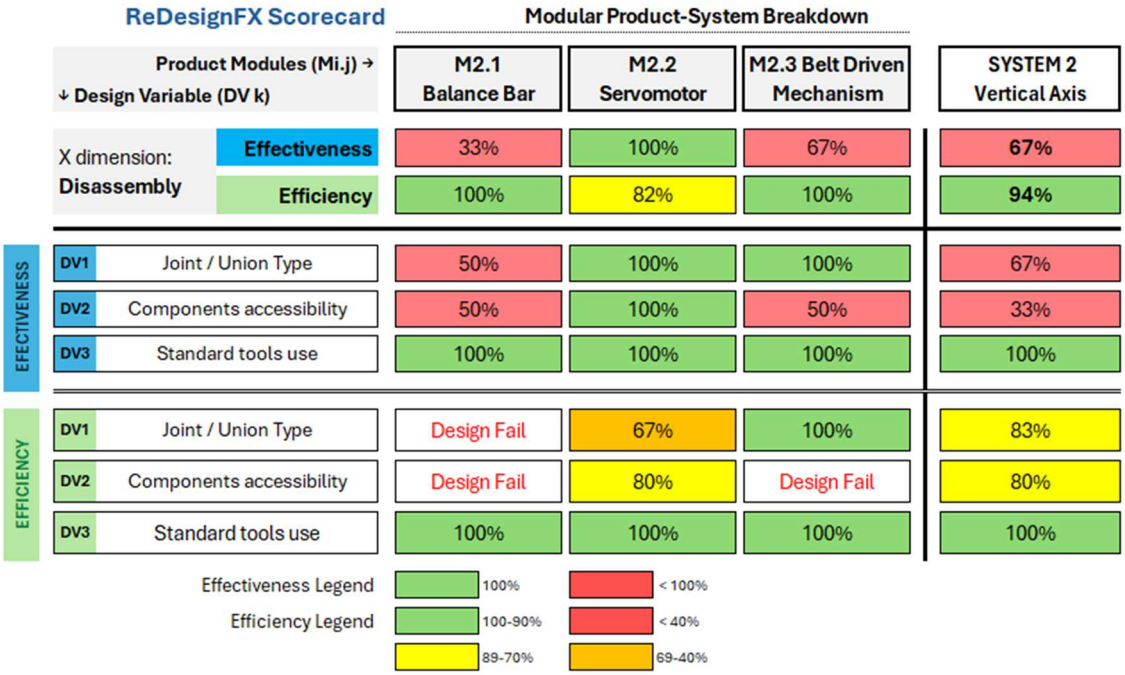

Fig. 6 - Design-for-Disassembly performance of current (reversed engineered) robot machine design.

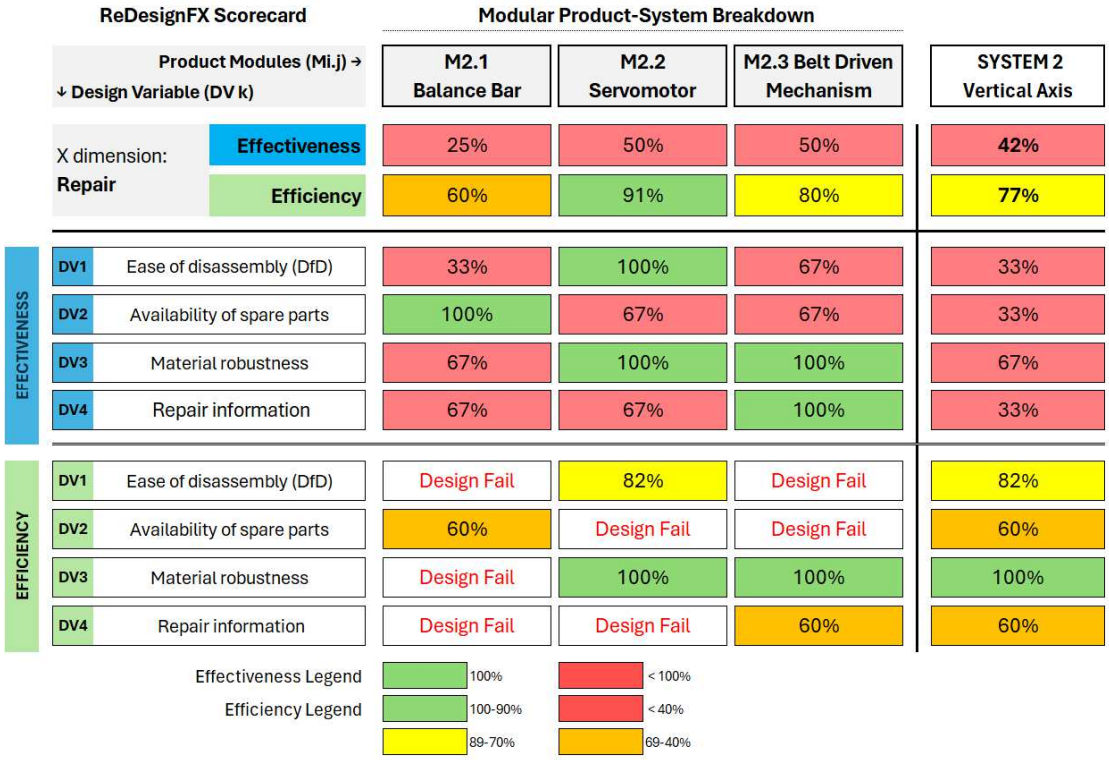

Fig. 7 - Design-for-Repair performance of current (reversed engineered) robot machine design.

3.3.2 Assessment for the Modules Redesigned

In Figure 8 is presented the final result regarding Design-for-Disassembly of the redesigned modules M2.1, M2.2, M2.3, thus of System 2 (Vertical Axis). The effectiveness was know all assured to the updated design requirements and in terms of efficiency of design only the DV2 Components Accessibility was not possible to achieve maximum level (5).

Figure 9 shows the final results regarding the Design-for-Repair of the redesigned Vertical Axis System and its modules. All the design issues were solved, passing all the effectiveness thresholds.

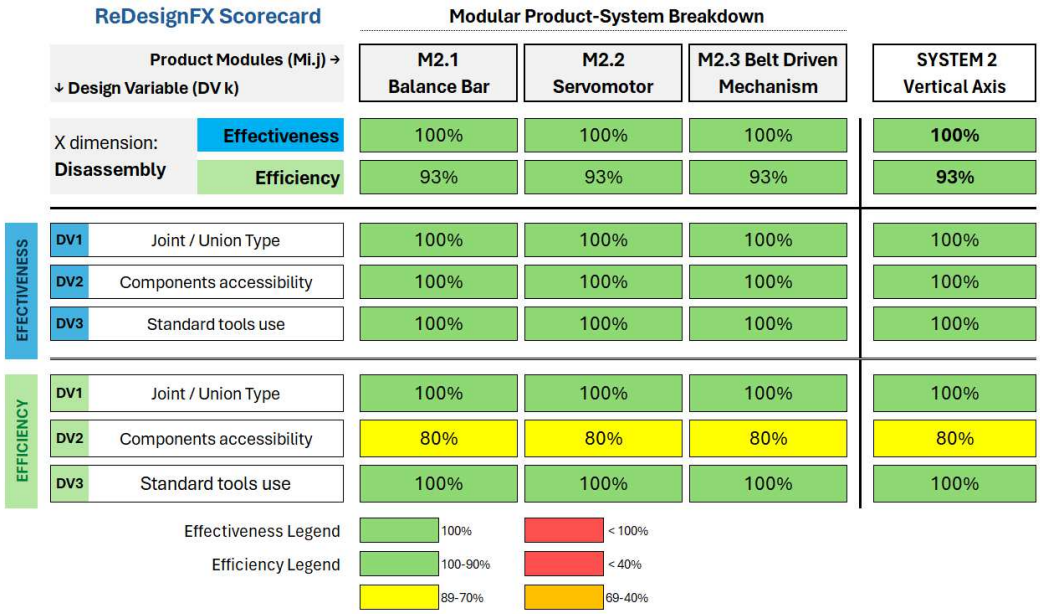

Fig. 8 - Design-for-Disassembly performance of redesigned robot machine design.

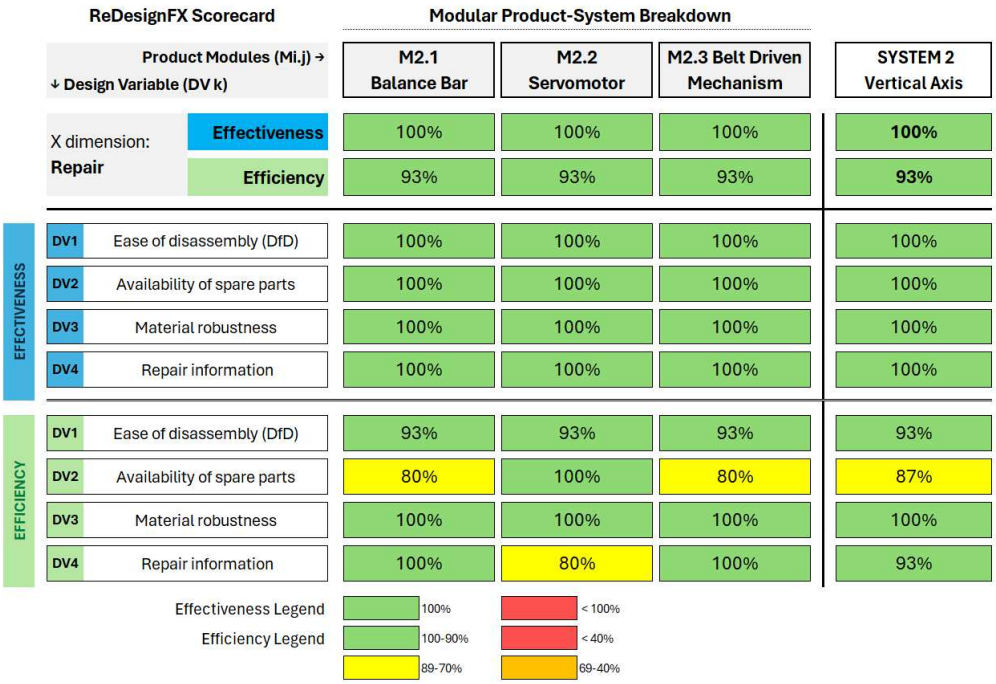

Fig. 9 - Design-for-Repair performance of redesigned robot machine design.

Some design variables were not possible to attain top level criteria for efficiency of design (DV2 Availability of Parts for M2.1 and M2.3, 80% of performance, and DV4 for repair information of M2.2). Nevertheless, the overall result achieved is very good and the improvement of DfD of all modules provide a direct impact in the reparability, as it was intended.

The new methodology of ReDesignFX, here in the context of remanufacturing operation, proved to be effective to map the design trade-offs and act as an integration methodology for product design performance for complex products as industrial robot machines.

4. CONCLUSIONS

This work presents a model for product redesign encompassing multidimensional assessment, ReDesignFX, considering design-for-X guidelines, either for new product development or product instance redesign in circular economy strategies application for product life extension (Design-for-Reuse, -Repair; -Refurbish, etc.). The model was applied in a proof-of-concept of a system redesign in the context of a real-based remanufacturing operation of an robot machine, where design-for-disassembly and design-for-repair were assessed for performance in the old machine (reverse engineered) and the new redesigned version.

The new methodology of ReDesignFX, here in the context of remanufacturing operation, proved to be effective to map the design trade-offs and act as an integration methodology for product design performance for complex products as industrial robot machines.

Despite the strong points of the method, there are shortcomings that need to be developed. The information mapping for a given product at a redesign stage must be detailed, either for a novel redesign version, or parts of a existing product (system or machine). The data sources must be coherently integrated (user feedback, maintenance records, repair history, etc.) and even to consider digital platforms data access (PDM or PLM softwares). Finally, the methodology should be tested in a complete design-for-remanufacturing of a new product or product version, to explore and demonstrate all its capabilities for design performance trade-offs and the relations between R-Strategies and D-Strategies.

AKNOWLEDGMENTS

This work is funded via European Union's Horizon Europe programme 'RENEE' (under grant agreement no 101138415). Special thanks to Campetella Robotic Center for their help and support, in particular to Simone Saraceni and Elia Campetella.

REFERENCES

[1] Atilano, L., Martinho, A., Silva, M.A., Baptista, A.J. (2019). Lean Design-for-X: Case study of a new design framework applied to an adaptive robot gripper development process. Procedia CIRP, 84, pp. 667-672. https://doi.org/10.1016/j.procir.2019.04.190.

[2] Bogue, R. (2007). Design for disassembly: A critical twenty-first century discipline. Assembly Automation, 27(4), pp. 285-289. https://doi.org/10.1108/01445150710827069.

[3] , S., Sandez, S., Bolaños Arriola, J., Faludi, J., Balkenende, R. (2025). Empirical evaluation of reparability scoring systems for validity and reliability. Resources, Conservation and Recycling, 218, 108211. https://doi.org/10.1016/j.resconrec.2025.108211.

[4] De Fazio, F., Bakker, C., Flipsen, B., Balkenende, R. (2021). The Disassembly Map: A new method to enhance design for product repairability. Journal of Cleaner Production, 320, 128552. https://doi.org/10.1016/j.jclepro.2021.128552.

[5] Dombrowski, U., Schmidt, S., Schmidtchen, K. (2014). Analysis and Integration of Design for X Approaches in Lean Design as basis for a Lifecycle Optimized Product Design. Procedia CIRP, 15, pp. 385-390. https://doi.org/10.1016/j.procir.2014.06.023.

[6] Fegade, V., Shrivatsava, R.L., Kale, A. V. (2015). Design for Remanufacturing: Methods and their Approaches. Materials Today: Proceedings, 2(4-5), pp. 1849-1858. https://doi.org/ 10.1016/j.matpr.2015.07.130.

[7] Mesa, J.A. (2023). Design for circularity and durability: An integrated approach from DFX guidelines. Research in Engineering Design, 34(4), pp. 443-460. https://doi.org/10.1007/ s00163-023-00419-1.

[8] Mesa, J.A., González-Quiroga, A. (2023). Development of a diagnostic tool for product circularity: A redesign approach. Research in Engineering Design, 34(4), pp. 401-420. https://doi.org/10.1007/s00163-023-00415-5.

[9] Montgomery, L., Fucci, D., Bouraffa, A., Scholz, L., Maalej, W. (2022). Empirical research on requirements quality: A systematic mapping study. Requirements Engineering, 27(2), pp. 183-209. https://doi.org/10.1007/s00766-021-00367-z.

[10] Muñoz, S., Hosseini, M.R., Crawford, R.H. (2024). Towards a holistic assessment of circular economy strategies: The 9R circularity index. Sustainable Production and Consumption, 47, pp. 400-412. https://doi.org/10.1016/j.spc.2024.04.015.

[11] Paul, M., Gong, S. Q.-C., Löffler, J., Reinhart, G. (2024). Enhancing product design for remanufacturing: Guidelines and their implementation in integrated remanufacturing systems. Production & Manufacturing Research, 12(1), 2396363. https://doi.org/10.1080/ 21693277. 2024.2396363.

[12] Roskladka, N., Bressanelli, G., Miragliotta, G., Saccani, N. (2023). A Review on Design for Repair Practices and Product Information Management. Em E. Alfnes, A. Romsdal, J. O. Strandhagen, G. Von Cieminski, & D. Romero (Eds.), Advances in Production Management Systems. Production Management Systems for Responsible Manufacturing, Service, and Logistics Futures (Vol. 692, pp. 319–334). Springer Nature Switzerland. https://doi.org/10. 1007/978-3-031-43688-8_23.

[13] Sassanelli, C., Urbinati, A., Rosa, P., Chiaroni, D., Terzi, S. (2020). Addressing circular economy through design for X approaches: A systematic literature review. Computers in Industry, 120, 103245. https://doi.org/10.1016/j.compind.2020.103245.

[14] Serrat, O. (2017). Design Thinking. Em O. Serrat, Knowledge Solutions (pp. 129-134). Springer Singapore. https://doi.org/10.1007/978-981-10-0983-9_18.

[15] Soh, S., Ong, S.K., Nee, A.Y.C. (2016). Design for assembly and disassembly for remanufacturing. Assembly Automation, 36(1), 12–24. https://doi.org/10.1108/AA-05-2015-040.

[16] Zhang, L., Chu, X., Xue, D. (2019). Identification of the to-be-improved product features based on online reviews for product redesign. International Journal of Production Research, 57(8), pp. 2464-2479. https://doi.org/10.1080/00207543.2018.1521019.

TRACK - E: Civil Engineering Applications

Buildings, Bridges and Infrastructures
Materials Characterization
Wood Mechanics and Timber Engineering
Structural Analysis,
Structural Integrity
Experimental Tests and Structural Monitoring
Concrete and Composite Structures
Metallic Structures
Structural Rehabilitation
Case Studies

Proceedings IRF2025: 8th International Conference on Integrity-Reliability-Failure
In Engineering, Materials, Manufacturing and Biomechanics. Porto 15-18 July 2025
DOI: https://doi.org/10.24840/978-972-752-323-8

PAPER REF: 22234

CUTTING-EDGE GROUND PENETRATING RADAR FOR HIGH-PRCEISION IDENTIFICATION OF BARS IN CONCRETE SLABS

Wael Zatar[1(*)], Hien Nghiem[2]

[1]College of Engineering and Computer Sciences, Marshall University, Huntington, West Virginia, USA
[2]Marshall University Research Corporation, Marshall University, Huntington, West Virginia, USA
[(*)]*Email:* zatar@marshall.edu

ABSTRACT

A new algorithm has been developed for automatically detecting rebar locations and diameters in reinforced concrete structures using ground-penetrating radar (GPR) techniques. This study formulates the speed of electromagnetic waves in reinforced concrete using two-way travel time and bi-quadratic equations, which approximate hyperbolic signatures. An established algorithm has been leveraged to create a computer program that allows for automated analysis of GPR data collected from survey grids. The developed evaluation approach is validated by testing a reinforced concrete slab and a beam on a functional bridge. The proposed methodology demonstrates exceptional signal processing capabilities and effectively identifies rebar information, highlighting its efficiency.

Keywords: Reinforced-concrete structures, non-destructive evaluation, ground-penetrating radar, rebar depth, rebar diameter.

INTRODUCTION

For several decades, ground-penetrating radar (GPR) has been used in geophysics for soil exploration. Since the early 1990s, advancements in high-frequency antennas, as well as sophisticated software and hardware systems, have made GPR a rapid and reliable method for assessing concrete structures. This technique has been effectively applied to monitor and evaluate bridge decks [1], detect the size and location of rebar within concrete [2], and estimate the cover and thickness of bridge deck concrete [3], [4].

This study utilizes GPR data to determine the depth and size of rebar in reinforced concrete slabs. A novel computer algorithm has been developed to accurately extract the hyperbolas representing rebar in the radargram. The introduction of new methods for determining the time zero and electromagnetic wave velocity offers significant advantages over existing techniques, enhancing the accuracy and reliability of the assessment. Additionally, bi-quadratic and theoretical equations for hyperbolas have been formulated to evaluate rebar spacing and depth. The comparison of experimental and theoretical curves provides valuable insights into the size of the rebar.

GPR SYSTEM AND DATA PROCESSING

Ground-penetrating radar (GPR) is an electromagnetic (EM) technique that uses radar pulses to create images of the subsurface. This technology relies on the propagation of high-frequency electromagnetic waves transmitted from a radar antenna. For most civil engineering applications, the wave frequency typically ranges from 200 MHz to 2.6 GHz. Two key physical

properties that influence GPR performance are dielectric constant and electrical conductivity, which affect how electromagnetic waves propagate through different materials.

As GPR energy travels through a medium, it experiences attenuation, meaning radar energy is lost. In resistive materials—such as dry sand, ice, or dry concrete—the signal remains strong for longer, allowing it to penetrate greater depths [5], [6]. Conversely, in conductive materials like salt water and wet concrete, GPR energy is absorbed more quickly, limiting its effective range. Because of these characteristics, GPR is well-suited for inspecting construction materials such as concrete, sand, wood, and asphalt [7].

The dielectric constant of a material indicates the speed at which radar energy travels through it. Ground Penetrating Radar (GPR) transmits electromagnetic (EM) waves into concrete and measures the time it takes to travel back after reflecting off embedded objects. The depth of these objects can be obtained by multiplying the two-way travel time by the wave speed. In air, GPR energy propagates at almost the speed of light, corresponding to a dielectric value of 1. Dielectric values typically range from 3 to 12 for construction materials, translating to radar wave velocities between 0.178 and 0.089 meters per nanosecond [8].

When radar energy encounters a subsurface or embedded object or a boundary between materials with different electrical conductivity and dielectric values—such as rebar, voids, or other inhomogeneous materials—it reflects to the surface and is detected by the receiving antenna [9]. The greater the difference in these values, the stronger the reflections. For instance, embedded rebar in concrete slabs produces a strong reflection because it is a conductive material. A GPR antenna consists of a transmitter (T) and a receiver (R); the transmitter sends the signal, while the receiver captures the reflected signal. This study chose a 1.6 GHz antenna with a 58 mm T-R offset (the distance between the transmitter and receiver) for the GPR system.

Data collection and acquisition

The data collection was conducted with meticulous attention to detail, with the direction chosen to be perpendicular to the steel rebars (i.e., parallel to the longer slab edge). The ground-coupled antenna, operating at a frequency of 1.6 GHz, was consistently used for all RC slab specimens.

Rebar depth and diameter

The shape of a hyperbola in ground-penetrating radar (GPR) data is influenced by two primary factors [5]: (1) scan spacing, where smaller spacing (i.e., more scans per meter) results in wider hyperbolas, and (2) wave velocity, where higher velocities (associated with lower dielectric constants) produce wider hyperbolas, and lower velocities produce narrower ones. To derive the theoretical equation of the hyperbola, the following assumptions are made:

- The positive peaks of the reflected waves from the rebar correspond to the negative peaks of the transmitted wave, indicating a phase reversal.
- The transmitted wave reflects at the surface of the rebar along the shortest two-way travel path.

The transmitting and reflection paths can be obtained as follows (Figure 1):

$$L_1 = \sqrt{(z + r - r\cos\alpha)^2 + \left(X - \frac{S}{2} - r\sin\alpha\right)^2} \tag{1a}$$

$$L_2 = \sqrt{(z + r - r\cos\alpha)^2 + \left(X + \frac{S}{2} - r\sin\alpha\right)^2} \tag{1b}$$

where: $\tan\alpha = X/z$; $X=x_p-x$ is the distance between the rebar and the center line of the transmitter and receiver (TR) in the horizontal direction; z is the depth of the rebar center; r is

the rebar radius; S is the spacing of the transmitter and receiver; x_0 is the horizontal coordinate of the rebar; x is horizontal coordinate of the antenna. Those parameters are illustrated in Figure 1.

Consider the peak point of the hyperbola; the two-wave travel time is expressed by Equation (2), where t_0 is time zero; t_p is the time of the hyperbola peak. Consider a point on the hyperbola; the two-wave travel time can be obtained, as can be depicted in Equation (3).

$$t_p - t_0 = \frac{\sqrt{4z^2+S^2}}{V_s} \tag{2}$$

$$t_i - t_0 = \frac{L_1+L_2}{V_s} \tag{3}$$

Substituting Eq. (1) and Eq. (2) into Equation (3) results in producing Eq. (4).

$$t_i = (t_p - t_0)\frac{\sqrt{(z+r-r\cos\alpha)^2+\left(X-\frac{S}{2}-r\sin\alpha\right)^2}+\sqrt{(z+r-r\cos\alpha)^2+\left(X+\frac{S}{2}-r\sin\alpha\right)^2}}{\sqrt{4z^2+S^2}} + t_0 \tag{4}$$

Equation (4) depicts the hyperbolic curve from a rebar embedded in RC. The suggested steps for solving for the rebar depth (z) and radius (r) in Equation (4) are as follows:

- Estimate the electromagnetic wave velocity.
- Calculate the rebar depth using Equation (2).
- Identify the coordinates at the peak of the hyperbola.
- Calculate the rebar radius using Equation (4)

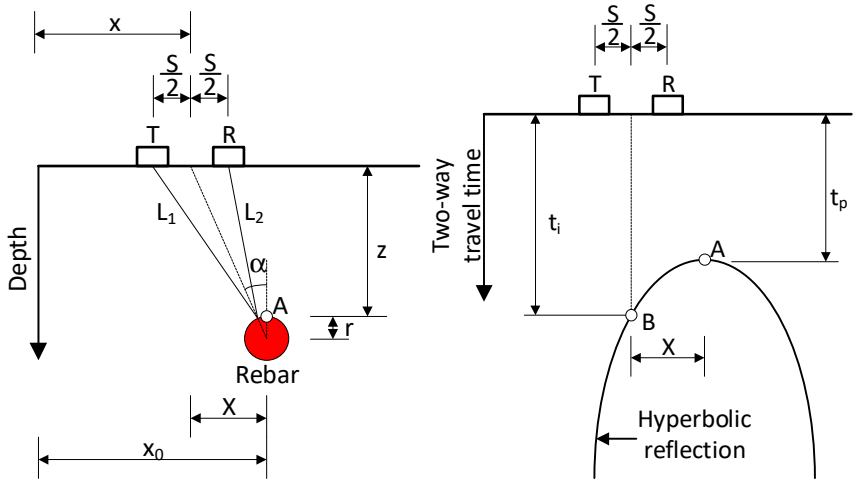

(a) Wave travel path (b) Hyperbolic reflection

Fig. 1 - Reflected wave from a rebar.

Determination of the coordinates at the peak of the hyperbola

The locus of the positive peak reflections from the rebars extracted from a radargram are not smooth curves, and their peak coordinates (t_p and x_p) are not provided. A biquadratic equation can approximate the curves to determine the coordinates as follows:

$$t_i \approx Ax^4 + Bx^3 + Cx^2 + Dx + E \tag{5}$$

The reason for choosing biquadratic Equation (5) is its close fit to theoretical hyperbola (Equation 4) with extremely high precision, as demonstrated in Figure 2. The x_p coordinate represents the horizontal position of the rebar, whereas t_p corresponds to its depth. The peak coordinates (t_p and x_p) can be identified by solving the first derivative of Equation (5).

$$\frac{dt_i}{dx} = 0 \tag{6}$$

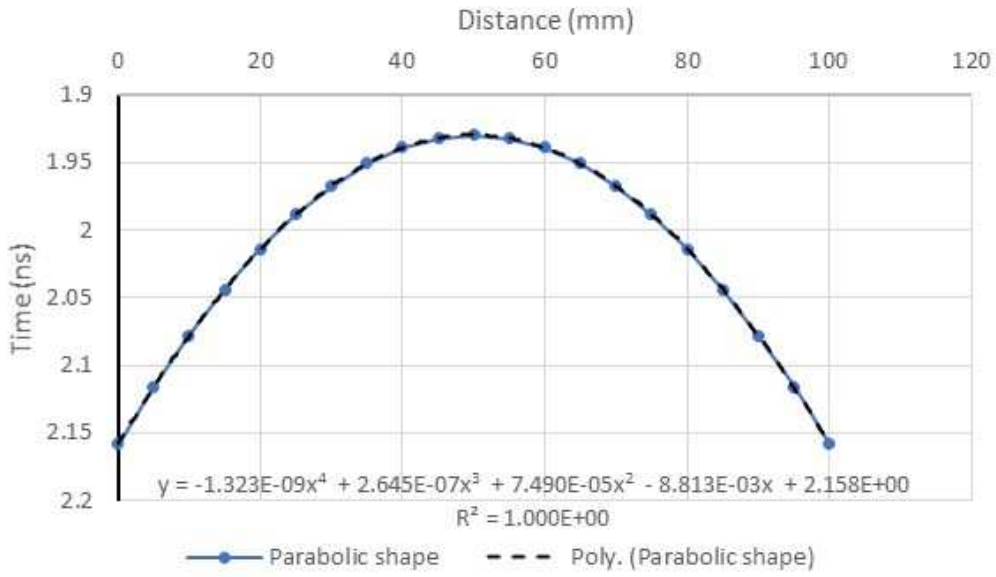

Fig. 2 - Biquadratic approximation.

The authors developed a computer program with a fully graphical interface using Delphi to address the limitations of the post-processing software in current commercial Ground Penetrating Radar (GPR) devices. Utilizing the principles and equations mentioned above, the program can automatically detect and determine the depth and size of rebar, as well as the electromagnetic wave velocity in concrete slabs. It identifies and fits all hyperbolic reflections represented by positive radargram peaks using biquadratic equations. An iterative method was employed to solve Equation (4) and accurately determine the unknown values necessary to fit the biquadratic Equation effectively.

EXPERIMENTAL PROGRAM

A reinforced concrete (RC) slab was developed and tested to assess the effectiveness of the in-house software. The specimen, referred to as S1, measures 914 mm in length, 610 mm in width, and 89 mm in thickness, as illustrated in Figure 3. This slab incorporates three different rebar diameters (#3, #5, and #7), all positioned at the same depth with a consistent spacing of 203 mm. The RC slab specimens were cast using ready-mix concrete sourced from in-transit mixers, followed by curing and testing under controlled laboratory conditions.

GPR testing was performed on a dynamic and functional bridge beam, with the cross-section depicted in Figure 4. The beam was scanned in both longitudinal and transverse directions. However, the transverse scan data, which may have been influenced by the presence of voids within the beam, were excluded from this study. The longitudinal scans specifically aimed to identify the internal stirrups.

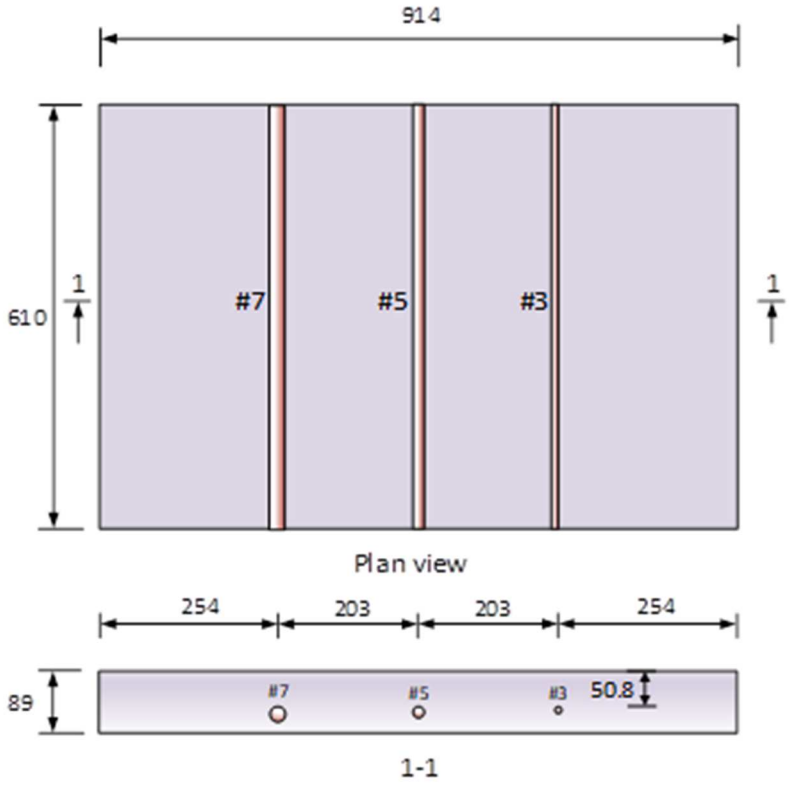

Fig. 3 - Details of the RC slab specimen (units in millimeters).

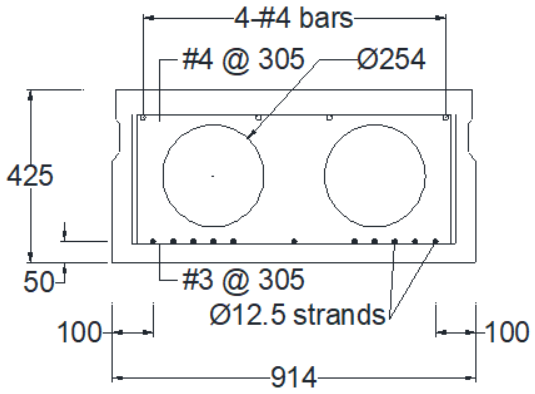

Fig. 4 - Cross section of the bridge beam (units in millimeters).

RESULTS AND CONCLUSIONS

The radargram shown in Figure 5 depicts the GPR scan conducted on slab S1, which reveals the presence of three rebars identified by their hyperbolic reflections. Figure 6 displays the positive peaks of these rebar reflections alongside theoretical hyperbolic curves for different types of rebar. The diameter of the rebar was determined by finding the diameter corresponding to the maximum R-squared value, as illustrated in Figure 7. This analysis provides crucial insights into the composition and characteristics of the slabs. Additionally, Table 1 compares rebar depth and diameter, indicating that the maximum variation in rebar diameter stays within 10 percent.

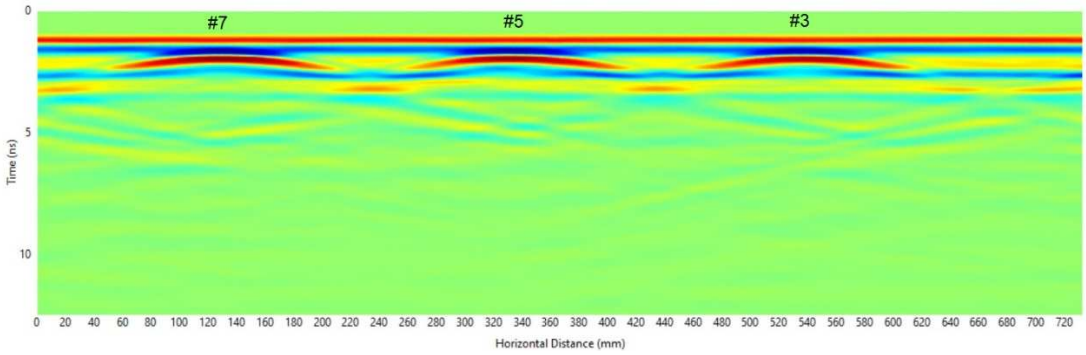

Fig. 5 - Radargram of slab specimens S1.

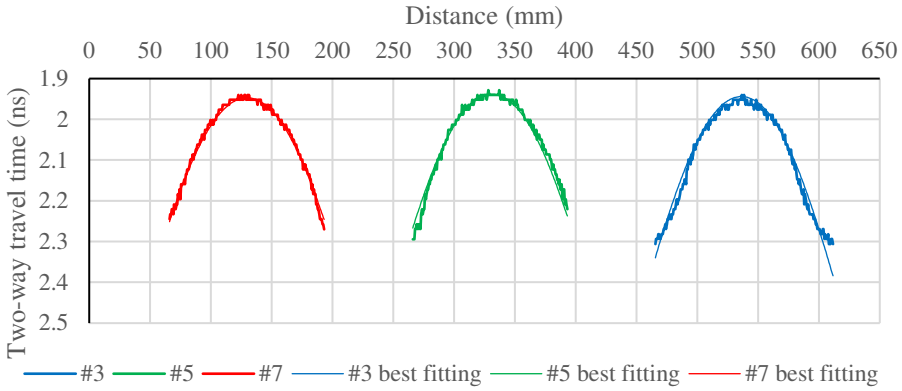

Fig. 6 - Hyperbolas and best fit curves for rebars.

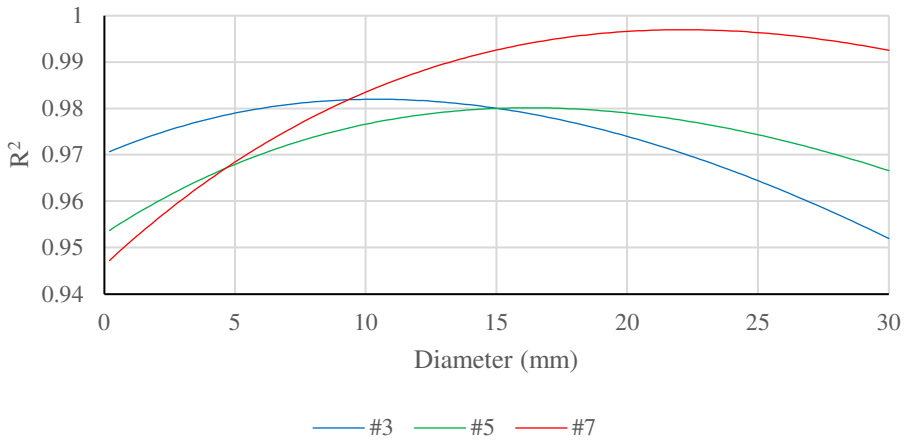

Fig. 7 - R^2 for slab specimens S1.

Table 1 - Rebar diameters and depths for S1 slab.

Rebar No./Diameter (mm)	Designed depth (mm)	Calculated diameter/depth (mm)	Diameter/ Depth differences (%)
#3/9.525	50.8	10.4/49	9.2/3.5
#5/15.875	50.8	16/48	0.8/5.5
#7/22.225	50.8	22.2/49	0.1/3.5

Figure 8 presents a radargram obtained from a longitudinal scan of the bridge beam. While some stirrup signals appear blurred due to the influence of internal voids, several stirrups were accurately detected. As shown in Figure 9, the estimated diameters of the detected stirrups range from 10 mm to 13.2 mm, closely matching the actual diameter of 12.7 mm.

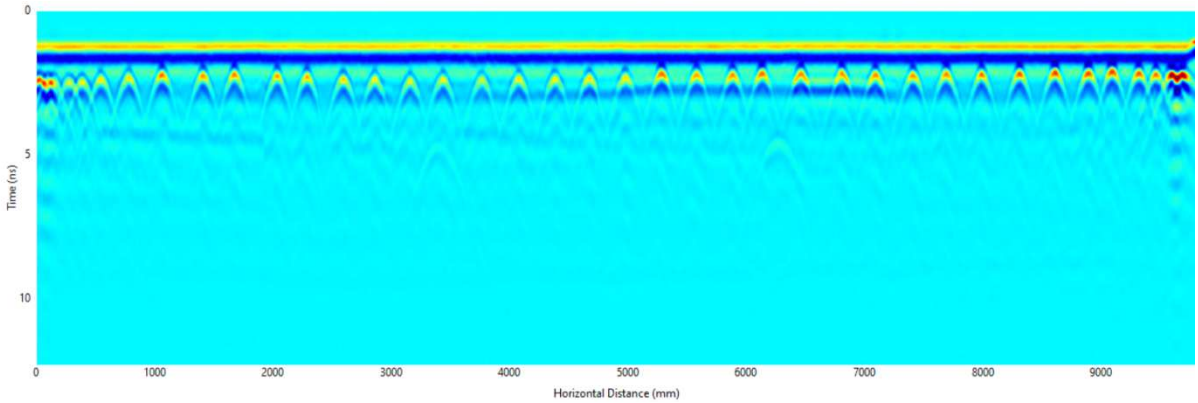

Fig. 8 - Radargram of the real bridge beam.

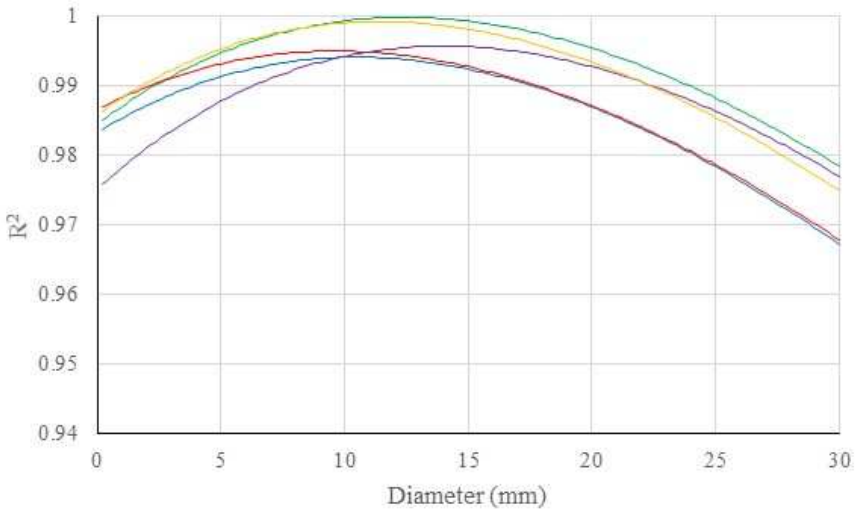

Fig. 9 - R^2 for the real bridge beam.

REFERENCES

[1] Alani AM, Aboutalebi M, Kilic G. Applications of ground penetrating radar (GPR) in bridge deck monitoring and assessment. Journal of Applied Geophysics, 2013, 97, pp.45-54.

[2] He XQ, Zhu ZQ, Liu QY, Lu GY. Review of GPR rebar detection. In PIERS proceedings 2009, pp.804-813.

[3] Zatar, W., Ruiz, F., Nghiem, H., "Revolutionizing concrete bridge assessment: implementing nondestructive scanning for transformative evaluation," Applied Sciences, 2024.

[4] Zhou F, Chen Z, Liu H, Cui J, Spencer BF Fang G. Simultaneous estimation of rebar diameter and cover thickness by a GPR-EMI dual sensor. Sensors, 2018, 18(9), p. 2969.

[5] Zatar, W., Ruiz, F., Nghiem, H., "Revolutionizing Concrete Bridge Assessment: Implementing Nondestructive Scanning for Transformative Evaluation," Applied Sciences 14 (24), 11590, 2024.

[6] Zatar, W., "Impact of environmental factors on condition assessment of concrete bridge decks using nondestructive testing," Risk-Based Strategies for Bridge Maintenance, pp.193-204, 2023.

[7] Zatar, W., Ruiz, F., Nghiem, H., "Vulnerability assessment of timber piles by bending wave and dispersive wave testing methods," Bridge Maintenance, Safety, Management, Digitalization and Sustainability, IABMAS 2024, Copenhagen, Denmark 2024.

[8] GSSI. Concrete Handbook, GPR inspection of concrete.

[9] Zatar, W., Nguyen, T., and Nguyen, H., "Predicting GPR Signals from Concrete Structures Using Artificial Intelligence-Based Method," Advances in Civil Engineering 2021 (1), 6610805.

Proceedings IRF2025: 8th International Conference on Integrity-Reliability-Failure
In Engineering, Materials, Manufacturing and Biomechanics. Porto 15-18 July 2025
DOI: https://doi.org/10.24840/978-972-752-323-8

PAPER REF: 22235

POST-TENSIONED RODS OF AGING WATER NAVIGATION STRUCTURES: A NOVEL EVALUATION STRATEGY FOR ENHANCED SAFETY AND INTEGRITY

Wael Zatar[1(*)], Hien Nghiem[2]

[1]College of Engineering and Computer Sciences, Marshall University, Huntington, West Virginia, USA
[2]Marshall University Research Corporation, Marshall University, Huntington, West Virginia, USA
[(*)]*Email:* zatar@marshall.edu

ABSTRACT

Post-tensioned Tainter gate anchorages that utilize trunnion anchor rods have been widely used in many dams across the United States, particularly in the Mississippi Valley, Great Lakes region, and the Southwestern and Northwestern Divisions. This study aims to evaluate the impact of a failed rod or multiple failed rods on the remaining rods' stress distribution and on the rod groups' overall capacity within the same anchorage box. A comprehensive experimental investigation was conducted on post-tensioned anchorages with various rod configurations. The experiments involved a scaled anchorage system featuring a post-tensioned concrete trunnion girder with nine high-strength post-tensioning rods. Finite element analyses simulating different failure scenarios of the trunnion rods were validated using data from the detailed experimental study. The numerical results effectively predicted changes in rod loads under various loading and de-tensioning conditions.

Keywords: Navigation structures, dam spillways, asset management, trunnion rods, post-tensioned anchorage.

INTRODUCTION

The United States Army Corps of Engineers (USACE) manages a large inventory of dams that utilize Tainter gates to regulate water flow. Tainter gates are considered one of the most effective solutions for controlling dam spillways. Across the United States, a diverse array of dams featuring post-tensioned Tainter gate anchorages. The highest concentration of these dams is found in the Mississippi Valley Division (MVD), Great Lakes and Rivers Division (LRD), Southwestern Division (SWD), and Northwestern Division (NWD) [1].

O'Donnell [2] discussed essential considerations for designing prestressed concrete anchorages for large Tainter gates. For the piers and girders, concrete with a strength of 5000 psi is required; however, higher-strength concrete may be necessary for large gates. The amount of prestressing was calculated based on various load conditions, and the actual final load on the prestressing steel should not exceed 60 percent of the steel's minimum ultimate strength. Due to stress losses in the steel caused by factors such as elastic shortening of the concrete, creep, and plastic flow, the initial tension on the steel—immediately after the anchorages are seated—should not exceed 70 percent of the ultimate strength of the steel.

Between 2010 and 2017, testing of ten dams across the United States revealed significant maintenance challenges and opportunities for performance enhancement. Eight of these dams exhibited failures in their post-tensioned trunnion rods. A thorough evaluation of 5,371 greased trunnion post-tensioned rods uncovered 22 instances of breakage and six cases of slipping

gripping hardware. Additionally, the Markland Dam and the Greenup Dam faced critical issues, with 202 rods on the Markland Dam and 76 rods on the Greenup Dam showing substantial cantilever bending or corrosion. Addressing these issues is crucial to preventing further failures in the post-tensioned trunnion systems.

Abela and Abela [3] conducted a case study that analysed an existing trunnion girder and its greased post-tensioned anchors before load testing. Their analysis assessed the capacity of the structural members using a finite-element (FE) model and investigated the likelihood of a critical anchor failure. This was based on test data obtained from non-destructive dispersive wave propagation testing and load testing of similar anchors at other dams. The analysis results revealed a higher-than-expected probability of a critical anchor failing. It indicated that a significant flood event could jeopardize the post-tensioned anchorage system. In response, two contingency plans were proposed: one involving the replacement of the anchors and another suggesting the addition of a steel exoskeleton wrapped around the trunnion girder, complete with new anchors.

Abela [4] assessed the adequacy of a passive anchorage system under increased hydrostatic loading through FE analysis and existing structural and mechanical design manuals. This study highlighted several key elements for evaluating an existing passive anchorage system, including analyzing the behavior of the anchorage system using FE models, considering Von Mises stress and the elongation of the system, understanding both historical and current codified guidance, applying the correct classification, and accounting for corrosion of embedded anchors. Malik and Zatar [5, 6] focused on structural health monitoring approaches to support waterway infrastructure. Nguyen et al. [7] and Zatar et al. [8, 9] reported successful methods for analytical and non-destructive testing of concrete structures.

The research team performed non-destructive laboratory testing and FE analyses on a scaled model of a Tainter gate used in navigation dams. The objective was to assess force distribution and evaluate the increased forces experienced by the remaining post-tensioned trunnion rods resulting from the failure of one to three of these rods.

SCALED MODEL OF TAINTER GATE STRUCTURE

The scaled model of the Tainter gate structure includes several key components: a concrete beam, pedestals, a steel girder, steel columns, and high-strength threaded rods, as illustrated in Figure 1. The concrete beam has dimensions of 120 × 24 × 30 inches (length × width × height) and is supported by three steel pedestals that are spaced 3 feet apart. A steel girder (shown in Figure 2) is responsible for transferring forces from two hydraulic actuators to the trunnion rods, conveying these loads to the concrete beam. The horizontal distance from each hydraulic actuator to the center of the concrete beam is 3 feet. Supporting the hydraulic actuators are two steel columns with wide-flange cross sections (W5×19). All structural components were fabricated at a dedicated facility, including the concrete beam, steel girder, columns, and pedestals. Additionally, nine high-strength threaded rods are arranged in a 3×3 grid with 8-inch spacing to simulate the trunnion rods in Tainter gate structures. The mechanical properties of these rods are detailed in Table 1.

The lateral loads, representing the combined effects of water pressure and wind load transferred from the Tainter gate to the girder, are simulated using two hydraulic actuators. Each actuator has a maximum capacity of 196 kips and a corresponding pressure limit of 5,000 psi. The test setup includes nine load cells mounted at the rods' ends on the concrete beam's rear side (Figure 1), along with two additional load cells attached to the hydraulic actuators to monitor applied forces. All load cells have a 50-ton capacity and a 2.0 mV/V sensitivity.

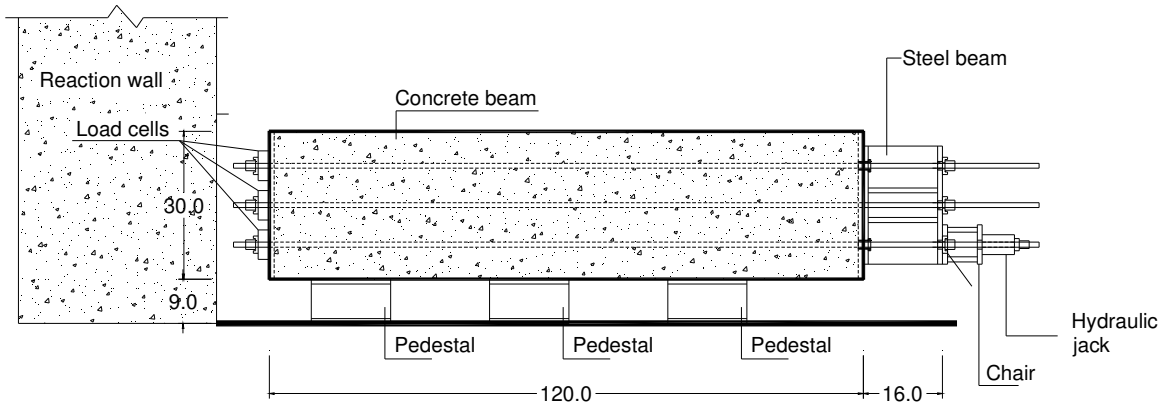

(a) Side view

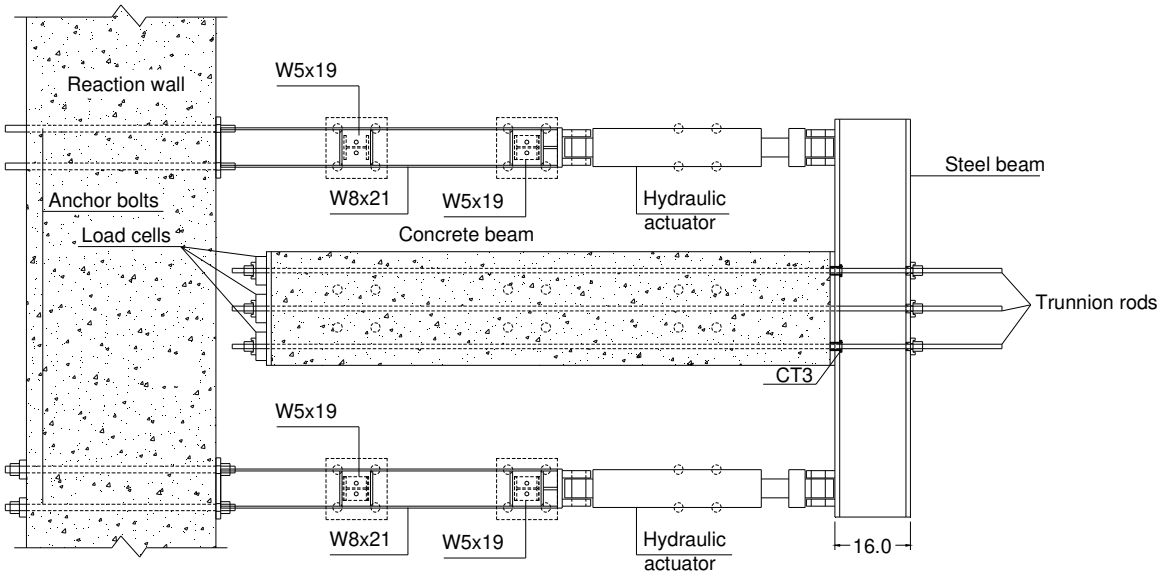

(b) Plan view

Fig. 1 - Schematic of the scale model test.

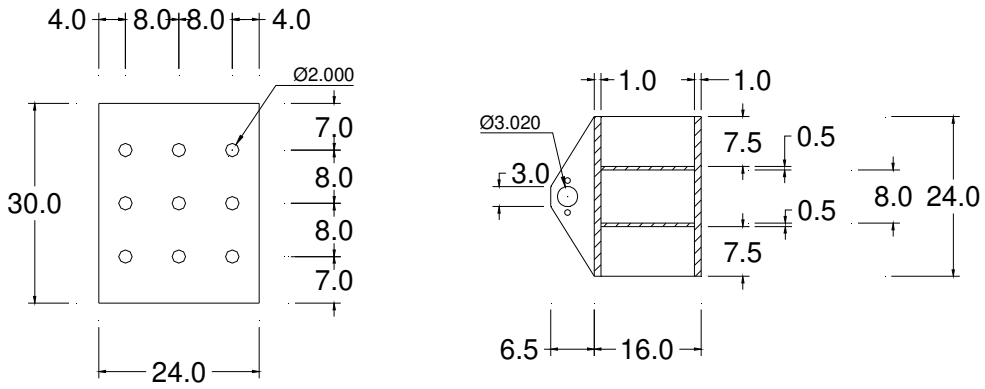

Fig. 2 - Cross sections of the concrete beam (left) and steel beam (right).

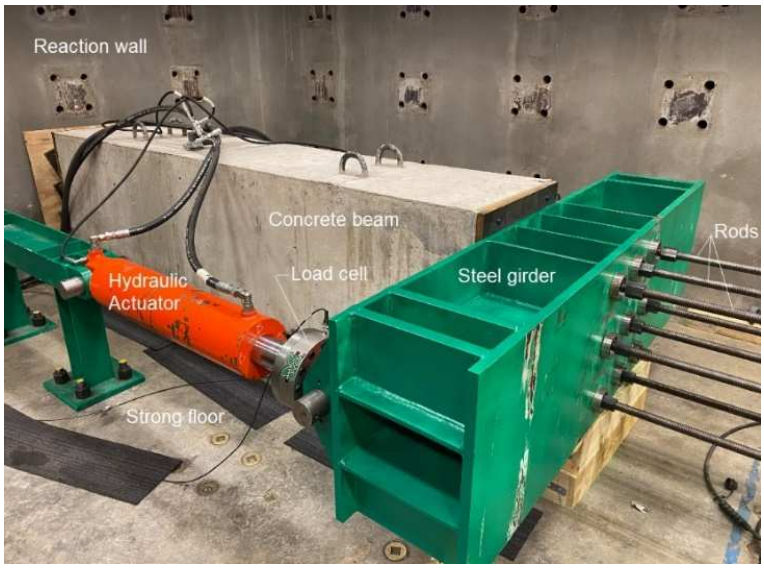

Fig. 3 - Three-dimensional view of testing system.

Table 1 - Threaded rods' properties.

Properties	Value
Diameter (in.)	1.0
Cross section area (in.^{2})	0.85
Minimum ultimate strength (kips)	128
Total length (in)	168

TEST PROCEDURE

The experimental program simulated various damage scenarios by accounting for the failure of one to three trunnion rods. In the laboratory, the rods were de-tensioned accordingly to represent these failure cases. A scenario involving the failure of three rods represents a critical condition that could reduce the system's capacity by up to one-third. With a maximum of three failed rods, over 30 possible configurations were identified. Tests were conducted at four levels of pre-tension, expressed as percentages of the minimum ultimate strength of the rods. Each test followed a three-step process:

1. Pre-tensioning all rods, ensuring that the force in each rod was adjusted so that the difference between the maximum and minimum pre-tension forces did not exceed 1.0 kip.
2. De-tensioning the selected rods to reflect the failure scenarios.
3. Applying external loading through hydraulic actuators.

It is important to note that pre-tensioning one rod affects the force levels in the other rods. As a result, the pre-tensioning process was repeated iteratively until the force variation among all rods fell within the 1-kip tolerance. Loading was applied incrementally through two hydraulic actuators and held briefly at four pressure levels: 1200 psi, 1700 psi, 2200 psi, and 2700 psi. These pressures corresponded to total applied forces of 92 kips, 130 kips, 169 kips, and 207 kips, respectively. After completing the loading cycle, the actuators were fully unloaded to return the system to zero pressure.

FINITE ELEMENT ANALYSIS

A finite element (FE) model was developed to simulate the scaled model testing, as shown in Figure 4. This model consists of 1,440 solid elements representing the concrete beam, 752 shell elements for the steel girder, 9 bar elements for the trunnion rods, and 58 interface elements to represent the contact between the concrete beam and the steel girder. The interface elements are designed to transmit only compressive stresses. The de-tensioning of the rods is simulated by deactivating the corresponding bar elements, which are assigned zero stiffness; as a result, they do not contribute to the structural behavior of the model. The material properties used in the simulation, including Young's modulus, Poisson's ratio, compressive strength, and yield strength, are detailed in Table 2.

Table 2 - Material properties.

Material	Young's modulus (ksi)	Poisson's ratio	Strength (ksi)
Concrete	4095	0.2	4
A36 steel	29000	0.3	60
150 ksi steel	30500	0.3	120

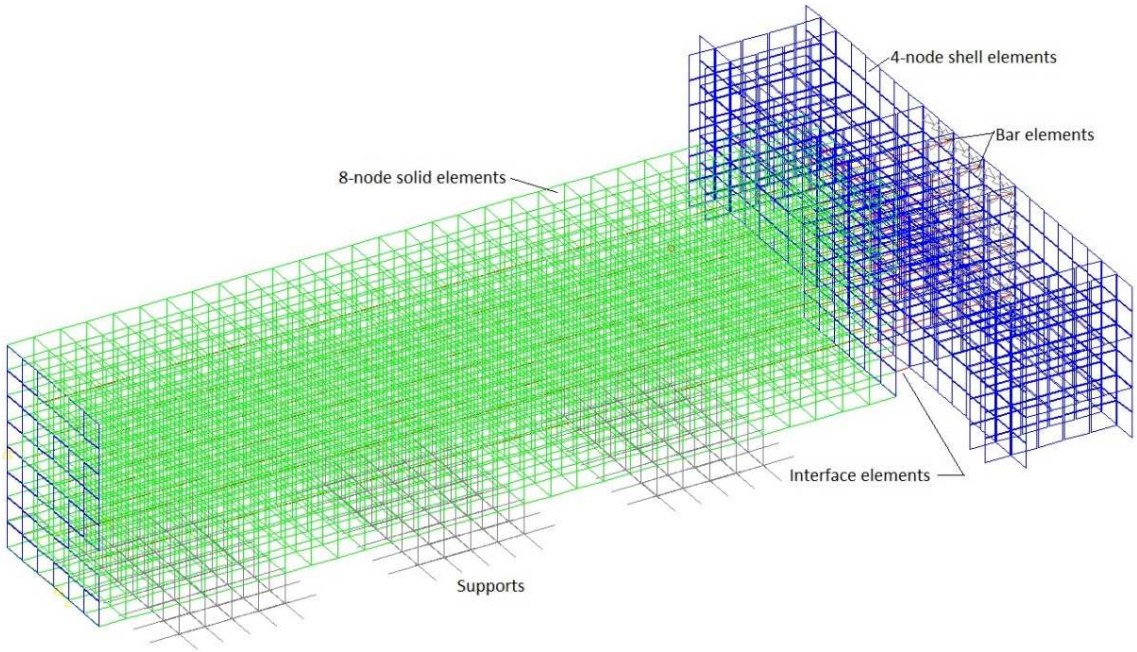

Fig. 4 - Three-dimensional view of FE model.

Figure 5 depicts the rods numbered from 1 to 9. Six specific configurations, referred to as C1 through C6, were utilized to compare the finite element analysis (FEA) results with those obtained from scaled model tests. In configurations C2 through C6, the rods that are not present are designated as de-tensioned rods.

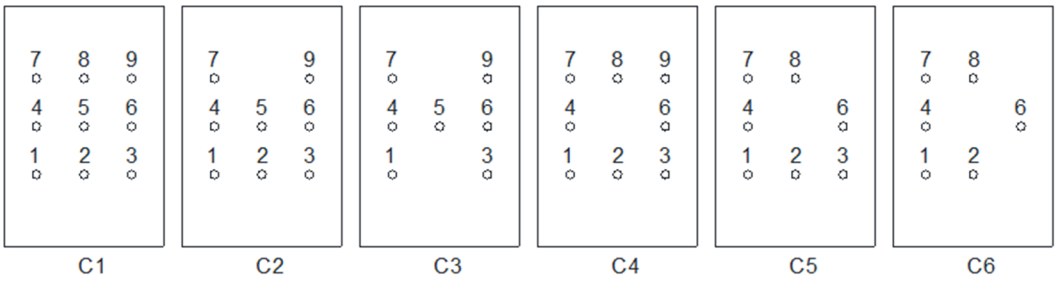

Fig. 5 - Configurations in FEA.

RESULTS AND CONCLUSIONS

In the first configuration (C1), where no rods are de-tensioned, the average initial pre-tension force obtained from the scaled model tests is recorded at 77.3 kips. In comparison, the finite element analysis (FEA) produces a slightly lower value of 77 kips. This close alignment between experimental and analytical results underscores the reliability of both methods in assessing pre-tension forces.

To further illustrate this point, Figure 6 (a-f) provides a comprehensive overview of the forces acting in each rod for configurations C1 through C6. These configurations were tested under a consistent pre-tension level of 60 percent and a pressure set at 2700 psi. The data presented in the figure includes results from both the scaled model tests and the FEA, allowing for a direct comparison between empirical evidence and numerical simulations.

The findings exhibit a fair to good agreement between the results from the FEA and those obtained through experimental tests across all configurations examined. This level of consistency is noteworthy, as it confirms the validity of the FEA model as a predictive tool in this context. The results indicate a strong correlation between the pre-tension forces determined from the FEA and the scaled model tests. The discrepancies observed between the two methods range from 0 percent to 4.6 percent, which suggests a high degree of accuracy in the analytical predictions. Such results are crucial for understanding the system's performance under different loading conditions and can be instrumental in guiding future design optimizations.

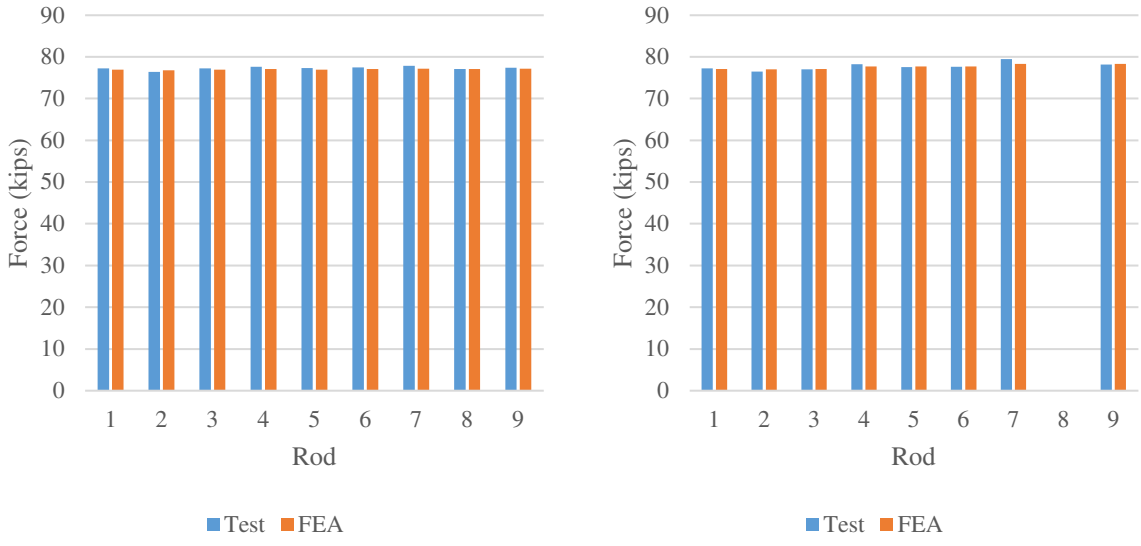

(a) C1 (b) C2

Fig. 6 - Comparison of forces in the rods (a-b).

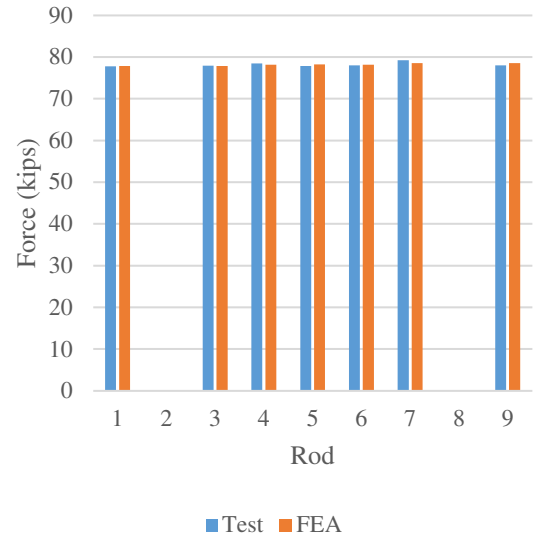

(c) C3

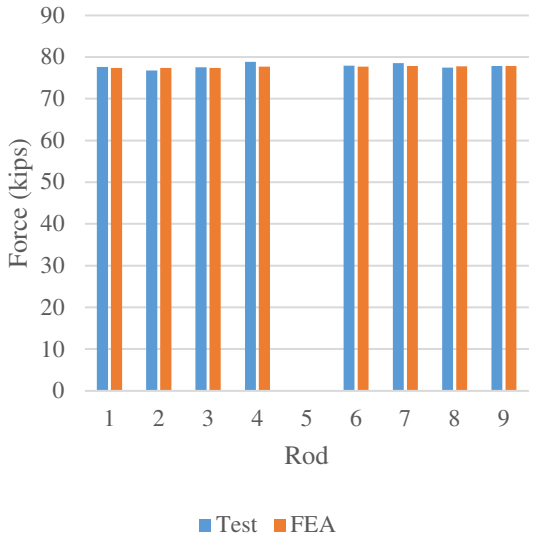

(d) C4

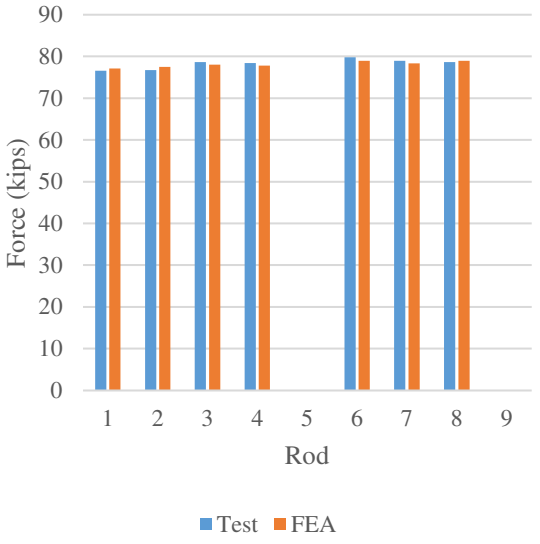

(e) C5

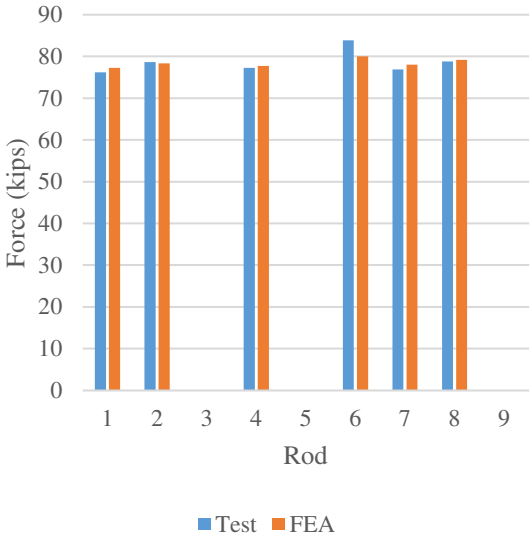

(f) C6

Fig. 6 - Comparison of forces in the rods (c-f).

REFERENCES

[1] Zatar, W., Nghiem, H., Ray, J., Nguyen, H., Anderson, S., "Evaluating Post–Tensioned Trunnion Girders: A Comparative Study of Scale Model Tests and Numerical Analyses," 14th International Workshop on Structural Health Monitoring (IWSHM), Stanford University, Palo Alto, CA, September 2023.

[2] O'Donnell, K.O. 1965. "Prestressed concrete anchorages for large Tainter gates," In Proc., 10th Annual Convention of the Prestressed Concrete Institute, Precast/Prestressed Concrete Institute, Chicago.

[3] Abela, C.M., Abela, A.A. "Evaluation of an Existing Steel Box Trunnion Girder and Its Post-tensioned Anchors before Lift-off Testing: Case Study," Practice Periodical on Structural Design and Construction, 20(4), p.04014052, 2015.

[4] Abela, C.M. "Evaluating Existing Passive Anchorage Systems for Tainter Gates," ASCE Practice Periodical on Structural Design and Construction, 23(1), p.04017032, 2017.

[5] Malik, H., Zatar W. "Software agents to support structural health monitoring (SHM)-informed intelligent transportation system (ITS) for bridge condition assessment," IWSHM 2019, Stanford University, CA, 2019.

[6] Malik, H., Zatar W. "Agent based routing approach to support structural health monitoring informed, intelligent transportation system," Journal of Ambient Intelligence and Humanized Computing, Volume 11, PP1031-1043, 2020.

[7] Nguyen, H. Zatar W., Mutsuyoshi, H. "Hybrid fiber-reinforced polymer girders topped with segmental precast concrete slabs for accelerated bridge construction," Journal of the Transportation Research Record, Volume 2407, issue 1, pp. 83-93, 2014.

[8] Zatar W., Nguyen, H. "Condition assessment of ground-mount cantilever weathering-steel overhead sign structures," Journal of Infrastructure Systems, Volume 23, Issue 4, 2017.

[9] Zatar, W., Nguyen, H., Nghiem, H. "Ultrasonic pitch and catch technique for non-destructive testing of reinforced concrete slabs," Journal of Infrastructure Preservation and Resilience, Volume 1, Issue 1, pp. 1-13, 2020.

Proceedings IRF2025: 8th International Conference on Integrity-Reliability-Failure
In Engineering, Materials, Manufacturing and Biomechanics. Porto 15-18 July 2025
DOI: https://doi.org/10.24840/978-972-752-323-8

PAPER REF: 22258

STRUCTURAL DAMAGE ALERT THROUGH ARTIFICIAL NEURAL NETWORKS

Danilo de Santana Nunes[1(*)], José Luis Vital de Brito[2], Graciela Nora Doz[2]

[1]Department of Engineering and Computing, State University of Santa Cruz, Ilhéus, Brazil
[2]Department of Civil and Environmental Engineering, University of Brasília, Brasília, Brazil
[(*)]*Email:* dsnunes@uesc.br

ABSTRACT

This paper presents a routine for damage detection based on Artificial Neural Networks (ANNs). The first step was to define the structure's regions most susceptible to damage based on stresses and deformed shape of the updated numerical model. The second step was to train an ANN using the natural frequencies of the intact and damaged models as input data, and vectors that indicate the position and magnitude of damage as expected output. A feed-forward backpropagation ANN was used. The procedure was used to assess the structural condition of a cable-stayed footbridge. A new dynamic test was performed and a vector composed of the newly identified natural frequencies was input into the ANN, which indicated the presence of damage. The damage scenario was applied to the numerical model. The difference between the frequencies of the updated and damaged model, and experimental values was less than 2%.

Keywords: Damage detection, neural networks, numerical model, natural frequencies.

INTRODUCTION

Different methods, conventional and dynamic, have been applied to identify structural damage. The most common approach for damage detection based on dynamic data, also used in this study, comprises the stages of modal identification and update of the numerical model (Azam et al., 2019; Cong et al., 2021). The analysis involves the design and calibration of the structure model, serving as a reference to evaluate the current and long-term condition of the structure (Chisari et al., 2015). One challenge of diagnosis is the characterization of the unknown relationship between field measurements and damage patterns through the development of robust algorithms with the ability to detect, locate, and quantify damage (Abdeljaber and Avci, 2016; Gulgec et al., 2019). In this regard, this study sought a damage detection procedure to characterize this relationship through Artificial Neural Networks (ANNs).

RESULTS AND CONCLUSIONS

From the stress analysis and deformed shape of the structure, some regions were initially selected as critical. This information, together with the data provided by the structural design (steel reinforcement), showed the sections with the greatest evidence of suffering damage between the initially selected. Figure 1 shows, respectively, the bending moments and deformed shape due to the permanent loads (self-weight + experimental stay forces), with emphasis (!) on some regions, and the regions judged as critical in yellow (D1, D2, D3 and D4). The ANN provided an output vector with positive and non-zero values in two components, which represent damages at D2 and D4. The reduction of geometric properties of the elements, the approach used in this study to simulate damage, were approximately 26% and 3%.

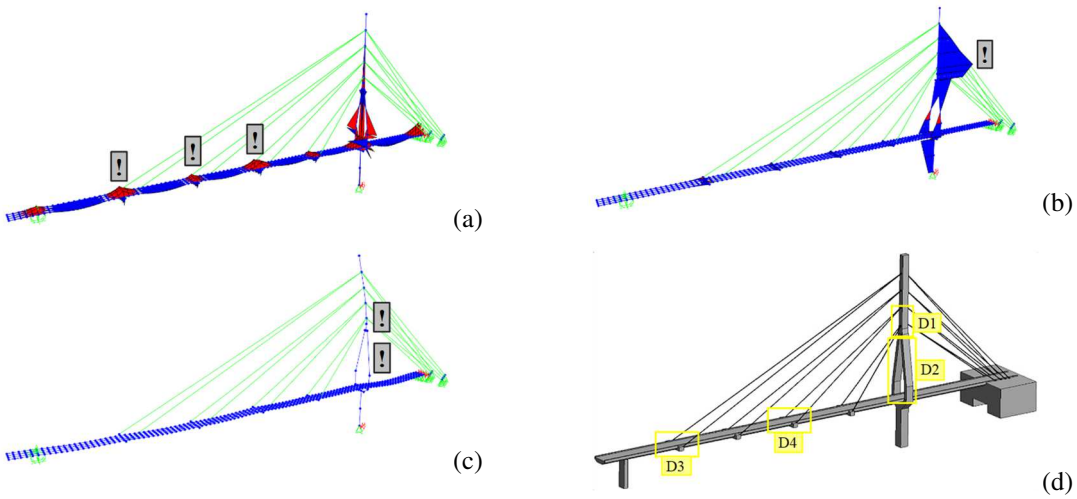

Fig. 1 - (a) (b) Bending moments and (c) Deformed shape due to permanent load, and (d) "Critical" regions.

In order to evaluate the result provided by the ANN, the damages and new stay forces were inserted into the numerical model, simulating the current condition of the footbridge as well as the natural frequencies of the first four flexural mode shapes ($f_{\text{damaged model}}$). Table 1 shows a comparison between the numerical and experimental frequencies from second test ($f_{\text{test 2}}$).

Table 1 - Comparison between the numerical (damaged model) and experimental frequencies from test 2.

Experimental flexural mode shape	$f_{\text{test 2}}$ (Hz)	$f_{\text{damaged model}}$ (Hz)	Difference (%)
1st	1.616	1.612	0.25 ↓
2nd	3.284	3.225	1.80 ↓
3rd	5.405	5.453	0.89 ↑
4th	8.408	8.367	0.49 ↓

This comparison demonstrates the coherence of the results provided by the ANN since, with the insertion of the provided damage vector and the new prestressing forces of the stays, the frequencies of the numerical and experimental models showed a maximum difference of 1.80%, in the second natural frequency, demonstrating the ability of ANN to detect multiple damage.

REFERENCES

[1] Azam SE, Rageh A, Linzell D. Damage detection in structural systems utilizing artificial neural networks and proper orthogonal decomposition. Structural Control and Health Monitoring, 2019, 26(2), pp.1-24.

[2] Cong Y, Sin-Chi K, Liam JB, Campbell RM. Implementing bridge model updating for operation and maintenance purposes: examination based on UK practitioners' views. Structure and Infrastructure Engineering, 2021, 18(12), pp.1638-1657.

[3] Chisari C, Bedon C, Amadio C. Dynamic and static identification of base-isolated bridges using genetic algorithms. Engineering Structures, 2015, 102(1), pp.80-92.

[4] Abdeljaber O, Avci O. Nonparametric structural damage detection algorithm for ambient vibration response: utilizing artificial neural networks and self-organizing maps. Journal of Architectural Engineering, 2016, 22(2), pp.1-14.

[5] Gulgec NS, Takáč M, Pakzad SN. Convolutional neural network approach for robust structural damage detection and localization. Journal of Computing in Civil Engineering, 2019, 33(3), pp.1-11.

Proceedings IRF2025: 8th International Conference on Integrity-Reliability-Failure
In Engineering, Materials, Manufacturing and Biomechanics. Porto 15-18 July 2025
DOI: https://doi.org/10.24840/978-972-752-323-8

PAPER REF: 22290

DAMAGE DETECTION IN BRIDGES USING COMBINED MODAL STRAIN ENERGY AND SPECTRAL FINITE ELEMENT METHODS

Mohammad Vahidi[1(*)], Gholamreza Ghodrati Amiri[2]

[1]Dep. Civil Engineering, Faculty of Engineering, South Tehran Branch, Islamic Azad University, Tehran, Iran
[2]Natural Disasters Prevention Research Center, School of Civil Engineering, Iran ust, Tehran, Iran
[(*)]*Email:* mohammadvahidi1001@gmail.com

ABSTRACT

Bridges are one of the most important infrastructures in the transportation industry, and monitoring the health of bridges on their condition and behavior is of great importance. A new and efficient two-step method for damage detection in elastic supports of a steel girder is presented. First, the spectral finite element (SFE) method is used to model the element's damage along the length of the girder with the definition of micro-damage. In the second step, two methods of modal strain energy (MSE) and modal flexibility (MF) are used to detect the location of damage. To simulate damage in elastic supports, the idea of reducing stiffness has been used. The modal strain energy method has been successful in determining the location of damage compared to the modal flexibility method.

Keywords: Spectral finite element, modal strain energy, modal flexibility method, damage detection, elastic supports.

INTRODUCTION

Bridges and their accessories are exposed to various micro-damage during their lifetime. One of the components of bridges is neoprene and its elastic supports, which makes it difficult to detect damage and is often associated with error. To reduce the error in damage detection of elastic supports, the SFE method can be used. SFE is a powerful method that has the flexibility of finite element modeling and also brings the accuracy of pseudo-spectral methods and reduces the computational cost (Kudela 2007, Vahidi 2023). MSE and MF are damage detection methods based on vibration characteristics. In comparison, MSE is more sensitive than other vibration-based methods in damage detection (Pandey 1994, Vahidi 2023).

RESULTS AND CONCLUSIONS

To use the advantages of the spectral finite element method and its governing equations, an eight-node beam element was defined in the OpenSees software (Vahidi 2023).

Element beamvahidi $eleTag $Node1 ... $Node8 $A $E $G $Iz $g $ρ $matTag $transfTag;

An experimental testing model has been used to verify the performance of the proposed method (Tan 2017). First, the steel girder is modeled with the Element beamvahidi taking into account the definition of micro-damage and elastic support conditions. The geometric characteristics of the girder and the length of the damaged elements are shown in Figure 1. Table 1 shows the material properties. Simulation of damage in elastic supports has been done with 10, 15, 20, and 25% stiffness reduction. By modal analysis of the structure and obtaining the mode responses, MSE and MF damage indices are calculated with Equations. 1 and 2, respectively (Pandey 1994, Vahidi 2023). The peaks in Figures 1 and 2 indicate damage locations.

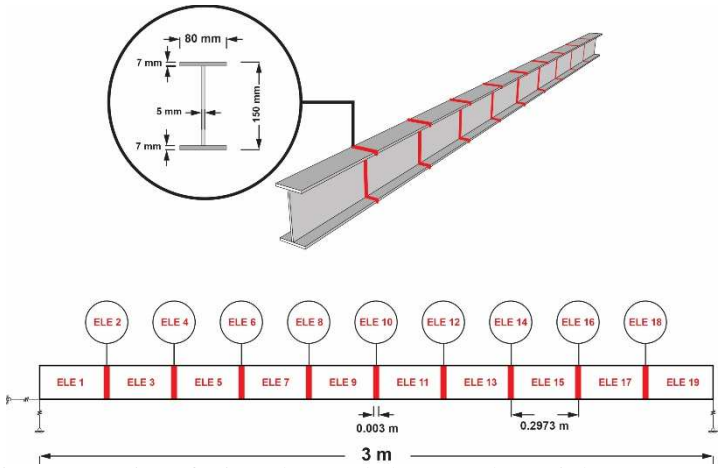

Fig. 1 - **L**ocation of micro-damaged elements along girder span.

Table 1 - Material properties of specimens.

E_{gider} (Pa)	1.75 E+11
ρ (kg/m^3)	7850
$L_{damage\ micro}$ (m)	0.003
A (m^2)	0.0018
I (m^4)	6.77E-6
E_{spring} (Pa)	6.67E+8

$$\beta_{ji} = \frac{\left[\left(\varphi''^{*}_{ji}\right)^2 + \sum_{i=1}^{nm}\left(\varphi''^{*}_{ji}\right)^2\right] * \left[\sum_{i=1}^{nm}\left(\left[\varphi''_{ji}\right]\right)^2\right]}{\left[\left(\varphi''_{ji}\right)^2 + \sum_{i=1}^{nm}\left(\left[\varphi''_{ji}\right]\right)^2\right] * \left[\sum_{i=1}^{nm}\left(\varphi''^{*}_{ji}\right)^2\right]} \quad (1)$$

$$MFMDI = \frac{\left[\sum_{i=1}^{m}\frac{1}{\omega_i^2}\varphi_i\varphi_i^T\right]_d - \left[\sum_{i=1}^{m}\frac{1}{\omega_i^2}\varphi_i\varphi_i^T\right]_h}{\left[\sum_{i=1}^{m}\frac{1}{\omega_i^2}\varphi_i\varphi_i^T\right]_h} \quad (2)$$

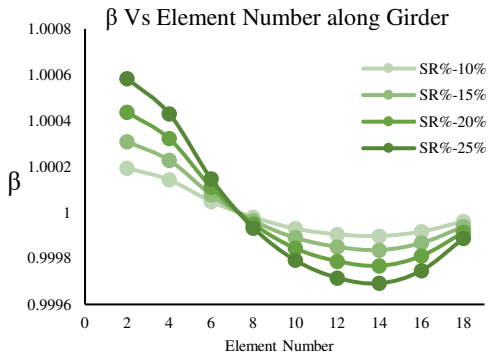

Fig. 2 - Plot of β vs element number.

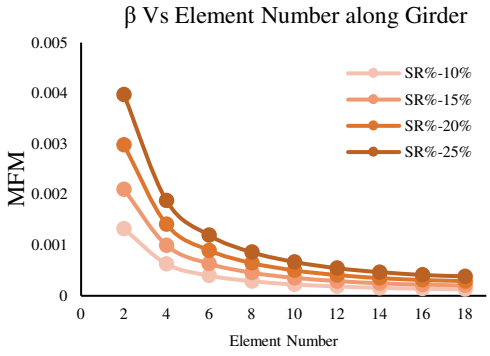

Fig. 3 - Plot of MFM vs element number.

Figures 2 and 3 present the obtained damage indices. The MSE method detected the damage at 0.297 m in the first element damage, near the support. The MF method correctly identified the damage location only in the first bending mode. While higher modes resulted in errors in damage localization. The combined method of SFE and MSE damage index has worked correctly and is capable of damage detection in elastic supports.

REFERENCES

[1] Kudela, Paweł; Krawczuk, Marek; Ostachowicz, Wiesław. Wave propagation modelling in 1D structures using spectral finite elements. J. Sound and Vibration, 2007, 300.1-2: 88-100.

[2] Vahidi, Mohammad, et al. "Conflation of Modal Strain Energy, Spectral Finite Element, and Machine Learning Techniques for Damage Detection in Multi-span Steel Girder Bridges with Variable Sections." Structures 57, (2023): 105086.

[3] Pandey, A.K.; Biswas, M. Damage detection in structures using changes in flexibility. Journal of sound and vibration, 1994, 169.1: 3-17.

[4] Tan, Zhi Xin, et al. Detecting damage in steel beams using modal strain energy based damage index and Artificial Neural Network. Engineering Failure Analysis, 2017, 79: 253-262.

Proceedings IRF2025: 8th International Conference on Integrity-Reliability-Failure
In Engineering, Materials, Manufacturing and Biomechanics. Porto 15-18 July 2025
DOI: https://doi.org/10.24840/978-972-752-323-8

PAPER REF: 22377

DAMAGE STATE PREDICTION OF RC-BRIDGES SUBJECTED TO PIER SCOURING AND EARTHQUAKES

Aref Jozi(*), Ali Raoof Mehrpour Hosseini, Mehran Seyed Razzaghi
Department of Civil Engineering, Qazvin Branch, Islamic Azad University, Qazvin, Iran
(*)*Email:* arefjozi@gmail.com

ABSTRACT

Reliable and rapid damage detection in RC bridges under the combined effects of scouring and earthquakes is vital for the resilience assessment of transportation infrastructure. However, there is a lack of literature assessing and predicting the simultaneous effects of random pier scouring and seismic events on RC bridges. Therefore, this study employs non-linear time history analyses on the finite element models to evaluate the behavior of RC bridges and generate a dataset for the development of an ANN model. This study aims to provide an ML-based Graphical User Interface (GUI) for predicting the damage state of multi-span RC bridges.

Keywords: RC-bridges, multi-hazard, FEA, machine learning, damage detection.

INTRODUCTION

RC bridges are vital to transportation networks. Hence, assessing their seismic vulnerability is key to risk management of transportation systems (Ren et al., 2021). The combined effect of scouring and earthquake has proven to be a major factor in bridge failures, particularly in flood-prone rivers. Scouring occurring near bridge foundations significantly impacts the seismic response of bridge components, such as the overall base shear of the structure and the pounding forces between the elements of the superstructure (Hosseini et al., 2023). The vulnerability of bridges can be assessed using in-situ techniques or numerical analyses (i.e., finite element analysis). These methods have been widely used and have provided valuable data. However, they have complex and time-consuming processes (Kazemi et al., 2023). Therefore, the demand for a precise and rapid estimation of damage state bridges facing multi-hazard scenarios still remains. Accordingly, in this study, a multi-layer artificial neural network was developed to conduct multiclass damage state (DS) detection, followed by identifying performance metrics, a confusion matrix, and optimal hyperparameters to ensure the integrity of the proposed ANN model. Finally, the results were used to introduce an estimation tool (i.e., a GUI) for identifying the DS of RC bridges.

RESULTS AND CONCLUSIONS

Nonlinear dynamic analyses were conducted on the bridge models using the OpenSees software. The results of the nonlinear analyses were collected in a dataset with 1200 data points, including earthquake, soil, scour depth, and structure-related features. In order to train the ANN model, the dataset was randomly grouped into a training set and a test set with 80% and 20%, respectively. Moreover, the target was the DS of the bridge piles based on Kowalsky Limit State Definitions. After training and testing the ANN model, five-fold cross-validation and random search were employed to obtain the optimal hyperparameters. Accordingly, the confusion matrix and performance metrics derived from the ANN model are shown in Figure 1**Error! Reference source not found.**(a).

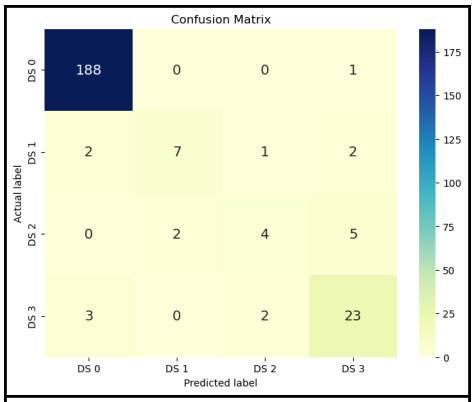

	precision	recall	f1-score	support
0	0.97	0.99	0.98	189
1	0.80	0.67	0.73	12
2	0.75	0.27	0.40	11
3	0.72	0.82	0.77	28

(a)

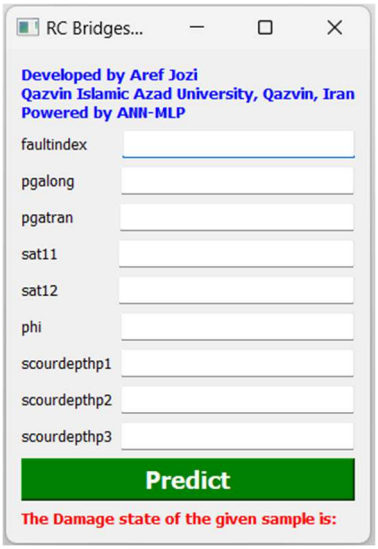

(b)

Fig. 1 - (a) Confusion matrix and performance metrics; (b) GUI of the predictor.

Due to the dataset's identity and the imbalanced distribution of the DS classes obtained from FE analyses, the ANN model performed differently in the majority and minority classes. The ANN model performed suitably in predicting DS0 and DS3, which are the majority classes, with a proportion of 92% of the test samples. Additionally, the accuracy of the ANN model for the training and test set was 98.8% and 93.0%, respectively. The results prove that the ANN exhibits excellent performance in accurately predicting the DS of the studied RC bridges.

In the end, a user-friendly tool powered by the trained ANN model was developed. As demonstrated in Figure 1(b), the GUI operates by first receiving the main features and then predicting the DS of the introduced RC bridge. It is important to note that the predictor achieves optimal accuracy when the input values are within the minimum and maximum range of the training dataset.

REFERENCES

[1] Hosseini A, Razzaghi M, Shamskia N. A Numerical Study on the Seismic Performance of a RC-Bridge with Random Pier Scouring. Journal of Structural Engineering and Geotechnics, 2023, 12, pp.75-89.

[2] Kazemi F, Asgarkhani N, Jankowski R. Machine learning-based seismic response and performance assessment of reinforced concrete buildings. Archives of Civil and Mechanical Engineering, 2023, 23, pp.1-21.

[3] Ren J, Song J, Ellingwood B. Reliability assessment framework of deteriorating reinforced concrete bridges subjected to earthquake and pier scour. Engineering Structures, 2021, 239, pp.11-23.

Proceedings IRF2025: 8th International Conference on Integrity-Reliability-Failure
In Engineering, Materials, Manufacturing and Biomechanics. Porto 15-18 July 2025
DOI: https://doi.org/10.24840/978-972-752-323-8

PAPER REF: 22388

PUR SANDWICH PANELS SUBJECTED TO BLASTS AT SHORT STANDOFF DISTANCES

Florea Dinu [1, 2], Calin Neagu[1,2(*)], Andreea Onea[1], Paul Zdrenghea[1], Mihai Senila[3], Robert Laszlo[4], Emilian Ghicioi[4]

[1]Politehnica University Timisoara, Timisoara, 300006, Romania
[2]Romanian Academy, Timisoara Branch, Timisoara, 300223, Romania
[3]Technical University of Cluj-Napoca, Cluj-Napoca, Romania
[4]Nat. Inst. Research and Develop. in Mine Safety and Protection to Explosion INSEMEX, Petrosani, Romania
[(*)]*Email:* calin.neagu@upt.ro

ABSTRACT

Light weight polyurethane foam panels are largely used for envelopes in different kind of buildings. One of their benefits is a good strength to weight ratio under transverse loads. However, under extreme loading conditions, e.g., external explosions, PUR panels can be severely damaged or even destroyed. The study presented in the paper describes the results obtained on PUR wall sandwich panels tested for blasts at short standoff distances. The panels are arranged as single span systems supported on side rails and tested for increasing charge weights until failure. Increasing standoff is a cost-effective way to reduce vulnerability and mitigate wall failure. The ultimate capacity also depends on the number of self-tapping screws that are used to attach the panels to the supporting members.

Keywords: Light steel-based façade, wall sandwich panel, external blast, robustness.

INTRODUCTION

Sandwich panels, which are also known as composite panels, are widely used in construction systems for the external walls and roofs of industrial, commercial, or other types of building. One common solution is the two steel-sheet facings (one internal and one external) and low-density polyurethane foam core sandwich panel PUR [1]. For wall applications, the two faces are generally flat or lightly profiled [2]. Wall sandwich panels are typically designed from the weather/climate related conditions of the site (wind and thermal actions, thermal comfort). The design provisions for sandwich panels are based to a large degree on test results [3]. In case of extreme pressures generated by an explosion, the flexural resistance of the wall elements can be exceeded, resulting in damage or failure, and possibly in further structural damage at the interior [4]. For such extreme cases, the flexural demands can be very high, so it can be extremely difficult to provide economical solutions. In such cases, the panels may be designed to allow the development of catenary forces by using appropriate design and detailing. Because the blast pressure decreases rapidly with distance, the increase in the standoff between a potential threat and the structure is a cost-effective way to reduce vulnerability and mitigate wall failure of protection.

This study investigated the capacity of light steel-based PUR sandwich panels to resist the effects of external blasts produced at short distance from the façade. The walls were tested incrementally until failure by keeping the standoff distance constant and increasing the charge weight.

RESULTS AND CONCLUSIONS

The wall sandwich panels considered for the experimental program are 100 mm thick and 1000 mm wide (Figure 1Fig. a). The two steel faces are lightly profiled, with a rib height of 1.5 mm, and the insulating core is made from rigid polyurethane foam PUR with a characteristic weight of 40 kg/m^3. The external and internal steel faces are 0.4 mm thick and are made from S250GD nominal steel. The panels are fixed to the side rails using 6 self-drilling screws 5.5x135 mm at each end. The span between the side rails is 1.9 m. The blast tests were performed using charges made from cylindrical cartridges with height-to-diameter ratio of 6.5. The equivalent mass of TNT of the explosive (or eTNT) was equal to unity. The charges were positioned 3.0 meters away from the wall's midspan and 1.5 meters above the ground. Charge weights started from 8 cartridges (T1 = 1.144 kg) and were gradually increased by two cartridges to T4 = 2.09 kg, until the failure of the panels. This study refers to a testing series for left span systems. Figure 1b shows a snapshot with large deformations of the panels during last test T4. The recording was fast enough to visualize the shock wave of the explosion. For clarity, the shock wave was transformed using background-oriented schlieren (BOS), based on image subtraction technique, see Figure 1c. Blast charges detonated at close distance produce high intensity pressure waves, much beyond those considered in classic design of enclosures; the pressure distribution is highly nonuniform and varies significantly in magnitude over the wall elements.

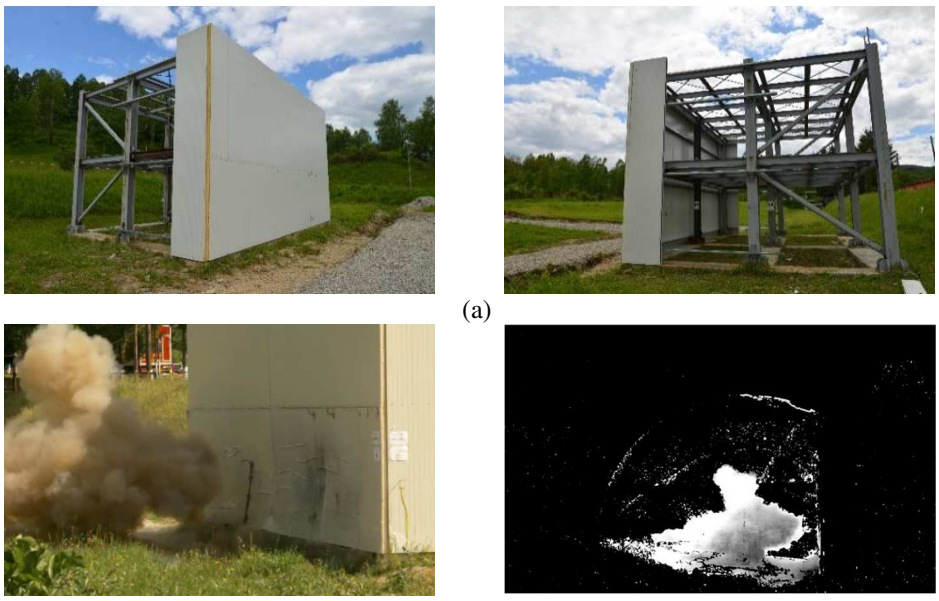

(a) (b) (c)

Fig. 1 - Views with the blast model (a), detonation of a charge (b), and the visualization of the shock wave propagation and reflection using background-oriented schlieren (BOS) (c).

REFERENCES

[1] Davies J. Sandwich panels. Thin-Walled Structures. 1993;16(1-4): pp.179-98.

[2] Dinu F, Neagu C, Senila M. Wall sandwich panels with steel facings and PUR foam core under transverse loading: Experimental testing and numerical model calibration. Engineering Structures. 2024 Dec 15;321:119014.

[3] ECCS 127. ECCS no. 127/ CIB no. 320,. European Convention for Constructional Steelwork; 2009.

[4] Dusenberry D, Schmidt J, Hobelmann P, Mlakar P, Lin L, Smilowitz R, et al. Blast protection of buildings, ASCE/SEI 59-11. 2011.

Proceedings IRF2025: 8th International Conference on Integrity-Reliability-Failure
In Engineering, Materials, Manufacturing and Biomechanics. Porto 15-18 July 2025
DOI: https://doi.org/10.24840/978-972-752-323-8

PAPER REF: 22394

PRELIMINARY SCENARIO OF EXPECTED EARTHQUAKE DAMAGE IN THE BUILDING STOCK OF SÃO MIGUEL, AZORES

Maria João Barros(*), Margarida Machado Pires
Faculty of Sciences and Technology, Universidade dos Açores, Açores, Portugal
(*)*Email:* maria.jf.barros@uac.pt

ABSTRACT

The Azores, a nine island Portuguese archipelago located in the North Atlantic Ocean, between North America and Europe, in the Azores micro-plate, is an area of severe seismic activity, due to its geotechnical framing and volcanic activity. Earthquakes are inevitable but their consequences are not. Since hazard cannot be reduced, we must reduce exposition and building stock vulnerability, to mitigate seismic hazard. The purpose of this study is to assess the seismic vulnerability and the average estimated damage grade, for moderate to high seismic intensities, of the residential building stock in São Miguel Island, Azores, based on a representative sample of buildings. The obtained results were compared with a previous study performed in Faial. This methodology can be used on other islands and repeatedly with updated data as a powerful tool for local and regional authorities.

Keywords: Building stock, seismic vulnerability, vulnerability index, damage grade.

INTRODUCTION

The purpose of this paper is to assess the seismic vulnerability and the average estimated damage grade, for moderate to high seismic intensities, of the residential building stock in São Miguel Island, Azores, based on a representative sample of buildings, following three stages. Since buildings are not all the same, we can expect different consequences/damages on buildings facing the same earthquake. So, first, to have a detailed characterization of the building stock, regarding the building typology, materials, construction technologies and conservation state, a Residential Building Stock Survey was used. Secondly, since the construction scheme found in São Miguel can be translated directly to the other islands, four different classes of vulnerability were defined based on the survey and on historical data related to destruction occurred during seismic crisis faced on the Azorean islands, namely the latest main event which affected the islands of Faial and Pico in 1998. Eight relevant parameters were selected, and a vulnerability index was calculated from this series of parameters, each parameter being assigned a weight according to its importance. For each one of the parameters, the four vulnerability classes were considered. Afterwards, the vulnerability index and the mean damage grade were evaluated for each building in the sample. Finally, the seismic vulnerability evaluation of the building stock of São Miguel Island through the average of global vulnerability index and the average estimated damage grade is done, for moderate to high seismic intensities.

RESIDENTIAL BUILDING STOCK CHARACTERIZATION

The Residential Building Stock Survey (RBSS) was developed by the University of the Azores, in the framework of the Green Islands Project, a project which associated the Massachusetts

Institute of Technology and several Universities in Portugal (Fortuna et al., 2010). With RBSS it was possible to characterize in a detailed manner the building stock of the Azores regarding the building envelope and surroundings. This survey was applied to a representative sample of 500 households in São Miguel, distributed by municipalities according to population concentration.

The methodology involved preliminary data collection followed by field work, consisting of building external and internal visual surveys upon arrival at the location of the building, and inhabitant interviews.

The external visual survey included the external pathologies of the building facade and, as much as possible, building dimensions and physical (envelope) characteristics. The objective of the internal visual survey was to gather information about the characteristics of the interior of the household unit (floor covering and ceiling covering, ceiling height, amongst others) and its interior pathologies (type and location). The data that could not be obtained by visual survey was retrieved from the interviewed residents.

From the survey results it is possible to define the most common residential household unit typology in São Miguel Island: single family buildings are the dominant type of housing. These residential buildings are mostly connected to other buildings on one side or two sides (row house) and there are also detached houses. Apartment buildings exist but in smaller numbers.

The most common number of floors in residential buildings is 3 (including ground floor), 57.6%, followed by 2 floors, 29.0%, and 11.2% of the buildings have 4 floors.

Of the 500 inquiries that were made, 33.2% did not know the approximate year of construction of the building. Of the remaining, the majority mentioned that the building was originally constructed before 1940. A high concentration of frequencies occurs between 1980 and 1999 with a continued concentration from 2000 to 2005 (Table 1). This is consistent with a construction boom that occurred after the 1980's and lasted until 2007.

Table 1 - Percent of buildings per year range of construction of the building [1].

Before 1940	1940-1949	1950-1959	1960-1979	1980-1989	1990-1999	2000-2005	2006-2008	2009-2010
14.6	2.0	5.2	11.8	11.8	10.2	8.6	2.2	0.4

The residential building stock in São Miguel Island, like in the other Azorean islands, is still mostly constituted of a traditional construction system, basically stone masonry load-bearing walls and timber floor slabs and roof trusses. In some cases, this traditional construction has been subject to modifications, namely the replacement of the timber floor structure (planks and beams) with a reinforced concrete slab, again being supported by load-bearing stone masonry walls. This modification can affect only the service areas (kitchens and bathrooms) or a more extended area.

The most common types of external walls are stone walls, with or without masonry mortar (45.8%), and aggregate concrete masonry units' walls (35.4%). There are only a few cases of double aggregate concrete masonry unit walls (0.8%).

As to the external rendering of the external walls, the most used material is cement mortar (63.2%). Lime mortar is also referred to in the case of external stone walls. Ceramic wall tiles, wood or natural stone are not very common.

In most cases the walls are 25 cm thick or 35 cm thick. For about four decades, 25 cm walls have dominated. Before 1950, walls are typically thick. After a progressive transition period, thinner walls (35 cm and 25 cm) become more common. However, it is expected that 35 cm thick walls (including rendering) will become dominant in the future, as opposed to thinner walls, due to thermal legislation. It is worth noting that in 22.4% of the cases the walls are 55 cm thick or more, most of them pertaining to buildings built before 1960, probably stone walls.

According to the RBSS results, the most common resistant structure of the buildings is reinforced concrete (54.6%), followed by stone masonry resistant structure (33.0%). Other types (steel, wood) are very uncommon.

Most dwellings are covered with a roof (94.8%), namely a gable roof (73.0%). One part roof refers to 4.2% of the cases and the remaining (17.6%) refers to more than two-part roofs. Flat (2.4%) or leaning slabs (0.4%) are only used in a small part of the sample.

Most roofs are supported by a discontinuous support structure of wood (39.2%) or by a slab (30.2%). However, in a noticeable number of cases the type of support of the roof could not be determined (30.6%).

In most cases, the type of floor structure is a slab, usually solid (44.4%) or slight (18.4%). It is also common to find wood floor structures (10.2%). Mixed cases are also represented (5.6%) but not so much metallic structure, which are found only in 0.2% of the cases.

In the study sample, many buildings are placed between two buildings of equal size (43.8%) or between two unequal-sized buildings (23.6%). A smaller portion are isolated buildings (10.2%) and an even smaller number of buildings are placed between two larger buildings (4.8%). Cases of buildings connected to a smaller (4.8%) or larger (5.0%) building are not very significant.

To complete the characterization of the existing residential building stock, the degradation state was evaluated using an empirical method based on field work, through which the existing (detectable) defects were gathered. The methodology was applied to each of the surveyed household units, resulting in an External Degradation Level (EDL) for each of them (Machado Pires and Barros, 2011).

The index EDL has six possible discrete values: 0, no visually detectable degradation, good, light, medium, broad and extensive degradation, 5.

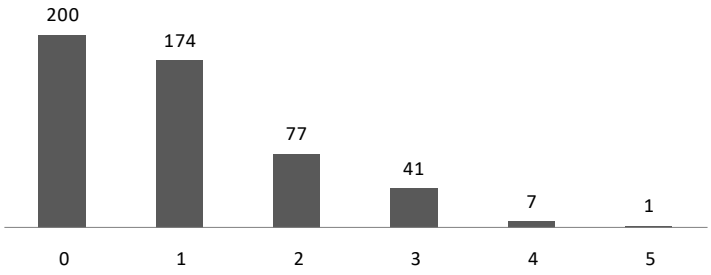

Fig. 1 - EDL results (Machado Pires and Barros, 2011).

The first task was to identify the main external pathologies that can affect the residential buildings (only the facades) and the affected location on the building facade. The approach was based on a ranking of importance concerning the affected area (extension) and depth of the problem. The results are shown in Figure 1.

From these results, 40% of the surveyed residential building stock shows no visually detectable degradation. However, 25% of the surveyed residential buildings need medium to large repair works (EDL=2, 3, 4 or 5).

VULNERABILITY ASSESSMENT METHODOLOGY

The assessment of the building stock vulnerability proposed is based in a vulnerability index calculated from a series of parameters, each parameter being assigned a weight according to its importance, as described in Table 2 (Neves et al., 2012).

Table 2 - Parameters description and their assigned weight.

Parameter	Description	Weight
P1	Type of resisting system	1.50
P2	Quality of the resisting system	2.50
P3	Maximum distance between floors	0.75
P4	Number of floors	1.50
P5	Household position	1.50
P6	Horizontal diaphragms	1.00
P7	Roofing system	1.00
P8	Conservation State	1.00

The parameters were defined from the survey variables and their combinations. For each one of the eight parameters, four vulnerability classes are considered, based on the RBSS results and on recent historical data related to destruction occurred during seismic crisis faced on other Azorean islands, namely the latest main event which affected the islands of Faial and Pico in 1998. The relationship between the survey variables and the parameters is explained below (Tables 3 to 10).

The type of resisting system was obtained from the knowledge of the main resisting structure of the building and the type of external walls.

Table 3 - P1 Type of resisting system.

Type of resisting system	Vulnerability class
Reinforced concrete/Steel	A
Timber	B
Stone masonry and mortar	C
Stone masonry; Unknown	D

The quality of resisting system was obtained from the knowledge of the main resisting structure of the building, year of construction and last rehabilitation/strengthening.

Table 4 - P2 Quality of the resisting system.

Type of resisting system	Year of construction of the buildings / Nature of last Rehabilitation or Strengthening	Vulnerability class
Reinforced concrete / Metallic	Before 1959	C
	From 1960 to 1979	B
	From 1980	A
Stone masonry with or without mortar; Unknown	Before 1959	D
	From 1960 to 1979	D
	From 1980	D
Stone masonry with or without mortar; Unknown	Reinforcement of structure with braces Reinforcement of structure with walls´ reinforcement	A

The maximum slenderness of resisting walls was obtained from the knowledge of the average ceiling height (h) and external walls thickness (s).

Table 5 - P3 Maximum slenderness of resisting walls.

Slenderness	Vulnerability class
$\frac{h}{s} \leq 9$	A
$9 < \frac{h}{s} \leq 15$	B
$15 < \frac{h}{s} \leq 20$	C
$\frac{h}{s} > 20$	D

In Tables 6, 7 and 8, the parameters were obtained directly from the survey.

Table 6. P4 - Number of building floors including ground floor.

Number of building floors	Vulnerability class
1 floor	A
2 or 3 floors	B
4 or 5 floors	C
6 or more floors	D

The Roofing system was obtained from the knowledge of the type of coverage of the housing unit, type of support structure of inclined roof coverage and predominant type of resistant structure of the building.

Table 7 - P5 – Household position.

Typology	Household position	Vulnerability class
Single-family row house	Between two buildings of equal size	A
	Between two larger buildings	B
	Between two smaller buildings	D
	Between two unequal-sized buildings	C
	1 smaller building	C
	1 larger building	B
Single-family isolated dwelling house Single-family connected house		A

Table 8 - P6 Horizontal diaphragms.

Horizontal diaphragms	Vulnerability class
Solid slab Slight slab Flat slab Metallic Mixed Slab	A
Wood floor structure Unknown	C

Table 9 - P7 Roofing system.

Roofing system	Vulnerability class
Slab + Flat paving stone	A
Slab + Leaning paving stone	B
Slab + One part roof	B
Flexible roofing system + One part roof	B
Slab + Roof with more than two parts	C
A, B, C + Predominant type of resistant structure (Stone masonry, metallic)	D
Flexible roofing system + Roof with more than two parts	C

The conservation state was obtained from the knowledge of the complementary EDL.

Table 10 - P8 Conservation state.

Conservation state	Vulnerability class
0 or 1	A
2	B
3	C
4 or 5	D

Finally, the vulnerability index was determined.

Table 11 - Vulnerability index.

Parameters	Class C_{vi}				Weight	Vulnerability index
	A	B	C	D	p_i	$I_v^* = \sum_{i=1}^{8} C_{vi} \times p_i$
1. Structural building system						$0 < I_v^* \leq 537.5$ Normalized index $0 \leq I_v \leq 100$
P1 Type of resisting system	0	5	20	50	1.50	
P2 Quality of the resisting system	0	5	20	50	2.50	
P3 Maximum slenderness of resisting walls	0	5	20	50	0.75	
P4 Number of floors	0	5	20	50	1.50	
2. Interaction						
P5 Household position	0	5	20	50	1.50	
3. Floor slabs and roofs						
P6 Horizontal diaphragms	0	5	20	50	1.00	
P7 Roofing system	0	5	20	50	1.00	
4. Conservation status and other elements						
P8 Conservation State	0	5	20	50	1.00	

A vulnerability level is also proposed, by aggregating values into levels or classes, as shown in Table 12.

Table 12 - Vulnerability levels.

Vulnerability index	I_v
Very low	0-20
Low	20-40
High	40-60
Very high	>60

The mean damage grade (MDG, μ_D) of a building subjected to a certain seismic intensity, I, according to the macroseismic scale, can be calculated as below (Ferreira et al., 2008):

$$\mu_D = 2.5(1 + tanh(I + 6.25V_i - 13.1)/2.3) \quad (1)$$

with V_i given by [3]

$$V = 0.592 + 0.0057 \times I_v \quad (2)$$

and the vulnerability index I_v taken from Table 11.

RESULTS AND CONCLUSIONS

With the methodology adopted for the seismic vulnerability evaluation, a normalized vulnerability index is obtained for each building, and it is possible to estimate the MDG.

It should be pointed out that in this study ruins and buildings not inhabited were not considered.

Figure 2 shows the results of the vulnerability index assessment method applied to the 500 buildings sample. As can be seen, around 54% of the building stock has a vulnerability index under 30. Still, about 8% have a vulnerability index over 55.

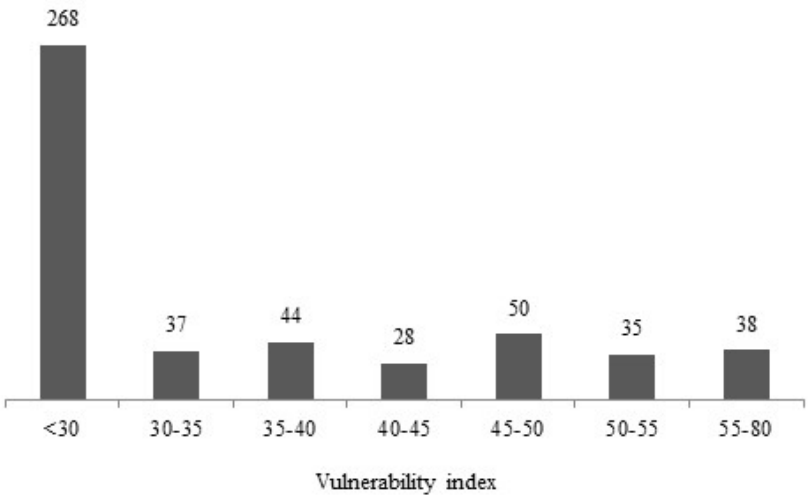

Fig. 2 - Vulnerability index results distribution per number of buildings.

The results also show that the mean value of the vulnerability index for the studied buildings is 28. This is not unexpected, since more than 50% of the building stock in the sample is reinforced concrete.

The results of this study are as expected when compared with a previous study performed in Faial (Neves et al., 2012), since the construction scheme found in São Miguel can be translated directly to the other islands.

According to the study performed in Faial, the vulnerability index obtained was 41.62. These two cases when compared indicate a lower seismic risk exists in São Miguel Island, when considering a hypothetical scenario of equal seismic hazard and exposure.

As can be seen in Figure 3, most buildings pertain to very low or low vulnerability levels and only a few to very high level.

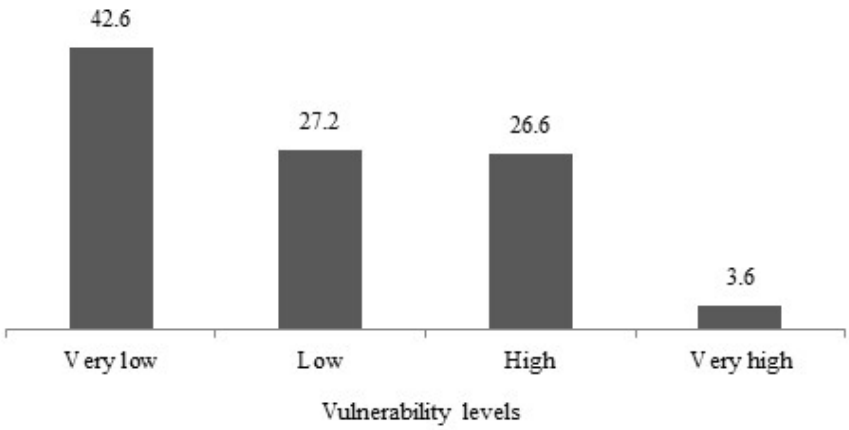

Fig. 3 - Vulnerability levels results distribution per percentage of buildings.

Concerning the MDG, a mean value of μ_D=1 and μ_D=2 for moderate to high intensities (*I*=VII and *I*=VIII), respectively, was obtained.

Since 30% of buildings pertain to high to very high vulnerability levels, for seismic intensity *I*=X we can expect a MDG μ_D=4.

Since this is not a complex methodology, homeowners can apply it as a first step to evaluate buildings vulnerability and identify retrofit needs. Applying this methodology can also aid as a guidance to potential home buyers providing information on their prospective home vulnerability.

It could be used on any Azorean island to map risk areas of high and very high vulnerability index buildings, to help local emergency teams identify specific measures and actions needed in case of an earthquake.

Local and regional authorities can also use this methodology to outline incentives and subsidies to achieve a resilient building stock.

With a growth in tourism due to government policies there has been an increase in building rehabilitation mostly in urban areas, so it would be interesting for future work to apply this innovative methodology now presented to an updated building stock.

REFERENCES

[1] Ferreira, M.A., Proença, J.M., Oliveira, C.S., Vulnerability assessment in educational buildings – inference of earthquake risk. A methodology based on school damage in the July 9, 1998, Faial earthquake in the Azores. The 14th World Conference on Earthquake Engineering, Beijing, China, October 12-17, 2008.

[2] Fortuna, M., Estrela Rego, I., Rosa Nunes, J., Machado Pires, M., Barros, M. J., Cunha, R., Inquérito ao Consumo de Energia em Edifícios de Habitação, 2010, Green Islands Project, UAc - MIT Portugal.

[3] Machado Pires, M.M., Barros, M. J., Residential Building Stock Survey in São Miguel Island, Azores: Pathologies and State of Degradation, Proceedings of the XII DBMC International Conference on Durability of Building Materials and Components, volume II, pp.933-941, 2011.

[4] Neves, F., Costa, A., Vicente, R., Sousa Oliveira, C., Varum, H., Seismic vulnerability assessment and characterization of the buildings on Faial Island, Azores. Bull Earthquake Eng, 10, pp.27-44, 2012.

Proceedings IRF2025: 8th International Conference on Integrity-Reliability-Failure
In Engineering, Materials, Manufacturing and Biomechanics. Porto 15-18 July 2025
DOI: https://doi.org/10.24840/978-972-752-323-8

PAPER REF: 22402

EFFECT OF SUSTAINABLE GRAPHENE DERIVATIVE ON 3D PRINTING OF CEMENTITIOUS MATERIALS

Mohd Mukarram Ali[1], Rashid K. Abu Al-Rub[2], Fawzi Banat[3], Tae-Yeon Kim[1(*)]

[1]Department of Civil and Environmental Engineering, Khalifa University, Abu Dhabi, 127788, UAE
[2]Department of Mechanical and Nuclear Engineering, Khalifa University, Abu Dhabi, 127788, UAE
[3]Department of Chemical and Petroleum Engineering, Khalifa University, Abu Dhabi, 127788, UAE
[(*)]*Email:* taeyeon.kim@ku.ac.ae

ABSTRACT

This study examines the influence of a sustainable graphene derivative, namely date syrup-based graphene-coated sand hybrid (D-GSH), on 3D-printed cement mortar (3DPC). The incorporation of D-GSH improved compressive strength and ductility of 3DPC over silica fume (SF). The experimental results showed that adding 0.5% D-GSH enhanced the compressive stress and strain capacity by 68% and 25%, compared with a mix involving SF. These improvements are due to the reinforcing action of D-GSH that increase load-bearing capacity and ductility, leading to steady reduction in post-peak stress, thereby mitigating the possibility of sudden failure of the 3D-printed structure.

Keywords: Additive manufacturing, D-GSH, Nanomaterials, Compressive strength.

INTRODUCTION

3D printing is a method that involves the layer-by-layer connection of materials to produce objects using 3D model data. Compared to conventional construction, 3DPC is more efficient, necessitates less labor, consumes less time to construct, and has the potential to provide more flexibility in developing building designs. The major challenge in 3DPC is to obtain the optimal printable mix proportion, which will have a direct influence on the fresh and hardened properties of 3DPC. In this study, the Delta WASP 3D-printer was employed along with an extruder [1]. This study investigates the compressive stress-strain relation of 3DPC by incorporating a sustainable graphene derivative named date syrup-based graphene-coated sand hybrid (D-GSH), and results were compared with a mix containing silica fume (SF). The D-GSH is produced from date syrup, a sustainable carbon source abundantly available in the UAE and surrounding areas. This is achieved through pyrolysis, a technique in which graphene nano-sheets are integrated into the vast desert sand found in this region [2]. The detailed procedure of the production of D-GSH is shown in Figure 1(a).

RESULTS AND CONCLUSIONS

The printable mix proportions of 3DPC involving 5% SF (55) and D-GSH at concentrations of 0.3% (D03) and 0.5% (D05) are shown in Table 1 [3]. All ingredients were expressed in terms of percentage by mass. The D-GSH was sonicated using an ultrasonic wave mixer to disperse it in the cement matrix. To perform a compression test, 3D-printed cubes of dimensions 50 mm × 50 mm × 50 mm were printed for mixes S5, D03, and D05 as shown in Fig. 1(b). The compressive stress-strain curve was plotted for each mix after 28 days of curing as shown in Fig. 1(c). The compressive stress-strain curves reveal that D-GSH in 3DPC improves both strength and ductility, i.e., it can withstand more strain before reaching the failure point when

compared with SF. The mix with 0.5% D-GSH achieved 68% higher compressive strength and 25% greater strain capacity compared to a mix containing 5% SF. On the other hand, 0.3% D-GSH showed a 55% increase in strength and a 19% enhancement in strain capacity. The improved performance of D-GSH mixtures is due to increased load-bearing capacity and superior energy absorption, as demonstrated by a slow drop in post-peak stress.

Table 1 - Printable mix proportions.

Mixes	Cement (%)	Sand (%)	Water (%)	Silica fume (%)	D-GSH *(% by sand weight)*	Super-Plasticizer (%)	Water-to-cement (w/c)
S5	55.00	18.00	22.00	5.00	-	-	0.40
D03	59.90	16.30	23.40	-	0.30	0.10	0.39
D05	59.90	16.10	23.40	-	0.50	0.10	0.39

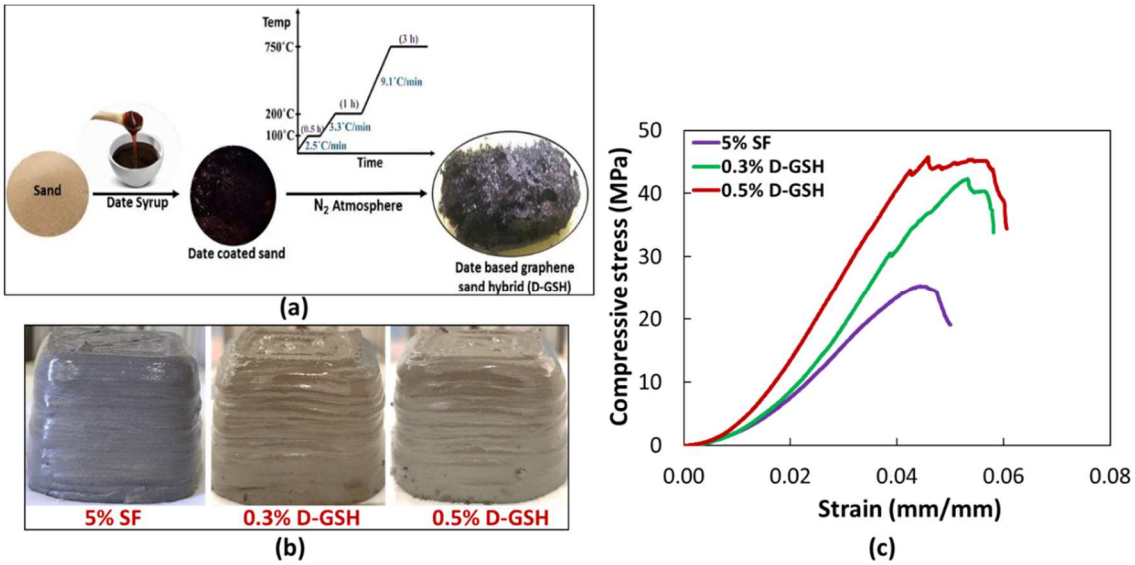

Fig. 1 - (a) Process of D-GSH production [2]; (b) 3D-printed cubes; and (c) Compressive stress vs. strain.

In conclusion, adding D-GSH remarkably improves the compressive strength and ductility of 3DPC compared with a mix containing SF. For instance, the addition of 0.5% D-GSH showed significant enhancements, highlighting its potential for superior load-bearing capacity and energy absorption, reducing sudden failure risks of 3D-printed structures.

ACKNOWLEDGMENTS

The authors acknowledge the support of Khalifa University ADAM Group (No. 8474000163) and Research & Innovation Grant (No. 8474000617).

REFERENCES

[1] Ali, M.M., et al. (2024). Influence of carbon nanotubes on printing quality and mechanical properties of 3D printed cementitious materials. Developments in the Built Environment, 18, 100415. https://doi.org/10.1016/j.dibe.2024.100415.

[2] Khan, S., et al. (2019). Sustainable synthesis of graphene-based adsorbent using date syrup. Scientific Reports, 9(1), 18106. https://doi.org/10.1038/s41598-019-54597-x

[3] Ali, M. et al. (2024). Enhancing the printing quality and mechanical properties of 3D-printed cement composites with date syrup-based graphene coated sand hybrid. Developments in the Built Environment, 20, 100582. https://doi.org/10.1016/j.dibe.2024.100582.

Proceedings IRF2025: 8th International Conference on Integrity-Reliability-Failure
In Engineering, Materials, Manufacturing and Biomechanics. Porto 15-18 July 2025
DOI: https://doi.org/10.24840/978-972-752-323-8

PAPER REF: 22414

THERMAL AND MECHANICAL RESISTANCE OF WOOD CONNECTIONS IN SINGLE SHEAR, WITH AND WITHOUT PROTECTION

João Campos Aguiar[1], Elza M M Fonseca[2(*)]

[1]Master in Mechanical Engineering, Instituto Superior de Engenharia (ISEP), IPP, Porto, Portugal
[2]INEGI/LAETA and Instituto Superior de Engenharia (ISEP), IPP, Porto, Portugal
[(*)]*Email:* elz@isep.ipp.pt

ABSTRACT

Currently, in the construction sector, there is an increase in the use of laminated wood structural elements. The safety design of these structures is essential, with special attention to mechanical connections. In a fire event, structures must withstand the demands imposed for a sufficiently long time, thus ensuring the safe evacuation of occupants. Despite being a combustible material, wood is highly resistant to fire due to the char formation that allows the core to be insulated. This resistance can be further improved, increasing the response time to fire, with the use of insulating and non-combustible materials, such as gypsum plasterboard, an efficient and widely used solution.

Keywords: Wood connection, fire resistance, thermal model, mechanical model.

INTRODUCTION

To carry out a robust bibliographic review that is aligned with the state of the art, recent and relevant articles on the topic in the study were analyzed. For this purpose, VOSviewer was used, a tool for building and analyzing bibliometric networks. As a starting point, a search was carried out in the Web of Science database, due to its scope and quality in the repository of scientific articles. The keywords “Fire” and “Timber” or “Thermomechanical” and “Timber” were used, with a time filter for publications from 2021 onwards. This approach allows us to obtain the 500 most relevant records, which were exported to a detailed analysis with VOSviewer. Bibliometric analysis will enable us to identify the most cited authors in recent articles that address the main keywords. Figure 1 a) shows the citation map resulting from the analysis carried out with VOSviewer. This map highlights the relevance of some authors cited in this literature review, including different authors (A. Bartlett, 2018; A. Buchanan, 2022; A. Frangi,2010; E. Fonseca, 2022; F. Wiesner, 2019; M. Audebert, 2019), [1-6]. The graphic representation highlights the connections and influence of these authors in the development of the subject, reinforcing its importance in the state of the art. The bibliometric analysis of the occurrence of keywords, shown in Figure 1 b), allowed us to identify the terms most frequently used in the articles resulting from the search. The resulting map highlights the predominance of terms such as “fire”, “timber”, “wood”, “fire resistance” and “mass timber”, reflecting the main areas of research on the topic addressed. However, the absence of relevant connections with the keyword “thermomechanical” stands out, which, despite being used in the search, did not play a central role nor did it have significant connections with other important keywords. This result reinforces the perception that the thermo-mechanical approach is still little explored or recognized in current investigations, indicating a possible opportunity for future studies, which is the main objective of the present work.

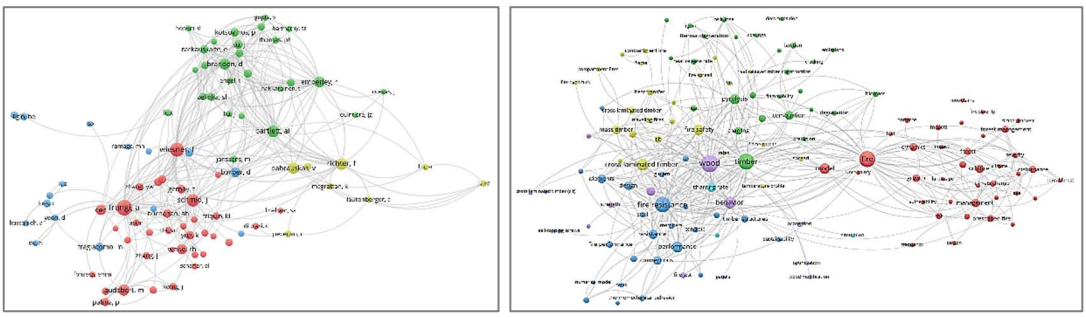

(a) (b)

Fig. 1 - VOSviewer results: (a) Citation map; (b) Keyword map.

In this work, a validation model will be presented to calibrate the developed computational model. The validation will be obtained with experimental results from a tested connection without protection in tensile and submitted to fire conditions. With the calibrated computational model, a protected connection will be presented to ensure the thermal resistance of this type of connection.

DEVELOPED MODEL AND VALIDATION OF UNPROTECTED CONNECTION

The computational model developed in this work was previously tested with experimental and numerical results given by Audebert et al. [7]. A thermal and mechanical comparison was realized in different steps. The connection geometry and all material properties are according to the ''Connection B_2003'' from [7], [8], [9]. The connection was submitted externally to fire conditions [10]. In the developed numerical model, the blue zone represents the wood material and violet represents the dowels in steel material.

In the first step, thermal and transient analysis with non-linear material was realised in the developed computational model with ANSYS®, compared with the experimental (TCi_Exp) tests and numerical (TCi_Num) results from Msc-Marc software [7]. The temperatures in the experimental tests were obtained with four thermocouples placed inside the wood connection, at the central (TC1_Exp, TC2_Exp) and the lateral (TC3_Exp, TC4_Exp) mid-height members [7]. Figure 2 represents the comparison of the temperature evolution in the four measured nodes and the comparison with the developed computational model (TCi). Also, it shows the timber connection with steel dowels, representing one-quarter of the entire model due to the symmetries of the vertical and horizontal plans. Until the time of fire exposure in the 1800s, the temperature was between 20 and 942 ºC, close to the presented solution by the authors [7] of 20-911ºC. The numerical values are close to the referenced and are satisfactory.

In the second step, a structural and incremental non-linear material analysis was realised in the developed computational model with ANSYS®, compared with the numerical results from [7]. Symmetric boundary conditions were considered. Also, interactions between wood connection and fasteners were allowed using contact elements and a friction coefficient. The load is applied by an imposed incremental pressure load. The results obtained in the developed connection are shown in Figure 3. The maximum mechanical resistance of the connection at ambient temperature was 259.1 kN. According to the tested connection [7] the load-carrying capacity of this connection at ambient temperature is 269.4 kN, which represents a relative difference with the calculated value of 3.98%.

Lastly, in the same Figure 3 the thermomechanical analysis is presented, where the maximum resistant load was equal to 4.1 kN, under fire exposure in the 1800s. This value represents a load ratio under fire exposure of 1.6% concerning 259.1 kN.

Mesh, element length 6 mm in maximum.
(Blue - wood; Violet - steel)
3D unprotected model (¼ mesh)

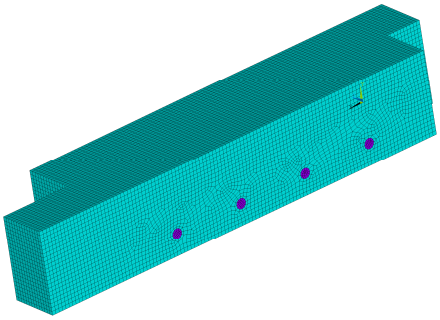

Temperatures in cross-section,

1800s 3600s

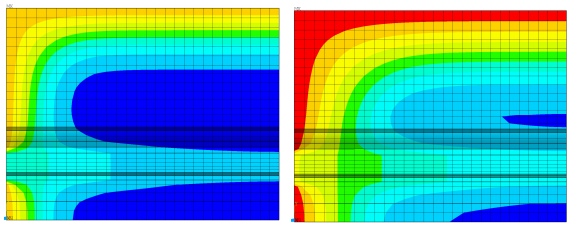

Temperatures in the connection, 3600s

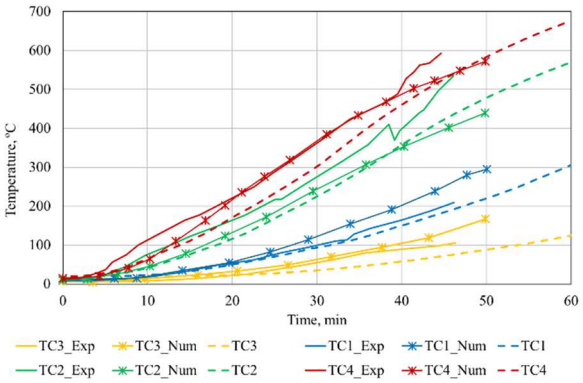

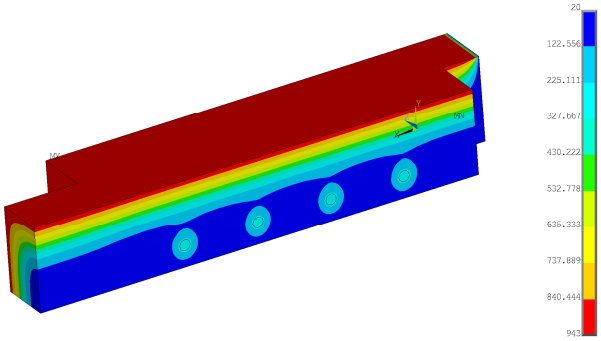

20 - 943ºC

Temperatures in wood material, 1800s

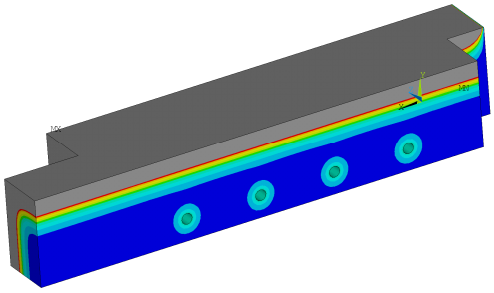

Temperatures in wood material, 3600s

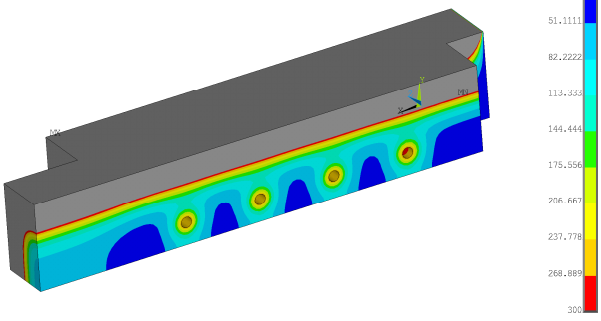

20 - 300ºC

Temperatures in steel dowels, 1800s

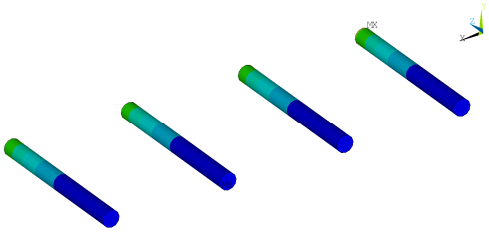

Temperatures in steel dowels, 3600s

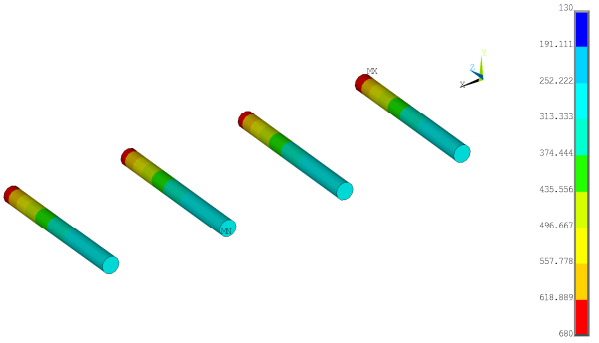

130 - 680ºC

Fig. 2 - Thermal model in unprotected connection, results and temperature calculation.

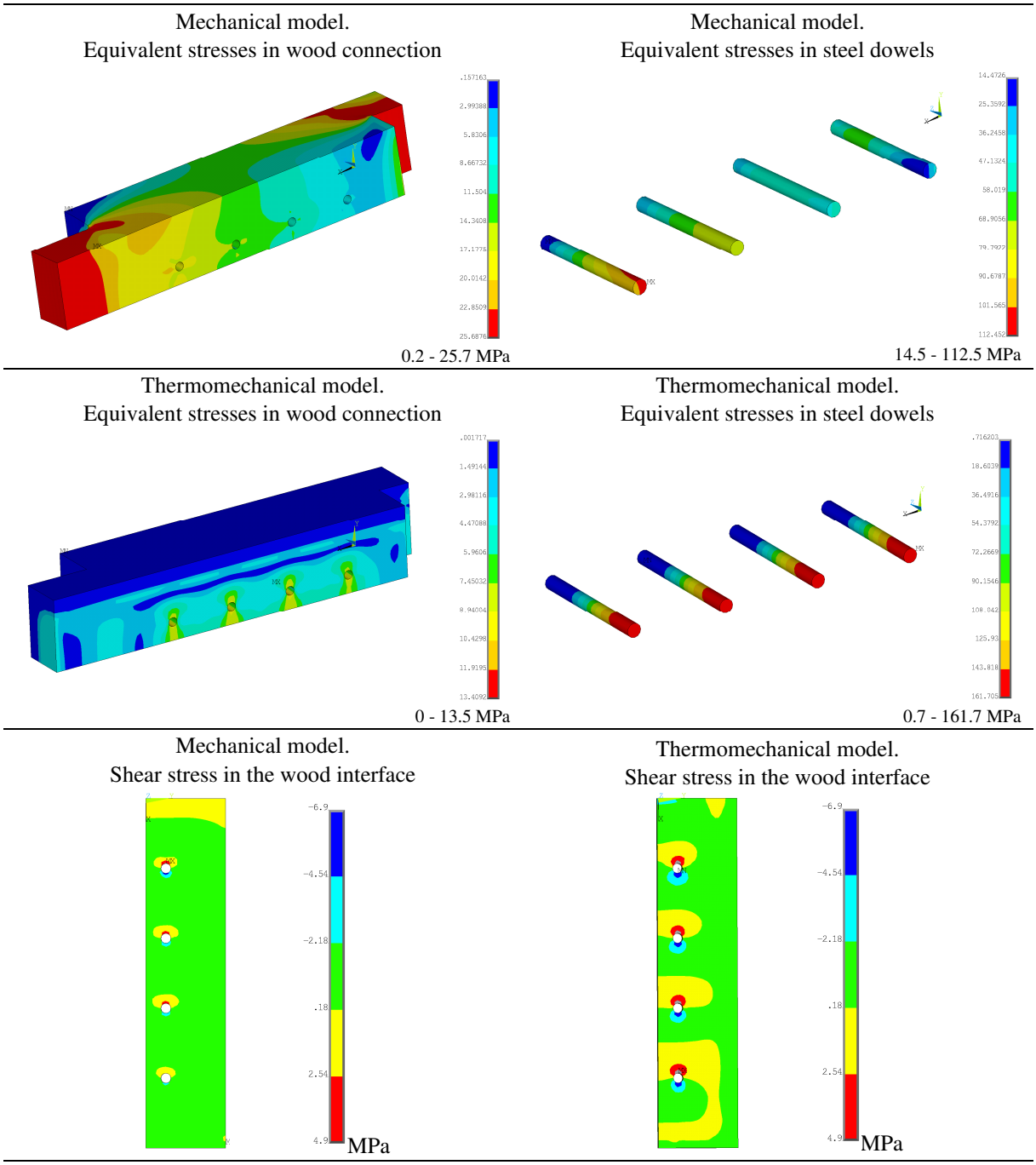

Fig. 3 - Mechanical and thermomechanical model in unprotected connection. Results for the maximum load of 259.1 kN at ambient temperature and the maximum load of 4.1 kN with fire exposure at 1800s.

With fire exposure, the char layer in wood material (in grey colour) increases but remains intact in the core element. The steel material transports the effect of heat inside the connection and the temperature reaches higher values near the dowels. The time-temperature history in Figure 2 agrees well with the time exposure in all four nodal positions with experimental and numerical results from [7]. The comparison between mechanical and thermomechanical results (Figure 3) shows the level of reached stresses for the incremental mechanical load at ambient temperature and with the imposed thermal load in the 1800s. The mechanical properties were included in the thermomechanical model with the stress-strain behaviour dependent of the temperature.

DEVELOPED MODEL OF PROTECTED CONNECTION

For connections with insulating material, EC5, 1-2 [11] proposes two options for the protection material: gypsum (type A, F or H) or wood-based panels, using different simplified equations.

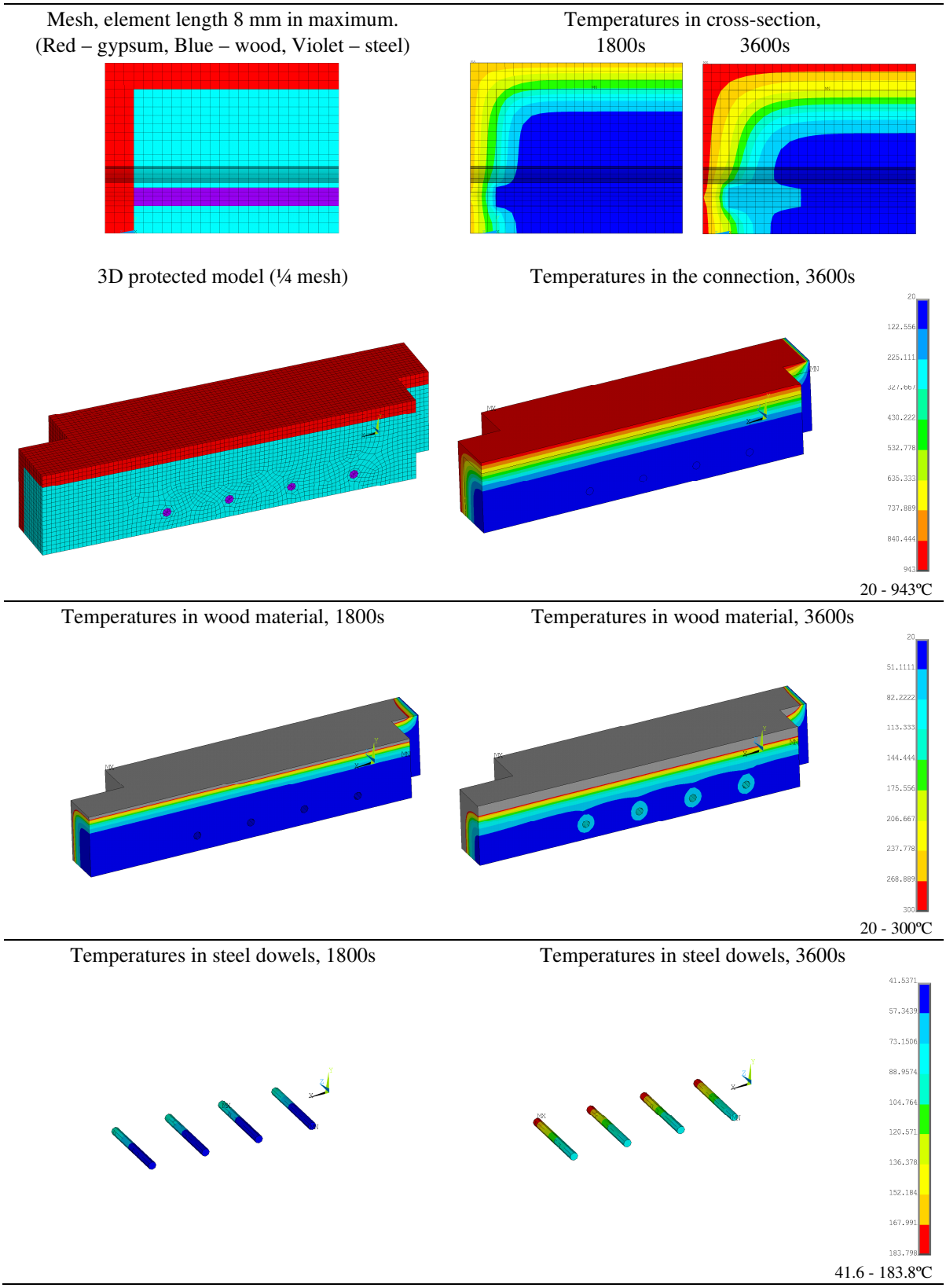

Fig. 4 - Thermal model in protected connection, results and temperature calculation.

In this work, the studied protected connection requires a protection layer thickness of the panel equal to 18 mm for gypsum plasterboard type F, assuming a standard fire resistance period of 60 min or if gypsum type A or H the fire protective panel thickness is 23 mm. For gypsum, the material properties are according to the literature, [12], [13]. For the protected connection, a regular mesh was increased in depth to 23 mm, with the thickness of the fire protective panel. Figure 4 represents the temperature results in the protected connection for different time instants. Figure 5 compares different nodal positions in the protected and unprotected connection.

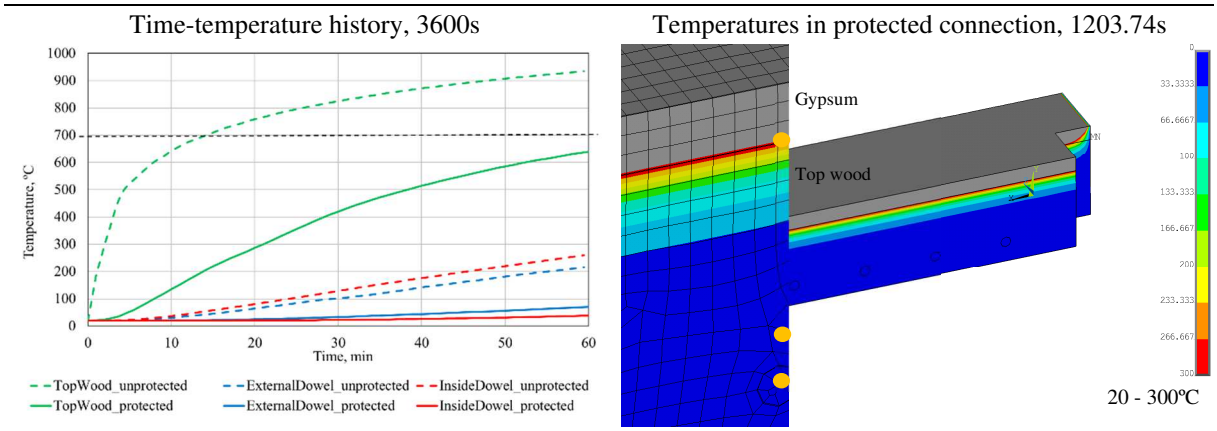

Fig. 5 - Thermal model in protected and unprotected connection, results and temperature calculation.

The protection using gypsum panels prepared to 60 min of fire exposure, protects the connection during 1203.74s. This is because the contact between the temperature in gypsum affects the starting charring in the wood material at 300 ºC. There is a temperature decrease with the use of protection compared with unprotected connections. After 3600s of fire exposure, the difference is greater, around 300 ºC and the gypsum temperature is still below the degradation temperature of 700 ºC in the material [14]. Inside the connection, the temperature is less than 100 ºC in the protected connection compared to the unprotected connection, which is more than 200 ºC. Furthermore, the front dowel is protected with the gypsum panel and the temperature remains lower than with wooden material.

CONCLUSIONS

There is a significant increase in the use of wood in construction solutions, mainly in the context of sustainability and mitigation of carbon emissions. This trend confirms the need to study the behaviour of wood connections, particularly under fire conditions. Despite being a renewable material with favourable properties, such as forming a char layer that contributes to fire resistance, the variability of fire conditions and different geometric configurations present challenges in standardising its performance. In this context, gypsum plasterboard has proven to be an efficient and widely applied solution as passive protection, standing out for its role in improving the fire resistance of connections. On the other hand, numerical analysis is essential for evaluating different construction solutions, with or without protective materials. Despite their complexity, due to the interaction of materials with non-linear behaviour and transient

thermal action, numerical models offer a promising method to predict the degradation of wooden elements and correlate them with fire resistance criteria. The development of this work aimed to carry out a thermal and mechanical study on wooden connections with steel dowels, with and without fire protection.

REFERENCES

[1] A. I. Bartlett, R. M. Hadden, L. A. Bisby, «A Review of Factors Affecting the Burning Behaviour of Wood for Application to Tall Timber Construction», Fire Technol., vol. 55, pp.1-49, 2018, doi: 10.1007/s10694-018-0787-y.

[2] A. Buchanan e B. Östman, Fire Safe Use of Wood in Buildings, First. Boca Raton: CRC Press, 2022. doi: 10.1201/9781003190318.

[3] A. Frangi, V. Schleifer, M. Fontana, E. Hugi, «Experimental and Numerical Analysis of Gypsum Plasterboards in Fire», Fire Technol., vol. 46, pp.149-167, 2010, doi: 10.1007/s10694-009-0097-5.

[4] E. M. M. Fonseca, P. A. S. Leite, L. D. S. Silva, V. S. B. Silva, H. M. Lopes, «Parametric Study of Three Types of Timber Connections with Metal Fasteners Using Eurocode 5», Appl. Sci., vol. 12, p. 1701, 2022, doi: 10.3390/app12031701.

[5] F. Wiesner, L. Bisby, «The structural capacity of laminated timber compression elements in fire: A meta-analysis», Fire Saf. J., vol. 107, pp.114-125, 2019, doi: 10.1016/j.firesaf. 2018.04.009.

[6] M. Audebert, D. Dhima, A. Bouchaïr, A. Frangi, «Review of experimental data for timber connections with dowel-type fasteners under standard fire exposure», Fire Saf. J., vol. 107, pp.217-234, 2019, doi: 10.1016/j.firesaf.2019.102905.

[7] M. Audebert, D. Dhima, M. Taazount, A.Bouchaır, «Thermo-mechanical behaviour of timber-to-timber connections exposed to fire», Fire Saf. J., vol. 56, pp.52-64, 2013, doi: 10.1016/j.firesaf.2013.01.007.

[8] EN 1993-1-2:2005, Eurocode 3. Design of steel structures. Part 1-2: General rules – Structural fire design. 2005, Brussels.

[9] EN 1995-1-1:2004, Eurocode 5. Design of timber structures. Part 1-1: General- Common rules and rules for buildings. 2004, Brussels.

[10] EN1991-1-2:2003, Eurocode1. Actions on structures. Part1-2: General actions –Actions on structures exposed to fire. 2003, Brussels.

[11] EN1995-1-2:2004, Eurocode 5. Design of timber structures. Part 1-2: General Structural fire design. 2004, Brussels.

[12] I. Rahmanian, Y. Wang, «Thermal Conductivity of Gypsum at High Temperatures A Combined Experimental and Numerical Approach», Acta Polytechnica, vol. 49 (1), pp.16-20, 2009.

[13] Andrea Frangi, Vanessa Schleifer, Mario Fontana, Erich Hugi, «Experimental and Numerical Analysis of Gypsum Plasterboards in Fire», Fire Technology, vol. 46, pp.149-167, 2010.

[14] K. Ghazi Wakili, E. Hugi, «Four Types of Gypsum Plaster Boards and their Thermophysical Properties Under Fire Condition», Journal of Fire Sciences, vol. 27, pp.27-43, 2009.

Proceedings IRF2025: 8th International Conference on Integrity-Reliability-Failure
In Engineering, Materials, Manufacturing and Biomechanics. Porto 15-18 July 2025
DOI: https://doi.org/10.24840/978-972-752-323-8

PAPER REF: 22415

PROGRESSIVE COLLAPSE OF THE SURFSIDE CONDOMINIUM POOL DECK

Mehrdad Sasani(*)

Department of Civil and Environmental Engineering, Northeastern University, Boston, MA 02115, USA
(*)*Email:* sasani@neu.edu

ABSTRACT

On June 24, 2021, Champlain Towers South, a 12-story condominium in the Miami suburb of Surfside, Florida, United States, partially collapsed, killing 98 people. Analyses and available evidence indicate that progressive collapse of the Surfside condominium pool deck began with punching shear failure at a slab-column connection followed by punching shear failures of neighboring slab-column connections. This paper presents a likely scenario of the initial failure and the subsequent progressive collapse of the pool deck that preceded the towers' partial collapse.

Keywords: Champlain Towers South, progressive collapse, punching shear failure.

INTRODUCTION

Analyses and available evidence indicate that the progressive collapse of the Champlain Towers South condominium pool deck (Surfside, Florida, USA) likely began with punching shear failure at the K-13.1′ slab-column connection (see Figure 1) followed by punching shear failures of neighboring slab-column connections. Analyses of the pool deck and lobby-level parking garage response, the vertical separation at the corner of the planter box above column K-13.1′ observed a few weeks prior to the collapse (Miami Herald, 2022), and eyewitness accounts indicating that the pool deck failure took place minutes before the tower collapse (Miami Herald, 2021), all point to punching shear failure at the K-13.1′ slab-column connection as the initiating event that led to the collapse. As a result of this punching shear failure, the majority of the gravity load that had been carried by column K-13.1′ needed to be transferred to neighboring columns, thereby increasing the punching shear demand on their slab-column connections. This, in turn, initiated a chain reaction of punching shear failures of the neighboring slab-column connections and the progressive collapse of the pool deck. The pool deck collapse area was bounded on its south and north sides by a foundation wall and the southern edge of the tower, respectively. On its east and west sides, the pool deck collapse area was bounded by a construction joint (and the Jacuzzi) and the columns on axis G.1 (and adjacent to the line of the long north-south shear wall), respectively.

RESULTS AND CONCLUSIONS

Based on the results of the collapse analysis, for the two most critical columns, K-13.1′ and J.1-15 (see Figure 1), Table 1 shows the punching shear demand-capacity ratios under the estimated loading at the time of the deck collapse. Note that no load factors, no strength reduction factors, and no live loads (except those of the parked cars) are included. The results from a nonlinear analytical model of the pool deck show that the failure at K-13.1′ would propagate to the neighboring slab-column connection. Such a collapse propagation would continue further until a majority of the pool deck slab-column connections failed through punching shear.

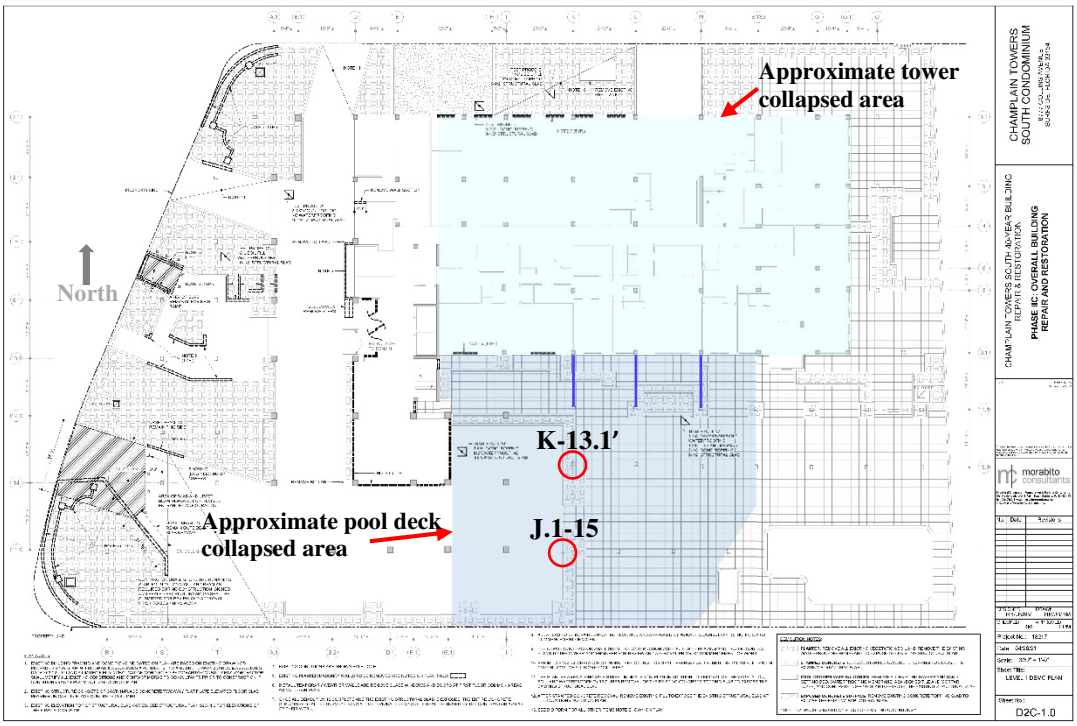

Fig. 1 - Champlain Towers South and pool deck.

Given the condition of and significant demand at the slab-wall connection on the south side, the slab would break away from the wall during the progressive collapse described above.

Table 1 - Punching shear demand (V_d) divided by punching shear capacity (V_c) for the two most critical columns under pool deck dead loads and parked car live loads with nominal capacities estimated based on ACI 318 (2019) and Eurocode 2 (2004).

	Column K-13.1' (12x16 in; 305x407 mm)	**Column J.1-15 (12x16 in; 305x407 mm)**
V_d / V_c (ACI 318)	0.77	0.74
V_d / V_c (Eurocode 2)	0.84	0.81

ACKNOWLEDGMENTS

The author would like to thank Mr. Allyn Kilsheimer of KCE structural Engineers and the Town of Surfside for supporting this study. The findings and conclusions are those of the author.

REFERENCES

[1] Miami Herald. Surfside condo was 'screaming' as an alarming crack formed just weeks before the collapse. S. Blaskey, B. Conarck, and N. Nehamas, 2022.

[2] Miami Herald. The collapse reconstructed: Ten witnesses describe what they saw and heard. S. Blaskey, B. Conarck, A. Leibowitz, and A.C. Chacin, 2021.

[3] ACI 318. Building code requirements for structural concrete and commentary. ACI 318-19, Farmington Hills, MI, 2019.

[4] Eurocode 2: Design of Concrete Structures, Part 1-1: General Rules and Rules for Buildings. European Committee for Standardization, Brussels, BS EN 1992-1-2, 2004.

Proceedings IRF2025: 8th International Conference on Integrity-Reliability-Failure
In Engineering, Materials, Manufacturing and Biomechanics. Porto 15-18 July 2025
DOI: https://doi.org/10.24840/978-972-752-323-8

PAPER REF: 22416

EVALUATION OF CONTACT AREAS FOR EACH CONSTITUENT MATERIAL USING X-RAY CT IMAGE ANALYSIS

Kosei Shibahara, Kotaro Sasai(*), Kiyoyuki Kaito

Graduate School of Engineering, The University of Osaka, Osaka, Japan
(*)*Email :* k.sasai@civil.eng.osaka-u.ac.jp

ABSTRACT

Concrete degradation phenomena involve two types of failure mechanisms: cohesive failure and adhesive failure, both of which significantly affect the durability of concrete. Understanding the locations where these degradation phenomena occur and their progression processes is crucial for accurate performance evaluation of concrete. X-ray imaging is an effective non-destructive method for observing the internal structure of specimens. Therefore, in this study, X-ray CT image analysis was conducted on mortar specimens to visualize and quantify the degradation phenomena. Specifically, three-dimensional restructured data were constructed using X-ray CT, and image analysis was performed to evaluate the porosity and the contact area between material boundaries within the specimens. This research contributes to the understanding of concrete degradation mechanisms.

Keywords: X-ray CT, Image Analysis, Segmentation.

INTRODUCTION

Concrete is a composite material composed of coarse aggregates, fine aggregates, cement, and other components. However, in current design methods, concrete is often treated as a homogeneous and unified layer. Due in part to such methods, little is known about the properties of individual components and the interactions at their boundaries, and behavior within the mixture, such as pore connectivity, has not been well understood. Consequently, there remains an issue where the understanding of deterioration phenomena in concrete, such as cracking and delamination, from a microscopic perspective has not yet been fully achieved.

Literature has seen advancement in microscopic studies using X-ray CT equipment for infrastructure materials such as concrete. For instance, a study used the large synchrotron radiation facility SPring-8 to quantify porosity and pore connectivity through image analysis (Michael et al.,2008). Another study employed X-ray μ-tomography to observe the microstructure and durability issues of concrete, calculating the pore pathways from the concrete surface to the interior of the specimen (Landis et al.,2000). Thus, image analysis techniques using X-ray CT equipment are effective for elucidating phenomena within concrete.

Within concrete, the deterioration mechanisms vary depending on the type of material in contact with the pores. For example, cohesive failure may occur at the boundaries between the pores and asphalt, while delamination may occur at the boundaries between the pores and aggregates. Therefore, in this study, non-destructive testing using X-ray CT equipment is conducted with the aim of calculating statistical quantities related to the factors influencing material properties and deterioration. Specifically, the study calculates porosity, aggregate filling ratio, and the adhesive surface area between materials and pores, to identify the deterioration phenomena and internal structures.

RESULTS AND CONCLUSIONS

The left image in Figure 1 shows a cross-sectional image obtained after observing the specimen using an X-ray CT scanner, with pores extracted through image processing. In this analysis, segmentation was performed by applying binarization using a thresholding process. The black areas represent the pores, while the white areas correspond to other materials such as aggregates and cement. By performing this binarization with varying threshold values, as shown in the right image of Figure 1, it becomes possible to visualize the positional information and distribution of the materials in three-dimensional data. The yellow regions represent the aggregates, the green regions represent the cement, and the blue regions represent the pores.

Through this binarized image analysis, it is possible to calculate the pore filling ratio and the aggregate filling ratio. Furthermore, by extracting the contours of the regions, the contact surface area between the pores and the materials can be calculated.

In this study, image analysis focusing on the pores within concrete specimens was conducted using non-destructive measurement with an X-ray CT scanner. By evaluating the porosity and the contact surface area between the materials and pores through three-dimensional image analysis, this research contributes to the understanding of deterioration mechanisms such as cohesive failure and adhesive failure.

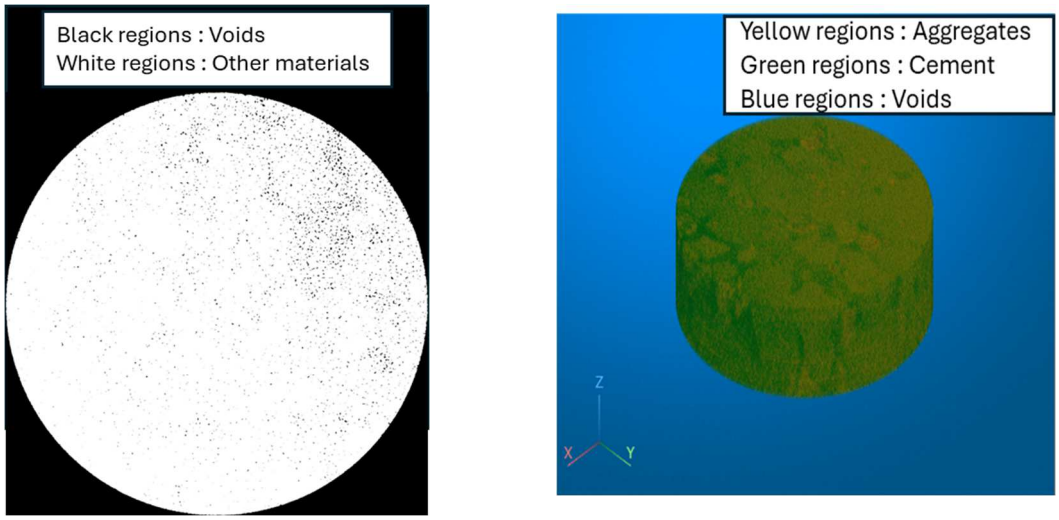

Fig. 1 - Binarized X-ray CT Image (left) and Internal Composition Distribution (right).

REFERENCES

[1] Michael Angelo B. Promentilla, Takafumi Sugiyama, Takashi Hitomi, Nobufumi Takeda. Characterizing the 3D Pore Structure of Hardend Cement Paste with Synchrotron Microtomography. Journal of Advanced Concrete Technology Vol.6, No.2, pp.273-286, June 2008.

[2] E.N. Landis, A.L. Petrell, S. Lu, E. N. Nagy. Examination of pore structure using three-dimensional image analysis of microtomographic data. Concrete Science and Engineering, Vol.2, December 2000, pp.162-169.

Proceedings IRF2025: 8th International Conference on Integrity-Reliability-Failure
In Engineering, Materials, Manufacturing and Biomechanics. Porto 15-18 July 2025
DOI: https://doi.org/10.24840/978-972-752-323-8

PAPER REF: 22420

FWI IMAGING OF FAULTS AND FRACTURES IN ROCKS

Paula Rayane Lopes de Andrade[1(*)], José Agnelo Soares[2], Carlos Alberto Mendonça[1], Carlos Moreno Chaves[1], Andre Luis Ferreira da Silva[3]

[1]USP/IAG, University of São Paulo, São Paulo, Brazil
[2]UFCG/UAM,Federal University of Campina Grande, Campina Grande- PB, Brazil
[3]USP/POLI, University of São Paulo, São Paulo, Brazil
[(*)]*Email:* paulaandrade@usp.br

ABSTRACT

The Full Waveform Inversion (FWI) technique, still relatively unexplored as a nondestructive evaluation method, was numerically assessed for its capability to detect events associated with internal heterogeneities within rock blocks. The simulations carried out using FWI aimed to analyze the resolution of this technique in identifying internal fractures within a square domain of metric dimensions, representing a quarry block under conditions similar to those found in situ. The potential of FWI was particularly highlighted in distinguishing different structural configurations by employing a reduced number of source-receiver pairs. Additionally, forward modeling tests were performed, providing a detailed analysis of events recorded in the resulting seismograms.For implementing the FWI technique, developed through the Devito Project software, the study began with a homogeneous model as a basic reference, followed by an intermediate model featuring a single well-defined internal fracture. Finally, a more complex model was evaluated, characterized by the simultaneous presence of multiple internal fractures of varying dimensions and positions. The results proved promising, confirming FWI's potential to efficiently identify and characterize complex internal structures in rock blocks using a relatively simple source-receiver configuration.

Keywords: FWI, rocks, Imaging, Quarries.

INTRODUCTION

Full Waveform Inversion (FWI) is a high-resolution seismic imaging technique involving the minimization of the difference between measured and numerically simulated state-variable values at receivers,achieved through optimization algorithms.

FWI was proposed by [20], reformulating the migration imaging originally introduced by [3, 4] as a local optimization problem, aiming to minimize the squared difference between recorded and modelled data. Comprehensive reviews of this method are provided by [21] and [6]. Initially, FWI applications were prominent in the oil, gas, and seismology fields. However, it is also widely employed as a Non-Destructive Testing (NDT) technique, particularly in ultrasonic testing aimed at detecting the position,size, and orientation of flaws. [17] highlights this approach as a nonlinear optimization problem for flaw mapping in an aluminum plate. Besides demonstrating the potential of FWI for flaw detection, this study proposes using a limited number of ultrasonic sensors as a novel NDT approach. The work takes ultrasonic imaging via FWI as a starting point for NDT applications, similar to the goal of the present research. However, its approach was purely numerical without experimental validation, and another aspect to consider is the investigation scale, which corresponds to the millimeter range. Following this line of research, [7] utilized an ultrasonic imaging technique based on Elastic Least-Squares ReverseTime Migration (ELSRTM), considering variable density as well as

variations in longitudinal and shear wave (S-wave) velocities, to address imaging challenges in heterogeneous structures. Furthermore, numerical results were experimentally verified at a millimeter scale. FWI has demonstrated promising support in non-destructive testing investigations. It is well-documented that purely experimental NDT systems can detect structural damage but generally do not provide detailed information regarding flaw parameters, such as exact location and size. Experimental approaches are typically compared with a reference model without flaw presence and analyzed by qualified professionals [10]. Such models can detect flaws but lack precision regarding flaw location and dimensions [2]. Consequently, there has been an increasing number of studies combining computational methods with experimental NDT, yielding improved results in material investigations.This combined approach became feasible with advances in complete signal storage, enabling the integration of experimental data with numerical simulation models and achieving more accurate outcomes.Several studies address this topic [18, 2, 1].

Given the gaps identified above regarding the application of FWI in rocks at a metric scale, the present study aims to obtain a velocity model (block imaging) compatible with flaw identification through events recorded at receivers. Thus, it enables the imaging of the rock block using a database that is easier to acquire compared to the comprehensive data coverage required by linear tomography imaging methods.

THEORETICAL FORMULATION

Acoustic Wave Equation

In this work, the state variable is defined as the solution of the acoustic wave equation given by Equation (1) [20].

$$\begin{aligned} &\frac{1}{C^2}\frac{d_u^2(t,x)}{dt^2} - \nabla^2 u \quad (t,x) = q \; in \; \Omega \\ &u \quad (.,0) = 0 \\ &\frac{d_u(t,x)}{dt} \; |_{t-0} = 0 \\ &u\,(x,t)|_{\delta\Omega} = 0 \end{aligned} \tag{1}$$

Optimization Problem

The full waveform inversion (FWI) is a nonlinear optimization problem that involves minimizing the quadratic difference between the observed (or real) seismograms represented by the variable u_{obs} and the synthetic seismograms u_{pred}, both measured at receiver locations.

$$\begin{aligned} &\min J = \int_0^T \int_\Omega (u_{pred}(c,t,x) - u_{obs}(t,x))^2 \delta(x - x_r) dx dt \\ &\frac{1}{C^2}\frac{d^2 u_{pred}(t,x)}{dt^2} - \nabla^2 u_{pred}(t,x) = q \; in \; \Omega \\ &u_{pred}(.,0) = 0 \\ &\frac{du_{pred}(t,x)}{dt} \; |_{t-0} = 0 \\ &u_{pred}(x,t)|_{\delta\Omega} = 0 \\ &C_{min} \leq c \leq C_{max} \quad \text{(Equation 2)} \end{aligned} \tag{2}$$

The variable xr represents the position of the receivers. Thus, the wave equation presented (Equation (1)) is used to solve the optimization problem using gradient-based algorithms. For this purpose, sensitivities are determined, and the problem is converted into an unconstrained problem using the Lagrangian:

$$L\left(u_{pred}(c;t,x),c,\lambda_{1,},\lambda_{2,}\lambda_{3,}\lambda_{4,}\right) =$$

$$\int_0^T \int_\Omega (u_{pred}(c;t,x) - u_{obs}(t,x))^2 \delta(x - x_r) dxdt \; +$$

$$- \int_0^T \int_\Omega \lambda_1 \left(\frac{1}{C^2} \frac{d^2 u_{pred}(t,x)}{dt^2} - \nabla^2 u_{pred}(t,x) \; + \eta \frac{du_{pred}(t,x)}{dt} - q \right) dxdt \; +$$

$$- \int_0^T \int_\Omega \lambda_2 u_{pred}(0,x) dxdt - \int_0^T \int_\Omega \lambda_3 \frac{du_{pred}(t,x)}{dt} \Big|_{t-0} \; dxdt - \int_0^T \int_\Omega u_{pred}(t,x) dxdt =$$

$$J - \lambda^T F \tag{3}$$

The adjoint equation (Equation (4a)) and sensitivity equation (Equation (4b)) are obtained by applying optimality conditions, that is, by imposing the Gateaux derivatives with respect to the variablesu_{pred} and design variable c to be equal to zero.

$$L_{\,u\,pred}\left(u_{pred}(c;t,x),c,\lambda_{1,},\lambda_{2,}\lambda_{3,}\lambda_{4,}\right) = \frac{\partial L}{\partial u_{pred}} = \frac{\partial J}{\partial u_{pred}} - \lambda^T \frac{\partial F}{\partial u_{pred}} = 0 \tag{4 a}$$

$$L\left(u_{pred}(c;t,x),c,\lambda_{1,},\lambda_{2,}\lambda_{3,}\lambda_{4,}\right) = \frac{\partial L}{\partial c} = \frac{\partial J}{\partial c} - \lambda^T \frac{\partial F}{\partial c} = 0 \tag{4b}$$

The adjoint problem is obtained by multiplying Equation (4a) by a test function, integrating over time and space, and applying the divergence theorem (Equation (5)):

$$\frac{1}{C^2} \frac{d^2 \lambda_1(t,x)}{dt^2} - \nabla^2 \lambda_1(t,x) = u_{pred} - u_{obs}$$

$$\lambda_1(T,x) = 0$$

$$\frac{d\lambda_1(t,x)}{dt}$$

$$\lambda_1\,(T,x)\,|_{\delta\Omega} = 0 \tag{5}$$

NUMERICAL IMPLEMENTATION

The FWI approach requires a wavefield simulator to solve the forward problem by numerically solving the wave equation. The same program module is utilized to compute the gradient of the Lagrangian, which provides the direction for the optimization algorithm [23, 11]. The Devito program [http://www.opesci.org/devito] has been employed in geophysical studies (Louboutin, et al., 2017) and enables the same calculations to be performed with finite differences representing rock blocks.Programming with Devito uses the SymPy symbolic algebra package, facilitating code implementation in Python notebooks, generating efficient and precise code for wavefield modeling and gradient determination in minimization routines that effectively implement the inverse imaging problem.

Initially, parameters are defined, and subsequently, the wave equation is solved for a domain representing a real field. The wave equation is solved in domain Ω with an initial estimate c = 0. From this solution, two computed fields are obtained corresponding to the fields at the receiver positions. These values represent the state variable (u), allowing calculation of the residual used in the objective function and the solution of the adjoint problem. Sensitivities calculated from the adjoint problem solution are provided alongside the objective function to the minimize function from the SCIPY library, employing the L-BFGSB optimization algorithm.

To ensure successful implementation and adequate results, some adjustments were necessary. Initially, dobs represents the pressure values at the receivers in the true model, and d_{pred} represents the receiver values for the initial model. In this work, the values of dobs d_{obs} and d_{pred} were very close to zero.

Consequently, the objective function $(d_{obs} - d_{pred})^2$reached values extremely close to zero, which is the lowest value attainable by the objective function. This caused the optimizer to reach the minimum of the function without finding a distribution that could further reduce it, resulting in early termination in the first iteration without achieving a satisfactory inversion. The solution was normalized between 0 and 1, preventing the objective function from approaching zero and allowing proper optimization.

METHODOLOGY

The developed methodology numerically investigates the waveform recorded by the sensors, comparing it to the expected response for a homogeneous block and highlighting identifiable events related to reflections at internal interfaces. To achieve realistic simulations, a two-dimensional (2D) numerical model of a 1 m x 1 m rock block was simulated using five sensors and one source, initially assuming constant velocity. The acquisition method utilized was the oblique incidence test, termed “reflective mode,” consisting of transmitter-receiver pairs positioned on the same edge of the block.

The ultrasonic pulses used in the simulation have a central frequency of 30 kHz. According to the discretization shown in Figure 1, a spatial spacing of 0.01 cm was adopted, resulting in a numerical grid with 101 points in both X and Y directions. The Figure presents the velocity models adopted for simulations with heterogeneities within the 1-meter block.

To evaluate the method’s sensitivity under different geological contexts, simulations were conducted considering two primary scenarios: a homogeneous sample and a heterogeneous sample. The heterogeneous model was designed to represent internal inclusions characterized by lower velocities, simulating various internal fractures. The homogeneous model has the same dimensions but contains no inclusions.

In summary, the simulations represent homogeneous and heterogeneous media with dimensions and velocity contrasts close to the parameters presented in Table 1, whose values were adopted as baseline parameters in all analyses. Additionally, simulations with variations in the time window (Tn) and different levels of velocity contrast (low and high contrast) were conducted to complement the evaluation of results.

The employed velocities aim to realistically represent typical rock media, using compressional wave velocities (V_P) widely reported in specialized literature: $V_P = 5.5\ Km\backslash$s for igneous/metamorphic rocks, such as granite, and $V_P = 3.3\ Km$s for fluids present in pores (air).

Table 1 - Initial parameters used in the Waveform Analysis simulation with the Devito Project.

Initial parameters	
Number of receivers and sources.	$N_{fonte} = 1$ $N_{receptor=5}$
Domain dimension.	$Shape = (101, 101)$ Spacing= (0.01, 0.01) cm Origin= (0., 0.)
Time	$T_0 = 0$ $T_0 = 0.9$ (milissegundos)
Frequência Ricker	$F_0 = 30\ Hz$
Domain velocity (high velocity contrast).	$V_{rocha} = 5.5\ km^{-1}$ $V_{fratura} = 0.3\ km^{-1}$
Domain Types and Fracture	Circular inclusion, Fracture Vertical and Fracture horizontal

Table 2 - Simulated models and dimensions of their internal structures.

Model and Dimensions	$V_{hom}(km\ s^{-1})$	$V_{het}(km\ s^{-1})$
Model 1 (Horizontal Fracture)	X = 1 cm ; Y= 20 cm	5.5 and 0.3
Model 2 (Vertical Fracture)	X= 20 cm ; Y= 1 cm	5.5 and 0.3

In Figure 1, seismograms are presented (1-d, 1-e, and 1-f). The main seismic (ultrasonic) events expected in reflective mode are: direct wave (event-1), reflection from the opposite side of the block(event-2), and reflection from internal heterogeneities within the block (event-3). Thus, event-1 corresponds to the direct wave observed as the first amplitude peak present in the simulated model's seismic traces, event-2 corresponds to reflection from the opposite side, and event-3 corresponds to a heterogeneity within the medium. This concept of events is discussed by [5]. The presence or absence of an "event-3" can characterize a rock block as homogeneous or heterogeneous. In numerical modeling, considering the reflective mode (oblique incidence test), these events were observed in models with various heterogeneities (circular, planar, etc.) as shown in Figure 1, having minimum dimensions on the order of 1 to 2 cm inside a 1 m edge block (simulations at 30 kHz).

Considering the heterogeneity model Figure 1 and oblique incidence test in a heterogeneous medium, three types of heterogeneities were considered: spherical inclusion Figure 1, horizontal fracture Figure 1, and vertical fracture Figure 1. The presence of a third event Figure 1 is considered as reflection from internal heterogeneities within the block (event-3). From the identification of these events, the velocity of the medium can be estimated from the direct wave. Knowing the thickness of the block, this velocity can also be estimated from event-2. A homogeneous block should yield very close velocity estimates from events 1 and 2 and should not exhibit events of type 3. The presence of the third event was observed in the seismograms for each type of heterogeneity.

Complementing the event analyses is the state variable field. The state variable field (wave propagation) for the heterogeneous medium with a vertical fracture simulated in the oblique incidence test (Figure 2) confirms the events observed in the seismic traces Figure 1. It can be observed that the first recorded events correspond to the direct wave (event-1), the second event is the reflection from the opposite side of the block (event-2), and the third event corresponds to reflection from internal heterogeneities within the block (event-3).

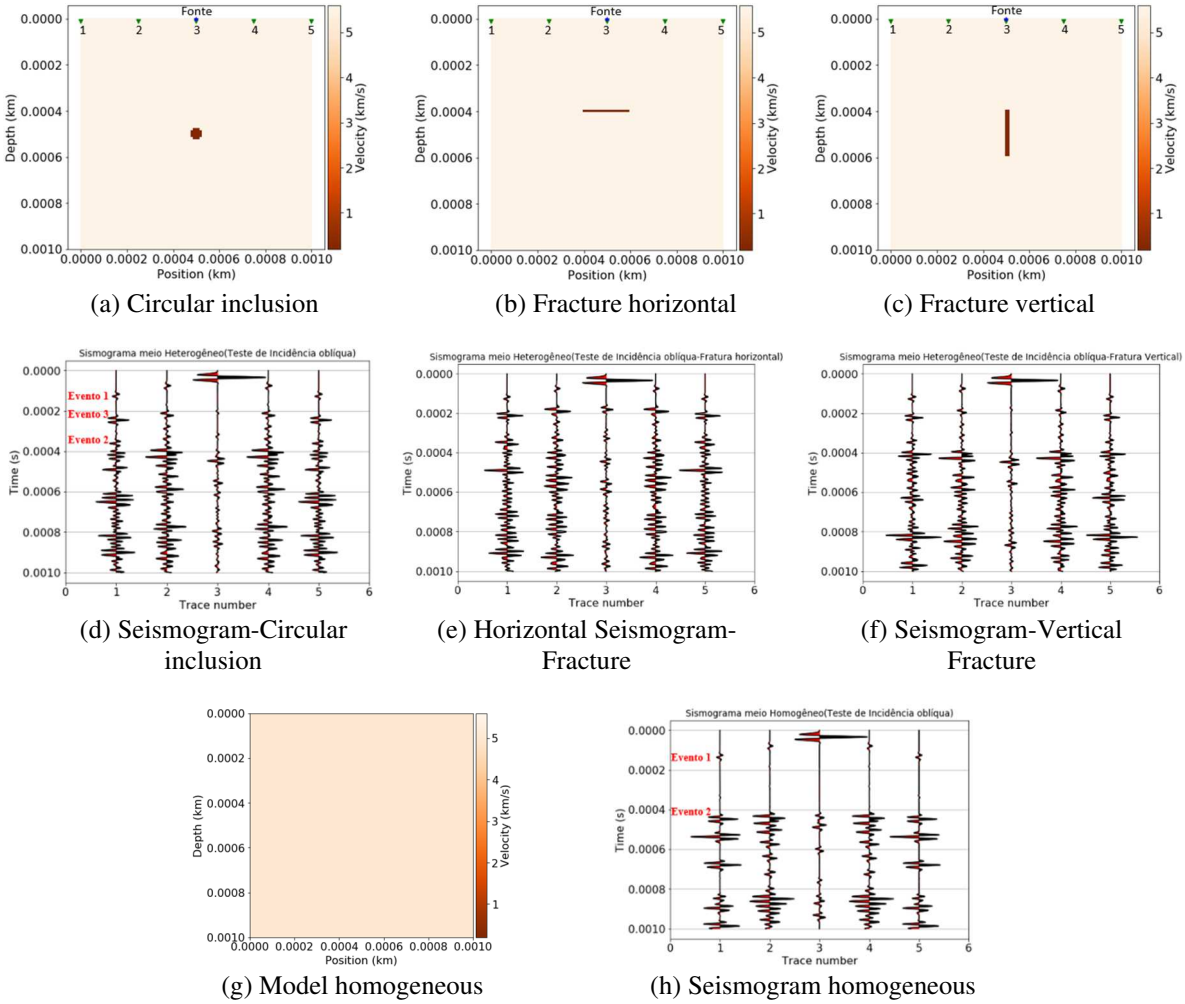

(a) Circular inclusion (b) Fracture horizontal (c) Fracture vertical

(d) Seismogram-Circular inclusion (e) Horizontal Seismogram-Fracture (f) Seismogram-Vertical Fracture

(g) Model homogeneous (h) Seismogram homogeneous

Fig. 1 - Heterogeneities e Homogeneous and respective seismograms: circular inclusion, horizontal fracture and vertical.

Another observed aspect is that the wave passes through the heterogeneity and quickly recomposes with a very small time difference, influencing the measured transit time. This phenomenon is known as wavefront healing. This phenomenon was first observed by [22] with observations focused on the effects of diffractions on transit time delays. In ray theory, waves preserve the accumulated time changes incurred by passing through an anomaly somewhere along their path between source and receiver. Due to intrinsic diffraction (’wavefront healing’), finite-frequency wavefronts do not behave in this way. Diffraction acts to fill irregularities in the wavefront. Moreover, diffracted waves with significant amplitude can interfere with the direct wave and introduce bias in transit time measurements [13]. This phenomenon has been reported extensively, highlighting the necessity of accounting for wavefront healing effects, as it represents one of the main deficiencies of Ray.

Theory [15, 14, 9, 16, 19, 8, 12]. In studies of rock blocks on a metric scale, this phenomenon has not yet been observed in the literature, despite its well-known occurrence in seismological contexts. Such a phenomenon would invalidate the application of Linear Transit Time Tomography under Straight Ray Theory assumptions. This approach will also be complemented by cross-correlation methods. The state variable field was also obtained for heterogeneous media with horizontal fractures and spherical inclusions; however, due to their similarity, only one representative case was chosen for presentation.

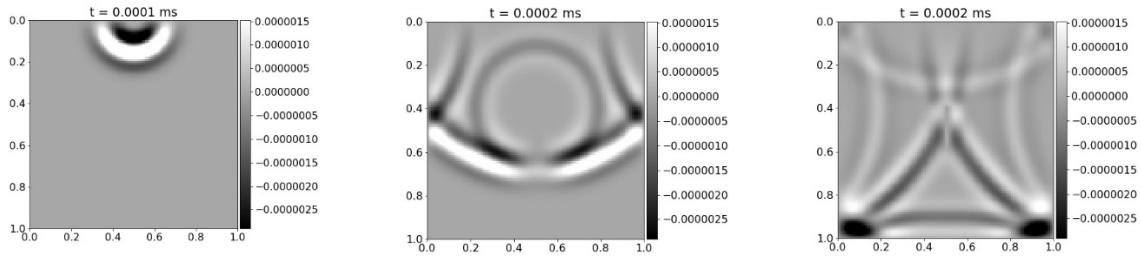

(a) Time = 0.0001 ms. (b) Time = 0.0002 ms. (c) Time = 0.0002 ms.

Fig. 2 - State variable field in time between 0.0001 ms and 0.0002 ms for heterogeneous médium with vertical fracture.

For the development of FWI, three synthetic models were generated: Model 1 - Horizontal Fracture, Model 2 - Vertical Fracture, and Model 3 - Scattering with multiple internal fractures. The number of sources (three) and receivers (ten) were arranged to simplify imaging.

DISCUSSIONS

Considering the three simulated models for the rock block within a square domain measuring 1m x 1m, each containing internal structures. Model 1 represents a rock block typically extracted from quarries, usually having more than one free face available for assessment tests and featuring flat surfaces. Three ultrasonic pulse sources are applied simultaneously and punctually at the upper edge of the block. This source is modelled using a Ricker wavelet pulse with a frequency of f = 30 kHz (the same used for subsequent presented models). We observe that through FWI, Model 1 was precisely inverted.

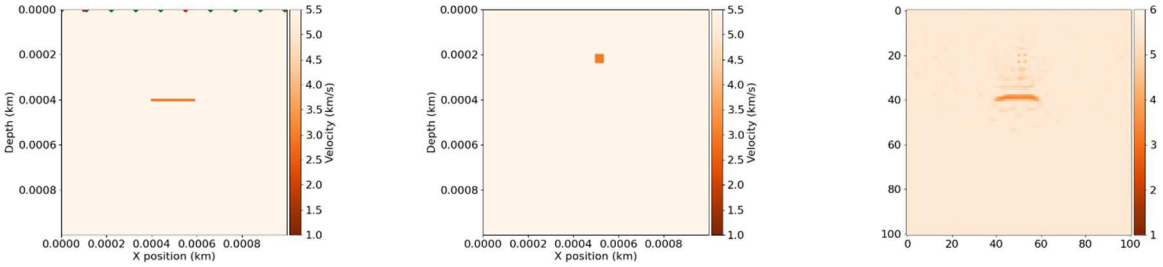

(a) True Model and Tx-TR (b) Initial model (c) Inversion results

Fig. 3 - Model 1: Horizontal Fracture. (a) True model indicating the locations of sources and receivers, (b) initial model used, and (c) result of FWI inversion.

In Model 2, the square domain represents a rock block containing a centralized internal vertical fracture, allowing analysis of the effect of fracture position on wave propagation. It is observed that the inversion was satisfactory for this model, providing good resolution for vertically positioned fractures (Figure 4). Starting from an initial model containing a fracture represented by only 4 pixels, the inversion closely approached the true model, despite displaying some spurious velocities in its vicinity.

Model 3, termed scattering, assumes fractures distributed in various positions along the x and y directions of the block, with dimensional variations in length and width. The complexity of this model allows evaluation of the implementation's quality. For Model 3 (Figure 5), starting from the same initial model, some spurious velocities are more evidently found in the obtained inversion, particularly near the central fracture. However, other fractures were recognized similarly to the true model. Different fractures were detected with varying resolutions, even with a limited number of source-receiver pairs, further confirming the efficiency of the FWI technique in identifying internal heterogeneities in rock blocks.

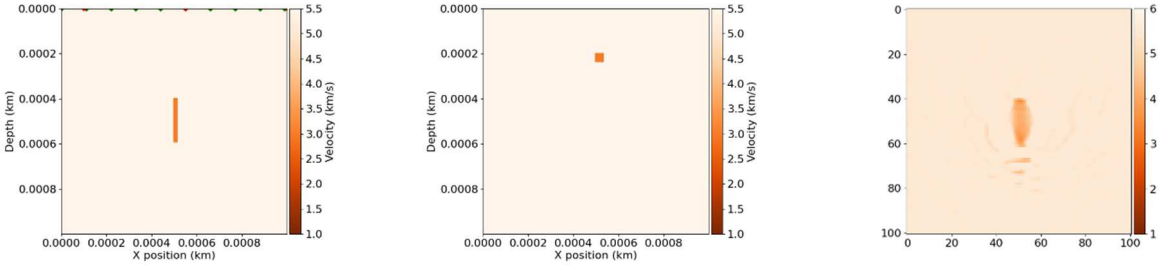

(a) True Model and Tx-TR (b) Initial model (c) Inversion results

Fig. 4 - Model 2: Vertical Fracture. (a) True model with sources and receivers, (b) initial model, and (c) result of FWI inversion.

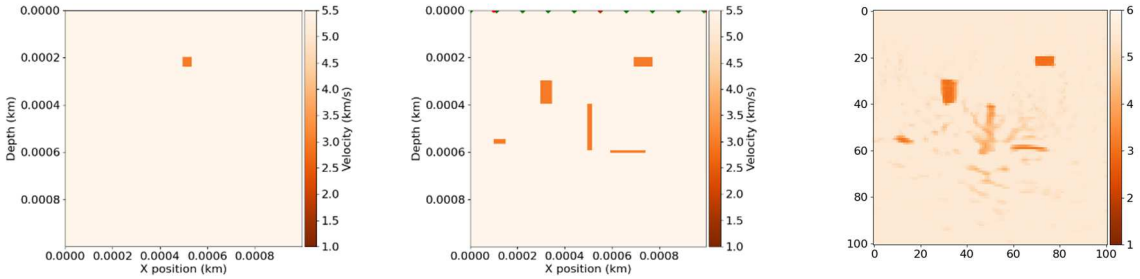

(a) Inicial Model (b) True model for FWI (c) FWI Result

Fig. 5 - FWI imaging results using an initial model of a plate with uniform velocity (1.b). Image (1.a) shows the location of the defect, and FWI accurately locates the heterogeneity at the position (1.c).

CONCLUSION

The identification of events in the seismograms obtained through oblique incidence tests demonstrates potential in characterizing the medium in terms of homogeneity and possible internal features, evidenced by the distinct presence of events 1, 2, and 3. The application of the Full Waveform Inversion (FWI) technique, still relatively unexplored as a non-destructive evaluation method, proved capable of imaging for detecting internal structures in rock blocks. The numerical simulations conducted also allowed evaluating the proposed technique's capability in identifying internal structures within a metric-scale square domain, resembling conditions typically found in situ in quarry blocks. FWI showed significant potential in identifying these structures using a reduced number of source-receiver pairs, representing its main advantage compared to conventional tomography, a technique requiring a larger number of source-receiver pairs. This advantage relates to the phenomenon of Wavefront Healing, which significantly compromises the resolution of traditional tomographic methods but has a reduced impact on the FWI technique.

REFERENCES

[1] Y. Amitt et al. Time-domain full-waveform inversion for ultrasonic imaging of embedded defects. Ultrasonics, 54(2): pp.665-678, 2014.

[2] E.G. Bazulin et al. Inverse ultrasonic imaging using full-waveform inversion. Ultrasonics, 91: pp.29-35,2019.

[3] Jon F. Claerbout. Toward a unified theory of reflector mapping. Stanford Exploration Project, 1971.

[4] Jon F. Claerbout. Fundamentals of geophysical data processing. McGraw-Hill, 1976.

[5] Dale Ensminger, Leonard J. Bond. Ultrasonics: Fundamentals, Technologies, and Applications.CRC Press, Boca Raton, 3rd edition, 2011.

[6] Andreas Fichtner. Full seismic waveform modelling and inversion. Springer Science & Business Media, 2010.

[7] Qing He, Wenjie Wang, Zhen Liu, Yan Zhang. Numerical and experimental study on ultrasonic imaging based on elastic least-squares reverse time migration for detecting flaws in heterogeneous structures. Ultrasonics, 110:106271, 2021.

[8] Qinya Liu, Frederik J. Simons. Influence of microstructure on wavefront healing: 2-d numerical simulations. Geophysical Journal International, 188(3): pp.1025-1042, 2012.

[9] Anthony Lomax. The wavelength smoothing effect and mislocation sensitivity of least squares traveltime inversion. Geophysical Research Letters, 21(16): pp.1739-1742, 1994.

[10] A.V. Lopatin et al. Computational aspects of full-waveform inversion in ultrasonic nondestructive testing. Russian Journal of Nondestructive Testing, 53(5): pp.341-349, 2017.

[11] Mathias Louboutin, Philipp Witte, Michael Lange, Navjot Kukreja, Fabio Luporini, Gerard Gorman, Felix J. Herrmann. Full-waveform inversion, part 2: Adjoint modeling. The Leading Edge, 37(1): pp.69-72, 2018.

[12] Alison E. Malcolm, James A. Scales. Tomographic resolution and finite-frequency effects of a wave-equation migration velocity analysis method. Geophysics, 76(5):R181-R192, 2011.

[13] D. Montelli, G. Nolet, F. A. Dahlen, G. Masters, E. R. Engdahl, S.-H. Hung. Finite-frequency tomography reveals a variety of plumes in the mantle. Science, 303(5656): pp.338-343, 2004.

[14] Gerd Mueller. Seismic imaging of wavefront healing. Geophysical Journal International, 108(3): pp.787-800, 1992.

[15] Guust Nolet. Seismic wave propagation and seismic tomography. Elsevier Science Publishers B.V., 15: pp.1-23, 1987.

[16] Guust Nolet, Frederik A. Dahlen. Wave front healing and the evolution of seismic delay times.Journal of Geophysical Research: Solid Earth, 105(B8): pp.19043-19054, 2000.

[17] Daniel Seidl. Iterative reconstruction methods for ultrasonic imaging in nondestructive testing.Journal of Nondestructive Evaluation, 35(2):1-15, 2016.

[18] Daniel Seidl et al. Full-waveform inversion in ultrasonic nondestructive testing. Journal of Sound and Vibration, 400:147-161, 2017.

[19] Frederik J. Simons, Frederik A. Dahlen, Guust Nolet. Resolution analysis of finite-frequency tomography. Geophysical Journal International, 157(1): pp.276-287, 2004.

[20] Albert Tarantola. Inversion of seismic reflection data in the acoustic approximation. Geophysics, 49(8): pp.1259-1266, 1984.

[21] Jean Virieux, St´ephane Operto. An overview of full-waveform inversion in exploration geophysics. Geophysics, 74(6):WCC1–WCC26, 2009.

[22] E. Wielandt. On the validity of the ray approximation for interpreting delay times. In G. Nolet, editor, Seismic Tomography, pp.85-98. Reidel, Dordrecht, 1987.

[23] Ren´e ´Edouard Plessix. A review of the adjoint-state method for computing the gradient of a functional with geophysical applications. Geophysical Journal International, 167(2): pp.495-503, 2006.

Proceedings IRF2025: 8th International Conference on Integrity-Reliability-Failure
In Engineering, Materials, Manufacturing and Biomechanics. Porto 15-18 July 2025
DOI: https://doi.org/10.24840/978-972-752-323-8

PAPER REF: 22422

ESTABLISHMENT OF A LOAD CARRYING CAPACITY FORMULA FOR REINFORCING FOUNDATIONS OF POWER TRANSMISSION TOWERS

Nanaka Sakamura[1(*)], Tomonori MurakamiI[2], Manabu Matsushima[1], Hidenori Yoshida[1]

[1]Faculty of Creative Engineering, Kagawa University, Kagawa, Japan
[2]Department of Power Engineering, Sikoku Research Institute Inc., Kagawa, Japan
[(*)]*Email:* s21t118@kagawa-u.ac.jp

ABSTRACT

Transmission towers that support overhead power lines are constructed to facilitate the transmission and reception power between power plants and substations. In Japan, the foundations of transmission towers have been identified as being affected by aging and non-compliance with standards. Additionally, due to the intensification of extreme weather and natural disasters caused by recent global warming, especially the uplift forces caused by rising wind loads, it is strongly needed to reinforce the foundations against them. Focusing on the bending and shear failure modes, which are brittle failure modes of unreinforced foundations, a strength evaluation formula is developed for unreinforced foundation structures in this study. To validate the developed strength capacity formulas, the reinforcement effectiveness was verified for each failure mode through 1/6-scale model tests. We considered (1) bending cracking and (2) bending yielding for bending failure, and (3) shear cracking and (4) shear yielding for shear failure. For (1) bending cracking and (3) shear cracking, the evaluation formulas accurately reproduced the actual behavior. However, the results for (2) bending yielding and (4) shear yielding were less satisfactory.

***Keywords*:** Transmission tower foundation, unreinforced concrete, repair and reinforcement, strength calculation

INTRODUCTION

Aging has become a serious issue in managing various infrastructures in Japan, and transmission towers face similar difficulties. Many of the foundations of transmission towers are unreinforced or have insufficient reinforcement, and it has been pointed out that they may be non-compliant with standards. Unlike ordinary foundations, transmission tower foundations are subjected to extraordinary conditions in which they are greatly affected by wind loads acting on the tower in addition to the weight of the tower and the earth pressure. Wind loads exert compressive forces at some points on the foundation and pull-up forces at others. Of these two forces, the uplift force caused by wind load is the dominant external force acting on the transmission tower foundation and is an essential issue in their design and reinforcement. This is because large uplift forces due to wind loading can cause brittle failures, such as pull-out shear failure and bending failure, in the foundation of transmission towers.

Under such circumstances, the intensification and frequency of disasters have become a significant problem in recent years. Azegami et al. point out that wind speed tends to increase as temperature rises due to global warming. Specifically, a 2℃ rise in temperature increases wind speed by an average of 8.6 m/s, and a 4℃ rise by an average of 10.2 m/s. As a result, the wind load on buildings may also increase [1]. In fact, the maximum wind speed of 48.2 m/s

was observed in Typhoon No. 21 in 2008 [2]. On the other hand, it is expected to be difficult to secure financial resources in the future due to the effects of the declining birthrate, aging population, and population decrease. Tax revenues are projected to decrease to 89, and social security expenditures will increase to 186 in 2040, taking the actual results as of 2018 as 100[3]. However, despite the declining population, the demand for electric power is increasing due to the recent utilization of ICT devices and AI, and it is strongly required to maintain it as one of the most essential social infrastructures from the viewpoint of a stable power supply in the future.

PREVIOUS STUDIES

Studies on the maintenance of transmission tower foundations have been conducted in the past. Reinforced concrete structures such as transmission tower foundations are often damaged by alkali-silica reaction which is one of the deteriorating properties of concrete. Okazaki et al. focused on the fact that a method for comprehensively evaluating the stress state of steel bars in members of deteriorated reinforced concrete structures has not been developed, and they constructed the methods for estimating the stress state in them and evaluating the structural integrity [4]. However, they did not evaluate the durability of the structures based on the effect of rational and economical reinforcement.

Yamamoto et al. conducted pull-up tests on a 1/6-scale model specimen to examine a repair method for unreinforced concrete foundations. As a result, it was confirmed that inserting reinforcement bars from the column section of the foundation had some reinforcing effect, but this test was limited to reinforcing the column section only.

PURPOSES

This study aims to develop a formula to predict the strength of bending and shear by focusing on the representative brittle failure modes of an unreinforced foundation, i.e., bending failure mode and shear failure mode. Specifically, the formula to predict the strength of bending cracking, shear cracking, bending yielding, and shear yielding were proposed, and their validity was examined through the tests using a reduced-scale specimen of an actual structure.

MODEL OF TEST SPECIMEN

SPSM1 Specimen

The SPSM1 specimen is an unreinforced bending failure specimen. The plan and side views of the SPSM1 specimen are shown in Figures.1 and 2, respectively. These figures show that sixteen M10 bolts (10mm diameter, fully threaded) were used for support, four at each

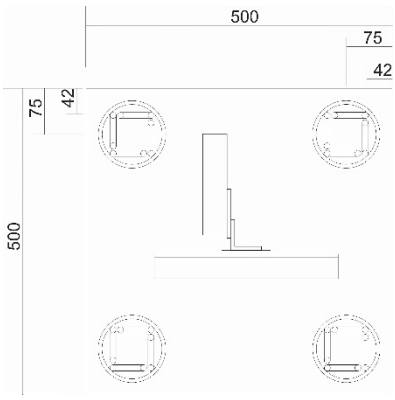

Fig. 1 - Plan view of SPSM1.

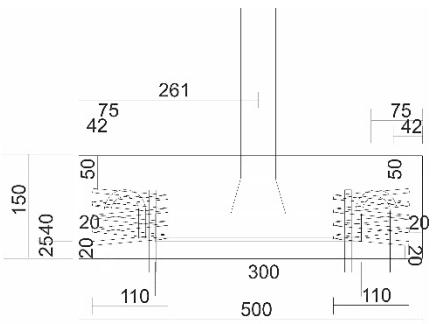

Fig. 2 - Side view of SPSM1.

corner, and four D6@20 spiral bars (6mm diameter, 20mm pitch) were used. These support and anchorage bars were used to reproduce the conditions on the underside of the specimen as pin rollers during loading and to anchor the specimen to the girders. The ends of the support and anchorage bars on the specimen side were hooked to ensure that they were secured to the specimen. On the trestle side of the rebar for support and anchorage, a length of 200mm was exposed, and a nut (nominal diameter 10mm × 2-face width 17mm × height 8mm) and washer (thickness 2mm × inner diameter 10.5mm × outer diameter 21mm) were used to secure the trestle to the M10.

SPSM2 Specimen

The SPSM2 specimen was a bending failure test specimen, and eight D6 bending reinforcement bars were placed to evaluate the effect of the bending reinforcement bars. For the SPSM2 specimen, concrete was placed up to 120mm from the bottom of the slab and allowed to cure in air for one week. After placing reinforcement bars on the top of a slab, concrete with a layer thickness of 30mm was placed. To ensure anchorage between the existing floor plate and the newly placed concrete, anchorage bars D6 (6mm in diameter and 40mm in length) were also placed. The plan and cross-sectional views of the SPSM2 specimen are shown in Figures 3 and 4, respectively.

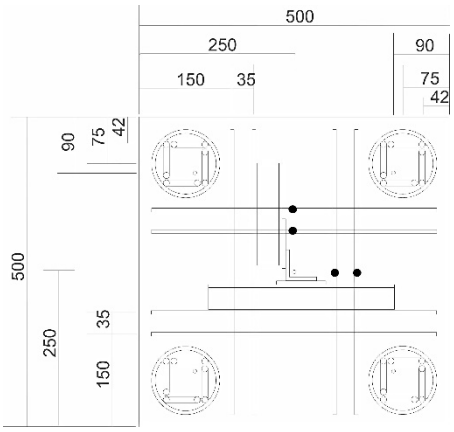

Fig. 3 - Plan view of SPSM2.

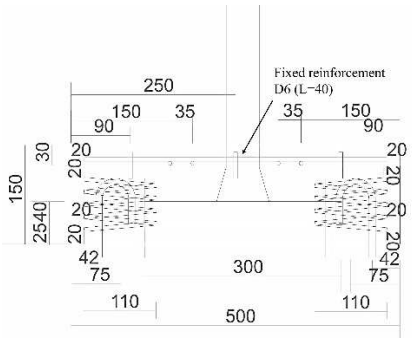

Fig. 4 - Side view of SPSM2.

SPSN1 Specimen

Since the SPSN1 specimen is an unreinforced shear failure specimen, 16 bending reinforcement bars, D6, were placed to prevent bending failure. Unlike the SPSM2 specimen, during the curing process, the concrete is placed at one time, rather than adding bending reinforcement bars and placing additional concrete. In order to ensure the anchorage of the bending reinforcement bars, they were bent in a U-shape. The plan and cross-sectional views of the SPSN1 specimen are shown in Figures.5 and 6, respectively.

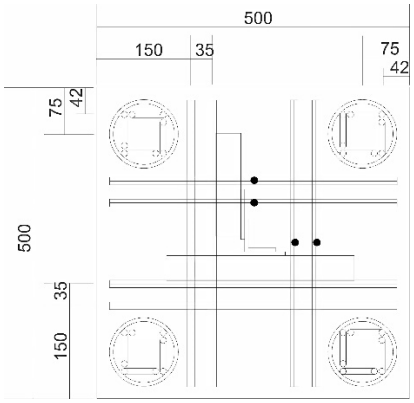

Fig. 5 - Plan view of SPSN1.

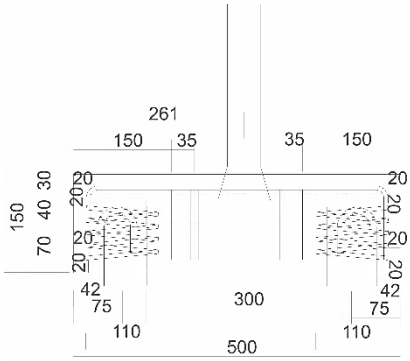

Fig. 6 - Side view of SPSN1.

SPSN2 Specimen

The SPSN2 specimen is almost identical to the SPSN1 specimen, differing only in placing three additional shear reinforcement bars with their tips bent into a hook shape. The SPSN2 specimen is also a shear failure test specimen. To evaluate the shear reinforcement, three D6 shear reinforcement bars were placed in addition to sixteen D6 bending reinforcement bars. As with the SPSN1 specimen, concrete was placed in a single step. The bending reinforcement bars were bent in a U-shape to ensure the anchorage of the reinforcement bars. Strain gauges were attached to four of the 16 bending reinforcement bars, two each in the longitudinal and shortitudinal directions of the anchors. Moreover, strain gauges were attached to the upper part of all three shear reinforcement bars, and to the lower part of one of them. Figures 7 and 8 show the plan and side views of the SPSN2 specimen, respectively.

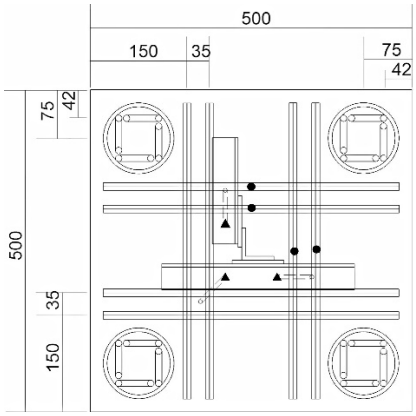

Fig, 7 - Plan view of SPSN2.

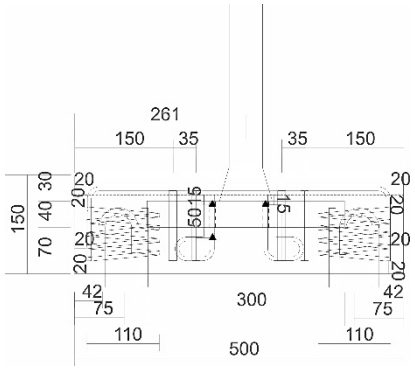

Fig. 8 - Side view of SPSN2.

Anchor material

Details of the steel portion of the test specimen are shown in Figure 9. The steel portion consists of the main legs, mounting plate, and anchor material. Though the test specimen is 1/6 scale of an actual foundation slab, it is necessary to verify the sizes and strength of the anchor specifically. The strength of the anchor was designed using not only the general structural analysis equation but also Chan's solution to ensure that the anchor can bear higher assumed forces.

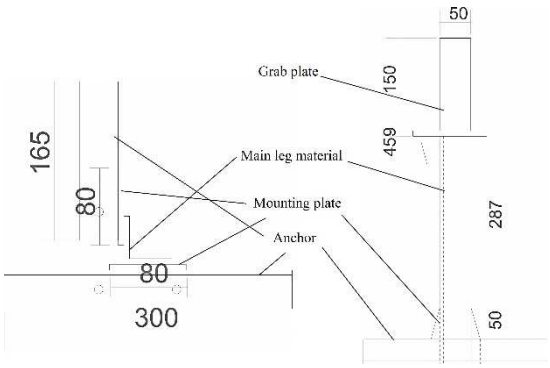

Fig. 9 - Anchor material.

First, the maximum stress in the cross-section is given by

$$\sigma_{\max} = \frac{M}{Z_{\max}} \tag{1}$$

where M is the bending moment.

$$Z_{\max} = \frac{bh^2}{6} \tag{2}$$

where b and h are the cross-sectional width and height, respectively. The bending moment is evaluated by the following equation:

$$M = \frac{kP}{A} \times \frac{l^2}{2} \tag{3}$$

where k is the safety factor (usually 1.5), A and l are the bearing area and length of anchor, respectively.

$$y(z) = -\frac{P}{4EI\beta^3} e^{-\beta z}(\sin\beta z + \cos\beta z) \tag{4}$$

The bending moment is obtained by differentiating Chan's solution twice. Comparing this value with one obtained from the general structural analysis equation, the bending moment obtained from Chan's solution was larger. Therefore, the sizes of the anchor material (SS400) were determined to be 40mm × 40mm × 5mm (thickness) so that the force acting on the anchor material, calculated based on the bending moment obtained from Chang's solution, would be less than the anchor's strength of 245N/mm^2. In Equation (4), EI is the bending stiffness, z is an axial coordinate, and y is a lateral displacement. β is defined by

$$\beta = \sqrt[4]{\frac{k_h b}{4EI}} \tag{5}$$

where b is the height of the anchor (40mm), and K_h is the reaction force coefficient of concrete, expressed as

$$K_h = \frac{E_c A_c}{l_c} \tag{6}$$

where E_c, A_c and l_c are the elastic modulus, cross-sectional area and length of concrete, respectively. Assuming that two directions, y and z directions, are semi-infinite, and that the remaining one direction has the unit width, the following equation is obtained.

$$K_h \fallingdotseq E_c \tag{7}$$

CALCULATION OF SPECIMEN'S STRENGTH

When reinforcing a structure, it is necessary to qualitatively and quantitatively evaluate the effectiveness of the reinforcement method. For this evaluation, formulae based on mechanics that can reproduce phenomena are considered to be valid. In this study, we developed such formulae and compared experimental and numerical values to evaluate the reliability and usefulness of the formulae. As for the calculations, the strength of bending cracking, shear cracking, bending yielding, and shear yielding were calculated using parameters such as the number of reinforcement bars and concrete thickness in advance of the experiment. The calculation method for these capacities is shown below.

Strength of Bending Crack

Yield Line Theory is employed to calculate the strength of bending cracking. In Yield Line Theory, two fracture lines which are bold lines shown in Figure 10 are assumed. The parameters, B and h, are defined as displayed in Figure 11.

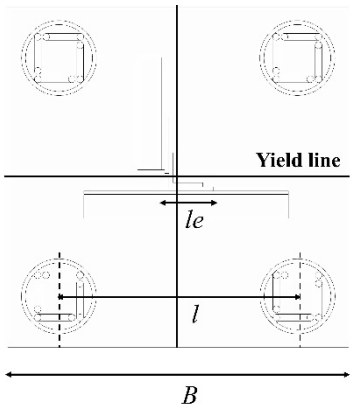

Fig. 10 - Concept figure for Yield Line Theory.

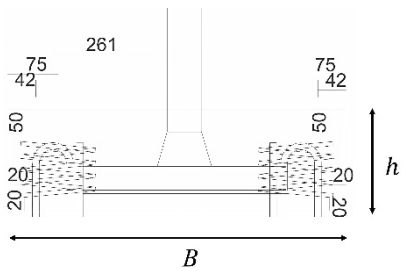

Fig. 11 - Parameters, B and h, of Yield Line Theory.

The fracture lines are modeled as simple beams as shown in Figure 12, The strength is calculated using the equation derived from conservation energy law, which states that the work done by the load acting on the simple beams is equal to the internal energy stored in the simple beams. and this is used to construct the calculation equation. Assume that an external load acts on the object and that the deformation changes from 0 to δ as it goes from 0 to *P*. External work *W* is then defined as follows.

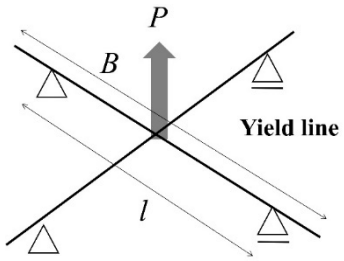

Fig. 12 - Simple beams for Yield Line Theory.

$$W = \int_0^{\delta} P(x)dx = \frac{1}{2}P\delta \tag{8}$$

Suppose that the circle has radius $\frac{l}{2}$ and angle θ, its arc is defined as

$$r = \frac{l}{2}\theta \tag{9}$$

Arc *r* is strictly a curve, whereas the angle θ is small, arc *r* can be approximated as a straight lin. Therefore, the arc length δ is expressed as (see Figure 13)

$$\delta = \frac{l}{2}\theta \tag{10}$$

Substituting Eq. (10) into Eq. (8), we obtain

$$W = \frac{1}{2}P\frac{l}{2}\theta = \frac{1}{4}Pl\theta \tag{11}$$

Assume that the rotation angle changes from 0 to θ as the bending moment goes from 0 to *M*. The internal energy U_0 stored in the beam is equivalent to the external work. The following integral can express the external work.

$$U_0 = \int_0^{\theta} M(\theta)d\theta \tag{12}$$

where the bending moment $M(\theta)$ is a function of the rotation angle θ. In spring and bar deformation, there is a proportional relationship between moment and angle of rotation. Thus, we obtain the following relation:

$$M(\theta) = k\theta \tag{13}$$

The internal energy U_0 shown in Equation (12) is the energy in the half of the beam shown in Figure 12, which is doubled for the entire beam. If there are two beams, as shown in Figure 10, it is doubled further. Note the above statement, the following equation is obtained from Equation (13):

$$U = 4 \times U_0 = 2M(\theta)\theta \tag{14}$$

In general, external work is energy added to the system from the outside, and some or all of which is stored in the system as internal energy. In particular, all of the external work *W* is converted to internal energy *U* because there is no energy loss in the elastic deformation range. From Equations. (11) and (14), the following equation is derived:

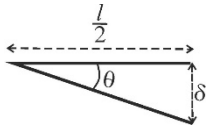

Fig. 13 - Strings and angles.

$$\frac{1}{4}Pl\theta = 2M\theta \tag{15}$$

From Equation (15), we obtain

$$P = \frac{8M}{l} \tag{16}$$

On the other hand, as shown in Figure 11, when a bending moment M acts on the cross section which has b of width and h of height, the vertical stress $\sigma(y)$ in the cross section is

$$\sigma(y) = \frac{M}{I} y \tag{17}$$

where I is the second-order moment of the cross-section of the beam. This equation shows that the vertical stress $\sigma(y)$ increases as the distance from the neutral axis, i.e., the horizontal line at which the vertical stress $\sigma(y)$ is zero, increases, and that the vertical stress $\sigma(y)$ attains maximum value at the point where y is maximum.

$$\sigma_{\max} = \frac{M}{I}\frac{h}{2} \tag{18}$$

When the maximum stress $\sigma_{\max}$ reaches the tensile strength σ_t of concrete, the bending cracking occurs in the concrete, and the bending moment M_t at this time can be obtained as follows.

$$M_t = \frac{I}{\frac{h}{2}}\sigma_t = \frac{\frac{bh^3}{12}}{\frac{h}{2}}\sigma_t = \frac{1}{6}bh^2\sigma_t \tag{19}$$

Therefore, the strength P_t at which the bending cracking occurs in the concrete can be obtained by substituting Equation (19) into Equation (16) as follows:

$$P_t = \frac{\frac{4}{3}bh^2}{l}\sigma_t \tag{20}$$

b in Equation (19) corresponds to the length B of the fracture line in the reduced model of the foundation minus the length l_e of the rigid mounting plate, and thus

$$P_t = \frac{4}{3}\frac{(B-l_e)h^2}{l}\sigma_t \tag{21}$$

can be obtained. The following relationship is established between the tensile strength of concrete and its compressive strength; σ_t and σ_c.

$$\sigma_t = 0.23\sigma_c^{\frac{2}{3}} \tag{22}$$

Strength of Bending Yielding

The strength of bending yielding is calculated from the moment at which the reinforcing bar in a reinforced concrete structure exceeds its elastic range and begins to yield. The moment of bending yielding on the cross-section of a reinforced concrete, M_y, is obtained by substituting the yield strength of the bar, σ_s, the cross-section area per a bar in tension, a_s, the number of bars, n, and the resistance distance, z, into the following equation.

$$M_y = \sigma_s a_s n z \tag{23}$$

This distance z is defined as the vertical distance between the following two lines of action;

-The line of action of the combined force of the compressive stresses in the concrete

-The line of action of the combined force of the tensile stresses in the bars

Therefore, z is defined by the following equation

$$z = h_{at} - \frac{a}{2} \tag{24}$$

where h_{at} is the effective height and a is a value determined by approximating the concrete arbitrary compressive stress distribution with a rectangular stress block. The compressive stress distribution in the cross-section of concrete is nonlinear. The maximum compressive stress in the cross-section of a concrete occurs at the top of the cross section when a load is applied from above to a simple beam. This compressive stress distribution is approximated by a rectangular stress block using the following scheme.

-The magnitude of the stress is $0.85f_{\mathrm{c}}$

-The height of the rectangular stress block, a, is equivalent to $\beta_1 \cdot c$

where β_1 is a coefficient based on the material property of the concrete and is usually set to 0.85.

Substituting A=0.85c into Eq. (24) yields

$$z = h_{\mathrm{at}} - \frac{0.85c}{2} \tag{25}$$

where c is generally defined by the following approximate formula.

$$c \approx \frac{h_{\mathrm{at}}}{7} \tag{26}$$

Substituting Equation (26) into Equation (25), we obtain

$$z = h_{\mathrm{at}} - \frac{a}{2} = h_{\mathrm{at}} - \frac{1}{2} \cdot \frac{0.85h_{\mathrm{at}}}{7} = \left(1 - \frac{0.425}{7}\right) h_{\mathrm{at}} \approx \frac{7}{8} h_{\mathrm{at}} \tag{27}$$

Equation (28) is obtained by substituting Equation (27) into Equation (23) as follows:

$$M_{\mathrm{y}} = \frac{7}{8} \sigma_{\mathrm{s}} a_{\mathrm{s}} n h_{\mathrm{at}} \tag{28}$$

Furthermore, substituting Equatiom (28) into Equation (16), the strength of bending yielding M_{y} is given by

$$M_{\mathrm{y}} = \frac{7\sigma_{\mathrm{s}} a_{\mathrm{s}} n h_{\mathrm{at}}}{l} \tag{29}$$

Strength of Shear cracking

To begin with, the strength of shear cracking of the specimen is considered equivalent to the shear strength of concrete. In this study, the shear failure plane was set up in advance because it is necessary to evaluate the shear strength of concrete at the plane where shear failure occurs. The shear failure plane is assumed to occur at an angle of 45 degrees from the point where the anchor and the mounting plate join, as shown in Figure 14. The vertical component of the shear forces acting on the assumed shear failure plane of the concrete is balanced by the uplift forces on the main legs, when the shear failure of concrete occurs on the plane. The equation for the balance of these forces is Equation (30)

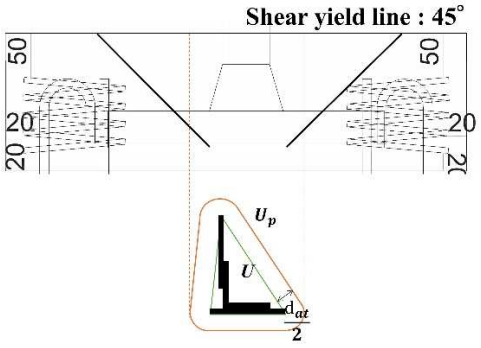

Fig. 14 - Assumed shear failure surface.

$$P_{\mathrm{c}} = U_{\mathrm{p}} d_{\mathrm{at}} \tau_{\mathrm{p}} \tag{30}$$

The effective shear height d_{at} is the length from the center of the bending reinforcement bars in two directions to the bottom of the anchor. As an exception, when bending reinforcement bars are not placed, the height d_{at} is from the top of the floor plate of a foundation to the bottom of an anchor. U_{p} is the circumference of the area lined in red shown in Figure 14 and can be defined by the following equation.

$$U_{\mathrm{p}} = U + \pi d_{\mathrm{at}} \tag{31}$$

In general, the shear strength of concrete, τ_{p}, depends on the material and structural properties. For the former, it is known that the shear strength of concrete, τ_{p}, is related to one of the material properties, f_{c}, and is proportional to $\sqrt{f_{\mathrm{c}}}$. As for the latter, it is known that the shear strength of concrete is affected by structural properties such as cross-sectional force, cross-sectional dimension, and cracking. Thus, the shear strength of concrete, τ_{p}, is defined by the following equation.

$$\tau_{\mathrm{p}} = 0.2\beta_{\mathrm{p}}\beta_{\mathrm{d}}\beta_{\mathrm{r}}\sqrt{f_{\mathrm{c}}} \tag{32}$$

where the coefficient of 0.2 is determined by a number of experimental results and is set so that the shear strength of concrete, τ_{p}, in Equation (32), agrees with the mean value obtained from experimental results as closely as possible. In addition, the coefficients:

β_{P}: Coefficient related to the reinforcement ratio of the bending reinforcement bars

β_{d}: Coefficient related to the shear effective height

β_{r}: Coefficient related to the shear span ratio

are defined as follows, respectively:

$$\beta_{\mathrm{p}} = \sqrt[3]{100P_{\mathrm{nu}}} \tag{33}$$

$$\beta_{\mathrm{d}} = \sqrt[4]{\frac{1000}{d_{\mathrm{at}}}} \tag{34}$$

$$\beta_r = 1 + \frac{1}{1 + \frac{0.25U_{\mathrm{p}}}{Bd_{\mathrm{at}}}} \tag{35}$$

The reinforcement ratio of the bending reinforcement bars in the floor is given by the following equation.

$$P_{\mathrm{nu}} = \frac{a_{\mathrm{s}}n}{Bd_{\mathrm{at}}} \tag{36}$$

The shear strength of the transmission tower foundation is the sum of the shear strength of concrete, P_{c}, which is mentioned above, and that of the shear reinforcement bars, P_{s}.

$$P_s = nA_{\mathrm{s}}\sigma_{\mathrm{y}}\alpha \tag{37}$$

where n and A_{s} are the number and cross-section of shear reinforcement bars within the shear failure area, respectively. Furthermore, σ_{y} and α are the yield stress and its factor of shear reinforcement bars, respectively.

TESTS AND RESULTS

In the tests, tensile strength, specimen displacement, the strain of the bar in the specimen, and concrete cracking were measured. Only in the case of SPSM1, the strain of the reinforcement bar in the test specimens was not measured because the reinforcement bar was not placed. In this chapter, the strengths of bending cracking, shear cracking, bending yielding, and shear yielding are calculated using the above formulae, and then the test results are compared with their strengths. Furthermore, the adaptability of the formulae is examined through the comparison of measured values and values calculated by formulae.

SPSM1 Specimen

The SPSM1 specimen expressed the expected failure behavior. The specimen in which bending cracking occurred at 58kN subsequently failed due to bending cracking mode. A plan view of a sketch of the cracked concrete is shown in Figure 15. The calculated and experimental strengths of bending cracking are 54.3kN and 58.0kN, respectively as displayed in Figure 16. Therefore, the formula can adequately estimate not only the strength of bending cracking but also the curve of displacement and loading relations.

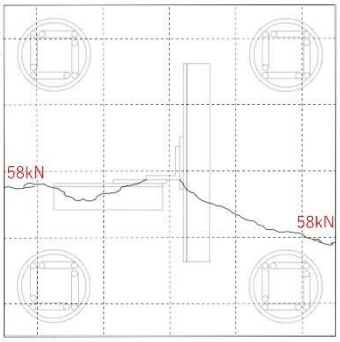

Fig. 15 - Sketch of the cracked concrete (plane view, SPSM1).

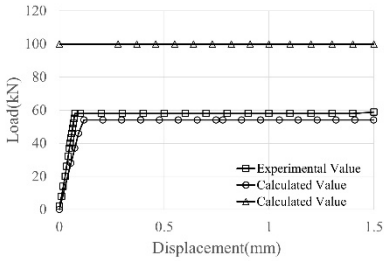

Fig. 16 - Displacement - load relations (SPSM1).

SPSM2 Specimen

The SPSM2 specimen behaved differently from what was expected. The specimen in which bending cracking occurred at 46kN subsequently failed in a different mode without transitioning to bending yielding failure.

First, the bending cracking occurring at 46kN of the uplift force is discussed according to the values of the strain gauge (see Figure 17) attached to the bending reinforcement bars. Initially, the values of all four strain gauges exhibited similar behaviors. However, at around 46kN of the uplift force, the values of each of the four strain gauges began to differ, and the values of two gauges, CH0103 and CH0406, increased rapidly. This suggests that bending cracking occurred at approximately 46kN.

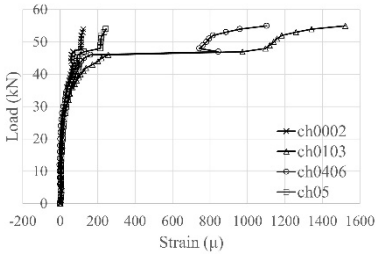

Fig. 17 - Strain values for bending reinforcement bars (SPSM2).

Next, Figures.18 and 19 show the plan and side views of a sketch of the cracked concrete, respectively. According to these figures, the causes that led to the unexpected failure of the SPSM2 specimen are discussed. As shown in Figures 18 and 19, bending cracks appeared on the top of the specimen parallel to the direction of the longer anchor. Then, on the side surface of the specimen, the bending cracks formed downward from the top. After that, horizontal cracks formed around the specimen when the bending cracks reached a point about 30 mm from the top where the joint surface of the reinforced concrete existed. The unexpected failure of the SPSM2 specimen is considered to be due to insufficient bonding between the concrete placed before and later.

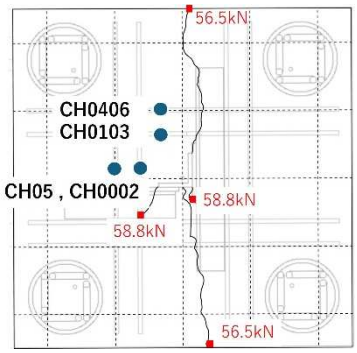

Fig. 18 - Sketch of the cracked concrete (plan view, SPSM2).

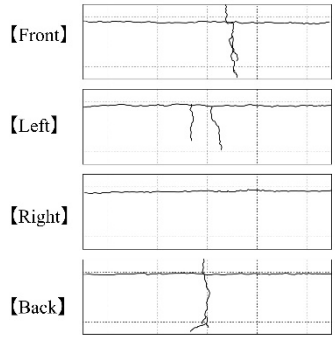

Fig. 19 - Sketch of the cracked concrete (side view, SPSM2).

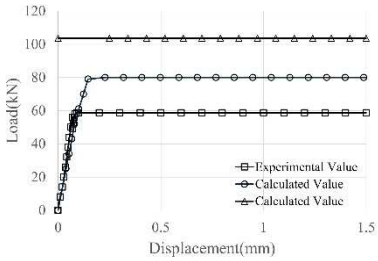

Fig. 20 - Displacement - load relations (SPSM2).

The calculated and experimental strengths of bending cracking are 54.3kN and 46.0kN, respectively, as displayed in Figure 20. Therefore, not only the strength of bending cracking but also the curve of displacement and loading relations can be adequately estimated by the formula. On the other hand, the shear cracking strength and bending yielding strength could not be compared with the experimental values because the specimens exhibited unexpected failure modes.

SPSN1 Specimen

The SPSN1 specimen expressed the expected failure behavior. The specimen in which bending and shear cracking occurred at 47.0kN and 57.0kN, respectively, subsequently failed due to shear cracking mode. Figure 21 shows a plan view of a sketch of the cracked concrete.

As shown in Figure 22, all four strain gages attached bending reinforcement bars exhibit similar behavior and were not yielded, which indicates that bending yielding did not occur in the SPSN1 specimen. The calculated and experimental strengths of bending cracking are 47.0kN and 54.3kN, and those of shear cracking are 57.0kN and 58.1kN, respectively, as displayed in Figure 23. As indicated in Figure 23, not only the strength of bending and shear cracking but also the curve of displacement and loading relations can be adequately estimated by the formulae.

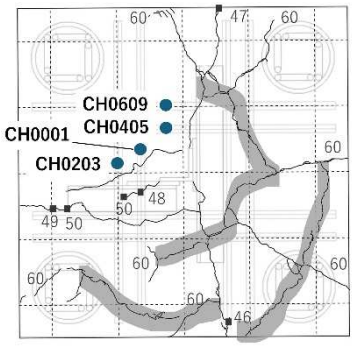

Fig. 21 - Sketch of the cracked concrete (plan view, SPSN1).

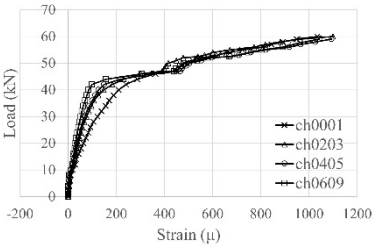

Fig. 22 - Strain values for bending reinforcement bars (SPSN1).

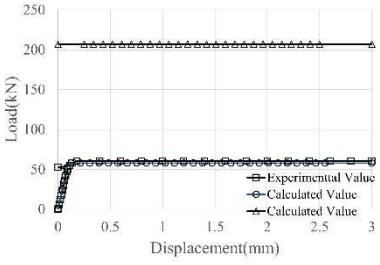

Fig. 23 - Displacement - load relations (SPSN1).

SPSN2 Specimen

The SPSN2 specimen behaved differently from what was expected. The specimen in which bending cracking occurred at 50kN and shear cracking occurred at 57.5kN subsequently failed in a different mode without transitioning to shear yielding failure.

First, the fact that the bending cracking occurring at 50kN of the uplift force is discussed according to the values of strain gauges attached to the bending reinforcement bars (see Figure 24). At the beginning, the values exhibited similar behaviors till 50.0kN at which the inclination of load-strain relations changed. This suggests that the bending cracking occurred at approximately 50.0kN.

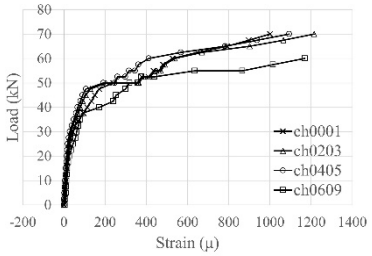

Fig. 24 - Strain values for bending reinforcement bars (SPSN2).

Next, the fact that the shear cracking occurred at 57.5kN of the uplift force is discussed according to the values of strain gauges attached to the shear reinforcement bars (see Figure 25). The values of three strain gauges attached above the anchors exhibited similar behaviors until 57.5kN at which the inclination of load-strain relations changed. This suggests that the shear cracking occurred at approximately 57.5kN.

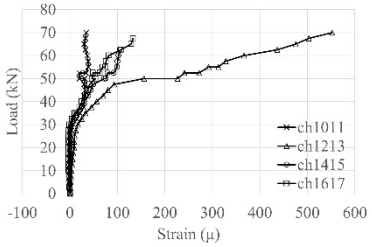

Fig. 25 - Strain values for shear reinforcement bars (SPSN2).

Furthermore, the plan and side views of a sketch of the cracked concrete are shown in Figures 26 and 27, respectively. As shown in these figures, the specimen in which cross the bending cracking occurred at 50.0kN of the uplift force, followed by the shear cracking in almost concentric circles as shown in the dashes.

We now consider why the unexpected failure mode occurred. Around the center of the lower part of the anchor, the uplift force usually induces a compressive field in the horizontal direction and a tensile field in the vertical direction. However, in this specimen, the fixing between the shear reinforcement bars and the concrete becomes stronger due to the hook installed at the end of the shear reinforcement bars, which resulted in greater tensile force than that without the hook. The concentrated compressive force in the horizontal direction and the tensile force in the vertical direction as described above also resulted in a larger shear force, which is considered to be the reason for the large strain value measured by strain gage CH1213. On the other hand, Figures 28 and 29 show that the shorter anchor is located at 74.4mm from the side and 80.0mm from the top. Around the left end of the shorter anchor, as the anchor is pulled up, shear forces are concentrated by the similar mechanism as described above in parallel to the anchor-concrete interface. The displacement jump across the interface between the anchor and the concrete caused the shear-opening cracks that reached the sides of the specimen, which brought about the specimen to fail.

The calculated and experimental strengths of bending cracking are 54.3kN and 46.0kN, and those of shear cracking are 58.1kN and 57.5kN, respectively as displayed in Figure 28. Therefore, not only the strength of bending and shear cracking but also the curve of displacement and loading relations can be estimated enough by the formulae. On the other hand, the shear yielding strength could not be compared with the experimental values because the specimens exhibited unexpected failure modes.

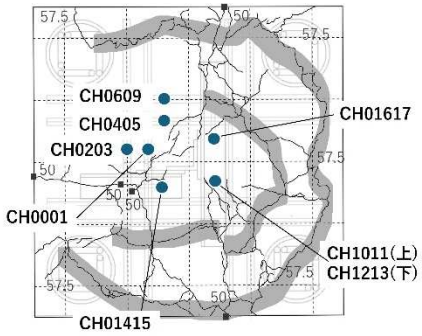

Fig. 26 - Sketch of the cracked concrete (plan view, SPSN2).

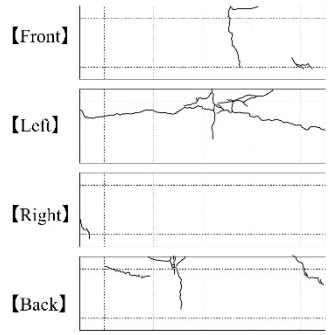

Fig. 27 - Sketch of the cracked concrete (side view, SPSN2).

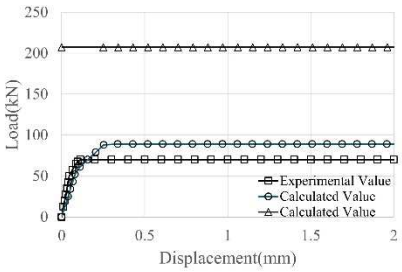

Fig. 28 - Displacement - load relations (SPSN2).

CONCLUSIONS

This study focuses on the unreinforced foundation of transmission towers with safety issues such as insufficient strength and severe disasters. Since it is difficult to replace these foundations from the viewpoint of financial resources, there is a need for more rational and economical repair and reinforcement. This study aims to examine the appropriate arrangement of structural members and the number of reinforcement bars so that the foundation can be reinforced reasonably and economically and to verify the validity of the proposed calculation formula through pull-up tests on a 1/6-scale model of a real structure.

As a result, there were good agreements between the values obtained using the formulae and the experimental values for the bending and shear cracking strength, confirming the validity of the formulae and convincing that they are sufficiently useful for evaluating the strength of actual transmission tower foundation.

Though we tried to verify the bending and shear yielding strength, the specimens did not exhibit the bending and shear yielding failure, making a comparison of the calculated and experimental values impossible. The reason why the experimental values in terms of bending yielding were not obtained seems to be the insufficient bonding between the concrete placed before and later. As for this, it is considered that the problem can be solved by making the joint surface rougher and increasing the number of anchorage reinforcement bars. The reason why the experimental values in terms of shear yielding were not obtained seems to be that the cracks emanating from the edge of the anchor reached the side of the concrete and progressed to macroscopic failure. As for this, it is considered that the problem can be solved by keeping a sufficient concrete cover and a separation distance between the anchor and the side of a concrete.

Future tasks should address the issues mentioned above, such as the number of anchorage reinforcement bars and the location of the anchor.

REFERENCES

[1] Yasuhiko Azegami: Study on the Influence of Global Warming on Typhoon Normal at Landfall in the Japanese Islands, Journal of Wind Engineering Research, No.27, pp.127-133, 2022.

[2] Ministry of the Environment, Japan: Results of Impact Assessment on Intensification of Disasters due to Climate Change: Typhoons Growing Stronger - What Risks Are We Facing? - . pp.12-17, 2023.10 (in Japanese).

[3] Ministry of Finance, Japan: Report of the Study Group on Declining Population and Economic Growth, Chapter 8, 2020.6 (in Japanese).

Proceedings IRF2025: 8th International Conference on Integrity-Reliability-Failure
In Engineering, Materials, Manufacturing and Biomechanics. Porto 15-18 July 2025
DOI: https://doi.org/10.24840/978-972-752-323-8

PAPER REF: 22427

IMPORTANCE OF FAILURE MODES IN THE ROBUSTNESS OF 4 BOLT-PER-ROW END-PLATE STEEL CONNECTIONS

Daniel Luís Nunes[1(*)], Adrian Liviu Ciutina[2]

[1]CMMC, Faculty of Civil Engineering, Politehnica University Timisoara, Timisoara, Romania
[2]CCTFC, Faculty of Civil Engineering, Politehnica University Timisoara, Timisoara, Romania
[(*)]*Email:* daniel.nunes@upt.ro

ABSTRACT

The extended steel end-plate beam-to-column connection is a key-parameter in the behaviour of moment-resisting frames. The usual configuration is by considering two bolts-per-row. However, a four-bolts-per-row configuration could offer a more reliable solution for achieving improved robustness performances for both the connection and the buildings in which higher levels of robustness are required. In this context, based on a FE parametric study, an indicator showing the closeness of the failure mode 2 of steel bolted end-plate connections to mode 1 or mode 3 is proposed and discussed with comparison to similar two bolts-per-row configuration.

Keywords: Steel end-plate steel connections, failure modes, 4 bolt-row, strength, ductility.

INTRODUCTION

The connections of steel structures in unbraced frames play a key role in the overall performance of a building, particularly under extreme loading conditions that exceed the nominal values considered during the design phase. A determining factor in the behaviour of the connections is their configuration, which significantly influences the response characteristics of the connections in terms of strength, stiffness, and ductility. The classical configuration of bolted beam-to-column connections with extended end plates features a two-row vertical arrangement, which involves brittle failure following the yielding and failure of the first tensioned bolts [1]. The plastic behaviour of such connections is not integrated into the current design codes, which limits performance-based structural analyses under extreme actions, such as robustness analyses. In this context, connection configurations with four bolts in a single row can offer advantages in scenarios where the classical configuration cannot provide a satisfactory level of structural robustness. However, post-elastic behaviour may lead to superior plastic resistance capacity and adequate ductility. Recent studies on this type of connection have focused on analyzing equivalent T-elements (similar to T-stubs - Figure 1), based on existing analytical characterization offered by the codes, which applies to the classical configuration with two bolts-per-row.

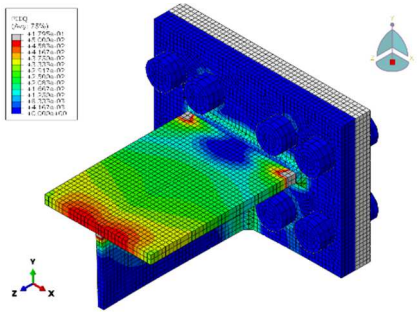

Fig. 1 - IPE360 yield zones before bolt rupture for 4B_I360_t20_M20_P3.

However, this characterization is limited to the elastic response domain of the connection and does not analyze the interaction between bolts disposed on different rows [2]. The paper aims to present a parametric numerical study using FEM on 2 and 4 row T-elements, based on previous results obtained on experimental tests.

RESULTS AND CONCLUSIONS

Considering the spectral nature of the failure modes (FM) - where FM 2 can be closer to FM 1 or FM 3), the indicator $\delta_{2\text{-}3}$ is calculated, ilustrating the closenest to FM 3 or FM 1:

$$\delta_{2-3} = \frac{|F_{T.2.Rd} - F_{T.1.Rd}|}{|F_{T.2.Rd} - F_{T.3.Rd}| + |F_{T.2.Rd} - F_{T.1.Rd}|} \quad (01)$$

In the given context a value near 0% indicates a tendency towards FM 1, while a value close to 100% suggests a tendency towards FM 3. According to the obtained results (Figure 2), the evolution of the yield and maximum forces is correlated with the closeness to either FM 1 or 3. For specimens which retain characteristics with tendency towards FM 1, the gains between 2B and 4B are small, or even negative. In the other side of the spectrum both strength values present a clear increase in the cases in which the failure characteristics tend towards FM 3.

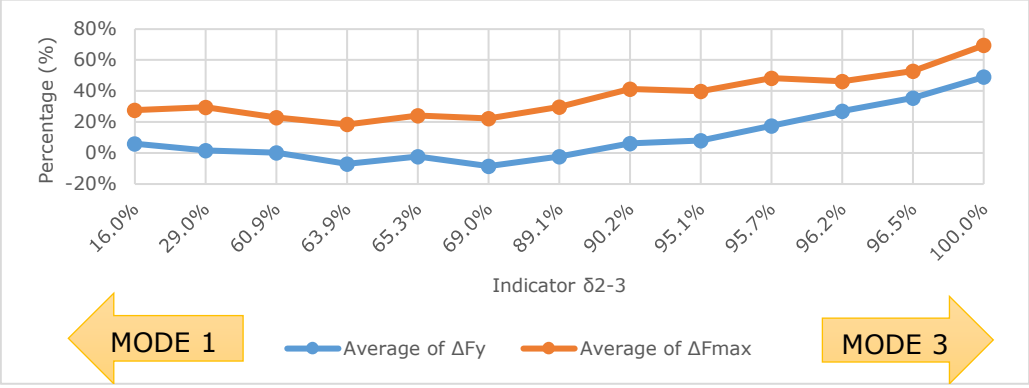

Fig. 2 - Average 2B-4B yield and maximum strength gains in relation to mode tendency.

The evolution of the results in relation to the indicative $\delta_{2\text{-}3}$ is significant. Configurations showing a $\delta_{2\text{-}3}$ value of 89.1% to 96.2%, indicating a FM 2 leaning towards FM 3 exhibited better outcomes in terms of both strength and ductility. Thus, the $\delta_{2\text{-}3}$ ratio serves as an important indicator for achieving a desirable balance between strength and ductility across different configurations.

REFERENCES

[1] F. Dinu, I. Marginean, D. Dubina, “Experimental testing and numerical modelling of steel moment-frame connections under column loss,” Engineering Structures, n 151, 2017.

[2] D.L. Nunes, A. Ciutina, “Behaviour of end-plate steel connections with 4 bolts per row under large deformations,” em 9th International Conference on Steel and Aluminium Structures (ICSAS19), Bradford, 2019.

Proceedings IRF2025: 8th International Conference on Integrity-Reliability-Failure
In Engineering, Materials, Manufacturing and Biomechanics. Porto 15-18 July 2025
DOI: https://doi.org/10.24840/978-972-752-323-8

PAPER REF: 22429

WONDERING ABOUT FIRE RESISTANCE OF TRADITIONAL PORTUGUESE CONSTRUCTION

João Rodrigues[1], Daniela Miranda[1], Naim Sedira[1, 2(*)], Cristina Reis[1, 3], Sandra Cunha[1, 2], Jorge Pinto[1, 2]

[1]UTAD, Vila Real, Portugal
[2]C-MADE, Polo UTAD, Vila Real, Portugal
[3]CONSTRUCT, FEUP, Porto, Portugal
[(*)]*Email:* naimsedira@utad.pt

ABSTRACT

Climate change as resulting in catastrophic urban scenarios such as uncontrolled fires, disruptive floods, bad air quality, among other. In terms of fires, unfortunately, there are several recent ones that resulted in deaths and loss of properties. Portugal, is also included in this set. This paper intends to give a contribution on the fire impact mitigation on traditional Portuguese construction. Thus, the type of local solid timber, the contribution of the skin of the tree in the fire resistance and a pre-burnout treatment is considered in this research. The first experimental results are shown and discussed in this document.

Keywords: Fire resistance, solid timber, traditional construction, mitigating failure.

INTRODUCTION

Fire impact on urban areas has been increasing sharply [1]. Los Angeles wildfires is one example. In Portugal, this situation is also occurring, Figure 1.

Fig. 1 - Fire in Vila Pouca de Aguiar, Portugal, september 2024.

In traditional Portuguese construction, it is very likely to have timber structural elements such as pavements, roofs, stairs, among other. In case of fire, these elements tend to burn which causes a decreasing of the cross section and, consequently, a structural degradation consequence. There are some technical building possibilities that can contribute in terms of

mitigating this structural impact. In this document, the type of timber, the contribution of the skin of the tree in the fire resistance and a pre-burnout treatment are the fire resistance technics that considered. Several samples of solid timber were prepared and tested in laboratory in order to evaluate its fire resistance contribution, Figure 2. The main results are presented. This team have done some works in this topic [2].

Fig. 3 - Laboratory tests.

REFERENCES

[1] Débora Ferreira, Alexandre Araújo, Elza Fonseca, Paulo Piloto, Jorge Pinto (2017). Behaviour of non-loadbearing tabique wall subjected to fire – Experimental and numerical analysis. Journal of Building Engineering. Volume 9. pp. 164-176.

[2] Jorge Pinto, Vanessa Vasconcelos, Romeu Monteiro, Sara Tapa, Isabel Bentes. 2021. Um contributo na temática dos riscos tecnológicos em ambiente urbano. CONREA`21 - O Congresso da Reabilitação. Livro de atas. UA Editora. 1ª edição - junho de 2021. pp. 127-133. ISBN 978-972-789-699-8. DOI https//doi.org/1048528/gy68-v843.

Proceedings IRF2025: 8th International Conference on Integrity-Reliability-Failure
In Engineering, Materials, Manufacturing and Biomechanics. Porto 15-18 July 2025
DOI: https://doi.org/10.24840/978-972-752-323-8

PAPER REF: 22434

DETERMINATION OF THE AERODYNAMIC FORCE DISTURBANCE INDEX FOR ANALYSIS OF NEIGHBORHOOD EFFECTS IN TALL BUILDINGS SUBJECTED TO WIND

João da Costa Pantoja[1(*)], Gabriela Villoslada[2], José Luiz Vital de Brito[2], Thiarly Feitosa Afonso de Lavôr[2]

[1]UNB, Dept. of Technology, University of Brasília, Brasília, Brazil
[2]UNB, Dept. of Structures Engineering, University of Brasília, Brasília, Brazil
[(*)]*Email:* joaocpantoja@gmail.com

ABSTRACT

The presence of obstacles around a building can interfere with the wind flow, modifying the pressure on the facades and, consequently, the resulting forces and moments. These interferences can generate protection effects or increase the pressure coefficients. Therefore, it is important to study the behavior of wind on buildings in the presence of surroundings to better understand these effects and ensure the safety of the structures. Most physical characteristics cannot be predicted with complete certainty and generate random results, with some of these results being more frequent than others. Reliability analyses are commonly used to examine the behavior of structures subjected to such effects, and one of these analyses is to consider the beta reliability index, which has several representations and, in this case, the determination of beta is proposed, not being considered a failure criterion, but rather as a change in the state of the aerodynamic force. In this sense, this work presents the determination, through reliability, of the aerodynamic force disturbance index, that is, how much the drag force and the force transversal to the wind direction are being modified due to the presence of neighbors, in order to evaluate the behavior of the wind effects from the CAARC (Commonwealth Advisory Aeronautical Research Council) standard tall building model, using experimental data generated in a wind tunnel. The standard tall building model was evaluated in different positions, subjected to variable aerodynamic force actions, in isolation and with the existence of different neighbours. Probabilistic concepts are presented, discussed, and in the results were analysed response surface graphs of the aerodynamic disturbance force generated for the configurations adopted by the neighbors in relation to the CAARC isolated for beta variation indexes. With the results found, it was observed that the existence of neighbors affects the average values of the data, as well as the aforementioned index, both for increase and reduction in relation to isolated building, depending on the situation, and this is evidenced by the surface graphs comparing them to other researches. Therefore, this study presents interpretations that can help in predicting the behavior of tall buildings subjected to wind loads in the presence of neighbors.

Keywords: Neighborhood effect, Wind tunnel, Reliability index, reliability.

INTRODUCTION

Natural systems can be described deterministically, but in a limited way. In many everyday situations, classical descriptions work well, but as systems become more complex, these approaches are inadequate (Kroetz, 2015). According to Blessmann (1985), the existence of obstacles can interfere with the wind flow of a building, which leads to changes in the pressures on the facades, and consequently, in the resulting forces and moments, due to the interaction between this and other structures that are around it, that is, in neighboring regions. These

interferences can occur in several ways, such as generating protection effects, reducing or increasing pressure coefficients. The objective of this work is to analyze the behavior of the wind flow in buildings with the presence of neighbors based on experimental data generated in a wind tunnel conducted by Lavôr (2023), taking as a calculation basis structural reliability criterion of a tall building subjected to the action of the wind, isolated and with different neighbors.

RESULTS AND CONCLUSIONS

The isolated CAARC and CAARC + neighbor were studied, as shown in Figure 1. The situations with the presence of the neighbor in the locations are called "A1", "A3", "A6", "B1", "B7", "B9", "C1", "C3" and "C5". "V0" indicates that the largest facade of the neighbor is perpendicular to the wind direction (neighbor at 0°), while "V90" indicates that the smallest facade of the neighbor is perpendicular to the wind (neighbor at 90°). All neighbors have the same dimensions as the CAARC.

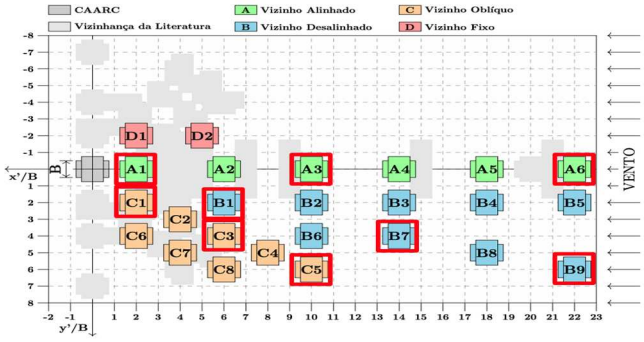

Fig. 1 - Neighbors under study. Source: Adapted from Lavôr, 2023.

The aerodynamic force disturbance index (Δβ) was obtained by calculating the difference between the Monte Carlo simulations performed on the isolated CAARC and the CAARC + neighboring, followed by the calculation of Beta according to equation (1). This index represents how the wind flow varies according to the change and positioning of these neighbors.

$$\beta = \Phi^{-1}(1 - P_f) \tag{1}$$

Where Φ^{-1} is the inverse of the standard normal cumulative probability density function and P_f is the probability of failure. By comparing the concepts of structural reliability and the aerodynamic force disturbance index (Δβ) obtained, it is clear that there is a difference between the commonly used reliability and that proposed in this study, where the disturbance index obtained through reliability will have another interpretation, opposite to the usual one, so that the higher the value of β, the greater the disturbance and the more one distribution equals another, the beta value tends to be closer to zero, and it is even possible to obtain negative β values, which can be attributed to changes in wind flow.

REFERENCES

[1] Kroetz, H.M. Meta-modelagem em confiabilidade estrutural. Dissertação de mestrado – Escola de Engenharia de São Carlos, Universidade de São Paulo, São Paulo, 2015.

[2] Blessmann, J.O Vento Na Engenharia Estrutural / Joaquim Blessmann. - 2. Ed. – Porto Alegre: Editora Da Ufrgs, 2013. 240 P, 1985.

[3] Lavôr, T.F.A. Efeitos De Vizinhança Associados A Fenômenos Aerodinâmicos Quase-Estáticos E Ressonantes. Tese De Doutorado Em Estruturas E Construção Civil, Departamento De Engenharia Civil E Ambiental, Universidade De Brasília, Brasília, Df, 267, p. 2023.

Proceedings IRF2025: 8th International Conference on Integrity-Reliability-Failure
In Engineering, Materials, Manufacturing and Biomechanics. Porto 15-18 July 2025
DOI: https://doi.org/10.24840/978-972-752-323-8

PAPER REF: 22441

NUMERICAL SIMULATION OF THE FIRE PROTECTION EFFECT AND LOAD LEVEL ON GLT TIMBER COLUMNS

Paulo A.G. Piloto[1(*)], Manuel D. Lorenzo [2], Ana B. Ramos Gavilán [2], Javier Sánchez-Haro [3]

[1]GICoS, Instituto Politécnico de Bragança, Bragança, Portugal
[2]Departamiento de Ingeniería Mecánica, Universidad de Salamanca, Zamora, España
[3]Departamiento de Ingeniería Mecánica y Estructural, Universidad de Cantabria, Santander, España
[(*)]*Email:* ppiloto@ipb.pt

ABSTRACT

The next generation of the Eurocode EN 1995-1-2 modifies the Effective Cross-Section Method (ECSM), where an adequate char depth reduces the initial timber cross-section. This char depth is based on the notional char layer (European Charring Model-ECM) and a zero-strength layer to compensate for the loss of strength and stiffness of heated but uncharred wood. The remaining effective cross-section has wood's strength and stiffness properties at room temperature and may be used to determine the load-bearing capacity. This investigation deals with gypsum-protected Glue Laminated Timber (GLT) columns under fire. The finite element method is also used to determine the fire resistance time based on a geometrical and material nonlinear analysis (GMNIA). Doubling the number of protection layers, from 12.5 mm thick to 25 mm thick, the fire resistance increases by an amount of 72% to 100% when the load level changes from 6% to 36%, with respect to load bearing at room temperature.

Keywords: Fire, Glue Laminated Timber, Gypsum protection, columns, load level.

INTRODUCTION

This research explores the principles and efficacy of gypsum-based fire protection for GLT columns. The thermal insulation is provided by gypsum and naturally by the char layer. As a sustainable and renewable building material, timber has seen a resurgence in modern architecture due to its aesthetic appeal, low environmental footprint, and structural versatility. The Glued-laminated timber (GLT) is prevalent for its strength and ability to span significant distances, making it suitable for columns and beams in mid- to high-rise buildings. However, timber's combustibility raises concerns about fire safety, especially for load-bearing structural elements.

ANALYSES, MATERIALS AND METHODS

This investigation used a simply supported timber column, with 1.2 m between supports and a cross-section of 100x80 mm^2. The material grade is spruce GL24h with a density of 365 kg/m^3 (wet). The EN14080 [1] specifies the characteristic strength under compression and bending. The material is considered orthotropic, assuming the modulus of elasticity parallel to the grain of 11.5 GPa. The design of compressive strength along the grain is 24 MPa. Based on these basic values, the orthogonal direction effect of the material [2], and the temperature reduction effect on strength and stiffness [3], one can define the orthotropic mechanical behaviour of this wood species, neglecting the effect of bond integrity between lamellas. The mechanical effect of the gypsum layer was neglected, considering only its thermal effect. The thermal properties

of the protection material are based on gypsum plasterboard with a density of 832 [kg/m³] and multiple layers of12.5 [mm] thickness according to prEN1995-1-2 [3]. The simulations, Figure 1, included an elastic buckling analysis to determine the first mode of instability and the bucking load, a second analysis using GMNIA to determine the buckling resistance at room temperature, a third analysis using the incremental non-linear thermal solution to determine the temperature in materials over time, and finally an incremental GMNIA analysis to determine the fire resistance time.

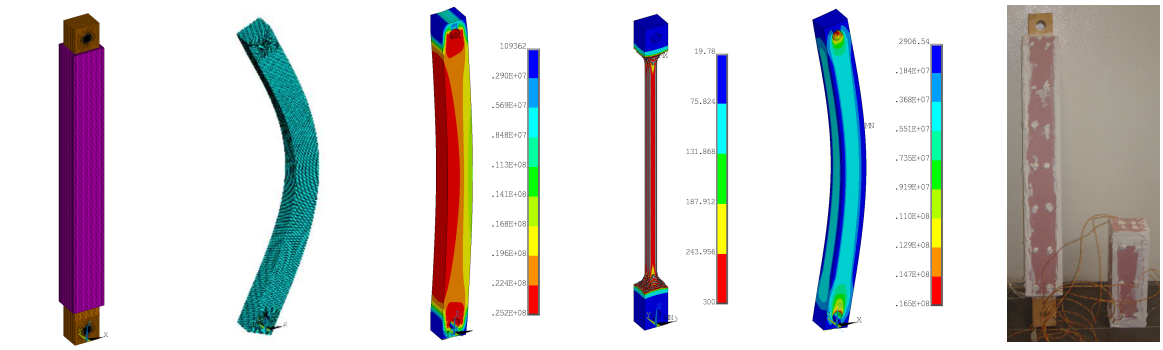

a) Finite element mesh (column with a single protection layer).

b) First buckling mode for the timber column.

c) Load-bearing capacity at room temperature (172380 N) (von Mises stress).

d) Temperature on the residual cross-section (t=2700s) with a single protection layer

e) Deformed column with a single protection layer (t=2700s) with

f) Experimental specimen and dummy with double protection layer.

Fig. 1 - Validated finite element model.

RESULTS AND CONCLUSIONS

The fire resistance is determined by the last time step of the incremental solution where it is possible to maintain the equilibrium. The fire resistance of the timber column when using a single gypsum layer was found to be 21, 27, 31 and 37 min. These limits were modified to 43, 52, 58 and 65 min when using a double gypsum layer. These results were determined with 6%, 12%, 21% and 36 % of the load-bearing capacity at room temperature. The fire resistance increases with the number of protection layers and decreases with the load level, see the contraction axial displacement “C” over time in Figure 2.

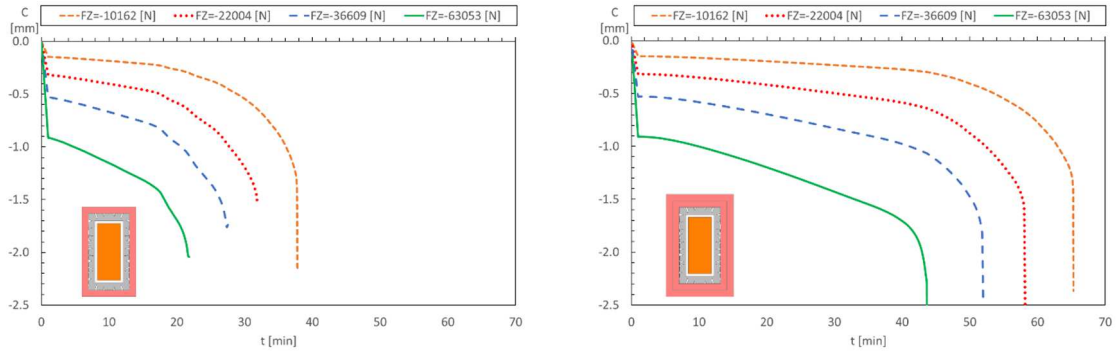

Fig. 2 - Influence of load and protection levels on the compression behaviour of GLT under fire.

REFERENCES

[1] CEN, «EN 14080 - Timber structures — Glued laminated timber and glued solid timber Requirements», CEN, n. June. pp.1-110, 2013.

[2] USA - Department of Agriculture (Forest Service), «Wood Handbook», 2010.

[3] CEN, «pr EN 1995-1.2, Eurocode 5: Design of timber structures - Part 1-2: General Structural fire design», CEN. CEN - European Committee for Standardization, Brussels, 2023.

Proceedings IRF2025: 8th International Conference on Integrity-Reliability-Failure
In Engineering, Materials, Manufacturing and Biomechanics. Porto 15-18 July 2025
DOI: https://doi.org/10.24840/978-972-752-323-8

PAPER REF: 22443

COHESIVE ZONE MODEL STRATEGY IN FINITE ELEMENTS SIMULATION OF MECHANICAL BEHAVIOR OF REINFORCED CONCRETE CORBEL STRENGTHENED BY CFRP

Veselin Stankov[1(*)], Dimitar Dontchev[1], Ivelina Ivanova[2] Jules Assih[2]

[1]Department of Applied Mechanic, University of Chemical Technology and Metallurgy, Sofia, Bulgaria
[2]Department of Civil Engineering, University of Reims Champagne-Ardenne, Reims, France
[(*)]*Email:* stankov_veselin@uctm.edu

ABSTRACT

Reinforced concrete (RC) corbels are structural elements, often used in the construction of bridges, buildings, and manufactories. The load-bearing capacity of these structures could be reduced due to execution and design errors, corrosion, aggressive environments, changing of design codes or the function of constructions, etc. The use of composite materials for strengthening and rehabilitation of reinforced concrete structures has been one of the most promising technologies in the field of structural materials engineering in recent decades. The deterioration of the structures due to the fall of the mechanical properties of the materials requires the development of new techniques of rehabilitation and reasonable control of the behavior of constitutive materials. Thus, knowledge of the mechanical behavior of the constituent materials and their loading history (at any point in the structure) is necessary to evaluate the strength of a structure and its durability. The experimental investigation is a highly resource-demanding process. Finite element (FE) simulation reduces the cost of scientific research, but the choice of the right modeling strategy is crucial for proper results especially when the confined zone of a strengthened concrete section has to be simulated.

Keywords: Reinforced concrete, Column, Corbel, Strengthening, CFRP, Finite element analysis, CDP model.

INTRODUCTION

The RC corbel is imposed on compression, tension, shear loads, and bending. The importance and the complexity of the mechanical behavior of these structures lead the researcher to investigate different strategies for strengthening and repairing [1], [2], [3]. The solution of strengthening the structures with carbon fiber-reinforced polymers (CFRP) is promising, but there is a lack of knowledge on how to improve the load-bearing capacity. The use of experimental research which results serves for validating the FE simulation provides a robust framework extending the tools for detailed investigation of the mechanical behavior of constitutive materials.

An experimental champagne was developed to characterize the constitutive materials. The obtained data is needed to be introduced in FE simulation. Special attention was paid to characterizing the CFRP mechanical behavior because the obtained data is crucial for cohesive zone modeling.

The considered model of RC corbel was developed by [4] and later extended by [5]. This paper aims to simulate the mechanical behavior of RC corbel strengthened by wrapping with three layers of CFRP because in this model, the confined zone of concrete could be highlighted. The

first validation of the FE model was done by a nonstrengthened RC corbel and then, parametrical research was performed with RC corbel strengthened by wrapping with three layers of CFRP. Four models were developed using different strategies of strengthening as below:

- Model with “Tie” contact
- Model with “Cohesive” type contact
- Model with additional cohesive FE elements
- 3D deformable elements for the composite layers and for the epoxy resin separately

EXPERIMENTAL WORK

The experimental work done by [1] was used, to validate the FE model. Nevertheless, an experimental campaign was conducted, for characterising the mechanical properties of constitutive materials. The constitutive materials are concrete, steel bars reinforcements, epoxy resin adhesive, and carbon fabrics, Table 1. The concrete compressive strength was characterized by cylindrical specimens whose dimensions are 320mm in height and 160mm in diameter. The specimens were tested through a special tool named compressometer. This tool provides four gauge measuring deformation. Three of them are placed vertically, measuring the longitudinal deformation and the resting one measure the transversal deformation. With this tool, the concrete compressive strength, Young's Modulus, and Poisson's ratio were obtained. The other materials where tested by simple tension.

Table 1 - Properties of constitutive materials.

Materials	**Young's Modulus (GPa)**	**Ultimate Strength (MPa)**	**Poisson's ratio**
Concrete	30±2	33.2±2	0.25
Steel bars	200±1	610±10	0.3
Adhesive	4.1±1	36±1	0.41
Fabrics	86±1	775±65	0.45

The column of the RC corbel has a 1,00m height and the section of the column is 150/300mm. The corbel is trapezoidal with a cantilever encastred symmetrically on both sides of the column. The length of the cantilever projection of RC corbels is 250mm, with 150mm width. The dimensions of the structure are presented in Figure 1. The reinforcement of the column consists four longitudinal bars with a 14mm diameter and a stirrup paced every 90mm. The main reinforcement of the RC corbel is a 10mm diameter placed at 25 mm from the top edge of the horizontal concrete surface. Two crossbars with the same diameter were welded to ensure the anchorage of the main reinforcements, at its ends. Strain gauges were glued to the steel reinforcement to measure the strain during the experimental tests. The strain gauges were protected from humidity and physical damage. To reduce interference induced during testing by other machines three-wire cable was soldered to the strain gauge. Wood plates were placed at the support, to avoid the local crushing of the concrete. The structure where tested in a revers position compared to the reality. The load on the corbel is applied as a reaction produced by a hydraulic jack acting on the base of the column.

FE SIMULATION

One very important step in preparing the model for FE simulation is the proper choice of mechanical behavior of constitutive materials. For the concrete "Concrete Damaged Plasticity" (CDP) model were applied, because the failure mechanism assumed is tensile cracking and compressive crushing, and also it could reproduce the irreversible deformations.

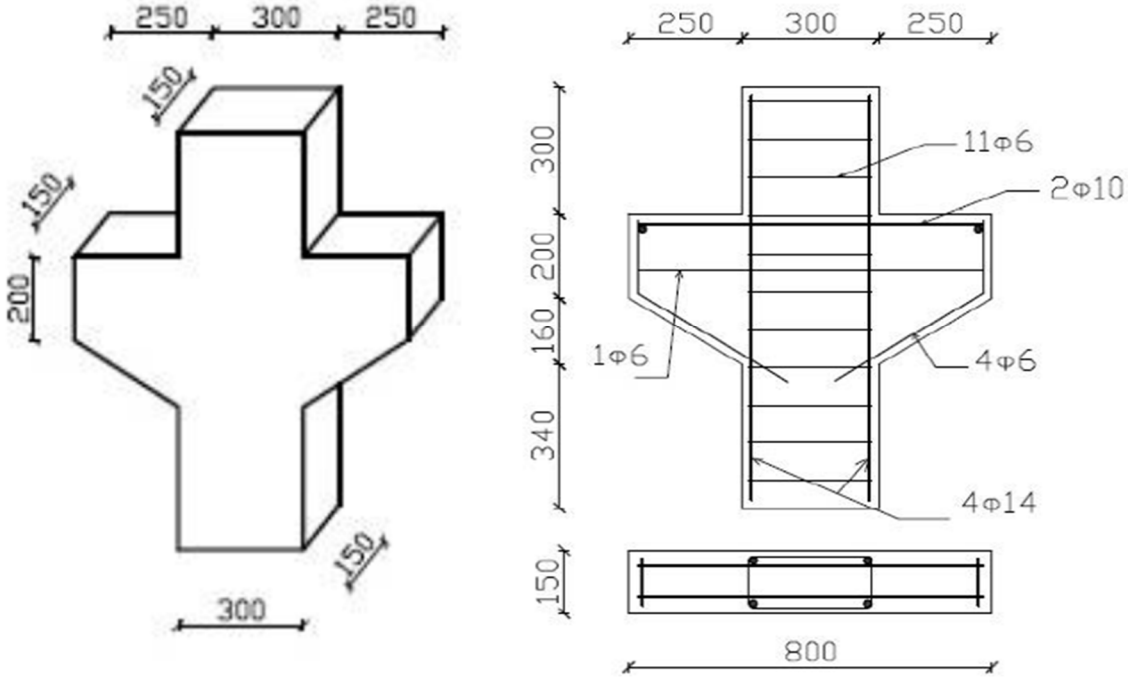

Fig. 1 - Dimentions of RC corbel [1].

The CDP model for the concrete section was incorporated by [2] and later was extended by [3] for cyclic loading. In this model, five parameters describe the failure mechanism of concrete:

- dilation (dilatancy angle) angle ψ measured in the p–q plane at high confining pressure – applied value - 36;
- flow potential eccentricity - ϵ, defining the rate at which the hyperbolic flow potential approaches its asymptote - applied value 0.1;
- ratio between the biaxial compressive yield strength *fb0*and the uniaxial compressive yield strength *fc0* - applied value -1.16;
- ratio of the second invariant of the stress on the tensile meridian, defining the form of the yield surface. The following conditions have to be met $0.5 < Kc < 1$, applied value – 0.66;
- viscosity parameter μ - not applied for explicit analysis.

In the nonlinear analysis need to be introduced the stress-strain curve in compression and in tension. But if we want to simulate the crack pattern, the damage parameter has to be introduced. The damage parameter – D describes the change of Young's Modulus during the loading. This parameter varies from 0 to 1. When D = 1, the structure is completely collapsed, but when D=0, the Hook's low is valid. Based on the experience of [4] the model proposed by [5] was applied. This model is developed based on the research of [6] and [7]. In the model, the compressive behavior curve is divided into three parts Figure 2. The first part is linear, and it is

based on Eurocode EN 1992-1-1. The second and third parts describe the nonlinear behavior under cyclic load. The slope given by the cyclic load represents the damage parameter D.

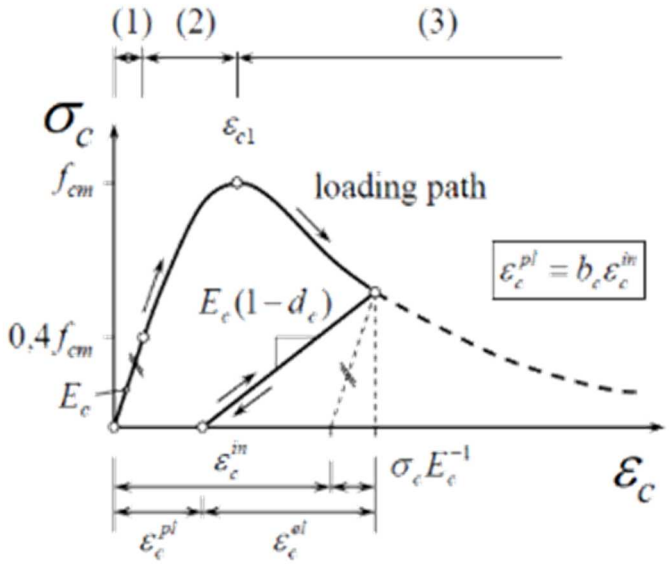

Fig. 2 - Compressive behavior of concrete [2].

$$\sigma_{c(1)} = E_{ci}\varepsilon_c \tag{1}$$

$$\sigma_{c(2)} = \frac{E_{ci}\frac{\varepsilon_c}{f_{cm}} - \left(\frac{\varepsilon_c}{\varepsilon_{cm}}\right)^2}{1 + \left(E_{ci}\frac{\varepsilon_c}{f_{cm}} - 2\right)\frac{\varepsilon_c}{\varepsilon_{cm}}} f_{cm} \tag{2}$$

$$\sigma_{c(3)} = \left(\frac{2 + \gamma_c f_{cm}\varepsilon_{cm}}{2f_{cm}} - \gamma_c\varepsilon_c + \frac{\varepsilon_c^2\gamma_c}{2\varepsilon_{cm}}\right)^{-1} \tag{3}$$

$$\gamma_c = \frac{\pi^2 f_{cm}\varepsilon_{cm}}{2\left[\frac{G_{ch}}{l_{eq}} - 0.5 f_{cm}\left(\varepsilon_{cm}(1-b) + b\frac{f_{cm}}{E_0}\right)\right]^2} \tag{4}$$

G_{ch} - cracking energy

l_{eq} - characteristic length, which depends on the mesh size, the type of finite element and the direction of the crack

f_{cm} – the compressive strength of concrete

$$\frac{\sigma_t(w)}{f_{tm}} = \left[1 + \left(c_1\frac{w}{w_c}\right)^3\right]e^{-c_2\frac{w}{w_c}} - \frac{w}{w_c}(1 + c_1^3)e^{-c_2} \tag{5}$$

$$d_t = 1 - \frac{1}{2 + a_t}\left[2(1 + a_t)\,exp\left(-b_t\varepsilon_t^{ck}\right) - a_t\,exp\left(-2b_t\varepsilon_t^{ck}\right)\right] \tag{6}$$

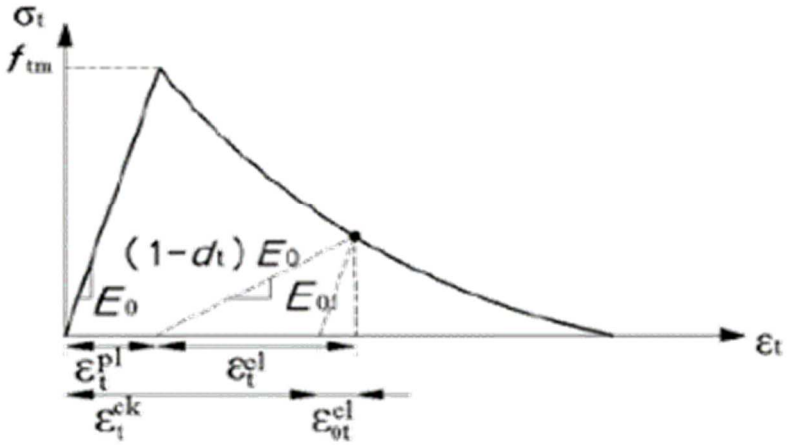

Fig. 3 - Strain-stress curve in tension of concrete [2].

$$b_t = \frac{f_{t0} l_{eq}}{G_f}\left(1 + \frac{a_t}{2}\right) = \frac{0.453 f_{ck}^{2/3}}{G_f} l_{eq} \tag{7}$$

W_c – the rupture □ra□k opening
f_{tm} – tensile strength
G_f – □ra□king energy
C1 and C2 – □oeffi□ient □al□ulated a□□ording to CEB-FIB 2010

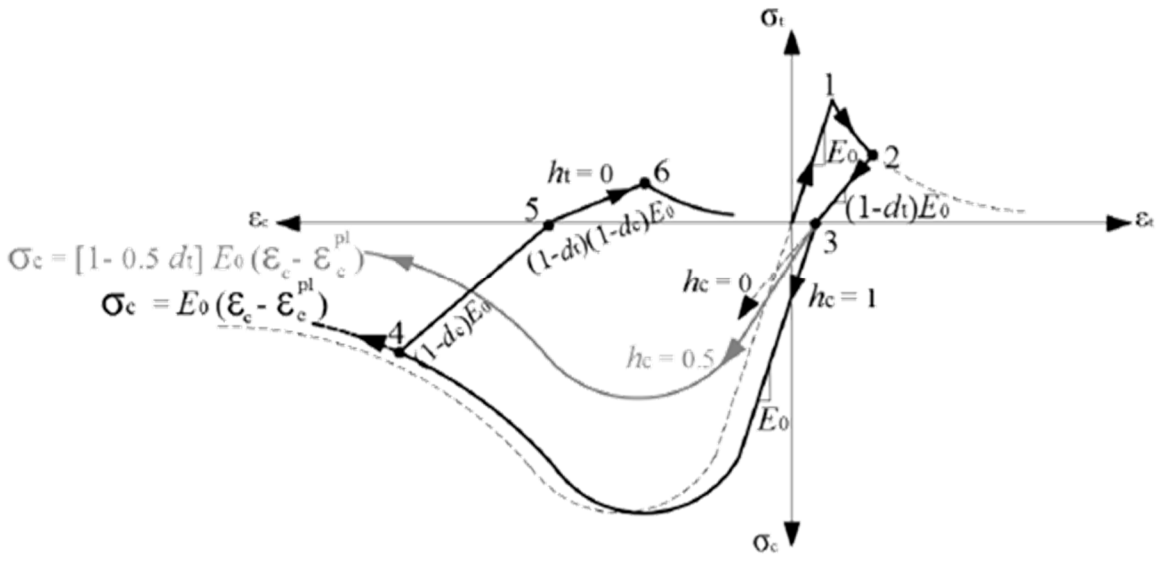

Fig. 4 - Behavior of concrete under cyclic load for CDP model [2].

$$d_c = 1 - \frac{1}{2+a_c}\left[2(1+a_c)\,exp(-b_c\varepsilon_c^{ch}) - a_c\,exp(-2b_c\varepsilon_c^{ch})\right] \tag{8}$$

$$b = \frac{\varepsilon_c^{pl}}{\varepsilon_c^{ch}} \qquad b_c = \frac{1.97(f_{ck}+8)}{G_{ch}}\,l_{eq} \qquad a_c = 7.873 \tag{9}$$

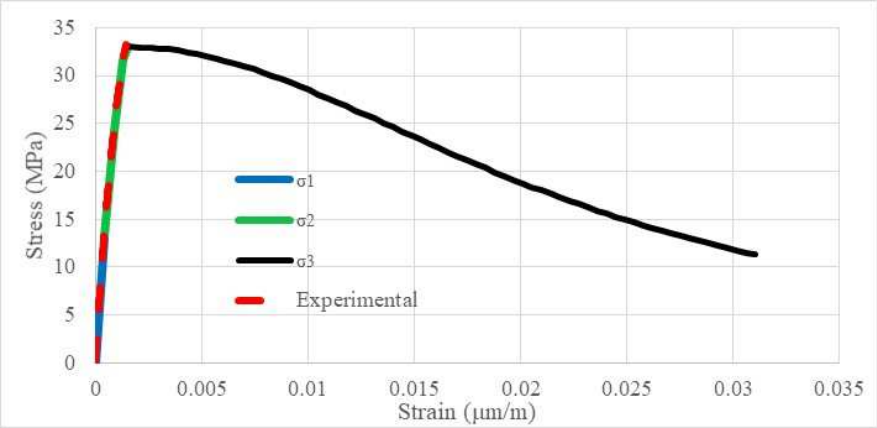

Fig. 5 - Comparing the experimental result with CDP model.

Figure 5 shows a comparison of the experimental result with the CDP model. The experimental data is presented with a red dashed line. The first linear part of the curve is given with a blue line, the second ascending part is given with a green line and the last descending part is given with black line. It could be noted, that the experimental data fits very well with the analytical model.

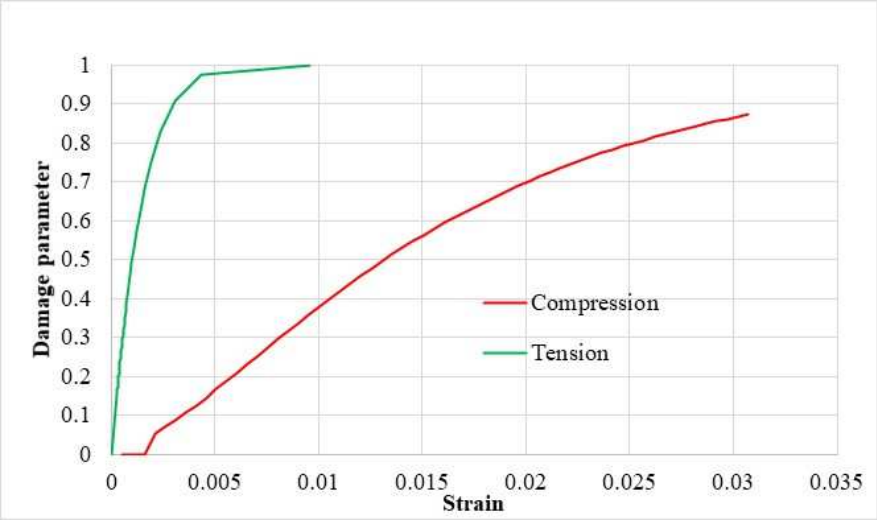

Fig. 6 - Damage parameter in tension and in compression.

Figure 6 shows the calculated damage parameters for the behavior on tension (in green) and in compression (in red), calculated based on the previously described equation for the CDP model. For the steel reinforcement Elastic-perfectly plastic models are applied. The behavior model is presented in Figure 7.

The data obtained from the experimental campaign for the adhesive is insufficient for nonlinear analysis. An additional finite element where used, for the adhesive, named cohesive element. This element helps the simulation for correct transmitting of the displacements of the no-coincided nodes between the concrete surface and CFRP. The cohesive elements have only a

translation degree of freedom. The Traction-Separation Law was used to define the behavior of adhesive. This model consists three components of separation – two parallel to the interface and one perpendicular. The base model of the Traction-separation Law is depicted in Figure 8.

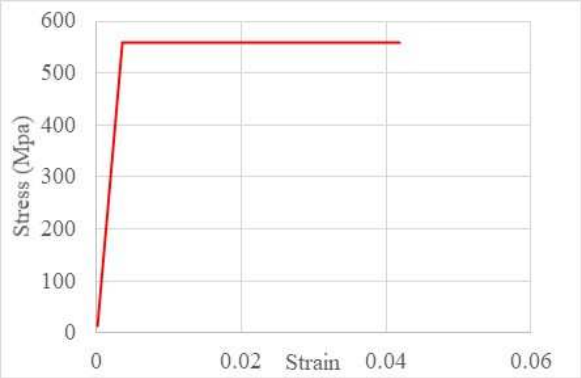

Fig. 7 - Elastic-perfectly plastic models for steel reinforcement.

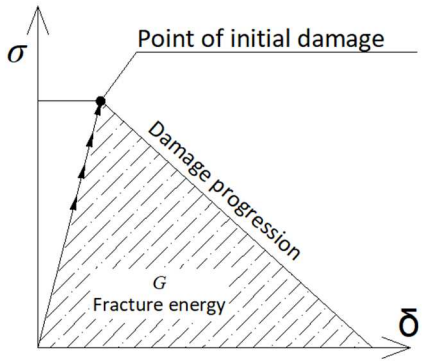

Fig. 8 - Traction-separation Law.

The strain-stress curve of the behavior starts with a linear increasing of stress until the initial point of damage. After that, a loss of rigidity of the structure appears and a reduction of the stress. The obtained closed surface by the curve gives the fracture energy of the structure. The chosen criterion for initial damage is the quadratic nominal strain criterion, where the damages start when a quadratic interaction function involving the nominal strain ratios reaches a value of one and it is presented by the fooling equation [3], [4]:

$$\left\{\frac{\langle\varepsilon_n\rangle}{\varepsilon_n^0}\right\}^2 + \left\{\frac{\varepsilon_s}{\varepsilon_s^0}\right\}^2 + \left\{\frac{\varepsilon_t}{\varepsilon_t^0}\right\}^2 = 1 \tag{10}$$

According to [3] an effective displacement have to be introduced as follow:

$$\delta_m = \sqrt{\langle\delta_n\rangle^2 + \delta_s^2 + \delta_t^2} \tag{11}$$

Figure 9 describe the traction-separation behavior for mixed mode of damage. The stress acting at the interface of material is traction, which is presented on the vertical axis. The other two axes present the magnitude of normal and shear separation. The unshaded triangles on vertical planes describe the pure mode of normal and shear stresses. The mixed mode damage is represented by the intermediates planes combined with the vertical axis, because of the traction applied.

The fracture energy depends on the mixed mode and it can be defined by power law fracture criterion. This criterion states that failure under mixed-mode conditions is governed by a power law interaction of the energies required to cause failure in the individual modes and it's given by the following expression:

$$\left\{\frac{G_n}{G_n^C}\right\}^\alpha + \left\{\frac{G_s}{G_s^C}\right\}^\alpha + \left\{\frac{G_t}{G_t^C}\right\}^\alpha = 1 \tag{12}$$

When $G_s^C = G_t^C$ the critical fracture energies during deformation purely along the first and the second shear, directions are equal, it is recommended to use the Benzeggagh-Kenane fracture criterion (BK) [4]. This criterion is given by:

$$G_n^C + (G_s^C - G_n^C)\left\{\frac{G_S}{G_T}\right\}^\eta = G^C \tag{13}$$

With $G_S = G_s + G_t, G_T = G_n + G_S$ and η are material parameters.

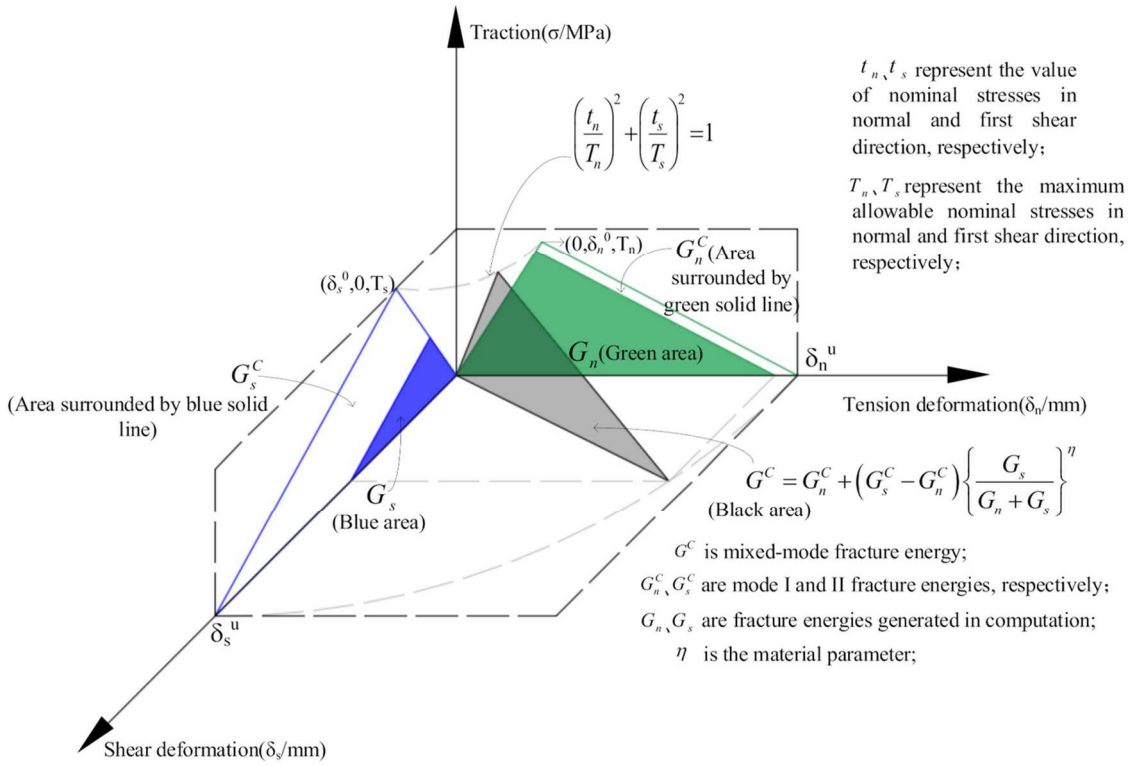

Fig. 9 - Mixed-mode response in cohesive elements [2].

The CFRP sheet was modeled using the HASHIN DAMAGE [5]model. This model is suitable for elastic-brittle materials because it can predict anisotropic damage. The failure modes are tension and compression separately for the matrix and for the fibers. The Young's Modulus of fibers E1 is calculated using the Rule of Mixture, where it is assumed, that the strain on fiber is equal to the strain on the matrix. E2 of the composite material was determined by the equation given by [6], [7].

$$\frac{E_2}{E_m}=\frac{1+\zeta\eta V_f}{1-\eta V_f} \tag{14}$$

$$\eta=\frac{\frac{E_f}{E_m}-1}{\frac{E_f}{E_m}+\zeta} \tag{15}$$

Where ζ – is a reinforcement geometrical parameter

E_f – Young's Modulus of fibres

V_f – fiber volume fraction

E_m – Young's Modulus of the matrix

$V_m = 1\text{-}V_f$.

Based on the research of [5] three layers of CFRP were considered in the model with a thickness of 0,566 mm. The aim of the article is to investigate different strategies for modeling the contact of CFRP sheets. Four models were developed with the following strategy:

- using constrain type Tie to connect the CFRP plies to, assuming perfect contact

- using cohesive behavior of contact for connection between CFRP and concrete surface

- using orphan mesh and defining additional finite cohesive elements, who are between the concrete surface and CFRP

- using a 3D deformable element for every plies of CFRP and for adhesive between plies depicted in Figure 10.

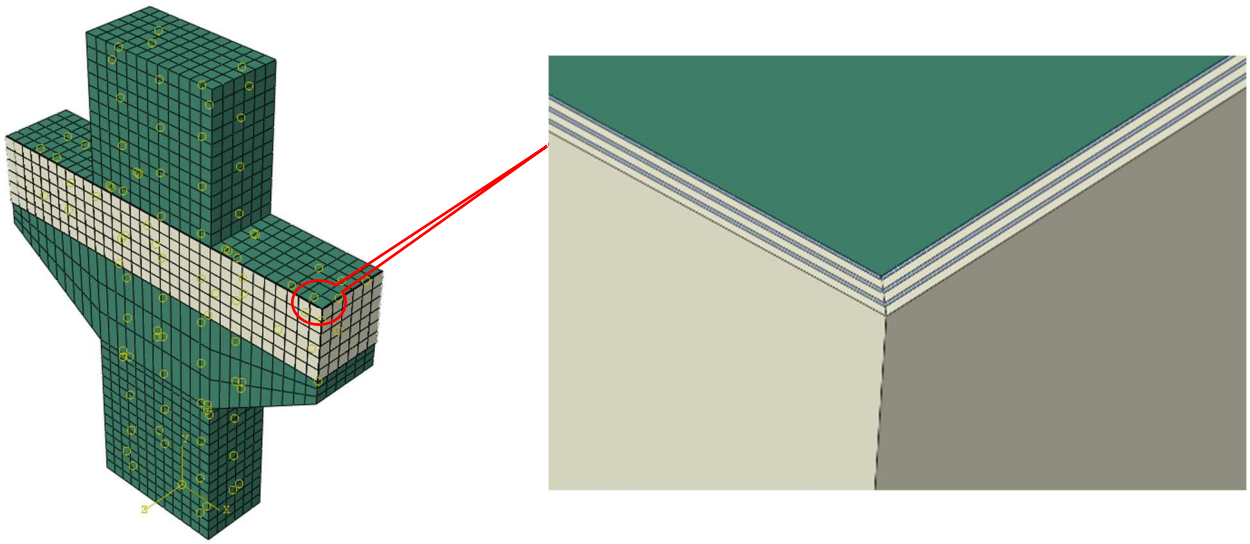

Fig. 10 - zoom on the corner of model of RC corbel strengthened with CFRP using 3D deformable elements for each plies.

The performed analysis is Dynamic Explicit. The finite elements used in the simulation are as follows:

- for the concrete section - an 8-node linear brick with reduced integration and hourglass control named C3D8R;

- for the CFRP sheet - a 4-node doubly curved thin or thick shell with reduced integration and hourglass control, finite membrane strains named S4R for all models except the model with 3D deformable elements for each ply;

- for the CFRP sheet with 3D deformable elements for each ply - an 8-node quadrilateral in-plane general-purpose continuum shell with reduced integration with hourglass control and finite membrane strains named SC8R;

- for steel reinforcement - a 2-node linear 3-D truss named T3D2;

- for adhesive - an 8-node three-dimensional cohesive element COH3D8.

The analysis is controlled by displacement. The steel reinforcement is dispersed in the concrete volume through using “Embedded region” technique. Smoot step is defined smoothly applying the load.

RESULTS AND CONCLUSIONS

On the main tensioned bars, a strain gauge was glued – G1 in the encastered zone. The data obtained from this strain gauge is compared with that obtained by the FE simulation. The FE model was successfully validated with the experimental data and comparative analysis was done with different modeling strategies.

Figure 11 presents the results from all models compared with the experimental data. The models with cohesive type contact and Tie contact gave the same results. The best result is obtained by the model with cohesive elements generated by orphan mesh. The stable time of the model with 3D deformable elements for each plies is 3.59153e-08.

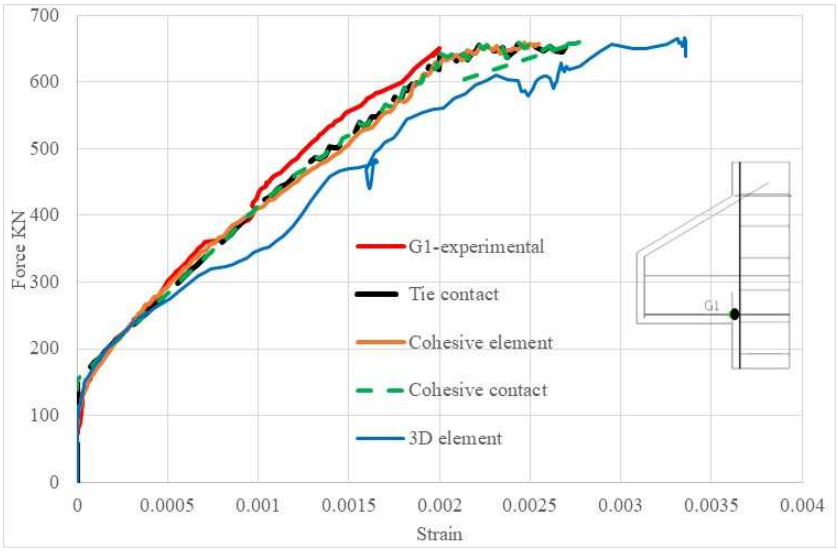

Fig. 11 - Comparing result from FE models with experimental data.

Compared with the others - 1.46552e-06 it is much less. That means that the model with 3D deformable elements for each ply could be optimized because it represents in a good way the delamination of the CFRP. Zooming on the Force-Strain curve it could be noticed - Figure 12, that the model with cohesive elements (brown line) and with 3D deformable elements are very close to the experimental data and represent the confined zone of concrete with acceptable accuracy.

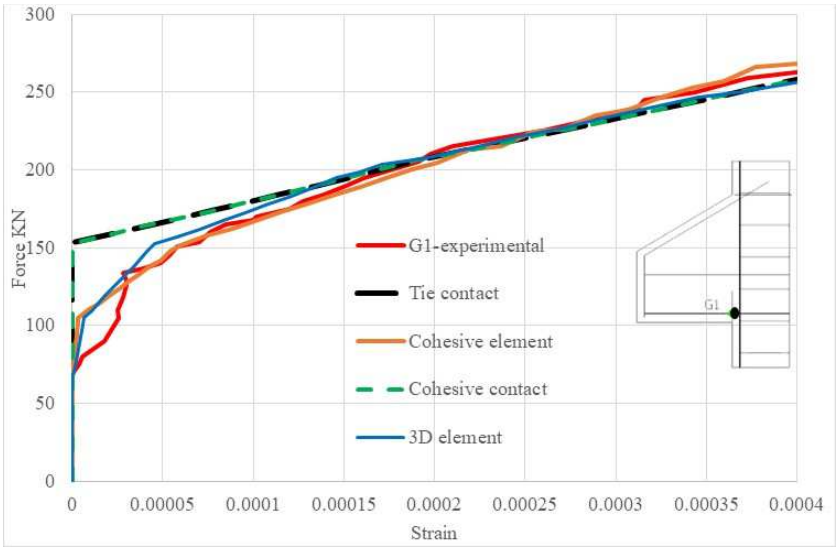

Fig. 12 - Zoom on the result comparing FE models with experimental data.

Observing the curve of the model with 3D deformable elements (blue line) in Figure 11, it could be concluded that this model loses stability. The possible reason for this phenomenon could be micro-crack propagation or plastic deformation because the strain at which the difference appears is almost the same - 7.37E-4. The most interesting FE model is this one with incorporated 3D deformable elements for the composite layers and the epoxy resin separately, but this model demands high resource consumption

CONCLUSION

The FE models were successfully validated with the experimental data. In this research, the best model, who clearly represent the crack pattern, load-bearing capacity, and the behavior of the main tensioned bars has a cohesive element. The model with incorporated 3D deformable elements is promising, but an optimization is needed.

ACKNOWLEDGMENT

This work was supported by the Bulgarian Foundation of Scientifical Research under contract КП-06-Н57/13-926, 2021- Mechanical investigation of reinforced concrete structures by natural fiber fabrics under dynamic loading.

REFERENCES

[1] V. Stankov, "Étude du comportement mécanique d'un assemblage poteau-console courte en béton armé renforcé ou réparé par collage de matériaux composites," 2021. [Online]. Available: http://www.theses.fr/2021REIMS026/document.

[2] V. Stankov, I. Ivanova, J. Assih, D. Dontchev, "Numerical modeling of mechanical behavior of a reinf orced concrete column-short corbel assembly strengthened by bonding a CFRF," IOP Conf Ser Mater Sci Eng, vol. 1276, no. 1, p.012023, Feb. 2023, doi: 10.1088/1757-899x/1276/1/012023.

[3] V. Stankov, I. Ivanova, J. Assih, D. Dontchev, "Numerical simulation of mechanical behavior of reinforced concrete column - short corbel assembly repaired and strengthened by bonding composite materials," IOP Conf Ser Mater Sci Eng, vol. 1323, no. 1, p.012008, Dec. 2024, doi: 10.1088/1757-899X/1323/1/012008.

[4] Khadraoui A. Delmas Y, "Analyse et modélisation du comportement mécanique des consoles courtes en béton armé," Thèse de doctorat, UFR Sciences de Reims, Reims, 1998.

[5] "Discipline : Génie Civil et Mécanique Ivelina Ivanova," 2013.

[6] J. Lubliner, J. Oliver, S. Oller, E. Oñate, "A plastic-damage model for concrete," Int J Solids Struct, vol. 25, no. 3, pp.299-326, Jan. 1989, doi: 10.1016/0020-7683(89)90050-4.

[7] J. Lee, G. L. Fenves, "Plastic-Damage Model for Cyclic Loading of Concrete Structures," J Eng Mech, vol. 124, no. 8, pp.892-900, Aug. 1998, doi: 10.1061/(ASCE)0733-9399(1998)124:8(892).

[8] B. Alfarah, F. López-Almansa, S. Oller, "New methodology for calculating damage variables evolution in Plastic Damage Model for RC structures," Eng Struct, vol. 132, pp.70-86, Feb. 2017, doi: 10.1016/j.engstruct.2016.11.022.

[9] Z.P. Bažant, B.H. Oh, "Crack band theory for fracture of concrete," Matériaux et Constructions, vol. 16, no. 3, pp.155-177, May 1983, doi: 10.1007/BF02486267.

[10] D.A. Hordijk, "Tensile and tensile fatigue behaviour of concrete; experiments, modelling and analyses," Heron, vol. 37, no. 1, 1992.

[11] M. Smith, ABAQUS/Standard User's Manual, Version 6.9. United States: Dassault Systèmes Simulia Corp, 2009.

[12] M.H. Kabir, S. Fawzia, T.H.T. Chan, M. Badawi, "Numerical studies on CFRP strengthened steel circular members under marine environment," Materials and Structures/Materiaux et Constructions, vol. 49, no. 10, pp.4201-4216, Oct. 2016, doi: 10.1617/s11527-015-0781-5.

[13] "Structural retrofitting of reinforced concrete beams using carbon fibre reinforced polymer yasmeen taleb obaidat." [Online]. Available: http://www.byggmek.lth.se

[14] P.P. Camanho, "Failure criteria for fibre-reinforced polymer composites," 2002.

[15] M. Kenane and M.L. Benzeggagh, "Mixed-mode delamination fracture toughness of unidirectional glass/epoxy composites under fatigue loading," 1997.

[16] Z. Hashin, "Failure Criteria for Unidirectional Fiber Composites," J Appl Mech, vol. 47, no. 2, pp.329-334, Jun. 1980, doi: 10.1115/1.3153664.

[17] J. Halpin, "Effects of environmental factors on composite materials," Ohio, 1996.

[18] J.C.H. Affdl, J.L. Kardos, "The Halpin-Tsai equations: A review," Polym Eng Sci, vol. 16, no. 5, pp.344-352, May 1976, doi: 10.1002/pen.760160512.

[19] "Discipline : Génie Civil et Mécanique Ivelina Ivanova," 2013.

Proceedings IRF2025: 8th International Conference on Integrity-Reliability-Failure
In Engineering, Materials, Manufacturing and Biomechanics. Porto 15-18 July 2025
DOI: https://doi.org/10.24840/978-972-752-323-8

PAPER REF: 22446

SENSITIVITY ANALYSIS OF A RAILWAY TEMPERATURE PREDICTION MODEL

Ary V.N. Frigeri[1(*)], Rubia M. Bosse[1], Paulo A.G. Piloto[2], Manuel Minhoto[2]

[1]Federal University of Technology - Paraná, Guarapuava, Brazil
[2]GICoS, Instituto Politécnico de Bragança, Portugal
[(*)]*Email:* aryviniciusnf@gmail.com

ABSTRACT

Rail temperature prediction plays a crucial role in ensuring railway safety, as extreme temperatures can cause local buckling and track instability. This study conducts a reliability-based sensitivity analysis of a previously developed prediction model using MATLAB and UQLab. Two analyses were performed: a global sensitivity analysis considering all parameters as random variables and a Data-Driven Sensitivity Analysis incorporating measured data for key variables to refine the model and enhance its practical applicability. Results indicate that uncertainties in convection and solar absorption are the most influential parameters affecting the response statistics of the rail temperature predictions. Future work will focus on refining parameter distributions and conducting Monte Carlo simulations to improve model accuracy and assess its reliability in unmeasured conditions.

Keywords: Railway, prediction model, temperature, sensitivity analysis.

INTRODUCTION

Rail temperatures play an important role in a railway track mechanical behaviour. High temperatures can lead to track buckling, whereas low temperatures can cause fragile rupture. Railways are structures exposed to open weather conditions with a high amplitude of temperature changes during the day and over the seasons. Thus, prediction models have been developed to predict these temperatures and predict instabilities before they happen (Wu et al., 2010). This study conducts a reliability-based sensitivity analysis of a previously developed prediction model to identify the evaluate the influence of parameter uncertainties on rail temperature predictions. The prediction model was implemented in MATLAB, and the UQLab toolbox was utilized to perform the analysis (Marelli et al., 2022).

METHODS

The model is described in Equation (1) and uses an energy balance to model the temperature of the rail (T_r) and takes into consideration other parameters such as solar radiation (SR), convection coefficient (h_{conv}) and other geometric considerations (Piloto et al., 2022; Zhang et al., 2008). Two main sensitivity analyses are presented. First considering all parameters of the model as random variables and second excluding parameters when measured data is available. In both cases, parameters are modelled with uniform distributions within a given range. In this paper, we are using mainly Sobol Indices (SI) to measure the sensitivity of the prediction model.

$$SR \cdot \alpha_s A_s - \left[h_{conv} A_c (T_r - T_{air}) + \epsilon_{res} \sigma A_r \left(T_r^4 - T_{sky}^4\right)\right] = \rho C V \frac{dT_r}{dt} \quad (1)$$

For the second analysis, field measured data (Piloto et al., 2022) of solar radiation, ambient temperature (T_{amb}) and convection coefficient by using Equation (2) are used, thus not

modelling them with a probability distribution. Additionally, in the first analysis, single step solutions of the model are used by UQLab to calculate the Sobol indexes, whereas on the second analysis, the solutions account for an entire day of measurements.

$$h_{conv} = \begin{cases} 5.6 + 4 \cdot w_s; w_s \leq 5m/s \\ 7.2 \cdot (w_s)^{0.78}; w_s > 5m/s \end{cases} \quad (2)$$

RESULTS AND CONCLUSIONS

The results of the first analysis (Figure 1a) show a strong dependency on the ambient temperature (T_{amb}), followed by the convection coefficient (h_{conv}) and the profile area subject to convection (A_c), indicating that that the predominant energy exchange type is via convection, since all these parameters form the convection part of the model. Since these parameters can easily be determined by measuring them, it is possible to remove most of the input random parameters from the analysis to further investigate the other predominant terms of the model, which is discussed in the second analysis. The second analysis (Figure 1b) indicates that the parameters with higher influence are: the area subject to the incoming solar radiation (A_s), followed by the area subject to convection (A_c). These results demonstrate that the most influential energy exchange methods might be convection and solar energy absorption. In addition, the latter might also support the efforts to better model the A_s parameter, not only as a probability distribution but with a deterministic approach as discussed in other studies (Hong et al., 2019; Piloto et al., 2022).

The next steps include refining statistical distributions for key parameters and conducting Monte Carlo simulations with them and comparing with measured data, to estimate how well the model behaves when extrapolating or modelling not-measured environment data.

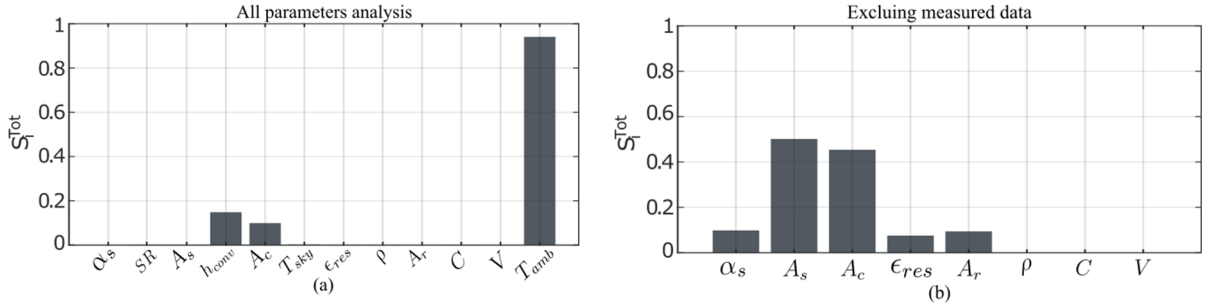

Fig. 1 - Total Sobol indices for different analysis.

REFERENCES

[1] Hong SU, et al. A Rail-Temperature-Prediction Model Considering Meteorological Conditions and the Position of the Sun. International Journal of Precision Engineering and Manufacturing. 2019;20(3): pp.337-346. doi:10.1007/s12541-019-00015-1

[2] Marelli S, et al. UQLab User Manual – Sensitivity Analysis. Chair of Risk, Safety and Uncertainty Quantification, ETH Zurich; 2022.

[3] Piloto PA, Frigeri AVN, Minhoto M, Silva DA. Validation of a rail temperature model with experimental measurements. Proceedings of the Institution of Mechanical Engineers, Part F: Journal of Rail and Rapid Transit. Doi:10.1177/09544097221074782.

[4] Wu Y, et al. A Review on Recent Developments in Rail Temperature Prediction for use in Buckling Studies. In: Conference on Railway Engineering; 2010.

[5] Zhang YJ, Lee S. Modeling Rail Temperature with Real-Time Weather Data. In: Transportation Research Circular. E-C126 2008.

Proceedings IRF2025: 8th International Conference on Integrity-Reliability-Failure
In Engineering, Materials, Manufacturing and Biomechanics. Porto 15-18 July 2025
DOI: https://doi.org/10.24840/978-972-752-323-8

PAPER REF: 22449

STRUCTURAL REHABILITATION: SOLAR DA BARONESA, SÃO JOÃO DEL REI - MG

Luciana Bracarense Coimbra[1(*)], Paloma Stefanie Silva[2]

[1]COARQ, Professor of the Architecture and Urban Planning Course (DAUAP), Federal University of São João Del Rei, São João Del Rei, Brasil.
[2]COARQ, Student of the Architecture and Urban Planning Course (DAUAP), Federal University of São João Del Rei, São João Del Rei, Brasil.
[(*)]*Email:* lubracarense.coimbra@ufsj.edu.br

ABSTRACT

With ongoing research, we seek to develop guidelines for intervention in Solar da Baronesa with a view to its structural rehabilitation. It is a 19th century building, inventoried and located in the Historic Center of the Municipality of São João Del Rei, MG. Once such a study has been launched, the need to expand the initial purpose with a prior design of the intervention that is identified as necessary is also moving forward.

Keywords: Structural rehabilitation, intervention guidelines, pathologies.

INTRODUCTION

The general theme of the research presented here – Structural Rehabilitation of Old Buildings – has as its preliminary focus a set of buildings already inventoried in the Historic Center of the Municipality of São João Del-Rei – MG. The choice of buildings from the selected set was based on the elements they have in common: (a) the time frame of the constructions, the 19th century (Figure 1); (b) the nature of damages and pathologies identified and recorded in the surveys. Among them, the object of study was the Solar da Baronesa, located at Rua Sebastião Sete, n°17 and n°21, heritage of the Federal University of São João Del Rei (UFSJ). Initially, the intention was to develop intervention guidelines with a view to its structural rehabilitation.

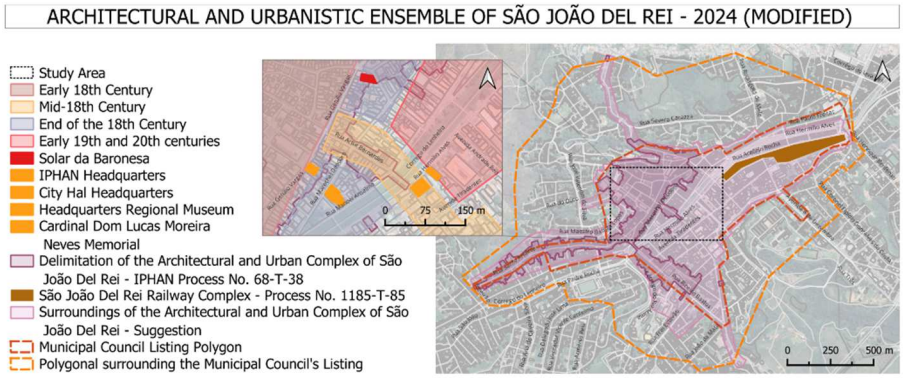

Fig. 1 - Delimitation of the municipality's preservation perimeters, highlighting, through stains, the time frame of the buildings and the study area. Source: IPHAN, edited by the authors. 2024.

Depending on the question to be answered "what type of guideline can be defined for an intervention based on a preliminary analysis of the stability and resistance conditions of the building?" some basic questions were asked: (a) Are there pathologies that compromise the stability of the building? (b) Is there any insecurity regarding the resistance of the building or

any of its elements? (c) How do the materials behave and how the structure works? It was hypothesized that the answers to such questions fall within the field of emergency and/or preventive needs, capable of avoiding greater and reckless damage; the team responsible for developing the restoration project is made up of four teachers (three architects and a civil engineer) and a graduate student in the scientific initiation phase, all from the Architecture and Urban Planning Course at UFSJ.

In an inspection and technical assessment carried out on 07/11/2024, by the office of the National Artistic Heritage Institute (IPHAN) of the municipality, pathologies and signs of degradation were identified in some rooms, frames and coverage, in addition to the need for repairs in specific locations.

RESULTS AND CONCLUSIONS

The conservation and restoration project of the Solar da Baronesa Cultural Center at UFSJ (Figure 2) will follow the standards determined by IPHAN, contained in the Manual for preparing cultural heritage preservation projects (Technical Notebooks 1).[1]

Fig. 2 - Panoramic view of Solar da Baronesa. Source: internet.

In this first stage (coverage recovery): updating the cadastral survey of the wooden frame and roof; analysis and evaluation of the state of conservation of the wooden framework of the roof structure, such as scissors, rafters and slats, checking for the existence of wood-eating insects, broken parts, missing parts or any problem that could compromise the safety of the roof of the old mansion; analysis of the degree of degradation of the tiles, porosity, broken tiles, lack of binding; analysis and selection of tiles that can be reused as “spout”; analysis of the eaves to identify points with infiltration of rainwater, the presence of vegetation trapped in the tiles and possible damage caused by these; whatever the solution adopted to restore the roof, it must receive a thermal blanket below the layer of tiles for better protection against rainwater infiltration.

REFERENCES

[1] Brasil. Patrimonial Letters. 3. ed. Rio de Janeiro: IPHAN, 2004.

[2] Cóias, V. Structural Rehabilitation of Old Buildings. 2. ed. Lisboa: IST PRESS, 2007.

[3] Cóias, V. Inspections and tests in building rehabilitation. 2. ed. Lisboa: IST PRESS, 2009.

[4] La Pastina Filho, J. Roof Conservation: manual. Brasília: IPHAN, 2005.

[1] Manual for preparing cultural heritage preservation projects. Prepared by José Hailon Gomide, Patrícia Reis da Silva, Sylvia Maria Nelo Braga. Brasília: Ministry of Culture, Monumenta Program Institute, 2005. (Technical notebooks 1).

Proceedings IRF2025: 8th International Conference on Integrity-Reliability-Failure
In Engineering, Materials, Manufacturing and Biomechanics. Porto 15-18 July 2025
DOI: https://doi.org/10.24840/978-972-752-323-8

PAPER REF: 22465

NUMERICAL AND EXPERIMENTAL INVESTIGATION OF REINFORCED CONCRETE BEAM STRENGTHENED WITH NATURAL FABRICS

Veselin Stankov[1(*)], Dimitar Dontchev[1], Ivelina Ivanova[2], Jules Assih[2], Ghiwa Bou Abdallah[1,2]

[1]Department of Applied Mechanic, University of Chemical Technology and Metallurgy, Sofia, Bulgaria
[2]Department of Civil Engineering, University of Reims Champagne-Ardenne, Reims, France
[(*)]*Email:* stankov_veselin@uctm.edu

ABSTRACT

Reinforced concrete (RC) beams are widely used structural elements in constructing buildings, manufactories, and bridges. However, these structures are exposed to different conditions, that reduce their load-bearing capacity such as excessive load, aggressive environment, and fatigue from dynamic loads. One traditional solution is to strengthen the structures using steel plates or fiber-reinforced polymers, but these solutions consider complex installation procedures, high costs, and environmental pollution. This study aims to explore the potential of natural fibers as an alternative for strengthening RC structures, finding sustainable and cost-effective strengthening techniques, and trying to reduce carbon emissions.

Keywords: Natural fabrics, reinforced concrete beam, strengthening, finite elements.

INTRODUCTION

The RC beams are a crucial structural element of buildings, bridges, etc. The need to extend their service life faces the structural engineer of choosing the right strengthening technic. Many researchers work on strengthening of RC structure[1], [2], [3]. However there is still a lack of knowledge in this field that prevents the industry to go further applying natural fibers. Combining numerical and experimental approaches, this study provides a robust framework for investigating the mechanical behavior of reinforced concrete beams strengthened by natural fibers.

The experimental investigation starts with characterization of vegetable fabrics and it was donne by [4]. Then, RC beam with and without strengthening was produced and subjected to four-point bending tests. The considered parameters are load-bearing capacity, mechanical behavior of tensile reinforcements, and crack propagation.

Using finite element (FE) analysis, a detailed model was developed. The model is calibrated and validated using the experimental data. Based on reliable FE model, parametric studies were conducted exploring the behaviour of RC beam strengthened by different configuration of natural fibers.

The results is promising and give the opportunities to extend the research and the use of these innovative materials in structural applications.

EXPERIMENTAL WORK

The experimental investigation starts with characterizing the constitutive materials. In this research, the natural fiber of hemp was considered. The constitutive materials are concrete, steel reinforcement, natural fabrics of hemp and adhesive. Every material was separately characterized.

Cylindrical specimens were produced to characterize the concrete, and tests were performed on compression. Normal concrete was used with a maximum aggregate of 16 mm. The cylinder dimensions are 160mm in diameter and 320mm in height. The cylinders were tested on compression and the compressive strength was obtained. The tension strength was obtained by a four-point bending test. Strain gauges were glued to capture the deformation with an acquisition system.

The steel reinforcements were characterized by a simple tensile test, but a strain gauge-type rosette was glued to measure the local deformation.

The hemp and the adhesive were also tested by a simple tensile test with a strain gauge-type rosette glued. The obtained data is given on Table 1.

Table 1 - Properties of constitutive materials.

Materials	Young's Modulus (GPa)	Ultimate Strength (MPa)	Poisson's ratio
Concrete	30±2	33.2±2	0.25
Steel bars	200±1	610±10	0.3
Adhesive	4.1±1	36±1	0.41
Hemp fabrics	63±5	24±3	

The considered experimental model is a simple beam subjected to four point bending. The beam has 2700 mm length, 130 mm width and 300 mm height, Figure 1.

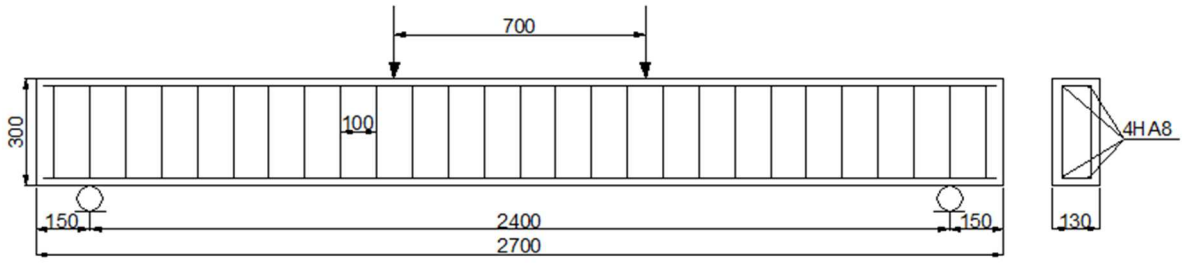

Fig. 1 - Dimensions of the beam

Strain gauges were glued on the tensioned steel reinforcements, who capture the deformation. The data were collected through acquisition system. Four-point bending were chosen to avoid shear stress.

NUMERICAL INVESTIGATION

Modelling the mechanical behaviour of concrete structure is significant challenge to the engineer because this material is anisotropic have completely different behaviour on traction and compression. The Concrete Damaged Plasticity model was chosen for the concrete material, because it can simulate the concrete behaviour with good accuracy and it is available on explicit analysis. The failure mechanism is described by 5 parameters as fallow:

- dilation (dilatancy angle) angle ψ measured in the p–q plane at high confining pressure – applied value - 36;
- flow potential eccentricity - ϵ, defining the rate at which the hyperbolic flow potential approaches its asymptote – applied value 0.1;
- ratio between the biaxial compressive yield strength *fb0*and the uniaxial compressive yield strength *fc0* - applied value -1.16;
- ratio of the second invariant of the stress on the tensile meridian, defining the form of the yield surface. The following conditions have to be met 0.5< *Kc*<1, applied value - 0.66;
- viscosity parameter μ - not applied for explicit analysis.

RESULTS AND CONCLUSIONS

Numerical simulation was developed, based on the experimental investigation. A simple experimental test was conducted for the characterization of constitutive materials. The data from this experimental campaign was introduced to the FE model.

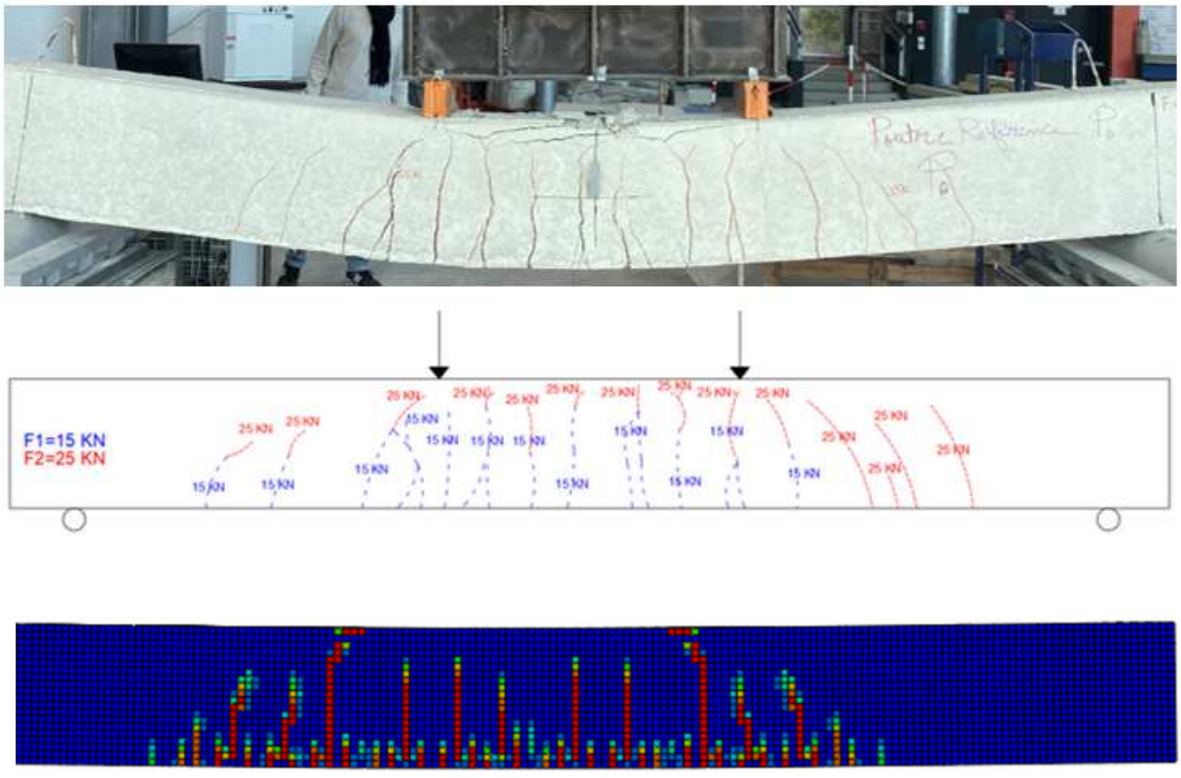

Fig. 2 - Crack pattern on Experimental and FE model.

Figure 2 presents the crack pattern on four point bending test on structure, compared with FE simulation. The load-bearing capacity, crack pattern, and mechanical behavior of the structure without strengthening were successfully reproduced. This validate the model and allow parametric studies. Different straightening configuration was tested as parametric analysis and the result was described. The analytical model used on the FE model was described by choosing the best model strategy. The result is promising and opens questions about future research.

ACKNOWLEDGMENT

This work was supported by the Bulgarian Foundation of Scientifical Research under contract КП-06-Н57/13-926, 2021- Mechanical investigation of reinforced concrete structures by natural fiber fabrics under dynamic loading.

REFERENCES

[1] V. Stankov, "Étude du comportement mécanique d'un assemblage poteau-console courte en béton armé renforcé ou réparé par collage de matériaux composites," 2021. [Online]. Available: http://www.theses.fr/2021REIMS026/document.

[2] V. Stankov, I. Ivanova, J. Assih, D. Dontchev, "Numerical modeling of mechanical behavior of a reinf orced concrete column-short corbel assembly strengthened by bonding a CFRF," IOP Conf Ser Mater Sci Eng, vol. 1276, no. 1, p. 012023, Feb. 2023, doi: 10.1088/1757-899x/1276/1/012023.

[3] V. Stankov, I. Ivanova, J. Assih, D. Dontchev, "Numerical simulation of mechanical behavior of reinforced concrete column - short corbel assembly repaired and strengthened by bonding composite materials," IOP Conf Ser Mater Sci Eng, vol. 1323, no. 1, p. 012008, Dec. 2024, doi: 10.1088/1757-899X/1323/1/012008.

[4] G. Bou Abdallah, "Renforcement de Structures en Béton Armé par des Matériaux Biosourcés," 2024. [Online]. Available: http://www.theses.fr/2024REIMS051/document.

Proceedings IRF2025: 8th International Conference on Integrity-Reliability-Failure
In Engineering, Materials, Manufacturing and Biomechanics. Porto 15-18 July 2025
DOI: https://doi.org/10.24840/978-972-752-323-8

PAPER REF: 22572

CONTRIBUTION TO THE STUDY OF THE INFLUENCE OF DATE PALM FIBERS ON THE CREEP AND RUTTING OF BITUMINOUS MIXTURES

Ferkous Saci Abdellhakim[1(*)], Ramdane Kahlouche[2]

[1]Civil engineering department, University M'Hamed Bougara Boumerdes,
[2]Public works department, University Mouloud Mammeri Tizi-Ouzou,
[(*)]*Email:* s.ferkous@univ-boumerdes.dz

ABSTRACT

The use of plant fibers as modifiers in bituminous mixtures has gained significant attention due to their potential to enhance mechanical properties and promote sustainability. This study explores the influence of date palm fibers (DPF) on the creep and rutting behavior of bituminous mixtures. An experimental campaign was conducted, preparing nine (09) mixtures with varying fiber lengths (1 cm, 3 cm, and 5 cm) and concentrations (0.1%, 0.3%, and 0.5%) using the dry process, alongside a control mixture. The mechanical performance was evaluated through a uniaxial static creep test, based on an oedometric apparatus, and a rutting test. The results reveal that both fiber content and length significantly influence the mixture's resistance to creep and rutting. Mixtures incorporating 3 cm fibers exhibited superior rutting resistance, while those with low fiber content (0.1%) demonstrated improved creep resistance. The study concludes that the mechanical behavior of fiber-modified mixtures is highly dependent on the deformation domain, with no direct correlation observed between creep and rutting performance. Furthermore, this research highlights the dual benefit of using date palm fibers: enhancing the mechanical properties of bituminous mixtures and valorizing an abundant agricultural waste material in our country. These findings contribute to the development of sustainable and high-performance asphalt mixtures, offering practical solutions for infrastructure improvement and waste management.

Keywords: Date palm fibers, creep behavior, rutting resistance, oedometric apparatus, sustainable development.

INTRODUCTION

Bituminous mixtures are the cornerstone of flexible pavement construction, prized for their durability, flexibility, and economic feasibility [1]. However, as traffic loads and environmental stresses on pavements increase, there is a growing demand for improved mechanical properties such as enhanced resistance to creep and rutting [2]. These deformations, which are caused by long-term exposure to traffic and temperature variations, undermine the service life of pavements, making it imperative to develop more robust asphalt mixtures [3], [4]. In this context, numerous studies have explored the potential of using various modifiers to improve the performance of bituminous mixtures, particularly through the incorporation of sustainable materials such as plant fibers. These fibers are renewable, environmentally friendly, and can significantly influence the rheological properties of asphalt [5]. Among the various fibers investigated, natural fibers such as cellulose, polypropylene, and rice husk have shown promise in enhancing the mechanical properties of asphalt mixtures [6], [7]. Date palm fibers, being abundant in arid regions and a byproduct of agriculture, have also attracted attention as a

potential modifier for bituminous mixtures [8]. Their low cost and availability make them an attractive alternative to synthetic modifiers [9].

The valorization of agricultural waste, such as date palm fibers, is a critical step toward sustainable development. In many regions, particularly in arid and semi-arid areas, date palm cultivation generates significant amounts of agricultural waste, including leaves, stems, and fibers [10]. These waste materials are often burned or discarded, contributing to environmental pollution and resource inefficiency [11]. By incorporating date palm fibers into bituminous mixtures, this study not only addresses the challenge of improving pavement performance but also contributes to the sustainable management of agricultural waste. Previous research has demonstrated that the use of agricultural waste fibers in construction materials can reduce environmental impact while enhancing material properties [12], [13]. Previous studies have demonstrated that the incorporation of fibers into bituminous mixtures can improve their resistance to fatigue, moisture damage, and thermal cracking [14]. Fiber reinforcement has been shown to reduce the potential for cracking and rutting by enhancing the mixture's resistance to permanent deformation under stress [15]. For instance, fibers like polypropylene have been studied for their ability to reduce the rate of creep under static load conditions [16], while cellulose fibers have been reported to improve the stiffness and fatigue properties of asphalt mixtures [6].

The mechanical performance of fiber-modified bituminous mixtures is influenced by multiple factors, including the type, length, and concentration of the fibers [5], [17]. Studies on the impact of fiber length have found that longer fibers generally improve rutting resistance but may reduce the resistance to creep [2]. Additionally, the interaction between fiber concentration and binder properties is critical, as excessive fiber content may disrupt the mixture's cohesion and reduce its workability [1]. Recent research has further highlighted the potential of natural fibers in improving the sustainability and performance of asphalt mixtures. For example, studies have shown that sisal and coir fibers can enhance the tensile strength and fatigue life of asphalt mixtures [18], [19]. Similarly, the use of jute fibers has been reported to improve the rutting resistance and aging resistance of asphalt binders [20]. Furthermore, the incorporation of waste materials such as recycled tire rubber and plastic fibers has been explored as a means of enhancing the mechanical properties of asphalt mixtures while addressing environmental concerns [21], [22]. Given the complexity of these interactions, further investigation into the specific effects of date palm fibers (DPF) on both creep and rutting behavior is warranted. By examining mixtures with varying fiber lengths (1 cm, 3 cm, and 5 cm) and concentrations (0.1%, 0.3%, and 0.5%), this study aims to provide valuable insights into how these variables affect the overall performance of bituminous mixtures under different deformation conditions. In particular, understanding the relationship between creep and rutting behavior in fiber-modified mixtures can help optimize their design for practical use in pavement construction [4], [23].

This study aims to evaluate the influence of date palm fibers on the creep and rutting behavior of bituminous mixtures, considering fiber length and concentration as key variables. By addressing the dual challenge of improving pavement performance and valorizing agricultural waste, this research contributes to the development of sustainable and high-performance asphalt mixtures for modern infrastructure needs.

MATERIALS AND METHODS

Asphalt

The physical properties of the binder used for this study are shown in Table 1. It is 35/50 penetration grade pure bitumen purchased from the Naftal Company, the most used product in road construction in Algeria.

Table 1 - Physical properties of asphalt.

Test type	Standard	Result	Algerian specifications
Penetration at 25°C (1/10mm)	EN 1426	42.3	40-50
Softening Point Ring and Ball "SPRB" (°C)	EN 1427	54.50	47-61
Ductility at 25°C (cm)	EN 13589	100	≥ 60

Aggregates

The aggregates used in this study are the fractions commonly used in Algeria for the production of bituminous mixes intended for wearing courses, taken from Ain Touta (Batna) quarry in the northern region of Algeria. Their characteristics are set in Table 2. They fully comply with Algerian specifications [24].

Table 2 - Characteristics of the aggregates – classes 0/3, 3/8, 8/15 and 7.2/10.

	Volume mass (t/m3)	LA	MDE
0/3	2.67	-	-
3/8	2.68	21.40	08.00
8/15	2.68	24.92	06.74
Algerian Specifications		≤ 25%	≤ 20%

Date palm fiber

Date palm fiber is extracted from the palm tree waste in Tamanrasset, in the southern region of Algeria. The following procedure is adopted: First, the palm fiber strips are separated into individual fibers in water to facilitate their defibration. The individual fibers are thoroughly washed with water mixed with a few drops of bleach to remove impurities and the lignin layer that surrounds the fibers and hinders adhesion. Then, the selection of fibers is based on their size and strength. Fibers with low strength and small dimensions are discarded to minimize variability. The selected fiber lengths are 1 cm, 3 cm, and 5 cm, while efforts are made to maintain a relatively uniform diameter along the useful section (see Figures 1-3). The fibers are cut to the required lengths using a razor blade.

Fig. 1 - Image of DPF of 1cm.

Fig. 2 - Image of DPF of 3cm.

Fig. 3 - Image of DPF of 5cm.

Asphalt mixtures

The studied formulation concerns a semi-coarse asphalt concrete (SCAC) 0/14, made from granular classes 0/3, 3/8, and 8/15, and a 40/50 grade bitumen. This type of bituminous concrete is frequently used for road surfacing.

The optimum binder content (OBC) of the mixtures was determined using the Marshall and Duriez tests [25, 26]. For the reference mix, the OBC value is 5.59%. The grading curve of the reference asphalt mix is presented in Figure 4. This is in accordance with the grading curve required for this type of asphalt concrete [24].

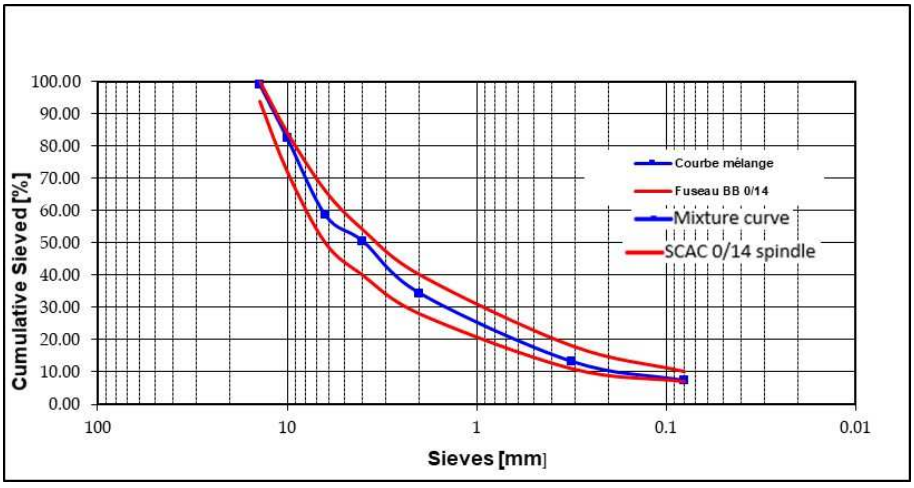

Fig. 4 - Grading curve of the reference asphalt.

Experimental Design

The experimental campaign aims to determine the influence of plant-based fibers on the mechanical properties of bituminous mixes. To achieve this, creep and rutting tests [27, 28] were conducted to evaluate the mixtures' resistance to permanent deformation. After establishing the control mix and its parameters, plant-based fibers were incorporated using the dry process, where they are added to the mixture during the mixing of components. Two variables were considered: the length and the concentration of the plant-based fibers. For the length, three values were chosen (1 cm, 3 cm, and 5 cm), and for the concentration, three percentages were selected (0.1%, 0.3%, and 0.5%) of the total mass of the mix. By combining these three lengths with the three percentages, nine (09) mixtures were prepared (Table 3 and Table 4).

Table 3 -The mixtures for different lengths and percentages of fibers.

Mixtures	1cm			3cm			5cm		
	0.1%	0.3%	0.5%	0.1%	0.3%	0.5%	0.1%	0.3%	0.5%

Table 4 - The percentage of fibers added for each dosage.

Fibers (%)	0.1%	0.3%	0.5%
Weight (g)	3.6	10.8	18

RESULTS AND DISCUSSION

Creep Behavior

To make the comparison of results as straightforward as possible, we will present the findings in two parts : first, we will examine the influence of the fiber content on deformation, and then, by fixing the fiber content, we will analyze the influence of the fiber length.

Influence of fiber content

We aim to investigate the influence of the added fiber content on the creep of asphalt mixes (with the fiber length parameter fixed), under a constant load of 10 kg and a constant temperature of 60°C. This is done by plotting the deformation-recovery curve of each mixture alongside that of the control sample for comparison (see Figures 5,7,9). For each curve, a bar graph is plotted to visually compare the improvement (see Figures 6,8,10).

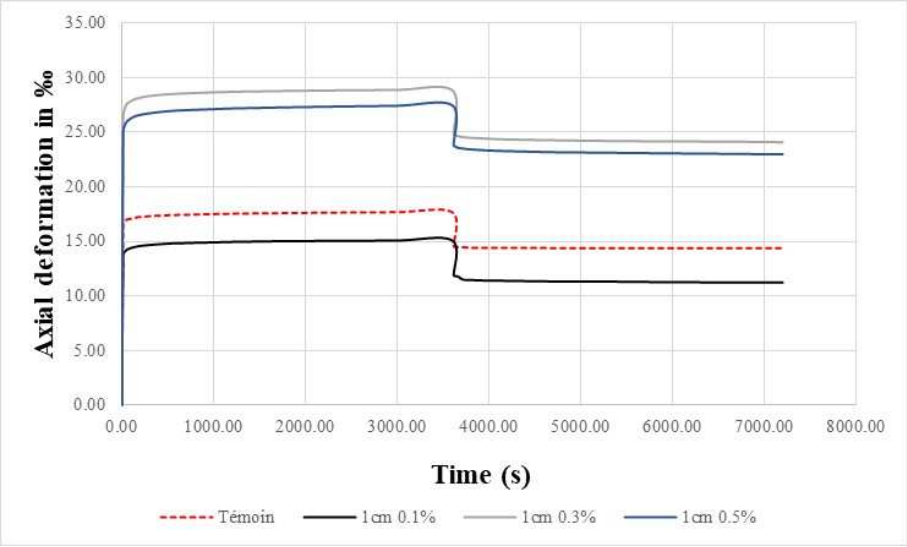

Fig. 5 - Creep-recovery curves for 1 cm fibers at different fiber contents.

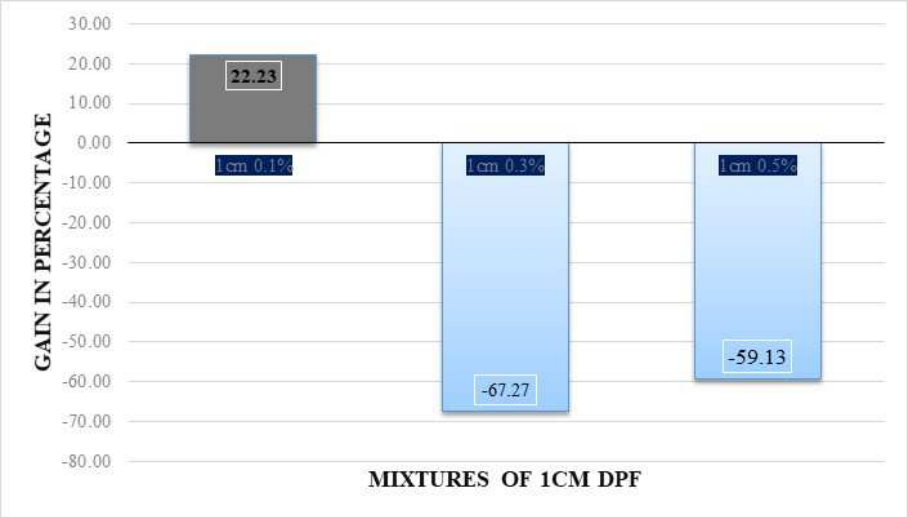

Fig. 6 - Improvements in 1 cm fiber mixtures.

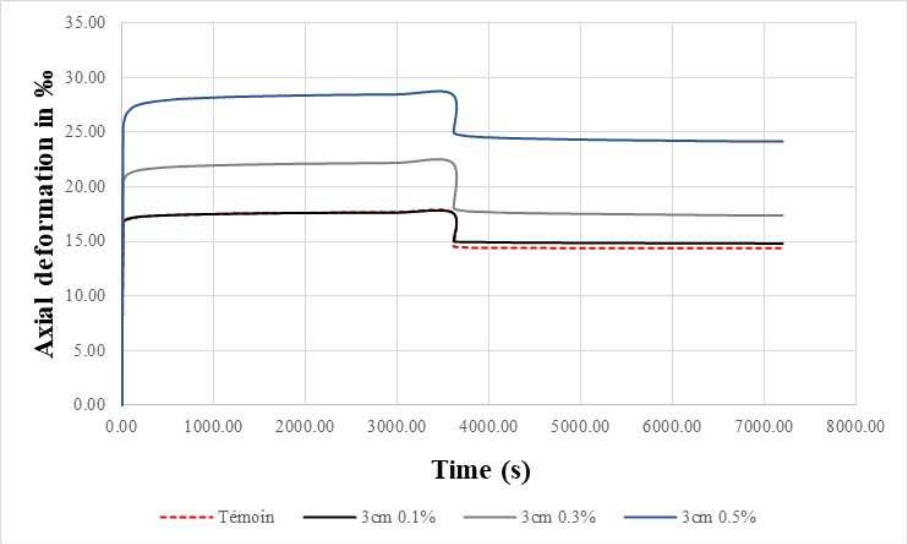

Fig. 7 - Creep-recovery curves for 3 cm fibers at different fiber contents.

Fig. 8 - Improvements in 3 cm fiber mixtures.

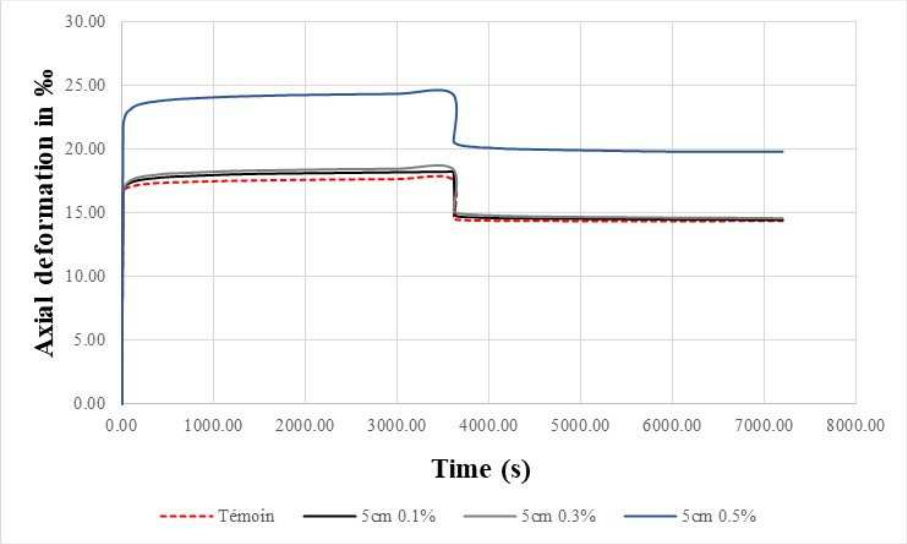

Fig. 9 - Creep-recovery curves for 5 cm fibers at different fiber contents.

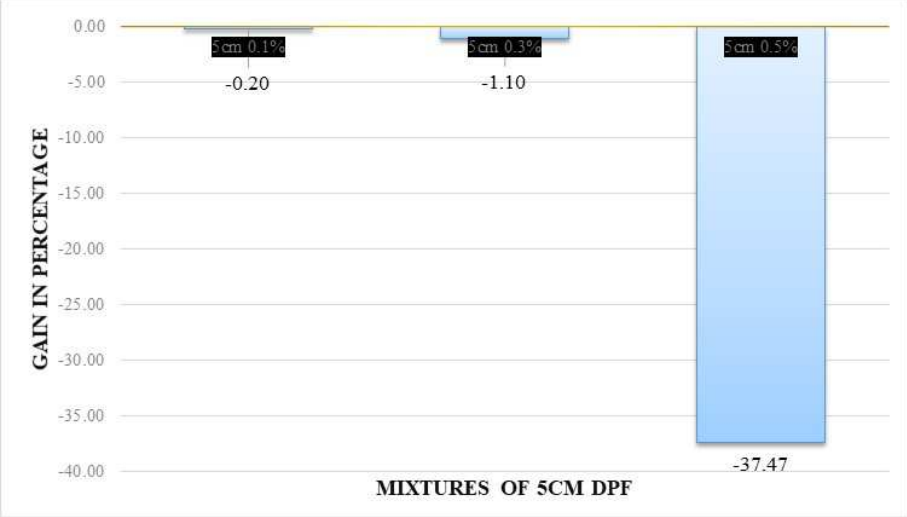

Fig. 10 - Improvements in 5 cm fiber mixtures.

Influence of fiber length

We aim to investigate the influence of the added fiber content on the creep of bituminous mixes (with the fiber content parameter fixed), under a constant load of 10 kg and a constant temperature of 60°C. This is done by plotting the deformation-recovery curve of each mixture alongside that of the control sample for comparison (see Figures 11, 13, 15). For each curve, a bar graph is plotted to visually compare the improvement (see Figures 12, 14, 16).

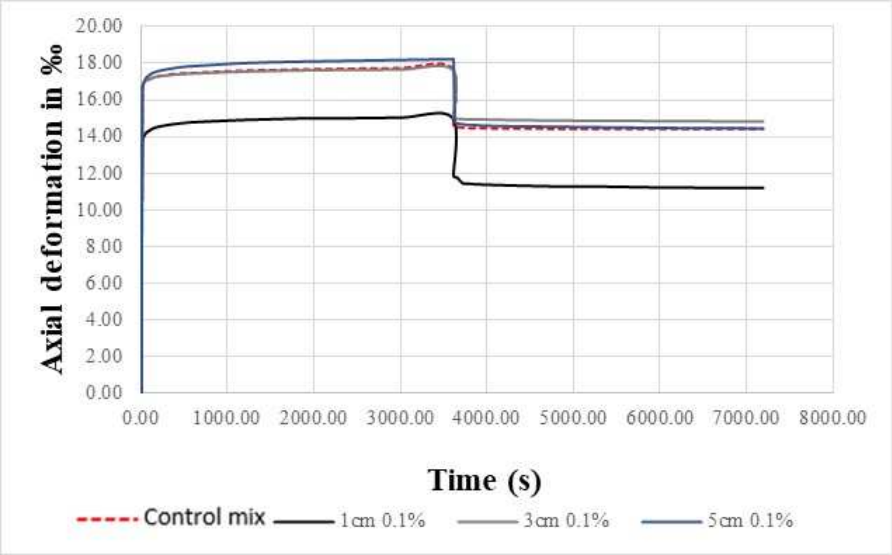

Fig. 11 - Creep-recovery curves of mixtures with 0.1% fiber content for different lengths.

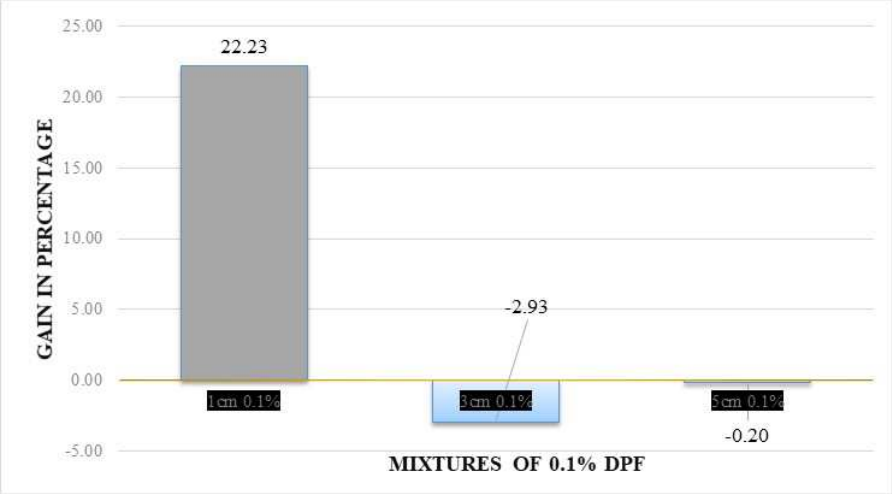

Fig. 12 - Improvements in mixtures with 0.1% fiber content.

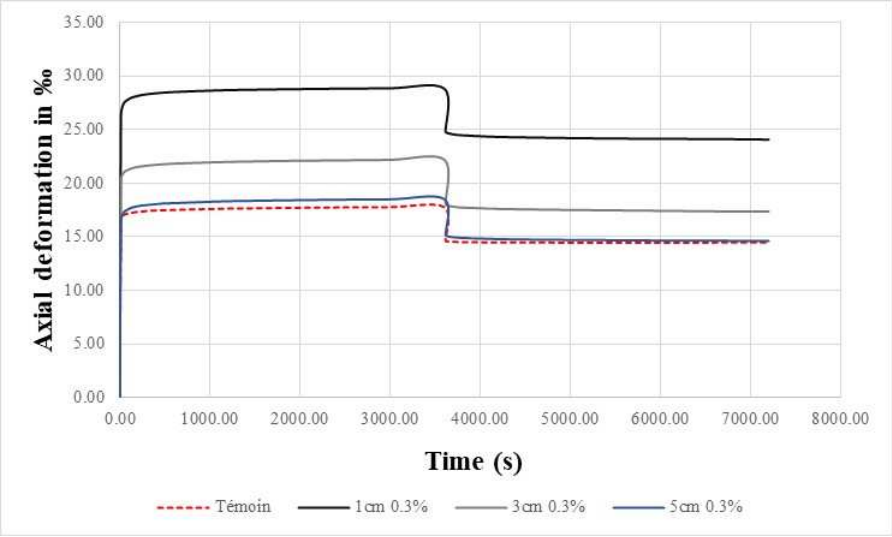

Fig. 13 - Creep-recovery curves of mixtures with 0.3% fiber content for different lengths.

Fig. 14 - Improvements in mixtures with 0.3% fiber content.

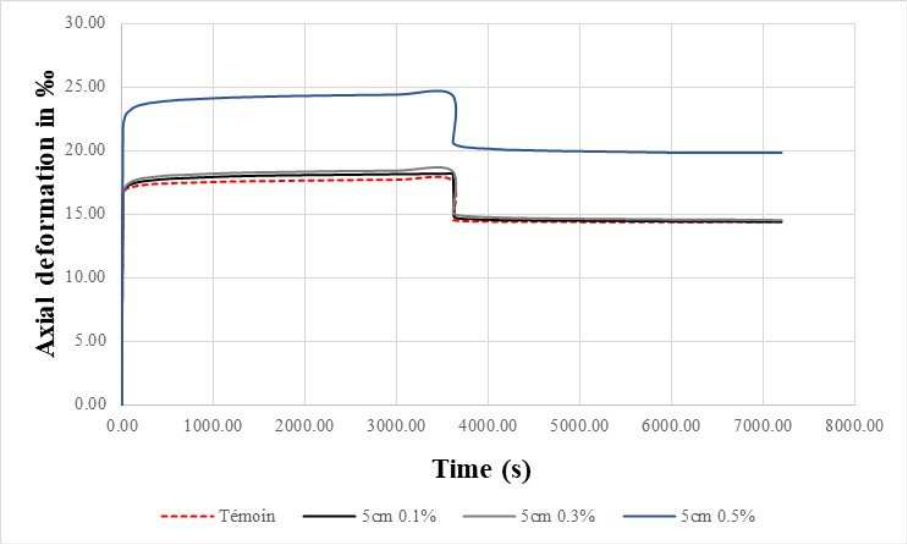

Fig. 15 - Creep-recovery curves of mixtures with 0.5% fiber content for different lengths.

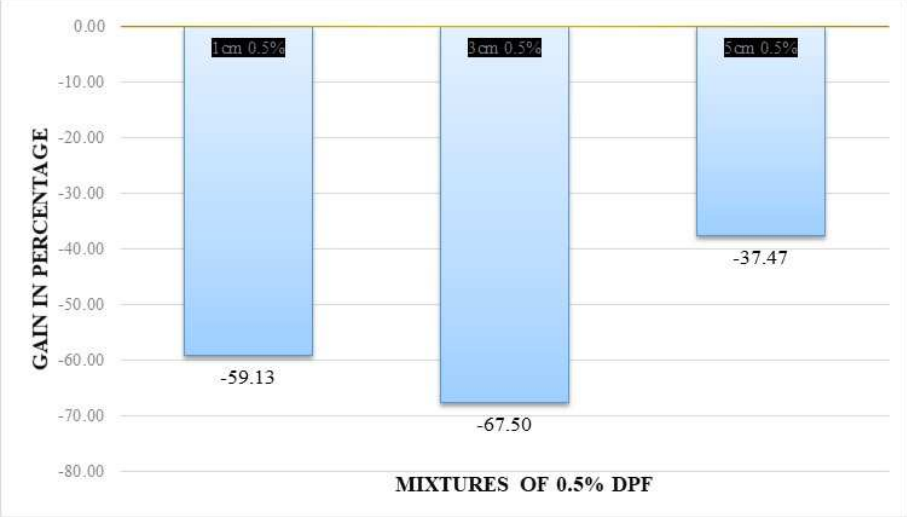

Fig. 16 - Improvements in mixtures with 0.5% fiber content.

Static creep tests have shown that all the tested mixes exhibited similar curves. These mixes all displayed irreversible permanent deformation after the recovery test. The results indicate that the general trend is a decrease in the creep resistance of the mixture, except for the case of mixtures with low fiber content (0.1%). When comparing the different mixtures in terms of improvement calculated based on the control mixture, from the perspective of fiber content, it is observed that mixtures with a fiber content of 0.1% generally show significantly higher improvements compared to other mixtures, which exhibit substantial declines. Furthermore, the mixture with 0.1% fiber content and 1 cm fiber length shows an improvement of 22.23%, while the other two mixtures with 0.1% fiber content and 3 cm and 5 cm fiber lengths show declines of less than 3%. However, observations based on fiber length do not provide any clear indication. As observed, the higher the fiber content, the lower the static creep resistance. This proportionality between fiber content and the percentage of voids is highlighted by the bar graph plotted from the PCG test for some mixtures (see Figure 17).

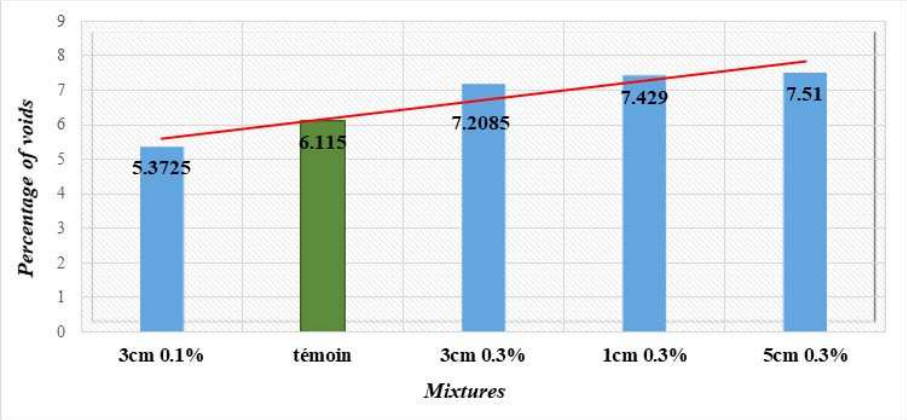

Fig- 17 - Percentage of voids for some mixtures.

Rutting Behavior

The test aims to evaluate, under given testing conditions, the rutting resistance of a bituminous mixture prepared and compacted in the laboratory. The rutting tests were conducted at the laboratory of EPTRC (Public Roadworks Company) in Berrouaghia, Medea Province, in the north region of Algeria. They allowed us to perform the test for five (05) mixtures: (control; 1 cm 0.3%; 3 cm 0.1%; 3 cm 0.3%; and 5 cm 0.3%).

The graph showed in Figure 18, illustrates the Rutting curves ln(RD) = fct(ln(N)). It is plotted as ln(RD) versus ln(N) for each specimen of the same composition subjected to the test. The values of the rut depth percentage (RD) at N load cycles are excluded if the rut depth exceeds 15% of the specimen's thickness after N load cycles [28].

The rutting tests (Figure 18) showed that all the tested mixes exhibited the same linear trend curves, with the general equation: $\ln(RD) = a \times \ln(N) + b$.

We compared all the results at the last point (N = 10,000 cycles, ln(N) = 9.21).

The results indicate that the mixtures with [3 cm 0.1%] and [3 cm 0.3%] provide better rutting resistance compared to the control mixture, unlike the other two mixtures [1 cm 0.3%] and [5 cm 0.3%].

For the same fiber content, 0.3%, the 3 cm mixtures perform better than the 1 cm and 5 cm mixtures. In terms of improvement, the 5 cm mixture shows a decline of over 14%. Between the two 3 cm mixtures, 0.1% and 0.3%, there is a slight difference (0.8%) in improvement (Figure 19).

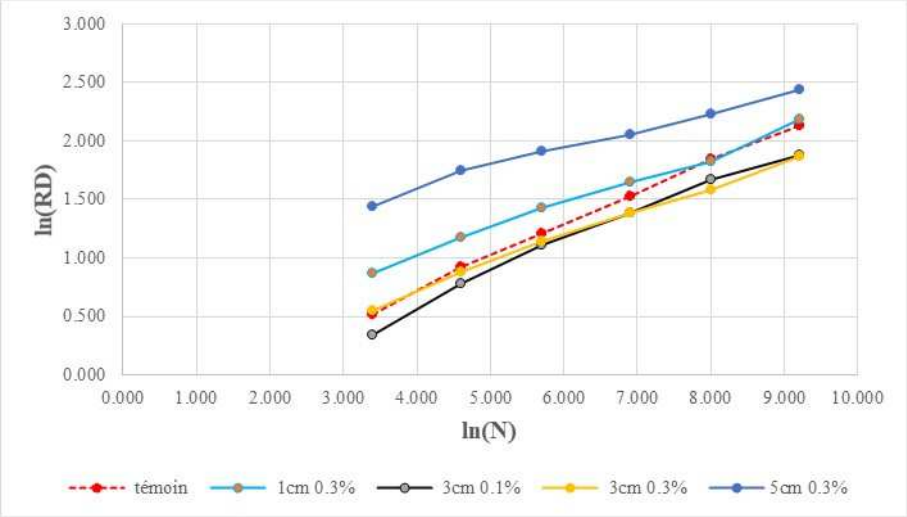

Fig. 18 - Rutting curves ln(RD) = fct(ln(N)).

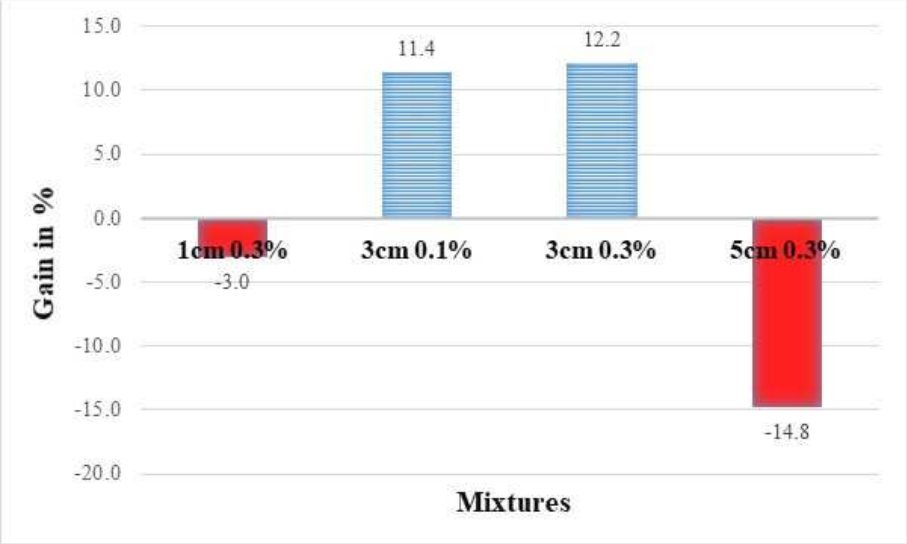

Fig. 19 - Improvement in rutting resistance for different mixtures.

CONCLUSION

In this work, we focused on modifying bituminous mixes using date palm fibers (DPF) from waste date palm trees and studying their influence on creep and rutting. To achieve this, we incorporated DPF using the dry process, considering two variables: fiber length and concentration (fiber content). Consequently, nine (09) mixtures and one control mixture were subjected to testing.

First, we conducted a mix design study to arrive at the mixture that best meets the required specifications. This mixture was used throughout the experimental process.

We developed a uniaxial static creep test based on oedometric equipment. This apparatus allows for the application of a constant stress and controlled temperature during the test.

The results obtained indicate that the general trend is a decrease in the creep resistance of the mixture, except for mixtures with low fiber content (0.1%). This may be justified by the increase in the percentage of voids as the fiber content increases.

Additionally, we performed rutting tests on several mixtures. The results show that the 3 cm mixtures provide better rutting resistance compared to the others.

Apparently, there is no correlation between the results of the two tests; mixtures that performed poorly in the creep test yielded good results in the rutting test. We can justify this conclusion by noting that static creep belongs to the domain of small deformations, while the rutting test belongs to the domain of large deformations.

In light of these results, several recommendations can be made for the continuation of this research :

- Complete other tests to determine the percentage of voids in all mixtures, in order to confirm the justification for the decrease in creep resistance.
- Complete the rutting test, particularly for the [1cm 0.1%] mixture, which yielded the best result in terms of creep resistance.
- Eliminate the 5cm mixtures and replace them with 2cm mixtures. Additionally, change the fiber content from 0.5% to 0.2% and 0.4%.

ACKNOWLEDGMENTS

The authors would like to thank USTHB (LEEGO) for its support, EPTRC (Public Roadworks Company) for carrying out the tests and university M'Hamed Bougara Boumerdes for technical helps.

REFERENCES

[1] G.D. Airey, "Rheological properties of styrene butadiene styrene polymer-modified road bitumens," Fuel, vol. 82, no. 14, pp.1709-1719, 2003.

[2] M. Fakhri, S. Ahmadi, "Influence of glass fiber on the rutting resistance and dynamic behavior of stone matrix asphalt," Construction and Building Materials, vol. 136, pp.174-183, 2017.

[3] H. Kim, D.N. Little, R.L. Lytton, "Fatigue and healing characterization of asphalt mixtures," Journal of Materials in Civil Engineering, vol. 15, no. 1, pp.75-83, 2003.

[4] S.C. Huang, R.E. Robertson, M.R. Legg, "Impact of aging on the properties of asphalt binders," Transportation Research Record, vol. 1590, no. 1, pp.1-10, 2007.

[5] M. Chen, J. Lin, "Mechanistic analysis of fiber-modified asphalt mixtures," Journal of Materials in Civil Engineering, vol. 17, no. 1, pp.58-65, 2005.

[6] F.E. Pérez-Jiménez, A.H. Martínez, R. Botella, "Fatigue performance of asphalt mixtures modified with cellulose fibers," Construction and Building Materials, vol. 30, pp.56-62, 2012.

[7] S. Tapkın, "The effect of polypropylene fibers on asphalt performance," Building and Environment, vol. 43, no. 6, pp.1065-1071, 2008.

[8] M. Arabani, S.A. Tahami, "Evaluation of the effects of date palm fibers on the mechanical properties of hot mix asphalt," Construction and Building Materials, vol. 150, pp.590–596, 2017.

[9] A.I. Al-Hadidy, Y.Q. Tan, "Mechanistic approach for polypropylene-modified flexible pavements," Materials & Design, vol. 30, no. 4, pp.1133-1140, 2009.

[10] F.M. Al-Oqla, S. M. Sapuan, "Natural fiber reinforced polymer composites in industrial applications: Feasibility of date palm fibers for sustainable automotive industry," Journal of Cleaner Production, vol. 66, pp.347-354, 2014.

[11] R. Khiari, M.F. Mhenni, M.N. Belgacem, E. Mauret, "Chemical composition and pulping of date palm rachis and Posidonia oceanica - a comparison with other wood and non-wood fiber sources," Bioresource Technology, vol. 101, no. 2, pp.775-780, 2010.

[12] A. Ashori, "Wood–plastic composites as promising green-composites for automotive industries," Bioresource Technology, vol. 99, no. 11, pp.4661-4667, 2008.

[13] O. Faruk, A.K. Bledzki, H.P. Fink, M. Sain, "Biocomposites reinforced with natural fibers: 2000-2010," Progress in Polymer Science, vol. 37, no. 11, pp.1552-1596, 2012.

[14] F.M. Nejad, A.R. Azarhoosh, G.H. Hamedi, "Effect of reclaimed asphalt pavement on mechanical behavior of asphalt mixtures," Materials & Design, vol. 31, no. 8, pp.4050-4055, 2010.

[15] S. Liu, S.S. Pang, Z. Dong, "Effects of fiber reinforcement on the properties of asphalt concrete," Construction and Building Materials, vol. 68, pp.220-228, 2014.

[16] F. Xiao, S.N. Amirkhanian, "Utilization of recycled crumb rubber modifier in asphalt pavements," Journal of Materials in Civil Engineering, vol. 21, no. 6, pp.327-335, 2009.

[17] A. Modarres, H. Hamedi, "Developing durable pavement mixtures through the use of waste materials," Construction and Building Materials, vol. 68, pp.110-117, 2014.

[18] R. Muniandy, B.B. Huat, "Laboratory evaluation of palm fiber and glass fiber in hot mix asphalt," Journal of Transportation Engineering, vol. 132, no. 7, pp.574-579, 2006.

[19] H.M.R.D. Silva, J.R.M. Oliveira, J. Peralta, "Incorporation of natural fibers in asphalt mixtures: A sustainable perspective," Resources, Conservation and Recycling, vol. 54, no. 4, pp.330-338, 2010.

[20] J. Zhu, S. Wu, J. Zhong, "Effect of jute fiber on asphalt binder properties," Materials & Design, vol. 58, pp.348-353, 2014.

[21] D. Lo Presti, "Recycled tire rubber modified bitumens for road asphalt mixtures: A literature review," Construction and Building Materials, vol. 49, pp.863-881, 2013.

[22] F. Moreno-Navarro, M. Sol-Sánchez, M.C. Rubio-Gámez, J. Jiménez del Barco Carrión, "The use of recycled materials in asphalt pavements: State of the art," Materials, vol. 11, no. 4, p.701, 2018.

[23] S. Wu, L. Montalvo, "Effects of recycled fibers on mechanical properties of asphalt mixtures," Construction and Building Materials, vol. 25, no. 5, pp.1918-1922, 2011.

[24] Organisme de contrôle technique des travaux publics. Recommandations sur l'utilisation des bitumes et des enrobés bitumineux à chaud, Ministère des travaux publics, Alger: Février, 2004.

[25] EN 12697-34, Bituminous mixtures - Test methods for hot mix asphalt - Part 34: Marshall test. 2012.

[26] Norme NF P 98-251-1 : Essais statiques sur mélanges hydrocarbonés - Partie 1 : Essai DURIEZ sur mélanges hydrocarbonés à chaud. 2002.

[27] [EN 12697-46], Bituminous Mixtures - Test Methods - Part 46: Cracking and Low-Temperature Properties by Uniaxial Tensile Tests.

[28] [EN 12697-22], Bituminous Mixtures - Test Methods - Part 22: Wheel Tracking Test, 2020.

Proceedings IRF2025: 8th International Conference on Integrity-Reliability-Failure
In Engineering, Materials, Manufacturing and Biomechanics. Porto 15-18 July 2025
DOI: https://doi.org/10.24840/978-972-752-323-8

PAPER REF: 22577

NUMERICAL ANALYSIS OF THE SHORT-TERM BEHAVIOR OF A SEMI-INTEGRAL ABUTMENT UNDER CYCLIC LATERAL LOADING

Pedro H.S. Silva[1(*)], Yuri D.J. Costa[2], Carina M.L. Costa[2], Jorge G. Zornberg[3]

[1]Res. Inst. on Mines and the Environment, Univ. of Quebec at Abitibi-Temiscamingue, Rouyn-Noranda, Canada
[2]Department of Civil Engineering, Federal University of Rio Grande do Norte, Natal, Brazil
[3]Department of Civil, Architectural and Environmental Engineering, University of Texas at Austin, Austin, USA
[(*)]*Email:* dosp01@uqat.ca

ABSTRACT

A two-dimensional finite element numerical model for a semi-integral bridge abutment was developed to investigate the lateral earth pressures on the abutment and the deformation in the backfill soil for daily cycles of expansion-contraction of the bridge superstructure. The numerical simulations showed that lower pressures concentrated at the top, mid-height, and bottom of the abutment, whilst higher pressures took place at the upper and lower thirds of the abutment, which is inconsistent with typical earth pressure distributions assumed from the theoretical pressure distributions and in design guidelines for integral bridge abutments. Deformation in the backfill soil provoked the development of a settlement trough adjacent to the abutment, which extended to a horizontal distance of about one abutment height. The deformation magnitude was deemed sufficient to negatively impact the bridge performance soon after the start of the bridge operation.

Keywords: Bridge abutment, numerical simulation, finite element method, cyclic loading.

INTRODUCTION

A two-dimensional finite element (FE) analysis was performed to investigate lateral earth pressures on the abutment and deformations in the backfill soil of a semi-integral bridge abutment under daily cycles of expansion-contraction of the bridge superstructure. The developed FE numerical model was validated against data collected in field from earth pressure cells installed on the retained soil side of the bridge abutment. Figure 1 shows details of the geometry in the vicinity of the bridge abutment. More details about the FE model and its validation can be found in Silva et al. (2023).

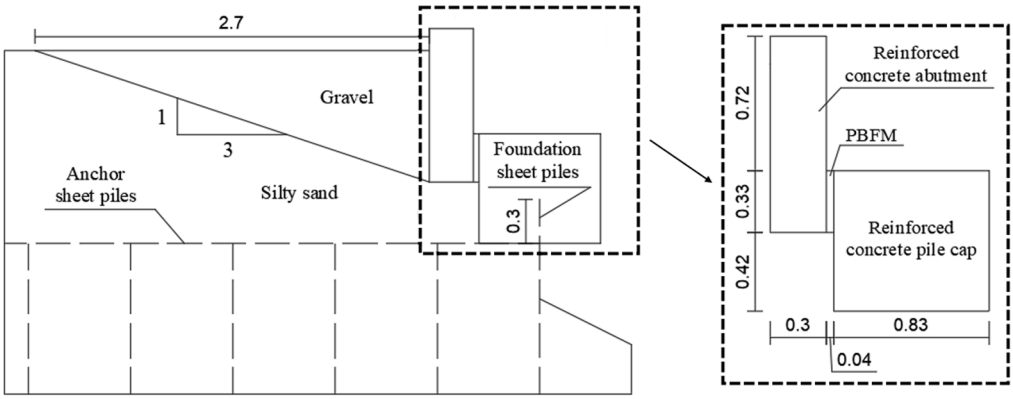

Fig. 1 - Details of the FE model in the vicinity of the bridge abutment (dimension in meters).

RESULTS AND CONCLUSIONS

Figure 2 shows peak lateral earth pressure distributions for selected daily cycles. Pressure distributions due to at-rest, active and passive conditions, as well as those predicted using the design methods specified in document PD6694-1 (BSI, 2011) and in the Massachusetts Department of Transportation's Bridge Design Guidelines (MassDOT, 2020), are also plotted for comparison. After the cycle no. 1, higher pressures occurred at the upper and lower thirds of the abutment, while lower pressures took place at the top, mid-height, and bottom of the abutment. The lateral pressures on the abutment exceeded the PD6694-1 distribution over the upper and lower thirds of the abutment. MassDOT's solution gave lateral pressures higher than those due to the daily cycles over the middle and lower thirds of the abutment, while underestimated lateral pressures in the upper third. Except for cycle no. 1, predicted distributions differed significantly from the theoretical pressure distributions.

Figure 3 presents profiles of the deformed backfill surface for selected daily cycles. According to the adopted sign convention, downward vertical displacements (i.e., settlements) are represented as positive. The displacement profiles showed the formation of a settlement trough in the backfill, with maximum settlements close to the backfill-abutment interface. Major settlements on the backfill surface extended to a horizontal distance of about one abutment height. The differential settlement between the abutment and the retained backfill that takes place after the lateral movements of the bridge superstructure, as shown in Figure 3, is commonly known as a "bump-at-the-end-of-the-bridge" and can lead to discomfort and potentially unsafe driving conditions (Al-Ani et al., 2018).

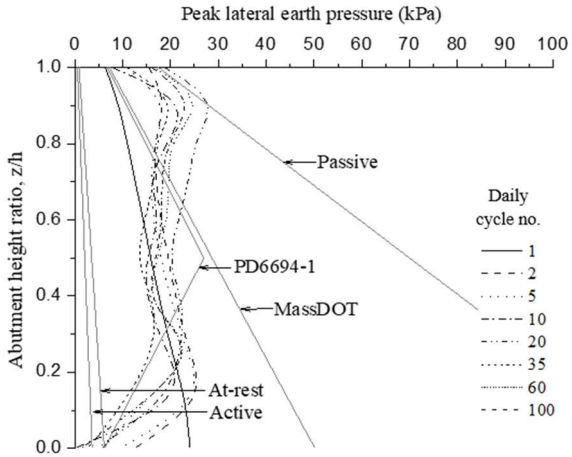

Fig. 2 - Lateral earth pressure distributions.

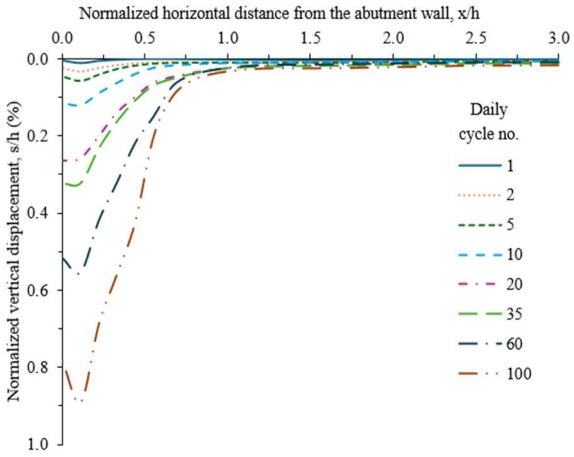

Fig. 3 - Deformed backfill surface profiles.

REFERENCES

[1] Al-Ani M, Murashev A, Palermo A, Andisheh K, Wood J, Goodall D, Lloyd N. Criteria and guidance for the design of integral bridges. Proc Inst Civ Eng – Bridge Eng, 2018, 171(3), pp.143-154. https://doi.org/10.1680/jbren.17.00014.

[2] BSI. PD6694-1:2011 – Recommendation for the design of structures subject to traffic loadings to BS EN 1997-1:2004. London, UK, BSI, 2011.

[3] MassDOT. LRFD bridge design guidelines. Boston, USA, 2020.

[4] Silva PHS, Costa YDJ, Walter JR, Kouchaki BM, Zornberg JG, Costa CML. Numerical evaluation of a semi-integral bridge abutment under cyclic thermal movements. Transportation Geotechnics, 2023, 39, 100938. https://doi.org/10.1016/j.trgeo.2023.100938.

Proceedings IRF2025: 8th International Conference on Integrity-Reliability-Failure
In Engineering, Materials, Manufacturing and Biomechanics. Porto 15-18 July 2025
DOI: https://doi.org/10.24840/978-972-752-323-8

PAPER REF: 22603

NUMERICAL ASSESSMENT OF PROGRESSIVE COLLAPSE IN REINFORCED CONCRETE FRAMES WITH MASONRY INFILL

Jessenia Gabriela Peñaloza Morán(*), Ingrid Xavier de Oliveira, Fábio Fleming Leitão, Nathan Shauer, Hugo Luiz Oliveira, Gustavo Henrique Siqueira

School of Civil Engineering, Architecture and Urban Planning, Department of Structures, University of Campinas (Unicamp), Campinas, São Paulo, Brazil
(*)*Email:* gpenalozamoran@gmail.com

ABSTRACT

The study of progressive collapse is crucial because structural collapse leads to significant economic impacts and the potential loss of human lives, as demonstrated in incidents such as Ronan Point, the Murrah Federal Building, and the World Trade Center. This paper uses the pushdown methodology to analyze the sensitivity of the models to mesh refinement in reinforced concrete frames with infill masonry walls subjected to progressive collapse. Developed in OpenSees, the model incorporates distributed plasticity elements with fiber sections and a three-strut representation for infill walls. The analysis compares two formulations: force-based and displacement-based. The findings emphasize the influence of modeling assumptions on the structural response under progressive collapse scenarios.

Keywords: Progressive collapse, pushdown analysis, masonry infill walls, numerical modeling.

INTRODUCTION

Progressive collapse occurs when the failure of a primary structural element triggers a chain reaction, leading to a disproportionate collapse of the entire system [14]. In recent years, researchers have placed on studying structural behavior under progressive collapse conditions, particularly following historical events such as the collapse of the World Trade Center towers (New York, 2001), the Murrah Federal Building (Oklahoma, 1995), and the Ronan Point building (London, 1968) [4, 15].

The progressive collapse of structures during extreme events is unlikely, meaning that designing buildings with excessive robustness can be impractical and costly. Therefore, studying secondary resistance mechanisms, which act as safety features to reduce the risk of progressive collapse during such events, is essential. These mechanisms include flexural action, compressive arch action, tensile catenary action, Vierendeel frame action, and the impact of non-structural components like infill walls and partitions [1, 4, 15].

Two approaches can be used to analyze structures subject to progressive collapse: they are the indirect and the direct method. The indirect method sets rules to enhance structural robustness, while the direct method analyzes structural response. Among the nonlinear static analysis techniques used in direct methods, the pushdown methodology evaluates how structures respond to the removal of critical elements [20].

The finite element method is a widely used tool to analyze structures subject to progressive collapse and is available in various software such as OpenSees, ABAQUS, SAP2000, and LS-DYNA [1, 2]. Beams and columns can be modeled with distributed plasticity elements and fiber

sections, with a corotational geometric formulation, as it allows capturing secondary resistance mechanisms occurring in beams, such as flexural action, compressive arch action, and tensile catenary action [3, 6, 20].

There are two main formulations for analyzing nonlinear structures: the displacement-based formulation (stiffness method) and the force-based formulation (flexibility method). The displacement-based formulation benefits from mesh refinement to minimize discretization errors in nonlinear analysis. On the other hand, the force-based formulation achieves higher accuracy by adjusting integration points or subdividing elements [13, 17].

Secondary resistance mechanisms, such as non-structural elements, significantly enhance a structure's ability to resist progressive collapse. Recent studies have increasingly focused on the role of infill walls, as they contribute to the redistribution of forces when a primary load-bearing element fails under vertical loading conditions [16, 18, 19].

This study uses a pushdown method to analyze reinforced concrete frames with infill masonry walls. It examines the influence of mesh refinement using force-based and displacement-based formulations in OpenSees software [10], aiming to highlight the impact of modeling assumptions on the structural response under progressive collapse.

METHODOLOGY

In this work, the pushdown methodology is implemented using the OpenSees software to analyze the progressive collapse of a reinforced concrete structure. The research investigates the influence of beam mesh refinement on the frame's structural response in relation to progressive collapse, focusing on both force-based and displacement-based formulations. Three aspects are analyzed: (i) the variation in the number of elements, (ii) the variation in the number of integration points, and (iii) the variation in the size of the elements at the ends of the beams.

The numerical model is verified against the experimental pushdown test described in [7], which examines the behavior of a reinforced concrete frame with masonry infill walls. The frame comprises two stories and four spans at a scale of 1:3 and is designed according to the Chinese code for moment resisting frames [11, 12]. The second floor has concrete infill walls in all its spans. The unconfined concrete compressive strength for the second floor is 41.3 MPa, while for the second floor, it is 31.8 MPa. The masonry walls have a compressive strength of 12.8 MPa.

The beams and columns are composed of 4 mm diameter confining stirrups with a yield strength of 235 MPa and an ultimate strength of 322 MPa. In addition, an 8 mm diameter longitudinal reinforcement with an average yield strength of 415 MPa, an ultimate strength of 588 MPa, and a rupture strain of 0.19.

The beams and columns are modeled with distributed plasticity elements and fiber sections. Two models are analyzed, one with a forced-based formulation and the other with a displacement-based formulation. The masonry walls are represented by the macro model proposed by [6], which recommends using three-strut model in each span of the frame, as shown in Figure 1. The diagonals are modeled using compression truss elements. The equivalent width of the main diagonal is calculated using Equation (1) and Equation (2) proposed by the Masonry Standards Joint Committee (MSCJ) [9].

$$\omega_{inf} = \frac{0.3}{\lambda_{strut} \cdot \cos(\theta_{strut})} \tag{1}$$

$$\lambda_{strut} = \left[\frac{E_m \cdot t_{inf} \cdot \sin(2\theta_{strut})}{4 \cdot E_{bc} \cdot I_{bc} \cdot H_{inf}}\right] \quad (2)$$

where, H_{inf} is the height of infill wall (mm); L_{inf} is the length of the infill wall; $\theta_{strut} = \tan^{-1}\left(H_{inf}/L_{inf}\right)$ represents the angle of infill diagonal with respect to the horizontal (degrees); I_{bc} is the moment of inertia of bounding column for bending in the plane of the infill (mm^4); t_{inf} is the thickness of the infill wall (mm); E_{bc} is the modulus of elasticity of bounding columns (MPa); and E_m is the modulus of elasticity of masonry in compression (MPa). The modulus of elasticity of the masonry wall is obtained with the MSCJ equation $E_m = 900 \cdot f'_m$ [9], where f'_m is the compressive strength of concrete masonry (MPa).

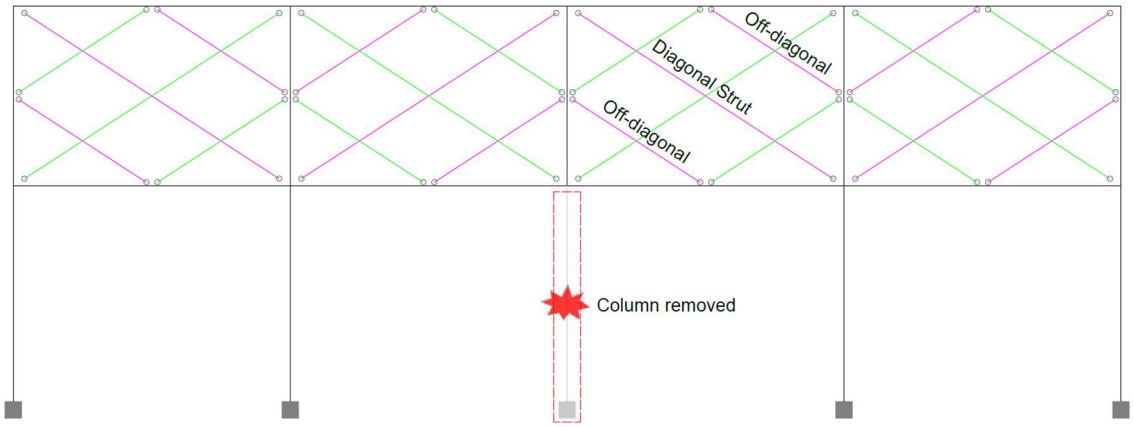

Fig. 1 - Representation of the macro model of the infill frame.

The constitutive material models define concrete using Concrete01 and the longitudinal reinforcement bars using Steel01. The uniaxial Concrete01 model is based on the Kent-Scott-Park formulation (see Figure 2a), while Steel01 follows the FEDEAS model (see Figure 2b) [10]. The section is modeled using a fiber section approach, allowing differentiation between unconfined concrete, confined concrete, and longitudinal reinforcement bars. The maximum compressive strength of confined concrete and its corresponding strain are determined using the Chang and Mander formulations [5, 8].

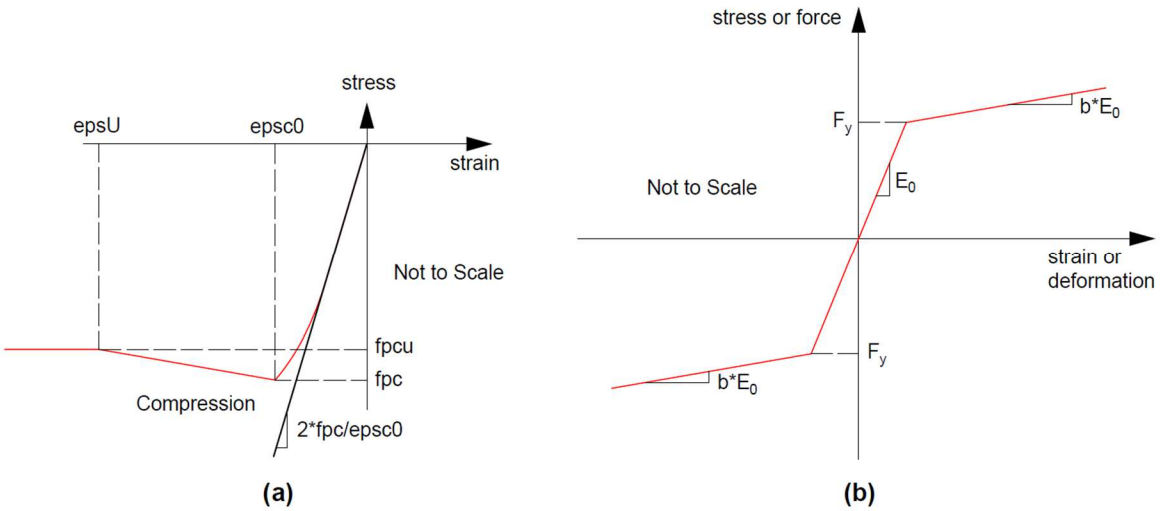

Fig. 2 - Material constitutive models in OpenSees: (a) Concrete01 and (b) Steel01.

The pushdown methodology implemented consists of the removal of the central column of the first level (see Figure 1) and applying gravity loads. Then, incremental displacements are imposed on the top node of the removed column, obtaining the pushdown curve, which represents the relationship between the applied vertical displacement and the reaction forces at that node.

The model is verified by comparing the pushdown curve obtained with the experimental results and the micro model of [7]. Additionally, it is compared with the macro-model curve from [6], which also replicates the experimental test described in [7].

RESULTS AND DISCUSSION

Three aspects are analyzed: (i) the variation in the number of elements, (ii) the variation in the number of integration points, and (iii) the variation in the size of the elements at the ends of the beams. Each case was analyzed using both force-based and displacement-based formulations. The column mesh is kept constant across all analyses, with eight elements per column and two integration points per element (see Figure 3).

The figures presented next show a comparison between various reference pushdown curves. These include the curves obtained in the experimental and micro model of [7] and the pushdown curve of the macro model of [6]. In addition, the curves derived from the mesh analysis for both force-based and displacement-based formulations are included, allowing a comprehensive evaluation of the performance of the models and their sensitivity to different modeling approaches.

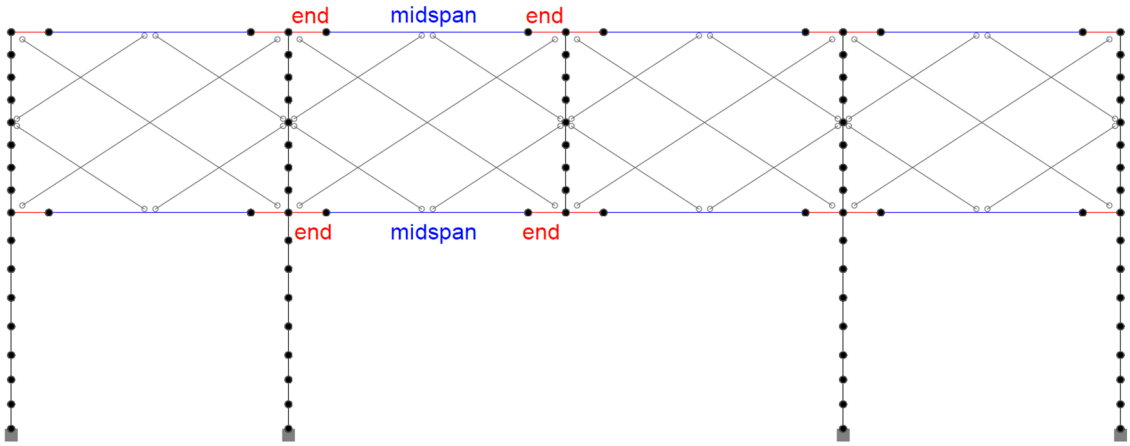

Fig. 3 - Representation of the mesh in the infill frame.

The study analyzed the variation in the number of elements in the midspan of beams, considering 2, 4, 6, 8, 10, 12, and 14 elements. The force-based and displacement-based formulations showed sensitivity to changes in the number of elements, as observed in Figure 4 and Figure 5.

The analysis of the variation of the integration points is performed on the midspan of the beams, considering 2, 3, 4, and 5 integration points, each evaluated with elements of 2, 4, 6, 8, 10, 12, and 14 in the midspan of the beams. The beam ends, modeled with a single element and two integration points, have a length of 0.231m.

The results obtained with the force-based formulation show that, in all cases, the pushdown curves vary when the number of integration points is changed. Figure 6 presents the results for the case of 10 elements in the midspan of the beams. All cases encountered convergence issues

when using 4 and 5 integration points. On the other hand, the displacement-based formulation shows no variation in the curves when modifying the number of integration points. Figure 7 shows the variation of the integration points for 10 elements in the midspan of the beams.

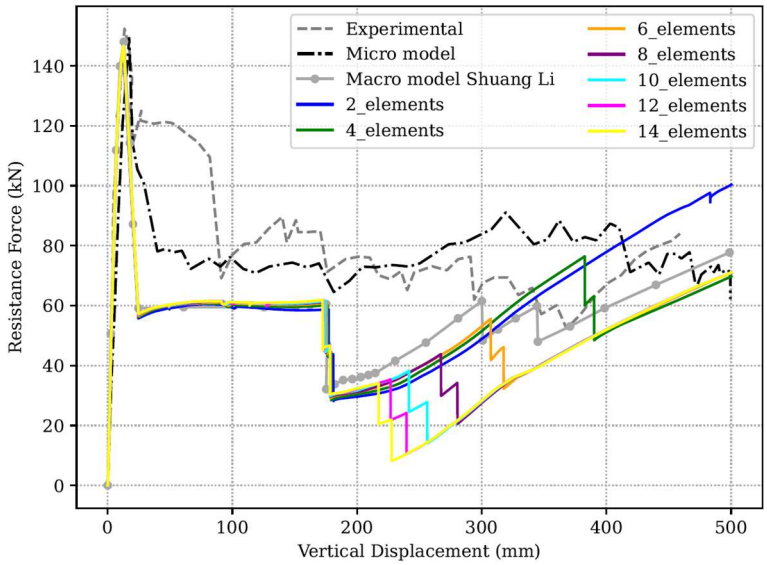

Fig. 4 - Comparison of pushdown curves with different numbers of midspan elements using a force-based formulation.

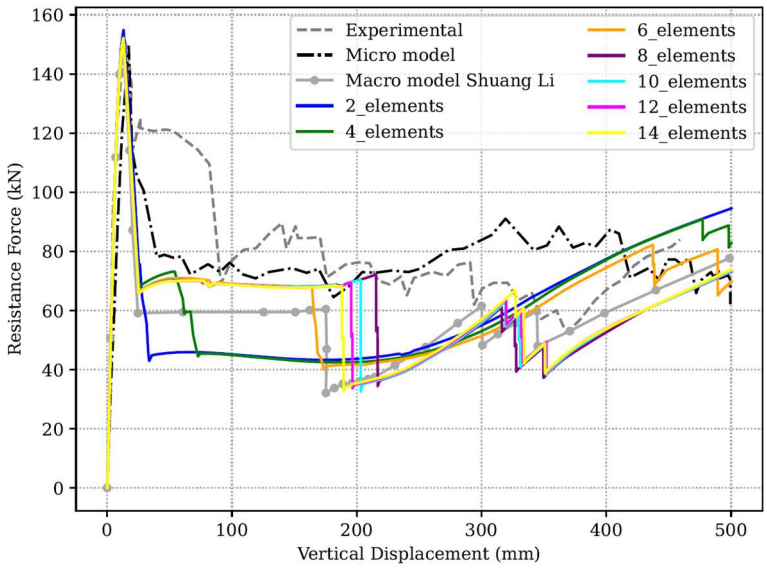

Fig. 5 - Comparison of pushdown curves with different numbers of midspan elements using a displacement-based formulation.

For the beams ends, the study evaluated two lengths—0.231 m and 0.35 m—modeling each with 1, 2, and 3 elements. For the force-based formulation, six elements and two integration points were used in the midspan of the beams, as these parameters provide the best fit for the curve. In the case of the displacement-based formulation, 10 elements and two integration points were used in the midspan of the beams, resulting in the best curve fit for that formulation, as observed in the previous analysis.

Figure 8 and Figure 9 show the results for the force-based formulation, while Figure 10 and Figure 11 show the results for the displacement-based formulation. Both formulations show sensitivity to changes in the size and number of elements at the beam ends.

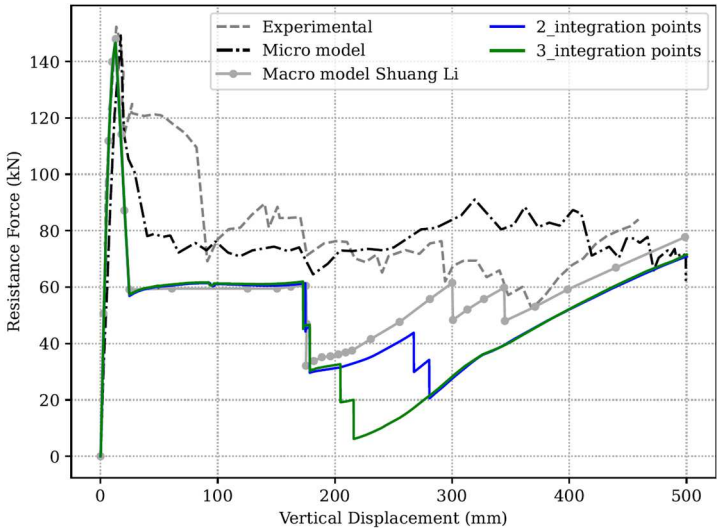

Fig. 6 - Comparison of pushdown curves with different numbers of integration points at midspan using force-based formulation. Case with 10 elements in midspan beams.

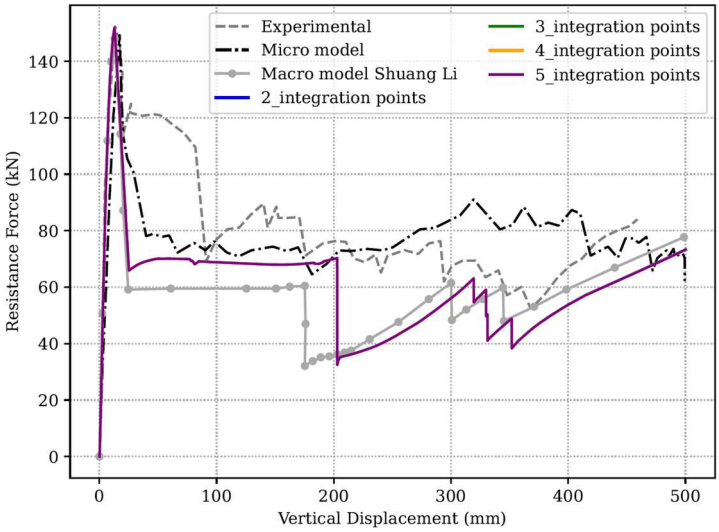

Fig. 7 - Comparison of pushdown curves with different numbers of integration points at midspan using displacement-based formulation. Case with 10 elements in midspan beams.

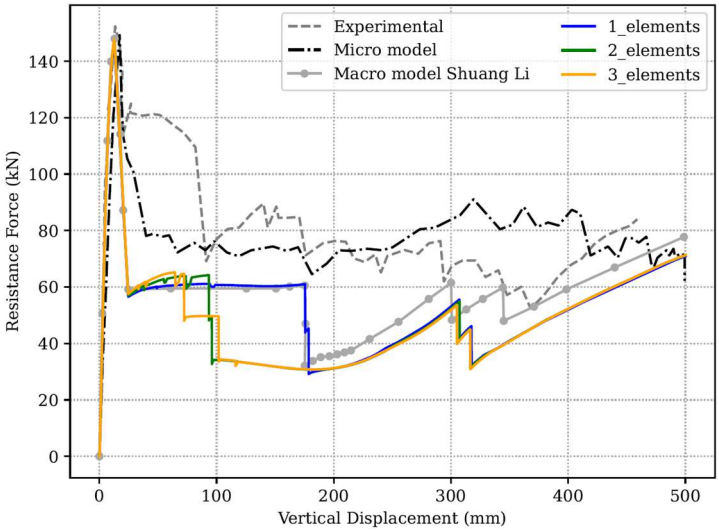

Fig. 8 - Comparison of pushdown curves by varying the size (0.231 m) and the number of elements at the ends of the beams using a force-based formulation.

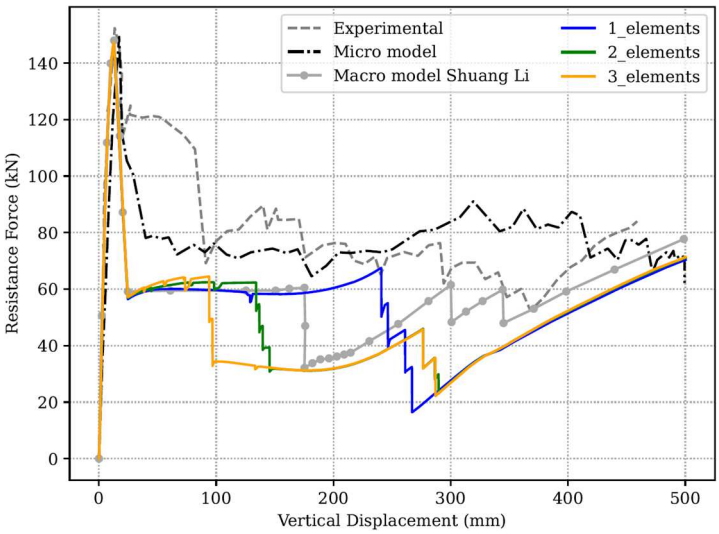

Fig. 9 - Comparison of pushdown curves by varying the size (0.350 m) and the number of elements at the ends of the beams using a force-based formulation.

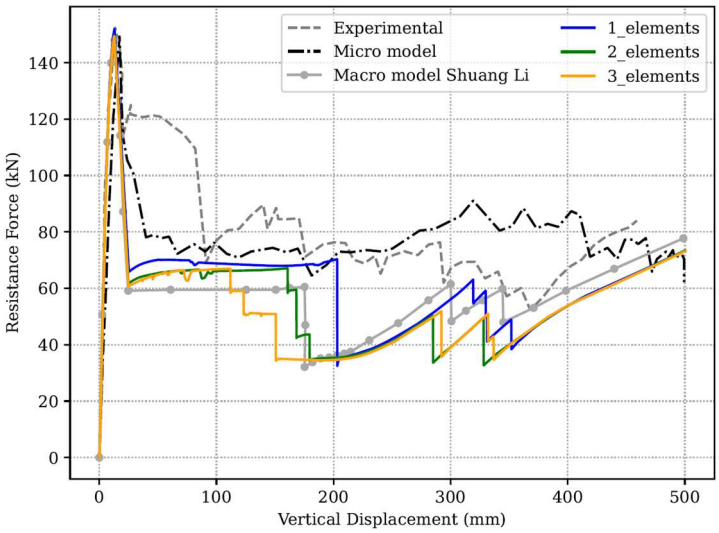

Fig. 10 - Comparison of pushdown curves by varying the size (0.231 m) and the number of elements at the ends of the beams using a displacement-based formulation.

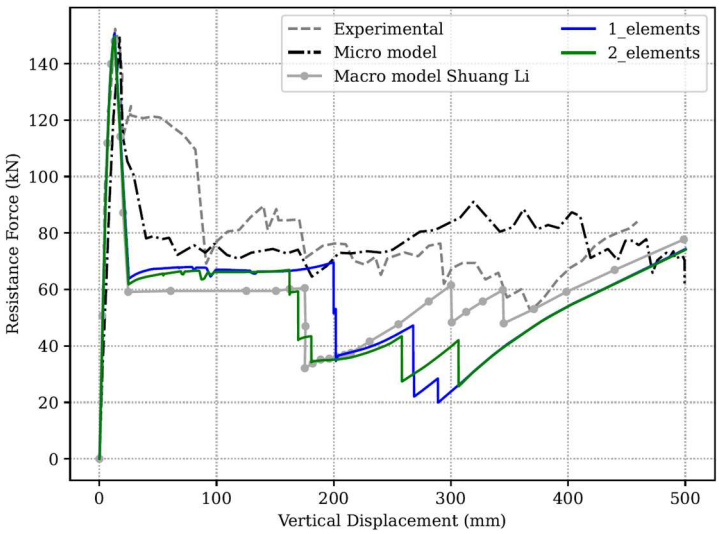

Fig. 11 - Comparison of pushdown curves by varying the size (0.350 m) and the number of elements at the ends of the beams using a displacement-based formulation.

Based on the analyses performed, it was observed that the number of elements and the integration points must be adjusted according to the chosen formulation. The parameters were selected for the force-based and displacement-based formulations, which allow a better approximation to the pushdown curve obtained by [6], as shown in Figure 12.

The optimal parameters for the force-based formulation are six elements in the beam midspan, one element at each end (0.231m for the end elements), eight elements for the columns, and two integration points per element. For the displacement-based formulation, the optimal configuration consists of ten elements in the beam midspan, two elements at each end (0.231m for the end elements), eight elements for the columns, and two integration points per element.

Figure 12 compares the pushdown curves with optimal parameters obtained in this study with the experimental and micro-model curves from [7] and the macro-model curve from [6]. The pushdown curves from this work show close agreement with those reported in [6], verifying the model developed using the OpenSees software.

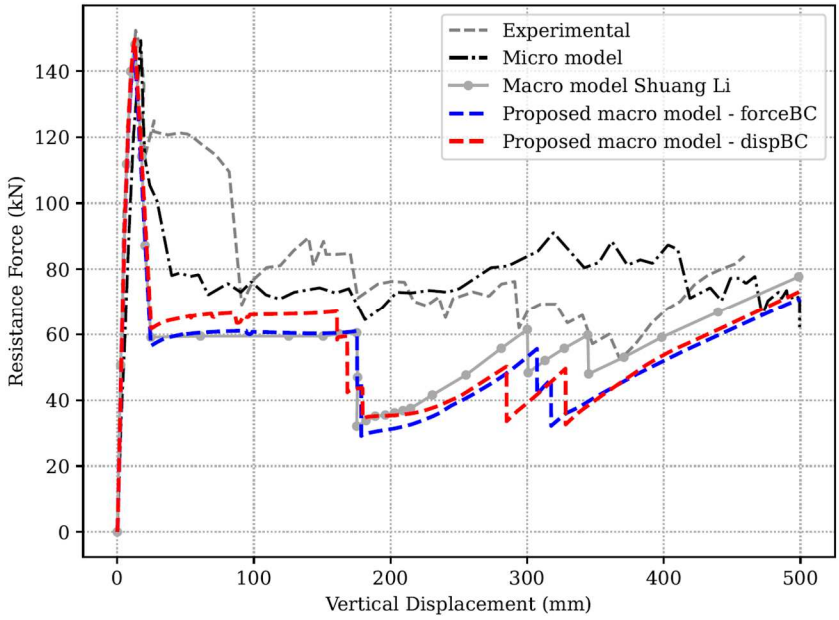

Fig. 12 - Comparison of force-based and displacement-based formulations with optimal parameters.

CONCLUSIONS

This study developed a macro model for pushdown analysis, exploring the influence of beam mesh refinement on the structural response of reinforced concrete frames with infill walls under progressive collapse. The proposed macro model was implemented in OpenSees using distributed plasticity elements with fiber sections for beams and columns and a three-strut model to represent the masonry walls. The pushdown methodology was applied to two formulations: force-based and displacement-based.

The macro model was verified by comparing its pushdown curve with the curves obtained from the experimental test and the micro model, both developed by [7], and the macro model presented in [6]. The pushdown curve generated in this study shows close agreement with the results reported in [6], confirming the satisfactory performance of the model implemented in OpenSees software.

The results of the beam mesh analysis show that the displacement-based and force-based formulations respond differently according to the mesh parameters, requiring specific adjustments for each. Both formulations are sensitive to variations in the number of elements in the midspan of the beams and the size and number of elements at the ends of the beams. The force-based formulation is sensitive to the number of integration points at the midspan of the beams. In contrast, the displacement-based formulation is not sensitive to the number of integration points at the midspan of the beams.

This study highlights the importance of correctly choosing the mesh and formulation parameters in progressive collapse analysis, as these factors significantly affect the model.

ACKNOWLEDGMENTS

The authors acknowledge the support provided by the Coordenação de Aperfeiçoamento de Pessoal de Nível Superior - Brazil (CAPES) - Funding Code 001 and the Fundação de Amparo à Pesquisa do Estado de São Paulo (FAPESP), Brazil - Process No. 2024/07576-0. Fábio F. Leitão thanks the Federal University of Acre for granting the leave necessary to pursue his doctoral studies.

REFERENCES

[1] Adam, J.M. et al. Research and practice on progressive collapse and robustness of building structures in the 21st century. Engineering Structures, Elsevier, v. 173, pp.122-149, 2018. Available at: <https://doi.org/10.1016/j.engstruct.2018.06.082>.

[2] Alhafian, S. Seismic Progressive Collap Concrete Frame Structu Applied Element M. Tese (Doutorado) - Heriot-Watt University, 2013. Available at: <http://hdl.handle.net/10399/2740>.

[3] Arshian, A.H.; Morgenthal, G.; Narayanan, S. Influence of modelling strategies on uncertainty propagation in the alternate path mechanism of reinforced concrete framed structures. Engineering Structures, Elsevier, v. 110, pp.36-47, 2016. Available at: <https://doi.org/10.1016/j.engstruct.2015.11.019>.

[4] Azim, I. et al. Factors influencing the progressive collapse resistance of rc frame structures. Journal of Building Engineering, v. 27, 2020. Available at: <https://doi.org/10.1016/j.jobe.2019.100986>.

[5] Chang, G.; Mander, J.B. Seismic energy based fatigue damage analysis of bridge columns: Part I-Evaluation of seismic capacity. National Center for Earthquake Engineering Research Buffalo, NY, 1994. Available at: <https://scholar.google.com.br/scholar?cluster=2445273563174106768&hl=es&as_sdt=0,5>.

[6] Li, S. et al. Modeling methods for collapse analysis of reinforced concrete frames with infill walls. Journal of Structural Engineering, American Society of Civil Engineers, v. 145, n. 4, p. 04019011, 2019.

[7] Li, S. et al. Experimental and numerical study on progressive collapse process of rc frames with full-height infill walls. Engineering Failure Analysis, Elsevier, v. 59, pp.57-68, 2016.

[8] Mander, J.B.; Priestley, M.J.; Park, R. Theoretical stress-strain model for confined concrete. Journal of structural engineering, American Society of Civil Engineers, v. 114, n. 8, pp.1804-1826, 1988. Available at: <https://doi.org/10.1061/(ASCE)0733-9445(1988)114: 8(1804)>.

[9] Masonry Standards Joint Committee (MSJC). Building code requirements for masonry structures. [S.l.], 2011.

[10] Mazzoni, S. et al. Opensees command language manual. Pacific earthquake engineering research (PEER) center, Berkeley, California, United States, v. 264, n. 1, pp.137-158, 2006.

[11] Ministry of Housing and Urban Rural Development (GB50010). Code for design of concrete structures. [S.l.]: China Architecture and Building Press Beijing, 2010.

[12] Ministry of Housing and Urban Rural Development (GB50011). Code for seismic design of building. [S.l.]: China Architecture and Building Press Beijing, 2010.

[13] Neuenhofer, A.; Filippou, F.C. Evaluation of nonlinear frame finite-elementmodels. Journal of structural engineering, American Society of Civil Engineers, v. 123, n. 7, pp.958-966, 1997. Available at: <https://doi.org/10.1061/(ASCE)0733-9445(1997)123: 7(958)>.

[14] Nyunn, S. et al. Numerical studies on the progressive collapse resistance of multi-story rc buildings with and without exterior masonry walls. Structures, Elsevier, v. 28, pp.1050-1059, 2020. Available at: <https://doi.org/10.1016/j.istruc.2020.07.049>.

[15] Qian, K.; Li, B.; Ma, J.-X. Load-carrying mechanism to resist progressive collapse of rc buildings. Journal of Structural Engineering, American Society of Civil Engineers, v. 141, n. 2, p.04014107, 2015. Available at: <https://doi.org/10.1061/(ASCE)ST.1943-541X. 0001046>.

[16] Sasani, M. Response of a reinforced concrete infilled-frame structure to removal of two adjacent columns. Engineering Structures, Elsevier, v. 30, n. 9, pp.2478-2491, 2008. Available at: <https://doi.org/10.1016/j.engstruct.2008.01.019>.

[17] Scott, M.H.A Tale of Two Element Formulations. 2020. Published by Portwood Digital. Accessed: 2025-02-23. Available at: <https://portwooddigital.com/2020/02/23/ a-tale-of-two-element-formulations/>.

[18] Tsai, M-H; Huang, T-C Effect of interior brick-infill partitions on the progressive collapse potential of a rc building: linear static analysis results. International Journal of Civil and Environmental Engineering, Citeseer, v. 3, n. 2, pp.108-114, 2009. Available at: <https://www.academia.edu/81075433/Effect_Of_Interior_Brick_Infill_Partitions_On_The_ Progressive_Collapse_Potential_Of_A_Rc_Building_Linear_Static_Analysis_Results>.

[19] Zhang, Q. et al. Reliability analysis of reinforced concrete structure against progressive collapse. Reliability Engineering & System Safety, Elsevier, v. 228, p.108831, 2022. Available at: <https://doi.org/10.1016/j.ress.2022.108831>.

[20] Yu, X.H. et al. Uncertainty and sensitivity analysis of reinforced concrete frame structures subjected to column loss. Journal of Performance of Constructed Facilities, American Society of Civil Engineers, v. 31, n. 1, p.04016069, 2017.

TRACK - F: Biomechanical Applications

Mechanics and Design of Protheses
Biomaterials and Biocompatibility
Stress Monitoring
Dental and Orthopaedic Biomechanics
Sports and Rehabilitation Biomechanics
Biofluid Mechanics
Modelling of Biomechanical Systems
Advanced Bioimaging
Medical Devices
Case Studies

Proceedings IRF2025: 8th International Conference on Integrity-Reliability-Failure
In Engineering, Materials, Manufacturing and Biomechanics. Porto 15-18 July 2025
DOI: https://doi.org/10.24840/978-972-752-323-8

PAPER REF: 22237

FAILURE OF AN AUTO-BELAY DEVICE

David Eager(*)

University of Technology Sydney, Faculty of Engineering and Information Technology, Sydney, Australia
(*)*Email:* David.Eager@uts.edu.au

ABSTRACT

This paper discussed the incident where an 8-year-old girl fell 7 m from a rope ladder on 30 July 2022. The indoor play centre operator was charged and pleaded guilty to two breaches of the Occupational Health and Safety Act. The operator was fined $60,000 plus costs.

Keywords: Indoor climbing, artificial climbing structures, risk management, self-belay device.

INTRODUCTION

The incident occurred at an indoor play centre in Melbourne, Australia. The incident involved an 8-year-old girl falling 7 m from a rope ladder while she was attending a friend's birthday party [1]. She became detached from a self-belay device suffering non-fatal traumatic injuries.

RESULTS AND CONCLUSIONS

It was concluded that the incident was a direct result of grossly inadequate maintenance. Safety Engineering, the manufacturer of the self-belay device requires all operators to recertify their devices annually. The self-belay devices are either refurbished and given a one-year additional warranty, or they are discarded and replaced with a new self-belay device. The estimated usage period of the self-belay system which failed was 43 months.

Excessive wear of the components within the self-belay device allowed sufficient movement of the locking anchors for the device to malfunction (Figures 1-3). The movement of the locking anchors allowed the key to be removed when the worn connector was not fully engaged which allowed the participant to commence climbing while not secure.

Fig. 1 - Side view of the heavily worn self-belay device which failed depicting the locking key removed when the connector is not fully engaged [2].

Fig. 2 - Disassembled and partially reassembled heavily worn self-belay device which failed depicting a single locking lever engaged within the worn connector partially engaged [2].

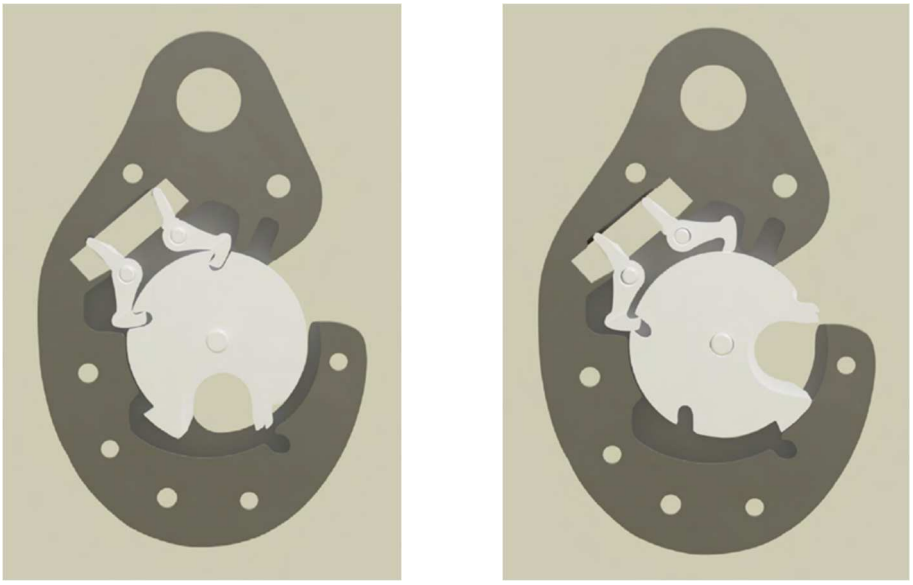

Fig. 3 - Sectional view of the self-belay device: Right: depicting the twin locking levers engaging with the three locking disks as it was designed to operate; and Left: depicting a single locking lever prematurely engaged with the three locking disks before the locking disk have rotated to the locking position [2].

REFERENCES

[1] https://au.news.yahoo.com/8yo-girl-horror-fall-climbing-045357466.html.

[2] Eager D., Entertainment Velocity 'Funtopia Maribyrnong' incident of 30 July 2022, University of Technology Sydney, Australia, 3 September 2023.

Proceedings IRF2025: 8th International Conference on Integrity-Reliability-Failure
In Engineering, Materials, Manufacturing and Biomechanics. Porto 15-18 July 2025
DOI: https://doi.org/10.24840/978-972-752-323-8

PAPER REF: 22417

THERMOMECHANICAL SIMULATION MODELS FOR EVALUATING THERMAL RISKS IN BONE DRILLING FOR DENTAL IMPLANTS

Irea López García[1(*)], David Agudo del Río[2], Jose Ángel López Campos[2], Jose Ramón Fernández García[3], Mercedes Gallas-Torreira[4], Jacobo González Baldonedo[2], Miguel Miguez Coto[1], Sofía Suárez García[2]

[1]Dpt. Mech. Engineering Universidade de Vigo, E-36310 Vigo, Spain
[2]CINTEX, Universidade de Vigo , Dpt. Mech. Engineering, E-36310 Vigo, Spain
[3]Department Applied Mathematics, Higher School of Telecommunications Engineering, Vigo, Spain
[4]Oral Medicine, Oral Surgery and Implantology Unit, Faculty of Medicine and Odontology, The Health Research Institute Foundation, University of Santiago de Compostela, Santiago de Compostela, Spain.
(*)*Email:* irealopez@gmail.com

ABSTRACT

The demand for dental implants has increased due to greater awareness of oral health, an aging population, and the rise in conditions that lead to tooth loss, such as periodontal disease and trauma. Implants provide an effective solution for restoring masticatory function and improving the quality of life. However, the placement procedure presents a critical challenge during bone drilling. High rotational speeds of the drills can lead to a rise in tissue temperature, which may induce cellular necrosis and compromise implant osseointegration. This study presents two computational simulation models, to assess and quantify the thermal risks associated with drilling: The Finite Element Method (FEM) and Smooth Particle Hydrodynamics (SPH). Additionally, an experimental validation is proposed to determine the accuracy of each model under real-world conditions.

Keywords: Dental implants, temperature, FEM, SPH, drilling.

INTRODUCTION

The dental implant placement procedure is a highly precise surgical process, and various factors can influence its success. The procedure involves drilling into the maxillary or mandibular bone to create a space for the implant. This drilling is one of the most critical aspects, as it is performed using high-speed rotary burs, typically around 2000 rpm, generating significant heat in the drilling area [1]. This heat can damage the bone and compromise implant integration. Thermal damage is a major concern, as temperatures exceeding 50°C can induce bone necrosis, negatively affecting healing and osseointegration [2]. To avoid such complications, it is crucial to maintain the temperature in the drilling area below 47°C, which presents a challenge in managing the speed and technique used during the drilling process.

METODOLOGY

Two computational simulation models based on the FEM and SPH methods are developed. The system experiences high deformations, and thus, the proper functioning of the FEM calculation depends on setting a maximum deformation threshold for its elements, beyond which they will be deleted. Under these conditions, the SPH method is proposed as an alternative, as it has been specifically developed for configurations involving high deformation.

RESULTS AND CONCLUSIONS

The heat transfer within the tissue due to drill friction during the drilling process is thoroughly analysed. The results obtained reveal significant differences between the models. In the FEM model, heat transfer is almost negligible, suggesting that the model does not fully capture the thermal effects of the drilling process. It is concluded that this outcome may be influenced by the element deletion procedure, in which elements are removed fast during the simulation, preventing the occurrence of a realistic temperature increase. On the other hand, the SPH model yields more realistic results, showing temperature increases close to 20ºC (Figure 1). This model appears to better capture the dynamics of heat generation and transfer, offering a more accurate representation of the temperature effects during the drilling process.

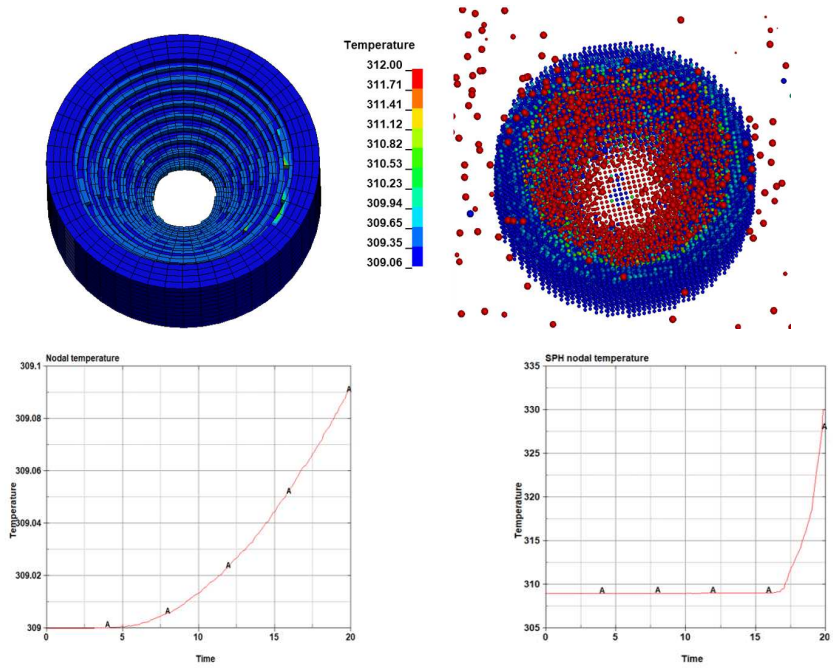

Fig. 1 - Deformation and thermal results of both FEM (left) and SPH (right) models.

Additionally, an experimental test is proposed using a commercial material such as ABS, as its mechanical properties are well-documented and consistent, which facilitates comparative analysis. This contrasts with bone, which is a complex and heterogeneous biological tissue whose composition and mechanical characteristics can vary significantly between individuals and under different conditions. The idea is to use ABS to evaluate the performance of the simulation models in a controlled environment, thereby enabling a more accurate and reliable comparison. This approach will help identify which model most effectively approximates real-world conditions.

REFERENCES

[1] B.K.E. El-Kholey, S. Ramasamy, S. Kumar R, A. Elkomy. Effect of Simplifying Drilling Technique on Heat Generation During Osteotomy Preparation for Dental Implant, Implant Dent., vol. 26, n.o 6, pp.888-891, dic. 2017, doi: 10.1097/ID.0000000000000692.

[2] A. Eriksson, T. Albrektsson, B. Grane, D. McQueen. Thermal injury to bone: A vital-microscopic description of heat effects», Int. J. Oral Surg., vol. 11, no. 2, pp.115-121, abr. 1982, doi: 10.1016/S0300-9785(82)80020-3.

Proceedings IRF2025: 8th International Conference on Integrity-Reliability-Failure
In Engineering, Materials, Manufacturing and Biomechanics. Porto 15-18 July 2025
DOI: https://doi.org/10.24840/978-972-752-323-8

PAPER REF: 22447

PVA-BG58S-CL-BASED BARRIER MEMBRANES FOR GUIDED TISSUE/BONE REGENERATION THERAPY

Isabela dos Santos Gonçalves[1], Vitor Gabriel Poli de Lima[1], Tiago Moreira Bastos Campos[2], Marcos Jacobovitz[3], Paulo Henrique Salles de Carvalho[1], Luana Marotta Reis de Vasconcellos[4], Ivone Regina de Oliveira[1(*)]

[1]Institute for Research and Development, University of Vale do Paraíba, São José dos Campos, SP, Brazil
[2]Federal University of Pelotas, Pelotas, RS, Brazil
[3]Private Clinic, São Carlos, SP, Brazil
[4]Institute of Science and Technology, Paulista State University, São José dos Campos, SP, Brazil
[(*)]*Email:*ivonero@univap.br

ABSTRACT

To enhance the bioactive and osteogenic properties of membranes, this study evaluated the production of membranes that combine the biocompatibility of the hydrophilic synthetic polymer (polyvinyl alcohol - PVA) with the osteogenic effects of chlorinated bioactive glasses (BG58S-Cl). The synthesized BG58S-Cl exhibited porosity, and its particles were successfully incorporated into PVA nanofibers, as demonstrated by FT-IR and SEM analyses. This material shows significant potential for application in guided bone regeneration.

Keywords: Chlorinated bioactive glasses, PVA, nanofiber, electrospinning.

INTRODUCTION

Periodontitis is an infectious disease of multifactorial origin, which originates from a periodontogenic bacterial biofilm that colonizes the surfaces of the teeth, resulting in an inflammatory reaction to microbial aggression. In the absence of adequate treatment, it can lead to the gradual destruction of the periodontal ligaments, cementum and alveolar bone. In guided tissue/bone regeneration therapy (GTR/GBR), a barrier membrane is placed between the fibrous tissues and the bone defect to prevent unwanted incursions of fibrous tissues into the bone defect, thus allowing the regeneration of quality bone. Currently, there are a significant number of biodegradable barrier membranes available on the market. However, a very common problem is that the membranes are not bioactive/osteogenic, that is, they are incapable of inducing a favorable osteogenic response and integration with the host tissue, resulting in many cases in displacement/expulsion of the membrane, requiring a new surgical procedure and replacement of the implant (Matos et al. 2023). Aiming to improve the bioactive and osteogenic properties of the membrane, this work evaluated the production of membranes that integrate the biocompatibility of the hydrophilic synthetic polymer (polyvinyl alcohol - PVA) with the osteogenic effects of chlorinated bioactive glasses (BG58S-Cl), using the electrospinning equipment.

RESULTS AND CONCLUSIONS

Evaluating the results from Figure 1, it is possible to observe that the spectral analysis revealed characteristic bands of PVA, such as those at 1092 cm^{-1} (C–O stretching), 1425 cm^{-1} (C–H bending vibration), 1700 cm^{-1} (C=O group), 2930 cm^{-1} (C–H stretching vibrations), and 3300

cm^{-1} (O–H intermolecular hydrogen bonding) (Nataraj et al 2020 and Fraga 2022). The BG58S-Cl bands were located between 900-1000 cm^{-1} and 1000-1030 cm^{-1} (Vicrery C and Nedelec J 2016). No significant changes were observed in the spectra of PVA membranes containing BG58S-Cl, possibly due to the overlap of bands from both materials.

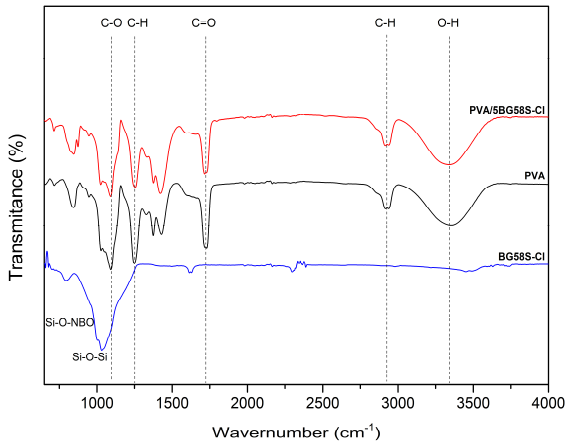

Fig. 1 - FTIR spectra of BG58S-Cl and the membranes PVA and PVA/BG58S-Cl.

Figure 2(a) reveals the presence of some pores in the BG58S-Cl particles, which enhances their interaction with the surrounding tissue, promoting cell adhesion and growth. Figures. 2(b) and 2(c) present micrographs of the membranes, with or without BG58S-Cl, showing the incorporation of the bioactive particles into the fibers, a factor that could bring bioactivity to the polymeric membranes.

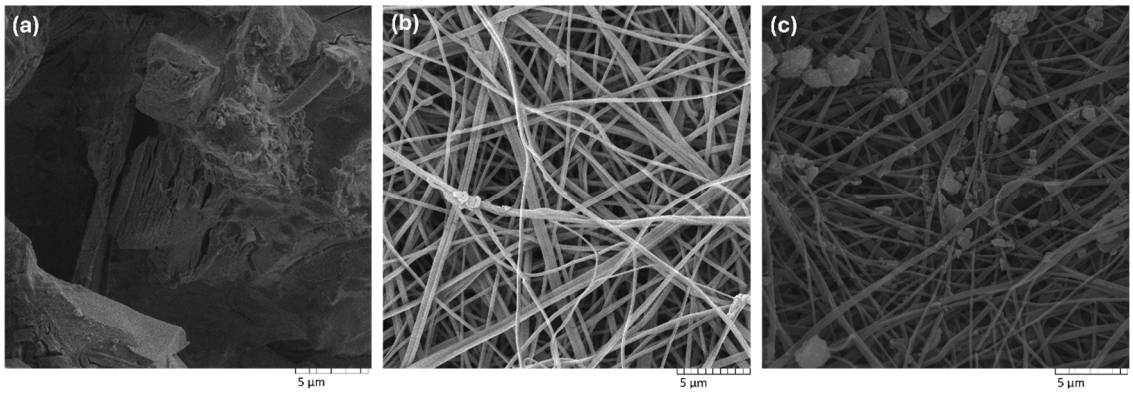

Fig. 2 – SEM images (a) BG58S-Cl particles, (b) PVA nanofibers, and (c) PVA nanofibers containing BG58S-Cl particles.

REFERENCES

[1] Fraga G. Curativos produzidos a partir de nanofibras de PVA contendo cloranfenicol. Dissertação (Mestrado em química), Universidade Estadual do Oeste do Paraná, 2022.

[2] Matos R et al. Polyvinylpyrrolidone nanofibers incorporating mesoporous bioactive glass for bone tissue engineering. Biomimetics, 2023, 8, p.206.

[3] Nataraj D, Reddy R, Reddy N. Crosslinking electrospun poly (vinyl) alcohol fibers with citric acid to impart aqueous stability for medical applications. European Polymer Journal, 2020, 124, p.109484.

[4] Vichery C, Nedelec J. Bioactive glass nanoparticles: from synthesis to materials design for biomedical applications. Materials, 2016, 9, p.288.

Proceedings IRF2025: 8th International Conference on Integrity-Reliability-Failure
In Engineering, Materials, Manufacturing and Biomechanics. Porto 15-18 July 2025
DOI: https://doi.org/10.24840/978-972-752-323-8

PAPER REF:22448

SILK FIBROIN-PVP-NPG-BASED BARRIER MEMBRANES FOR TISSUE REGENERATION THERAPY

Ivone Regina de Oliveira[1(*)], Isabela dos Santos Gonçalves[1], Tiago Moreira Bastos Campos[2], Leandro José Raniero[1], Luana Marotta Reis de Vasconcellos[3], Fernando dos Santos Ortega[1], João Henrique Lopes[4]

[1]Institute for Research and Development, University of Vale do Paraíba, São José dos Campos, SP, Brazil
[2]Federal University of Pelotas, Pelotas, RS, Brazil
[3]Institute of Science and Technology, Paulista State University, São José dos Campos, SP, Brazil
[4]Department of Chemistry, Technological Institute of Aeronautics, São José dos Campos, SP, Brazil
[(*)]*Email:* ivonero@univap.br

ABSTRACT

This study aimed to evaluate electrospun membranes for guided tissue/bone regeneration composed of silk fibroin (SF), poly(vinylpyrrolidone) (PVP) and treated graphene nanoplatelets (GNP-T). The membranes, produced using the electrospinning method, exhibited continuous, defect-free nanofibers. The study indicates that the choice of solvents and the crosslinking method directly impact the physicochemical properties of SF membranes. The functionalization of GNP with chemical groups compatible with the matrix resulted in a stronger and more stable bond, ensuring that the GNP remained adhered to the fibers.

Keywords: Barrier membranes, silk fibroin, nanoparticles, tissue regeneration.

INTRODUCTION

Guided tissue/bone regeneration (GTR/GBR) employs biocompatible membranes to restore the architecture and functionality of periodontal tissues by preventing epithelial and connective tissue migration. This allows progenitor cells in the periodontal ligament to regenerate alveolar bone, connective attachment, and periodontal tissues. Traditionally, synthetic or collagen-based membranes, with or without calcium phosphate-based grafts, have been used. However, these membranes often lack sufficient mechanical strength and biological functionality to endure surgical handling, maintain integrity during healing, and resist forces such as cellular traction and wound contraction. To overcome these limitations, this study developed hybrid electrospun membranes integrating the biocompatibility of silk fibroin (SF) and the synthetic polymer poly(vinyl pyrrolidone) (PVP) with graphene nanoplates (GNP). This combination aimed to improve mechanical strength, preserve structural integrity, and enhance osteogenic properties, offering a promising solution for clinical applications in GTR/GBR.

RESULTS AND CONCLUSIONS

The study indicates that the choice of solvents directly impact the physicochemical properties of SF membranes. Formic acid (AF) promotes the formation of a greater number of β-sheets, while HFIP favors the formation of α-helices, influencing the final conformation of silk fibroin films. From the analysis of Figure 1(b), it is possible to observe nanofibers with a smooth, continuous morphology and no beads using HFIP (Hong H et al. 2020). GTR/GBR barrier membranes must have mechanical strength to withstand handling, implantation, and the bone regeneration process, resisting cellular traction forces and wound contraction during healing.

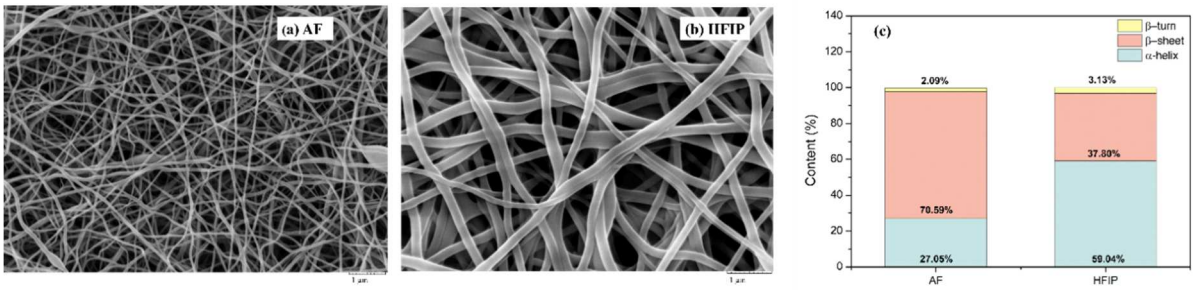

Fig. 1 - SEM images of silk fibroin (SF) nanofibers dissolved in (a) formic acid (AF), (b) hexafluoroisopropanol (HFIP), and (c) the content of the components that make it up in the amide I region.

The functionalization of GNP with chemical groups compatible with the matrix resulted in a stronger and more stable bond, ensuring that the GNP remained adhered to the fibers. The improved mechanical properties indicated good dispersion of GNP in the matrix and the formation of bonds between GNP-T and the nanofibers (Khan T et al. 2023). Figure 2 presents the results obtained after the electrospinning of PVP/GNP membranes.

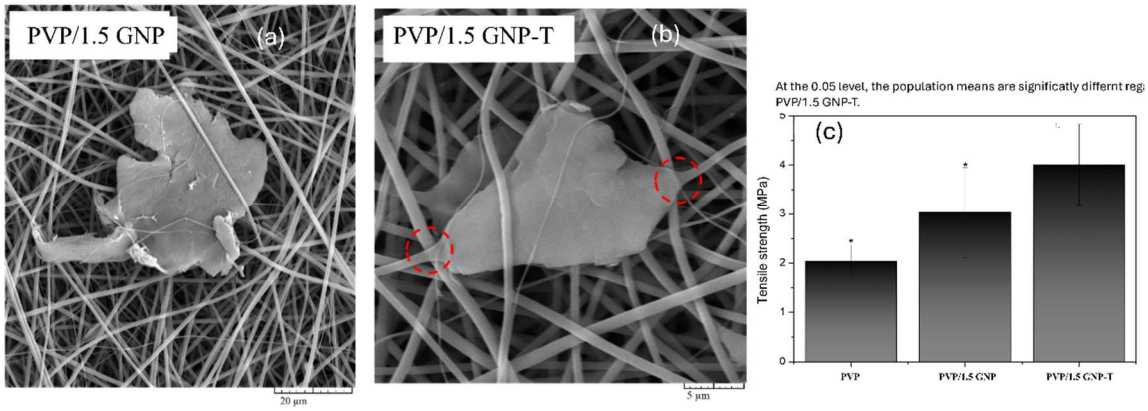

Fig. 2 - SEM images of PVP nanofibers containing GNPs, (b) GNP adhered to the fiber after functionalization, and (c) tensile strength of membranes.

FT-IR spectra also confirmed the retention of SF's chemical structure post-incorporation, as evidenced by Amide I, II, and III bands at approximately 1618 cm^{-1}, 1514 cm^{-1}, and 1230 cm^{-1}, respectively (Liu Z et al. 2022). The absence of changes in the spectra and fiber morphology indicates that the interactions between SF, PVP and GNP did not significantly alter the primary or secondary chemical structure of the protein.

REFERENCES

[1] Hong H *et al*. Cytocompatibility of modified silk fibroin with glycidyl methacrylate for tissue engineering and biomedical applications. Biomolecules, 2020, 11, p.35. v. 11, n. 1, p.35.

[2] Khan T, Aslam M, Basit M. *et al.* Graphene-embedded electrospun polyacrylonitrile nanofibers with enhanced thermo-mechanical properties. Journal of Nanoparticle Research, 2023, 25, p.1-7.

[3] Liu Z *et al*. Electrospinning silk fibroin/graphene nanofiber membrane used for 3D wearable pressure sensor. Polymers, 2022, 14, p.3875.

Proceedings IRF2025: 8th International Conference on Integrity-Reliability-Failure
In Engineering, Materials, Manufacturing and Biomechanics. Porto 15-18 July 2025
DOI: https://doi.org/10.24840/978-972-752-323-8

PAPER REF: 22454

MECHANICAL ANALYSIS OF THE KNEE OF A BIPED ROBOT

Gerardo García Liñán(*), Sergio Sierra Segura, Juan César BeltránMorales, Pedro de Jesús García Zugasti[1],Ludy Magnolia Valdez Martínez[1], Juan Gabriel Sandoval Granja, Juana Elizabeth de la Rosa Hernández

Instituto Tecnológico de San Luis Potosí, San Luis Potosí México.
(*)*Email:* gerardogarcia.linan80@gmail.com

ABSTRACT

The present work is the design of a humanoid robot called TGK with movement capabilities. Likewise, it performs high-risk tasks for a person, in this way it can be used in other applications, such as, for example, it could function as a Rescue Robot.It is proposed to create a humanoid robot that is sufficiently capable of walking in a controlled environment, and can lift objects in its path. For this reason, the analysis of the knee is carried out since it is one of the basic mechanisms of the robot. This paper presents the design and basic mathematical analysis of the knee of a biped for educational purposes to facilitate calculations for students of these subjects.

Keywords: biomechanics, design, reliability, mathematical analysis, equations.

INTRODUCTION

In the field of robotics, the development of bipedal robots that mimic human locomotion has presented one of the greatest technical and mechanical challenges. The knee, as an essential part of the locomotion system, plays a crucial role in the stability and efficiency of movement. Understanding and mathematically modelling the behavior of the knee of a bipedal robot is key to the design and optimization of robots that can walk, run, or adapt to different types of terrain effectively.

The mathematical analysis of a robot's knee not only allows understanding its kinematic and dynamic behavior, but also facilitates the prediction of the forces and moments acting on its components, as well as its interaction with the rest of the system. These mathematical models are fundamental for the design of actuators, the selection of materials, and the implementation of control algorithms that ensure stable and efficient locomotion.

This article aims to explore the methods used to mathematically analyze the knee of a biped robot. Kinematic models describing joint motions, methods for calculating forces and moments, and techniques used to improve robot stability and control will be presented. In addition, the importance of considering human biomechanics in the design of these systems will be discussed, in order to achieve more natural and adaptive movements. Through this analysis, we aim to offer a comprehensive view of the challenges and advances in the study and design of the knee of a biped robot.

THEORY

Mechanical analysis of a bipedal robot knee in the field of robotics is critical to understanding how the robot's motion and stability can be designed and optimized. Here are some key points that are typically considered in such analysis:

1. Knee Kinematics: This involves studying the motions and positions of the moving parts of the robot's knee. Mathematical models are used to describe the geometry and trajectory of joint movements.
2. Dynamics: This refers to the forces and moments acting on the knee during movement. It is essential to calculate how these forces affect the robot's performance and how they can be mitigated to improve efficiency and durability.
3. Load Analysis: The load-bearing capacity of the materials and structures that make up the robot's knee is assessed. This includes considerations of the mechanical stress and strength of the materials used.
4. Stability and Balance: How the bipedal robot's balance and stability can be maintained during various activities and under different terrain conditions is investigated.
5. Actuator Design: Actuators are key components that provide motion to the robot knee. We analyze how they can be designed to optimize performance and minimize energy consumption.
6. Control and Feedback: Control algorithms are developed that allow the robot to move accurately and respond to changes in its environment. Sensory feedback plays a crucial role in this aspect.
7. Impact of Human Biomechanics: In some cases, the robot knee can be designed taking into account biomechanical principles learned from the functioning of the human knee, to achieve more natural and efficient movements.

In summary, mechanical analysis of the knee of a bipedal robot combines elements of mechanical engineering, biomechanics, and control to create robotic systems that are stable, efficient, and capable of performing a wide range of movements.

The study of the mechanical motion of the knee of a bipedal robot involves a combination of kinematic and dynamic modelling. The main equations and concepts used in these analyses are presented below:

1. Inverse Kinematics (Position and Motion)

In inverse kinematics, the goal is to determine the joint angles required (in this case, the knee) to reach a desired position in space.

General Equation of Joint Motion Kinematics

If the knee is modelled as a crank-type mechanism (with a geometry similar to a lever system), the equations governing joint motion can be described by the law of cosines and the geometric relationships between the links of the system.

For a knee, motion can be modelled as a two-link system: the femur (upper part) and the tibia (lower part), connected by the knee joint.

If we define:

θ_1: Knee flexion angle (between femur and tibia).

L_1: Length of the femur.

L_2: Length of the tibia.

x and y: : Cartesian positions of the foot with respect to the origin.

The position equation in inverse kinematics can be expressed as:

$$\text{Foot position} = (\theta_1)=(x,y) \quad (1)$$

Where the angle θ_1 depends on the lengths L_1 and L_2, and the position of the foot (x,), obtained from the law of cosines:

$$x=L_1\cos(\theta_1)+L_2\cos(\theta_1+\theta_2) \quad (2)$$

$$y=L_1\sin(\theta_1)+L_2\sin(\theta_1+\theta_2) \quad (3)$$

In this case, θ_2 is the angle of the tibia relative to the femur.

2. Velocity Kinematics

The analysis of joint velocities is essential to understand dynamic motion. For a bipedal robot, the angular velocity $\dot{\theta}_1$ of the knee can be derived from the relationship between the velocities of the moving parts.

Relationship between joint speeds:

$$\dot{x}=\frac{d}{\mathrm{dt}}\,(L_1\cos(\theta_1)+L_2\cos(\theta_1+\theta_2)) \quad (4)$$

$$\dot{y}=\frac{d}{\mathrm{dt}}\,(L_1\sin(\theta_1)+L_2\sin(\theta_1+\theta_2)) \quad (5)$$

By deriving these expressions, we obtain the necessary angular velocities at each joint:

$$\dot{\theta}_1=\frac{\dot{x}*\left(L_1 sin(\dot{\theta}_1)+L_2 sin(\theta_1+\theta_2)\right)-\dot{y}*(L_1 cos(\theta_1)+L_2 cos(\theta_1+\theta_2))}{L_1*L_2*\sin(\Theta_2)} \quad (6)$$

3. Dynamics (Newton's Second Law and Models of Motion)

To analyze the dynamics of the knee, the equations of motion that describe the forces and moments that affect the joint are used. This can be done using Newton's second law or the Lagrange method.

Forces and moments at the knee:

For each knee joint, the equations of motion can be written using Newton's law for rotations:

$$\tau=\mathrm{I}\cdot\alpha+\tau_{\mathrm{ext}} \quad (7)$$

Where:

τ is the torque applied at the joint.

I is the moment of inertia of the leg part (femur or tibia) about the joint.

α is the angular acceleration of the joint.

τ_{ext} is the external moment due to external forces (such as the weight of the leg or contact with the ground).

Calculation of the moment of inertia *I* of moving parts:

$$I=\frac{1}{3}mL^2 \quad (8)$$

Where m is the mass of the part (femur or tibia) and L is the length of the part. This calculation can be extended to more complex systems that include the geometric characteristics of each segment.

Lagrange equations for knee motion:

The Lagrange principle is a powerful tool for deriving the equations of motion of a complex dynamic system. The Lagrange function L is defined as:

$$L=T-U \tag{9}$$

Where:

T is the kinetic energy of the system (which depends on the joint velocities).

U is the potential energy (due to gravity and other external forces).

The Lagrange equation is expressed as:

$$\frac{d}{dt}\left(\frac{\partial \mathrm{L}}{\partial \mathrm{q_1}}\right)-\frac{\partial L}{\partial \mathrm{q_1}}=0 \tag{10}$$

Where $\dot{q}_1$ is the generalized coordinate of the joint (for example, the angle θ_1 of the knee) and $\dot{q}_1$ is the associated velocity.

4. Stability and Control

Dynamic analysis also includes the study of the stability of the knee under different loading and motion conditions. Stability equations are derived from the equation of motion in terms of stiffness and damping matrices, allowing control algorithms to be designed that ensure the robot maintains its balance.

Knee control using feedback:

Knee control is typically performed using a PID control or a dynamic model-based controller to ensure the knee moves stably and efficiently during locomotion.

This mathematical analysis provides a framework for understanding the mechanical behavior of a bipedal robot's knee, from basic motion to the complex dynamic forces involved in its operation. These models allow for optimization of robot design, improved performance, and ensuring stability during walking and other activities.

RESULTS AND CONCLUSIONS

Some robots are intended for use in the home, assisted living facilities, and hospital settings. They work to automate some physical tasks that an older person may not be able to do, such as feeding themselves, brushing their teeth, getting in and out of bed, getting in and out of a wheelchair, and adjusting the bed for maximum comfort. In some cases, robots are conceived as part of a ubiquitous computing system, combining cameras and other sensors in the environment and computer-controlled devices (such as light switches, doors, and televisions). In others, robots serve SAR functions, such as promoting physical and cognitive exercise.

Biomechanical and dynamic motion models: Several biomechanical models have been developed to gather data on the nature of stress exerted on body structures and tissues by loads and forces during manual assembly processes [1]. Tools used to collect and/or analyze data on manual assembly jobs included lifting limitations according to the National Institute for Occupational Safety and Health (NIOSH) guideline for biomechanical measurement according to Waters in their work published in 1994; worker posture during the task according to OWAS guidelines on measuring risk or injury [2]; Methods Time Measurement (MTM) cycle time [3]; and the Rapid Upper Extremity Assessment (RULA)[4], a measure of risk factors associated with upper extremity disorders; the 3D University Static Strength Prediction Program (3DSSPP) [5]; psychophysical approach [6];

Most of the biomechanical models mentioned are used to estimate muscle forces in static postures. However, the effects of inertia are not accounted for in these models; therefore, static models alone are not considered accurate enough to offer truly predictive data [7].

Much of the research conducted on human dynamic movement has been conducted using multi-segment models developed to evaluate force or torque moments applied about the axis of joints with the joint at various angles. Most of this research describes the biomechanical modeling of a single body part. A small proportion of that research has been directed specifically at full-body models for activities involving both the lower extremities

In addition to the above, Winter classified the attachment moments to be positive when the pull direction is counter-clockwise and negative when clockwise, as shown in Figure 1 [8], the same model is presented in this work which can be seen further in Figure 2.

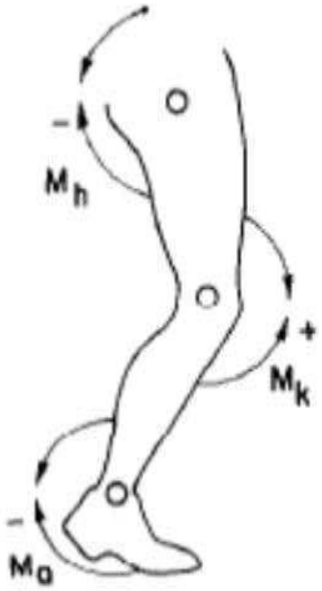

Fig. 1 -. Joint force moment profile at the ankle, knee and hip during walking.

Fig. 2 - TGK robot leg; the lower part is the one that will make contact with the ground, the central link functions as a knee and the two upper cylindrical joints represent the equivalent of a hip.

The robot's drive system has been proposed in an arrangement of two four-bar mechanisms linked together by a common link, similar to a knee, as shown in Figure 3. Therefore, this arrangement of mechanisms has two degrees of freedom.

To determine how each of the robot's legs moves, it is necessary to start from a kinematic diagram, which provides a general relationship between the positions of each of the mechanism segments [9]. The diagram was created considering the hip of the robot at the top while the ankle is at the bottom. From this diagram the restriction equations are determined for one of the legs (symmetry is assumed, both legs are equal), these equations are based on a 'closed loop' and therefore are equal to zero. The lengths of the links are constant with magnitudes I1, I2, I3 and I4, respectively. Likewise, the separations between the pivots of the 'knee' link (a, b, c, f), the 'hip' link (d) and the 'ankle' link (e) are also of constant magnitude [10].

Leg constraint equations

The angles between the links change as the inclination of the leg changes. The first constraint equations to be determined are those corresponding to the position along the ‘X’ axis (1) and those corresponding to the position along the ‘Y’ axis (2). Where a is the angle that will be applied by the motor or actuator to the system.

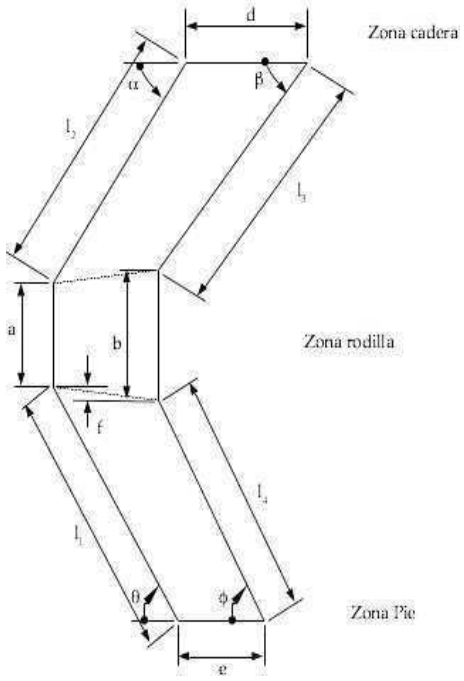

Fig. 3 - Kinematic diagram of a robot leg.

REFERENCES

[1] S. Kumar, Biomechanis in Ergonomics, vol. 1. 2015.

[2] O. Karhu, P. Kansi, I. Kuorinka, "Correcting working postures in industry: A practical method for analysis," Appl. Ergon., vol. 8, no. 4, pp.199-201, 1977.

[3] C. João, D.L.M. De Almeida, "Analysis of the Methods Time Measurement (MTM) Methodology through its Application in Manufacturing Companies," Flex. Autom. Intell. Manuf., vol. 1, no. March, pp.2-9, 2009.

[4] A.E. Dimate, D.C. Rodríguez, A.I. Rocha, "Percepción de desórdenes musculo-esqueléticos y aplicación del método RULA en diferentes sectores productivos: una revisión sistemática de la literatura," Rev. la Univ. Ind. Santander. Salud, vol. 49, no. 1, pp.57-74, 2017.

[5] R. Huangfu, T. Gao, L. Cao, S. Gallagher, "Multiple tasks input tool for 3D Static Strength Prediction Program," no. September, pp.2-3, 2015.

[6] J.E. Fernandez, R.J. Marley, "The development and application of psychophysical methods in upper-extremity work tasks and task elements," Int. J. Ind. Ergon., vol. 44, no. 2, pp.200-206, 2014.

[7] E. Mathieu, S. Crémoux, D. Duvivier, D. Amarantini, P. Pudlo, "Biomechanical modeling for the estimation of muscle forces: toward a common language in biomechanics, medical engineering, and neurosciences," J. Neuroeng. Rehabil., vol. 20, no. 1, pp.1-12, 2023.

[8] A. Al-zuheri, L. Luong, K. Xing, "Biomechanical Assessment of Lower Limbs Using Support Moment Measure at Walking Worker Assembly Lines," Ergon. - A Syst. Approach, p.232, 2012.

[9] T. Minato, M. Shimada, H. Ishiguro, S. Itakura, "Development of an Android Robot for Studying Human-Robot Interaction," pp.424-434, 2004.

[10] D. Feil-Seifer, M.J. Mataric, "Human-robot interaction," Invit. Contrib. to Encycl. Complex. Syst. Sci., pp.4643-4659, 2009.

Proceedings IRF2025: 8th International Conference on Integrity-Reliability-Failure
In Engineering, Materials, Manufacturing and Biomechanics. Porto 15-18 July 2025
DOI: https://doi.org/10.24840/978-972-752-323-8

PAPER REF: 22457

INVESTIGATING THE DISTAL CONNECTION STRENGTH OF A FUSED FILAMENT FABRICATED PROSTHETIC SOCKET

Clara Phillips[1(*)], Aaryan Nagpal[2], Mark Kortschot[3], Fae Azhari[1]

[1]Department of Mechanical and Industrial Engineering, University of Toronto, Toronto, Canada
[2]Department of Engineering Science, University of Toronto, Toronto, Canada
[3]Department of Chemical Engineering and Applied Chemistry, University of Toronto, Toronto, Canada
[(*)]*Email:* cl.phillips@mail.utoronto.ca

ABSTRACT

The connections used for assembling parts made with fused filament fabrication (FFF) can potentially become weak points in a multi-part structure, yet their strength is largely underreported in the literature. Lower-limb prosthetic socket manufacturing is one application where the adoption of FFF is hindered due to lack of guidance on how to reliably attach the distal end of the socket to the remaining prosthetic limb. Here, a comparison of the tensile strength of two attachment hardware types (hex-nuts and heat-set inserts) embedded in FFF samples is provided, and an approach for predicting failure of hardware samples using a stress-gradient condition is discussed. Predicted values are within 11% of experimental results. A case study of a prosthetic socket subjected to axial and bending moment loading is introduced, aiming to facilitate FFF adoption for prosthetic socket manufacturing.

Keywords: Fused filament fabrication, assembly hardware, finite element analysis, brittle failure criteria, prosthetic sockets.

INTRODUCTION

A lower-limb prosthetic socket is the connecting interface between a prosthesis and the user's residual limb. Therefore, each socket must be custom made to comfortably fit the user's unique physiology. Additive manufacturing, particularly fused filament fabrication (FFF), has become a popular technique for fabricating prosthetic sockets due to its ability to easily create custom, organically shaped structures. However, clinicians hesitate to fabricate sockets with FFF, as there is insufficient evidence of their structural integrity. In particular, the distal end of the socket (where it connects to the remaining prosthesis) is subject to extreme stress concentrations due to the connecting hardware. Only in one study have researchers directly measured the effective failure stress of AM material surrounding hardware (Burhan and Crawford, 2004).

In this study, we aim to predict tensile failure in the FFF material at stress concentrations caused by standard hardware. A prosthetic socket case study is used. FFF parts are orthotropic and exhibit brittle failure when loaded transversely to their printed layers. When in operation, sockets are loaded transversely to their layers, and have proven to fail in a brittle manner by delamination (mode I fracture) (van der Stelt et al., 2021). Therefore the failure criterion used in the finite element analysis (FEA) in this study is based on both the ultimate tensile stress and the stress-gradient condition (Kwon, 2021). Custom samples were created for testing the tensile strength of the FFF material surrounding embedded hardware (heat-set inserts and hex-nuts). Discrepancies between predicted (FEA) and experimental failure loads of these samples are discussed.

RESULTS AND CONCLUSIONS

Custom hardware samples were subjected to tensile loading until failure, and digital image correlation (DIC) was used to qualitatively assess the fracture initiation sites and the progression of brittle failure. Load *vs.* displacement curves for two FFF materials (PLA and carbon-fiber infused PLA) used with heat-set inserts and hex-nuts are shown in Figure 1A.

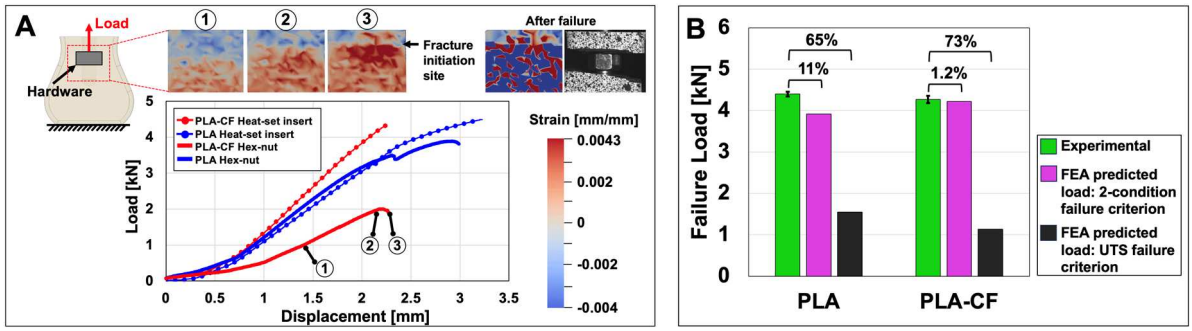

Fig. 1 - (A) Failure load curves for hardware samples with DIC results of a PLA-CF hex-nut sample; (B) Experimental *vs.* predicted failure loads.

Failure loads of the heat-set insert samples were predicted with FEA using a failure criterion where two conditions must be met (Kwon, 2021). The first condition states that, for failure to occur, the effective stress must be greater or equal than the transverse *UTS* of the material. The second condition, which relies on the stress gradient, is expressed in Equation (1):

$$\sigma_l \geq \left(\left| \frac{d\sigma_l}{ds} \right| 2E\Upsilon \right)^{\frac{1}{3}} \tag{1}$$

where σ_l is the local stress, E is the transverse elastic modulus, Υ is a material constant equivalent to the critical energy release rate of the material, and $d\sigma_l/ds$ is the stress gradient along the failure path, s. To predict failure, both conditions must be satisfied. Here, transverse E and *UTS* were measured from tensile coupon tests (ASTM D3039) where layers were printed perpendicular to the tensile load. The fracture toughness used to calculate Υ was estimated by considering the notches at the layer boundaries as small V-notches. The width of these notches have been reported to be up to 0.5 mm wide. By using the 2-condition criterion compared to the single *UTS* criterion, predicted errors decrease from 65% to 11% for the PLA sample and from 73% to 1.2% for the carbon-fiber PLA sample (Figure 1B).

The failure of a whole socket structure is also predicted and compared to experimental results. Here, an equivalent tensile load calculated from a combination of bending moment and axial load from a ground reaction force is applied, and the socket is connected to the prosthesis with heat-set inserts. Through this work, we aim to enhance the adoption of FFF for the prosthetics sector and other industries that rely on the functional performance of FFF parts.

REFERENCES

[1] Burhan D, Crawford R. Design and manufacture of an attachment fitting for transtibial prosthetic sockets using selective laser sintering. Materials Science, 2004, pp.794-807.

[2] Kwon YW. Revisiting failure of brittle materials. Journal of Pressure Vessel Technology, 2021, 143, p.064503.

[2] Van der Stelt M, Verhamme L, Slump CH, Brouwers L, Maal TJJ. Strength testing of low-cost 3D-printed transtibial prosthetic socket. Journal of Engineering in Medicine, 2021, pp.1-9.

TRACK - G: Energy and Thermo-Fluid Systems

Energy Systems
Thermal Barrier Coatings
Heat and Mass Transfer
Combustion
Experimental Fluid Dynamics
Computational Fluid Dynamics
Solid-Fluid Interactions,
Interfacial Dynamics
Turbulence Analysis
Case Studies

Proceedings IRF2025: 8th International Conference on Integrity-Reliability-Failure
In Engineering, Materials, Manufacturing and Biomechanics. Porto 15-18 July 2025
DOI: https://doi.org/10.24840/978-972-752-323-8

PAPER REF: 22558

THE FLUID-STRUCTURE ANALYSIS OF VACUUM PUMPS IN SEMICONDUCTOR FABRICATION FACILITY FOR IDENTIFYING THE STRUCTURAL DAMAGE AND CRACK

Chan Lee(*), Hyun Gwon Kil
Faculty of Mechanical Engineering, University of Suwon, Hwaseong, Republic of Korea
(*)*Email:* clee@suwon.ac.kr

ABSTRACT

The present study conducts the flow-structure analysis of roots type vacuum pumps of semiconductor fabrication facility. The computed CFD results for internal pressure and temperature distributions of vacuum pumps are applied to structural analyses of the pumps. The coupled analysis results between flow and structure show that the deformation of pump structure is mainly resulted from the thermal expansion by hot gas in pump, and the deformed impeller and housing produce their severe contact and impact phenomena causing mechanical damage and crack.

Keywords: Vacuum pump, dynamic mesh, housing, rotor, clearance, CFD, FEM, FSI.

INTRODUCTION

Since the chemical deposition process (CVD) mainly used in the semiconductor industry requires a low and medium vacuum state of about 0.01 Torr, various types of vacuum pumps are used to maintain this vacuum state. However, the semiconductor process gas flowing into these types of vacuum pumps contains process by-products other than gas, and these process by-products are deposited inside the pump and are a major factor in collisions between the housing/rotor of the pump, and the rotor/rotor of the pump, which often causes pump failure during the process. Therefore, this study performs computational fluid dynamics analysis on the gas flow inside the roots type vacuum pump for semiconductor processing, and through this, the flow characteristics of pressure and temperature distribution inside the pump are identified when the vacuum pump is operated, and structural damage and cracks of the pump are identified by performing structural analysis based on the temperature and pressure data obtained through flow analysis.

RESULTS AND CONCLUSIONS

In this study, the Fluent code as a CFD software is used for viscous flow analysis inside the pump. In order to consider the abnormal effect on the position change of the rotor, a dynamic mesh is used. Figure 1 shows the pressure distribution among the flow analysis results, and Figure 2 shows the temperature distribution. As a result of the pressure distribution, it can be seen that gas is transferred due to the motion of the rotor rotation in the pump, and a pressure increase appears. In addition, as a result of the temperature distribution, the gas temperature rises due to compression caused by the motion of the rotor in the pump, and the connection part between the pumps is maintained at a low temperature due to the wall heat loss. The high temperature around the rotor causes thermal expansion of the rotor and the housing.

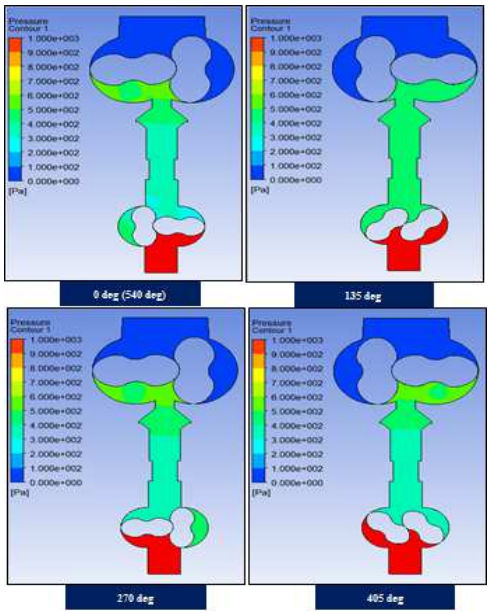

Fig. 1 - Pressure distribution of vacuum pumps.

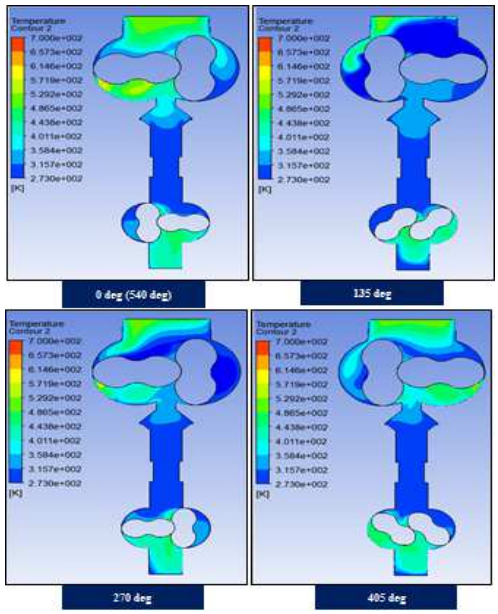

Fig. 2 - Temperature distribution of vacuum pumps.

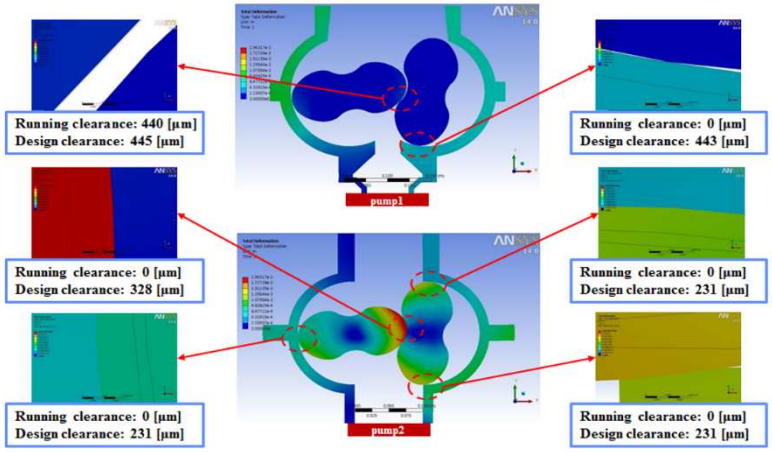

Fig. 3 - Deformation of rotors and housings of vacuum pumps.

Figure 3 shows the deformation values of the structural analysis when temperature and pressure are given as inputs. Since deformation is mainly caused by thermal expansion, as a result of selecting and analyzing several cases with a large temperature gradient, it is confirmed in Figure 3 that the rotor and the housing contact each other at the rotation angle of 280 deg. As shown in Figure 3, it can be seen that the running clearance becomes 0 by contacting at various parts of pump1 and pump2. This contact phenomenon is confirmed to be broken at the same angle as the simulation even in the actual operation field.

ACKNOWLEDGMENTS

This work was supported by the Korea Institute of Energy Technology Evaluation and Planning (KETEP) grant funded by the Korea government Ministry of Trade, Industry & Energy (MOTIE), Republic of Korea. (No. 2021202080026).

REFERENCES

[1] Lee C., Fluid-Structure Analysis of WH4400, Technical Report, LOT vacuum, 2010.

Proceedings IRF2025: 8th International Conference on Integrity-Reliability-Failure
In Engineering, Materials, Manufacturing and Biomechanics. Porto 15-18 July 2025
DOI: https://doi.org/10.24840/978-972-752-323-8

PAPER REF: 22600

TECHNICAL-ECONOMIC ASSESSMENT OF ETHANOL CONVERSION TO JET FUEL PRODUCTION CONSIDERING CADO TECHNOLOGY

York Castillo Santiago[1(*)], Rafael Menegassi de Almeida[2], Leandro Novaes[1], Jeiveison Gobério Santos Maia[1], Stefano Ferrari Interlenghi[1]

[1]SENAI Innovation Institute for Biosynthetics and Fibers, Rio de Janeiro,RJ 21941-857, Brazil
[2]Research and Development Center, PETROBRAS, Rio de Janeiro, RJ 21941-915, Brazil
[(*)]*Email:* ycsantiago@cetiqt.senai.br

ABSTRACT

In this work, a technical-economic evaluation of the production of sustainable aviation fuel (SAF) considering the Consolidated Alcohol Deoxygenation and Oligomerization (CADO) process, which is one of the most recent Alcohol-to-Jet (ATJ) technologies, was performed. For this purpose, the simulation of the CADO process was performed using the Aspen Plus v14.0 software, with fuel-grade ethanol serving as the primary raw material of the process. A self-developed method for economic and financial analysis was conducted by calculating the economic indicators of the process, such as the SAF's minimum selling price (MSP). The results indicated that to produce 13,232 kg of SAF, 5.93 kg of ethanol/kg-SAF and 7.87 kg of steam/kg-SAF were required as raw materials, while the technical indexes indicated that 1.58 kg of BTX (benzene, toluene, and xylene)/kg-SAF and 0.35 kg of naphtha/kg-SAF were produced as by-products. Regarding the economic assessment, a capital expenditure (CAPEX) of $USD 178.34 million was determined, of which the equipment required for the process contributed $USD 58.86 million. In the case of operating expenses (OPEX), the total value reached $USD 471.77 million, of which $USD 404.35 million were associated with the raw materials used. Finally, considering a 20-year investment horizon and a 10-year depreciation period, the MSP obtained was $ 2,829.70 per ton-SAF.

Keywords: Biofuels, Sustainable aviation fuel, Ethanol use, Bioenergy.

INTRODUCTION

According to the International Energy Agency (IEA 2025), the aviation sector was responsible for 2.5% of global energy-related CO_2 emissions in 2023. To mitigate the impact of global aviation, interest in more sustainable jet fuels has emerged. Among these fuels, sustainable aviation fuel (SAF) stands out, which is designed to be a “drop-in” alternative and can be blended directly with conventional jet fuel and used in existing aircraft without significant modifications to engines or infrastructure (Santiago et al. 2024). SAF can be obtained from several different routes, one of which is Alcohol-to-Jet (ATJ). One of the main advantages of the ATJ route consists in its use of ethanol as its primary raw material, which has some advantages such as large-scale production, price, established logistic chain, and market share compared to other alcohols (Watson et al. 2024). The ATJ process consists of three catalytic reaction steps: dehydration, oligomerization, and hydrogenation, with butanol and ethanol being the only two alcohols currently used in ATJ processes. The goal of this process is to convert short-chain alcohols (C2–C4) into longer hydrocarbons (C8–C16) (Lau et al. 2024).

A technology that differs from the conventional ATJ process is known as Consolidated Alcohol Deoxygenation and Oligomerization (CADO), which can transform alcohols into hydrocarbons in a single step without the percentage of water in the alcohol affecting the SAF selectivity (Hannon et al. 2020). The CADO technology was developed by Vertimass in partnership with Oak Ridge National Laboratory (ORNL) at a scale of ~2 kg ethanol per day using V- or Ga-supported ZSM-5 to convert aqueous ethanol (40% wt. H_2O, 350 °C, 4 bar) to liquid hydrocarbons, which are separated from H_2O and light gases (burned for process heat) in a decanter (Eagan et al. 2019). According to Hannon et al. (2020) the product distribution obtained for the CADO process is concentrated in the typical jet fuel range (C7 to C16), with 40% by weight of the product distribution and about 57% aromatics corresponding to a mixture of benzene, toluene, and xylene (BTX). This excess of aromatics is beneficial, as when mixed with aviation fuel (up to a maximum of 25% vol.), it improves certain properties, including elastomeric swelling, material compatibility, and lubricity characteristics (Wang et al. 2020).

Recently, the economic viability of CADO technology has been analyzed by different authors, such as Klein et al. (2023) developed a computational model to evaluate the impact of feedstock and by-product selection on the overall economics of a North American biorefinery producing SAF, identifying the benefits of selecting a higher-yielding fuel alcohol, i.e., ethanol over isobutanol. The results indicated that it is possible to sell SAF at $ 3.15 per gallon of gasoline-equivalent (GGE) and produce carboxylic acids and esters. Anekwe et al. (2024) performed a techno-economic evaluation of a single-step transformation of wet ethanol vapor to hydrocarbons using a Ni-doped HZSM-5 catalyst. The authors determined that the annualized capital and operating costs for converting wet ethanol to fuel blending stocks were predicted to be $0.05/L, indicating that at an oil price of $100/BBL (Barrel of Crude Oil), the expected MSP for CADO-produced fuel blending stocks are similar to conventional gasoline prices. However, at an oil price of $60/BBL, the MSP for CADO-derived blending stocks is not competitive with conventional gasoline.

Therefore, this work aims to indicate the main findings of the technical-economic evaluation of SAF production through CADO technology in the Brazilian context, aiming to identify the viability of scaling up this process.

MATERIALS AND METHODS

The previously described CADO process, which obtains SAF, naphtha, and BTX, was simulated in Aspen Plus v14.0 (Aspentech). The Block Flow Diagram (BFD) of the process is shown in Figure 1, divided into three hierarchies: A100 – reaction section, A200 – gas separation section, and A300 – purification section.

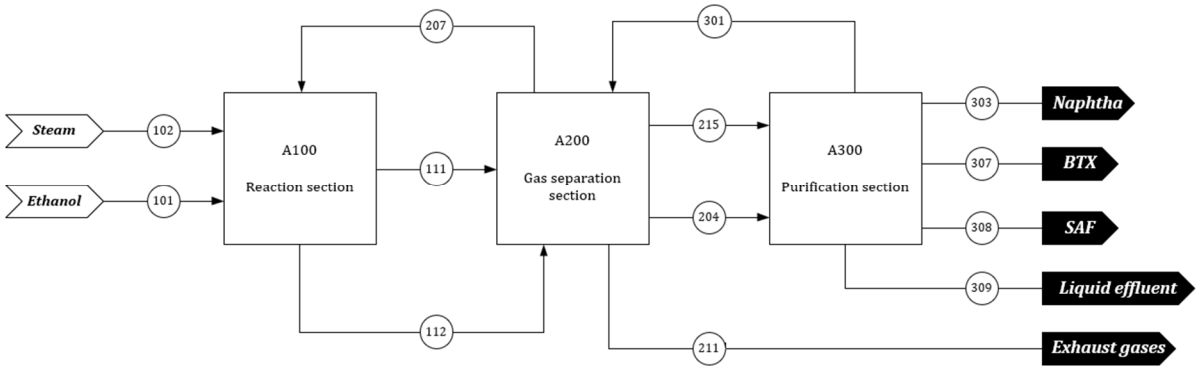

Fig. 1 - Block flow diagram of CADO process.

Due to the polar nature of water and ethanol, sections A100 and A200 were simulated using the non-random two liquid-Redlich Kwong (NRTL-RK) activity model, while hydrocarbon separation in the distillation section (A300) was conducted with the Peng-Robinson equation of state (Haydary 2019). A (P,T) flash was conducted in the frontier of A200 to A300 in order to change the thermodynamic model.

The Process Flow Diagram (PFD) of area A100 is shown in Figure 2. The raw material of the process is hydrated ethanol with a mass composition of 92.5% ethanol and 7.5% water. The liquid hydrated ethanol at 25 °C and atmospheric pressure (stream 101) is pumped via P-101 and vaporized in heat exchanger E-101. It is subsequently mixed with medium-pressure steam (at 12 bar), resulting in stream 105, which passes through valve V-101 to reduce the pressure to 6 bar, operating pressure of R-101. The mixture is then heated again in exchangers E-102 and E-103 to ensure the operating temperature of reactor R-101. The gases produced in the reactor (stream 109) are used as working fluid in exchangers E-101 and E-102 before being sent to area 200 as stream 111.

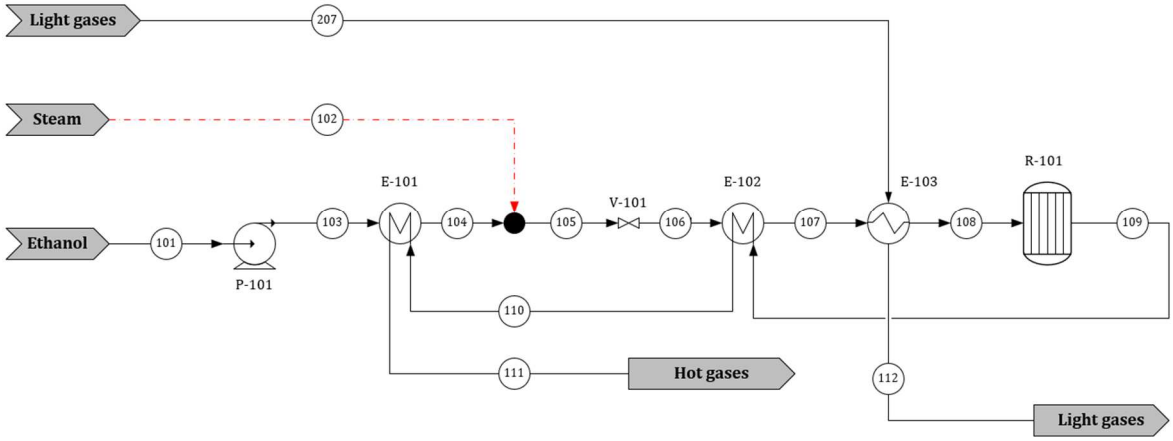

Fig. 2 - Process flow diagram of A100.

The PFD of area A200 is shown in Figure 3. The reactor products (stream 111) are cooled in exchanger E-201 and introduced into decanter V-201. The generated gas stream 202 is sent to the combustion chamber (R-201), where it is mixed with compressed air (stream 206) and light gases from area 300 (stream 301) to produce stream 207, which will be used in the energy integration of exchanger E-103 (A100).

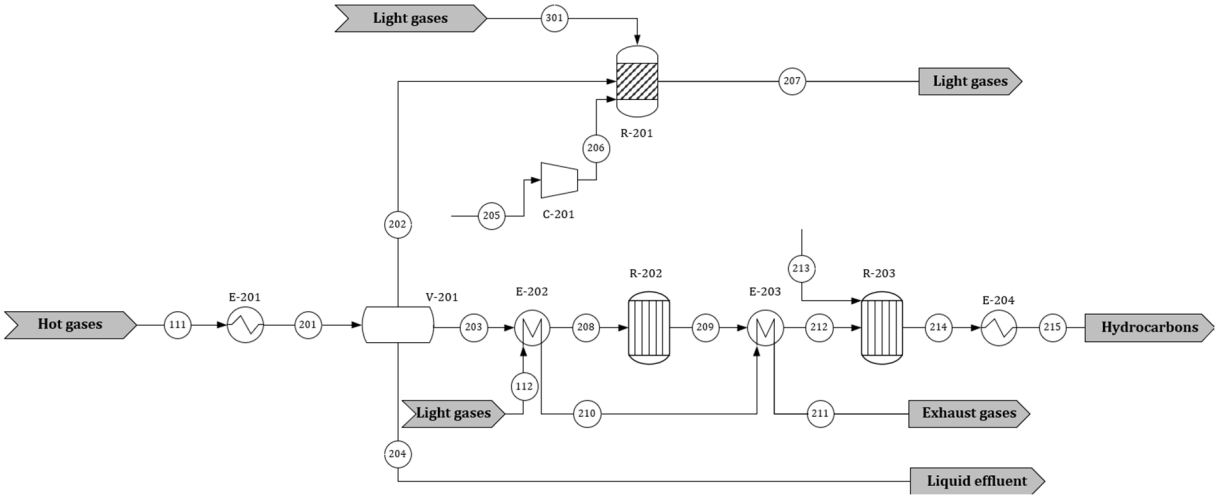

Fig. 3 - Process flow diagram of A200.

The liquid stream produced in the decanter (stream 203), which contains the hydrocarbons and aromatics generated in R-101, is heated in the E-202 exchanger to obtain a phase change and sent to an alkylation reactor (R-202) and later to a hydrogenation reactor (R-203). The alkylation reaction converts the excess aromatics and small paraffins into hydrocarbons in the C7-C12 range, generating stream 215. Finally, the organic phase of the decanter is stream 204, which will later be mixed with other liquid effluents generated during the process.

The A300 PFD is shown in Figure 4. The hydrocarbons and aromatics from A200 (stream 215) are sent to a first distillation column (C-101), where light gases (stream 301), liquid effluent (stream 302), naphtha (stream 303), and a stream with a mixture of heavier hydrocarbons and aromatics (stream 304) are generated. This last stream is sent to the second distillation column (C-302), where BTX and SAF are produced, which are cooled to 30°C respectively in exchangers E-301 and E-302, generating streams 307 and 308.

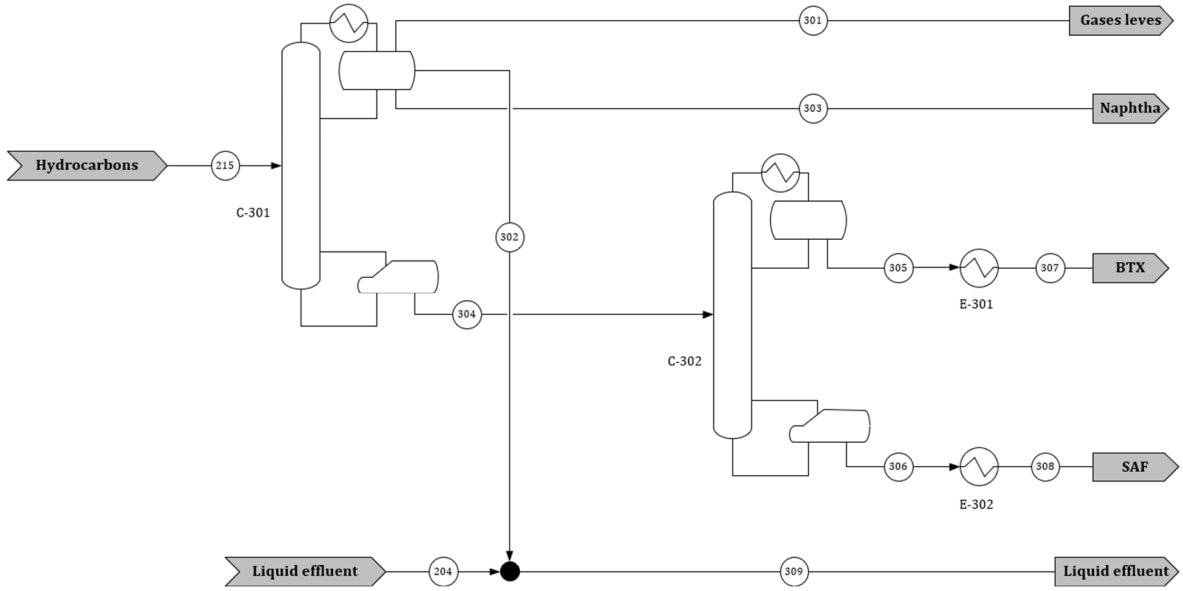

Fig. 4 - Process flow diagram of A300.

Table 1 shows the main assumptions for the economic evaluation of the processes, from which the additional capital costs related to the construction of the plant (such as instrumentation, piping, civil construction, and electrification) are estimated, as well as the operational costs of the process.

Table 1 - Assumptions for economic evaluation.

Type of main product	Basic chemical
Technology Readiness Level (TRL)	Pilot (5 to 7)
Availability of information	Medium
Process severity	High
Type of material handled	Fluids
Plant size	Large

Equipment acquisition costs were estimated based on the assumptions mentioned in Table 1 and results obtained from Aspen Process Economic Analyzer v14.0 (APEA). These costs were calculated for the main plant area (ISBL; Inside Battery Limits) and the auxiliary area (OSBL; Outside Battery Limits), such as storage tanks for raw materials and products and systems for supplying utilities to the main process.

The total equipment acquisition cost served as the primary basis for calculating the other CAPEX items. Expenses for equipment installation, piping, electrical work, instrumentation, and other related costs are also estimated using APEA software and added to the plant's direct and indirect costs. The sum of the equipment acquisition and installation costs results in the installed cost of the plant also referred to as direct costs in this work. Indirect costs, including construction, office, and off-site costs, are added to this value. The value obtained in this last item includes expenses for freight, taxes on acquisition, engineering, administrative area, and contract fees. The project contingency must increase the sum of these installments, and, finally, the values must be updated over time and by location.

The MSP corresponds to the selling price that results in a zero net present value (NPV) at the end of the project's investment horizon. Therefore, the MSP corresponds to the price guaranteeing the minimum financial return the investor desires to justify the investment risk. Some financial assumptions must be considered when constructing the cash flow, which are presented in Table 2.

Table 2 - Financial assumptions defined for the construction of cash flow.

Item	Value
Project lifetime	20 years
Engineering, procurement, and construction time	2 years
Land purchase factor (% of ISBL + OSBL)	2.0%
CAPEX distribution	1st year: 60.0% 2nd year: 40.0%
Financing type	None
Minimum Acceptable Rate of Return (MARR)	14.44%
Brazilian taxes	34.0%
Depreciation method	Straight line
Depreciation period	10 years
Residual value (% CAPEX)	20.0%

RESULTS AND DISCUSSION

Table 3 contains the technical indices obtained via simulation for the process, products, raw materials, and utilities (cooling water, electricity, heating, and catalyst). For each kg of SAF produced, 5.93 kg of ethanol, 7.87 kg of steam, 0.74 kg of catalyst, and 0.28 kW of electricity are necessary.

Table 3 - Financial assumptions defined for the construction of cash flow.

Item	Value	Technical Index
Ethanol	78,553 kg/h	5.93 kg/kg-SAF
Steam	104,083 kg/h	7.87 kg/kg-SAF
Electricity	3,738 kW	0.28 kW/kg-SAF
Cooling water	13,894 ton/h	1.05 ton/kg-SAF
Natural Gas	969,986 kg/h	73.3 kg/kg-SAF
Catalyst	5,688 kg/h	0.43 kg/kg-SAF
Naphtha	4,621 kg/h	0.35 kg/kg-SAF
BTX	21,118 kg/h	1.59 kg/kg-SAF
SAF	13,232 kg/h	-

It is worth mentioning that the high natural gas index (73.3 kg/kg-SAF) is mainly associated with the fact that it is used as feedstock to produce steam (stream 102 in Figure 2) that is mixed with ethanol at the beginning of the process; however, steam is also generated to be used in the reboilers of the two distillation columns. A high demand for cooling water is also observed as it is used as the cooling medium in four heat exchangers (E-201, E-204, E-301, E-302) and the condensers of the distillation columns.

Regarding economic assessment, the results indicated that the total investment in equipment is $USD 51.18 million, where 58.32% of this value is associated with the area destined for the allocation of the plant's main equipment (known as Inside Battery Limits), while 41.68% is attributed to the area destined for the allocation of the plant's auxiliary equipment (known as Outside Battery Limits), as indicated in Figure 5a. Considering the industrial capacity of the plant and that the products obtained from the CADO process are stored for 7 days, the capacity (and investment) of the storage tanks are high, $USD 22.24 million (43.47% in Figure 5b). This value, combined with the large amount of piping required, leads to a high OBSL. Furthermore, the installation, indirect field, and non-field costs are included in the CAPEX, which has a value of $USD 178.37 million, considering a location factor of 0.97, as shown in Table 4.

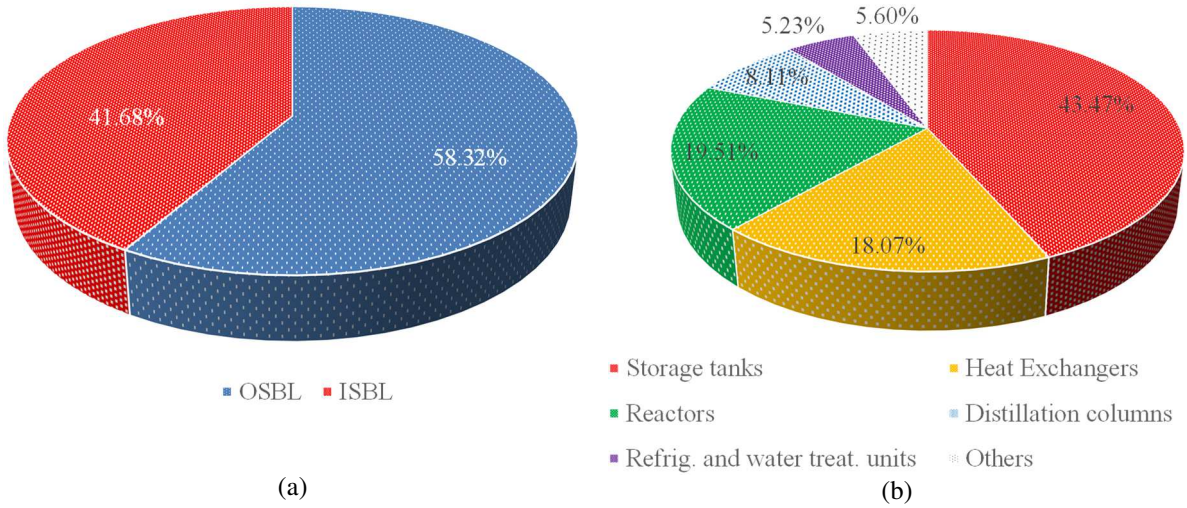

Fig. 5 - Distribution of equipment costs by area and by equipment.

Table 4 - Value calculated for CAPEX.

Item	Value
Equipment costs	$USD 51.18 million
Unscheduled equipment (% of equipment costs)	15.0%
Total equipment costs	**$USD 58.86 million**
Installation costs	
Piping, Civil, Steel, Instrumentals, Electrical, Insulation, and Paint Costs	**$USD 48.87 million**
Indirect field costs	
Field office staff and Construction indirect	**$USD 15.33 million**
Non-field costs	
Freight, Taxes and permits, Engineering, GA overheads, Contract fee	**$USD 23.95 million**
Project contingency	30.0%
Time update factor	0.96
Location factor	0.97
Project CAPEX	**$USD 178.37 million**

Table 4 shows that the higher contribution to CAPEX comes from direct costs, specifically the total cost of equipment and plant adaptation, including piping, Civil, Steel, Instrumentation, Electrical, Insulation, and painting costs. The second-highest costs are associated with non-field costs, mainly taxation, due to the scenario being in Brazil with a 34% tax rate.

OPEX formed by the variable, direct fixed, and indirect fixed costs correspond to $USD 471.68 million, in which ethanol (raw material) acquisition cost had the higher contribution with $USD 359.91 million, as indicated in Table 5.

Table 5 - Value calculated for CAPEX.

Item	Value
Raw materials	$USD 359.91 million
Chemical inputs and utilities	$USD 44.44 million
Total variable costs	**$USD 404.35 million**
Direct fixed costs	
Labor costs	$USD 1.84 million
Supply and maintenance costs	$USD 2.14 million
Administrative overhead, Manufacturing overhead Taxes and insurance, Patents and royalties	$USD 11.02 million
Total direct fixed costs	**$USD 15.00 million**
Indirect fixed costs	
Location factor	$USD 52.42 million
Project OPEX	**$USD 471.77 million**

Finally, considering the OPEX, CAPEX, and a minimum attractive rate of return of 14.44%, the MSP of SAF was 2,829.7 $USD/ton. This value is approximately three times higher than conventional kerosene fossil, 918.75 $USD/ton, according to Intratec Solutions (2025), which is a trend that has already been reported in the literature by some authors (Santiago et al. 2024),(Zwiercheczewski de Oliveira et al. 2024). It is worth noting that the MSP is calculated by balancing costs, including project investment, operating costs, and taxes; it also considers the sale of products and by-products and the financial return at the end of the investment horizon, as indicated in Figure 6. It can be observed that the price of ethanol (raw material) has the greatest influence on the MSP with 67%, followed by indirect fixed costs (10%).

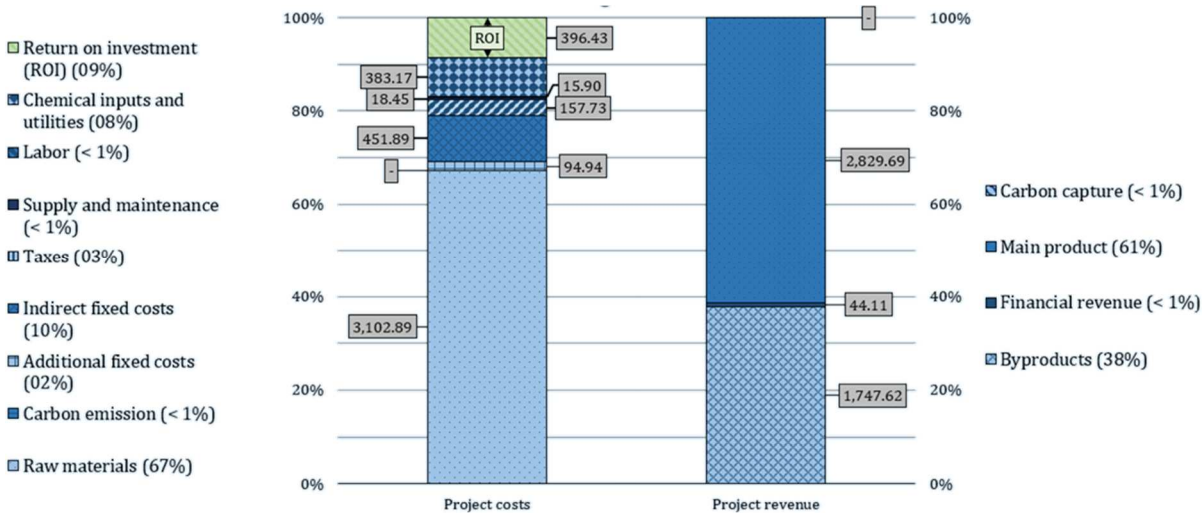

Fig. 6 - MSP calculation distribution.

The ethanol price in 2024 for the Brazilian context was $USD 572.72/ton, considerably impacting the MSP of SAF. In the case of indirect fixed costs, its value is influenced by administrative, manufacturing, distribution, and selling, as well as research and development costs. Regarding project revenue, it is evident that SAF (main product) has the largest share with 61%; nevertheless, it is worth mentioning that the by-products (naphtha and BTX) have a considerable contribution with 38%, mainly the BTX because it is produced in greater quantities than SAF. Therefore, for the MSP of SAF produced through CADO technology to be competitive with the value of fossil kerosene, it is necessary to reduce the ethanol prices by 50% or combine a smaller reduction in the price of ethanol (i.e., 20 or 30%) and increase the price of BTX by 30%, as indicated in Figure 7. None of the other variables (e.g. catalyst price or project CAPEX) had a significant influence on the reduction in the MSP value.

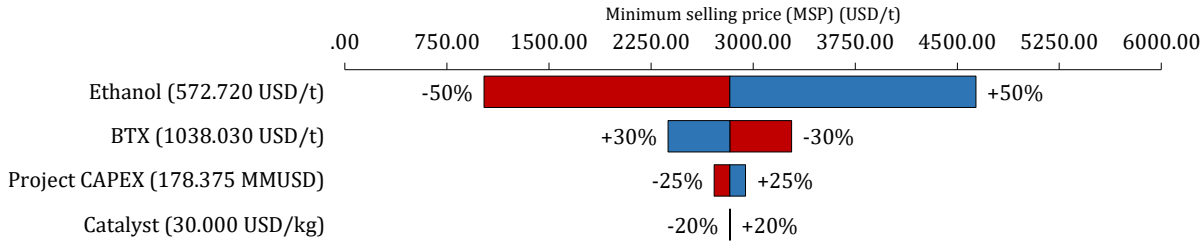

Fig. 7 - MSP tornado chart.

CONCLUSIONS

In this study, an economic assessment of SAF production through CADO technology was carried out. According to the results, it was observed that 5.93 kg of ethanol and 7.87 kg of steam were necessary to produce 1 kg of SAF, where byproducts, such as naphtha and BTX, presented technical indexes of 0.35 kg/kg-SAF and 1.59 kg/kg-SAF, respectively. Regarding economic assessment, it can be concluded that a significant investment ($USD 22.24 million) was required to purchase storage tanks for the products obtained in the CADO process. Furthermore, it was possible to observe the large share of the price of ethanol (76.3%) in OPEX, indicating that the raw material cost will have an enormous impact on the MSP (2,829.7 $USD/ton) of SAF. Finally, although the MSP of SAF is three times higher than that of fossil jet fuels, some strategies, such as carbon credits and new policies, can be implemented to make SAF competitive. Furthermore, it was concluded that a reduction in the ethanol cost and an increase in the BTX price could cause the price of SAF obtained through CADO technology to be more competitive. For future studies, the environmental impact of the complete process, including the comparison with other technologies, should be evaluated through life cycle assessment methodology.

REFERENCES

[1] Anekwe IMS, Lora EES, Subramanian KA, et al (2024). Techno-economic and life-cycle analysis of single-step catalytic conversion of bioethanol to fuel blendstocks over Ni-doped HZSM-5 zeolite catalyst. Energy Conversion and Management: X 22:. https://doi.org/10.1016/j.ecmx.2024.100529.

[2] Eagan NM, Kumbhalkar MD, Buchanan JS, et al (2019). Chemistries and processes for the conversion of ethanol into middle-distillate fuels. Nat Rev Chem 3: 223-249.

[3] Hannon JR, Lynd LR, Andrade O, et al (2020). Technoeconomic and life-cycle analysis of single-step catalytic conversion of wet ethanol into fungible fuel blendstocks. Proceedings of the National Academy of Sciences 117:12576-12583. https://doi.org/10.1073/pnas.1821684116.

[4] Haydary J (2019). Chemical Process Design and Simulation: Aspen Plus and Aspen Hysys Applications, 1st edn. Wiley.

[5] IEA (2025) Aviation. In: IEA - Energy systems. https://www.iea.org/energy-system/transport/aviation. Accessed 10 Feb 2025.

[6] Intratec Solutions (2025) Industry Economics Worldwide. In: Oil & Energy prices. https://www.intratec.us/products/industry-economics-worldwide#industrial-utilities-pricescosts, Accessed 22 Jan 2025.

[7] Klein BC, Scheidemantle B, Hanes RJ, et al (2023). Economics and global warming potential of a commercial-scale delignifying biorefinery based on co-solvent enhanced lignocellulosic fractionation to produce alcohols, sustainable aviation fuels, and co-products from biomass. Energy Environ Sci 17:1202–1215. https://doi.org/10.1039/d3ee02532b.

[8] Lau JIC, Wang YS, Ang T, et al (2024). Emerging technologies, policies and challenges toward implementing sustainable aviation fuel (SAF). Biomass Bioenergy 186:107277. https://doi.org/https://doi.org/10.1016/j.biombioe.2024.107277.

[9] Santiago YC, Guimaraes HR, Chagas MF, et al (2024). Production of Sustainable Aviation Fuel in Brazil Integrating Biochemical and Thermochemical Routes. Techno-economic and Environmental Assessment Considering Alcohol to Jet and Fischer-tropsch Strategies. Chem Eng Trans 109:73–78. https://doi.org/10.3303/CET24109013.

[10] Wang H, Yang B, Zhang Q, Zhu W (2020). Catalytic routes for the conversion of lignocellulosic biomass to aviation fuel range hydrocarbons. Renewable and Sustainable Energy Reviews 120:109612. https://doi.org/https://doi.org/10.1016/j.rser.2019.109612.

[11] Watson MJ, Machado PG, da Silva A V, et al (2024). Sustainable aviation fuel technologies, costs, emissions, policies, and markets: A critical review. J Clean Prod 449:141472. https://doi.org/https://doi.org/10.1016/j.jclepro.2024.141472.

[12] Zwiercheczewski de Oliveira P, Porto de Souza Vandenberghe L, Amaro Bittencourt G, et al (2024). Sustainable Aviation Fuel Production. In: Brar SK, Osorio Gonzalez CS, Soccol CR, Saini R (eds) The Microbiology of the Drop-in Biofuel Production. Springer Nature Switzerland, Cham, pp.221-243.

Proceedings IRF2025: 8th International Conference on Integrity-Reliability-Failure
In Engineering, Materials, Manufacturing and Biomechanics. Porto 15-18 July 2025
DOI: https://doi.org/10.24840/978-972-752-323-8

PAPER REF: 22642

A DELAYED ACCEPTANCE APPROACH WITH MARKOV CHAIN MONTE CARLO METHOD TO CONTACT FAILURES IDENTIFICATION IN MULTILAYERED COMPOSITES MEDIUM

Luiz A.S. Abreu[1(*)], Helcio R.B. Orlande[2]

[1]Department of Mechanical Engineering and Energy, Rio de Janeiro State University, Rio de Janeiro, Brazil
[2]Department of Mechanical Engineering, Federal University of Rio de Janeiro, Rio de Janeiro, Brazil
[(*)]*Email:* luiz.abreu@iprj.uerj.br

ABSTRACT

The integrity analysis of multilayered composite structures is critical in many applications, including aerospace, pipe joints, and refrigeration systems. Recent studies have demonstrated the effectiveness of Bayesian techniques in identifying contact failure regions through non-intrusive thermal measurements. However, these methods are computationally expensive, prompting efforts to develop more efficient approaches. This study employs a Markov Chain Monte Carlo method with a Delayed Acceptance strategy to reduce computational costs. Two models are considered: a high-cost model that provides accurate solutions for low thermal conductivity and large thickness cases, and a reduced-cost model based on the Partial Lumped System, which simplifies the problem by averaging temperatures across the thickness but sacrifices precision for high Biot numbers, as encountered in heat conduction problems involving low-conductivity or thick materials. The reduced model serves as an initial evaluation for candidate points, which are later reassessed with the full model, enhancing computational efficiency. Results using simulated temperature measurements show that the methodology effectively reduces computational costs while maintaining solution accuracy, even for test cases with various failure shapes.

Keywords: Composite structures, Bayesian approach, thermal contact conductance, delayed dcceptance MCMC, classical lumped models.

INTRODUCTION

The integrity analysis of multilayered composite structures has numerous practical applications in aerospace engineering, pipe joints, and refrigeration systems (Abreu et al., 2014; Gay, 2015; Madhusudana, 2014). Bayesian techniques, combined with thermal analysis and the estimation of thermal contact conductance, have proven effective in identifying contact failure regions through non-intrusive temperature measurements. However, these methods are computationally expensive, which has led to significant research efforts focused on reducing computational costs (Abreu et al., 2014, 2018; Ozisik and Orlande, 2021). Some approaches leverage measurement data and define likelihood functions in a transformed domain, particularly when combined with analytical or hybrid methods for solving partial differential equations, such as the Generalized Integral Transform Technique (GITT) (Abreu et al., 2018; Ozisik and Orlande, 2021).

To address these challenges, this study applies the Markov Chain Monte Carlo (MCMC) method with a Delayed Acceptance strategy to improve computational efficiency (Orlande et al., 2014; Ozisik and Orlande, 2021). The approach considers two mathematical-physical models: a high-cost model that provides accurate solutions for low thermal conductivity and large thickness cases and a reduced-cost model based on the Partial Lumped System (PLS). The

reduced model simplifies the problem by averaging temperatures across the thickness, retaining essential physical characteristics while significantly lowering computational demand. However, its accuracy diminishes in cases where the Biot number is greater than 0.1, such as in low-conductivity or thick materials (Kulacki, 2018; Ozisik, 1993).

The reduced model serves as an initial evaluation for candidate points in the posterior distribution, which are then reassessed using the full model. This strategy minimizes unnecessary evaluations, focusing computational resources on candidates with higher acceptance potential, thereby improving efficiency without compromising accuracy. Further details on this methodology, as applied in a different context, along with additional references on the employed techniques, are available in the literature.

PHYSICAL PROBLEM AND MATHEMATICAL FORMULATION

The general problem proposed in this work involves a two-layered plate subjected to a prescribed heat flux, $q(x, y, t)$, on one face, while the opposite face exchanges heat with the environment at a room temperature T_∞ with a heat transfer coefficient h. Heat losses through the edges are considered negligible. At the interface between the layers, a spatially varying thermal contact conductance, $h_c(x)$, is assumed. This parameter is directly related to contact failures.

REFERENCES

[1] Abreu, L.A., Orlande, H.R.B., Kaipio, J., Kolehmainen, V., Cotta, R.M., Quaresma, J.N.N., 2014. Identification of Contact Failures in Multilayered Composites With the Markov Chain Monte Carlo Method. J. Heat Transfer 136, 101302-101302. https://doi.org/10.1115/1.4027364.

[2] Abreu, L.A.S., Orlande, H.R.B., Colaço, M.J., Kaipio, J., Kolehmainen, V., Pacheco, C.C., Cotta, R.M., 2018. Detection of contact failures with the Markov chain Monte Carlo method by using integral transformed measurements. Int J Therm Sci 132, pp.486-497. https://doi.org/10.1016/j.ijthermalsci.2018.06.006.

[3] Gay, D., 2015. Composite materials: design and applications, Third edition. ed. CRC Press, Taylor & Francis, Boca Raton.

[4] Kulacki, F.A., 2018. Handbook of thermal science and engineering. Springer Berlin Heidelberg, New York, NY.

[5] Madhusudana, C.V., 2014. Thermal Contact Conductance, Mechanical Engineering Series. Springer International Publishing, Cham.

[6] Orlande, H.R.B., Dulikravich, G.S., Neumayer, M., Watzenig, D., Colaço, M.J., 2014. Accelerated Bayesian Inference for the Estimation of Spatially Varying Heat Flux in a Heat Conduction Problem. Numerical Heat Transfer, Part A: Applications 65, 1–25. https://doi.org/10.1080/10407782.2013.812008.

[7] Ozisik, M.N., 1993. Heat Conduction. John Wiley & Sons.

[8] Ozisik, M.N., Orlande, H.R.B., 2021. Inverse Heat Transfer: Fundamentals and Applications, 2nd ed. CRC Press, Boca Raton. https://doi.org/10.1201/9781003155157.

Proceedings IRF2025: 8th International Conference on Integrity-Reliability-Failure
In Engineering, Materials, Manufacturing and Biomechanics. Porto 15-18 July 2025
DOI: https://doi.org/10.24840/978-972-752-323-8

PAPER REF: 23498

AN EXPERIMENTAL METHOD TO MEASURE BICYCLE TIRES ROLLING RESISTANCE AT THE SANGALHOS VELODROME

Pedro de Figueiredo Vieira Carvalheira[1(*)], Octávio Nuno Chaves de Freitas Cardoso[2]

[1]Universidade de Coimbra, ADAI, Departamento de Engenharia Mecânica, Coimbra, Portugal.
[2]Escola Superior de Tecnologia e Gestão de Viseu – Instituto Politécnico de Viseu, Viseu, Portugal
[(*)]*Email:* pedro.carvalheira@dem.uc.pt

ABSTRACT

The Sangalhos velodrome, like the majority of velodromes, has a track with variable positive bank angle in all perimeter. To make accurate measurements of the aerodynamic drag force of cyclists riding bicycles at the velodrome it is necessary to measure accurately the bicycle tires rolling resistance and cornering drag force at the velodrome. To measure accurately the rolling resistance of bicycle tires at the Sangalhos velodrome an experimental method was developed and is presented. The method developed is based on the conservation of mechanical energy, considers the kinetic energy and potential gravitational energy of the set cyclist + bicycle and considers the following forces and torque acting on the set cyclist + bicycle: weight; ground normal reaction force; tires rolling resistance force, aerodynamic drag force, tires cornering drag force and friction torque of the rear wheel freewheel mechanism. The measurements were made in a straight segment in the inner zone of the track with levelled surface, null bank angle and with the same surface characteristics as the racing track. The method considers the tires rolling resistance coefficient (CRR) constant during the measurement. Measurements made with a time trail bicycle and a cyclist in full racing gear, with a low rolling resistance clincher tire with a latex inner tube combination in both wheels, gave a standard deviation of ±6.7% around the measured mean value of the tires CRR.

Keywords: Rolling resistance coefficient, bicycle tires, experimental method, velodrome.

INTRODUCTION

The aerodynamic drag force is the most important resistive force acting on road racing cyclists when the slope of the road is less than 2 % (Rinard et al., 2018). Accurate measurements of the aerodynamic drag force of cyclists riding bicycles in a velodrome requires accurate measurements of the bicycle tires rolling resistance and cornering drag force in the same velodrome, because the velodrome is characterized by having positive bank angle in all perimeter and each velodrome has specific track surface roughness characteristics. It was necessary to develop this method to measure the rolling resistance of bicycle tires, to make accurate measurements of the drag area, the product of drag coefficient (C_D) by the frontal area (A), of cyclists in the velodrome. CRR measurements were made in a straight segment, in the most inner zone of the velodrome track, where track surface is horizontal, the bank angle is null and the ground surface characteristics, including roughness, are similar to the ground surface of the racing track. The rolling resistance of clincher bicycle tires depends on the tire, inner tube used, inflation pressure, temperature of the tire, vertical load on the tire, rim width, displacement speed of the bicycle relative to the ground surface (Biernan, 1997) and surface roughness of the ground (Sun et al., 2024). To eliminate the influence of the following factors on the rolling resistance of the tires on the measurement of the cyclist drag area, we measured

the rolling resistance of the bicycle tires using the same tires, inner tubes, inflation pressure, rim width and surface roughness as will be used when measuring the cyclist drag area. We measure the rolling resistance of the tires at a temperature and vertical load on the tire as close as possible to the values of temperature and load used during the aerodynamic drag tests. The measurements of the rolling resistance are made at very low velocity, generally in the range of 2-7 km/h, so that the rolling resistance force is large when compared to other resistive forces that act in the cyclist and bicycle, such as the aerodynamic drag, the tire cornering drag and the tangential component of the weight.

RESULTS AND CONCLUSIONS

Table 1 presents results of CRR obtained in 6 measurements made at Sangalhos velodrome, its mean and standard deviation. The tires, inner tubes, internal rim width and pressure were the same in the front and rear wheels of the bicycle. The tires used were the Vittoria Corsa Pro Speed TUBE/TLR 24-622. The inner tubes used were the Vredestein Race Superlite Latex 20/25-622 with a 50 mm Presta valve and mass of 0.050 kg. The inflation pressure used in both tires was 90 psi (621 kPa). The rims of both wheels were of the crochet type with 17.0 mm internal width (17C). The front wheel was a DT SWISS ARC 1100 DI 700C RB 80 5/100, the rear wheel was a ZIPP WH SP9 CC V2 700R SR 11S WHT. The value reported in the literature for CRR for the same tires, a slightly heavier inner tube, a Vittoria Competition Latex 19/23-622 inner tube with a 48 mm Presta valve and mass of 0.080 kg, and in a velodrome track, is CRR = 1.475E-3 at 130 psi (897 kPa) inflation pressure (Aerocoach, 2024).

Table 1 - Results of CRR obtained in 6 measurements made at Sangalhos velodrome.

Meas. No.	**1**	**2**	**3**	**4**	**5**	**6**	**Mean**	**St. Dev.**
CRR	1.520E-3	1.405E-3	1.238E-3	1.399E-3	1.364E-3	1.443E-3	1.395E-3	9.357E-5

An experimental method was developed to measure the rolling resistance of bicycle tires at the Sangalhos velodrome. This method is based on the conservation of mechanical energy. Results of CRR measurements made at Sangalhos velodrome with given tires, inner tubes, and inflation pressure are presented and compared with results found in the literature for the same tires, in a velodrome track, at a different inflation pressure, and using slightly heavier latex inner tubes.

REFERENCES

[1] Aerocoach. Clincher tyre rolling resistance performance in track cycling. https://www.aero-coach.co.uk/clincher-tyre-rolling-resistance-performance-in-track-cycling. 2024. accessed: 20/03/2025.

[2] Biernan J. Special Articles. https://www.bicyclerollingresistance.com/specials/, 2022, accessed: 20/03/2025.

[3] Rinard D, Guzik, D, Kuerner, D, Hamilton, I, Schottler, J, Barry, N. White Paper SystemSix. Cannondale, June 25, 2018, pp.1-49.

[4] Sun Z, Premarathna WAAS, Anupam K, Kasbergen C, Erkens SMJG. A state-of-the-art review on rolling resistance of asphalt pavements and its environmental impact. Construction and Building Materials 411 (2024) 133589.

Proceedings IRF2025: 8th International Conference on Integrity-Reliability-Failure
In Engineering, Materials, Manufacturing and Biomechanics. Porto 15-18 July 2025
DOI: https://doi.org/10.24840/978-972-752-323-8

PAPER REF: 23499

AN EXPERIMENTAL METHOD TO MEASURE BICYCLE TIRES ROLLING RESISTANCE AT A ROAD ROUNDABOUT

Pedro de Figueiredo Vieira Carvalheira[1(*)], Octávio Nuno Chaves de Freitas Cardoso[2]

[1]Universidade de Coimbra, ADAI, Departamento de Engenharia Mecânica, Coimbra, Portugal.
[2]Escola Superior de Tecnologia e Gestão de Viseu – Instituto Politécnico de Viseu, Viseu, Portugal.
[(*)]*Email:* pedro.carvalheira@dem.uc.pt

ABSTRACT

In racing events it is important to have the lowest possible rolling resistance to maximize the bicycle velocity. In this work an experimental method was developed to measure accurately the rolling resistance of bicycle tires in a road surface, where the measurements are made in a roundabout. The method is based on the conservation of mechanical energy, considers the kinetic energy and potential gravitational energy of the set cyclist + bicycle and considers the following forces and torque acting on the set cyclist + bicycle: weight; ground normal reaction force; tires rolling resistance force, aerodynamic drag force, tires cornering drag force and friction torque of the rear wheel freewheel mechanism. To measure accurately the rolling resistance, it is necessary to measure previously the aerodynamic drag area (CdA) of the set cyclist + bicycle, in the same position in the bicycle and with the same gear used when the rolling resistance is measured, and to measure the tires cornering stiffness (C_α). The results of rolling resistance are presented in non-dimensional format as rolling resistance coefficient (CRR), which is considered constant during the measurements. The advantage of this method is that is not necessary to make the topographic survey of the roundabout because when the bicycle makes a complete turn, the altitude of the initial point is equal to the altitude of the final point. CRR measurements were made with a time trial bicycle used in race events and a cyclist in full racing gear, with different bicycle racing tires and inner tubes, at different temperatures and at the same inflation pressure, and the results of several measurements are presented.

Keywords: Rolling resistance coefficient, bicycle tires, experimental method, road test.

INTRODUCTION

This experimental method was developed because it was necessary to measure the tires rolling resistance of a time trial bicycle in the road to predict its performance, select the best tires, inner tubes and inflation pressure to use in the time trial race of the UCI Granfondo Coimbra Region 2025, held in the 1st March 2025. The measurements were made in the inner zone of a roundabout in a trajectory with constant radius. The roundabout was chosen to have small bank angles and a surface roughness similar to the surface roughness of the road where the race was made. The measurements of the rolling resistance were made at very low velocity, generally in the range of 2-11 km/h, so that the rolling resistance force was large when compared to the other resistive and propulsive forces that act in the cyclist and bicycle, such as the aerodynamic drag, the tire cornering drag and the tangential component of the weight (Martin et al., 1998; Vorotovic et al., 2013). To consider the aerodynamic drag of the cyclist and bicycle, the aerodynamic drag area of the set cyclist + bicycle, in the same position in the bicycle used in the tests and using the same gear, was measured previously. To limit the aerodynamic forces on the set cyclist + bicycle due to the wind, the measurements were only considered valid when the wind speed at 10 m height was less than 5.0 km/h. The rolling resistance of clincher bicycle

tires depends on the tire, inner tube, inflation pressure, tire temperature, vertical load on the tire, rim width, displacement speed of the bicycle relative to the ground surface (Biernan, 2022) and surface roughness of the ground (Sun et al., 2024). The measured mean profile depth (MPD) of the road surface macrotexture where the CRR measurements were made was 1.290±0.144 mm.

RESULTS AND CONCLUSIONS

Figure 1 presents results of the evolution of CRR with tire temperature for three different combinations of tires and inner tubes in the front and rear wheels. The results are presented with error bars equal to the standard deviation of the measured CRR. Figure 1 also presents the measured CRR values reported in the literature for the Continental GP 5000 tires and 0.080 kg latex inner tubes, at 90 psi inflation pressure, using a 77 cm diameter drum (Biernan, 2019).

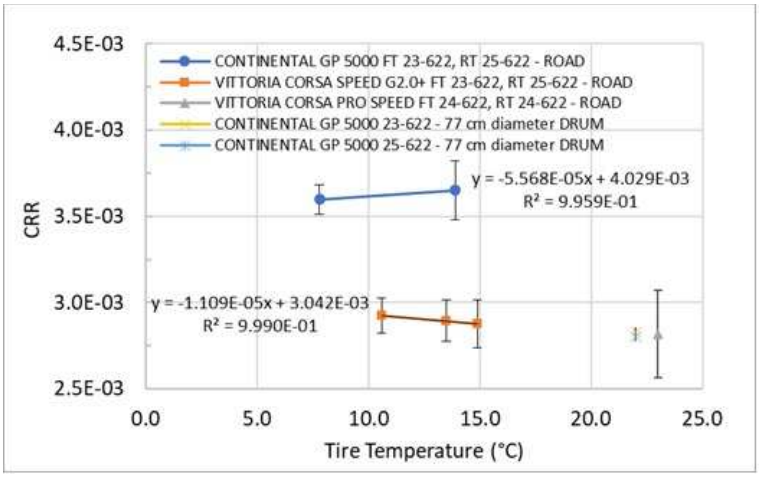

Fig. 1 - Evolution of CRR with tire temperature for three different tires and inner tubes at 90 psi pressure.

ACKNOWLEDGMENTS

We would like to thank Eng. César Abreu and ACIV – Associação para o Desenvolvimento da Engenharia Civil for providing the equipment and measuring the MPD at the test site.

REFERENCES

[1] Biernan J. Continental Gran Prix 5000 Comparison: 23, 25, 28, and 32 mm Compared. https://www.bicyclerollingresistance.com/specials/gran-prix-5000-comparison, 2019-02-19, accessed: 20/03/2025.

[2] Biernan J. Special Articles. https://www.bicyclerollingresistance.com/specials/. 2022, accessed: 20/03/2025.

[3] Martin JC, et al., Validation of a Mathematical Model for Road Cycling Power. Journal of Applied Biomechanics, 1998, 14(3): 276-291.

[4] Sun Z, Premarathna WAAS, Anupam K, Kasbergen C, Erkens SMJG. A state-of-the-art review on rolling resistance of asphalt pavements and its environmental impact. Construction and Building Materials 411 (2024) 133589.

[5] Vorotovic GS, Rakicevik VV, Mitic SR, Stamenkovic DD. Determination of Cornering Stiffness Through Integration of a Mathematical Model and Real Vehicle Exploitation Parameters. Faculty of Mechanical Engineering Transactions, Belgrade, 2013, 41, 66-71.

Proceedings IRF2025: 8th International Conference on Integrity-Reliability-Failure
In Engineering, Materials, Manufacturing and Biomechanics. Porto 15-18 July 2025
DOI: https://doi.org/10.24840/978-972-752-323-8

Paper REF: 23512

HIERARCHICAL CARBON NANOTUBE ARCHITECTURES FOR EFFICIENT INTERFACIAL SOLAR-DRIVEN WATER EVAPORATION

Yongyi Zhang[1,2(*)]

[1]Suzhou Institute of Nano-Tech and Nano-Bionics, Chinese Academy of Sciences, Suzhou 215123, China
[2]School of Nano-Tech and Nano-Bionics, Univ. Science and Technology of China, Hefei 230026, China
[(*)]*Email:* yyzhang2011@sinano.ac.cn

ABSTRACT

Global freshwater scarcity is intensifying worldwide, yet conventional seawater desalination technologies remain inadequate for economically disadvantaged regions due to excessive energy consumption, high operational costs, and technical complexity. Consequently, developing sustainable, cost-effective, and simplified desalination approaches suitable for remote or resource-constrained communities has become increasingly imperative. SIVG represents an emerging approach to obtaining potable water resources, characterized by environmentally friendly attributes, minimal energy demands, negligible pollution, low capital expenditures, and compatibility with decentralized deployment. Despite rapid advancements and extensive exploration into various photothermal materials and structural configurations, significant challenges persist, including insufficient photothermal conversion efficiency and elevated energy thresholds. Hence, further advancements in high-performance photothermal evaporative systems are critically needed.

Keywords: Potable water resources, desalination, photothermal conversion, water purification technologies.

RESULTS AND DISCUSSION

In recent years, our group has developed multidimensional photothermal water-evaporation structures based on CNT fibers, CNT films, and CNT aerogels, specifically targeting efficient photothermal energy utilization and precise regulation of evaporation enthalpy. As shown in Figure 1a, by combining CNT fibers and cotton yarns into hybrid twisted yarn architectures, we achieved pronounced gradient photothermal differences of 5 °C between CNT and cotton regions at the microscale. As a result, the crafted fabric evaporator has a superior evaporation rate of 2.83 kg m^{-2} h^{-1} and an exceptional outdoor freshwater yield reaching 12.7 kg m^{-2} h^{-1}, which is the highest value reported among 2D fabric evaporators.

Inspired by mangrove forests growing in salty shoals (Figure 1b), an adaptive tree-like evaporator was fabricated by rolling cotton threads and punched (pin-holed) CNT film into modified photothermal bundles and further weaving them into root-leaf-like structures, enabling uncoated cotton bundles as dense roots for extracting and transporting water and coated part as leaves with open holes for evaporation. Meanwhile, the evaporator exhibited highly efficient evaporation performance across diverse complex aqueous environments.

Additionally, as shown in Figure 1c, leveraging CNT aerogels possessing hierarchical porous frameworks and integrating polymers such as polyvinyl alcohol (PVA) and polyethyleneimine (PEI), we developed interfacial weakly hydrated CNT-based photothermal hydrogels characterized by low evaporation enthalpy. The obtained hybrid hydrogel achieved a high

evaporation rate of 3.55 kg m^{-2} h^{-1} with an efficiency of 92.0 % under 1 sun irradiation, and particularly a superior self-evaporation rate of 0.49 kg m^{-2} h^{-1} in the dark. Our team has also concurrently explored the rational design and modulation of hierarchical porous structures for photothermal evaporation systems, alongside the development of outdoor water collection devices, thereby contributing essential technical and theoretical foundations for advancing solar-driven water purification technologies.

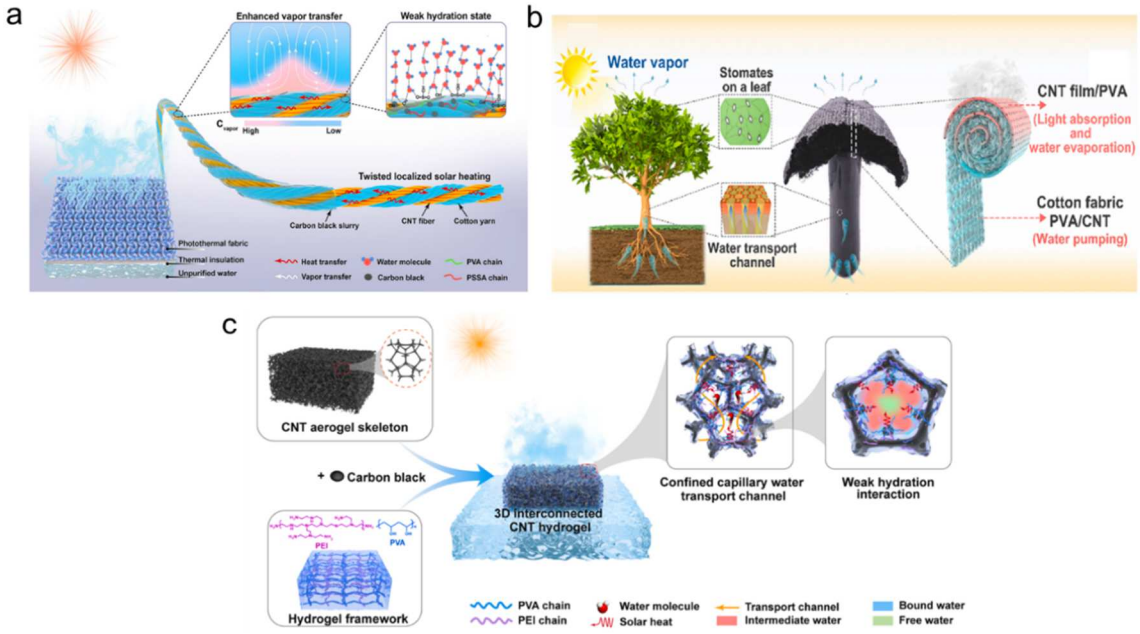

Fig. 1 - Rational design of (a) CNT fibers, (b) CNT films, and (c) CNT aerogel for solar-driven interfacial evaporation.

REFERENCES

[1] L. Zhao, Z. Yang, J. Wang, Y. Zhou, P. Cao, J. Zhang, P. Yuan, Y. Zhang, Q. Li, Boosting solar-powered interfacial water evaporation by architecting 3D interconnected polymetric network in CNT cellular structure, Chem. Eng. J., 2023, 451, 138676.

[2] L. Zhao, L. Zhang, Z. Yang, T. Zhou, P. Cao, L. Chen, Y. Zhang, T. Qin, Z. Yong, K. Wu, Q. Li, Twisted integration of high-efficiency photothermal/water-transported yarns for boosting solar-powered fabric evaporator, Chem. Eng. J., 2024, 490, 151605.

[3] P. Cao, P. Yuan, L. Zhao, Z. Yang, Y. Zhang, B. Wang, Y. Cao, Z. Yong, Y. Niu, J. Zhang, Q. Li, Plant-inspired multi-environmentally adaptive, flexible, and washable solar steam generation fabric, Chem. Eng. J., 2023, 471, 144286.

[4] L. Zhao, J. Zhang, P. Cao, L. Kang, Q. Gong, J. Wang, Y. Zhang, Q. Li, Fast water transport reversible CNT/PVA hybrid hydrogels with highly environmental tolerance for multifunctional sport headband, Composites Part B-Engineering, 2011, 211, 108661.

[5] P. Cao, L. Zhao, J. Zhang, L. Zhang, P. Yuan, Y. Zhang, Q. Li, Gradient heating effect modulated by hydrophobic/hydrophilic carbon nanotube network structures for ultrafast solar steam generation, ACS Appl. Mater. Interfaces, 2021, 13, 19109-19116.

[6] P. Yuan, C. Men, L. Zhao, P. Cao, Z. Yang, Y. Niu, Y. Zhang, Y. Yu, Q. Li, Spontaneous salt-preventing solar-thermal water evaporator with a high evaporation efficiency through dual-mode water transfer, ACS Appl. Mater. Interfaces, 2022, 14, 15549-15557.

TRACK - H: Industrial Engineering

Systems Engineering
Manufacturing Engineering
Production Systems for Metallic Materials
Production Systems for Polimeric Materials
Safety Engineering
Sustainable Technologies and Processes
Risk Assessment
Product Reliability
Operations Management
Case Studies

Proceedings IRF2025: 8th International Conference on Integrity-Reliability-Failure
In Engineering, Materials, Manufacturing and Biomechanics. Porto 15-18 July 2025
DOI: https://doi.org/10.24840/978-972-752-323-8

PAPER REF: 22173

NEW DESIGN FOR SEMI-INDUSTRIAL 6-APA PRODUCTION: TECHNICAL AND ECONOMIC REVIEW

Akbar Esmaeili(*) Sajjad Fereidooni

Department of Chemical Engineering, North Tehran Branch, Islamic Azad University, Tehran, Iran.
(*)*Email:* akbaresmaeili@yahoo.com

ABSTRACT

The intermediate 6-ammoniopenicillanic acid (6APA), crucial for antibiotic production, is derived from penicillin. This study focused on optimizing enzyme usage and substituting butanol for methanol in the powder-washing stage. Various amounts of penicillin G-amidase enzyme were tested, revealing maximum efficiency with a 2:1 ratio of penicillin to enzyme (50 grams enzyme for 100 grams penicillin). Additionally, using butanol instead of methanol for washing the powder post-filtration proved effective. Butanol reduced residual solvent levels and increased drying speed, making the process more economical. The substitution cut costs by approximately 10% due to butanol's lower price and faster drying. This study is the first to demonstrate butanol as a viable alternative to methanol and optimize enzyme use in 6APA production.

Keywords: 6-ammoniopenicillanic acid (6APA), Penicillin, Penicillin G-amidase enzyme. Butanol, Methanol, Enzyme optimization.

INTRODUCTION

6-ammoniopenicillanic acid (6APA) is a vital intermediate in the production of antibiotics, particularly penicillin derivatives, which are essential for treating bacterial infections (Smith et al., 2020). This compound is derived from penicillin through the action of penicillin G-amidase, an enzyme critical in the antibiotic manufacturing process (Jones & Lee, 2018). However, the high cost of enzymes and solvents, such as methanol, can significantly impact production expenses. Optimization of enzyme usage is crucial due to the substantial cost associated with these biocatalysts. Studies have shown that improving the efficiency of enzyme reactions can lead to cost savings and enhanced productivity (Williams & Brown, 2019). Furthermore, the solvent used in post-filtration washing stages, typically methanol, also affects the overall process efficiency and cost. Methanol, while effective, is relatively expensive and has environmental drawbacks (Adams et al., 2021). Recent research suggests that butanol, a cheaper and more environmentally friendly solvent, could be a viable alternative to methanol in the washing process (Harris & Davis, 2022). Butanol's lower cost and faster drying properties could reduce production costs and improve process efficiency. This study explores both the optimization of enzyme use and the substitution of butanol for methanol, aiming to enhance the economic and operational aspects of 6APA production.

RESULTS AND CONCLUSIONS

In this study, the enzymatic process for producing 6-ammoniopenicillanic acid (6APA) was examined with varying amounts of enzyme. The highest efficiency was observed with a 2:1 ratio of enzyme to penicillin powder, using 50 grams of enzyme for 100 grams of penicillin powder, which is more effective than the previously reported optimal amount of 60 grams (Blaha et al., 1975).

During the penicillin fermentation process, samples were taken every 12 hours over 200 hours and analyzed for PMV, morphology, nitrogen content, glucose levels, PAA concentration, and PEN G. Results showed that PMV and microorganism count increased up to approximately 90 hours, stabilizing after that. PEN G levels increased steadily, reaching 21,000 IU by 200 hours. PAA levels were maintained by injecting 40% PAA, while corn oil and ammonium sulfate (30%) were used to manage foam and nitrogen levels, respectively. Glucose was maintained at 55% through continuous injection.

Following filtration, the penicillin was mixed with butyl acetate, treated with potassium carbonate to transfer penicillin to the aqueous phase, and processed enzymatically. The enzymatic reaction, conducted at 26°C and pH 7, concluded after 2 hours, followed by butanol filtration. This study is the first to utilize butanol instead of methanol for washing the powder, which expedited drying and reduced costs compared to previous methods (Vandamme et al., 1998). The substitution of butanol led to approximately 10% cost savings by removing the need for two additional tanks and integrating ammonium sulfate and corn oil into the fermentation medium. The optimal concentrations were found to be 2 grams per liter for corn oil and 5 grams per liter for ammonium sulfate.

Quality tests of the 6APA powder showed no significant differences in antimicrobial activity compared to standard and methanol-washed 6APA powders. The new method proved to be more economical and efficient, with comparable antimicrobial properties.

REFERENCES

[1] Esmaeili A, Haseli M. Electrospinning of thermoplastic carboxymethyl cellulose/poly (ethylene oxide) nanofibers for use in drug-release systems. Mater Sci Eng C Mater Biol Appl, 2017, 77, p.p1117-1127.

[2] Abian O, Mateo C, Fernandez-Lorente G, Guisan JM, Fernandez-Lafuente R. Improving the industrial production of 6-APA: enzymatic hydrolysis of penicillin G in the presence of organic solvents. Biotechnol Prog, 2003, 19(6), pp.1639-1642.

[3] Shim K-M, Kim C-J. Study on the dither random noise for improving the bias stability of ring laser gyroscope. J Inst Control Robotics Systems, 2006, 12(11), pp.1065-1073.

[4] Chisti Y, Moo-Young M. On the calculation of shear rate and apparent viscosity in airlift and bubble column bioreactors. Biotechnol Bioeng, 1989, 34(11), pp.1391-1392.

[5] Masoumi S, Esmaeili A. In vivo, in vitro, and antibacterial activity of Fe3O4@ RIF-BUP-CMCs-modified by fatty acids nanoparticles to remove drug liver toxins. Appl Nanoscience, 2020, 10(11), pp.4149-4160.

[6] Esmaeili A, Khodaei M. A new and enzymatic targeted magnetic macromolecular nanodrug system which delivers methadone and rifampin simultaneously. ACS Biomater Sci Eng, 2019.

[7] Vandamme E, De Baets S, Vanbaelen A, Joris K, De Wulf P. Improved production of bacterial cellulose and its application potential. Polym Degrad Stab, 1998, 59(1-3), pp.93-99.

[8] Masoumi S, Esmaeili A. New method of creating hybrid of buprenorphine loaded rifampin/polyethylene glycol/alginate nanoparticles. Int J Biol Macromol, 2020.

[9] Blaha JM, Knevel AM, Hem SL. High-pressure liquid chromatographic analysis of penicillin G potassium and its degradation products. J Pharm Sci, 1975, 64(8), pp.1384-1386.

[10] Ashraf Z, Bais A, Manir MM, Niazi U. Novel penicillin analogues as potential antimicrobial agents; design, synthesis and docking studies. PLoS One, 2015, 10(8).

Proceedings IRF2025: 8th International Conference on Integrity-Reliability-Failure
In Engineering, Materials, Manufacturing and Biomechanics. Porto 15-18 July 2025
DOI: https://doi.org/10.24840/978-972-752-323-8

PAPER REF: 22188

SOME OF THE GOVERNING PARAMETERS OF THE MACHINE SETTINGS DURING THE MANUFACTURING PROCESSES OF MASS PRODUCTION IN METALWORKING INDUSTRIES

Jayanta Kumar Banerjee(*), Julián Rivera-Rodríguez, Luis Cruz-Zapata
Dep. Mechanical Engineering, University of Puerto Rico at Mayagüez (UPRM), Mayagüez, Puerto Rico
(*)*Email:* jayanta.banerjee@upr.edu

ABSTRACT

Some of the limiting factors in constant volume deformation processes as well as in subtractive and additive manufacturing processes are outlined. In the processes where the volume of the workpiece material does not change, like rolling, forging, extrusion, etc., the total effective true strain that corresponds to the maximum force or stress is the governing parameter. In subtractive manufacturing processes, like machining, grinding, sand blasting, super- polishing, etc., the material removal rate (MRR) is the governing parameter. In additive manufacturing processes, like casting, molding, welding, etc., the governing parameter is the total solidification time (TST) of the material transforming from liquid to solid. Here the fluid flow and heat transfer affect TST.

***Keywords*:** Volume constancy, material removal rate, Chvorinov's equation for TST.

INTRODUCTION

In mass-scale manufacturing processes in the metalworking industries, the workpiece material as well as the tool material are not as precise as those used in research or teaching laboratories at the universities. For example, the workpiece material is not always homogeneous, isotropic, and hence does not always follow the yield criteria and their associated plastic flow rules. The present paper gives some examples from materials forming, materials removal and materials additive processes, to demonstrate how some of the machine setting parameters can control the production rate and the product quality of the processes in mass scale manufacturing.

RESULTS AND CONCLUSIONS

Materials Forming Processes: In materials forming processes, such as rolling, forging, extrusion, etc. the total volume of the workpiece material does not change, only its form changes. In a simple uniaxial process like wire drawing, the volume of the workpiece material, V = A*L, where L is the length of the workpiece material and A is its cross-sectional area at any time during the forming process. If V = A*L is constant, its first derivative, dV = A (dL) + L (dA) = 0. Again, if we stop the tensile machine when the uniaxial force F = A*S, (S being the uniaxial true tensile stress) reaches its maximum value, then F = A*S is maximum. Hence, by the same argument, the first derivative of a maximum is zero. Thus, dF = d (A.S) = A (dS) + S (dA) = 0.

Combining mathematically these two physical concepts of plasticity [1], (equations of the derivatives of volume V and force F, namely dV and dF) and using the true stress – strain relationship (Ludwik's Law): S = K (E^n) , K being the strength constant of the workpiece

material, E the true strain, and n being the work-hardening (strain-hardening) exponent of the workpiece material, it can be demonstrated in a few simple algebraic steps that E = n when F reaches its maximum value. Hence the tensile machine, like an Instron, can control the process by stopping it when the optimum true strain, E reaches n, or when the machine records a maximum force, F.

Materials Removal Processes: During the material removal processes, such as machining, grinding and other forms of abrasive machining, the rate of materials removal from the workpiece can be easily controlled by the machine tools performing the removal operation, such as on a CNC lathe, milling machine or a simple drill press [2]. For the first two cases, Figures 1A and 1B describe the parameters used in each operation to obtain the material removal rate (MRR).

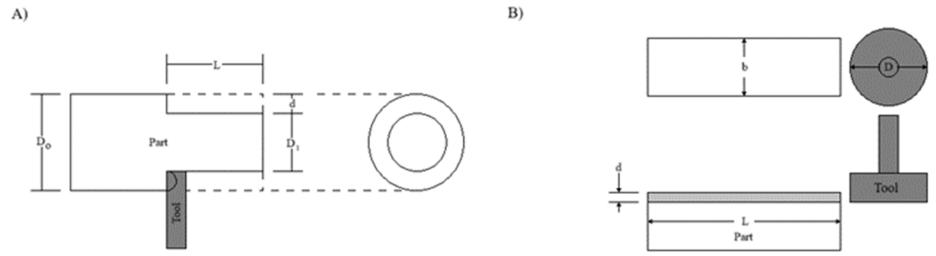

Fig. 1 - A) Turning on a Lathe Process Diagram and B) Milling Process Diagram.

For example, following Figure 1 B) for the milling process, L is the machined length (mm), t is the machining time (min), b is the machining width (mm), d is the depth of cut (mm) and f is the tool feed rate (in/min). Furthermore, with some mathematical steps, the Material Removal Rate (MRR) can be derived. Hence, the MRR, (V), that governs the production rate can be given by a simple function of the machine settings: V = v*d*f, where v is the cutting speed (mm/min.), d the depth of cut (mm/pass), f the tool feed per rotation of the workpiece (mm). Thus, the rate of production can be controlled by the machine settings (cutting speed, tool feed rate and depth of cut). The product quality depends on tool wear, supply of cutting fluids, machine tools' "Chatter" vibration and the surface finish as well as the dimensional tolerance of the final product.

Materials Addition Processes: Unlike volume constancy and volume reduction, in these processes the volume can increase by a significant proportion. A simple daily experience is freezing water into ice cubes where the volume increases. Here also the product quality is governed by the precision of the machine tools used in the processes [3]. In molding, casting and welding, the Total Solidification Time (TST) is the main governing parameter, as expressed by Chvorinov's equation: TST = C [Volume / Surface Area]^2, where C is the mold constant.

REFERENCES

[1] Banerjee JK, Fundamental parameters of plasticity for the design of products in mass scale manufacturing in metalworking industries. Proceedings of the Mechanics and Materials in Design (M2D) International Conference, Madeira, Portugal, 2022. pp.203-204.

[2] Velez JL, Banerjee JK, Aponte A. Problems of heat, mass and momentum transfer in manufacturing processes: A brief review. American Transactions on Engineering and Applied Sciences. 2015.

[3] Groover MP. Fundamentals of Modern Manufacturing: Materials, Processes and Systems (5th edition). John Wiley, New York, USA. 2015. Chapter 10, pp.242-244.

Proceedings IRF2025: 8th International Conference on Integrity-Reliability-Failure
In Engineering, Materials, Manufacturing and Biomechanics. Porto 15-18 July 2025
DOI: https://doi.org/10.24840/978-972-752-323-8

PAPER REF: 22398

STRUCTURE FORMATION IN LUBRICATING GREASES AS A RESULT OF APPLIED FRICTIONAL STRESS

Erik Kuhn(*)

TREC, Faculty of Technology and Computer Sciences, Hamburg University of Appl. Sc., Hamburg
(*)*Email:* erik.kuhn@haw-hamburg.de

ABSTRACT

The structure of lubricating greases, meaning the geometry and arrangement of the solid substance, changes during a friction process. Similar to the friction of, for example, steel-steel pairings and their surface behavior, an optimized structure develops in lubricating greases. So far, this can only be observed indirectly (via the shear stress profile) during a friction process. This study analyzes possibilities that provide important insights into the driving forces behind structural changes. It becomes evident that stable behavior is also an attractor for the friction process in lubricating grease.

Keywords: Lubricating grease, nonequilibrium, entropy production.

INTRODUCTION

Lubricating greases essentially consist of a base oil and a solid substance. The structure of a lubricating grease is defined as the geometry and distribution of this solid substance. Such geometries can vary significantly, for example, in the form of long fibrils, platelets, spherical shapes, etc. The arrangement of the agglomerates, in turn, can be either homogeneous or highly heterogeneous.

The question of why a grease reacts in the observed manner when mechanical energy is applied seems interesting. In other words, what are the driving forces behind the processes taking place? It has been investigated in many processes [1] that the behavior over time, under continuous energy input, tends toward a steady state. Such behavior is also well known from tribological studies. A particularly remarkable phenomenon occurs when disturbances arise, leading to the formation of new structures [1], [2]. This is not necessarily mandatory, but it becomes possible when certain conditions far from equilibrium prevail.

In the study presented here, evidence is provided that such structure formation is also possible in friction-stressed viscoelastic lubricants.

RESULTS AND CONCLUSIONS

Unfortunately, it is currently not possible to make structure formation in a grease during a tribological process "visible." It is also unclear whether such a structure would manifest, for example, as a new solid distribution, a new agglomerate geometry, or both (e.g., Bénard cells). However, it is possible to investigate conditions that serve as prerequisites for the formation of new structures far from equilibrium. It has been shown [3] that one prerequisite is the occurrence of an instability. A criterion for the occurrence of instability is described by [3] and involves the description of entropy production caused by emerging disturbances.

$$P = \frac{dS_i}{dt} = \sum_p J_p X_p \geq 0 \tag{1}$$

$$\frac{1}{2}\frac{\partial}{\partial t}\delta^2 S = \sum J_p X_p = P > 0 \tag{2}$$

$$\frac{1}{2}\frac{\partial}{\partial t}\delta^2 S = \sum_p \delta J_p \delta X_p \tag{3}$$

In Equation (2), the left-hand side corresponds to a Lyapunov function, and near equilibrium, all disturbances are damped. This stability criterion is proposed by [3]. Equation (3) examines the disturbed process near non-equilibrium. Here, the right-hand side represents the so-called excess entropy. If the contribution of the excess entropy is negative, an instability may occur. Here *J* is the thermodynamic flux and *X* a thermodynamic force.

For the general shearing of a grease volume (friction within the grease), the frictional energy is expressed as $(\tau \cdot \gamma \dot{:} V)$ [4].

For the contribution of the excess entropy, it is shown that

$$\frac{1}{2}\frac{\partial}{\partial t}(\delta^2 S) = \left(\frac{V}{T}\right)^2 \left[\frac{\gamma^3}{\lambda^2}\frac{\partial \tau}{\partial \psi}\left(\lambda\frac{\partial \tau}{\partial \psi} - \tau\frac{\partial \lambda}{\partial \psi}\right)\right](\delta\psi)^2 + \frac{1}{\lambda}\left(\frac{\partial \tau}{\partial \dot{\gamma}}\dot{\gamma} + \tau\right)^2 (\delta\dot{\gamma})^2 \tag{4}$$

Only the terms that make a relevant contribution are displayed [5]. Here ψpresents the solid content, λ the thermal conductivity. The dependencies considered were $\tau(\psi, \dot{\gamma})$ and $\lambda(\psi)$. And we find the condition to get a possibility for instability with

$$\frac{\partial \lambda}{\partial \psi} > 0 \tag{5}$$

In this presentation, experimental rheometer results are further shown for the interpretation of the criterion in (5). The possibility of structure formation is considered, and criteria are presented.

In a further study, the thixotropic behavior is examined from the perspective of additional entropy production, and an analytical description and interpretation are attempted for the grease behavior during the resting phase of a rheometer experiment. This work is not included in this abstract.

REFERENCES

[1] Prigogine I., Nicolis G.: Biological order, structure and instabilities. Quart. Reviews of Biophysics 4,2 &3 (1971).

[2] Gershman I.S., Gershman E.I., Fox-Rabinovich G.S., Veldhuis S.C.: Description of seizure process for gas dynamic spry of metal powders from non-equilibrium thermodynamic standpoint. Entropy 18,315, 2016.

[3] Prigogine,I.: Time, structure and fluctuations. Science, vol.20, nr. 4358,1978.

[4] Kuhn E., Balan C.: Experimental procedure for the evaluation of the friction energy of lubricating greases. Wear, 209, 1997.

[5] Jetschke, G: Mathematic of selforganisation (in German). Vieweg,1989

Proceedings IRF2025: 8th International Conference on Integrity-Reliability-Failure
In Engineering, Materials, Manufacturing and Biomechanics. Porto 15-18 July 2025
DOI: https://doi.org/10.24840/978-972-752-323-8

PAPER REF: 22409

SmartMTQM - SIMPLIFICATION OF THE MTQM METHOD FOR APPLICABILITY IN SMEs

Christian Kern[1*], Robert Refflinghaus[1], Jochen Deuse[2], David Lenze[2]

[1]RIF Institute for Research and Transfer, Department of Process Optimization, Dortmund, Germany
[2] RIF Institute for Research and Transfer, Department of Production Systems, Dortmund, Germany
[(*)]*Email:* christian.kern@rif-ev.de

ABSTRACT

When planning manual assembly processes, it is necessary to examine both the methods of time planning and the methods for predicting human reliability in order to achieve efficient and stable production processes. For this purpose, at the institute of the authors the assembly planning method MTQM (Methods Time and Quality Measurement), which brings together the above-mentioned planning areas, was developed in the field of basic research [1]. However, until now, the application of MTQM requires experience and expert knowledge in the analysis of human reliability, especially in determining and evaluating performance shaping factors (PSF) [2]. In small and medium-sized enterprises (SMEs), the required experience and methodological competence in the above-mentioned areas is usually insufficient, so that the application of MTQM requires further support. For this reason, this article presents a simplified screening procedure that precedes the original MTQM method.

Keywords: Manual Assembly Operations, Human Reliability, Human Error Probability, Methods Time and Quality Measurement, Screening-Tool, Process Reliability.

INTODUCTION AND APPROACH

Using a simplified MTQM procedure (called smartMTQM), SMEs with manual assembly processes all over the world and across industries can easily identify work steps that have an increased probability of producing defective or inferior parts in order to carry out a more in-depth analysis in the next step. The focus is on the simple application of MTQM without in-depth methodological knowledge, so that an initial defect assessment can be carried out and critical process steps can be presented.

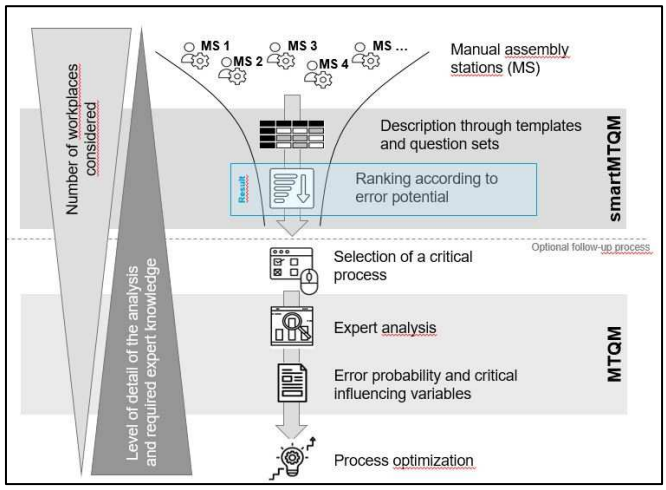

Fig. 1 - Overall structure of two-stage (smart)MTQM procedure.

Figure 1 visualizes the overall analysis process combining smartMTQM as a simplified procedure as well as the potentially following more comprehensive expert procedure MTQM and shows the methodology underlying the research concept. As part of the research activities, existing configurations in manual assembly with regard to mental and physical stress were clustered industry-specifically in order to generate PSF sets consisting of PSFs relevant for the respective industry. In the next step, the PSF sets were condensed into predefined PSF templates (relevant PSFs including their characteristics) for specific assembly conditions (e.g. the influence of workplace contamination was weighted significantly differently in the pharmaceutical sector than in a metalworking company). In addition, task clusters were identified in terms of complexity, difficulty and the proportion of simultaneous manual and mental processes and characterized by sets of questions.

RESULTS AND CONCLUSIONS

In the context of a SME characterized by diverse manual assembly processes and substantial product diversification, the initial step in a targeted optimization is to identify the assembly process with the greatest error potential. smartMTQM is designed to facilitate this identification process. At the beginning of the smartMTQM process, the user describes the considered workstations using templates and sets of questions. These templates are used, for example, to query the type of assembly (e.g. large-scale assembly or small-scale production), the environmental conditions (e.g. climate or noise) and other relevant aspects (e.g. ergonomics). By answering the sets of questions, the specific assembly process is also recorded. Answering these questions and describing them using the templates provided does not require much expert knowledge, for example in the areas of time management and ergonomics. Following this basic description of the considered processes, a ranking of the workstations according to their error potential is created and given to the user using the smartMTQM calculation logic. This ranking makes a targeted examination of individual manual assembly processes possible through an in-depth analysis of the error potential, thus significantly reducing the analysis effort. The more comprehensive MTQM process can be used for further detailed analysis with subsequent optimization. In summary, the result of smartMTQM method facilitates a low-effort determination of the risk ranking of multiple workplaces. The ranking-based risk forecast can then be utilized to specifically identify critical workplaces, which in the subsequent step can be subjected to an in-depth risk analysis using the more comprehensive MTQM procedure to design production processes that are reliable and economically feasible.

ACKNOWLEDGMENT

This Project is supported by the Federal Ministry for Economic Affairs and Climate Action (BMWK) on the basis of a decision by the German Bundestag.

REFERENCES

[1] Refflinghaus R, Kern C (2018) On the track of human errors - Procedure and results of an innovative assembly planning method. Procedia Manufacturing 21:157-164.

[2] Refflinghaus R, Blackert L, Kern C, Trostmann T (2019) Quality improvement in manual assembly by software-based evaluation of human misconduct Proceedings of the 29th European Safety and Reliability Conference. ESREL 2019, S 361-369.

Proceedings IRF2025: 8th International Conference on Integrity-Reliability-Failure
In Engineering, Materials, Manufacturing and Biomechanics. Porto 15-18 July 2025
DOI: https://doi.org/10.24840/978-972-752-323-8

PAPER REF: 22432

COMPUTATIONAL MATHEMATICAL MODELING OF AIRFLOW IN A CABIN-TYPE SOLAR DRYER USED FOR DRYING SUGAR CANE BAGASSE

Lindomar Matias Gonçalves[1], Alexandre Melo de Oliveira[2], Amir Zacarias Mesquita[3], Daniel José de Oliveira Ferreira[4], Hugo César Coelho Michel[5]

[1]UNIFEI, Institute of Pure and Applied Sciences, Federal University of Itajubá, Itabira campus, Brazil.
[2]IFSP Federal Institute of São Paulo, Votuporanga campu, Brazil.
[3] Nuclear Technology Development Center (CDTN), Belo Horizonte, Brazil.
[4,5]Federal University of Minas Gerais, Department of Engineering, Belo Horizonte, Brazil.
(*) *Email:* lindomar@unifei.edu.br

ABSTRACT

The use of solar energy as an alternative energy source has increased in recent years, driven by the search for renewable energy solutions. Solar dryers are a low-cost and technically feasible technology. Electricity is used only to power fans for forced convection, when applicable. Studying the behavior of air within the equipment is crucial to determining the efficiency of the solar dryer. This study aimed to model the airflow behavior inside an empty cabin-type solar dryer used to dry sludge from steel wire drawing. Furthermore, various simulations of variables were proposed to analyze heat exchange and air homogenization within the dryer. The analysis of the results allowed the determination of the efficiency of the solar dryer to dry the studied residue. The numerical model was developed using the Engineering Equation Solver (EES) software, considering variations in air temperature, mass flow rate, density, and solar radiation. After simulation of all possible scenarios, detailed information was extracted to determine the optimal kinetics for the drying process.

Keywords: Computational mathematical model; solar dryer; Airflow; Steel wire drawing sludge.

INTRODUCTION

The generation of industrial solid waste has increased significantly worldwide, and one method still used is landfill disposal for certain types of solid waste. However, the pursuit of sustainable processes and the integration of waste into the development of new products have become necessary. The circular economy seeks to minimize environmental impacts by reducing waste disposal, which requires a profound cultural change.In Brazil, the sugar-energy sector has gained prominence in recent years due to its high potential for energy cogeneration. According to [2], sugarcane bagasse is used to meet the energy needs of production processes, and surplus energy is commercialized throughout the national grid. Improving the efficiency of bagasse processing is essential to meet the demand for ethanol while maintaining the self-sustainability of the industry.

Sugarcane bagasse, the main by-product of sugar-ethanol plants, is used as a boiler fuel to produce steam, which powers turbines and generates electricity. Combustion efficiency is directly related to the bagasse's moisture content, which is approximately 50% on a wet basis (W.B.) after sugarcane milling. Therefore, to maximize its use as an energy source, bagasse must undergo a drying process [9].

To dry the bagasse, a cabin-type solar dryer is used. Its structure comprises wood (freijó) commonly used in aircrafts due to its high mechanical strength and low density, galvanized steel components, and fiberglass for thermal insulation. The goal is to increase the residence time of heated air within the dryer, in order to achieve higher thermal efficiency during the bagasse drying process. To achieve this objective, the EES numerical simulation software (Engineering Equation Solver) will be utilized. A notable feature of EES is its highly precise thermodynamic and transport property database for hundreds of substances, enabling its effective use for equation-solving capabilities.

Using solar energy through solar dryers for bagasse drying is a technically and economically viable alternative, offering environmental advantages due to its renewable nature and the absence of greenhouse gas emissions.

THEORETICAL FRAMEWORK

Drying can be defined as the removal of water, or any other liquid, from a solid material in the form of vapor into an unsaturated gas phase (usually air) through a thermal vaporization mechanism at a temperature below the liquid's boiling point. The aim of drying is to reduce the product's moisture content, creating unfavorable conditions for microbial growth, increasing shelf life, reducing weight (facilitating transportation), and, in some cases, enhancing nutritional content and flavor.

In drying operations, the fundamental variables are the product's moisture content, temperature, relative humidity, and air flow pressure. For fixed air temperature and flow pressure, there is an equilibrium relationship between the relative humidity of the air and the moisture content of the product. When the drying process begins (with an initial moisture content under controlled thermal parameters), variations in moisture diffusivity and dependencies of thermal properties on water content and temperature are crucial parameters for assessing the efficiency of the drying process [3].

Drying involves simultaneous heat and mass transfer between the product being dried and the air flow until the equilibrium moisture content is reached. Generally, in drying processes, heat is transferred to the product by convection and, in some cases, by radiation. This energy partially penetrates the product, facilitating moisture migration.

Mathematical modeling in drying processes is essential for the simulation and design of drying equipment. Drying is a complex phenomenon that simultaneously involves heat and mass transfer. The additional challenge in modeling solar drying processes lies in the varying climatic conditions during the drying process [3].

According to [4], solar drying using solar collectors has been shown to be efficient, but numerical and theoretical investigations of the drying parameters are necessary. From the study, the need for a new mathematical model was identified to achieve new results through experiments with sweet basil.

DRYING METHODS AND TYPES OF DRYERS

The first and most widely used drying method in tropical regions is natural drying. For agricultural products, after physiological maturation, the moisture content is high. The product, still in the plant (or placed on the ground, boards, screens, or racks), is dried by absorbing incident solar radiation and wind action. Over time, the product achieves the desired moisture content for storage, but remains vulnerable to rain, bird attacks, rodents, and insects, resulting

in significant losses. For residue drying, the process is slow and subject to moisture reabsorption.

Dryers can be classified according to the method of heating the drying air. When air is heated using solar energy, dryers are called solar dryers. When heating is achieved through other energy sources (fossil fuel combustion, electric heating, etc.), they are referred to as artificial dryers. Hybrid dryers combine solar energy with a conventional energy source.

Industries commonly use convective drying methods that involve airflow, with thermal energy sourced from electricity, LPG or fuel oil. Fossil fuels are still widely used in industries, but they often entail high costs. In remote areas, particularly rural regions, solar energy is commonly used for air heating [5].

According to [5], solar energy drying methods are divided into two major groups based on air circulation: passive and active. In passive dryers, air circulation is driven by thermal energy. In active dryers, air circulation is provided by an electric fan. Active dryers have an additional cost due to the use of fans, but they achieve higher drying speeds compared to passive dryers.

TECHNICAL CONSIDERATIONS FOR DRYER ANALYSIS

Drying processes involve simultaneous heat transfer (from the surroundings to the product's surface, and subsequently to its interior) and mass transfer (from the product's interior to its surface and, subsequently, to the surroundings). In these processes, the heat and mass transfer coefficients (between air and the product) and the product parameters (size, density, and moisture content) continuously vary. These parameters are influenced by the thermal characteristics of the airflow (temperature, humidity, and flow rate) and the chemical composition of the product. Each product tolerates a maximum temperature without sustaining damage or adverse chemical changes in its nutritional and sensory qualities. This temperature depends on the type of food being dried, its intended use, the moisture content, and the degree of maturity.

The key parameters for the technical evaluation of solar dryers [6] include:

- Physical characteristics of the dryer;
- Thermal efficiency of the dryer.

The main physical characteristics of a dryer are the following:

- Dryer classification (type);
- Geometric configuration; dimensions;
- Materials used in construction;
- device weight;
- Drying capacity and load density;
- area and number of drying screens;
- ease of loading and unloading the product from the device;
- Solar energy collection area.

In general, the dimensions and shape of a dryer are parameters that are directly used to evaluate its drying capacity, as they determine the number of drying screens and their area.

METODOLOGY

The proposed dryer is coated both internally and externally with painted galvanized steel sheets to protect the wooden structure (preventing damage caused by moisture during the drying process) and to protect the thermal insulation. All walls of the dryer casing are internally thermally insulated with fiberglass.

In the dryer (Figure 1), solar radiation passes through the glass cover and reaches the metal plate that absorbs solar radiation (painted in matte black). Airflow enters at ambient temperature through a rectangular screened channel, absorbs heat by convection from the absorber plate located at the bottom of the internal casing, passes through the tray containing the residue to be dried (removing moisture), and exits the dryer through a circular duct. A fan system installed in the vent ensures the necessary airflow to maximize the removal of moisture from the bagasse.

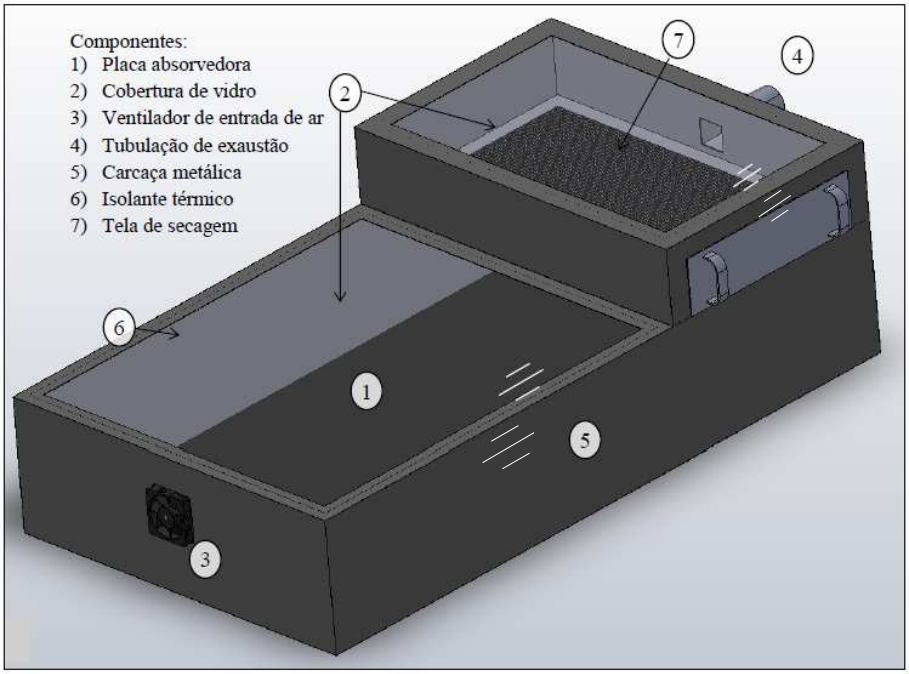

Fig. 1 - Schematic representation of the cabin-type solar dryer.

The bagasse will be placed on a drying screen constructed in the form of a drawer installed within the drying chamber. This drawer can be inserted and removed from the drying chamber to load and unload the residue, aided by a handle. The drying chamber is covered with glass, enhancing the absorption of solar radiation by the residue and accelerating the drying process.

The geometric configuration of the dryer forces the airflow to pass through the tray containing the bagasse to be dried [7], promoting uniform airflow and reducing drying heterogeneity (commonly observed in most dryers). Preliminary numerical analyzes confirm greater homogeneity in airflow and lower thermal losses compared to many traditional dryers.

Experimental results will enable energy balance analysis and evaluation of the efficiency of the dryer solar collector.

The sensible energy absorbed by airflow (Eautil) can be determined as a function of the airflow mass flow rate (), the specific heat of air at constant pressure (c_p), and the ambient inlet (T_{amb}) and outlet (Tout) temperatures of the airflow from the device: device:

$$E_S = \int \dot{m}\, c_p \left(T_{out} - T_{amb}\right) dt \tag{1}$$

By measuring the inlet and outlet air temperatures of the dryer airflow (using temperature sensors) and the airflow velocity (using an anemometer), it is possible to experimentally determine the sensible energy absorbed by the airflow.

When the total solar energy incident on the dryer's cover is measured, it becomes possible to determine the device's overall thermal efficiency.

$$E_T = \int GA\, dt \tag{2}$$

$$\eta_T = \frac{E_S}{E_T} \tag{3}$$

Here ETE_TET is the total energy, AAA is the collection area, GGG is the incident radiation flux, and (T is the thermal efficiency.

Furthermore, it becomes possible to quantify the thermal losses of the dryer.

$$E_P = E_T - E_S \tag{4}$$

The First Law of Thermodynamics establishes the equivalence between thermal energy (heat) and mechanical energy (work), based on the principle of conservation of energy, which states: Energy cannot be created or destroyed, only transformed from one form to another [8]. Where the work ($\boldsymbol{\tau}$) given in joules (J), when added to the change in internal energy ($\boldsymbol{\Delta U}$), will be equal to the amount of heat (Q).

$$Q = \tau + \Delta U \tag{5}$$

The second law of thermodynamics establishes the conditions under which energy transformations (thermal and mechanical) are possible. Work can be fully converted to heat, but heat cannot be fully converted to work. This transformation is achieved through a heat engine [8].

$$\tau = Q_1 - Q_2 \tag{6}$$

Where Q1 is the amount of heat supplied, Q2 is the amount of heat lost and is the work obtained.

Efficiency of the heat engine: It is the ratio of the work performed due to the heat supplied by a hot source (the efficiency is expressed as a percentage). The Kelvin-Planck formulation of the Second Law of Thermodynamics (Clausius) states that it is impossible to construct a device that, by itself, i.e., without external intervention, can transfer heat from a body to another body at a higher temperature [8]. The change in the thermofluidynamic behavior of the air heated inside the equipment will be analyzed using mathematical models using EES as the computational tool, with formulas extracted from the books and literature. It is a general equation solving program that can numerically solve thousands of coupled algebraic and non-linear differential equations.

Some parameters will be decisive for the simulation using the tool mentioned above.

- Simulation of sensible energy through the variation of mass times the enthalpy (hhh) changes as a function of time;
- Variation of solar radiation as a function of time, fixing the area of the solar dryer;
- Determining thermal efficiency as the ratio of sensible energy to thermal energy;
- Quantifying the thermal losses of the equipment through the variation of thermal energy and sensible energy;
- The amount of heat through the variation of energy added to the work performed;
- And finally, the work is the variation of the amount of heat lost relative to the amount of heat supplied.

All parameters are crucial for achieving adequate efficiency for the equipment.

RESULTS AND CONCLUSIONS

An energy balance in the device characterizes the most significant energy losses of the system and allows the establishment of the structural changes necessary for the solar dryer to become competitive and technically feasible. An important parameter for controlling the drying process is the measurement of sensible energy, as it allows for identifying the thermal efficiency of the equipment. Figure 2 shows the variation of the air temperature inside the equipment. It can be observed that the behavior is linear, as the variation in density is directly proportional to the temperature change.

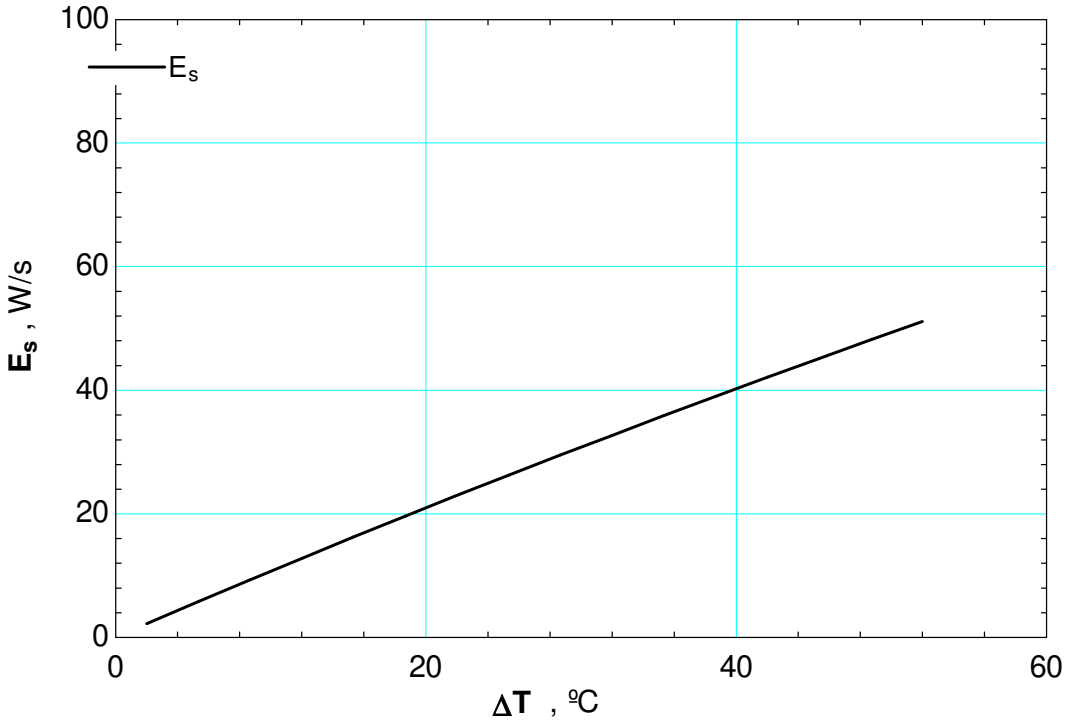

Fig. 2 - Representation of Sensible Energy as a Function of Temperature Variation.

In the solar dryer, ambient air is blown through a fan to promote heat transfer by convection with the absorber plate, which is painted in matte black with a high absorbance of incident solar radiation. The heated air flow, through convection, passes through the drying chamber and exits via a screened tube. The dryer reaches steady state after the first few hours of testing. As solar radiation increases, the temperature inside the dryer increases, leading to the maximization of sensible energy. This is directly related to the increase in thermal energy, which, in turn, reduces the amount of water present inside the equipment through the exhaust system. Since the area of the equipment is fixed (1.8 m²), the variation in solar radiation as a function of time will significantly influence the interior of the equipment. As shown in Figure 3, the higher the incident solar radiation on the absorber plate of the equipment, the higher the thermal efficiency.

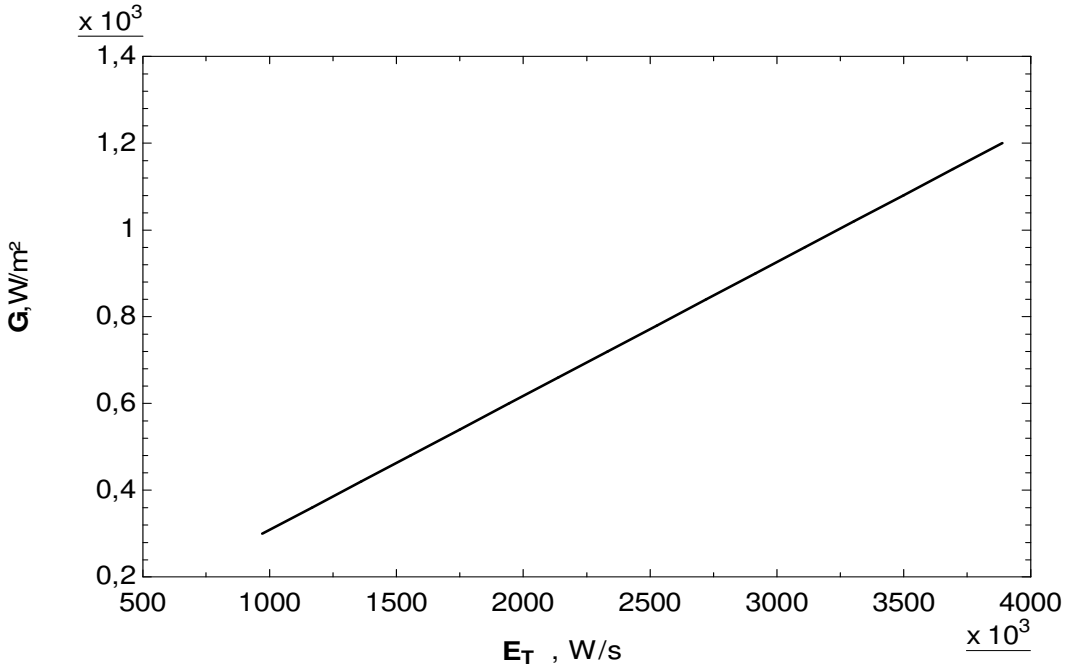

Fig. 3 - Representation of Sensible Energy as a Function of Temperature Variation.

The increase in thermal efficiency occurs because the equipment is not loaded; otherwise, if the equipment were loaded, the curve would exhibit sinusoidal behavior. Since the variation in density is very low as it involves only heated air, the curve is linear. However, when the dryer is loaded, there is a significant increase in density due to the increase in temperature. Initially, there is a peak in thermal efficiency, as the flow rate is constant and the air flow within the equipment is also constant. As solar radiation affects the medium, the curve tends to become linear, which is due to the proximity between the external air temperature and the internal air temperature. However, the internal air temperature is higher because it is heated by an absorber plate painted matte black, in a controlled environment. The global thermal efficiency will depend on the receiver area, which is related to the temperature gain of the air in the dryer.

Energy losses in the equipment are of utmost importance to determine, as reducing them will increasingly enhance the thermal efficiency of the equipment. As shown in Figure 4, the instantaneous simulated thermal efficiency of the dryer increased in a parabolic shape.

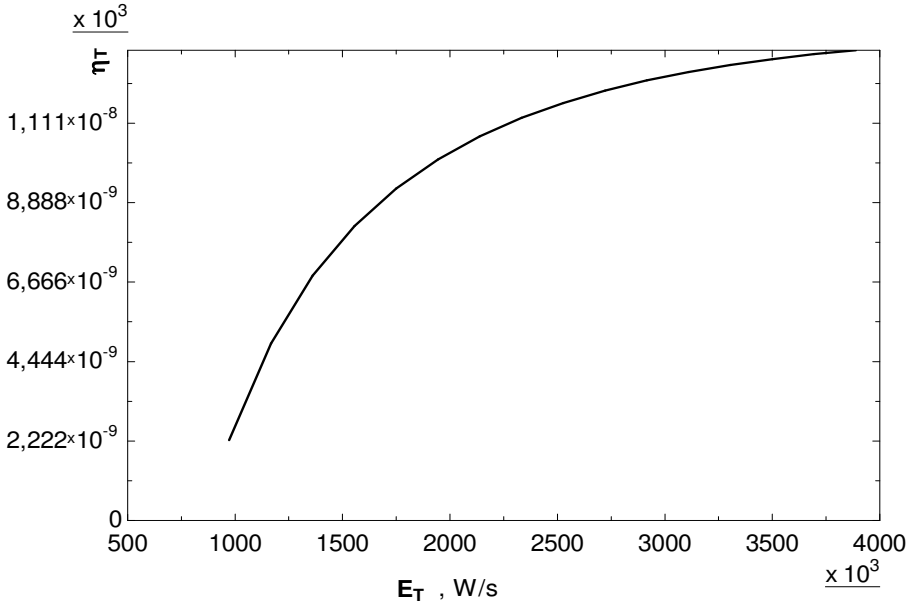

Fig. 4 - Representation of the Thermal Efficiency of the Solar Dryer.

The fact that a linear curve was not achieved can be explained by the fact that efficiency increases with temperature, and when the system reaches steady state, it behaves linearly. Since thermal efficiency is related to the increase in air temperature inside the equipment and there is initially a significant temperature difference between the inlet and outlet, the curve is exponential. However, when the equipment stabilizes the air temperature, that is, reduces the temperature difference between the inlet and outlet, the curve tends to become linear. This occurs because the equipment does not have a load to remove the sensible energy from the air. The thermal losses of the equipment occur because of the difference in energy present in the heated air and the energy received, based on the dryer area. As shown in Figure 5, the increase in equipment losses is proportional to the increase in efficiency. When the system reaches steady state, the losses reach their maximum value.

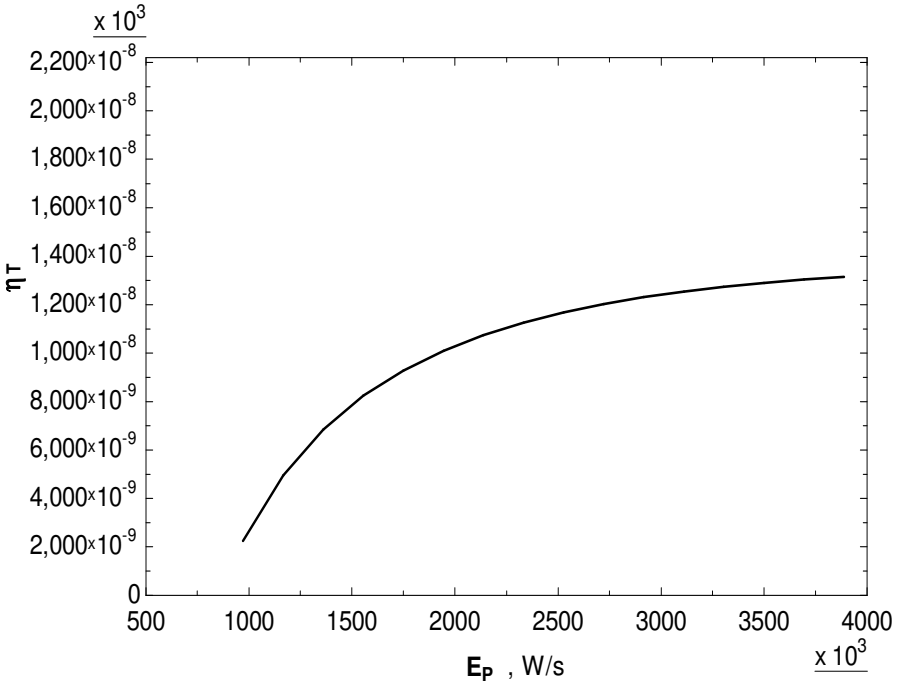

Fig. 5 - Representation of losses in relation to the thermal efficiency of the solar dryer.

It is clear that if the dryer reached higher temperatures, it would be necessary to review the insulation system, although this is not required when using solar energy, as the air heating capacity is limited. Depending on the increase in losses, more studies such as equipment exergy analysis would be necessary, which would require additional measures and studies that were not addressed in this work. This analysis works with the energy balances of the entire system, aiming to reduce losses. The initial analysis of a solar dryer using a simulation tool, in this case, the EES software, is crucial to obtain initial parameters to understand the drying behavior. When a process is simulated, the possibility of errors in the experimental tests is minimized. Studying the energies present in a process or equipment, as well as the losses, is necessary to achieve the maximum efficiency of a solar dryer. The thermal efficiency of the equipment, under stable temporal conditions, presents linear behavior, which is not the case under normal conditions. However, they serve as input parameters and to define control goals for the equipment. Mathematical methods, as well as simulation, have been increasingly used in various fields, especially in engineering. The losses of equipment that uses thermal energy as a source, which comes from insulation, are higher at the beginning of the process, maintaining linear behavior as the process stabilizes. In the energy evaluation of the solar dryer, considering that the energy source is solar, it is a factor of extreme relevance in the current global energy market scenario. Finally, it can be inferred that the analysis and simulation of the data performed allowed the main objective of this article to be achieved, which is to outline the initial drying behaviors with the equipment empty, prior to drying the sugarcane bagasse.

REFERENCES

[1] F-Chart Software. Engineering Equation Solver (EES): Commercial and Professional Versions. Madison, EUA, 2005. 297p.

[2] Dantas, GU. A., Legey, L. F.L., Mazzone, A. Energy from sugarcane bagasse in Brazil: An assessment of the productivity and cost of different technological routes. Review article Renewable and Sustainable Energy Reviews, Volume 21, May 2013, pp.356-364.

[3] Ramos, N.I.; Brando, T.R.S.; Silva, C.L.M. Simulation of solar drying of grapes using an integrated heat and mass transfer model. Original Research Article Renewable Energy, Volume 81, September 2015, pp.896-902.

[4] Gulcimen, F.; Karakaya, H.; Durmus, A. Drying of sweet basil with solar air collectors. Original Research Article Renewable Energy, Volume 93, August 2016, pp.77-86.

[5] Sekyere, C.K.K.; Forson, F.K.; Adam, FW Experimental investigation of the drying characteristics of a mixed mode natural convection solar crop dryer with back-up heater. Original Research Article, Renewable Energy, Volume 92, July 2016, pp.532-542.

[6] Leon, M. A., Kumar, S., and Bhattacharya, S.S.. C.A Comprehensive Procedure for ther Performance Evaluation of Solar Food Dryers. Renewable and Sustainable Energy Reviews, v. 6, pp.367-393, 2002.

[7] Ferreira, A. G.; Gonçalves, L.M.; Maia, C.B. Solar drying of a solid waste from steel wire industry. Original Research Article Applied Thermal Engineering, Volume 73, Issue 1, 5 December 2014, pp.104-110.

[8] EngelL, Y A; Boles, M A. Termodinâmica. 5a edição. So Paulo: MacGraw-Hill, 2009.

[9] H. Lee, H.O. Kim, D.H. Lee, D.H. Choi et al. G. Kim, 'Fixed Bed Drying of Sugarcane Bagasse Using Solar Energy', Journal of the Korean Wood Science and Technology, vol. 52, no. 1, pp.47-57, 2024, doi: 10.5658/WOOD.2024.52.1.47.

Proceedings IRF2025: 8th International Conference on Integrity-Reliability-Failure
In Engineering, Materials, Manufacturing and Biomechanics. Porto 15-18 July 2025
DOI: https://doi.org/10.24840/978-972-752-323-8

PAPER REF: 22440

ENHANCING MULTI-MATERIAL RECYCLING IN THE AUTOMOTIVE INDUSTRY: A STUDY ON CRYOGENIC TREATMENT FOR IMPROVED MATERIAL SEGREGATION

Romeu Matos[1(*)], Ivan Pereira[1], Bruna F. Oliveira[2], Flávia Barbosa[2,3], Vitor Paulo[4], Maria G. Fernandes[1]

[1]CATIM, Technological Centre for the Metalworking Industry, Porto, Portugal
[2]INEGI, Porto, Portugal
[3]LAETA/INEGI, Porto, Portugal
[4]GLN Plast, Leiria, Portugal
[(*)]*Email:* romeu.matos@catim.pt

ABSTRACT

Recycling multi-material compounds in the automotive industry, such as composites and metals, poses significant challenges due to tightly bonded structures that hinder separation processes. These difficulties result in high recycling costs and environmental impacts. This study explores cryogenic treatment as a method to enhance material segregation by inducing brittleness in bonded interfaces. The effects of different cryogenic cycles, particularly exposure time, were analyzed using mechanical testing to separate metal components from composite materials. Optimized conditions for the segregation of PBT-GF30 and metals were tested, exploring cryogenic treatment as a possible approach to improving recycling efficiency in the automotive sector.

Keywords: Automotive sector, cryogenic treatment, multi-material segregation, recycling.

INTRODUCTION

The automotive industry faces significant challenges in recycling multi-material compounds, which often consist of tightly bonded materials such as composites and metals (Maldonado-Guzmán et al., 2021). These complex bonds hinder the separation process, increasing recycling costs and environmental impacts due to reliance on landfill or incineration. Cryogenic treatment has emerged as a possible technique for improving material segregation by increasing the material's brittleness (Deshmukh et al., 2022). Cryogenic treatment entails subjecting materials to cryogenic temperatures (generally considered to be below -150°C), mainly using liquid nitrogen, to effect modifications in their physical properties (Kalia, 2010). The exposure to such low temperatures induces thermal contraction, which occurs at varying rates depending on the material's composition (Zohuri, 2018). This effect proves especially beneficial for multi-material systems, as the differential contraction may compromise the interfacial adhesion between heterogeneous components like composites and metals (Hemath Kumar et al., 2017). Moreover, cryogenic treatment can improve the mechanical properties of specific metals by promoting microstructural refinement (Yan et al., 2021). In the domain of recycling, the primary function of cryogenic processing is to facilitate the fragmentation and separation of bonded materials. By controlling these mechanisms, cryogenic treatment appears as a valuable approach to enhance the efficiency of material recovery processes, minimize waste, and support sustainable recycling methodologies.

In this context, this study investigates the impact of different cryogenic cycles on the segregation efficiency of these compounds, with a specific focus on the effect of exposure time

at cryogenic temperatures. By exposing the multi-material samples to varying cryogenic conditions, the research aims to identify optimal parameters for segregating material interfaces, facilitating effective separation. Key metrics such as exposure time and the force applied to remove the metallic screws in different experimental conditions were analysed to evaluate the pertinence of the cryogenic treatment for multi-material recycling.

MATERIALS AND METHODS

The studied component is a glass fibre reinforced polybutylene terephthalate (PBT-GF30) automotive part, produced by injection molding, containing embedded metallic inserts (Figure 1). The component included three types of inserts: two M10 round-head screws, ten M5 square-head screws, and four spacer washers. A total of 15 components (n=15) were used in the experiments, 5 with no cryogenic treatment and 10 that were exposed to a different cryogenic treatment. All of them were subjected to a fast removal of the metallic inserts at ambient temperature.

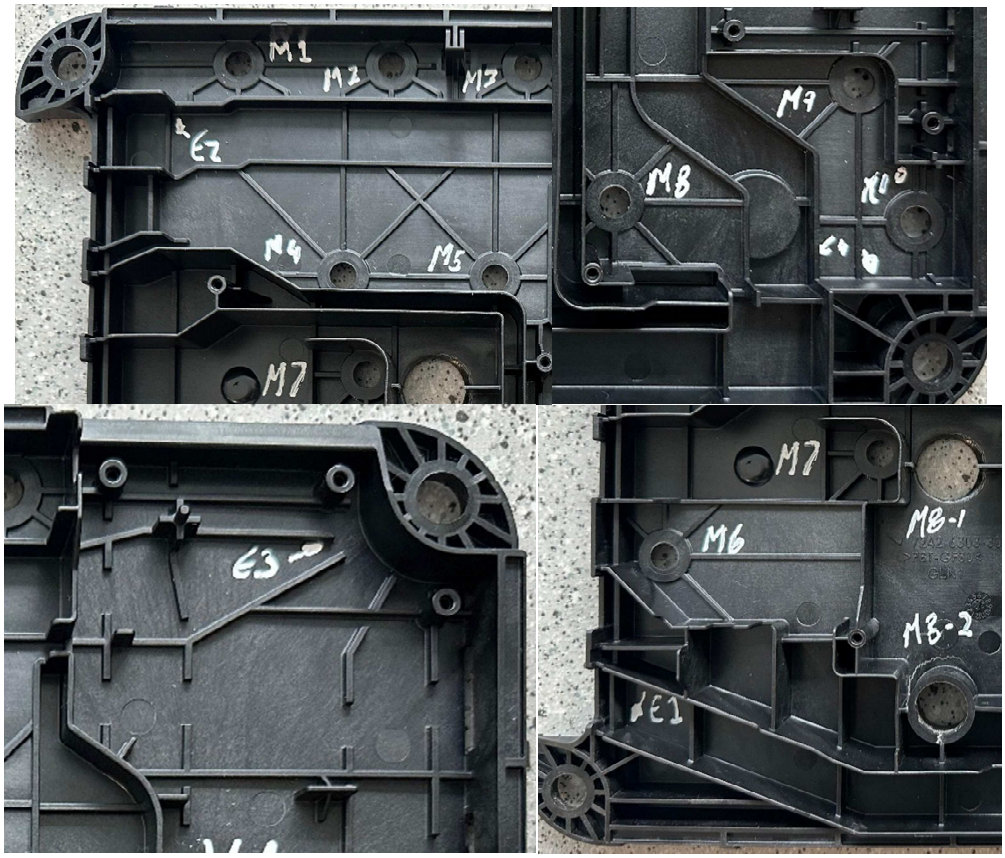

Fig. 1 - Metallic inserts layout.

Cryogenic treatment

The first step in the experimental procedure for the PBT-GF30 component is cryogenic treatment. The experimental setup (Figure 2) consisted of a 60 L nitrogen bottle (Figure 2a) connected via a hose (Figure 2b) to a 25 L aluminum pot (Figure 2d). Three components at a time were submerged in the pot (Figure 2c)), for different timed tests, as indicated in Table 1. The temperature of the components during the treatment reached -197 ºC and remained at it until their removal.

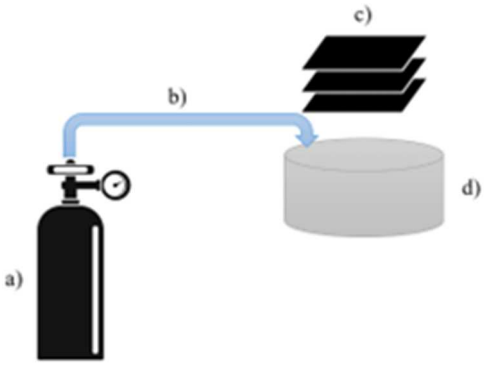

Fig. 2 - Cryogeny experimental setup, based on (Oliveira et al., 2025).

Table 1 - Plan of experiments

Test	Number of components	Time submerged
1	5	2 h
2	5	3 h

After the cryogenic treatment, the components were left outside to heat up to the ambient temperature. Then, the same components were subjected to compression tests for the removal of the metallic inserts.

Compression tests

The screws were positioned within the injection mold and secured to the base material by their heads, while the spacer washers were fully embedded in the polymer, as illustrated in **Error! Reference source not found.**. Compression tests were performed at ambient temperature using an Instron 5969 testing machine equipped with a die and counter-die for insert extraction. The removal process was performed by applying a compressive force at a constant speed of 50 mm/min. This loading mechanism induced three primary phenomena:

- **Zone 1:** detachment of the insert from the base material by traction in zone 1;
- **Zone 2:** detachment of the insert from the base material by shear in zone 2;
- **Zone 3:** shear stress on the base material itself.

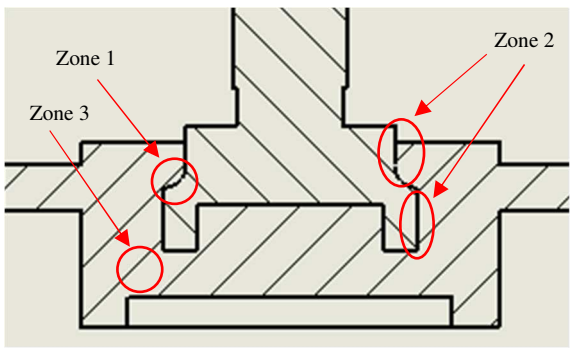

Fig. 3 - Layout of the M5 insert.

The primary force occurred in Zone 3, as shear stress acted directly on the base material.

RESULTS AND CONCLUSIONS

As mentioned, the base material (PBT-GF30) is a hybrid polymer, which contains approximately 30 % short-embedded glass fiber reinforcement. The variation of the glass fibers length as well as their orientation results from various phenomena, such as flow velocity, injection temperature, cooling time, injection pressure, among others. Consequently, their orientation has both a predictable component and a random aspect.

All these variables increase the uncertainty regarding fiber positioning and, consequently, the local mechanical behavior, as well as the interaction between the base material and the insert.

Table 2 presents the results obtained for components that did not undergo any cryogenic treatment, considering five samples. The results effectively demonstrate significant variability among the trials, as evidenced not only by the sample's standard deviation but also by the standard amplitude, calculated as:

$$\varepsilon_F = \frac{(F_{Max} - F_{Min})}{F_{Max}}, \quad (1)$$

where:

F_{Max} represents the maximum extraction force among the five pieces;

F_{Min} represents the minimum extraction force among the five pieces.

Table 2 - Results and analysis of the experiments carried out with untreated (no cryogenic treatment) pieces for the maximum force required to remove the inserts.

	Maximum Force (F)[N]					**Average (F_μ) [N]**	**Standard Deviation (F_σ) [N]**	**Standard amplitude (ε_F) [%]**
	Piece 1	**Piece 2**	**Piece 3**	**Piece 4**	**Piece 5**			
Spacer-1	8530	7609	7047	7563	8434	7837	630	17,4%
Spacer 2	6667	7153	6563	10340	7713	7687	1551	36,5%
Spacer 3	7386	7153	7731	9919	7708	7979	1111	27,9%
Spacer 4	7655	8056	7439	7799	7707	7731	225	7,7%
M5-1	5133	5292	4860	4986	4855	5025	188	8,3%
M5-2	5145	5228	4868	4866	4773	4976	198	8,7%
M5-3	5063	4984	4674	4625	4605	4790	216	9,0%
M5-4	4735	4900	4759	4679	4642	4743	99	5,3%
M5-5	5118	5330	4796	4965	5087	5059	197	10,0%
M5-6	4748	4818	4468	4502	4479	4603	167	7,3%
M5-7	4923	5238	4697	4894	4743	4899	212	10,3%
M5-8	4973	4928	4394	4750	4688	4747	230	11,6%
M5-9	4389	4875	4615	4772	4823	4695	197	10,0%
M5-10	4806	4774	4359	4564	4637	4628	180	9,3%
M10-1	9494	9715	6735	6670	6378	7798	1656	34,3%
M10-2	9551	9420	7251	7804	7658	8337	1069	24,1%

The results also indicate that ε_F is generally higher for spacer washers and the M10 round-head bolts, than the case of M5 square-head bolts. However, even in the latter case, the minimum ε_F is 5.3%, and the maximum ε_F reaches 11.6%, with an average ε_F for this type of insert being 9.0%.

These results stem from the previously mentioned randomness, which is associated both with the material itself and the injection process. To some extent, the high variability of the spacers can be explained, as they are located at the extremity of the piece, where these factors are amplified.

Table 3 presents the average maximum removal force for the 5 pieces, the standard deviation, and the range for the untreated specimens, as well as those subjected to cryogenic treatment for 2 hours and 3 hours. Additionally, the difference between the mean results of the cryogenic treatment (2 and 3 hours) and the untreated pieces were calculated as:

$$\Delta F_{2h} = \frac{(F_{\mu}[2h\ cryogenic\ treatment] - F_{\mu}[No\ treatment])}{F_{\mu}[No\ treatment]}, \quad (2)$$

$$\Delta F_{3h} = \frac{(F_{\mu}[3h\ cryogenic\ treatment] - F_{\mu}[No\ treatment])}{F_{\mu}[No\ treatment]}, \quad (3)$$

where:

$F_{\mu}[No\ treatment]$ is the average of the maximum force required for five pieces with no treatment;

$F_{\mu}[2h\ cryogenic\ treatment]$ is the average of the maximum force required for five pieces with 2h cryogenic treatment;

$F_{\mu}[2h\ cryogenic\ treatment]$ is the average of the maximum force required for five pieces with 2h cryogenic treatment.

Table 3 - Results and analysis of the experiments all pieces for the maximum force required to remove the inserts.

	No treatment			**2h Cryogenic treatment**				**3h Cryogenic treatment**			
	F_{μ} [N]	**F_{σ} [N]**	**ε_F [%]**	**F_{μ} [N]**	**F_{σ} [N]**	**ε_F [%]**	**ΔF_{2h} [%]**	**F_{μ} [N]**	**F_{σ} [N]**	**ε_F [%]**	**ΔF_{3h} [%]**
Spacer-1	7837	630	17,4%	7795	256	7,1%	-0,5%	7736	524	14,5%	-1,3%
Spacer 2	7687	1551	36,5%	7723	256	7,7%	0,5%	7863	591	16,2%	2,3%
Spacer 3	7979	1111	27,9%	7750	175	4,8%	-2,9%	7737	223	7,6%	-3,0%
Spacer 4	7731	225	7,7%	7830	333	9,5%	1,3%	7633	487	14,2%	-1,3%
M5-1	5025	188	8,3%	5005	206	9,1%	-0,4%	4965	218	11,6%	-1,2%
M5-2	4976	198	8,7%	4993	198	9,4%	0,3%	4902	141	7,7%	-1,5%
M5-3	4790	216	9,0%	4888	155	7,1%	2,0%	4822	88	4,5%	0,7%
M5-4	4743	99	5,3%	4725	113	4,9%	-0,4%	4750	198	9,4%	0,1%
M5-5	5059	197	10,0%	5116	200	8,1%	1,1%	4980	134	6,9%	-1,6%
M5-6	4603	167	7,3%	4631	128	6,1%	0,6%	4532	125	7,3%	-1,5%
M5-7	4899	212	10,3%	4801	280	12,2%	-2,0%	4707	187	10,1%	-3,9%
M5-8	4747	230	11,6%	4725	206	10,5%	-0,5%	4703	92	5,1%	-0,9%
M5-9	4695	197	10,0%	4616	101	5,1%	-1,7%	4571	89	4,6%	-2,6%
M5-10	4628	180	9,3%	4697	174	8,3%	1,5%	4566	159	9,3%	-1,3%
M10-1	7798	1656	34,3%	7919	1577	31,0%	1,5%	7668	1374	29,0%	-1,7%
M10-2	8337	1069	24,1%	8643	984	21,5%	3,7%	8313	909	22,0%	-0,3%

The results show a slight improvement in the consistency of the outcomes obtained for the components after cryogenic treatment, particularly for the spacer-type inserts and the M10 inserts. However, both still exhibit a wider range of results compared to the M5 inserts.

The average of ΔF_{2h}, considering all the inserts, is 0.3% higher than the components that underwent no thermal treatment, while the average of ΔF_{3h} is 1.2% lower than those that did not undergo any thermal treatment. Given the approximately 10% variability (ε_F), it is not possible to conclude that cryogenic treatments (2 and 3 hours) significantly influenced component removal behavior. If there is any modification in the structure of the base polymer, it would be lower than the variability associated with the material and injection process. This also suggests that cryogenic thermal treatments did not have a significant impact on the plastic/metal bonding when subject to a compressive force at a constant speed of 50 mm/min. These findings underline the need for further research into polymer embrittlement mechanisms during cryogenic treatments and the mechanical behavior of fiber-reinforced polymers.

REFERENCES

[1] Deshmukh, K. A., Chopra, S., Khajanji, P., Deshmukh, A., Peshwe, D. R. (2022). Effectiveness of cryogenic treatment on PBT composites: prediction of interfacial interaction parameter and its influence on filler bonding and wear performance. Polymer Bulletin, 79(1), pp.381-405. https://doi.org/10.1007/s00289-020-03501-z.

[2] Hemath Kumar, G., Mohit, H., Purohit, R. (2017). Effect Of Deep Cryogenic Treatment On Composite Material For Automotive Ac System. In Materials Today: Proceedings (Vol. 4). www.sciencedirect.comwww.materialstoday.com/proceedings.

[3] Kalia, S. (2010). Cryogenic processing: A study of materials at low temperatures. Journal of Low Temperature Physics, 158(5-6), pp.934-945. https://doi.org/10.1007/s10909-009-0058-x.

[4] Maldonado-Guzmán, G., Garza-Reyes, J.A., Pinzón-Castro, Y. (2021). Eco-innovation and the circular economy in the automotive industry. Benchmarking, 28(2), pp.621-635. https://doi.org/10.1108/BIJ-06-2020-0317/FULL/XML.

[5] Oliveira, B.F., Gonçalves, T.I., Gonçalves, R., Lourenço, E., Oliveira, C., Paulo, V., Barbosa, F.V. (2025). Assessing the environmental impact of cryogenic treatment in recycling scenarios for PBT-GF30 components. Sustainable Materials and Technologies, 44, e01298. https://doi.org/10.1016/j.susmat.2025.e01298.

[6] Yan, Y., Liu, K., Luo, Z., Wang, M., Wang, X. (2021). Effect of cryogenic treatment on microstructure, mechanical properties and distortion of carburized gear steels. Metals, 11(12). https://doi.org/10.3390/met11121940.

[7] Zohuri, B. (2018). Cryogenic Technologies. In Physics of Cryogenics, pp.1-51. Elsevier. https://doi.org/10.1016/b978-0-12-814519-7.00001-x.

Proceedings IRF2025: 8th International Conference on Integrity-Reliability-Failure
In Engineering, Materials, Manufacturing and Biomechanics. Porto 15-18 July 2025
DOI: https://doi.org/10.24840/978-972-752-323-8

PAPER REF: 22466

DEVELOPMENT OF WOK SEVERITY INDEX FOR BAKERY OPERATIONS

Olasunkanmi Salami Ismaila(*), Desmond Ayobami Oladeji

Dep. Mechanical Engineering, College of Engineering, Federal University of Agriculture, Abeokuta, Nigeria
(*)*Email:* ismailaso@funaab.edu.ng

ABSTRACT

This study investigated the ergonomic risks associated with bakery operations, focusing on personal factors, task factors, and environmental factors. The potential severity and likelihood of occurrence for all identified risk factors were evaluated on a scale from 1 to 5. The risk index was calculated by multiplying the likelihood of occurrence by the potential severity for each risk parameter. The relative weights of the risk factors' parameters were determined by dividing each cumulative risk index by the total cumulative risk index. Similarly, the relative weights of the ergonomic risk factors were obtained by dividing the cumulative risk index for each factor by the sum of all cumulative risk indices. The total risk index for each factor was computed by summing the products of the relative weights and the risk indices of the parameters constituting the factor. The Work Severity Index (WSI) was calculated by summing the products of the relative weights and the risk indices of the ergonomic risk factors. The risk values were then categorised into three categories: low, medium, and high risk. Findings reveal a low overall risk level, with the mean Work Severity Index (WSI) calculated as 7.88 (±1.79), indicating manageable ergonomic risks. The WSI categorisation showed that while the majority of subjects exhibited low-risk levels, several workers had medium-risk scores, highlighting areas requiring attention. Specifically, WSIs of 9.55, 9.27, 8.82, 10.32, and 10.20 were classified as medium risk, whereas scores such as 6.26, 5.84, 6.40, 6.57, and 5.84 fell within the low-risk range.

Keywords: Ergonomic risk, work severity index, bakery operations, occupational safety, musculoskeletal disorders.

INTRODUCTION

Bakeries are integral to food production, creating diverse products such as bread, pastries, and cakes. However, the labor-intensive nature of bakery work poses various ergonomic challenges. These challenges stem from repetitive tasks, awkward postures, prolonged standing, and exposure to harsh environmental conditions such as high temperatures and noise. Addressing these risks is essential to protect workers from musculoskeletal disorders (MSDs) and other occupational hazards (Aghilinejad et al., 2016; Gu et al., 2016). This study aimed to develop a Work Severity Index (WSI) to evaluate and categorize ergonomic risks in bakery operations. By integrating personal, task, and environmental factors, the WSI provides a quantitative approach for assessing workplace safety and identifying areas requiring intervention.

RESULTS AND CONCLUSIONS

The mean WSI across the bakery workers was 7.88 (±1.79), indicating a low overall ergonomic risk. However, several medium-risk scores highlighted areas of concern:

Personal Factors: Workers with limited experience (≤5 years) or high BMI (≥30 kg/m²) were more prone to injuries. Subject 8, with a BMI of 39.96 kg/m², exhibited the highest personal risk.

Task Factors: Prolonged standing, awkward postures, and heavy lifting contributed to medium risk levels. Tasks involving poor hand coupling or excessive twisting were particularly hazardous.

Environmental Factors: Ambient temperatures averaging 35.41°C and noise levels of 92.72 dB posed significant risks. Though vibration levels (0.20 m/s²) were within acceptable limits, the combined impact of environmental conditions exacerbated worker discomfort.

Medium-risk WSIs were observed for subjects 1 (9.55), 2 (9.27), 6 (10.32), and 7 (10.20), underscoring the need for targeted interventions.

Table 1 - Work Severity Indices and Categorisation of these Indices.

Subject	Total Risk Index for Personal Factor ($TRI_{personal\ factor}$	Total Risk Index for Task Factor ($TRI_{task\ factor}$	Total Risk Index for Environmental Factor	Work Severity Index (WSI)	Categorisation of Work Severity Index
1	5.70	11.31	11.63	9.55	Medium
2	4.86	11.31	11.63	9.27	Medium
3	9.28	2.26	8.08	6.26	Low
4	8.00	2.26	8.08	5.84	Low
5	3.48	11.31	11.63	8.82	Low-Medium
6	8.02	11.31	11.63	10.32	Medium
7	7.68	11.31	11.63	10.20	Medium
8	9.69	2.26	8.08	6.40	Low
9	9.63	5.48	4.53	6.57	Low
10	8.00	2.26	8.08	5.84	Low
11	6.48	5.48	11.63	7.59	Low
Mean	**7.35**	**6.96**	**9.69**	**7.88**	**Low**
SD	**2.01**	**4.33**	**2.44**	**1.79**	

The WSI model incorporated weighted contributions from all assessed parameters:

$$\text{Work Severity Index} = 0.33\text{x}\boldsymbol{TRI}_{personalfactor} + 0.38\text{x}\boldsymbol{TRI}_{tasfactor} + 0.29\text{x}\boldsymbol{TRI}_{environmentalfactor}$$

Python facilitated parameter adjustments to validate the model's sensitivity and applicability across various scenarios.

The WSI framework provided actionable insights into ergonomic risks. Workers with high BMI and minimal experience were identified as vulnerable groups, necessitating tailored interventions. Redesigning workstations to minimize awkward postures and implementing scheduled breaks could mitigate task-related risks. Environmental risks, particularly high temperatures and noise levels, require engineering controls such as improved ventilation and noise-dampening solutions.

The study's findings align with previous research emphasizing the link between ergonomic risk factors and occupational injuries (Ghamari *et al*., 2010; Ismaila *et al*., 2020). While the overall risk level was low, medium-risk scores underscore the importance of continuous monitoring and proactive safety measures.

This study highlights the utility of the WSI as a comprehensive tool for assessing ergonomic risks in bakery operations. By identifying medium-risk areas, the model facilitates targeted interventions to enhance workplace safety and worker well-being.

REFERENCES

[1] Aghilinejad M, Ehsani A, Talebi A, Koohpayehzadeh J, Dehghan N. Ergonomic risk factors and musculoskeletal symptoms in surgeons with three types of surgery: open, laparoscopic, and microsurgery. Medical Journal of the Islamic Republic of Iran, 2016, 30, pp.467-467.

[2] Ghamari F, Mohammadbeigi A, Khodayari M. (2010). Work stations revision by ergonomic posture analyzing of arak bakery workers. Zanjan University of Medical Sciences, 2010, 18(70), pp.80-90.

[3] Gu, J.K., Charles, L.E., Andrew, M.E., Ma, C.C., Hartley, T.A., Violanti, J.M., Burchfiel, C. M. (2016). Prevalence of work-site injuries and relationship between obesity and injury among US workers: NHIS 2004-2012. Journal of Safety Research, 2016, 58, pp.21-30.

[4] Ismaila, S.O., Oriolowo, T.K., Kuye, S.I., Adekunle, N.O., Adewumi, B.A., Alabi, A. (2020). Ergonomic risk assessment of maintenance job in a gas power station. Sigurnost, 2020, 62(1), pp.47-60.

[5] Tatipamula, V., Rao, R. (2021). Ergonomic assessment of work-related musculoskeletal discomfort faced by bakery workers. International Journal of Creative Research Thoughts, 2021, 9(7), pp.2320-2882.

Proceedings IRF2025: 8th International Conference on Integrity-Reliability-Failure
In Engineering, Materials, Manufacturing and Biomechanics. Porto 15-18 July 2025
DOI: https://doi.org/10.24840/978-972-752-323-8

PAPER REF: 22571

RELIABILITY ESTIMATION IN INDUSTRIAL SYSTEMS: A PROBABILITY-BASED APPROACH TO FAILURE PREDICTION

Daniel Sanin-Villa[1(*)], Juan Camilo Tejada[2], Adrián Felipe Martinez[3]

[1]Universidad EAFIT, Medellín, Colombia.
[2]Departament of Engineering Studies for Innovation, Universidad Iberoamericana Ciudad de México
[3]Instituto Tecnológico Metropolitano, Medellín, Colombia.
[(*)]*Email:* dsaninv2@eafit.edu.co

ABSTRACT

Reliability modelling is essential for predicting failures and optimizing maintenance. Traditional methods usually assume constant failure rates, but real-world failures exhibit complex behaviors. This study analyzes operational time data from 50 work orders, fitting Weibull, Normal, Log-Normal, and Exponential distributions. Parameters were estimated using maximum likelihood estimation, and model selection was based on Kolmogorov-Smirnov (KS), Akaike Information Criterion (AIC), and Anderson-Darling (AD) tests. The best-fitting distribution enhances failure prediction, supporting data-driven maintenance decisions. The findings contribute to optimizing asset reliability, reducing downtime, and improving predictive maintenance strategies.

Keywords: Reliability, probability distributions, Weibull, predictive maintenance.

INTRODUCTION

Reliability analysis is essential in industrial maintenance for failure prediction and schedule optimization. Traditional models often assume a constant failure rate, favoring the Exponential distribution, but real-world failures require more flexible statistical models. Previous studies highlight the advantages of Weibull modelling (Djeddi et al., 2020), the role of parametric lifetime distributions (Şaşmaztürk et al., 2024), and the integration of statistical models into maintenance frameworks (Yang et al., 2024). This study analyzes 50 work orders to fit Weibull, Normal, Log-Normal, and Exponential distributions, evaluating model fit using Kolmogorov-Smirnov (KS), Akaike Information Criterion (AIC), and Anderson-Darling (AD) tests. The results support a data-driven approach for predictive maintenance.

RESULTS AND CONCLUSIONS

The methodological approach in this study involves analysing the operational time of an industrial asset by fitting different probability distributions to the observed data. The dataset consists of recorded operational times statistically modelled using Weibull, Normal, Log-Normal, and Exponential distributions. To determine the best-fitting model, the parameters of each distribution are estimated using maximum likelihood estimation, and their fit is evaluated through statistical tests. In Figure 1, the fitted probability distributions are presented. The histogram represents the observed data, while the plotted curves correspond to the probability distributions fitted to the dataset. Each distribution is analysed to assess its accuracy in modelling asset reliability and predicting failure times.

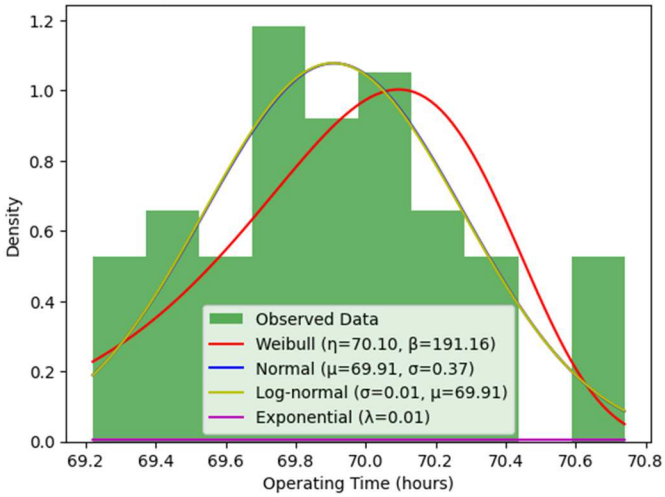

Fig. 1 - Fitting Probability Distributions to Operating Times.

Table 1 presents the results of the goodness-of-fit tests for the Weibull, Normal, Log-Normal, and Exponential distributions fitted to the operational time data.

Table 1 - Goodness-of-Fit Test Results for Different Distributions.

Distribution	KS Statistic	KS p-value	AIC	Anderson-Darling Statistic
Weibull	0.094	0.7313	150.54	N/A
Normal	0.0626	0.9826	142.48	0.1913
Log-Normal	0.0634	0.9804	142.45	N/A
Exponential	0.6285	1.226e-19	624.72	22.6970

The KS test evaluates the similarity between empirical and theoretical distributions, where higher p-values indicate a better fit. AIC compares model performance, favouring lower values, while the AD test assesses deviations, particularly in the tails. The Normal and Log-Normal distributions best fit the operational time data, with the Normal distribution showing the lowest AIC, highest KS p-value, and a low AD statistic, suggesting a near-symmetric failure pattern. The Weibull distribution demonstrated an acceptable fit but was less optimal. The Exponential distribution performed the worst, confirming that a constant failure rate assumption does not reflect the observed data. These findings support using data-driven reliability models for predictive maintenance, considering variations in failure behavior. Future research should expand the dataset and incorporate advanced statistical techniques, such as Bayesian inference, to improve reliability estimations.

REFERENCES

[1] Djeddi A.Z., Hafaifa A., Guemana M., Kouzou A. Gas turbine reliability modelling based on a bath shaped rate failure function: modified Weibull distribution validation. Life Cycle Reliability and Safety Engineering, 2020, 9, pp.437-448.

[2] Şaşmaztürk M.S., Ertem A., Ulusoy S.K. Parametric and Non-Parametric Reliability Analysis of The Propeller Unit of an Aircraft Fleet. Researcher, 2024, 4(01), pp.94-106.

[3] Yang X., He Y., Liao R., Cai Y., Dai W. Mission reliability-centered opportunistic maintenance approach for multistate manufacturing systems. Reliability Engineering & System Safety, 2024, 241, pp.109693.

SPECIAL SESSIONS
(SYMPOSIA)

SYMPOSIUM - 1
Experimental Mechanics and Instrumentation

J.F. Silva Gomes[)]
Faculty of Engineering, University of Porto, Portugal

Proceedings IRF2025: 8th International Conference on Integrity-Reliability-Failure
In Engineering, Materials, Manufacturing and Biomechanics. Porto 15-18 July 2025
DOI: https://doi.org/10.24840/978-972-752-323-8

PAPER REF: 22146

OPTICAL TECHNIQUES IN EXPERIMENTAL MECHANICS: A STATE-OF-THE-ART OVERVIEW

J.F. Silva Gomes(*)
Faculty of Engineering, University of Porto, Porto, Portugal
(*)*Email:* sg@fe.up.pt

ABSTRACT

Optical techniques are a broad range of methods that utilize light to analyze and characterize materials, structures, and processes. These techniques have revolutionized experimental mechanics by providing non-contact, high-resolution methods for measuring mechanical properties and deformations. In this paper, we explore the state-of-the-art optical techniques used in experimental mechanics, their typical engineering applications, and the future prospects of this field.

Keywords: Experimental mechanics, optical methods, noncontact techniques.

INTRODUCTION

Experimental mechanics aims to understand the behaviour of materials and structures under various loading conditions. Traditionally, strain gauges and extensometers were used to measure mechanical quantities. However, optical techniques have emerged as powerful alternatives due to their non-invasive nature, high accuracy, and ability to capture full-field information. These techniques are integral to both scientific research and practical applications in various industries, including mechanical and civil engineering, biomechanics, and materials science. In this paper we delve into the optical methods that have transformed experimental mechanics.

TYPICAL ENGINEERING APPLICATIONS

Digital Image Correlation (DIC): DIC is a modern full-field optical technique that tracks surface displacements by analyzing images of speckle patterns. It provides strain maps and deformation fields with high spatial resolution. This method can be used in material testing, structural health monitoring, and biomechanics, among many other applications. Recent advancements in DIC include the development of 3D DIC systems that can measure out-of-plane movements and the integration of machine learning algorithms to improve data analysis.

Electronic Speckle Pattern Interferometry (ESPI): ESPI measures surface displacements by analyzing interference patterns produced by laser light reflected from the surface of the specimen. Typical applications can be found in fracture mechanics, fatigue testing, and vibration analysis.

Holographic Interferometry: Holographic interferometry captures the phase information of light waves to visualize deformations. It is used as a powerful optical technique in non-destructive testing, stress analysis, and modal analysis.

Shearography: Shearography detects surface and under surface defects by comparing speckle patterns before and after loading. This is commonly used in composite material inspection, adhesive bonding assessment, and aerospace components.

Photoelasticity: Photoelasticity is an optical technique that has been used for decades to study stress distribution in transparent materials. It is based on the birefringence property of materials, where a change in stress can alter the material's refractive index.

Moiré Techniques: Moiré methods use the superposition of optical gratings to measure displacements and strains. It is a classical optical technique for the strain analysis of mechanical components, strain gauge calibration, and residual stress measurement.

Thermoelastic Stress Analysis (TSA): TSA exploits the temperature-dependent optical properties of materials to visualize stress fields. It is often applied over aerospace structures, automotive components, and weld inspection.

Digital Holography: Digital holography records the complex wavefront of light, enabling 3D deformation analysis. This method allows microscale deformation measurement, MEMS characterization, and biological tissues.

Fiber Optic Sensors: Fiber Bragg gratings and Fabry-Perot interferometers embedded in optical fibers provide strain and temperature measurements. Typical applications can be found in structural health monitoring, civil engineering, and oil pipelines.

High-Speed Imaging: High-speed cameras capture transient events (impact, fracture, and vibration) with frame rates up to millions per second. This method is applied in ballistic testing, crash simulations, and impact analysis.

CONCLUSIONS AND FUTURE DIRECTIONS

Optical techniques are extensively used for characterizing the mechanical properties of materials, such as composites, metals, and polymers. Structural health monitoring is another area where optical techniques shine. They can detect damage and monitor the integrity of structures like bridges, buildings, and aircrafts. At the microscale and nanoscale, optical techniques are indispensable for measuring the mechanical behavior of materials, which is crucial for the development of microelectromechanical systems (MEMS) and nanotechnology.

The future of experimental mechanics lies in the integration of optical techniques with computational mechanics. This synergy will enable the development of more accurate models and simulations. Optical techniques will play a vital role in the development of new materials, such as metamaterials and nanocomposites, by providing insights into their behavior at different scales.

REFERENCES

[1] Jones I., Iadicola, M. (2018). A Good Practices Guide for Digital Image Correlation. International Digital Image Correlation Society.

[2] Ming-Tzer Lin, Cosme Furlong & Chi-Hung Hwang, Editors (2021). Advancement of Optical Methods & Digital Image Correlation in Experimental Mechanics, Proceedings of the 2020 Annual Conference on Experimental and Applied Mechanics. Springer.

[3] Rastogi P.K. (2007). Experimental stress analysis. Alpha Science International Ltd.

[4] Rastogi P.K. (2000). Digital speckle pattern interferometry and related techniques. John Wiley & Sons.

[5] Sutton M.A., Orteu J.J., & Schreier H. (2009). Image correlation for shape, motion and deformation measurements: Basic concepts, theory and applications. Springer Science & Business Media.

Proceedings IRF2025: 8th International Conference on Integrity-Reliability-Failure
In Engineering, Materials, Manufacturing and Biomechanics. Porto 15-18 July 2025
DOI: https://doi.org/10.24840/978-972-752-323-8

PAPER REF: 22178

DETERMINE WATER VELOCITY IN CHECK VALVES WITH DIFFERENT GEOMETRY IN MICROCHANNELS MANUFACTURED BY 3D PRINTING (SLA)

Richard Chamorro, Víctor H. Cabrera-Moreta(*)
Mechanical Engineering Department, Universidad Politécnica Salesiana, Quito, Ecuador
(*)*Email:* vcabrera@ups.edu.e

ABSTRACT

Microfluidics is a promising technology that offers advantages such as reduced resource consumption, cost and time. Additive Manufacturing is a key ally of microfluidics, enabling the creation of microchannels with high precision and quality. Devices with check valves of different dimensions were produced using stereolithographic SLA. The check valves had a height and width of 600, 700 and 800 micrometers, in order to estimate the impact of valve size on fluid velocity.

The results showed that the fluid velocity increased with respect to the size of the check valve. This is because larger check valves offer less resistance to flow. The factors that influence the flow resistance in a microfluidic channel are channel shape, channel width and surface roughness. The fluid velocity was observed to vary along the channel geometry, with higher values in the vicinity of the check valve. This is because the check valve creates a zone of turbulence that increases the fluid velocity.

Fluid retention in the ridges of the devices is an important factor for mixing samples and reagents, as it allows the fluids to combine uniformly. The devices fabricated in this study will be used in biomedicine for laboratory testing, ensuring more accurate results.

Keywords: Microfluidic; SLA; check valves; velocity.

INTRODUCTION

Three-dimensional (3D) printing using additive manufacturing is an innovative technique that creates objects from a digital design, adding material layer by layer. Unlike traditional methods that remove material to give shape, 3D printing adds material to obtain the precise shape of the desired object [5].

Inspired by stereolithography (SLA) developed in the 1980s [6], 3D printing has become fundamental in various biomedical and engineering applications. In 2015, ISO/ASTM 52900 established standards to unify terminology and categorize types of 3D printers [7]. Among the most commonly used types are: Fused deposition (FDM) 3D printers: these use a plastic wire that is melted and deposited layer by layer, with an accuracy of between 0.1 and 0.3 mm and a printing speed of 10 to 100 mm/s [6]. Selective laser sintering (SLS) 3D printers: Use a laser to sinter metal powder, with an accuracy of 0.05 to 0.1 mm and a print speed of 10 to 100 mm/s [8].

Fused deposition modelling (MJF) 3D printers: Use a printhead to deposit plastic powder and a laser to fuse the layers, with an accuracy of 0.1 to 0.2 mm and a print speed of 10 to 100 mm/s [9]. These systems offer different levels of precision and speed, suitable for a variety of

applications. 3D printing has revolutionized the manufacturing of medical devices, prototypes and functional parts, among other uses.

Fluid microsystems (FM) manipulate fluids at micrometer and nanometre scales, using tiny channels to study microorganisms and analyze organic molecules [10]. These systems offer advantages such as efficient use of samples and reagents, high sensitivity and reduced analysis time.

The field of MF is constantly growing, with new applications and emerging technologies. Check valves are crucial in microfluidic applications, allowing flow control in one direction [7].

Active and passive methods have been proposed for their implementation, with various materials and designs. These devices are fundamental in biological assays and other microfluidic applications.

In the microscopic domain, the Reynolds number is a crucial measure to predict whether the flow will be laminar or turbulent [16].

On the other hand, the surface tension of fluids in microscale open channels affects their behavior, generating additional pressures and phenomena such as capillarity [17]. These effects are fundamental in the design and operation of microfluidic devices, impacting their efficiency and analytical capabilities.

METHODOLOGY

The image below, Figure 1, summarizes the methodology used in this study.

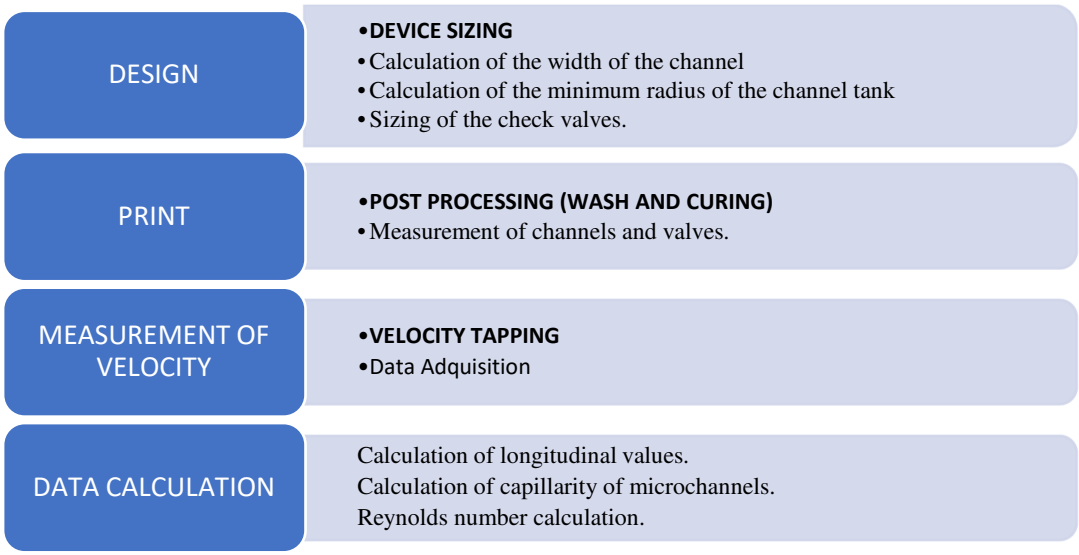

Fig. 1 - Methodology of the Design, Printing, Measurements and Data Analysis [21, 22].

Check valve device design

The sketch of the check valve devices was made in a specialized CAD tool for 3D modelling called SolidWorks, Figure 2, where the appropriate dimensioning of the micro-device was placed.

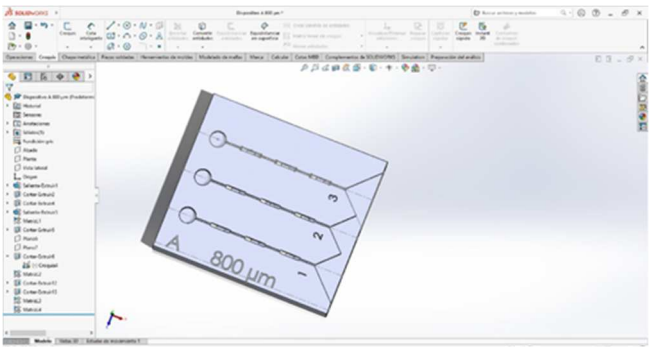

Fig. 2 - 3D Modelling in SolidWorks.

Channel width tolerance

To determine the printer's printing tolerance, previous studies on the margin of error in measurements smaller than 1000 µm were analyzed. Nine trials were conducted with three devices, each with three test channels. The check valves varied by 100 µm between devices (600, 700 and 800 µm).

For the check valves, the correlation coefficient between valve tolerance and amplitude increase was approximately 0.0075, suggesting a very weak or insignificant correlation between these two variables. This indicates that an increase in valve tolerance does not consistently affect the increase in amplitude in the check valves.

In contrast, for the channel, it was not possible to calculate a correlation coefficient because we only have one data set. However, it was observed that the channel gain (140 µm) is equal to the channel tolerance (140 µm) in this case. This suggests that, in this sample, the channel increase is directly related to the channel tolerance, indicating that an increase in channel tolerance translates directly into a channel increase in the check valves.

Therefore, while the tolerance in the check valves appears to have a negligible correlation with the increase in amplitude, the channel tolerance appears to be directly related to the increase in channel in the check valves.

Volume calculation using SolidWorks

The volume of a microdevice was calculated using a computer-aided design (CAD) tool, Figure 3. This software allowed each component of the device to be accurately modelled.

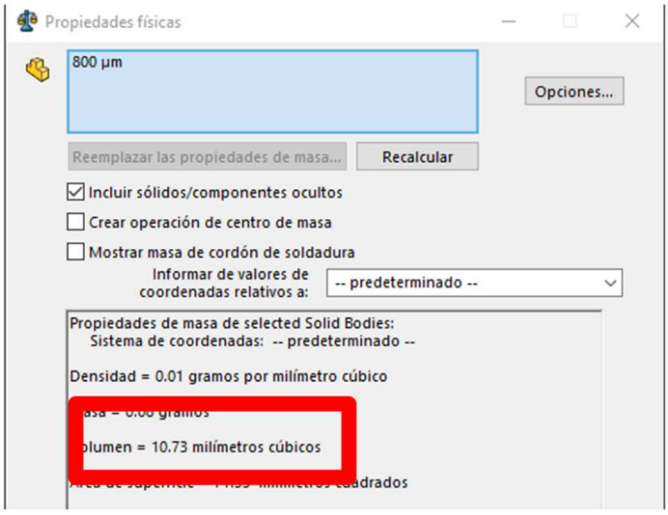

Fig. 3 - 800 µm microchannel volume in SolidWorks software.

Printing of devices with check valves

The following text describes the steps for printing the micro devices. The 3D printing process is divided into the following steps (Figure 4):

Fig. 4 - 3D printing process and post-processing. A. Design of the device in specialised software. B. VAT 3D printer. C. Washing machine. D. UV curing machine.

Measure Velocities

Measuring velocities in microchannels involves recording the fluid's movement, which is then processed using specialized software to determine displacement, time, and velocity. To measure velocities in three devices, they are coated with hydrophilic adhesive paper, Figure 5. The devices are then placed on the base of a Dino-Lite digital microscope and leveled. Using a pipette, the volume of fluid needed to fill the channel is measured, and the fluid, consisting of distilled water and vegetable dye, is placed in the microchannel reservoir. The advance of the fluid is recorded using DinoCapture 2.0 software.

For data acquisition, a specialized software called Tracker is used to calculate fluid velocity in the microchannels, Figure 6. Videos of the fluid's advance are imported into the software without a scale, so a coordinate axis is added, and the calibration tool is used to reference the measurements in the video. To calculate velocity, a mass is added in the software to manually or automatically track the moving fluid, marking its points as it moves and generating a table of time data, distance in x, distance in y, and velocity.

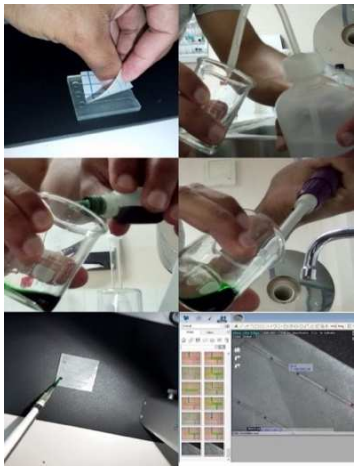

Fig. 5 - Velocity tapping. A. Gluing of hydrophilic adhesive paper on the device. B. Distilled water. C. Distilled water with vegetable dye. D. Measuring the volume of water with the pipette. E. Placement of water in the device. F. Recording of the fluid flow in the DinoCapture 2.0 software.

Calculation of longitudinal values

To determine the total length of the microchannels, it is necessary to calculate the displacement in the x-axes. From these values, the magnitude of the displacement can be obtained by vector addition. Finally, the actual length of the channel is obtained by adding the magnitudes of the x-displacements.

Calculation of Reynolds Number

The Reynolds number is an indicator that defines the flow behavior of the fluid, classifying it as laminar or turbulent. This dimensionless value is obtained by the ratio between the inertial forces and the viscosity acting on the fluid.

In a laminar flow, the fluid particles move in parallel layers without mixing with each other, which is associated with a low Reynolds number. In contrast, a turbulent flow presents a chaotic and disorganized movement of the particles, characterized by a high Reynolds number.

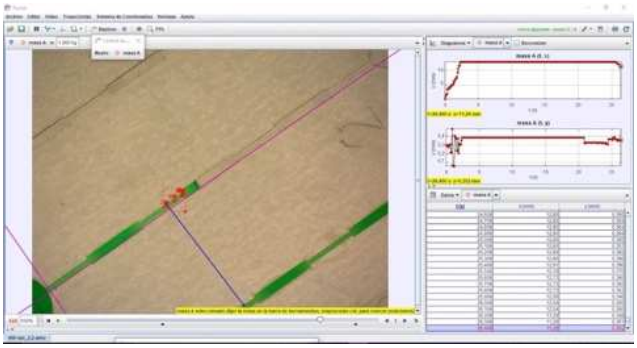

Fig. 6 - Acquisition of velocity data in the software (Tracker).

In other words, the Reynolds number allows us to determine whether the flow of a fluid is smooth and orderly (laminar) or chaotic and agitated (turbulent).

$$Re = \frac{\rho * v * D}{\mu} \quad (1)$$

Where:

Re: Reynolds number

ρ: fluid density (kg/m³)

v: fluid velocity (m/s)

D: hydraulic diameter (m)

μ: fluid dynamic viscosity (Pa-s)

RESULTS AND DISCUSSION

Each microdevice integrates a reservoir that holds the precise amount of fluid for its path through the channel, Figures 7&8. The device has a variable sized check valve, available in 600, 700 and 800 micrometer options. The function of the valve is to hold the fluid momentarily before releasing it and allowing it to reach the end of the channel, where a vent is located.

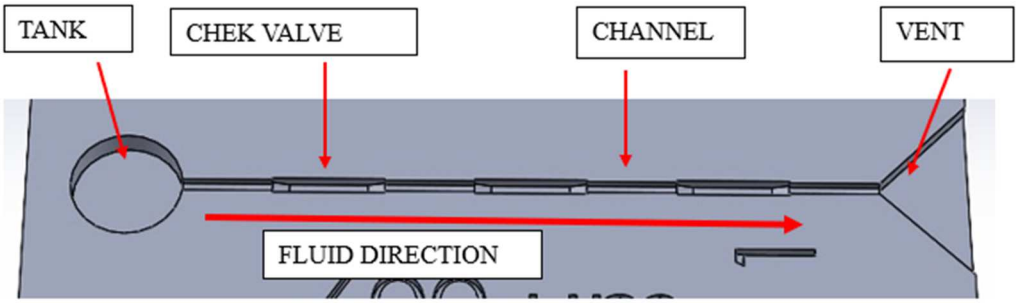

Fig. 7 - Device sectioning.

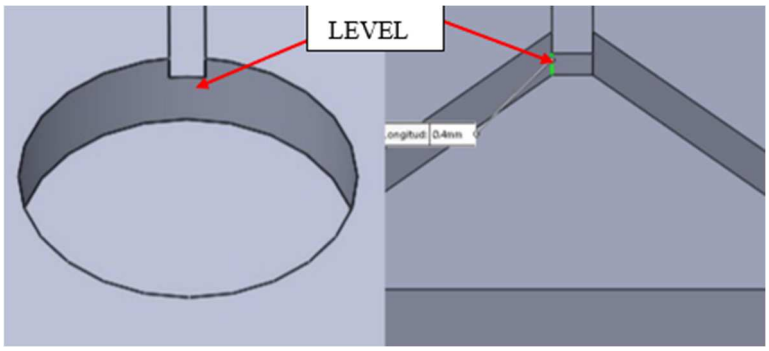

Fig. 8 - Cross-section of the device.

Device cross-section

The channel has a cross section of 400 micrometers wide by 400 micrometers high. The reservoir has a height difference of 900 micrometers and the outlet has a height difference of 400 micrometers, allowing the fluid to flow forward. The check valve of the first device has a width of 600 micrometers and a height of 600 micrometers, Figure 9.

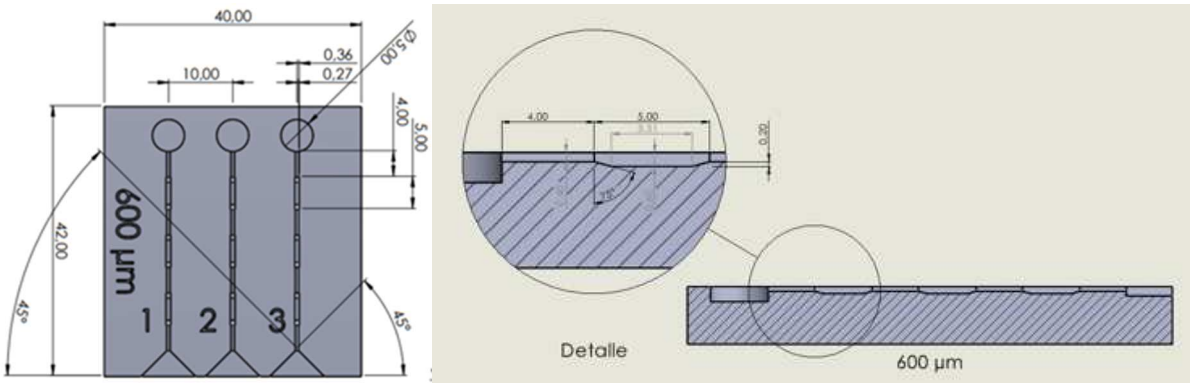

Fig. 9 - Cross-section of the 600 micron device.

Overall dimensions of the devices

The main dimensions of the devices are measured in millimeters (mm) and are detailed in the table (Table 1).

Table 1 - Table Type Styles.

Dimensions	Unity	D - 600	D - 700	D - 800
Channel width	(mm)	0.54	0.54	0.54
Channel depth	(mm)	0.4	0.4	0.4
Device radius	(mm)	5	5	5
Check valve amplitude	(mm)	0.71	0.795	0.880
Check valve depth	(mm)	0.60	0.70	0.80

Printing of the devices

The measurements of the (600 µm) device are shown below, Figure 10. The printing of 3 devices with check valves of different sizes (600 µm) was carried out on the stereolithography 3D printer (SLA).

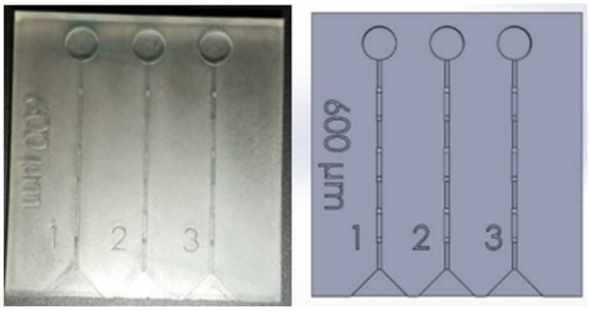

Fig. 10 - Device dimensioning 600 microns.

Calculation of the channel dimensioning

The print quality is affected by various environmental and printer parameters that cannot be adjusted. As a result, the results are lower than expected. The following table shows the standard deviation of the 400 micrometer channel (Table 2) as well as the 600 micrometer check valves (Table 3).

Table 2 - Measurements of the channels in the different devices.

Channel 600 µm			**Channel 700 µm**			**Channel 800 µm**		
C1	C2	C3	C1	C2	C3	C1	C2	C3
406	400	410	430	430	431	448	451	416
404	396	413	424	410	426	423	403	409
Average = 418 µm								
Standard Deviation = 15.61								

Table 3 - 600 µm valve dimensions.

Channel 1	**Channel 2**	**Channel 3**
594	617	625
594	590	606
589	594	632
Average = 605 µm Standard Deviation = 16.26		

Graphical separation into blocks

Considering the geometrical shape of the device, it was divided into blocks. This division was done both graphically and by tabulating data, taking into account the length of the channel and the changes in direction of the channel.

Blocks of the (600 µm) device

The 600 µm device was divided into 7 blocks, because it has 3 check valves, these blocks are represented by letters of the alphabet (Figure 11).

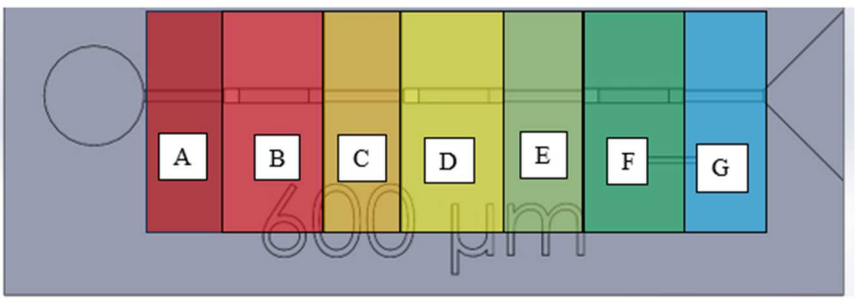

Fig. 11 - Block separation of the 600 µm device.

Tabulation of data

In the breakdown of the data, velocity statistics, including capillarity and Reynolds number, were analyzed. In addition, longitudinal velocity scatter plots, box and whisker plots of the block velocity and an analysis of the retention times were created.

Device statistics

The frequency histograms of the 600-, 700- and 800-micron devices reveal a leptokurtic distribution of velocities, with a concentration of values in the lower ranges, Figure 12. This distribution indicates that most of the velocities are close to the central measurement, with a positive skewness that shifts the data to the left of the distribution. In other words, a higher frequency of low velocities is observed, which can be attributed to fluid detentions at the crests.

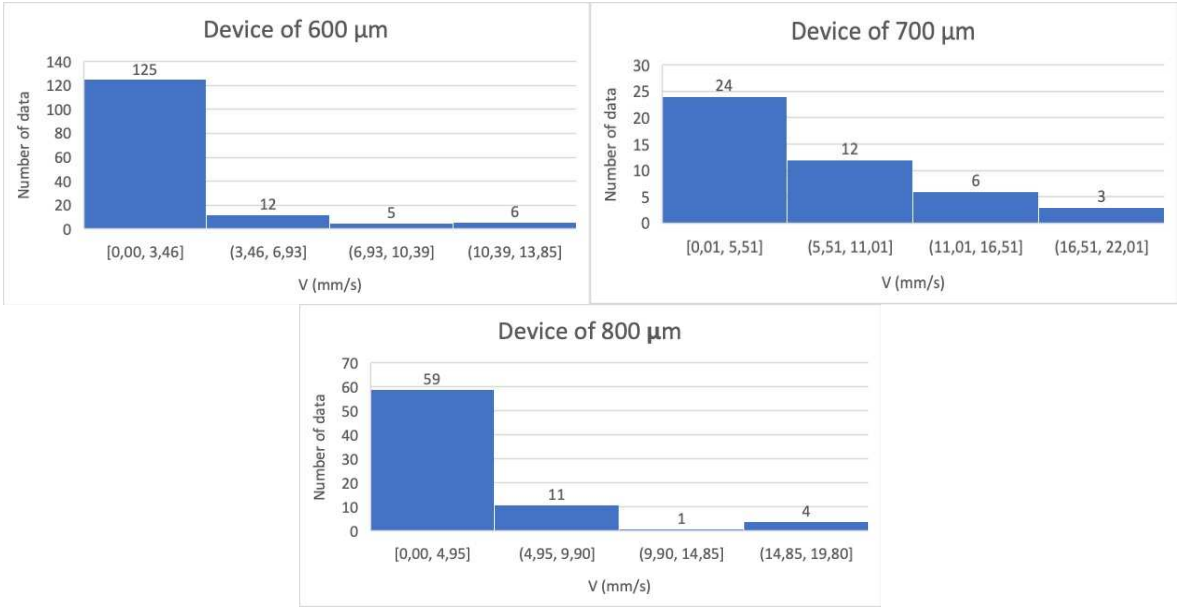

Fig. 12 - Histograms of the speed (mm/s) of the 600, 700 and 800 micron devices.

The velocity values of the devices a median of 2.2318 mm/s, with a high standard deviation showing that the velocity data is far from the mean standard deviation.

Tabulation of data

Capillary flow is defined as the spontaneous imbibition of a liquid in narrow channels without the application of external forces. In the case of water as a fluid in microchannels, intermolecular attractive forces are overcome by adhesion forces between the liquid and the channel surface, which drives capillary flow.

$$Pc = \frac{2 * 72.8\frac{N}{m} * cos(55°)}{\left(\frac{4x10^{-4}\ m}{2}\right)} = 417.56\ Pa \tag{5}$$

Speed vs. length

The relationships between velocity and length are shown for the 3 devices. The data are grouped into blocks according to device geometry and velocity changes. The graph of length (L) vs velocity (V) of the 600 micron device, Figure 13, shows a larger dispersion of velocity data in blocks A, C and E. Furthermore, no linear trend is observed, which makes it difficult to properly analyze the relationship between velocity and length.

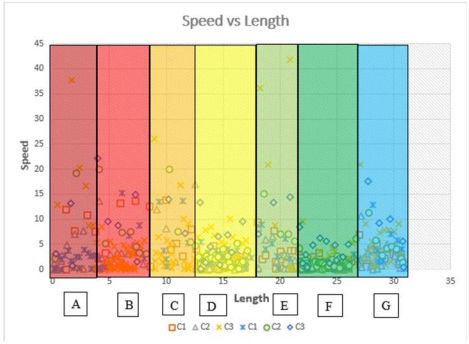

Fig. 13 -Speed of 600 µm.

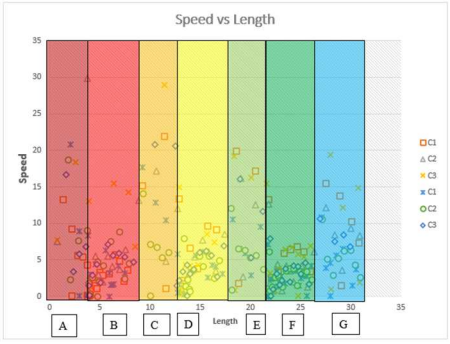

Fig. 14 - Speed of 700 µm.

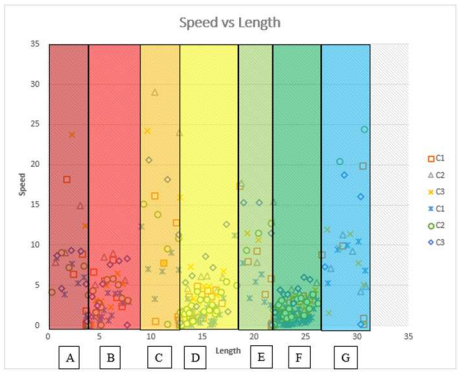

Fig. 15 - Speed of 800 µm.

The scatter plot of length (L) vs velocity (V) of the 700 micron device, Figure 14, reveals a larger scatter of velocity data in blocks C, E and G. This suggests heterogeneity in the flow behavior in these blocks. In addition, prolonged fluid retention is observed in valve blocks B, D and F, which could indicate a blockage (Figure 14).

Analysis of the scatter plot of length (L) vs velocity (V) of the 800 micron device, Figure 15, showed a greater dispersion of the velocity data in blocks A, C and G. This finding suggests heterogeneity in the flow behavior in these blocks. Additionally, prolonged fluid retention was observed at the start of the valves in blocks B, D and F, which could be indicative of a blockage (Figure 15).

Tabulation of data

An analysis of speed versus length was carried out by dividing the devices into blocks according to their geometry.

600 micron check valve device

A box and whisker plot were produced for the velocity data of the 7 blocks of the 600 micrometer device. The analysis of the velocity in the microdevice shows that the average velocities in channels A, C and G are similar, while the velocity in channel E is slightly lower. The largest velocity variations are found in the C-D and E-F sections, which could be related to the presence of valves B and F. Average velocity per channel: Channels A, C and G have similar average velocities, between 3.8 and 3.9 mm/s. Channel E has a slightly lower average velocity of 3.7 mm/s. Velocity variation: The largest velocity variations are found in sections C-D (decrease of 2.294 mm/s) and E-F (decrease of 2.898 mm/s). Valves B and F seem to generate a significant increase in velocity in sections B-C (0.932 mm/s) and F-G (3.048 mm/s). The velocity variation between A and B is negative (-0.774 mm/s), indicating a possible loss of energy in this section.

A box-and-whisker plot was produced for the velocity data of the 7 blocks of the 700 micrometer device, Figure 16. Fluid flow appears to be fastest in sections C, E and G, and slowest in sections A and B. Check valves B, D and F appear to be functioning correctly, as they are preventing backward flow of the fluid. Average velocity: The highest average velocity is found in section C (10.141), followed by section G (7.088) and section E (7.665). The lowest average speed is found in section B (3.563). Velocity variation: The highest velocity variation is found between sections B and C (6.578), indicating an abrupt change in fluid flow. The other velocity variations are smaller, but still significant.

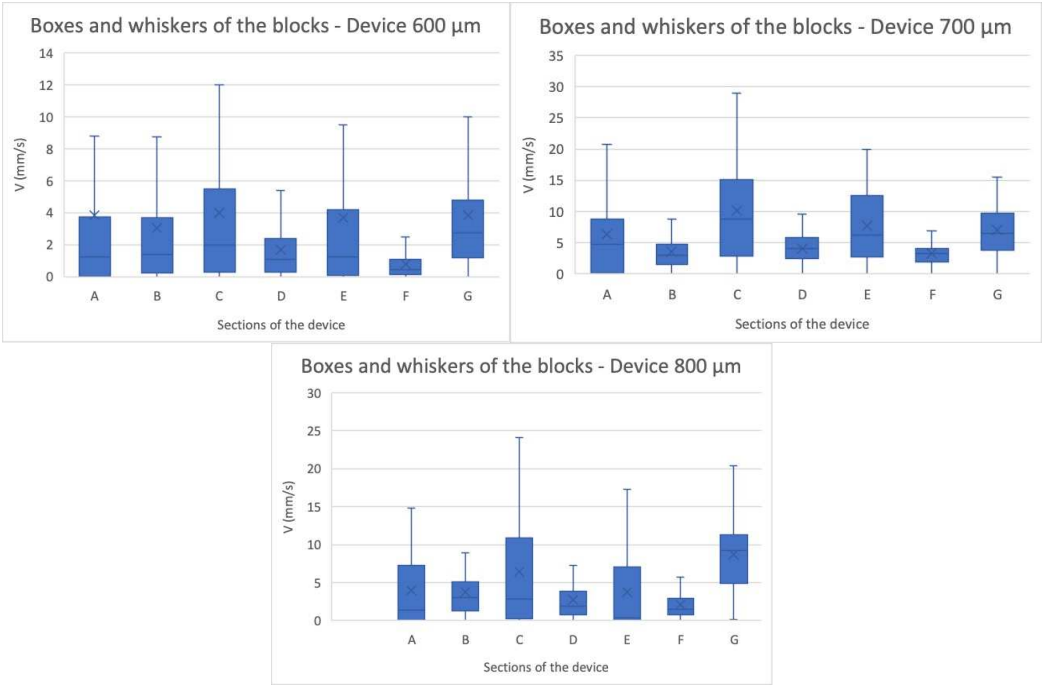

Fig. 16 - Boxes and whiskers of the speed of the blocks.

A box and whisker plot were constructed to analyze the distribution of the velocity data in the 7 blocks of the 800 micrometer device, Table 4. Average velocity: The average velocity in the tank is 3.928 mm/s. The highest average velocity is found in section G (8.71 mm/s) and the lowest in section F (2.071 mm/s). Sections A, B, E and G have relatively similar average velocities, while sections C and D have significantly different average velocities. Velocity variation: The largest velocity variation is found between sections C and D (-3.737 mm/s), indicating a significant reduction in flow velocity. The second largest velocity variation is between sections F and G (6,639 mm/s), indicating a considerable increase in flow velocity. The velocity variations between sections A-B, D-E and E-F are relatively small. Section C appears to be a critical point in the flow, with a significant reduction in velocity. Section G has the highest average velocity and the largest velocity variation at the end of the device.

Table 4 -Statistical measurements of the speed (mm/s) of the 600, 700 and 800 micrometre devices.

Statistical speed measurements (mm/s)		
Device	Avarage	Standard Deviation
D – 600	0.895	4.019
D – 700	3.8	5.092
D – 800	2	4.751
Average	2.231	4.620

A uniformly decreasing velocity trend is observed for the 700 and 800 micron devices. In the case of the 700 micron device, the velocity decreases gradually in both the channels and the check valves. This results in an adequate decrease in fluid velocity without an increase in the last channel prior to venting.

Box and whisker plots of the devices

The box and whisker plots in (Figure 17) show the distribution of the velocity data for the three devices. It can be seen that the data from the 600 and 800 micron devices show a positive skewness, indicating that the velocity values are concentrated towards the lower values. In contrast, the data from the 700 micron device are more symmetrical, with a slight positive skewness.

Table 5 - Speed variation of the 600 µm device.

	A	**B**	**C**	**D**	**E**	**G**
Average speed	3.83	3.05	3.99	1.69	3.71	3.85
Section	A-B	B-C	C-D	D-E	E-F	G
Variation	-0.78	0.93	-2.29	2.01	-2.9	3.85

Table 6 - Speed variation of the 700 µm device.

	A	**B**	**C**	**D**	**E**	**F**	**G**
Average speed	6.31	3.56	10.14	4.15	7.67	3.27	7.09
Section	A-B	B-C	C-D	D-E	E-F	F-G	G
Variation	-2.75	6.58	-5.99	3.51	-4.39	3.81	7.09

Table 7 - Speed variation of the 800 µm device.

	A	**B**	**C**	**D**	**E**	**F**	**G**
Average speed	3.93	3.78	6.47	2.73	3.77	2.07	8.7
Section	A-B	B-C	C-D	D-E	E-F	F-G	G
Variation	-0.15	2.69	-3.74	1.04	-1.7	6.64	8.7

After performing the tests and taking the corresponding measurements in the three printed devices, Tables 5, 6, 7 and 8, it could be observed that the 600 micron device the fluid flowed along the micro channel with a deficient retention of the fluid in the valves, while in the 700 micron device the speed was gradually reduced, but in the last retention valve an increase in speed was noticed, making the system a little deficient for its purpose.

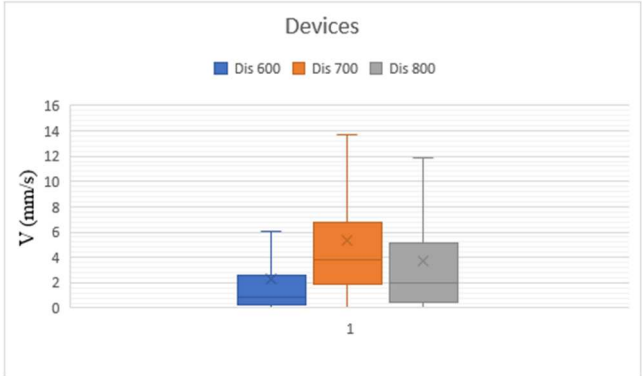

Fig. 17 - Boxes and whiskers of the devices.

In the case of the 800 micron device is where the fluid velocity was gradually reduced until it reached the end without any irregularity being visible at the moment of decreasing the fluid

velocity and giving the necessary guidelines in each valve to be able to reduce the velocity significantly, but without obstructing the passage of the fluid.

Table 8 - Statistical measurements of the speed in (mm/s) of the 600, 700 and 800 micron devices.

M.Esadisticas	**D-600 mm/s**	**D-700 mm/s**	**D-800 mm/s**
Maximum value	6.1	13.7	11.9
Third quartile	2.6	6.745	5.11
Median	0.895	3.8	2
First quartile	0.2	1.89	0.5
Minimum value	0.00086	0	0.0005

CONCLUSION

In this technological proposal, it has been demonstrated that the application of specific post-processing parameters, such as cleaning the channels with air for 5 minutes and curing the parts for 12 minutes at 60 degrees Celsius, prevents deformation of the micro devices and microchannels manufactured by 3D printing. The results of the hydraulic tests carried out on these devices showed that they have a good hydraulic behavior. The water flow velocity in the microchannels is uniform and no obstructions are observed.

The capillarity result in the microchannel with distilled water was 417.56 Pa. This indicates that the water has a strong tendency to move up the channel walls due to the cohesive force between its molecules. This phenomenon is important in microfluidics, as it can be used to control the movement of fluids in miniaturized devices.

The printing of microchannels with widths of 800, 700 and 600 microns, and integrated check valves. The results showed that: The printed channels had good geometry and dimensional accuracy. The check valves functioned correctly, allowing fluid flow in one direction and blocking it in the opposite direction. The printing tolerance was ± 10 microns for the channels and ± 20 microns for the check valves.

Devices were designed with a channel width of 540 µm, considering the tolerance between real and printed measurements in SLA 3D printing. The average channel width obtained was 410 µm, with an error of 10% with respect to the desired width of 400 µm.

The 600, 700 and 800 micrometer devices show significant variations in fluid velocity along their channel sections and check valves. In the 600 micrometer device, an average velocity of 3.828 units was observed, with noticeable variations between channel sections and check valves. In the 700 micrometer device, the average velocities range from 3,274 mm/s to 10,141 mm/s, with the greatest variation between sections C and D. Finally, in the 800 micrometer device, the average velocity is 3,928 mm/s, with noticeable variations between sections, especially between C and D, and between F and G. These results highlight the significant influence of check valves and channel sections on fluid velocity in microdevices, which is crucial for their design and optimization in applications requiring precise control of fluid velocity.

The results for the three devices (600, 700 and 800 micrometers) show that the fluid velocity varies significantly across the devices, influenced by the channel sections and check valves. In the 600 micrometer device, the average velocity was 3,828 units, with noticeable variations between channel sections and check valves. The differences in velocity between the sections indicate the influence of the check valves and the channel sections on the fluid velocity. On the other hand, in the 700 micrometer device, an average velocity varying between 3.274 mm/s and

10.141 mm/s was observed, with the largest variation between sections C and D (5.989 mm/s). This indicates that the check valves and variations in channel section have a significant impact on the fluid velocity in this device. Finally, in the 800 micrometer device, an average velocity of 3.928 mm/s was found, with the largest variation between sections C and D (-3.737 mm/s). Section G had the highest average velocity and the largest velocity variation at the end of the device.

REFERENCES

[1] Y. Valencia García, "Diseño de un producto industrial mediante técnicas de impresión 3D y nuevos materiales," Sep. 2020, Accessed: Dec. 16, 2023. [Online]. Available: https://riunet.upv.es:443/handle/10251/150763.

[2] V. Sharma, M. Gyanprakash D., P. Gupta, J. Ramkumar, "Analysis of circuit current in electrochemical micromachining process under the application of different waveforms of pulsed voltage," J Manuf Process, vol. 75, pp.110-124, Mar. 2022, doi: 10.1016/j.jmapro.2022.01.006.

[3] P. Guía, G. Pincheira. Diseño e Implementación de un Sistema Contínuo de Impresión 3D FDM. Memoria para optar al Título de Ingeniero Civil Mecatrónico.

[4] G.L. Goh, H. Zhang, T.H. Chong, W.Y. Yeong, "3D Printing of Multilayered and Multimaterial Electronics: A Review," Advanced Electronic Materials, vol. 7, no. 10. John Wiley and Sons Inc, Oct. 01, 2021. doi: 10.1002/aelm.202100445.

[5] N.C. Zuchowicz, J.A. Belgodere, Y. Liu, I. Semmes, W.T. Monroe, T.R. Tiersch, "Low-Cost Resin 3-D Printing for Rapid Prototyping of Microdevices: Opportunities for Supporting Aquatic Germplasm Repositories," Fishes, vol. 7, no. 1, Feb. 2022, doi: 10.3390/fishes7010049.

[6] I. Gibson, D. Rosen, B. Stucker, M. Khorasani, "Additive Manufacturing Technologies."

[7] K. Puebla, K. Arcaute, R. Quintana, R. B. Wicker, "Effects of environmental conditions, aging, and build orientations on the mechanical properties of ASTM type i specimens manufactured via stereolithography," Rapid Prototyp J, vol. 18, no. 5, pp.374-388, 2012, doi: 10.1108/13552541211250373.

[8] L. Romano, M. Stampanoni, "Microfabrication of X-ray optics by metal assisted chemical etching: A review," Micromachines, vol. 11, no. 6. MDPI AG, Jun. 01, 2020. doi: 10.3390/MI11060589.

[9] P. Bettotti, "Hybrid Materials for Integrated Photonics," Advances in Optics, vol. 2014, pp.1-24, Jun. 2014, doi: 10.1155/2014/891395.

[10] G.M. Whitesides, "The origins and the future of microfluidics," Nature, vol. 442, no. 7101. pp.368-373, Jul. 27, 2006. doi: 10.1038/nature05058.

[11] A.Y. An, K.Y.G. Choi, A.S. Baghela, R.E.W. Hancock, "An Overview of Biological and Computational Methods for Designing Mechanism-Informed Anti-biofilm Agents," Frontiers in Microbiology, vol. 12. Frontiers Media S.A., Apr. 13, 2021. doi: 10.3389/fmicb.2021.640787.

[12] T.M. Squires, S.R. Quake, "Microfluidics: Fluid physics at the nanoliter scale."

[13] G. Filo, E. Lisowski, J. Rajda, "Design and flow analysis of an adjustable check valve by means of cfd method," Energies (Basel), vol. 14, no. 8, Apr. 2021, doi: 10.3390/en14082237.

[14] W. Al-Faqheri, F. Ibrahim, T. H. G. Thio, M. M. Aeinehvand, H. Arof, M. Madou, "Development of novel passive check valves for the microfluidic CD platform," Sens Actuators A Phys, vol. 222, pp.245-254, Feb. 2015, doi: 10.1016/j.sna.2014.12.018.

[15] D. Paez, C. R. Suribabu, Y. Filion, "Method for Extended Period Simulation of Water Distribution Networks with Pressure Driven Demands," Water Resources Management, vol. 32, no. 8, pp.2837-2846, Jun. 2018, doi: 10.1007/s11269-018-1961-1.

[16] J.P. Brody, P. Yager, "Low Reynolds number micro-fluidic devices," 1996. [Online]. Available: https://www.researchgate.net/publication/267375361.

[17] J.P. (James P.) Hartnett, T.F. (Thomas F). Irvine, Y.I. Cho, G. Alanson. Greene, Advances in heat transfer. Volume 34. Academic Press, 2001.

[18] D.S. Kim, K.-C. Lee, T.H. Kwon, S.S. Lee, "Micro-channel filling flow considering surface tension effect. Institute of Physics Publishing Journal of Micromechanics and Microengineering. Micro-channel filling flow considering surface tension effect," 2002. [Online]. Available: http://iopscience.iop.org/0960-1317/12/3/307.

[19] A. Olanrewaju, M. Beaugrand, M. Yafia, D. Juncker, "Capillary microfluidics in microchannels: From microfluidic networks to capillaric circuits," Lab on a Chip, vol. 18, no. 16. Royal Society of Chemistry, pp.2323-2347, Aug. 21, 2018. doi: 10.1039/c8lc00458g.

[20] D. Yang, M. Krasowska, C. Priest, M.N. Popescu, J. Ralston, "Dynamics of capillary-driven flow in open microchannels," Journal of Physical Chemistry C, vol. 115, no. 38, pp.18761-18769, Sep. 2011, doi: 10.1021/jp2065826.

[21] J.P. Kruth, "Material incress manufacturing by rapid prototyping techniques," CIRP Annals, vol. 40, no. 2, pp.603-614, 1991.

[22] S.K. Balavandy et al., "Scalable 3d printing method for the manufacture of singlematerial fluidic devices with integrated filter for point of collection colorimetric analysis," Analytica Chimica Acta, vol. 1151, p.238101, 2021.

Proceedings IRF2025: 8th International Conference on Integrity-Reliability-Failure
In Engineering, Materials, Manufacturing and Biomechanics. Porto 15-18 July 2025
DOI: https://doi.org/10.24840/978-972-752-323-8

PAPER REF: 22384

ULTRA-SENSITIVE MICROCRACK-BASED STRAIN SENSORS FOR REAL-TIME STRUCTURAL INTEGRITY MONITORING

Jae-Hwan Lee,[1,2] Seung-Kyun Kang[1,2,3,4(*)]

[1]Department of Materials Science and Engineering, Seoul National University, Republic of Korea
[2]Research Institute of Advanced Materials (RIAM), Seoul National University, Republic of Korea
[3]Interdisciplinary Program of Bioengineering, Seoul National University, Republic of Korea
[4]Nano Systems Institute SOFT Foundry, Seoul National University, Republic of Korea
[(*)]*Email:* kskg7227@snu.ac.kr

ABSTRACT

This study develops a highly sensitive strain sensor to detect and monitor internal structural cracks in real time. Utilizing intentionally introduced microcracks in metal thin films, the sensor achieves exceptional sensitivity and is fabricated on polymer substrates for surface attachment. A wireless, battery-free data acquisition system using NFC technology ensures efficient, maintenance-free operation. Finite element analysis (FEA) simulations reveal the relationship between internal crack locations and surface strain profiles, enabling crack localization and size prediction using a sensor array. This technology advances industrial safety diagnostics by enabling real-time, proactive structural health monitoring.

Keywords: Safety monitoring, strain sensor, continuous monitoring, pipe cracking.

INTRODUCTION

Structural damage in industrial facilities can lead to significant economic losses and safety hazards. Specifically, cracks and fractures in critical infrastructure such as pipelines often begin as localized microstrain, which, if left unaddressed, can escalate into catastrophic failures. Existing post-damage response methods focus on repairs after damage has occurred, making it challenging to prevent accidents and associated economic losses during maintenance processes. To address these challenges, a proactive approach is needed that enables real-time monitoring of surface microstrain before damage occurs, allowing for preemptive maintenance.

Cracks inside materials induce surface strain, often at extremely small levels. Detecting such strain externally requires highly sensitive diagnostic sensors with a gauge factor exceeding 1,000. Furthermore, real-time monitoring of strain to continuously track crack progression necessitates the development of wireless diagnostic sensors. Beyond sensor development, understanding the correlation between internal crack-induced deformation and the resulting surface strain profile is crucial. This requires interpreting these relationships based on the material's mechanical properties. Additionally, to address discrepancies between crack locations and sensor placement, a sensor array configuration is essential. By analyzing strain variations across multiple sensors in the array, the crack's location and propagation can be effectively identified.

This research aims to go beyond simply developing a high-sensitivity strain sensor. It also seeks to establish a comprehensive diagnostic framework that integrates strain measurement, crack location prediction, and real-time wireless data acquisition, ultimately advancing structural health monitoring technologies.

RESULTS AND CONCLUSIONS

This study successfully developed a highly sensitive strain sensor capable of detecting and monitoring internal structural cracks.[1,2]. By intentionally introducing microcracks into metal thin films, the sensors leveraged the opening and closing of these cracks to achieve exceptional sensitivity. The sensors were fabricated on polymer substrates with thicknesses in the tens of micrometers and attached to structural surfaces, enabling effective monitoring of internal crack propagation. Through repeated fatigue testing, the microcrack distribution and size were precisely controlled, enhancing both the reproducibility and sensitivity of the sensors. Additionally, mock pipe experiments confirmed that the sensors effectively detected crack propagation in real-world scenarios.

A wireless data acquisition system was also developed to collect sensor data without wired connections. Using near-field communication (NFC) technology, the system enabled efficient, real-time data transmission while eliminating the need for batteries. This battery-free energy harvesting approach significantly reduced maintenance costs and ensured continuous operation.

Moreover, the relationship between internal crack locations and surface strain profiles was analyzed using finite element analysis (FEA). The strain distributions were evaluated under various angles and distances between cracks and sensor placement. These analyses demonstrated that by deploying at least three sensors in an array, the crack's position and size could be predicted. The study further revealed that the resolution and spacing of the sensor array are critical factors influencing the detectable range of cracks. Proper sensor array design is essential to optimize detection performance while accounting for sensor resolution limitations.

The developed strain sensor, utilizing metal thin films with microcracks, demonstrates exceptional sensitivity and reproducibility, enabling the detection and monitoring of structural cracks with high accuracy. By integrating a wireless, battery-free data acquisition system and utilizing finite element simulations, this research provides a robust framework for real-time structural health monitoring. The proposed technology offers a significant advancement in proactive maintenance strategies by ensuring industrial safety and improving operational efficiency.

REFERENCES

[1] J.-H. Lee et al., Hypersensitive meta-crack strain sensor for real-time biomedical monitoring. Sci. Adv. 10, eads9258 (2024).

[2] J.-H. Lee et al., A Fully Biodegradable and Ultra-Sensitive Crack-Based Strain Sensor for Biomechanical Signal Monitoring. Adv. Funct. Mater. 34, 2406035 (2024).

Proceedings IRF2025: 8th International Conference on Integrity-Reliability-Failure
In Engineering, Materials, Manufacturing and Biomechanics. Porto 15-18 July 2025
DOI: https://doi.org/10.24840/978-972-752-323-8

PAPER REF: 22389

LABORATORY INVESTIGATION OF MECHANICAL PROPERTIES ON HALF-SCALLED GLASS FIBRE REINFORCED PLASTIC BOGIE FOR THE FREIGHT WAGONS

Jan Chvojan(*), Roman Jozefy

Research and Testing Institute in Pilsen (VZU Plzen), Dynamic Testing Laboratory, Pilsen, Czech Republic
(*)*Email:* chvojan@vzuplzen.cz

ABSTRACT

Static and dynamic properties of the half scale GFRP innovative low track force, low noise bogie are investigated based on static and dynamic loading of the bogie on the test bench. The bogie was loaded with four hydraulic actuators according to the FEM calculation and calculated and measured values were compared. The fatigue test of the bogie has been performed after static and dynamic investigations.

Keywords: GFRP - Glass Fibre Reinforced Plastic, loading, test bench, strains, stresses, half – scale bogie, WHR – Welsh Highland Railways.

INTRODUCTION

This paper was created based on an international research project where the main goal was to demonstrate the ability of an innovative bogie design to operate in service with lower track forces and environmental impact in comparison with conventional freight bogie designs. The revolutionary design employs a frame of glass-fibre reinforced plastic (GFRP) and integrates suspension and damping functions within the composite bogie frame. The assembly of the bogie was performed in the Dynamic Testing Laboratory of VZU Plzen from individual parts, delivered from the producer or an own production: lower and upper frames, axle ties, central pivot, axle boxes, wheel sets and inter-frame and sliding elements. Before the assembly both upper and lower bogie frames were instrumented with strain gauges. Some of them were used to set loading levels and do monitoring during the fatigue test. In order to do an analysis of the stresses the strain gauge transducers of the company HBM and Vishay were used. The fiber optic sensors were also integrated to compare the strains measured this way with strain gauge measurement. The main goal of the test was to demonstrate that the GFRP bogie frames are able to withstand the loads coming from WHR car bodies in normal operation condition. The existing bogies of both vehicles have a mass of $m+ = 1{,}500\ kg$ and would be replaced by GFRP bogies ($m+ = 855\ kg$). The bogie should withstand both the operational and exceptional loads of freight vehicles. For this purpose, a special test bench was developed, manufactured and assembled, using which the GFRP half - scale bogie was tested. This composite bogie equipped with two wheelsets was set up, each wheel was put on to one block, containing short rail with load cell for measuring the wheel reactions.

RESULTS AND CONCLUSIONS

Vertical, longitudinal, lateral forces and twist were statically applied in many combinations corresponding to various driving modes on the track, and the responses to strain gauges and fiber optics sensors were measured and strength evaluated. The fatigue test was performed with

blocks in accordance with the proposed values given from the calculations with testing frequency of 2,5 Hz. The applied forces are graphically shown in Figure 1, the test bench with the GFRP half - scale bogie is shown in Figure 2.

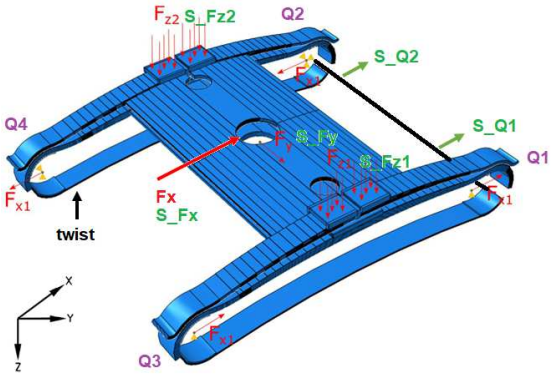

Fig. 1 - Scheme of loading of the bogie.

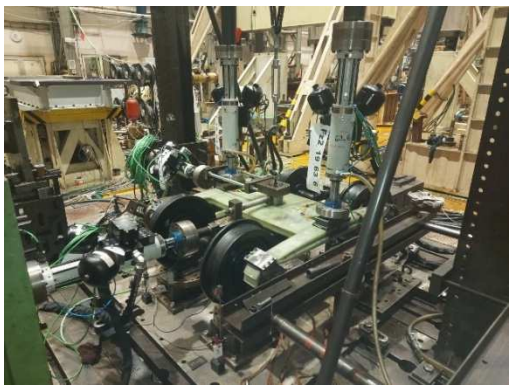

Fig. 2 - Loading set-up with tested bogie.

Results of static tests have been got including strains on individual strain gauges given for each load case. Except of this, the reactions and displacements have been also measured. For strain gauge rosettes also the strains in principal directions ε1, ε2 and the angle φ of the maximum principal strain from the rosette is calculated. Based on performed investigations during static, dynamic and fatigue test several results were obtained and some conclusions can be made. An example of actual loading forces during the fatigue test is given in Figure 3.

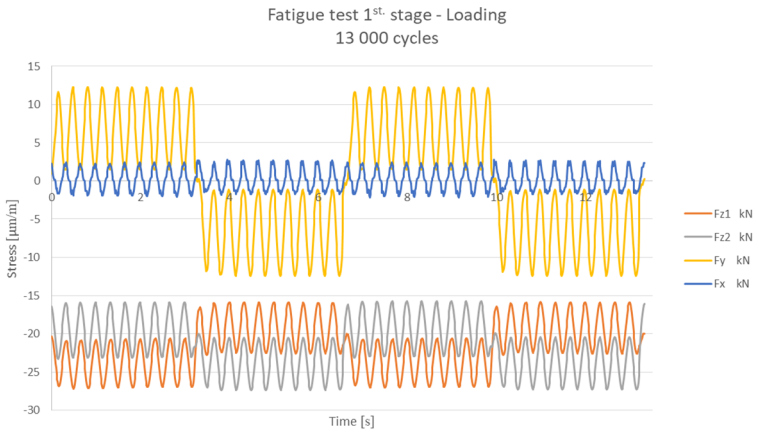

Fig. 3 - Actual values of loading forces.

Measured values of longitudinal and sheer stresses are substantially lower than those obtained from FEM calculations. No stresses exceeded the allowable values. Values of vertical and torsional stiffness and damping were also calculated and their comparison with the values of the real steel bogie will be carried out. During the performed fatigue tests no damage on the bogie was observed.

REFERENCES

[1] Chvojan J, Jozefy R, Vaclavik J., Experimental research of static and dynamic properties of a half-scale GRP bogie, VZU-VZ-54/21/17, 2021.

[2] P. Schönhuber, J. Lekue, Eureka E! 11157 Ecobogie, Analysis of Structural Integrity and Dynamic Behaviour, IFS-Bericht 01/2020, RWTH Aachen University.

Proceedings IRF2025: 8th International Conference on Integrity-Reliability-Failure
In Engineering, Materials, Manufacturing and Biomechanics. Porto 15-18 July 2025
DOI: https://doi.org/10.24840/978-972-752-323-8

PAPER REF: 22413

IN-LINE ALTERNATIVE FOR NON-DESTRUCTIVE TESTING IN WIRE ARC ADDITIVE MANUFACTURING BASED ON ELECTROMAGNETIC EMISSIONS

Douglas Silva Marques Serrati[1(*)], João Pedro de Sousa Oliveira[2], Telmo G. Santos[1,3]

[1]UNIDEMI, Department of Mechanical and Industrial Engineering, NOVA School of Science and Technology, Universidade NOVA de Lisboa, Caparica, Portugal
[2]CENIMAT|i3N, Department of Material Science, NOVA School of Science and Technology, Universidade NOVA de Lisboa, Caparica, Portugal
[3]Intelligent Systems Associate Laboratory, LASI, 4800-058, Guimarães, Portugal
[(*)]*Email:* d.serrati@campus.fct.unl.pt

ABSTRACT

The process Wire Arc Additive Manufacturing (WAAM) offers cost-effective and efficient production of large and complex metal parts. However, quality assurance remains a challenge, as traditional testing methods are often unsuitable for the in-process assessment of structural integrity. This study investigates alternatives for an in-line non-destructive testing (NDT) technique based on Electromagnetic Emissions (EME) for monitoring the quality of WAAM components. By leveraging EME, it is possible to detect potential flaws, such as cracks or porosity, during the manufacturing process without interrupting production. This technique not only enhances product reliability but also reduces costs associated with post-process inspection and repair.

Keywords: Non-Destructive Testing, Wire Arc Additive Manufacturing, Real-Time Monitoring, Quality Assurance.

INTRODUCTION

Additive Manufacturing processes has rapidly evolved, with WAAM becoming prominent for its ability to produce large metal parts with high deposition rates. However, WAAM also introduces specific challenges related to the mechanical and structural integrity of parts due to high thermal gradients, rapid cooling rates and the formation of residual stresses and defects, like porosity or cracks. Traditional inspection techniques are conducted after the completion of the fabrication process, because during the WAAM process, however, excessive heat input and the irregular surface of the fabricated part prevent the use of ultrasonic equipment, eddy currents, and other methodologies (Serrati et al., 2023). Furthermore, when a flaw is identified after the fabrication of a component, it must either be reworked or discarded. Making in-line inspection feasible allows for real-time repairs, thereby reducing rework and repair times. Thus, there is a need for an in-line NDT approach that can evaluate structural integrity and identify defects in real time.

EME signals generated during WAAM can be utilized to detect anomalies indicative of potential flaws (Li et al., 2022). High-speed camera footage, sound acquisition with laser-optical microphone (LO Mic) and photodiode sensor for 660nm (Ph 660nm) wavelength were used to monitor the WAAM deposition of AWS ER90S steel. All these signals are observed alongside the conventional voltage and current signals.

This study explores the development and application of an EME-based in-line NDT technique specifically designed for the WAAM process.

RESULTS AND CONCLUSIONS

Using walls constructed via the WAAM process, where layer depositions were intentionally performed with and without defects, variations in the signals from all sensors were analyzed. This approach allows for comparing sensor signals between defect-free and with defect layers.

Significant variations in the sensor readings indicate the feasibility of training and adapting software to detect flaw in real-time. Figure 1 shows the graphical behavior of a WAAM layer with and without defects.

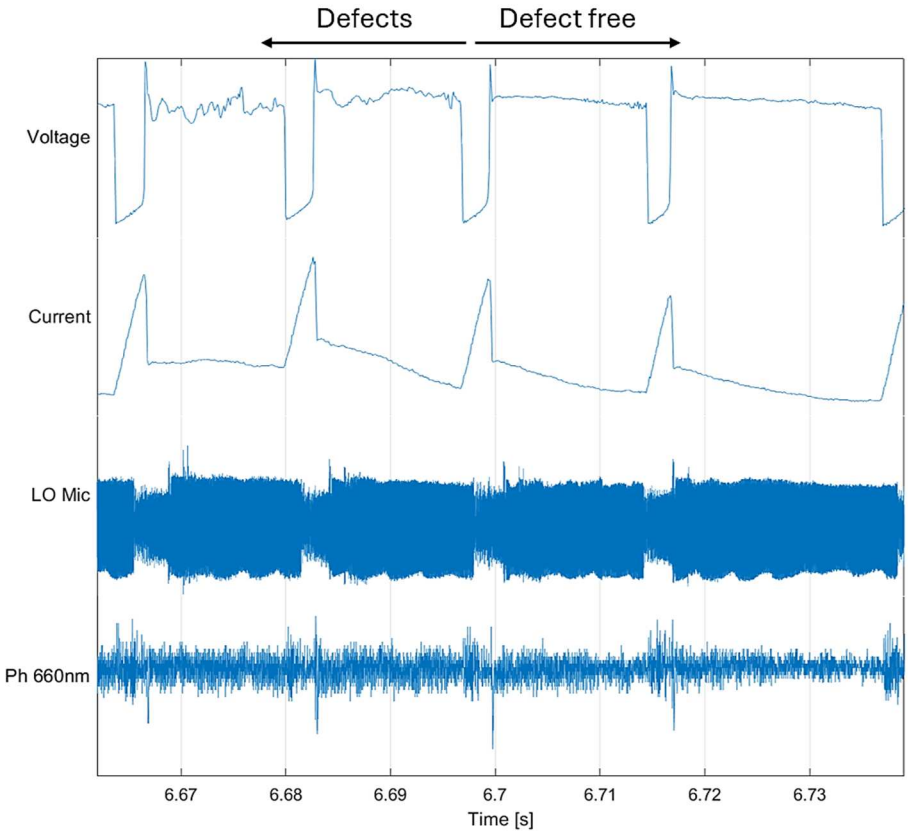

Fig. 1 - Graphical behavior of sensors in a layer deposited with and without defects in WAAM process.

This new approach facilitates the design of simpler, more cost-effective systems that are as efficient as existing methods, opening new possibilities for in-line monitoring of the WAAM process to enable early defect prediction during manufacturing.

Future work may also enable this software to classify the type of flaw occurring.

REFERENCES

[1] Serrati DSM, Machado JAM, Oliveira JP, Santos TG. Non-destructive testing inspection for metal components produced using wire and arc additive manufacturing. Metals. 2023;13(4):648. doi:10.3390/met13040648.

[2] Li Y, Polden J, Pan Z, Cui J, Xia C, He F, Mu H, Li H, Wang L. A defect detection system for wire arc additive manufacturing using incremental learning. J Ind Inf Integr. 2022;27:100291. doi: 10.1016/j.jii.2021.100291.

Proceedings IRF2025: 8th International Conference on Integrity-Reliability-Failure
In Engineering, Materials, Manufacturing and Biomechanics. Porto 15-18 July 2025
DOI: https://doi.org/10.24840/978-972-752-323-8

PAPER REF: 22424

COMPARISON OF X-RAY AND TERAHERTZ METHODS IN NON-DESTRUCTIVE TESTING OF PYROTECHNIC OBJECTS

Waldemar Swiderski(*), Tomasz Krzeminski
Military Institute of Armament Technology, Zielonka, Poland
(*)*Email:* waldemar.swiderski@wp.pl

ABSTRACT

The basic method in non-destructive testing of pyrotechnic objects is the X-ray method. Experimental studies using terahertz radiation have shown that the terahertz transmission method can also be used to test smaller pyrotechnic objects. In this article, we present the results of comparative experimental studies conducted on gasifier imitators with intentionally introduced defects and on real objects.

Keywords: Non-destructive testing, pyrotechnic materials, terahertz radiation, X-ray.

INTRODUCTION

In the last twenty-five years, there has been a dynamic development of techniques using terahertz radiation (THz) (Yun-Shik, 2009). Terahertz waves are characterized by unique properties. For many years, due to the lack of appropriate sources and detectors in this range, they were not used in non-destructive testing. Terahertz radiation is characterized by a high ability to penetrate dielectric materials. They are reflected by metals. Non-destructive testing of pyrotechnic materials (solid rocket propellants) is a standard procedure required before their use. Any defects in their internal structure (air bubbles, structural inhomogeneities, foreign bodies) can have a negative effect on their operation. The basic non-destructive testing method used in their evaluation is the X-ray method. However, there are cases in which X-ray images are difficult to interpret. The conducted experimental preliminary studies have shown that the terahertz method can be an auxiliary method in the testing of pyrotechnic materials (Hlosta et al., 2022; Swiderski et. al., 2024).

RESULTS AND CONCLUSIONS

The principle of operation of the X-ray and terahertz transmission methods is similar. The radiation source and the detector detecting this radiation are located on opposite sides of the tested object. They consist in recording an image in a dedicated range of radiation after the radiation generated by the source passes through the tested object. Defects in the internal structure of the tested material are imaged as a result of the difference in the physical parameters of the defects and the basic material. Causing differences in the absorption and reflection of the dedicated radiation.

As a model for preparing a gas generator charge imitator, it was decided to use a powder pressure accumulator (PAC) which is an element of one of the anti-aircraft missiles. The product was selected due to its simple geometry and small size. The imitator samples had the shape of a cylinder with a diameter of approx. 25 mm and a height of approx. 85 mm. The technological process of its production was carried out so that air bubbles, which were defects, were created in the internal structure. An example of the test result is presented in Figure 1.

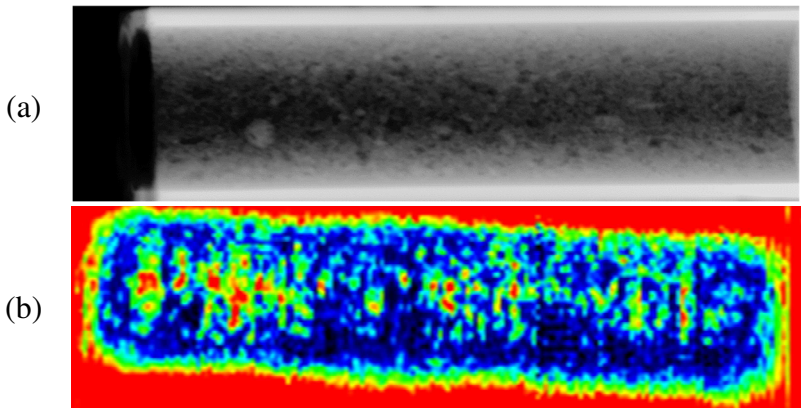

Fig. 1 - (a) X-ray image and (b) THz image of the sample.

Figure 2 shows the results of non-destructive testing of a gas generator for an anti-aircraft missile. The basic material of the generator was not covered with an inhibitor layer because internal defects were detected in it by X-ray. The defects are poorly visible on the X-ray image. The terahertz image taken at a frequency of 300 GHz shows more clearly visible inhomogeneities in the structure of the gas generator. It should also be noted that the structure of the gas generator manufacturing technology is visible on the terahertz image, which is not visible on the X-ray image. The technology of making a gasifier consists in rolling a flat layer of material from which a cylinder-shaped generator is created. In the censer of the cylinder, layers of rolled material can be seen. This can be seen in the terahertz image, where the center of the gasifier stands out.

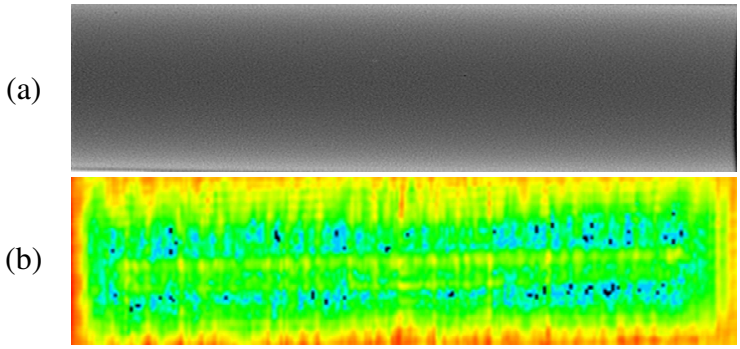

Fig. 2 - A gas generator for a rocket without an inhibitor a) X-ray image b) Terahertz image.

As experimental studies have shown, the terahertz transmission method can be an interesting alternative for non-destructive testing of small-diameter pyrotechnic objects. It should also be noted that, in comparison to the X-ray method, it is safe for the operator. It does not require such safeguards as the X-ray method.

REFERENCES

[1] Yun-Shik L., Principles of Terahertz Science and Technology, Springer, 2009.

[2] Hlosta P., Nita M., Powala D., Swiderski W., Terahertz radiation in non-destructive testing of composite pyrotechnic materials, Composite Structures, 2022, 279, 114770.

[3] Swiderski W., Description of the research work of the project "Innovative methods of terahertz diagnostics in selected key applications in military and security" - TeraDiag, WITU Publishing House, 2024.

Proceedings IRF2025: 8th International Conference on Integrity-Reliability-Failure
In Engineering, Materials, Manufacturing and Biomechanics. Porto 15-18 July 2025
DOI: https://doi.org/10.24840/978-972-752-323-8

PAPER REF: 22437

RELIABLE CONTINUOUS FORCE MEASUREMENT AT AMBIENT AND ELEVATED TEMPERATURES WITH STRAIN GAUGES USING THE EXAMPLE OF BOLTED JOINTS

Tobias Held(*), Jens Peth, Christoph Friedrich

Machine Elements, Fastening Systems, Product Innovation (MVP), Institute of Engineering Design, Department of Mechanical Engineering, University of Siegen, Germany.
(*)*Email:* tobias.held@uni-siegen.de

ABSTRACT

The paper deals with the theory and practical use of reliable determination of values measured with foil strain gauges in an extended temperature range of 20 °C ≤ T ≤ 150 °C using the example of determining the preload force of a bolted joint. As it will be shown, significant deviations from the mechanical strain rate must be expected if the components are not designed for thermal suitability. However, even when used at ambient temperature (T = 20 °C), an incorrect approach can lead to significant measurement errors. For both applications, the potential of error is illustrated by means of tests; conclusions are drawn how this can be avoided.

Keywords: Strain gauges, preload measurement, bolted joints, elevated temperature.

INTRODUCTION AND THEORETICAL PRINCIPLES

Strain gauges are used today in a wide range of technical products, which can be both simple (e.g. load cells) and complex (e.g. wind turbine to monitor the deformations of the rotor blades and the tower structure). It is also suitable to use them to monitor the operating behavior of machines and their components (e.g. on screw connections, cf. [1]). The principle always utilized when measuring with strain gauges is that the electrical resistance of a conductor wire with current flow changes exactly proportionally to an external mechanical load, which stretches (increase in resistance) or compresses (decrease in resistance) it. By precisely determining the change in resistance relative to the nominal resistance using a suitable electronic circuit (Wheatstone bridge, application necessary due to typically very small amounts of change) and comparing it with a known reference value (calibration), it is possible to determine forces, torques, deformations or pressures (transducer design) or calculate mechanical stresses (stress analysis) [2,3].

Figure 1 shows the basic structure of a foil strain gauge and its attachment to a component to be analyzed. The central element is the continuous conductor wire (measuring grid), which has a meandering shape and represents a precisely defined electrical resistance. The most important requirement for its material is that the relationship between the amount of strain and the relative change in resistance should be as linear as possible; Ni-Cu (Constantan) or Ni-Cr (NiChrome) alloys are often used. Applied to a carrier foil, there is a transition to electrically conductive soldering pads at the beginning and end of the measuring grid, which serve to contact the connecting wires. To protect the sensitive conductor wire from external influences, it is usually covered with a thin, transparent cover film. The connection to the test specimen to be analyzed is made by adhesive bonding, for which two-component adhesives are used in most cases for the foil strain gauges considered here. They cure under the influence of temperature and pressure (approx. 0.7-4.8 bar at 100-180 °C, depending on the process time), as does the epoxy-

phenolic adhesive used here 'Micro Measurements M-Bond 610'. The task of the bond is to transfer the local strain ε of the component to the measuring grid as unrestrictedly as possible and to initiate a change in resistance. For this purpose, a clean and error-free execution of the strain gauge application is essential for the quality of the measurement result.

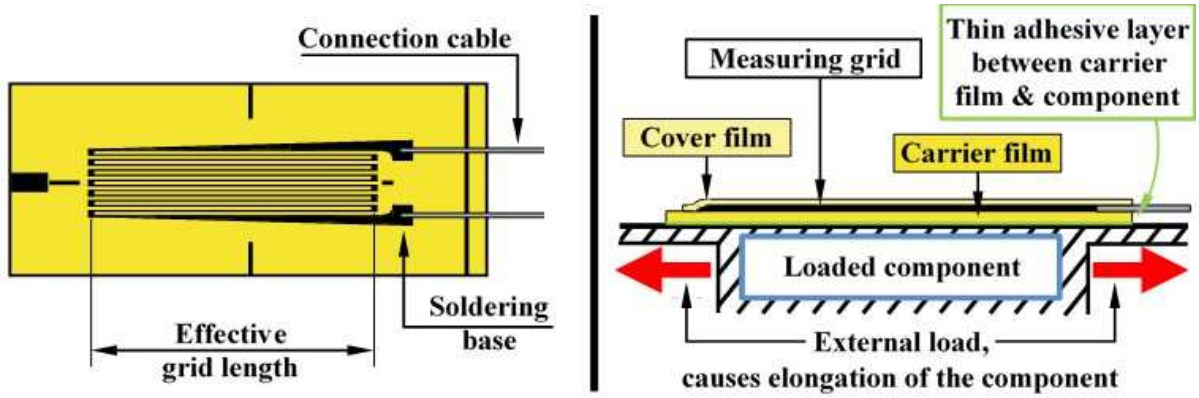

Fig. 1 - Structure of a foil strain gauge with metallic measuring grid, top view (left, with transparent cover foil in reality), side view with component (right, coloring of the cover foil for clarification).

Since the mechanical strain of the component to be analyzed is small in most cases, the electrical resistance change of the deformed conductor is also small and is typically in the range of 0.0001 - 0.01 Ω per Ω nominal resistance [3]. For this reason, an electrical circuit is required that makes it possible to detect the smallest changes in resistance with reliability. The Wheatstone measuring bridge (WB), an arrangement of four electrical resistors R_1-R_4, which are imaged in different variants by strain gauges, is classically used for this purpose. Figure 2 shows two circuit diagrams of the WB taken from standard literature (left, completely identical in function) and the embedding of a measuring strip applied to a bolt in the WB (right). Independently of the graphical representation, the resistors are arranged in a circle and connected to each other.

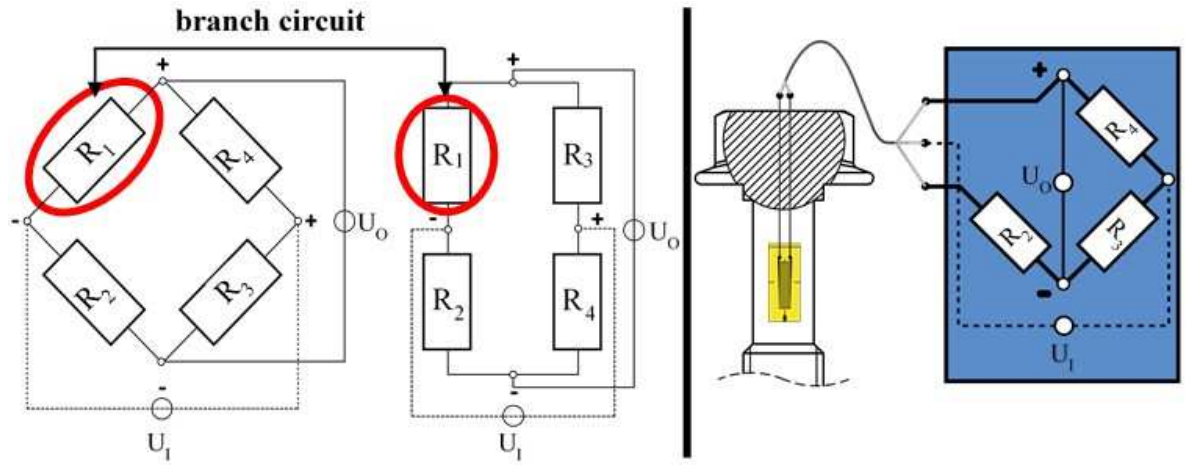

Fig. 2 - Functionally identical circuit diagrams of the Wheatstone bridge (left) and integration of a single strain gauge into the circuit. In this case, the resistors R2-R4 must be substituted by electrical fixed resistors of the same value. Based on [2] (left) and [1] (right).

If a constant input voltage U_I in a low volt range (usually 1 V ≤ U_I ≤ 10 V [2, 3] resp. 2,5 V ≤ U_I ≤ 10 V [4]) is supplied between two opposing bridge arms, an output voltage U_O (in the millivolt range [3]) occurs between the remaining arms precisely when the nominal resistance

of the strain gauges changes due to an applied load. By using a measurement amplifier, the signal can be amplified into the volt range and used for further processing [3]. Based on the electrotechnical laws underlying the WB (Kirchhoff rules), the number N of measuring strips on the specimen ($N \in \{1, 2, 4\}$) and their orientation (vertical, horizontal) can be used to compensate for disturbance variables, e.g. due to bending moment or temperature influences. This is possible because the strain values of opposite measuring strips are summed up, while those of adjacent strips are subtracted, as shown in equation 1 (with k as a proportional factor between strain and change in resistance, which is usually specified by the strain gauge´s manufacturer):

$$\frac{U_0}{U_I}\left[\frac{mV}{V}\right] = \frac{k}{4} \cdot (\varepsilon_1 - \varepsilon_2 + \varepsilon_3 - \varepsilon_4) \tag{1}$$

Figure 3 illustrates common variants that are suitable for determining the preload force on bolted joints (suitability for strain measurement on the tension rod, application method 'outer application of strain gauges on the bolt shaft'). As described, the bolt elongation leads to a change in resistance of the WB and therefore to a change of the measured voltage with a given supply voltage. To determine the bolt force [N], we need to use a calibrated reference such as a load cell. A linear function then can be used to transform any measured signal to a force.

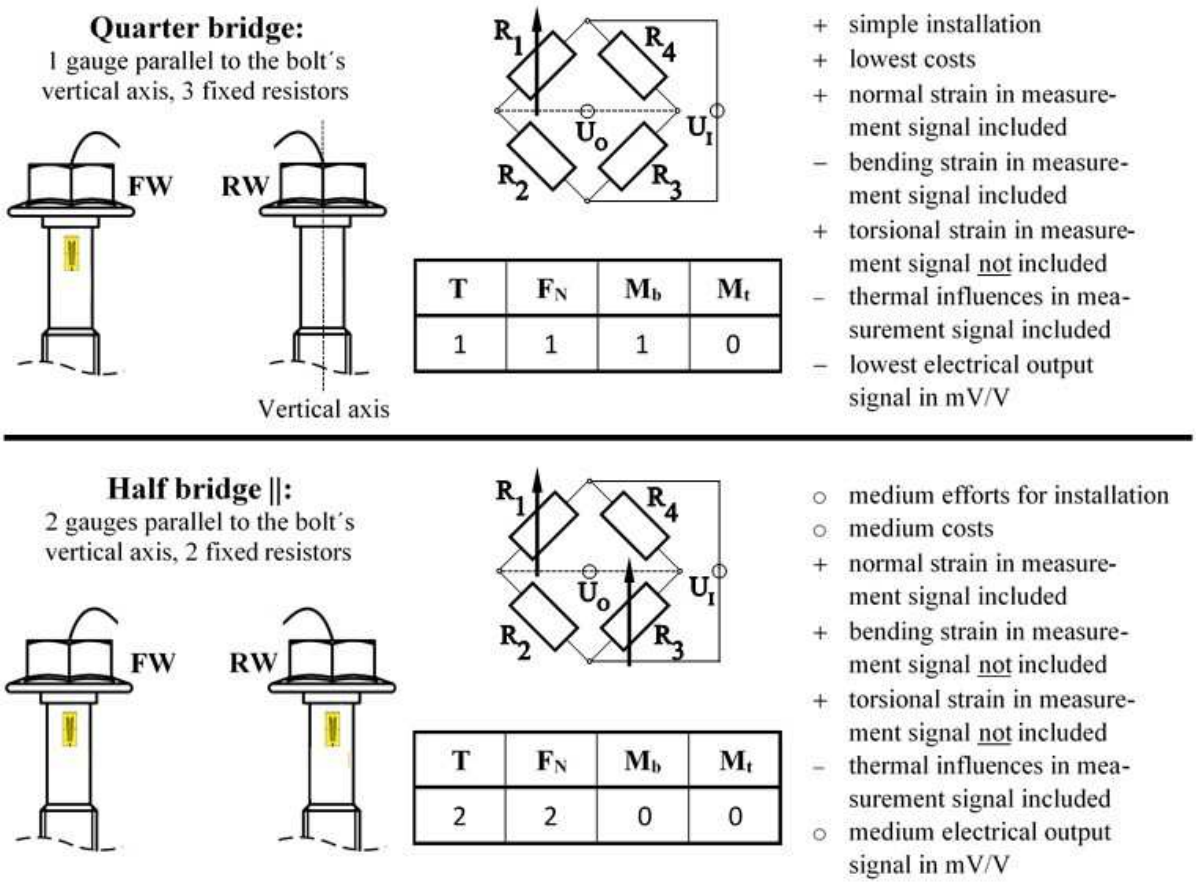

Fig. 3a - Selection of suitable variants of the WB for determining a bolt´s preload force (≙ normal strain), pictorial presentation of the strain gauges on the bolt shaft (front/rear view FW/RW), circuit diagrams of the bridges (centre), resulting signal components (tables) and the individual advantages and disadvantages (gradiation + / ∘ / -), after [5].

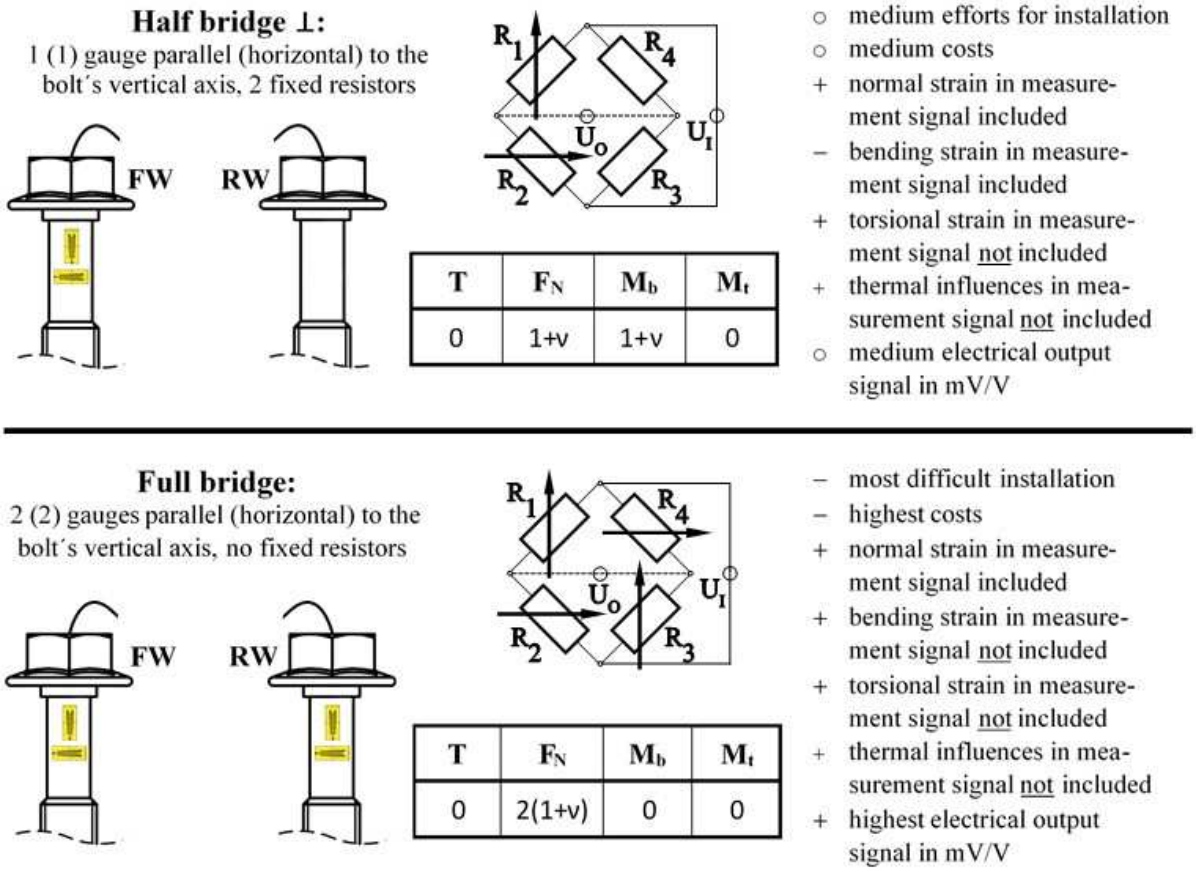

Fig. 3b - Continuation of Fig. 3a.

Although the use of four strain gauges connected in a full bridge allows the largest possible output signal and, in theory, complete compensation of bending, torsion and temperature influences, practical use shows that this is only partially true due to manufacturing inhomogeneities on sides of gauge manufacturer and also user. In particular, high operating temperatures T_A (20 °C < T_A ≤ 150 °C) can lead to a significant deviation from the desired mechanical signal component. However, errors can also occur at room temperature, which can be avoided by the correct selection and arrangement of. In the following, the corresponding error potential is explained and it is indicated how reliable measurement results can be generated.

In the following, all strain gauges are applied to bolts of size M10 x 90 10.9 (material: 40CrMo4) with a continuous thread extending below the bolt´s head similar to DIN 6921, whereby the first 17 mm of the thread below the head were machined in such a way that a flat surface of diameter d = 7.8 mm with low surface roughness was created. The gauges were then applied to this surface and a temperature-resistant connection cable was routed through a vertical hole drilled via the bolt´s head with a diameter of d = 1.6 mm. Unless otherwise specified, strain gauges of the type “J5K” from the manufacturer “Micro Measurements Inc.” were used in all measurements carried out, which were applied with the high-temperature, heat-curing two-component epoxy-phenol adhesive “M-Bond 610” (also Micro Measurements Inc.). All peripheral components such as measuring cables, solder etc. were selected based on their suitability for temperatures up to T = 150 °C and have been used unchanged in all tests.

FORCE MEASUREMENT WITH STRAIN GAUGES AT AMBIENT TEMPERATURE

This chapter uses examples to illustrate that the choice of circuit type (according to Figure 3) must always be made according to the expected measurement task in terms of cost and benefit. It can be seen that even minor factors can lead to considerable deviations from the desired mechanical signal component and threaten to falsify the measured variable.

A. Influence of an unsteady operating temperature

If a strain gauge-based application is not used continuously in a room with a constant temperature, it will probably experience certain temperature changes. Even small temperature changes ΔT, such as those that can occur during the course of a normal day, are sufficient to cause a significant distortion of the measurement signal. This is not only due to the thermally induced change in length of the conductor wire as a function of its expansion coefficient α, but also, for example, due to the thermally induced change in the resistance of a metallic conductor itself, as this increases with rising temperature [2] (lattice atoms have more kinetic energy and thus impede the flow of free electrons, which are responsible for the current flow). The k-factor as a correlation between the change in stress and strain (equation 1) also changes with the operating temperature [2].

To illustrate the effect, quarter, half (orthogonal, parallel) and full bridge circuits are considered as shown in Figure 3, which are subjected to a moderate temperature increase of $\Delta T = 15$ °C from $T_1 = 20$ °C to $T_2 = 35$ °C (rate of change: 1 °C/min). After a holding time of 60 min, controlled cooling with rate of 1 °C/min was done. Before starting the test, all bolts were pre-tempered for approx. 12 hours under supply voltage (1 V) at a constant temperature of $T_1 = 20$ °C in a climatic chamber and then used in the test untensioned (i.e. without clamping part and nut). The (apparent) force F_{ap} was measured, which was caused solely by the temperature change but was not mechanically present (thermal drift). Figure 4 shows the recorded measurement curves.

While a bolt equipped with a full bridge circuit experiences almost no thermally induced signal change, an orthogonally manufactured half bridge variant experiences a slight temperature change of approx. 70 N, which is, however, completely reversible. As a WB formed in this way just compensates for temperature influences, the theory is confirmed by the measurement result. A different picture emerges when using a quarter bridge circuit and a half bridge arrangement with two strain gauges mounted in parallel and arranged offset by 180° at the same height. In both cases, there is a constant change (increase) in the measurement signal, which changes to an almost stationary state when T_2 is reached. This is approximately 600-700 N (quarter bridge) or 800 N (half bridge) above the zero point and in real use this means a superposition with the mechanically induced signal. If, for example, clamping parts made of aluminum with $\alpha_{th,AL} \approx 24\text{e-}06\ K^{-1} > \alpha_{th,FE} \approx 11\text{e-}06\ K^{-1}$ are clamped with these steel bolts, the preload force increases due to the greater expansion of the aluminum parts. It remains unclear which part of the signal is due to the actual increase in elongation and which is due to the occurrence of a temperature change. This leads to the risk of misinterpreting the measurement result.

B. Influence of an uneven counter surface

As shown in the previous section, the use of strain gauge technology is highly sensitive to a change in the operating temperature. However, other influencing variables, such as the

occurrence of a bending moment due to an uneven mating surface, can also lead to considerable deviations if the wrong circuit is selected, which can also result in misinterpretations.

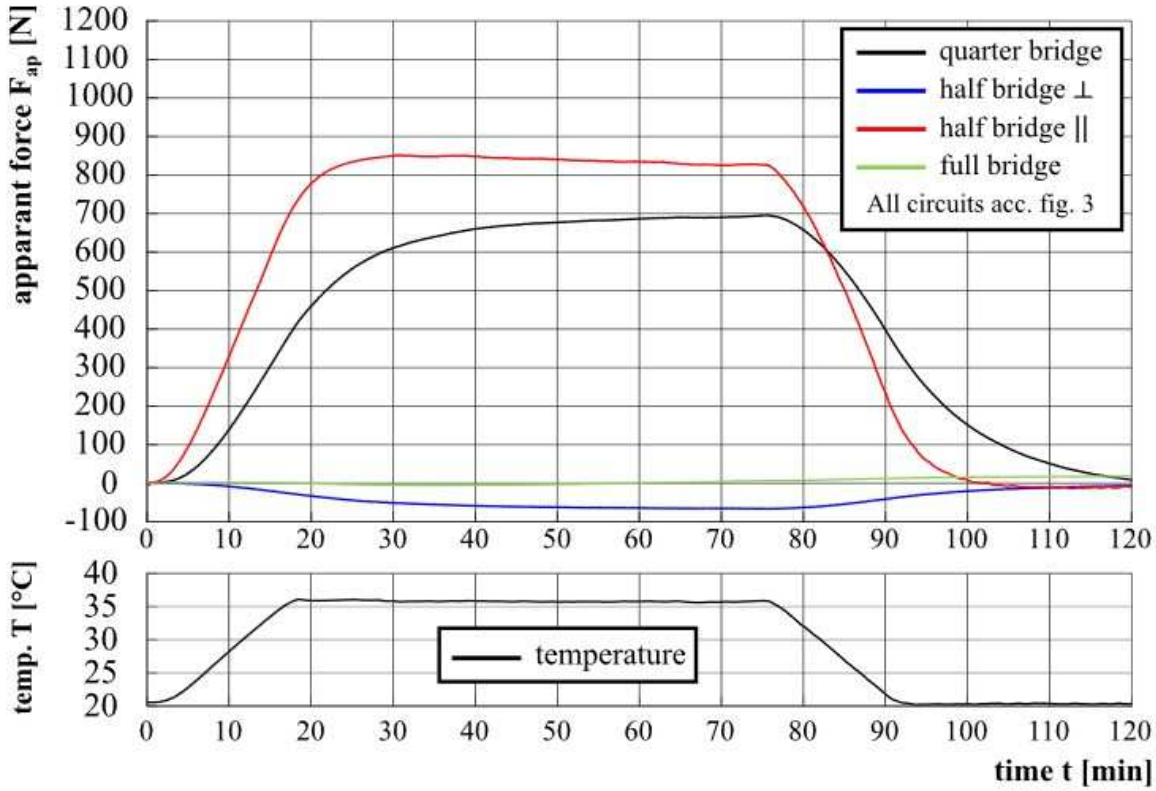

Fig. 4 - Effect of a moderate temperature increase of ΔT = 15 °C from T1 = 20 °C up to T2 = 35 °C on the measured force signal of a sensor screw manufactured with different circuit types.

The bolt variants described above (quarter bridge, half bridge orthogonal, half bridge parallel, full bridge configuration) were fastened within a uniaxial tensile test rig and loaded torsion-free with an axial force F_{ax} = 10 kN (≙ F_P) and afterwards again analyzed.

A load cell installed in the test rig and located within the load level served as a reference source in each test. A DIN 434 wedge disc with an inclination of 8% (≈ 4.57°) was attached below the bolt head in each case, which resulted in an uneven load distribution in the bolt shaft.

Figure 5 shows a detailed image of the test configuration mounted in the test rig (left) and the stress distribution within the bolt determined using the finite element method (equivalent stress according to von Mises), which results when loaded to F_P = 10 kN (right):

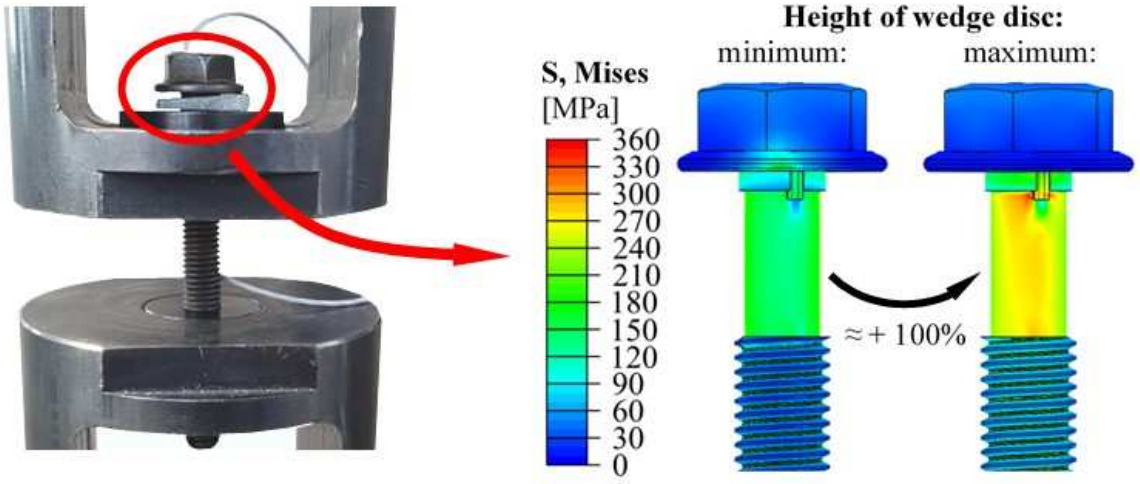

Fig. 5 - Close-up view of the test bolt installed in the tensile testing machine with wedge disc (left) and resulting numerically determined stress distribution (equivalent stress according to v. Mises from FEA; FP = 10 kN)

All tests were carried out at a constant ambient temperature and the load on the target preload F_P was applied purely axially within approximately 30 seconds using a hydraulic pump. Preload and reference force of the fully compensated load cell were measured continuously. The loading process was carried out in stages and the mean force increase was then approximated using a linear equation. Figure 6 illustrates the methodology (left) and shows the measurement results obtained in this way (right), which are well suited for comparison.

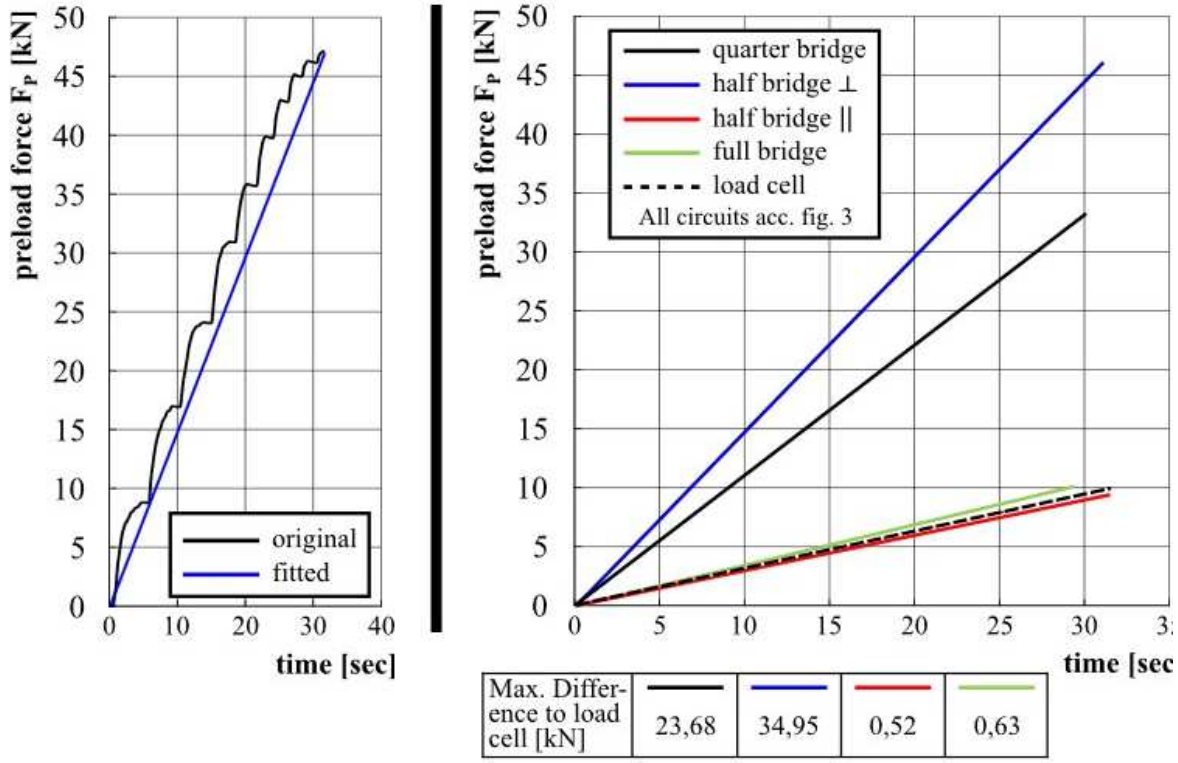

Fig. 6 - Deviation of the bolt preload forces from the load cell reference signal with torsion-free tensile load to F_P = 10 kN with tightening against a wedge disc with 8 % inclination angle according to DIN 434.

With presence of a bending moment (here wedge disc), the quarter bridge circuit shows a significant deviation in relation to the load cell signal (factor of around 3.5). With the half bridge circuits, the result is the opposite of Figure 4, as the orthogonal variant shows force differences similar to quarter bridge circuit (deviation by a factor of 4.5), whereas the parallel variant is consistently close to the reference curve (load cell, black dashed line). This proves that the circuit can be compensated as shown in Figure 3. This also applies to the full bridge variant, which does not show any significant deviations from the reference at any time (this also means on the other hand, that no bending moment can be evaluated).

C. Influence of the supply voltage

Up to now, all tests have been done with a supply voltage (U_I) of 1V, which is a relative low value. As a general rule, higher values always have advantages, as they can be used to realize a higher output voltage U_O (as a further parameter in addition to the strain) and thus a larger measurement signal is generated. This makes it possible, for example, to better detect smaller amounts of strain because the circuit reacts more sensitive to loads. Nevertheless, the selection of a higher value of U_0 is associated with certain risks, as the measuring area can heat up excessively, because the metallic measuring grid represents an electrical resistance that emits heat to the carrier material and sample body due to the applied electric current. Because many properties of the measuring system are temperature-dependent, a signal drift or hysteresis, i.e. signal curves that are out of phase with increasing and decreasing strain, can occur [2].

In practice, this means that the supply voltage should always be selected depending on the nominal resistance R of the strain gauges used and the measurement task; common values for the electrical resistance R are 120 Ω, 350 Ω or 1000 Ω. While low-resistance (120 Ω) variants tend to heat up the measuring area at high supply voltages, the use of higher-resistance gauges (e.g. 1000 Ω) results in significantly less thermal stress under the same conditions [2]. Although these are much more sensitive to interference pulses from electric and magnetic fields [3], which is why the selection of a medium-resistance gauge (350 Ω) with a moderate supply voltage (1-2.5 V) is usually a good compromise [5]. If the amount of strain to be measured on the componente is not sufficient to generate a processable output signal with this parameter configuration, the outer dimensions can be reduced.

FORCE MEASUREMENT WITH STRAIN GAUGES AT ELEVATED TEMPERATURE

With regard to the reliable determination of measured values, elevated temperatures in particular can cause considerable problems and deviations. As already explained, this is due to the fact that the physical effects that are utilized when measuring with strain gauges are themselves dependent on the temperature and change their characteristics with it. Nevertheless, it is possible to record safe and reliable signals even under simultaneous mechanical and thermal stress. The following section outlines how this can be achieved.

D. Occurrence of a thermal drift

As already shown in Figure 4, when strain gauges are used, an apparent force F_{ap} occurs even at small temperature increases of $\Delta T = 15$ °C, which can lead in a misinterpretation of the measurement result. The values that this force can assume in the most unfavorable case are illustrated in Figure 7.

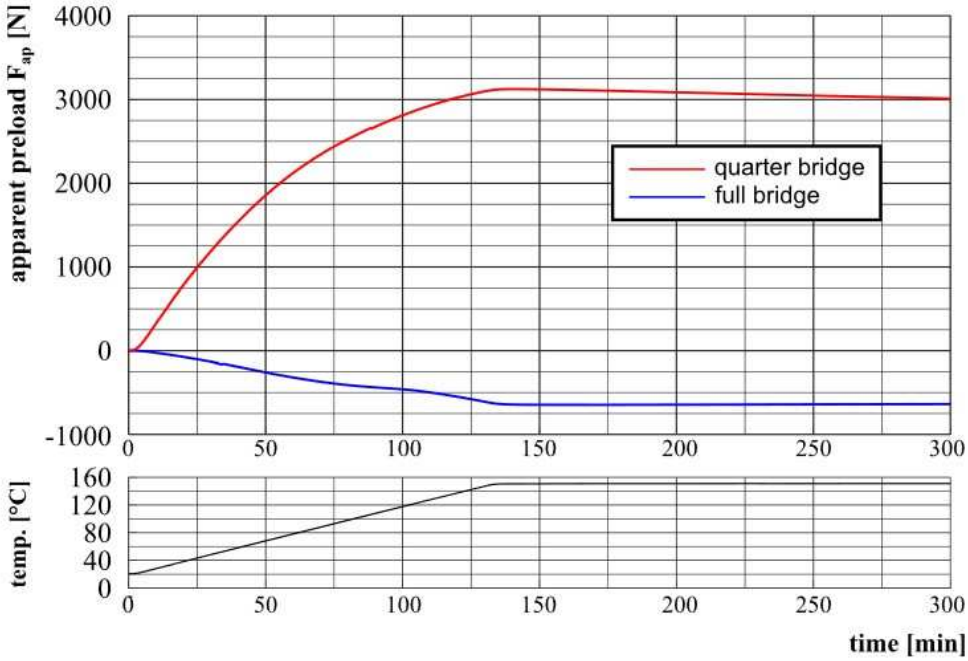

Fig. 7 - Thermal drift of quarter- and full bridge circuit when heated to T = 150 °C (no preloading of bolt).

Bolts with quarter and full bridge arrangements are placed untensioned in a climate chamber and heated from T_1 = 20 °C to T_2 = 150 °C at a rate of 1 °C/min. The bolt force is measured until the target temperature is reached, whereas the cooling phase is not considered further.

The quarter bridge configuration results in a thermal drift of F_{ap} = 3000 N, which eliminates any suitability for high temperatures regardless of the gauge type used. While the full bridge arrangement should theoretically be fully compensated against temperature influences, a temperature variation of F_{ap} = -650 N nevertheless occurs, which may be due to unavoidable manufacturing inhomogeneities (see chapter 'Introduction').

E. Relevance of the real thermal suitability of the used strain gauge

The product catalogues or websites of the strain gauge manufacturers indicate that a relatively large number of gauge types are approved for temperature ranges of 150-200 °C. Provided that the peripheral components are also suitable for these ranges, good quality and stable measurement results should be expected. In practice, however, this approval is by no means a guarantee of reliable results. Even if the structure or materials of the measuring strips are often similar, there are only a few that ultimately fulfil the central requirement of stability of the measuring signal under simultaneous thermal and mechanical load.

Two strain gauge variants are analyzed, which are applied to the bolt shaft in a full bridge arrangement. Three specimens of each type were identically manufactured, temperature-resistant peripheral components were used in all cases. Table 1 compares some basic characteristics of the gauges. All bolts were tensioned with solid steel sleeves made of 42CrMo4 (outer diameter d_{out} = 40 mm, grip length l = 20 mm) and nuts according to DIN 6331 to preload F_P = 30 kN and then exposed to a constant operating temperature of T_2 = 150 °C for four hours with heating and cooling starting from T_1 = 20 °C and a rate of 1 °C/min. This was followed by further exposure at T_1 for 500 minutes. The time-continuous preload signal of the bolts was recorded. Due to the utilization of clamped massive steel components, which were used far

below their thermal and mechanical limit load capacity, no preload changes caused by the fastening system were to be expected. Figure 8 shows the measurement results as a mean value (continuous curve section) with upper and lower deviation (dashed curve sections, each calculated from N = 3 individual measurements).

Table 1 - Characteristics of the strain gauge types used.

		Gauge Type 1	**Gauge Type 2**
Constructional design:		single grid	
Nominal resistance:		350 Ohm	
Connection of signal cables:		soldering pad (not pre-wired)	
Materials:	Carrier film:	PEEK	Polyimide
	Measuring Grid:	Constantan (Cu-Ni-Alloy)	Karma (Ni-Cr-Alloy)
	Cover film:	PEEK	Polyimide
Authorized temperature range:		-40 to +200 °C	-75 to +205 °C

While gauge type 2 shows an almost stationary behavior even when preloading after a swing-in process, which only takes place in the phase of thermal change, several effects can be observed using gauge type 1. Although a swing-in process also takes place here, after reaching the target temperature this changes into a phase of uniform creep with a similar negative gradient, which cannot be explained by a mechanically induced change in strain. After a relatively short time period of t = 375 min = 6.25 hr, an apparent drop in prestressing force of 5.2 % on average is recorded. After assuming the initial temperature, an average force difference of 3.75 % remains for gauge type 1, while type 2 returns exactly to the originally set force.

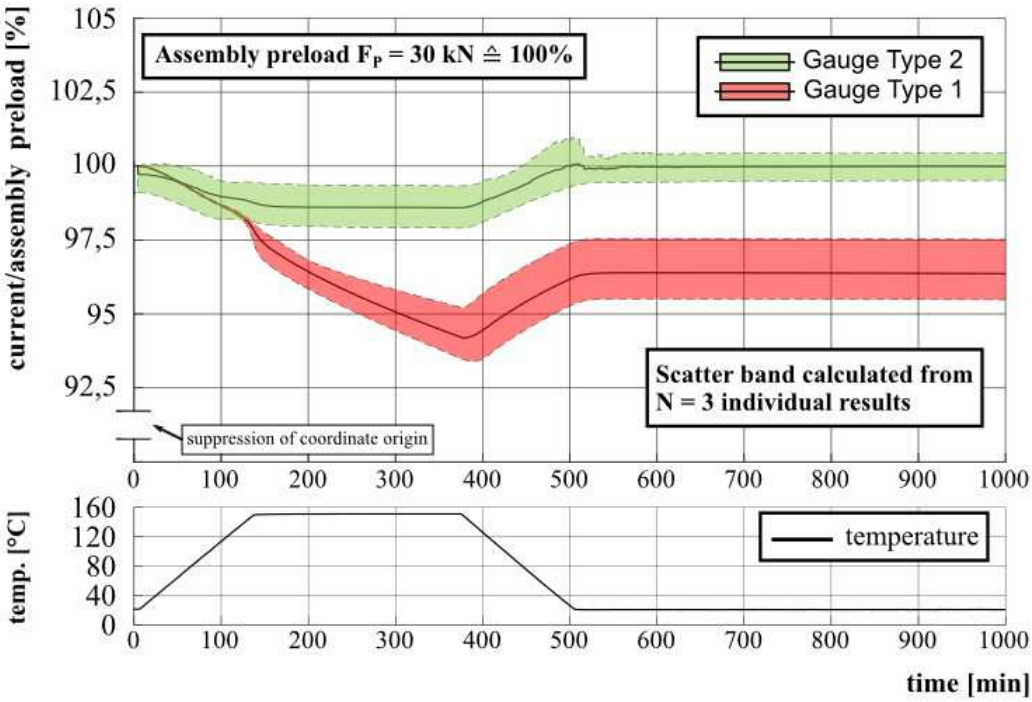

Fig. 8 - Behaviour of a suitable (type 2) and unsuitable (type 1) strain gauge under mechanical load (FP = 30 kN) at a high operating temperature (T = 150 °C). On the Y-Axis, only the relevant information area is shown (suppression of the coordinate origin).

At this point it must be noted that the operating temperature of T = 150 °C represents a very high load for conventional foil strain gauges, at which the peripheral components such as the measuring cable and solder will reach their permissible limits.

Gauge type 2 is also used in [5] as the exclusive gauge for all strain gauge measurement tasks in a range of 20 °C ≤ T ≤ 150 °C.

As already shown in Fig. 4 and Fig. 7, a low thermal drift occurs even with the compensated full bridge arrangement, which can also be seen in both curves in Fig. 8. The following chapter shows how this significantly can be reduced, so that the measurement signal describes the mechanical signal much more accurately.

F. Effect of an additional frictional resistance for the almost complete elimination of the thermal drift

With a relatively simple additional procedure, it is possible to achieve almost complete compensation of the thermal drift that occurs in practice even with bolts with four measuring strips in a full bridge arrangement. For this purpose, a further resistive element must be inserted within the electrical circuit, which is able to compensate for the thermally induced change in the output voltage. A so called friction resistor of the type “N2B-TR-H22A-00010” (Micro Measurements Inc.) is used, which is soldered into two adjacent bridge arms due to the design and therefore has two “inputs”. The WB is closed via a common, centered output. Figure 9 shows the friction resistor of this type (left, greatly enlarged) and its arrangement within the Wheatstone bridge (right).

The conductor loops themselves have an output resistance of 1 Ω, which can be specifically adjusted by careful rubbing with an eraser, and are made of Balco wire (Ni-Fe alloy). The key feature of this alloy, which is specifically exploited, is that its resistance changes proportionally to temperature. If the apparent force F_{ap} assumed by the mechanically unloaded bridge circuit at a specific operating temperature T_2 (bridge detuning) is known, the required resistance compensation can be calculated and adjusted by rubbing a conductor loop, which depends on the sign of F_{ap} (- / +; see Fig. 4). The result is a nearly stationary behavior of the measuring bridge when exposed to the target temperature T_2, which allows a significantly more realistic assessment of the mechanical signal component (Figure 10).

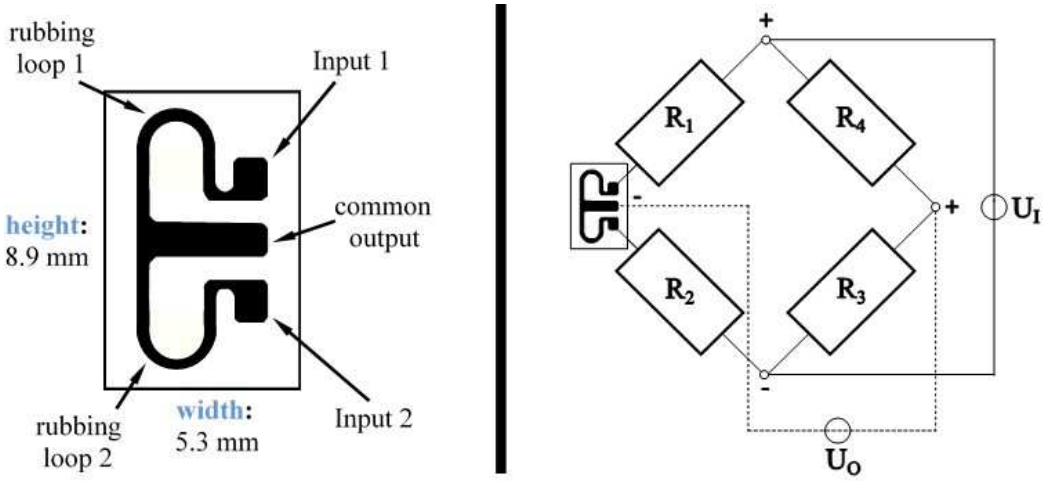

Fig. 9 - Frictional resistance "N2B-TR-H22A-00010" (left) and its arrangement in the WB (right).

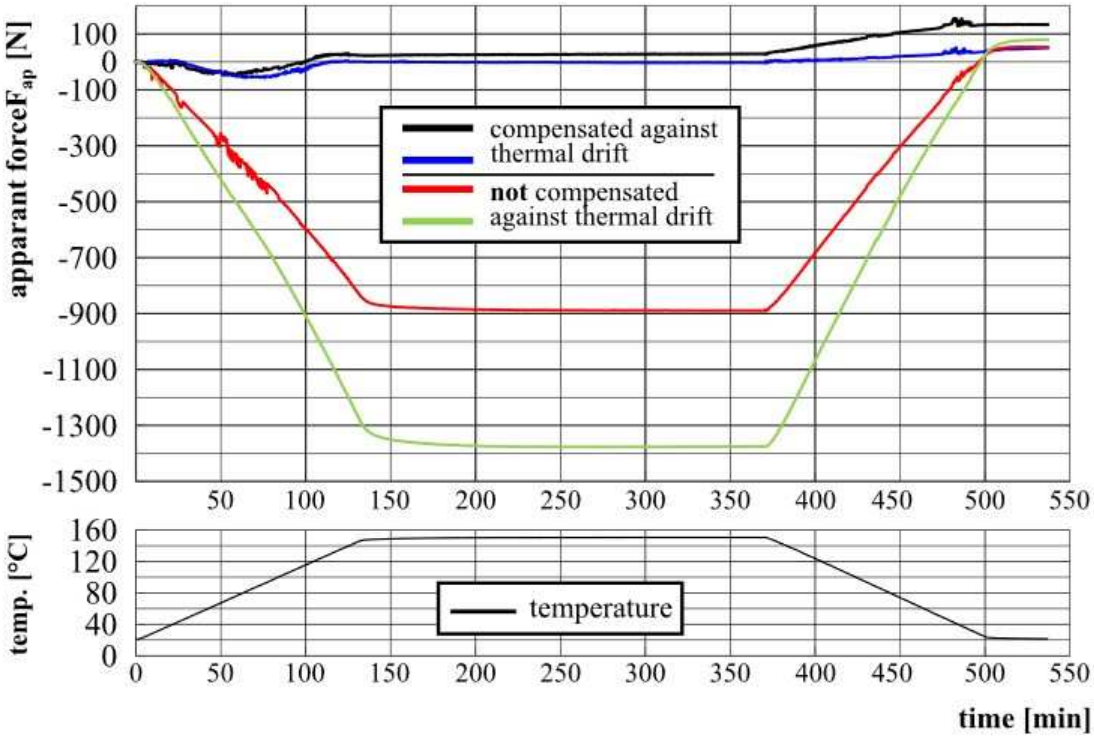

Fig. 10 - Effect of an additional and specifically adjustable frictional resistance integrated into the WB for almost completely elimination of the thermal drift, illustrated by two curves each.

PRACTICAL EXAMPLE: PRELOAD RELAXATION MEASUREMENT USING STRAIN GAUGE APPLIED BOLTS

As mentioned in the introductory chapter, strain gauges can be used in a wide range of applications to determine mechanical parameters. Finally, a practical example is illustrated in which strain gauges are used to continuously measure the decrease in preload due to relaxation effects.

A bolting system consisting of a sensor bolt in a full bridge arrangement (gauge type: J5K), which is clamped with a nut according to DIN 6331 against a 20 mm high aluminum clamping part (EN AW-6082) to an assembly preload of F_P = 30 kN, is examined. The subject of the investigation is the influence of different temperatures (T = 20 °C, 100 °C, 120 °C, 150 °C), which is why the thermal drift of all bolt specimens was compensated by an additional friction resistor (see previous chapter). After assembly, all test parts were placed in a preheated climate chamber for t = 100 hr and then removed again and cooled down at room temperature (T = 20 °C).

After facing the thermal load, an increase in preload can be seen at all exposure temperatures T > 20 °C, which is due to a greater expansion of the aluminum clamping parts compared to the steel components. In the following 100 hr, there is a continuous decrease in the preload due to plastification within the bolting system in all cases, which increases with the temperature. After finally reaching T = 20 °C, all curves switch to a stationary state, which amount is smaller the higher the thermal load. This is a good indication that the sensor bolts adapted to the measuring task determine reliable values.

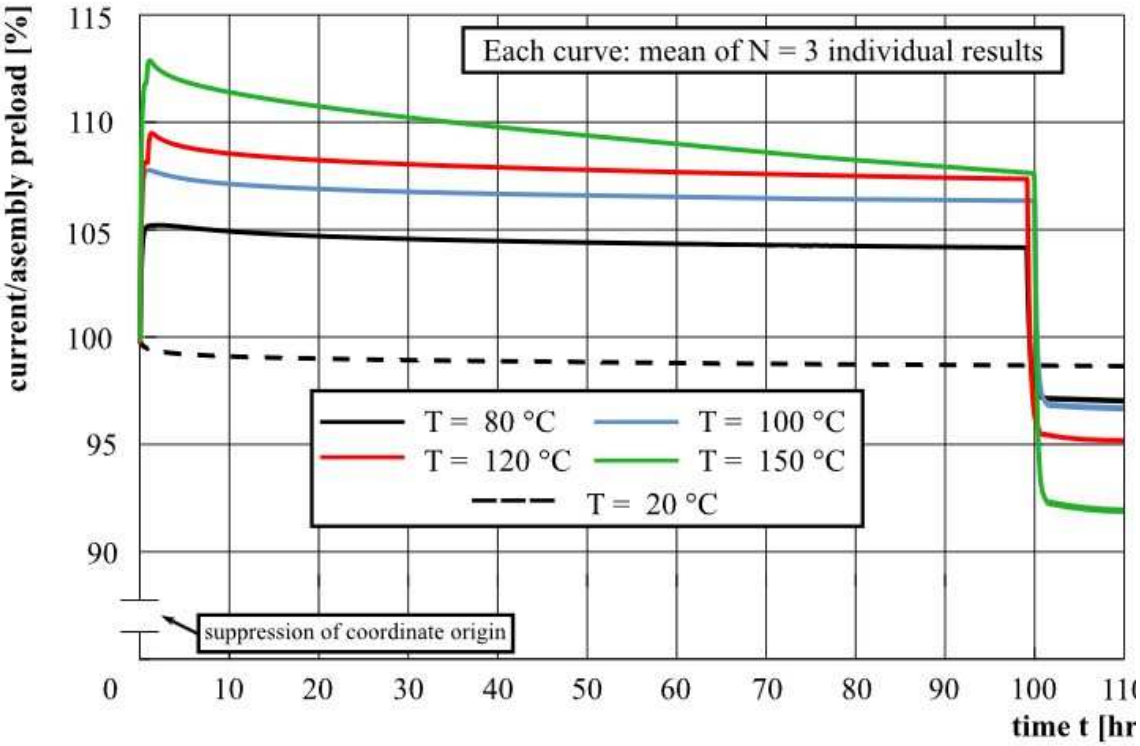

Fig. 11 - Preload relaxation curves of bolted joints with aluminium at elevated temperatures determined with strain gauges. On the Y-Axis, only the relevant information area is shown (suppression of the coordinate origin). Additional measurements can be found in [6].

SUMMARY AND OUTLOOK

The safe and reliable determination of preload force on bolted joints using strain gauges is also possible at high operating temperature of up to 150 °C. However, it is essential that the entire measuring system is designed from the beginning for these operating conditions, which includes the correct choice of adhesive, connection cables and gauges. Additionally the installation procedure has to be done precisely with experience.

It has been shown, even the theoretically fully compensated full bridge circuit shows a significant thermal drift, which is superposed to the mechanical signal and thus leads to a falsification or misinterpretation of the measurement results. Due to the usage of a friction resistor, this effect can be almost completely eliminated. The results of this paper show, that even at room temperature a minimal temperature increase can cause significant deviations in non-adapted circuits. This leads to incorrect measurement results. For measuring in laboratory this leads to differences from reality and possibly misinterpretation, even if all strain gauges are calibrated with standardized conditions; for control intention in mechatronic series products it leads to wrong control in operation. In practice of products bending moments can occur – also this does influence the measurement signal (see example with wedge disc above).

As outlook it should be considered, that the influences shown above are fundamental to define, also for preload sensing bolted joints - which are a real opportunity to combine sensor information and fastening in one component of modern intelligent products. Besides this

preload measurements also show integrity of the joints themselves, especially for thermal induced preload loss for different material combinations or operating at elevated temperature; to determine this more in detail, permanently projects are in progress.

REFERENCES

[1] Dümpelmann C. Erfassung der Strukturintegrität durch Messung der zeitabhängigen Vorspannkraft in Schraubenverbindungen. Dissertation Universität Siegen, universi, 2020.

[2] Keil S. Dehnungsmessstreifen. Springer Fachmedien Wiesbaden, Wiesbaden, 2017.

[3] Hoffmann K. Eine Einführung in die Messung mit DMS-Streifen. Hottinger Baldwin Mess-technik, 2000.

[4] Hannah R. Strain Gage Users' Handbook. Chapman & Hall, London, 1994.

[5] Held T. Dissertation Universität Siegen (in progress), 2027.

[6] Peth C. Einflüsse auf das Vorspannkraftrelaxationsverhalten von Schraubenverbindungen im Leichtbau. Dissertation Universität Siegen, universi, 2022.

Proceedings IRF2025: 8th International Conference on Integrity-Reliability-Failure
In Engineering, Materials, Manufacturing and Biomechanics. Porto 15-18 July 2025
DOI: https://doi.org/10.24840/978-972-752-323-8

PAPER REF: 22634

EFFECT OF CARBON /ARAMID FIBER REINFORCEMENT ON THE IMPACT TOLERANCE OF LAMINATES

Paweł Przybylek(*), Andrzej Komorek, Robert Szcepaniak, Tomasz Zahorski
The Polish Air Force University, Faculty of Aviation, Dvwizonu 303 str. No.35, 08-530 Dęblin
(*)p.przybylek@law.mil.pl

ABSTRACT

The aim of this study is to present the influence of hybrid laminates with carbon/aramid reinforcement on strength properties after impact. The puncture resistance tests and residual strength properties after impact were performed with three values of energy: 3, 5, 10 [J]. Two types of carbon fabric (GG 280T, DYF 160/25) one of aramid (KK 170T) and hybrid, aramid - carbon type (KPiS-T-A-007) of fabric were used. After impact testing, three-point bending tests were performed to identify the residual strength of the laminates. The surface area of damage on the impacted and the opposite side of the composite were measured. Reinforcement of fibre fabric GG280T has the greatest effect on increasing the strength, however the addition of the DIY 160/25 carbon fibre fabric reduces them.

Keywords: Laminates, fibres reinforcement composites, impact resistance.

INTRODUCTION

Composite laminates are increasingly used to produce components of vehicles in civil and military aerospace, marine and automotive industries [Cătălin et al., 2025]. Fiber-reinforced polymers are very important for engineering applications due to their high specific stiffness, fatigue performance, good chemical and thermal resistance [Ni, et al. 2024]. The choice of fibres plays an equally important role in creating composites [Claus et al.2020]. Different fibre reinforcement types offer strain energy absorption potential, which is beneficial for residual properties. The knowledge of a dynamic response of a structure with regard to the used reinforcement and its impact tolerance are necessary for exploiting them in applications. [Fan, et al.2024]. The aim of this article is to present the results of the impact tolerance and puncture resistance test as well as residual strength properties after an impact performed with different energy hybrid laminates.

RESULTS AND CONCLUSIONS

Four types of reinforcements were used in various configurations placed into an epoxy resin matrix L 285 cured by hardener H 285 in proportion100:40 weight share. The following types of reinforcement were used to produce the laminates:

- Aramid fiber fabric KK 170 T, 170 g/m^2 basis weight, 2x2 twill weave;
- Carbon fiber fabric GG 280 T, 160 g/m^2 basis weight, 2x2 twill weave;
- Carbon fiber fabric DYF 160/25, 220 g/m^2 basis weight, plain weave, dynanotex flat fabric;
- Hybrid (aramid/carbon) fabric KPiS-T-A-007, 165 g/m^2 ,twill weave.

Eight composite control panels with 7 layers of reinforcement were prepared for the experimental tests, Figure 1: 1 - 4 layers of GG280 T and 3 layers of KK170 T; 2 -4 layers of KK170 T and 3 layers of GG 280 T; 3 - 8 layers of KPiS-T-A-007; 4 – 8 layers of KK 170 T; 5 – 5 layers of GG 280 T and 2 layers of DYF 160/25; 6 – 5 layers of DYF 160/25 and 2 layers of GG 280 T; 7 - 8 layers of GG 280 T; 8 – layers of DYF 160/25. The composites were prepared by manual lamination and then placed in a hydraulic press for 24 hours under a pressure of 23 tons (1MPa). The following experimental tests were carried out and later the achieved properties were analysed:

- Puncture resistance test (at the drop tower CEAST 9340 INSTRON): The Impact Resistance [N/m], Peak Force [N], Peak Energy [J];
- Charpy impact test (at the research station GALDABINI IMPACT 25: Resilience [kJ/m^2]
- Three-point bending strength test: bending strength σ_{fM} [MPa], elastic modulus E [MPa],
- Surface Area of the damage on the impact side [mm^2] and on the side opposite to the impact side.

The experimental tests concern the impact resistance test and residual strength properties after an impact performed with three values of Energy (3, 5, 10 [J]) on a drop tower.

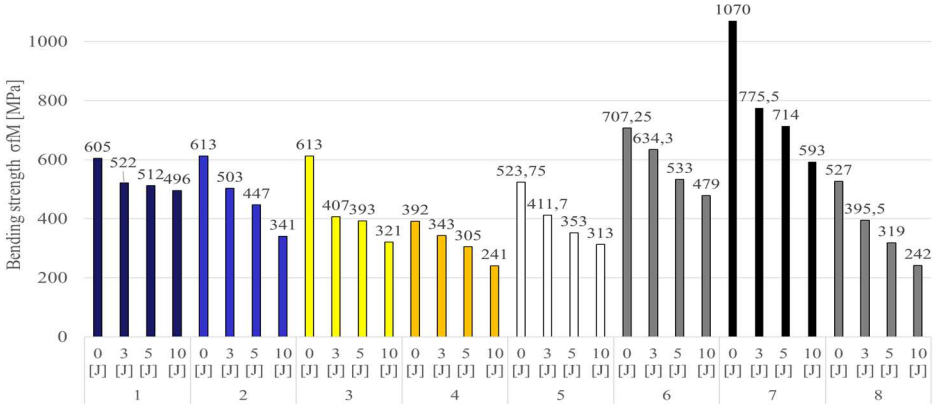

Fig. 1 - Bending strength σ_{fM} [MPa] after an impact of all composites.

- The addition of the GG 280 T carbon fibre fabric has the greatest effect on increasing the strength but the addition of the DIY 160/25 carbon fibre fabric reduces them;
- The addition of KK170 T aramid fibre fabric has the best effect on impact resistance;
- Material No. 1, obtained the smallest deterioration of bending strength after impact, respectively by about 20% for the impact energy of 10 [J];

REFERENCES

[1] Fan, Q.; Duan, H.; Xing, X. A review of composite materials for enhancing support, flexibility and strength in exercise. Alex. Eng. J. 2024, 94, pp.90-103.

[2] George Cătălin Cristea, et al, Influence of Resin Grade and Mat on Low-Velocity Impact on Composite Applicable in Shipbuilding,2025, Polymers17, 355, https://doi.org/10.3390/ polym17030355.

[3] Fan, Q.; Duan, H.; Xing, X. A review of composite materials for enhancing support, flexibility and strength in exercise. Alex. Eng. J. 2024, 94, pp.90-103.

[4] Ni, K. et al. Low-velocity impact and post-impact compression properties of carbon/glass hybrid yacht composite materials. Ocean Eng. 2024, 292, 116448.

Proceedings IRF2025: 8th International Conference on Integrity-Reliability-Failure
In Engineering, Materials, Manufacturing and Biomechanics. Porto 15-18 July 2025
DOI: https://doi.org/10.24840/978-972-752-323-8

PAPER REF: 22644

CORRELATING FLEXURAL ULTRASOUND ATTENUATION PARAMETER TO SENSITIZATION BASED ON FABRY-PEROT RESONATOR PRINCIPLE

Songwei Wang, Haiying Huang(*)

Department of Mechanical and Aerospace Engineering, University of Texas at Arlington, Arlington, TX, USA
(*)*Email:* huang@uta.edu

ABSTRACT

Ultrasound attenuation in polycrystalline materials is sensitive to microstructure changes such as recrystallization, fatigue, sensitization, etc. This study introduces the principle of Fabry-Perot resonator for measuring the attenuation parameter of dispersive flexural waves. The results demonstrate that the flexural ultrasound attenuation parameter correlated well with the degree of sensitization (DoS) in aluminum-magnesium (Al-Mg) alloy samples, leading to a fast and non-destructive technique to characterize DoS.

Keywords: Fabry-Perot resonator, sensitization, flexural wave, ultrasound attenuation, degree of sensitization, aluminum-magnesium (Al-Mg) alloys.

INTRODUCTION

Previous studies on the effect of microstructural changes on ultrasound attenuation parameter used either longitudinal or shear waves because of their non-dispersive nature. Dispersive flexural waves are rarely used for attenuation measurement because wave dispersion changes the shape of the wave packet, making comparing the amplitudes of two consecutive wave packets difficult. When exposed to elevated temperature for an extended period, Aluminum-magnesium (Al-Mg) alloys experience sensitization, i.e. the formation of β-phase Al_2Mg_3 precipitates at the grain boundaries. This microstructure changes makes Al-Mg alloys more susceptible to intergranular corrosion and stress corrosion cracking. The standard technique for quantifying sensitization requires submerging matchstick samples in acid solution and measuring the material loss after 24 hours of soaking. This approach is time consuming and cannot track the progression of sensitization in the same sample. Other researchers have studied non-destructive ultrasound attenuation for sensitization characterization. Even though these studies demonstrated that sensitization changes the ultrasound attenuation parameters, the large measurement uncertainty hinders the detection of small sensitization development. Recently, the authors presented a mathematical proof that a flexural beam is a mechanical Fabry-Perot resonator (FPR). This study extends the FPR fringe analysis to study the influence of sensitization on the flexural ultrasound attenuation parameter.

RESULTS AND CONCLUSIONS

Assuming a harmonic shear force $Fe^{i\omega t}$ is applied at the left end of a flexural beam, the harmonic response of the beam, measured at the right end $x = l$, can be solved as

$$w_{FP}(l,f) = Fe^{-i\boldsymbol{\beta} l}[1 + r^2 e^{-i(2\beta_r l)} + r^4 e^{-i(4\beta_r l)} + \cdots], \quad (1)$$

in which $r^2 = e^{-2\beta_i l}$ represents the round-trip attenuation of the flexural wave. The FPR fringe spectrum of the flexural beam is the amplitude of $W_{FP}(l,f)$, i.e.,

$$I_{FP}(l,f) = F[1 + r^2\cos(2\beta_r l) + r^4\cos(4\beta_r l) + \cdots]. \quad (2)$$

Thus, the fringe frequency spectrum, i.e., the spectrum of $I_{FP}(l,f)$, has fringe frequency peaks with amplitude $A_1 = r^2$, $A_2 = r^4$, etc. The attenuation parameter α can then be determined from the amplitudes of the first and second fringe frequency peak A_1 and A_2 as

$$\alpha = r^2 = 20\log\left[\frac{A_1}{A_2}\right]/2. \quad (3)$$

Matchstick samples having a length of 10 mm and a square cross-section of 6.35 mm^2 were machined from as-received AA5456 cold-rolled plates. Before heat treatment, the impulse response of each matchstick samples was measured by shining a high-power laser pulse on one end surface to excite flexural ultrasound waves and measuring the displacement at the other end of the sample using a laser interferometer. The fringe spectrum of the flexural FPR is calculated from the fast Fourier transform (FFT) of the impulse response. Applying a second FFT on the fringe spectrum produces the fringe frequency spectrum, from which the attenuation parameter can be determined using equation (3).

The samples were heat-treated at 120°C inside an oven. At selected heat treatment intervals, two samples were removed from the oven and the attenuation parameters were measured, after which the Degree of Sensitization (DoS) of these samples were measured using the material loss test. In addition to AA5456 samples, reference samples made of AA5052, which are more immune to sensitization, were tested. Figure 1 shows the correlation of the flexural ultrasound attenuation parameter with the DOS. AA 5456 samples experienced substantial sensitization development while the sensitization of AA5052 samples is neglectable. For both materials, the flexural ultrasound attenuation parameter correlates well with DoS. The flexural attenuation parameter changed significantly with sensitization and the measurement uncertainty is relatively small. These results demonstrate that the flexural ultrasound attenuation parameter have the potential to be used for fast and non-destructive quantification of DoS.

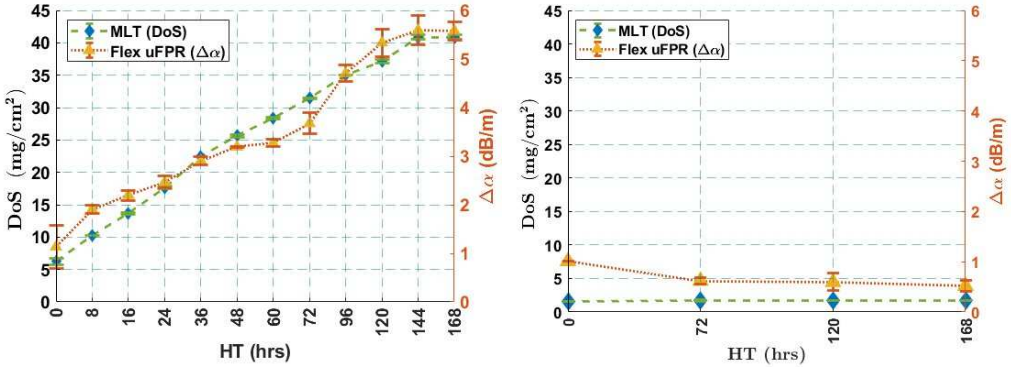

Fig. 1 - Correlation of flexural ultrasound attenuation parameter change and Degree of Sensitization for (a) AA5456 and (b) AA5052.

REFERENCES

[1] Li, F., et al. Measurements of degree of sensitization (DoS) in aluminum alloys using EMAT ultrasound. Ultrasonics, 2011, 51(5), pp.561-570.

[2] Chukwunonye, C.U., et al., Sensitization in aluminum alloys: effect on acoustic parameters, Corrosion, 2018, 74(11), pp.1237-1244.

[3] Wang, S. and Huang, H., Determining ultrasound attenuation parameter from fringe spectrum of ultrasound Fabry-Perot Resonator (UFPR), 2024, Proc. 12949,1294918.

SYMPOSIUM - 3
Digital Manufacturing

J.C. Outeiro(*) and H.P. Cherukuri(*)
Dept. of Mechanical Engineering & Engineering Science
University of North Carolina at Charlotte, U.S.A.

(*)Associate Editor for papers in this Symposium

Proceedings IRF2025: 8th International Conference on Integrity-Reliability-Failure
In Engineering, Materials, Manufacturing and Biomechanics. Porto 15-18 July 2025
DOI: https://doi.org/10.24840/978-972-752-323-8

PAPER REF: 22462

EXPERIMENTAL EVALUATION AND NUMERICAL SIMULATION OF HIGH-SPEED MILLING OF INCONEL 718 USING CERAMIC TOOLS

Marcos Valério Ribeiro[1,2], Necati Uçak[1,3(*)], Ahmed Razin[1], Jose Outeiro[1]

[1]Digital Engineering for Advanced Manufacturing Laboratory (DEAM Lab), Center for Precision Metrology, Department of Mechanical Engineering and Engineering Science, University of North Carolina at Charlotte, Charlotte, NC, 28223, United States
[2]Department of Materials and Technology, São Paulo State University, Av. Ariberto Pereira da Cunha 333, Guaratinguetá, SP, 12516-410, Brazil
[3]Department of Mechanical Engineering, Faculty of Engineering and Natural Sciences, Ankara Yıldırım Beyazıt University, 06010 Ankara, Türkiye
[(*)]*Email:* nucak@charlotte.edu

ABSTRACT

In this study, high-speed machining of Inconel 718 was investigated using SiAlON ceramic tools with different cutting parameters under dry conditions. For that purpose, a series of face milling tests combined with 3D numerical simulations were performed at cutting speeds of 700, 914, and 1219 m/min, feeds per tooth of 0.076, 0.102, and 0.152 mm/tooth, an axial depth of cut of 1.5 mm, and a radial depth of cut of 24.3 mm. The cutting performance was evaluated in terms of measured and simulated forces, temperature, tool wear, and surface integrity.

Keywords: Inconel 718, high-speed machining, Finite Element Method (FEM), tool wear, surface integrity.

INTRODUCTION

Inconel 718 is one of the most widely used nickel-based super alloys in critical industries such as aerospace, automotive, and energy due to its high mechanical and physical properties especially at high temperatures and severe working conditions (Bartolomeis et al. 2021). However, it is also considered a difficult-to-cut material as a result of its high strength, work hardening tendency, and built-up edge formation (Zhang et al. 2024). Under dry and high-speed machining conditions, these inherent properties result in substantial thermo-mechanical loads, contributing significantly poor surface integrity and accelerated tool wear (Shu et al. 2024). Therefore, improvement of tool performance and productivity in machining operations of Inconel 718 is considered as a major challenge (Bartolomeis et al. 2021).

In this study, the evolution of forces in axial, feed, and transverse directions and thermo-mechanical loads acting on the machined surface at different cutting speeds (700-1219 m/min) and feeds per tooth values (0.076-0.152 mm/tooth) were investigated in high-speed face milling of Inconel 718 in down milling direction. The tests were performed under dry conditions using SiAlON ceramic inserts (Kyocera 6030) placed in a toolholder (Seco R220.26-0050-RN1204.6A) with six cutting inserts. It was aimed to improve process productivity by investigating the high-speed machining performance of Inconel 718 while ensuring the surface integrity required for the application through experimental approaches and digital technologies.

RESULTS AND CONCLUSIONS

Figure 1a shows the numerical model developed in Abaqus FEA software to simulate face milling operation. The employed material properties and parameters of constitutive models (Johnson-Cook plasticity and damage) used in simulation of the processes can be found in references (Zhang et al. 2024) and (Shu et al. 2024). Figure 1b show the measured forces depending on employed cutting parameters. The maximum forces were observed in axial direction while the minimum forces were measured in the feed direction under all conditions. This can be associated with the selected low depth of cut value (1.5 mm) in comparison to large nose radius value (12.7 mm). In general, increase in cutting speed led to a decrease in forces due to higher thermal loads acting between tool and workpiece interfaces. In case of transverse forces, higher feed per tooth values led to higher cutting forces due to the increased mechanical loads. Similar results were also observed in case of axial forces except the lowest feed per tooth value. This can be attributed to ploughing dominant process conditions at low feed per tooth. The tool wear tests performed at the cutting speed of 914 m/min and feed of 0.102 mm/tooth showed that a maximum flank wear value of 0.54 mm was reached after a machining time of 16 s.

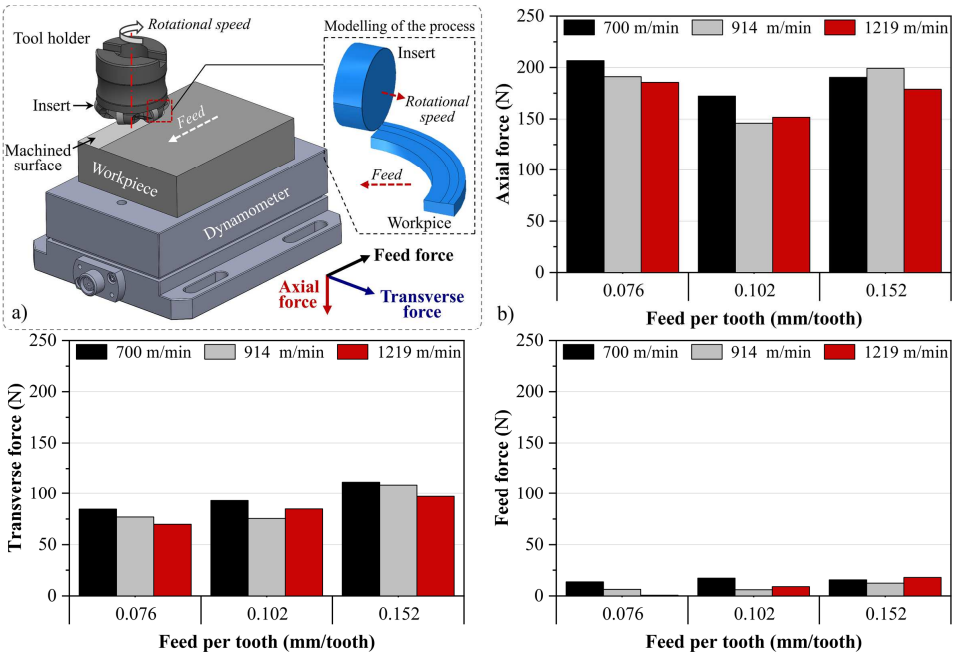

Fig. 1 - a) Numerical model and b) measured forces.

Future studies will focus on experimental/numerical investigation of tool wear and surface integrity characteristics of machined surfaces including surface roughness, surface and subsurface residual stresses, microstructural changes, and subsurface hardness variation.

REFERENCES

[1] De Bartolomeis A, Newman ST, Jawahir IS, Biermann D, Shokrani A. Future research directions in the machining of Inconel 718. J Mater Process Technol 2021, 297, 117260.

[2] Zhang P, Wang S, Zhang J, Sun Y, Zhou H, Yue X. Research on high speed machining mechanism and tool wear mechanism of nickel-based superalloy 718. Vacuum 2024, 229, 113538.

[3] Shu A, Ren J, Zhou J. Mechanical properties of machined surface for high-speed machining Inconel 718 considering microstructural evolution. J Manuf Process 2024, 124, pp.1143-1158.

Proceedings IRF2025: 8th International Conference on Integrity-Reliability-Failure
In Engineering, Materials, Manufacturing and Biomechanics. Porto 15-18 July 2025
DOI: https://doi.org/10.24840/978-972-752-323-8

PAPER REF: 22463

DEVELOPMENT OF A DIGITAL TWIN OF AN INTELLIGENT ROBOT-ASSISTED FINISHING SYSTEM FOR POLISHING METAL ADDITIVE MANUFACTURED COMPONENTS

Jose Outeiro[1(*)], Tero Kaarlela[2], Necati Uçak[1], Noel Greis[1], Harish Cherukuri[1]

[1]Digital Engineering for Advanced Manufacturing Laboratory (DEAM Lab), Center for Precision Metrology, Department of Mechanical Engineering and Engineering Science, University of North Carolina at Charlotte, 9201 University City Blvd., Charlotte, 28223, NC, USA
[2]Department of Production Technology, Centria University of Applied Sciences, Ylivieska 84100, Finland
[(*)]*Email:* jc.outeiro@charlotte.edu

ABSTRACT

This paper presents the design and deployment of a Digital Twin (DT) of an Intelligent Robot-Assisted Finishing System (iRAFS) for finishing components obtained by Metal Additive Manufacturing (MAM). This DT is a digital representation of the physical system (iRAFS), composed of a centrifugal disc finisher assisted by a collaborative robot to hold the component and to control its movements inside the media during the finishing process. The DT integrates a bidirectional communication for real-time data acquisition and process control to enhance the precision and efficiency of the finishing process of MAM. It is used for monitoring, programming and controlling the physical system, reducing the downtime thus improving productivity. This work establishes a foundation for the implementation of intelligent DT-driven systems in advanced manufacturing, promoting productivity and process reliability.

Keywords: Digital Twin, Robotic, Drag Finishing, Additive Manufacturing.

INTRODUCTION

Additive manufacturing (AM)is one of the advanced manufacturing methods, enabling the production of components from a three-dimensional model by joining materials layer by layer [1]. To increase the overall utility and profitability of AM, automated and flexible methods are required for the finishing process of AM production. The key to increasing AM profitability is to adopt advanced technologies such as robotics for the finishing process. While collaborative robots feature advanced functionality for human-robot collaboration, the programming methods remain primitive. Programming using the teach pendant requires expertise in the specific robot model and the physical presence of the operator. Replacing the teach pendant by a more user-friendly programming option that does not require programming is necessary. While hand-guiding provides a user-friendly programming option, physical presence and production interruption are necessary to program robots. Although utilizing VR as a high-level user interface for programming and teleoperating robots has been studied previously, the previous solutions do not offer location and time-independence [2]. Web-based eXtended Reality (WebXR) enables device-independent VR application development and distribution [3]. In addition, Message Queuing Telemetry Transport (MQTT) enables authentication, authorization, and encryption to ensure cybersecure CPS implementation.

This paper presents an intelligent DT-driven approach for location-independent robot programming. The presented approach utilizes virtual reality (VR) as the high-level user interface and MQTT communication protocol to provide a location- and time-independent way to teleoperate and program a collaborative robot. The focus is on teleoperation, monitoring, and

programming a collaborative robot for AM finishing applications. The presented approach extends the previous work [2] by adding location and time-independence to increase production flexibility.

RESULTS AND CONCLUSIONS

A DT of an Intelligent Robot-Assisted Finishing System (iRAFS) was developed. This system is illustrated in Figure 1 and is composed of (1) a centrifugal disc finisher from Mass Finishing model RF-50, (2) a collaborative robot from Universal Robot model UR30 mounted in a (3) pedestal in granite. This system is installed in the Depart. of Mechanical Engineering and Engineering Science at the University of North Carolina at Charlotte. As a complete digital representation of the physical system (iRAFS), this DT integrates a bidirectional communication for monitoring, programming and controlling the physical system, reducing the downtime thus improving productivity.

This DT is operated through WebXR user interface built using the Unity game engine to enable a realistic environment for the robot teleoperator. The components and kinematics of the robot are based on the model files at ROS industrial package. The communication layer is based on the MQTT protocol. Both MQTT broker and WebGL-based DT are hosted on a cloud server to enable location-independent teleoperation. Fig. 1 shows both physical and digital twins.

The presented DT-driven approach enables device and location-independent programming and teleoperation of a collaborative robot manipulating 3D-printed metallic components in a centrifugal finisher. The presented approach does not require expertise in robotics or the utilization of a teach pendant. This DT was tested using several XR headsets including Apple Vision Pro and Meta Quest.

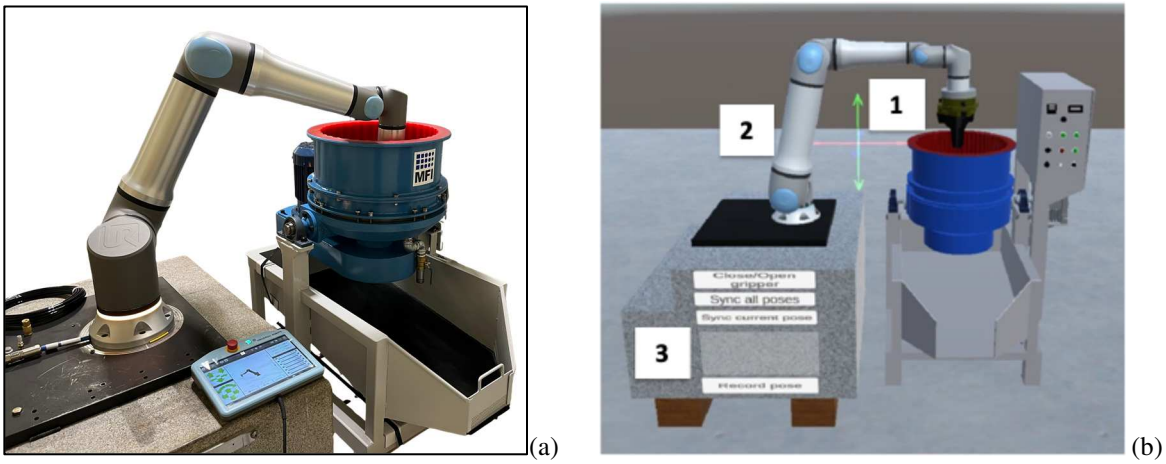

(a) (b)

Fig. 1 - (a) Physical system (iRAFS) and corresponding (b) Digital Twin.

REFERENCES

[1] B. Bigliardi, E. Bottani, E. Gianatti, L. Monferdini, B. Pini, A. Petroni, Sustainable additive manufacturing in the context of industry 4.0: a literature review, Procedia Computer Science 232 (2024), pp.766-774, 5th International Conference on Industry 4.0 and Smart Manufacturing (ISM 2023). https://doi.org/10.1016/j.procs.2024.01.076.

[2] G. Garg, V. Kuts, G. Anbarjafari, Digital twin for fanuc robots: Industrial robot programming and simulation using virtual reality, Sustainability 13 (18) (2021). https://doi.org/10.3390/su131810336,

[3] J. Gonzales, Run webassembly with apache, https://wasmlabs.dev/articles/apache-mod-wasm/ (2022).

Proceedings IRF2025: 8th International Conference on Integrity-Reliability-Failure
In Engineering, Materials, Manufacturing and Biomechanics. Porto 15-18 July 2025
DOI: https://doi.org/10.24840/978-972-752-323-8

PAPER REF: 22578

MEMETIC-BASED BIOGEOGRAPHY HYBRID ALGORITHM FOR OPTIMIZATION OF MECHANICAL SYSTEMS

Arcílio Carlos Ferreira Peixoto[1(*)], Carlos Conceição António[2]

[1]Faculty of Engineering, University of Porto, Porto, Portugal
[2]INEGI/LAETA, Faculty of Engineering, University of Porto, Porto, Portugal
[(*)]*Email:* up202209749@up.pt

ABSTRACT

The science of biogeography was described through mathematical equations in 1967 by Robert MacArthur and Edward Wilson. In 2008, Dan Simon presented an algorithm called biogeography-based optimization, or BBO, which used some of the principles and definitions described in MacArthur and Wilson's book. The objectives of this work were to study the behavior of the BBO method when it is hybridized with other evolutionary search methods and to analyze the effect of its application to some examples of mechanical engineering systems. Alongside some BBO modifications used in the literature, the operators considered in the hybridization study are the genetic recombination (crossover) and the local search, aiming to overcome the limitations and difficulties that arise when using the original BBO.

Keywords: Memetic algorithms; biogeography-based optimization; population-based algorithms.

INTRODUCTION

Engineering problems have become increasingly complex, making their analytical resolution practically impossible to complete in many situations. Numerical solution methods have, therefore, been given greater focus. Optimization, which fits into this category, has become one of the most pivotal subjects in the day-to-day of a modern engineer specifically because there is not an area in engineering where optimization is not involved in some way. Biogeography is the study of the distribution of species and ecosystems in geographical space over geological time (Wilson and MacArthur, 1967). Biogeography-based optimization is an evolutionary algorithm (EA), introduced in 2008 by Dan Simon (Simon, 2008), that optimizes a function by iteratively and stochastically improving its solutions according to a quality measure or fitness function.

BBO APPROACH MODEL

The science of biogeography, created in the 19th century, was considered to be descriptive and historical, but in 1967, Robert MacArthur and Edward Wilson published The Theory of Island Biogeography (Wilson and MacArthur, 1967), where they tried to describe this phenomenon in mathematical equations. These models have tried to describe how species move from one island to another, how new species appear, and how they become extinct.

BBO is a population-based global optimization algorithm, proposed by Dan Simon in 2008 (Simon, 2008). As it is implied, this method uses the science of biogeography, that represents the study of the distribution of species over time and space, to study the search space in search of an optimum point. The BBO algorithm uses the models described by MacArthur and Wilson

(Wilson and MacArthur, 1967), to represent the different process of biogeographical evolution, such as habitats, migration and cataclysmic events. In this algorithm each solution is considered a habitat, where its suitability to preserve life will represent the fitness of the Genetic Algorithms. A habitat with a high habitat suitability index (HSI) will represent a solution with good fitness while a poor habitat (a habitat with low fitness) will have a low HSI. The algorithm will then evolve its solution to maximize (or minimize) the HSI of the best solutions by emigrating and immigrating features of the different habitats. Good solutions are associated with habitats with high HSI, while habitats with low HSI are associated with bad solutions. Solutions with high HSI are more resistant to change, so solutions with high HSI tend to share characteristics with low HSI solutions. The diversity of individuals is related to HSI, so when an individual arrives in a habitat with low HSI, the habitat's HSI tends to increase.

Migration Operator

This process uses the migration rates of each solution to probabilistically share information between habitats. The immigration rate λ_S is used to determine whether a selected characteristic of each solution will change. If a given solution S_i has a characteristic which is selected to enter the migration process, then the emigration rate μ_S of the other solutions will decide which of the solutions will migrate a characteristic (SIV) to this solution S_i. This process is quite similar to other reproduction processes from GAs, but this method differs from them in a very important aspect. In GAs, reproduction by recombination is used to create new solutions, while BBO migration is used to modify existing solutions. It is, therefore, possible to say that, unlike the reproduction process of the GA, the migration of the BBO is an adaptive process. The migration rates, presented in (Zheng, Sueqin, Zhang, and Chen, 2019), are then given by,

$$\lambda_S = I\frac{n}{n} \tag{1}$$

$$\mu_S = E\left(1 - \frac{i}{n}\right) \tag{2}$$

where E represents the point where the emigration rate reaches its maximum, I represents the point where the immigration rate reaches its maximum (normally $E = I = 1$), i represents the solution ranking after being placed in descending order and n represents the number of solutions on the population.

The use of linear models to describe the migration process is usually sufficient in the optimization algorithm. But Ma (Ma, An analysis of the equilibrium of migration models for biogeography, 2010) also presented several different options to describe the migration operator, such as the trapezoidal and sinusoidal model, which have been used to obtain several good results (Peixoto and António, 2025).

Ma and Simon also presented a new variation of the migration operator in their algorithm, named blended BBO (Ma and Simon, Blended biogeography-based optimization for constrained optimization, 2011). This change created a migration operator that mixes each component of an immigrating solution (H_i) with the corresponding component of the emigrating solution (H_j), as follows:

$$H_i'(d) = \alpha H_i(d) + (1-\alpha)H_j(d) \tag{3}$$

where α is a number between $[0,1]$, which can be a predetermined or random value.

Mutation Operator

Cataclysmic events can drastically change the HSI of a natural habitat, this process is represented in this algorithm as a mutation on the SIV of a solution. Each element of the population has an associated probability, which indicates the probability of expecting a priori that there is a solution to the problem in question. Solutions with a very low or very high HSI are equally unlikely to mutate and solutions with a medium HSI are relatively likely. If a solution S has a low probability P_i, then the probability of it being mutated is high. On the other hand, a solution with a high probability will have fewer opportunities to mutate. This can be implemented, using the following formula,

$$m_i = m_{\max}\left(\frac{1 - P_i}{P_{\max}}\right) \tag{4}$$

where $m_{\max}$ is a parameter defined by the user, that represents the maximum mutation rate and $P_{\max}$ is the maximum of P_i in the population, P_i is then calculated as,

$$P_i = \begin{cases} P_0 = \dfrac{1}{1 + \sum_{k=1}^{n} \dfrac{\lambda_0 \lambda_1 \dots \lambda_{k-1}}{\mu_1 \mu_2 \dots \mu_k}}, & i = 0 \\ P_i = \dfrac{\lambda_0 \lambda_1 \dots \lambda_{i-1}}{\mu_1 \mu_2 \dots \mu_i \left(1 + \sum_{k=1}^{n} \dfrac{\lambda_0 \lambda_1 \dots \lambda_{k-1}}{\mu_1 \mu_2 \dots \mu_k}\right)}, & 1 \le i \le n \end{cases} \tag{5}$$

This method makes it possible to improve solutions with low HSI. Furthermore, with the use of elitism, which guarantees that the best solutions are kept in the study space, mutation adds some guarantee that the algorithm won't get stuck in a local optimum.

Hybridization Operators

The performance of the standard algorithm, when subject to some problems of optimization of mechanical systems (Peixoto and António, 2025), was lacking. With the algorithm having several issues on the final generations of its process. But it also showed great promise in its initial generations, where the global search was a bigger factor. So, a couple of modifications were introduced to improve the quality of the performance of the algorithm.

Initially, a mutation cycle, in which the mutation operators are used several times in the same generation, only allows for the addition of improved solutions. A solution injection process (Conceição António, A multilevel genetic algorithm for optimization of geometrically nonlinear stiffened composite structures, 2002; Conceição António, A hierarchical genetic algorithm for reliability based design of geometrically non-linear composite structures, 2001) was also added, where the last 10 % of the population was replaced by new solutions at the end of each generation. All these processes were added in an initial iteration of the studies to improve the diversity of the algorithm's population.

Then a recombination process through crossover was added to the algorithm to improve the exchange of genetic information. For the implementation of these operators, it was also necessary to implement a binary decoder and encoder since most of the operators and heuristics of the BBO method are in the real domain. Three operators, the single-point crossover (SP) (António, 2022), multi-point crossover (MP) (António, 2022), and the uniform crossover (U) (Eshelman, Caruana, and Schaffer, 1989). Recombination processes are based on the selection of a couple for each child that will be generated, these are called Mating Selection Mechanisms. This work used studied two different MSM.

The first one is denoted by *Independent Selection-based Fitness* (ISbF), and it is proceeded as follows:

The current population is divided into two groups according to the fitness of each solution, the best (elite) group and the worst group of solutions (Conceição António, A multilevel genetic algorithm for optimization of geometrically nonlinear stiffened composite structures, 2002). Each group provides a parent, which is selected through a roulette method (equation 3.1). The two stochastic procedures are independent. Then the offspring created will all be placed in the population, replacing every solution not belonging to the elite.

$$P\left(\boldsymbol{x}_j^k\right) = \frac{f\left(\boldsymbol{x}_j^k\right)}{\sum_{j=1}^{N_{\text{pop}}} f\left(\boldsymbol{x}_j^k\right)} \tag{4}$$

where $f\left(\boldsymbol{x}_j^k\right)$ represents the fitness value of the solution and N_{pop} the size of the population.

The second strategy for MSM, denoted by Previous Elites-based Selection (PEbS), is proceeded as follows:

The first parent is selected from the current population with a probability equal to the migration rate (proportional to rank position). The second parent is selected randomly from the best solutions stored in previous generations. Then, the offspring created by crossover will be evaluated. The new population will be composed using the best solutions from the current population and the offspring. The enlarged population is sorted by fitness, and the worst individuals are eliminated to restore the original size of the population.

A Hooke-Jeeves algorithm was also added as a local search optimizer, to improve the final generations' performance. This operator will allow for an improvement of the search velocity, allowing for the algorithm to reach the end solution with greater ease. The Hooke-Jeeves method is common in the world of optimization, since it allows for an efficient search for spaces of great dimensions, even if the objective function is very complex. This method and its parameters were altered, so that its performance and synergy with the other operators was greatly improved.

RESULTS AND CONCLUSIONS

The algorithm was applied to four different examples in the mechanical systems area. The first example focused on the minimization of the cost of a welded beam design. This non-linear problem was subject to a different number of constraints, ranging from the displacements to the size constraints and the allowable stresses. The results obtained were compared to a reference value retired from the literature (Help, s.d.). The second example also wanted to minimize the cost of a mechanical system, this time a welded gusset design, having constraints related to its size and allowable stresses. The results were also compared to a reference value from the literature (Gonçalves, 2023), which was obtained from a genetic algorithm with local search and controlled mutation. The third example required the minimization of the potential energy of a spring and weight system. This ten variable problem only had constraints related to its size and shape, to impede the possibility of interference between nodes. This examples' reference value was obtained from (Vanderplaats, 1984). Finally, the fourth example represented the optimization of a 10-bar truss problem by minimizing the weight of the system, through the reduction of the area. The reference value was obtained from a augmented genetic algorithm

(Aminifar, Aminifar, & Nazarpour, 2013). The best results, obtained from the fully hybridized algorithm, are exposed and compared to the reference values are in Table 1.

Table 1 - Best result obtained for the four examples.

Example	Best Value	Reference Value
1	1.7192	1.7248523085
2	3214.375	3228.13
3	-4416.36	-4416
4	2182.267	2261.42

The results shown above all surpass the reference values obtained from the literature, so it is possible to say that the algorithm had a good performance overall. It is important to note that these were the best results obtained from the fully hybridized algorithm, which means, the BBO including the blended migration approach (Ma and Simon, Blended biogeography-based optimization for constrained optimization, 2011), crossover operators and a Hooke-Jeeves local search method. The original algorithm, without modifications, didn't obtain good values, due to the lack of population diversity in its final generations, but showed great promise with its great global search in the initial generations.

There was also a necessity to perform some statistical tests, to better understand the impact of the new additions to the method. For that, the Friedman (Friedman, 1937) and Wilcoxon (Wilcoxon, 1945) test were used. The average results for the different statistical tests are presented in Table 2.

Table 2 **-** Average results from the statistical tests.

Test	P-Value
Migration	0.773111
Mutation	0.23349
Crossover	0.287532
Crossover Operators (PEbS)	0.392943
Crossover Operators (ISbF)	0.465267
Local Search	0.056681

As it is possible to note from the table above, the inclusion with the most significance was the local search having the lowest average P-value. The inclusion of the crossover also had some significance, even though not as much as the difference between the two mutation operators. Of all the different inclusions and different operators, the different migration operators (not shown in the table) had the least amount of significance, having the highest average P-value.

REFERENCES

[1] Aminifar, F., Aminifar, F., Nazarpour, D. (2013). Optimal design of truss structures via an augmented genetic algorithm. Turkish Journal of Engineering & Environmental Sciences, 37, pp.56-68.

[2] António, C.C. (2022). Optimization of Mechanical Systems. Porto: Efeitos Gráficos.

[3] António, C.C. (2001). A hierarchical genetic algorithm for reliability based design of geometrically non-linear composite structures. Composite Structures, 54, pp.37-47.

[4] António, C.C. (2002). A multilevel genetic algorithm for optimization of geometrically nonlinear stiffened composite structures. Struc. Multidisc. Optim., 24, pp.372-386. doi:10.1007/s00158-002-0249-4.

[5] Eshelman, L., Caruana, A., Schaffer, J. (1989, June 4-7). Biases in the crossover landscape. Proceedings of the third international conference on genetic algorithms, pp.10-19.

[6] Friedman, M. (1937). The use of ranks to avoid the assumption of normality implicit in the analysis of variance. Journal of the American Statistical Association, 32(200), pp.674-701.

[7] Gonçalves, H.F. (2023). Development and implementation of memetic models for the optimal design of mechanical systems. Porto: Faculdade de Engenharia da Universidade do Porto.

[8] Help, M. (n.d.). Welded Beam Design Optimization. (MAPLE) Retrieved Março 2024, from https://www.maplesoft.com/support/help/maple/view.aspx?path=applications%2FWeldedBeam.

[9] Ma, H. (2010). An analysis of the equilibrium of migration models for biogeography. Information Sciences, 180, pp.3444-3464.

[10] Ma, H., Simon, D. (2011). Blended biogeography-based optimization for constrained optimization. Engineering Applications of Artificial Intelligence, 24, pp.517-525.

[11] Peixoto, A.C., António, C.C. (2025). Memetic-Based Biogeography Optimization Model for the Optimal Design of Mechanical Systems. Mathematics, 13(3), 492. doi:https://doi.org/10.3390/math13030492.

[12] Simon, D. (2008). Biogeography-based optimization. IEEE Transactions on Evolutionary Computation, 12(6), pp.702-713.

[13] Vanderplaats, G.N. (1984). Numerical optimization with MATLAB Programming. New York: McGraw Hill.

[14] Wilcoxon, F. (1945). Individual Comparisons by Ranking Methods. Biometrics Bulletin, 1(6), pp.80-83.

[15] Wilson, E.O., MacArthur, R. (1967). The Theory of Island Biogeography. Princeton: Princeton University Press.

[16] Zheng, Y., Sueqin, L., Zhang, M., Chen, S. (2019). Biogeography-Based Optimization: Algorithms and Applications. Beijing: Science Press Beijing.

Proceedings IRF2025: 8th International Conference on Integrity-Reliability-Failure
In Engineering, Materials, Manufacturing and Biomechanics. Porto 15-18 July 2025
DOI: https://doi.org/10.24840/978-972-752-323-8

PAPER REF: 22723

DYNAMIC TRACKING WITH INTELLIGENT COLLISION AVOIDANCE BASED ON OCTREE STRUCTURE FROM POINT CLOUD FOR AUTOMATIC COLLABORATION

Wen-Yang Chang[1,2(*)], Zi-Wei Wang[1], Zheng-Xun Huang[3]

[1]Department of Mechanical and Computer-Aided Engineering, National Formosa University, Yunlin, Taiwan.
[2]Smart Machine and Intelligent Manufacturing Research Center, National Formosa University, Yunlin, Taiwan.
[3]National Formosa University, Department of Power Mechanical Engineering, Yunlin, Taiwan.
[(*)]*Email:* wenyang@nfu.edu.tw

ABSTRACT

The intelligent technologies and the automation industries have become the modern trend in recent years. Specially, the robots and AGVs (Automated Guided Vehicle) are also many applications in various industries and thus become one of the indispensable machines in the assembly line. However, the probability of collision among robots, AGVs, machines, and people etc. is very high during complex works. Therefore, this paper studies the intelligent system of collision avoidance based on octree structures from point cloud for automatic collaboration using dynamic 3D point cloud tracking. For the intelligent system of collision avoidance, the point cloud model firstly achieves tracking the 3D pose of the robot by the octree radius search. Second, the system detects people and machines entered the scene by octree point cloud change detector. A minimum distance between the point cloud models of the object and the robot for collision avoidance is calculated by the octree point cloud search. Finally, the connection between the intelligent system of collision avoidance and the robot controller is the TCP/IP protocol. The results showed that the system calculation time of each frame for collision avoidance is about 0.067s and the distance error of collision is 0.76 cm when the linear velocity of the robot is 30 mm/s. The external objects can be captured and detected in real-time by the algorithm of the octree point cloud change detector for intelligent collision avoidance.

Keywords: Dynamic Tracking, Point cloud model, Collision avoidance, Real-time.

INTRODUCTION

In recent years, the artificial intelligent technology has gradually been introduced into the industry. During intelligent manufacturing, the robots, automated guided vehicles (AGV), autonomous mobile robots (AMR) have also been widely used in various fields which become the most important mechanical tools of dynamic moving. In addition, the demand for human, robot, or machine cooperation has been increasing in collaborative environment. The safety protection of collaborative environment in real time is also very paramount importance. However, it has been difficult to distinguish between the external force generated by a collision and intended contact for collaborative operation. Several approaches have been studied during the past years for collaborative environment, such as inertial sensors [1], laser scanners [2], vision-based approach [3,4], stereo vision system [5-6], or depth camera [7]. The inertial sensors depended on a special suit with sensors and the limitation of motion capture of the suit wearer only, where the surrounding is unmonitored. For laser scanners that provided high resolution but with relatively low processing speed, because each line of the scanned scene is

sampled separately and directly. In general, the depth camera processes the large point data to distinguish the external object that is generated by a collision and is intended contact for collaborative operation. Therefore, this paper studies the intelligent system of collision avoidance based on octree structures from point cloud for automatic collaboration using dynamic 3D point cloud tracking.

RESULTS AND CONCLUSIONS

Experimental Setup and Methods

The system setup mainly had a depth camera, 2 6-axis robots, a worktable with a vise as shown in Figure 1(a). The depth camera monitors the surrounding environment of the robot and generates point cloud model data, as shown in Figure 1(b). The model of the depth camera is Azure Kinect Developer Kit, which frame rate is 30 fps with USB type C connector. The resolutions of depth camera and color camera are 1MP and 12MP, respectively. The field of interest of width and the operating range are $120^{\circ} \times 120^{\circ}$ and 0.25 - 2.21 meters, respectively. The robot is a six-axis robot, model Fanuc M-16iB/20 with R-30iA controller. The payload, reach, and repeatability are 20 kg, 1667 mm, and 00.08 mm, respectively.

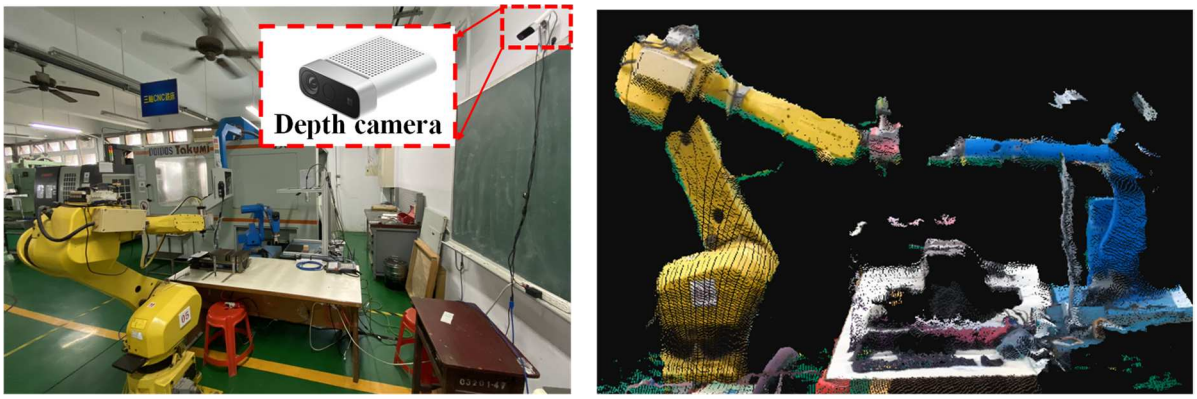

(a) (b)

Fig. 1 - Dynamic 3D tracking with intelligent collision avoidance (a) Experimental setup (b) Unprocessed point cloud of dynamic model.

Point Cloud Building Methods

The point cloud data is generated by a depth camera which uses Time-of-flight (ToF) theory [3]. The principles of ToF include the pulsed light theory and the continuous-wave modulated light theory. The depth camera mainly uses the continuous-wave modulated light theory to calculate the depths of the scene, as shown in Figure 2(a).

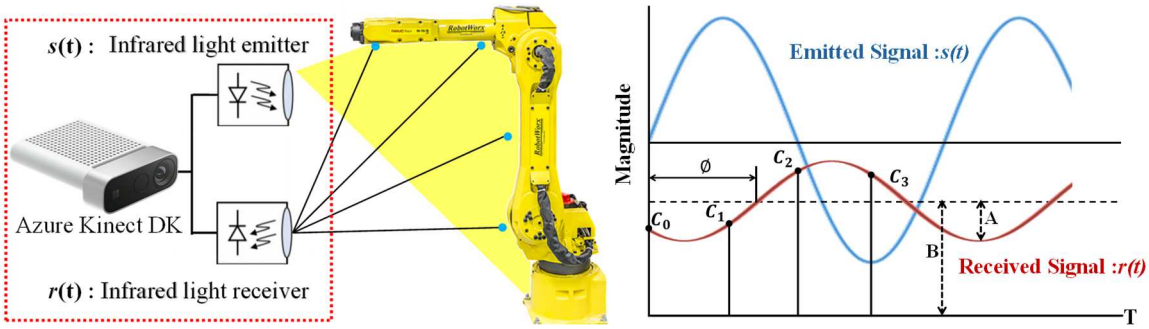

(a) (b)

Fig. 2 - Point cloud building using depth camera (a) Emitted and received signals of continuous-wave modulation (b) Cross-correlation of depth information.

The s(t) and r(t) are the optical powers of the emitted and received signals, as shown in formula below:

$$s(t) = a_1 \cos(2\pi f t) + a_2 \quad and \quad r(t) = A\cos(2\pi f t - 2\pi f \tau) + B$$

Where a_1, A and a_2, B are the amplitude and the offset of the modulated emitted and received signals, respectively. f is the signal frequency and τ is the time delay between the emitted and received signals, $\emptyset$=2πft is the phase shift. Figure 2(b) is the cross-correlation of depth information and the depth value d of the objects at each pixel is computed as follows formula:

$$d = \frac{c}{4\pi f}\emptyset = \frac{c}{4\pi f} tan^{-1}(\frac{C_3 - C_1}{C_0 - C_2})$$

Where c is the light speed, C_0, C_1, C_2,and C_3 are the time occupied by 0°, 90°, 180°, and 270° in the reflected wave, respectively.

Octree Structure from Point Cloud for Dynamic Change Detector

After modelling the point cloud model of the robot arm and its surroundings through Euclidean clustering segmentation, the point cloud model of the robotic arm needs to be monitored and performed dynamic tracking for intelligent collision avoidance. It is also necessary to detect external objects such as people or machinery that suddenly enter the scene during monitoring. Therefore, this study uses the algorithm of Octree point cloud change detector with fixed-radius near neighbours search [7] to detect the external objects. Assume that the search ball S(q,r) is defined by point q and radial r and the half of a side length of Octree cube is e. , as shown in Figure 3(a).

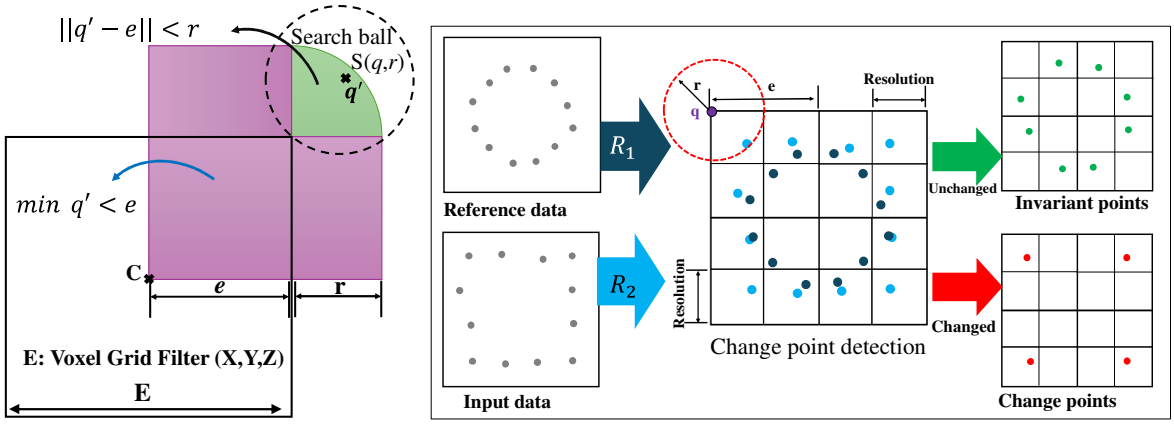

(a) (b)

Fig. 3 - Octree search. (a) a fixed-radius near neighbors search; (b) Cross-correlation of depth information.

Then, the Octree cube is detected to check if it overlaps with the search ball S(q,r) as bellow:

$$||q' - e|| < r \quad \text{where } max\ q' < e + r \text{ and } min\ q' < e$$

After this algorithm calculates each point q_i, we can obtain the change points and can know the spatial change between the points, as shown in Figure 3(b). Where resolution is the smallest voxel side length of octree cube, R_1 is the point cloud models of the robot and the surrounding environment, and R_2 is the point cloud model of the scene. In the intelligent system of collision avoidance, the system needs to detect and generate the point cloud models when any external objects enter the scene.

In order to monitor and prevent collisions for intelligent collision avoidance, it is necessary to continuously capture the point cloud model of the system in each frame for three-dimensional dynamic tracking. Each frame is originally classified by an algorithm of Euclidean cluster extraction. This algorithm calculates the minimum distance to cluster point cloud data between different groups by setting a threshold distance. The clustering definition formula of objective function, B_i, is as follows:

$$B_i = \sum_{j=1}^{k} \sum_{i=1}^{n} min||P_i^{(j)} - C_j||^2 \quad \geq D_{th}$$

Where k and n are number of clusters and number of cases, respectively. P_i and C_j are the case i and centroid cluster j of point cloud data, respectively. D_{th} is the maximum distance threshold. In order to perform grouping, each data point is assigned to the nearest cluster centroid. The nearest is typically determined using the Euclidean distance, as shown in Figure 4. The robot (blue), environment (black), and external (green) objects of point cloud are extracted using the Euclidean cluster. Then, the group collision (red) of point cloud based on Octree search distance (magenta) can be dynamically detected for intelligent collision avoidance

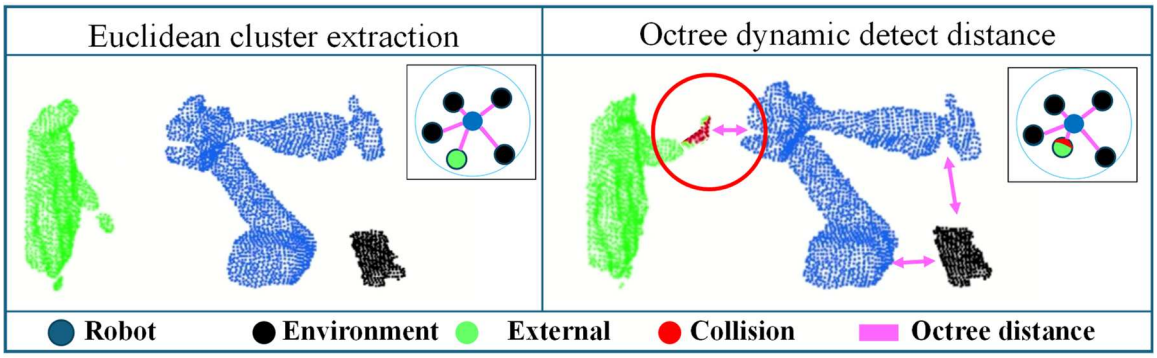

Fig. 4 - Dynamic tracking for intelligent collision avoidance based on Euclidean extraction and Octree distance detection.

For collision verification, the experiment mainly tested the errors of anti-collision detection at different distances. The distances for safe detection are 18, 20, 22,25, 27,30,32, and 35 cm. During experiment, the robot continuously operates at a fixed linear speed of 30 mm/s. The robot will immediately stop if the external objects enter the safe distance of collision avoidance. Then, the actual distance of collision avoidance was measured with 10 numbers of measurement, as shown in Figure 5(a). The range of average error is about 0.73 cm~0.925 cm and the range of average error rate is about 2.28%~4.78%, as shown in Figure 5(b). Results showed that the errors at different distances are stable when the robot arm moves at the same linear speed. The collision avoidance sy[1] stem have a fairly reliable system accuracy.

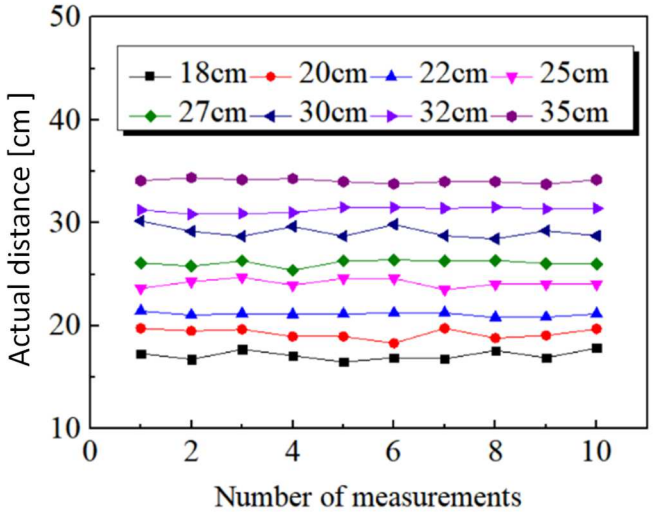

(a)

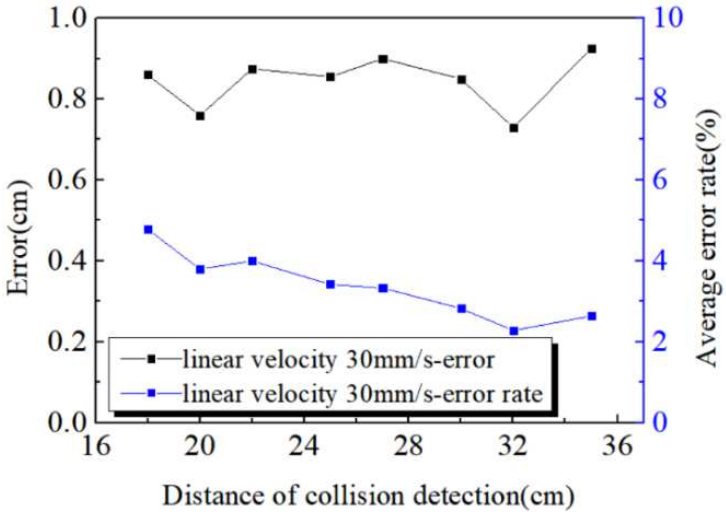

(b)

Fig. 5 - Anti-collision detection avoidance (a) Actual distance of collision avoidance at different distances (b) The errors and average error rate of different distances.

This study developed the real-time tracking system of 3D dynamic and the intelligent system of collision avoidance and obtained results summarizes as follows: The result of the real-time tracking system shows that the point cloud of the robot can track the 3D pose of the robot by the algorithm of the octree point cloud search. The results of the intelligent collision avoidance show that the external objects can be captured in real-time by the algorithm of the octree point cloud change detector and the system can detect collision.

REFERENCES

[1] Heonmoo K., Yosoon C., 3D location estimation and tunnel mapping of autonomous driving robots through 3D point cloud registration on underground mine rampways. Underground Space, 2025,22, pp.1-20.

[2] Mohammad S., Pedro N., Minimum distance calculation using laser scanner and IMUs for safe human-robot interaction, 2019 Robotics and Computer-Integrated Manufacturing, 2019, 58, pp.33-42.

[3] Thomas O. D., Stephen A. G., Alex A. G., Predicting uncertainty in vision-based satellite pose estimation using deep evidential regression, Aerospace Science and Technology, 2025, 160, p.110055.

[4] Yunliang J., Kailin L., Zhen Y., Haoyu Z., Xiongtao Z., Monocular visual anti-collision method based on residual mixed attention for storage and retrieval machines, Expert Systems with Applications, 2024, 255, p.124640.

[5] Victor M. N., Rasika R.M. A.,Zifu L., Ryozo N., Tofael A., Development of a Machine stereo vision-based autonomous navigation system for orchard speed sprayers, Computers and Electronics in Agriculture, 2024, 227, p.109669.

[6] Prasanth K.D., Naga P.B.M., Rajalakshmi P., Stereo vision based object detection for autonomous navigation in space environments, Acta Astronautica, 2024, 218, pp.326-329.

[7] Dong L., Chen S.H., Chen Z., Wu Y., Chu L.Y.L., Xue F., 4D point cloud-based spatial-temporal semantic registration for monitoring mobile crane construction activities, Automation in Construction, 2024, 165, p.105576.

Proceedings IRF2025: 8th International Conference on Integrity-Reliability-Failure
In Engineering, Materials, Manufacturing and Biomechanics. Porto 15-18 July 2025
DOI: https://doi.org/10.24840/978-972-752-323-8

PAPER REF: 22783

INTEGRATED TWIN-TRANSITION MATURITY MODEL: APPLICATION TO A MECHATRONIC SME

João N. Ruivo[1,2], A.J. Baptista[1], Américo L. Azevedo[1,2]

[1]INESC-TEC, Faculty of Engineering, University of Porto, Porto, Portugal
[2]Faculty of Engineering, University of Porto, Porto, Portugal
[(*)]*Email:* joao.ruivo@inesctec.pt

ABSTRACT

The increasing global awareness of climate change and its associated consequences pose new environmental, economic, and social challenges to businesses, with particular emphasis on small and medium enterprises (SMEs), who possess limited capacity and resources to adapt and meet established goals. One emerging concept to tackle this problem is that of Twin-Transition, which aims to combine both digital and green transitions. However, it is often unclear for companies (particularly SMEs) how they position themselves regarding this dual transition. This work conducted, initially, a state-of-art review of existing proposals and models in both digital and green domains focused on SMEs. Secondly, it integrated a previously developed Digital Maturity Assessment Model with an original Green Assessment one, combining two complementary concepts - Sustainability (following a Triple Bottom Line perspective) and Circularity (incorporating topics such as R-Strategies, "D-Strategies", Energy and Materials flows). Both areas were set to be assessed on a 5-level scale, with emerging concepts being integrated, such as the perspectives of Restoration and Regeneration on the Green Assessment. The proposed model was then applied to a company in the mechatronics sector for initial testing and validation.

Keywords: Twin-Transition, Maturity Model, Digital, Green, Sustainability, Circularity.

INTRODUCTION

The latest report from the Intergovernmental Panel on Climate Change (IPCC) has shed light on the significant impact of human activities on global warming, with global surface temperature rising by 1.1°C in 2011-2020 (Calvin et al., 2023). Despite efforts being made individuals, governments and enterprises, indicators tend to aggravate each year, leading to the European Union setting the goal to become carbon neutral by 2050 (The European Green Deal - European Commission, 2021). To achieve this, it has established, through the 'European Growth Model', 'Twin-Transition' (digital and green transitions) to be a key factor in the change needed (European Commission, 2021). However, it is still necessary to delve deeper into how these two transitions complement each other, as, for example, a fully digitalized green transition will make new solutions possible, but it may also make environmental performance data forgeries more likely (European Commission. Joint Research Centre., 2022). The difficulty to implement measures that will fulfil this transition tends to be higher for SMEs, which end up being more constrained in terms of their scope of action, due to a lack of support supply and lack of capital (Rizos et al., 2016). The aim of this work was to propose a novel Twin-Transition Maturity Assessment Model aimed at SMEs which have less resources to evaluate the sustainability of their business development models, when and if supported on digital tools. To achieve this model, there was an initial state-of-art review of most used structures, as well as,

key concepts identified as relevant to address in the created model. The obtained model was then applied to a Portuguese SME for testing and for a first real-based validation. This paper is structured as follows: firstly, an overview of the performed state-of-art review is carried out, regarding Twin-Transition, Digital Maturity Assessment, Green Maturity Assessment, existing maturity models and the main gaps identified; secondly, it describes the development of the proposed Maturity Model, detailing each one of its modules and sub-modules, as well as, the scales adopted for their assessment; finally there it is presented the results and analysis of the first application to a SME in the mechatronics sector.

STATE-OF-ART REVIEW

In order to map previous studies on existing Twin-Transition Maturity Assessment models on SMEs, the bibliographic research undertaken followed an organized approach by applying the following query at Scopus database:

((“Twin-Transition”) AND (Assessment OR Mapping OR Maturity OR Roadmap OR “Digital Transformation” OR Digitalization OR “Industry 4.0”) AND (Green OR Sustainability OR “Circular Economy” OR Circularity OR R-Strategies) AND (SME OR “Small Medium Size”))

Since the concept of Twin-Transition (TT) is very recent, the literature on maturity assessment models for SMEs are still scarce as well of success cases for the double transition. Nevertheless, despite the challenges, it is observed that while pursuing technological innovation, companies are still capable of making a Green transition (Rehman et al., 2023). The same way, (Chatzistamoulou, 2023) concludes that data supporting the idea that digital transformation can help with the transition to sustainability, and this effect seems to be consistent throughout the robustness checks that have been done. Moreover, (Chatzistamoulou, 2023) also argued that, in general, SMEs appear to be determined to adopt a sustainability enhancing strategy. In fact, the adoption of i4.0 technologies does allow companies to create their own roadmaps towards Circular Economy (CE), in the short, medium and long-term (Findik et al., 2023). (Findik et al., 2023) also observed that it was still not possible for them to observe the dynamic interactions between i4.0 technologies and CE practices. Regarding digitalization, companies should focus on the adoption of AI technologies, since they are strongly related to the ability of eco-innovating (Diodato et al., 2023). Likewise, digital investments do indeed spur the capability of eco-innovation (Montresor and Vezzani, 2022). (Li et al., 2023) concluded (albeit for the construction sector) that businesses should invest more in digital infrastructure and keep improving their digital capabilities because these are essential for attaining green innovation. (Ortega-Gras et al., 2021) concluded that CE can be highly boosted through the implementation of 3 specific i4.0 technologies: Big Data, AI, and IoT, to monitor energy consumption and dynamic analysis to support CE energy management. Nevertheless, a careless and excessive adoption of digital technologies can sabotage environmental objectives and targets, due to being too energy intensive, so it is important to recognize its potential but also its limitations (Bianchini et al., 2023). When studying the TT in Romanian SMEs, (Ogrean and Herciu, 2021) concluded that the first obvious step for any Romanian SME looking to build its future competitive strategy would be to conduct a thorough and impartial self-analysis on sustainability and digitization (compared to industry/national peers, benchmarking). As for a possible survey/maturity model and the scales used for measuring each question, (Mehedintu and Soava, 2022) argue that better results could be achieved if a quantitative and qualitative approach is taken. Regarding a possible organization model, (Burinskienė and Nalivaikė, 2024) proposed a 6-dimension framework to assess Twin-Transition, but they recognize it fails to consider government policies and regulatory environment, as well as the fact that 6 dimensions could fall short in evaluating TT. As for the implementation of a survey, when matters related

to TT are involved, typically there is a high dependency on external support, for clarifications, by participants (Perossa et al., 2023). The literature research identified different gaps presented in Table 1:

Table 1 - Results and gaps identified in the literature review.

Result/Gap	**Reference**
Digitalization does encourage the Green transition and SMEs are generally keen on making it. I4.0 technologies positively influence this, so they must be considered.	(Rehman et al., 2023) (Chatzistamoulou, 2023) (Findik et al., 2023) (Li et al., 2023) (Ortega-Gras et al., 2021)
Interactions between I4.0 technologies and CE practices should be studied.	(Findik et al., 2023) (Diodato et al., 2023) (Montresor & Vezzani, 2022)
Evaluating a company's maturity in these domains is desirable.	(Ogrean & Herciu, 2021)
TBL approach for Sustainability assessment could be of interest.	(Elkington, n.d.) (Spaltini et al., 2024)
It is important to study the implications diverse dimensions of digitalization can have on sustainability/CE dimensions.	(Bianchini et al., 2023) (Kumar & Sharma, 2024)
Considering the regulatory/government environment is relevant for the success of TT.	(Burinskienė & Nalivaikė, 2024)
An index that allows for an overall performance assessment could be useful.	(Benedetti et al., 2023)
Undertaking a maturity assessment model should be done, ideally, with external monitoring.	(Perossa et al., 2023)

METHODOLOGY

The proposed Maturity Model has its foundations on a sequential maturity assessment rational of both the Digital Maturity Assessment and Green Maturity Assessment, which were subsequently composed of different key modules, according to the frameworks and concepts identified on the literature review and original developments. Regarding the creation of the Digital Maturity Assessment Module, a deep analysis on an existing model by (P. Senna et al., 2023) was done, some updates were conducted (e.g. new trends such Generative Artificial Intelligence, Digital Product Passport traceability) and was used as a foundation for the proposed model.

This digital maturity assessment model is particularly appealing, as it focus on being generalizable, meaning it could be easily adapted to the mechatronics industry, which was the objective of this work and because at the time of its creation, existing gaps from other models were studied and addressed, such as the missing of key aspects regarding I4.0 and lack of alignment with current beliefs regarding the uptake of technology. This maturity model uses the Technology-Organization-Environment (TOE) framework, which was kept for this new one. In this context, the sub-modules that composed the Digital Module were:

- D1 - Technology;
- D2 - Organization;
- D3 - Environmental Context.

The D3's name differs from what is typical according to the TOE framework in order to avoid misconceptions with a new module for the Sustainability domain. Figure 1 presents the architecture for the maturity assessment model, where the digital assessment domain is on the left side of the diagram.

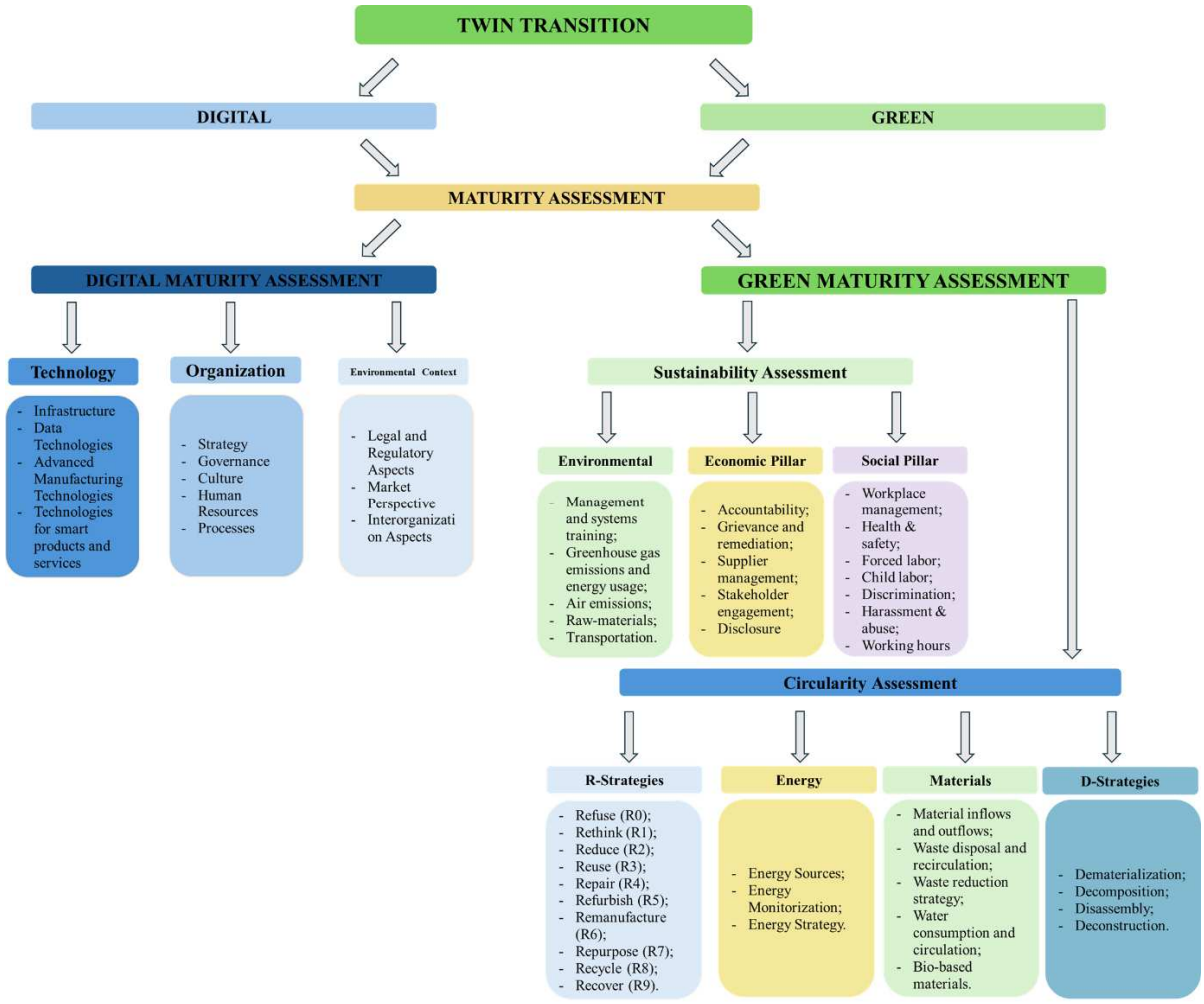

Fig. 1 - Maturity Model Overview.

D1 considers all relevant technologies to an organization which are already in use, available for purchase or in development/implementation phases through research, development and innovation actions. It takes into account the degree of complexity, the need for compatibility with current hardware and/or legacy systems, and the technologies being created for use in data-driven services or smart products (P. Senna et al., 2023). It also addresses vertical and horizontal integration, as well as communication and the exchange of information with external actors (P. Senna et al., 2023). D1 seeks to consider and assess any pertinent technology that is being used, developed, or in the process of being implemented. Its goal is to investigate the company's information sharing and communication with external actors, as well as its vertical and horizontal integration. The intricacy of the technologies being used, their compatibility with

current hardware, and the adoption of higher cyber-security standards are all discussed. It considers the technology incorporated into goods and services to allow for intelligent operation and autonomous features. Furthermore, it aims to comprehend the entire scope of information systems (IS) across the entire enterprise, including their architecture and integration, the technologies employed, and their compatibility, for both data-driven services and intelligent goods. It also assesses the degree of automation and the use of robotics. Lastly, the maturity model assesses how well the Digital Product Passport (DPP) is implemented and verifies which key technologies are either now in use or are slated to be deployed (P. Senna et al., 2023). D2 dimension regards the organization's profile, complexity of managerial structure, financial availability, as well as the digital strategy outlined. Moreover, aspects related to the workforce formal education, training, competencies, and skills, as well as the retainment of talent, are also part of the topics within this dimension. The connections established within, and between, internal subunits of a company can lead to innovative actions, which may be further enhanced through a greater decentralization of the organic structure. Finally, topics related to the business and operational processes of the organization, such as the engineering, production, planning and control, supply chain and quality management are also taken into account on the evaluation of the organization dimension (P. Senna et al., 2023). D3 dimension focuses on the organization's setting and its environment. It regards external factors, such as the market positioning, the opportunities for technological innovation from novel technologies, as well as the regulatory framework and funding opportunities. The intense and high-level competitive environment has been a stimulant to innovation since the 1960s, while the regulatory framework and funding opportunities are key factors in the adoption of digital technologies.

For the purpose of evaluating a company's maturity, the initial 6-level scale from (P. Senna et al., 2023) was normalized in 5 levels, where the two first levels where merged (Digitization and Communication):

- L1: I3.0 - Digitization and Communication - Generically, this level reflects that most processes are carried out manually or they are at the beginning of their digitization stage, thus not defined. The company has no knowledge of the scope and impact of digital technologies or I4.0. Conventional processes and business models remain standard, and there are few, if any, digital initiatives in place. Some systems may exhibit a simple structure and interconnectivity, and traditional communication and operation channels are still widely used;
- L2: I4.0 - Visibility - There are initial digitization initiatives as well as a digital strategy vision. Systems that allow for decision-making are being developed, supported by collected data and business visibility. For I4.0 concepts and technologies, there are official strategies and plans of action, the majority of which are still at planning or early development stages;
- L3: I4.0 - Transparency - The company has started establishing a digital culture and long-term vision. It is clear that knowledge is the basis for decision-making, with significant investments and defined strategies in place for the adoption of I4.0 technologies;
- L4: I4.0 - Predictability - A series of steps has been implemented to digitalize operations and processes. Digital culture and strategy are widely spread across all levels of the workforce. Maturity Model Development (D4G) 26 Forecasting future scenarios and events, as well as collecting real-time data, are the foundations for autonomous decision-making;
- L5: I4.0 - Flexibility/Adaptability - A series of actions have been deployed to digitalize operations and processes, with complete integration and full autonomy and self-adjusting

skills in every procedure. Employees undergo continuous education and training programs to solidify and improve both hard and soft skills. Within the hierarchy, career development and leadership are defined and nurtured. Smart products and data-driven services with servitization capabilities and supporting activities are available.

As (Münnich et al., 2023) state, there are various maturity models that aim to address either the current state of digitalization or sustainability, but very few aim to support both digital and green dimensions. Knowing this, an analysis on existing maturity models for the creation of the green module was done, trying to understand what was regarded as indispensable and gaps found. A key aspect taken in the development was to consider two independent (but complementary) modules in the Green Maturity Assessment: Sustainability and Circularity. The Ellen MacArthur Foundation, committed to creating a circular economy, developed a framework called Circulytics (Ellen MacArthur Foundation, 2020). In it, they intend to help companies monitor their performance regarding CE. It enables businesses to highlight their transformational achievements and pinpoint areas that require improvement, aligned with the three design-driven principles of CE: removing waste and pollution, reusing products and materials, and regenerating the environment (Ellen MacArthur Foundation, 2020).

A Green transition is only possible by combining two complementary concepts, sustainability and circularity, since as (Walker et al., 2022) concluded, circularity and sustainability are two distinct yet related concepts. Working towards a Circular Economy is a mean of achieving Sustainability, since CE can contribute positively to achieving positive sustainability impacts, including SDGs, but is not a sufficient condition (a given circular economy business can retrieve unsustainable operations for a company, either environmental or in social terms). Nevertheless, one key point that (Mang and Reed, 2020) highlight is that until recently, the main goals of sustainable and green practices were to reduce harm to the environment and public health, while making better use of resources. This effectively slows down the degradation of the planet's natural systems but is not sufficient for the level of current climate crisis that we face (global warming, pollution, or biodiversity losses). Furthermore, and as the literature shows (Calvin et al., 2023), the planet is still rapidly deteriorating, so this approach per se is not enough. To counter this, regenerative practices must be deployed, as they aim to create human systems that can coexist with natural systems, or evolve in a way that produces benefits for both parties and a higher overall expression of life and resilience, in addition to reversing the degradation of the earth's natural systems (Mang et al., 2016).For the creation of the Sustainability module, the Triple Bottom Line framework was used to group the necessary topics companies need to address and weigh how they are doing:

- S1 - Environment;
- S2 - Economic;
- S3 - Social.

S1 aims to evaluate whether the company has deployed an environmental management system and respective systems training, GHGs emissions and energy usage and transportation. S2 addresses economic-related matters, such as accountability, grievance and remediation, supplier management, stakeholder engagement, disclosure and facilities. S3 tackles questions regarding workplace management, health, safety, forced labour, child labour, discrimination, harassment and abuse, working hours and social inclusion. For this module, the topics chosen were selected according to what the literature review showed as most important. The topics for this module were:

- C1 - R-Strategies;
- C2 - D-Strategies;
- C3 - Energy; - assessing the implementation of renewable resources;
- C4 - Materials.

C1 aims to go through each R individually from the R-Strategies, as they were found to be a very useful tool to measure circularity, as it evaluates a different range of topics, from refusing to use raw materials on the creation of products, to recovering energy from discarded products, thus fostering circularity; C2 addresses D-Strategies, given that these could act as enablers for the R-Strategies. This D-Strategies suggestion includes Dematerialization, Decomposition, Disassembly and Deconstruction; C3 intends to evaluate several energy-related topics, to understand the main energy sources used by companies, the proportion between renewable and non-renewable, if there is active monitoring of consumptions and if there is a defined energy strategy defined, in order to reduce the overall energy consumption and/or improve energy efficiency. C4 aims to evaluate the material inflows and outflows, as well as waste management and water consumption strategies.

Given that the planetary situation has significantly worsened, as the IPCC report concluded, it was important to reinforce the idea that it is not enough to pursue eco-efficient actions to achieve carbon neutrality. Currently, it is more and more important that companies are aware of and pursue restorative and regenerative measures, that allow for the recovery of heavily degraded ecosystems and environments and to sequester carbon from the atmosphere. With this in mind, to evaluate a company's performance in the 2 proposed dimensions (and respective 7 modules), a 5-level scale was adapted from (Mang and Reed, 2020), that takes into consideration the up mentioned problematics:

- Conventional - Externalises all/most environmental/social topics which are not regulated (Staying within the law);
- Green - Focus on quality assurance, health and safety, code of conduct, some environmental/social initiatives (Less bad impact);
- Sustainable - Sustainability vision, CO2 carbon neutrality target and action plan, business focus missing (Not increasing additional harm);
- Restorative - Ambitious frontrunner implementing circular economy principles in strategy, business model and product/service design (Humans doing things to nature);
- Regenerative - Transformative leader: business strategy and R&D create success through holistically net-positive solutions (Humans doing things as nature);

Despite the implementation of a 5-level scale, since the restorative and regenerative actions are still in current research development and can be hard or for the moment impossible to apply in mechatronic companies, in some questions the 5th level was not used. Depending on the question, most were limited to level 2 (green), level 3 (sustainability) or level 4 (restorative) as it was considered that, as of today, it is still not possible in many cases to reach restorative or regenerative scenarios under existent technologies or procedures. With this approach, the objective was to mirror as realistically as possible a company's state, neither creating a better or worse looking scenario. Taking this into account, the maximum attainable limit, according to the complete list of topics covered in the Maturity Assessment Survey, for the Circularity module is 3.675 and for the Sustainability module is 3.

APPLICATION EXAMPLE AND RESULTS DISCUSSION

The proposed Maturity Model was applied to a Portuguese SME in the Mechatronics industry sector (to be addressed as Company A, for confidentiality purposes), for an initial testing of the developed TT assessment methodology. The overall results are shown in the tables (Table 1, 2, 3) below. Table 2 presents the results regarding the digital assessment with a global average of 3.74 of maturity for this company, which means that is close to a Predictability level (L4) and therefore in a good maturity.

Table 2 - Company A's Digital Maturity Assessment results

Digital Maturity Assessment				
Dimensions	Technology (max=5)	Organization (max=5)	Env. Context (max=5)	Average (max=5)
Company A	3.56	4.25	3.4	3.74

In regard to the sustainability assessment, the average for the company's maturity was 2.185, meaning that it is slightly above L2 ("Green" as "doings less bad actions") but this result affected as a poor result on Environmental component (1.46), doing just above what the regulations and laws oblige, where the economic and social were results was 2.6, so, no far away from the maximum value for the use scale.

Table 3 - Company A's Green Maturity Assessment - Sustainability results

Green Maturity Assessment – Sustainability				
Dimensions	Env.Sustainability (max=2.9)	Economic(max=3.2)	Social (max=2.9)	Total Green Average (max=3.3375)
Company A	1.46	2.6	2.6	2.185

On the circularity results, the maturity level was good on the R-Strategies 3.1/3.8, fair (L2 "Green") on the D-Strategies and Energy aspects 2/3.5 and 2/3.8 respectively, and 1.5/3.6 what is a poor result (L1 conventional actions and do accordingly to the regulations).

Table 4 - Company A's Green Maturity Assessment - Circularity results

Green Maturity Assessment – Circularity				
Dimensions	R-Strategies (max=3.8)	D-Strategies (max=3.5)	Energy(max=3.8)	Materials (max=3.6)
Company A	3.1	2	2	1.5

To better extract the maturity trade-offs between the digital and the green domains, the assessment Figure 2 presents the plot of results on the Digital Technology module versus the overall Green Maturity. This diagram allows the discoverey of the interactions between digital and green, namely by relating the pairs that maximize the TT maturity, and those that show more debility regarding the company's current status (operation and product wise). For company A, the pair Tech<>Green Maturity show the best results (both above Level 3). The

worse result is related to the pair Tech<>Environmental Sustainability, and Tech<>Materials (circularity module) that can relates to the need of doing more on the waste reduction level and to choose less environmental impact materials.

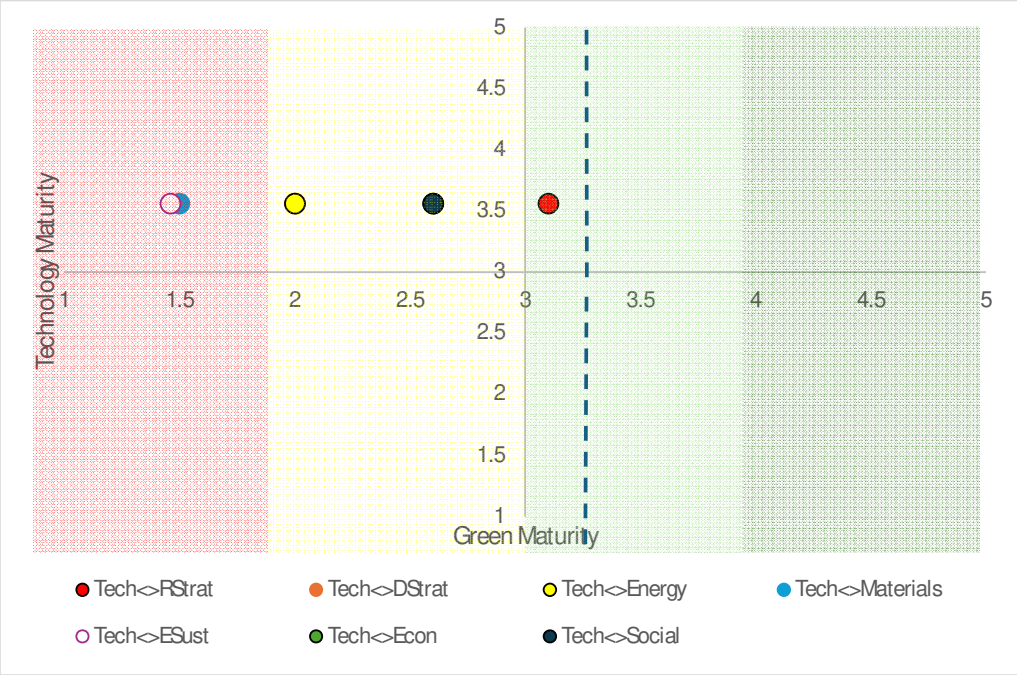

Fig. 2 - Company A's results, Technology-Green Pair.

Figure 3 presents the plot of Organization Maturity on the Digital domain versus the overall Green Maturity. The best result pair is Organization<>R-Strategies, with the Organization above 4th level (predictability) and above 3 on the green maturity (sustainable).

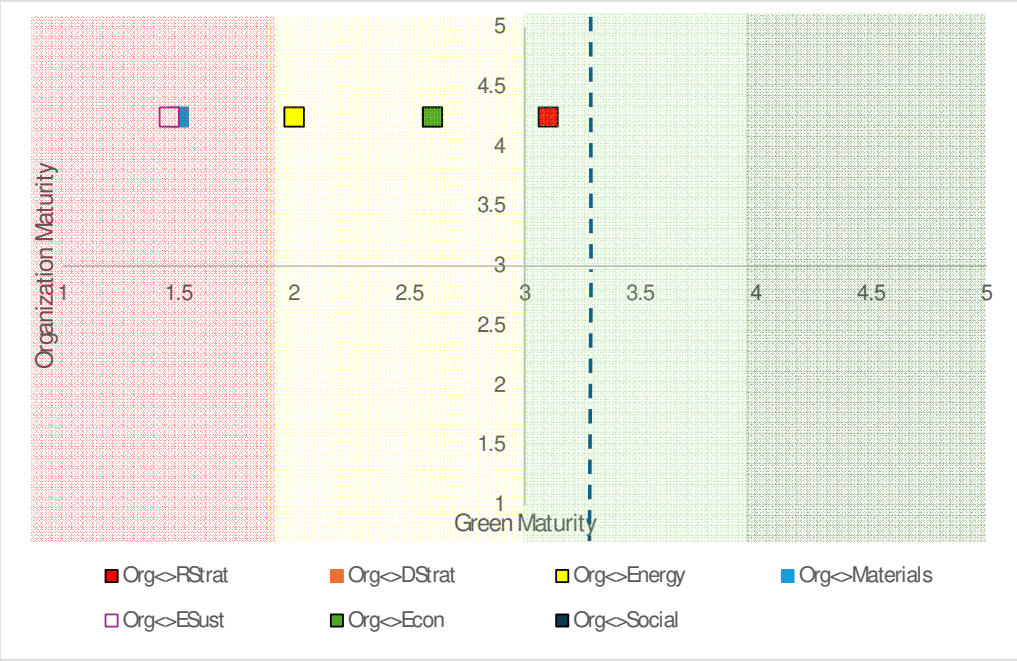

Fig. 3 - Company A's results, Organization-Green Pair.

As an overall conclusion, Company A's results show that it is well-established within i4.0, scoring high in all Digital modules and performing well in some Green modules (R-Strategies, Economic and Social. Despite its heavily advanced digital maturity, almost reaching level 4 on the Digital scale (Predictability), with solid advances in the implementation of the DPP standing out, there is room for improvement in the automation levels and the adoption of robotic technologies. It is important to understand that due to the company's nature, it can be difficult, as of now, to achieve better results in Materials module for circularity. Nevertheless, the implementation of an environmental management system and subsequent evaluation of environmental performance would be vital to improve the results obtained in the Environmental Sustainability module.

CONCLUSIONS AND FUTURE WORK

This paper presents an original Twin-Transition Maturity Assessment Model focused on Small and Medium Size companies' context and specificalities. The Digital dimension was based on a previously developed model by INESC TEC, with some changes and updating being made to better match the proposed context of SMEs and meet nowadays standards and trends. It managed to define a clear structure for the maturity assessment model through a literature review, which allowed for the key dimensions to be defined (TOE framework, Triple Bottom Line framework and main Circularity concepts). The model was tested in a real base assessment for a Portuguese Mechatronic SME. Despite the novel aspects introduced, that include an emergent measurement for "Green Development" by means of companies acting also in Restorative and Regenerative activities and operations, the model must be further tested in more companies, and in more industrial sectors. Moreover, it would be of high importance to develop an additional tool that could allow the study and bilateral analysis of the synergies between Digital and Green concepts, i.e., how higher digitalization levels may influence a company's Green performance and vice-versa. Such a tool would then allow concrete roadmapping to be carried out alongside companies that undertake the proposed Maturity Model.

AKNOWLEDGMENTS

This work is funded via INESC TEC's Plurianual programme (under agreement no. UIDB/50014/2020).

REFERENCES

[1] Benedetti, I., Guarini, G., Laureti, T. (2023). Digitalization in Europe: A potential driver of energy efficiency for the twin transition policy strategy. Socio-Economic Planning Sciences, 89, 101701. https://doi.org/10.1016/j.seps.2023.101701.

[2] Bianchini, S., Damioli, G., Ghisetti, C. (2023). The environmental effects of the "twin" green and digital transition in European regions. Environmental and Resource Economics, 84(4), pp.877-918. https://doi.org/10.1007/s10640-022-00741-7.

[3] Burinskienė, A., Nalivaikė, J. (2024). Digital and Sustainable (Twin) Transformations: A Case of SMEs in the European Union. Sustainability, 16(4), 1533. https://doi.org/10.3390/su16041533.

[4] Calvin, K., Dasgupta, D., Krinner, G., Mukherji, A., Thorne, P. W., Trisos, C., Romero, J., Aldunce, P., Barrett, K., Blanco, G., Cheung, W. W. L., Connors, S., Denton, F., DiongueNiang, A., Dodman, D., Garschagen, M., Geden, O., Hayward, B., Jones, C., … Péan, C. (2023). IPCC, 2023: Climate Change 2023: Synthesis Report. Contribution of Working Groups I, II and III to the Sixth Assessment Report of the Intergovernmental Panel on Climate Change [Core Writing Team, H. Lee and J. Romero (eds.)]. IPCC, Geneva, Switzerland. (First). Intergovernmental Panel on Climate Change (IPCC). https://doi.org/10.59327/IPCC/AR6-9789291691647.

[5] Chatzistamoulou, N. (2023). Is digital transformation the Deus ex Machina towards sustainability transition of the European SMEs? Ecological Economics, 206, 107739. https://doi.org/10.1016/j.ecolecon.2023.107739.

[6] Diodato, D., Huergo, E., Moncada-Paternò-Castello, P., Rentocchini, F., Timmermans, B. (2023). Introduction to the special issue on "the twin (digital and green) transition: Handling the economic and social challenges". Industry and Innovation, 30(7), pp.755-765. https://doi.org/10.1080/13662716.2023.2254272.

[7] Elkington, J. (n.d.). Enter the Triple Bottom Line.

[8] Ellen MacArthur Foundation. (2020). Circulytics: Measuring circular economy performance. https://www.ellenmacarthurfoundation.org/resources/circulytics/resources.

[9] European Comission. (2021). EU countries commit to leading the green digital transformation | Shaping Europe's digital future. https://digital-strategy.ec.europa.eu/en/news/eu-countries-commit-leading-green-digital-transformation.

[10] European Commission. Joint Research Centre. (2022). Towards a green & digital future: Key requirements for successful twin transitions in the European Union. Publications Office. https://data.europa.eu/doi/10.2760/977331.

[11] Findik, D., Tirgil, A.,Özbuğday, F.C. (2023). Industry 4.0 as an enabler of circular economy practices: Evidence from European SMEs. Journal of Cleaner Production, 410, 137281. https://doi.org/10.1016/j.jclepro.2023.137281.

[12] Kumar, L., Sharma, R.K. (2024). Examining interdependencies among solution dimensions for sustainable development in SMEs based on Industry 4.0 concept. Kybernetes. https://doi.org/10.1108/K-09-2023-1674.

[13] Li, L., Yi, Z., Jiang, F., Zhang, S., Zhou, J. (2023). Exploring the mechanism of digital transformation empowering green innovation in construction enterprises. Developments in the Built Environment, 15, 100199. https://doi.org/10.1016/j.dibe.2023.100199.

[14] Mang, P., Haggard, B., & Regenesis. (2016). Regenerative Development: A Framework for Evolving Sustainability (1st ed.). Wiley. https://doi.org/10.1002/9781119149699.

[15] Mang, P., Reed, B. (2020). Regenerative Development and Design. In V. Loftness (Ed.), Sustainable Built Environments (pp.115-141). Springer US. https://doi.org/10.1007/ 978-1-0716-0684-1_303.

[16] Mehedintu, A., Soava, G. (2022). A Structural Framework for Assessing the Digital Resilience of Enterprises in the Context of the Technological Revolution 4.0. Electronics, 11(15), 2439. https://doi.org/10.3390/electronics11152439.

[17] Montresor, S., Vezzani, A. (2022). Digital Technologies and Eco-Innovation. Evidence of the Twin Transition from Italian Firms. SSRN Electronic Journal. https://doi.org/10.2139/ssrn.4094997.

[18] Münnich, M., Stange, M., Süße, M., Ihlenfeldt, S. (2023). Integration of Digitization and Sustainability Objectives in a Maturity Model-Based Strategy Development Process. In H. Kohl, G. Seliger, F. Dietrich (Eds.), Manufacturing Driving Circular Economy (pp.918-926). Springer International Publishing. https://doi.org/10.1007/978-3-031-28839-5_102.

[19] Ogrean, C., Herciu, M. (2021). Romania's SMEs on the Way to EU's Twin Transition to Digitalization and Sustainability. Studies in Business and Economics, 16(2), pp.282-295. https://doi.org/10.2478/sbe-2021-0040.

[20] Ortega-Gras, J.-J., Bueno-Delgado, M.-V., Cañavate-Cruzado, G., Garrido-Lova, J. (2021). Twin Transition through the Implementation of Industry 4.0 Technologies: Desk-Research Analysis and Practical Use Cases in Europe. Sustainability, 13(24), 13601. https://doi.org/10.3390/su132413601.

[21] P. Senna, P., Barros, A.C., Bonnin Roca, J., Azevedo, A. (2023). Development of a digital maturity model for Industry 4.0 based on the technology-organization-environment framework. Computers & Industrial Engineering, 185, 109645. https://doi.org/10.1016/ j.cie.2023.109645.

[22] Perossa, D., Acerbi, F., Rocca, R., Fumagalli, L., Taisch, M. (2023). Twin Transition cosmetic roadmapping tool for supporting cosmetics manufacturing. Cleaner Environmental Systems, 11, 100145. https://doi.org/10.1016/j.cesys.2023.100145.

[23] Rehman, S.U., Giordino, D., Zhang, Q., Alam, G. M. (2023). Twin transitions & industry 4.0: Unpacking the relationship between digital and green factors to determine green competitive advantage. Technology in Society, 73, 102227. https://doi.org/10.1016/j.techsoc. 2023.102227.

[24] Rizos, V., Behrens, A., Van Der Gaast, W., Hofman, E., Ioannou, A., Kafyeke, T., Flamos, A., Rinaldi, R., Papadelis, S., Hirschnitz-Garbers, M., Topi, C. (2016). Implementation of Circular Economy Business Models by Small and Medium-Sized Enterprises (SMEs): Barriers and Enablers. Sustainability, 8(11), 1212. https://doi.org/10.3390/ su8111212.

[25] Spaltini, M., Terzi, S., Taisch, M. (2024). Development and implementation of a roadmapping methodology to foster twin transition at manufacturing plant level. Computers in Industry, 154, 104025. https://doi.org/10.1016/j.compind.2023.104025.

[26] The European Green Deal-European Commission. (2021, July 14). https://commission. europa.eu/strategy-and-policy/priorities-2019-2024/european-green-deal_en.

[27] Walker, A.M., Opferkuch, K., Roos Lindgreen, E., Raggi, A., Simboli, A., Vermeulen, W.J.V., Caeiro, S., Salomone, R. (2022). What Is the Relation between Circular Economy and Sustainability? Answers from Frontrunner Companies Engaged with Circular Economy Practices. Circular Economy and Sustainability, 2(2), pp.731-758. https://doi.org/10.1007/ s43615-021-00064-7.

SYMPOSIUM - 5

Computer Methods, Artificial Intelligence and Experiments in Biomedicine

Sónia I.S. Pinto(*) and Luisa C. Sousa(*)

Dept. of Mechanical Engineering, Faculty of Engineering University of Porto, Portugal
Institute of Science and Innovation in Mechanical and Industrial Engineering, Portugal.

(*)Associate Editor for papers in this Symposium

Proceedings IRF2025: 8th International Conference on Integrity-Reliability-Failure
In Engineering, Materials, Manufacturing and Biomechanics. Porto 15-18 July 2025
DOI: https://doi.org/10.24840/978-972-752-323-8

PAPER REF: 22471

NUMERICAL MODELING OF RED BLOOD CELLS INTERACTIONS WITH VISCOELASTIC MEMBRANES

Rosaire Mongrain[1(*)], Hristo Valtchanov[1], Renzo Cecere[2]

[1]Department of Mechanical, McGill University, Montreal, Canada
[2]Department of Surgery, Division of Cardiac Surgery, McGill University, Montreal, Canada
[(*)]*Email:* rosaire.mongrain@mcgill.ca

ABSTRACT

Heart failure is amongst the most important cardiovascular diseases associated with an important death rate. The gold standard of treatment of end stage heart failure is transplantation. However, because of the severe shortage of potential organ donors, mechanical pumps have been developed for long term support. Blood damage remains an important issue with these implants and constitutes the most important failure modes. The principal consequence are hemolysis (rupture of the red blood cells or RBCs) and thrombosis (formation of blood clot). A simulation model is presented to study hemolysis in the context intercellular interaction taking into account the viscoelasticity of the cell membrane. It is reported that viscoelasticity appears to be associated with lower maximal cell strains and thus possibly related to hemolysis.

Keywords: Red blood cells, cells collisions, viscoelastic membrane, hemolysis.

INTRODUCTION

In its 2019 update, the American Heart Association reported 377 599 deaths linked to heart failure [1]. The gold standard for the treatment of heart failure is transplantation. However, there is an important shortage of suitable organ donors. For this reason, mechanical pumps have been designed to assist the heart in its pumping function. Hemolysis and thrombosis are the principal failure modes for these mechanical devices [2]. Indeed, under supra-physiological flow conditions, RBCs are susceptible to rupture (hemolysis), which poses severe risks to patient safety [5]. Advancements in RBC membrane modeling have progressed from simple strain-energy based hyperelastic formulations to more sophisticated mathematical descriptions incorporating spectrin network and viscoelasticity [3]. This paper presents simulations of red blood cells collisions taking into account the viscoelasticity of the membrane.

RESULTS AND CONCLUSIONS

Unsteady incompressible finite-finite volume computational fluid dynamics simulations are executed using Ansys Fluent™ with a fully Eulerian methodology for modeling the membrane deformation [3, 4]. The methodology uses the volume-of-fluid (VOF) multiphase numerical scheme [3]. The momentum conservation equation is solved for the mixture velocity and density field common to both phases, given below:

$$\frac{\partial}{\partial t}(\rho\vec{v}_m) + \frac{\partial}{\partial x_i}(v_i\rho\vec{v}_m) = \nabla\cdot\boldsymbol{\sigma} + b(\phi_c,\nabla\phi_c)\vec{f} \quad \forall\, i \in \{1,2,3\} \qquad (1)$$

where $\boldsymbol{\sigma}$ is the fluid stress tensor, which is modelled with a Newtonian viscosity and $\vec{f}$ is an immersed-boundary force and the term $b(\phi_c,\nabla\phi_c) = |\nabla\phi_c|$ is an indicator term to locate the interface between plasma and hemoglobin phases. Viscoelasticity is modelled using a simple mixing model where membrane viscosity (μ_m) combined is with the cytoplasm (μ_c) and plasma viscosities (μ_p) [5]:

$$\mu = \begin{cases} (1 - b(\phi_c, \nabla\phi_c))\mu_c + \mu_m b(\phi_c, \nabla\phi_c) \; if \; \phi_c \geq 0.5 \\ (1 - b(\phi_c, \nabla\phi_c))\mu_p + \mu_m b(\phi_c, \nabla\phi_c) \; if \; \phi_c \leq 0.5 \end{cases} \quad (2)$$

with μ_m=0.3 [$\mu Pa{\cdot}s{\cdot}m$], μ_c=5.024·10^{-3} [$Pa{\cdot}s$] and μ_p=1.024 ·10^{-3} [$Pa\ s$]. Simulations were performed with 2 and 4 cells, Figure 1 illustrates the RBC collisions and maximum strains.

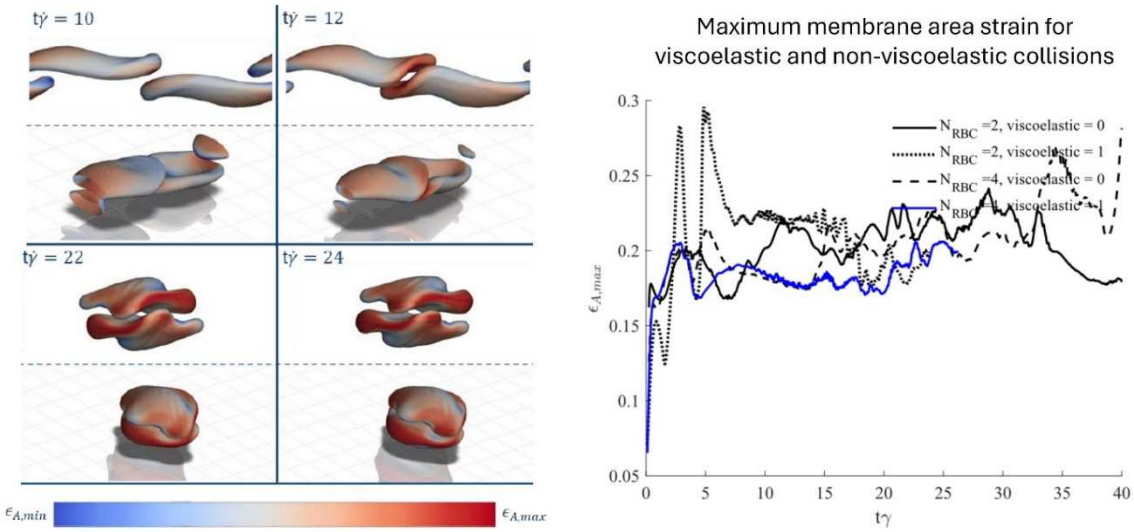

Fig. 1 - (a) Ilustration of the RBC deformation during collision and (b) Maximum membrane area strain during collisions at 20,000 s-1 for 2 and 4 cells with and without viscoelasticity.

When comparing the 4-cell viscoelastic collision case with its non-viscoelastic counterpart (purely elastic), it appears that the peaks of the non-viscoelastic case are higher during collisions (Figure 1b), but the overall mean membrane strain is similar for both viscoelastic and non-viscoelastic cases. It is hypothesized that the viscous stress absorbs and damps membrane response to the high frequency load experienced during collisions at high shear rate, preventing excessive strains that may lead to hemolysis (corroborated experimentally) [6]. As mean strain is similar between viscoelastic and non-viscoelastic cases however, viscoelasticity does not negate the effect of collisions [4].

ACKNOWLEDGMENTS

The authors gratefully acknowledge the funding by NSERC The Natural Sciences and Engineering Research Council of Canada.

REFERENCES

[1] Connie W. Tsao et al., AHA Statistical Update, Heart Disease and Stroke Statistics—2022 Update: A Report From the American Heart Association, Circulation, 45:e153-e639, 2022.

[2] G Roland, P Pauli, Computational Fluid Dynamics for Mechanical Circulatory Support Device Development in Mechanical Support for Heart Failure pp.399-427, 2022.

[3] Valtchanov H et al., Simulation of the effect of hemolysis on thrombosis in blood-contacting medical devices, Medical Engineering & Physics, 131: 104218, 2024.

[4] Ansys F Solver theory guide, Ansys Inc. Release 15: 249, 2013.

[5] Mills J, Qie L, Dao M, et al. Nonlinear elastic and viscoelastic deformation of the human red blood cell with Optical Tweezers. Mcb-Tech Science 1: pp.169-180, 2004.

[6] Watanabe, N., et al. (2018). Visualization of erythrocyte deformation induced by supraphysiological shear stress. Int. J, of Artificial Organs, 41(12), pp.838-844.

Proceedings IRF2025: 8th International Conference on Integrity-Reliability-Failure
In Engineering, Materials, Manufacturing and Biomechanics. Porto 15-18 July 2025
DOI: https://doi.org/10.24840/978-972-752-323-8

PAPER REF: 22580

COMPUTED FFR USING WINDKESSEL AND VISCOELASTIC MODELS - VALIDATION WITH LEFT CORONARY PATIENT CASES

M. Fernandes[1,2(*)], L.C. Sousa[1,2], M.P.L Parente[1,2], S. Silva[3], S.I.S. Pinto[1,2]

[1]University of Porto, Engineering Faculty, Porto, Portugal
[2]Institute of Science and Innovation in Mechanical and Industrial Engineering (LAETA-INEGI), Porto, Portugal
[3]Institute of Electronics and Informatics Engineering of Aveiro (IEETA), University of Aveiro, Aveiro, Portugal
[(*)]*Email:* mcfernandes@fe.up.pt

ABSTRACT

The current clinical method used to assess the fractional flow reserve (FFR) in stenosed coronary arteries is invasive, costly, and time-consuming. Therefore, this procedure, which allows the quantification of the functional severity of the stenosis has on blood flow, should be replaced by a non-invasive one, which is being developed by the authors. In patient-specific coronary artery models with stenosis, numerical simulations were carried out in ANSYS® Fluent using a combination of mathematical models to accurately model the velocity, pressure, and rheology of blood. These models, namely a 3-element Windkessel pressure model, a Womersley velocity model and the simplified Phan-Thien/Tanner (sPTT) viscoelastic model, assure that patient-specific properties are considered and, therefore, make the simulations very close to real blood flow. Numerically, the FFR was obtained and compared to the invasive value obtained at the hospital through catheterization. The simulations returned accurate FFR results for the sample of 5 patients (average relative error (RE) = 14.0%, minimum RE = 2.7%). However, before clinical application of the tool, more patients need to be studied, which is currently underway.

Keywords: Fractional flow reserve, Windkessel model, Simplified Phan-Thien/Tanner model, Stenotic coronary arteries, Hemodynamic Simulations.

INTRODUCTION

Atherosclerosis is a medical condition that is caused by the narrowing of arteries due to the development of atheroma (also called atherosclerotic plaque). The chances of developing this disease grow naturally with age, but are also intensified by poor lifestyle choices, like sedentarism or smoking. The plaque leads to poor circulation, which results in poor oxygenation of tissues and uneven blood flow. This disease is silent and can irreversibly harm the patient through life-threatening acute myocardial infarction (heart attack). Cardiologists have developed a parameter named fractional flow reserve (FFR) in 1993 to assess the functional severity that stenoses have on blood flow inside diseased arteries, and it has been the gold standard ever since [1].

This nondimensional parameter is calculated by the division of the aortic pressure and the pressure 20 mm distal to the stenosis. A hyperaemic state is induced through the administration of adenosine, a substance that promotes maximum vasodilation of the vessel, to facilitate the movement of the pressure sensors inside the vessels. This parameter, which is measured through catheterization, can cause more damage to the lumen. Compared to the invasive technique, the numerical analysis of blood flow in atherosclerotic coronary arteries could make the diagnosis of cardiovascular diseases more affordable and quicker. Therefore, using computational

methodologies as an alternative is preferred and they have been extensively studied in the literature [2], but not necessarily using the most accurate and patient-specific physiological conditions. The authors have studied different models, from simpler to more complex, to obtain a computational tool with two characteristics that are imperative for clinical application: high accuracy and low computational time [1], [3]. Aspects such as Windkessel models with many elements, blood rheology, and fluid-structure interaction (FSI) between lumen and the artery wall have been studied, as well as their possible impact on the computational FFR determination [4], [5]. In these works, the authors have concluded that complex models are associated with more parameters which are most times impossible to calculate through patient-specific data. Yet, their complexity does not translate to more accurate numerical FFR values, so less complex and quick models can be used instead.

At the present moment, to correctly depict the real physiological conditions of each patient, our tool uses a Womersley profile to define the periodic and pulsatile velocity profile at the inlet. In addition, it uses a 3-element Windkessel model to define the outlet pressure profiles. Finally, blood viscoelasticity is considered because it is essential for producing realistic simulation results, and a simplified Phan-Thien/Tanner (sPTT) rheology model was used. The simultaneous use of these 3 models in physiologically realistic simulations of blood flow in coronary arteries with stenoses is novel in the literature. These boundary conditions and rheological models were incorporated as User-Defined Functions (UDFs) in ANSYS® Fluent software, where the numerical simulations were run.

In this work, the authors want to validate their methodology in several left coronary arteries (LCAs) with stenosis and use a sample of 5 patient-specific cases, whose Computed Tomography (CT) images, invasive FFR, and clinical data was provided by the medical doctors at the Cardiology Department of Gaia/Espinho Hospital Centre (CHVNG/E).

METHODOLOGY

Various steps were required in the process of numerically obtaining the FFR. At first, the three-dimensional geometries were created through image segmentation of CT images. Then, the programming of the complex models used in the boundary conditions. Then, the numerical simulation settings were run and the computational FFR was calculated. More details on the methodology are provided in this section.

3D Model: Segmentation and Hyperaemization

Five patients were studied, and their LCA CT scans were provided by the Cardiology Department of Gaia/Espinho Hospital Centre (CHVNG/E) in resting conditions. The set CT scans are collected in consecutive parallel planes, which allow for the 3D reconstruction of the left coronary tree. This was performed using MIMICS® software and finalised in 3-matic®.

To simulate the invasive procedure used to measure the FFR, the lumen of the LCA needs to be converted to a maximum vasodilation setting. According to [11], [12], the intravenous administration of adenosine of 140 μg/kg/min is the value that according the clinical practice leads to the maximum vasodilation of a vast number of patients, and it produces an increase of cross-sectional area by a factor of 2.04. This process required the measurement of the values of the areas at resting state for many cross-sections, and, after calculating the area values for the hyperaemic state, the new cross-sections were drawn in their place. Using a loft feature, the different cross-sections were unified to create the hyperaemic model, used in the numerical simulations. The geometric differences of this process can be viewed in Fig.

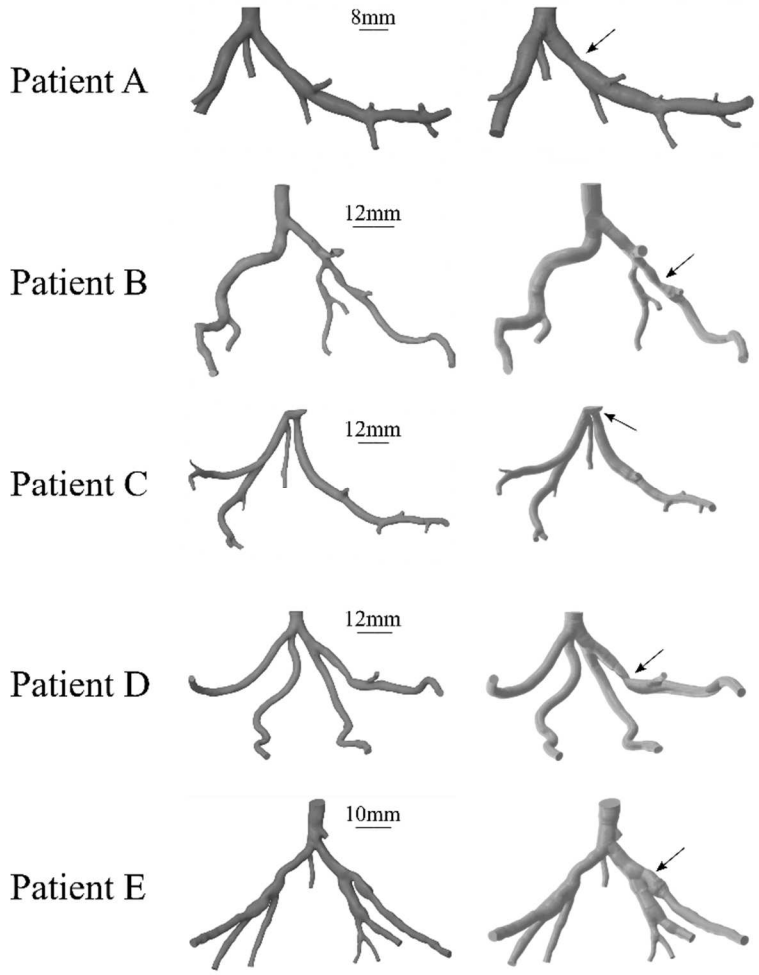

Fig. 1 - Model of the lumen of the coronary artery for all patients in resting and hyperaemic states. The stenosis locations are highlighted with an arrow.

Boundary Conditions and Fluid Properties: Definition

Numerical simulations of blood flow through fluid-flow equations demands the definition of the boundary conditions as well as the viscosity of the fluid. In this section, the used models are explained, as well as the used equations. All the following models were programmed in language C and compiled in ANSYS® Fluent as user-defined functions (UDFs), since these models are not contained in the software. The rheology of blood is the same for all patients, while the UDFs for velocity and pressure are patient-specific and, therefore, with different parameters for each patient case.

Inlet boundary: Velocity profile

The chosen inlet velocity profile was the Womersley profile, used to model pulsatile flow:

$$v(r,t) = \frac{AR^2}{i\mu\alpha^2}\left(1 - \frac{J_0\left(i^{1.5}\alpha\frac{r}{R}\right)}{J_0(i^{1.5}\alpha)}\right)e^{i\omega t} \quad (1)$$

The axial velocity, v, is a function of the radial distance from the centreline to any point, r, time, t, the radius of the artery, R, the pressure gradient, A, the cardiac frequency, ω, the dynamic viscosity of blood, μ, the first-order Bessel function, J_0, and the imaginary number, i. Moreover,

it also depends on α, which is the Womersley number. This non-dimensional parameter is the ratio between transient inertial forces and viscous forces, and it is measured with the artery radius, the density of blood, ρ, its dynamic viscosity, and the cardiac frequency [4]:

$$\alpha = R\sqrt{\frac{\rho\omega}{\mu}} \tag{2}$$

The cardiac frequency and the inlet area are patient-specific information. The former is obtained by analysis of the clinical data and conversion to hyperaemia conditions [11], while the latter was obtained by measuring the area in ANSYS® SpaceClaim, a geometry modulation software.

Outlet boundary: Pressure profile

Moreover, the chosen pressure boundary condition was a three-element Windkessel model [6], [13] (Figure 2). The model is applied to each outlet of the coronary trees. Q_0 and P_0 are the outlet volume flow rate and pressure, respectively, R_p is the proximal resistance and, after this resistance, p_d is the pressure at the arteriolar and capillary level. After this node, there are two elements in parallel, namely R_d, the distal resistance, and C_a, the arterial capacitance.

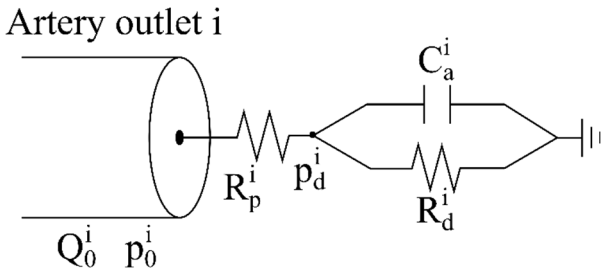

Fig. 2 - 3-element Windkessel model used to model the outlet pressures in the coronary tree.

The incorporation of patient-specific data in the pressure boundary conditions is done through the calculation of the total arterial capacitance, C_t, and the total resistance, R_t. These global properties are combined information of the outlet areas to calculate the distal and proximal resistances. Moreover, the diastolic blood pressure (DBP) and systolic blood pressure (SBP) values, provided by the medical doctors in resting conditions, are used to calculate the mean arterial pressure (MAP) in hyperaemic conditions and then used to obtain C_t and R_t [14].

Blood rheology: Viscoelasticity

Due to its composition (plasma, red blood cells, white blood cells, and platelets), blood is a complex fluid with viscoelastic properties. In this work, the viscoelasticity of blood was modelled according to the works of [10], using a simplified Phan-Thien/Tanner model:

$$\boldsymbol{\tau} = \boldsymbol{\tau}_s + \boldsymbol{\tau}_e \tag{3}$$

$$\boldsymbol{\tau}_s = 2\mu_s \boldsymbol{D} \tag{4}$$

$$\left[f(\boldsymbol{\tau}_{e_k})\right]\boldsymbol{\tau}_{e_k} + \lambda_K \boldsymbol{\tau}^*_{e_k} + \alpha_k \frac{\lambda_k}{\mu_{e_k}}(\boldsymbol{\tau}_{e_k} \cdot \boldsymbol{\tau}_{e_k}) = 2\mu_{e_k}\boldsymbol{D} \tag{5}$$

$$f(\boldsymbol{\tau}_{e_k}) = 1 + \frac{\lambda_k \varepsilon_k}{\mu_{e_k}} tr(\boldsymbol{\tau}_{e_k}) \tag{6}$$

For this multi-modal model, the shear stress vector, $\boldsymbol{\tau}$, is the sum of the vector of shear stress of the solvent part, $\boldsymbol{\tau}_s$, and the vector of the elastic properties of the fluid, $\boldsymbol{\tau}_e$. The viscosity of the solvent of blood, μ_s (plasma, considered a Newtonian fluid), and the strain rate tensor, $\boldsymbol{D}$ are

necessary to calculate the solvent shear stress. Moreover, the elastic portion depends on its viscosity, μ_e, the extensibility coefficient, ε, the relaxation time, λ, the mobility factor, α, the trace of the stress tensor, $tr(\boldsymbol{\tau}_e)$, and the upper-convected derivative of the elastic stress tensor, $\boldsymbol{\tau}_e^*$. The k are the different modes, 1 through 4 (Table 1).

Table 1 - Values for the parameters of the sPTT viscosity model. Adapted from [10].

Modes	$\mu_{e,k}$ **[Pa s]**	λ_k **[s]**	α_k
1	0.05	7	0.06
2	0.001	0.4	0.001
3	0.001	0.04	0.001
4	0.0016	0.006	0.001
Solvent	μ_s = 0.0012 [Pa s]		

Numerical Settings

In ANSYS® Fluent, a Green-Gauss node-based solution method was implemented in the gradient property. A SIMPLE computation scheme was implemented to perform the coupling of pressure and velocity. To eliminate the errors produced by the initialization process, 5 cardiac cycles were simulated, and the results for the last cycle were retrieved for all patient cases. Using the stenosis locations certified by cardiologists (seen in Figure 1), the distal plane was defined 20mm downstream the stenosis location and parallel to blood flow in the lumen, whereas the aortic plane was defined at a miniscule distance of 0.001mm from the inlet. In these planes, the spatial-average pressure values were measured every 0.005 seconds.

RESULTS AND DISCUSSION

Figure 3 contains the total pressure distribution in the lumen at the peak systolic velocity (PSV), which is the time instance of the maximum inlet velocity and therefore, maximum contraction of the myocardium. It is possible to see the difference between the pressure values reached at the same point of the cardiac cycle (maximum inlet velocity). In fact, while the flow of patient A reaches a maximum pressure value of 605.1 Pa, patient C witnesses a maximum pressure value of 1749.7 Pa, which is almost three times bigger. Hence, this figure shows that flow is patient specific and, thus, the same pressure profile should not be applied to each studied artery.

For all cases, the maximum pressure value is located near the inlet, before the bifurcations. It is also clear that the presence of curvatures acts as an obstacle to flow, reducing its total pressure. This is most evident in the case of patient B. In addition, the presence of stenoses leads to a pressure drop, which is mostly evident in the cases of patients B and D. This coincides with the medical indication of the severity of the stenoses, since these patients possess the highest severity out of the total sample (75%, and 95% stenosis, respectively). Even though the entire circulatory system is not represented in the geometry, it is clear that this pressure drop influences flow downstream of the coronary artery because these patients exhibited symptoms of cardiovascular problems.

To calculate the FFR, the temporal-averaged distal pressure and aortic pressure values were calculated through the trapezoidal rule:

$$p = \frac{\Delta t}{2}\left[p_{t_0} + 2 * \left(p_{t_1} + \cdots + p_{t_{n-1}}\right) + p_{t_n}\right] \quad (7)$$

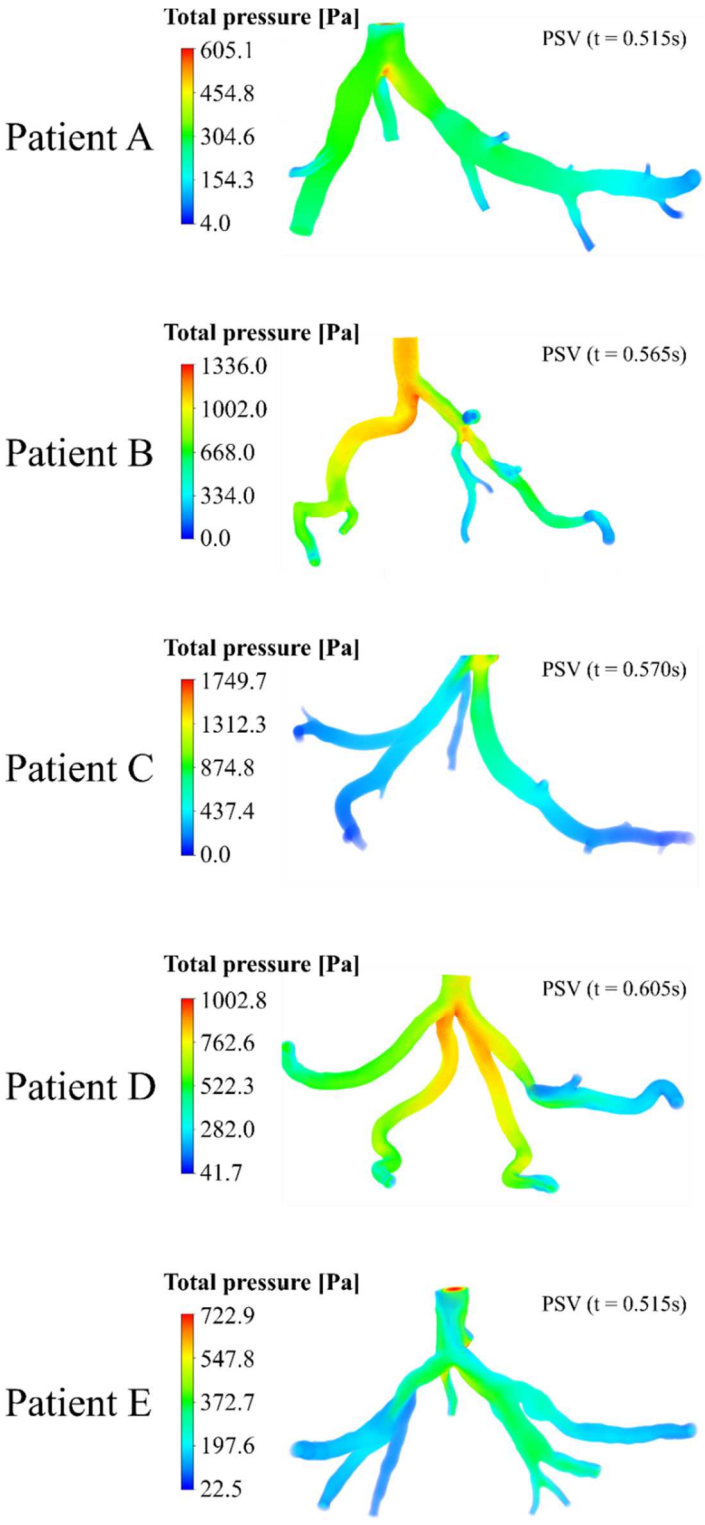

Fig. 3 - Pressure distribution at the respective peak systolic velocity (PSV) time instances for all patient cases.

The numerical FFR results obtained in the numerical simulations representative of the fifth cardiac cycle are displayed in Table 2, as well as the invasive FFR value provided by medical doctors at CHVNG/E. The relative error (RE) between the two FFR values, admitting the invasive FFR is the real FFR value, is also displayed.

Table 2 - FFR values: numerically computed, invasive, and their relative error (RE).

Patient case	Computed FFR	Invasive FFR	RE (%)
Patient A	0.890	0.93	2.7%
Patient B	0.498	0.58	14.1%
Patient C	0.888	0.81	9.6%
Patient D	0.442	0.61	27.5%
Patient E	0.503	0.60	16.2%

It can be said that the computational FFR is relatively low for all patient cases. While the maximum registered RE was 27.5%, the lowest value is only 2.7%. The average RE is 14.0% and the median RE is 14.1%. The authors think that these results are promising, and the tool should be tested with further patients.

CONCLUSIONS AND FUTURE WORK

The present work focused on further validating numerical methods regarding the prediction of FFR in stenotic left coronary arteries. This numerical tool, developed by the authors, is currently on a validation period, using already available reconstructed patient geometries.

So far, the results are promising. In fact, the findings of this study highlight the importance that patient-specific flow modelling has on the accuracy of the results. Therefore, generic boundary conditions should not be used, and each patient needs to be studied individually.

The computational fractional flow reserve values were relatively low across all patient cases, with a maximum relative error of 27.5% and a minimum of 2.7%. The average RE was 14.0%, and the median RE was 14.1%. These results are promising and suggest that the computational tool used in this study has potential for clinical application.

However, this potential is conditioned by the future works, yet to be implemented. The main challenge the authors face is expanding the patient sample size to include a broader range of FFR values, stenoses severities, and geometric features. This step would help in validating the computational FFR tool and increasing its accuracy as much as possible.

The authors recognize the difficulty in finding the necessary data for each patient case. The study is interest in the study of left coronary arteries only, and in patients that have not been subjected to any vascular reconstructive procedures, like coronary artery bypass grafting (CABG). Moreover, the files of medical data, especially images, should be available in the formats that can be accessed by available software. For instance, medical imaging obtained through alternative methods, such as MRI or angiographic projections, are read through programmes that are not available to the authors, limiting the number of patients that can be studied. However, the authors of the study are in the process of gathering more patients that fulfil our criteria, and the tool will be validated with more patient cases in the near future.

ACKNOWLEDGMENTS

Authors gratefully acknowledge the financial support of FCT (Portugal) regarding the R&D Project “CADS-FACT – PTDC/EMD-EMD/0980/2020” and the PhD fellowship “2024.01624.BD”, the Engineering Faculty of University of Porto, the Institute of Science and Innovation in Mechanical and Industrial Engineering, the Cardiovascular R&D Unit of the Medicine Faculty of University of Porto, and the Cardiology Department of Gaia/Espinho Hospital Centre.

REFERENCES

[1] M. Fernandes, L.C. Sousa, C.C. António, S. Silva, S.I.S. Pinto. A review of computational methodologies to predict the fractional flow reserve in coronary arteries with stenosis. J. Biomech., 2025, 178, pp.1-14.

[2] A. Corti, C. Chiastra, M. Colombo, M. Garbey, F. Migliavacca, S. Casarin. A fully coupled computational fluid dynamics – agent-based model of atherosclerotic plaque development: Multiscale modeling framework and parameter sensitivity analysis. Comput. Biol. Med., 2020, 118, pp.1-19.

[3] M. Fernandes, L.C. Sousa, C.C. António, S.I.S. Pinto. Accuracy and temporal analysis of non-Newtonian models of blood in the computational FFR – Numerical implementation. Int. J. Non. Linear. Mech., 2024, 161, pp.1-11.

[4] M. Fernandes, L.C. Sousa, C. C. António, S.I.S. Pinto. Modeling the Five-Element Windkessel Model with Simultaneous Utilization of Blood Viscoelastic Properties for FFR Achievement: A Proof-of-Concept Study. Mathematics, 2023, 11(24), pp.1-19.

[5] M.C. Fernandes, L.C. Sousa, C.F. de Castro, J.M.L.M. da Palma, C.C. António, S.I.S. Pinto. Implementation and Comparison of Non-Newtonian Viscosity Models in Hemodynamic Simulations of Patient Coronary Arteries. Adv. Struct. Mater., 2022, 175, pp.403-428.

[6] N. Westerhof, J.W. Lankhaar, B.E. Westerhof. The arterial windkessel. Med. Biol. Eng. Comput., 2009, 47(2), pp.131-141.

[7] E. Romano, L.C. Sousa, C.C. António, C.F. Castro, S.I.S. Pinto. Non-Linear or Quasi-Linear Viscoelastic Property of Blood for Hemodynamic Simulations. Adv. Struct. Mater., 2020, 132, pp.127-139.

[8] B.C. Good, S. Deutsch, K.B. Manning, Hemodynamics in a Pediatric Ascending Aorta Using a Viscoelastic Pediatric Blood Model. Ann. Biomed. Eng., 2016, 44(4), pp.1019-1035.

[9] T. Bodnár, A. Sequeira, M. Prosi. On the shear-thinning and viscoelastic effects of blood flow under various flow rates, Appl. Math. Comput., 2011, 217(11), pp.5055-5067.

[10] L. Campo-Deaño, R.P.A. Dullens, D.G.A.L. Aarts, F.T. Pinho, M.S.N. Oliveira. Viscoelasticity of blood and viscoelastic blood analogues for use in polydymethylsiloxane in vitro models of the circulatory system. Biomicrofluidics, 2013, 7(3), pp.1-12.

[11] R.F. Wilson, K. Wyche, B.V. Christensen, S. Zimmer, D. D. Laxson. Effects of adenosine on human coronary arterial circulation. Circulation, 1990, 82(5), pp.1595-1606.

[12] P. Sharma et al.. A framework for personalization of coronary flow computations during rest and hyperemia. Proc. Annu. Int. Conf. IEEE Eng. Med. Biol. Soc. EMBS, 2012, pp.6665-6668.

[13] A. Jonášová, J. Vimmr. On the relevance of boundary conditions and viscosity models in blood flow simulations in patient-specific aorto- coronary bypass models. Int. J. Numer. Method. Biomed. Eng., 2021, 37(4), pp.1-14.

[14] A. Deyranlou, J.H. Naish, C.A. Miller, A. Revell, A. Keshmiri. Numerical Study of Atrial Fibrillation Effects on Flow Distribution in Aortic Circulation. Ann. Biomed. Eng., 2020, 48(4), pp.1291-1308.

Proceedings IRF2025: 8th International Conference on Integrity-Reliability-Failure
In Engineering, Materials, Manufacturing and Biomechanics. Porto 15-18 July 2025
DOI: https://doi.org/10.24840/978-972-752-323-8

PAPER REF: 22581

ANALYSIS OF HYPEREMIC STATE GENERATED IN PATIENT SPECIFIC RIGHT CORONARY ARTERIES USING CURRENT OR AUTOMATIC IN-HOUSE SOFTWARE

F.P Oliveira[1,2(*)], G. Rodrigues[1,2], L.C. Sousa[1,2], J. Festas[1,2], S.I.S. Pinto[1,2]

[1]University of Porto, Engineering Faculty, Porto, Portugal
[2]Institute of Science and Innovation in Mechanical and Industrial Engineering (LAETA-INEGI), Porto, Portugal
[(*)]*Email:* up202004230@edu.fe.up.pt

ABSTRACT

Accurate hyperemic state modeling is essential for non-invasive Fractional Flow Reserve assessment in coronary artery disease. Current methods, such as SimVascular, are time-intensive, user-dependent, and prone to amplified errors in branching regions, as demonstrated for a chosen patient. An in-house software was developed to automate the hyperemia transformation of patient-specific right coronary artery geometries from CT scans. Initial results show that the in-house software consistently recreates a uniform centerline, maintaining anatomical fidelity. It aims to significantly reduce processing time and eliminate user-induced variability. Although further refinement is needed for complex regions, this tool shows strong potential to streamline FFR workflows, reducing reliance on skilled personnel and enhancing CAD diagnostics.

Keywords: Coronary artery segmentation, patient-specific right coronary arteries, hyperemia, manual segmentation methods, automatic segmentation methods.

INTRODUCTION

Coronary artery disease (CAD) remains one of the leading causes of morbidity and mortality worldwide and is characterized by the narrowing or partial obstruction of the coronary arteries due to the buildup of atherosclerotic plaque. Fractional Flow Reserve (FFR) has become the gold standard parameter for assessing the significance of coronary stenosis and guiding clinical decisions regarding revascularization (Fernandes et al., 2023). Traditionally, FFR is measured invasively in a procedure that requires pharmacological induction of hyperemia, causing a vasodilation of approximately 2.04 times the original diameter of the patient's vessels (Wilson et al., 1990). Although highly accurate, this invasive approach presents several challenges, and the use of pharmacological agents to induce hyperemia can cause different adverse effects, further limiting the accessibility and performance of this method (Fearon et al., 2003; Tesche and Gray, 2020).

To combat these limitations, non-invasive computational have emerged, using patient-specific coronary artery geometries created from imaging techniques combined with computational fluid dynamics (CFD) simulations or machine learning algorithms to estimate FFR and therefore improve the accuracy of CAD diagnosis (Fernandes et al., 2023).

The most crucial step in the FFR calculation workflow is the coronary artery reconstruction, since it will dictate each patient's physiological and anatomical condition. These geometries need to be under a hyperemic state, mimicking the traditional invasive procedure. There are

well-established software tools available for generating 3D coronary artery geometries from computed tomography (CT) scans performed in clinical environment. It happens that most commercially available software demand high early financial investment and may be more optimized for larger vessels, rather than coronary arteries. Among these, SimVascular represents a strong open-source alternative. SimVascular, developed at Stanford University, is an open-source software designed for cardiovascular modeling and simulations, allowing integration of patient-specific CT scans. Its open-source nature supports custom coding, enabling user-defined operations like hyperemia simulation, which is essential for comparing invasive and computational FFR. Hyperemia can be achieved through a Python script that uniformly dilates each segmented artery layer, simulating the effect of adenosine-induced vasodilation (Raluca Monica et al., 2012).

In parallel, an innovative and fully automated software has been in development at FEUP and INEGI. This Python-based in-house software integrates advanced region-growing techniques and centerline extraction to enhance accuracy and computational efficiency in coronary artery segmentation, while significantly reducing the time consumed (Updegrove et al., 2017). This approach aims to address key disadvantages found in existing available software by implementing a semi-automatic segmentation algorithm that will ensure high patient-specific fidelity (Festas et al., 2023). This software is expected to automatically induce a hyperemic state in the generated 3D geometries, but validation and testing is still needed in order to evaluate its accuracy.

For that reason, right coronary arteries (RCA) generated using both the *in-house* software and SimVascular will be compared in order to help validating its efficiency, highlighting the key advantages of one over another.

METHODOLOGY AND RESULTS

SimVascular was used to obtain the final hyperemic right coronary artery (RCA) model, in order to compare it with the in-house software. For this, SimVascular was selected due to being one of very few available software in which it was possible to uniformly dilate the geometry after segmentation, even if only the user-selected slices with an external Python script.

3D RCA CONSTRUCTION USING SIMVASCULAR

Path Creation

Even though SimVascular is widely used and provides a comprehensive pipeline for image-based cardiovascular modeling, the software requires significant time and pre-procedural practice in order to correctly use its tools, as many operations demand manual input and fine-tuning. When working with patient-specific data, it is crucial to preserve anatomic information, so this geometry construction needs to be performed numerous times in order to obtain consistency, minimizing user-derived errors.

The first step involves defining the centerline of the RCA by manually placing a sequence of points along the artery in multiple cross-sectional views of the CT scans (Figure 1). The user must manually adjust and refine the control points to ensure smooth transitions in regions with high curvature, avoiding abrupt changes that could compromise the final model. This process has to be done for each branch of the RCA separately.

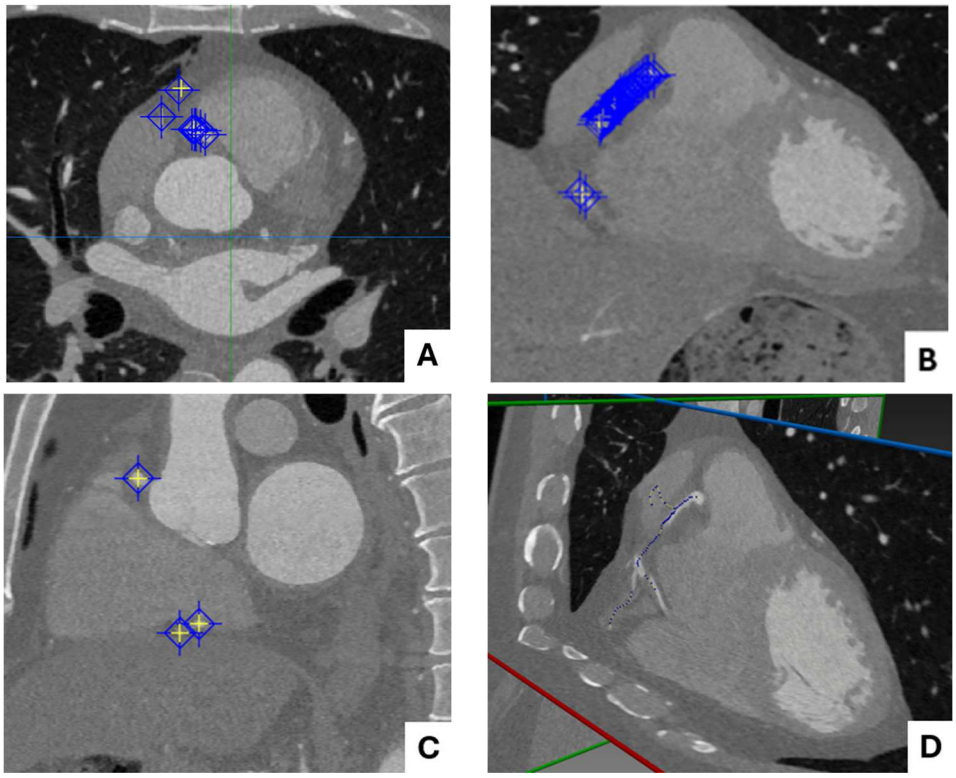

Fig. 1 - Path creation example in axial (A), coronal (B) and sagital (C) planes, plus 3D representation (D) using SimVascular.

SimVascular also allows for 3D visualization using volume rendering, which helps the user in case of low-quality imaging. Even so, this feature needs to be used carefully with cautious threshold selection due to its liability in coronary arteries, especially in stenotic and branching regions, as seen in Figure 2 below. It should be used as a way to ensure the paths are following their anatomical way.

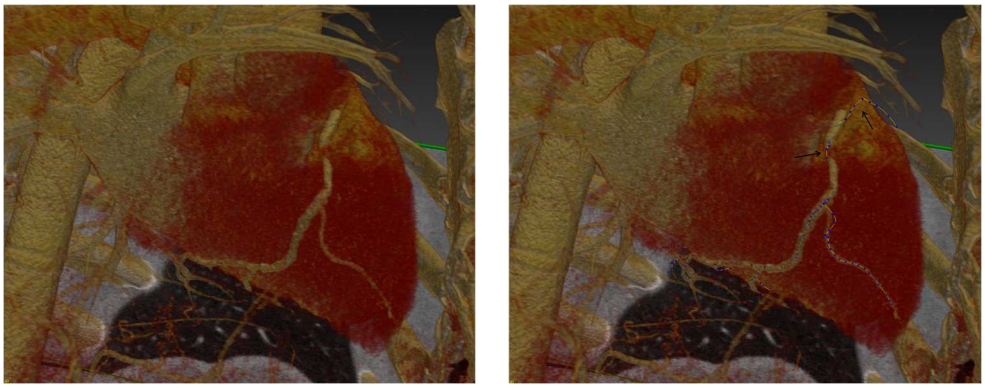

Fig. 2 - Default threshold volume rendering feature in SimVascular with the respective generated paths.

Segmentation

Segmentation is the most critical and user-dependent step. From each previously marked point in the paths, or additional in more detailed regions, the boundaries of the RCA must be manually delineated by the user, defining the lumen in every slice. One particularly helpful feature of SimVascular's segmentation workflow is that it aligns each plane orthogonally to the vessel's

centerline, ensuring users draw their contours perpendicularly to the lumen, which greatly improves accuracy. By using the SplinePoly function within SimVascular's segmentation window, it is possible to closely match the patient-specific's RCA lumen shape, provided the image quality is sufficient. Figure 3 below illustrates this process, as it shows a cross-sectional view of the coronary artery in grayscale, alongside its respective SplinePoly segmentation outlining the circular lumen boundary.

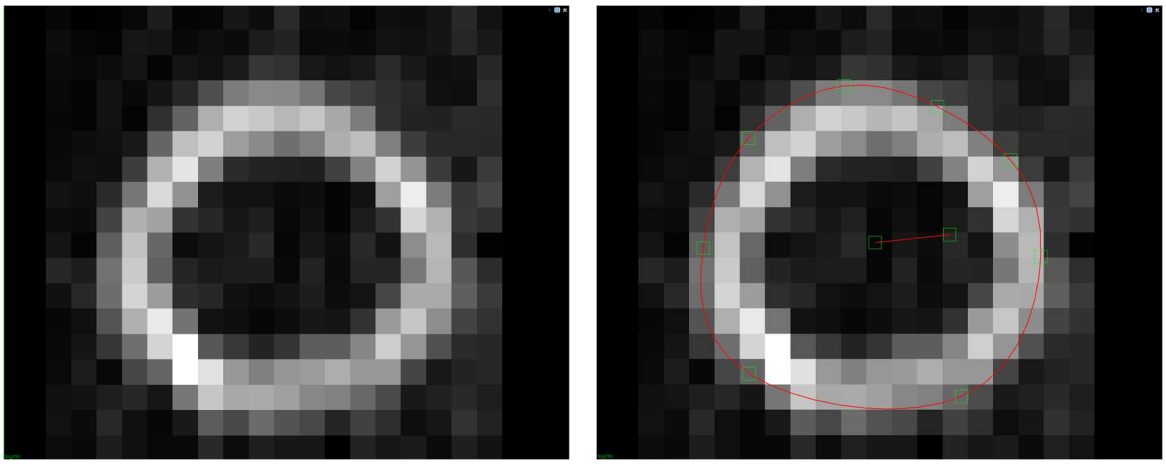

Fig. 3 - Segmentation example using SplinePoly.

However, this procedure is not ideal for coronary arteries due to poor image resolution at high magnification, such as in secondary branches (Figure 4C), which translates into a challenging contour detection. Also, this important step is highly dependent on the user's expertise in medical imaging, which can sometimes compromise the final geometry.

As illustrated in Figure 4A, the segmentation process begins in a proximal region near the aorta. The cross-sectional view captures the vessel's lumen, which appears approximately circular in these region, though subtle deviations can exist and translate into important patient-specific data. These imposed boundary lines reflect the careful step-by-step delineation of each layer, accounting for variations in pixel intensity and potential edge artifacts.

Further downstream, Figure 4B represents this patient's stenotic region. Stenoses can present significant challenges for accurate segmentation due to irregular lumen shapes, reduced blood flow, and potential plaque deposits that may not fully absorb the contrast agent. The cross-sectional image reveals how the vessel narrows and takes on a more elliptical or distorted appearance, while the 3D view confirms the severity and location of the lesion. Carefully identifying lumen boundaries in these sections is the most essential step during segmentation, since it is the most impactful feature for the FFR. Over or underestimation of stenosis severity can substantially impact computational simulations of blood flow and clinical decision-making. Figure 4C shows the task of segmentation becoming more challenging in secondary branches, as blood flow is reduced and the contrast agent may not fully penetrate irregular areas, leaving the vessel walls less clearly defined.

Model Generation

SimVascular constructs the resting state 3D model by interpolating between the segmented slices. However, as the resulting surface may contain artifacts or inconsistencies, additional smoothing may still be necessary, Figure 5. The user must check for abrupt variations in vessel diameter and ensure that the model maintains anatomical realism.

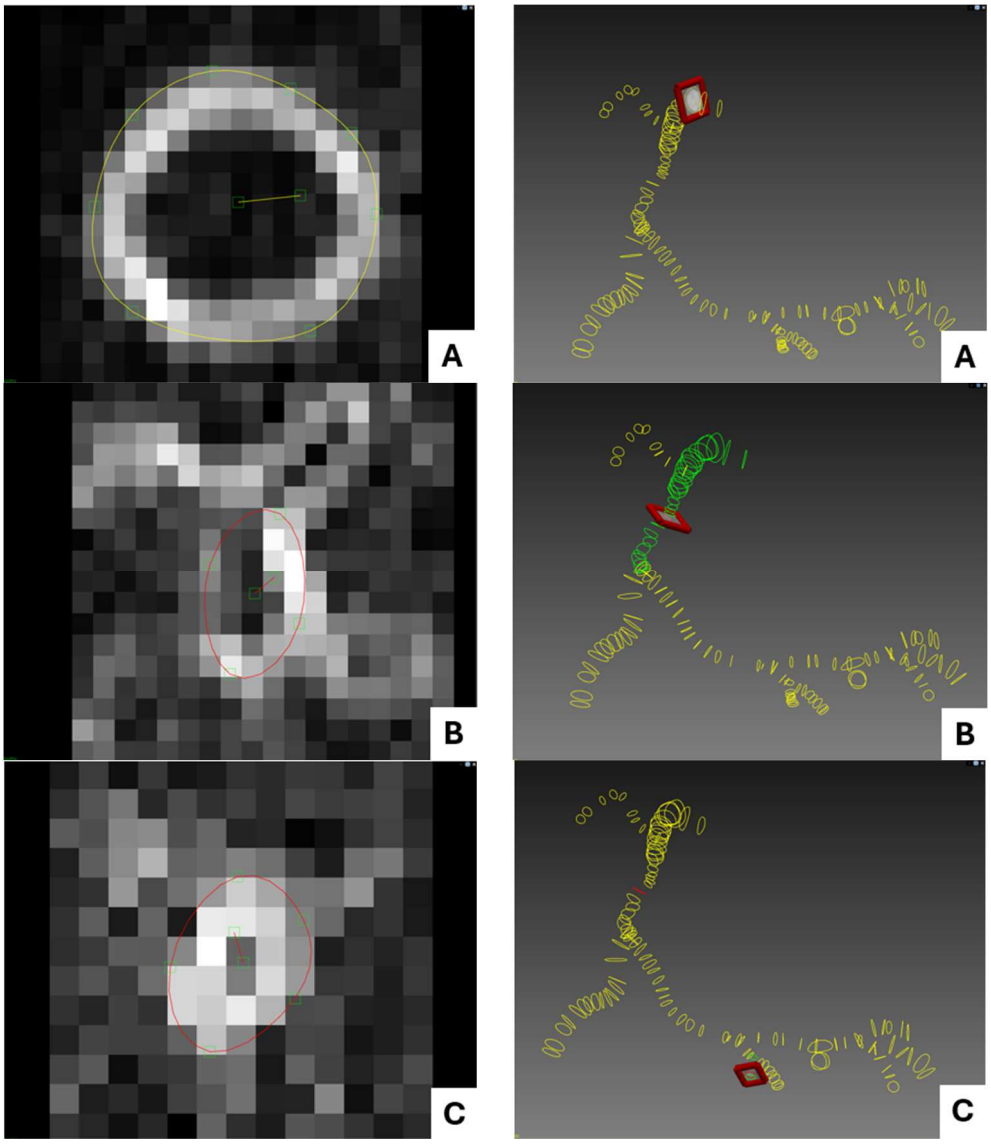

Fig. 4 - RCA lumen proximal to the aorta (A), in a stenotic region (B) and in a secondary branch (C) in SimVascular.

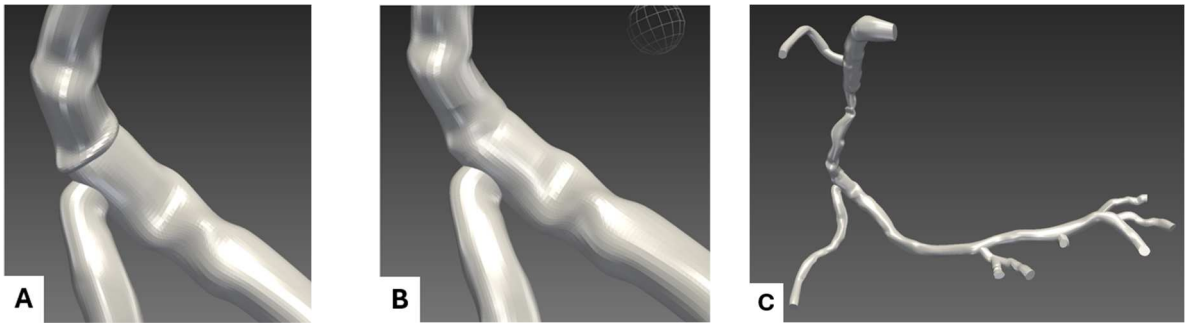

Fig. 5- Unsmoothed model (A), Smoothed model (B) and final resting state model (C) in SimVascular.

Smoothing the reconstructed vascular surface must be approached selectively, focusing on small regions where artifacts or irregularities are most pronounced, rather than globally across

the entire model. This local smoothing approach helps preserve the authentic anatomy of the model as a whole, correcting critical areas, such as arterial bifurcations, stenotic segments, or sharp curvatures, which reduces abrupt changes caused by SimVascular's slice-to-slice interpolation. By maintaining a balance between surface refinement and morphological accuracy, it is possible to achieve a more realistic 3D representation for subsequent analyses or procedural planning.

Hyperemia Induction in SimVascular

This mandatory step for future FFR calculation was performed using a created Python script in parallel with SimVascular. This script is able to capture the segmented contour groups as an input and scale each layer to a selected magnitude, maintaining the needed fidelity with the resting state geometry. This reveals to be crucial to preserve patient-specific anatomic details, which will help in obtaining an accurate FFR. To emulate a clinically realistic hyperemic condition, a uniform scaling factor of 2.04 was applied, ensuring that the vessel experiences a constant dilation of this magnitude along its entire length. This approach reflects a global vasodilation representative of maximal hyperemia and translates into more accurate non-invasive FFR assessments in the future (Wilson et al., 1990).

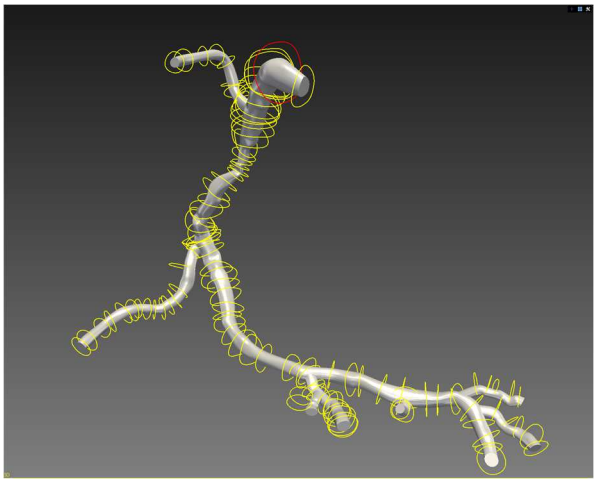

Fig. 6 - Hyperemic state segmentation vs Resting state model in SimVascular.

Figure 6 above shows the comparison between the original resting state model and the obtained hyperemic RCA. In a physiological context, arterial expansion is constrained by surrounding tissues and other biomechanical factors that limit in which directions vasodilation occurs. In this workflow, however, the vasodilation effect is simulated solely by scaling each cross-sectional layer. As a result, certain branches unexpectedly overlapped or collided following the uniform scaling, particularly at bifurcation points. These intersections were then manually adjusted, positioning the segments in a more anatomically plausible manner, not affecting their geometry, only their location. This troubleshooting step is not an ideal reflection of the body's natural behavior, and it can lead to some loss of patient specific anatomy in those edited bifurcation regions.

Throughout most of RCA, the script successfully scaled the lumen diameter by the requested 2.04 times, a feature not commonly found in other vascular modeling software. Figure 7 below shows these minor user edits performed, along with the final hyperemic state model of the RCA.

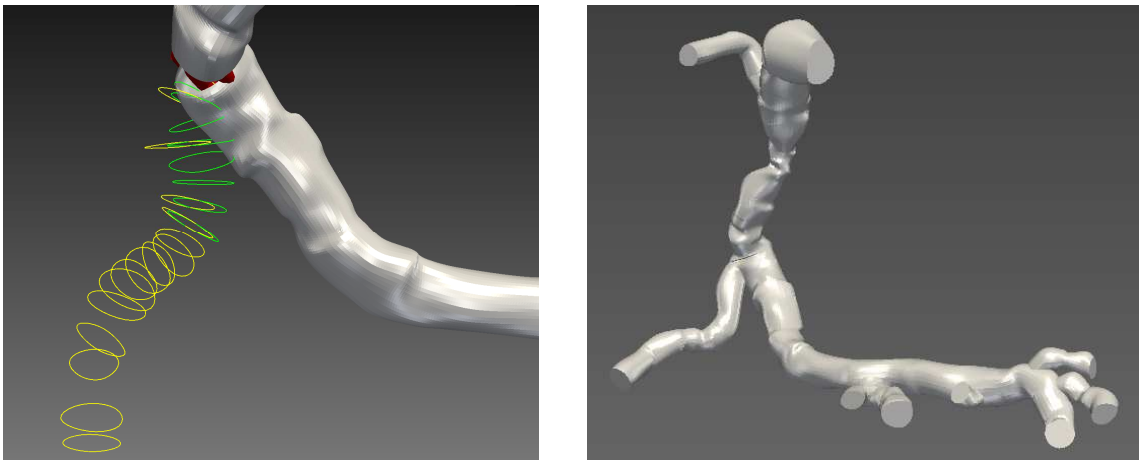

Fig. 7 - Old (green) and adjusted (yellow) segmentation of the secondary branch, and the final model of the hyperemic RCA.

Even though SimVascular brings several advantages and is capable of helping to maintain patient-specific anatomy, this software only allows for strict manual segmentation, in which the user has to go through the CT scan images as a whole and pinpoint the limits of the target vessel in each layer. This is a highly user-biased methodology, and the image quality can be poor when segmenting coronary vessels due to the high scaling needed, which besides being highly time consuming, can translate into user-derived errors. Since the resting state geometry construction is so dependent on the user, minor inaccuracies might emerge in the final geometry, which could lead to a loss of patient-specific data. Also, SimVascular allows only for the segmentation of one artery branch at a time, meaning that bifurcation regions will be less accurate, since the software computes these areas separately.

By allowing for the implementation of external Python scripts, SimVascular efficiently addresses several issues not regarded by other commercial options, despite its user-based drawbacks.

3D RCA CONSTRUCTION USING IN-HOUSE AUTOMATIC SOFTWARE

In order to overcome the limitations inherent to existing segmentation tools, usually time-consuming manual workflows and difficulties in accurately capturing severe stenoses, an innovative, fully automated in-house software solution has been under development at FEUP and INEGI. Unlike conventional manual approaches, which demand extensive operator input and often translate into inconsistent results, this Python-based framework leverages advanced region-growing techniques, gradient-informed segmentation, and centerline-based expansion to achieve fast and highly accurate vessel delineation (João et al., 2023). By progressively refining each coronary segment in multiple stages, the software attains greater fidelity in challenging anatomical regions, including those with reduced lumen diameter or lower contrast enhancement. Moreover, this design offers considerable flexibility compared with deep learning-based alternatives, which typically rely on large, labeled datasets and may not generalize well across diverse patient populations. Through the combination of computational efficiency and anatomical precision, the in-house software lays the groundwork for more robust and streamlined coronary artery modeling.

Building on this foundational work, the in-house software has been further enhanced to incorporate a second major and crucial feature: generating patient-specific hyperemic geometries. While the original version excelled at automatically producing resting-state

coronary anatomies, ongoing refinements now apply physiologically informed dilation factors to each vessel segment, simulating vasodilation under hyperemic conditions. The aim is to replicate, in a realistic yet automated manner, the artery's expansion during induced hyperemia, thereby enabling non-invasive assessments of functional severity in coronary lesions.

SIMVASCULAR VS. AUTOMATIC IN-HOUSE SOFTWARE

Although still at a relatively early stage of development, the in-house software already demonstrates key capabilities that distinguish it from more established commercial platforms, regarding hyperemia. As seen in Figure 8, this software can reliably extract a centerline, which is a particularly valuable workflow for analyzing how a coronary artery might behave under maximal vasodilation, an essential step for non-invasive FFR evaluations. While the initial implementation focuses on scaling layers within the main branch of the RCA, preliminary results confirm that the overall script is stable and accurate in capturing global luminal expansion. Manual adjustments are not required, keeping user intervention minimal.

By contrast, SimVascular provides a semi-automated environment in which clinicians or researchers contour slice-by-slice and apply smoothing or lofting operations to generate the 3D model. This process can yield anatomically detailed reconstructions, especially if the user meticulously corrects each layer. However, the manual workload can become substantial for cases involving multiple branches and severe stenoses, particularly if the user seeks to maintain high geometric fidelity. Additionally, most commercially available options do not offer a dedicated hyperemia feature. Even though SimVascular allows for it, there is the need of an external Python script in order to perform the operation. As a result, each branching segment must be checked individually to avoid unrealistic overlaps or collisions.

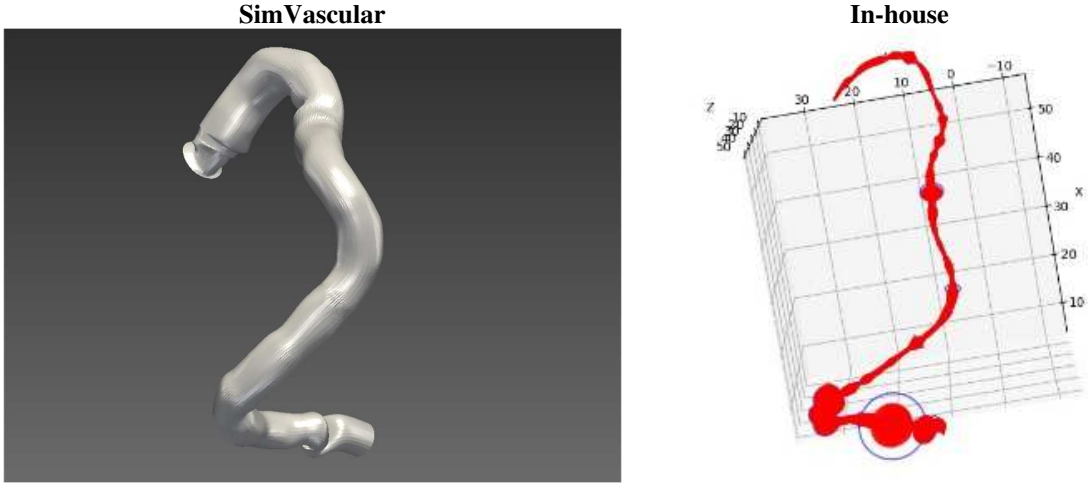

Fig. 8 - Qualitative analysis of hyperemic state generated RCA's main branch in SimVascular vs generated centerline in the in-house software.

CONCLUSIONS AND FUTURE WORK

The in-house method aims to produce a more uniformly smooth lumen, applied equally along the artery from the proximal to the distal portions, because it systematically scales cross-sectional layers rather than interpolating between manually drawn contours. SimVascular reconstructions, on the other hand, may exhibit slight variations in surface roughness or lumen

tapering, partly attributable to slice-by-slice edits and the user's criteria for preserving small anatomical details. Interestingly, while SimVascular's interactive workflow can capture subtle geometries if the user invests time in manual refinements and has expertise in medical imaging, the in-house hyperemia script supports a much faster, largely automated process, aiming to take only a few minutes to convert a set of CT scans into a hyperemic model accurately.

In its current form, the in-house software has generated promising preliminary results by successfully dilating a patient's RCA main branch by approximately twofold without significant geometric artifacts or discontinuities. These findings indicate that the underlying framework for centerline extraction and cross-sectional dilation is both robust and efficient. The next phases of development will focus on refining the dilation algorithm to better handle complex multi-branch anatomies and reduce any remaining collisions, aiming ultimately for a fully automated hyperemic transformation that accurately reflects patient-specific constraints. By combining these improvements with the existing automated segmentation pipeline, clinicians and researchers will be able to obtain both resting-state and hyperemic 3D models in a fraction of the time required by traditional methods, helping them to analyze each patient's 3D geometry and conclude about possible conditions. Also, this software will streamline the non-invasive FFR calculation workflow, significantly reducing the time needed to be obtained.

ACKNOWLEDGMENTS

Authors gratefully acknowledge the financial support of FCT (Portugal) regarding the R&D Project "CADS-FACT – PTDC/EMD-EMD/0980/2020", the Engineering Faculty of University of Porto, the Institute of Science and Innovation in Mechanical and Industrial Engineering, the Cardiovascular R&D Unit of the Medicine Faculty of University of Porto, and the Cardiology Department of Gaia/Espinho Hospital Centre.

REFERENCES

[1] Fearon, W.F., Farouque, H.M., Balsam, L.B., Caffarelli, A.D., Cooke, D.T., Robbins, R.C., Fitzgerald, P.J., Yeung, A.C., Yock, P. G. (2003). Comparison of coronary thermodilution and Doppler velocity for assessing coronary flow reserve. Circulation, 108(18), pp.2198-2200. https://doi.org/10.1161/01.Cir.0000099521.31396.9d.

[2] Fernandes, M., Sousa, L.C., António, C.C., Pinto, S.I.S. (023). Modeling the Five-Element Windkessel Model with Simultaneous Utilization of Blood Viscoelastic Properties for FFR Achievement: A Proof-of-Concept Study. Mathematics, 11(24), 4877. https://www.mdpi.com/2227-7390/11/24/4877.

[3] Festas, J. et al., Exploring a Python-Based Semi-Automatic Approach for Coronary Artery Segmentation Proceedings of 44th Ibero-Latin American Congress on Computational Methods in Engineering (CILAMCE), 2023.

[4] Raluca Monica, C., Tarcolea, M., Vlasceanu, D., Cotrut, M.C. (2012). Virtual 3D reconstruction, diagnosis and surgical planning with Mimics software. International Journal of Nano and Biomaterials, 4, pp.69-77. https://doi.org/10.1504/IJNBM.2012.048212.

[5] Tesche, C., Gray, H.N. (2020). Machine Learning and Deep Neural Networks Applications in Coronary Flow Assessment: The Case of Computed Tomography Fractional Flow Reserve. Journal of Thoracic Imaging, 35. https://journals.lww.com/thoracicimaging/fulltext/2020/05001/machine_learning_and_deep_neural_networks.11.aspx.

[6] Updegrove, A., Wilson, N.M., Merkow, J., Lan, H., Marsden, A.L., Shadden, S.C. (2017). SimVascular: An Open Source Pipeline for Cardiovascular Simulation. Ann Biomed Eng, 45(3), pp.525-541. https://doi.org/10.1007/s10439-016-1762-8.

[7] Wilson, R.F., Wyche, K., Christensen, B.V., Zimmer, S., Laxson, D.D. (1990). Effects of adenosine on human coronary arterial circulation. Circulation, 82(5), 1595-1606. https://doi.org/10.1161/01.cir.82.5.1595.

Proceedings IRF2025: 8th International Conference on Integrity-Reliability-Failure
In Engineering, Materials, Manufacturing and Biomechanics. Porto 15-18 July 2025
DOI: https://doi.org/10.24840/978-972-752-323-8

PAPER REF: 22583

SEMI-AUTOMATIC CONSTRUCTION OF 3D CORONARY GEOMETRIES IN HYPEREMIA CONDITIONS FOR FFR ACHIEVEMENT - DEVELOPMENT OF A PYTHON SOFTWARE

G. Rodrigues[1,2(*)], M. Fernandes[1,2], L.C. Sousa[1,2], J. Festas[1,2], S.I.S. Pinto[1,2]

[1]University of Porto, Engineering Faculty, Porto, Portugal
[2]Institute of Science and Innovation in Mechanical and Industrial Engineering (LAETA-INEGI), Porto, Portugal
[(*)]*Email:* up201907214@edu.fe.up.pt

ABSTRACT

This study presents a semi-automatic computational framework capable of constructing 3D coronary arteries under hyperemic conditions, conditions where the fractional flow reserve (FFR) was obtained in the hospital. This computational software was developed in Python with the final goal of patient-specific hemodynamic replication and FFR computational prediction instead of the invasive one achieved in the hospital. The input of the developed numerical tool in Python is computed tomography (CT) scans, and the desired output is the 3D geometry in hyperemia conditions. The cross-sectional area along all the artery was enlarged compared to resting conditions.

Keywords: 3D geometry reconstruction, semi-automatic methods, hyperemia, Python, software development, fractional flow reserve.

INTRODUCTION

Coronary artery disease (CAD) is a leading cause of death. The measurement of the fractional flow reserve (FFR) allows medical doctors to assess the severity of stenoses developed in this disease, and it is currently measured invasively by the administration of chemicals that produce hyperemia (maximum vasodilation). As an alternative to the invasive procedure, which can be risky for patients in debilitated conditions, numerical simulations could be performed to measure the FFR (Fernandes et al., 2024). These simulations are performed on reconstructed patient-specific coronary arteries in hyperaemia conditions, by manually (Martins et al., 2023) altering the geometry of the segmented artery obtained through computed tomography (CT) imaging at the medical facilities. The increase of the cross-sectional area of the vessels is done through the values obtained in the work of Wilson et al. (1990). However, this procedure takes many hours, and the researcher can introduce geometric errors in the process. Therefore, an automatic method is preferred.

Through the programming in Python language, the authors of the present study have developed a semi-automatic computational framework with the objective of constructing 3D models of coronary arteries, under hyperemic conditions from the CT images. The images, as well as invasive values of the FFR, were collected by medical doctors at the Vila Nova de Gaia/Espinho Hospital Centre (CHVNG/E) from patients displaying symptoms of CAD. This framework, along with numerical simulation software, has the goal of contributing to the implementation of computational hemodynamics as a robust alternative to the invasive procedure used to measure the FFR in hospitals. As a result, the tool can provide personalized cardiovascular diagnostics and bridge the gap between imaging and clinical decision-making. In addition, the tool highlights how numerical simulations have the potential to aid medical doctors in the diagnosis and treatment choice stages.

METHODOLOGY

The 3D mask of the artery geometry obtained through the In-House software (Festas et al., 2023) is the input (Figure 1a). In this work, operations of skeletonization (Figure 1b.) are made using the sci-kit image library which allows for the reduction of the structure into a volumeless skeleton constituted of points while preserving its shape and main characteristics.

With the usage of a code made in NumPy it becomes possible to identify terminal points of the branches (Figure 1c) using neighbourhood analysis on a 3x3x3 voxel neighbourhood cube. The first method of detection is through voxel connectivity, the points that only have one neighbour are considered potential terminal points and later validated if when temporarily erased its closest point becomes a terminal point. The second method of detection is by identifying the points with two neighbours in which the angle between them is less than a certain threshold. The terminal points that belong to very small branches that rapidly enter the main branch are disconsidered since they will not significantly change the results but demand a lot of extra unnecessary work. The last step in this terminal point processing is the identification of the blood flow inlet and the outlets, which is done by analysing the coordinates.

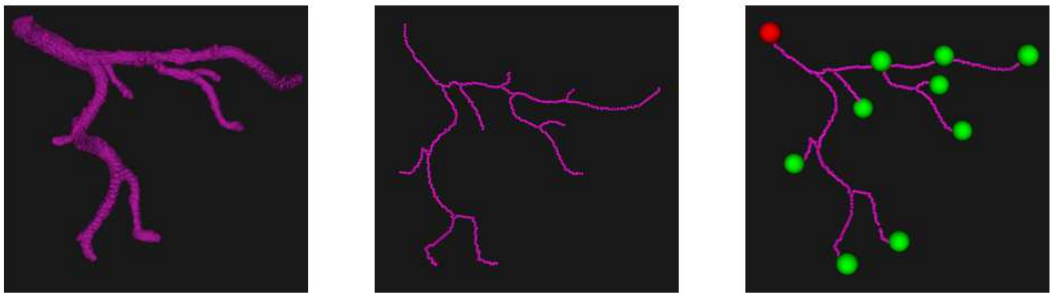

Fig. 1 - Key Process stages in terminal point definition: (a) input In-House geometry, (b) creation of the artery skeleton using Skimage morphology package, (c) definition of the terminal points as Seed and target points (in red and green, respectively).

The next stage is all about the execution of preprocessing operations for the geometry to correctly serve as input to the VMTK library. Beginning at each of the terminal points the next closest point is collected iteratively for a certain number of points. After this semi branch is composed it is possible to perform an interpolation separately for x, y and z using "*np.polyfit"* with a degree decided by the Akaike information criteria which punishes higher degrees. With this it is possible to obtain the tangent at the endpoint and to create a plane normal to that tangent which will intersect the STL model and give origin to a contour (Figure 2a) with which the structure will be clipped and then capped into a closed surface (Figure 2b).

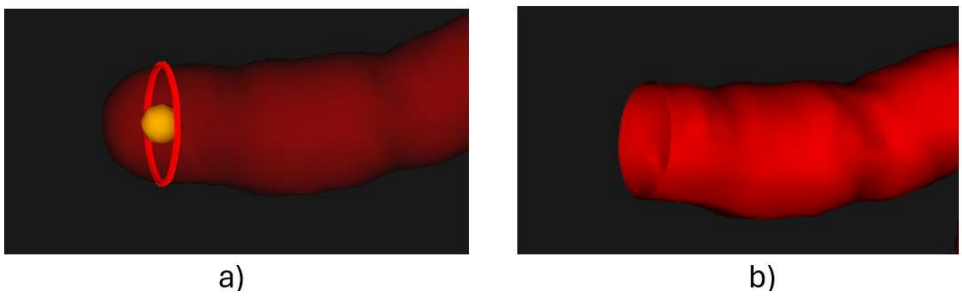

Fig. 2 - Phases of the pre-processing stage: (a) terminal zone of the geometry with endpoint (in yellow) and contour (in red), (b) clipped and capped terminal surface.

With the geometry processed VMTK is used to extract the centerline (Figure 3a) using "*vmtkCenterlines"* which can compute the shortest and most central path through the vessel geometry and multiple branches and gives as output a "*VTKPolyData"* with the coordinates of the center points, the centerlines and individual point data such as "*MaximumInscribed-SphereRadius*" which gives maximum radius of the sphere that can fit inside the vessel. With this new more accurate centerline, it is possible to use *"vmtkBranchExtractor"*, which can segment the centerline into multiple branches (Figure 3b). After this is done the next is to go through the points and retrieve notorious data such as the "*MaximumInscribedSphereRadius"* which is later organized by branch and its values augmented by a factor of 2.04 to create the hyperemic geometry. The last step to get the hyperemic geometry ready for the simulation software (Figure 3c) is to again do the previous steps done in the preprocessing stage to get a clean-cut capped terminal zone of the branch.

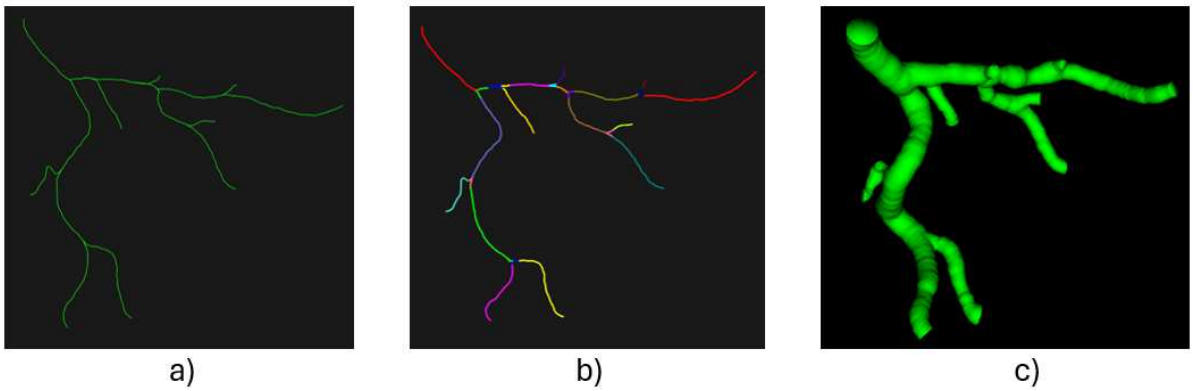

Fig. 3 - Phases in VMTK stage: (a) centerline extraction in VMTK, (b) separation into branches in VMTK, (c) hyperemic geometry ready for computational simulations.

After obtaining the 3D coronary geometries, it becomes possible to run patient-specific simulations to obtain the FFR calculations. It starts by forming a mesh that is the best balance between computational time and result accuracy and with the boundary conditions definition with user-defined functions (UDFs) written in C for inlet velocity and outlet pressures for each patient case, with a 3-element Windkessel model for pressure and a Womersley model for velocity all the while the blood rheology being described by the simplified Phan-Thien/Tanner model which accounts for the viscoelasticity of this fluid. A finite element approach was used regarding the solution of the blood flow models, set to unsteady flow with a time-step of 0.005 s for 3 consecutive cardiac cycle each with the duration of 0.72s. The momentum and UDFs functions being discretized by a second order upwind-scheme and the velocity pressure coupled governing equations were solved using a SIMPLE algorithm at each time-step. Two planes were defined, one 0.1 mm after the inlet surface and the other 20 mm after the apex of the stenosis. The pressure data was retrieved in the last cardiac cycle to reduce errors introduced by the initialization of the simulations.

RESULTS AND CONCLUSIONS

To compare the accuracy of the segmented geometries, the authors compared the output of their computational framework with the output using hyperemic geometry obtained in MIMICS® (a commercial software dedicated to the segmentation of medical imaging, including coronary CT scans), resulting FFRs obtained in the most realistic hemodynamic conditions as possible.

Table 1 - Comparison between the Computed FFR with In-House Software to obtain the 3D Geometry and the Computed FFR with Mimics software to obtain the 3D Geometry.

Parameter	Value	Relative Error
Computed FFR with In-House Software	0.457	
Computed FFR with Mimics Software	0.498	8.59%

As can be seen in the table above (Table 1) the relative error is 8.59% which is acceptable and serve as a proof of concept that the project is on the right track, since the semi-automatic geometry is a good substitute for what is usually the golden standard, the manual segmentation geometry. The difference in FFRs can be traced back to errors in both geometries. The commercial software geometry is quite labour intensive which opens the potential for error and the In-House geometry still needs further refinement in the stenosis zones and bifurcation zones since considering that the radius is expanded in a 3-D sphere and not just in the plane of the section some problems can arise. The expansion of the radius can make it so that the stenosis is not enlarged correctly due to the fact that it is surrounded by much larger spheres that when expanded can just involve the entire zone and prevent the correct expansion of the narrowed structure, which could result both in the disappearance of the characteristic narrowing or on the contrary result into a structure in which the narrowing happens all of the sudden and peaks rapidly causing an effect similar to one of a orifice plate. This 3-D expansion of the spheres can also cause problems in the geometry in the bifurcation zones since from one center point to the other the maximum inscribed radius of the sphere suddenly gets much bigger and when expanded creates a sudden much bigger sphere like shape with center in the bifurcation zone, that generates what appears to be a discontinuity in what should be a smooth, continuous geometric structure.

The objective of making a python-based semi-automatic software that could produce these hyperemic geometries in a fast and accurate way was achieved all the while depending on a very small quantity of inputs.

In regards to the next stages, the main objective is to test the In-House software for a bigger sample of patients and obtain their FFR's in order to try to achieve its validation by comparing them to the FFR's obtained invasively, and the FFR's obtained for the 3D geometries manually produced using the Mimics® commercial software. This involves testing the software for a much larger data base, right coronary arteries, left coronary arteries, stenosis with different severities, stenosis situated in different locations, all to see if the software is indeed able to reconstruct the coronary arteries in the hyperemic state in a swift way that makes its usage plausible in a clinical context.

REFERENCES

[1] Fernandes, M. et al., Fractional Flow Reserve Prediction Using In-House Computational Methods - Validation With Several Patient Cases, Proceeding of 9th Euro. Cong. on Comp. Meth. in App. Sci. and Eng., 2024. DOI:10.23967/eccomas.2024.265.

[2] Wilson, R.F. et al., Effects of adenosine on human coronary arterial circulation, Circulation, 1990, 82, pp.1595-1606.

[3] Festas, J. et al., Exploring a Python-Based Semi-Automatic Approach for Coronary Artery Segmentation, Proceedings of 44th Ibero-Latin American Congress on Computational Methods in Engineering (CILAMCE), 2023.

Proceedings IRF2025: 8th International Conference on Integrity-Reliability-Failure
In Engineering, Materials, Manufacturing and Biomechanics. Porto 15-18 July 2025
DOI: https://doi.org/10.24840/978-972-752-323-8

PAPER REF: 22584

EQUIPMENT AND ADVANCES FOR MEASURING FATIGUE IN OFFICE SETTINGS: A SYSTEMATIC REVIEW

Seyed Iliya Pezeshki[1(*)], Joana Cristina Guedes[1,2], João Santos de Baptista[1,2]

[1]Lab. Prevention of Occupational and Environmental Risks, PROA: Fac. Engineering, U. Porto, Portugal
[2]Assoc. Lab. for Energy, Transports and Aeronautics, LAETA, Fac. Engineering, U. Porto, Portugal
[(*)]*Email :* up202103483@up.pt

ABSTRACT

Fatigue in humans is a condition that decreases activity, performance, and cognitive abilities due to sensations like tiredness, drowsiness, sleepiness, and burnout. It can be categorized as objective or subjective, where objective fatigue results from prolonged mental, emotional, or physical exertion that depletes cognitive resources and energy, while subjective fatigue is the personal perception of tiredness, encompassing physical weariness, mental exhaustion, and a general lack of energy. It is influenced by mentally challenging or stressful tasks and indirectly affected by physical activities that reduce alertness, mental focus, motivation, and other psychological factors. Although fatigue has been extensively studied in fields such as transportation, emergency response, and healthcare, there remains a lack of a comprehensive, unified database for quantitatively measuring fatigue in office environments. Given its negative impact on productivity, understanding fatigue in office settings is crucial. Establishing a database that provides precise information on the causes and effects of fatigue, along with reliable measurement techniques, would be valuable for future research. To address this gap, a systematic review is proposed to investigate the relationship between office workers' sedentary status throughout their workdays and the resulting fatigue-induced pains and cognitive function reductions.

Keywords: PRISMA, pain, occupational, office worker.

INTRODUCTION

Fatigue is a well-documented factor in reducing human performance across various fields (Williamson et al. 2005). It can be categorized as objective, resulting from prolonged cognitive or physical effort, or subjective, which is the personal perception of tiredness and exhaustion (Bustos et al. 2021). Fatigue affects response and decision-making time, leading to human error, particularly in high-risk professions such as military service, driving, and offshore work (Meijer, Robb, and Smit 2017; Sant'Anna and Hilal 2021). However, even in low-risk environments like office work, fatigue can contribute to health issues and productivity losses (Arezes et al. 2020). Office workers are prone to musculoskeletal disorders, psychological issues, and absenteeism, all of which negatively impact individual well-being and organizational efficiency (Abdulameer, Finteel, and Flayyih 2020; Lima and Coelho 2018; Rizzo, Peresson, and Larese Filon 2012).

Fatigue assessment methods include subjective tools like the Nordic Musculoskeletal Questionnaire and Cornell Musculoskeletal Discomfort Questionnaires (Bazazan et al. 2019; Chaiklieng and Poochada 2021) and objective tools such as Electroencephalography (EEG) and surface Electromyography (EMG) (Fu et al. 2022; Mota-Carmona et al. 2022; Ramirez-Moreno et al. 2021). However, many of these methods are intrusive, time-consuming, and impractical

for office settings (Pimenta et al. 2013). With advancements in technology, non-intrusive fatigue assessment methods using computers and machine learning have gained interest (Bustos et al. 2019; Bustos et al. 2021; Ramos et al. 2020). Machine learning enables computers to improve performance based on data, showing potential for fatigue detection, though its application in office work remains underexplored. Despite office work being less risk-prone than other professions, research on fatigue in this sector is limited. This study aims to address this gap by reviewing available methodologies for fatigue assessment in office environments.

RESULTS AND CONCLUSIONS

A total of 31 studies were selected for analysis. Among them, various equipment and methodologies were used to measure fatigue, as depicted in the accompanying chart, Figure 1. The chart categorizes the number of articles utilizing different equipment for assessing muscle-related and brain-related fatigue. Specifically, questionnaires were the most commonly used method for assessing brain fatigue (14 articles), followed by heart rate variability (HRV) (3 articles) and cognitive tests (1 article). For muscle fatigue, electromyography (EMG)/electrocardiography (ECG) was the most frequently used method (7 articles), followed by questionnaires (4 articles), other logging tools (1 article), and HRV (1 article). This data highlights the predominant reliance on subjective assessments and underscores the potential for further exploration of objective, non-intrusive fatigue measurement techniques.

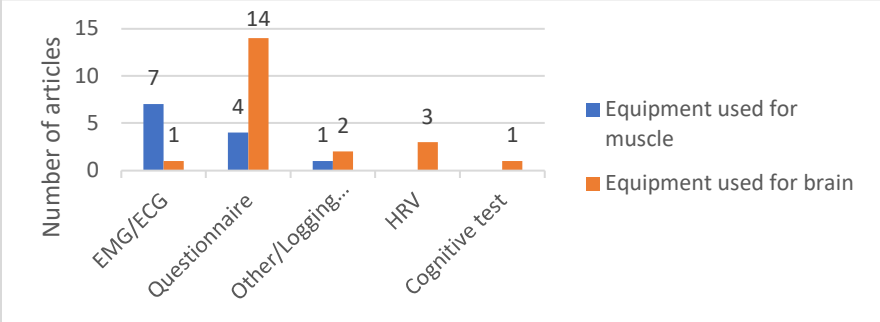

Fig. 1 - Clustered-column chart of the different equipment used for fatigue detection (made by Microsoft Excel).

The findings from this study will contribute to the development of more practical, cost-effective, and scalable solutions for monitoring and mitigating fatigue in office work settings. By identifying and optimizing assessment techniques, this research aspires to enhance workplace health, reduce fatigue-related inefficiencies, and pave the way for future advancements in non-intrusive fatigue detection systems.

REGISTRATION AND PROTOCOL

The protocol for this systematic review has been registered on PROSPERO with the reference number CRD42023408696.

REFERENCES

[1] Abdulameer, M.M., Finteel, A.K., Flayyih, S.K. (2020). Exercise therapy for musculoskeletal pain among office workers: A narrative review. Journal of Pain Management, 13(2), pp.115-118.

[2] Arezes, P.M., Baptista, J.S., Carneiro, P., Castelo Branco, J., Costa, N., Duarte, J., Guedes, J.C., Melo, R.B., Miguel, A.S., Perestrelo, G. (Eds.), Studies in Systems, Decision and Control (Vol. 277). Springer International Publishing. https://doi.org/10.1007/978-3-030-89617-1.

[3] Bazazan, A., Dianat, I., Feizollahi, N., Mombeini, Z., Shirazi, A.M., Castellucci, H. I. (2019). Effect of a posture correction–based intervention on musculoskeletal symptoms and fatigue among control room operators. Applied Ergonomics, 76, pp.12-19. https://doi.org/10.1016/j.apergo.2018.11.008.

[4] Bustos, D., Guedes, J.C., Alvares, M., Baptista, J.S., Vaz, M., Torres Costa, J.C. (2019). Real time fatigue assessment: Identification and continuous tracing of fatigue using a physiological assessment algorithm. Studies in Systems, Decision and Control, 202, pp257-265. https://doi.org/10.1007/978-3-030-14730-3_28.

[5] Bustos, D., Guedes, J.C., Pratas, P., Vaz, M.P., Costa, J.C.T., Fernandes, R.J., Baptista, J.S. (2021). Fatigue detection through physiological assessment during real-life occupational situations: Preliminary results. pp.49-55. https://doi.org/10.24840/978-972-752-279-8_0049-0055.

[6] Chaiklieng, S., Poochada, W. (2021). Assessment of Muscle Fatigue and Potential Health Risk of Low Back Pain Among Call Center Workers. In Lecture Notes in Networks and Systems (Vol. 273, pp.54-61). https://doi.org/10.1007/978-3-030-80713-9_8.

[7] Fu, Y.L., Liang, K.C., Song, W., Huang, J.L. (2022). A hybrid approach to product prototype usability testing based on surface EMG images and convolutional neural network classification. Computer Methods and Programs in Biomedicine, 221. https://doi.org/10.1016/j.cmpb.2022.106870.

[8] Lima, T.M., Coelho, D.A. (2018). Ergonomic and psychosocial factors and musculoskeletal complaints in public sector administration – A joint monitoring approach with analysis of association. International Journal of Industrial Ergonomics, 66, pp.8594. https://doi.org/10.1016/j.ergon.2018.02.006.

[9] Meijer, K., Robb, M., Smit, J. (2017). Shift work fatigue in the petroleum industry: A proactive fatigue countermeasure. Proceedings - SPE Annual Technical Conference and Exhibition, 0. https://doi.org/10.2118/187048-MS.

[10] Mota-Carmona, J.R., Pérez-Escamirosa, F., Minor-Martínez, A., Rodríguez-Reyna, R. M. (2022). Muscle fatigue detection in upper limbs during the use of the computer mouse using discrete wavelet transform: A pilot study. Biomedical Signal Processing and Control, 76. https://doi.org/10.1016/j.bspc.2022.103711.

[11] Pimenta, A., Carneiro, D., Novais, P., Neves, J. (2013). Monitoring Mental Fatigue through the Analysis of Keyboard and Mouse Interaction Patterns. In Lecture Notes in Computer Science (including subseries Lecture Notes in Artificial Intelligence and Lecture Notes in Bioinformatics): Vol. 8073 LNAI (pp.222-231). https://doi.org/10.1007/978-3-642-40846-5_23.

[12] Ramirez-Moreno, M.A., Carrillo-Tijerina, P., Candela-Leal, M.O., Alanis-Espinosa, M., Tudon-Martinez, J.C., Roman-Flores, A., Ramirez-Mendoza, R.A., Lozoya-Santos, J.J.D., Ramírez-Moreno, M.A., Carrillo-Tijerina, P., Candela-Leal, M.O., Alanis-Espinosa, M., Tudón-Martínez, J.C., Roman-Flores, A., Ramírez-Mendoza, R.A., Lozoya-Santos, J.J.D. (2021). Evaluation of a Fast Test Based on Biometric Signals to Assess Mental Fatigue at the Workplace-A Pilot Study. International Journal of Environmental Research and Public Health, 18(22). https://doi.org/10.3390/ijerph182211891 WE - Science Citation Index Expanded (SCI-EXPANDED) WE - Social Science Citation Index (SSCI).

[13] Ramos, G., Vaz, J.R., Mendonça, G.V., Pezarat-Correia, P., Rodrigues, J., Alfaras, M., Gamboa, H. (2020). Fatigue Evaluation through Machine Learning and a Global Fatigue Descriptor. Journal of Healthcare Engineering, 2020, pp.1-18. https://doi.org/10.1155/2020/6484129.

[14] Rizzo, M., Peresson, M., Larese Filon, F. (2012). Approccio alla valutazione dello stress lavoro-correlato in un'Azienda Sanitaria. Giornale Italiano Di Medicina Del Lavoro Ed Ergonomia, 34(3), pp.716-719.

[15] Sant'Anna, D.A.L.M. de, Hilal, A.V.G. de. (2021). The impact of human factors on pilots' safety behavior in offshore aviation companies: A brazilian case. Safety Science, 140. https://doi.org/10.1016/J.SSCI.2021.105272.

[16] Williamson, R.J., Purcell, S., Sterne, A., Wessely, S., Hotopf, M., Farmer, A., Sham, P. C. (2005). The relationship of fatigue to mental and physical health in a community sample. Social Psychiatry and Psychiatric Epidemiology, 40(2), pp.126-132. https://doi.org/10.1007/S00127-005-0858-5.

Proceedings IRF2025: 8th International Conference on Integrity-Reliability-Failure
In Engineering, Materials, Manufacturing and Biomechanics. Porto 15-18 July 2025
DOI: https://doi.org/10.24840/978-972-752-323-8

PAPER REF: 22640

PRINCIPAL COMPONENT ANALYSIS AND HIDDEN MARKOV MODELS OF ELECTRICAL SUBMERSIBLE PUMPS DATA TO FAILURE DETECTION

Paulo Yoshio Kuga(*), Alberto Luiz Serpa

FEM/UNICAMP, School of Mechanical Engineering, Universidade Estadual de Campinas, Campinas, São Paulo, Brazil.
(*)*Email:* p204451@dac.unicamp.br

ABSTRACT

In Electrical Submersible Pump (ESP) operations, several sensors provide real-time data related to operation monitoring, such as electrical current, pressure, temperature, vibration and others. In the proposed article, the intent is to use a Principal Component Analysis (PCA) to identify anomalous behaviour in time series. Moreover, a Hidden Markov Model (HMM) is used to classify abnormalities and provide insights about their probabilities.

Keywords: ESP failures, time-series failure detection, Hidden Markov Models, Principal Component Analysis.

INTRODUCTION

Most ESP failure detection studies use supervised learning (Mohammed, 2023; Yang et al., 2022; Lastra and Xiao, 2022) with methods like SVM, K-Means, and Boosted Trees. These require labelling when the failure happened, which is not always feasible. This work explores unsupervised techniques, applying PCA and HMM to detect failures without prior knowledge. HMM has been previously used in failure prediction (Zhou et al., 2010; Smyth, 1994).

The objective using PCA is to show up combined components that represent major variance of measured signals, that contains corrupted sections. Some physical properties can be measured through its combinations, for example power and impedance may reveal intrinsically current and voltage. The PCA generates components, and HMM is applied to it. This model provides a hidden state model that brings insights about probabilities of abnormalities in the ESP time-series.

RESULTS AND PRELIMINAR CONCLUSIONS

An example of PCA and filtering applications is stated on Figure 1. The original set of signals is merged with a noise. Then, it's randomly recombined. To reduce noise effect, a low-pass filter is applied, and PCA is applied. It is possible to, preliminarily, conclude that the original set of signals is recovered, in this simple preliminary problem, put as a test.

As stated in Figure 2, the norm-2 is obtained and an HMM model is applied. For each segment in the dataset, a hidden state is inferred. This allows to have insights about the abnormality and its probability of occurrence. In the figure, the abnormality is predicted at state 3, but the usage of the model is going to be studied further.

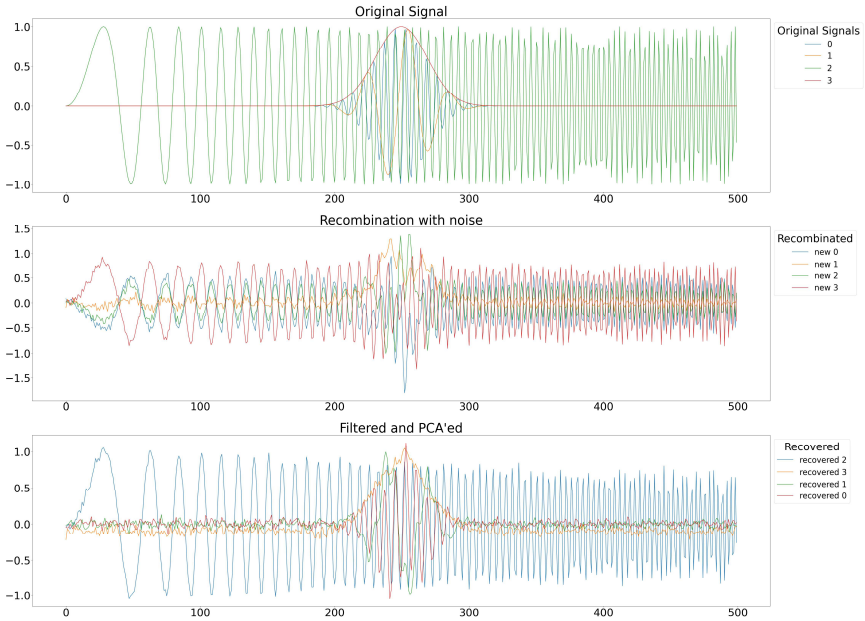

Fig. 1 - The simulated procedure proposed in this article for PCA.

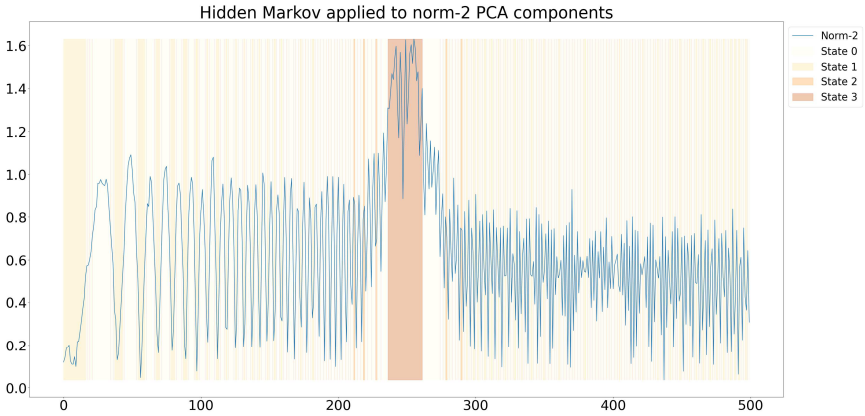

Fig. 2 - HMM for the norm-2 (Square) result of PCA components. The abnormality was revealed through state 3.

REFERENCES

[1] Lastra, R., Xiao, J. Machine Learning Engine for Real-Time ESP Failure Detection and Diagnostics. SPE Middle East Artificial Lift Conference and Exhibition, 2022 - 10.2118/206935-MS.

[2] Mohhamed, A. Data driven-based model for predicting pump failures in the oil and gas industry. Engineering Failure Analysis, v. 145, p.107019, 2023. ISSN 1350-6307.

[3] Smyth, P. Hidden Markov models for fault detection in dynamic systems. Pattern Recognition, v. 27, n. 1, pp.149-164, 1994. ISSN 0031-3203.

[4] Yang, P., Chen, J., A fault identification method for electric submersible pumps based on DAE-SVM. Shock and Vibration, v. 2022, n. 1, p.5868630, 2022.

[5] Zhou, Z.-J, Hu, C., Xu, D., Chen, M., Zhou, D. A model for real-time failure prognosis based on hidden markov model and belief rule base. European Journal of Operational Research, v. 207, n. 1, pp. 269-283, 2010. ISSN 0377-2217.

Proceedings IRF2025: 8th International Conference on Integrity-Reliability-Failure
In Engineering, Materials, Manufacturing and Biomechanics. Porto 15-18 July 2025
DOI: https://doi.org/10.24840/978-972-752-323-8

PAPER REF: 22648

ALIGNING CORONARY AND VENTRICULAR SEGMENTATIONS FOR AN INTEGRATED ASSESSEMENT OF CARDIAC FUNCTION

J. Festas[1,2(*)], A.F.A. Senra[1,2], L.C. Sousa[1,2], S.I.S. Pinto[1,2]

[1]University of Porto, Engineering Faculty, Porto, Portugal
[2]Institute of Science and Innovation in Mechanical and Industrial Engineering (LAETA-INEGI), Porto, Portugal
[(*)]*Email:* up201705997@up.pt

ABSTRACT

Coronary artery disease (CAD) remains a leading cause of mortality worldwide, highlighting the need for effective treatment strategies and enhanced patient care. Traditionally, CAD diagnosis involves evaluating coronary arteries through shape evaluation and hemodynamic measurements such as fractional flow reserve (FFR). However, not all coronary regions flagged as potentially compromised necessarily impact the ventricular myocardium. To accurately assess cardiac function, it is essential to analyze absolute myocardial perfusion alongside coronary hemodynamics. This project aims to integrate hemodynamic analysis of the coronary arteries with myocardial perfusion assessment, establishing a spatial correlation between coronary artery outlets and specific ventricular segments. By leveraging consistency in image acquisition techniques, both relying in computed tomography (CT), we developed novel in-house segmentation algorithms in Python to achieve this goal.

Keywords: Coronary artery disease, myocardial perfusion, hemodynamic, image acquisition techniques, segmentation algorithms, Python.

INTRODUCTION

Coronary artery disease (CAD) remains the leading global cause of mortality due to its detrimental effects on myocardial perfusion and cardiac functionality. The condition is predominantly driven by atherosclerotic plaque accumulation within the coronary arteries, which progressively impairs blood flow. Such blockages can result in myocardial ischemia, infarction, or heart failure. Effective clinical management requires more than the identification of anatomical stenoses; it necessitates an understanding of the functional repercussions of these lesions. Despite advancements in diagnostic imaging and pressure-based assessments, discerning physiologically significant lesions continues to pose a challenge. Not all anatomically apparent lesions manifest as perfusion deficits.

Fractional Flow Reserve (FFR) and Computed Tomography Angiography (CTA) have become integral tools in evaluating coronary artery patency and stenotic severity. FFR is well-established for its ability to quantify the physiological impact of coronary stenoses by measuring pressure gradients across lesions during pharmacologically induced hyperemia. Recent developments have enabled non-invasive FFR assessment using computational models derived from CTA imaging (De Bruyne et al., 2012). Concurrently, Computed Tomography Perfusion (CTP) imaging offers temporal insights into myocardial blood flow, providing critical information about ischemia. The synergistic use of CTA and CTP has demonstrated improved diagnostic accuracy in identifying functionally significant coronary lesions (George et al., 2011).

Nevertheless, the clinical application of CTA-derived FFR and CTP often occurs in silos. This disjointed analysis impairs spatial correlation between coronary lesions and their downstream myocardial effects, thereby limiting the capacity to draw comprehensive conclusions regarding cardiac function.

To address this disjunction, we introduced a suite of Python-based segmentation pipelines specifically developed for coronary arteries (Festas et al., 2023) and the left ventricular myocardium (Senra et al., 2024). Additionally, we proposed a novel co-registration methodology utilizing the aorta as a common anatomical anchor, as it is consistently present in both CTA and CTP datasets. This technique facilitates the spatial alignment of coronary anatomy with myocardial perfusion data.

The integration of these datasets culminates in a unified spatial map that enables precise association between coronary anatomical features and their physiological consequences. This approach promises a more nuanced and clinically valuable understanding of CAD by concurrently analyzing anatomical and perfusion-based markers of disease severity.

METHODOLOGY

Coronary Artery Segmentation

To extract accurate vessel geometry from Computed Tomography Angiography (CTA) scans, our coronary artery segmentation approach was crafted to address typical challenges like undersegmentation and limited contrast near stenotic regions. The process begins with a region-growing technique initiated at a user-defined seed within the aorta. This step segments an initial underdeveloped representation of the coronary structure, followed by its separation from the aorta.

The enhancement phase then applies a three-part refinement process implemented in Python, relying on the scikit-image and numpy libraries. This procedure operates on a preprocessed 3D CTA volume and is structured as follows:

1. **Dual Region-Growing Phase:**

Using two duplicated image arrays, this step runs side-by-side region growing to separately isolate the coronary arteries and the aorta. By adjusting the Hounsfield Unit (HU) threshold dynamically and removing overlapping voxels, the method improves the accuracy of boundary identification. The iterative growth is carefully controlled—constrained by maximum HU values and relative volume change thresholds—to avoid capturing unrelated high-density tissues, which helps prevent oversegmentation.

2. **Gradient-Informed Vessel Tracking:**

This phase enhances boundary clarity, especially in curved or poorly contrasted vessel regions. A Frangi vesselness filter, known for emphasizing tubular shapes, is applied to identify likely vessel candidates. Voxels are then selected within a 3D region of interest based on a hybrid of intensity and gradient measures. This step is critical where intensity alone is insufficient to define vessel edges, allowing for more robust and refined segmentation.

3. **Centerline Propagation and Continuity Recovery:**

Areas of severe narrowing often interrupt prior segmentation attempts. To address this, a centerline skeleton of the segmented structure is computed, and terminal branches are extended directionally. These projections rely on both voxel intensity and connectivity cues to predict

vessel continuation. Once missing portions are reconstructed, the earlier steps are repeated to re-integrate the full vessel path.

By combining these strategies, the final segmentation output reflects a highly detailed and continuous reconstruction of the coronary arteries, Figure 1 shows the differences these steps make on the final segmentation. This robustness extends to anatomically intricate areas, allowing for more dependable structural analysis that supports downstream clinical and research applications. [3].

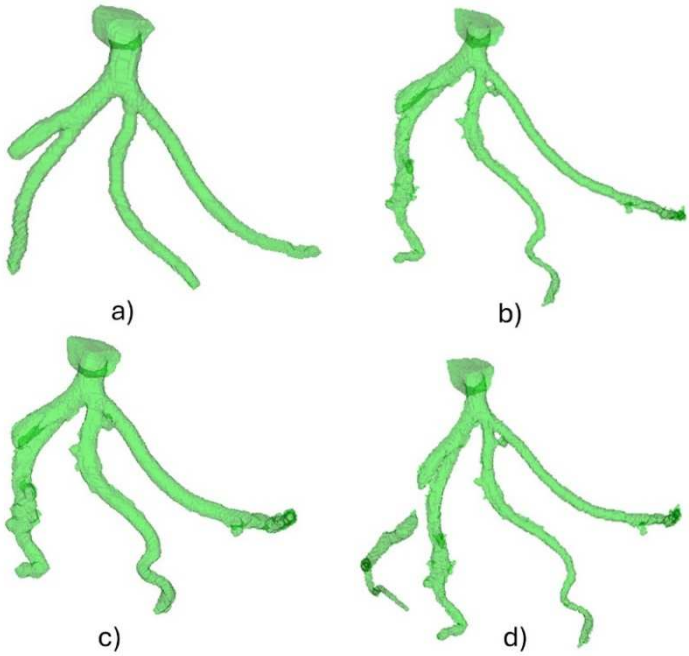

Fig. 1 - a) Coronary Artery right after separation from the aorta; b) Increase in total segmentation vi aside by side region growing; c) Improvement of boundaries using gradient informed región growing; d) Inclusion of a missing Branch retrieved via centerline propagation.

Left Ventricle Segmentation

Segmenting the left ventricle (LV) from dynamic computed tomography perfusion (CTP) images presents substantial challenges, primarily due to inherent limitations in image quality, the presence of motion artifacts, and considerable anatomical variability over the cardiac cycle. To overcome these obstacles, we implemented a semi-automated pipeline in Python designed for reliable and efficient segmentation of the LV using limited manual intervention.

The workflow initiates with a manual indication of the mitral valve region on a selected CTP frame with optimal contrast. This input defines the mitral valve plane, offering a crucial anatomical boundary between the atrium and ventricle. From this landmark, a targeted region of interest (ROI) containing the LV is extracted for further processing.

Segmentation within this ROI unfolds in two primary stages. Region-growing methods are applied from both long-axis and short-axis views to outline the blood-filled cavity of the left ventricle. These multi-view approaches enhance the segmentation's spatial robustness and reduce sensitivity to image noise or partial volume effects. The myocardial wall is identified by refining the inner and outer boundaries using morphological transformations and strategic image rotations. These steps improve delineation across varying orientations and ensure the contours remain anatomically consistent.

After initial segmentation, a post-processing phase removes residual non-ventricular structures and artifacts. This refinement is achieved by combining anatomical priors from both axis planes with morphological operations that enforce spatial coherence. Figure 2 shows the different stages of this segmentation process.

A reference frame—typically the image with peak contrast enhancement—is selected to define a baseline LV mask. This frame serves as the foundation for tracking changes throughout the dynamic sequence.

To extend the segmentation across all timepoints, the cavity in the reference image is used as a spatial anchor. For each subsequent frame, the algorithm searches within a constrained window around the prior segmentation. This search relies on intensity-based thresholding that adapts dynamically to the contrast agent's temporal dynamics—compensating for wash-in and wash-out effects. The assumption underpinning this approach is that although contrast intensity varies, ventricular shape and location remain relatively stable over short time intervals. In cases where this assumption breaks down—due to significant motion or contrast degradation—the method allows for fallback strategies such as increased thresholding stringency or manual correction, although such interventions were seldom necessary in practice.

The end result is a time-resolved map of the left ventricular cavity. This facilitates the construction of contrast time-attenuation curves, enabling extraction of clinically meaningful perfusion parameters critical for evaluating myocardial function. [4]

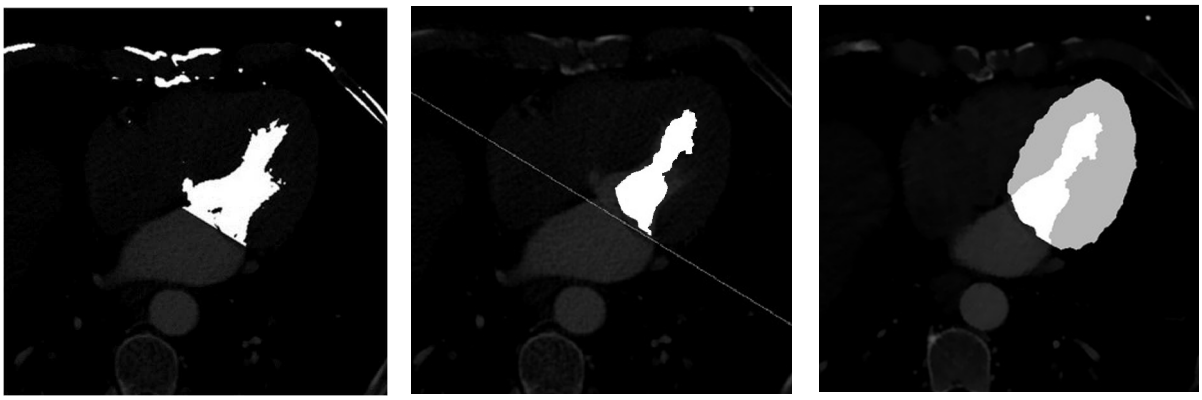

Fig. 2 - a) Identification of ROI above the mitral plane; b) Segmentation of the blood filled cavity with the representation of the mitral plane; c) Propagation of the segmentation to the myocardium.

Alignment Strategy

To achieve a unified spatial framework that links anatomical and functional cardiac data, accurate alignment between the coronary artery structures extracted from CTA and the left ventricular myocardium segmented from CTP is critical. This alignment is anchored by the aorta—a common anatomical feature visible in both imaging modalities—which serves as a stable reference despite differences in resolution and contrast.

In the high-resolution CTA-based coronary segmentation pipeline, the process begins with user input: a seed placed in the ascending aorta. This initiates region growing that captures both the aorta and the left ventricle. Through a combination of intensity thresholding, binary morphological filtering, and a minimum-cost path strategy, the algorithm iteratively identifies the aortic valve, a key anatomical boundary separating the aorta from the heart chambers. Once the valve is detected, the coronary arteries are separated from the aortic structure, and the segmentation pipeline proceeds as described previously.

By contrast, the lower resolution and higher noise levels of CTP imaging make automated valve detection more error-prone. In these cases, manual input is introduced to specify the aortic valve location in a selected axial slice, allowing the segmentation to proceed and extract the CTP-based aorta mask.

After both aortas have been successfully segmented, the CTA and CTP datasets are spatially co-registered through a rotational optimization process. One segmented aorta volume is rotated relative to the other to find the orientation that yields maximum volumetric overlap. The resulting transformation matrix is then applied to align the full coronary artery model and the left ventricle mask into a shared anatomical coordinate space.

By using the aorta as a central anatomical anchor, this alignment method ensures that subsequent spatial analyses—such as correlating coronary branches with myocardial perfusion territories—are anatomically coherent. This cross-modality consistency is critical for clinical applications, particularly when dealing with heterogeneous image quality, different acquisition timings, or patient movement between CTA and CTP scans.

RESULTS

The coronary artery segmentation algorithm was first evaluated using a dataset provided by the collaborating hospital. Six patient cases were tested, with segmentation results compared against manual annotations generated using a commercial cardiovascular analysis platform. The method achieved a mean Dice similarity coefficient of 0.845, indicating strong agreement with expert-defined ground truth.

To assess scalability, the same segmentation pipeline was applied to 100 patients from a publicly available dataset. When compared to the provided reference labels, the method achieved a mean Dice coefficient of 0.7747, confirming reliable performance across varied imaging conditions and anatomical variability. Figure 3 shows a final segmentation of a left coronary artery.

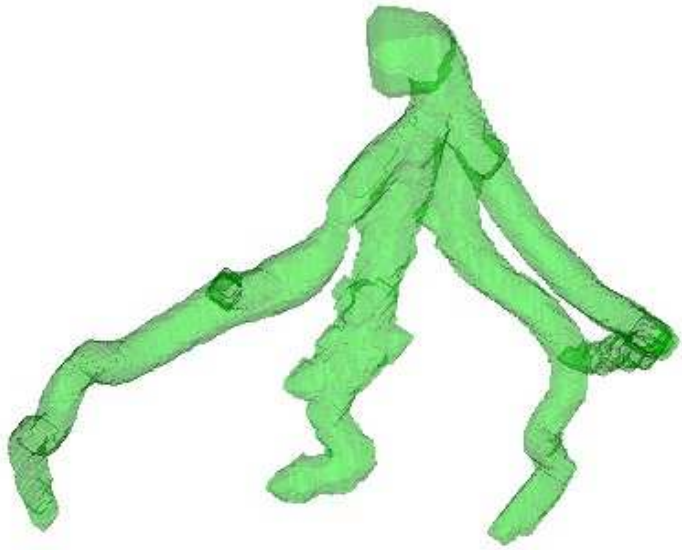

Fig. 3 - A segmented result for a single left coronary artery, with a focus on the reconstructed vessel after all steps re reprocessed because a new Branch was found via centerline propagation.

Left ventricle segmentation from CTP volumes was tested qualitatively on two patient cases from the hospital dataset, the 3d volume of 1 can be seen in Figure 4. While formal metrics are pending, visual inspection showed promising results across all timepoints, including low-contrast phases of the contrast-enhanced sequence. The consistent segmentation of the LV cavity over time also enabled the construction of a time-volume curve, capturing the evolution of contrast-filled blood volume throughout the cardiac cycle. This visualization, in Figure 5, serves as a foundation for future dynamic perfusion analysis and parameter extraction.

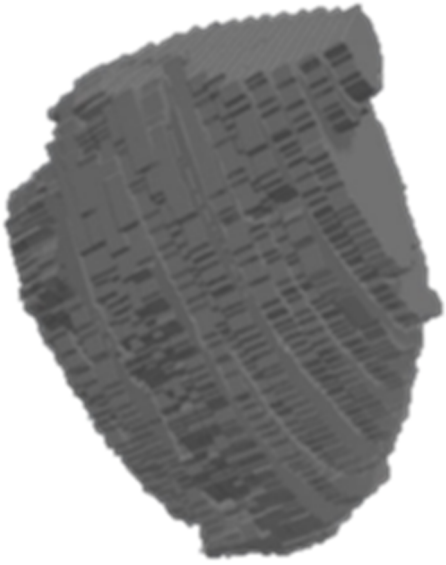

Fig. 4 - A segmented result for a single CTP volume, demonstrating successful delineation of the ventricular myocardium.

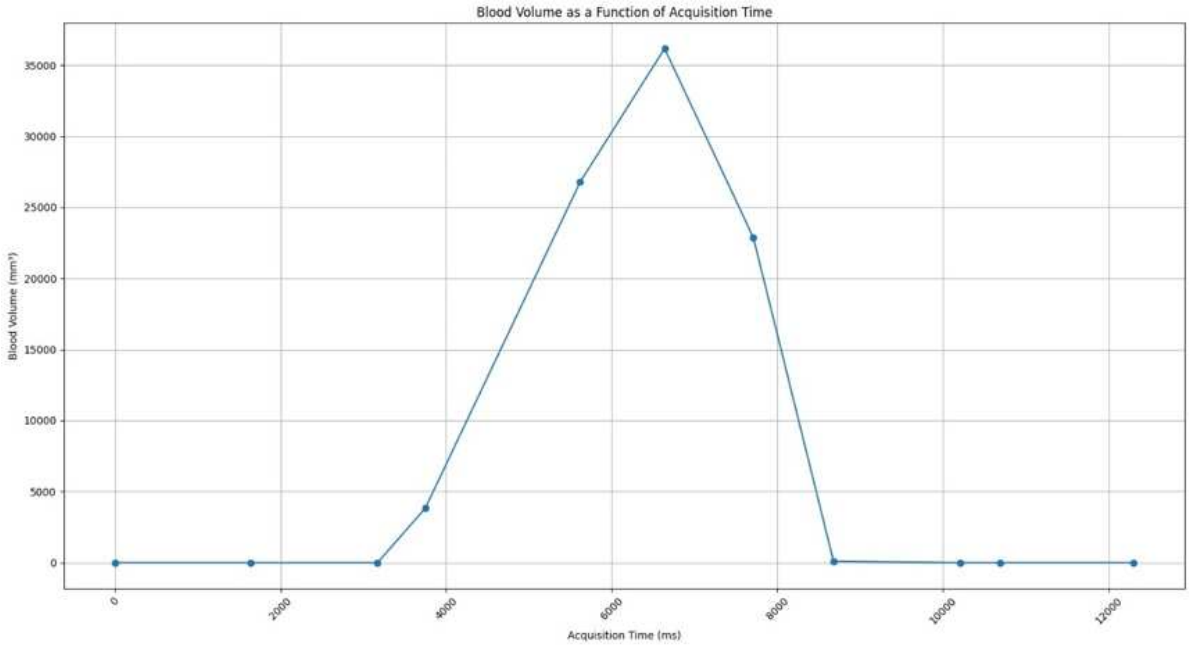

Fig. 5 - Evolution blood with contrast in the cavity throughout the acquisition time [4].

CONCLUSIONS AND FUTURE WORK

This study introduces a fully developed computational pipeline that encompasses segmentation of the coronary arteries and the LV, alongside an aorta-based alignment method designed to unify anatomical and functional cardiac imaging data. The proposed framework stands out for its precision and practicality, achieved without reliance on deep learning methodologies.
The coronary artery segmentation module has been rigorously validated using both clinical and publicly available datasets. It achieved Dice similarity coefficients of 0.845 and 0.7747, respectively, aligning closely with outcomes from more resource-intensive, state-of-the-art systems. These results highlight the accuracy, flexibility, and practical relevance of the method, particularly in diverse imaging conditions where traditional deep learning approaches may struggle without large training datasets.

The LV segmentation process, though still being refined, has shown encouraging performance in its early applications. It has maintained consistent accuracy across all phases of contrast-enhanced CTP image sequences, including those with suboptimal quality. The resulting segmentations enable the derivation of time-volume curves, which serve as a basis for estimating dynamic perfusion parameters. These metrics hold significant clinical value for assessing myocardial function and diagnosing ischemic conditions.

Equally important is the alignment strategy based on the aorta, which successfully bridges CTA and CTP datasets by spatially registering segmented structures. This method ensures anatomical consistency across imaging modalities, allowing for the precise mapping of coronary perfusion territories onto the myocardium. Such integration is pivotal for evaluating the physiological impact of coronary artery lesions.

Collectively, the framework demonstrates not only robustness across imaging environments but also clear potential for clinical translation. By linking anatomical structures to their functional consequences, this approach supports a more holistic understanding of coronary artery disease and facilitates comprehensive cardiac evaluation.

Despite the promising outcomes achieved thus far, several areas remain open for refinement and further investigation to strengthen the system's clinical utility. The most pressing task is to undertake a rigorous quantitative validation of the LV segmentation algorithm. This will enable a more objective evaluation of its accuracy across different phases of the cardiac cycle and under varied contrast enhancement levels. Through such analysis, critical timepoints and anatomical regions where segmentation may falter can be identified and systematically improved.

Concurrently, work is advancing on the development of an automated hyperemia model tailored for the coronary arteries. This component is central to enabling computational simulation of FFR, offering a non-invasive alternative for assessing the hemodynamic significance of coronary lesions. Automating hyperemia modeling is expected to substantially streamline functional evaluation without requiring pharmacological or catheter-based interventions.

Another major trajectory for development is the establishment of a detailed perfusion-to-artery mapping framework. The objective here is to spatially associate localized perfusion signals in the ventricular myocardium with their corresponding coronary artery branches. By defining myocardial perfusion at the segmental level and linking it to proximal arterial structures, the framework could determine whether specific lesions exert a physiologically meaningful impact on cardiac function. This level of integration is essential for differentiating between anatomically visible but functionally insignificant stenoses and those that warrant intervention.

Together, these future enhancements aim to evolve the current system into a comprehensive, non-invasive diagnostic platform. Such a tool would not only capture the structural complexity of coronary artery disease but also elucidate its functional consequences—enabling clinicians to make more informed, patient-specific treatment decisions.

REFERENCES

[1] De Bruyne, B. et al. Fractional Flow Reserve–Guided PCI for Stable Coronary Artery Disease, The New England Journal of Medicine, 2014.

[2] Magalhães, T.A. et al. Combined coronary angiography and myocardial perfusion by computed tomography in the identification of flow-limiting stenosis - The CORE320 study: An integrated analysis of CT coronary angiography and myocardial perfusion, Journal of Cardiovascular Computed Tomography, 2015.

[3] Festas, J. et al., Exploring a Python-Based Semi-Automatic Approach for Coronary Artery Segmentation, Proceedings of 44th Ibero-Latin American Congress on Computational Methods in Engineering (CILAMCE), 2023.

[4] Senra A.F.A. et al., Semi-Automatic Construction of Heart Left Ventricle from Dynamic CTP Images Development of Python Software, Master's Thesis, Faculdade de Engenharia da Universidade do Porto, 2024.

SYMPOSIUM - 6

Innovative Engineering Education: From Lessons to Emerging Practices

Sónia I.S. Pinto[1(*)] and Rosaire Mongrain[2(*)]

(1) Mech. Engineering Department, Faculty of Engineering University of Porto, Porto, Portugal
(2) Mechanical Engineering Department, McGill University, Montreal, Canada

(*)Associate Editor for papers in this Symposium

Proceedings IRF2025: 8th International Conference on Integrity-Reliability-Failure
In Engineering, Materials, Manufacturing and Biomechanics. Porto 15-18 July 2025
DOI: https://doi.org/10.24840/978-972-752-323-8

PAPER REF: 22472

IMPLEMENTATION OF DESIGN ACTIVITIES FOR CAPSTONE ENGINEERING TEAMS FOR COMMUNICATION SKILLS

Rosaire Mongrain(*), Mark Driscoll
Department of Mechanical, McGill University, Montreal, Canada
(*)*Email:* rosaire.mongrain@mcgill.ca

ABSTRACT

This paper reports observations made during a 5-year implementation of Capstone Engineering Projects for Medical Technologies Design at McGill University. This effort was realized in the context of a NSERC Engineering Design Chair for unifying the capstone projects across all departments in the Faculty of Engineering in order to strengthen the diversity of students design training. Communication is a key skill for ensuring teams success, especially for multidisciplinary work. Communication skills were evaluated using direct and indirect assessment tools. The direct assessment tools are a set of specific design activities that were elaborated to develop several skills including communication. It is reported that teams acquired the required communication skills based on the graded work and survey results.

Keywords: Capstone course, Multidisciplinary Team, Communication skills, Design Activities.

INTRODUCTION

A NSERC Design Chair (Natural Sciences and Engineering Research Council of Canada) was put in place in 2019 in the Faculty of Engineering at McGill University [1]. The NSERC Chairs in Design Engineering were established to improve the level and quality of design engineering activity within Canadian universities through multidisciplinary and interdisciplinary training to support the growing demand for design engineering talent for emerging fields such as climate change technologies [2, 3], aerospace [4] and medical technologies [5]. The specific field this NSERC Chair in Design was the Design of Medical Technologies. A cornerstone specific talent is communication. Indeed, communication is key in clarifying the design objectives, learning disciplinary languages and organizing resources. It should be emphasized that communication is paramount for establishing accountability, avoid misinterpretation and conflict. We present a set of Design Activities which include specific tasks meant to develop communication skills.

RESULTS AND CONCLUSIONS

The investigation is illustrated with the final year Capstone course. In this course, students work in teams of four students on a common design project during the entire academic year. The Canadian accreditation body for engineering programs in Canada is the CEAB (Canadian Engineering Accreditation Board) [6]. CEAB has developed graduate attributes to establish national standards for engineering education [6]. There are 12 graduate attributes to assess the engineering programs which include Communication skills [6, 7]. The CEAB description for the Communication skills attribute (CS) reads: “An ability to communicate complex engineering concepts within the profession and with society at large.”. The CS attribute was assessed with several graded design activities. The developed Design Activities are labelled with Design Activity Numbers (DANs). The following DANs were included for assessing the written and oral communication skills: DAN 5 (Conceptual Design Report); DAN 6

(Embodiment Design Report); DAN 8 (Oral presentation of the group project); DAN 9: (Presentation of the working prototype) and DAN 10 (Final Project Report).

The specific CEAB indicators that were assessed include [6]:

CS.1 - Understands, interprets and/or assesses oral, written, graphical or visual communications

CS.2 - Produces written research papers, engineering reports and design documentation

CS.3 - Demonstrates competency in the oral communication of complex engineering concepts

CS.4 - Demonstrates an ability to give and/or effectively respond to clear instructions

Figure 1(a) shows the results from the 2022-2023 year that incorporates the CS indicators and Figure 1(b) reports the results of student surveys that were performed at the end of the Capstone course. We note that the majority of students exceed expectations for the CS attribute. An alumni survey revealed that 70% were satisfied with the quality of the Communication skills.

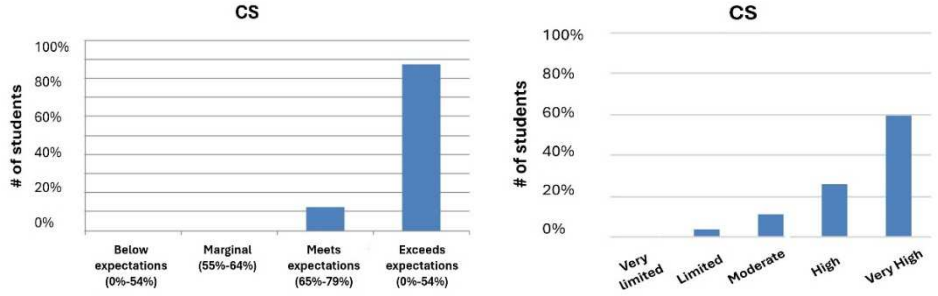

(a) (b)

Fig. 1 - (a) Direct assessment (with the DANs) and (b) Indirect assessment (surveys) of the Communication skills attribute for the Capstone class in Winter 2023.

In general, the assessment of the CS indicates that the majority of students have demonstrated a high level of communication skills by the end of their program. This confirms that the Design Activities provide favorable conditions to develop this very important soft skill. The indirect assessments also reveal that more opportunities to develop the skills would be beneficial.

ACKNOWLEDGMENTS

The authors gratefully acknowledge the funding by NSERC The Natural Sciences and Engineering Research Council of Canada.

REFERENCES

[1] NSERC Chairs in Design Engineering (www.nserc-crsng.gc.ca/Professors-Professeurs/ CFS-PCP/ CDE-CGC_eng.asp).

[2] A Kolmos et al., Interdisciplinary project types in engineering education, European Journal of Engineering Education 49(2): pp.257-282, 2023.

[3] U Beagon et al., Preparing engineering students for the challenges of the SDGs: what competences are required? European Journal of Engineering Education 48(1): pp.1-13, 2023.

[4] A Seth et al., MADE: A Multidisciplinary Computational Framework for Aerospace Engineering Education, IEEE Trans Educ. 66(76): pp.622 - 631, 2023.

[5] A Singh et al., Improving Biomedical Engineering Education Through Continuity in Adaptive, Experiential, and Interdisciplinary Learning Environments. J Biomech Eng 140(8): 2018.

[6] Accreditation Board | Engineers Canada

[7] ceab_graduate_attributes_and_their_definitions.pdf.

Proceedings IRF2025: 8th International Conference on Integrity-Reliability-Failure
In Engineering, Materials, Manufacturing and Biomechanics. Porto 15-18 July 2025
DOI: https://doi.org/10.24840/978-972-752-323-8

PAPER REF: 22592

SUCCESS LEVEL OF MECHANICAL ENGINEERING STUDENTS OF THE ENGINEERING FACULTY OF UNIVERSITY OF PORTO IN MATHEMATICAL ANALYSIS III COURSE UNIT FROM 2017 TO 2023

S.I.S. Pinto[1,2], L. Madureira[1(*)], S.M. Zvacek[3]

[1]University of Porto, Engineering Faculty, Porto, Portugal
[2]Institute of Science and Innovation in Mechanical and Industrial Engineering (LAETA-INEGI), Porto, Portugal
[3]Independent Consultant for Higher Education, CollegeTeachingCoach.com, Castle Rock, CO, USA
[(*)]*Email:* luisarm@fe.up.pt

ABSTRACT

Over several years of teaching, two professors of the *Mathematical Analysis III* course unit in the Mechanical Engineering Department at the Faculty of Engineering, University of Porto (Portugal), observed a perceived variation in student success rates before, during, and after the COVID-19 pandemic. To investigate this trend, they conducted a study to analyze the changes and their underlying causes. The success rate increased from 75% before the pandemic (academic year 2019/2020) to 84% during the pandemic (academic year 2020/2021). Additionally, the percentage of students scoring between 14 and 16 increased by 13–17%, while the percentage of those scoring between 17 and 20 (the maximum score) increased by 3–4% during the pandemic. This trend can be attributed to several facilitating factors introduced during the pandemic. One key factor was the mandatory reduction in exam duration from 2 hours to 1 hour and 30 minutes, which consequently led to lower exam complexity and reduced difficulty levels.

Keywords: Mathematical analysis, course unit, success level, mechanical engineering.

INTRODUCTION

The academic success of university students is influenced by a variety of interconnected factors, as highlighted in recent literature. Chaudhary and Singh (2022) [1] conducted a meta-analysis on the key elements affecting teaching and learning in higher education, identifying pedagogical, psychological, and institutional factors as determinants of academic performance. Among these, teaching methods play a central role, as different pedagogical approaches can significantly influence how students acquire knowledge and develop skills. Kirschner and Hendrick (2020) [2] explored this issue by analyzing fundamental principles of educational psychology and their practical application in teaching, emphasizing the importance of evidence-based instruction. Beyond pedagogical aspects, individual factors such as student motivation are also critical for academic success. Sell (2019) [3] discussed how different learning strategies and motivational mechanisms impact student performance, highlighting the need for approaches that foster self-regulation and active engagement in the learning process. Student well-being in the academic environment is another essential element, as identified by Konstantinidis (2024) [4], who conducted an integrative review of the literature to understand how the educational context influences students' emotional and psychological well-being. Finally, instructor support can be a key determinant of learning and academic success. Tao et al. (2022) [5] conducted a meta-analysis on the relationship between perceived teacher support,

student engagement, and academic achievement, concluding that students' perception of instructor support has a significant impact on their motivation and academic outcomes.

Given the considerable impact of teaching methodologies, student motivation, well-being, and instructor support on academic performance, it is essential to examine how these factors have evolved over time and under varying circumstances. The COVID-19 pandemic introduced unprecedented challenges to higher education, significantly affecting pedagogical practices and students' learning experiences. Gaining insight into how these disruptions influenced academic success is crucial for identifying trends and potential areas for improvement in engineering education.

In this context, two professors of Mathematical Analysis III course unit in the Mechanical Engineering Department at the Faculty of Engineering of the University of Porto (Portugal), Professors Luísa Madureira and Sónia Pinto, undertook a study to assess the academic success of students in this subject before, during, and after the pandemic.

METHODOLOGY

During the academic years 2017/2018, 2018/2019, 2019/2020, and 2020/2021, the Mechanical Engineering program at the Faculty of Engineering of the University of Porto followed the *Integrated Master in Mechanical Engineering* structure, a five-year degree program. However, starting in the academic year 2021/2022, the program transitioned to a *Bachelor in Mechanical Engineering*, a three-year degree that remains the current structure. This change was part of a broader educational reform, aligning the curriculum with international standards and adapting the program to a more modular system.

Despite this structural modification, the content of the *Mathematical Analysis III* course unit has remained unchanged from 2017/2018 to 2023/2024, ensuring consistency in the topics covered and learning objectives. No external influences have affected the syllabus, instructional methodologies, or assessment criteria throughout these seven academic years. Additionally, Professor Luísa Madureira has consistently been responsible for this course unit throughout the entire period, ensuring continuity in teaching practices and evaluation methods.

At the university level in Portugal, the grading system follows a 0 to 20 scale, where 0 represents the lowest score and 20 the highest. Students are considered to have passed the course if they achieve a score of 10 or higher. This standardized grading system provides a clear benchmark for evaluating student performance and academic achievement.

RESULTS

Figure 1 illustrates the percentage of students who achieved *"Approval"* and *"Not Approval"* in the *Mathematical Analysis III* course unit within the Mechanical Engineering program from the academic years 2017/2018 to 2023/2024. The academic years 2017/2018, 2018/2019, and 2019/2020 correspond to the period before the COVID-19 pandemic, while 2020/2021 and 2021/2022 represent the years affected by the pandemic. The academic years 2022/2023 and 2023/2024 are considered the post-pandemic period.

Figure 2 illustrates the percentage of students who did not achieve approval ("*Not Approval"*, score below 10) and the distribution of different success levels among those who did ("*Approval"*, score equal to or higher than 10). A score between 10 and 13 corresponds to

"*Sufficient" Approval* (yellow region in Figure 2), a score between 14 and 16 indicates "*Good" Approval* (green region in Figure 2), and a score between 17 and 20 represents "*Very Good" Approval* (blue region in Figure 2).

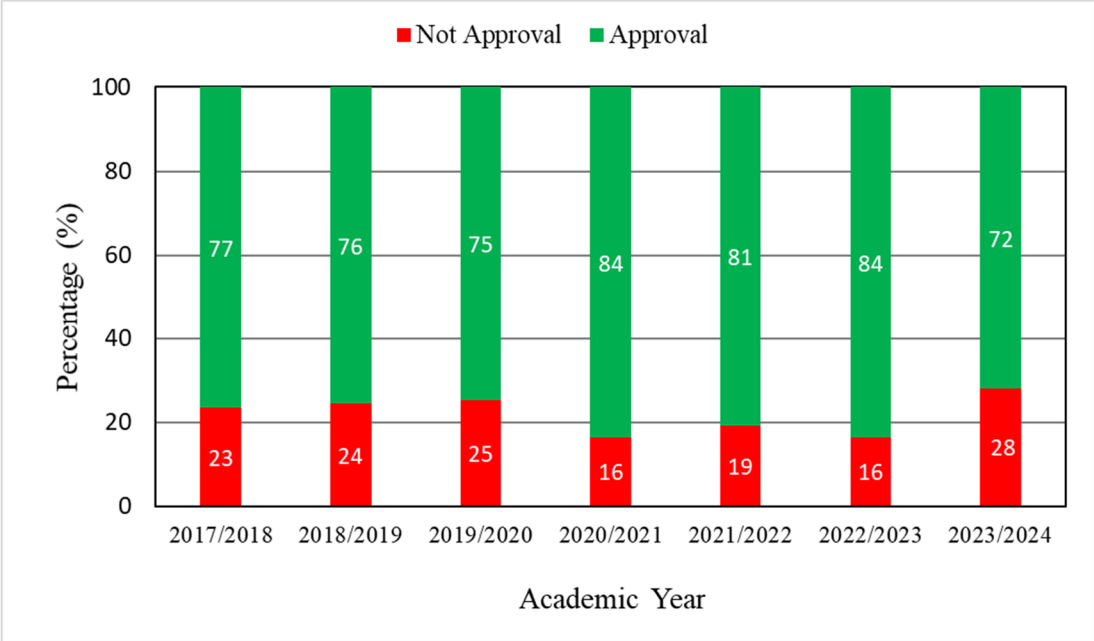

Fig. 1 - Percentage of *"Approval"* and *"Not Approval"* of Mechanical Engineering Students in the Course Unit Mathematical Analysis III along the years, since the academic year 2017/2018 to 2023/2024.

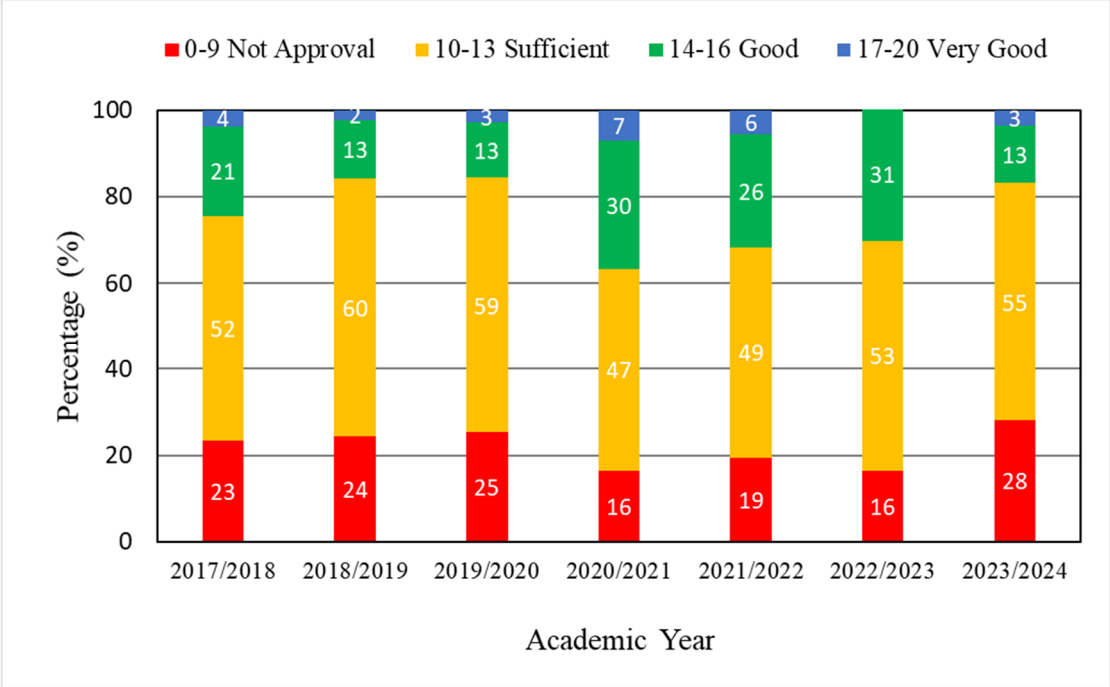

Fig. 2 - Percentage of *"Not Approval"*, *"10-13 Sufficient"* Approval, *"14-16 Good"* Approval, *"17-20 Very Good"* Approval of Mechanical Engineering Students in the Course Unit Mathematical Analysis III along the years, since the academic year 2017/2018 to 2023/2024.

DISCUSSION AND CONCLUSIONS

Before the COVID-19 pandemic, during the academic years 2017/2018, 2018/2019, and 2019/2020, mechanical engineering students maintained a relatively stable success rate, ranging between 75% and 77%, while the failure rate ranged between 23% and 25% (see Figure 1, red region). Figure 2 also reveals a consistent trend across the three approval score levels. The only notable change was an increase of 10% in the number of students achieving a score higher than 14 from the academic year 2017/2018 to the academic years 2018/2019 and 2019/2020.

During the COVID-19 pandemic, in the academic years 2020/2021 and 2021/2022, the success rate increased by approximately 9–10% (see Figure 1). Additionally, Figure 2 indicates that students achieved higher scores. The percentage of students scoring between 14 and 16 increased by 13–17%, while the percentage of those scoring between 17 and 20 increased by 3–4%. This trend can be attributed to several facilitating factors, including a reduction in the duration of evaluation exams imposed by higher education authorities due to pandemic-related restrictions. Specifically, the exam duration was reduced from 2 hours to 1 hour and 30 minutes. As a result, questions had to be shorter and, consequently, less complex.

In the 2022/2023 academic year, after the pandemic, the evaluation exam duration returned to 2 hours. However, the percentage of students failing the course remained similar to that observed during the pandemic years (see Figure 1). Nonetheless, students' scores declined due to the removal of several facilitating factors mentioned previously. Notably, no students achieved scores of 17 or higher (see Figure 2). It was only in the 2023/2024 academic year that the trend returned to pre-pandemic levels, with a success rate of 72% and a failure rate of 28% (see Figure 1). Furthermore, as shown in Figure 2, the distribution of success levels in 2023/2024 closely mirrors that of the pre-pandemic years, particularly those before 2019/2020.

REFERENCES

[1] Chaudhary, P., Singh, R. A meta-analysis of factors affecting teaching and student learning in higher education. Front. Educ., 2022, 6. https://doi.org/10.3389/feduc.2021.824504.

[2] Kirschner, P., Hendrick, C. How learning happens: Seminal works in educational psychology and what they mean in practice, Routledge, 2020.

[3] Sell, H. Motivation and learning strategies for college success, 6th ed., Taylor & Francis, 2019.

[4] Konstantinidis, A. An integrative review of the literature on the factors influencing student well-being in the learning environment, International Journal of Educational Research Open, 2024, 7, 100384.

[5] Tao Y., Meng, Y., Gao, Z., Yang, X. Perceived teacher support, student engagement, and academic achievement: A meta-analysis, Educational Psychology, 2022, 42.

Proceedings IRF2025: 8th International Conference on Integrity-Reliability-Failure
In Engineering, Materials, Manufacturing and Biomechanics. Porto 15-18 July 2025
DOI: https://doi.org/10.24840/978-972-752-323-8

PAPER REF: 22620

ENHANCING MECHANICAL ENGINEERING EDUCATION: HANDS-ON MACHINING PROJECTS FOR SKILL DEVELOPMENT

A.M.P. de Jesus[1(*)], R.D.F.S. Costa[1,2], V.F.C. Sousa[1,2], T.E.F. Silva[2]

[1]DEMec, Department of Mechanical Engineering, University of Porto, R. Dr. Roberto Frias s/n, 4200-465 Porto, Portugal
[2]INEGI, Institute of Science and Innovation in Mechanical and Industrial Engineering, R. Dr. Roberto Frias 400, 4200-465 Porto, Portugal
[(*)]*Email:* ajesus@fe.up.pt

ABSTRACT

The introduction of novel and innovative teaching strategies in any field of knowledge is proven to be more effective in transmitting the information to the students, capturing their interest and making them more willing to be involved in the classroom, eager to learn something new. Mechanical engineering students are no exception to this. In fact, the field of manufacturing processes is full of practical applications, with numerous opportunities for hands-on laboratory projects. This paper presents an improved teaching method applied to the machining module of Advanced Production Technologies II, a discipline taught in the master's degree branch of Materials and Technological Processes of the Mechanical Engineering course at the Faculty of Engineering of the University of Porto (FEUP). The purpose of this module was to put the students in contact with different instrumented machinability studies, at first for the orthogonal cutting and cylindrical turning of metallic alloys, and later for the drilling of composite materials, more precisely CFRPs (carbon fibre reinforced polymers). The use of different materials under the same machining conditions makes it possible to compare the results for each case and select the most fit for a determined application. By taking the students to the laboratory and allowing them to observe the real challenges felt in an industrial environment, their preparation for the job market improves exponentially, surpassing candidates which only assisted to theoretical classes without applying the learned concepts with real conditions. The improved concepts learned by the students with this enhanced methodology are also highlighted and discussed.

Keywords: Machinability, metals, CFRPs, laboratory classes, hands-on projects.

INTRODUCTION

The machinability of a material, for example a metal alloy, depends on several factors, such as the power required to machine, tool life, surface finish or chip disposal. The specific cutting pressure (k_c) in machining, a critical factor to evaluate the machinability of a material, stands for the power of cut per unit volume of material removed. This is usually understood as a mechanical property relative to the cut of the material, which allows to estimate the cutting force as long as the undeformed chip section is known, but it depends on the chip thickness. This property is essential in the orthogonal cutting and turning processes performed in metallic materials, since it determines how the material behaves to the chosen cutting conditions, i.e., its resistance to cutting (Silva et al., 2022). Through its study and determination via experimental testing, it becomes possible to assess the material's machinability and, thus, to establish a connection bridge between both processes, highlighting the similarities and

differences between the 2D (orthogonal cutting) to the 3D cutting (cylindrical turning) (Sujuan et al., 2021). Cutting load is significant as an indicator of the operation stability and energy requirements of the machining process. Combined with chip morphology characterization, it allows the identification of favourable cutting scenarios in the post processing stage, envisioning an increase of the production rate and quality of the finished product. Additionally, it allows the determination of the specific cutting power, which, due to being sensitive to material's imperfections, can help to understand if the typical materials defects and heterogeneities compromise the machinability of steels (Stepan et al., 2011). Merchant (Merchant, 1945) made an important contribution in the orthogonal cutting field with his studies, establishing a relation for the orientation of the cutting plane at the base of the chip. This relation was developed based on the hypothesis that the cutting plane is the one which produces the lowest average shear stress. One of the practical consequences of this relation is the demonstration that the use of cutting fluids during machining processes allows the reduction of the friction coefficient and, therefore, a reduction in the cutting loads (Jesus, 2019).

Conversely, the drilling of composite materials possesses distinct challenges. The abrasive nature of their fibres causes an excessive tool wear, leading to a constant drill replacement and, therefore, reducing the process efficiency at the same time its cost is increased (Xu, 2021). Moreover, the CFRP's anisotropic nature hinders the drilling process, resulting in defective holes, which is the case of fibre pull-out or delamination (Chen, 2023). This affects the hole dimensional precision and component structural integrity, compromising its application, reason why it must be avoided (Costa, 2023). Composite materials, such as CFRPs, are widely used in aeronautical and automotive applications where the quality is of utmost importance, due to their enhanced mechanical and physical properties, such as high strength-to-weight ratio and corrosion resistance, for example (Xu, 2023). For this reason, several authors have studied this process, testing different approaches with distinct composite configurations and tool geometries, varying the machining parameters to obtain the best outcomes possible (Sun, 2023).

The machinability of metals and CFRPs raises different perspectives and challenges. In this paper, both approaches will be addressed through experimental testing, firstly comparing the orthogonal cutting and cylindrical turning operations on three distinct metallic alloys and secondly performing drilling tests on two different composite materials. These were fundamental for the students to understand the dynamics of each process and to comprehend how the machinability of each material is assessed.

METHODOLOGY

The laboratory hands-on project of the machining module in focus was centred on machinability studies of metals and CFRPs. During the laboratory classes, students were in contact with three different instrumented machinability studies, specifically the orthogonal cutting of metallic alloys, the cylinder turning of the same metallic alloys, and the drilling of CFRPs.

Metallic Alloys

For the first two cases, three different metals were selected with the objective of comparing their machinability. These are, respectively, the St52 steel, a high resistance unalloyed structural steel; the aluminium alloy AA6082, a medium strength alloy with excellent corrosion resistance; and a brass alloy. The purpose of using the same metals in two different processes was for the students to understand and be able to perform the transferability from 2D (orthogonal cutting) to 3D (cylinder turning) cutting, highlighting the main similarities and differences between them.

In the orthogonal cutting process (Figure 1a), two tools with a PVD (physical vapour deposition) TiAlN coating were used, with rake angles of 5º and 12º. The three materials were tested with the same cutting speed and three uncut chip thicknesses (around 0.35 mm, 0.6 mm and 0.7 mm). The acquisition of loads was made through an Advantech USB-4711A portable data acquisition module with a 5kHz data sampling rate, as seen in Figure 1b, and a Kistler multichannel charge amplifier, present in Figure 1c.

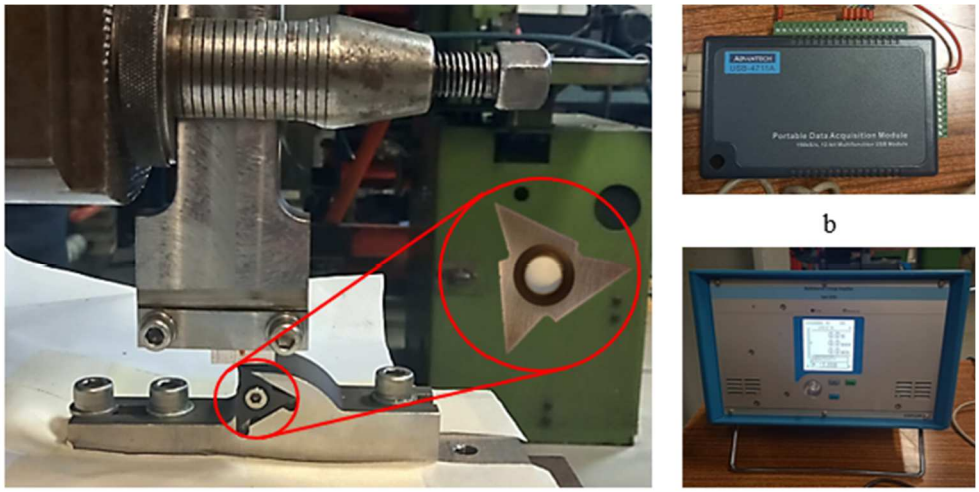

Fig. 1 - (a) Orthogonal cutting process with a 12º cutting tool, (b) portable data acquisition module, and (c) Kistler multichannel charge amplifier.

As for the cylinder turning, it was carried out on a horizontal lathe EFI DU20 with 5.9 kW power, under dry conditions. A load cell was mounted on the lathe's tool carriage and levelled in order to ensure the alignment of the cutting tool with the centre of rotation of the fixation chuck. The load measurement and acquisition equipment was the same than in the orthogonal cutting tests. The turning insert had a chip-breaker, and the same coating of the orthogonal cutting test insert was used. The parameters used were two spindle speeds (1800 rpm and 2500 rpm), three feeds (0.05mm/rev, 0.1mm/rev and 0.2mm/rev) and three depths of cut (0.1mm, 0.2mm and 0.3mm) with two repetitions for each combination. The selected values represented finishing conditions. Figure 2 shows the cylinder turning process and the turning insert used in the experimental tests.

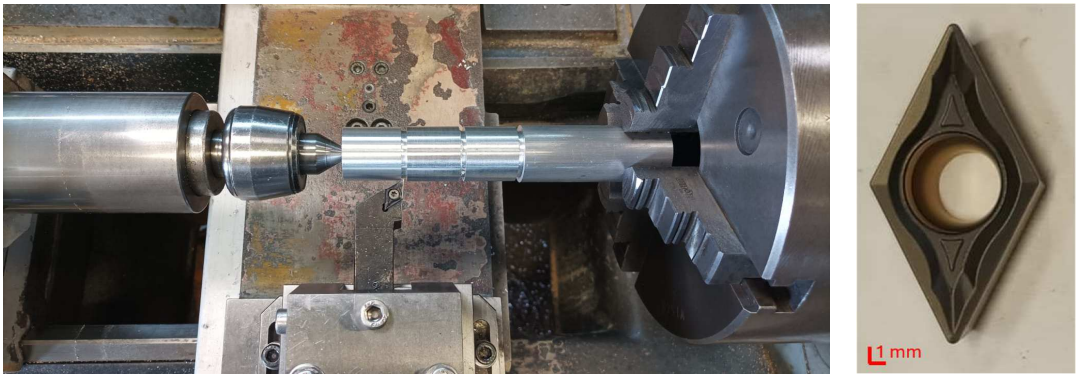

Fig. 2 - (a) Cylinder turning process, and (b) 55º DCMT11T turning insert.

The orthogonal cutting goals were for the students to generate the specific cutting pressure vs. uncut chip thickness curves for each material, and to compare the specific cutting pressures between the different materials and draw conclusions regarding their machinability according

to the cutting loads/power criterion. It was also intended to verify the size effect (phenomenon where the unit cutting force increases with the chip thickness decreasing), to discuss the generated chip's geometry, to compute the friction coefficient and shear strength of the material and to verify the Merchant's theory for the cases where the chip thickness ratios were evaluated.

On the other hand, the turning process had as objectives the generation of the specific cutting pressure vs. feed for each material and cutting speed, and to compare the specific cutting pressures between the orthogonal cutting and turning, assessing the transferability from the 2D to the 3D cutting. Moreover, it was intended to evaluate the effect of cutting speeds, compare the surface roughness and chips for each set of machining conditions, and to use all the gathered data to perform a proper machinability analysis of the three metallic alloys.

Composite Materials

For the CFRP case, two different plates were used, one with a thermosetting resin, epoxy, and unidirectional fibres (0°), UD, and another with a thermoplastic resin, polyamide, and bidirectional fibres, BD, in the two main orthogonal directions (0/90°). The aim of this approach was for the students to understand the influence of the fibre orientation and resin nature on the machinability of composite materials. To perform the drilling tests, four different helicoidal drills were chosen, with variations both in terms of geometry and coating, so that the students could understand the influence of each tool detail in the cutting loads and also in the drilled hole. These are shown in detail in Figure 3, being, respectively, a CVD (chemical vapour deposition) NCD (nanocrystalline diamond) conventional drill (A), a CVD NCD double point angle drill (B), a PVD TaC (tantalum carbide) conventional drill (C), and an uncoated conventional drill (D). All of the drills had a 6 mm diameter, 120º point angle and 30º helix angle. Additionally, drill B had a 60º second point angle.

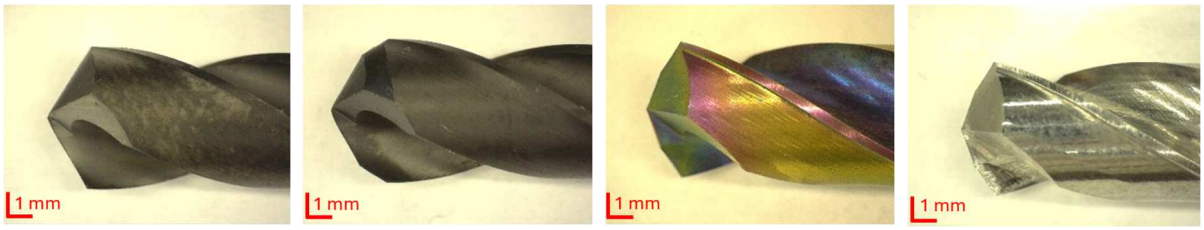

a b c d

Fig. 3 - Tools used in the CFRP drilling tests: (a) NCD coated conventional drill, (b) NCD coated double point angle drill, (c) TaC coated conventional drill, and (d) uncoated conventional drill.

A single cutting speed was used for every case, equal to 110 m/min, which corresponded to a spindle speed of 5836 rpm. Two feed values were used, 0.1 mm/rev and 0.3 mm/rev, equivalent to 584 mm/min and 1751 mm/min, respectively. The intention of using such values was to test both low and high values, for the students to be able to identify more easily the differences between both feeds. All the tests were repeated just once, as this was enough to demonstrate the process to the students for didactic purposes, hence there was no need for a minimum of three repetitions for each condition to guarantee a statistical significance in the collected data.

Regarding the equipment, present in Figure 4, an Okuma CNC machine with a Kistler dynamometer for drilling (Fx, Fy, Fz and Mz) was used for the tests, which were performed under dry conditions, alongside a DinoLite microscope for a more detailed sample analysis and an x-ray machine. The latter is commonly used as a non-destructive test to analyse the drilled holes, revealing discontinuities in the material. An image processing and analysis software in Python language was used to determine the delamination factors of each hole, which correlate both the diameter and area of the nominal hole and the delaminated area to quantify the damage extension around the hole.

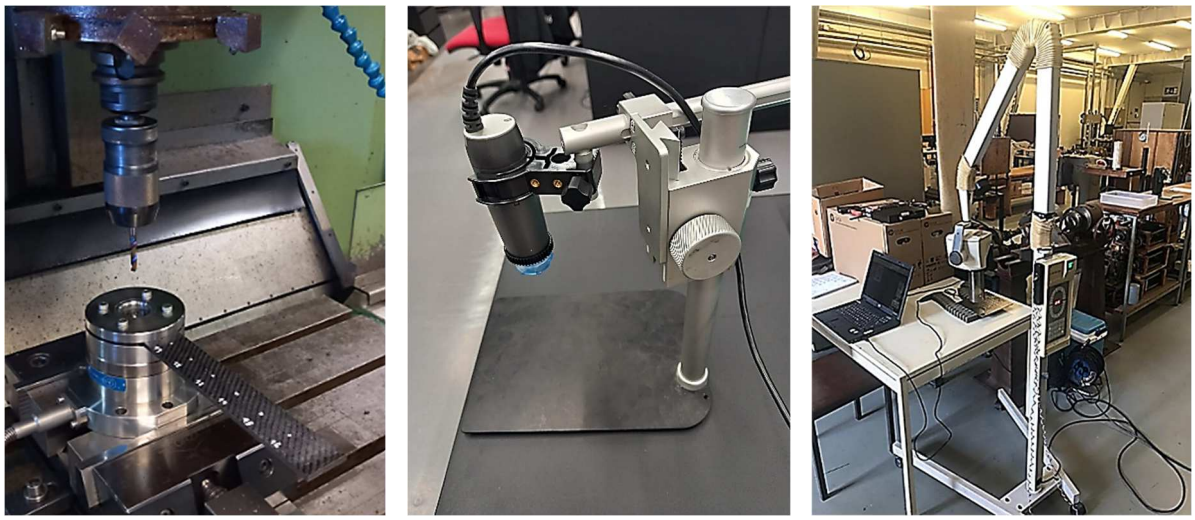

a b c

Fig. 4 - (a) OKUMA CNC machine with drilling setup, (b) DinoLite microscope, and (c) X-ray analysis machine.

Conversely to the processes for the metallic alloys, the aim of these tests was for the students to compare quantitatively the loads obtained during the drilling operations, relating these with the chosen parameters, tool geometry and coating, and qualitatively evaluate the hole quality by visual inspection, and microscopic and x-ray images, as well as discuss the nature of the chips generated during the drilling tests.

RESULTS

The practical component of this work consisted of the experimental testing of each of the mentioned processes in the laboratory with the students present, so they could attentively observe their performance and later on perform the respective analysis of the obtained data.

Metallic Alloys

Figure 5 depicts a comparison of the specific cutting pressure in a St52 steel between the orthogonal cutting (2D) and the turning (3D) processes as a function of the uncut chip thickness (2D)/feed (3D). In the 2D case, the specific cutting pressure is more easily controlled, as it is a simpler situation, whereas in the 3D case, the continuous variation in chip thickness and the additional effects of rotation make it a more complex problem.

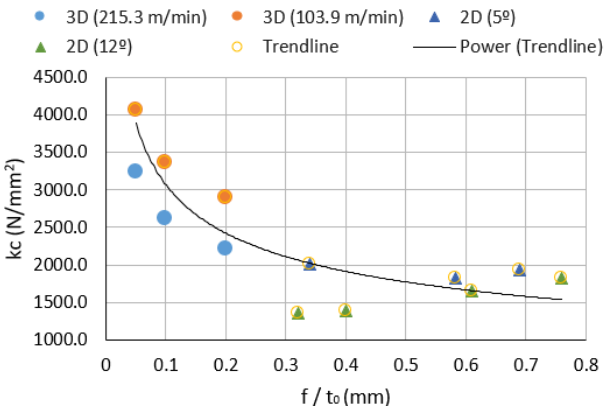

Fig. 5 - Specific cutting pressure as a function of the feed/uncut chip thickness in St52 steel comparison for the 2D and 3D cutting.

Through the graph analysis, a correlation between the orthogonal cutting and the turning processes was established. The specific cutting pressure is reduced with the increment of feed (f) for the cylindrical turning and the initial thickness (t_0) for the orthogonal cutting, behaviour justified because lower feed values generate higher specific cutting pressure due to the relative increasing effect of friction with respect to the material plastic deformation/fracture. The k_c values are higher in the 3D process than in the 2D for lower f / t_0 values, indicating that the cylindrical turning may involve higher initial loads for unit cut area, owing to the higher complexity of the tool-chip contact. It is also seen that higher cutting speeds result in lower specific cutting pressures, explained by the thermal effect in the material, which reduces its resistance to cut.

Comparing the three materials, the aluminium alloy AA6082 had the lowest specific cutting pressure, which made it clear that it is the easiest material to machine, from the three studied, and the St52 steel had the highest k_c, due to its high hardness.

Figure 6 shows a DinoLite microscope image of a chip resultant from the orthogonal cutting process performed in the ST52 steel. It was measured using the DinoCapture software to determine the chip thickness (t_c) which, alongside the undeformed chip/cutting thickness (t_c), is fundamental in the calculation of the cutting ratio (r) and the respective side flow ratio (R).

Fig. 6 - DinoLite microscope image of an orthogonal cutting St52 chip with measurement.

After the orthogonal cutting tests, the students used the Merchant theory to determine the chip's shear angle through the friction coefficient between the chip and the tool's rake face, as well as the tool's attack angle. Afterwards, they used the tool's rack angle and the calculated cutting ratio (r) to determine the real shear angle and compare both values to assess the respective error. This led to a better understanding from the students of the differences between the analytical calculations and the experimental values taken from real conditions.

A roughness analysis was also performed in the cylindrical turning materials, from which it was concluded that it greatly increases proportionally with the feed increase in the three materials. For the steel, an increment in the spindle speed reduces slightly the surface roughness of the freshly cut material, and in the aluminium, this only happens for the 0.2 mm/rev feed; however, in the brass, lower spindle speeds rise the surface roughness. In general terms, the brass shows the highest average roughness values, with the aluminium presenting the lowest ones.

Through the metal machinability tests, the students learned the differences between these 2D and 3D processes, and that the orthogonal cutting can be applied to the cylindrical turning with some limitations, although these lose relevance as the penetration increases in relation to the tool tip radius.

Composite Materials

Table 1 shows the maximum axial forces (Fz) registered during the drilling tests for each set of machining conditions in the holes performed on both CFRP plates.

Table 1 - Maximum axial forces obtained from the UD and BD drilling tests.

Drill	A		B		C		D	
Feed (mm/rev)	0.1	0.3	0.1	0.3	0.1	0.3	0.1	0.3
UD Fz (N)	117.83	171.63	121.34	183.31	106.64	144.78	95.50	157.96
BD Fz (N)	59.23	92.44	76.85	79.28	51.94	77.87	43.64	75.40

From the loads analysis, there is a clear maximum force increase with the rise of the feed, meaning that lower feeds are preferable. Comparing both CFRP configurations, the BD results in much lower axial forces than the UD. This is explained by the epoxy resin, which being thermosetting, is more rigid and resistance than the thermoplastic, generating higher loads. Between all the drills, the uncoated conventional drill (D) has the best performance, with lower forces generated. Although tool A in the BD CFRP had a higher force for the feed of 0.3 mm/rev, the CVD NCD double point angle drill (B) had generally the worst performance, resulting in higher forces. This outcome was not expected, since a drill with an additional cutting edge should perform a better cut and result in lower forces, but it was a good opportunity to show the students that sometimes in practice not everything goes according to the expected, differently from the theory, due to external factors. In addition, the low number of holes drilled contributes to a high variance in the results and lower reliability in them, reason why this was just a process demonstration, and, in the industry, more repetitions are done, to compensate for these errors and to establish a pattern with the same outcomes for the same conditions.

Figure 7 shows an example of a hole drilled in a unidirectional thermosetting CFRP plate. An uncoated conventional twist drill was used with the following parameters: cutting speed of 110 m/min and feed of 0.3 mm/rev. The severe feed employed, alongside the unidirectional nature of the fibres, which is less resistant to damage than a bidirectional disposition, led to a strong delamination in the fibre direction.

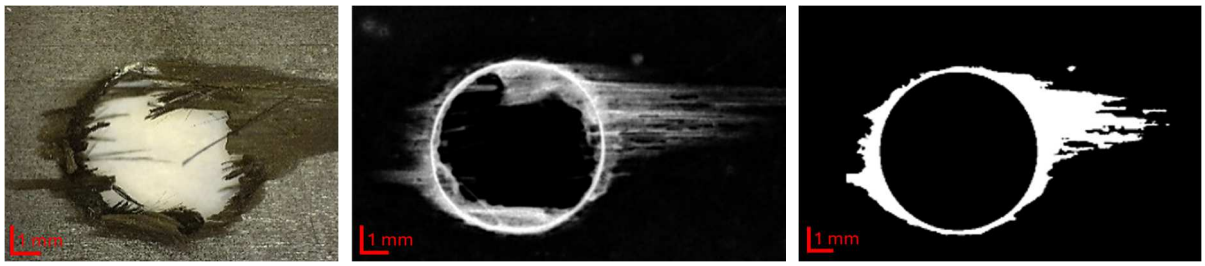

a b c

Fig. 7 - Drilled hole in a unidirectional epoxy CFRP plate: (a) DinoLite microscope image, (b) x-ray image, and (c) binary image.

On the other hand, Figure 8 depicts the same situation as Figure 7, however in this case for a hole drilled under the same conditions in a bidirectional (0/90°) thermoplastic CFRP plate.

Several conclusions can be assessed from the comparison of a hole drilled in the two different CFRP configurations. The first method the students used was a visual analysis, when the plates were withdrawn from the CNC machine. Their observation is highlighted in the DinoLite microscope images, which was that the UD plate had much severe defects than the BD. Since the fibres are just aligned in a single direction, they are more prone to pull-outs, whereas in the BD the fibres are distributed in two perpendicular directions, resulting in a more resistant material. Besides this, the x-ray image denotes that the epoxy resin results in a cleaner image, since the hole and the pulled fibres are highlighted from the rest of the plate, whereas the

polyamide revealed all the fibres in the composite, resulting in a noisier image, which compromises its analysis.

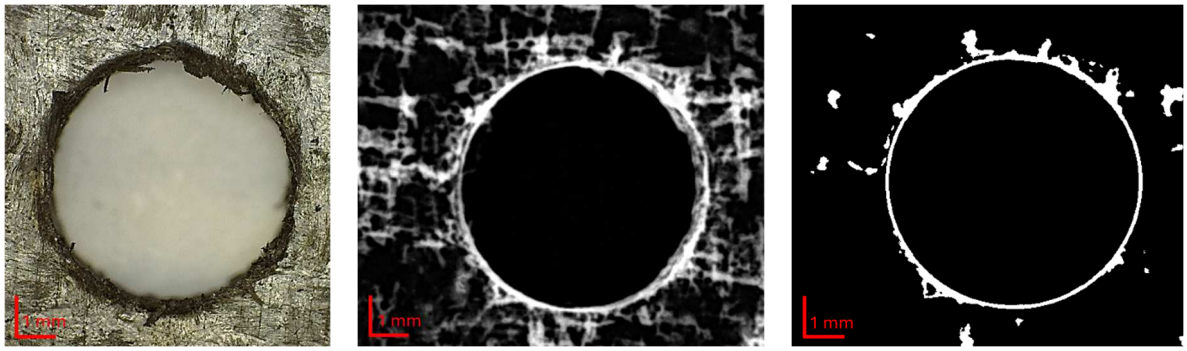

a b c

Fig. 8 - Drilled hole in a bidirectional polyamide CFRP plate: (a) DinoLite microscope image, (b) x-ray image, and (c) binary image.

The resultant chips from the drilling tests were also analysed. In the case of the epoxy, they were in the form of a powder, since this is a thermosetting resin, meaning that it retains its solid state and cannot be reshaped with the heat, breaking more easily. In contrast, the polyamide resulted in continuous chips, which is in accordance with its thermoplastic nature, as it deforms significantly before breaking. When the feed was low, 0.1 mm/rev, they presented a long form, but when it increased to 0.3 mm/rev, a high feed value, the chips broke easily, being short.

Table 2 presents the delamination factors that were determined based on the binary images obtained from the UD holes in the image processing and analysis software in Python, for each drill and feed used. The reason behind the delamination factors being only considered for the holes in the unidirectional plate was not only in the fibre direction, but also in the matrix. The main motive is that, as confirmed before, the UD holes had much more delamination than the BD, explained by the single direction of its fibres. In spite of that, since epoxy resin was the matrix of this CFRP configuration, as seen in the binary image (Figure 6b), the x-ray highlights the hole and the damaged zones, leaving the rest of the plate in a single black pattern. Nevertheless, for the polyamide resin (Figure 7b), the composite fibres stand out in the image around the hole, and may sometimes be wrongly considered delamination, when in reality in most cases they are just noise.

Table 2 - Delamination factors obtained from the UD holes with each drill and respective feeds.

Drill	A		B		C		D	
Feed (mm/rev)	0.1	0.3	0.1	0.3	0.1	0.3	0.1	0.3
Fda	1.251	1.416	1.376	1.804	1.508	1.526	1.389	2.982

The delaminations factors follow the same tendency as the registered loads, more precisely that a higher feed increases the hole delamination. Moreover, the highest delamination was observed in drill D, the uncoated drill, which showed the students the benefits of a proper tool coating in machining. On the other hand, drill A had the lowest delamination, proving that the CVD NCD coating is the most efficient one.

Figure 9 shows an example of tool wear observed after the tests, which was more prominent in the PVD TaC drill. Although the number of performed holes was not much significative, some signs of abrasive wear on the secondary cutting edge and an aluminium BUE (built-up edge)

on the primary cutting edge. This showed the students that a machining tool's lifetime is constantly reduced from the first moment they are submitted to experimental testing.

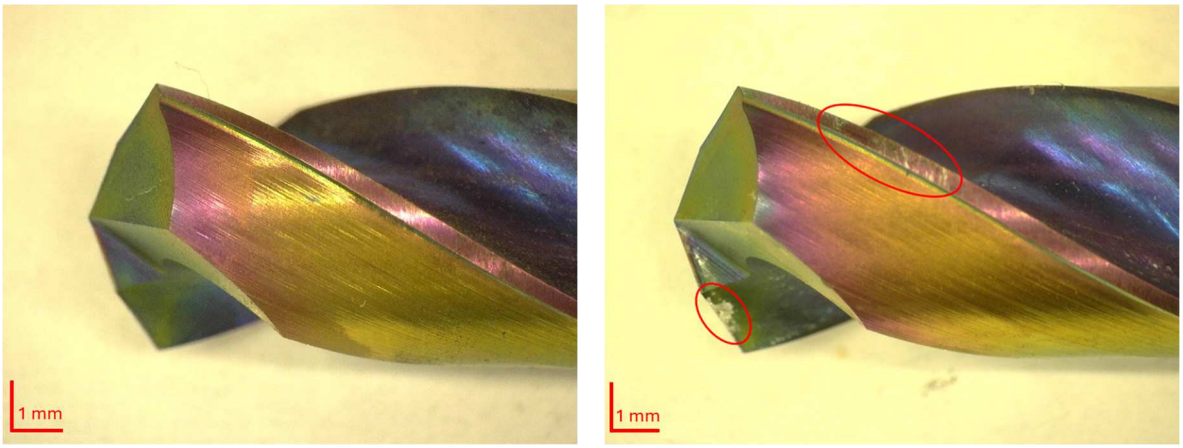

(a) (b)

Fig. 9 - TaC-coated drill DinoLite microscope image: (a) before the tests, and (b) after the tests.

CONCLUSIONS

The use of alternative teaching methods adapted for a deeper student integration, fostering their interaction with the practical work, such as handling the testing specimens and machining tools by themselves or observing a process taking place in real time, resulted in an increase of their attention span and ability to better understand the transmitted concepts compared to a similar class, where their direct participation and involvement was not required. In fact, this was observed through the reports delivered and presentations made at the end of the machining module, which demonstrated the skills developed in this practical project and proved the enhancement of their education. With the implementation of hands-on machining projects, the motivation growth of the students was clearly visible, since they felt part of the process, as if they were already in a real company situation solving engineering problems with the gathered knowledge. In these cases, the transition to the labour market is smoother and more efficient, with the students being able to clearly show the recruiters what they learned in the university and apply the same procedures to real situations when they are already working in mechanical engineering companies.

ACKNOWLEDGMENTS

The authors gratefully acknowledge the "Fundação para a Ciência e a Tecnologia" (FCT) for the financial support through Grant Number 2024.05867.BDANA. The authors also acknowledge Project Hi-rEV – Recuperação do Setor de Componentes Automóveis (C644864375-00000002) cofinanced by Plano de Recuperação e Resiliência (PRR), República Portuguesa through NextGeneration EU.

REFERENCES

[1] Chen, R., Li, S., Zhou, Y., Qiu, X., Li, P., Zhang, H., Wang, Z. Damage formation and evolution mechanisms in drilling CFRP with prefabricated delamination defects: simulation and experimentation. Journal of Materials Research and Technology, 2023, 26, pp.6994-7011.

[2] Costa, R.D.F.S., Sales-Contini, R.C.M., Silva, F.J.G., Sebbe, N., Jesus, A.M.P. A critical review on fiber metal laminates (FML): from manufacturing to sustainable processing. Metals, 2023, 133, 638.

[3] Jesus, A.M.P. Fundamentos do corte: teoria e exercícios. 2019.

[4] Merchant, M.E. Mechanics of the metal cutting process II. Plasticity conditions in orthogonal cutting. Journal of Applied Physics, 1945, 16 (6), pp.318-324.

[5] Silva, T., Sousa, V., Silva, F., Jesus A.M.P. On the suitability of instrumented orthogonal cutting tests towards cutting load modelling in turning operations. International Conference Innovation in Engineering. Springer International Publishing, 2022, pp.339-350.

[6] Stepan, G., Dombovari, Z., Muñoa, J. Identification of cutting force characteristics based on chatter experiments. CIRP Annals, 2011, 60 (1), pp.113-116.

[7] Sujuan, W., Tao, Z., Wenping, D., Zhanwen, S., To, S. Analytical modelling and prediction of cutting forces in orthogonal turning: a review. International Journal of Advanced Manufacturing Technology, 2022, 119, pp.1407-1434.

[8] Sun, Z., Geng, D., Meng, F., Zhou, L., Jiang, X., Zhang, D. High performance drilling of T800 CFRP composites by combining ultrasonic vibration and optimized drill structure. Ultrasonics, 2023, 134, 107097.

[9] Xu, J., Geier, N., Shen, J., Krishnaraj, V., Samsudeensadham, S. A review on CFRP drilling: fundamental mechanisms, damage issues, and approaches toward high-quality drilling. Journal of Materials Research and Technology, 2023, 24, pp.9677-9707.

[10] Xu, J., Lin, T., Davim, J.P., Chen, M., Mansori, M.E. Wear behavior of special tools in the drilling of CFRP composite laminates, 2021, 476, 203738.

Proceedings IRF2025: 8th International Conference on Integrity-Reliability-Failure
In Engineering, Materials, Manufacturing and Biomechanics. Porto 15-18 July 2025
DOI: https://doi.org/10.24840/978-972-752-323-8

PAPER REF: 22637

DISCUSSING INTERNATIONAL STUDENT MOBILITY IN AND OUT OF PORTUGAL

Catarina F Castro(*)

Mechanical Engineering Department, Faculty of Engineering, University of Porto, Porto, Portugal
(*)*Email:* ccastro@fe.up.pt

ABSTRACT

International student mobility significantly impacts individuals seeking for academic excellence, cultural exchange, economic growth, and international understanding in an increasingly interconnected world. Governments are increasingly looking to international education systems, developing policies to enhance individuals' social and economic prospects, providing incentives for greater efficiency in schooling, and helping to mobilise resources to meet rising demands. Portugal's emphasis on internationalization and the quality of education has contributed to enhance global perspectives.

Keywords: Student mobility, learning environment, progression in education, internationalization.

INTRODUCTION

International student mobility refers to the movement of students across borders for educational purposes. Students participate in exchange programs, where they attend a foreign institution for a semester or academic year. This offers them exposure to different cultures, education systems, and languages. Countries that attract international students often see economic benefits through tuition fees, living expenses, and student-related spending. International students can contribute to a diverse cultural environment, enriching the local community [1]. In almost all countries, the share of international students has increased since 2013, despite the disruptions due to the COVID-19 pandemic. In many countries, international students make up more than 10% of the student body at tertiary level. The European Union's ministers agreed on reaching a target of at least 20% of students that spend some part of their studies or training abroad. "Mobility for learning purposes" includes the outbound flux from the home country in order to study or undertake training, considering that support for mobility is a main aspect of Erasmus +, the EU program for education and training [2]. Exposure to different academic systems, building international networks, and enhancing employability by being able to speak multiple languages or having international experience. Portugal's job market for international students is growing, especially in fields like technology, engineering, and business.

DISCUSSION

Portugal is a participant in the Erasmus+ program, which allows European students to study abroad within the EU [3]. This initiative has significantly increased student mobility in and out of Portugal. Portugal offers a wide range of programs in fields such as engineering, business, technology, architecture, arts, and social sciences. While Portuguese is the official language, many universities in Portugal offer English-taught programs, particularly at the postgraduate level. This is particularly attractive to international students, especially from non-Portuguese-

speaking countries. The influx of international students has had positive effects on Portuguese society and the economy. The number of international students in Portugal has been steadily rising, especially from non-EU countries. Portugal has been active in the Erasmus Mundus Actions. The country is attracting students not only from Europe but also from countries like Brazil (due to the shared language), China, India, and other parts of the world.

Students are driven to seek different institutions and different societies outside their known environment [4]. International student mobility is deeply interconnected with employment opportunities, both during the studies and after graduation [5]. International student mobility opens doors to job opportunities both during and after studies, providing students with invaluable experience, income, and professional networks. While there are challenges such as language barriers and work permit restrictions, many countries provide avenues for students to transition to the workforce post-graduation. Moreover, international students are seen as important contributors to the host country's economy and workforce, benefiting from their education while providing diversity and global perspectives to the job market. English and local language skills are often necessary for better integration and career advancement. Portugal has also been offering favourable policies for highly skilled graduates, particularly in sectors like tech.

CONCLUSIONS

Studying abroad opens up many networking opportunities with professors, professionals, and fellow students from different parts of the world. This network can prove to be crucial in securing job opportunities after graduation, either in the host country or in the student's home country or another region. Many international students also engage with alumni networks, career fairs, and university-sponsored job placement services to find opportunities in their field. The proposed study explores the strategic importance of international student mobility in the Portuguese context addressing cultural perspectives, economic benefits and employment opportunities.

REFERENCES

[1] Roy, Achinto, et al. "Outcomes of international student mobility programs: A systematic review and agenda for future research." Studies in Higher Education 44.9 (2019): pp.1630-1644.

[2] López-Duarte, Cristina, Jane F. Maley, Marta M. Vidal-Suárez. "International mobility in higher education: students' attitude to international credit virtual mobility programs." European Journal of Higher Education 13.4 (2023): pp.468-487.

[3] López-Duarte, Cristina, Jane F. Maley, Marta M. Vidal-Suárez. "Main challenges to international student mobility in the European arena." Scientometrics 126.11 (2021): pp.8957-8980.

[4] Castro, C.F., M.R. Barbosa. "International Student Mobility: An Empirical Study Based on FEUP Mechanical Engineering Data." Educ. Sci. 2021, 11, 36. 2021.

[5] Gutema, Dandi Merga, Sukrit Pant, Shahrokh Nikou. "Exploring key themes and trends in international student mobility research - A systematic literature review." Journal of Applied Research in Higher Education 16.3 (2024): pp.843-861.

Proceedings IRF2025: 8th International Conference on Integrity-Reliability-Failure
In Engineering, Materials, Manufacturing and Biomechanics. Porto 15-18 July 2025
DOI: https://doi.org/10.24840/978-972-752-323-8

PAPER REF: 23600

ENHANCING ENGAGEMENT IN COMPUTATIONAL FLUID MECHANICS: A REVIEW ON THE USE OF INTERACTIVE VIDEOS AND IN-CLASS QUIZZES IN HIGHER EDUCATION

S.I.S. Pinto[1,2(*)]

[1]University of Porto, Engineering Faculty, Porto, Portugal
[2]Institute of Science and Innovation in Mechanical and Industrial Engineering (LAETA-INEGI), Porto, Portugal
[(*)]*Email:* spinto@fe.up.pt

ABSTRACT

Teaching Computational Fluid Mechanics (CFM) at high education level presents unique challenges due to its mathematical complexity and reliance on simulation tools. Prior pedagogical research has emphasized the importance of instructional models such as cognitive apprenticeship and T-shaped instructional design in addressing these challenges. This paper offers a narrative review of the author's continued pedagogical experience in CFM, focusing on the integration of interactive instructional videos and in-class quizzes. These tools have been observed to enhance student engagement, foster deeper understanding, and promote autonomous learning. The approach aligns with cognitive apprenticeship principles - such as modeling, scaffolding, and reflection - while supporting interdisciplinary thinking as encouraged by T-shaped education. Although no formal data were collected, this review includes qualitative observations gathered from the last academic years in the Master's program in Computational Mechanics at the University of Porto. The discussion is supported by relevant literature and offers insights for improving learning in simulation-based engineering courses.

Keywords: Computational Fluid Mechanics, Cognitive Apprenticeship, Interactive Learning.

INTRODUCTION

Computational Fluid Mechanics (CFM) is a core component of many engineering programs of high education, requiring students to integrate mathematical modelling, physical reasoning, and computational tools. However, the abstract nature of the subject, combined with the steep learning curve of commercial simulation platforms such as ANSYS Fluent, often results in student disengagement or superficial learning. Modern pedagogical frameworks offer strategies to improve learning outcomes in complex technical domains. One such approach is the cognitive apprenticeship model, which emphasizes guided learning through real-world tasks, combining elements like modelling, coaching, scaffolding, and reflection. Complementing this is the T-shaped instructional design, which promotes deep disciplinary knowledge along with the ability to apply concepts across domains. In their previous work, Pinto and Zvacek (2020) applied these principles to redesign the CFM course in the Master's in Computational Mechanics at the University of Porto, enhancing student learning through contextualized instruction and active methodologies. Building upon this foundation, the present review focuses on two specific tools recently adopted in this course: interactive videos and in-class quizzes. These resources have been integrated to extend the cognitive apprenticeship approach and strengthen both conceptual understanding and student autonomy. This paper reviews these practices in light of current educational literature and offers reflective insights based on the author's experience over multiple academic years.

RESULTS AND CONCLUSIONS

The integration of interactive instructional videos and in-class quizzes has significantly enriched the teaching approach in CFM. Although no systematic data collection has been carried out, consistent qualitative observations suggest improved student engagement, confidence, and performance in simulation-based tasks.

The interactive videos, developed by the instructor using ANSYS Fluent, follow cognitive apprenticeship principles by explicitly modelling expert thinking and step-by-step problem-solving strategies. Students can engage with the material asynchronously, reviewing complex procedures - such as mesh generation or turbulence modelling - at their own pace. This scaffolding allows them to internalize concepts before applying them independently during practical sessions or project work.

In-class quizzes have served both formative and diagnostic functions. Delivered in short formats throughout the semester, these quizzes assess students' understanding of key theoretical and computational topics, such as discretization schemes or residual convergence. The immediate feedback and low-stakes nature of the quizzes support reflection and self-regulation, two essential components of cognitive apprenticeship. Furthermore, these activities have contributed to the development of T-shaped competencies by encouraging students to transfer core concepts into varied problem contexts.

Pedagogical literature supports these findings. Mayer's (2009) theory of multimedia learning underscores the value of combining visual and verbal channels, while Brame (2016) highlights how well-designed videos can improve attention and retention. Similarly, Gikandi et al. (2011) show that formative quizzes with feedback enhance learning, particularly in higher education settings.

Student feedback gathered informally over the years reflects appreciation for both resources. Many students reported that the videos helped them grasp challenging concepts and feel better prepared for practical tasks. Others highlighted how quizzes helped them stay on track and monitor their own progress.

Overall, these tools have proven to be effective extensions of a pedagogical framework rooted in cognitive apprenticeship and interdisciplinary skill development. Their adaptability and low implementation cost also make them suitable for broader application in simulation-intensive engineering education.

REFERENCES

[1] Pinto, S.I.S.; Zvacek, S.M. (2020). Cognitive apprenticeship and T-shaped instructional design in computational fluid mechanics: Student perspectives on learning. Journal of the Royal Society of Medicine Open, 50(1). https://doi.org/10.1177/0306419020915725.

[2] Mayer, R.E. (2009). Multimedia Learning (2nd ed.). Cambridge University Press.

[3] Brame, C.J. (2016). Effective educational videos: Principles and guidelines for maximizing student learning from video content. CBE - Life Sciences Education, 15(4).

[4] Gikandi, J.W.; Morrow, D.; Davis, N.E. (2011). Online formative assessment in higher education: A review of the literature. Computers & Education, 57(4), 2333-2351.

[5] Kay, R.H. (2012). Exploring the use of video podcasts in education: A comprehensive review of the literature. Computers in Human Behavior, 28(3), pp.820-831.

SYMPOSIUM - 7

Condition-Based Maintenance: Reliability, Proactivity and Practice

Suzana Lampreia[1(*)], Teresa Morgado[2(*)] and A. M. Pereira[3(*)]

[(1)]Portuguese Naval Academy, Lisbon, Portugal
[(2)]Polytechnic University of Lisbon, Lisbon, Portugal
[(2)]Polytechnic University of Leiria, Leiria, Portugal

(*)Associate Editor for papers in this Symposium

Proceedings IRF2025: 8th International Conference on Integrity-Reliability-Failure
In Engineering, Materials, Manufacturing and Biomechanics. Porto 15-18 July 2025
DOI: https://doi.org/10.24840/978-972-752-323-8

PAPER REF: 22460

FAILURE MODES, EFFECTS, MECHANISM AND CRITICALITY ANALYSIS (FMMECA) OF INTERVAL CONTROL VALVE (ICV)

Iara Tammela(*), Rodolfo Cardoso, Igor de Souza Pinto, Luiz Antonio de Oliveira Chaves, Mateus Carvalho Amaral, Nelson Victor Costa da Silva

Instituto de Ciência e Tecnologia (ICT), Universidade Federal Fluminense (UFF), Rio das Ostras, Brasil
(*)*Email:* nelsonvictor@id.uff.br

ABSTRACT

Interval Control Valves (ICVs) are active flow control devices installed in oil wells that are operated remotely from the surface and perform the function of optimizing fluid production and improving management to increase the recovery factor, especially in reservoirs that have more than one productive zone. However, ICVs have a significant failure rate, especially after ten years of operation, because they operate in extreme pressure, load and flow conditions with erosive and corrosive components, which justifies and makes it essential to evaluate their reliability and useful life in the context of Intelligent Completion (IC) for loss prevention. The aim of this article is to apply the Failure Modes, Mechanisms, Effects, and Criticality Analysis (FMMECA) methodology to ICVs used in intelligent completion systems for offshore wells. Based on ISO 14224 guidelines and Petrobras technical standards N-2781 and N-2782, 132 failure sequences were identified, with a description of the modes, mechanisms and causes for each functional failure of the valve integrated into the system. To assess the risk associated with each failure sequence, an adaptation of the FMECA methodology was applied, incorporating the failure mechanism as an additional parameter in determining the criticality index and risk tolerability. The results highlighted critical failures that require more robust controls, and suggested alternative methods to mitigate the probability of occurrence or the severity of the failure effects. Therefore, the analysis made a contribution by recommending strategies to reduce risks to acceptable levels, promoting a balance between reliability and safety in the Intelligent Completion system.

Keywords: Maintenance. RCM. FMECA. Intelligent Completion. Interval Control Valve.

INTRODUCTION

Smart completion systems incorporate permanent downhole sensors and interval control valves (ICVs) that are actuated from the surface, allowing production and hydrocarbon injection activities to be actively monitored, evaluated and managed in real time (Aljubran; HorneE, 2021). ICVs play a crucial role in improving production performance and controlling fluid flow in oil wells, and are a key component for managing operations in intelligent completion systems (Yang et al., 2019). The proper adjustment of valve configurations such as Interval Control Valves (ICVs) makes it possible to maximize hydrocarbon recovery and improve reservoir flow efficiency (GUAN et al., 2020).

Although real-time monitoring is already a reality in wells operating under intelligent completion technologies, there is still much room for improvement if operations and the oil and gas industry are to achieve satisfactory levels of safety (Al-Hajji; Onikoyi, 2022). These improvements are essential to increase the level of security of monitoring operations and ensure

that interventions are targeted based on accurate information (Atamuradov et al., 2017; Calabrese et al., 2019; Al-Hajji; Onikoyi, 2022).

In order to be able to efficiently manage operations and faithfully demonstrate the integrity of the completion system, it is essential that a robust set of data and information on parameters and variables of interest is collected continuously (Mathew et al., 2012; Chen; Tsui, 2013). However, there is a gap regarding how to select the appropriate parameters to manage the asset, and this activity is usually based on the empirical knowledge of expert engineers (Zhou et al. 2023). According to the authors, this creates a need to establish methods that can help these experts to more accurately identify the appropriate monitoring and management parameters, in order to drastically reduce the volume of data to be monitored and the efforts made.

Therefore, it is justified to identify the functional failures of the ICV, relating them to the potential precursors of failure, so that, in later stages, we can move on to a discussion of which parameters and variables are sufficiently representative for monitoring the degradation and management models of the specialist team. With this in mind, the aim of this article is to propose a mechanism-oriented failure modes, effects and criticality (FMECAM) analysis of the ICV based on its functional failures to serve as a support for future work to identify the necessary parameters for monitoring and creating failure interpretation rules.

REFERENCES

[1] Al-Hajji, H.; Onikoyi, A. Well Integrity Solutions Using Intelligent Field Remote Surveillance and Monitoring Systems. International Petroleum Technology Conference. 2022.

[2] Aljubran, M.J.; Horne, R. Surrogate-Based Prediction and Optimization of Multilateral Inflow Control Valve Flow Performance with Production Data. 2021, v. 36, n. 01, pp.224-233.

[3] Atamuradov, V. et al. Prognostics and Health Management for Maintenance Practitioners - Review, Implementation and Tools Evaluation, 2020, v. 8, n. 3.

[4] Chen, N.; Tsui, K.L. Condition monitoring and remaining useful life prediction using degradation signals: revisited. 2013, v. 45, n. 9, pp.939-952.

[5] Rahman, M.S. et al. Study on heavy metals levels and its risk assessment in some edible fishes from Bangshi River, Savar, Dhaka, Bangladesh. 2012, v. 134, n. 4, pp.1847-1854.

[6] Mathew, S.; Alam, M.; Pecht, M. Identification of Failure Mechanisms to Enhance Prognostic Outcomes. 2012, v. 12, n. 1, pp. 66-73.

Proceedings IRF2025: 8th International Conference on Integrity-Reliability-Failure
In Engineering, Materials, Manufacturing and Biomechanics. Porto 15-18 July 2025
DOI: https://doi.org/10.24840/978-972-752-323-8

PAPER REF: 22468

MAIS METHOD FOR GULLY'S RISK ANALYSIS

Ana Luiza Alves de Oliveira(*), Nathaly Sarasty Narvaes, João da Costa Pantoja
Urbanism and Architecture Faculty, University of Brasilia, Brasilia (DF), Brasil
(*)*Email:* ana.luiza@unb.br

ABSTRACT

Methods for reliability and risk analysis have been developed and explored in recent years. In the context of public policy management for the Federal District (DF) of Brazil, a collaboration between researchers of the University of Brasília and the Civil Defense of the DF led to the development of the MAIS Method - a methodology based exclusively on visual inspection parameters to assess the risk of damage to buildings and infrastructure caused by gully erosion. The approach involves visual monitoring and the determination of key risk parameters. The methodology was applied to a case study in Chácara 74, Sol Nascente (DF), identifying critical parameters for gully assessment, such as connection to a community, slope gradient, and gully progression. Additionally, the study presents the parameter intervals and the calibration process. Ultimately, a reliability level for the analyzed gully was determined as "moderate-high".

Keywords: Reliability, risk, gully, multi-factor criteria, monitoring engineering.

INTRODUCTION

The quantified reliability analysis of complex engineering systems aims to provide a rational basis for decisions related to their safe and economical operation (Martin et al., 1983). The concept of reliability introduces a distinct approach to safety in engineering, shifting the focus from detailed stress calculations and individual member behavior to the quantification of uncertainties inherent in structural performance, loading conditions, and material properties. Structural reliability analysis and prediction emphasize not only accurate representation of the underlying physics but also the development of models that are realistic, sufficiently simple, and practical, incorporating probabilistic descriptions of both loads and resistances (Melchers & Beck, 2018). This approach operates under the assumption that past performance can inform future behavior. Ultimately, it represents a departure from traditional deterministic methods, offering a framework that integrates risk, uncertainty, and probabilistic reasoning into engineering practice.

By quantifying the probability of failure and its potential consequences, reliability-based methods provide a scientific foundation for risk-informed decision-making and resilience planning. Established techniques such as Monte Carlo simulation, the First-Order Reliability Method (FORM), and the Second-Order Reliability Method (SORM) are widely accepted by the scientific community and are routinely employed to estimate the failure probability of systems both in structural engineering and in disaster risk management.

In addition to ensuring structural safety, reliability analysis plays a critical role in the broader context of disaster risk assessment, supporting the evaluation of system vulnerabilities under extreme events such as earthquakes, floods, and landslides. Building on these principles and addressing the need for mapping and monitoring risk areas in the Federal District (DF), Brazil,

the Civil Defense of DF and the University of Brasília (UnB) have established a partnership. The initiative aims to identify and assess areas susceptible to environmental hazards, particularly those affected by gully erosion. Its goal is to develop a methodology based on reliability principles to support decision-making and prioritize interventions.

A gully is a "small hollow or channel worn in earth or unconsolidated material, as on a hillside, by running water and through which water runs only after a rain or the melting of ice or snow; it is larger than a rill and smaller than a stream channel" (Ostercamp, 2008). This landform develops as a result of the displacement of soil or soft rock particles by concentrated surface runoff, which leads to the formation of distinct, narrow incisions. These incisions are typically deeper and wider than rills and generally convey water only during and immediately following intense rainfall or snowmelt events.

According to Oliveira et al. (2013), a survey conducted in 2009 identified 1,094 rills and gullies throughout the Federal District, occupying an area of 64.88 hectares, which corresponds to 0.01% of the DF's surface (Figure 1). Although this is considered a relatively small area, these are highly impacted zones that are difficult to restore. This data reinforces the need for the partnership established to develop a methodology for assessing environmental risk related to gullies. This methodology is intended to be both easy to apply and adaptable to different contexts, and it will be explained in the next section

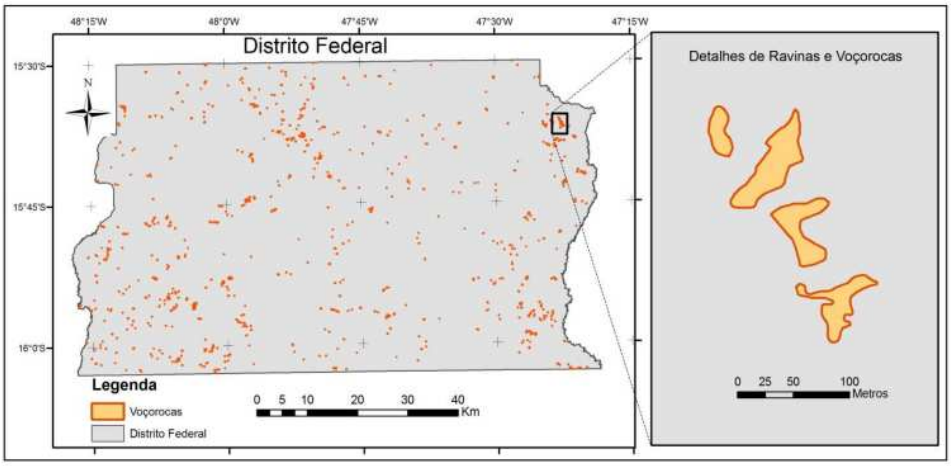

Fonte: Oliveira et. Al., 2013.

Fig. 1 - Spatial distribution of ravines and gullies present in the Federal District.

Reliability index β

Due to the complexity involved in obtaining the probability of failure, several analytical methods have been developed as alternative ways to evaluate it. Some of these approaches use the concept of the **reliability index**, β. It represents the shortest distance from the origin of the standard normal space of the random variables to the performance function. The mean of the performance function $G_{(x)}$ is given by the following expression:

$$\mu_G = \mu_R - \mu_S \tag{1}$$

Where μ_R and μ_S are the means of capacity and demand, respectively.

The reliability index, β, is defined as:

$$\beta = \frac{\mu_G}{\sigma_G}$$

The β index indicates the distance from the average safety margin, since $G_{(x)} = 0$. Figure 2 graphically displays the β index in one dimension. The idea behind the β index is that the distance from the mean value of G to the limit state surface provides a good measure of the system's reliability. This distance is expressed in terms of the standard deviation of G, denoted as σ_G (Madsen et al., 1986).

The **target reliability index**, β_t, is considered a control parameter for optimization. This parameter reflects the investment of material placed in the structure. The more material that is invested in the critical areas, the lower the expected loss. This type of optimization is mostly applied when potential economic losses outweigh the risk to human life. When the expected loss of life or health is significant, the ideal level of reliability becomes more controversial. This often leads to a cost-benefit analysis, where the system's reliability is translated into a cost-per-life-saved metric.

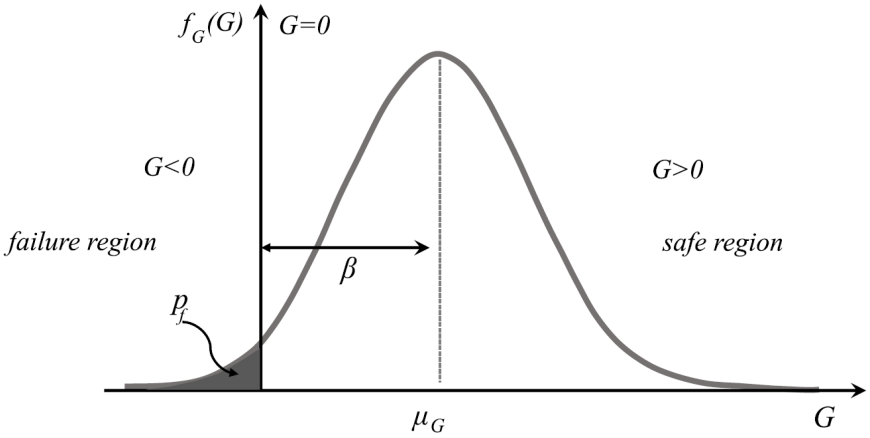

Fig. 2 - β index.

METHOD OF ASSESSMENT BY INTEGRITY AND SAFETY FOR GULLIES

Originally developed for the structural evaluation of reinforced concrete buildings, the Method of Assessment by Integrity and Safety - MAIS Method - integrates sensorial inspection with probabilistic reliability analysis, providing a rapid and practical approach to assessing structural condition and safety (Oliveira, 2021). Intended as an initial screening tool to support decision-making, it functions as a multi-criteria methodology that quantifies degradation based on observable parameters. This adaptation integrates both qualitative inspection - through sensorial evaluation - and quantitative safety analysis, by incorporating a reliability index into the integrity model.

The Brazilian Standard NBR 16747:2020 – Building Inspection – Guidelines, Terminology and Procedures defines sensorial inspection as "*Assessment of a product's attributes through the sensory organs in order to evoke, measure, analyze, and interpret reactions to the characteristics of materials as perceived by the five senses: sight, smell, taste, touch, and hearing*" (ABNT, 2020). In contemporary contexts, where fast-paced conditions and limited time, equipment, or financial resources are common, sensorial inspection offers a fast, methodologically grounded, and efficient alternative. It was developed to meet the market demand for quick inspections without the use of testing equipment, while still ensuring reliable results. This concept is used in MAIS Method, as shown in Figure 3.

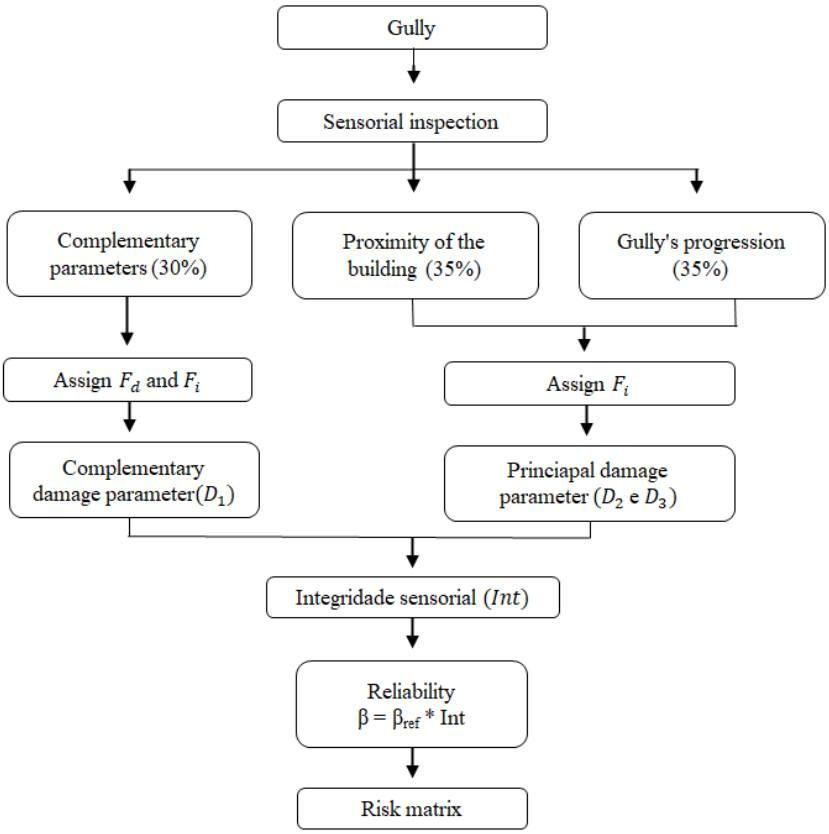

Fig. 3 - MAIS Methodology for gully.

The first step of the method is to select and identity the gully to be inspected and its area of influence. Once the inspection area of the gully is defined, the *in loco* sensorial inspection is carried out. During this stage, a set of technical parameters related to the gully's morphological and environmental characteristics, shown in Table 1, are systematically evaluated. Each parameter is associated with a predefined Damage Factor (F_d), which represents its relative importance in the overall degradation process, reflecting the significance of the parameter in terms of functionality and risk. Additionally, each parameter is classified into specific intervals based on field observations, and an Intensity Factor (F_i) is assigned accordingly. It represents the severity and progression of the damage, capturing the degree of degradation present at the time of inspection. This structured approach allows for the consistent quantification of damage severity and relevance using observable features. It is time-dependent and context-sensitive, requiring the inspector to consider environmental conditions. The inspector assigns a qualitative interval to each of the 14 parameters observed *in situ*. Each interval is associated with an F_i value, while the corresponding F_d is assigned based on the type of damage observed.

Following a more comprehensive analysis of the gully's behavior and in consultation with domain experts, it was determined that the final two parameters: 13) gully progression and 14) proximity to the erosive factor - should be assigned greater significance, as they represent the primary drivers of structural degradation and associated risk. These are defined as core parameters and their damages (D_1 *and* D_2) are directly integrated into the risk formulation. The remaining parameters (1 through 12), considered supporting parameters, have their individual damage contributions quantified using Heidecke's damage model, via Equation 1.

$$D_3 = (1{,}9738\ {F_i}^2 - 1{,}1187\ F_i + 0{,}1513) * F_d \quad (1)$$

Table 1 - Parameters and intervals for the sensorial inspection of gullies.

Item	Parameters	Damage Factor (Fd)	Intervals	Intensity Factor (Fi)
1	Cross-section	0,35	V	0,35
			U	0,65
2	Gully's slope	0,65	0 - 30%	0,35
			> 30% - 60%	0,65
			> 60% - 90%	0,85
			> 90%	1
3	Shallow gully size	0,85	Nonexistent	0
			Small (up to 5 cm)	0,35
			Medium (> 5 cm to 30 cm)	0,65
			Large (> 30 cm)	1
4	Upstream ground slope	1	Slightly sloped (up to 5°)	0
			Moderately sloped (> 5° – 15°)	0,65
			Sloped (> 15° – 25°)	0,85
			Steep (> 25°)	1
5	Plan view shape	0,35	Polygonal	0,35
			Branched	0,65
			Bifurcated	0,85
			Linear	1
6	Land use and cover	1	forestry	0
			Natural vegetation	0
			Agriculture and pasture	0,65
			Exposed soil	0,85
			Urban area	1
7	Building standard	0,65	High	0,35
			Medium	0,65
			Low	0,85
8	Sewage system quality	0,35	Good	0,35
			Medium	0,85
			Poor	1
9	Garbage collection frequency	0,35	Daily	0
			Two or three times a week	0
			Weekly	0,35
			Fortnightly or less	0,65
10	Paving quality	0,35	Good	0,35
			Medium	0,85
			Poor	1
11	Drainage system quality	0,35	Good	0,35
			Medium	0,85
			Poor	1
12	Presence of debris	0,65	None	0
			Low	0,65
			Medium	0,85
			High	1
13	Gully progression	--	Reduced	0
			Stationary	0
			Slow	0,65
			Fast	1
14	Proximity to erosive factor	--	> 100 m	0,35
			> 50 m - 100 m	0,65
			> 20 m - 50 m	0,85
			up to 20 m	1

Heidecke's degradation model was selected because it reflects the progressive behavior observed in most natural deterioration processes. This formulation captures an initially slow degradation phase - the initiation phase - followed by an accelerated loss of integrity - the propagation phase - once a critical threshold is reached, as proposed by Tuutti (1982). The 3D graphic in Figure 4 illustrates the behavior described by this equation, highlighting both phases. Although it is challenging to pinpoint the exact critical point, it is evident that the propagation phase has greater significance than the initiation phase, since the initial degradation occurs slowly and its effects are less pronounced. Therefore, the scale adopted for the parameters in this study was calibrated to the following discrete values: (0; 0.35; 0.65; 0.85; 1.0), which captures the transition into the propagation phase and emphasizes its importance.

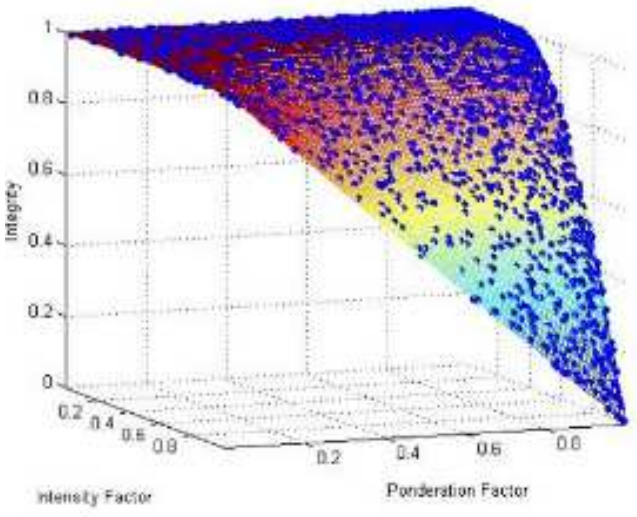

Fig. 4 - Heidecke's integrity model.

To mitigate the subjectivity inherent to human inspection and incorporate a safety margin, the MAIS method was expanded to include probabilistic risk analysis, resulting in a combined integrity-reliability indicator. The reliability, C, is defined as the complement of the probability of failure, P_f , that is as shown on Equation 1:

$$C = 1 - P_f \tag{1}$$

The reliability index (β) by MAIS method is computed by the following equations:

$$\mathrm{C} = 1 - \left\{\left[D_{imáx}\left(1 + \frac{\sum_{i=1}^{m} D_i - D_{imáx}}{\sum_{i=1}^{m} D_i}\right) x \frac{m}{2m-1}\right] x\, \beta_{ref}\right\} \tag{2}$$

$$\beta_{mais} = \mathrm{C} x \beta_{ref} \tag{3}$$

where:

D_i Individual damage of each parameter;
$D_{imáx}$ Maximum individual damage among the parameters;
m Number of parameters;
β_{mais} Approximate Reliability index of MAIS method;
β_{ref} Reference reliability index.

The direct, linear coupling between the integrity and the reliability index is grounded in the assumption of a proportional interdependence between gully integrity and structural safety. In this formulation, a reduction in physical integrity corresponds directly to a decrease in reliability. The adoption of a linear relationship facilitates computational simplicity, enhances methodological transparency and eliminates the need for empirically defined correction functions. Given that the reliability index (β) is statistically robust - being derived from probabilistic frameworks such as First-Order Reliability Method (FORM) or Monte Carlo simulations - it provides a suitable scalar for transforming qualitative integrity assessments into a quantitative measure of structural safety.

In the present study, the adopted reference reliability index (β_{ref}) is 4.0, in accordance with the recommendations of fib Bulletin 62 (2010) and aligned with the values prescribed for new structures classified under Consequence Class 3 (CC3) – High consequence class – in the Eurocode framework (CEN, 2002), as presented in Table 2.

Table 2 - Reference reliability index.

Consequence Class	**Minimum Reference Period**	**β New**	**β Repaired**	**β Existing**
		WN	WD	WN
CC0	1 year	3.3	2.3	2.8
CC1 – Low**	15 years	3.3	2.3	2.8
CC2 – Medium**	15 years	3.8	2.8	3.3
CC3 – High**	15 years	4.3	3.3	3.8

Notes:

1. Classes 0 and 1 (CC0 and CC1) – applied only in situations where there is no risk to human life.
2. WN – Wind non-dominant forces
3. WD – Wind dominant forces
4. In this case, the reliability index (β) represents the minimum level for human safety under the given circumstances and consequence classes.
5. ** Classified based on the provisions of Annex C of Eurocode (EN 1990) (CEN, 2002).

Accordingly, the classification of this result, after the reliability index is integrated with the findings of the sensorial inspection, is presented in Table 3, which is an adapted version of the risk matrix previously shown in Table 4.

Table 3 - Risk Matrix – Severity × Probability.

Risk Matrix		**Consequence**			
		Low	**Medium**	**High**	**Very High**
Failure Probability	Very High	0.68	0.52	0.24	0.00
	High	1.28	0.68	0.52	0.24
	Moderate-High	1.80	1.28	0.68	0.52
	Moderate	3.41	1.80	1.28	0.68
	Low	3.72	3.41	1.80	1.28
	Very Low	4.00	3.72	3.41	1.80

Table 4 - Risk Matrix – Severity × Probability.

VERY DANGEROUS ZONE			
Nível	**Confiabilidade**		
Very High	0	to	0.24
High	> 0.24	to	0.68
Moderate-High	> 0.68	to	1,80
Moderate	> 1.80	to	3,41
Low	> 3.41	to	3,72
Very Low	> 3.72	to	4
VERY SAFE ZONE			

CASE STUDY

Based on the analysis of the Zoning of Geological Risk Areas in Brasília – Federal District (DF) report (SGB, 2022) and the Activity Reports issued by the Government of the Federal District (GDF) in 2015 and 2023, which address geological and environmental risks in various regions, the implementation of the monitoring project prototype was decided for Chácara 36 situated in Administrative Region XXXII – Sol Nascente/Pôr do Sol. These locations were selected due to their high risk of flash floods and erosion (gullies), as well as their distinct socio-environmental characteristics. Figure 5 provides an overview of the location of these areas in relation to the Sol Nascente Administrative Region.

Fig. 5 - Chácara 36 Field visit (31/01/2024).

According to the Technical Report by the State Secretariat of Public Security of the Federal District (GDF, 2023), Chácara 36 lies on a slope, with its lower end below street level. The area shows signs of severe gully in sandy, low-cohesion soils, indicating high soil vulnerability. Combined with the lack of drainage, waste accumulation, poor vehicle access, and unregulated growth, the region faces increased risks of flooding, landslides, and sheet erosion, with no

mitigation measures in place. Therefore, the selection of Chácara 36 as the implementation site for the monitoring project prototype is both strategic and necessary. The proposed methodology is crucial for the assessment of the numerous gullies present in the Federal District and for providing technical support to civil defense actions.

Studies using drone technology made it possible to identify that, during a field visit conducted on May 25, 2024, the gully had an area of 409 m² and a perimeter of 106 m. Figure 5 presents aerial images captured on that day. In August 2024, a technical visit was conducted to carry out the sensorial inspection of the area and the application of the MAIS Method. The evaluation and the results of which are presented in **Error! Reference source not found.**Table 5.

Table 5 - Gully Assessment – Chácara 36.

Item	**Parameters**	**Intervals**	**Damage** (D_1, D_2 and D_3)
1	Cross-section	U	0,09
2	Gully's slope	> 30% - 60%	0,17
3	Shallow gully size	Small (up to 5 cm)	0,00
4	Upstream ground slope	Sloped (> 15° – 25°)	1,00
5	Plan view shape	Linear	0,35
6	Land use and cover	Urban area	1,00
7	Building standard	Low	0,41
8	Sewage system quality	Poor	0,35
9	Garbage collection	Fortnightly or less	0,09
10	Paving quality	Poor	0,35
11	Drainage system quality	Poor	0,35
12	Presence of debris	High	0,65
13	Gully progression	Reduced	0,00
14	Proximity to erosive	up to 20 m	1,00
		Integrity adjacent factors (Int_1)	**0,06**
		Integrity gully advancement (Int_2)	**1,00**
		Integrity proximity to erosive factor (Int_3)	**0,00**
		Integrity (Int)	**0,37**
		Reference beta (βref)	**4,00**
		Sensorial beta (βsensorial)	**1,47**

After the evaluation, the result indicated that the gully presents a risk level of 1.47, which corresponds to a “moderate-high” level according to the risk matrix. The result is considered accurate, as the situation is dangerous; however, since there has been no progression, the Civil Defense should monitor its development. There is no immediate need to evacuate the area. The population must remain alert and leave in case of rainfall, but a full evacuation is not currently necessary.

CONCLUSIONS

The MAIS Method demonstrates significant potential as a rapid and practical tool for assessing gully-related environmental risks. Its integration of sensorial inspection with reliability analysis provides an innovative, low-cost approach that is particularly suitable for regions facing urgent and resource-limited risk scenarios. The method's ability to translate qualitative field

observations into quantifiable indicators supports more structured and informed decision-making, as evidenced by its application in Chácara 36. The resulting classification of a "moderate-high" risk level shows that the methodology can effectively identify and communicate critical risk conditions.

Nonetheless, while the results confirm the method's overall validity and usefulness, further calibration is recommended to enhance its precision and generalizability. The weights and intervals used in the risk formulation, especially for core parameters, should be refined through additional case studies and longitudinal monitoring. Expanding its application across a broader range of environmental and socio-urban contexts will help ensure the robustness and scalability of the methodology, reinforcing its role as a decision-support tool for civil defense and public policy.

REFERENCES

[1] Associação Brasileira de Normas Técnicas. NBR 16747:2020 - Inspeção Predial - Diretrizes, Conceitos, Terminologia e Procedimento. Rio de Janeiro: ABNT, 2020.

[2] Governo do Distrito Federal (GDF). Secretaria de Estado de Segurança Pública do Distrito Federal. Coordenação de Gestão de Riscos de Desastres. Gerência de Proteção Comunitária III. Relatório de Atividades: Monitoramento de Áreas de Riscos Vila Madureira e Condomínio Recanto da Paz – Chácara 36. Brasília: GDF, 2023.

[3] International Organization for Standardization. ISO 31000:2018 – Risk management - Guidelines. Geneva: ISO, 2018.

[4] Martin P, Strutt JE, Kinkead N. A review of mechanical reliability modelling in relation to failure mechanisms. Liverpool: University of Liverpool; Cranfield: Cranfield Institute of Technology; Warrington: UKAEA, 1983.

[5] Oliveira ALA. Método Acoplado Integridade e Segurança – MAIS para a Avaliação de Patrimônios Históricos em Estruturas de Concreto Armado. Tese de Doutorado, University of Brasília, Brasília, 2021.

[6] Oliveira BEN, Matricardi EAT, Chaves HML, Bias ES. Identificação dos processos erosivos lineares no Distrito Federal através de fotografias aéreas e geoprocessamento. Geociências (São Paulo), 2013, 32(1), pp.152-165.

[7] Osterkamp WR. Annotated definitions of selected geomorphic terms and related terms of hydrology, sedimentology, soil science and ecology. Reston, Virginia: U.S. Geological Survey, 2008. (Open File Report 2008-1217).

[8] Serviço Geológico do Brasil (SGB). Antiga Companhia de Pesquisa de Recursos Minerais (CPRM). Setorização de Áreas de Risco Geológico em Brasília – Distrito Federal. Brasília: SGB, 2022.

[9] Tuuttii, K. Corrosion Steel inconcrete. Swedish cement and concrete research institute. Stockolm. 1982.

Proceedings IRF2025: 8th International Conference on Integrity-Reliability-Failure
In Engineering, Materials, Manufacturing and Biomechanics. Porto 15-18 July 2025
DOI: https://doi.org/10.24840/978-972-752-323-8

PAPER REF: 22519

DATA-DRIVEN POST-EARTHQUAKE REPAIRABILITY ASSESSMENT OF CORRODED RC BRIDGE PIERS

M. Sadeghi, P. Poorahad A., M.R. Shiravand(*)

Faculty of Civil, Water and Environmental Engineering, Shahid Beheshti University, Tehran, Iran
(*)*Email:* m_shiravand@sbu.ac.ir

ABSTRACT

Bridges are key components of transportation infrastructures, and any interruption in their serviceability can cause serious environmental, social, and economic issues. Reinforced concrete (RC) bridge piers undergo permanent deformation due to the severe damage in the plastic hinge region, primarily caused by the fixed-base condition. Despite their satisfactory seismic performance, which allows them to withstand lateral deformation without significant reductions in strength, ductility, or stiffness, the permanent damage often demands reconstruction. Over time, ageing factors, such as corrosion, lead to a significant reduction in strength, ductility, and lateral stiffness, intensifying the damage sustained by the piers, which in turn, increases the likelihood of the reconstruction after a seismic event [1].

Keywords: Corrosion, machine learning, concrete bridge, post-earthquake repairability.

INTRODUCTION

The corrosion-induced deterioration includes a reduction of the cross-sectional area and mechanical properties of the steel reinforcing bars, as well as a decrease in the compressive strength of the concrete [2]. As shown in Figure 1, this deterioration manifests visually through the formation of cracks on the concrete surface and degradation of the concrete cover, which increases the risk of moisture and corrosive substances penetrating the structure. The degradation of reinforcing steel also deteriorates concrete confinement and the bond between the reinforcements and concrete. Additionally, these corrosion-induced degradations affect the failure mode of reinforced concrete piers and can lead to shear-associated failures, even in ductile-designed structures [3]. Ultimately, the consequences of corrosion can compromise the safety and longevity of reinforced concrete infrastructure.

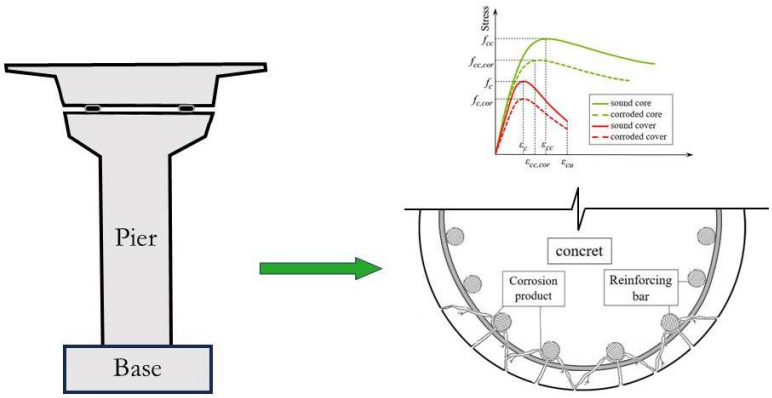

Fig. 1 - The impact of corrosion of the reinforcing bars on the formation of cracks and the reduction in mechanical properties of concrete bridge piers.

Machine learning (ML) methods can effectively tackle challenges and limitations in structural and earthquake engineering problems. ML algorithms provide powerful tools for solving problems as an alternative to traditional experimental and numerical tests with minimal human intervention. Moreover, ML predictive models estimate new points or find patterns in data without necessitating a deep understanding of the physical laws and theories behind the phenomena, provided that a comprehensive and relevant database is prepared [4].

RESULTS

In this paper, a comprehensive database that includes data, as input features, regarding geometrical, material, detailing, loading conditions, and corrosion-related parameters from a large number of experiments which performed cyclic load tests on corroded RC bridge piers is gathered. The outputs of the database comprise residual strength and residual drift ratio, which are essential for evaluating the post-earthquake repairability of corroded RC piers. Five machine learning models – linear regression, decision tree, support vector regression, K-nearest neighbors, and bagging regression – are employed for data fitting. Bayesian search is used for hyperparameter optimization. R-squared and root mean squared error metrics are utilized as metrics considered for selecting the most accurate model.

REFERENCES

[1] Todorov B, Billah AM. Post-earthquake seismic capacity estimation of reinforced concrete bridge piers using Machine learning techniques. Structures: Elsevier; 2022. pp.1190-206.

[2] Vu NS, Li B. Seismic performance of flexural reinforced concrete columns with corroded reinforcement. 2018.

[3] Lee H-S, Kage T, Noguchi T, Tomosawa F. An experimental study on the retrofitting effects of reinforced concrete columns damaged by rebar corrosion strengthened with carbon fiber sheets. Cement and concrete research. 2003;33: pp.563-570.

[4] Poorahad Anzabi P, Shiravand MR, Mahboubi S. Machine Learning-Aided Prediction of Seismic Response of RC Bridge Piers Exposed to Chloride-Induced Corrosion. The International Conference on Net-Zero Civil Infrastructures: Innovations in Materials, Structures, and Management Practices (NTZR): Springer; 2024. pp.1409-1421.

Proceedings IRF2025: 8th International Conference on Integrity-Reliability-Failure
In Engineering, Materials, Manufacturing and Biomechanics. Porto 15-18 July 2025
DOI: https://doi.org/10.24840/978-972-752-323-8

PAPER REF: 22598

DETERMINATION OF ACOUSTOELASTIC COEFFICIENTS FOR STRESS ESTIMATION OF A CONCRETE ELEMENT SUBJECTED TO FLEXURAL LOADING

Aayush Joshi[1,2(*)], Kranti Jain[2], Ajay Chourasia[3]

[1]Dep. Civil Engineering Women Institute of Technology, Dehradun-248001, Uttarakhand, India.
[2]Dep. Civil Eng. National Inst. of Technology, Uttarakhand Srinagar, Pauri Garhwal, Uttarakhand, India.
[3]Structural Engineering Division, Central Building Research Institute, Roorkee, Uttarakhand, India.
[(*)]*Email:* aayushjoshi.phd19@nituk.ac.in,

ABSTRACT

This study investigates the acoustoelastic response of concrete elements under flexural loading by determining acoustoelastic coefficients for stress estimation. Ultrasonic pulse velocity (UPV) measurements were conducted in both tensile and compressive zones, revealing a linear variation with applied stress, an increase in the compression zone and a decrease in the tension zone. The acoustoelastic coefficients were determined using linear curve fitting of the relative velocity variation as a function of stress. The derived coefficients provide a quantitative framework for non-destructive stress assessment in concrete structures, enhancing the reliability of ultrasonic techniques for structural health monitoring.

Keywords: Acoustoelastic effect, stress level, UPV, flexural loading, SHM.

INTRODUCTION

Since the development of the theory of acoustoelasticity, the majority of research on concrete has been conducted under uniaxial compressive loading conditions[1,2,3]. To quantify this behavior, acoustoelastic coefficients are determined using linear curve fitting of the relative velocity variation as a function of applied stress. The linearized form [4]:

$$\frac{\Delta V_{ij}}{V_{ij}^{0}} = \sigma_{11} A_{ij} + C \qquad (1)$$

Equation (1) is used to determine the coefficient , which characterizes the stress sensitivity of UPV. To extend the scope of acoustoelasticity to flexural loading conditions, the present investigation adopts a similar approach to evaluate its feasibility in such scenarios. In the past research have been carried out and wave velocity variation for flexural loading has been investigated in tension zone [5].

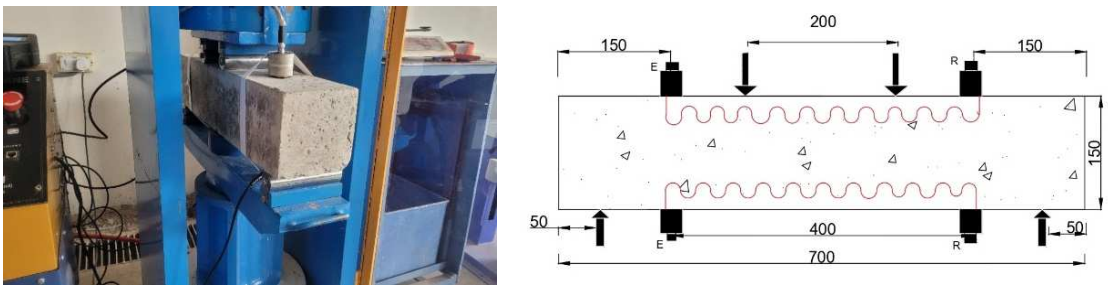

Fig. 1 - A schematic diagram showing transducer arrangement for propagation of longitudinal wave (LW) in compression zone (top) and tension zone (bottom) in a concrete specimen.

In the present study, two ultrasonic pulse analyzers were employed one dedicated to the tension zone and the other to the compression zone to measure ultrasonic pulse velocity in both regions independently. An extended experimental consisting CTM with 100 kN flexural attachment was used to apply flexural load (Figure 1). Pulse analysis was done using Proceq PL200. The loading conditions used were an incremental flexural load with a load step of 1 kN was used. This load step was selected on hit and trail basis depending uspon cube test and 4-point bend test conducted on 100x100x500 (mm) beams. The specimens were loaded to a stress level of 50-60 % of the ultimate compressive strength, this stress level was selected to avoid any observable mechanical damage to the specimen, to transducers and other equipment.

RESULTS AND CONCLUSIONS

Ultrasonic pulse velocity (UPV) exhibited stress-dependent behaviour under flexural loading, with distinct trends in the compression and tension zones. In the compression zone (upper beam region), UPV increased linearly with stress, consistent with acoustoelastic responses observed under uniaxial compression. In contrast, the tension zone (lower region) showed a linear decrease in velocity, with a higher magnitude of relative variation compared to compression.

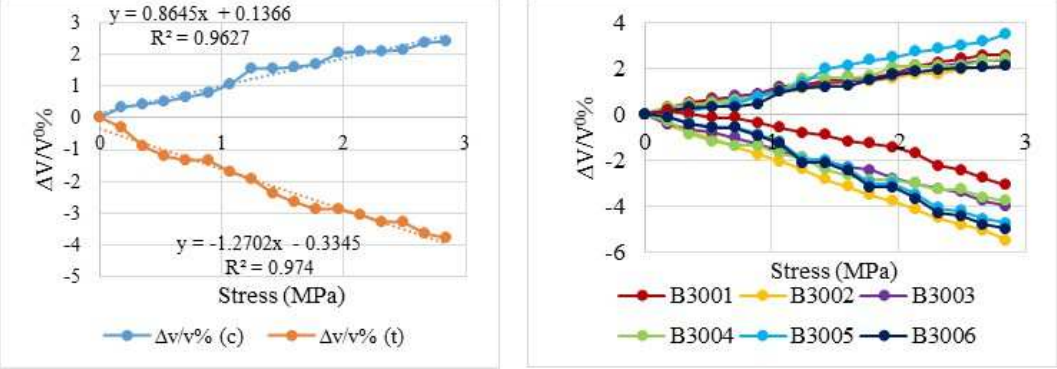

Fig. 2 - Velocity variation with stress and determination of acoustoelastic coefficients using linear curve fitting

Across different concrete mix designs, UPV trends remained predominantly linear, except in cases where microcracking introduced anomalies. On average, the compression zone exhibited a 2.5% velocity increase, indicating a stiffening effect, while the tension zone showed a 4% decrease, aligning with acoustoelastic principles. As shown in figure 2 Acoustoelastic constants were determined for all the specimens.

REFERENCES

[1] Bompan, K.F.; Haach, V.G. (2018). Ultrasonic tests in the evaluation of the stress level in concrete prisms based on the acoustoelasticity. Construction and Building Materials, 162, pp.740-750. https://doi.org/10.1016/j.conbuildmat.2017.11.153.

[2] Hughes, D.S.; Kelly, J.L. (1953). Second-Order elastic deformation of solids. Physical Review, 92(5), pp.1145-1149. https://doi.org/10.1103/PhysRev.92.1145.

[3] Shokouhi, P., et al. (2012). Surface wave velocity-stress relationship in uniaxially loaded concrete. ACI Materials Journal, 109(2), pp.141–148. https://doi.org/10.14359/51683700.

[4] Lillamand, I.; Chaix, J.F.; Ploix, M.A.; Garnier, V. (2010). Acoustoelastic effect in concrete material under uni-axial compressive loading. NDT and E International, 43(8), pp.655-660. https://doi.org/10.1016/j.ndteint.2010.07.001.

[5] Carnot, L.N. (2019). The Influence of Concrete Nonlinear Elastic Behavior under Tensile Stresses on Longitudinal and Shear Ultrasonic Pulse Propagation. Russian Journal of Nondestructive Testing, 55(12), pp.918-927. https://doi.org/10.1134/S1061830919120076.

Proceedings IRF2025: 8th International Conference on Integrity-Reliability-Failure
In Engineering, Materials, Manufacturing and Biomechanics. Porto 15-18 July 2025
DOI: https://doi.org/10.24840/978-972-752-323-8

PAPER REF: 22633

ADOPTION OF INDUSTRY 4.0 TECHNOLOGIES FOR PRODUCTIVITY IMPROVEMENT IN MANUFACTURING SYSTEMS - A REVIEW

Mohammed Iltefat Quraishi[1(*)], Prashant M. Ambad[2]

[1]Department of Mechanical Engineering, Maharashtra Institute of Technology, Aurangabad, India.
[2]Professor, School of Mechanical and Manufacturing Sciences, JSPM University, Pune, India.
[(*)]*Email:* qiltefat@gmail.com

ABSTRACT

In the era of Industry 4.0, every manufacturing industry is striving to improve its production process, reduce wastage and increase productivity. To achieve this goal, a well-established system of Total Productive Maintenance (TPM) has been widely adopted. TPM focuses on keeping all equipment in top working condition without breakdowns and also without delays in all manufacturing processes. Industrial Internet of Things (IIoT) systems can be successfully used to create effective smart factories (manufacturing facilities) in which higher levels of efficiency can be reached which is the ultimate goal of TPM program. In this context, this article presents a literature review on the application of IIoT technologies in different manufacturing systems for productivity improvement, particularly in maintenance of the equipments. Firstly we present an overview of the principal concepts and technologies of Industry 4.0. Then the maintenance management and various maintenance strategies adopted for the upkeep of the equipments are presented mainly focussing on predictive maintenance. After that, the Predictive Maintenance (PdM), which uses Industrial Internet of Things (IIoT) to detect any potential problems in the machines and equipments before they occur is dealt with in detail. As the main contributions, this study discusses the current trends, challenges and limitations in the application of IIoT technologies in today's industry. We concluded that the advanced technologies in Industry 4.0 renders for the development of smart factories contributing to revolutionizing manufacturing by increasing flexibility, enhancing machine downtime, costs, control and quality of production.

Keywords: Predictive Maintenance, TPM, IIoT, Industry 4.0

INTRODUCTION

Industry 4.0 has introduced a new era for manufacturing industries, where the Industrial Internet of Things (IIoT) is playing a crucial role in enhancing the quality and maintenance of manufacturing systems. Every manufacturing industry is striving to improve its production process, reduce wastage and increase productivity. By adopting the cutting-edge technologies and methodologies, manufacturing companies can achieve significant improvements in productivity, efficiency, and profitability. Quality related waste can be minimized by identifying root causes and implementing corrective actions. Through TPM and Predictive Maintenance, industries can optimize their processes and minimize quality-related errors. Apart from visible losses, there are also concealed losses that affect the profitability of the company. The implementation of Industry 4.0 concepts can help in identifying these concealed losses and taking corrective measures to prevent them.

The use of IoT-based solutions in the industrial setting is considered very promising by the research community and the industry. The notion that Manufacturing industry needs to transform into predictive manufacturing has motivated our study. To facilitate the development of systems that help in realizing the integration of Industry 4.0 technologies in conventional TPM operations to leverage the benefits of TPM programs in the manufacturing systems, there is a need for a detailed review providing broader insight and knowledge into the domain of Industry 4.0. The present paper reviews literature on various Industry 4.0 technologies currently in use in industrial tasks and how they can offer new opportunities for management strategies. This analysis also provides broader insight and knowledge of the recent trends and existing challenges, highlighting key aspects occurring in the implementation of IoT technologies in a smart factory.

The paper also examined the various predictive maintenance practices within an I4.0 environment. It also envisioned the possibility of adopting different information and communication technologies (ICTs) in various industrial operations and to help diagnose mechanical and electrical failures, so that organizations could establish more assertive corrective interventions and preventive planning while providing real-time information to managers. The paper is organized as follows: Section 2 illustrates the background, providing an overview of the main aspects of Industry 4.0 and Total Productive Maintenance; Section 3 illustrates the importance the maintenance management, digitalization of maintenance and the various maintenance strategies adopted. Section 4 contains the discussion on current practices, key drivers, benefits, challenges and limitations in implementation of Industry 4.0; Finally, in Section 5 the conclusions of the study are provided.

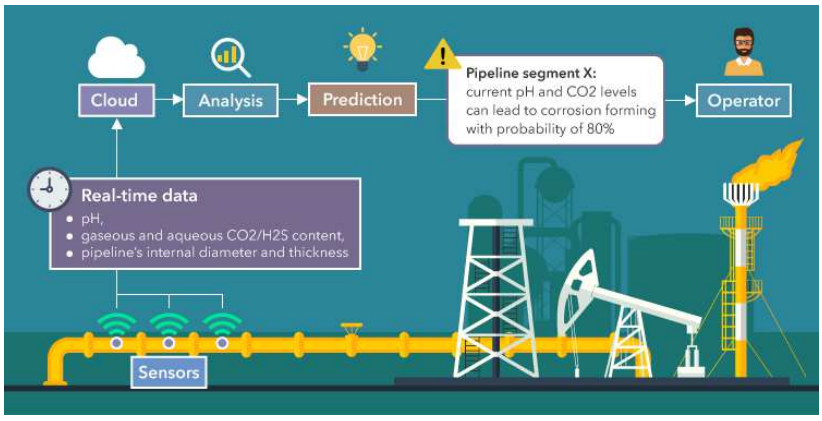

Fig. 1 - IoT for Predictive Maintenance.

REFERENCES

[1] Federico Civerchia, et al., Industrial Internet of Things Monitoring Solution for Advanced Predictive Maintenance Applications, Journal of Industrial Information Integration (2017), doi: 10.1016/j.jii.2017.02.003.

[2] Yahya Mohammed Al-Naggara, et al., 18th CIRP Conference on Modelling of Machining Operations Condition monitoring based on IoT for predictive maintenance of CNC machines, Procedia CIRP 102 (2021), pp.314-318.

[3] Filip Hardt, et al., Innovative Approach to Preventive Maintenance of Production Equipment Based on a Modified TPM Methodology for Industry 4.0, Appl. Sci. 2021, 11, 6953.

[4] Guilherme Luz Tortorella, Flavio S. Fogliatto, Paulo A. Cauchick-Miguel, Sherah Kurnia, Daniel Jurburg Integration of Industry 4.0 technologies into Total Productive Maintenance practices, International Journal of Production Economics 240 (2021).

AUTHOR INDEX

A

Abdallah, Ghiwa B. - 355
Abdelhakim, Ferkous S. - 359
Abreu, Luiz A.S. - 417
Abu Al-Rub, Rashid K. - 293
Agnelo, José S. - 307
Agudo del Río, David - 389
Aguiar, João C. - 295
Ali, Mohd M. - 293
Aliha, Mohammad R.M. - 125, 131
Almeida, Beatriz - 99, 213
Amaladoss, Arun W. - 221
Amaral, Mateus C. - 597
Amaral, Pedro - 147
Ambad, Prashant M. - 613
Andrade, Paula R.L. - 307
António, Carlos C. - 81, 509
Anzabi, Pooria P. - 609
Apuleo, Gianvito - 77
Arce, Isidro - 99
Assih, Jules - 339, 355
Azevedo, Américo L. - 521
Azhari, Fae - 401

B

Bak, Mateusz - 73
Bali, Güntaç - 141
Banat, Fawzi - 293
Bancaleiro, Tiago - 145
Bandeira, Cirlene F. - 25, 27, 53
Banerjee, Jayanta - 429
Baptista, Manuela C. - 35, 37
Baptista, Joao S. - 559
Baptista, António J. - 243, 521
Barbosa, Flávia - 445
Bardenstein, David - 77
Barros, Maria João - 283
Batista, Juliana T. - 55
Bosse, Rubia M. - 351
Botelho, Edson C. - 53
Boukhaoua, Sid Ali - 63
Braga, Maria H. - 29, 33, 35, 37
Brazda, Michal - 61
Brito, José L.V. - 275, 335
Busko, T.O. - 13

C

Cabrera-Moreta, V.H. - 205, 463
Camerini, Cesar G. - 67
Camp, Lucas S.K. - 151
Campos, Tiago M.B. - 391, 393
Cardoso, Otávio N.C.F. - 419, 421
Cardoso, Rodolfo - 597
Carvalheira, Pedro F.V. - 419, 421
Carvalho, Paulo H.S. - 391
Carvalho, David - 35
Casarejos, Enrique - 233
Castello, Daniel A. - 151
Castro, Catarina F. - 591
Cecere, Renzo - 535
Cesnavicius, Ramunas - 187
Chamorro, Richard - 463
Chang, Yoon-Suk - 127
Chang, Wen-Yang - 515
Chaussumier, Michel - 93
Chaves, Carlos M. - 307
Chaves, Luiz A.O. - 597
Chern, Shin Y. - 237
Cherukuri, Harish - 507
Chourasia, Ajay - 611
Chvojan, Jan - 479
Ciminello, Monica - 77
Ciutina, Adrian L. - 331
Coimbra, Luciana B. - 353
Coluccia, Antonio - 113
Concilio, Antonio - 77
Constantinescu, Andreea - 159
Corbani, Silvia - 151
Costa, Jose M. - 37
Costa, Michelle L. - 53
Costa, Yuri D.J. - 373
Costa, Carina M.L. - 373

Costa, Rúben D.F.S. - 581
Costa, Emmanuel A.A.M. - 151
Cruz-Zapata, Luis - 429
Cunha, Sandra - 333

D
Dargel, Alrik - 41
de Almeida, Rafael M. - 407
De Pasquale, Giorgio - 113
Deng, Hanzhong - 91
Deuse, Jochen - 433
Dias, Sérgio - 99
Dinu, Florea - 159, 281
Dmytrenko, O.P. - 13, 97
Dontchev, Dimitar - 339, 355
Doz, Graciela N. - 275
Driscoll, Mark - 575
Dzugan, Jan - 61

E
Eager, David - 387
Esmaeili, Akbar - 427

F
Fallah, Arash Y. - 193
Fang, Zong R.D. - 231
Farajiani, Farhad - 111
Faria, Ricardo - 81
Farias, Camila A. - 67
Fernandes, José R. - 213
Fernandes, Maria C. - 537, 555
Fernandes, Maria G. - 445
Fernández García, Jose R. - 389
Ferreira, Daniel J.O. - 435
Festas, João - 545, 555, 565
Figueira, Joana - 35
Fleming Leitão, Fábio - 375
Fonseca, Elza M.M. - 295
Freitas, Ângela - 35
Friedrich, Christoph - 485
Frigeri, Ary V.N. - 351
Fujita, Katsuhide - 157

G
Gallas-Torreira, Mercedes - 389
Gaponov, A.M. - 13
Garcia-Gil, Pablo - 233
Garofalo, Giovanni - 179
Gerritzen, Johannes - 41
Ghayomian, Rasoul - 125
Ghicioi, Emilian - 281
Ghodrati Amiri, Gholamreza - 277
Głowacka, Karolina - 87
Gomes, Beatriz - 33, 35
Gonçalves, Isabela S. - 391, 393
Gonçalves, Lindomar M. - 435, 39
González Baldonedo, Jacobo - 389
Granja, Juan G.S. - 395
Greis, Noel - 507
Gröger, Benjamin - 41
Gude, Maik - 41
Guedes, Joana - 559
Guedes Sobrinho, Anne B. - 55
Guerreiro, Nuno - 35
Guerrero-Miguel, D.J. - 135
Guo, Jingbo - 11
Gutiérrez-Moizant, R. - 135

H
Han, Mengze - 11
Habbouche, Houssem - 63
Hebda, Aleksander - 95
Held, Tobias - 485
Henschel, Sebastian - 115
Heravi, Farshad N. - 243
Hernández, Juana E.R. - 395
Horng, Jeng-Haur - 237
Hosseini, Ali R.M. - 279
Hosseinzadeh, Javad - 131
Huang, Haiying - 501, 143
Hübner, Sarah - 115

I
Il'in, P.P. - 13, 97
Interlenghi, Stefano F. - 407
Ismaila, 'Olasunkanmi S. - 451
Ivanova, Ivelina - 339, 355
Ivascu, Denis - 159

J
Jacobovitz, Marcos - 391
Jafari, Mohammad Ali - 193
Jain, Kranti - 611
Janiszewski, Jacek - 71

Jesus, Abílio M.P. - 581
Joo, Hwan-Jae - 127
Joshi, Aayush - 611
Jozefy, Roman - 479
Jozi, Aref - 279
Juiña, L.J. - 205

K

Kaarlela, Tero - 507
Kahlouche, Ramdane - 359
Kaito, Kiyoyuki - 305
Kang, Seung-Kyun - 477
Karam-Abian, M. - 235
Karolczuk, Aleksander - 21
Kern, Christian - 433
Khaledi, Yaser - 201
Khaledi, Soroush - 201
Khalvati, Amir H. - 193
Kilikevicius, Sigitas - 187
Kim, Tae-Yeon - 293
Kim, Min-Su - 133
Klemenc, Jernej - 239
Köhler, Daniel - 41
Komorek, Andrzej - 71, 73, 499
Kortschot, Mark - 401
Koukolikova, Martina - 61
Krüger, Lutz - 115
Krzeminski, Tomasz - 483
Kuga, Paulo Y. - 563
Kuhn, Erik - 431
Kulish, M.P. - 13, 97
Kupfer, Robert - 41
Kurek, Marta - 95
Kurochka, L.I. - 97
Kuryliuk, A.M. - 13, 97
Kuryliuk, V.V. - 13, 97
Kuzmych, L.V. - 13, 97
Kuzmych, S.A. - 13, 97

L

Łagoda, Tadeusz - 87, 95
Lamperova, Katarina - 181
Lampreia, Suzana - 145, 147
Landim, Julia C. - 53
Laszlo, Robert - 281
Lavôr, Thiarly F.A. - 335
Learth, João P. - 67
Lebre, Hugo - 35
Lee, Jae-Hwan - 477
Lee, Chan - 405
Leen, S.B. - 235
Leite, António - 99
Lenze, David - 433
Li, Jiasheng - 85
Li, Ying - 61
Liao, Sheng J. - 237
Lima, Vitor G.P. - 391
Lima Jr., Onofre R. - 53
Liñán, Gerardo G. - 395
Liu, Yang - 91
Liu, Wei L. - 237
Liutkauskiene, Kristina - 187
Longère, Patrice - 179
Lopes, João H. - 393
López Campos, Jose A. - 389
López García, Irea - 389
López Garcia, Irea - 233
Lopez Lago, Marcos - 233
Lorenzo, Manuel D. - 337
Lourari, Abdel Wahhab - 63

M

Mabru, Catherine - 93
Machado Pires, Margarida - 283
Madureira, Luísa R. - 215, 577
Mahmoudi, A.H. - 123
Maia, Beatriz A. - 29, 35
Maia, Jeiveison G.S. - 407
Makashev, Kuanysh - 15
Małecka, Joanna - 87, 95
Małys, Sławomir - 95
Marchello, Gabriele - 243
Marczak, Rogério J. - 129
Margaria, Luca - 113
Martinez, Adrian F. - 455
Martínez, Ludy M.V. - 395
Martins, Rodrigo - 35
Marton, Martin - 181
Masiewicz, Joanna - 69, 75
Matos, Romeu - 445
Matsushima, Manabu - 317
McMullan, E.D. - 123
Meguid, Shaker A. - 3
Melo, Francisco Q. - 215

Melzer, Daniel - 61
Mendonça, Carlos A. - 307
Mercurio, Umberto - 77
Meschut, Gerson - 41
Mesquita, Amir Z. - 39, 435
Michel, Hugo C.C. - 435
Miguez Coto, Miguel - 233, 389
Minhoto, Manuel - 351
Miranda, Daniela - 333
Momenian, S. - 131
Mongrain, Rosaire - 535, 575
Montoro, Sérgio R. - 25, 27, 53
Morais, Raul - 213
Morales, Juan C.B. - 395
Morgado, Teresa - 145, 147
Moshatghi, Somayeh - 125
Mota, Izabel O. - 25, 27, 53
Moura, Vanessa N.P. - 195
Mousavi, A. - 131
Moussaoui, Kamel - 179
Murakami, Tomonori - 317

N

Nagode, Marko - 239
Nagpal, Aaryan - 401
Neagu, Calin - 159, 281
Neto, Celio A.C. - 67
Nghiem, Hien - 259, 267
Nobile, Riccardo - 89
Nogueira, Carla C.G. - 25
Novaes, Leandro - 407
Novak, Lovro - 239
Nunes, Danilo S. - 275
Nunes, Daniel L. - 331

O

Okano, Toshihiko - 157
Oladeji, Desmond A. - 451
Oliveira, Miguel - 99, 213
Oliveira, João P.S. - 481
Oliveira, Alexandre M. - 435
Oliveira, F. Bruna - 445
Oliveira, Ivone R. - 391, 393
Oliveira, Alexandre M. - 39
Oliveira, Ana L.A. - 599
Oliveira, Andersson G. - 195
Oliveira, Francisco P. - 545
Oliveira, Hugo L. - 375
Onanko, A.P. - 13, 97
Onanko, Y.A. - 13, 97
Oneea, Andreea - 281
Orlande, Helcio R.B. - 417
Ortega, Fernando. S. - 393
Outeiro, Jose - 505, 507

P

Palmeira, Alexandre A. - 27
Pantoja, João C. - 335, 599
Parandavar, P. - 235
Parente, Marco P.L. - 537
Parghazeh, Amir - 201
Parreira, Renata M. - 25
Parsania, Hossein - 125, 131
Paul, Henryk - 21
Paulo, Vitor - 445
Pavlenko, O.L. - 13
Pawel, Przybylek - 499
Pegado, Helio A. - 169
Peixoto, Arcílio C.F. - 509
Pellone, Lorenzo - 77
Peñaloza Morán, Jessenia G. - 375
Pereira, Diego M.G. - 169
Pereira, Fábio - 99, 213
Pereira, Ana C.C. - 27
Pereira, Ivan - 445
Pereira, Mário - 145, 147
Peth, Jens - 485
Pezeshki, Seyed I. - 559
Phillips, Clara - 401
Pietras, Daniel - 125, 131
Piloto, Paulo A.G. - 337, 351
Pinchuk-Rugal, T.M. - 13, 97
Pinheiro, José M. - 33
Pinto, Jorge - 333
Pinto, Joana V. - 35
Pinto, Igor S. - 597
Pinto, Sónia I.S. - 537, 545, 555, 577, 565, 593
Popov, S.A. - 97
Prażmowski, Mariusz - 21, 87
Prior, Tomás - 35
Przybyłek, Pawel - 69, 73, 75

Q

Qu, Junsheng - 31

Quraishi, Mohammed I. - 613

R

Rafiei, Camellia - 125
Rahnavard, Alireza - 193
Rajabi-Kafshgar, A. - 131
Ramírez-Berasategui, M. - 135
Ramos Gavilán, Ana B. - 337
Raniero, Leandro J. - 393
Razin, Ahmed - 505
Razzaghi, Mehran S. - 279
Rduch, Jacek - 221
Refflinghaus, Robert - 433
Reis, Cristina - 333
Reis, Gabriel R.P. - 129
Reis, Rômulo P.B. - 195
Reis, Anna - 61
Ribeiro, Marcos V. - 505
Rio, David A. - 233
Ritto, Thiago G. - 151
Rivera-Rodríguez, Julián - 429
Rodrigues, João - 333
Rodrigues, Gonçalo - 545
Rodrigues, C. - 555
Rubio, D. - 205
Rugal, A.G. - 13, 97
Ruivo, João N. - 243, 521

S

Sadeghi, Melina - 609
Sadowski, Tomasz - 125, 131
Sakamura, Nanaka - 317
Sánchez-Haro, Javier - 337
Sanin-Villa, Daniel - 455
Santiago, York C. - 407
Santos, Telmo G. - 481
Santos, André M. - 53
Sarasty, Nathaly N. - 599
Sasai, Kotaro - 305
Sasaki, Kensuke - 157
Sasani, Mehrdad - 303
Sathikh, Peer M. - 231
Schlichter, Malte - 41
Sedira, Naim - 333
Segura, Sergio S. - 395
Senila, Mihai - 159, 281
Senra, A.F.A. - 565
Serpa, Alberto L. - 563
Serra, Roger - 149
Serrati, Douglas S.M. - 481
Seruga, Domen - 239
Shangguan, Yiming - 31
Shauer, Nathan - 375
Shibahara, Kosei - 305
Shiravand, Mahmoudreza - 609
Silva, Jairo O. - 27
Silva, Andre L.F. - 307
Silva, Paloma S. - 353
Silva, Jocinaldo A.P. - 191
Silva, Antônio A. - 191
Silva, Márcio D. - 191
Silva, Nelson V.C. - 597
Silva, Antônio A - 195
Silva, Pedro H.S. - 373
Silva, Samuel - 537
Silva, Tiago E.F. - 581
Silva Gomes, J.F. - 461
Simões, José - 145, 147
Siqueira, Gustavo H. - 375
Skarka, Wojciech - 221
Skrobacz, Sebastian - 87
Śliwiński, Daniel - 71
Soares, José A. - 55
Sokol, Milan - 181
Song, Xiu - 91
Sousa, Luisa C. - 537, 545, 555, 565
Sousa, Vítor F.C. - 581
Stankov, Veselin - 339, 355
Sturm, Ralf - 155
Suárez García, Sofía - 389
Surand, Martin - 93
Suzuki, Takuma - 157
Swiderski, Waldemar - 483
Szczepaniak, Robert - 69, 73, 75, 499

T

Tabatabai, Habib - 111
Tammela, Iara - 597
Tejada, Juan C. - 455
Thermou, Georgia - 15
Tissot, Maxime - 93
Tong, M. - 235
Topkaya, Tolga - 141
Tria, Djalel Eddine - 63
Triantafyllou, Savvas - 15

U
Uçak, Necati - 505, 507

V
Vahidi, Mohammad - 277
Vale, Antonio B. - 37
Valiollahi, Arash - 143
Valtchanov, Hristo - 535
Varum, Humberto S.A. - 5
Vasconcellos, Luana M.R. - 391, 393
Velhinho, Alexandre - 145
Venglar, Michal - 181
Vieira, Manuel F. - 37
Villalba, A. - 205
Villoslada, Gabriela - 335

W
Wang, Lei - 91
Wang, Songwei - 501
Wang, Wenjing - 31
Wang, Xiangjie - 23
Wang, Yuzhu - 149

X
Xavier de Oliveira, Ingrid - 375
Xie, Liyang - 101

Y
Yan, Ruiguo - 31
Yang, Heejun - 127
Yeh, Jim C. - 237
Yehorov, S.V. - 97
Yoshida, Hidenori - 317
Yu, Minju - 133

Z
Zahorski, Tomasz - 69, 499
Zatar, Wael - 259, 267
Zdrenghea, Paul - 159, 281
Zeng, Xiangli - 31
Zhang, Xiong - 85
Zhang, Yongyi - 423
Zornberg, Jorge G. - 373
Zugasti, Pedro J.C. - 395
Zvacek, Susan M. - 577

About the Book:

This book contains all extended abstracts or full papers accepted for presentation in the *IRF2025 - 8th International Conference on Integrity-Reliability-Failure,* held in Porto/Portugal, 15-18 July 2025.

IRF2025 is the eighth international gathering of a prestigious series of Integrity-Reliability-Failure conferences coordinated by the International Scientific Committee on Mechanics and Materials in Design. This series of conferences started in 1999 and they are wholly devoted to advances in assessing the integrity, reliability and failure of engineering systems, materials, manufacturing and biomechanics.

The organisation of IRF2025 was jointly sponsored by the University of Porto, the University of Toronto and the Portuguese Society of Experimental Mechanics. The conference attracted over 160 contributions, with 148 accepted submissions involving 454 authors from 27 different countries.

The conference themes, which address novel and advanced topics on Integrity, Reliability and Failure, focused on Theory, Experiments and Applications in Engineering, including Composite and Advanced Materials, Fatigue and Fracture Mechanics, Structural Dynamics, Mechanical Design and Prototyping, Civil Engineering Applications,, Biomechanical Applications, Energy and Thermo-Fluid Systems, and Industrial Engineering, among other topics.

ISBN: 978-972-752-323-8
DOI: https://doi.org/10.24840/978-972-752-323-8